Lecture Notes in Civil Engineering

K. K. Pathak
J. M. S. J. Bandara
Ramakant Agrawal *Editors*

Recent Trends in Civil Engineering

Select Proceedings of ICRTICE 2019

Springer

Lecture Notes in Civil Engineering

Volume 77

Series Editors

Marco di Prisco, Politecnico di Milano, Milano, Italy

Sheng-Hong Chen, School of Water Resources and Hydropower Engineering, Wuhan University, Wuhan, China

Ioannis Vayas, Institute of Steel Structures, National Technical University of Athens, Athens, Greece

Sanjay Kumar Shukla, School of Engineering, Edith Cowan University, Joondalup, WA, Australia

Anuj Sharma, Iowa State University, Ames, IA, USA

Nagesh Kumar, Department of Civil Engineering, Indian Institute of Science Bangalore, Bengaluru, Karnataka, India

Chien Ming Wang, School of Civil Engineering, The University of Queensland, Brisbane, QLD, Australia

www.EngineeringBooksPDF.com

Lecture Notes in Civil Engineering (LNCE) publishes the latest developments in Civil Engineering - quickly, informally and in top quality. Though original research reported in proceedings and post-proceedings represents the core of LNCE, edited volumes of exceptionally high quality and interest may also be considered for publication. Volumes published in LNCE embrace all aspects and subfields of, as well as new challenges in, Civil Engineering. Topics in the series include:

- Construction and Structural Mechanics
- Building Materials
- Concrete, Steel and Timber Structures
- Geotechnical Engineering
- Earthquake Engineering
- Coastal Engineering
- Ocean and Offshore Engineering; Ships and Floating Structures
- Hydraulics, Hydrology and Water Resources Engineering
- Environmental Engineering and Sustainability
- Structural Health and Monitoring
- Surveying and Geographical Information Systems
- Indoor Environments
- Transportation and Traffic
- Risk Analysis
- Safety and Security

To submit a proposal or request further information, please contact the appropriate Springer Editor:

– Mr. Pierpaolo Riva at pierpaolo.riva@springer.com (Europe and Americas);
– Ms. Swati Meherishi at swati.meherishi@springer.com (Asia - except China, and Australia, New Zealand);
– Dr. Mengchu Huang at mengchu.huang@springer.com (China).

All books in the series now indexed by Scopus and EI Compendex database!

More information about this series at http://www.springer.com/series/15087

www.EngineeringBooksPDF.com

K. K. Pathak · J. M. S. J. Bandara ·
Ramakant Agrawal
Editors

Recent Trends in Civil Engineering

Select Proceedings of ICRTICE 2019

Springer

www.EngineeringBooksPDF.com

Editors
K. K. Pathak
Indian Institute of Technology (BHU)
Varanasi, India

J. M. S. J. Bandara
University of Moratuwa
Colombo, Sri Lanka

Ramakant Agrawal
Medi-Caps University
Indore, India

ISSN 2366-2557 ISSN 2366-2565 (electronic)
Lecture Notes in Civil Engineering
ISBN 978-981-15-5194-9 ISBN 978-981-15-5195-6 (eBook)
https://doi.org/10.1007/978-981-15-5195-6

© Springer Nature Singapore Pte Ltd. 2021
This work is subject to copyright. All rights are reserved by the Publisher, whether the whole or part of the material is concerned, specifically the rights of translation, reprinting, reuse of illustrations, recitation, broadcasting, reproduction on microfilms or in any other physical way, and transmission or information storage and retrieval, electronic adaptation, computer software, or by similar or dissimilar methodology now known or hereafter developed.
The use of general descriptive names, registered names, trademarks, service marks, etc. in this publication does not imply, even in the absence of a specific statement, that such names are exempt from the relevant protective laws and regulations and therefore free for general use.
The publisher, the authors and the editors are safe to assume that the advice and information in this book are believed to be true and accurate at the date of publication. Neither the publisher nor the authors or the editors give a warranty, expressed or implied, with respect to the material contained herein or for any errors or omissions that may have been made. The publisher remains neutral with regard to jurisdictional claims in published maps and institutional affiliations.

This Springer imprint is published by the registered company Springer Nature Singapore Pte Ltd.
The registered company address is: 152 Beach Road, #21-01/04 Gateway East, Singapore 189721, Singapore

www.EngineeringBooksPDF.com

Organising Committee

Chief Patron

Shri R. C. Mittal, Chancellor, Medi-Caps University, Indore

Patrons

Shri Gopal Agrawal, Pro-Chancellor, Medi-Caps University, Indore
Prof. Dr. Sunil K. Somani, Vice-Chancellor, Medi-Caps University, Indore

General Chair

Dr. D. K. Panda, Dean (Engineering)

Organizing Committee Chair

Dr. Ramakant Agrawal, Head (Civil)

Program Chairs/Volume Editors

Dr. K. K. Pathak, IIT(BHU) Varanasi
Dr. J. M. S. J. Bandara, University of Moratuwa, Colombo, Srilanka
Dr. Ramakant Agrawal, Medi-Caps University, Indore

www.EngineeringBooksPDF.com

Program Committee

Dr. Akil Ahmed, IIT, New Delhi
Dr. B. B. Das, NITK, Suratkal
Dr. Deepak Khare, IIT, Roorkee
DR. Goutam Das Gupta, Columbia University, New York
Dr. M. S. Hora, MANIT, Bhopal
Dr. Prachand Man Pradhan, Kathmandu University, Nepal
Dr. Reshma Rughooputh, University of Mauritius, Mauritius
Dr. R. K. Shrivastava, SGSITS, Indore
Dr. Sandeep Chaudhary, IIT, Indore
Dr. Sanjeev Chaudhary, IIT, Bombay
Dr. Sanjeev Saxena, CSIR-AMPRI, Bhopal
Dr. Vinod Tare, IIT, Kanpur
Dr. Vivek B., BITS Pilani, Dubai

Publicity Chairs

Mr. Alok Rarotiya
Mr. Shashank Agrawal
Mr. Vinay Joshi

Publication Chairs

Dr. Ramakant Agrawal
Mr. Chaitanya Mishra
Ms. Megharima Dutta
Ms. Nikita Thora

Registration Chairs

Mr. Ashwin Parihar
Mr. Raj Joshi
Ms. Monika Pagare

www.EngineeringBooksPDF.com

Session Management Chairs

Dr. Rajeev Kumar
Dr. S. M. Narulkar
Mr. A. K. Deora
Mr. Ajit Kumar Jain
Mr. Ruchir Lashkari

Local Arrangement Chairs

Mr. Deepak Patel
Mr. Deepak Jain
Mr. Ubaid Hanfee

Members

Mr. Bhupendra Sirbiya
Mr. Anurag Tripathi
Mr. Ashwin Sharma
Mr. Abhishek Agrawal
Ms. Shweta Mandloi
Mr. Yash Mothe
Mr. Ankit Soni
Mr. Ajay Sinha

www.EngineeringBooksPDF.com

Preface

This Lecture Notes in Civil Engineering volume contains documented versions of the papers accepted at the International Conference on Recent Trends and Innovations in Civil Engineering, 2019 (ICRTICE-2019). The conference was held during September 26–28, 2019 at Medi-Caps University, Indore (Madhya Pradesh), India.

This conference was a platform for academicians, researchers, and industry delegates to present their research and contributions. The conference highlighted emerging research on different disciplines of Civil Engineering. The objective of this International Conference was to provide opportunities for the participants to interact and exchange ideas, experience, and expertise in the recent technological trends. Along with sharing, an array of lectures from eminent personalities in this field was delivered to bring value to the conference.

The inauguration was held in the presence of Mr. Philip Mathew (ACC Limited) and Dr. S. Bandara (University of Moratuwa, Colombo) on September 26 with their enlightening talks. The keynote talks were delivered by Dr. K. K. Pathak (IIT (BHU) Varanasi) and Dr. Manish Mudgal (AMPRI-CSIR, Bhopal). The conference had been a good opportunity for participants from across the country. The sessions were a perfect learning place with speakers from diverse expertise.

The sessions were mentored by academic leaders from IITs, Industries, and other Institutes like Dr. Dilip Wagela, Dr. H. K. Mahiyar, Dr. R. K. Shrivastava, Dr. Sandeep Choudhary, Dr. Saiket Sarkar, Dr. Vijay Rode, and Dr. S. M. Narulkar. The areas covered in the sessions included Structural Engineering, Transportation Engineering, Geotechnical engineering, Concrete Technology, Water Resources Engineering, Environmental Engineering, Construction Technology and Management, and recent technical topics that align with the theme of the conference. There were 82 papers in 7 sessions that filled the gaps in the recent researches and suggested new measures and tools for improvising the existing state of research and applications of the new techniques and innovations.

A committee of external and internal reviewers was formed for a rigorous peer review of submitted papers which were 184 in number. For maintaining the quality of the conference, the committee took full efforts and helped to shortlist 82 papers

www.EngineeringBooksPDF.com

for the presentation. We are thankful to all the reviewers. Our acknowledgements are due also to Prof. Aakash Chokrovorty and Mr. Maniarasan Gandhi who were a constant support for communications with the Springer publications.

Finally, we take the privilege to thank all sponsors, committee members, volunteers, participants, press, print, and electronic media for the success of the conference.

Varanasi, India — K. K. Pathak
Colombo, Sri Lanka — J. M. S. J. Bandara
Indore, India — Ramakant Agrawal

www.EngineeringBooksPDF.com

Contents

Structural Engineering

Wind Analysis of High-Rise Building Using Computational Fluid Dynamics 3
Prafulla Kishor Sharma and Suresh R. Parekar

Structural Performance of Modular Buildings: A Review 19
Ashok Jammi and Arul Jayachandran Sanjeevi

Application of Artificial Neural Network (ANN) in the Prediction of Displacement of RC Frame Subjected to Earthquake 43
R. Prabhakara, Pallavi Patil, Narayana Harish, and H. N. Jagannatha Reddy

Fatigue Crack Growth Analysis Using Surrogate Modelling Techniques for Structural Problems 55
Geetu G. Kumar, T. Sivaranjani, D. V. T. G. Pavan Kumar, and C. L. Mahesh Kumar

Dynamic Response of RC Slab Under Drop Test Retrofitted with CFRP Strips Using NSM Technique 67
Nandeesh M. Sreenivasappa, Arjun R. P. Reddy, H. N. Jagannatha Reddy, and R. Prabhakara

Experimental Studies to Demonstrate the Effect of Clamping Reinforcement on Shear Strength of GPC Adopting Push-Off Specimens 83
N. R. Harish Kumar, Sachin R. Biradar, R. Prabhakara, and H. Jagannatha Reddy

Evaluation of Flexural Behaviour of Post-tensioned RC Beams Strengthened Using CFRP Laminates with NSM Technique 95
Vathsala, H. N. Jagannatha Reddy, and R. Prabhakara

www.EngineeringBooksPDF.com

Analysis of Isotropic and Orthotropic Sandwich Bridge Decks 109
Preeti Agarwal, P. Pal, and P. K. Mehta

The Effect of Angle of Web Opening for Prediction of Ultimate Failure Load of Castellated Beams by Experimental Investigation 121
Amol J. Mehetre and Rajashekhar S. Talikoti

Free Vibration Frequencies of Lock Gate Structure 135
Deepak Kumar Singh, Priyaranjan Pal, and Shashi Kant Duggal

Introspecting System Identification in Numerical Technique for Inverse Identification Process 149
Shalem Ernest and U. K. Dewangan

Effect of Steel Ratio on Dynamic Response of HSC Two Way Slab Strengthened by Entrenched CFRP Strips Using Drop Test 157
Arjun R. P. Reddy, Nandeesh M. Sreenivasappa, R. Prabhakara, and H. N. Jagannatha Reddy

Damage Detection Techniques to Identify the Unknown Damage Parameters from the Structural Response Data in Beam: A Review 175
Bhawna Patel and U. K. Dewangan

Studies on Rotation Capacity and Torsional Strength of Normal, Medium- and High-Strength RC Beams 185
M. R. Prakash, Katta Venkataramana, R. Prabhakara, and B. Manjunatha

Manufacturing of an Economical Single Degree-of-Freedom Shake Table 197
Ketan N. Bajad and Manisha V. Waghmare

Behaviour of Different Lateral Stability Structural Systems for the Tall Steel Structures Under Wind Loads 211
Abhimanyu Pandey and R. K. Tripathi

To Compare ATC 40 and FEMA 440 Methods for Computation of Performance Point 223
Ankit Sandilya and Rajesh Kumar Tripathi

Non-linear Dynamic Analysis of a Multi-storey Building Subjected to Earthquakes 231
Arjit Verma, P. Pal, and Y. K. Gupta

Finite Element Modeling of Precast Diaphragms Concrete and Their Connections 243
Raj Joshi, Astha Jhawar, Megharima Datta, Ashwin Parihar, and Ubaid L. Hanfee

www.EngineeringBooksPDF.com

T-Beam Bridge Girder Analysis Using Finite Element Modeling for IRC Loading 255
Dhaker Rahul and U. K. Dewangan

Flexural Strengthening of Steel Structures with Fiber-Reinforced Polymers and Analysis Using ANSYS 271
Prabhudeva Gunthati and Mohit Jaiswal

Study on Sensitivity of PZT Signatures for Damage Detection in RC Columns—A Numerical Study 283
Venkat Shivaram Yedlapati and Mallika Alapati

Experimental Studies on Flexural Behaviour of RC Beams Strengthened with High Performance Concrete Layer 291
Aravindkumar Harwalkar and Ashwini S. Ingale

Health Monitoring of Civil Structures by Pulse Compression-Based Digital Frequency Modulated Thermography 307
J. A. Siddiqui and Sachin Patil

Transportation Engineering

Application of Remotely Piloted Unmanned Aerial Vehicle in Construction Management 319
Tirth Patel, Vishal Suthar, and Naimish Bhatt

Spatial Pavement Information System for Transportation Networks Based on Distress Features in Nagpur City Using RS and GIS 331
Y. B. Katpatal, Kaddak Harashal, and M. S. Mukesh

Evaluation of Strength Development of Untreated and Treated Red Mud with Gypsum as a Road Construction Material 343
K. Sarath Chandra and S. Krishnaiah

Strength Characteristics of Cement-Stabilized Recycled Asphaltic Pavement (RAP) for Pavement Applications 351
V. K. Vidyashree, K. H. Mamatha, and S. V. Dinesh

Feasibility of Recycled Tyre as Reinforcing Material for Pavements 363
B. N. Vinod Raj, K. H. Mamatha, and S. V. Dinesh

Partial Replacement of Moorum with Fly Ash in Embankment 381
Sagar D. Turkane and Sandeep K. Chouksey

Scour Around Bridge Abutments in Clay Bed 393
Anoop Kumar, B. N. Advith Ganesh, Shubham Vats, P. Sumanth, T. Gangadharaiah, and K. H. Mamatha

www.EngineeringBooksPDF.com

Analysis of Pedestrian Crossing Behavior at Uncontrolled Intersections 405
S. P. Niveditha and K. M. Mallesha

Utilization of RAP in Flexible Pavements 419
Bhavana Suresh, K. H. Mamatha, and S. V. Dinesh

Influence of Long-Term Laboratory Aging on Properties of Binder 431
S. Tejeshwini, B. Gowtham, K. H. Mamatha, S. V. Dinesh, and Anand Tadas

Pavement Evaluation Using Falling Weight Deflectometer (FWD) 445
D. Nayana, K. H. Mamatha, S. V. Dinesh, and T. R. Lokesh

Geotechnical Engineering

Design of Blanket by Adding Different Percentages of Soil 459
Hardev Singh

Challenges in Design and Construction of Pile Foundation in Non-liquefiable and Liquefiable Soil 467
M. K. Pradhan, G. R. Reddy, and K. Srinivas

Improvement of Clayey Subgrade by Using Ferro-Sand 485
Ambika Priyadarshini Mishra, Rupashree Ragini Sahoo, and Pradip Kumar Pradhan

Soil Subgrade Stabilization Using Non-woven Polypropylene Geotextile 501
Ayush Mittal and Shalinee Shukla

Assessment of Scaling Effects on Plugging of Driven Piles Using Image Analysis 513
G. Sreelakshmi, M. N. Asha, and S. Nandish

Performance Evaluation of Bio-Stabilized Soils in Pavements 523
V. Divya and M. N. Asha

Effect of Granular Pile Stiffness on Load Distribution for Piled Raft 531
Jitendra Kumar Sharma and Raksha Rani Sanadhya

Performance Evaluation of Expansive Soil Using Animal Bone Ash 547
Jitendra Kumar Sharma and Abdul Shahid Qureshi

www.EngineeringBooksPDF.com

Concrete Technology

High Performance Concrete Mixed with Combinations of Mineral Admixtures 563
Bhargav Reddy Isanaka, M. Abdul Akbar, P. Perumal, and R. Sai Priyanka

Effect of Fly Ash as Replacement of Fine Aggregate on Strength Enhancement of Concrete 573
K. C. Panda, S. S. Samantaray, and S. Jena

Bacterial Concrete for the Development of Sustainable Construction—A Review 587
S. Jena, B. Basa, and K. C. Panda

Effect of Aggregate Ratio Using Non-pozzolanic Mineral Filler Waste on the Property of Self Compacted Concrete 601
V. C. Panchal and G. R. Vesmawala

Strength and Drying Shrinkage of High Strength Self-Consolidating Concrete 615
V. A. Shruthi, Ranjitha B. Tangadagi, K. G. Shwetha, R. Nagendra, C. Ranganath, Bharathi Ganesh, and C. L. Mahesh Kumar

Creep Characteristics of High Strength Self Compacting Concrete 625
Ranjitha B. Tangadagi, V. A. Shruthi, Bharathi Ganesh, M. V. Vasudev, R. Nagendra, and C. Ranganath

Effects of Cigarette Butts in Fly Ash Cement Bricks 637
Chaitanya Mishra, Aayush Verma, Aditya Ratra, Ankit Jain, Anuj Agrawal, Anuj Dodeja, and Anuj Dubey

Influence of Copper Slag Properties on Behaviour of Cement Mortars and Concrete 649
D. Arpitha and C. Rajasekaran

Monitoring Methods of Concrete from Early Age Strength Gain of Concrete: A Review 659
Tripti Sonker, Anupam Rawat, and Rakesh Kumar

An Experimental Study on Strength Development in Concrete by Incorporating Rice Husk Ash as Replacement to Cement with Recycled Aggregate for Low Volume Roads 679
D. Sai Bharadwaj and Adepu Ramesh

Influence of Partial Replacement of Cement by Industrial Wastes on Properties of Concrete 693
Nikhil Kumar Verma

www.EngineeringBooksPDF.com

Water Resource Engineering

Bathymetric Mapping for Shallow Water Using Landsat 8 via Artificial Neural Network Technique 717
Arun Patel, S. K. Katiyar, and Vishnu Prasad

Land Suitability Assessment for Agriculture Using Analytical Hierarchy Process and Weighted Overlay Analysis in ArcGIS ModelBuilder 735
Ayush Tiwari and Sunil Ajmera

Dynamic Analysis of Tunnels in Western Ghats of Indian Peninsula: Effect of Shape and Weathering 763
Mohammad Zaid and M. Rehan Sadique

Trend Analysis and Rainfall Variability of Monthly Rainfall in Sheonath River Basin, Chhattisgarh 777
Shashikant Verma, A. D. Prasad, and Mani Kant Verma

Performance Evaluation of Pench Command Area of Maharashtra, India Using Spatial Approach 791
Digambar S. Londhe, Y. B. Katpatal, and Garima Newar

Regional Frequency Analysis Using L-Moment Methodology—A Review 811
Ramgopal T. Sahu, Mani Kant Verma, and Ishtiyaq Ahmad

Fluctuation of Pressure Due to Bends in Venturimeter 833
S. Masalvad Shravankumar, Rallapalli Alice Grace, Kaveti S. Venkatesh, Ruthika Gujjula, and Anjali Gujjari

UV/Fe^{+3} Photolysis Process Optimization Using Response Surface Methodology for Decolorization of Reactive Red 120 Dye Simulated Wastewater 847
Bhatt Dhruv and Makwana Abhipsa

Relative Wave Run-Up Parameter Prediction of Emerged Semicircular Breakwater 867
Suman Kundapura, Subba Rao, and Vittal Hegde Arkal

Study of Pavement Unevenness Using Sensor-Based Smartphone Software 879
Mandeep Kaur Arora, Mahesh Ram Patel, and Abhyuday Titiksh

Detection of Flood Hazard Using QGIS 899
Shivani Soni and A. D. Prasad

Comprehensive Study on Foamed Bitumen 907
Shweta Mandloi, Sarvesh Kumrawat, and Vinay Deulkar

www.EngineeringBooksPDF.com

Water Lettuce for the Improvement of River Water Quality in Pune Metropolitan Area 919
Jayeshkumar Maheshkumar Bhagwat, Veruval Devadas, and Bharati V. Mahajan

Non-parametric Trend of Drought and Its Future Applicability: A Case Study of Sagar Station 939
A. Vishwakarma, M. K. Choudhary, and M. S. Chauhan

Effect of Dam Reservoir Interaction on Response of Dam Subjected to Dynamic Load 945
Pooja D. Girme and Manisha V. Waghmare

A Small-Scale Study for the Treatment of Grey Wastewater Through Free Surface Constructed Wetlands Using Water Hyacinth Plant 963
Anudeep Nema, Dhaneesh K. H, Kunwar D. Yadav, and Robin A. Christian

Real-Time Flood Analysis Using Artificial Neural Network 973
Vijendra Kumar and S. M. Yadav

Development of Synthetic UH by Using Geomorphologic Instantaneous Unit Hydrograph (GIUH) Based Nash Model 987
A. Agrawal and R. K. Shrivastava

Environmental Engineering

The Selection of Wastewater Treatment Units Based on Analytical Hierarchical Process 1003
Atul Sharma and Nekram Rawal

Bibliometric Analysis of Constructed Wetlands in Wastewater Treatment 1021
Nandini Moondra, Robin A. Christian, and Namrata D. Jariwala

Assessment of Carbon Foot Print: A Case Study of SVNIT Campus 1029
Bibin K. Suresh, Nandini Moondra, and Bhaven N. Tandel

Removal Efficiency of Heavy Metals by Washing the Contaminated Soil Using Effective Leaching Agents 1041
J. Sumalatha, R. Prabhakara, and P. V. Sivapullaiah

Pre-monsoon Analysis of Vehicular Pollution on Highly Traffic Loaded Squares of Indore City 1053
Ruchir Lashkari and Ramakant Agrawal

Stress–Strain Behavior of Municipal Solid Waste in Undrained Loading Condition 1063
Sandeep Kumar Chouksey

www.EngineeringBooksPDF.com

Settlement Behavior of Municipal Solid Waste Using Constitutive Modeling Approach 1069
Sandeep Kumar Chouksey

Performance Comparison of Microbial Fuel Cell: A Case Study with Different Effluents 1075
Prateek Jyotishi and Dal Chand Rahi

Microbial Fuel Cell: An Application for Dairy Wastewater Treatment and Electricity Generation 1083
Prateek Jyotishi and Dal Chand Rahi

Construction Technology and Management

Analyzing Labor Productivity for Reinforcement Installation Using Artificial Neural Network in India 1093
Jignesh M. Mistry and Geetha K. Jayaraj

www.EngineeringBooksPDF.com

About the Editors

Dr. K. K. Pathak is Professor in the Department of Civil Engineering IIT (BHU) Varanasi since April 2016. Before that he was a professor in the Department of Civil & Environmental Engineering, NITTTR Bhopal. He has also served as Scientist in CSIR from 1996 to 2011. Dr. Pathak received his B.Tech and M.Tech from KNIT Sultanpur and MNNIT Allahabad, in 1991 and 1993, respectively. He obtained his Ph.D from IIT Delhi in the area of computational solid mechanics in 2001. He has published more than 300 papers in journals and conference proceedings. He is a Fellow of Institution of Engineers (India). He is a recipient of the prestigious George Oomen Memorial Prize, The Metallurgical and Materials Engineering Division Prize and E. P. Nicoles Prize by the Institution of Engineers (India) in 2004, 2009 and 2011, respectively. He was the editor of Journal of Modelling and Simulation in Design and Manufacturing and Journal of Engineering, Science & Management Education. Dr. Pathak has delivered many invited talks in Conferences and STTP programs. His research interests include structural analysis and design, structural shape optimization, computer simulation of manufacturing processes, material characterization using miniature testing methods, finite element analysis, artificial intelligence and software development.

Dr. J. M. S. J. Bandara is a Senior Professor in Civil Engineering, University of Moratuwa. He graduated from the University of Moratuwa as a Civil Engineer and obtained his Ph.D. in Transportation Engineering with specialization in Airport Planning from The University of Calgary, Canada. He has over 35 years of experience in teaching and research. Currently, he is serving as the Head, Department of Civil Engineering, University of Moratuwa and Director of Intelligent Transport Systems Research Center. Dr. Bandara is a Chartered Engineer and a Fellow of Chartered Institute of Logistic & Transport, Sri Lanka. He is also the current President of Sri Lanka Evaluation Association and President of Highway Engineering Society, Sri Lanka. Dr. Bandara has served in a number of national level committees in the areas of public transport, traffic planning, airport development, road safety, highway engineering, monitoring & evaluation, and environmental assessment. He is a member of the editorial advisory board of the

www.EngineeringBooksPDF.com

Journal of Advanced Transportation. There are over 200 national and international research publications in the above areas and joint patent for UniRoad Traffic Signal System to his credit.

Dr. Ramakant Agrawal is Professor and Head in the Department of Civil Engineering, Medi-Caps University Indore. He received his B.E. and M. Tech. from Maulana Azad College of Technology (REC), Bhopal, and obtained his Ph.D in structural engineering from Maulana Azad National Institute of Technology, Bhopal. He has more than 21 years of teaching experience. His research interests include soil-structure interaction, high-performance concrete and structural health monitoring. He has published 15 research papers in reputed journals. He is Life Member of Indian Society of Technical Education.

www.EngineeringBooksPDF.com

Structural Engineering

www.EngineeringBooksPDF.com

Wind Analysis of High-Rise Building Using Computational Fluid Dynamics

Prafulla Kishor Sharma and Suresh R. Parekar

Abstract In the analysis of high-rise structure wind pressure is a more effective lateral load than seismic force for larger time period. Therefore, buildings over 60 m height are generally analyzed for wind loads. In wind analysis building behaves as a cantilever structure. In this study, experimental work was carried out using wind tunnel setup for three models (circular, hexagonal, and octagonal). Drag coefficients were noted down from the experiments for different plan of structure. Same models were prepared and analyzed in ANSYS 16.0 with full scales. The results obtained from tests are compared with the values of CFD and with the values available in IS 875(Part-3)2015.

Keywords Wind pressure · CFD analysis · Wind tunnel · ANSYS 16.0 · Drag coefficient

1 Introduction

Mainly three factors—strength, stability, and rigidity—are considered for the design of structure. Strength is the main factor in design of low-height structures. However, as the height of the structure increases, rigidity and stability requirements become predominating. Nowadays, engineering techniques are used to increase the stiffness of the elements rather than depending upon the dead weight for stabilization. Wind tunnel is used for the experimental work on the models of different shapes, height, and plan of the structures. For the preparation of models, geometric similarity is used, and for velocity application kinematic similarity is used. Thus, three models are prepared using the geometrical similarities for the test. Then tests are conducted on the models and observations are recorded. In wind tunnel, drag is observed by sensor and the value of drag coefficient is displayed on the panel.

P. K. Sharma (✉) · S. R. Parekar
Department of Civil Engineering, AISSMS COE, Pune 411001, India
e-mail: prafullasharma26@gmail.com

S. R. Parekar
e-mail: srparekar@gmail.com

© Springer Nature Singapore Pte Ltd. 2021

K. K. Pathak et al. (eds.), *Recent Trends in Civil Engineering*, Lecture Notes in Civil Engineering 77, https://doi.org/10.1007/978-981-15-5195-6_1

www.EngineeringBooksPDF.com

1.1 Drag

The flow of wind is considered in two dimensions, that is, along the flow and transverse to the flow of wind. The term along the flow of wind is known as drag and in the transverse direction is known as lift. The fluid force exerted on the moving body is generally inclined to the direction of motion. There are two components of force: one is in the direction of motion called as drag (F_D) and another perpendicular to the direction of motion called as lift (F_L). In symmetrical bodies such as cylinder, sphere, and so on, the total force is drag force and the lift is zero. Drag is classified into three types. First is frictional drag which is caused due to shear stress; second is pressure drag which is caused due to separation of flow; and third is deformation drag due to deformation of fluid particles. Deformation of particles occurs when viscous force is predominant than inertia force (Fig. 1).

Drag force is the sum of frictional drag and pressure drag

$$F_D = F_{Df} + F_{Dp} \tag{1}$$

where

F_{Df} = frictional drag and F_{Dp} = pressure drag.

The mathematical expression for drag coefficient is given as

$$F_D = C_D A \frac{\rho v 2}{2} \tag{2}$$

where

F_D = drag force (N), C_D = drag coefficient, V = flow velocity (m/s).

ρ = density of air as a fluid (1.2 kg/m^3 for air at NTP).

A = particular frontal area of the body (m^2).

In Eq. (2), $\frac{\rho v 2}{2}$ is known as dynamic pressure of flowing fluid.

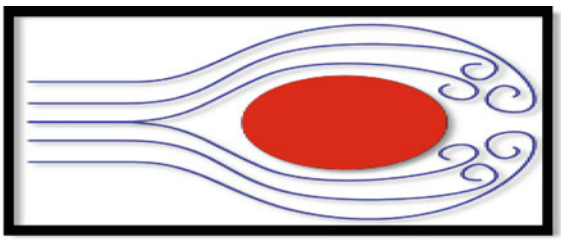

Fig. 1 Drag coefficient

www.EngineeringBooksPDF.com

2 Literature Review

Anoop et al. [1] investigated the scope and limitation of suitable code of practice for wind loads from IS 875-Part III(1987) in predicting the wind-induced overall structural loads with the help of wind tunnel test results from selected Indian projects. Since the design codes for wind-load-based design of buildings were framed on the basis of research work conducted on a range of conventional building shapes, several decades ago it is important to check the given standards with the current building design and standard.

Irwin [2] studied the challenges that are faced in modern high-rise buildings and the basic concepts of wind engineering, like wind statistics and wind profiles. Extreme wind speeds statistics and its importance are discussed. Further optimization of shape stiffness, effect of mass and damping and some concepts of wind tunnel testing are discussed.

Kwon and Kareem [3] stress the need to understand better the underlying commonalities and differences among the major international wind loading codes/standards, which are also constantly being revised and updated. A comprehensive comparison of wind loads and their effects on tall buildings is conducted utilizing major international codes/standards: ASCE 2010 (USA), CNS 2012 (China), NBCC 2010 (Canada), ISO 2009, and IWC 2012 (India).

Sevalia and Vasanwala [4] discussed about the potential of CFD to supersede traditional wind tunnel studies as a more cost-effective and time-saving design tool. Further, a comprehensive study of wind effects on the circular and square plan shaped tall buildings of same area. It was stated that the architect and civil engineer jointly modify the shape of building so that the tall buildings perform better during strong gust of wind.

Daemei and Bahrami [5] studied wind aerodynamics and flow characteristics of triangular-shaped tall building and CFD simulation in order to assess drag coefficient. The simulations were conducted on seven models with height 120 m (40 stories) in two phases. In the first phase, drag coefficient is assessed on tall buildings with triangular section and drag is calculated for the same building by providing chamfer, rounded-edge and recessed. Building scaled is the ratio of width to one-sixth of height of the building. In the next phase, the aerodynamic forms of setback, taper, helical were employed on basic model to figure out which one has best performance. From the above two phases, compare the results of with and without aerodynamics effect.

www.EngineeringBooksPDF.com

3 Methodology of Computational Fluid Dynamics

3.1 Dimensional Analysis of Drag

The functional relation of drag is given as

$$F_D = f_1(L,\ \rho,\ \mu,\ v,\ K,\ g,\ \eta) \tag{3}$$

$$F_D = f_2\left(\mu, \frac{\rho VL}{\mu}, \frac{V}{\sqrt{K}\Big/\rho}, \frac{V}{\sqrt{gL}}\right) \tag{4}$$

In Eq. (4), $\frac{\rho VL}{\mu}$ is known as Reynolds number (Re); $\frac{V}{\sqrt{K}\Big/\rho}$ is known as Mach number (Ma), and $\frac{V}{\sqrt{gL}}$ is known as Froude number (Fr).

$$C_D = f_3\left(\eta, \frac{\rho VL}{\mu}, \frac{V}{\sqrt{K}\Big/\rho}, \frac{V}{\sqrt{gL}}\right) \tag{5}$$

$$C_D = f_4(\eta,\ Re) \tag{6}$$

where

L = characteristic length, V = moving velocity, ρ = mass density of air as a fluid.

μ = viscosity, K = modulus of elasticity, F_D = drag.

When the free surface of the object is partly immersed, Froude number is predominant, whereas if fully immersed Reynolds or Mach number is predominant.

When the fluid is considered incompressible, Reynolds number (Re) is predominant.

When compressibility effect of fluid considers Mach (Ma) is predominant.

The value of different shape drag obtained by IS 875(Part-3) 2015 is mentioned in the table −25, clause 7.4.2.2.

3.2 Analysis by Using ANSYS 16.0

Step-by-step procedure is followed:

www.EngineeringBooksPDF.com

Fig. 2 Domain size

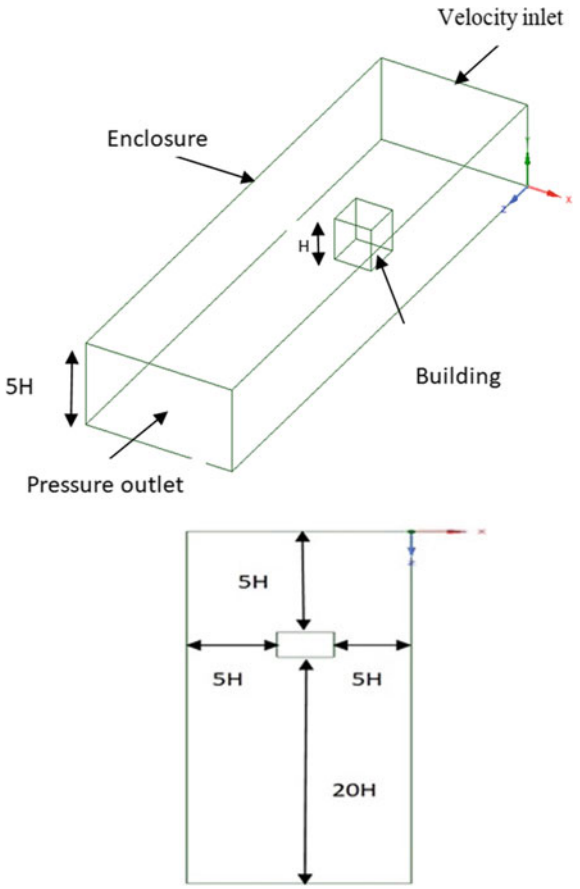

3.3 Figure Below Shows the Geometry of the Enclosure with Building Model

See Fig. 2.

3.4 Meshing

In meshing, boundary conditions are applied to the enclosure and the model and then the sizing of mesh is done. By sizing of mesh, fine and smooth mesh is generated (Fig. 3).

www.EngineeringBooksPDF.com

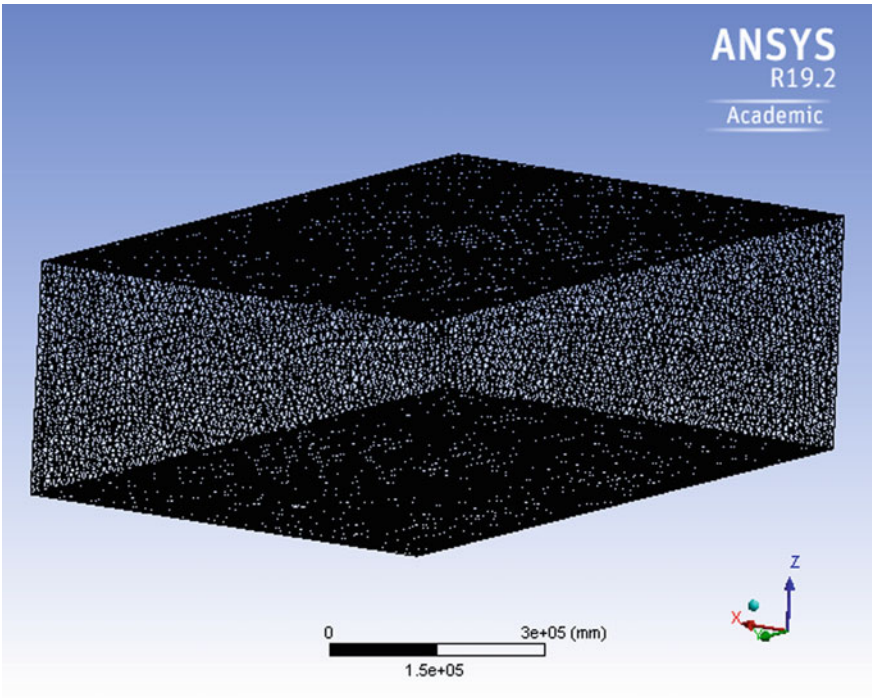

Fig. 3 Meshing

3.5 Setup

In setup, property such as K-ε epsilon model equation is selected for analysis purpose, where K is the turbulence kinetic energy and epsilon (ε) is the turbulence energy. Material properties used for analysis are: fluid as air and wood as solid. In boundary condition inlet velocity and pressure outlet are applied to the enclosure. Reference values such as area of model are also applied.

3.6 Solution

Initializations of parameters that are to be worked out are drag coefficient (C_d) and lift (C_l). Then type of solution such as hybrid or standard is selected and input for number of iterations is given.

www.EngineeringBooksPDF.com

Table 1 Description of model

S. no.	Shape of model	Diameter/breadth (m)	Height (m)
1	Circular	30	60
2	Hexagonal	30	60
3	Octagonal	30	60

3.7 Result

Result shows the output of the above analysis in the form graphs of C_d and value of C_d and also by velocity streamline flow sows friction and wake back side of model.

4 Experimental Work

4.1 Model Description

In the experimental work, three models (circular, octagonal, and hexagonal) were prepared by using geometric similarity between prototype and model. Scale used is 1:250, which means 1 cm of model to 250 cm of prototype (Table 1).

4.2 Material

Wooden material is used for making models, and brass pipe of diameter 3 mm is fixed in the model for measuring the pressure at different points.

4.3 Wind Tunnel

All the three models were tested in wind tunnel for measuring drag coefficient. The wind tunnel is of open type. The size of wind tunnel is 1.2 m × 4.8 m for which the maximum velocity of flow limits to 30 m/s. The size of test section is 1000 mm × 300 mm x × 300 mm and the capacity of measuring drag and lift is from 0 to 20. The velocity applied in experimentation is taken from zonal consideration in which the considered zone is Pune having wind velocity of 39 m/s. Using kinematic similarity, velocity of fluid flow is reduced. Reduced inlet velocity is applied to the models placed in wind tunnel and verified using digital anemometer having capacity of 30 m/s. And the results are displayed on the control panel and also on the manometer (Fig. 4).

www.EngineeringBooksPDF.com

Fig. 4 Wind tunnel

Fig. 5 Circular model for wind tunnel

Tests on wind tunnel are carried out if the following conditions are satisfied:

- Geometrical similarity between the model and the prototype. The modeled structure is geometrically similar to their full-scale counterparts.
- Reynolds number effect on pressure and forces is minimized.
- Wind tunnel test section longitudinal pressure gradient is accounted.

www.EngineeringBooksPDF.com

Fig. 6 Hexagonal model for wind tunnel

- The size of model is 8% less than test section.
- Kinematic similarity exists between the model and the prototype.
- Wind tunnel is consistent with the required measurement.

There are three types of wind tunnel test models commonly used:

1. Rigid pressure (PM)
2. Rigid high-frequency base balanced
3. Aero elastic (AM)

Figures 5, 6 and 7 are the models prepared to be tested in wind tunnel:

5 Results and Discussion

The values of drag coefficient for circular, hexagonal, and octagonal shapes are obtained from IS 875(Part-3) 2015 and are mentioned in the table −25, clause 7.4.2.2.

In experimental work, the values of drag coefficient are obtained and are displayed on the board of control panel of wind tunnel.

www.EngineeringBooksPDF.com

Fig. 7 Octagonal model for wind tunnel

Analytical values are obtained from CFD analysis using ANSYS 16.0. Velocity streamline in Fig. 9 shows the frictional effect of fluid flow on the model and diversion of flow. After performing CFD analysis the graph of iterations versus C_d is plotted and the values of pressure and viscous coefficient are obtained. Summing pressure and viscous coefficient, we get drag coefficient. CFD analysis is compared with the trustworthy existing approaches like tests on models in wind tunnel.

Drag coefficients are obtained by using wind tunnel for three models and are tabulated in Table 2. The values obtained by CFD and IS 875 are also mentioned in Table 2.

The details of the results obtained in the experimental setup and CFD are shown in Figs. 8, 9, 10, 11, 12, 13, 14, 15 and 16.

Table 2 Comparison of drag coefficient

Plan shapes	IS 875-2015 (Part 3)	Wind tunnel	ANSYS 16.0
Circle	0.50	0.60	0.56
Hexagon	1.20	0.70	0.82
Octagon	1.10	0.70	0.79

www.EngineeringBooksPDF.com

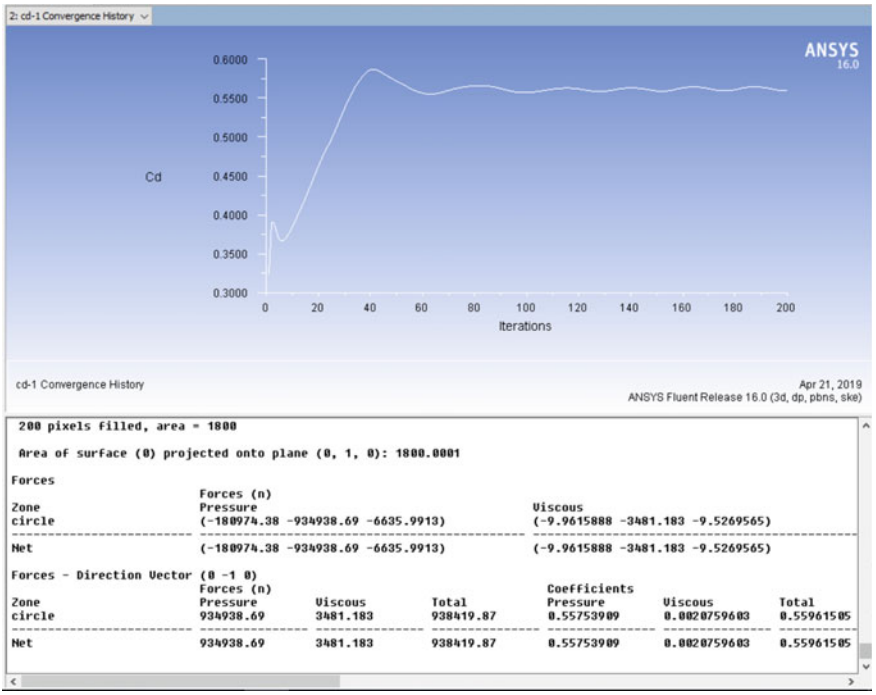

Fig. 8 Drag coefficient for circular shape by CFD

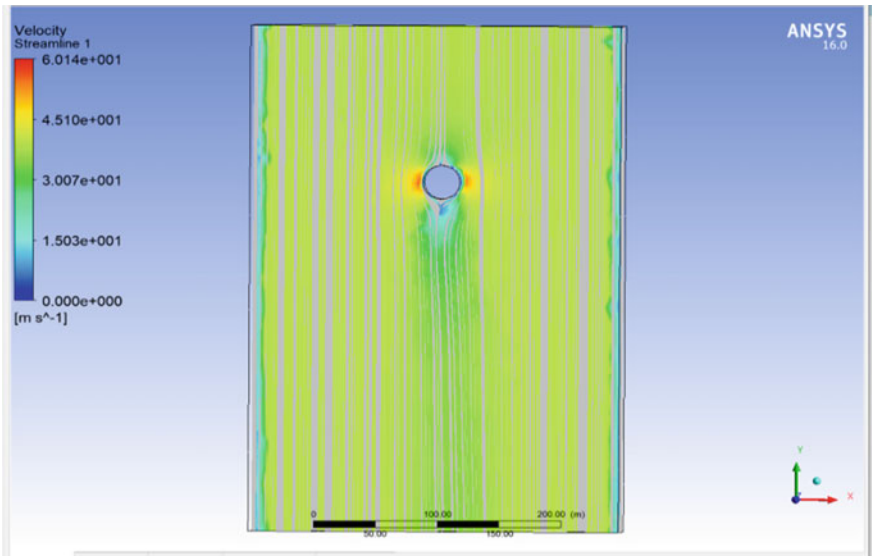

Fig. 9 Velocity streamlines for circular shape by CFD

www.EngineeringBooksPDF.com

Fig. 10 Drag coefficient for circular shape by wind tunnel

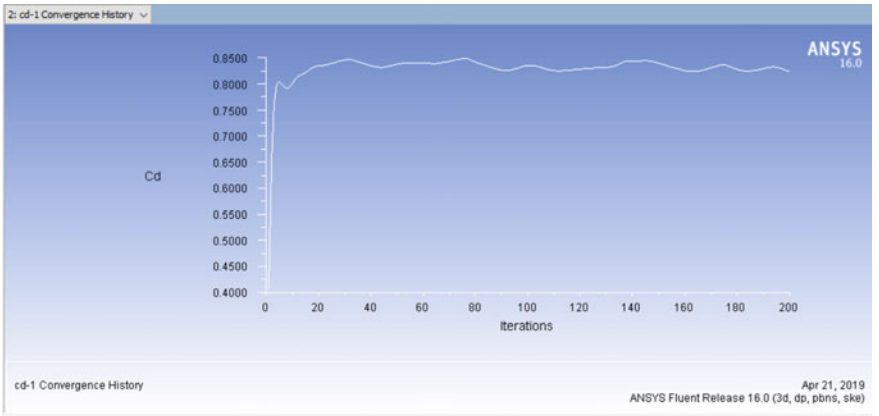


```
 turbulent viscosity limited to viscosity ratio of 1.000000e+05 in 202 cells
   200  1.2694e-02  3.6572e-05  7.0551e-05  3.6586e-05  2.0440e-03  5.2689e-06  8.2350e-01  0:00:00    0

Forces

                          Forces (n)
Zone                      Pressure                                  Viscous
hexagonal                 (-234543.49 -1379333.1 -49282.917)        (-40.68491 -1603.9108 -354.81236)
------------------------  ------------------------------------------------------------------------------
Net                       (-234543.49 -1379333.1 -49282.917)        (-40.68491 -1603.9108 -354.81236)

Forces - Direction Vector (0 -1 0)
                          Forces (n)                                Coefficients
Zone                      Pressure        Viscous         Total     Pressure        Viscous          Total
hexagonal                 1379333.1       1603.9108       1380937   0.8225482       0.00095647232    0.82350467
------------------------  --------------  --------------  --------  --------------  ---------------  ----------
Net                       1379333.1       1603.9108       1380937   0.8225482       0.00095647232    0.82350467
```

Fig. 11 Drag coefficient for hexagonal shape by CFD

www.EngineeringBooksPDF.com

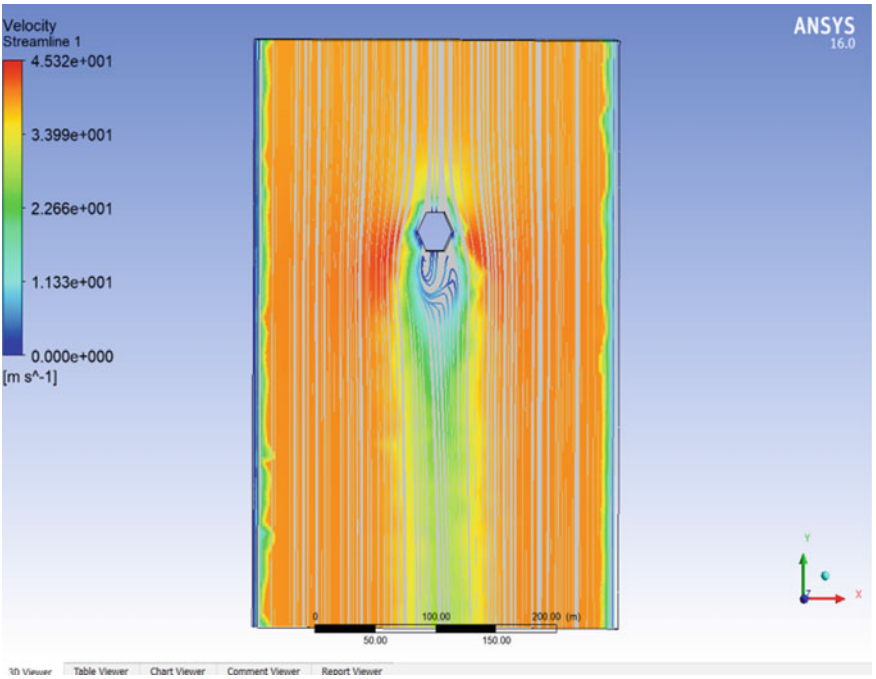

Fig. 12 Velocity streamlines for hexagonal shape by CFD

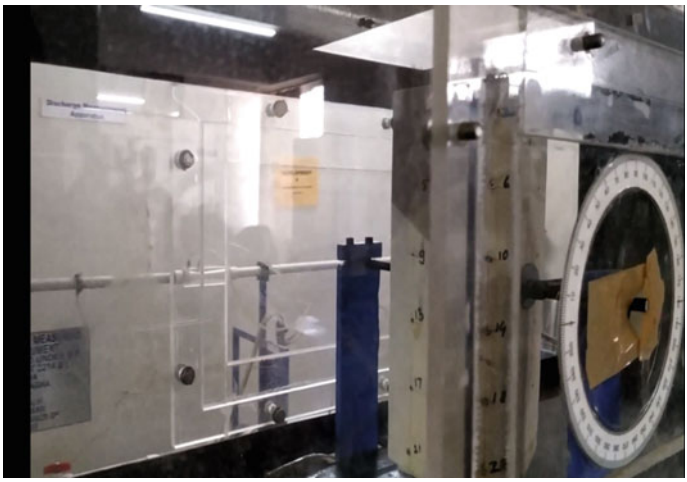

Fig. 13 Drag for hexagonal shape by wind tunnel

www.EngineeringBooksPDF.com

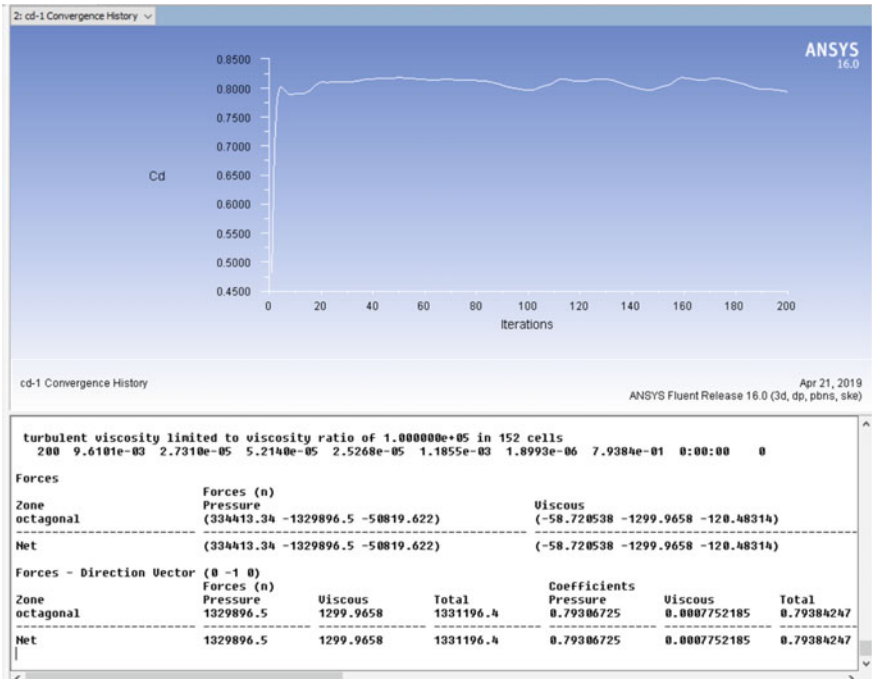

Fig. 14 Drag coefficient for octagonal shape by CFD

6 Conclusions

The velocity streamline shows the flow diversion and friction on model and the development of vortex at backside of the model. The results obtained by experimental setup and CFD are close as compared to the values obtained by using IS 875(Part-3)2015. In circular plan the values obtained by tests and CFD are overestimating the values obtained by IS 875(Part-3)2015. However, in the other two models, the values of test results and CFD underestimate the values obtained from IS 875(Part-3)2015.

www.EngineeringBooksPDF.com

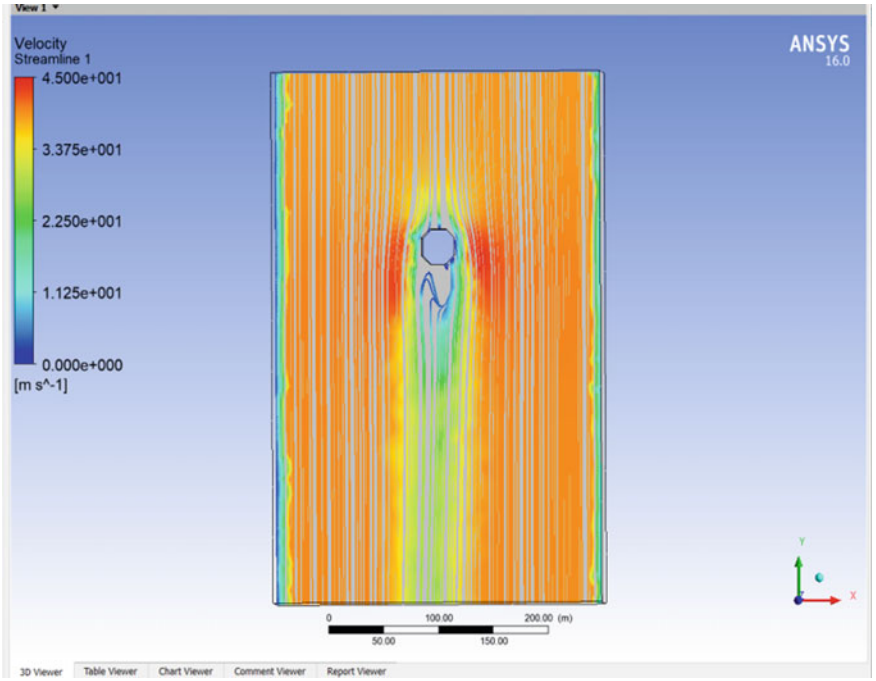

Fig. 15 Velocity streamlines for octagonal shape by CFD

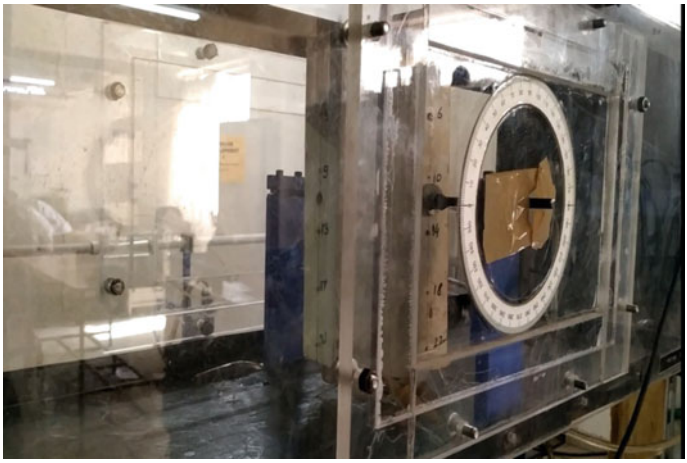

Fig. 16 Drag coefficient for octagonal shape by wind tunnel

www.EngineeringBooksPDF.com

References

1. Anoop et al C (2012) Suitability of IS 875 provisions for assessing wind loads on high rise buildings: scope and limitations VI National Conference on Wind Engineering 2012, Dec. 14–15
2. Irwin PA (2009) Wind engineering challenges of the new generation of super-tall buildings. J Wind Eng Ind Aerodyn 97:328–334
3. Kwon DK, Kareem A (2013) Comparative study of major international wind codes and standards for wind effects on tall buildings. Eng Struct 51:23–35
4. Sevalia JK, Vasanwala SA (2012) Comparative Study of wind flow effect on tall building using computational fluid dynamics. In: 8th Biennial conference on structural engineering convention (SEC-2012)
5. Daemei AB, Bahrami P et al (2018) Study on wind aerodynamic and flow characteristics of triangular shaped tall buildings and CFD simulation in order to assess drag. Ain Shams Eng J

www.EngineeringBooksPDF.com

Structural Performance of Modular Buildings: A Review

Ashok Jammi and Arul Jayachandran Sanjeevi

Abstract This paper presents a detailed review of research in the structural performance of modular buildings. Modular construction refers to 3D units that are fully fabricated in the factory and are assembled onsite to create complete buildings or parts of a building. This paper presents the advantages, different components, and materials used for modular construction. It also outlines the different load transfer mechanisms in modular buildings. The progress of research on the analysis of modular buildings under different actions is compiled, and conclusions are drawn based on available research. The authors suggest the use of cold-formed steel shear wall system as a lateral load resisting system owing to its specific advantages.

Keywords Modular buildings · Lateral load · Connections · Cold-Formed steel shear wall panels

1 Introduction

Modular construction has its roots extending over the last 15 years in many sectors of building industry. With gear up of automation in the manufacturing industry, the production rates increased out beating the past, which depended on the industrial workforce. At the same time, the workforce in the building industry started to decline—both skilled and unskilled labor—owing to many reasons. Also, with the advances in design and information technologies, combined with attention given by the industry to address cost, schedule, and labor issues, it led to *Re-thinking construction* (Egan) in the UK. This phenomenon led to a greater increase in offsite manufacture (OSM) [1]. In modular construction, the majority of the value of construction work takes place in the manufacturing environment. The economic, environmental, structural, and sustainable advantages of modular construction are [1, 2]:

A. Jammi (✉) · A. J. Sanjeevi
Indian Institute of Technology Madras, Chennai, India
e-mail: ashokjammi10994@gmail.com

A. J. Sanjeevi
e-mail: arulsteel@gmail.com

© Springer Nature Singapore Pte Ltd. 2021

K. K. Pathak et al. (eds.), *Recent Trends in Civil Engineering*, Lecture Notes in Civil Engineering 77, https://doi.org/10.1007/978-981-15-5195-6_2

www.EngineeringBooksPDF.com

- Speed of construction onsite. As the majority of the construction takes place in the manufacturing environment, construction onsite becomes rapid. This leads to early completion of the project and early return of capital investment to the client.
- Increased productivity in the factory and reduced requirement of onsite labor. Only installation of modules is to be done onsite, which is done by specialist teams.
- Reduced disturbance and disruption to adjacent sites, especially in heavy trafficked areas.
- Lightweight, less material use, and less wastage compared to onsite construction.
- The structure can be dismantled (especially whole steel modular buildings) and reused on another site.
- Quality of construction is enhanced as the product is factory-based (controlled environment). Also, provision for checks in a simulated environment.
- Short exposure to the weather or other site constraints to a construction operation. So, it can be constructed even in rainy seasons without any additional protection measures for the site or the materials.
- Good quality of acoustic and thermal insulation as the walls between modules are double skinned.

Owing to the above advantages, modular construction is considered as "technology coming of age" [1].

Modular construction concept is a subset of offsite manufacture (OSM). For a better understanding of different forms of OSM, Gibb (1999) classified them into four levels, as shown in Table 1. Levels 0 and 1 represent a majority of current constructional practices. Level 0 represents fully onsite construction like reinforced cement concrete or masonry.

Level 1 represents some prefabricated elements like roof trusses, precast beams, and columns. Level 2 involves prefabricated 1D or 2D structural systems like wooden frames, cold-formed steel framing systems. To these frames, other elements are

Table 1 Various levels of OSM technologies (*Source* Lawson et al. [2])

Level	Components	Description of technology
0	Materials	Basic materials for site intensive construction; e.g., concrete, brickwork
1	Components	Manufactured components that are used as part of sit-intensive building processes
2	Elemental or planar systems	Linear or 2D components in the form of assemblies of structural frames and wall panels
3	Volumetric systems	3D components in the form of modules used to create major parts of buildings, which may be combined with elemental systems
4	Complete building systems	Complete building systems, which comprise modular components, and are essentially fully finished before delivery to the site

www.EngineeringBooksPDF.com

attached. Level 3 involves a major proportion of prefabricated elements like bathroom pods, lift, stair units, and modular units. Level 4 involves offsite manufacture of complete building systems, as shown in Fig. 1. Higher the level of OSM, higher is the proportion of prefabricated components. This leads to an approximately proportionate reduction of overall construction time.

Table 2 gives the overall idea of where the offsite manufacture (OSM) is popular. Generally, cellular-type buildings are constructed using the modular technique.

Fig. 1 Modular unit at G + 1 level being lifted and placed. (*Source* Amarco Modular)

Table 2 Construction sectors most relevant to the use of offsite manufacturing (*Source* Mark Lawson and Ogden [1])

Levels of offsite manufacture (OSM)				
Sectors for which OSM is most relevant	Structural frames	2D panels	Mixed construction	Fully modular systems
Housing	–	Often	–	Rarely
Apartments—multistorey	Often	Often	Rarely	Often
Student residences	Rarely	Often	Rarely	Widely used
Military accommodation	–	–	–	Widely used
Hotels	Rarely	Rarely	Often	Widely used
Office buildings	Widely used	–	Rarely	Rarely
Retail buildings	Widely used	–	Rarely	Rarely
Health sector buildings	Widely used	Rarely	Rarely	Widely used
Educational buildings	Widely used	–	Rarely	Often
Mixed use	Often	Rarely	Widely used	–
Industrial	Widely used	–	Rarely	–
Sports buildings	Widely used	Rarely	Rarely	Rarely
Prisons and security buildings	Rarely	–	Rarely	Widely used

www.EngineeringBooksPDF.com

Transportability is the major factor limiting the module sizes. So to increase the carpet area two or more partially or fully opened modular units may be combined [1].

While there are many advantages of modular construction, it is to be noted that, to reap the maximum benefit careful survey has to be done considering the magnitude of the project, availability of materials, and access to prefab industry, and so on. One of the challenges that modular construction is facing is the reluctance of people to diverge from traditional building practices. Also, the lack of established design codes or guidelines on modular practice implicates the clients to place faith in the design and construction firm regarding the quality and reliability of the project. In this paper, the modular construction is being considered from a structural perspective. First, the materials used are introduced, followed by types of modular construction, and then followed by connections in modular buildings.

2 Materials

The materials that are commonly used for modular constructions are mainly steel (hot rolled and cold formed), precast concrete, and timber.

2.1 Steel

Using steel in modular construction has revolutionized its applicability by reducing the construction time, the versatility of design, and easy transportation of modules. According to Ferdous et al. [3], as of now, 12 stories is the tallest project that has been constructed with steel as core and 32 stories with steel as a frame. Light gauge steel (LGS) modules extend up to eight stories. Using LGS framing is ideal for modular construction because of its efficient use of the material and ability to be integrated into a sophisticated manufacturing process.

Forms of modular construction prevailing in the industry, using steel are as given in [1]:

- Continuously supported modules.
- Open-sided or corner-supported modules.
- Non-load-bearing modules—supported by a separate structure.

2.2 Precast Concrete

Precast units include 2D units such as slabs and walls and 1D units such as beams and columns. It reduces the requirement of formwork and scaffolding, thereby save costs onsite. It has good fire resistance, thermal insulation, and acoustic insulation capacity. According to Ferdous et al. [3], as of now, 44 stories is the tallest project

www.EngineeringBooksPDF.com

that has been undertaken using precast concrete panels or systems. The precast joints between the columns and beams are designed for moment-free condition and carry only gravity loads. The lateral loads are resisted by shear walls. The beams and wall panels were precast including the hollow core slab and staircases.

Forms of modular building construction that use precast concrete elements are as given in [1]:

- Frame and floor slab
- Cross-wall construction
- Twin-wall construction
- Tunnel form construction.

2.3 Timber

For a long time, timber is prevailing in the building industry, especially in residential buildings. Timber is used as secondary beams, floor material, and wall panels. Now cross-laminated timber (CLT) is being adopted in many modular constructions. Owing to its possibility of load transfer in more than one direction to achieve diaphragm action, it offers a plethora of possibilities in buildings [4]. It is a 2D timber product where panels are made using cross-wise glued lamellas with an uneven number of layers ultimately resulting in symmetrical cross-section. Along the length, they are joined by finger joints. Using CLT eight stories is the tallest modular project that has been constructed [4].

3 Structural Types

Generally, four types of structural types are adopted in modular construction:

- Load-bearing wall type module.
- Corner-supported module.
- Non-load-bearing modules.
- Modules placed around a central concrete or steel core.

The differentiating factor is the load path. This difference in the load path brings about the change in their performance under various actions, like lateral load, gravity load, dynamic load, and so on. So the analysis and design procedures vary depending on the structural type chosen. The choice of the structural type depends on so many factors, like availability of resources, availability of design experts and fabrication feasibility, the height of the building, the intended utility of the building, and so on. The description of the above types is given in the following section.

www.EngineeringBooksPDF.com

3.1 Load-Bearing Wall Type

This type of modules is primarily made of light gauge steel, as shown in Fig. 2. In this case, the load will be transferred through the side walls of the modules. In this case, the resistance of wall panels to axial compression is the major factor to be considered, as it governs the design. The wall panels are made up of light steel C sections at 300–600 mm spacing between centers. This type of construction limits the building height from 4 to 8 stories [6]. The type of complex loading that the wall panels are subjected to is as given in [5]:

- Additional moments developed due to eccentricities in the direct wall to wall bearing caused by manufacturing defects and inaccurate module installation and loading from the floors and ceilings which are applied at the face of the wall.
- Restraint provided by floors and ceilings which depends on their diaphragm action.
- Unquantified stabilizing effect from the sheathing boards, which restrain minor-axis buckling.
- In taller buildings, second-order effects (P−Δ) play a key role due to sway and other eccentricities.

Based on the experiments done by Lawson et al. [5], light steel wall with sheathing (gypsum board on one side and OSB board on another side), the following failure modes are observed to occur:

- Local crushing of cross-section in compression, as shown in Fig. 3.
- Global buckling of the wall about major axis, as shown in Fig. 4.
- Board pulls out from wall studs, leading to loss of composite action.

The restraint provided by the sheathing led to a 62% increase in buckling resistance, and a 2.2% increase in slenderness ratio [7]. As the load eccentricity increases, the axial compression capacity also reduces. In this study by Lawson et al., BS 5950-1 and NSSS (National Structural Steelwork Specification) is used for assessing

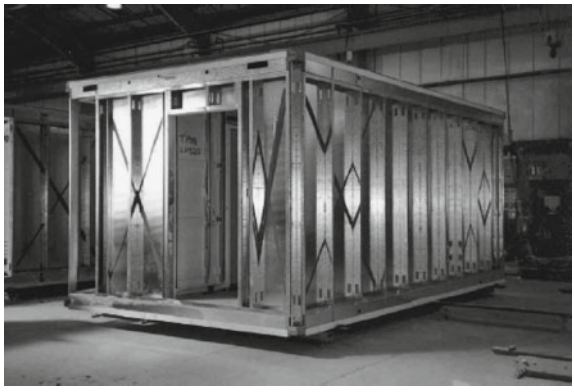

Fig. 2 Load-bearing wall type module. (*Source* Lawson et al. [5])

www.EngineeringBooksPDF.com

Fig. 3 Local crushing of C section in compression. (*Source* Lawson et al. [5])

Fig. 4 Global buckling of the wall about major axis. (*Source* Lawson et al. [5])

the relevant performance of the buildings, such as influences of construction tolerances, assessing sway stability by applying notional horizontal load, and so on. The summary of research done by Lawson et al. on load-bearing type module is given in Table 3, as mentioned in [7–9] (Fig. 5).

For buildings with unsymmetrical plan across different floors, the load transfer takes place through a shear core [7]. These core walls will be of stiff concrete and

www.EngineeringBooksPDF.com

Table 3 Summary of research done on load-bearing wall type modules

Effect considered	Experimental type/analytical procedure	Conclusion
1. Compression resistance of Modular walls	2300 mm × 600 mm wide wall panels with three 100 mm deep C sections with two 15 mm plasterboards on one side and 11 mm OSB on the other side	1. Increased moment of inertia due to composite action with sheathing material 2. Reduced crushing resistance during eccentric loading is attributed to reduced compression area 3. Buckling curve used in BS 5950-1 for cold-formed sections is conservative
2. Influence of initial eccentricities and constructional tolerances on additional forces and moments in wall modules	An empirical equation is proposed, taking into account all the positional, manufacturing, and geometric tolerances. $\delta_h < e + nh/10000 = 5n + 3n = 8n$ where n is the number of stories	1. An absolute out of verticality of maximum 80 mm is recommended
3. Applicability of BS 5950-1 in modular construction using notional horizontal load approach	The effect of eccentricity is empirically converted to an equivalent horizontal load which produces the same moment at the base	1. The notional horizontal varies from 0.5 to 0.9% when expressed as a percentage of vertical load applied to the module, which agrees with BS 5950-1
4. Second-order effects in the design of corner columns	Each frame is analyzed as shown	1. The eccentricity of load that is acting on the corner columns should not be taken less than 35 mm 2. In-plane stiffness of wall panels to which they are connected may restrain them, but in case of the partially open-sided module or the case when the wall has openings in it—it may not restrain
5. Module connection behavior	Tie connection was tested at a re-entrant corner to assess tensile strength	1. Figure 6 shows the best solution for the module to corridor connection

(continued)

www.EngineeringBooksPDF.com

Table 3 (continued)

Effect considered	Experimental type/analytical procedure	Conclusion
6. Robustness	Support to one corner of a module is removed, and tie forces are assessed using finite-element analysis	1. Minimum horizontal tying force should be taken as 30 kN for lightweight modules 2. For the considered module to module connections, a tying force of 40 kN can be resisted

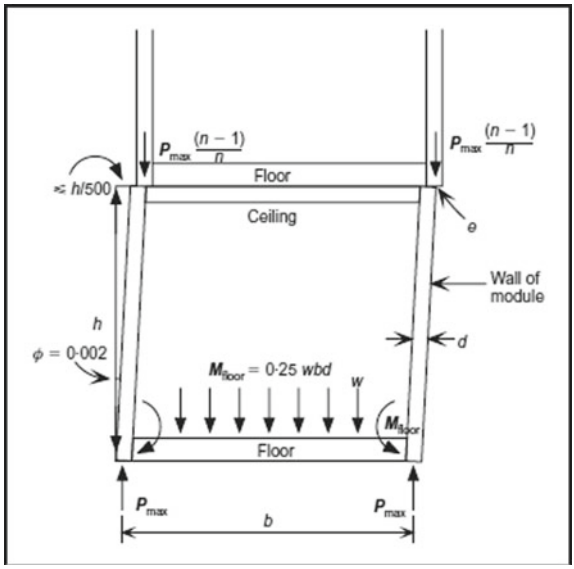

Fig. 5 Second-order effect analysis. (*Source* Lawson et al. [5])

can be placed as central core. They can be connected through bolted plates in the horizontal direction, and modules with stiff concrete walls are introduced. Together they efficiently transfer lateral loads [10].

3.2 Corner-Supported Modules

These are used for heavily loaded structures, where load transfer takes place through corner posts which are joined axially to get a column action. The corner posts used are—hollow sections for cold-formed steel, and I section for hot rolled steel as shown in Fig. 6.

These modules support more flexibility than load-bearing wall type but are more costly than fully light steel systems [8]. Since resistance to lateral load is critical

www.EngineeringBooksPDF.com

Fig. 6 Corner-supported module. (*Source* SteelConstruction.info)

in taller buildings, corner-supported modules are a more feasible option because the elements can be connected both horizontally and vertically at the beam-column junctions. Each frame of the module can be braced using concentric or eccentric braces [9] or stiff concrete walls [10].

Figures 6 and 7 show the difference between the braced frame of modular building and conventional building. The difference comes in the detailing. In the conventional frame, at an interior joint, four braces, two beams, and two columns join. But in a modular building, these are offset due to inter-modular connections, as shown in Fig. 6. This leads to complexity in analysis, especially at the points where plastic hinges are to be formed. As a result, we have to perform nonlinear analysis to predict the behavior of these structures. Software such as SAP2000, ETABS, OpenSees, RAUMOKO are used for carrying out building nonlinear dynamic analysis, and ABAQUS and ANSYS are used to analyze connection behavior. A detailed description of connections in modular buildings will be discussed in the forthcoming sections. An overall picture of the work done on corner-supported modules is given in Table 4.

At this point it would be befitting to consider the behavior of cold-formed shear wall panels with steel sheathing, under combined lateral and gravity load actions and the various analytical and computational models that are developed to assess their behavior. This would be of interest in assessing the overall building performance as

www.EngineeringBooksPDF.com

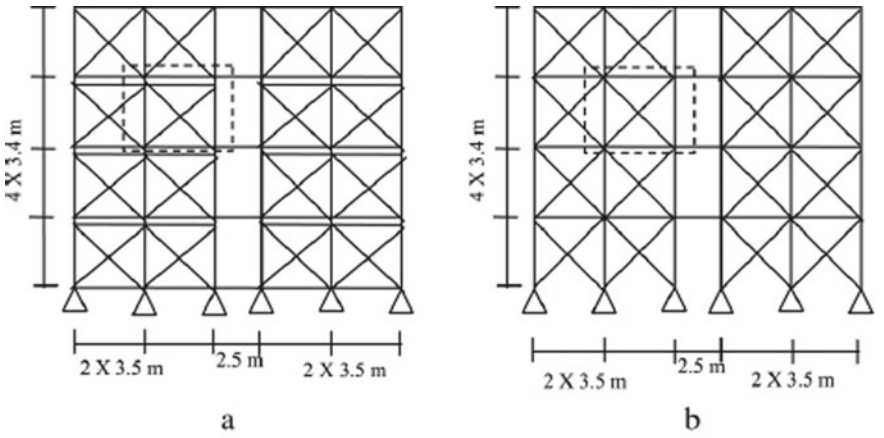

Fig. 7 **a** Modular frame building; **b** Conventional frame building. (*Source* Lawson et al. [8])

the behavior of individual wall panel governs the lateral and gravity load resistance of the whole modular building. There has been considerable research done on the behavior of steel sheathed cold-formed wall panels in terms of the tension field action of the steel sheathing, development of plastic hinges at the anchorage points, and frame sheathing interaction in the panel. It would be of great advantage to study these systems and incorporate them in modular steel buildings for better lateral, and gravity load performance in low and mid-rise as these systems are lightweight, weld-free and can be easily modulated into 2D or 3D applications (Fig. 9).

3.3 Non-load-Bearing Modules

This is a type of modular construction where the gravity and lateral loads are taken by a steel frame and modules are placed into the infill space of the frames. These are shown in Fig. 10.

These modules are not designed to carry any structural loads except the loads acting during transportation. The design is mainly concerned with the frame action of the primary frame rather than the modular action. So, these modules are mainly made of light-weight steel. Bathroom pods or small pant rooms are generally manufactured as non-load-bearing modules [2].

There is not much research exclusively related to this as this doesn't fall into the category of modular action. To investigate the behavior, the research relating to framed structures can be accessed with an understanding of gravity and inertial loads imposed by modular units.

www.EngineeringBooksPDF.com

Table 4 Summary of prominent research done on corner-supported modules

Effect considered	Experimental setup/analytical procedure	Conclusions
1. Seismic performance evaluation—comparing regular-braced frame with modular frame in terms of stiffness, strength, inelastic force and deformation, and energy dissipation characteristics [11]	MSB-braced specimen of one-storey high with one-bay cross-braced panel extracted and scaled from a typical four-storey modular building The nonlinear analysis was carried out using SeismoStruct	1. In regular specimen the onset of nonlinearity was by brace buckling, whereas in MSB it was due to column yielding 2. Beyond ductility of 2 MSB specimens showed higher energy dissipation per cycle till failure
2. Inelastic behavior of braced modular frames, assessing their demands and capacities [11]	The external-braced frame was modeled as 2D—frame supporting half of the building mass. The floor was modeled as a rigid plate. Elastoplastic material model was employed, and inelastic steel beam-column frame element was used for column members	1. The study of inter-storey drift demand shows that the first storey experiences a high concentration of inelasticity 2. The first mode dominated the response
3. Force modification factors related to seismic overstrength and ductility are considered [12]	Nonlinear static pushover analysis	1. Due to high redundancy in the MSB frame system at the joints, they possess high overstrength than given by NBCC 2005 for regular frames. The values are 1.9–2.5 as opposed to 1.3
4. Brace-induced column action in capacity design [13]	Nonlinear static pushover analysis	SRSS method was not found conservative, and so the direct summation (DS) method was recommended
5. New lightweight steel double-skin panels (shown in Fig. 8) as lateral load-resisting system in framed modular buildings [14]	1. 2 types of experiments were performed—framed modular system and double-skin steel panels with or without panel strengthening 2. Also, hysteresis curves were obtained for the proposed panel system using dynamic analysis 3. Ductile behavior of panels at large roof drifts was predicted by the rigid plastic analysis	1. Slender double-skin steel panels follow theoretical flexural behavior 2. The proposed lightweight steel panels can be used as an effective supplementary lateral load resisting system 3. The behavior of this lateral load resisting system can be predicted by single-wall hysteresis

(continued)

www.EngineeringBooksPDF.com

Table 4 (continued)

Effect considered	Experimental setup/analytical procedure	Conclusions
6. Inelasticity distribution along the height of the MSB and maximum drift demand due to various ground motion intensities were studied [15]	Incremental dynamic analysis with OpenSees.	1. Increment dynamic analysis was proved to be effective in providing insight into the seismic behavior of the structure 2. Vertical connections between modules can be effectively made directly by connecting the ceiling beams to floor beams directly rather than at connecting columns

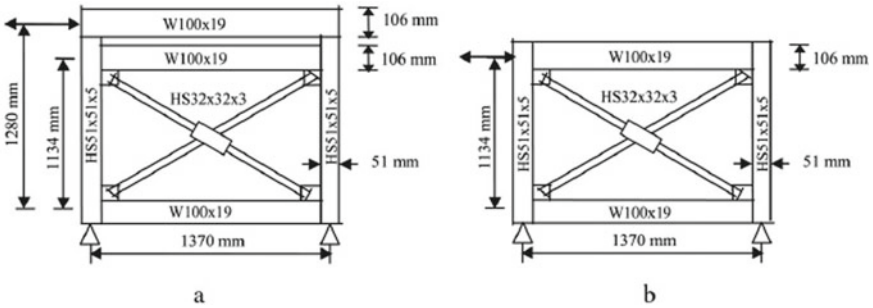

Fig. 8 Zoomed-in view of the dotted line in Fig. 6 **a** Modular frame; **b** Conventional frame. (*Source* [10])

Fig. 9 Double-skin steel panel. (*Source* Hong et al. [14])

www.EngineeringBooksPDF.com

Fig. 10 Non-load-bearing modules placed into a primary frame structure. (*Source* Steel Construction. info)

3.4 Modules Placed Around a Central Steel or Concrete Core

As the height of the building increases beyond ten stories, the wind loads acting on the structure increase enormously, leading to large lateral drifts. So, in MSB, an additional lateral load resisting system has to be constructed as a central concrete or steel core to transfer the horizontal loads to the foundation [6]. The structural interaction between modules and core defines the span and height to which the modules can be extended.

Figure 11 shows Europe's tallest modular tower (28 stories)—Apex house in Wembley. It demonstrates the power of load-bearing core for modular tall buildings. However, this type of construction actually deprives the building to be called purely

Fig. 11 Modular construction with concrete core. (*Source* Apex Modular)

www.EngineeringBooksPDF.com

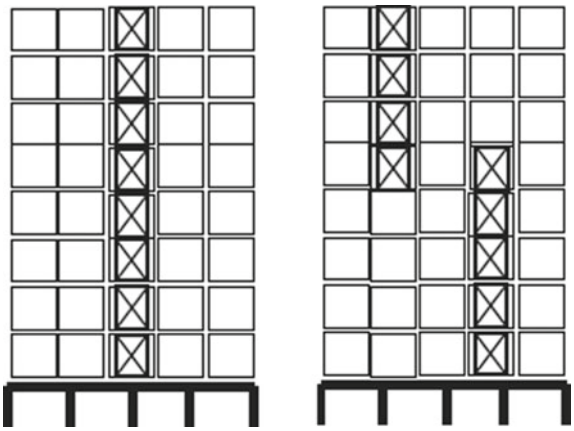

Fig. 12 Conceptual arrangements of the lift core made possible with the new system. (*Source* Gunawardena et al. [10])

modular as it requires onsite construction also, thereby increasing the construction time. So, an innovative, flexible structural system using prefabricated modules is proposed by Gunawardena et al. [10]. They proposed a structural system in which elevator core, formed by prefabricated modules, will be the primary lateral load resisting system, as shown in Fig. 12. They are connected through bolted plates in the horizontal direction, and modules with stiff concrete walls are introduced. Together they efficiently transfer lateral loads.

Given the overview of different structural types, load-bearing modules are suitable for low- and mid-rise buildings, 8–10 stories high. For high-rise buildings central concrete core or steel core is necessary for resisting the lateral loads.

4 Behavior of Modular Buildings During Wind and Earthquake

The behavior of modular buildings in the case of wind and earthquake varies with type of modules and connections adopted. However, few experimental and simulation studies have been carried out on the behavior. Michael Sadeghinia et al. [17] have investigated the behavior of shear wall and slab inter-connections between RCC modules for a 40-storey modular building under seismic and wind loading. Walls and slabs are modeled in SAP2000. The slabs were 200 mm thick for shear core and for modules they used composite slab 250 mm thick. The following are the behavioral plots they obtained (Figs. 13, 14 and 15).

They concluded that in low-rise-braced structures the shear mode displacements are more dominant and will determine the lateral stiffness of the structure. In medium to high rise, the dominant mode flexure is similar to regular buildings. The total

www.EngineeringBooksPDF.com

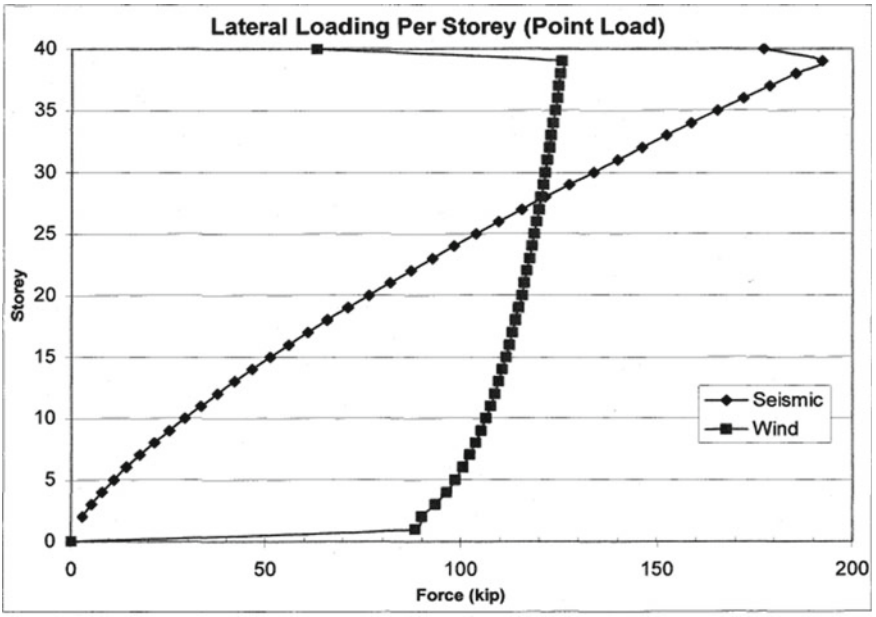

Fig. 13 Lateral loading per storey due to point load. (*Source* Sadeghinia [17])

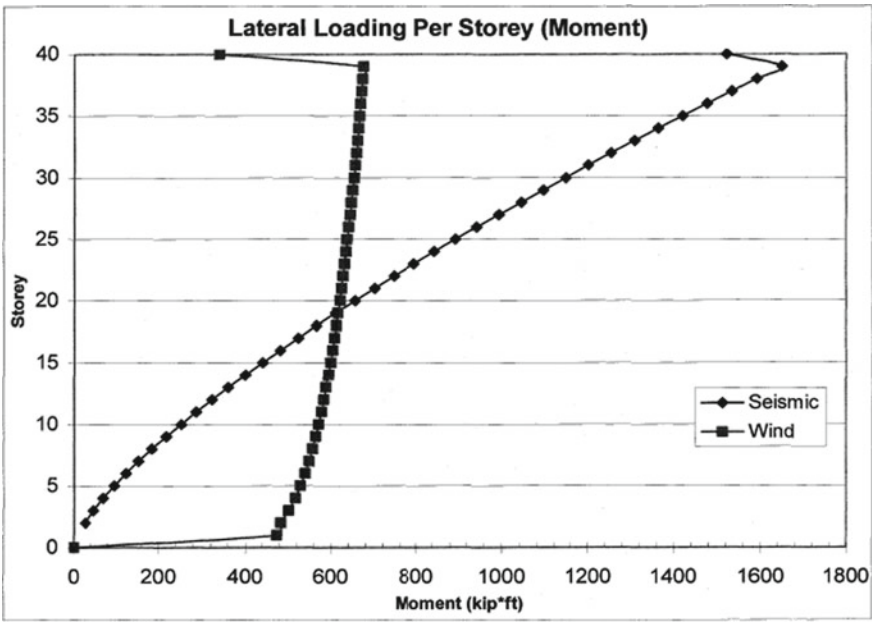

Fig. 14 Lateral loading due to moment. (*Source* Sadeghinia [17])

www.EngineeringBooksPDF.com

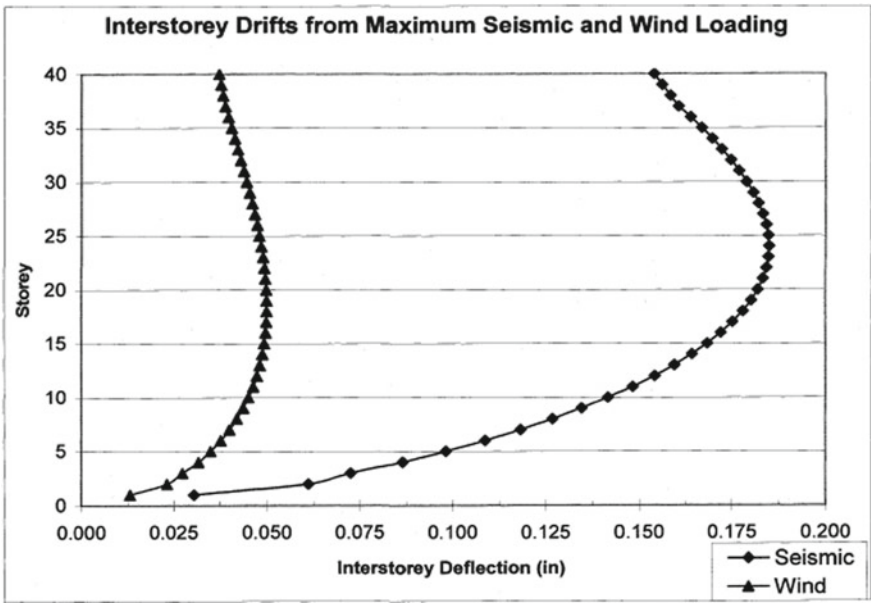

Fig. 15 Inter-storey drifts. (*Source* Sadeghinia [17])

deflections, even the inter-storey ones, indicate the flexural mode behavior dominating the shear mode. Some frame action is evident, but even the frame action is mostly attributable to the frame behaving in flexure.

Tharaka Gunawardena et al. [18] also analyzed a 10-storey building in SAP2000 for wind and seismic conditions. The following pushover curves are obtained (Fig. 16):

They concluded that the wall dimensions required for controlling deflections and contributing to lateral load transfer is 10.8 m × 5.4 m.

These researches have concluded that the modular systems are capable of resisting the lateral load in par with regular buildings and importance should be given to inter-modular connections and module dimensions.

5 Connections

Connections are the crucial components for effective integration and load transfer between the modules. Especially in modular steel buildings, the inter-modular (horizontal and vertical) connections are of key importance for resisting lateral loads due to dynamic and wind action. Also, the redundancy at the connections determines the robustness of the building. As in conventional steel framed buildings, there are no standard connection systems for modular buildings [3]. Sometimes even if the

www.EngineeringBooksPDF.com

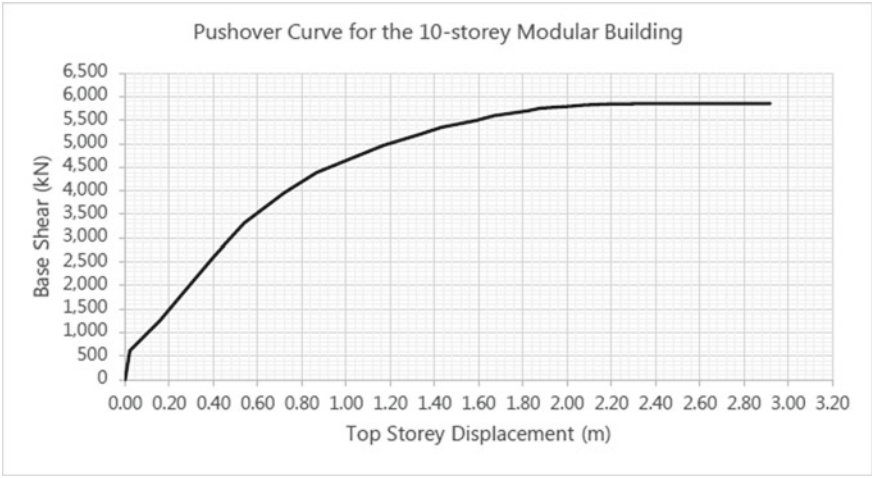

Fig. 16 Pushover curve for 10-storey modular steel building. (*Source* Gunawardena et al. [18])

connection is the same as conventional steel building, the behavior is observed to be completely different, owing to the modular nature of the construction. This was shown by Annan et al. [16] in case of stringer-to-beam connection. Generally, the stringer-to-beam connection is designed to transfer vertical shear force. But this study shows that they must be designed to transfer significant axial load and bending moment also. Traditionally used rotational spring to represent semi-rigid connections will not predict the axial force developed in modular floor stringers. So, every building is tailored with a different connection system based on the designers' discretion. So it is a topic of investigation which many researchers across the globe have focused upon.

The following are some of the major connection types (module to module) considered:

- Vertical post-tensioned connections [19]
- Vector Bloc modular connector [20]
- Steel bracket connection [21]
- Bolted connections [22]
- An innovative interlocking system [25].

5.1 Vertical Post-tensioned Connections

Figure 13 shows the proposed connection by Sanches et al. [19]. This type of connection consists of a post-tensioned threaded rod encased in an HSS column and a steel box placed between two modules. The threaded rod extends throughout the entire length of the columns to provide proper vertical connectivity amongst the modules

www.EngineeringBooksPDF.com

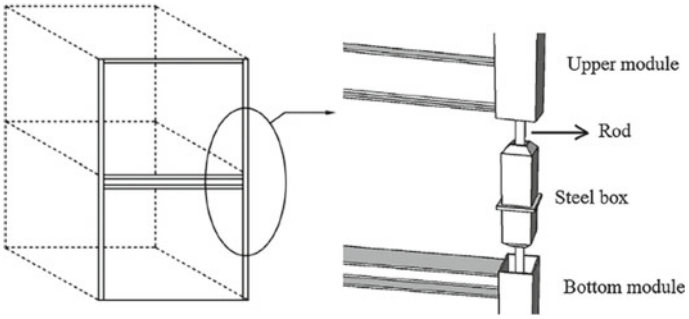

Fig. 17 Schematic representation of vertical post-tensioned connection. (*Source* Sanches et al. [19])

and is anchored against the end plates at column ends. In this study cyclic response of a post-tensioned column base connection for steel frame was obtained by quasi-static tests. The results corroborated that this connection eliminates the need for onsite welding while providing adequate lateral resistance and energy dissipation (Fig. 17).

This post-tensioned column specimen behavior was compared with the welded specimen in terms of their initial stiffness and energy dissipation capacity and was found to perform better. Alleviating welding onsite which reduces the speed of construction by interfering with the assembly process, the proposed connection behaves adequately in seismic scenarios.

5.2 VectorBloc Modular Connector

This is a cast steel connector developed by VectorBloc corp. The HSS beams can be connected directly to the columns, and it also supports inter-modular connections. This study was done to validate the use of this connector in a living facility to be built [20]. A corner connection has been studied for axial behavior in both tension and compression. The experiment and finite-element modeling showed that the failure loads of the connection are much higher than factored design loads of the proposed living facility. The compression failure mode is ductile, but the tension failure—due to rupture of socket head cap screws (SHCS)—connects lower bloc to upper bloc. So the connection has to be improved to perform better in tension (Fig. 18).

5.3 Steel Bracket Connections

The steel bracket type (Fig. 15) connections are experimentally investigated by [21] under different loading conditions. A baseline analytical model was proposed using

www.EngineeringBooksPDF.com

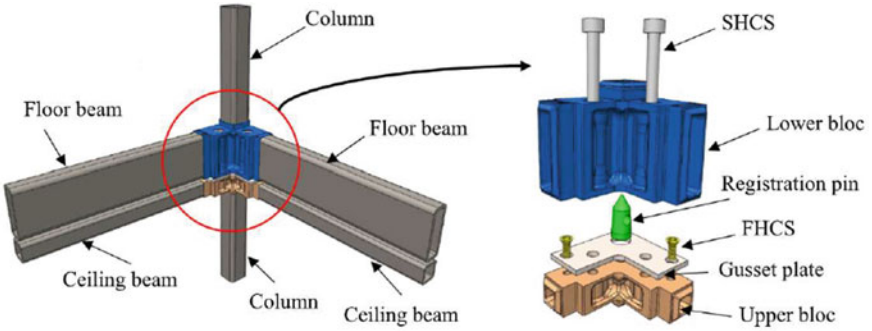

Fig. 18 VectorBloc connector (corner). (*Source* Dhanapaul et al. [20])

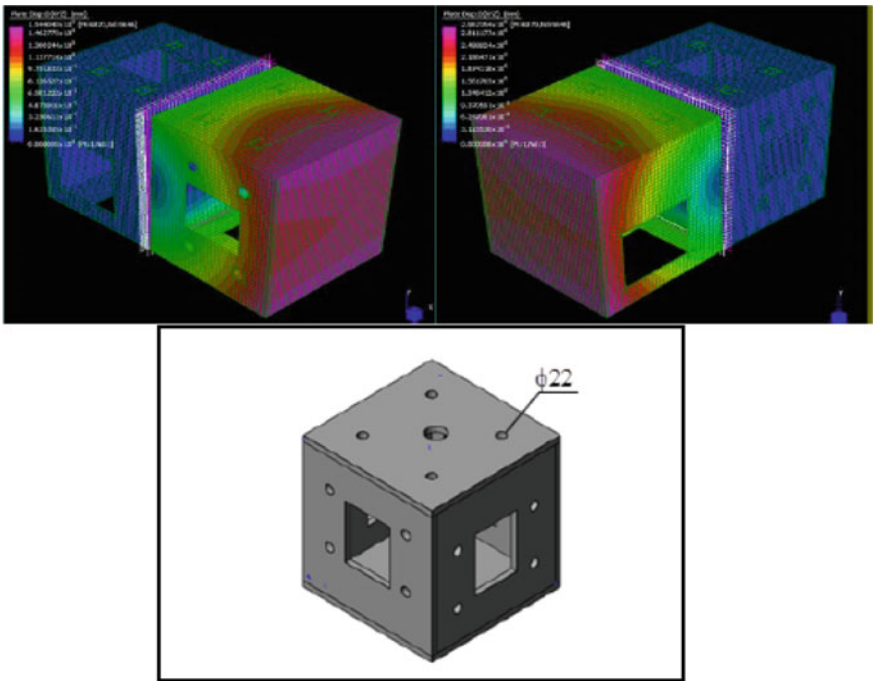

Fig. 19 Steel bracket connection. (*Source* Hwan Doh et al. [21])

Strand7 software. The experiments revealed that the failure was due to exceeding tensile capacity of the bolts in both shear and simply supported tests. The connection failure was ductile and no bracket failure has occurred (Fig. 19).

www.EngineeringBooksPDF.com

5.4 Bolted Connections

Several works are carried out by Liu et al. [23] and Doh et al. [21] on bolted connections in terms of innovating a new configuration to suit the modular construction scenario. The bolted connection is most preferable because it is very versatile to assemble onsite and also bolted connections fail only upon reaching the ultimate load, giving a considerable room for utilizing the capacity of connected members. Liu et al. [23] proposed a new fully bolted connection (Fig. 16b) to connect a truss to the column and a column to column. They conducted an experimental and FEA study using ABAQUS on the proposed connection and gave simple formulas to calculate the strength of the connection under static and cyclic load. They agreed well with the tests and FEA. En-Feng Deng et al. [22] proposed a bolted connection (Fig. 16a) with a welded cover plate and conducted experimental tests on seven full-scaled specimen and proposed a design formula. The tests proved that the proposed connection could induce moment resisting frame action and are capable of developing the full strength of connected beams. Although the proposed connection is a typical semi-rigid type and can be used only for ordinary moment frame systems, by adding triangular-shape stiffeners or inner diaphragm, they can be used for special moment frame systems. The ductility and energy dissipation capacity were found to be satisfactory. According to Lacey et al. [24], most of the existing studies are based on single load action, and specific consideration has to be given to combined action and developing theoretical models on a bolted connection (Fig. 20).

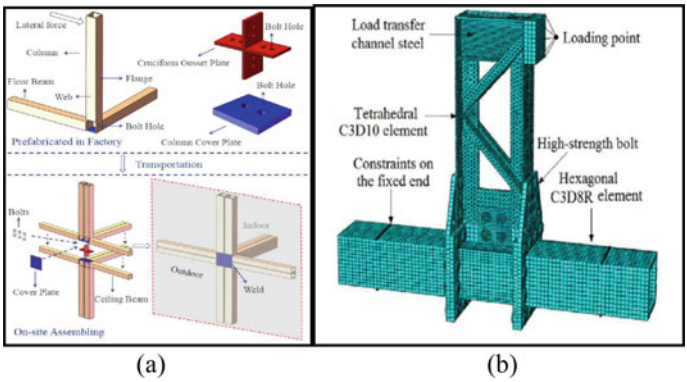

Fig. 20 **a** Bolted connections. (*Source* En-Feng Deng et al. [22]) **b** Bolted connections. (*Source* Liu et al. [23])

www.EngineeringBooksPDF.com

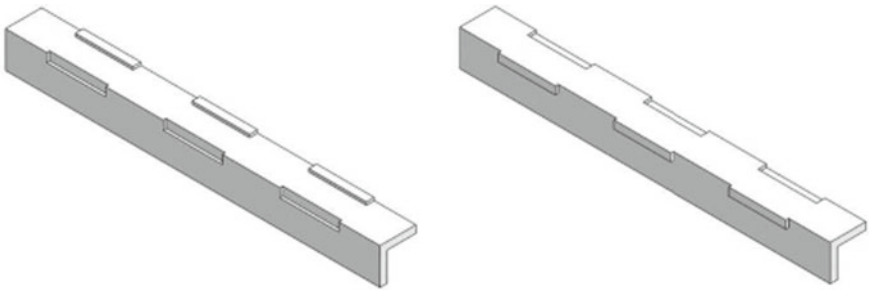

Fig. 21 Innovative interlocking system. (*Source* Pezman Sharafi et al. [25])

5.5 An Innovative Interlocking System

Pezman Sharafi et al. [25] proposed an innovative interlocking system based on the premise that topological interlocking has several advantages over traditional construction. That means providing mechanical attachment by geometric features like tongues and grooves, where motions required for assembly are simple—push, tilt, slide, twist, or spin. In the practical scenario, access to intermodular connections is a very difficult task. So this type has been suggested. Experimental and numerical analysis show that this connection can significantly improve the integrity of each modular unit with the other, and performance is adequate in lateral load action (Fig. 21).

6 Conclusions

The materials, structural framework, and connection systems in modular buildings have been introduced, and the progress of research has been reviewed. Modular construction was briefly introduced, and its advantage over traditional construction has been highlighted. Hence there is a necessity for developing design guidelines for modular construction so that it would be beneficial for design firms to take up the construction with solid support. Lateral load resisting systems play a key role in mid- and high-rise buildings. Not much investigation has been done in the literature to develop a methodology, which incorporates the local behavior of cold-formed steel wall panels for assessing the global structural performance of modular buildings. Also, the effect of connections—wall to wall, wall to floor, and inter-storey wall to wall connections—in developing the anticipated resistance of the wall is to be inspected further. So, a detailed study of cold-formed steel wall panels is recommended. There is a need for a new structural system with cold-formed steel framing, compatible for mid- and high-rise applications with adequate lateral load resistant system.

www.EngineeringBooksPDF.com

References

1. Mark Lawson CG, Ogden R (2017) Design in Modular Construction 71(1), https://doi.org/10.1080/10464883.2017.1260969
2. Lawson RM, Prewer J, Trebilcock PJ, Modular Construction using Light Steel Framing : an Architect' s Guide. SCI publication- P272, ISBN 1895198283
3. Wahid Ferdous TDN, Bat Y, New advancements, challenges and opportunities of multi-storey modular buildings—a state of the art review. Eng Struct 183:883–893.https://doi.org/10.1016/j.engstruct.2019.01.061
4. Gijzen R, MSc Thesis Modular cross-laminated timber buildings
5. Lawson RM, Byfield MP, Popo-Ola SO, Grubb PJ (2008) Robustness of light steel frames and modular construction. Proc Inst Civ Eng Struct Build 161(1):3–16. https://doi.org/10.1680/stbu.2008.161.1.3
6. Lawson RM, Richards J (2010) Modular design for high-rise buildings. Proc Inst Civ Eng Struct Build 163(3):151–164
7. Lawson RM (2016) Modular Construction in light steel framing for residential buildings
8. Lawson RM, Ogden RG, Bergin R (2014) Application of modular construction in high-rise building., 1–5, https://doi.org/10.1061/(asce)ae.1943-5568.0000057
9. Annan CD, Youssef MA, El Naggar MH (2009) Experimental evaluation of the seismic performance of modular steel-braced frames. Eng Struct 31(7):1435–1446. https://doi.org/10.1016/j.engstruct.2009.02.024
10. Gunawardena T, Ngo T, Mendis P, Alfano J (2016) Innovative flexible structural system using prefabricated modules. J Archit Eng 22(4):05016003. https://doi.org/10.1061/(asce)ae.1943-5568.0000214
11. Annan CD, Youssef MA, El Naggar MH (2009) Seismic vulnerability assessment of modular steel buildings. J Earthq Eng 13(8):1065–1088. https://doi.org/10.1080/13632460902933881
12. Annan CD, Youssef MA, El Naggar MH (2009) Seismic overstrength in braced drames of modular steel buildings. J Earthq Eng 13(1):1–21. https://doi.org/10.1080/13632460802212576
13. Fathieh A, Mercan O (2016) Seismic evaluation of modular steel buildings. Eng Struct 122:83–92. https://doi.org/10.1016/j.engstruct.2016.04.054
14. Hong SG, Cho BH, Chung KS, Moon JH (2011) Behavior of framed modular building system with double skin steel panels. J Constr Steel Res 67(6):936–946. https://doi.org/10.1016/j.jcsr.2011.02.002
15. Mercan O (2013) Thesis -Nonlinear dynamic analysis of modular steel buildings in two and three dimensions, 214
16. Annan CD, Youssef M, Naggar MH (2005) Analytical investigation of semi-rigid floor beams connection in modular steel structures. In: 33rd annual general conference Can. Soc. Civ. Eng. Cite this Publ., pp 1–9, https://doi.org/10.13140/2.1.2010.3687
17. Sadeghinia M (2005) An analytical investigation into shear wall and slab interconnections between reinforced concrete modules for high rise buildings utilizing modular construction under extreme seismic loading and wind loading, PhD Thesis
18. Gunawardena T (2016) Behaviour of prefabricated modular buildings subjected to lateral loads PhD Thesis, 2016. ORCID: 0000-0001-6958-1470
19. Rafaela Sanches BR, Mercan O (2018) Experimental investigations of vertical post—tensioned connections for modular steel structures. Eng Struct 175:776–789, https://doi.org/10.1016/j.engstruct.2018.08.049
20. Jothiarun Dhanapal JV, Ghaednia H, Das S (2019) Structural performance of state of the art VectorBloc modular connector under axial loads. Eng Struct 183:496–509, https://doi.org/10.1016/j.engstruct.2019.01.023
21. Hwan Doh J, Ho NM, Miller D, Peters T, Carlson D, Lai P (2017) Steel bracket connection on modular buildings. J Steel Struct Constr 2(2), https://doi.org/10.4172/2472-0437.1000121

www.EngineeringBooksPDF.com

22. En-Feng Deng YD, Zong L (2018) Monotonic and cyclic rsponce of bolted connections with welded cover plate for modualr steel construction. Eng Struct 167(7):407–419, https://doi.org/10.1016/j.struct.2018.04.028
23. Liu XC, Pu SH (2015) Static and seismic experiment for bolted-welded joint in modualrised prefabricated steel structure. J Constr Steel Res 115(8):417–433, http://dx.org/10.1016/j.jcsr.2015.08.036
24. Andrew William Lacey WC (2019) Review of bolted inter-module connections in modular steel buildings. J Build Eng 23:207–219, https://doi.org/10.1016/j.jobe.2019.01.035
25. Pezman Sharafi BS, Mortazavi M (2018) Interlocking system for enhancing the integrity of multi-storey modular buildings. Autom Constr 85:263–272, http://doi.org/10.1016/j.autocon.2017.10.023

www.EngineeringBooksPDF.com

Application of Artificial Neural Network (ANN) in the Prediction of Displacement of RC Frame Subjected to Earthquake

R. Prabhakara, Pallavi Patil, Narayana Harish, and H. N. Jagannatha Reddy

Abstract The load response behavior of the structure subjected to earthquake load depends on many parameters. The responses can be broadly classified into three categories, namely zonal, soil, and structural response. Most of the designers and researchers rely upon the analytical method to see the complete performance of the structure which will enable them to design the structure for serviceability accurately. Several software have been developed to understand the structural behavior subjected to earthquake loading. The drawback of this analytical method is the failure of the models to represent explicitly important features like nonlinear behavior of structural system over the rate of change with time. It has been observed from the recent analytical studies that application of artificial neural network (ANN) is becoming very popular in the prediction of the behavior of the structure. In the present analytical studies, the ANN model was applied to predict the displacement of the structure using 462 data sets obtained from ETABS-16 results. The performance was compared over statistical parameters in terms of correlation coefficient (CC), root-mean-squared error (RMSE), and scatter index (SI). In addition, it was observed that ANN prediction provides an alternative method for predicting the structural behavior, especially in the case where it is difficult to model complex interaction.

Keywords Structural behavior · Response spectrum analysis · ETABS-16 · Artificial neural networks · Displacement · Statistical parameters

R. Prabhakara (✉)
Principal, Brindavan College of Engineering, Bengaluru 560063, India
e-mail: r.prabhakara@gmail.com

P. Patil
Department of Civil Engineering, Ramaiah Institute of Technology, Bengaluru 560054, India

N. Harish
Department of Civil Engineering, National Institute of Technology Goa, Ponda 403401, India

H. N. Jagannatha Reddy
Department of Civil Engineering, Bangalore Institute of Technology, Bengaluru 560004, India

© Springer Nature Singapore Pte Ltd. 2021

K. K. Pathak et al. (eds.), *Recent Trends in Civil Engineering*, Lecture Notes in Civil Engineering 77, https://doi.org/10.1007/978-981-15-5195-6_3

www.EngineeringBooksPDF.com

1 Introduction

Earthquake is defined as severe vibration of the earth, and it occurs due to the release of large amount of strain energy stored in the earth crust through the effective failure planes. The release of energy propagates vibration in horizontal and vertical directions which damage the structures. It is a challenging task for the engineers to design safe and economical structure which will perform satisfactorily against these types of natural calamities. Better understanding of the load response behavior of structure leads to safe and economical design. It was reported in the literature that the behavior of the structure under the earthquake loads is complicated because of several interconnected parameters, such as zone variation, soil characteristics, material properties, and structural system. Contemporary research in this area is on over the globe to obtain cost-effective structural systems which perform in a superior way during the earthquake. It is also supported by a fast computing system and latest developed software and it is possible to simulate actual load response behavior of the structure subjected to an earthquake with a high degree of accuracy. In this regard, the prediction of earthquake, artificial earthquake motion was used in seismic proof structural design and seismic hazard analysis to structure and machinery [1]. In this case, the fundamental and essential task is to set the earthquake hazard. There are various methods of simulating artificial earthquake motion; the method of superimposing sine wave to match the target response spectrum is widely used [1]. A response spectrum is simply a plot of the peak or steady-state response (displacement, velocity, or acceleration) of a series of oscillators of varying natural frequency, which are forced into motion by the same base vibration or shock. From the past, many analytical models were developed to study the load response behavior of structures [2–5], but they consume a lot of time and are expensive in terms of cost. To minimize the cost and time in conducting the analytical work, the soft computing tools like artificial neural network (ANN), adaptive neuro-fuzzy inference system (ANFIS), and so on [6–10] are widely used to predict an outcome.

Recently, researchers have used the ANN model in various fields of civil engineering [11, 12]. Külahcı et al. [13] used ANN to predict earthquake by random monitoring. Lagaros et al. [14] used ANN to predict nonlinear structural behavior. The seismic performance of liquid storage tanks using an ANN model was predicted by Razzaghi and Mohebbi [15]. Based on the results obtained, it was seen that the ANN model had great potential to predict the seismic performance of liquid storage tanks. Roxas and Ongpeng et al. [16] developed a way to predict the overall cost of the structure on Philippine construction project using the ANN model. Suryanita et al. [17] applied the ANN model for predicting the structural response (storey drift) of multi-storey reinforced concrete structures under the earthquake load in the Sumatra region. Khademi et al. [10] applied data-driven models to determine the displacement of concrete reinforced building. They used ANN, adaptive neuro-fuzzy inference system (ANFIS), and multiple linear regression model (MLR) to predict the displacements. Results obtained by them indicate that both the models showed excellent accuracy in predicting the displacements in a concrete frame.

www.EngineeringBooksPDF.com

From the literature review, it was found that response spectrum analysis for the RC building models subjected to earthquake loading, and the prediction of the deflection using artificial neural network was not carried out. In this study, an attempt has been made to obtain the deformation profile of a multi-storied building using the ANN model. In order to predict the performance of soft computing tool using backpropagation technique, the ANN model is used in the prediction of load response behavior and the influencing parameters.

2 Data Collection

Response spectrum of any building gives the plot of peak or steady-state response (displacement, velocity, or acceleration) of a series of oscillators of a varying natural frequency that are forced into motion by the same base vibration or shock. Three space frame models were considered in the present study. The floor plan was made identical (Fig. 1), whereas the numbers of stories were varied. Three space frame models (9 stories, 6 stories, and 3 stories) made up of reinforced concrete were considered (Figs. 2, 3 and 4). Fixed support condition was assumed, and soil–structure interaction effect was neglected in all models. Modal damping of 5% of the critical was considered in all models, in order to account for the material damping.

The design response spectrum functions for the RC building models subjected to earthquake loading are obtained from seismic hazard map of India. The performance of the structures in a space frame model was verified under zone III and IV for the locations such as Chennai, Kolkata, Delhi, and Mumbai, respectively. Response

Fig. 1 Typical floor plan

www.EngineeringBooksPDF.com

Fig. 2 Model 1: 3-storey

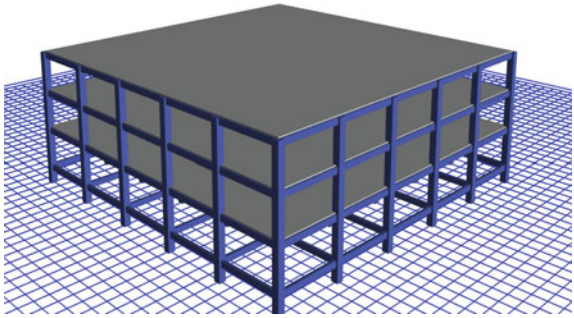

Fig. 3 Model 2: 6-storey

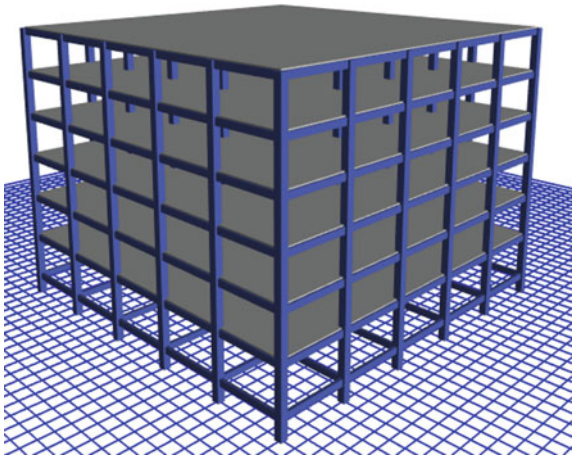

Fig. 4 Model 3: 9-storey

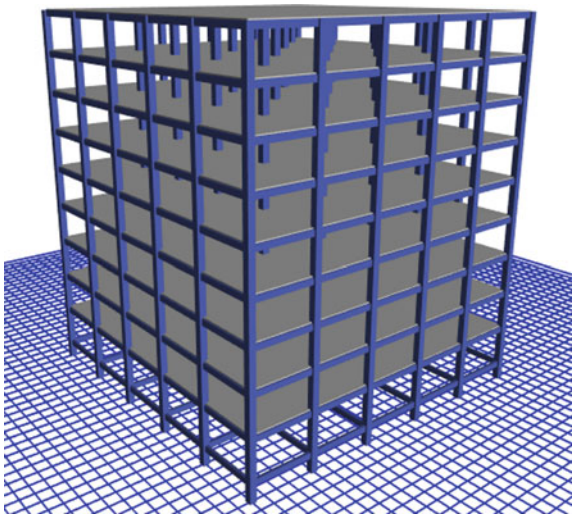

www.EngineeringBooksPDF.com

Table 1 Preliminary data of the space frame

Structural details				
Elements	Properties			Materials
Beams	230 × 450 mm			M30 concrete
Columns	500 × 500 mm			M30 concrete
Slab	175 mm			M30 concrete
Size of building	25 m × 25 m × 19.5 m			–
Number of stories: G + 2, G + 5, G + 8; typical storey height 3 m				
Loads on slabs and beams				
	Floor finishes kN/m^2	Live load, kN/m^2	Wall load, kN/m	Parapet load, kN/m (Exterior)
Floor slabs	1.5	3 (R = 0.25)	–	–
Roof slabs	1.5	1.5 (R = 0)	–	–
Floor beams	–	–	12.995	–
Roof beams	–	–	–	2.76

spectrum functions were obtained by taking three different ground conditions, which are hard, medium, and soft. The final loads on the frame and all other preliminary data of the plane frame model are given in Table 1.

The maximum and minimum values of data set for different single-family detached (SFD), SFV, and single-family attached (SFA) are shown in Table 2. The complete variation of the data set used for the data-driven models is shown in Fig. 5. The independent variables are zero peak acceleration (ZPA), SDS (design spectral accelerations at short periods), SD1 (design spectral accelerations at 1-second period), T0 and TS (characteristic time periods), soil condition, and building height. In addition, the dependent variable is displacement.

It was observed from Fig. 5 that the range and variation of data is appropriately distributed for both training and testing data set so that the prediction will be accurate.

3 Artificial Neural Network

An artificial neural network (ANN) is formed by a sequence of layers connecting each other through a neuron. ANN also has the ability to form nonlinear relationships between input and output parameters. Weighted input data is processed by ANN using various algorithms to obtain the desired output. The weight factors which are responsible for connections between the neurons in ANN are modified through the training process. With each iteration, the weight factors are modified, and at the end of the process, the desired output would be obtained. The focus here is to obtain the storey displacement with high accuracy, which will assist an engineer either in

www.EngineeringBooksPDF.com

Table 2 Range of data used for the development of ANN models

Network	Range	ZPA (g)	S_{DS} (g)	S_{D1} (g)	T_0 (sec)	Ts (sec)	Soil condition	Building height (m)	Displacement (mm)
SFD	Min	0.012	0.023	0.0053	0.041	0.210	1	1.50	1
	Max	0.125	0.600	0.4008	0.134	0.669	3	28.5	1810
SFV	Min	0.012	0.023	0.0053	0.041	0.210	1	1.50	–
	Max	0.125	0.600	0.4008	0.134	0.669	3	28.5	–
SFA	Min	0.012	0.023	0.0053	0.041	0.210	1	1.50	–
	Max	0.125	0.600	0.4008	0.134	0.669	3	28.5	–

www.EngineeringBooksPDF.com

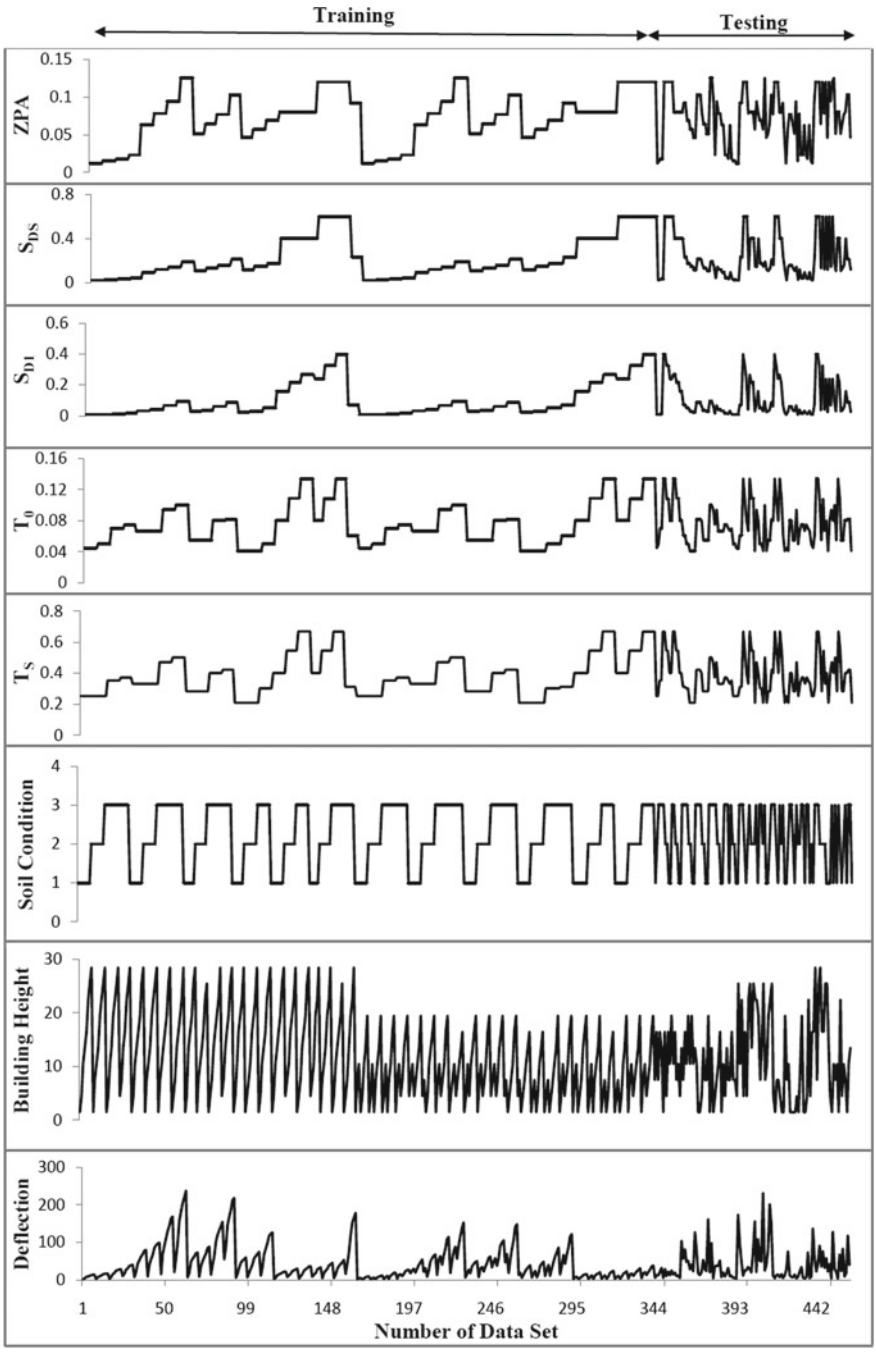

Fig. 5 The range of data set used in ANN model

www.EngineeringBooksPDF.com

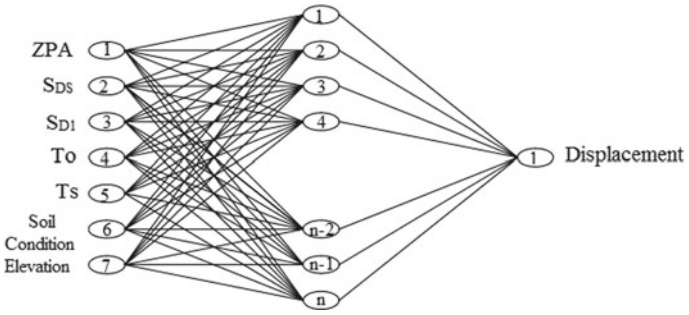

Fig. 6 Proposed backpropagation (BPNN) architecture

the design or in the evaluation of building condition due to earthquake loading and taking proper measures.

Backpropagation ANN with a Levenberg–Marquardt algorithm (LMA) (trainlm) [18] shown in Fig. 6 is used in this study. An input layer, hidden layer, and output layer together form the architecture of ANN. The input layer is formed by seven neurons, which denote seven input parameters. These include earthquake response spectrum functions (ZPA, S_{DS}, S_{D1}, T_0, and T_S), elevation, and soil condition. Whereas the output layer has one neuron, that is, to represent storey responses in the horizontal direction is shown in Fig. 6. With the help of response spectrum analysis, the data for target storey responses (displacement) was fed into the ANN, followed by errors and rate of prediction calculations. To achieve the highest rate of prediction, the number of hidden layer neurons, training parameters such as normalization range and learning rate are selected using trial-and-error. The aim of this ANN architecture was to obtain the ability to predict the storey displacement of the RC building models of any given elevation.

4 Results and Discussion

In the present study, ETABS-16 was used to analyze the structure with different storey height. A total of 462 data sets with seven independent variables, and one dependent variable were developed using ETABS-16. Data-driven model ANN was applied to predict the displacement of the structure. Further, the data set was divided appropriately into 80% for training, and the remaining 20% for testing the model. The accuracy of the model was checked by using statistical measures like correlation coefficient (CC), root-mean-square error (RMSE), and scatter index (SI), which are defined as:

$$CC = \frac{\sum_{i=1}^{n} \left(X_i - \bar{X}_i\right)\left(Y_i - \bar{Y}_i\right)}{\sqrt{\sum_{i=1}^{n} \left(X_i - \bar{X}_i\right)^2 \left(Y_i - \bar{Y}_i\right)^2}} \tag{1}$$

www.EngineeringBooksPDF.com

$$RMSE = \sqrt{\frac{1}{n}\sum_{i=1}^{n}(X_i - Y_i)^2} \tag{2}$$

$$SI = \frac{RMSE}{\overline{X_i}} \tag{3}$$

where X_i and Y_i are observed and predicted deflections, respectively, n is the number of data set used and $\bar{X}_i$ and $\overline{\bar{Y}_i}$ are averagely observed and predicted displacement, respectively.

5 Artificial Neural Network Model

In this study, the ANN model was developed using Matlab software [19], and the models were run in Lenova@ G50 with Intel® core ™ i5 CPU @ 2.67 GHz, and 4 GB RAM and 64-bit Windows 7 operating system. Initially, training and testing were carried out using different training algorithms and finally selected LMA as a better algorithm for the prediction model. Here the number of hidden layer and number of hidden nodes in the hidden layer were optimized for a constant 300 epochs in order to arrive at a better training algorithm.

Validation of the obtained results during the training and testing process, in the present study, was not done because the developed model was performing well with the test data set; hence there was no overfitting in the trained model. The CC, RMSE, and SI values are tabulated in Table 3. The CCs between observed output and predicted outputs were calculated using Eq. 1. The RMSE and SI between the observed output and predicted output were calculated using Eqs. 2 and 3, respectively.

The ANN model was trained for 346 data sets with hidden layers and varying hidden nodes in the hidden layers. It was observed in Table 3 that training CC was more than 0.9906, and RMSE was less than 6.22 for all ANN models. From this,

Table 3 Statistical measures of ANN model with different hidden layer and nodes

Model		CC	RMSE	SI
ANN1 (7-8-7-1)	Training	0.9906	6.2200	0.1436
	Testing	0.9895	6.5168	0.1591
ANN2 (7-13-7-1)	**Training**	**0.9930**	**5.3493**	**0.1235**
	Testing	**0.9911**	**5.9570**	**0.1454**
ANN3 (7-15-7-1)	Training	0.9933	5.2503	0.1212
	Testing	0.9906	6.1701	0.1506
ANN4 (7-20-7-1)	Training	0.9909	6.0884	0.1405
	Testing	0.9818	8.6414	0.2110

www.EngineeringBooksPDF.com

it was observed that the model was well trained with training data sets. Testing results obtained from the network for CC was more than 0.9818, and RMSE was less than 8.6414. This clearly shows that the ANN model is one of the better prediction models with accuracy and time-saving techniques. The ANN model was run for varying hidden nodes in the hidden layer, and the results were tabulated, as shown in Table 3. From Table 3, it was observed that with the ANN structure consisting of 7-13-7-1 gave better results compared to the other ANN structures. The scatter index for training and testing was less than 0.1436 and 0.2110, respectively, for all the ANN models. The CC graph for the best model that is ANN2 for training and testing CC was plotted, as shown in Figs. 7 and 8.

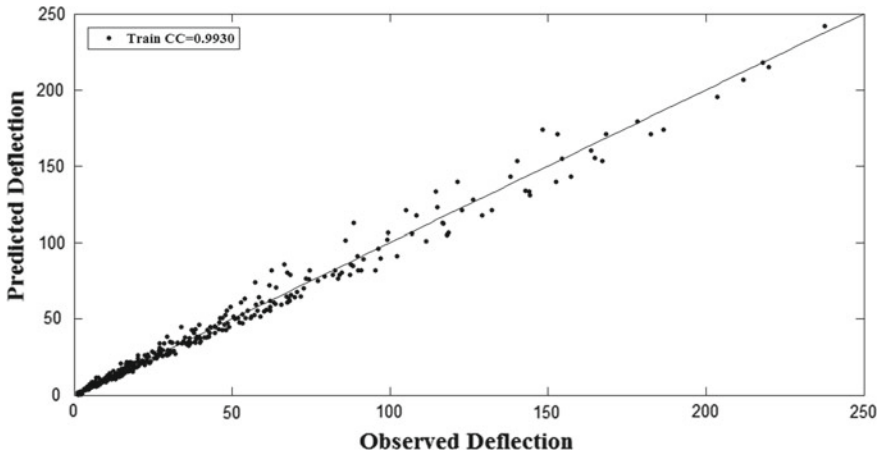

Fig. 7 45° Line training (7.13.7.1)

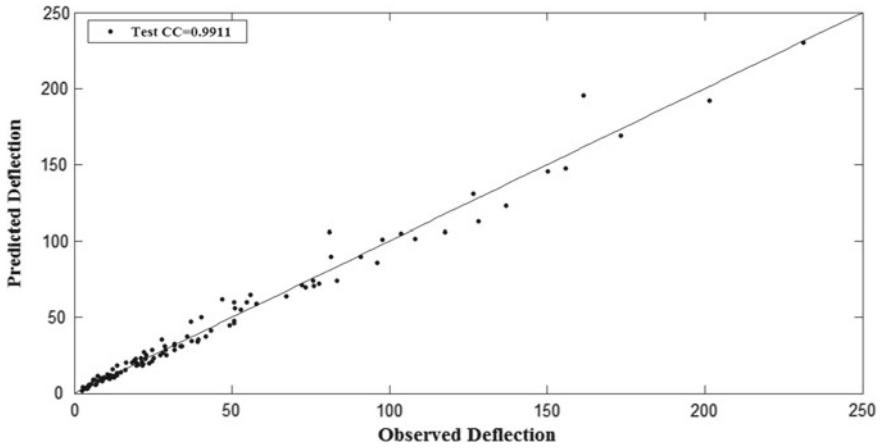

Fig. 8 45° Line test (7.13.7.1)

www.EngineeringBooksPDF.com

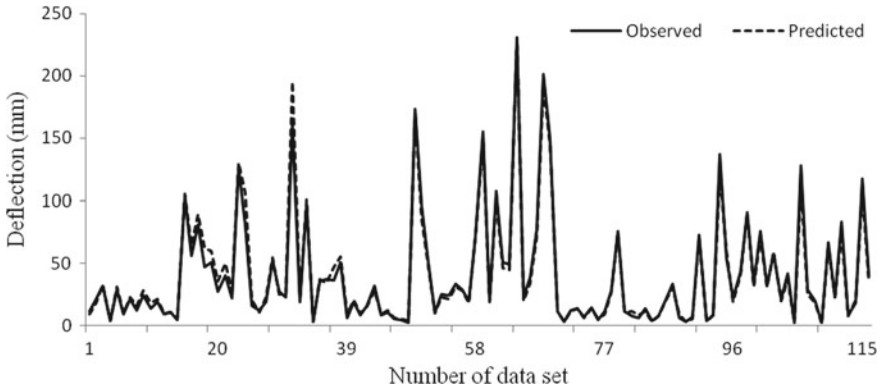

Fig. 9 Observed and predicting displacement

Figure 9 shows the behavior of displacement obtained from ETABS and ANN2 model. It was observed that displacement pattern for observed and predicted behaves in a similar manner. This concludes that ANN2 model has a capacity to predict any complex problem in the real world. So the ANN model can be used as an alternative tool for predicting the displacement of RC framed building when analyzed with the response spectrum method. From the results obtained we can conclude that our model does better than literature review models since our ANN training (7-13-7-1) model was found to be well trained with a CC of 0.9930 and also testing (7-13-7-1) model CC was coming about 0.9911. This signifies that the obtained model is a better while predicting the deflection.

6 Conclusions

In the present study, ETABS-16 was used to analyze the RC frame using response spectrum analysis to determine the deformation of the structure. The structure was analyzed for varying floor heights with constant bay. From the obtained data set, the ANN model was developed with hidden layers and varying hidden nodes with constant. The following conclusions were drawn:

- ANN trained with 462 data sets, the rate of prediction was calculated for displacement values in terms of CC are as high as 98%, and RMSE was less than 8.6414.
- The correlation coefficient CC falls in the range of 0.98 to 1 for all models. Hence they represent a strong positive relationship between independent and dependent variables.
- Based on the obtained results, it was inferred that ANN has the ability to make an early prediction of the structural response like storey drift of multi-storey buildings. This can be effectively used in a situation to assist FEM analysis further.

www.EngineeringBooksPDF.com

- Thus ANN can accurately model complex and nonlinear relationship among parameters of physical phenomenon such as those affecting the behavior of RC structure under response spectrum analysis.

Acknowledgements The authors are grateful to the Management, Brindavan College of Engineering, Bengaluru, India and the Director, National Institute of Technology Goa, India; for the support encouragement provided to them and for permission to publish.

References

1. Murthy CVR (2005) Earthquake tips, learning earthquake design and construction. Department of Civil Engineering, IIT Kanpur
2. Kunnath SK, Reinhorn AM, Park YJ (1990) Analytical modeling of inelastic seismic response of R/C structures. J Struct Eng 116(4):996–1017
3. Cavaleri L, Failla A, La Mendola L, Papia M (2005) Experimental and analytical response of masonry elements under eccentric vertical loads. Eng Struct 27(8):1175–1184
4. Belmouden Y, Lestuzzi P (2007) Analytical model for predicting nonlinear reversed cyclic behaviour of reinforced concrete structural walls. Eng Struct 29(7):1263–1276
5. Oh BK, Kim D, Park HS (2017) Modal response-based visual system identification and model updating methods for building structures. Comput Aided Civ Infrastruct Eng 32(1):34–56
6. Lazarevska M, Knezevic M, Cvetkovska M, Gavriloska TA (2014) Application of artificial neural networks in civil engineering. TehnickiVjesnik 21(6):1353–1359
7. Sharma V, Rai S, Dev A (2012) A comprehensive study of artificial neural networks. Int J Adv Res Comput Sci Softw Eng 2(10)
8. Alvanitopoulos PF, Andreadis I, Elenas A (2010) Neuro-fuzzy techniques for the classification of earthquake damages in buildings. Measurement 43(6):797–809
9. Arslan MH (2010) An evaluation of effective design parameters on earthquake performance of RC buildings using neural networks. Eng Struct 32(7):1888–1898
10. Khademi F, Akbari M, Nikoo M (2017) Displacement determination of concrete reinforcement building using data-driven models. Int J Sustain Built Environ
11. Li ZX, Yang XM (2008) Damage identification for beams using ANN based on statistical property of structural responses. Comput Struct 86(1):64–71
12. Harish N, Mandal S, Rao S, Patil SG (2015) Particle swarm optimization based support vector machine for damage level prediction of non-reshaped berm breakwater. Appl Soft Comput 27:313–321
13. Külahcı F, İnceöz M, Doğru M, Aksoy E, Baykara O (2009) Artificial neural network model for earthquake prediction with radon monitoring. Appl Radiat Isot 67(1):212–219
14. Lagaros ND, Papadrakakis M (2012) Neural network-based prediction schemes of the non-linear seismic response of 3D buildings. Adv Eng Softw 44(1):92–115
15. Razzaghi MS, Mohebbi A (2011) Predicting the seismic performance of cylindrical steel tanks using artificial neural networks. Acta Polytech Hungarica 8(2)
16. Roxas CLC, Ongpeng JMC (2014) An artificial neural network approach to structural cost estimation of building projects in the Philippines. In: Proceedings of DLSU Research Congress
17. Suryanita R (2016) The application of artificial neural networks in predicting structural response of multistory building in the region of Sumatra island. KnE Eng 1(1)
18. Hagan M, Menhaj M (1994) Training feedforward networks with the Marquardt algorithm. IEEE Trans Neural Netw 5:989–993
19. www.mathworks.com/access/helpdesk/help/pdf_doc/nnet/nnet.pdf (2017)

www.EngineeringBooksPDF.com

Fatigue Crack Growth Analysis Using Surrogate Modelling Techniques for Structural Problems

Geetu G. Kumar, T. Sivaranjani, D. V. T. G. Pavan Kumar, and C. L. Mahesh Kumar

Abstract This paper addresses the polynomial-based response surface models for fatigue crack growth problems. The fatigue crack growth behaviour of critical pin-loaded lug with through-the-thickness crack at a hole was analysed using finite-element (FE) tools. The stress intensity factor (SIF) and fatigue crack growth life for the incremental crack length of the attachment lug was predicted using Virtual Crack Closure Technique (VCCT) approach and crack growth laws, respectively. The polynomial-based surrogate model was built using the FE characterisation of the relationship between various crack parameters such as crack size, load applied, thickness, stress intensity factor and fatigue crack growth life. Then, using the developed model, stress intensity factors and fatigue crack growth life for various parameters were obtained without the help of FE tools. Hence, the computation cost of using finite-element tools was reduced.

Keywords Stress intensity factor · Fatigue crack growth life · Pin-loaded lug · Surrogate model

1 Introduction

The moving and the stationary operational duties of the mechanical systems are realised by the assembly of load transferring, which is known as the lug joint type. In such connection joints, due to cyclic loading, the contact pressure, high concentration stress factor and the fretting can lead to growth of crack initiation, and thus the growth of the crack can lead to the failure of the structure. A crack in a part will grow under conditions of cyclic applied loading and is called fatigue crack growth. In this work, damaged lug model was studied to predict the SIF. For each and every crack increment, the finite-element mesh was modified and then the SIF was obtained.

G. G. Kumar (✉) · C. L. Mahesh Kumar
Nitte Meenakshi Institute of Technology, Bengaluru, India
e-mail: geetugkumar@gmail.com

T. Sivaranjani · D. V. T. G. Pavan Kumar
Structural Technologies Division, CSIR-National Aerospace Laboratories, Bengaluru, India

© Springer Nature Singapore Pte Ltd. 2021

K. K. Pathak et al. (eds.), *Recent Trends in Civil Engineering*, Lecture Notes in Civil Engineering 77, https://doi.org/10.1007/978-981-15-5195-6_4

www.EngineeringBooksPDF.com

From the obtained SIF, incremental fatigue crack growth life was calculated using crack growth laws. In order to avoid the repeated finite-element analysis for each crack length and so on, here surrogate models were explored. Surrogate model is a type of engineering method used whenever the outcome or response cannot be measured easily, so a model of the response is used instead. Surrogate models are also known as response models, black-box models, meta-models or emulators and are simplified approximations of more complex, higher order models. Surrogate model explores the relationships between several input variables and one or more response variables.

Toribio [1] used the Paris law-based model to study the fatigue crack growth propagation in a plate, under cyclic loading, for the case of corner crack subjected to bending, tension and combination of both (tension + bending) loading conditions. Queipo [2] provided a broad discussion of the important issues that arise in surrogate-based analysis and optimisation. Using the data drawn from the high-fidelity models, the surrogate models were constructed to obtain the quick estimates of the objectives and the constraints at new design points, thereby creating the optimisation and sensitivity studies feasible. Boljanovic [3] and Mookaiya [4] evaluated the fatigue behaviour of the lug with through-the-thickness crack at the hole through numerical and analytical approaches.

2 Surrogate Modelling Techniques

The surrogate models available are polynomial response surface, kriging or Gaussian process regression, radial basis function, space mapping and artificial neural networks. In the present study, polynomial-based response surface model was explored. Polynomial response surface method (PRSM) is an approximation method, but they can be used because it is easy to estimate and apply, even when little is known about the process. These methods are used whenever there is a long computation time or complex problem where repeatedly the same operation will happen over and again. In order to avoid the computation time, response models can be built using the responses arrived from the design space variables and using those models further response results can be arrived for different design variables without much computation cost and time [2]. The polynomial regression is a type of regression analysis in which the relation between the dependent y and the independent variable x is modelled as a polynomial in x. Generally, these models are fit using the method of least squares. Polynomial-based RSM constructs the polynomial model by assuming the order and the coefficients that are unknown based on the regression analysis. The order of the polynomial and the number of design variables [5] involved are used to evaluate the number of coefficients required. Table 1 shows the different expressions based on the number of coefficients, order of the polynomial having single design

www.EngineeringBooksPDF.com

Table 1 A few examples of expressions available for the polynomial-based RSM

Order of polynomial	Regression
First (Linear)	$y = f(x) = ax + b$
Second (Quadratic)	$y = f(x) = ax^2 + bx + c$
Third (Cubic)	$y = f(x) = ax^3 + bx^2 + cx + d$
Fourth order	$y = f(x) = ax^4 + bx^3 + cx^2 + dx + e$
Fifth order	$y = f(x) = ax^5 + bx^4 + cx^3 + dx^2 + ex + f$

variable available for the polynomial-based response surface methods with single response.

The following procedure was adopted to arrive at the response models.

Quadratic response model, $y = ax^2 + bx + c$, where a, b and c are the coefficients to be determined.

2.1 Method of Least Squares

Residual (R) of the model

$$R = y - \left(ax^2 + bx + c\right) \tag{1}$$

Sum of squares of residuals is minimum

$$S = \sum_{i=1}^{n} \left[y_i - \left(ax_i^2 + bx_i + c\right)\right]^2 \tag{2}$$

To minimise the error, the above equation was partially differentiated and equated to zero as shown in (3)

$$\frac{\partial S}{\partial a} = 0, \frac{\partial S}{\partial b} = 0 \text{ and } \frac{\partial S}{\partial c} = 0 \tag{3}$$

Further solving the simultaneous equations obtained from differentiation, the coefficients can be estimated. Using the above method, polynomial-based single response surface models were derived for structural problems such as static, fatigue and fatigue crack growth. Here, the fatigue crack growth analysis of the attachment lug with single through-the-thickness crack specimen was considered for further study.

www.EngineeringBooksPDF.com

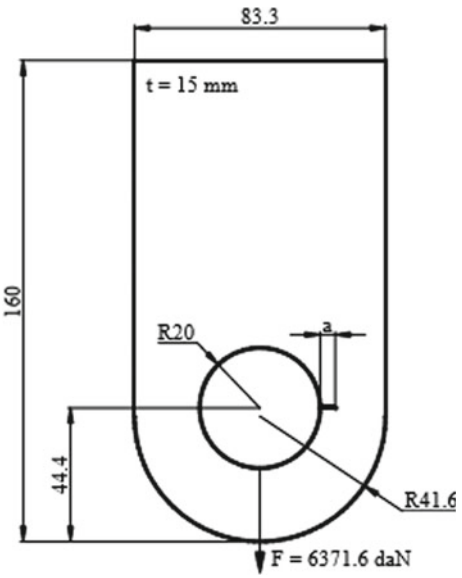

Fig. 1 Geometry of lug

3 Fatigue Crack Growth Analysis of Lug with Initial Through-the-Thickness Crack

3.1 Geometry of the Lug

SIF calculation was carried out for single through-the-thickness crack for a lug. The lug is subjected to axial loading with constant amplitude (P_{max} = maximum force = 63716 N and stress ratio $R = 0.1$), has a diameter of $2r = 40$ mm and the initial crack length $a = 5$ mm. The geometric sizes are shown in Fig. 1. The lug is made up of 7075 T7351 aluminium alloy having modulus of elasticity (E) as 72 GPa and Poisson's ratio as 0.3. The crack growth parameters are: C (intercept) is 6.9×10^{-12} m/cycles and m (slope) is 3.

3.2 Loads and Boundary Conditions

The lug is subjected to the stress level: $\sigma = \sigma_{max} = 98.1$ N/mm^2 and $\sigma_{min} = 9.81$ N/mm^2 and the corresponding axial force, $F_{max} = \sigma(\text{w} - 2\text{R})\, t = 63716$ N. The lug is clamped at the top end.

www.EngineeringBooksPDF.com

3.3 Analytical Procedure

Development of a suitable computational procedure for determining the crack growth is one of the main tasks in the study of lug-type structures. To accurately assess fatigue crack growth in lug, it is essential to analyse fatigue crack growth behaviour at the point of maximum stress concentration. The fatigue crack propagation life [6] can be described by the Walker equation (R ratio is 0.1), as shown in Eq. (4):

$$\frac{da}{dN} = \frac{C(\Delta K)^m}{(1-R)^{m(1-\lambda)}} \tag{4}$$

where da/dN = crack growth rate, C = intercept, m = slope on the log–log plot, K = stress intensity factor.

When the fatigue performance is taken into consideration, the presence of stress concentrators such as notches, corrosion pits, holes, cut outs, manufacturing damages is the main cause that greatly affects the structure. Owing to this, the initiation of the crack takes place which leads to the crack growth and then it even leads to the failure of the structure. In fracture mechanics, by examining the SIF, the fatigue behaviour of nonlinear stress fields can be obtained, as expressed in Eq. (5):

$$\Delta K = Y * \Delta S * \sqrt{\pi a} \tag{5}$$

where ΔK is the SIF range, Y is the corrective factor [3] and ΔS denotes applied stress range.

In failure analysis, the corrective factor that consists of two corrective functions are used to examine the geometry of the cracked lug, as shown in Eqs. (6–9)

$$Y = \left[\frac{w}{D} - 1\right] F_1\left[\frac{a}{l_1}, \frac{D}{H}\right] F_2\left[\frac{w}{D}, \frac{2a}{D}\right] \tag{6}$$

where 'w' is the width of the lug, 'D' is the diameter of lug and 'H' is height of the lug head.

$$F_1\left[\frac{a}{l_1}, \frac{D}{H}\right] = \frac{\frac{a}{l_1} f\left(\frac{D}{H}\right) + 10^{-3}}{\frac{a}{l_1} + 10^{-3}} \tag{7}$$

$$f\left(\frac{D}{H}\right) = 0.72 + 0.52\left(\frac{D}{H}\right) - 0.23\left(\frac{D}{H}\right)^2 \tag{8}$$

where $l_1 = \frac{w-D}{2}$

www.EngineeringBooksPDF.com

$$F_2\left[\frac{w}{D}, \frac{2a}{D}\right] = 27.754\left(\frac{2a}{D}\right)^5 - 44.092\left(\frac{2a}{D}\right)^4 + 12.485\left(\frac{2a}{D}\right)^3 + 12.988\left(\frac{2a}{D}\right)^2 - 9.037\left(\frac{2a}{D}\right) + 3.048 \quad (9)$$

Further, in the crack growth investigation, the above formula was used to arrive at the SIF for various crack lengths. By the means of FE tools, the fatigue failure analysis for an attachment lug with through-the-thickness crack was numerically tackled. Thus to define a complex stress state of a cracked lug, FE methods are used in a step-by-step procedure for the approximate increments of crack length.

3.4 FE Modelling and Fracture Mechanics Analysis

The FE model was developed using the given geometry, loading and boundary conditions. The CQUAD4 elements were used for generating the model. The load was applied at the centre of the lug hole using rigid body elements (RBE2) which were created for the lower half of the lug hole, as shown in Fig. 2. The mesh size of 0.5 mm was chosen based on the convergence study. The stress intensity factor results obtained from the FE analysis using VCCT approach were compared with the analytical results [3] and are shown in Table 2.

From the SIF obtained, the incremental fatigue crack growth life was calculated for each crack increments using the Walker equation and then the cumulative life

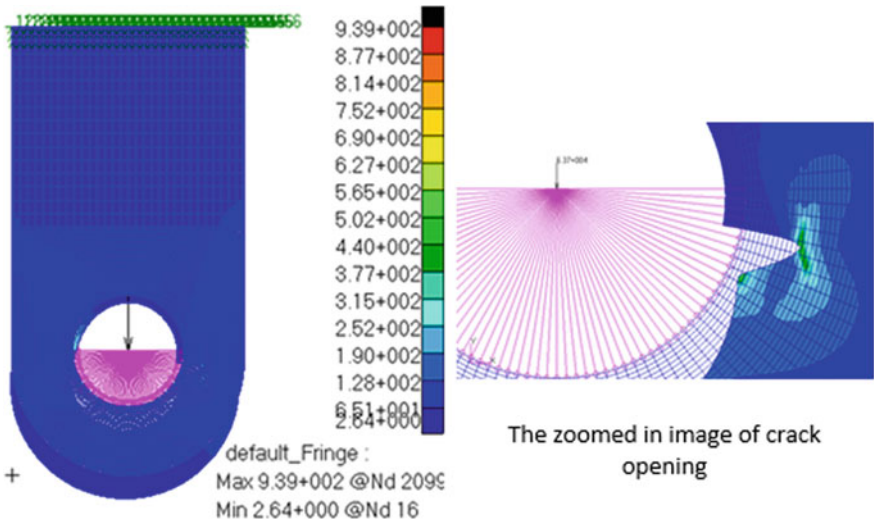

Fig. 2 FE model for lug

www.EngineeringBooksPDF.com

Table 2 SIF of lug for different crack sizes

Crack size (mm)	Beta (β)		Stress intensity factor K (MPa $\sqrt{m}$)	
	Analytical	FEM	Analytical	FEM
5.0	1.7866	1.81928	21.96	22.36
5.5	1.7278	1.74751	22.27	22.52
6.0	1.6813	1.68586	22.63	22.70
6.5	1.6455	1.63264	23.06	22.88
7.0	1.6188	1.58655	23.54	23.07
7.5	1.5997	1.54660	24.08	23.28
8.0	1.5866	1.51202	24.67	23.51
8.5	1.5782	1.48223	25.29	23.75
9.0	1.5730	1.45673	25.94	24.02
9.5	1.5700	1.43517	26.60	24.31
10.0	1.5682	1.41726	27.26	24.63

was calculated by the sum of all incremental lives. Using the above FE procedure, the SIF and fatigue crack growth life for different input variables such as crack size, thickness of the lug and loading were computed and those data were used to obtain the response surface model.

4 Polynomial-Based Response Model for Lug Analysis

In the present study, polynomial regression (linear, quadratic and cubic) was explored for single response arrived from single input variable. Using the training data generated, all the three models were trained and then the best model was chosen based on the error estimation. For the response surface model derivation using the generated data, MATLAB programmes were written and the root-mean-squared error was determined, which was used to find the best fit.

- Polynomial-based response model for SIF (output response) was obtained for different crack sizes (input variable) using the linear, quadratic and cubic polynomials with single variable and the results obtained from the model are given in Table 3.

From the above table, it is clear that cubic model outperforms both the linear and quadratic model with least error. The equation used for the cubic model was:

$$K = 3.323 \times 10^6(a^3) - 3.997 \times 10^4\left(a^2\right) + 472.3(a) + 20.59 \tag{10}$$

www.EngineeringBooksPDF.com

Table 3 Polynomial-based model to obtain the SIF

Design variable	Response (K (SIF) (MPa $\sqrt{m}$))						
Crack size (m) 'a'	FEM	Linear model	Error %	Quadratic model	Error %	Cubic model	Error %
0.0055	22.52	22.43	−0.4338	22.53	0.0491	22.53	0.0124
0.0060	22.70	22.66	−0.1652	22.69	−0.0145	22.70	0.0104
0.0065	22.88	22.89	0.0587	22.87	−0.0363	22.88	0.0110
0.0070	23.07	23.12	0.2246	23.06	−0.0311	23.07	0.0112
0.0075	23.28	23.35	0.3235	23.28	−0.0099	23.28	0.0113
0.0080	23.51	23.59	0.3459	23.51	0.0158	23.51	0.0111
0.0085	23.75	23.82	0.2822	23.76	0.0342	23.75	0.0092
0.0090	24.02	24.05	0.1282	24.03	0.0383	24.02	0.0091
0.0095	24.31	24.28	−0.1243	24.32	0.0171	24.31	0.0094
0.0100	24.63	24.51	−0.4822	24.62	−0.0397	24.63	0.0090
RSME		**0.0762**		**0.0087**		**0.00315**	
Validation of the response model							
Crack size	FEM	Cubic model					
0.0045	22.19	22.21					
0.0120	26.25	26.24					
0.0076	23.30	23.36					

Using the above obtained response surface model, for the intermediate values of crack sizes, SIF was calculated without the help of FE method and the results were validated with FEM results. Root-mean-squared error (RMSE) is known as the fit standard error and the standard error of the regression. It is defined as

$$RMSE = s = \sqrt{MSE} \tag{11}$$

where MSE is the mean squared error,

$$MSE = \frac{SSE}{V} \tag{12}$$

where SSE is the sum of squares due to error and is defined as

$$SSE = \sum_{i=1}^{n} \left(y_i - \widehat{y_i}\right)^2 \tag{13}$$

where y_i is the observed response value and $\widehat{y_i}$ is the fitted response value. 'v' is defined as the number of response values 'n' minus the number of coefficients 'm' from the response values.

www.EngineeringBooksPDF.com

Table 4 Polynomial-based model to obtain the fatigue crack growth life for varying stresses

Design variable	Fatigue crack growth life (N_f (cycles))				
Stress (N/mm^2) 'S'	FEM	Linear model	Error %	Quadratic model	Error %
94	55416	55050	0.6605	55403	0.0233
95	53684	53575	0.2036	53691	−0.0137
96	52024	52100	−0.1457	52039	−0.0292
97	50431	50625	−0.3831	50445	−0.0281
98	48903	49150	−0.5038	48911	−0.0164
99	47436	47675	−0.5026	47436	0.0005
100	46027	46200	−0.3744	46020	0.0166
101	44673	44725	−0.1141	44662	0.0252
102	43372	43250	0.2833	43364	0.0195
103	42102	41775	0.7785	42125	−0.0531
RMSE		**240.17**		**14.52**	
Validation of the response model					
Stress	FEM	Quadratic model			
92	59109	59003			
98.5	48162	48166			
106	38645	38761			

- Polynomial-based response model for fatigue crack growth life (output response) was obtained for different applied stresses (input variable) keeping the crack growth as constant from 5 to 10 mm having the crack growth increment of 0.5 mm, using the linear and quadratic polynomials and the results obtained from the model are given in Table 4.

From the above table, it is clear that quadratic model outperforms the linear model with the least error. The equation used for the quadratic model was:

$$K = 29.509\left(S^2\right) - 7288.6(S) + 479790 \tag{14}$$

Using the above obtained response surface model, for the intermediate values of applied stresses, fatigue crack growth life was calculated without the help of FEM and the results were validated with FEM results.

- Polynomial-based response model for fatigue crack growth life (output response) was obtained for different thickness of the lug (input variables) keeping the crack growth from 5 to 10 mm having the crack growth increment of 0.5 mm, using the linear, quadratic and cubic polynomials and the results obtained from the model are given in Table 5.

From Table 5, it is clear that cubic model outperforms both linear and quadratic models with the least error. The equation used for the cubic model was:

www.EngineeringBooksPDF.com

Table 5 Polynomial-based model to obtain the fatigue crack growth life for varying thickness

Design variable	Fatigue crack growth life (N_f(cycles))						
Thickness in mm '*t*'	FEM	Linear model	Error %	Quadratic model	Error %	Cubic model	Error %
0.0100	14445	12890	10.769	14500	−0.306	14451	−0.011
0.0105	16722	16168	3.316	16714	0.109	16727	0.004
0.0110	19227	19446	−1.138	19195	0.221	19231	0.011
0.0115	21970	22724	−3.431	21942	0.179	21974	0.012
0.0120	24949	26002	−4.218	24954	0.028	24967	−0.039
0.0125	28214	29280	−3.777	28233	−0.026	28220	0.007
0.0130	31737	32558	−2.586	31777	−0.082	31745	0.003
0.0135	35541	35836	−0.827	35587	−0.086	35552	0.000
0.0140	39639	39114	1.324	39663	−0.022	39651	−0.001
0.0145	44040	42392	3.740	44004	0.115	44054	−0.003
RMSE		**1080.52**		**39.09**		**4.52**	
Validation of the response model							
Thickness	FEM	Cubic model					
0.00800	7396	7420					
0.01225	26555	26552					
0.01600	59365	59169					

$$K = 1.421 \times 10^{10}\left(t^3\right) + 9.42 \times 10^{6}\left(t^2\right) - 12.37 \times 10^{4}(t) + 531.7 \qquad (15)$$

Using the above obtained response surface model, for the intermediate values of applied thickness, fatigue crack growth life was calculated without the help of FEM and the results were verified with FEM results.

5 Conclusions

Fracture mechanics analysis of the lug having single through-the-thickness crack was studied to find out the SIF for different crack lengths. The finite-element results were validated with the analytical results. Using the same FE procedure, training data were generated to develop the response surface model having SIF and fatigue crack growth life as response and crack length, thickness and applied load as input design variables. Root-mean-squared error (RMSE) was used to arrive at the best fit model. Cubic model was performing well for SIF prediction, when crack length was varied. Quadratic model was performing for fatigue crack growth life, for load variation. Cubic model was performing for fatigue crack growth life for thickness. The response models arrived at were checked for the values which were not present

www.EngineeringBooksPDF.com

in the training data to generate the models. Hence, the response surface model can be used in place of finite-element analysis, where repeated analyses or repeated long calculations are required. The real benefit of the developed surrogate models for SIF and fatigue crack growth life will be realised when those models are used in structural optimisation of aerospace/civil/mechanical structures where fatigue crack growth parameters act as design variables and fatigue crack growth life as constraint or objective.

Acknowledgments The authors would like to thank the authorities of CSIR - National Aerospace Laboratories, Bengaluru and Nitte Meenakshi Institute of Technology, Bengaluru, for their continuous support in carrying out the present work.

References

1. Toribio J, Matos J-C, González B (2017) Corrosion-fatigue crack growth in plates: amodel based on the Paris Law. https://doi.org/10.3390/ma10040439
2. Queipo NV, Haftka RT, Shyy W, Goel T, Vaidyanathan R, Kelvin Tucker P (2005) Surrogate-based analysis and optimization. J Progr Aerospace Sci 41(1):1–28
3. Boljanovic S, Maksimovic S (2017) Fatigue damage analysis of wing-fuselage attachment lug. In: 2nd international conference on structural integrity, vol 5, pp 801–808
4. Mookaiya K, Balaji S, Balakrishan SR (2013) Crack growth analysis in aircraft wing lug section and fatigue life estimation. Int J Eng Res Technol 2(6) ISSN: 2278-0181
5. Chandrashekar KS (2014) Engineering Mathematics-III. Sudha Publications
6. Keerthi HG, Sivaranjani T, Pavan Kumar DVTG, Manjuprasad M, Dinesh SV (2013) Fatigue life prediction of plates with multiple stress concentration zones using FEM. In: International conference on computer aided engineering (CAE-2013), IIT Madras

www.EngineeringBooksPDF.com

Dynamic Response of RC Slab Under Drop Test Retrofitted with CFRP Strips Using NSM Technique

Nandeesh M. Sreenivasappa, Arjun R. P. Reddy, H. N. Jagannatha Reddy, and R. Prabhakara

Abstract Slabs are two-dimensional structural elements in a storied building that provide large useful area for working during construction and even after occupancy. The effect of impact loads on slabs was not studied effectively due to lot of constraints, like lack of experimental setup, cost of sophisticated equipment, boundary conditions and so on. Drop test on slabs is gaining importance in recent years due to its simplicity in experimental setup while measuring the dynamic response of slabs under impact loads with a reasonable degree of accuracy. An experimental investigation was conducted on simply supported two-way RC slab under three drop heights to study the variation in the dynamic response of strengthened slab by near-surface mounting (NSM) technique over normal RC slabs. The dynamic response was studied over different height of impact and change in concrete grade, and the effect of strengthening was recorded using an accelerometer mounted at the bottom of slab. All the slabs were tested as simply supported with the drop weight impacting at the centre of the slab on the top surface. It was observed from this experimental result that the height of the drop and strengthening technique influence the dynamic behaviour of RC slab. Peak displacement, acceleration and damage index in terms of energy required per unit length of crack were compared to demonstrate change in the dynamic behaviour of RC slabs. It was interesting to note that the sudden change in the response of RC slabs over the different kinetic energy needs further detailed investigations.

N. M. Sreenivasappa (✉)
Department of Civil Engineering, M. S. Ramaiah Institute of Technology, Bangalore 560054, India
e-mail: nandeeshms@gmail.com

A. R. P. Reddy · H. N. Jagannatha Reddy
Department of Civil Engineering, Bangalore Institute of Technology, Bangalore, India
e-mail: arjunreddy.rp@gmail.com

H. N. Jagannatha Reddy
e-mail: jagannath.priyadhi@gmail.com

R. Prabhakara
Structural Engineering Division, Visvesvaraya Technological University, Belagavi 590018, India
e-mail: r.prabhakara@gmail.com

© Springer Nature Singapore Pte Ltd. 2021

K. K. Pathak et al. (eds.), *Recent Trends in Civil Engineering*, Lecture Notes in Civil Engineering 77, https://doi.org/10.1007/978-981-15-5195-6_5

www.EngineeringBooksPDF.com

Keywords NSM technique · Drop test · Dynamic response · Damage index

1 Introduction

Slabs are designed for static loading only; however, it is subjected to various sudden impact loads such as drop of objects during the construction, accidental events in industrial floor spaces and natural calamities. All these loads induce distress in the slabs for which they are not designed. The effect of impact loading on two-way slab is very rarely studied due to complex phenomenon with the involvement of many parameters and requires more time and requires difficult test setup, which has discouraged the widespread study [1]. In recent days, drop test has emerged as an effective way of studying the impact behaviour of slabs [2, 3]. The main reason for its popularity is simplicity of test setup and ease of experimentation. The drop test involves an impact of mass onto the slab and recording the response in terms of acceleration, velocity, displacement signatures and damage formation which are bound to vary with the change in kinetic energy given by Eq. 1.

TE = Static Energy stored due to the height of drop weight = Kinetic Energy of the drop weight just before impact.

$$\mathrm{TE} = \mathrm{mgH} = 1/2\mathrm{m}\,(\mathrm{gt})^2 \tag{1}$$

It has been observed from the literature that the dynamic response of the slab depends on the kinetic energy of the system (height of drop), and the influence of key parameters such as concrete grade, reinforcement ratio, geometry and boundary conditions needs to be understood from the design perspectives [4]. Retrofitting of existing structures is economically viable to push the service life of the structures over reconstruction of entire structure. Several strengthening methods and high-performance materials proved to be more efficient in the recent days. Out of many methods near-surface mounted (NSM) technique is one such retrofitting method gaining interest among the research community, which involves embedding of additional reinforcement in the form of bars or strips in the groove made in concrete cover [4, 5]. The use of NSM with CFRP strip is the latest method for increasing both flexural and shear strength of deficient reinforced concrete (RC) beams and slabs. The present study focused on the acceleration response of the RC slabs with change in grade of concrete (M20 and M70) for different drop heights of two-way RC slab retrofitted using NSM technique.

2 Literature Review

Owing to complexities involved in the testing of the slab under dynamic or impact loading, the available literatures are very less, however, a few of the literature surveyed are as follows:

www.EngineeringBooksPDF.com

Hrynk and Vecchio [6] studied the behaviour of NSC slabs and steel FRC slabs under high-mass, low-velocity impact and concluded the following:

- The crack pattern was observed to be aligned with the reinforcement grid on both the faces.
- Punching shear cracks were seen to form from the circumferential cracks around impact area.
- Impact capacity was measured as the total kinetic energy imparted to the slab.
- Effect of impact energy was not different for different reinforcement ratio but varied with the change in fibre content in the mix.
- Displaced shapes of slabs showed distinct punching cones under repeated loading.
- Inertial response of the slab under impact loading was believed to be the main cause of punching shear failure.

Ozgur et al. [7] presented an experimental and analytical study on the behaviour of reinforced concrete slabs under impact loading. Both experimental and analytical study considered application of impact loads to the specimens by dropping a standard weighing hammer of 5.25 kg from a height of 500 mm while varying the support conditions.

- The behaviour of slabs due to impact loads depends significantly on support type and support layout.
- Supports with higher stiffness showed lower acceleration, thus leads to lower velocity and displacements.
- Specimens with two opposite-sided support layout exhibited better performance compared to two adjacent-sided support layouts.
- The increase in damage with the number of drops resulted in decrease in accelerations.

Ramanna [8] in his doctoral thesis has shown that the use of near-surface mounted carbon fibre polymer (NSM-CFRP) reinforcement, such as FRP strips, produces an increase of flexural strength. In this study, the response of reinforced beams and slabs subjected to static or impact loads was observed. The experimental work consisted of a total of 23 number of beams and four slabs for testing. The performance of beams and slabs under impact loads was studied using the acceleration time histories. A single degree of freedom elasto-plastic was developed to capture their dynamic behaviour.

- Retrofitted slab was seen to show two times higher load carrying capacity than the control slab under static loading.
- The deflections in the retrofitted slab were found to be nearly half of the control slab which indicates that the slab was stiffened with the strengthening and thus ductility reduced.
- Retrofitted slab exhibited three times higher stiffness than control slab under dynamic loading.
- Strengthening of the slab was seen to avoid punching shear failure.

www.EngineeringBooksPDF.com

3 Objectives

The following objectives were identified for the present study:

- To conduct drop test on slabs to evaluate the dynamic response behaviour of slabs.
- To record the change in dynamic response of different grade of concrete and when slabs are strengthened with NSM technique.

4 Materials Used in the Current Study

The materials used in the present investigation were characterized in accordance with the standard procedure as follows:

CEMENT: OPC of 53 grade conforming to IS 12269-2013.

AGGREGATES: The fine and coarse aggregates confirming to IS 383-1970.

REINFORCEMENT: Confirming to IS 1786: 2008.

ADMIXTURE: For the present work, for M70 concrete, Master Glenium Sky 8233 was used and Siri plast was used for producing M20 concrete.

WATER: As per IS 456:2000, both for mixing and curing, potable water was used which was free from injurious salts.

CFRP laminates and the epoxy used were "Nitowrap CFP" and "Nitowrap 40" which was sponsored by FOSROC CHEMICALS, Bangalore, for retrofitting both NSC and HSC slabs.

The mix design of M20 was done in accordance with IS 10262, and M70 was done with 1.5% superplasticizer dosage as per Prabhakara et al. [9] mix design. The mix proportions, fresh properties and the strength gain with age are presented in Tables 1, 2 and 3, respectively.

5 Specimen Casting and Strengthening by NSM Technique

A total of 12 number of slabs were cast for impact test, out of which six were control slabs and six were NSM strengthened slab. Slabs of two grades M20 and M70 were casted with a reinforcement ratio of 0.341% to study the change in the dynamic

Table 1 Trial mix design specifications for NSC and HSC [10, 11]

Ingredient	M20	M70
Water/cement ratio	0.5	0.3
Cement	405.00 kg/m^3	500
Coarse aggregate	904.40 kg/m^3	714
Fine aggregate	801.33 kg/m^3	1000
Water	202.50 kg/m^3	150
Superplasticizer	Nil	7.47

www.EngineeringBooksPDF.com

Table 2 Fresh properties of concrete [10, 11]

Concrete	Property	Standard values	Obtained values
M20 (NSC)	Slump (mm)	Medium = 50–100	115
		High = 100–150	
	Compaction factor	Medium >0.92	0.944
		High >0.95	
M70 (HSC)	Slump (mm)	Medium = 50–100	108
		High = 100–150	
	Flow rate	>100%	124%

Table 3 Test results of concrete used for casting at different ages [10, 11]

Days	M20	M70
Compressive strength (MPa)		
3	15.11	49.05
7	24.29	65.07
28	26.47	71.61
Split tensile strength (MPa)		
3	1.83	4.06
7	2.31	5.47
28	2.63	5.95
Flexural strength (MPa)		
3	2.08	4.63
7	2.94	5.52
28	3.12	5.92

behaviour of slab with change in grade of concrete. The specimens casted were of size 1 m × 1 m × 0.1 m for studying the behaviour of slabs in impact loading by varying the grade of concrete for a constant reinforcement ratio. The dimensions and reinforcement details are provided in Fig. 1. The slabs without NSM strengthening were identified as control slabs with marking NSM0 and the strengthened slabs were designated as NSM1. The strengthening of slabs was done by NSM technique using CFRP strips. The strengthening was done in diagonal direction based on earlier researches [12]. A zone of NSM strengthening marked by L/5.31 from the ends of the slab was identified [8].

The groove size to embed the CFRP strips is arrived upon from previous literatures [13] and a typical groove dimensions with respect to the strip dimension is as shown in Fig. 2. The CFRP strip used in the study was 1.6 mm thick and 10 mm width. Based on these dimensions the groove depth was computed as 1.5 × 10 = 15 mm and groove width as 3 × 1.4 = 5.2 mm (Figs. 3 and 4).

www.EngineeringBooksPDF.com

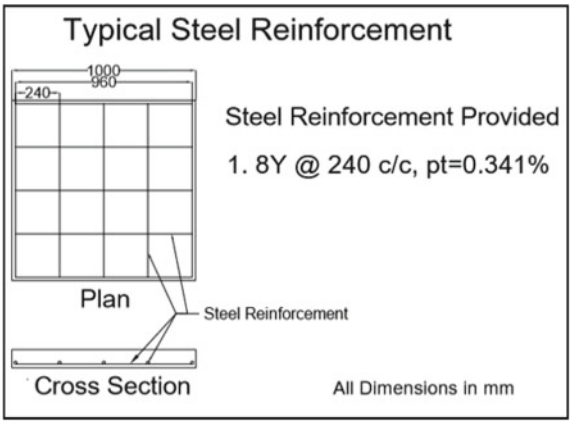

Fig. 1 Reinforcement details of slab

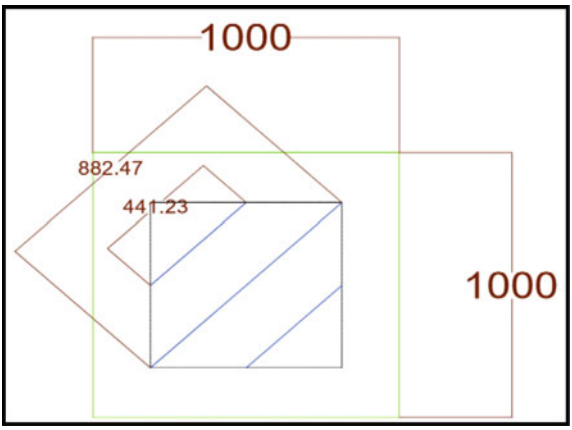

Fig. 2 Typical NSM strengthening

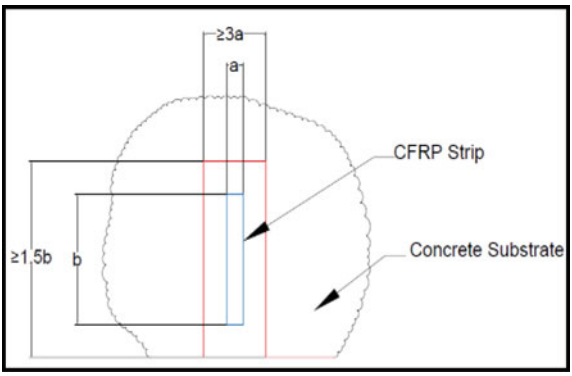

Fig. 3 Typical groove dimensions

www.EngineeringBooksPDF.com

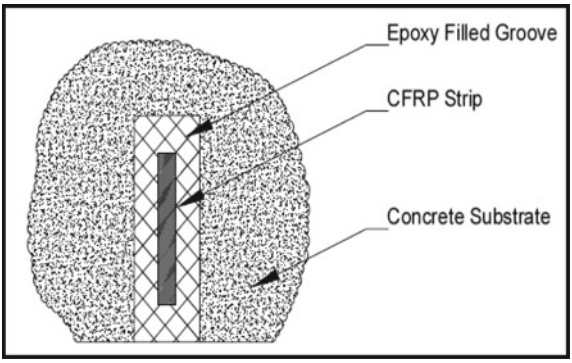

Fig. 4 Typical groove details

The system of strengthening involved the following steps:

1. Groove cutting: In this step the groove to be made is marked and cut along the required direction.
2. Chiselling: In this step the groove made from the cutting machine is widened to suit the required groove size.
3. Cleaning: The groove is then cleaned with an air blower to remove any fine dust remaining from the groove cutting procedure.
4. Primer application: In this step the primer, Nitowrap 30 is applied to the groove using a brush and left to set for 24 h.
5. Adhesive application: After 24 h have passed since the primer application of the epoxy, Nitowrap 40, which is prepared by mixing the base and hardener is applied onto the groove.
6. Installation of FRP strips: The CFRP strips which have been cut into required lengths and width are then inserted into the groove filled with epoxy.
7. Filling adhesive on top of strips: The top portion of the groove which has the strips exposed is then filled with another coat of epoxy to cover it completely.
8. Levelling of excess adhesive: The excessive adhesive applied is then scraped off from the groove sides to produce the finished product.
9. Curing: The strengthened specimen is then left to curing in air as specified by the company datasheet.

6 Experimental Setup

The impact test on slab was done using a drop test. The test setup consists of a drop weight, represented in Fig. 5; the loading frame was used; a pulley and a rope arrangement was fixed to lift the weight as shown in Fig. 6; and a four-channel dynamic data acquisition system (DDAS) (Figs. 7 and 8) and accelerometers used to study the response shown in Fig. 9 are used. The accelerometer was fixed on the bottom face of slab at the locations indicated in Fig. 10.

www.EngineeringBooksPDF.com

Fig. 5 Drop weight of 70 kg

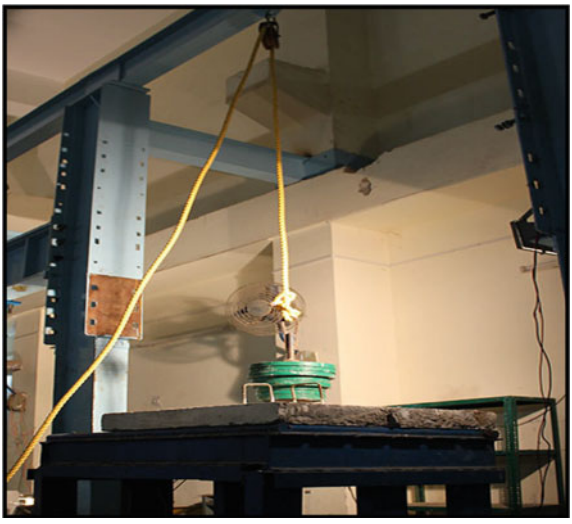

Fig. 6 Pulley and rope assembly

7 Experimental Procedure

All the slabs were dried and whitewashed, to have a smoother surface and to identify crack formation, propagation of cracks and measuring crack width during testing. The location to fix accelerometer at the centre of the slab and measurements of crack widths were marked on the tension face of the slab and the location of the drop mass striking point was marked on the compression face. The support condition for the slabs to be tested was simply supported on all four edges.

www.EngineeringBooksPDF.com

Fig. 7 Four-channel DDAS

Fig. 8 DDAS with software KAMPANA

In the present investigation, the drop mass was obtained from the work energy principles for total slab capacity. For the present study the drop mass was worked out to be 70 kg. The height of the drop was varied to give different impact energies to have different range of kinetic energy to the slab and to record variation in the response of slab under different impact energy. For this purpose, the drop weight of 70 kg was dropped from the height of 0.67, 1.33 and 2 m, respectively onto the different slabs. The total energy impacted due to different drop heights is shown in Table 4.

The total energy imparted to the slab will be in the form of kinetic energy which would be equal to the potential energy stored in the drop weight lifted to the respective

www.EngineeringBooksPDF.com

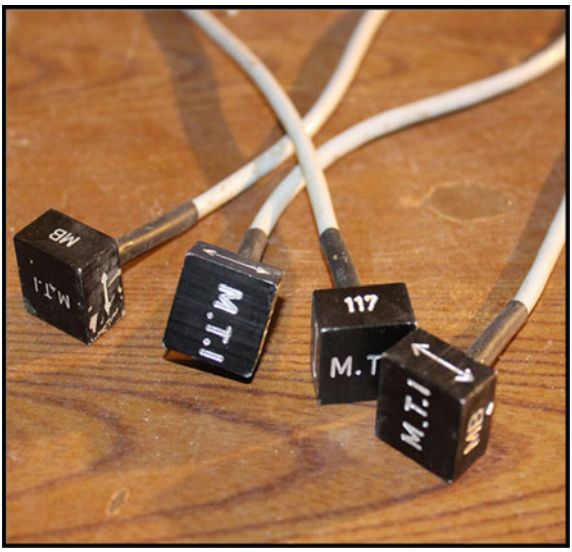

Fig. 9 Accelerometers

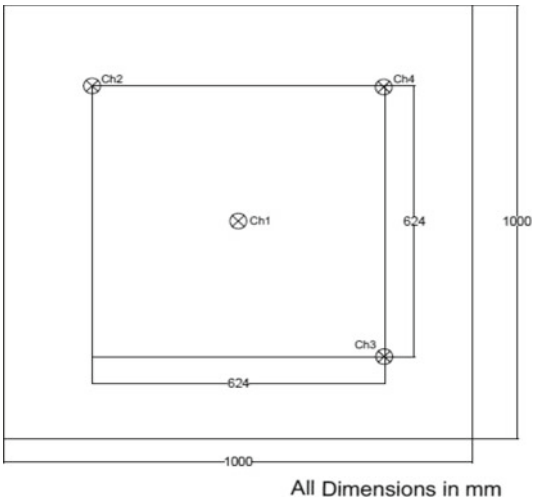

Fig. 10 Accelerometers location

Table 4 Impact energy on the slabs

Drop weight 'm' (kg)	Drop height 'H' (m)	Impact energy = m × g × H (Joules)
70	H1 = 0.67	460.01
	H2 = 1.33	913.31
	H3 = 2.00	1373.4

www.EngineeringBooksPDF.com

heights, and the drop was frictionless; hence it can be assumed that total energy would be converted without losses.

8 Test Results

These slabs were tested in the present investigation and the responses of each slab were obtained from the software "KAMPANA" of data acquisition system where the acceleration, velocity and displacement values were captured from the accelerometer placed at centre of the slab at the bottom portion. A typical data record from the software is as shown in Fig. 11.

For the current presentation, the data record of only the Ch1 accelerometer which was located on the bottom face of the concrete slab exactly below the drop impact is presented. The results from the test recorded in the central accelerometer are presented in Table 5. For easy comparison the same results are graphically represented comparing the acceleration response of the slabs for different drop heights, which is as shown in Fig. 12 (Figs. 13 and 14).

The crack pattern study of the slabs subjected to impact testing will help us to understand the failure behaviour of the slab under impact. Only the tension face (bottom face) cracking behaviour of the slabs was discussed as the compression face (top face) did not develop any crack. The cracks formed on the tension face due to drop impact were measured and a new index called damage index is formulated which is the ratio of energy absorbed per unit length of crack for different test specimen and presented in Table 6, and the same is represented in Fig. 15 to compare the values easily.

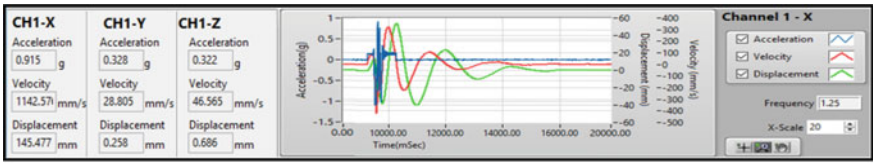

Fig. 11 Typical dynamic data recorded in KAMPANA software

Table 5 Response of the test slabs

Unstrengthened slab	Acceleration (g)	Strengthened slab	Acceleration (g)
M20/PT1/H1/NSM0	0.718	M20/PT1/H1/NSM1	0.341
M20/PT1/H2/NSM0	0.865	M20/PT1/H2/NSM1	0.43
M20/PT1/H3/NSM0	4.112	M20/PT1/H3/NSM1	0.72
M70/PT1/H1/NSM0	1.826	M70/PT1/H1/NSM1	0.664
M70/PT1/H2/NSM0	0.591	M70/PT1/H2/NSM1	1.455
M20/PT1/H3/NSM0	0.723	M70/PT1/H3/NSM1	3.808

www.EngineeringBooksPDF.com

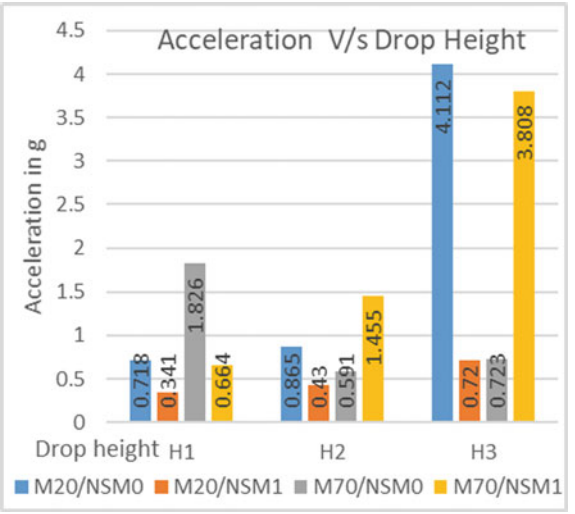

Fig. 12 Acceleration versus drop height

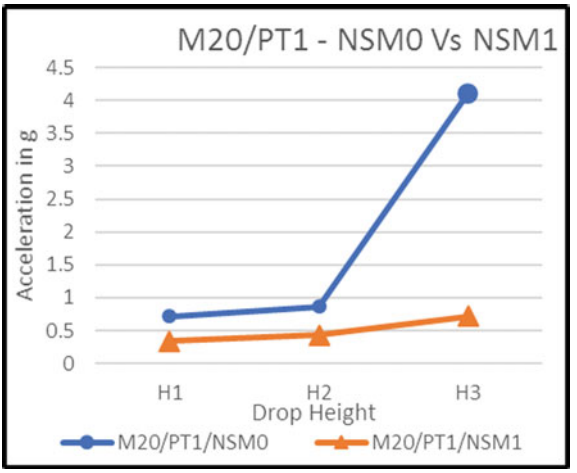

Fig. 13 Acceleration versus drop height for M20 slabs

9 Observations

The following observations were drawn from the experimental results:

1. The acceleration response of unstrengthened slab was observed to increase with increase in concrete grade only for drop height of 0.67 m, whereas it decreased with increase in grade for drop heights of 1.33–2.0 m.
2. It was recorded that with strengthening, the HSC slabs showed a decrease in acceleration for drop height H1 but it increased for drop heights H2 and H3.

www.EngineeringBooksPDF.com

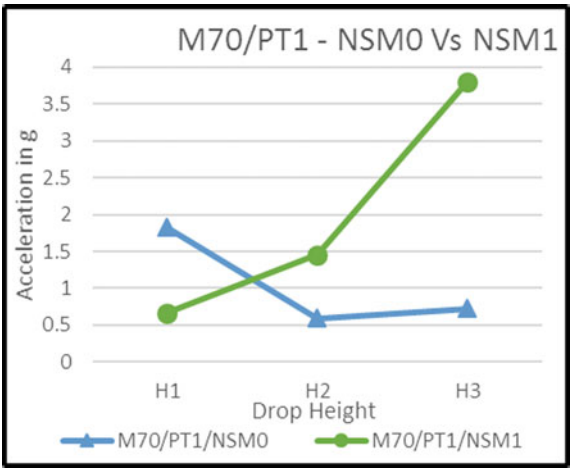

Fig. 14 Acceleration versus drop height for M70 slabs

Table 6 Crack length per unit slab area

SLAB ID	Energy impacted (J)	Crack length (mm)	Energy per unit length of crack (J/mm)
M20/PT1/H1/NSM0	460.01	2920	0.16
M20/PT1/H1/NSM1		2790	0.16
M20/PT1/H2/NSM0	913.31	3572	0.26
M20/PT1/H2/NSM1		3630	0.25
M20/PT1/H3/NSM0	1373.4	3443	0.40
M20/PT1/H3/NSM1		3030	0.45
M70/PT1/H1/NSM0	460.01	2120	0.22
M70/PT1/H1/NSM1		810	0.57
M70/PT1/H2/NSM0	913.31	3470	0.26
M70/PT1/H2/NSM1		2170	0.42
M70/PT1/H3/NSM0	1373.4	3710	0.37
M70/PT1/H3/NSM1		4130	0.33

3. Figure 13 shows the acceleration variation of both control slabs and strengthened slab of M20/PT1 with drop heights H1, H2 and H3. It was observed that with increase in drop height the acceleration response of slab increases for both control slab and strengthened slab. With strengthening, the acceleration of the slabs was seen to reduce when compared to control slab.
4. For M70 slab, it was observed from Fig. 14 that for control slabs the acceleration reduced when drop height increased from H1 to H2 and increased marginally with increase of drop height to H3. For strengthened slabs it was seen that the increase in drop heights increased the acceleration response successively from H1 to H3. Then comparing control and strengthened slabs it was recorded

www.EngineeringBooksPDF.com

that with strengthening, the acceleration was reduced for drop height H1 but increased for drop heights H2 and H3.

5. Crack length was seen to decrease nominally for all NSC test slabs with strengthening whereas the HSC slabs showed considerable decrease in crack length for drop heights H1 and H2 but increased marginally for drop height H3 with strengthening.
6. It was observed that for NSC control slabs the crack length increased with increase in drop height from H1 to H3 but reduced marginally for H3. In case of HSC slabs there was a steady increase in crack length with increase in drop height. NSC strengthened slabs also showed similar behaviour as NSC control slabs with increase in crack length from H1 to H2 drop height and a slight reduction from H2 to H3. Comparing both control and strengthened slabs the general trend was that there was decrease in crack length for all specimen except M20 specimen impacted from drop height H2 and M70 specimen impacted from drop height H3.
7. For control specimen with 0.34% reinforcement the crack length formed on the tension face is follows. For NSC with drop height H1 the crack length was 2920 mm, for H2 it was 3572 mm and for H3 it was 3443 mm. For HSC slabs the crack length for drop height H1 was recorded as 2120 mm, for H2 it was 3470 mm and for H3 it was obtained as 3710 mm. For NSC slabs it was observed that with increase in drop height from H1 to H2 the crack length increased by 22.33% and for increase in drop height from H2 to H3 it decreased by 3.98%. In case of HSC slabs the crack length increased by 63.68% for increase in drop height from H1 to H2 and further it increased by 6.92% for increase in drop height from H2 to H3. With increase in concrete grade from M20 to M70 the crack length for H1 decreased by 27.4%, for H2 it decreased by 2.8% and H3 it increased by 7.75%.
8. For strengthened specimen with 0.34% reinforcement the crack length formed on the tension face is as follows. For NSC with drop height H1, the crack length was 2790 mm; for H2 it was 3630 mm; and for H3 it was 3030 mm. For HSC

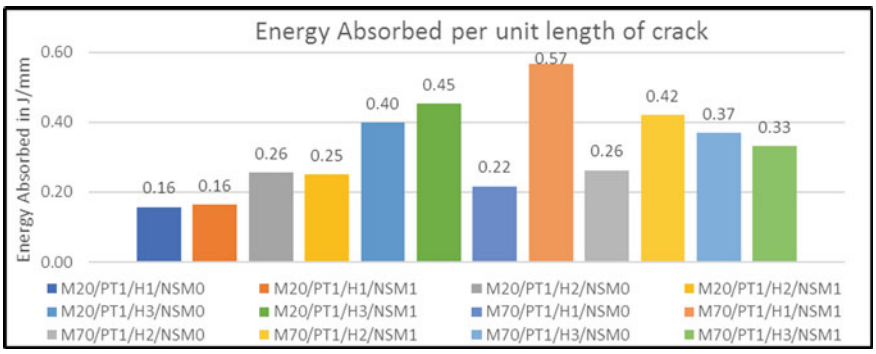

Fig. 15 Energy absorbed per mm of crack length

www.EngineeringBooksPDF.com

slabs the crack length for drop height H1 was recorded as 810 mm; for H2 it was 2170 mm; and for H3 it was obtained as 4130 mm. For NSC slabs it was observed that with increase in drop height from H1 to H2 the crack length increased by 30.1% and for increase in drop height from H2 to H3 it decreased by 16.53%. In case of HSC slabs the crack length increased by 167.9% for increase in drop height from H1 to H2 and further it increased by 90.32% for increase in drop height from H2 to H3. With increase in concrete grade from M20 to M70 the crack length for H1 decreased by 70.97%; for H2 it decreased by 40.22% and H3 it increased by 36.3%

9. When comparing control specimen and strengthened specimen, it was observed that with strengthening, the crack length of all slabs except NSC with drop height H2 and HSC with drop height H3 was found to reduce. For NSC slab with H1 drop height it decreased by 4.45%; for H2 it increased by 1.62%; and for H3 it decreased by 12%. In case of HSC slabs, for drop height H1 crack length reduced by 61.8%; for H2 it reduced by 37.46%; and for H3 it increased by 11.32%.
10. From Fig. 15 it was observed that for control slabs of NSC and HSC, the energy absorbed per mm of crack length increased with increase in drop height. Energy absorbed of NSC and HSC slab for drop height H2 was similar. For drop height H1, NSC had lower energy absorption per mm of crack length when compared to HSC, whereas for drop height H3, HSC had higher absorption than HSC.
11. For strengthened slabs it was observed that for NSC increase in drop height increased the energy absorption per mm of crack length, whereas for HSC it was found to decrease with increase in drop height.
12. Comparing both control slabs and strengthened slabs, upon strengthening, the increase in energy absorption was highest for HSC slab with drop height H1. The energy absorption did not change for NSC slab with drop height H1, whereas it was seen to decrease for NSC slab with H2 drop height and HSC slab with drop height H3.

10 Conclusions

From the observations made it can be concluded that for the given reinforcement ratio:

1. The acceleration response of NSC slabs decreased with strengthening for all drop heights.
2. Maximum change in response was recorded for highest impacting energy, where NSC slabs showed a significant decrease in response whereas HSC exhibited the opposite behaviour showing an increase in acceleration.
3. Crack length was observed to decrease significantly for HSC slabs when compared with NSC slabs for all cases except highest impact energy considered in the present study.

www.EngineeringBooksPDF.com

4. For control slabs of NSC, increase in drop height from H1 to H3 increased the energy absorbed per unit length of crack
5. For strengthened slabs of NSC, increase in drop height from H1 to H3 increased the energy absorbed per unit length of crack.
6. For control slabs of HSC, increase in drop height from H1 to H3 decreased the energy absorbed per unit length of crack.
7. With strengthening the energy absorbed per unit length of crack of HSC slab with drop height H1 and H2 increased but decreased for H3.

The study has shown promising results to represent the dynamic response of slabs under impact loads, however, further studies need to be conducted to understand the intricacies of the mechanical behaviour to predict the response mechanism of RC slabs under drop test.

References

1. Banthia N, Mindess S, Bentur A et al (1989) Exp Mech 29:63. https://doi.org/10.1007/BF02327783
2. Sangi AJ, May IM (2009) High mass, low-velocity impacts of reinforced concrete slabs. In: 7th LS-DYNA conference, UK
3. Krauthammer T, Zineddin M (2007) Structural concrete slabs under localized impact. Int J Impact Eng 34:1517–153. Anil Ö, Kantar E, Yilmaz MC (2015) Low velocity impact behavior of RC slabs with different support types. Constr Build Mater 93:1078–1088
4. Rizkalla S, Hassan T (2001) Various FRP strengthening techniques for retrofitting concrete structures. In CICE 2001 conference proceedings
5. Witkowski H, Kotynia R (2010) Bond between NSM Reinforcement and concrete. In: 8th fib Ph.D. symposium in Kgs, Lyngby, Denmark
6. Hrynyk TD, Vecchio FJ (2014) Behavior of steel fiber-reinforced concrete slabs under impact load. ACI Struct J 111(5)
7. Anil Ö, Kantar E, Yilmaz MC (2015) Low velocity impact behavior of RC slabs with different support types. Constr Build Mater 93:1078–1088. https://doi.org/10.1016/j.conbuildmat.2015.05.039
8. Ramanna-Sanjeevaiah N (2012) Static and impact load response of reinforced concrete beams and slabs with NSM-CFRP retrofitting. In: Doctor of Philosophy (PhD), dissertation, Civil/Environmental Engineering, Old Dominion University. https://doi.org/10.25777/wkb7-v478, https://digitalcommons.odu.edu/cee_etds/61
9. Prabhakara R et al (2006) Ultimate flexural strength of high strength concrete beams. Indian Concr J pp 40–50
10. Nandeesh MS, Reddy AR, Prabhakara R (2016) Investigations on effect of CFRP strips retrofitted using NSM method on two-way NSC and HSC slabs subjected to concentrated load. eISSN: 2319-1163|pISSN: 2321-7308 05(14)| ICRAES-2016
11. Reddy AR, Nandeesh MS, Prabhakara R (2015) Studies on strength and deformation behaviour of two-way NSC and HSC slabs under single point loading. eISSN: 2319-1163|pISSN: 2321-7308 05(14) ICRAES-2016
12. De Lorenzis L, Nanni A, La Tegola A (2000) Strengthening of reinforced concrete structures with near surface mounted FRP rods. In: International meeting on composite materials, PLAST 2000, proceedings, advancing with composites, pp 9–11
13. Bonaldo E, Barros JA, Lourenço PB (2005) Concrete slabs strips reinforced with epoxy-bonded carbon laminates into slits. University of Minho, Portugal

www.EngineeringBooksPDF.com

Experimental Studies to Demonstrate the Effect of Clamping Reinforcement on Shear Strength of GPC Adopting Push-Off Specimens

N. R. Harish Kumar, Sachin R. Biradar, R. Prabhakara, and H. Jagannatha Reddy

Abstract Mechanical properties of GPC are different compared over NSC; this is due to change in cracking behaviour under the application of load. Compressive strength, flexural strength, modulus of elasticity and in-plane shear strength are the important mechanical properties to be understood before it is used in practice. It has been observed that literatures available on in-plane shear strength of GPC are limited. The experimental investigation carried out in the present study is to study the in-plane shear strength of normal strength concrete (NSC) and geo polymer concrete (GPC) using push-off specimens. The grade of concrete and height of shear plane used are M30 and 100 mm, respectively. Dimensions of push-off specimen were 150 × 150 × 260 mm with two rectangular notches of 10 mm thick was cut, 100 mm apart along the longitudinal axis of loading and at equidistance from mid-depth. A total of 48 push-off specimens were tested (24 in each NSC and GPC, respectively), six push-off specimens with zero, one, two and three bars, respectively, crossing the shear plane. It was observed from experimental results that as the number of bars across shear plane increased the shear stress increased and in-plane shear strength of GPC was higher than NSC.

Keywords In-plane shear strength · NSC · GPC · Push-off specimen · Clamping reinforcement

N. R. Harish Kumar (✉) · S. R. Biradar
Civil Engineering Department, Sri Venkateshwara College of Engineering, Airport Road, VidyaNagara Cross, Bengaluru 562157, Karnataka, India
e-mail: harishnrgowda@gmail.com

S. R. Biradar
e-mail: sachinbiradar98@gmail.com

R. Prabhakara
Visvesvaraya Technological University, Belgaum 590018, India
e-mail: r.prabhakara@gmail.com

H. Jagannatha Reddy
Civil Engineering Department, Bangalore Institute of Technology, KR Road, VV Puram, Belgaum 560004, Karnataka, India
e-mail: jagannath.priyadhi@gmail.com

© Springer Nature Singapore Pte Ltd. 2021

K. K. Pathak et al. (eds.), *Recent Trends in Civil Engineering*, Lecture Notes in Civil Engineering 77, https://doi.org/10.1007/978-981-15-5195-6_6

www.EngineeringBooksPDF.com

1 Introduction

Cement is a widely used construction material. The production and processing of cement involves heating lime, also called calcination, which involves heating of materials at high temperature of around 14,000–15,000 °C which leads to depletion of natural resources and emission of carbon dioxide. Many methods have been tried to reduce the usage of cement by finding alternate cementitious material for cement. Geo polymer concrete is one such alternative to cement in concrete where cementitious material is replaced by fly ash [1]. Investigation is carried out on flexure, shear, torsion and so on, but it has been found from various literatures that investigation on estimation of shear strength is less. The failure in concrete elements in direct shear is sudden and brittle which is of type mode II failure and is of prime importance in corbels, brackets, shear walls, deep beams, reactor containment vessels and various connections of reinforced concrete structures [2]. The test methods generally followed to evaluate shear characteristics are Federation international de la Precontrainte (FIP) standard test, Japanese society of civil engineering (JSCE) standard method push-off test, Bairagi and Modhera model, but not one method is accepted globally as standard test [3]. To evaluate shear strength of concrete, push-off test has been used as this method is simple in the present study. A total of 48 push-off specimens were tested (24 in each NSC and GPC, respectively), six push-off specimens with zero, one, two and three bars, respectively, crossing the shear plane. Further in the present study, shear strength is being evaluated and compared between NSC and GPC of M30 grade by varying shear reinforcement across the shear plane. The push-off test is conducted by subjecting the specimen to axial force so that specimen fails along the predetermined shear plane; shear plane in push-off specimen is a plane which is located centrally along the longitudinal axis between the notches which are opposite to each other as shown in Figs. 1 and 2.

2 Scope of the Present Investigation

- To obtain the design mix proportion for GPC of grade M30 and NSC of grade M30 concrete which is widely used in the precast industry with end block strengthened to ensure failure along shear plane only.
- A total of 48 push-off specimens were tested (24 in each NSC and GPC, respectively). Six push-off specimens with zero, one, two and three bars, respectively, crossing the shear plane [4].
- It is proposed to observe the variation in shear stress values with varying number of bars across the shear plane of push-off specimens of both NSC and GPC as shown in Fig. 2a, b.

www.EngineeringBooksPDF.com

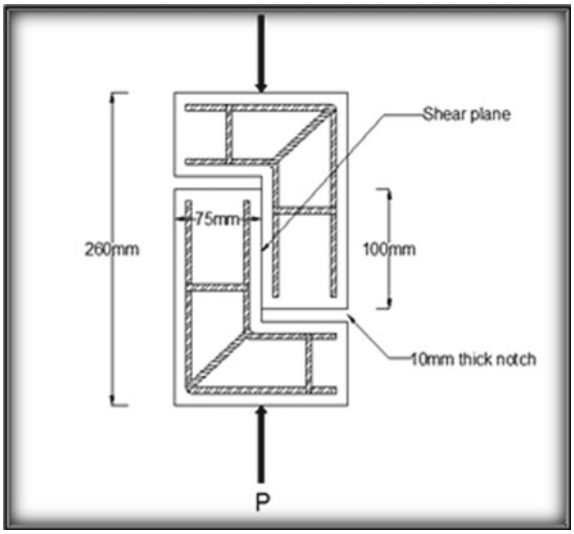

Fig. 1 Schematic diagram of push-off test specimen

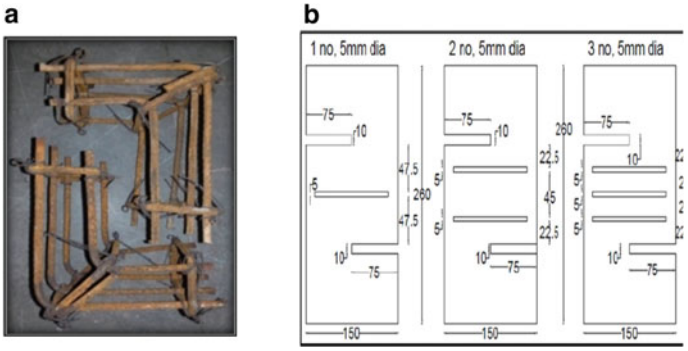

Fig. 2 L-shaped cage reinforcement, b Schematic diagram of push-off specimen with varying shear reinforcement

3 Characterisation of Materials Used in the Study

3.1 Cement

OPC 53 grade with specific gravity of 3.10 conforming to IS: 12269-1987 was used for normal strength concrete, and chemical composition is as follows (vide Table 1).

www.EngineeringBooksPDF.com

Table 1 Chemical composition of OPC 53 grade cement

Compound	CaO	SiO_2	Al_2O_3	Fe_2O_3	SO_3	MgO	Cl
In(%)	62.00	21.05	5.05	3.10	3.05	1.45	0.008

Table 2 Chemical composition of fly ash

Compound	SiO_2	Al_2O_3	Fe_2O_3	CaO	MgO	TiO_2	K_2O	Na_2O	SO_3	LOI (1000 C)	Moisture
In(%)	55.6	25.9	5.6	5.4	2.1	1.1	0.5	0.5	1.6	2.0	0.4

Table 3 Chemical composition of GGBS

Compound	SiO_2	Al_2O_3	Fe_2O_3	CaO	MgO	SO_3	S	MnO	Na_2O	K_2O	Cl
In(%)	33.7	18.9	0.8	32.5	10.9	0.9	0.5	0.4	0.32	0.99	0.009

3.2 Fly Ash

Class 'F' fly ash sourced from RTPS, Karnataka was used for GeoPplymer Concrete, and low calcium fly ash provides remarkable contribution to the fresh and mechanical properties of concrete (Table 2).

3.3 GGBS

Ground granulated blast furnace slag (GGBS) was replaced with 10% by weight of binders (Table 3).

3.4 Fine Aggregates

Locally available and as per the code IS 383-1970 was used. The specific gravity and bulk density was found to be 2.38 and 1691.00 kg/m^3, respectively.

3.5 Coarse Aggregate

Crushed aggregates with 12.50 mm downsize for GPC and 20 mm downsize for NSC as per the code IS 383-1970 having specific gravity 2.63 and bulk density of 1498 kg/m^3 was used, respectively.

www.EngineeringBooksPDF.com

3.6 Alkaline Solution

NaOH (flakes) and Na_2SiO_3 are used as alkali activator in the mix to produce solution for the GPC mix. NaOH solution with a concentration of 8 molar was used, as it was observed from the literature the mechanical properties of the concrete will be optimum around 8 molar. Sodium-based solutions (prepared one day prior) [5] were adopted in the experiment to make it economical and for practical applications.

3.7 Water

Potable water available in lab as per IS 456-2000. Mix design for NSC M30 was carried out according to IS: 10262-2009 and for GPC M30, Rangan [4–8] mix design was followed in the present studies. After several trails, the final mix designs obtained for both NSC and GPC are as shown in Table 4.

4 Experimental Investigation

The dimension of specimens was chosen after going through literature studies (150 × 150 × 260 mm). Specimen was provided with notches (75 mm × 10 mm) which was positioned at 100 mm from each other and perpendicular to the axis of the specimen as shown in Fig. 1. Notch tips define the vertical plane along which shear cracking is expected in the push-off specimen. Push-off test involves the application of a compressive force 'P' to produce a pure shear in the specimen. This is achieved by two 'L' blocks and the plane that connects these two blocks which is the proposed shear plane. It is important to outline that the shear plane direction must be coincident with the load direction in order to induce pure shear.

The specimens for push-off test were cast by adopting different percentage of clamping reinforcement across shear plane area. The main aim of introducing

Table 4 Mix proportions of NSC M30 and GPC adopted in the present investigation

Materials (kg/m^3)	NSC M30	GPC
Cement	348.33	–
Coarse aggregates	1146.8	1293.60
Fine aggregates	681.66	554
Water	191.58	–
Fly ash	–	382.14
GGBS	–	42.46
NaOH solids	–	36
Na_2SiO_3 solution	–	91

www.EngineeringBooksPDF.com

clamping reinforcement is to study the effect of shear reinforcement on shear strength, propagation of crack and the width of the crack pattern with different dosages in GPC and compare the results obtained with the normal concrete specimens. The specimens were reinforced with Fe500 5 mm dia. bar as illustrated in Fig. 2 [6] and variation of shear reinforcement is illustrated in Fig. 2a, b. Two 10 mm thick steel plates' of 75 mm length and 150 mm depth are welded at 100 mm apart, to induce notches at predetermined positions in the specimen.

4.1 Casting of Push-off Specimens

NSC and GPC push-off specimen were cast by rolling the mix in a pan mixer as per the mix design and casting in the moulds specified above. The required quantities of ingredients are batched. NaOH and Na_2SiO_3 solution prepared 24 h prior to be used [4]. The fly ash-based geo polymer concrete mix was dark and shiny. Both mixtures were very cohesive. Fresh concrete property test were performed and the slump values obtained were 80 and 100 mm for NSC and GPC, respectively. Standard test procedure has been followed and uniformity was also maintained to minimise the variation while mixing and casting.

4.2 Curing Method

NSC push-off specimens were moist cured. After which the moulds were de-moulded and all the NSC specimens were cured for standard curing period.GPC push-off specimens were taken out from the moulds after 24 h and then transferred to the steam curing chamber. The specimens were kept in steam curing chamber at 600 °C for about 24 h. At the end of curing period the specimens cooled in the chamber for about 3–4 h and then stored at room temperature until the day of testing [7].

Figure 3 shows the universal CTM of 2000 kN used to test all specimen. Steel bearing plates of size 10 × 150 mm length were placed at both ends of specimen to transfer load along the testing plane of strengthened end blocks. The load at first crack was noted for the specimen. Crack width was measured along the shear plane of specimen by using hand (Filar) microscope after the failure of specimen (Fig. 4, 5, 6 and 7).

5 Test Results

See Fig. 8 and Table 5.

From Tables 6 and 7, it was clear that the incorporation of shear reinforcement in both NSC and GPC specimens has resulted in better structural integrity before

www.EngineeringBooksPDF.com

Fig. 3 Test arrangement under CTM

Fig. 4 NSC with CR

failure. All the test specimens fractured over the shear plane zone. It was observed that specimens with clamping reinforcement did not separate till the end. The separation was observed for the specimens without clamping reinforcement. An attempt has been done to bring about a comparative study between the experimental data and various available codes and their expressions regarding the shear stress. The expressions which have been found from regression analysis are also brought into consideration.

According to ACI 318-11

$$Vu = 0.87As\,fy + K1Ac \tag{1}$$

where K1 = 400; Psi = 2.76 MPa.

www.EngineeringBooksPDF.com

Fig. 5 NSC without CR

Fig. 6 GPC with CR

Fig. 7 GPC without CR

According to IS 456: 2000

$$Vu = \tau_c bd + 0.87 fy Ast \quad (2)$$

www.EngineeringBooksPDF.com

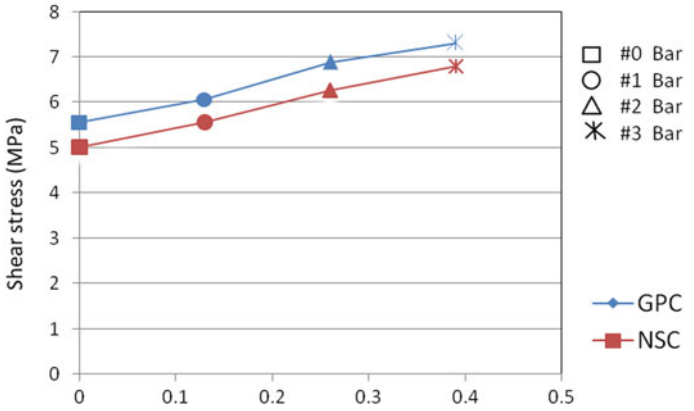

Fig. 8 Graph showing variation in shear stress with varying CR for both NSC and GPC

Table 5 Cube compressive strength of NSC and GPC concrete

Concrete type	Max aggregate size (mm)	Concrete Grade	Cube dimensions (mm)	Average compressive strength, f_{ck}(MPa)		Target strength (MPa)
				7 days	28 days	28 days
NSC	20	M30	150 × 150 × 150	24.12	38.73	38.25
GPC	12.5	M30	100 × 100 × 100	38.26	43.16	38.25

Table 6 Shear stress values of NSC

S. no.	Specimen designation	A_g (mm^2)	Stirrups	ρ%	f_y (MPa)	A_{st} (mm^2)	V (kN)	τ (MPa)
1	NSC/0B	15000	0	0	550	0	75.21	5.01
2	NSC/1B	15000	#1,5 mm ϕ	0.13	550	19.63	83.39	5.56
3	NSC/2B	15000	#2,5 mm ϕ	0.26	550	39.26	94.01	6.27
4	NSC/3B	15000	#3,5 mm ϕ	0.39	550	58.9	101.78	6.79

Table 7 Shear stress values of GPC

S. no.	Specimen designation	A_g (mm^2)	Stirrups	ρ%	f_y (MPa)	A_{st} (mm^2)	V (kN)	τ (MPa)
1	GPC/0B	15000	0	0	550	0	83.4	5.56
2	GPC/1B	15000	#1,5 mm ϕ	0.13	550	19.63	91.04	6.06
3	GPC/2B	15000	#2,5 mm ϕ	0.26	550	39.26	103.4	6.89
4	GPC/3B	15000	#3,5 mm ϕ	0.39	550	58.9	109.67	7.31

www.EngineeringBooksPDF.com

where τ_c max = 3.5 N/mm^2 (M30), τ_c max = 4.0 N/mm^2 (≥M40).

fck—Compressive strength of concrete, A_g—Gross area of concrete, ρ—Percentage shear reinforcement,

fy—Yield strength of steel, A_{st}—Area of steel, *Vu*—Ultimate load, τu—Ultimate shear stress, *b*—Width of shear plane and *d*—Depth of shear plane.

From the experimental results and the calculated values from the codal provisions, linear regression analysis was carried out separately for NSC and GPC to formulate prediction Eqs. 3 and 4, respectively,

$$\tau_u = 5.23 + 4.67\rho - 0.006\,f_{ck} \tag{3}$$

$$\tau_u = 5.77 + 4.71\rho - 0.006\,f_{ck} \tag{4}$$

The shear strength was calculated theoretically for all the tested specimens using the Eqs. 1 and 2. The ratio of experimental shear stress and calculated shear stress obtained for ACI, IS codes and predicted equation for NSC and GPC are tabulated in Tables 8 and 9, respectively (Figs. 9 and 10).

Table 8 Calculated shear stress values for NSC

S. no.	Specimens	τ(exp)/τ(cal)		
		ACI	IS	Predicted
1	NSC/0B	1.81	1.43	1.00
2	NSC/1B	1.66	1.35	0.98
3	NSC/2B	1.60	1.32	1.01
4	NSC/3B	1.52	1.26	0.99
Mean		1.64	1.34	0.99
SD		0.12	0.07	0.01
CV(%)		7.44	5.27	1.29

Table 9 Calculated shear stress values for GPC

S. no.	Specimens	τ(exp)/τ(cal)		
		ACI	IS	Predicted
1	GPC/0B	2.01	1.58	1.00
2	GPC/1B	1.81	1.46	0.98
3	GPC/2B	1.76	1.45	1.02
4	GPC/3B	1.63	1.36	0.99
Mean		1.80	1.46	0.99
SD		0.15	0.09	0.01
CV(%)		8.75	6.17	1.71

www.EngineeringBooksPDF.com

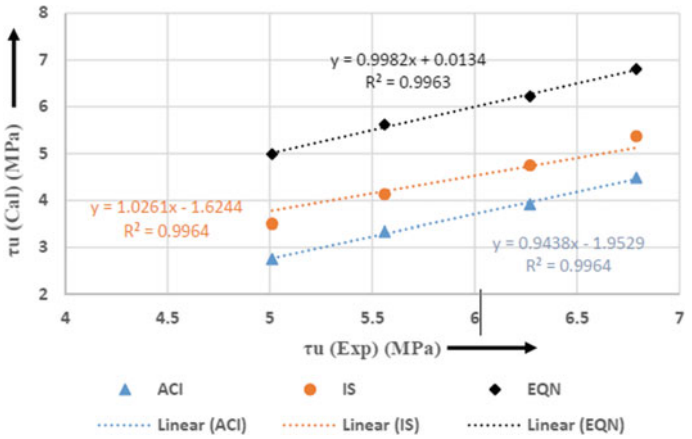

Fig. 9 Shear stress values: calc versus exp (NSC)

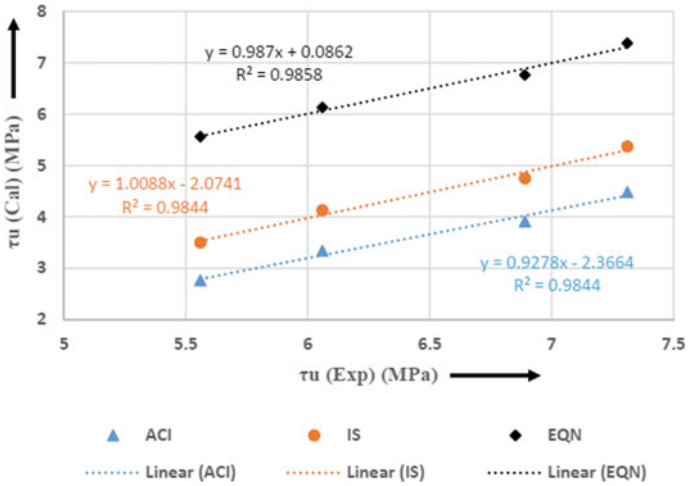

Fig. 10 Shear stress values: calc versus exp (GPC)

6 Conclusions

The ultimate load carrying capacity and ultimate shear stress values was better in specimens with clamped reinforcement than that which had no reinforcement across shear plane for both NSC and GPC.

It was observed from results that as the number of bars increased across the shear plane the values of shear stress of push-off specimens increased. In case of NSC, shear stress values of NSC/1B, NSC/2B and NSC/3B increased by 10.97, 25.15 and 35.53% when compared to NSC/0B, respectively. In case of GPC, shear stress value

www.EngineeringBooksPDF.com

of GPC/1B, GPC/2B and GPC/3B increased by 9, 23, 92, respectively, and 31.47% when compared to GPC/0B.

From experimental results it was observed that GPC had better shear stress carrying capacity when compared to NSC. Shear stress values obtained from predicted equation gave satisfactory results with mean of 0.99 for NSC and GPC and the coefficient of variation of 1.29 and 1.71% for NSC and GPC, respectively, ACI code gives good prediction of shear stress values with a mean of 1.64 for NSC and 1.80 for GPC, and the prediction equations gave satisfactory results mean 0.99 for both NSC and GPC. The coefficient of correlation obtained when experimental and theoretical compared was 0.99 in case of NSC and 0.98 in case of GPC; R2 (coefficient of correlation) value closer to 1 indicates perfect prediction.

References

1. Joseph B, Mathew G (2013) Interface shear strength of fly ash based geopolymer concrete. Annals Fac Eng Hunedoara 11(3):105
2. Lin IJ, Chang KY (1988) Shear-friction strength in orthogonally reinforced concrete with tension acting across the shear plane. J Chin Inst Eng 11(5):435–445. https://doi.org/10.1080/02533839.1988.9677094
3. Shaikh NN, Zeeshan M, Saba MM, Nirmala SB, Prabhakara R (2012) Inplane shear strength of normal, high strength and self compacting concrete using push-off specimen. In: Proceedings of international conference on advances in architecture and civil engineering (AARCV 2012), vol 21, p 169)
4. Aleem MA, Arumairaj PD (2012) Optimum mix for the geopolymer concrete. Indian J Sci Technol 5(3):2299–2301
5. Subhaja R (2015) Experimental investigation and strength characteristics of fly ash based geopolymer concrete. Int J Sci Res 4–4:164–166
6. Naserian R, Hosseini A, Marefat MS (2013) Assessment of shear transfer capacity of non-cracked concrete strengthened with external GFRP strips. Constr Build Mater 45:224–232. https://doi.org/10.1016/j.conbuildmat.2013.03.028
7. Hardjito D, Wallah S, Sumajouw Rangan (2004) On the development of fly ash-based geopolymer concrete. ACI Mater J 101:468–472
8. Olivia M, Nikraz H (2012) Properties of fly ash geo polymer concrete designed by Taguchi method. Mater Des 1980–2015(36):191–198. https://doi.org/10.1016/j.matdes.2011.10.036

www.EngineeringBooksPDF.com

Evaluation of Flexural Behaviour of Post-tensioned RC Beams Strengthened Using CFRP Laminates with NSM Technique

Vathsala, H. N. Jagannatha Reddy, and R. Prabhakara

Abstract A large number of investigations are available on the flexural evaluation of strengthened reinforced concrete beams using several structural materials and techniques. However, very limited information is available on the performance of strengthened post-tensioned (PT) beams. Carbon fibre-reinforced polymer (CFRP) strengthening material with near-surface mounted (NSM) technique has evolved as the promising material and method due to their superior performance. This paper focused on the structural strength and deformation behaviour of PT RC beams, and flexural strength with NSM technique using CFRP laminate. Four PT beams were tested in the present experimental and analytical investigation, in which one beam was regarded as control beam, and the remaining three beams with increase over the area of CFRP laminates by a factor of 1, 2 and 3, respectively. The aim of this experiment and analytical work was to demonstrate the strength and deformation behaviour of the PT beams tested under static condition over four points bending. The results revealed that the cracking and ultimate load-carrying capacity of strengthened PT beams increased linearly compared with control beams. Increase in ductility index with reduction in the deflection at the level of ultimate load was recorded for the strengthened PT beams.

Keywords CFRP laminate · Post-tensioned beams · NSM technique · Ductility index · Ultimate load

Vathsala (✉) · H. N. Jagannatha Reddy
Department of Civil Engineering, BIT, K R Road, Bangalore 04, India
e-mail: vathsalagowda@gmail.com

H. N. Jagannatha Reddy
e-mail: jagannath.priyadhi@gmail.com

R. Prabhakara
Structural Engineering Division, PG Center, VTU Belagavi, Belgaum 590018, India
e-mail: r.prabhakara@gmail.com

© Springer Nature Singapore Pte Ltd. 2021

K. K. Pathak et al. (eds.), *Recent Trends in Civil Engineering*, Lecture Notes in Civil Engineering 77, https://doi.org/10.1007/978-981-15-5195-6_7

www.EngineeringBooksPDF.com

1 Introduction

The performance of PSC structures over several decades under the environmental load has given many problems. It was observed that few PSC structures with high design reliability and maintenance have performed well. However, most of the PSC structures have shown distress. This is due to primitive design standards, poor quality of materials and construction, damage due to impact and exposure to the environmental loads [1]. The public and private agencies realised the effect of degradation of the structures, and the impact on the economy of the state started strengthening of the structure with reasonable cost as the complete replacement becomes uneconomical. The knowledge and the knowhow of strengthening or retrofitting of the structures is well developed, such as section enlargement, external bonding, warping, jacketing and near-surface mounted (NSM). Many investigations have been documented on the application of strengthening technique to enhance the strength and performance of the conventional structures. However, less information is there on the implementation of strengthening technique to the PSC structures. This is due to the fundamental fact that the cracking and deformations of PSC structures are slightly different compared with conventional structures [2]. Flexure, shear and anchorage zones are the vital regions in PSC beams which have to be strengthened by any method in order to keep the structures in operational mode, and thus has become the main objective. There are several strengthening methods available for the application and each one has its own merits and demerits. It has been observed from the available literature that strengthening using FRP has emerged as an effective alternative over others for the reason that of the mechanical properties of fibre composites. FRP materials are light in weight, have resistance to corrosion, demonstrate high tensile strength and are relatively uncomplicated to install [4–6]. This paper is focused on structural strength and deformation evaluation of post-tensioned (PT) beams and strengthened PT beam with NSM reinforcement technique.

2 Review on the Past Work

Seven decommissioned girders of the Eastern North Carolina Bridge erected in 1960 were strengthened, and their performance for fatigue behaviour was studied by Rosenboom and Rizkalla [7]. They strengthened the beams by near-surface mounted bars and strips and externally bonded strips and sheets with different CFRP systems. All girders were tested for flexure using monotonic loading system. Based on the experimental programme and analysis of test results, it was revealed that the use of CFRP materials as strengthening material reduces the stress ratio in the pre-stressing strands. In addition they were also more effective in controlling crack widths and increasing the stiffness. Barros et al. [8] evaluated the efficacies of external bond reinforcement (EBR) and NSM strengthening techniques for concrete beams. For this work, they cast 24 beams of size 120 × 170 × 1000 mm with distinct ratio of

www.EngineeringBooksPDF.com

longitudinal tensile steel reinforcement and tested statically under two-point loading condition. CFRP laminates were utilised for NSM technique and CFRP sheets were used with wet lay-up method for EBR technique and the obtained experimental results were compared. From their work, they concluded that for shear strengthening NSM technique was most effective with CFRP laminates rather than the fabrics. For shear strengthening of beam with more depth, laminates placed at 45° orientation were more effective than that of laminates at 90° orientation. Failure modes of beams strengthened with NSM technique were different from beams strengthened with EBR techniques.

An attempt was made by Bilotta et al. [9] to explore the behaviour of bonding between concrete surface and fibre-reinforced polymer systems in externally bonded and NSM techniques. For this, they developed an experimental programme consisting of 42 concrete prisms of size 160 × 200 × 300 mm, out of which 24 specimens were considered for EBR technique and 18 specimens for NSM technique. Carbon, glass and basalt fibre-reinforced polymers were used as strengthening materials in the form of strips, round and square bars. They conducted single shear test on concrete prism strengthened by FRP system. They analysed the performance of specimens in terms of load–slip relationship, mode of debonding and strain distribution. From their investigation, the authors concluded that with higher utilisation factor, NSM technique exploited the tensile strength of FRP materials rather than EBR technique. Also, the authors found that the process of debonding of FRP in NSM was delayed when compared to FRP systems in EBR technique.

An analytical solution developed by Jun Deng et al. [10] was utilised to calculate the flexural strength of beams strengthened by CFRP laminates. Because of symmetry, half of 3D FE model was considered for nonlinear analysis. All nodes at mid-span were restrained to produce the required symmetry. To represent the simple roll-supported condition, nodes at the end of the beam were restrained. The 8-node brick element (element Solid65) was used to represent concrete plate, in which the rebar was assumed to be smeared throughout the element. A 4-node shell element (element Shell43) was used to model steel beam. Combin39 element was used to model the shear studs connecting the concrete plate and the steel beam. The adhesive layer was modelled with 8-node brick elements (element Solid45). The beams were strengthened using one layer, three layers and five layers of unidirectional CFRP laminates with thickness of 1.27 mm and width of 76 mm. From their analyses, they concluded that pre-stressing force and permanent load did not alter the flexural strength of the beam. But flexural strength was reduced because of rupture of CFRP plate.

3 Experimental Studies

Totally, four PT beams of dimensions 230 mm × 300 mm × 3400 mm were cast. Out of four beams, one beam was considered as control beam. All the beams were designed according to IS: 1343 specification, and tested under static condition over

www.EngineeringBooksPDF.com

four points bending. Two bars of 12 mm diameter and two bars of 10 mm diameter of characteristic strength 500 MPa were provided as bottom and top reinforcements, respectively, for all beams. Two-legged 8 mm diameter bars were provided at a spacing of 170 mm, centre-to-centre along the length of the beam as shear reinforcement. Unbounded-type post-tensioning beams were achieved by placing sheathing pipe at an eccentricity of 106 mm. Anchorage system was provided at the end of the sheathing pipe which terminates at the end face of the beams.

3.1 Casting of Beam Specimens

In a concrete mixer, the M40 grade concrete was prepared and placed in the moulds where the reinforcement cage was placed. Needle vibrator was used to compact concrete and the top surface of the beam was properly finished using a trowel. Beams were de-moulded after 24 h.

3.2 Post-tensioning of Beams

Post-tensioning was done after curing period of 28 days. For post-tensioning, two numbers of high-tensile steel of 12.7 mm diameter were inserted into the sheathing pipe provided at the time of casting the beam. The applied stress needs to be balanced equally. So to achieve these two tendons of different lengths was placed on each side of the beam. The stressing was introduced in three levels: the stressing was done over a span of 2 h. Using wedges and barrels, the tendons were anchored at both edges. About 70% of ultimate strength was introduced in high-tensile pre-stressing steel as the stressing force. It was applied on each tendon at the longer side provided at the alternative ends, as shown in Fig. 1. The applied force was measured by measuring the elongation in each tendon. Gifford–Udall system was used for tendon anchorage system.

Fig. 1 Post-tensioning of beams

www.EngineeringBooksPDF.com

3.3 Strengthening of Beams by NSM Technique

After post-tensioning, beams were strengthened by NSM technique. Longitudinal groove of 50 mm width, 25 mm length and 3000 mm depth at the bottom side of the beam was made, to have an area of bonding of about 0.15 m^2 for NSM-1. CFRP strip was installed at the clean, epoxy-filled groove by maintaining gap of 20 mm between concrete face and laminate. Smooth finish of surface was achieved by uniform application of epoxy. Two grooves of 50 mm width and 25 mm depth, each by maintaining the gap of 40 mm and laminates were placed inside them to maintain bonding area of about 0.3 m^2 for NSM-2. For the beam NSM-3, three strips were placed in the three grooves by maintaining 20 mm spacing between them to achieve bonding area of about 0.45 m^2.

3.4 Testing of Beams

All the beams were tested for static loading condition under four-point bending condition. This setup was achieved in the loading frame of capacity 200 ton, as shown in Fig. 2. The deflection was measured at mid-span for each increment of 5 kN up to ultimate load. Development crack was observed and marked on beams.

4 Analytical Studies

In this work, finite-element analysis of the post-tensioned beam strengthened by NSM techniques using CFRPs has been carried out and compared over the experimental behaviour using ANSYS-R14.5. Half of the post-tensioned beam was modelled using top-down approach, by taking the advantage of the symmetry. Blocks for beams of size 230 × 300 × 3400 mm were developed for this work. Solid-65 element was used

Fig. 2 Test setup for testing the beams

www.EngineeringBooksPDF.com

to model concrete as it was suitable for cracking simulation. Using LINK-8 element, two bars of 12 mm diameter (Fe-500) were modelled as bottom reinforcements and two bars of 10 mm diameter (Fe-500) were modelled as top reinforcements for all beam models. Two-legged 8 mm diameter bars were modelled at a spacing of 170 mm, centre-to-centre along the length of the beam as shear reinforcement for flexural analysis models. Two numbers of high-tensile steel of 12.7 mm diameter were modelled using LINK-8 element at 106 mm from the bottom of the beam. Clear concrete cover of 25 mm was provided to the reinforcement, and meshing of the model was done. The Shell-63 element was selected to model the strengthening material CFRP laminate. This element has both bending and membrane capabilities. It also has six degrees of freedom system at each node. Since the beam and loading were symmetric, symmetrical boundary condition was applied, as has been shown in Fig. 3. The models were developed to represent the strengthening of post-tensioned beams strengthened by near-surface mounted technique using one strip, two strips and three strips of CFRP and is shown in Figs. 4, 5 and 6.

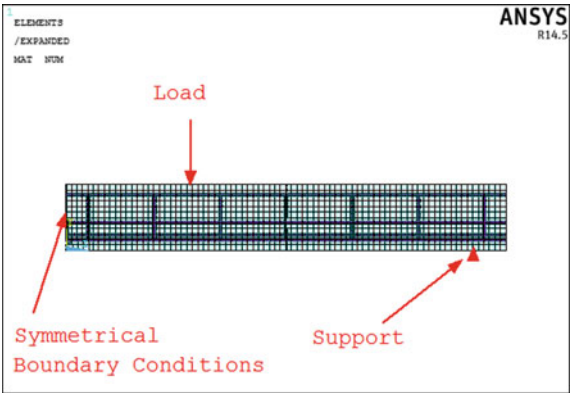

Fig. 3 Meshing and boundary conditions

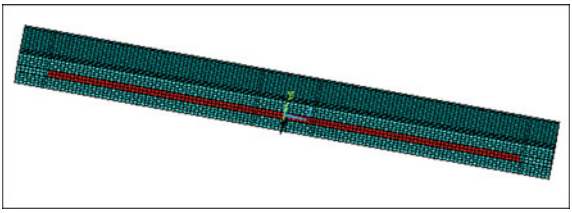

Fig. 4 Meshing details of NSM-1 beam model

www.EngineeringBooksPDF.com

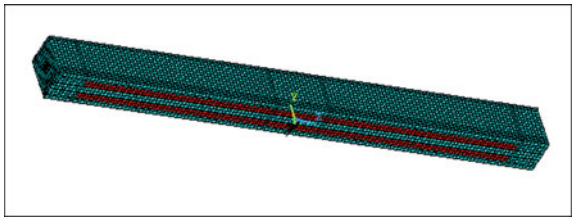

Fig. 5 Meshing details of NSM-2 beam model

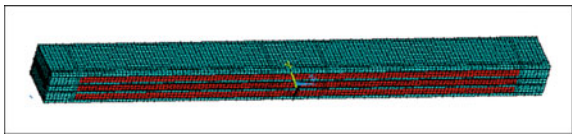

Fig. 6 Meshing details of NSM-3 beam model

5 History of Failure of Beams

5.1 Control Beam CBF

The objective of writing the history of failure of the control beam is to understand the cracking and deformation pattern of the control beam. The first crack appeared at 62 kN at the bottom of the beam in the mid-span region and the deflection was 2.93 mm. As the loading further increased, the identified crack propagated towards the top surface of the beam. Flexural cracks developed at an equidistant and symmetrically spread over the length of the beam. All developed cracks were vertical and secondary cracks were developed originating from the main cracks. Ultimately, the beam failed functionally at the load of 128 kN. The measured maximum central deflection was 24.98 mm. The failure pattern of the beam is shown in Fig. 7.

In finite-element analysis using ANSYS, the first crack developed at the origin, at the loading stage of 58 kN, as a red patch which spread over the mid-span, representing the development of flexural cracks. The crack pattern of reference model for flexural analysis at ultimate loading stage was as shown in Fig. 8. The ultimate load carried by the beam was 124 kN and the maximum deflection was 20 mm at the origin, that is, at the centre of the span.

Fig. 7 Cracking pattern for control beam CBF

www.EngineeringBooksPDF.com

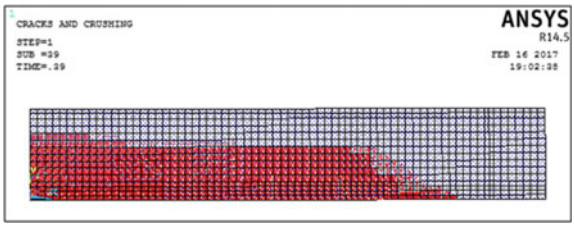

Fig. 8 Final crack pattern of control beam CBF

5.2 NSM-1

In NSM-1 beam the first crack was initiated at 88 kN, and the corresponding central deflection was 5.54 mm. Number of cracks developed was less compared to control beam. The crack pattern developed was as shown in Fig. 9. The crack had developed due to the bond between concrete and CFRP laminate. The ultimate load was 180 kN in experimental work, and the corresponding central deflection was 18.99 mm.

At loading stage of 70 kN, in ANSYS the crack started to appear at the mid-span of beam. The cracking model of the beam showed predominant flexural crack at the mid-span of the beam along with flexural shear cracks, which has been shown in Fig. 10. Massive cracks were observed near the support where CFRP laminate was terminated, indicating high stress concentration due to varying stiffness. Cracks were observed in the binding material around the external reinforcing element. The ultimate load carried by the beam and maximum deflection by the beam was 180 kN and 17.4 mm, respectively.

Fig. 9 Crack pattern for beam NSM-1

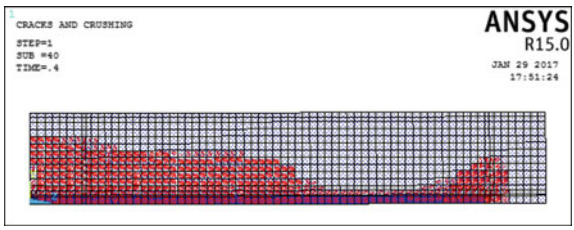

Fig. 10 Final crack pattern of beam NSM-1

www.EngineeringBooksPDF.com

Fig. 11 Crack pattern for beam NSM-2

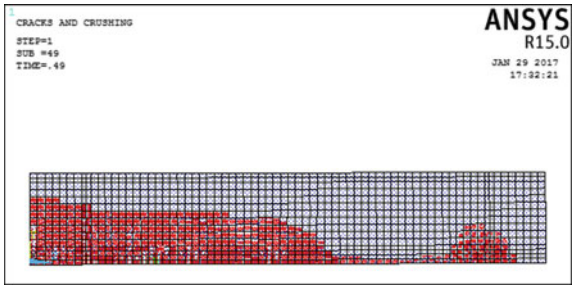

Fig. 12 Final crack pattern of beam NSM-2

5.3 NSM-2

In this beam, the first crack developed at 96 kN and the corresponding deflection was 4.37 mm. As loading increased, more number of cracks developed which were parallel, and the width of the cracks increased, as shown in Fig. 6. When loading approached ultimate load, a crack had developed at the bottom surface of the beam, which was between the two laminate strips near the right support, as shown in Fig. 11. The ultimate load was 190 kN, and the corresponding central deflection was 17.82 mm.

In finite-element analysis flexural crack started to appear at loading stage of 82 kN at the mid-span of the beam. Excessive cracking of concrete was observed at the zone where CFRP laminates were terminated. It was also observed that there was cracking of concrete around the strengthening material as shown in Fig. 12. The ultimate load sustained by the beam was 184 kN with the maximum deflection of 16.1 mm.

5.4 NSM-3

In beam NSM-3, even though the bonding area was more compared to NSM-2, the first crack was similar to that of previous beam, that is, 96 kN. The formation of cracks continued as loading proceeded and the numbers of crack were reduced and spacing between them was increased compared to all other beams in experimental work. As the bonding area was more, at the stage of ultimate load, sudden crack developed at the bottom near the support, as shown in Fig. 13. The ultimate load

www.EngineeringBooksPDF.com

Fig. 13 Crack pattern for beam NSM-3

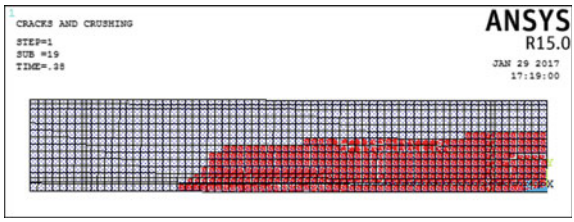

Fig. 14 Final crack pattern of beam NSM-3

sustained by this strengthened beam was 202 kN and the corresponding deflection was 11.69 mm.

During the finite-element analysis, the cracking model at the ultimate stage showed the pure flexural crack at the mid-span of the beam, which was initiated at the loading stage of 86 kN, but no shear or flexural shear cracks were observed, as shown in Fig. 14. No crack appeared at the end of CFRP laminate as observed in the experimental results. The maximum deflection of the beam was 12 mm along with ultimate load of 198 kN.

6 Load Deflection Behaviour of Beams

Load deflection behaviour of three beams along with control beams from experimental work has been presented in Fig. 15 along with the load deflection behaviour of control beam. During the initial stages of loading, strengthened beams showed linear behaviour compared over control beam. It was observed that the beam with three strips performed better in terms of initial stiffness and load-carrying capacity when compared to the other strengthened beams. From this, it was observed that as the bonding area increased, load-carrying capacity and stiffness of the beam also increased. There was no debonding of CFRP laminate that occurred in any of the beams strengthened by NSM technique. There was a similarity in failure modes of all three strengthened beams. Development of cracks at the ends of the laminate revealed that the terminating position of the strengthening material played vital role in the enhancement of load-carrying capacity of the beam.

www.EngineeringBooksPDF.com

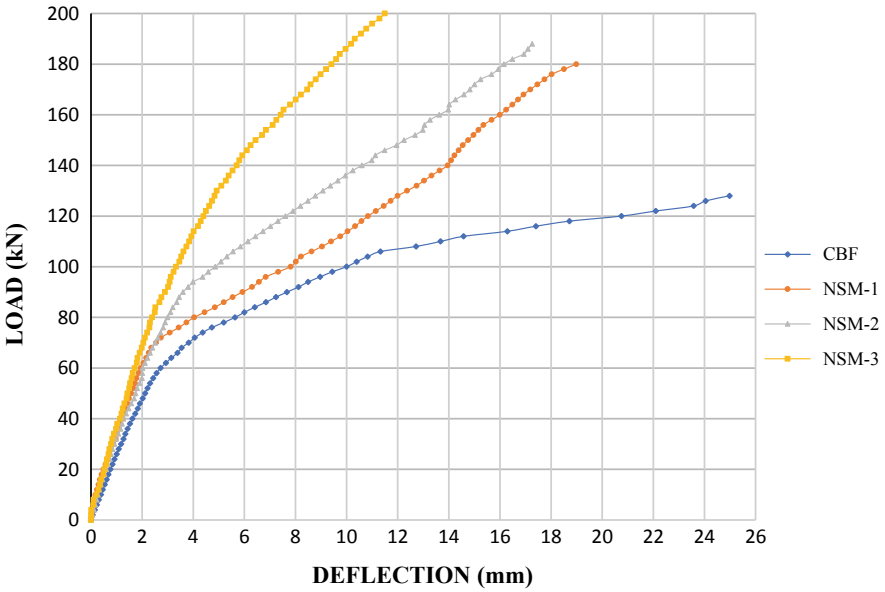

Fig. 15 Combined load deflection diagram of strengthened beams with control beam

7 Cracking, Working, Ultimate Loads and Deflections

The experimental cracking load (P_{cr}) was taken when first crack appeared on the beam and deflection corresponding to this load level was noted as deflection (Δ_{cr}) at first crack. Also, the ultimate load (P_u) and corresponding deflection (Δ_u) were noted. The working load (P_w) was obtained by dividing ultimate load (P_u) by a value of 1.5 and the corresponding deflection (Δ_w) was obtained from load deflection diagram and the values for control and strengthened beams are shown in Table 1. Ratio of ultimate and cracking loads of experimental and analytical results is shown in Table 2.

From Table 1, it was observed that load at initial crack and ultimate load for NSM-1 were increased by 42 and 40%, respectively, when compared to control beam, and

Table 1 Cracking, working, ultimate loads, deflections in flexure and ductility index

Beam	P_{cr} (kN)	Δ_{cr} (mm)	P_w (kN)	Δ_w (mm)	P_u (kN)	Δ_u (mm)	Δ_y (mm)	Ductility index (μ)
CBF	62	2.93	86	5.2	128	24.98	6.85	3.65
NSM-1	88	5.54	120	4.2	180	18.99	10.83	1.75
NSM-2	96	4.37	126	4.8	190	17.82	8.49	2.10
NSM-3	96	3.12	136	4.8	202	11.69	5.39	2.17

www.EngineeringBooksPDF.com

Table 2 Ratio of ultimate and cracking loads of experimental and analytical results

Beam	Experimental results			Analytical results			Ratio of P_u and P_{cr}	
	P_{cr} (kN)	P_u (kN)	Δ_u (mm)	P_{cr} (kN)	P_u (kN)	Δ_u (mm)	P_{cr} (exp)/P_{cr}(ana)	P_u (exp)/P_u (ana)
CBF	62	128	24.98	58	124	20	1.07	1.03
NSM-1	88	180	18.99	70	180	17.4	1.26	1
NSM-2	96	190	17.812	82	184	16.1	1.17	1.03
NSM-3	96	202	11.69	86	198	12.0	1.12	1.02

www.EngineeringBooksPDF.com

there was a decrease in central deflection of about 24%. In NSM-2, there was increase in the initial crack load and ultimate load by 54 and 48%, respectively, compared to control beam. In addition, deflection was decreased by 29%. In NSM-3 initial crack load and ultimate load were increased by 54 and 57%, respectively, compared to control beam. Central deflection was decreased by 53% compared to control beam. From Table 2, from the ratio of P_u and P_{cr}, analysis of control and strengthened post-tensioned beam using ANSYS was also validated.

8 Ductility Index

Ductility is calculated in terms of dimensionless ductility factor or ductility index (μ). This is calculated as the ratio of ultimate deflection (Δ_u) to the yield deflection (Δ_y) as given by Prabhakara et al. [11] in Eq. (1)

$$\mu = \frac{\Delta u}{\Delta y} \tag{1}$$

Bilinear method has been considered to analyse the ductility of strengthened post-tensioned beams. Here, the yield point is located by equating the area of the actual load deflection diagram to the bilinear system keeping the initial angle same in both the conditions. The ductility index (μ) for control and strengthened post-tensioned beams was calculated and presented in Table 1. The ductility index ranges from 2.44 to 4.8.

Generally, a high ductility index indicates that a structural member is capable of undergoing large deformations prior to failure. For beams with ductility index in the range of 3–5 is considered imperative for adequate ductility, especially in the areas of seismic design and redistribution of moments [11]. It has been observed from Table 1 that as the bonding area increased, ductility index was decreased.

9 Conclusions

Based on the experimental and analytical work, the following conclusions were drawn:

- Test results revealed that there was an increase in the first crack load of strengthened PT beams compared to control beam. However, increase in the first crack load was not proportional to the effective area of the strip.
- There was increase in initial stiffness of strengthened PT beams as compared to control beam. Therefore, the central deflection of the strengthened beam decreased with increase over the area of CFRP strips.

www.EngineeringBooksPDF.com

- Number of cracks developed in strengthened beams was less compared to control beams. However, ductility decreased over the increase in the area of CFRP strips.
- The PT beam strengthened by laminates with bonding area 0.45 m^2 was found to be more effective and the load-carrying capacity was increased compared to control beam.
- The experimental and analytical outcomes qualify the application of CFRP in NSM technique, as an effective tool to restore the flexural capacity of post-tensioned beams.

References

1. Carolin A (2003) Carbon fiber reinforced polymers for strengthening of structural elements. Doctoral thesis, Luleå University of Technology
2. Wight RG, Green MF, Erki MA (2001) Pre-stressed FRP sheets for post-strengthening reinforced concrete beams. J Compos Constr 5(4):214–220. https://doi.org/10.1061/(ASCE)1090-0268(2001)5:4(214)
3. Reed C, Peterman R (2004) Evaluation of pre-stressed concrete girders strengthened with carbon fiber reinforced sheets. J Bridge Eng 9(2):185–192. https://doi.org/10.1061/(ASCE)1084-0702(2004)9:2(185)
4. Larson KH, Peterman RJ, Rasheed HA (2005) Strength—fatigue behavior of fiber reinforced polymer strengthened pre-stressed concrete T- beams. J Compos Constr 9(4):313–326. https://doi.org/10.1061/(asce)1090-0268(2005)9:4(313)
5. Rosenboom O, Hassan T, Rizkalla S (2007) Flexural behavior of aged prestressed concrete girders strengthened with various FRP systems. Constr Build Mater 21(4):764–776. https://doi.org/10.1016/j.conbuildmat.2006.06.007
6. Kim YJ, Green M, Wight Gordon R (2008) Live load distributions on an impact-damaged prestressed concrete girder bridge repaired using prestressed CFRP sheets. J Bridge Eng 13(2):202–210. https://doi.org/10.1061/(ASCE)1084-0702(2008)13:2(202)
7. Rosenboom O, Rizkalla S (2006) Behavior of prestressed concrete strengthened with various CFRP systems subjected to fatigue loading. J Compos Constr 10(6):492–502. https://doi.org/10.1061/(ASCE)1090-0268(2006)10:6(492)
8. Barros JAO, Dias SJE, Lima JLT (2006) Efficacy of CFRP-based techniques for the flexural and shear strengthening of concrete beams. Cement Concr Compos 29(6):203–217
9. Bilotta A, Ceroni F, Di Ludovico Nigro E, Pecce M and Manfredi (2011). Bond efficiency of EBR and NSM FRP systems for strengthening concrete members. J Compos Constr 15(5): 757–772
10. Deng J, Lee M, Li S (2011) Flexural strength of steel–concrete composite beams reinforced with a prestressed CFRP plate. Constr Build Mater 25(1):379–384
11. Prabhakara R, Muthu KU, Meenakshi R (2006) Investigations on ultimate flexural strength and ductility behaviour of HSC beams. Indian Concr J 26(10):40–50

www.EngineeringBooksPDF.com

Analysis of Isotropic and Orthotropic Sandwich Bridge Decks

Preeti Agarwal, P. Pal, and P. K. Mehta

Abstract This paper presents the behaviour of isotropic and orthotropic sandwich bridge decks under IRC class-A wheel loading. In general, the fatigue damage of the bridge deck under the wheel load system is caused by stress concentration. Therefore, the stress concentration and displacement of simply supported steel and steel-polyurethane sandwich decks are determined using FEM. The models of both the decks are developed using ANSYS Workbench 14.0 and are analysed under area loading. The geometrical and material properties are taken from the reported results. The present results are compared with the reported literature and are found to be in good agreement. The optimum mesh size is chosen through a convergence study for discretizing the decks. It is found that the stresses in the steel deck are reduced from 40 to 85% and the maximum stress is reduced from 75 to 80% by using a sandwich deck system. The displacement of the sandwich deck system is found to be 85–90% less than that in the single-layer steel deck. Here, the thickness of the steel deck is equal to the sum of the two steel faceplates of the sandwich deck. The study shows that fatigue damage can be reduced in the steel bridge deck by using the sandwich deck system. The developed sandwich deck system shows good performance and proves to be an effective solution for the existing steel decks.

Keyword Sandwich deck · Steel deck · Displacement · Stress · FEM

P. Agarwal (✉) · P. Pal · P. K. Mehta
Department of Civil Engineering, MNNIT Allahabad, Prayagraj 211004, UP, India
e-mail: gotopreetiagarwal@gmail.com

P. Pal
e-mail: prpal@mnnit.ac.in

P. K. Mehta
e-mail: pradeep11@mnnit.ac.in

© Springer Nature Singapore Pte Ltd. 2021

K. K. Pathak et al. (eds.), *Recent Trends in Civil Engineering*, Lecture Notes in Civil Engineering 77, https://doi.org/10.1007/978-981-15-5195-6_8

www.EngineeringBooksPDF.com

1 Introduction

Fatigue damage in the bridge deck system poses a considerable challenge throughout the world. The main reason for fatigue damage of the bridge deck is stress concentration, which is caused by wheel load. So, it is important to study the stress concentration in the bridge deck system. Orthotropic sandwich decks (OWSDs) are of great importance in modern structural design. Orthotropic steel deck (OSD) is made of deck plates and may be stiffened by longitudinal ribs and transverse diaphragms. These are generally used in different kinds of steel bridges because of the inherent advantages, for example, lightweight, high load-bearing limit, convenient transportation and assemblage, and short construction time period. Most commonly, the moveable and long-span bridges are constructed with an orthotropic steel sandwich deck (OSSWD) because of its cost-effectiveness. OSSWD is also having low self-weight, which reduces stresses.

In the last few decades, numerous enhancements in inspection, maintenance and design were accomplished for OSSWD. An extensive literature is available on the orthotropic bridge deck (OBD) system and a few of them are presented below. OBD was first used in the mid-1930s for moveable bridges. Longitudinal and rolled stringers were used for supporting the OBD [1]. Cullimore and Smith [2] studied the stress concentration of non-sandwich orthotropic steel bridge deck subjected to local wheel loading using FEM. In OBD, Janss [3] investigated the fatigue resistance at the welds between a trapezoidal stiffener and the deck plate under transverse bending. Fatigue resistance is the main problem in OSD since it is directly and repeatedly loaded by vehicle. Most of the researchers found that the fatigue cracks occurred in between the stiffening rib and the bridge deck because of high-stress concentration [4, 5], which truly influences the traffic security on bridges. Pfeil et al. [6] investigated the structural behaviour of OSD with trapezoidal ribs under heavy vehicle loads, particularly where the fatigue cracks are prone to happen, using the finite element method. Xie and Chapman [7] suggested an alternative design method to improve the structural behaviour of the steel deck. The authors described the construction of steel–concrete–steel deck in which the plates were associated by bars, and were friction welded at both ends at the same time. Feldmann et al. [8] carried out the tests and calculative investigation to show the strengthening and stiffening effects and demonstrated the reasonableness of the steel-polyurethane steel (SPS) overlay strategy for general use. Romanoff and Varsta [9] presented a theory for web core sandwich plates to predict the bending response, local deformation, stress concentration and the effect of thick face plates. An investigation was carried out to reduce fatigue problem by introducing the reinforcing system. OBD was reinforced by two systems: (i) the sandwich steel plate system and (ii) the bonded steel plate system. The reinforcing system was used to stiffen the OSD to reduce the fatigue stress and to extend the fatigue life of OBD. In the bonded steel plate system, the bonding was done to the existing steel deck by attaching a secondary steel plate with a thin epoxy layer. The sandwich plate was composed of a thick solid polymer (polyurethane) core and two steel plates [10–12]. The risk of fatigue cracking during the whole life of OSD and

www.EngineeringBooksPDF.com

the problem of stress concentration under service vehicle loads, several possibilities were explored, for example, bonding a thin reactive powder concrete (RPC) layer underlying OSD [13, 14]. The sandwich steel-polyurethane bridge deck comprises a sandwich of two steel plates, filled by a strong polyurethane core. Polyurethane mass density is about 1/7 of the steel mass density. The sandwich core layer has low weight, high impact resistance, high stiffness, high insulation property and good damping. The polyurethane steel sandwich deck reduces the quantity of stiffeners, decreases the local stresses and self-weight of bridges. It provides a lesser steel surface exposed to corrosion [15]. Shan and Yi [16] studied numerically and experimentally the stress concentration law of steel-polyurethane sandwich deck under wheel load with and without stiffening rib.

In the present work, the isotropic and orthotropic sandwich bridge decks subjected to IRC class-A loading [17] are investigated. The effect of class-A load (wheel load) on a single-layer steel plate and a sandwich plate system without stiffening ribs is studied using the finite element method. Both the deck systems are considered to be simply supported. The stresses and displacements are calculated for a given load and the performances of decks are evaluated.

2 Modelling Process and Validation

The modelling procedure may be accepted if it gives comparative outcomes for the reported bridge models by other researchers. The model, shown in Fig. 1, is chosen for comparison. This was initially demonstrated by Shan and Yi [16]. The authors used SHELL-93 and SHELL-99 elements for modelling of single-layer steel deck and sandwich deck, respectively. Both elements are having eight nodes with six degrees of freedom at each node. In this study, SHELL-281 element, accessible in

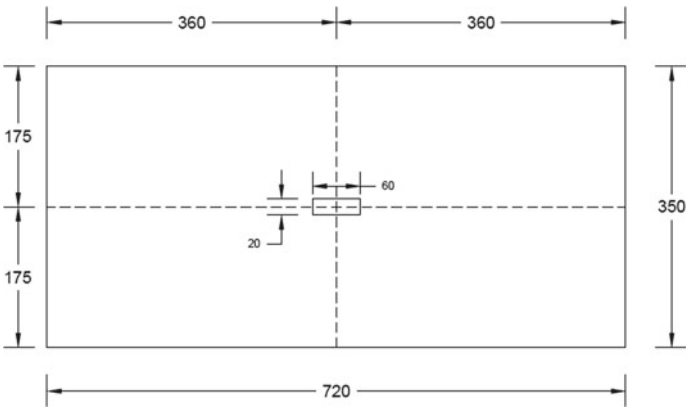

Fig. 1 Model of deck (dimensions are in mm)

www.EngineeringBooksPDF.com

Table 1 Material properties of steel and polyurethane

Material	Steel	Polyurethane
Gravimetric density (kN/m^3)	78.5	11.5
Yield strength (MPa)	335	–
Poisson's ratio	0.3	0.46
Elastic modulus (MPa)	2×10^5	800

ANSYS Workbench 14.0 [18], is used for the analysis of deck systems. This element is also having eight nodes with six degrees of freedom at each node.

Shan and Yi used a rectangular sandwich plate and a single-layer steel plate for the analysis of decks. The same models are studied here for validation. The length of the plate is 720 mm, width is 350 mm, and the thickness of lower and upper steel faceplates is 2 mm. The thickness of the core of the sandwich plate is 10 mm. The thickness of a single-layer steel plate is 4 mm. The model of the deck system is shown in Fig. 1. The material properties are presented in Table 1.

Both the single-layer steel deck and sandwich bridge deck are considered as simply supported on four edges. In the analysis, the wheel load is converted to a uniformly distributed area load of initially1.667 MPa [i.e. P/(60 × 20), where P is the jack force of 2 kN]. The stress concentration is studied for the steel-polyurethane sandwich bridge deck system. The mesh size of the element is taken as 20 mm along both the longitudinal and transverse directions. The bending normal stresses along both the directions are determined and compared. Stress points at the base of both decks are shown in Fig. 2. The stresses are determined at every 10 mm distance in both the longitudinal and transverse directions. The obtained results are presented in Figs. 3, 4, 5 and 6 for the area load. Figures 3 and 5 show the stresses in both the decks in X-direction at points 1–17 and 18–32, respectively. Figures 4 and 6 show the stresses in both the decks in Y-direction at points 1–17 and 18–32, respectively. The maximum stress occurs under the area load, as expected. The present results are compared and are found to be in close agreement with the reported results by Shan and Yi [16].

From the figures, it is observed that the stresses in the sandwich deck are less than about 1/3 of those in a single-layer steel deck. Hence, the verified modelling procedure considered may be extended to the real steel deck and sandwich deck models.

3 Model of Bridge Deck

In this section, a rectangular sandwich deck and a single-layer steel deck are modelled using the SHELL-281 element. SHELL-281 elements are reasonable for investigating the slender to modestly thick shell structures. Shan and Yi considered the dimensions of the bridge deck as follows: deck width = 1440 mm; deck length = 700 mm; and thickness of each steel faceplate of the sandwich plate = 2 mm. All dimensions of

www.EngineeringBooksPDF.com

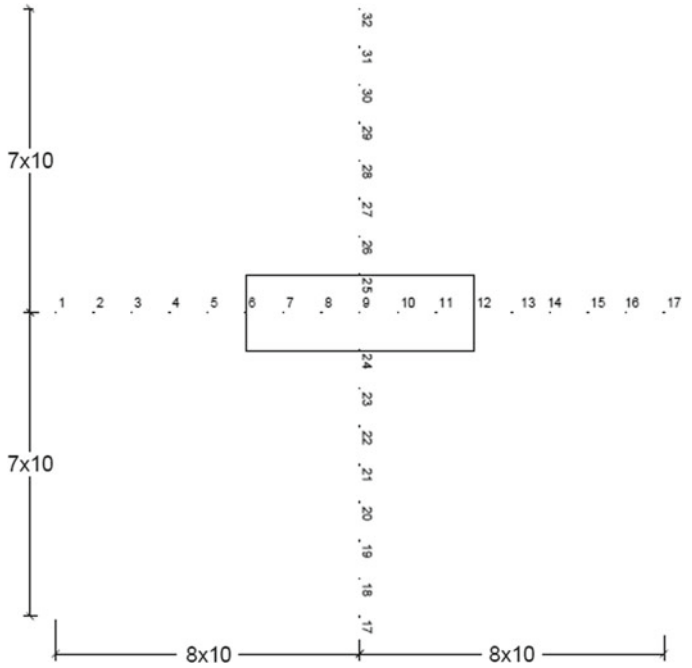

Fig. 2 Stress points of deck

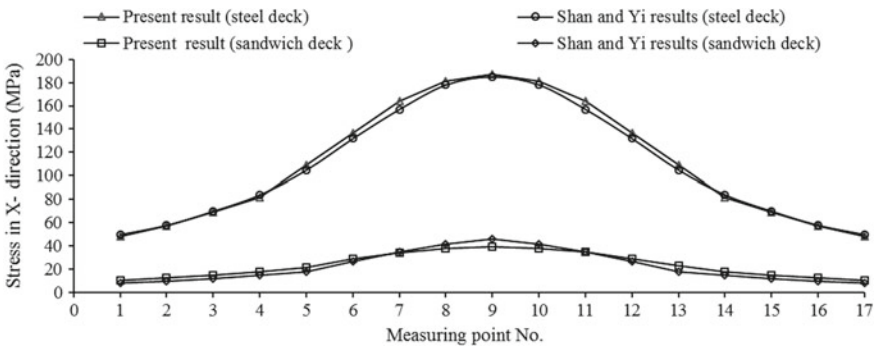

Fig. 3 Stress in X-direction at points 1–17

the deck, that is, length, width and thickness were scaled to 1/4 of the real deck size. In the present investigation: width of the steel deck = 5760 mm; length of the single layer of steel deck = 2800 mm; and the thickness = 16 mm, which are similar to the real bridge deck system. In the sandwich deck, the thickness of the lower and upper steel faceplates is considered as 8 mm. The total thickness of the steel-polyurethane sandwich deck is 40 mm. Material properties and boundary conditions adopted are

www.EngineeringBooksPDF.com

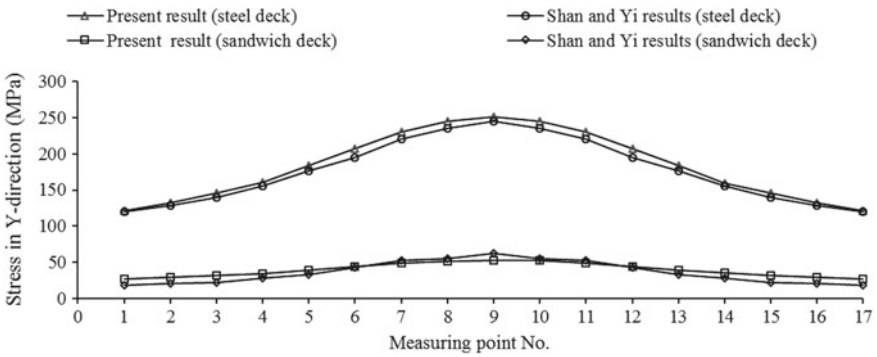

Fig. 4 Stress in Y-direction at points 1–17

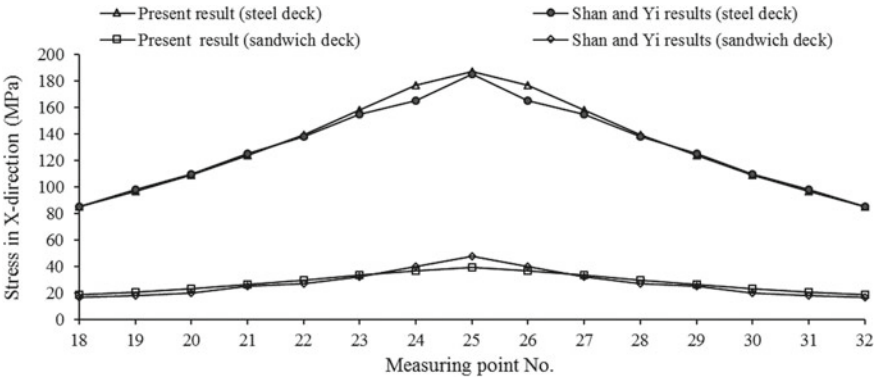

Fig. 5 Stress in X-direction at points 18–32

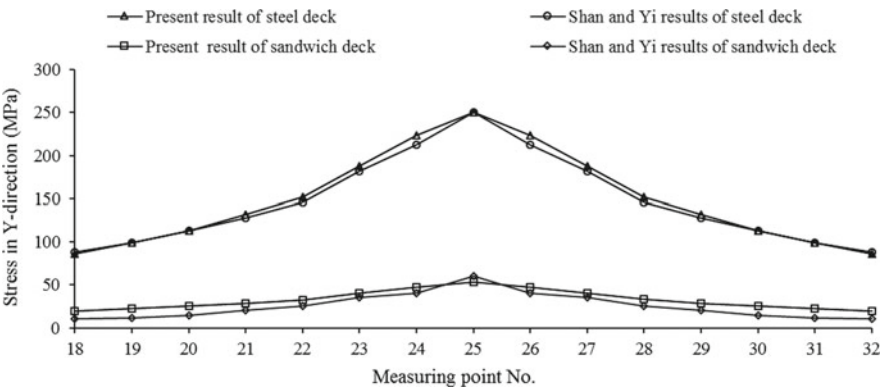

Fig. 6 Stress in Y-direction at points 18–32

www.EngineeringBooksPDF.com

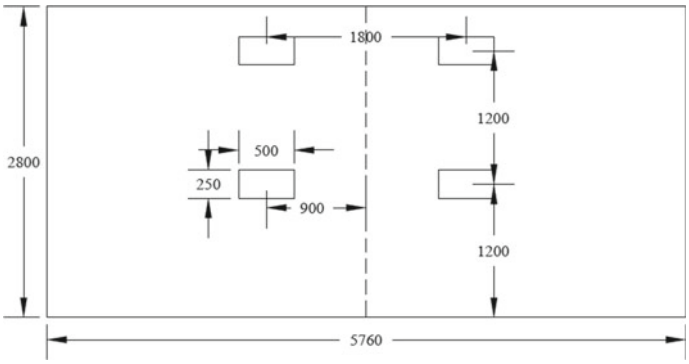

Fig. 7 Model of bridge deck system (dimensions are in mm)

the same as those considered by Shan and Yi. The heaviest wheel load of IRC class-A loading [17] (i.e. 57 kN), and the loading area of 500 × 250 mm are considered for the analysis of the bridge deck system. Four wheels of class-A load [17] act on both the sandwich deck and the single-layer steel deck. In the longitudinal direction, the distance of the rear wheel load from the edge of the plate is 1200 mm. In the transverse direction, the distance of the rear wheel load from the centre of the deck is 900 mm. Figure 7 shows the modal of the bridge deck system with load position.

3.1 Convergence Study

A convergence is studied to check the proper number of nodes required to accomplish the minimum error in the evaluated maximum deflection of a single-layer steel deck system. The obtained results are shown in Fig. 8. It is clearly observed that the results converge at the mesh size of 20 mm. To minimise the computational error, a mesh size of 20 mm is adopted for modelling the deck system.

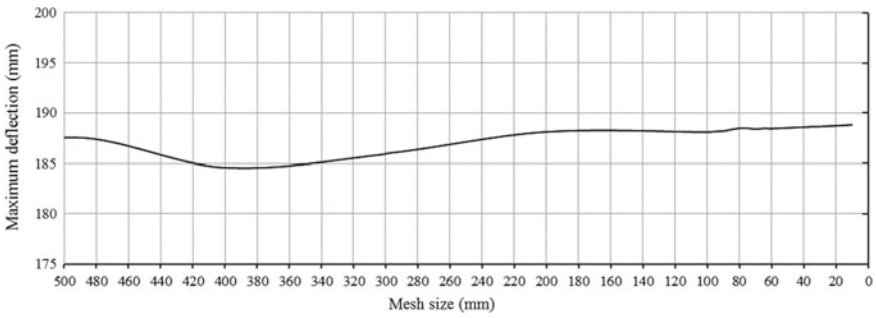

Fig. 8 Convergence study

www.EngineeringBooksPDF.com

4 Results and Discussion

This study determines the stresses and deflection of a single-layer steel deck and a sandwich deck subjected to the IRC class-A wheel load [17]. In the longitudinal direction, stresses are determined at a distance of 1200 mm from the edge of the plate. In the transverse direction, stresses are determined at a distance of 2000 mm from the edge of the plate. At every 40 mm distance, the stresses are determined along both the longitudinal and transverse directions. The deflection and stress contour of both the deck systems are shown in Figs. 9 and 10, respectively. Normal stress resultants of a single-layer steel deck and an orthotropic sandwich bridge deck are shown in Figs. 11, 12, 13 and 14. Figures 11 and 13 illustrate the stresses in both the decks in X-direction along width and length directions, respectively. Figures 12 and 14 illustrate the stresses in both the plate in Y-direction along width and length directions, respectively. In the two orthogonal directions, the bending normal stresses are plotted. A few interesting features are noted from the study due to the effects of the polyurethane material.

The maximum deflection of the steel deck is 187.68 mm, whereas it is 17.74 mm in the sandwich deck. The deflection of the sandwich deck is much lower than the single-layer steel deck. As seen in Figs. 11, 12, 13 and 14, the stresses in X and

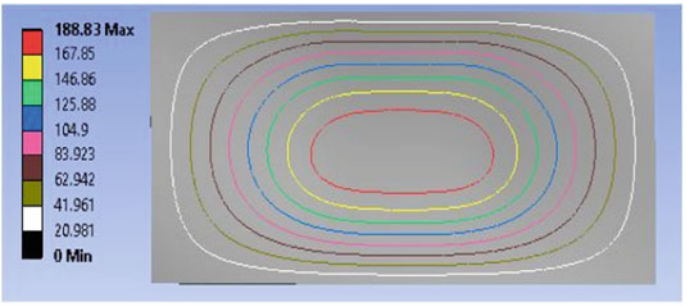

(a) Single layer steel deck

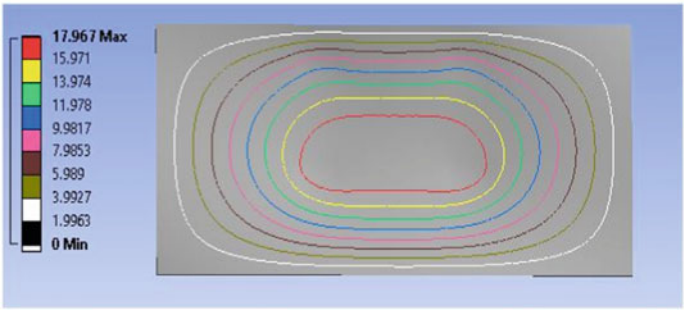

(b) Steel- polyurethane sandwich deck

Fig. 9 Deflection contour

www.EngineeringBooksPDF.com

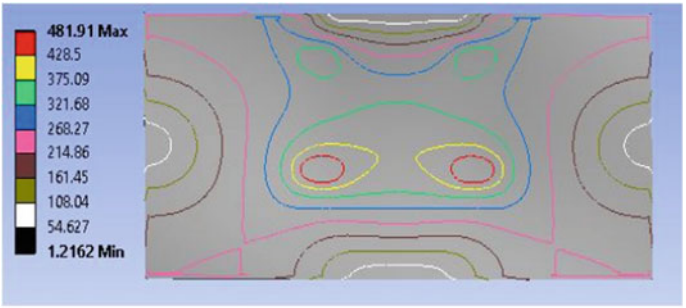

(a) Single layer steel deck

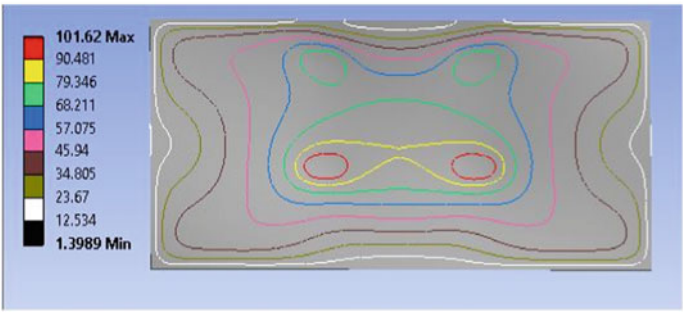

(b) Steel- polyurethane sandwich deck

Fig. 10 Stress contour

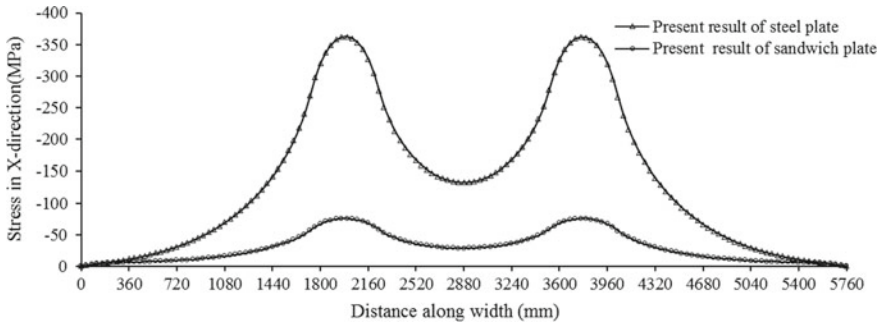

Fig. 11 Stress in X-direction along the width

Y directions of a single-layer steel deck are more than those in a sandwich deck. The stress distribution is found to be higher near the area of distribution load, as expected. The stress distribution curve is found to be steep for the single-layer steel deck, whereas it is flat for the sandwich deck. This indicates that the stress and its distribution are higher for a single-layer steel deck. It is observed that the stresses

www.EngineeringBooksPDF.com

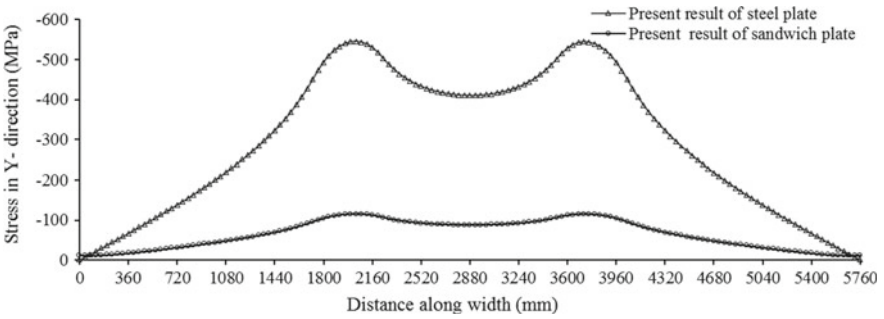

Fig. 12 Stress in Y-direction along the width

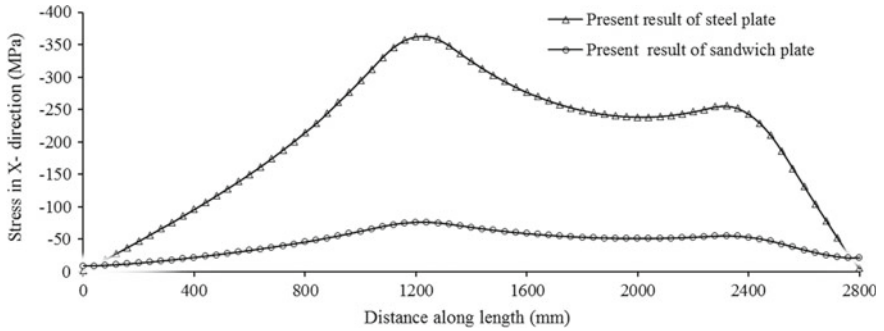

Fig. 13 Stress in X-direction along the length

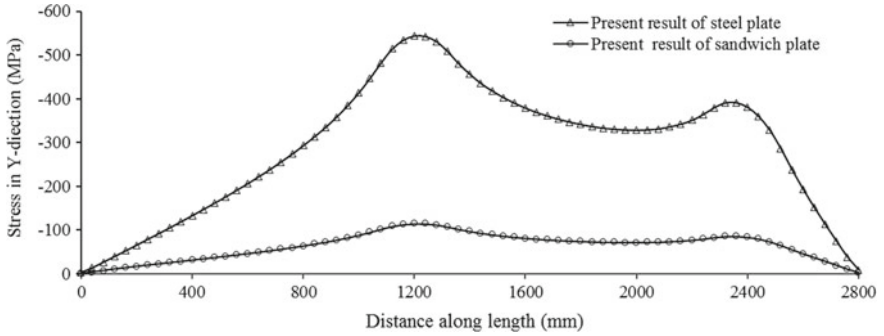

Fig. 14 Stress in Y-direction along the length

in the X-direction are less than that in the Y-direction. The stresses of the single-layer steel deck are greater than that in the sandwich deck. The outcomes described above provide the quantitative description of the bending stresses, which may be useful for the design of the bridge deck.

www.EngineeringBooksPDF.com

5 Conclusions

This study aims to demonstrate the effectiveness of polyurethane material in the deck system. Based on the study carried out so far, the following conclusions are drawn:

- The maximum stresses in both the decks are developed under the wheel load and are decreased rapidly outside the region immediately surrounding it.
- The stresses in the longitudinal direction are greater than those in the transverse direction.
- Stresses in the steel deck are reduced from 40 to 85% by using a sandwich deck system. Using 24 mm thick polyurethane core and 8 mm thick upper and bottom steel face plates, the maximum stress reduction of 75–80% is achieved.
- The performance of the sandwich deck is superior if the bending stress plays an important role in the design of the deck system.
- The displacement of the steel-polyurethane sandwich plate is 85–90% less than that in the single-layer steel deck under the effect of wheel loading.
- The sandwich deck system proves to be an effective alternative for strengthening old as well as new steel deck systems and is fit for traffic too.

Acknowledgments The authors acknowledge the Motilal Nehru National Institute of Technology Allahabad for providing the financial support under TEQIP-III.

References

1. Heins C, Firmage D (1979) Design of orthotropic deck bridges, in design of modern steel highway bridges. Wiley, New York
2. Cullimore M, Smith J (1981) Local stresses in orthotropic steel bridges deck caused by wheel loads. J Constr Steel Res 1:17–26. https://doi.org/10.1016/0143-974X(81)90029-8
3. Janss J (1988) Fatigue of welds in orthotropic bridge decks panels with trapezoidal stiffeners. J Constr Steel Res 9:147–154. https://doi.org/10.1016/0143-974X(88)90005-3
4. Wolchuck R (1990) Lessons from weld cracks in orthotropic decks on three European bridges. J Struct Eng 116:75–84. https://doi.org/10.1061/(ASCE)0733-9445(1990)116:1(75)
5. Cunninghame J, Beales C (1990) Fatigue crack location in orthotropic steel decks. In: Proceedings international association for bridges and structural engineering, Zurich, Switzerland, pp 17–26. http://doi.org/10.5169/seals-42842
6. Pfeil M, Battista R, Mergulhão A (2005) Stress concentration in steel bridge orthotropic decks. J Constr Steel Res 61:1172–1184. https://doi.org/10.1016/j.jcsr.2005.02.006
7. Xie M, Chapman J (2006) Developments in sandwich construction. J Constr Steel Res 62:1123–1133. https://doi.org/10.1016/j.jcsr.2006.06.025
8. Feldmann M, Sedlacek G, Geler A (2007) A system of steel-elastomer sandwich plates for strengthening orthotropic bridge decks. Mech Compos Mater 43:183–190. https://doi.org/10.1007/s11029-007-0018-y
9. Romanoff J, Varsta P (2007) Bending response of web-core sandwich plates. Compos Struct 81:292–302. https://doi.org/10.1016/j.compstruct.2006.08.021
10. Teixeira de Freitas S, Kolstein H, Bijlaard J (2010) Composite bonded systems for renovations of orthotropic steel bridge decks. Compos Struct 92:853–862. https://doi.org/10.1016/j.compstruct.2009.09.016

www.EngineeringBooksPDF.com

11. Teixeira de Freitas S, Kolstein H, Bijlaard J (2011) Sandwich system for renovation of orthotropic steel bridge decks. J Sandw Struct Mater 13:279–301. https://doi.org/10.1177/1099636210386848
12. Teixeira de Freitas S, Kolstein H, Bijlaard J (2013) Fatigue behavior of bonded and sandwich systems for strengthening orthotropic bridge decks. Compos Struct 97:117–128. https://doi.org/10.1016/j.compstruct.2012.10.019
13. Chen B, Shao X, Cao J (2012), Study of fatigue cracking for orthotropic steel bridge deck. J Eng Mech 29:170–174. http://en.cnki.com.cn/Article_en/CJFDTotal-GCLX201212026.htm
14. Shao X, Yi D, Huang Z, Zhao H, Chen B, Liu M (2013) Basic performance of composite bridge deck system with orthotropic steel deck and thin RPC layer. J Bridge Engg 18:413–428. https://doi.org/10.1061/(ASCE)BE.1943-5592.0000348
15. Teixeira de Freitas S, Kolstein H, Bijlaard J (2013) Lightweight reinforcement systems for fatigue-cracked orthotropic bridge decks. Struct Eng Int 23:458–467. https://doi.org/10.2749/101686613X13627347100356
16. Shan C, Yi Y (2016) Stress concentration analysis of an orthotropic sandwich bridge deck under wheel loading. J Constr Steel Res 122:488–494. https://doi.org/10.1016/j.jcsr.2016.04.011
17. IRC 6–2014: Standard specifications and code of practice for road bridges
18. ANSYS workbench 14.0, User Manual

www.EngineeringBooksPDF.com

The Effect of Angle of Web Opening for Prediction of Ultimate Failure Load of Castellated Beams by Experimental Investigation

Amol J. Mehetre and Rajashekhar S. Talikoti

Abstract A beam which has openings in its web portion is called castellated beam. For the preparation of castellated beams, fabrication of I section is done by cutting web portion and subsequently re-joining it one above the other. The popularity of castellated beams measures its advantageous structural applications. It expands the lives of millions every day combined with our pioneering business facilities. The objective of this research paper is to investigate new angle of web opening of the diamond shape in comparison with hexagonal and rectangular web opening to determine the ultimate load-carrying capacity and to avoid shear stress concentration at the corner of the rectangular and hexagonal opening which is responsible for failure of castellated beam. This paper studies the deflection performance and ultimate load-carrying capacity of castellated beams with a diamond, hexagonal and rectangular opening. To identify experimental results of this research, 24 beams were fabricated, tested and results are validated using ANSYS software. The variable considered in this research is the angle of opening 30°, 45° and 60° for diamond. The length of the opening for diamond and rectangle of castellated beams is equal. It is concluded that the ultimate load-carrying capacity of diamond web opening with 30° angle of opening is 47.86% more and has 47.5% less deflection compared to the hexagonal opening. The average load-carrying capacity of diamond web opening is 44.21% more and deflection 44.00% less than rectangular web opening.

Keywords Angle of opening · Length of opening · Ultimate load-carrying capacity · Deflection · ANSYS

A. J. Mehetre (✉)
Civil Engineering Department, LGNSCOE, SPPU Pune, Nashik, Maharashtra, India
e-mail: amol.mehetre@avcoe.org

R. S. Talikoti
Civil Engineering Departments, R. H. Sapat College of Engineering, Management Studies and Research, SPPU Pune, Nashik, Maharashtra, India
e-mail: rstalikoti@gmail.com

© Springer Nature Singapore Pte Ltd. 2021

K. K. Pathak et al. (eds.), *Recent Trends in Civil Engineering*, Lecture Notes in Civil Engineering 77, https://doi.org/10.1007/978-981-15-5195-6_9

www.EngineeringBooksPDF.com

1 Introduction

The construction industry demands castellated steel beams (CSBs) since many years because of the development of mechanised equipment used for cutting and welding. Manufacturing of such beams is done in an almost unlimited number of spans and depths. For both light and heavyweight loading conditions, a castellated beam (CB) is suitable. Earlier, the angle of cutting for CBs ranged from 45° to 70° but now, the proper standard cutting angle is 60°. Though 45° sections also exist, it is well known that these are near values. In practice, actual angles are slightly different from these to house other geometrical necessities. Castellated beams are commonly used in the areas of high steel cost and low labour cost.

For the improvement of moment of inertia, depth of a section and section properties of parent hot-rolled steel section are to be improved by castellation, as shown in Fig. 1. Parent section was of depth 150 mm whereas castellated beam was having depth of 225 mm. It increases the load-carrying capacity and control on a deflection. Web resists shear force whereas flange resists the bending moment. According to the theory of beam, the rolled steel I section is much effective for carrying bending and shear loads in the web. The results of castellation show 50% increase in the depth of the beam; 20 and 30% increase in strength and stiffness, respectively, for the same weight of the beam. The section modulus of the castellated beam is increased 2.25 times that of parent beam section. Ductwork can be done in the beams through the openings instead of going underneath of the beams. Finally, floor system depth reduces, as shown in Fig. 2.

Wang et al. [19–21] studied the CSBs with hexagonal fillet corner web opening to know the shear buckling behaviour of the web-post using finite-element method (FEM). The fillet corner hexagonal web opening CBs having circular and elongated circular opening were compared for various buckling capacity with various buckling modes. The proposed opening shape of the web-post in a CSB showed best structural performance as compared with circular openings. The load-bearing capacity of a proposed opening shape of CBs for the different capacities, like web-post buckling,

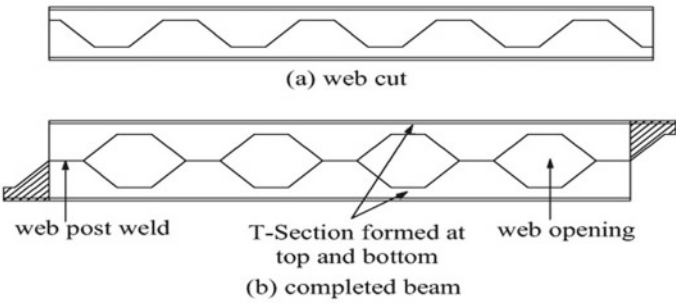

Fig. 1 Castellated steel beam with hexagonal openings IC225

www.EngineeringBooksPDF.com

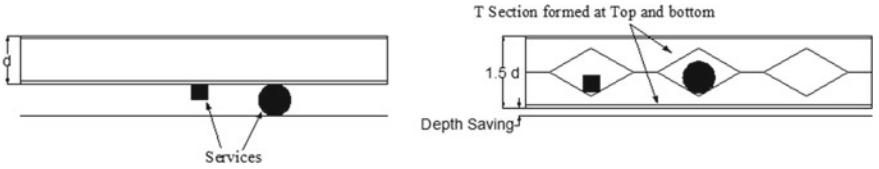

Fig. 2 Castellated steel beam with diamond openings usages for depth saving and attractive appearance

shear rupture capacity of the horizontal weld and the Vierendeel failure capacity, has the minimum value.

Durif et al. [3–5] have done investigation on sinusoidal web opening of cellular beams by experimental and numerical approach. The maximum strength of castellated beams with the sinusoidal opening was evaluated through the comparative study with FEM for different beam profile and opening shapes. The analytical model proposed by the authors' revealed that the analytical ultimate loads gave acceptable results compared to FEM results.

Ellobody [8, 9] studied the normal and high strength cellular steel beams by considering combine buckling modes with nonlinear analysis. The test was conducted with a variable like a different length, cross-section and loading condition. Different modes of failure were verified by developing the nonlinear 3D finite-element model. The cellular steel beams failed due to combined web distortional buckling. Web-post buckling modes showed a considerable decrease in the failure loads. The usage of high strength steel resulted in a considerable increase in the failure loads.

Gandomi et al. [10] predicted a model of the castellated beam for the load capacity using gene expression programming (GEP). Hosain and Speirs [11] investigated the effect of hole geometry on the modes of failure and ultimate strength of castellated beams. Kerdal and Nethercott [12] investigated various modes of failure associated with castellated beams because of web openings and welds, which are as follows:

1. Flexural failure mechanism; 2. Lateral-torsional buckling; 3. Vierendeel bending mechanism; 4. Weld rupture at web-post; 5. Shear buckling of web-post; and 6. Compression web-post buckling.

The maximum load capacity and its deflection were investigated by Morkhade and Gupta [13, 14]. Consideration for vertical load for steel beam with the circular and hexagonal opening was given. Optimization was done for spacing to diameter and aspect ratio. The analytical study to know the effect of web opening on the flexural response of a hybrid beam with circular, hexagonal, square and rectangular shape opening was done.

Tsavdaridis and D'Mello [17] investigated opening web shapes which are hexagonal, circular and elliptical opening of web. Extensive finite-element studies were done on web opening to examine Vierendeel failure. The structural behaviour of perforated beam is significantly affected by the shape of the web opening as shown in this research. It is in contrast to the rectangular shape of web opening which is used predominantly. Zirakian and Showkati [23] studied a distortional buckling by

www.EngineeringBooksPDF.com

using experimental investigation. The extrapolation techniques were used in addition to the test strengths to determine accurate critical loads of the beams. A comparison has been made among the theoretical predictions and the obtained test loads.

Thomas and Baskar [18] worked on the load-carrying capacity of thin-webbed castellated beams to propose an equation for understanding and the prominent modes of failure.

Wie-bin et al. [6, 16, 22] presented an analytical solution to determine the deflection under concentrated or uniformly distributed transverse loads of castellated/cellular beams with various web openings. Serviceability condition is checked for the design purpose with the deflection criteria. The analytical model for calculating deflection due to concentrated, uniformly applied transverse load has been developed. Also, the additional deflection due to vertical shearing effect at the opening is included. The theoretical bending deflection to overall deflection for finite-element investigation for cellular beams has been considered.

Pourbehi and Pirmoz [15] studied a critical issue in designing of web-post failure characteristic and failure modes of non-ductile nature of buckling. Castellated beams failed with web-post buckling are considered to study the shear characteristic using numerical analysis. The precision of the earlier projected design is calculated for the mild steel beam and it was investigated that the existing methods are insufficient to forecast the web-post buckling load of the beams.

Most of the existing researches were carried out for hexagonal, rectangle, circular and sinusoidal shape of the opening of castellated steel beams; however, very less study was reported on the opening angle of diamond shape. In fact, this opening angle is very useful for a load-carrying capacity of the section and its control on deflection. Therefore, in this paper, the emphasis is given on the opening angle of the diamond shape web opening and its effect over the castellated beams in terms of ultimate load-carrying capacity and deflection. Considering all these aspects, CSBs with a diamond, hexagonal and rectangle web opening, which is one of the recommended possible solutions for the incorporation of technical utility in the building structures, were tested for the occurrence of failure. This research includes a test on eight specimens out of one parent beam model and one hexagonal beam model, three for diamond and rectangle, respectively. CSBs model subjected to two-point vertical loads are shown in Figs. 3 and 4. The present study is primarily an experimental basis, and experimental programme is done on specimen up to occurrence of failure. Table 1 indicates the details of beam specimen in the form of span, angle of opening, and so on.

2 Experimental Program

A total of 24 numbers of CSBs ware fabricated for the experimental study followed by the guidelines according to ASTM [2] (ANSI/AISC 360-10, 2010) and David D [7] (2003) Steel Design Guide Series-2. Castellated beam is fabricated using ISMB 150 as a parent section for fabrication. Depth of such beam is kept 1.5 times more than the

www.EngineeringBooksPDF.com

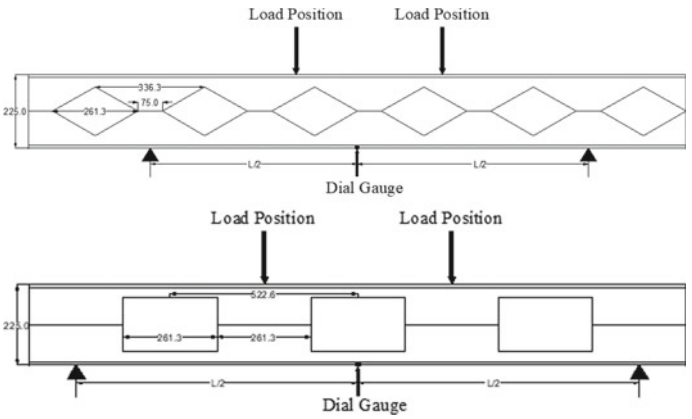

Fig. 3 Two-point loading and dial gauge in castellated steel beam with diamond and rectangular openings

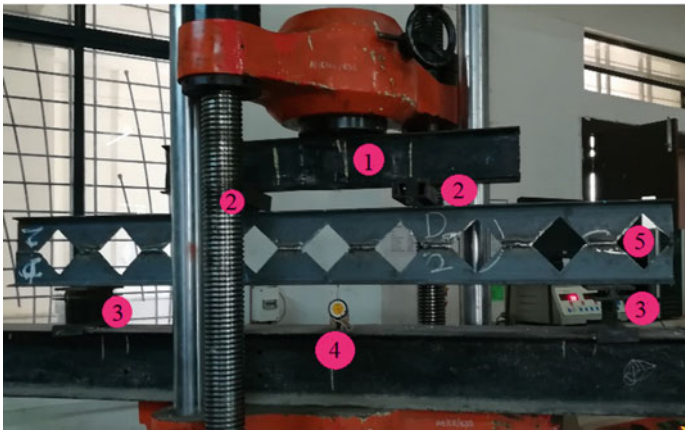

Fig. 4 Detailed view of the experimental setup. 1. Two-point loading assembly, 2. Loading point. 3. Support at solid part of the beam, 4. Dial gauge for maximum deflection at the centre of the span, 5. A castellated steel beam with 45° angle of opening $CSBID_2$

original depth, which becomes 225 mm after fabrication. The flange thickness is 8 mm whereas web thickness is 5 mm, keeping 150 mm depth of opening and fabricated length of 2000 mm. These beams are tested using 1000 kN universal testing machine (UTM) for flexural load. This paper includes testing of 24 CSBs, which is carried out to investigate the ultimate load-carrying capacity and deflection of CBs with a hexagonal opening having an angle of opening 60°, diamond opening with the angle of opening 30°, 45°, 60° and rectangle opening using an equal length as that of opening for diamond section by using the experimental method. The differences in load-carrying capacity and deflection of entirely fabricated CBs are presented,

www.EngineeringBooksPDF.com

Table 1 Identification of castellated steel beams

S. No.	Details of beams	Angle of opening Θ°	Depth of top or bottom T S_b or S_t	Depth of opening $D_O = h_o$ (mm)	Centre to centre spacing between two openings S (mm)	Number of openings
1	IP	–	–	–	–	–
2	CSBIH	45°	37.5	150	305.00	6
3	$CSBID_1$	30°	37.5	150	336.30	6
4	$CSBID_2$	45°	37.5	150	224.50	9
5	$CSBID_3$	60°	37.5	150	161.10	12
6	$CSBIR_1$	–	37.5	150	522.60	3
7	$CSBIR_2$	–	37.5	150	300.00	6
8	$CSBIR_3$	–	37.5	150	172.20	11

IP—Parent beam (I section), CSBIH—Castellated steel beam with hexagonal opening, CSBID—Castellated steel beam with diamond opening, CSBIR—Castellated steel beam with rectangular opening

and the results are validated using ANSYS software [1] (ANSYS version 16). The hexagonal 60° section is selected for comparison point of view because the section is widely used in practice.

3 Measurement Technique

All the beams are divided into three equal spans from the face of support and loaded with a two-point loading assembly. The loading point is applied at L/3 distance from the face of support. Gradually increasing load is applied until failure. The ultimate load and corresponding deflection of the specimen is recorded till the occurrence of failure. Deflection is noted on dial gauge placed at a distance L/2 from the face of support having a least count of 0.001 mm. By applying the same techniques ultimate load-carrying capacity of each beam at failure is observed and the deflection was noted on a dial gauge. The load and deflection is also recorded for parent section ISMB 150. The experimental setup is shown in Fig. 4. Care should be taken at the time of testing that the position of applied loads and support provision made is on the solid part of the web (refer Fig. 4). In the guideline given by ASTM, it is mentioned that concentrated load should not apply above the opening but the flexural testing is consider under two-point loading to face the practical difficulty.

www.EngineeringBooksPDF.com

4 Results and Discussion

The experiment shows the flange buckling in case of diamond opening as shown in Fig. 5, and web and flange buckling in case of rectangular web opening in tested beams, as shown in Fig. 6. By using experimental and software results, the graphs are plotted for deflected beams of a different angle of web opening. Experimental and software failure mode is same for rectangular web opening as shown in Figs. 7 and 8. Refer Table 2 for experimental ultimate load carrying capacity of castellated beams. Figure 9 shows comparison of ultimate load carrying capacity of tested beam specimen.

Fig. 5 Flange buckling is observed in the beam with diamond web opening $CSBID_1$

Fig. 6 A crack developed at the corner of rectangular web opening $CSBIR_2$

Fig. 7 Web and flange buckling is observed in the beam with rectangular opening $CSBIR_1$

www.EngineeringBooksPDF.com

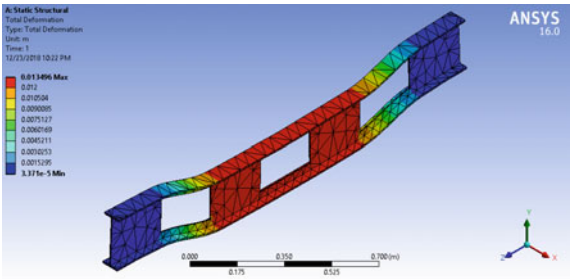

Fig. 8 Equivalent failure pattern in ANSYS for $CSBIR_1$

Table 2 Details of experimental ultimate load-carrying capacities of castellated beams

Types of CSBs	IP	CSBIH	$CSBID_1$	$CSBID_2$	$CSBID_3$	$CSBIR_1$	$CSBIR_2$	$CSBIR_3$
Ultimate loads (kN)	132.2	140	207	146	134	75	119	144

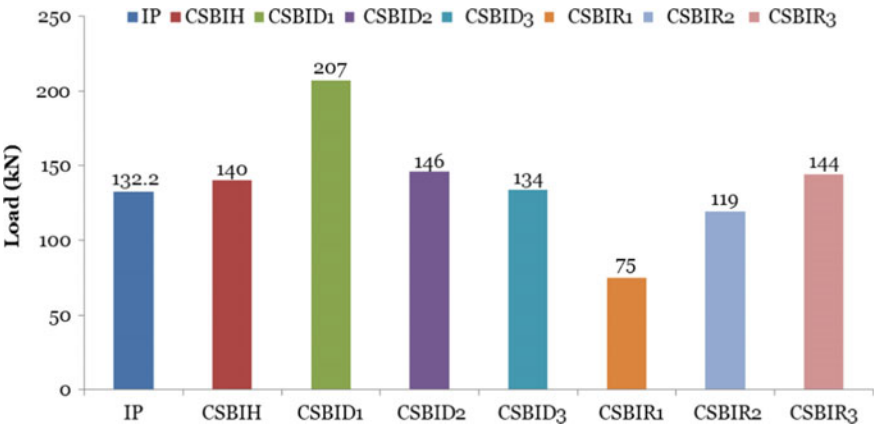

Fig. 9 Comparison of ultimate load-carrying capacity of tested beams specimen

4.1 Finite-Element Analysis

Thin to moderately thick-type shell structures are analysed using SHEEL-181 element in ANSYS modelling. This element consists of four nodes, and each node has six degrees of freedom. This element follows translation as well as rotation in x, y and z directions. (Using membrane option this element has only translational degree of freedom.) While creating a mesh, triangular option is used as a filler element. SHELL-181 is suitable in case of linear, nonlinear, large rotation and/or large strain applications. While doing nonlinear analysis the corresponding change in thickness

www.EngineeringBooksPDF.com

Table 3 Material properties used in ANSYS modelling

Material	ρ (kg/m^3)	E (MPa)	Poisson's ratio	F_y (MPa)	Element used
Steel	7850	200000	0.30	250	SHELL-181

of shell is considered. This element is supported by both full and reduced integration. It takes into account the load stiffness and effect of distributed pressure. Refer Table 3 for properties of material used in ANSYS modelling. Position of supports and loads for $CSBID_1$ is shown in Fig. 10. The maximum deflection of $CSBID_1$ is shown in Fig. 11.

For all eight cases, load vs deflection graphical representation of experimental and software readings are plotted in Figs. 12, 13, 14, 15, 16, 17, 18 and 19. From the plot, it is observed that experimental behaviour is nonlinear and software behaviour is linear. In software, materials have the given controlled properties. During experimentation, gas cutters were used due to which material properties have changed slightly. It may also happen that in ANSYS nonlinear stress–strain diagram is not incorporated during analysis (As reflected in Table 4).

Graphical representation of Fig. 9 has shown the load-carrying capacity of the tested sample. It is clearly observed that the load-carrying capacity of diamond web opening having 30° angle of opening shows maximum value amongst all tested CSBs.

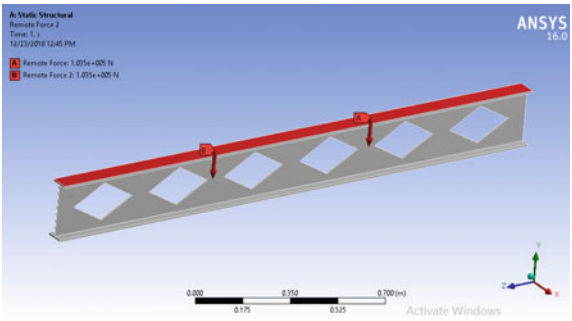

Fig. 10 Position of supports and loads for $CSBID_1$

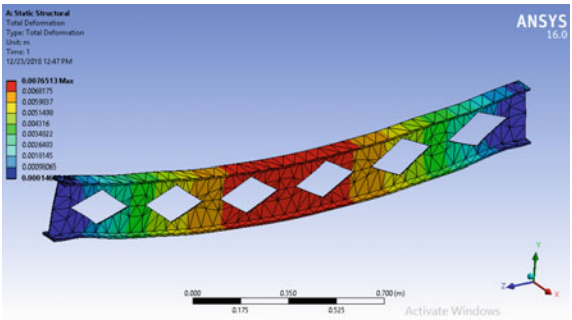

Fig. 11 Maximum deflection of $CSBID_1$

www.EngineeringBooksPDF.com

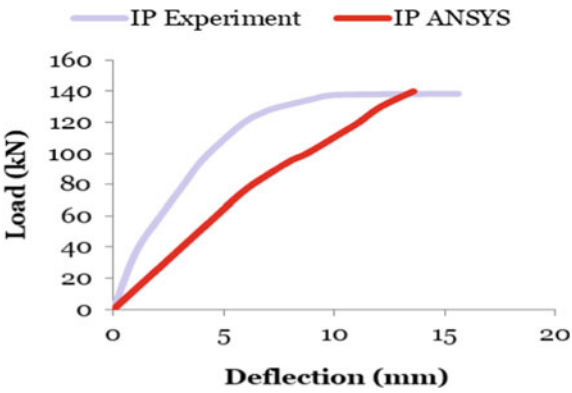

Fig. 12 Load versus deflection for IP

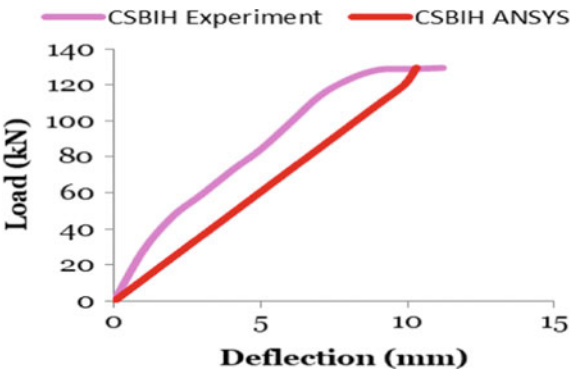

Fig. 13 Load versus deflection for CSBIH

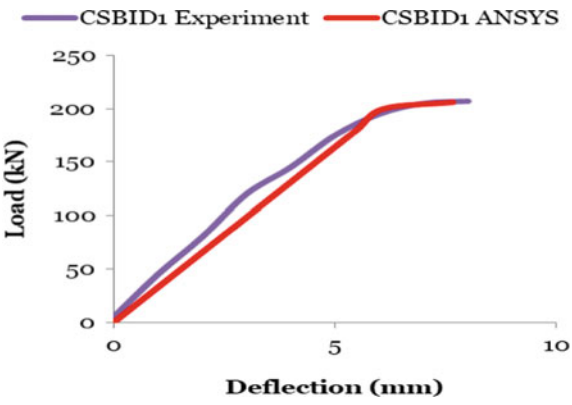

Fig. 14 Load versus deflection for $CSBID_1$

Similarly, the deflections of tested CSBs are shown in Fig. 20. All the values obtained for the deflection criteria were satisfying and the deflection criterion is given in code; hence all the sections designed for this experiment are conservative.

www.EngineeringBooksPDF.com

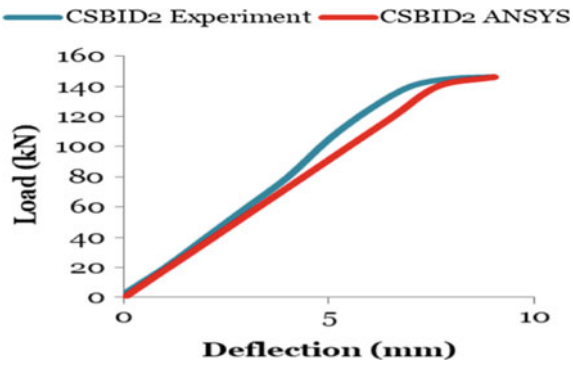

Fig. 15 Load versus deflection for $CSBID_2$

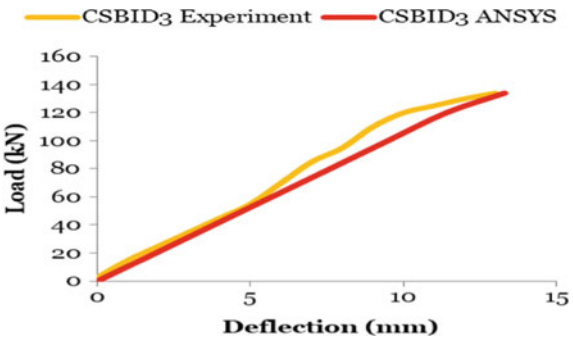

Fig. 16 Load versus deflection for $CSBID_3$

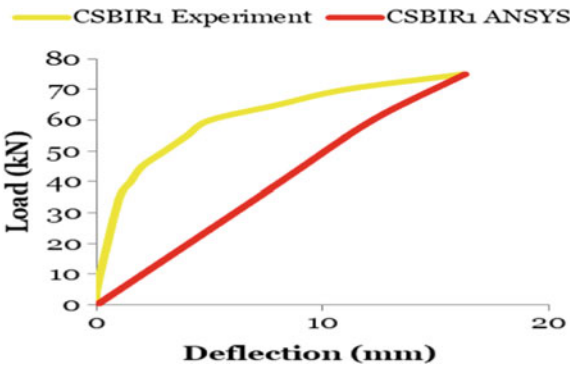

Fig. 17 Load versus deflection for $CSBIR_1$

5 Conclusions

Based on the above results, the following conclusions are drawn.

1. Ultimate load-carrying capacity of the castellated beam with diamond web opening is more as compared to castellated beam with the hexagonal opening.

www.EngineeringBooksPDF.com

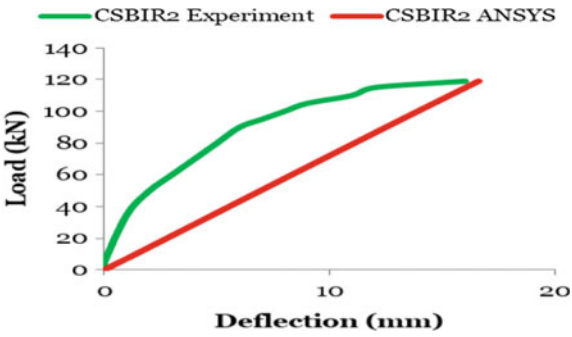

Fig. 18 Load versus deflection for $CSBIR_2$

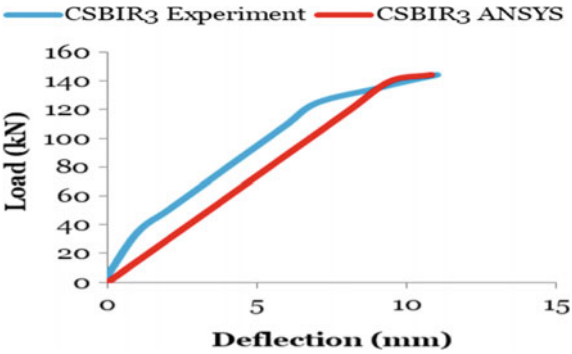

Fig. 19 Load versus deflection for $CSBIR_3$

Table 4 Comparison between experimental and software results of deflections of castellated beams

S. no.	Specimen	Deflection (mm)	
		Experimental	ANSYS
1	IP	15.60	15.52
2	CSBIH	11.20	10.31
3	$CSBID_1$	8.00	7.65
4	$CSBID_2$	9.00	9.03
5	$CSBID_3$	13.00	13.28
6	$CSBIR_1$	16.2	13.50
7	$CSBIR_2$	16.00	16.63
8	$CSBIR_3$	11.00	10.79

2. The load-carrying capacity of $CSBID_1$ compared to CSBIH is 47.85% more, that of $CSBID_2$ compared to CSBIH is 4.28% more and of $CSBID_3$ compared to CSBIH is 4.28% less.
3. The castellated beam with diamond web opening has performed structurally better than the hexagonal opening when compared in terms of distribution of stress, shear stress and modes of failure.

www.EngineeringBooksPDF.com

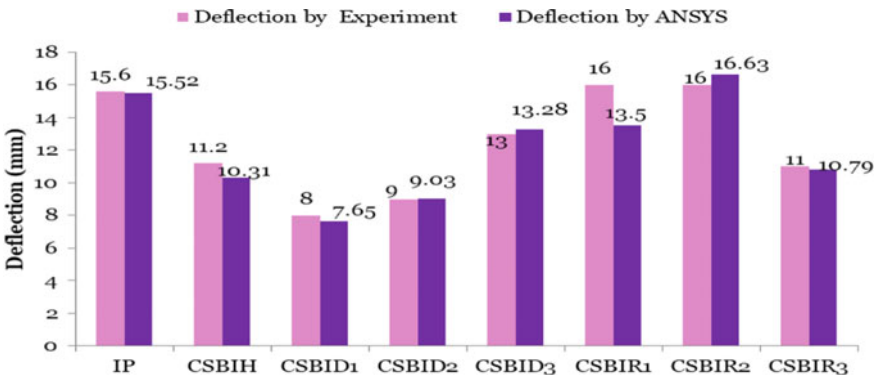

Fig. 20 Comparison of deflection of tested beam specimens with ANSYS results

4. Castellated beams with diamond web opening have maximum shear capacity compared to hexagonal web opening.
5. Experimental analysis shows that shear stress gets easily concentrated at the corners of hexagonal and rectangle web opening castellated beams.
6. Diamond web opening castellated beams show less deflection as compared to hexagonal and rectangle web openings.
7. Deflection of $CSBID_1$ compared to CSBIH is 40.00% less and that of $CSBID_2$ compared to CSBIH is 24.44% less and of $CSBID_3$ compared to CSBIH is 16.07% more.
8. On comparing the results of all diamond web opening castellated beams, it is found that a castellated diamond web opening with the angle of web opening 30° shows better performance compared to castellated beam with diamond web opening and the angle of web opening 45° and 60°.
9. Nature of the curves for experimental and ANSYS results are nearly the same as per the graphical representation.

The main outcomes of this study can be summarized as:

The 30° angle of opening of CSBs has shown good structural performances with hexagonal and rectangular openings in the form of the load-carrying capacity and deflection, mode of failure and the distribution of stresses. The CSBs with the hexagonal and rectangular opening have a lower shear carrying capacity compared to beams with diamond opening.

This work can be extended in terms of change in angle, such as the hexagonal, octagonal shape of opening by considering the variation in the angle of web opening.

References

1. ANSYS version 16.0 (2015) Inc. Canonsburg
2. American Institute of Steel Construction (2010) Specification for a structural steel building. ANSI/AISC 360-10. An American National Standard
3. Durif S, Bouchair A (2012) Behavior of cellular beams with sinusoidal openings. Procedia Eng 40:108–113
4. Durif S, Bouchair A, Vassar O (2014) Experimental and numerical investigation on web-post specimen from cellular beams with sinusoidal openings. Eng Struct 59:587–598
5. Durif S, Bouchair A (2016) Analytical model to predict the resistance of cellular beams with sinusoidal openings. J Constr Steel Res 121:80–96
6. Djebli B, Kerdal DE, Abidelah A (2014) The total deflection of composite cellular beams under transverse loading. Arabian J of Sci Eng. https://doi.org/10.1007/s13369-014-1227-z
7. David D (2003) Steel design guide series 2 steel and composite beams with web opening. American Institute of Steel Construction Inc
8. Ellobody E (2011) Interaction of buckling modes in castellated steel beams. J Constr Steel Res 67:814–825
9. Ellobody E (2012) Nonlinear analysis of cellular steel beams under combined buckling modes. Thin-Walled Struct 52(1):66–79
10. Gandomia AH, Tabatabaei SM, Moradian MH, Radfar A, Alavi A (2011) A new prediction model for the load capacity of castellated steel beams. J Constr Steel Res 67:1096–1105
11. Hosain MU, Speirs WG (1973) Experiments on castellated steel beams. Welding Research, American Welding Society and Welding Research Council 329–341
12. Kerdal D, Nethercott DA (1984) Failure modes for castellated beams. J Constr Steel Res 4:295–315
13. Morkhade SG, Gupta L (2015) An experimental and parametric study on steel beams with web openings. Int J Adv Struct Eng 7:249–260
14. Morkhade SG, Kshirsagar M, Dange R, Patil A (2019) Analytical study of effect of web opening on flexural behaviour of hybrid beams. Asian J Civil Eng https://doi.org/10.1007/s42107-019-00122-4
15. Pourbehi P, Pirmoz A (2015) Shear response of castellated steel beams. Int J of Steel Struct 15(2):389–399
16. Panedpojaman P, Thepchatri T (2013) Finite element investigation on deflection of cellular beams with various configurations. Int J of Steel Struct 13(3): 487–494. https://doi.org/10.1007/s13296-013-3008-z
17. Tsavdaridis KD, D'Mello C (2012) Vierendeel bending study of perforated steel beams with various novel web opening shapes through nonlinear finite element analyses. J Struct Eng138 (10):1214–1230
18. Thomas CA, Baskar K Assessment of load carrying capacity of thin-webbed castellated beam. Recent Adv Struct Eng https://doi.org/10.1007/978-981-13-0362-3_27
19. Wang P, Wang X, Ma N (2014) Vertical shear buckling capacity of web-posts in castellated steel beams with fillet corner hexagonal web openings. Eng Struct 75:315–326
20. Wang P, Ma Q, Wang X (2014) Investigation on Vierendeel mechanism failure of castellated steel beams with fillet corner web openings. Eng Struct 74:44–51
21. Wang P, Guo K, Liu M, Zhang L (2016) Shear buckling strengths of web-posts in a castellated steel beam with hexagonal web openings. J Constr Steel Res 121:173–18
22. Wie-bin Y, Nan-ting Y, Zhao-shui B, Li- ping W (2016) Deflection of castellated beams subjected to uniformly distributed transverse loading. Int J Steel Struct 16(3): 813–821
23. Zirakian T, Showkati H (2006) Distortional buckling of castellated beams. J Const Steel Res 62:863–871

Free Vibration Frequencies of Lock Gate Structure

Deepak Kumar Singh, Priyaranjan Pal, and Shashi Kant Duggal

Abstract The effect of incompressible fluid on free vibration frequencies of a stiffened lock gate structure is investigated. The formulation of a stiffened lock gate consists of plate and beam elements. Mindlin's plate bending and Euler's beam theories are used for the plate and the stiffener, respectively. The fluid is assumed to be inviscid and incompressible, having an irrotational flow. The infinite far boundary of the fluid domain is truncated near the lock gate structure using Fourier half-range cosine series expansion in the solution of the Laplace equation. Finite-element method (FEM) is used to establish interaction between the fluid and the lock gate. The finite-element formulation is then converted into computer code to determine the free vibration frequencies of the stiffened lock gate in the presence of fluid. The results are compared with the unstiffened lock gate by approximately keeping the same volume of material.

Keywords Lock gate · Stiffener frequencies · Fluid-structure interaction

1 Introduction

Lock gate is a structural component in the dam-reservoir system, which controls the flow of water. Interaction between the lock gate and the reservoir fluid considerably affects the response of the lock gate; hence it is important to study the fluid–structure interaction effect on the vibration of the lock gate. When a body vibrates at a frequency equivalent to free vibration frequency, the amplitude of vibration increases significantly which could lead to failure. In general, the free vibration frequency of any structure decreases in the presence of surrounding fluid than that in the absence

D. K. Singh (✉) · P. Pal · S. K. Duggal
Civil Engineering Department, MNNIT Allahabad, Prayagraj 211004, UP, India
e-mail: erdeepak.india@gmail.com

P. Pal
e-mail: prpal@mnnit.ac.in

S. K. Duggal
e-mail: shashi@mnnit.ac.in

© Springer Nature Singapore Pte Ltd. 2021

K. K. Pathak et al. (eds.), *Recent Trends in Civil Engineering*, Lecture Notes in Civil Engineering 77, https://doi.org/10.1007/978-981-15-5195-6_10

of fluid. So, the determination of free vibration frequencies becomes very important for such structures. As the overall mass of the fluidstructure system is increased in the presence of fluid, the frequency of any system is directly influenced by the mass of the whole system. The problems of fluid–structure interaction are addressed in open literature quite often, consisting of unstiffened gate and reservoir. The isotropic rectangular and circular plates vibrating in contact with water are also investigated by many researchers. Some of these contributions are presented in this study.

Free vibration analysis of annular [1] and circular [2] plates which are in contact of an incompressible, inviscid fluid was investigated. A theoretical method was proposed to determine the natural frequencies of free edge annular plates [3] and circular plates [4]. A novel far boundary is introduced for the infinite reservoir by truncating the far boundary near the structure [5]. An analytical Ritz approach was developed to investigate the plate-water system and validate the results with added virtual mass incremental (AVMI) factor approach [6]. The coupled problems of fluid and lock gate are investigated using FEM [7–11]. Free vibration analysis of liquid-filled containers was investigated using a meshless local Petrov-Galerkin (MLPG) approach [12]. The frequency of clamped circular plate bounded by incompressible, inviscid fluid was investigated [13]. A procedure for the vibration analysis of a rectangular plate placed at the bottom of a liquid-filled container was presented [14].

The aim of the investigation is to determine the free vibration frequencies of unstiffened and stiffened lock gates with or without the presence of fluid. Further, the frequencies are compared by approximately keeping the same volume of material in both unstiffened and stiffened lock gates. Undisturbed free surface condition is considered here when the lock gate is in contact with the fluid. The results may be useful for the engineers and designers for designing the lock gate structures.

2 Methodology

The model used in the present investigation is shown in Fig. 1. In actual, the free surface of the fluid domain is nonlinear in nature. But when the fluctuation of the

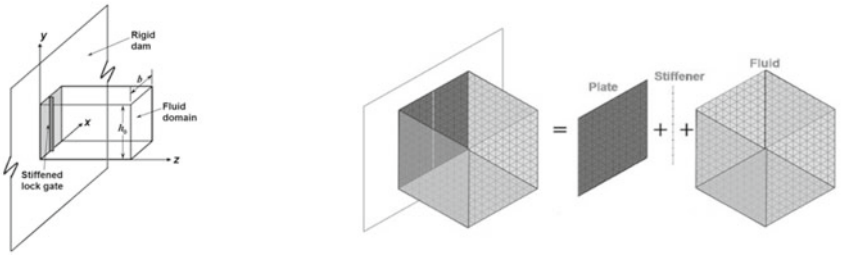

(a) Theoretical model (b) Numerical model

Fig. 1 Stiffened lock gate and fluid domain system

free surface is small in comparison to the depth of the fluid domain, the free surface may be assumed to be linear. Further, simplification is made by considering the free surface as undisturbed. The far boundary is truncated closer to the lock gate so as to minimise the computation time without influencing the results, very much.

3 Mathematical Formulation

The mathematical formulation for stiffened lock gate and fluid domain has been presented separately in the following section. Afterward, the finite-element formulation is done for coupling of both the domains which is finally converted into a computer code written in FORTRAN to evaluate the free vibration frequencies of the lock gate with and without fluid. The formulation for a lock gate structure may be found elsewhere [15].

3.1 Fluid Domain

The undisturbed free surface condition is assumed at the top surface of the fluid domain. The infinite length of the fluid domain is truncated near the lock gate numerically and which are as follows.

Governing equation
For inviscid, incompressible fluid, and irrotational fluid flow neglecting the static pressure, the value of fluid pressure may be written using Laplace equation as

$$\nabla^2 p = \nabla^2 p(x, y, z) = 0 \tag{1}$$

where ∇^2 is the Laplacian operator and p is the fluid pressure at a point at any instant of time over and above the static atmospheric pressure.

Boundary condition
It is assumed that there is no pressure change across the side surfaces of the fluid domain due to small generated displacement of the lock gate, as it vibrates along the rigid dam,

$$\text{At, } x = 0, \frac{\partial p}{\partial n}(0, y, z) = 0, \text{ and at, } x = b, \frac{\partial p}{\partial n}(b, y, z) = 0 \tag{2}$$

where b is the width of the fluid domain.

Also, it is assumed that there is no pressure change across the bottom surface of the fluid domain. It is also assumed that there is no surface wave, that is, the free surface is undisturbed,

$$\text{At, } y = 0, \frac{\partial p}{\partial n}(x, 0, z) = 0, \text{ and at, } y = h_0, p(x, h_0, z) = 0 \tag{3}$$

where h_0 is the depth of the fluid domain.

At the fluid–structure interface, pressure gradient has been generated and the pressure is assumed to be zero at the truncated far boundary surface,

$$\text{At, } z = 0, \frac{\partial p}{\partial n}(x, y, 0) = -\rho_f a, \text{ and at, } z = \infty(\text{far boundary}), p(x, y, \infty) = 0 \tag{4}$$

where a is the acceleration of fluid.

Development of truncated far boundary

The far boundary of the fluid domain can be considered sufficiently at a large distance away from the lock gate structure. The implementation of this condition, though easier, accounts for a large volume of computation time and space. Therefore, using some rational approximations, the truncated far boundary is developed. Using the Fourier half-range cosine series, the boundary condition at the far truncated boundary may be developed by solving Eq. (1) and represented as

$$p = 4h_0\rho_f a \times \sum_{m=0}^{\infty} \frac{(-1)^{(m+1)}}{\lambda_m^2} \cos\lambda_m \left(\frac{y}{h_0}\right) e^{-\left[\lambda_m\left(\frac{z}{h_0}\right)\right]} \tag{5}$$

where $\lambda_m = \frac{(2m-1)\pi}{2}$

$$\frac{\partial p}{\partial n} = \left(\frac{\partial p}{\partial n}\right)_{z=L} = \frac{-p}{h_0}\zeta_i \tag{6}$$

where L is the truncated length and $\zeta_i = \dfrac{\sum_{m=0}^{\infty} \frac{(-1)^{(m+1)}}{\lambda_m^2} \cos\lambda_m \left(\frac{y}{h_0}\right) e^{-\left[\lambda_m\left(\frac{z}{h_0}\right)\right]}}{\sum_{m=0}^{\infty} \frac{(-1)^{(m+1)}}{\lambda_m^3} \cos\lambda_m \left(\frac{y}{h_0}\right) e^{-\left[\lambda_m\left(\frac{z}{h_0}\right)\right]}}$

where x, y and z denote the axis along the side, height and fluid length, respectively.

3.2 Structural Domain

In the following section, the formulation of the lock gate structure (i.e. plate with stiffener) is presented. It comprises the formulation of the plate and the stiffener separately.

Plate element formulation
The displacement at any point within the plate element can be expressed as

$$\begin{Bmatrix} u \\ v \\ w \\ \theta_x \\ \theta_y \end{Bmatrix} = \sum_{i=1}^{9} N_i [I] \begin{Bmatrix} u_i \\ v_i \\ w_i \\ \theta_{xi} \\ \theta_{yi} \end{Bmatrix} \tag{7}$$

where u, v, w, θ_x and θ_y are the displacement at node i, N_i is the interpolation function and $[I]$ is the identity matrix. The stiffness matrix of the plate [15] is given by

$$\left[K_p\right] = \iint \left[B_p\right]^T \left[D_p\right] \left[B_p\right] t_p |J| d\xi d\eta \tag{8}$$

where $\left[B_p\right]$ is the strain displacement matrix, $[D_p]$ is rigidity matrix and $[J]$ is Jacobian matrix. The mass matrix of the plate element is given by

$$\left[M_p\right] = \iint [N]^T \left[m_p\right] [N] t_p |J| d\xi d\eta \tag{9}$$

where m_p is the mass matrix of the plate element.

Stiffener element formulation
The displacement field of the stiffener may be expressed as

$$\begin{Bmatrix} u_s \\ v_s \\ w_s \end{Bmatrix} = \begin{Bmatrix} u_{0s} - z\theta_{xs} \\ v_{0s} - z\theta_{ys} \\ w_{0s} \end{Bmatrix} \tag{10}$$

where u_s, v_s and w_s are displacements at any point in x, y and z directions, respectively. u_{0s}, v_{0s} and w_{0s} are the translations at the mid-plane of the stiffener. θ_{xs} and θ_{ys} are the rotations of the normal with respect to the undeformed mid-plane. z is the distance of the point from the mid-plane at which the displacements are determined. The stiffness matrix of the stiffener [15] is given by

$$[K_s] = \iint [B_s]^T [D_s][B_s] L_s O_s |J| d\xi d\eta \tag{11}$$

where $[B_s]$ is the strain displacement matrix, $[D_s]$ is the rigidity matrix and $|J|$ is Jacobian matrix. The mass matrix of the stiffener (i.e. beam element) is given by

$$[M_s] = \iint [N]^T [m_s][N] L_s O_s |J| d\xi \tag{12}$$

where m_s is the mass matrix of the stiffener element. After formulating the plate and the stiffener individually, both are combined to form the stiffened lock gate. In this study, a single stiffener is used to stiffen the lock gate system, where the stiffener may be placed edge to edge along the height or width of the plate. However, to coincide with the nodes of the stiffener and plate, the stiffener is to be placed on the centre nodal line of the plate.

4 Finite-Element Formulation

The resulting coupled solution is used for the evaluation of free vibration frequencies of the lock gate. Plate, stiffener and fluid are discretized using nine-noded isoparametric plate element, three-noded isoparametric beam element and twenty-seven-noded isoparametric brick element, respectively.

4.1 Governing Equation for the Fluid Domain

Finite-element formulation is presented [11, 15] considering top surface of the fluid to be undisturbed free surface.

Undisturbed free surface
The fluid domain is discretized (Fig. 1b) as an assemblage of finite elements assuming pressure to be the nodal unknown. The pressure at any point inside an element may be represented as

$$p = \sum_{i=1}^{n} N_i \bar{p}_i \tag{13}$$

N_i, $\bar{p}_i$ are the interpolation functions and nodal pressure values corresponding to node i, respectively, and n is the number of nodes in the element. Using the Galerkin's weighted residual method, the weighted average integral of Eq. (1) may be written in concise form to represent the fluid domain as

$$[G]\{\bar{p}\} = \{B\} \tag{14}$$

where $[G] = \sum \int_{\Omega_e} \left(\nabla N^T . \nabla N\right) d\Omega_e$ and $\{B\} = \sum_s \int_{\Gamma_e} N^T \frac{\partial p}{\partial n} d\Gamma_e$.

$\sum_s$ refers to the total boundary surface of the fluid domain and $N = [N_1, N_2, N_3 \ldots N_n]$

The boundary term {B} may split into several components that are available in the literature [11, 15], and after incorporating the boundary conditions, Eq. (14) yields

$$[G_i]\{\bar{p}\} = -\rho_f \left[R_{fs}\right]\{\bar{a}\} \tag{15}$$

where $[G_i] = [G] + \frac{1}{h_0}[R_{ti}]$, $\left\{R_{fs}\right\} = \sum_{S_{fs}} \int_{\Gamma_e} N^T N_s d\Gamma_e$ and $[R_{ti}] = \sum_{S_t} \int_{\Gamma_e} \left(N^T \zeta_i N\right) d\Gamma_e$

4.2 Governing Equation for the Gate

The undamped free vibration equation of the lock gate may be expressed as

$$[M]\left\{\ddot{\overline{X}}\right\} + [K]\left\{\overline{X}\right\} = \{0\} \tag{16}$$

where [M] and [K] are the assembled mass and stiffness matrices of the gate, respectively; $\left\{\ddot{\overline{X}}\right\}$ and $\left\{\overline{X}\right\}$ are displacement and acceleration vectors, respectively. Stiffness and mass matrices corresponding to each element are the summation of stiffness and mass matrices of the plate, and the contributions of stiffener to this element.

$$[M] = \left[M_p\right] + [M_s] \tag{17}$$

$$[K] = \left[K_p\right] + [K_s] \tag{18}$$

where subscripts p and s refer to plate and stiffener, respectively.

4.3 The Coupled Motion of the Lock Gate and the Fluid

In this section, the formulation of the lock gate and the fluid domain is combined together to enquire the effect of fluid on the lock gate structure. The motion of

the fluid–structure interface is prescribed by the movement of the stiffened gate. Replacing $\{\bar{a}\}$by$\left\{-\ddot{\overline{X}}\right\}$ in Eq. (15), the resulting equation is yielded as

$$[G_i]\{\bar{p}\} = \rho_f\left[R_{fs}\right]\left\{\ddot{\overline{X}}\right\} \tag{19}$$

When the effect of dynamic pressure is added to Eq. (16), it may be written as

$$[M]\left\{\ddot{\overline{X}}\right\} + [K]\left\{\overline{X}\right\} = \left\{\overline{f_s}\right\} \tag{20}$$

where $\left\{\overline{f_s}\right\}$ is the forcing term due to the fluid pressure at the interface.

$$\left\{\overline{f_s}\right\} = -\sum_{S_{fs}}\int_{\Gamma_e}[N_s]^T p d\Gamma_e = -\left[R_{fs}\right]^T\{\bar{p}\} \quad \text{since, p} = [N]\{\bar{p}\} \tag{21}$$

After substituting $\left\{\overline{f_s}\right\}$, Eq. (21) may be written as

$$[M]\left\{\ddot{\overline{X}}\right\} + [K]\left\{\overline{X}\right\} + \left[R_{fs}\right]^T\{\bar{p}\} = \{0\} \tag{22}$$

From Eq. (19), it is yielded as

$$\{\bar{p}\} = \rho_f[G_i]^{-1}\left[R_{fs}\right]\left\{\ddot{\overline{X}}\right\} \tag{23}$$

Substituting $\{\bar{p}\}$, Eq. (22) may be written as

$$\left[\overline{M}\right]\left\{\ddot{\overline{X}}\right\} + [K]\left\{\overline{X}\right\} = \{0\} \tag{24}$$

where $\left[\overline{M}\right] = [M] + \rho_f\left[R_{fs}\right]^T\left\{\ddot{\overline{X}}\right\}[G_i]^{-1}\left[R_{fs}\right]$.

5 Results and Discussion

The results of the investigation are presented in this section through a few examples. Free vibration frequencies of the lock gate are determined for clamped and simply supported on all edges. The lock gate and stiffeners are modelled as per Codal provisions, taking the minimum thickness of the plate to be 6 mm. The thickness of the stiffener plate is also taken to be 6 mm and outstand to be 14 $t_s\varepsilon$ (IS: 800-2007) [16], t_s is the thickness of stiffener and ε is the yield stress ratio $\left(\frac{250}{f_y}\right)^{\frac{1}{2}}$, f_y is the yield stress (250 MPa).

The lock gate is assumed to be isotropic, homogeneous, uniformly thick and elastic in nature. The fluid is assumed to incompressible, inviscid with a small amplitude, irrotational fluid flow, and the effect of hydrostatic pressure is neglected. The free vibration frequencies are presented in the form of non-dimensional frequencies as given below.

$$\Omega = \omega b^2 \sqrt{\frac{\rho_p t_p}{D_p}} \tag{25}$$

where, ω = free vibration frequency of the lock gate, b = width of the lock gate, ρ_p = mass density of lock gate = 7850 kg/m^3, t_p = thickness of the lock gate, D_p = flexural rigidity of the lock gate = $\frac{Et_p^3}{12(1-\upsilon^2)}$,

where, E = Young's modulus = 2.0×10^5N/mm^2, υ = Poissons's ratio

A convergence study is performed on the unstiffened square lock gate of 1.0 m height (A) and 1.5 m width (B), with a thickness of 10 mm, to decide the mesh size. The non-dimensional free vibration frequencies are plotted against the mesh size for both clamped and simply supported edges, as shown in Fig. 2. It is observed that the results are coming very close when the mesh size is 4 × 4, which is considered in this study to minimise the computational time.

Example 1 In this example, the first non-dimensional free vibration frequency of the unstiffened lock gate is determined by varying the length of the fluid domain from 0.25 to 1.5 m keeping the height (h_0) and width (b) of the fluid domain to 1.0 m. An unstiffened lock gate of 1.0 m width, 1.5 m depth and 10 mm thickness is considered. The results are shown in Fig. 3 for both clamped and simply supported edges.

It is observed that when the length of the fluid domain is varied, there is very little change in the frequencies of the lock gate after 1.0 m length of the far boundary for

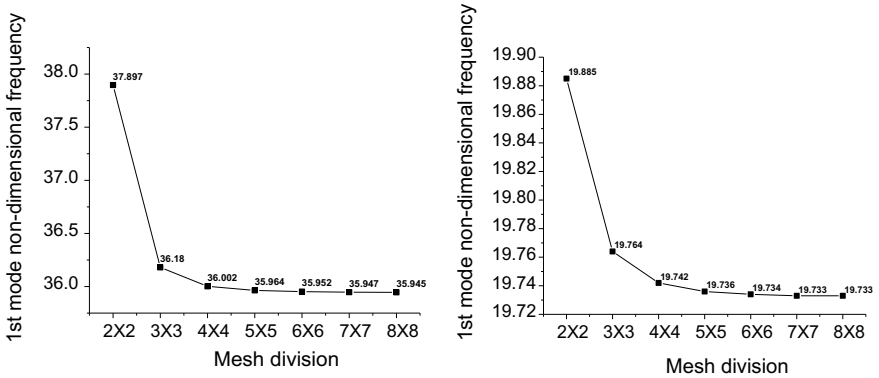

(a) Clamped unstiffened lock gate

(b) Simply supported unstiffened lock gate

Fig. 2 Convergence study

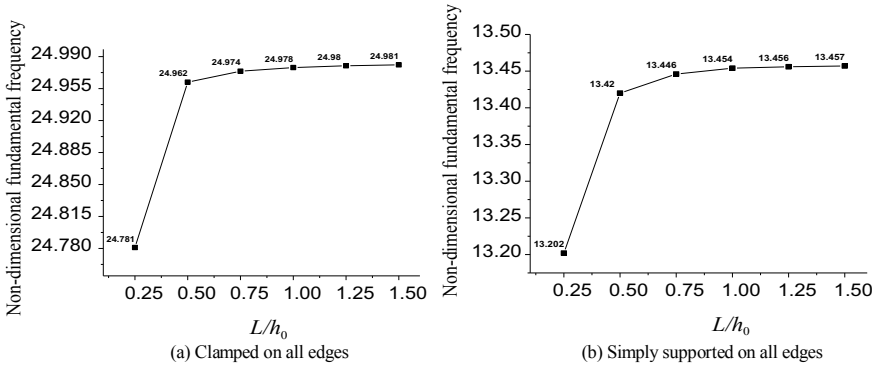

Fig. 3 First-mode non-dimensional frequencies of unstiffened lock gate

both the edge conditions. Therefore, the length of the fluid domain is truncated to 1.0 m length (L).

Example 2 In this example, an unstiffened square lock gate of 1.0 m width and 6 mm thick is considered. The width and height of the fluid domain are taken as 1 m because the width and height of the lock gate and truncated length of the fluid domain is 1.0 m, as found in Example 1. First, six non-dimensional free vibration frequencies are illustrated in Figs. 4 and 5 for clamped and simply supported on all edges, respectively.

The obtained results are comparable with the results available in the literature [6, 8] and found to be in good proximity.

Example 3 In this example, an unstiffened square lock gate is investigated by varying the thickness of the lock gate, that is, 6 and 10 mm. First, six non-dimensional free

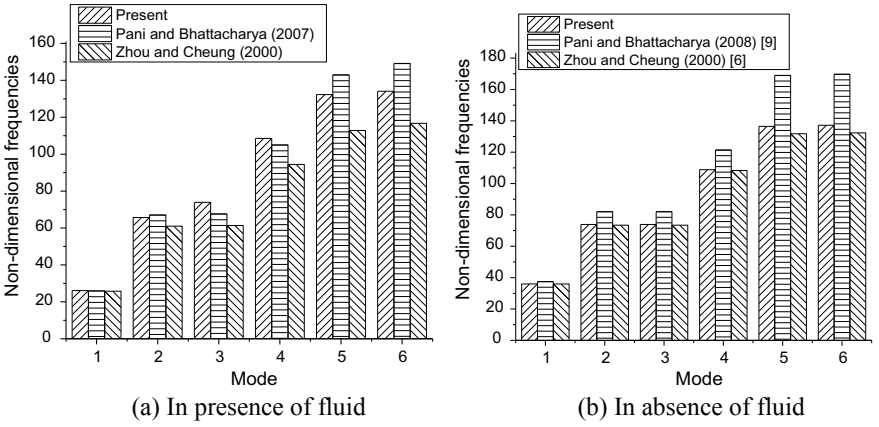

Fig. 4 Non-dimensional frequencies of clamped unstiffened lock gate

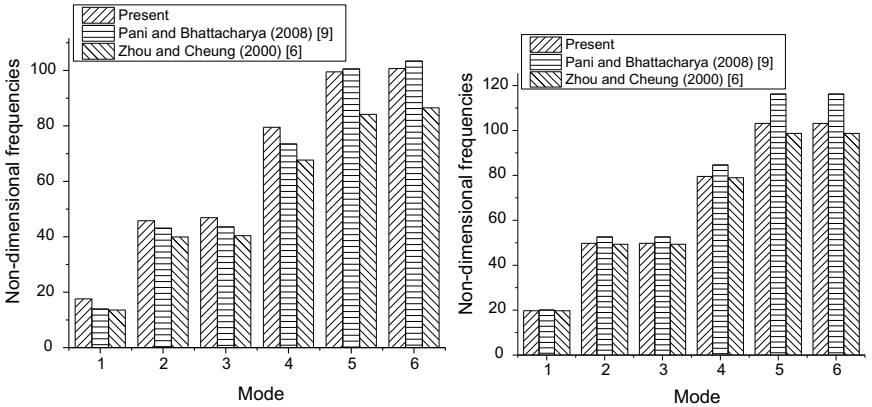

Fig. 5 Non-dimensional frequencies of simply supported unstiffened lock gate

vibration frequencies are illustrated in Figs. 6 and 7 for clamped and simply supported on all edges, respectively. It is found that there is almost no change in the results when the thickness of the lock gate is varied.

Example 4 In this example, a stiffened square lock gate of 1.0 m width and 6 mm thick and stiffener plate of 1.0 m length, 84 mm outstand and 6 mm thick is considered. Stiffened lock gate is compared with the unstiffened lock gate. First, six non-dimensional free vibration frequencies are illustrated in Figs. 8 and 9 for clamped and simply supported on all edges, respectively. It is found that when the plate is stiffened, free vibration frequencies are increased in both the cases of with and without the presence of fluid.

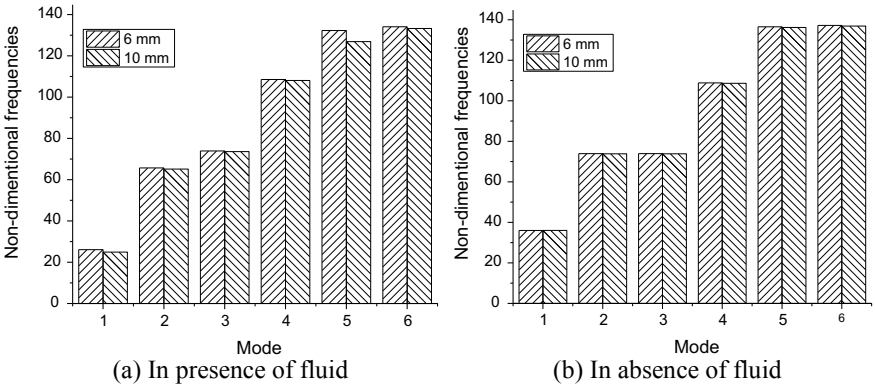

Fig. 6 Non-dimensional frequencies of clamped unstiffened lock gate

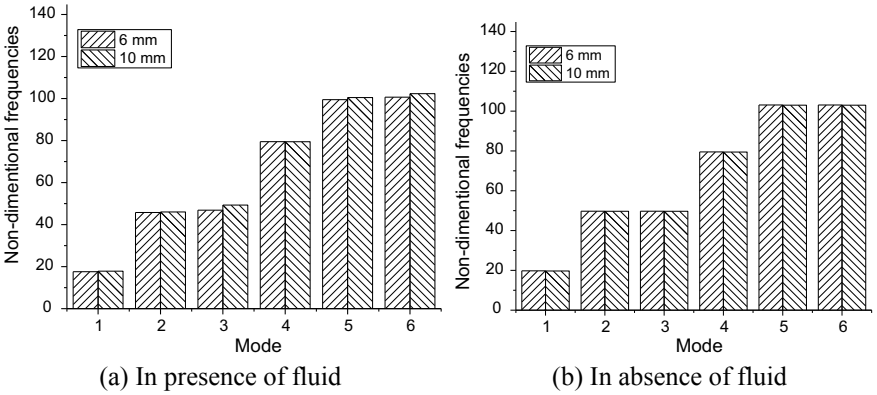

Fig. 7 Non-dimensional frequencies of simply supported unstiffened lock gate

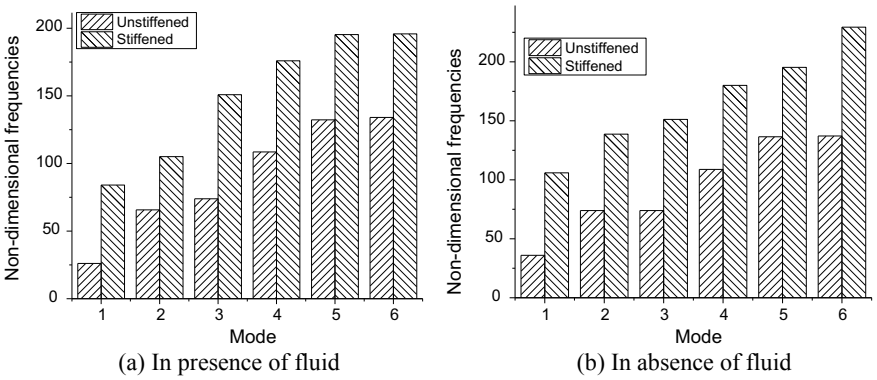

Fig. 8 Non-dimensional frequencies of clamped lock gates

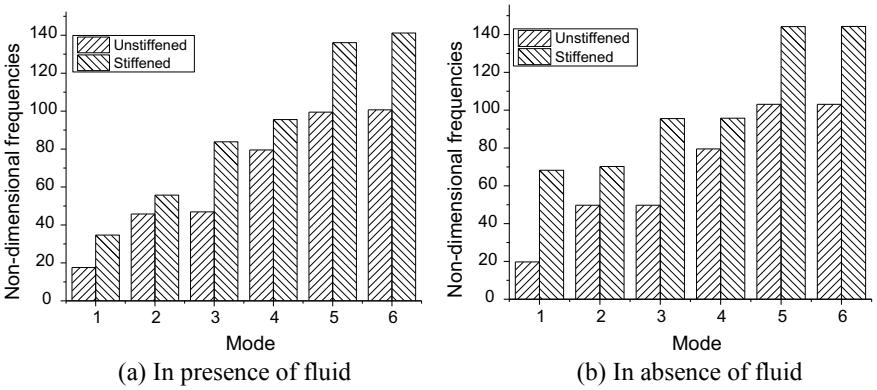

Fig. 9 Non-dimensional frequencies of simply supported lock gates

6 Conclusion

The free vibration frequencies of unstiffened and stiffened lock gate structure in the presence of reservoir fluid are investigated. The following conclusions are drawn based on the study carried out:

- No change in free vibration frequencies of the lock gate is noticed when the length of the fluid domain is increased beyond 1.0 m length.
- The free vibration frequencies are changed by a very small margin for the unstiffened lock gate in the presence and absence of fluid when the thickness of the lock gate is varied, that is, for 6 and 10 mm.
- Free vibration frequencies are increased when the lock gate is stiffened. The frequencies are increased by almost two times when the stiffened lock gate is considered, keeping almost the same volume of material as that of an unstiffened lock gate.

Acknowledgments The authors acknowledge the Motilal Nehru National Institute of Technology Allahabad for providing the financial support under TEQIP-III.

References

1. Amabili M, Frosali G, Kwak MK (1996) Free vibrations of annular plates coupled with fluids. J Sound Vib 191(5):825–846. https://doi.org/10.1006/jsvi.1996.0158
2. Amabili M (1996) Effect of finite fluid depth on the hydroelastic vibrations of circular and annular plates. J Sound Vib 193(4):909–925. https://doi.org/10.1006/jsvi.1996.0322
3. Amabili M, Kwak MK (1999) Vibration of circular plates on a free fluid surface: effect of surface waves. J Sound Vib 226:407–424. https://doi.org/10.1006/jsvi.1998.2304
4. Kwak MK, Amabili M (1999) Hydroelastic vibration of free-edge annular plates. Trans ASME 121:26–32. https://doi.org/10.1115/1.2893944
5. Maity D, Bhattacharyya SK (1999) Time domain analysis of infinite reservoir by finite element method using a novel far-boundary condition. Finite Elem Anal Des 32:85–96. https://doi.org/10.1016/S0168-874X(98)00077-8
6. Zhou D, Cheung YK (2000) Vibration of vertical rectangular plate in contact with water on one side. J Earthq Eng Struct Dyn 29:693–710. https://doi.org/10.1002/(SICI)1096-9845(200005)29:5%3c693:AID-EQE934%3e3.0.CO;2-V
7. Pani PK, Bhattacharyya SK (2006) Fluid-structure interaction effects on free vibration of a vertical rectangular lock gate using a near truncated boundary. Inst Eng (India)–Struct Div 86:187–194
8. Pani PK, Bhattacharyya SK (2007) Fluid-structure interaction effects on dynamic pressure of rectangular lock gate. Finite Elem Anal Des 43(10):739–748. https://doi.org/10.1016/j.finel.2007.03.003
9. Pani PK, Bhattacharyya SK (2008) Free vibration characteristics of a rectangular lock gate structure considering fluid-structure interaction. Adv Vib Eng 7(1):51–69
10. Pani PK, Bhattacharyya SK (2009) Finite element analysis of a vertical rectangular plate coupled with an unbounded fluid domain on one side using a truncated far boundary. J Hydrodyn 21(2):190–200. https://doi.org/10.1016/S1001-6058(08)60136-5

11. Pal P, Singh RR, Singh DK (2016) Free vibration frequencies of lock gate structure considering fluid structure interaction. Int J Adv Civ Eng Technol 1:1–22
12. Pal P (2010) Free-vibration analysis of liquid-filled containers using meshless local petrov-galerkin approach. Int J Recent Trends Eng Technol 3(2010):1–5
13. Tariverdilo S, Shahmardani M, Mirzapour J, Shabani R (2013) Asymmetric free vibration of circular plate in contact with incompressible fluid. Appl Math Model 37(2013):228–239. https://doi.org/10.1016/j.apm.2012.02.025
14. Cho DS, Kim BH, Vladimir N, Choi TM (2015) Natural vibration analysis of rectangular bottom plate structures in contact with fluid. Ocean Eng 103(2015):171–179. https://doi.org/10.1016/j.oceaneng.2015.04.078
15. Singh DK, Duggal SK, Pal P (2018) Free vibration analysis of stiffened lock gate structure coupled with fluid. J Struct Eng 45:1–9
16. IS 800 (2007) Indian standard, general construction in steel—code of practice, Bureau of Indian Standards, New Delhi

Introspecting System Identification in Numerical Technique for Inverse Identification Process

Shalem Ernest and U. K. Dewangan

Abstract In this paper, a new approach is developed for the system identification using finite element method (FEM) modelling concept. Matrices of the structural members are modelled using the stiffness matrix approach. A bridge truss structure is selected for the computational purpose. In the multiplication of the matrices element to element multiplication is used instead of conventional matrix multiplication. An algorithm has been developed of the same. MATLAB is used as a common platform for the computational purposes. Element to element computing concept has been applied in the algorithm for computing the global matrices. Eigen frequency evaluation technique along with the distributive computing concept is used to locate and predict the damage. The algorithm is able to detect the damage for single as well as multiple damaged members.

Keywords System identification · Finite element method · Bridge truss · Eigen frequency · MATLAB

1 Introduction

Generally when a structure is subjected to high load and high stress condition, these conditions can lead to damage in a structure. It is important to estimate the damage present in a structure because it rises the safety in operation of the structure. The detection of damage at an early stage can save a huge loss of life and money. Therefore, detection of damage has always been a significant issue for the researchers and the field industry [1].

When the performance of the structure changes with respect to the previous performance the structure can be said to be a damaged structure, this type of a structure can be identified by measuring the subsequent change in the structural properties [2]. Damage in any structural component can be a reason for the changes in the mass or stiffness distribution of the structural system, the modal properties such as natural

S. Ernest (✉) · U. K. Dewangan
Research Scholar, Raipur, India
e-mail: shalemernest@gmail.com

© Springer Nature Singapore Pte Ltd. 2021

K. K. Pathak et al. (eds.), *Recent Trends in Civil Engineering*, Lecture Notes in Civil Engineering 77, https://doi.org/10.1007/978-981-15-5195-6_11

frequencies, damping ratios, and mode shapes [3], may alter as well [4]. In order to measure the amount of damage the direct stiffness method as described in [5] can be used. The location of the element in global as well as in local stiffness matrix can be found out by [6] for structural system identification. The detection of damage can be done in non-prismatic reinforced concrete beam using mode shape curvature [7]. Based on dynamic response information the stiffness mutation position of tower truss [8] can be calculated.

The convergence of eigen frequency and its convergence criteria on a bridge truss structure has been discussed by [9].

A new numerical technique is developed and which uses the element to element multiplication of matrices along with the distributed mass concept for the prediction of damage in system identification. Eigen frequency evaluation technique along with the distributive computing concept is used to locate and predict the damage. The algorithm is able to detect the damage for single as well as multiple damaged members.

1.1 Theoretical Development

In this the Fig. 1 shows a horizontal axis x to which a plane truss element is inclined at an angle β. The figure presents a dual nodal displacement. One of which has the displacement vertical to element axis (i.e. u and v) while the displacements in the other set are in terms of global reference axis (i.e. ū and ṽ). In order to express the stiffness matrix in terms ū and ṽ transformation of ū and ṽ is important as the element stiffness is expressed in terms of ū and ṽ.

This association is known as coordinate transformation for two sets of nodal displacements (i.e. u, v and ū, ṽ) and the relationship works well for both of them. The relationship is

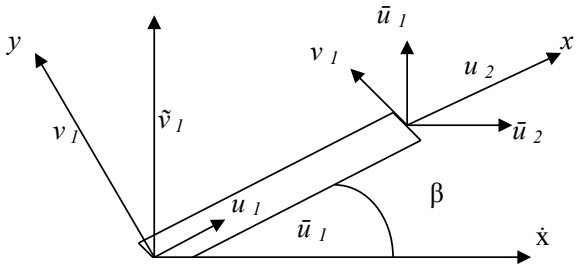

Fig. 1 Generalized two-dimensional truss element

$$\begin{Bmatrix} u_1 \\ v_1 \\ u_2 \\ v_2 \end{Bmatrix} = \begin{bmatrix} c & s & 0 & 0 \\ -s & c & 0 & 0 \\ 0 & 0 & c & s \\ 0 & 0 & -s & c \end{bmatrix} \begin{Bmatrix} \tilde{u}_1 \\ \tilde{v}_1 \\ \tilde{u}_2 \\ \tilde{v}_2 \end{Bmatrix} \tag{1}$$

where $c = \cos\beta$ and $s = \sin\beta$. Let us rewrite Eq. (1) as

$$\{d^e\} = [T]\{d'^e\} \tag{2}$$

To transform the element stiffness matrix. The articulation of strain energy is given as

$$U = \frac{1}{2}\{d^e\}[K^e]\{d^e\} \tag{3}$$

Substituting Eq. (2) into Eq. (3) in the terms of *xy*- coordinate system, we get

$$U = \frac{1}{2}\{d'^e\}^T[T]^T[K^e][T]\{d'^e\} \tag{4}$$

The expression for strain energy can be now stated as

$$U = \frac{1}{2}\{d^e\}[\check{K}^e]\{d'^e\} \tag{5}$$

In this [Ǩe] is the transformation element stiffness matrix. As the strain energy is reliant on the coordinate system the strain energy in (5) and (4) should be equivalent. Equating the Eqs. (4) and (5) we get

$$[\check{K}^e] = [T]^T[K^e][T] \tag{6}$$

Substitution of Eqs. (12) and (14) into Eq. (19) results in the transformation stiffness matrix

$$[\check{K}^e] = \frac{AE}{l}\begin{bmatrix} c^2 & cs & -c^2 & -cs \\ cs & s^2 & -cs & -s^2 \\ -c^2 & -cs & c^2 & cs \\ -cs & -s^2 & cs & -s^2 \end{bmatrix} \tag{7}$$

For the common nodal points this element stiffness matrix can be composed into the global matrix.

The element stiffness matrix can be derived by using the kinetic energy expression that is similar to the strain energy expression.

$$[\acute{M}^e] = [T]^T[M^e][T]] \tag{8}$$

Matrix multiplication can be carried out using the constant mass matrix gives. The lumped mass matrix can be acquired likewise and expressed below

$$[\acute{\mathrm{M}}^e] = \frac{\rho Al}{2}\begin{bmatrix} c^2 & cs & 0 & 0 \\ cs & s^2 & 0 & 0 \\ 0 & 0 & c^2 & cs \\ 0 & 0 & cs & s^2 \end{bmatrix} \tag{9}$$

After obtaining K(Global Stiffness) and M(Global Mass) Matrices the generalised problem is that of evaluating an eigenvalue ($\lambda = \omega 2$) which is a measure of frequency of vibration together with the corresponding eigen-vector U indicating the mode shape as is stated here

$$\mathrm{KU} = \lambda \mathrm{MU} \tag{10}$$

From the Eq. (9), we have

$$(\mathrm{K} - \lambda \mathrm{M})\mathrm{U} = 0$$

If the eigen vector is non-trivial, the required condition is

$$\det(\mathrm{K} - \lambda \mathrm{M}) = 0$$

This represents the characteristic polynomial in λ.

1.2 Lumped Mass Concept

This adds to the novelty of the work that instead of using the regular matrix multiplication, element to element matrix multiplication is carried out. In the normal matrix multiplication rows are multiplied with the column which means that the rows of the stiffness matrix are multiplied with the columns of the mass matrix, in doing so the location of the specific elemental is lost in the global matrix. By doing element to element matrix multiplication the location of the member is not lost.

1.3 Element to Element Multiplication Concept

Once, the global stiffness matrix is formed the global mass matrix is formulated in a similar manner, instead of lumped mass matrix a distributed form of mass matrix is used for the formulation of the global mass matrix. After the formation of the global stiffness and mass matrix they are multiplied using a regular matrix multiplication.

Taking the example of two matrices X and Y.

$$X = \begin{bmatrix} A & B \\ C & D \end{bmatrix} \quad Y = \begin{bmatrix} E & F \\ G & H \end{bmatrix}$$

On regular matrix multiplication the result will be:

$$X * Y = \begin{bmatrix} AE + BG & AF + BH \\ CE + DG & CF + DH \end{bmatrix}$$

On the other, when doing element to element matrix multiplication we get:

$$X * Y = \begin{bmatrix} A.E & B.F \\ C.G & D.H \end{bmatrix}$$

The advantage in doing so is that the location of the specific element is not lost and damage location can be identified.

2 Problem Formulation

The bridge truss displayed in Fig. 2 is used for the analysis with the initial undamaged cross sectional area $A = 101.6$ mm^2, having a modulus of elasticity $E = 69$ GPa along with. Damage has been introduced by replacing the original member with the member having reduced cross sectional area of 70 mm^2. The member 4 and 9 have been replaced with the damaged members.

The numbers marked in the circles represent the element/member numbers and the numbers not marked represent the node numbers. A mathematical modelling

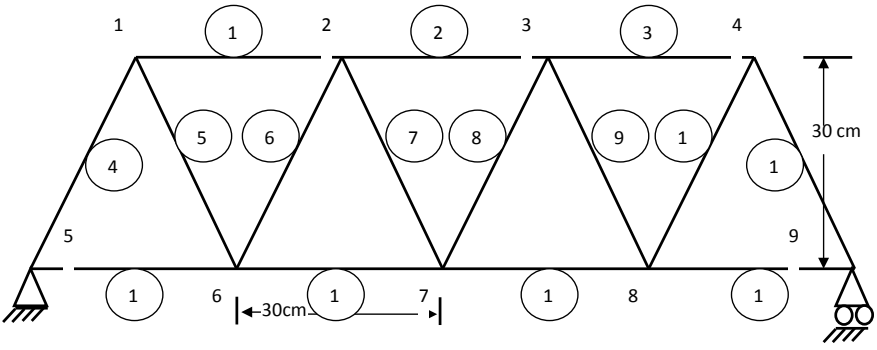

Fig. 2 Bridge truss showing elements and nodes

of the same has been done using the Finite Element Method. Finite element technique is used for the formulation of the stiffness and mass matrix of the structure. Distributed mass matrix formulation is used in the multiplication of mass and stiffness matrix formulation. Element to element multiplication is being used instead of the conventional matrix multiplication. The truss as depicted in Fig. 1 is used for all the computation purposes. MATLAB software has been used as a common platform for the development of the damage detection algorithm.

3 Results and Discussion

In the mathematical model the mass and the stiffness matrices have been constructed by using the finite element technique. Eigen frequency evaluation technique has been used to determine the frequency. The results obtained are as follows.

Blue bars on the positive side of the *x*-axis indicate the damaged member and on the negative side of the *x*-axis indicate the undamaged members.

From Fig. 3 it can be seen that the convention technique shows a mixed response of the damaged members and the results are not clear. Only by guessing the peak of the bar one can determine the damaged member. From Fig. 4 it can be seen that the damaged members can be predicted very clearly and in a very precise manner.

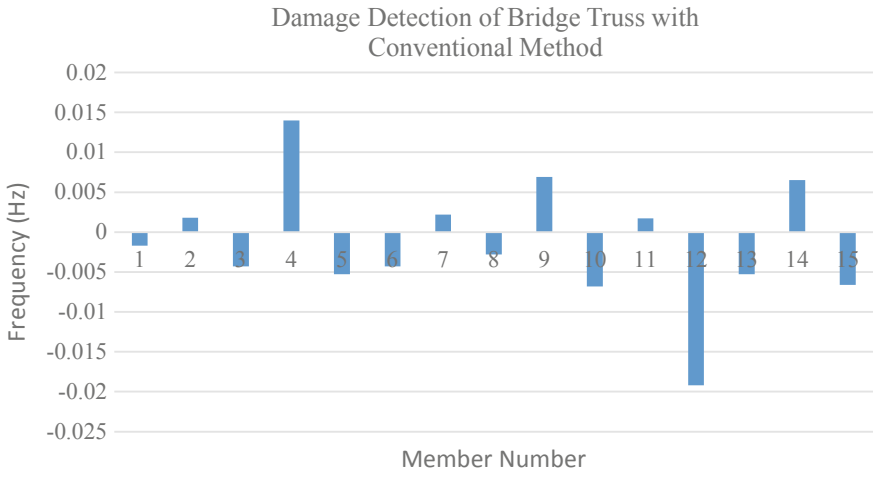

Fig. 3 Result of the developed algorithm showing multiple damaged members 4 and 9

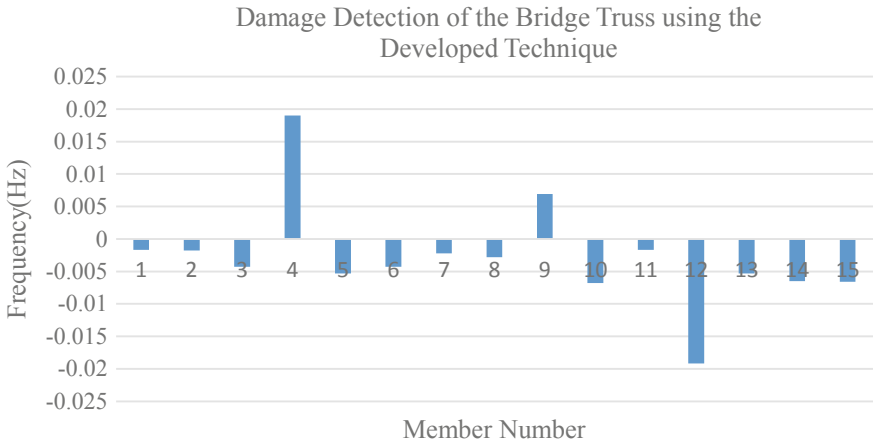

Fig. 4 Result of the developed algorithm showing multiple damaged members 4 and 9

4 Conclusion

The numerical technique which utilises the element to element matrix multiplication concept along with the distributed computing technique is developed. A bridge truss model is used for analysing the numerical technique. The mathematical model is simulated in MATLAB using Finite Element Technique. The graphs are plotted, from which the following inference can be drawn.

The algorithm can detect damage for single as well as multiple damaged members.

The algorithm is precise and more accurate than the conventional technique.

References

1. Kwon K, Lin R (2005) Robust damage location in structures using Taguchi method. J Struct Eng 131(4):629
2. Sain T, Kishen JMC (2006) Damage assessment in beams using inverse method. J Eng Mech ASCE 132:337–344, 2006
3. Huth O, Feltrin G, Maeck J, Kilic N, Motavalli M, Bridge R (2005) Damage identification using modal data: experiences on a prestressed concrete bridge 131:1898–1910
4. Scott MBP, Doebling W, Farrar CR (1989) A summary review of vibration-based damage identification methods. J Appl Mech 111(2):270–278
5. Unger JF, Teughels A, De Roeck G (2007) System identification and damage detection of a prestressed concrete beam. J Struct Eng 132:1691–1698
6. Dewangan UK (2011) Element locations in system identification *. Indian J Appl Res, 89–91
7. Saleh F, Supriyadi B, Suhendro B, Tran D (2004) Damage detection in non-prismatic reinforced concrete beams using curvature mode shapes. In: SIF2004 structural integrity and fracture. http://eprint.uq.edu.au/archive/00000836
8. Gao B, Li H, Liu Y (2008) Damage identification methods for support position of tower structure based on information extension. IEEE, pp 555–558

9. Ernest S, Dewangan UK (2016) Comparison of eigen frequency convergence criteria on a bridge structure. J Chem Pharm Sci 2:69–74
10. Barroso LR, Rodriguez R (2004) Damage detection utilizing the damage index method to a benchmark structure. J Eng Mech 130(2):142–151

Effect of Steel Ratio on Dynamic Response of HSC Two Way Slab Strengthened by Entrenched CFRP Strips Using Drop Test

Arjun R. P. Reddy, Nandeesh M. Sreenivasappa, R. Prabhakara, and H. N. Jagannatha Reddy

Abstract Higher performance of High Strength Concrete (HSC) slabs attracted the engineers to provide it as floor slabs in warehouses and heavy industries. These floor slabs are subjected to higher intensities of loads including drop of objects there by subjected to dynamic effect. It has been observed that the dynamic response behaviour of slabs are obtained with a reasonable accuracy by subjecting the elements to drop test. Steel ratio in slabs plays an important role in the static and dynamic response behaviour of slabs. In the present study, HSC two-way simply supported slab strengthened with entrenched CFRP strips were subjected to drop test. Accelerometer was mounted on the bottom of the slab to record the acceleration time graph. In the current study dynamic behaviour of HSC slabs were compared with the same configuration with entrenched strengthened slabs. The change in dynamic response was recorded and studied with the strengthening and found that dynamic parameters such as peak acceleration and damage index, measured as energy required to develop unit crack length caused by the impact were found to be dependent on the steel ratio. The strengthening technique was effective in reducing the peak acceleration of slabs.

Keywords Drop test · Two-Way slab · Dynamic response · Peak acceleration · Damage index

A. R. P. Reddy (✉) · H. N. J. Reddy
Department of Civil Engineering, Bangalore Institute of Technology, Bangalore, India
e-mail: arjunreddy.rp@gmail.com

H. N. J. Reddy
e-mail: jagannath.priyadhi@gmail.com

N. M. Sreenivasappa
Department of Civil Engineering, M. S. Ramaiah Institute of Technology, Bangalore, India
e-mail: nandeeshms@gmail.com

R. Prabhakara
Principal, Brindavan College of Engineering, Affiliated to VTU Belagavi, Bengaluru 560063, India
e-mail: r.prabhakara@gmail.com

© Springer Nature Singapore Pte Ltd. 2021

K. K. Pathak et al. (eds.), *Recent Trends in Civil Engineering*, Lecture Notes in Civil Engineering 77, https://doi.org/10.1007/978-981-15-5195-6_12

1 Introduction

Reinforced concrete structures are made out of linear elements like beams and columns, two dimensional elements slabs and rigid junction between beam and column and beam column connection between them have become majority of existing structures. In designing these structures, various load combinations are used. Slabs being an integral part of a structure and widely used structural member and these are generally designed to withstand static loading but are exposed to other forms of loads like impact loads from the time of their casting to throughout their design life. The impact loads may arise from dropping of building materials like bricks, blocks, formwork materials and cement bags during the construction of structure, accidental events in industrial floor spaces, natural calamities like landslides and rock fall impacts. All these loads induce distress in the slabs for which they are not designed.

Understanding the static behaviour of slabs and extrapolating this data in understanding the behaviour is not logical. Experimentations on impact behaviour of structural elements requires advanced test arrangements and devours additional time, In some cases it is delicate to the outcomes acquired in this manner and the accessible writing are less. It has been seen lately drop tests are turning out to be well known in light of their effortlessness and less utilization of time [1–3].

It is conceivable to acquire peak acceleration, velocity profile, damping coefficient and acceleration decay from accelerometers used in the drop test. The principle followed in the drop test is based on the energy principle, a fraction of load obtained from the static analysis is applied on to the slab to observe impact behaviour of slabs.

In the studies conducted, the failure of concrete subjected to impact was under localized effects like punching shear failure, concrete scabbing and perforation [4, 5]. To avoid these ill effects and provide suitable impact resistance HSC are preferred. HSC are increasing widely notaries in present day field application because of its point of interest like early strength gain, better durability, Impact and toughness characteristics. HSC are believed to show better durability and corrosion opposition in comparison to Normal Strength Concrete (NSC). HSC provides higher strength per unit cost, per unit weight and per unit volume thus can lead to reduced size and weight of structures. Higher compressive strength of concrete results in a higher modulus of elasticity and reduced specific creep, and thus increases stability and reduces deflections. These advantages along with high compressive strength of concrete has encouraged the usage of HSC in everyday use.

NSM (Near Surface Mounted) technique, in which shallow grooves are made in the concrete cover and these grooves are filed with the bar-shaped or strip-shaped FRP (Fiber Reinforced Polymers) elements as additional reinforcement and they are embedded in epoxy or cement resins (adhesives), which creates adhesion with the concrete, and provides anchoring. This method of NSM FRP technique has proved to enhance the flexural and shear strength of deficient Reinforced Concrete (RC) beams and slabs [6]. In the present study, the inertial response due to impact loading on HSC

slabs with variation in reinforcement ratio was studied along with its changes when strengthened with NSM technique.

2 Literature Review

The literatures available were less due to the complexity involved in testing the slabs under impact loading. The following literature reviews were carried out in the present study.

2.1 Prabhakara et al. [7]

In this study, a mix design procedure for HSC has been provided without use of silica fume. The study was conducted with 20 mm down-size aggregate with water content varying between 0.23 and 0.25. Concrete of strength up to 120 MPa was obtained. This method proved to be the best method for gaining more strength with less cement content.

2.2 Annadurai and Ravichandran [8]

The authors presented the mix design developed for high strength concrete with silica fume and high range water reducing admixture (HRWR). In this work, they selected the 53 grade OPC, 10 mm down coarse aggregates and river sand as materials. Using ASTM C 127 standard relative quantities and proportions for M60 grade of concrete was calculated. GLENIUM B233 was used as HRWR. The replacement of cement with 9% of micro silica and 0.9% HRWR gave maximum strength.

2.3 Andresson [9]

The load carrying capacity of concrete slabs subjected to concentrated loads are studied considering both static and impact loads. The slabs were casted with reinforcement meshes using shotcrete and some of the slabs were casted with steel fibre reinforced concrete (SFRC). Some slabs were casted with SFRC only, some with SFRC and mesh and one only Normal conventional concrete. Impact loads were given using a steel mass of 600 kg. The free fall height was varied from 1 to 2 m. The peak Impact load varied from 200 to 250 kN and the corresponding impulse load varied from 4 to 5.5 kNs. The slabs were observed to fail in flexure. The concrete fallout was observed to be less in SFRC slabs than the slabs with rebar mesh.

2.4 Yoo et al. [5]

In this study the compressive and flexural behaviour of normal strength concrete, steel fibre reinforced concrete with various fibre volume fractions were determined and further the slabs were strengthened in flexure using externally bonded FRP sheets using AFRP and CFRP and their behaviour under high strain loading was studied. Occurrence of flexure cracks, FRP deboning, spalling etc. reduced the dissipated energy. Strength of concrete was seen to increase with increase in strain rate and increase in volume of fibres.

2.5 Rankovic et al. [10]

They suggested to use of FRP for enhancing the strength properties by usage of GFRP, CFRP and AFRP and also by using different shapes of bars i.e., square, rectangular which increases the specific reinforcement area of the bar, and circular cross sections which offers ease to anchor during prestressing and by using strips which increase surface coefficient and reduces the risk of adhesion loss and with various surface configurations i.e., smooth, rough with spiral grooves or ribbed grooves choice is based on concrete cover. According to NSM technique, three kinds of failures were observed i.e. separation of adhesive, separation from concrete and tensile failure of FRP.

2.6 Ramanna [11]

The use of near surface mounted carbon fibre polymer (NSM-CFRP) reinforcement such as FRP strips holds a high potential for increasing the flexural strength. The studies were focused on response of reinforced beams and slabs subjected to static or Impact loads. The performance of beams and slabs under impact loads were evaluated using accelerations versus time relationship. A single degree of freedom elasto-plastic was developed to capture their dynamic behaviour. Among four slabs, two were control slabs and two were retrofitted slabs. One control slab was used for static and other for dynamic test similarly each retrofitted slabs was used for static and dynamic test. The drop height calculated for 400 lbs steel impactor to impact the slab was calculated using work-energy principles and it should match with the load applied upon the impact and if not it has to be revised. The control slabs experienced bigger cave compared to retrofitted slabs. The load carrying capacity of the retrofitted slab was found to be two times higher than the control slab.

3 Objectives

- To obtain the dynamic behaviour of slabs under impact loading.
- To analyse the change in behaviour of the test results over the change in reinforcement ratio and effect of strengthening the slab by NSM technique.

4 Materials Used in the Current Study

Materials used in the present investigation have been characterized in accordance with the standard procedure as follows:

CEMENT—OPC of 53 grade conforming to IS: 12269-2013 was used.
AGGREGATES—The fine and coarse aggregates used was confirming to the specifications as per IS 383-1970.
REINFORCEMENT—The reinforcing steel was confirming to the specifications as per IS 1786: 2008.
ADMIXTURE—for the present work, for M70 concrete, Master Glenium Sky 8233 was used which BASF Construction Chemicals (India) Private Limited commercially markets.
FOSROC CHEMICALS sponsored CFRP strips and epoxy used to bond the strips to concrete substrate, that is marketed under the name "Nitowrap CFP" and "Nitowrap 40" respectively was used in the present study for retrofitting the slabs. The mix design of M70 was done with 1.5% superplasticizer dosage as per Prabhakara [7] mix design. The mix proportions, fresh properties and the strength gain with age are presented in Tables 1, 2 and 3 respectively.

Table 1 Trial Mix design specifications for HSC [12, 13]

Ingredient	M70
Water/Cement ratio	0.3
Cement	500 kg/m^3
Coarse aggregate	714 kg/m^3
Fine aggregate	1000 kg/m^3
Water	150 kg/m^3
Superplasticizer	7.47 kg/m^3

Table 2 Fresh properties of concrete [12, 13]

Concrete	Property	Standard values	Obtained values
M70(HSC)	Slump (mm)	Medium = 50–100	108
		High = 100–150	
	Flow rate	>100%	124%

Table 3 Test results of concrete used for casting at different ages [12, 13]

Days	M70		
	Compressive strength (MPa)	Split tensile strength (MPa)	Flexural strength (MPa)
3	49.05	4.06	4.63
7	65.07	5.47	5.52
28	71.61	5.95	5.92

4.1 Specimen Casting and Strengthening by NSM Technique

The specimen were casted to carry out the tests for studying the behaviour of slabs in impact loading by increasing the reinforcement ratio. The dimensions and reinforcement details are given in Fig. 1.

The NSM technique with CFRP strips are used to strengthen the slabs. The strengthening was done in diagonal direction based of earlier researches [11, 14]. A zone of NSM strengthening marked by L/5.31 from the ends of the slab was identified. The typical strengthening system considered and the groove dimensions adopted for this investigation are shown in Figs. 2 and 3 respectively [15]. The strengthening was

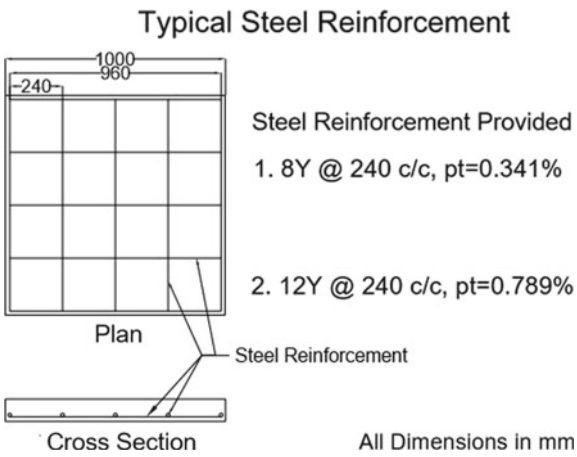

Fig. 1 Reinforcement details of slab

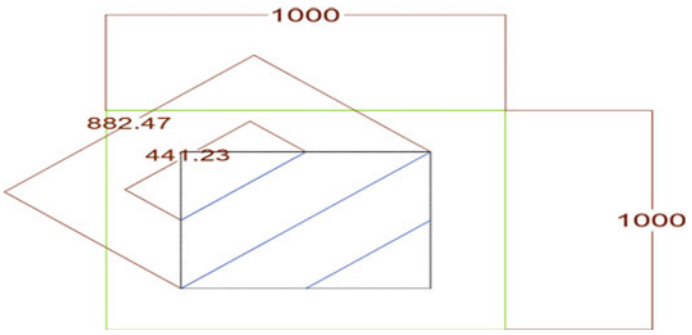

Fig. 2 Typical NSM strengthening

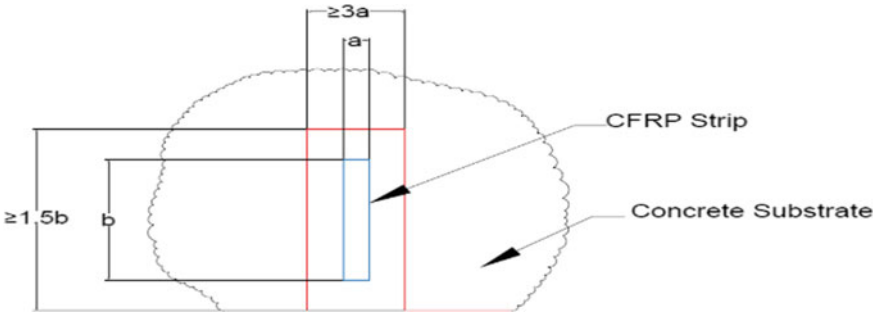

Fig. 3 Typical groove dimensions

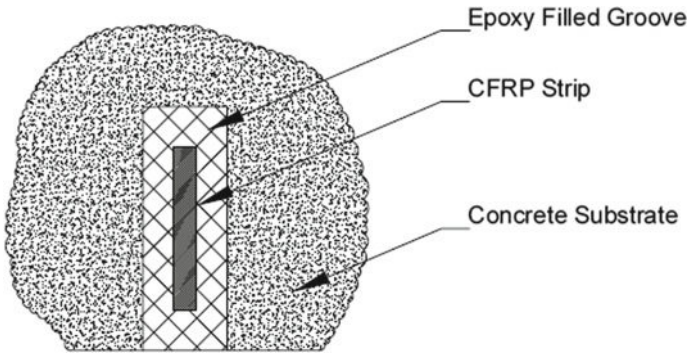

Fig. 4 Typical groove details

done by cutting a groove on the bottom face of the slab and embedding the CFRP strips in the epoxy that was filled in the groove cut out earlier to obtain the details as shown in the Fig. 4.

5 Experimental Setup

The Impact testing on slab was carried out by using a drop test. The test setup consists of a drop weight, the loading frame, which was used, a pulley and a rope arrangement was fixed to lift the weight as shown in the Figs. 5 and 6, and a four-channel dynamic data acquisition system (DDAS) and accelerometers used to study the response as shown in Figs. 7, 8 and 9 and accelerometer is placed at centre of the slab (Ch 1) as shown in Fig. 10.

5.1 Experimental Procedure

After a curing period of 28 days, the slabs were then allowed to dry and white washed to have a smoother surface to easily locate crack propagation and pattern. The accelerometer was fixed at the centre of the tension face as shown in Fig. 10. Then the specimen was mounted on the loading platform and the slabs were tested for simply supported end conditions [16]. In the study the drop mass was obtained from the work energy principles for total slab capacity. For the present study the drop mass was obtained as 70 kg. The height of the drop was varied to give different impact energies to have different range of kinetic energy to the slab and to record variation in the response of slab under different impact energy. For this purpose,

Fig. 5 Drop weight of 70 kg

Fig. 6 Pulley and rope assembly

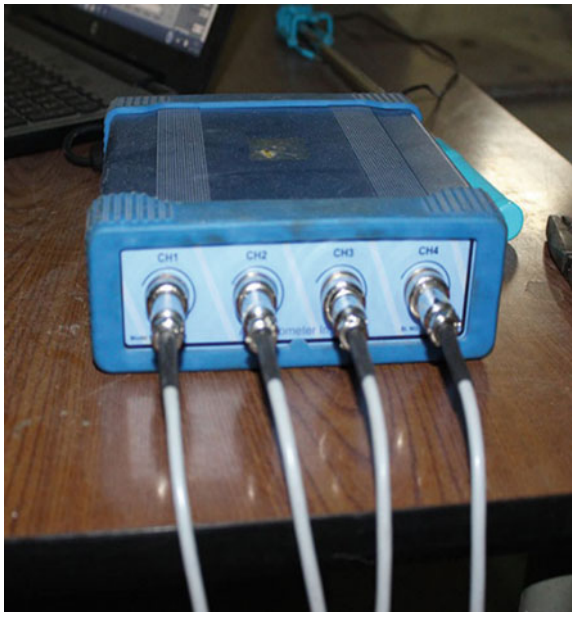

Fig. 7 Four-Channel DDAS

Fig. 8 DDAS with software KAMPANA

Fig. 9 Accelerometers

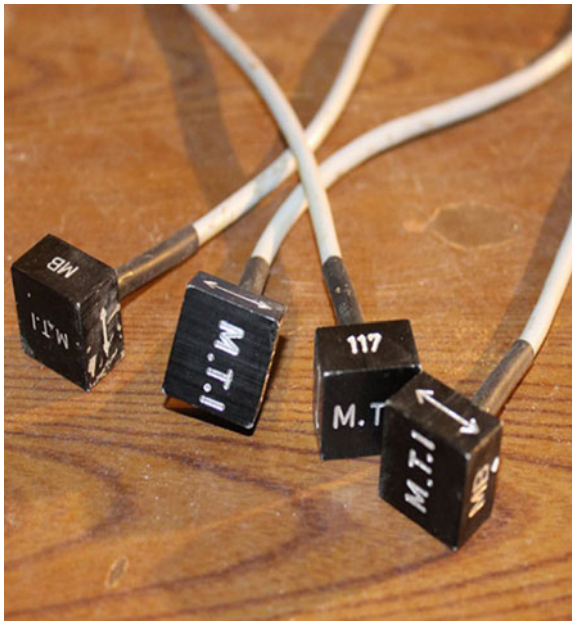

the drop weight of 70 kg was dropped from the height of 0.67 m, 1.33 m and 2 m respectively on to the different slabs. The total energy impacted due to different drop heights are shown in Table 4.

The total energy imparted to the slab will be in the form of kinetic energy which would be equal to the potential energy stored in the drop weight lifted to the respective

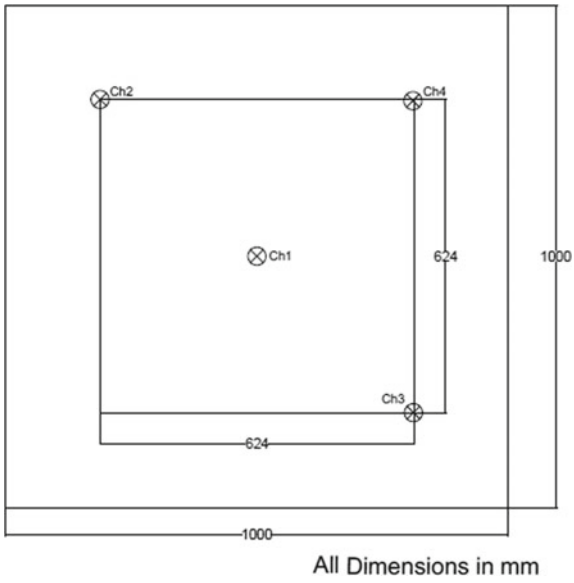

Fig. 10 Accelerometers location

Table 4 Impact Energy on the slabs

Drop weight 'm' (kg)	Drop height 'H' (m)		Impact energy = m × g × H (Joules)
70	H1	0.67	460.01
	H2	1.33	913.31
	H3	2.00	1373.4

heights and the drop was frictionless hence it can be assumed that total energy would be converted without losses.

6 Test Results

Totally twelve number of slabs were cast for impact test, out of which six were control slabs and six were NSM strengthened slab. These slabs were tested in the present investigation and the responses of each slab was obtained from the software "KAMPANA" of data acquisition system where the acceleration, velocity and displacement values were captured from the accelerometer placed at centre of the slab. The accelerometers will capture the response data of the test slab in all three axes. A typical data record from the software is as shown in Fig. 11.

The results from the test are presented in Table 5. A graphical representation of the experimental results comparing the acceleration response of the slabs for different drop heights is as shown in Figs. 12, 13, 14 and 15.

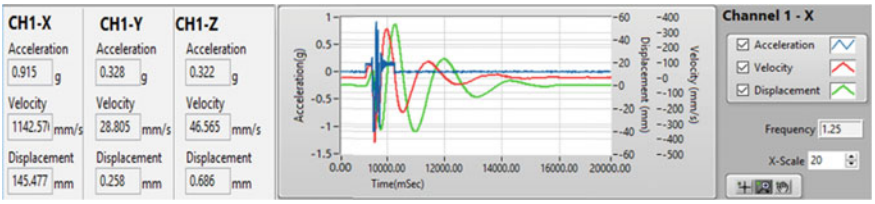

Fig. 11 Typical dynamic data recorded in KAMPANA software

Table 5 Response of the test slabs

Unstrengthened slab	Acceleration (g)	Strengthened slab	Acceleration (g)
M70/PT1/H1/NSM0	1.826	M70/PT1/H1/NSM1	0.664
M70/PT1/H2/NSM0	0.591	M70/PT1/H2/NSM0	1.455
M70/PT1/H3/NSM0	0.723	M70/PT1/H3/NSM0	3.808
M70/PT1/H1/NSM0	0.555	M70/PT1/H1/NSM0	0.367
M70/PT1/H2/NSM0	1.26	M70/PT1/H2/NSM0	0.699
M70/PT1/H3/NSM0	0.664	M70/PT1/H3/NSM0	0.468

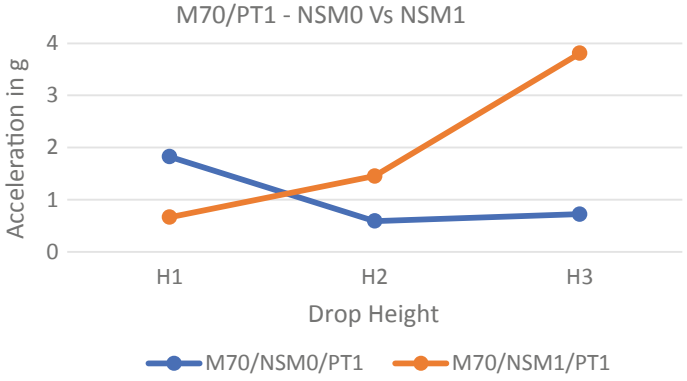

Fig. 12 Acceleration versus drop height for PT1 slabs

Impacted energy of a given slab was divided by its crack length measured to obtain the energy absorbed per unit length. The Crack length and energy absorbed of slabs are tabulated in Table 6 and the energy absorbed per unit length of crack amongst the slabs tested are compared in Fig. 16.

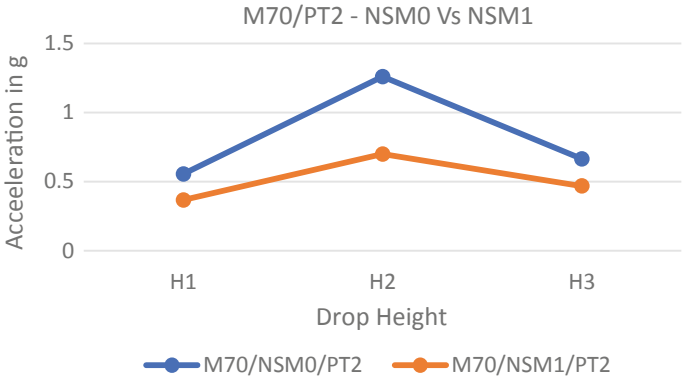

Fig. 13 Acceleration versus drop height for PT2 slabs

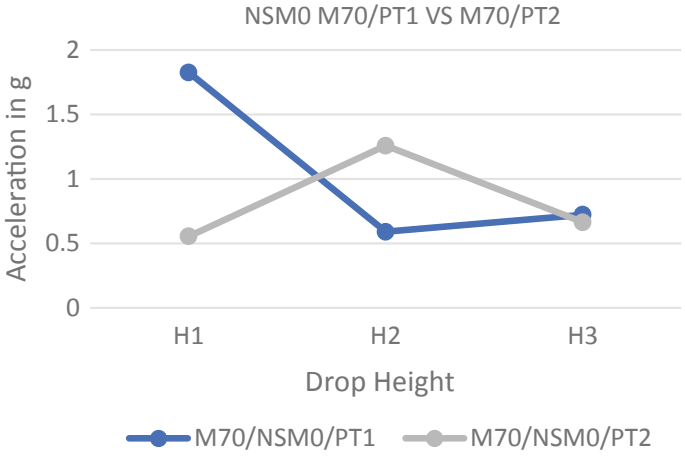

Fig. 14 Acceleration versus drop height for slabs

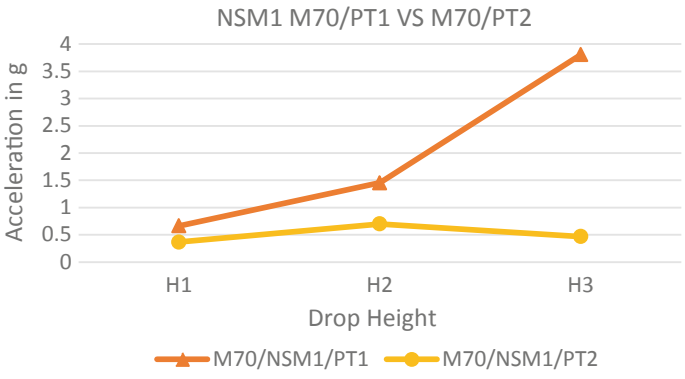

Fig. 15 Acceleration versus drop height for slabs

Table 6 Energy Absorbed per unit length of crack

Slab ID	Energy impacted (J)	Crack length (mm)	Energy per unit length of crack (J/mm)
M70/PT1/H1/NSM0	460.01	2120	0.22
M70/PT1/H1/NSM1		810	0.57
M70/PT1/H2/NSM0	913.31	3470	0.26
M70/PT1/H2/NSM1		2170	0.42
M70/PT1/H3/NSM0	1373.4	3710	0.37
M70/PT1/H3/NSM1		4130	0.33
M70/PT2/H1/NSM0	460.01	2190	0.21
M70/PT2/H1/NSM1		1380	0.33
M70/PT2/H2/NSM0	913.31	5070	0.18
M70/PT2/H2/NSM1		2930	0.31
M70/PT2/H3/NSM0	1373.4	7210	0.19
M70/PT2/H3/NSM1		4860	0.28

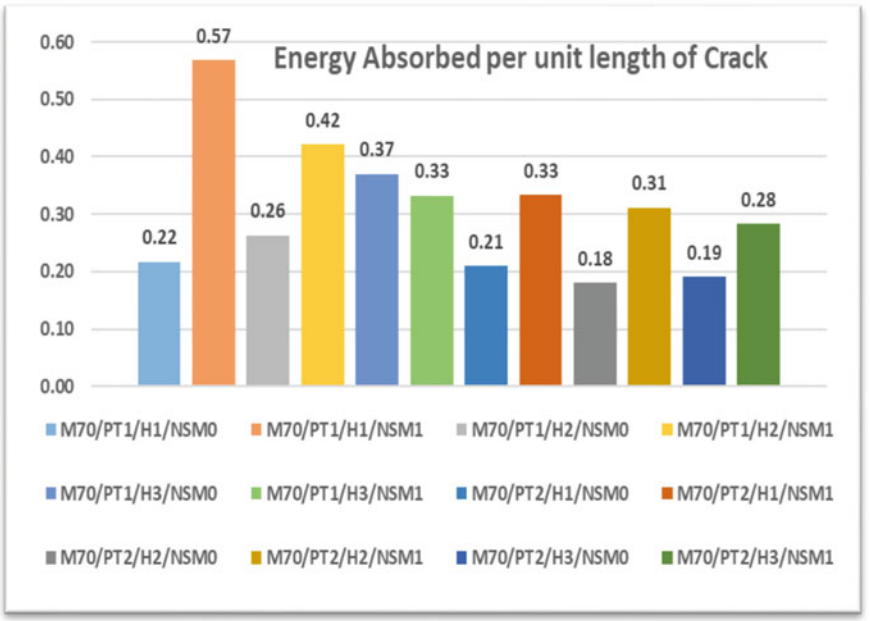

Fig. 16 Energy Absorbed per mm of crack length

7 Observations

The following observations were made from this study

1. For lower reinforcement ratio the acceleration response of unstrengthened- slab was seen to decrease with increase in drop height from H1 to H2 but increased marginally from H2 to H3 whereas it increased successively for strengthened slabs with increase in drop height as shown in the Fig. 12.
2. For higher reinforcement ratio both strengthened and unstrengthened slab showed higher response at drop height of H2 and lower at both H1 and H3 as shown in the Fig. 13.
3. For control slabs with reinforcement ratio of 0.341% the acceleration response decreased for increase of drop height from H1 to H2 and with further increase of drop height to H3 the acceleration increased. This behavior was exactly opposite to that of slabs with reinforcement ratio of 0.789% as indicated in Fig. 14.
4. It was observed that for strengthened slabs with increase in reinforcement ratio the acceleration response increased for drop height from H1 to H2 however on further increase in drop height to H3 the response of slab with 0.341% reinforcement ratio increased whereas the same decreased for 0.789% reinforcement slab as represented in Fig. 15.
5. It was observed that for control with PT1 reinforcement showed the higher energy absorption per mm of crack length compared to PT2 slabs at same drop height. For PT1 slabs the energy absorbed was observed to increase with increase in drop height whereas for PT2 slabs there was a decrease in energy absorbed with height changed from H1 to H2 and increased from H2 to H3.
6. For strengthened slabs it was observed that with increase in drop height the energy absorbed per mm of crack length was decreasing for both PT1 and PT2 slabs. The decrease was steep for PT1 slabs and gradual for PT2 slabs.
7. Comparing both control and strengthened slabs it was observed that maximum energy absorption increased for slab with PT1 reinforcement impacted from drop height H1 and decreased for PT1 slab with drop height H3. For all other slabs there was increase in energy absorption.

8 Conclusions

1. The slabs with lower reinforcement ratio, strengthening increased the acceleration response for increase in impact energy.
2. For higher reinforcement ratio, the strengthening of slab exhibited lower response when compared with unstrengthened slab for similar impact energy, this may be further examined.
3. For moderate impact energy there was an increase in acceleration response of strengthened slabs for both the reinforcement ratios but in case of highest impact energy considered the same trend was not observed. The reason for this phenomenon needs to be investigated in detail.

4. The dynamic behaviour of unstrengthened slabs through different drop heights is not showing the trend of expected observation over the increase in reinforcement ratio.
5. In control slabs with increase in reinforcement from PT1 to PT2 reinforcement showed a decrease in energy absorbed per unit length of crack with increase in drop height.
6. For strengthened slabs with increase in reinforcement from PT1 to PT2 reinforcement showed a decrease in energy absorbed per unit length of crack with increase in drop height.
7. With strengthening, it was observed that energy absorbed per unit length of crack for all the specimen increased except PT1 with drop height H3.
8. Further studies are to be conducted in detail to analyse the parametric studies of strengthened and unstrengthened slabs under impact loading.

References

1. Banthia N et al (1988) Impact testing of concrete using drop weight impact machine. Exp Mech, 63–69
2. Sangi AJ, May IM (2009) High mass, low-velocity impacts of reinforced concrete slabs, 7th LS-DYNA Conference, 2009, UK
3. Krauthammer T, Zineddin M (1995) Structural concrete slabs under localized impact, Fortifikatorisk Notat Nr 211/93, Norwegian defence constructive service
4. Hrynk TD, Vecchio FJ (2014) Behaviour of steel fibre reinforced concrete slabs under impact load. ACI Struct J 3(5)
5. Yoo DY et al (2012) Enhancing impact resistance of concrete slab strengthened with FRPs and steel fibres. In: Proceedings of the 6th international conference on FRP composites in civil engineering, CICE
6. Rizkalla S, Hassan T (2001) Various FRP strengthening techniques for retrofitting concrete structures
7. Prabhakara R et al (2006) Ultimate flexural strength of high strength concrete beams. Indian Concr J 40–50
8. Annadurai A, Ravichandran A (2014) Development of mix design of high strength concrete with admixtures. IOSR J Mech Civ Eng 3(5)
9. Andersson A (2014) Impact loading on concrete slabs: experimental tests and numerical simulations
10. Ranković S, Folić R, Mijalković M (2010). Effects of RC beams reinforcement using near surface mounted reinforced FRP composites. Facta universitatis-series: Archit Civ Eng 8(2):177–185
11. Ramanna N (2012) Static and impact load response of reinforced concrete beams and slabs with NSM-CFRP retrofitting PhD thesis submitted to Old Dominion University, USA
12. Sreenivasappa, N et al (2016) Investigations on effect of CFRP strips retrofitted using NSM method on two-way NSC and HSC slabs subjected to concentrated load. Int J Res Eng Technol eISSN: 2319–1163 | pISSN: 2321–7308 |05(14) | ICRAES-2016| Sep-2016
13. Reddy ARP et al (2016) Studies on strength and deformation behaviour of two-way NSC and HSC slabs under single point loading. Int J Res Eng Technol eISSN: 2319–1163 | pISSN: 2321–7308 | 05(14) | ICRAES-2016| Sep-2016
14. De Lorenzis L et al (2000) Strengthening of reinforced concrete structures with near surface mounted frp rods, International Meeting on Composite Materials, Milan, Italy

15. Bonaldo E et al (2005) Concrete slabs strips reinforced with epoxy bonded carbon laminates into slits, University of Minho, Portugal
16. Ozgur A et al. (2015), Low Velocity Impact Behaviour of RC Slabs with Different Support Conditions, Construction and Building Materials 2015.

Damage Detection Techniques to Identify the Unknown Damage Parameters from the Structural Response Data in Beam: A Review

Bhawna Patel and U. K. Dewangan

Abstract In this paper, the structural system identification technique is reviewed. The focus of this paper is to review mainly the state of art on damage detection techniques particularly, in beams. The various researchers have tried to find the unknown damage parameters from the structural field response data using various techniques, still, the unknown damage parameter identifications are a challenging issue using the field data. In this paper, a comparative review is presented using the various techniques applied by the researchers. Their findings and future scope of work are also presented. Finally, a conclusion in the current state of art review is presented.

Keywords Damage detection · Parameter identification · Structural field response · Beam

1 Introduction

Beams are used as an important structural component in many engineering structures like buildings, dams, bridges, flyovers, etc. Also, its other applications are wings of an airplane, machine, etc. Due to the aging of structure, extreme climatic condition, or extreme loading condition, there is a chance of deformation of the beam which will affect the load-bearing behavior of the structure and will lead to breakdown or collapse of the structure. Hence, it is necessary to identify the damage so that a warning system can be created to ensure user safety before the structure reaches the critical condition. A damage detection method is an automatic tool for engineers which can be utilized to recognize the existence of the damage and also the unknown damage parameter of the beam or any structure. Doebling et al. [1] have proposed many techniques to identify the damage.

B. Patel (✉) · U. K. Dewangan
National Institute of Technology, Raipur, India
e-mail: bpatel.phd2018.ce@nitrr.ac.in

U. K. Dewangan
e-mail: ukdewangan.ce@nitrr.ac.in

© Springer Nature Singapore Pte Ltd. 2021

K. K. Pathak et al. (eds.), *Recent Trends in Civil Engineering*, Lecture Notes in Civil Engineering 77, https://doi.org/10.1007/978-981-15-5195-6_13

According to Gawande and More [2], it has been seen that, in a beam when artificial damage is provided as notch and then the vibration is induced, the natural frequency changes. To verify this, a cantilever beam of 500 mm X 25 mm X 10 mm has been taken. A vibration test is performed on this beam without any damage and with notch made of various depths by wire cut electronic discharge machine (EDM). Result demonstrates that the natural frequency of vibration of structure varies with notch depth. As the position of notch moves toward the fixed end, natural frequency of beam decreases.

2 Damage Detection Method Classification

Damage detection methods in a beam or any structure can be classified as follows by Yan et al. [3].

2.1 The Local-Based Damage Detection Method

This method is used to detect local damage, i.e., damage of some of the components of the structure. In this method, the data to identify the unknown damage parameter are taken from the damaged structure only. Baseline data and data from the theoretical model of the undamaged structure are not used here. Thus, this method is very effective for small and regular dimension structures such as pressure vessel, bunker, silos, etc., and, for the main component of structures such as beam, column, slab, etc., CT scanning, ultrasonic test are examples for this method.

2.2 Global-Based Damage Detection Technique

This method is useful for on-site structural damage detection. This method is useful for some large and complicated structures such as dams, bridges, old monuments, etc. The data to identify unknown damage parameters are taken from a damaged structure. Also, baseline data and data from the theoretical model of the undamaged structure are required here.

For health assessment of any structure, firstly, it is considered a dynamic system with dynamic parameters as Mass, Stiffness, and Damper. As the dynamic parameters and the modal parameter and frequency-response parameter will change when damage emerges in the structure, this change in parameters will be considered as a signal for initial damage. The image processing technique is also used for damage detection, but internal damage in structure is not accurately accessible by this method. Thus, vibration-based damage detection technique is used. Other damage detection techniques like ultrasonic test and X-ray scanning can access the internal damage

very easily, but these methods are cumbersome and expensive. Also, for in-field damage detection, these methods are not suitable. Vibration techniques give in-field damage detection, and also this method is inexpensive, fast, and reliable.

Damage detection methods in beam or any structure based on vibration technique can be classified as follows by Yan et al. [3] in two types

2.3 Traditional Method

This method is based on the natural vibration characteristic of the structure. It utilizes only self-mechanism characteristics of structure such as mode shape, natural frequency, etc. The experimental setup is required in this method to measure the mode shape and damping, which require manual operation, so the chance of error is more, and tiny damage may not be detected. The method is very expensive and time-consuming.

- Traditional-type damage detection method: Change in natural frequency-based
- Traditional-type damage detection method: Change of structural flexibility or stiffness
- Traditional-type damage detection method: Change of structural vibration mode
- Traditional-type damage detection method: Transfer function (frequency–response function)
- Traditional-type damage detection method: Static information-based
- Traditional-type damage detection method: Power flow-based.

2.4 Modern Method (Intelligent Damage Diagnosis)

In this method, firstly, the vibration response of the structure is measured online, then these parameters are further considered for damage detection. The various techniques are as follows:

- *Wavelet analysis*
- *Neural network method*

Further, vibration-based structure damage detection is classified as:

- **Modal-based method**. Some dynamic characteristics are compared for a numerical model of structures and experimental model.
- **Non-modal-based method**. Change in the dynamic characteristics is directly compared without any numerical model.

3 Damage Detection Method in Beam

After going through many references, the category for finding the unknown damage parameters particularly in a beam is, methods based on natural frequency, image processing, mode shape, strain mode shape, dynamically measured flexibility, non-linear methods, neural network, and other.

3.1 Damage Identification Method in Beam: By Image Processing Technique

Mohan and Poobal [4] the image processing technique is also used for damage detection. In this method, a high-resolution camera of, say more than 10 megapixels, is used to take the image of the crack formed in the beam. Now, image is further processed which includes segmentation and reducing image sample. This can be automatically done by using software like MATLAB image processing toolbox. Now, the crack in a beam is detected as a result. But, internal damage in structure is not accurately accessible by this method. Also, ultrasonic image processing is used nowadays which provides a better result.

3.2 Damage Identification Method in Beam: Change in Natural Frequency-Based Technique

In this method, artificial damage in the form of crack for different depth is introduced in the beam. The mode shape amplitude of structure was generated before the damage. Then after damage, the mode shape amplitude was generated again. The mode shape amplitude of all the modes and frequency before and after the damage of beam are the unknown damage parameter, these results are compared. If there is any change in damage and undamaged response, then there is the existence of damage.

For this, a simply supported beam, 3.6 m long, 0.1 m thick, and 0.125 m wide, is selected for damage identification and artificial damage in the form of crack for different depths is introduced in the beam. In software ANSYS, the modal response of structure was generated before damage as well as after damage. The mode shape amplitude of all the modes before and after damage is taken as the unknown damage parameter. This parameter for all modes is separately compared for damage and undamaged case. The predicted locations for crack are within 1 cm near the mid-span and within 13.7 cm near the left quarter-span by Kim et al [5]. Thus, the damage is not exactly located by the author but is very near to the crack. This error was mentioned as a localization error.

3.3 Damage Identification Method in Beam: Mode Shape-Based

In this, artificial damage in the form of crack for different depths is introduced in the beam. The modal response of structure was generated before the damage. Then after damage, the modal response was generated again. The mode shape amplitude of all the modes and frequency before and after the damage of beam is the unknown damage parameter, these results are compared. If there is any change in damage and undamaged response, then there is the existence of damage.

As per the method of Kim et al. [5], a simply supported beam, 3.6 m long, 0.1 m thick, and 0.125 m wide, is selected for damage identification and artificial damage in the form of crack for different depth is introduced in the beam. In software ANSYS, the modal response of structure was generated before damage and then after damage. The mode shape amplitude of all the modes and frequency before and after the damage of beam is the unknown damage parameter. Now, pseudo-readings at the 289 nodal points of the DDM for each mode shapes are to be determined. For this, cubic spline functions were used. Modal sensitivities are then calculated for both before and after damages. The result shows that damage could be located with high accuracy. If the crack is present at the middle span, then the severity of the damage could be estimated with a relatively small size error and, if the crack is present at a quarter of span, then the severity of the damage could be estimated with relatively large-size error.

3.4 Damage Identification Method in Beam: Strain Mode Shape-Based

As per the method of Tan et al. [6], firstly, the vibration is induced in the beam and only the first mode of vibration response is used, for predicting the existence, location, and severity of the damage. For single-damage scenarios, damage detecting, locating, and quantification is done by, damage index β which is based on modal strain energy. Now, to calculate β, the response of beam in terms of mode shape of first bending mode is considered. Then a graph is plotted between damage index and distance along the beam. The further result can be drawn by the comparative plots.

Tan et al. [6] used a steel beam for damage identification. The graph is plotted between damage index and distance along the beam and among the input parameters. Now, in the graph, if single damage is observed, then equations are generated from regression analysis for each damage location. However, if the graph shows multiple numbers of damage, then we need to use Artificial Neural Networks (ANNs) to confirm the exact damage location, as research has shown that this method provides more accuracy.

3.5 Damage Identification in Beam: Neural Network-Based Methods

This is a modern approach for detection and evaluation of the damage in beam or any structure. In this study, firstly by the method of experimental modal analysis, the dynamic behavior of undamaged and damaged beam, i.e., vibration data such as natural frequencies and mode shape are obtained. Then same response parameters are computed by finite element simulations. Then these data are used to train the ANNs. The trained ANNs are then used to predict the severity and location of the double-point damage case.

Hakim et al. [7] have considered an I-beam for damage identification and assessment by the ANN-based method. According to this paper, natural frequencies of the beam of the initial five modes influence the damage parameter by 9.08% which is the highest percentage among all other modes. Therefore, we observe that, for predicting damage in the double locations, the first natural frequency of the vibration is the most important. Also, Pathirage et al. [8] have attempted to identify damage parameters by neural networking.

3.6 Damage Identification in Beam: Nonlinear Method

The nonlinear system identification method is used to predict the dynamic response of the system with nonlinear behavior. When the structural nonlinear behavior is considered, the nonlinear index has presented 100% of the true result by Luis et al. [9]. Thus, the nonlinear index is considered as a more sensitive method for damage detection.

Luis et al. [9] have considered a clamped-free beam for damage identification by the nonlinear method. Vibration is induced by placing the magnet near the free end of the beam, which causes a cubic stiffness effect and detected the damage by the nonlinear method. Then, to predict the dynamic response of the system by taking the nonlinear behavior under consideration, the Volterra series method of nonlinear system identification expanded in the Kautz orthonormal basis has been used.

3.7 Damage Detection in Steel–Concrete Composite Beam

In this method, the damage-sensitive features are considered to be deflection and rotation induced by moving load. Only the extreme value of dynamic response is required, for damage detection. Along with that more deflection and rotation are simultaneously monitored for increasing the accuracy of damage detection. No sensors are required. The result shows that when damage occurs, an envelope of

dynamic response in terms of deflection and rotation tends to increase. This effect can be considered for the development of an algorithm for damage detection. [10]

Çam et al. [11] have also presented in their paper about the damage detection technique in the beam. The paper induced artificial damage in the form of crack in a beam. Then the location and depth of damage were identified. Vibration has been introduced in the beam by impact shock. The response thus obtained in uncracked and artificially damage beams were compared in the frequency domain.

4 Gaps and Issues

Based on the literature review conducted, we identify some of the shortcomings in various methods mentioned in this paper. They are discussed below.

The local-based damage detection method is useful for the beam. Also, this method involves the contact-based technique, in which the damage detection parameters can be identified but not located exactly. This method is not applicable to the whole structure as well as complex structures [3]. In damage parameter detection method based on natural frequency, the predicted locations for crack are within 1 cm near the mid-span and within 13.7 cm near the left quarter-span by Kim et al. [5]. Thus, the damage is not exactly located by the author but is very near to the crack. Also, initial damage causes a very small change in natural frequency which is not detected during measurement. To overcome this difficulty, change in mode shapes can be considered for damage detection. Mode shape is more sensitive to damage than natural frequency. But this method is also not feasible because the damage is a local phenomenon which does not influence the lower mode. Also, mode shapes are often exposed to noise, the choice of the sensor also effect on damage parameter by Kim et al.[5]. The vibration-based damage detection technique is now used by many researchers for beam. But this method is not able to quantify the severity of the damage. Thus, presently, the computational intelligence techniques are used for damage identification. The most important of that is the ANNs. Also, optimization algorithms are used for some case. In ANNs, natural frequencies and mode shapes are taken as input for recognizing patterns in data. But, if these inputs are considered, then single damage may only be quantified, and large error may occur during multiple damage quantification. With the help of ANNs, an algorithm can be developed for obtaining accurate damage parameter and location.

5 Conclusion

This paper provides a collective survey of different damage detection techniques to identify the unknown damage parameter in the beam. The main aim of this study is to review the damage detection techniques for the beam. Here, we have taken more than 40 research papers for review. We have finalized our review based on two

features. First one is the method suitable for in-field. Secondly, the method based on the accuracy level for prediction of the location of the damage.

Based on the review, we concluded that local-based damage detection method is useful for the beam. Also, this method involves the contact-based technique, in which the damage detection parameters can be identified but not located. In the damage parameter detection method based on the natural frequency measurement technique, initial damage is not detected during measurement. Also, error during measurement or variation in ambient condition causes uncertainty in measured frequency. In the change in mode shapes method, the damage is not affecting the lower mode, so it can't be identified. Also, mode shapes are often exposed to noise, the choice of the sensor also effect on damage parameter.

Then, vibration-based damage detection technique is now used by many researchers for beam. But this method is not able to accurately quantify the severity of the damage. Thus, presently, the computational intelligence techniques are used for damage identification. In the future, we plan to survey various vibration-based and ANN-based damage detection techniques and also the non-contact-based technique as these are seen to be more useful if they are used together.

References

1. Doebling SW, Farrar CR, Prime MB (2019) A summary review of vibration-based damage identification methods. Shock Vib Digest 30(1998):91–105. https://doi.org/10.1177/058310249803000201
2. Gawande SH, More RR (2016) Effect of notch depth & location on modal natural frequency of cantilever beams. In: Structures, vol 8, Part 1. Elsevier, pp 121–129, https://doi.org/10.1016/j.istruc.2016.09.003 (November 2016)
3. Yan YJ, Cheng L, Wu ZY, Yam LH (2007) Development of vibration-based structural damage detection technique. In: Mech Syst Signal Process 21:2198–2211, https://doi.org/10.1016/j.ymssp.2006.10.002 (Elsevier)
4. Mohan A, Poobal S (2018) Crack detection using image processing: a critical review and analysis. Alexandria Eng J 57(2), 787–798, https://doi.org/10.1016/j.aej.2017.01.020 (June 2018, Elsevier)
5. Kim J-T, Ryu Y-S, Cho H-M, Stubbs N (2003) Damage identification in beam-type structures: frequency-based method versus mode-shape-based method. Eng Struct 25(1):57–67, https://doi.org/10.1016/s0141-0296(02)00118-9 (January 2003, Elsevier)
6. Tana ZX, Thambiratnama DP, Chana THT, Abdul Razak H (2017) Detecting damage in steel beams using modal strain energy based damage index and Artificial Neural Network. In: Engineering failure analysis, vol 79. Elsevier, pp 253–262, https://doi.org/10.1016/j.engfailanal.2017.04.035 (September 2017)
7. Hakim S, Abdul Razak H (2012) Damage detection of steel bridge girder using artificial neural networks. In: Steel Compos Struct 14(4):367–377, https://doi.org/10.12989/scs.2013.14.4.367 (April 2013)
8. Pathiragea CSN, Li J, Li L, Hao H, Liu W, Ni P (2018) Structural damage identification based on autoencoder neural networks and deep learning. In: Engineering structures, vol 172. Elsevier, pp 13–28, https://doi.org/10.1016/j.engstruct.2018.05.109 (October 2018)
9. Villania LGG, da Silvaa S, Cunha Jr A (2017) Damage detection in an uncertain nonlinear beam. In: Procedia engineering, vol 199. Elsevier, pp 2090–2095, https://doi.org/10.1016/j.proeng.2017.09.480

10. Kasinos S, Palmeri A, Lombardo M (2015) Using the vibration envelope as a damage-sensitive feature in composite beam structures. In: Structures, vol 1. Elsevier, pp 67–75, https://doi.org/10.1016/j.istruc.2014.10.001 (February 2015)
11. Çam E, Orhan S, Luy M (2015) An analysis of cracked beam structure using impact echo method. NDT & E Int 38(5), 368–373, https://doi.org/10.1016/j.ndteint.2004.10.009 (July 2005, Elsevier)

Studies on Rotation Capacity and Torsional Strength of Normal, Medium- and High-Strength RC Beams

M. R. Prakash, Katta Venkataramana, R. Prabhakara, and B. Manjunatha

Abstract Understanding of the beam behaviour in torsion along with bending and shear is very important for the complex design of buildings and as well as recent developments in neo-concretes. An experimental investigation was carried out to determine the response of normal, medium- and high-strength concrete beams when subjected to torsion. In the present investigation under standard testing conditions, the torsional behaviour of total 27 beams which are grouped into nine categories like NSC, MSC and HSC beams with identical geometrical conditions like width, depth, effective span and varied area of steel in longitudinal and transverse directions has been investigated. The beam properties like rotation capacity, ultimate torsional strength and failure pattern of the beams are studied. The results obtained from the experimental investigations are validated with the help of similar work as cited in the literature survey. Also, the parametric analysis had carried out for different models, theories and codal equations as suggested by the different investigators. The obtained torsional strength experimental values of NSC beams are well agreement with the predicted torsional strength for most of the codes available in the literature. The experimental values of MSC and HSC beams are close agreement with EURO code II results. It was also observed that the rotation capacity of the beams depends on the grade of concrete, longitudinal steel and spacing of transverse reinforcement.

Keywords Rotation capacity · Ultimate torsional strength · Failure pattern

M. R. Prakash (✉) · B. Manjunatha
Acharya Institute of Technology, Bangalore, Karnataka, India
e-mail: prakash@acharya.ac.in

B. Manjunatha
e-mail: manjunathab.ait@gmail.com

K. Venkataramana
NITK Surtkal, Mangalore, Karnataka, India
e-mail: ven.nitk@gmail.com

R. Prabhakara
Visvesvaraya Technological University, Bangalore, Karnataka, India
e-mail: r.prabhakara@gmail.com

© Springer Nature Singapore Pte Ltd. 2021

K. K. Pathak et al. (eds.), *Recent Trends in Civil Engineering*, Lecture Notes in Civil Engineering 77, https://doi.org/10.1007/978-981-15-5195-6_14

1 Introduction

Development in concrete technology resulted in new concretes with different engineering properties which attracted engineers and researchers. A lot of work taking place for improving quality of the concrete by various means, to maximize its performance. Addition of fibres, chemical and mineral admixtures improved the quality of concrete which resulted in Fibre-Reinforced Concrete (FRC), High-Performance Concrete (HPC), High-Strength Concrete (HSC), Self-Compaction Concrete (SCC), etc. HSC is often considered as a relatively new material over Normal Strength Concrete (NSC). The problems related to the heterogeneity of conventional concrete have been eliminated by the production of HSC. The microstructural studies of HSC have reported that dense, uniform and compact microstructure.

Torsional moment of structural elements plays a vital role in the design of buildings and bridges. Reinforced concrete members experience forces—axial, shear, bending and torsion [1–5]. In most of the design practices, the effect of bending moments and shear forces are considered as primary, and torsion as secondary. Torsion often appears along with bending and shears in the spandrel beam or in curved girders, beams in eccentrically loaded frames of multi-deck bridges and box girder bridges [6] are an example of such cases. Torsion becomes the main effect, where beams are curved in plan. These structures are often required to resist torsion and should be designed or at least be checked against torsion. The analysis and design for torsion are getting more importance amongst structural engineers.

The causes of torsional failure of reinforced concrete beams have not been fully explored [1]. In general, well-formulated empirical equations are available to predict the failure of the beam in terms of torsional strength. This is due to the lack of rationality in our approach to the problem of torsion. The behaviour of members under the effect of torsion is still a research subject extensively. Investigations have been carried out on a total 27 beams, in 9 varieties of beams such as NSC, 9 MSC and HSC, to understand the torsional behaviour by varied longitudinal and transverse reinforcement. To witness the influence of longitudinal steel, three beams in each category were prepared and tested having longitudinal reinforcement 2, 3 and 4% and also having transverse reinforcement of 8-mm-diameter stirrups at the spacing of 1D, 1.5D, 2D [7–9]. The span to depth ratio of the beam was maintained constant with a value of 8. The breadth and depth of the beam were also kept constant with 100 mm.

2 Experimental Procedures

The theories and codes used in the present analysis are skew-bending theory [10], space truss analogy, ACI [11], British standards-8110-97, Euro Code-I, Australian code-3600, Canadian standards-CSA [12] and Indian Standards-456-2000 [13]. The Eqs. (1–7) are as specified below.

$$T_{np} = \frac{x^2 y}{3}(0.85 f_r) \tag{1}$$

where T_{np} = Ultimate torsional strength of plain concrete beam, x and y = smaller and longer dimensions of the rectangular cross section, respectively, f_r = modulus of rupture of the concrete, MPa.

$$T_{uR} = \frac{2A_t b_1 d_1}{S_v}\left(0.85 f_y\right) \tag{2}$$

where T_{uR} = ultimate torsional moment at rupture, A_t = Area enclosed by the centre line of longitudinal bars mm^2, b_1 = breadth of beam at reinforcement, mm, d_1 = depth of beam at reinforcement, mm S_v = Spacing of the stirrups along the length of the member, mm, f_y = modulus of rupture of the concrete, MPa.

$$T_{cr} = \frac{\sqrt{f_c'}}{3}\left(\frac{A_{cp}^2}{p_{cp}}\right) \tag{3}$$

where T_{cr} = Torsional cracking moment, kN-m, f_c' = Concrete compressive strength, MPa,

A_{cp} = Area enclosed by outside perimeter of concrete cross section, mm^2.

p_{cp} = Outside perimeter of the concrete cross section, mm.

$$T_{us} = \frac{0.8 x_1 y_1 A_{sv}}{S}\left(0.87 f_{ys}\right) \tag{4}$$

where T_{us} = ultimate torque at stirrup spacing.

A_{sv} = Total cross-sectional area of the stirrup legs within a distance s_v, mm^2.

f_{ys} = Specified yield strength of the reinforcement, MPa;

S = Spacing of the stirrups along the length of the member, mm.

$$T_{us} = \frac{2A_t A_{sw} f_{ys}}{S}(\cot\theta_t) \tag{5}$$

where A_t = longitudinal reinforcement area mm^2, A_{sw} = total cross-sectional area of the stirrup legs within a distance s_v, mm^2, θ or θ_t = crack angle of twist, 45º.

$$T_{u1} = \frac{2A_k A_{sw} f_{ys}}{S}(\cot\theta_t) \tag{6}$$

where T_{u1} = Torque corresponding to stirrups.

$$T_{u2} = \frac{2A_s A_k f_y}{u_k}(\tan\theta_t) \tag{7}$$

Table 1 Concrete proportion

Mix	Cement (kg)	Water (lit)	W/B	F/A (kg)	CA (kg)	SP (%)
M-40	450	202.5	0.44	656.65	984.97	–
M-80	636	150	0.36	744	1050	2
M-100	750	150	0.20	470	1050	3

where T_{u2} = Torque corresponding to longitudinal steel; A_k = Area enclosed by the central lines of wall thickness, u_k = Perimeter of cross section.

2.1 Concrete Proportion

Prior to adopting the final mix proportions for different grades of concrete, numerous trial mixes were tried having the right consistency and workability [7–9, 14–16]. The results of these final proportions for M40, M80 and M100 concrete are given in the Table 1.

2.2 Specimen Testing

The cast beams were tested in specially fabricated equipment shown in Fig. 1, applying constant load increments as per Indian standards using loading frame at MSRIT laboratory.

Figure 1 shows the arrangements of the specimen in the loading frame having been secured to avoid any slip during the time of loading. When the beam is ready to

Fig. 1 Loading arrangement

take the load after it was secured in position, the lever was placed symmetrically by applying load uniformly by spreader beam. The spreader beam of ISHB 150 with 3 m length was used and the arm was adjusted by varying the angle to satisfy the required span of beam. The two arms attached to the rotating box are ISHB 150 of 1.5 m length. A proving ring with 50-kN capacity was used. Two dial gauges were fixed at 0.5 m distance from the centre of the cross section of the beam below the loading arm and the deflection at that point was recorded and converted to twist. The beam specimens were simply supported at two bearings, under which the roller supports were installed to release the restraint of longitudinal elongation of specimens during the test. The vertical load was applied using a 500-KN capacity hydraulic jack through spreader beam on torsional arms to produce the torque.

The details of the specimens are tabulated in Table 2. The first letter indicates the mix, the second number indicates the percentage of longitudinal reinforcement and the third indicates the spacing of stirrups. The effective length of the specimen was 800 mm. The total span provided was 1200 mm, 200-mm bearing on each side. To avoid the failure of the specimen at the support section, the support was provided with a higher amount of reinforcement than the test region. The beams were cast as per standards and tested using 500 tones loading frame under standard conditions. The results obtained were tabulated and analysed by using different codes and theories. The beams tested show the failure at centre of the beam as shown in Fig. 2 with the inclination of the cracks from 40° to 50° and the width of crack varied from 0.3 to 7 mm without any further increase in load.

3 Results and Discussions

3.1 Torsional Moment Versus Twist Curves for Reinforced NSC Beams

To know the behaviour of NSC reinforced beams, the important parameters like the concrete strength, ductility and influence of main bars (longitudinal) and stirrups (transverse), the variations of twist with respect to torsional moment were studied and plotted. A torsional moment vs twist curve of all NSC beams have been considered to understand their behaviour with the variation of main bars and stirrups, the torsional moment carrying capacity is depicted in Fig. 3. From Fig. 3, it was observed that the torsional moment exhibits linear elastic behaviour up to cracking and thereafter the non-linear behaviour exhibited. At the end of non-linear region, the failure of concrete takes place due to torsion moment. It has been noticed that, after cracking, the twist of beam rapidly increased due to yielding of the reinforcement and decreased the torsional moment carrying capacity. After yielding of reinforcement, twist moment carrying capacity got reduced. It was evident that as the spacing of stirrups increases the torque carrying capacity decreases. However, the spacing of stirrups is in the entire length of the beam, to avoid the failure of the beam at the supports, higher

Table 2 Ratio of experimental to theoretical torsional strength

Beam	Tμ (exp)/Tμ (theory)								
	Skew-bending theory	Space truss analogy	IS-456	AS-3600	BS-8110	ACI	Euro1	Euro2	CSA
NSC/2/1.0D	1.83	0.69	0.66	1.05	0.71	0.57	0.57	0.64	0.68
NSC/2/1.5D	1.88	1.00	0.96	1.52	1.03	0.84	0.84	0.62	0.99
NSC/2/2.0D	1.87	1.29	1.24	1.97	1.33	1.08	1.08	0.60	1.28
NSC/3/1.0D	2.04	0.77	0.74	1.17	0.79	0.64	0.64	0.47	0.76
NSC/3/1.5D	2.06	1.09	1.05	1.66	1.12	0.91	0.91	0.45	1.08
NSC/3/2.0D	1.96	1.33	1.28	2.03	1.37	1.11	1.11	0.41	1.32
NSC/4/1.0D	2.17	0.85	0.81	1.29	0.87	0.71	0.71	0.39	0.84
NSC/4/1.5D	2.11	1.15	1.11	1.75	1.18	0.96	0.96	0.36	1.14
NSC/4/2.0D	2.08	1.46	1.40	2.22	1.49	1.22	1.22	0.34	1.44
MEAN	2.0	1.07	1.03	1.63	1.10	0.89	0.89	0.47	1.06
SD	0.12	0.27	0.26	0.41	0.27	0.22	0.22	0.12	0.26
CV	0.06	0.25	0.25	0.25	0.25	0.25	0.25	0.25	0.25
MSC/2/1.0D	1.91	1.62	0.87	2.46	1.66	1.35	1.35	0.84	1.60
MSC/2/1.5D	1.80	2.21	1.19	3.37	2.27	1.85	1.85	0.77	2.19
MSC/2/2.0D	1.74	2.80	1.51	4.27	2.88	2.34	2.34	0.733	2.77
MSC/3/1.0D	2.08	1.80	0.97	2.74	1.84	1.50	1.50	0.62	1.78
MSC/3/1.5D	2.07	2.59	1.40	3.94	2.66	2.16	2.16	0.60	2.56
MSC/3/2.0D	1.98	3.24	1.75	4.92	3.32	2.70	2.70	0.56	3.20
MSC/4/1.0D	2.17	1.91	1.03	2.90	1.96	1.59	1.59	0.50	1.88
MSC/4/1.5D	1.96	2.48	1.34	3.78	2.55	2.07	2.07	0.43	2.45

(continued)

Table 2 (continued)

Beam	Tμ (exp)/Tμ (theory)								
	Skew-bending theory	Space truss analogy	IS-456	AS-3600	BS-8110	ACI	Euro1	Euro2	CSA
MSC/4/2.0D	1.88	3.09	1.67	4.71	3.17	2.58	2.58	0.40	3.06
MEAN	1.95	2.42	2.24	3.68	2.48	2.02	2.02	0.61	2.39
SD	0.14	0.57	0.69	0.82	0.59	0.48	0.48	0.15	0.57
CV	0.06	0.25	0.25	0.25	0.25	0.25	0.25	0.24	0.25
HSC/2/1.0D	2.19	2.05	1.11	3.12	2.10	1.71	1.71	1.07	2.03
HSC/2/1.5D	2.30	3.13	1.69	4.76	3.21	2.61	2.61	1.09	3.09
HSC/2/2.0D	2.29	4.10	2.21	6.24	4.21	3.42	3.42	1.07	4.05
HSC/3/1.0D	1.81	1.73	0.93	2.63	1.77	1.44	1.44	0.60	1.71
HSC/3/1.5D	2.11	2.91	1.57	4.43	2.99	2.43	2.43	0.67	2.88
HSC/3/2.0D	2.42	4.37	2.64	6.50	4.56	3.68	3.68	0.73	4.40
HSC/4/1.0D	2.16	2.09	1.13	3.17	2.14	1.74	1.74	0.54	2.06
HSC/4/1.5D	2.48	3.45	1.86	5.25	3.54	2.88	2.88	0.60	3.41
HSC/4/2.0D	2.57	4.68	2.52	7.12	4.80	3.90	3.90	0.61	4.62
MEAN	2.26	3.17	2.24	4.80	3.26	2.65	2.65	0.77	3.14
SD	0.22	1.08	0.69	1.61	1.11	0.90	0.90	0.23	1.07
CV	0.10	0.34	0.31	0.34	0.34	0.34	0.34	0.34	0.34

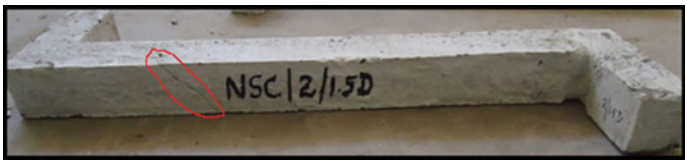

Fig. 2 Cracking pattern of specimen

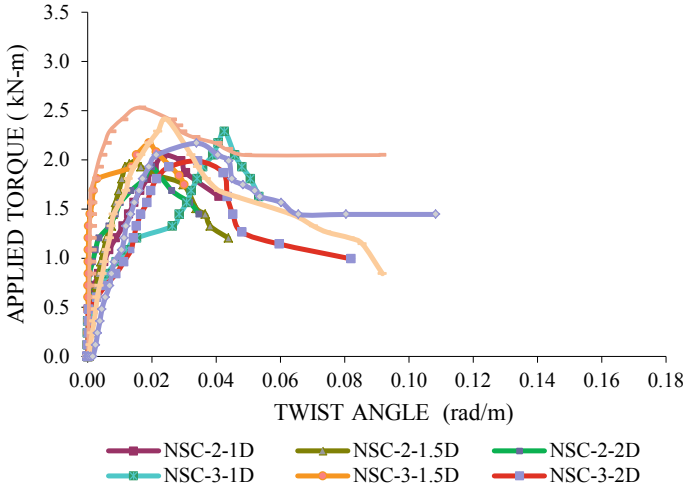

Fig. 3 Torsional moment versus twist curve for all NSC beams

reinforcement was provided. The longitudinal reinforcement ratio is less effective for torsional moment. The results obtained were compared with the earlier tested beams of MSC and HSC beams.

The combined graphs of all the reinforced beams of MSC and HSC were plotted and depicted in Figs. 4 and 5, in order to know the behaviour with respect to its strength, both longitudinal and transverse steel and stiffness. The variation of curves is as shown in Figs. 4 and 5. The curves of NSC, MSC and HSC drawn have shown the similar behaviour until the failure of concrete, as the torsional moment was applied. All the curves were observed to be linear and very close to each other, as the concrete failed to take the load and there was a sudden fall from linear variation till the concrete fails completely.

For the beams, as the transverse reinforcement ratio increases, the curves become steeper compared to the other beams having less transverse reinforcement ratio. It is observed from the graph that the beams prepared with HSC have a steeper slope than the MSC and NSC beams. As the amount of longitudinal reinforcement increases, the torsional moment carrying capacity also increases.

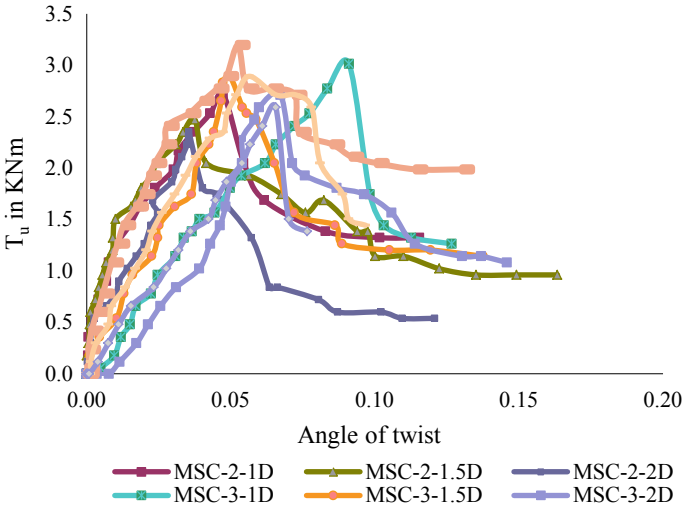

Fig. 4 Torsional moment versus twist curve for all MSC beams

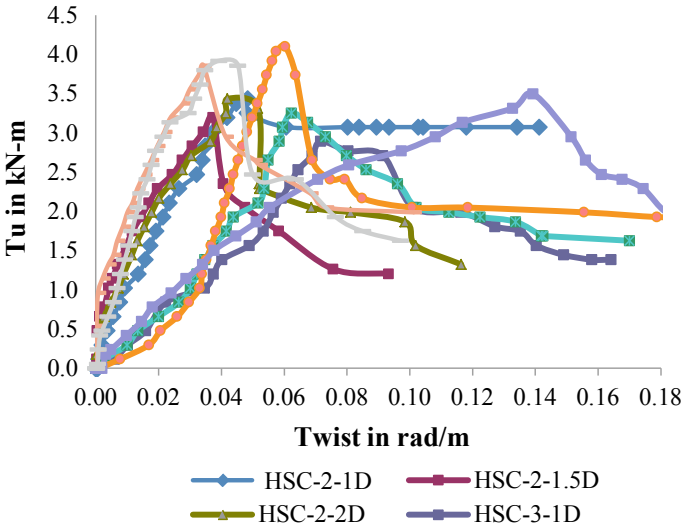

Fig. 5 Torsional moment versus twist curve for all NSC beams

3.2 Comparison of Torsional Strength of NSC, MSC and HSC Beams

The torsional strength of beams was calculated using the Eqs. 1–7, later ratio of the experimental to calculated strength value, mean, standard deviations (SD) and

coefficient of variation (CV) were determined and tabulated in Table 2. It can be observed that the determined mean values of torsional strength for NSC beams ratios were found higher than the experimental values, except for ACI and European codes. This indicates that, except for ACI European codes, all other standards have predicted the torsional capacities conservatively. The average of torque ratios shows that Indian standard and CSA were more successful in predicting the ultimate torques compared to other standards for NSC beams. The values submitted in the work for the MSC and HSC, the EURO code predicts better results, with mean of 0.61 and 0.77, SD = 0.15 and 0.23 and CV = 0.25 and 0.3, respectively. All the codes underestimate the experimental values.

Parametric analysis has been carried out for the data collected from various research papers published on the above topic from 1995 to 2008. Total 102 data from eight investigations are tabulated with the available parameters, presented in Table 3. It was found that, from the analysis of various theories, the results of Euro code-II predict better results with the MEAN = 0.62, SD = 0.21 and CV = 0.34.

4 Conclusions

1. It was seen that as the compressive strength of concrete is increased the torsional capacity of beams also increases. The increase in longitudinal reinforcement ratio was less effective for NSC beams compared to the torsional moment carrying capacity in MSC and HSC beams.
2. The beams with the same percentage of reinforcement, the torsional capacity of NSC beams is less compared with MSC and HSC beams. The rotation (twist) for NSC beams was greater when compared MSC and HSC beams.
3. It has been found that as the percentage of longitudinal reinforcement increases, the ultimate torsional shear stress of all the beams increases in the case of both experimental and literature data. As the spacing of transverse reinforcement increases in case of experimental and literature data, the torsional stress increases for all the reinforced beams.
4. The torsional stress increases as the total reinforcement increases for the experimental as well as the literature data.
5. For the experimental values of NSC reinforced beams, space truss analogy and IS-456 method predicts better results, with mean = 1.07, S D = 0.27, C V = 0.25 and for IS-456 method mean = 1.03, S D = 0.26, C V = 0.25, respectively.
6. For the experimental values of MSC reinforced beams, EURO code II predicts better results, with mean = 0.61, S D = 0.15, C V = 0.25.
7. For the experimental values of HSC reinforced beams, EURO code II predicts better results, with mean = 0.77, S D = 0.23, C V = 0.3.

Table 3 Details of literature data

Sl	Researcher	B (mm)	D (mm)	l/d	ρ_l (%)	P_t (%)	f_c (MPa)	No of data
1	Rasmussen and Baker [3]	160	241	12.45	4	1.83	36.3–109.8	12
2	Ashour et al. [5]	100	370	1.02–5.48	0.85	0.75	53.97–93.93	20
3	Koutchoukali and Belarb [6]	203	255	15.53	0.1–0.15	1.2–1.7	39–93	10
4	Fang and Shaiu [17]	350	464	6.68	0.6–2.0	0.6–2.0	33.5–78.33	16
5	Chiu et al. [7]	250–420	370–650	4.77–8.38	0.51–0.91	1.71–2.27	20–42.4	13
6	Amel and Ronagh [8]	127–254	118.3–346	5.02–16.91	0.74–3.31	0.71–2.27	20–42.4	11
7	Csikos and Hegedus [14]	130	117.3	17.05	0.74–1.48	0.74–1.34	20	12
8	Husem et al. [9]	150	250–300	1.67–2	1.2–2.2	0.66–0.91	66	8
Total								102

References

1. HSUT (1968) Torsion of structural concrete-behaviour of reinforced concrete rectangular members, torsion of structural concrete, SP-18, vol 18. American Concrete Institute, ACI Symposium Publication, pp 261–306
2. Hsu Thomas T C (1984) Torsion of structural concrete. Van Nostrand Reinhold Co., Inc., New York
3. Rasmussen LJ, Baker G (1995) Torsion in reinforced normal and high-strength concrete beams part 1: experimental test series. ACI Struct J 92(1):56–62
4. Indian Standard Structural use of Concrete, Part 1: Code of Practice for design and construction, BS 8110-1:1997
5. Ashour SA, Samman TA, Radain TA (1999) Torsional behaviour of reinforced high-strength concrete deep beams. Struct J 96(6):1049–1060
6. Koutchoukali NE, Belarbi A (2001) Torsion of high-strength reinforced concrete beams and minimum reinforcement requirement. Struct J 98(4):462–469
7. Chiu HJ, Fang IK, Young WT, Shiau JK (2007) Behavior of reinforced concrete beams with minimum torsional reinforcement. Eng Struct 29(9):2193–2205
8. Ameli M, Rounagh H (2007) Treatment of torsion of reinforced concrete beams in current structural standards. Division of Civil Engineering, School of Engineering, University of Queensland, QLD, 4072, Australia. Asian J Civil Eng (Build Hous) 8(5):507–519
9. Husem M, Oztekin E, Pul S (2011) A calculation method of cracking moment for the high strength concrete beams under pure torsion. Sadhana 36(1):1–15
10. Prakash MR, Vidya M, Manjunath H (2012) Cracking and torsional ductility behaviour of MSC and HSC plain beams. Int J Eng Res Ind Appl 2:1–10
11. Prakash MR, Sadanand P, Manjunath HR, Jagadeesh Kumar BG, Prabhakara R (2012) Cracking and torsional ductility behavior of HSC beams. Int J Civil Struct Environ Infrastruct Eng Res Dev (IJCSEIERD) 2(4):1–10. ISSN 2249-6866
12. Prakash MR, Vidya MS, Manjunath HR, Jagadeesh Kumar BG, Prabhakara R (2012) Torsional ductility behaviour of MSC and HSC plain beams. Int J Eng Res Ind Appl (IJERIA) 5(IV):23–36
13. Prakash MR, Sunil K, Prabhakara R (2013) Parametric analysis of torsional behaviour of plain normal and high strength concrete beams. MSR J Eng Technol Res 1(1):5–9
14. Csikos A, Hegedus I (2007) Torsion of reinforced concrete beams. In: 2nd International PhD Symposium in Civil Engineering, Budapest
15. Manjunath HR, Prakash MR, Pramod K, Prabhakara R, Venkatasubramanya BV (2013) Moment redistribution in two span continuous high strength concrete beams. Int J Multidiscip Res Adv Eng (IJMRAE) 5(I):151–167. ISSN 0975-7074
16. Prakash MR, Chinmayee Vikram Kumar, Prabhakara R (2017) Torsional behaviour of plain and reinforced normal strength concrete beams. Imp J Interdiscip Res 3(3):11–16
17. FangI K, Shiau JK (2004) Torsional behaviour of normal-and high-strength concrete beams. ACI Struct J 101(3):304–313

Manufacturing of an Economical Single Degree-of-Freedom Shake Table

Ketan N. Bajad and Manisha V. Waghmare

Abstract Shake table is the most effective and well-organized device than any other test for understanding the basic concepts of earthquake. This paper provides a well-organized, effective, economical, and affordable single-DOF shake table. It gives a straightforward and user-friendly platform for engineering students to practically understand and carry out the scientific study of earthquakes. The study proceeds with the proper designing and erection of a single DOF shake table with a payload of 30 kg and a frequency of 0–25 Hz. Steady-state analysis of an identical structure made of steel and aluminum is done in SAP2000, conventional shake table and designed shake table, and results are compared. Harmonic analysis (sinusoidal wave) of three structures with different height is carried out in SAP2000 in order to study the impact of their height on the seismic response of structure. Harmonic sinusoidal wave applied on the above structures in SAP2000 is obtained from the designed shake table. Data translation system and QuickDaq software are used for recording the harmonic data. The single-DOF shake table assembled with an economical cost of INR 50,000 only proved effective for seismic analysis of structures at the academic level. It is also seen that as the height of the structure increases, the displacement of structure increases, and the base shear decreases.

Keywords Degrees-of-freedom (DOF) · Earthquake · Frequency · Harmonic analysis · Shake table

1 Introduction

One of the catastrophes that make civil engineer think again and again, and apply their best of the knowledge to make the structure a whole resistive body is "Earthquake." Earthquakes are unpredictable, deadly, and scary. An earthquake occurs for a several

K. N. Bajad (✉) · M. V. Waghmare
Department of Civil Engineering, AISSMS COE, Pune 411001, India
e-mail: kbajad02@gmail.com

M. V. Waghmare
e-mail: manivw@gmail.com

© Springer Nature Singapore Pte Ltd. 2021

K. K. Pathak et al. (eds.), *Recent Trends in Civil Engineering*, Lecture Notes in Civil Engineering 77, https://doi.org/10.1007/978-981-15-5195-6_15

minutes, but the psychological and disastrous effect it made on the human society is long-lasting. No one can predict by what time the earthquake can occur and what will be its effects. In simple words, earthquake is unstoppable, but a structural engineer should always make efforts to reduce the hazardous effects of earthquake. It is a need of time to get ready, be better prepared, and be informed. Earthquake can never be stopped from occurrence, but structural engineers can be prepared for the better designs of structures. For this, the better platform is to have a practical understanding of earthquake occurrence on a small-scaled shake table. Shake table is the most effective and well-organized device than any other test for understanding the basic concepts of earthquake engineering and checking the response of structure to the ground vibrations during earthquake.

A complete theory about contribution and step-by-step evolution of shake table for practical needs in earthquake engineering has been presented. In recent years of nineteenth century, James Forbes and David Milne-Homes tried their best to establish the assembly for recording earthquake ground motions. The detailed history of shake table development was proposed by Muir Wood in 1980 [1, 2]. Efforts were being made to establish a correlation between shake table test and pseudo-dynamic test. For this, four models were subjected to shake table and pseudo-dynamic test. With a minimal error of 10%, correlation between two tests was established satisfactorily [3]. The behavior of massive RC structures such as gymnasium, high-rise building, museum, etc., subjected to earthquake event, was effectively studied by testing their proportionate scaled model on shake table. Results obtained from these test shows that shake table is the most reliable and cheaper model for study of the behavior of structures [4–9]. However, shake table was used as an apparatus for studying the seismic response of massive structures subjected to seismic excitations. Attempts were made for the development of shake table; a servo system of multi-degree-of-freedom (DOF) electro-hydraulic shaking table (EHST) was designed to replicate the desired acceleration vibration signal. Six-DOF shake table having three axes with hydraulic actuators was designed and tested for evaluating seismic performance of structures [10]. An electric shake table was also designed and assembled in order to train and create awareness among civilians and professionals about the disaster preparedness and training of emergency situations such as earthquake event. Dimensions of the designed shake table were 3-m each in length and width axes and have a capacity of 10 people [11].

In order to overcome the limitations of small-scaled structure testing on shake table, it was necessary to develop seismic design technologies to put forth the realistic picture of a massive structure subjected to a seismic event. For this purpose, a joint collaboration of US–Japan named “E-Defense/NEES Collaborative Research Program on Earthquake Engineering” developed the world’s largest 3D full-scale earthquake testing facility. There on, this facility proved effective in studying the seismic behavior of structure such as bridges, RC, and post-tensioned buildings, etc., at large scale [12–14]. A completed thesis about the process of rehabilitating a one-DOF shake table for use in seismic analysis of small-scale models in the School of Architecture [15].

As per the work performed by the above researcher, there is a need of a large-scale shake table with multiple DOF. Large-scale shake table is always costly and used for précised research work. On the other hand, in academic institutions, there is a need of understanding basic principles of earthquake engineering and ground vibration effects. The single degree-of-freedom (SDOF) shake table available for such basic purpose comes with cost INR 1–1.5 Lacs. This paper presents the methodology and different components required for the development of shake table with an economical cost up to INR 50,000 only.

This paper mainly focuses on (1) Designing and assembling an economical SDOF shake table, (2) Establishing the effectiveness of designed SDOF shake table with conventional horizontal shake table, and (3) Analyzing and studying the impact of height on the seismic response of the structure.

2 Designing and Assembling SDOF Shake Table

In this study, material used for the development of an economical shake table is thoroughly selected, examined, and designed. Prominently, wooden platform is used as shaker for a designed shake table. The wooden platform may get weaken recurrently but still may be economical. This is because the weight of steel platform is approximately 9 times than the weight of wood for the same volume; thus making it difficult to transport shake table assembly with steel plank. Also, wood offers electrical resistance and sound insulation better than steel. Moreover, the cost of steel plank is 2 times higher than that of the wooden plank.

Assembly of shake table is built with the help of lightweight steel angles. The wooden platform is connected to the steel angles by springs at its four corners. The arrangement is bolted with the help of nut and bolts. A 1000-RPM DC motor is placed at the center of wooden platform for providing determined frequency to the wooden platform. Figures 1 and 2 show the whole assembly and components of the designed shake table. Details of material used and specifications of the designed shake table are presented in Tables 1 and 2.

Plan dimensions of the designed shake table are tabulated in Table 3. Plan dimensions are selected so that the assemblies of the designed shake table should not require much more space to install in the SD laboratory, AISSMS COE.

3 Frequency Validation of Designed Shake Table

Frequency attained (0–25 Hz) on designed shake table is recorded using an accelerometer, data translator, and, QuickDaq software. Attained frequency of 24 Hz is shown in Fig. 3.

It is seen from Fig. 3, the attained frequency on designed SDOF shake table is 24 Hz.

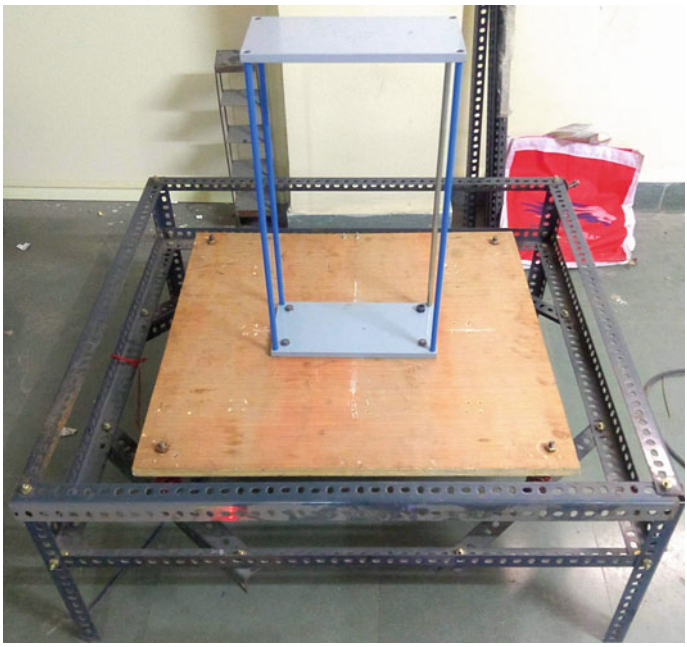

Fig. 1 Designed shake table assembly

Fig. 2 Components of designed shake table

Table 1 Material and dimensions of designed shake table

Material	Dimensions (mm)		
Steel angles	50 × 50		
Wooden platform	Thickness	Width	Length
	18	700	700
Steel springs	Diameter	Height	
	30	100	
Stainless steel nuts	Shape	Head dameter	Shank length
	Hexagon	9	10
Stainless steel bolts	Shape	Diameter	
	Hexagon	6	

Table 2 Specification of designed shake table

Property	Specification
Maximum payload	30 kg
Motor	1000-RPM DC motor
Frequency range	0–25 Hz
Frequency controller	L293D driver IC
Frequency controller technique	Pulse modulation

Table 3 Plan dimensions of designed shake table

Plan dimensions	Length (mm)	Width (mm)	Height (mm)
	930	930	400

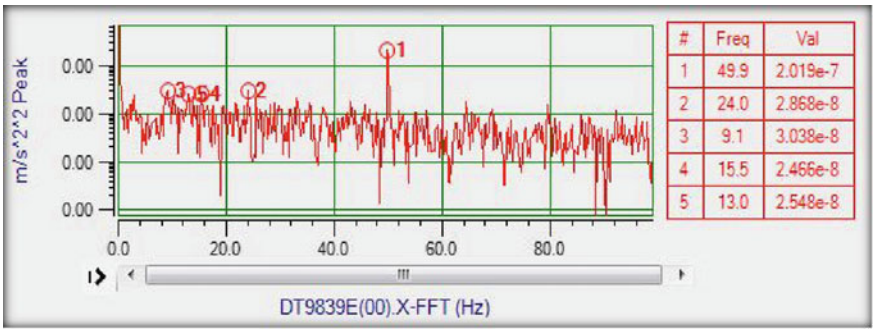

Fig. 3 Frequency attained (0–25 Hz) on designed shake table

4 Establishing the Effectiveness of Designed SDOF Shake Table with Conventional Horizontal Shake Table

4.1 Structural Models

A single-story structural model shown in Fig. 4 is used for steady-state analysis. Two different materials are used for making the asymmetrical single-story structural model (steel and Aluminium). The top and bottom plates and one circular column out of four columns are made of steel while the remaining three columns are made of aluminum. Details of material along with their properties and dimensions of the model are presented in Tables 4 and 5, respectively.

.

Fig. 4 Single-story structural model

Table 4 Material properties of single-story model used for steady-state analysis

			Material properties	
Part	Material	Mass (kg)	Mass density (kg/m^3)	Modulus of elasticity (N/m^2)
Column	Aluminum	0.3264	2700	69×10^9
Column	Steel	0.3037	7800	02×10^{11}
Slab	Steel	3.7294	7800	02×1011

Table 5 Dimensions of single-story model used for steady-state analysis

Part	Shape	Dimensions (mm)		
Column	Circular	Diameter (D)	Length (L)	
		10	500	
Slab	Rectangular	Thickness (T)	Width (B)	Length (L)
		10	150	300

4.2 Free Vibration Properties of Model Used for Steady-State Analysis

The modal frequency and time period of the structural model used for experimentation (Table 5) are obtained from modal analysis done in SAP2000 is presented in Table 6 and shown in Fig. 5.

Table 6 Modal frequency of structure obtained from SAP2000

Structural system	Mode	Time period (S)	Frequency (Hz)
Fixed-base single-story structure	1	0.07193	13.91

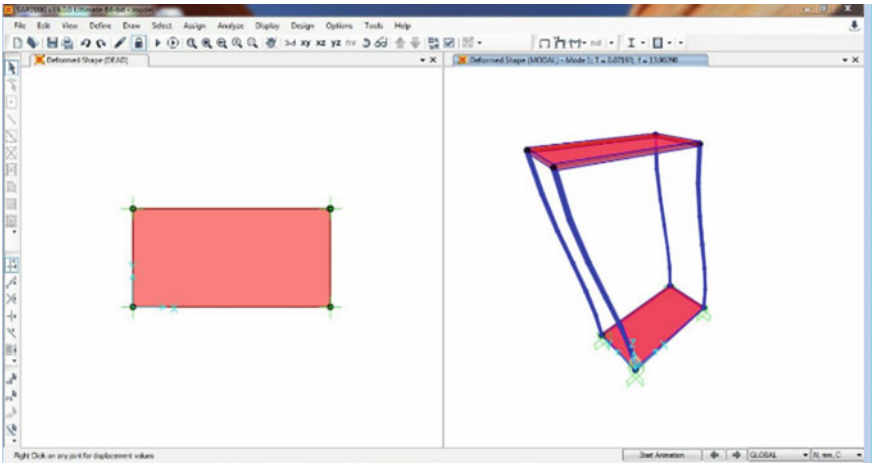

Fig. 5 Modal analysis in SAP2000

4.3 *Steady-State Analysis of Fixed-Base Single-Story Structure*

Firstly, displacement value at the level of roof is obtained by analyzing the modeled single-story structure in SAP2000 subjected to modal frequency of 13.91 Hz and amplitude of 2 mm as presented in Table 7 and shown in Fig. 6.

Secondly, Allen keys are used for fixing the model to the platform of a conventional shake table. With the help of concentric cam, harmonic loading of 2-mm amplitude and modal frequency of 13.91 Hz is applied to the single-story structural model. To record the result, the accelerometer is attached at the roof of the structure, and displacement is recorded as presented in Table 7 and shown in Fig. 7.

Finally, structure is fixed to the platform of designed shake table and displacement value subjected to a frequency of 13.91 Hz and amplitude of 2 mm is recorded and tabulated in presented in Table 7 and shown in Fig. 8.

Table 7 Steady-state analysis results in the direction of excitation

Mode	Frequency (Hz)	Time period (s)	Maximum displacement		
			SAP2000	Conventional shake table	Designed shake table
1	13.91	0.07193	3.65×10^{-9}	3.67×10^{-9}	3.19×10^{-9}

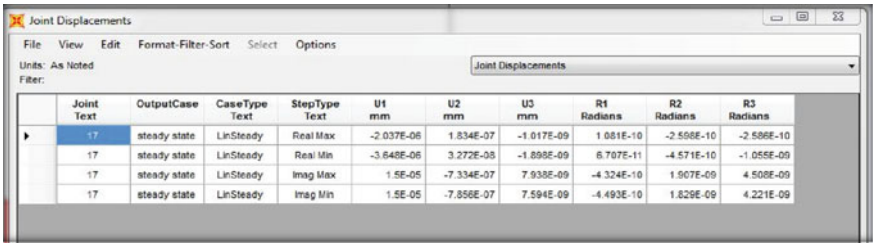

Fig. 6 Steady-state analysis results in the direction of excitation obtained from SAP2000

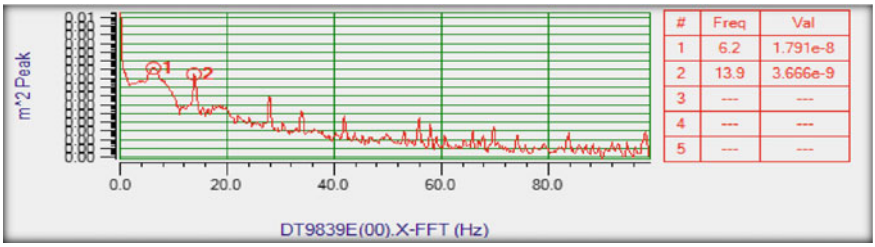

Fig. 7 Steady-state analysis results in the direction of excitation obtained from conventional shake table

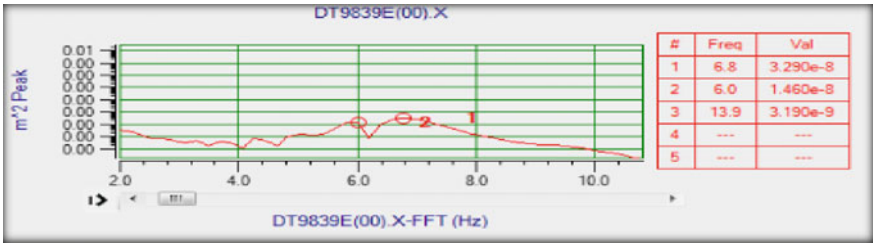

Fig. 8 Steady-state analysis results in the direction of excitation obtained from designed shake table

It is seen that the displacement analysis results as compared in Table 7 obtained by performing steady-state analysis on the conventional shake table and designed shake table differ by 12% only. However, the main purpose of a conventional shake table, to understand the structural behavior during earthquake event at the academic level is fully satisfied by designed shake table at a very reasonable cost.

5 Analyzing and Studying the Impact of Height on the Seismic Response of the Structure

5.1 Structural Models

Three structural models of varying height are modeled in SAP2000 for harmonic (sinusoidal wave) analysis. The top and bottom plates and four corner columns are made of a common material (aluminum). Top and bottom plates are 10 mm thick each and columns are rectangular strips of 25 mm wide and 3 mm thick. Details of material along with their properties and dimensions of model are shown in Tables 8 and 9, respectively.

Table 8 Material properties of single-story model used for harmonic (sinusoidal wave) analysis

		Material properties	
Part	Material	Mass density (kg/m^3)	Modulus of elasticity (N/m^2)
Column	Aluminum	2700	69×10^9
Slab	Aluminum	2700	69×10^9

5.2 Harmonic (Sinusoidal Wave) Analysis

Recorded harmonic wave applied to the three structures with varying height (Table 9) in SAP2000. The applied wave is recorded by placing an accelerometer at the platform of the designed shake table. Harmonic wave data recorded is shown in Fig. 9 is at an interval of 0.005 s for a total time of 61.44 s.

5.3 Harmonic (Sinusoidal Wave) Analysis Results

Maximum story displacement, base shear, time history, and frequency of structure in the direction of excitation obtained from harmonic (sinusoidal wave) analysis performed in SAP2000 are recorded and tabulated in Table 10. Figure 10 shows the time versus displacement graph and base shear versus height graph for structures in direction of excitation. Figure 11 shows the base shear versus height graph for structures in direction of excitation

From Fig. 10, it is seen that as the height of the structure increases displacement increases. Displacement of the structure depends upon the stiffness and as

Table 9 Dimensions of single-story models of varying height used for harmonic (sinusoidal wave) analysis

Structure no.	Length (mm)	Width (mm)	Height (mm)
01	150	300	**1200**
02	150	300	**800**
03	150	300	**400**

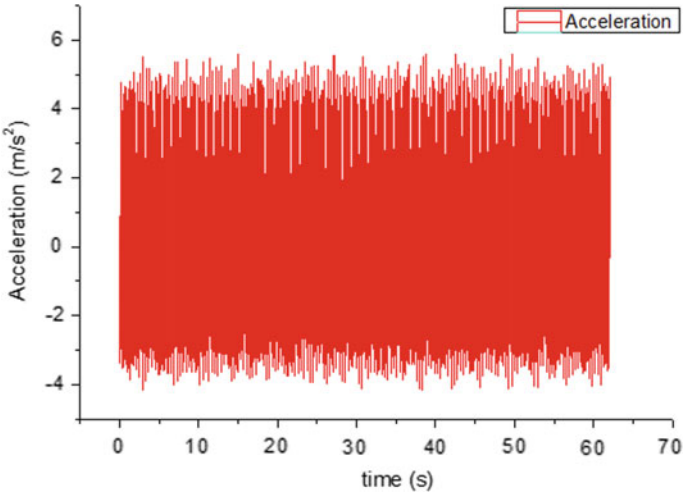

Fig. 9 The time series data recorded on designed shake table

Table 10 Maximum story displacement, base shear, time period, and frequency of structure in the direction of excitation obtained from harmonic (sinusoidal wave) analysis performed in SAP2000

Structure no.	Time period (s)	Frequency (Hz)	Max. story displacement (mm)	Base shear (N)
01	0.84	1.19	11.89	10.50
02	0.438	2.28	8.50	11.62
03	0.148	6.76	4.32	17.51

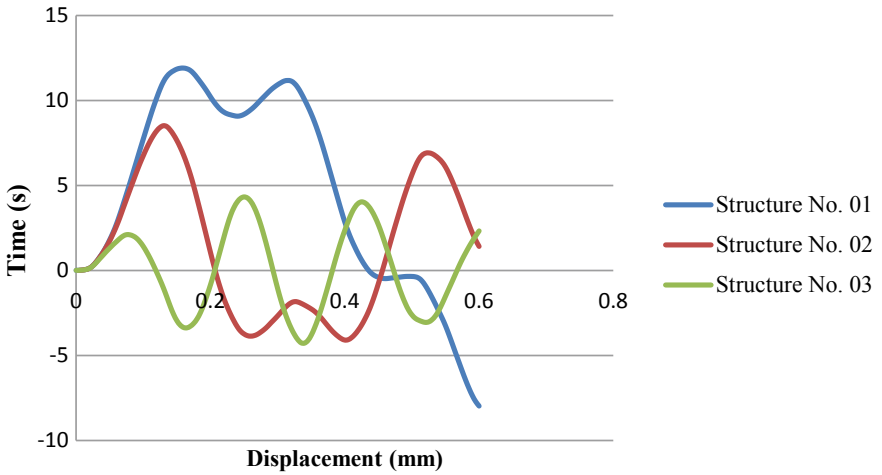

Fig. 10 Max. story displacement results for structures with varying height in the direction of excitation obtained from harmonic (sinusoidal wave) analysis performed in SAP200

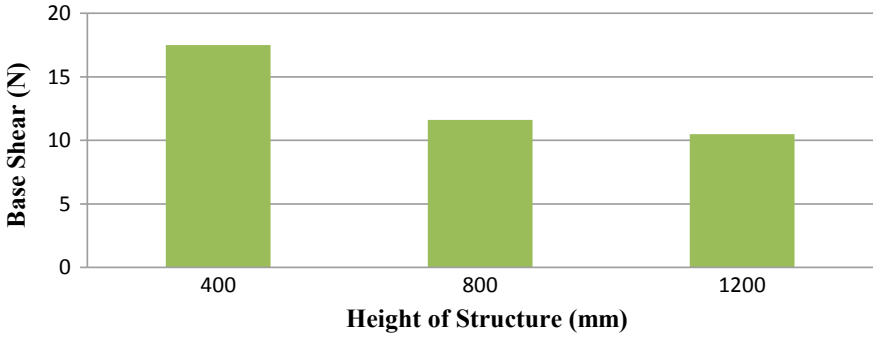

Fig. 11 Base shear results for structures with varying height in the direction of excitation obtained from harmonic (sinusoidal wave) analysis performed in SAP200

height increases, stiffness gets reduced, causing an increase in flexibility. Since more flexibility, more easy for the structure to get excited during earthquake.

From Fig. 11, it is seen that as the height of the structure increases, base shear decreases. Structure no. 01 have time period more than that of structure nos. 02 and 03. Structure with a higher time period is flexible than a structure with lower time period. Flexible structures experiences lower accelerations than structures with lower time period. As, flexible structures of higher time period are hard to excite during earthquake, they show lesser base shear value.

6 Conclusions

1. The designed shake table is able to carry a payload of 30 K g and have a vibrating frequency ranging from 0 to 25 Hz.
2. With a minimum error of 12% and economical cost up to INR 50,0000 only, the effectiveness of designed shake table can be established with a mechanical shake table which cost for INR 1–1.5 Lacs.
3. As the height of structure increases, the displacement of structure increases.
4. As the height of structure increases, the base shear of structure decreases.

References

1. Wood RM (1988) Robert Mallet and John Milne-Earthquakes incorporated in Victorian Britain. Earthq Eng Struct Dyn 17(01):107–142. https://doi.org/10.1002/eqe.4290170103
2. Severn RT, Stoten DP, Tagawa Y (2012) The contribution of shaking tables to earthquake engineering. In: 15th world conferences on earthquake engineering, Lisboa, vol 02, pp 1044–1054
3. Yamazaki Y, Nakashima M, Kaminsono T (1986) Correlation between shaking table test and pseudo dynamic test on steel structural models. BRI Research Paper No. 119, pp 82
4. El-Attar AG, White RN, Gergely P (1991) Shake table test of A 1/6 scale two-story lightly reinforced concrete building. Technical Report of National Center for Earthquake Engineering Research (NCEER)-91-0017
5. Shi W (2000) Shaking table experimental study of reinforced concrete high-rise building. In: 12th world conferences on earthquake engineering, Auckland-New Zealand. No 218
6. Kim S-E, Lee D-H, Ngo-Huu C (2007) Shaking table tests of a two-story unbraced steel frame. J Constr Steel Res 63(03):412–421. https://doi.org/10.1016/j.jcsr.2006.04.009
7. Liu W, Qin C, Liu Y, He W, Yang Q (2016) Shaking table tests on earthquake response characterization of a complex museum isolated structure in high intensity area. Hindawi Publishing Corporation, Shock and Vibration, pp 23. https://doi.org/10.1155/2016/7974090
8. Islam R, Md Hossain T, Bin Alam JMd, Ahmed M (2018) Study of dynamic behavior of a three story model frame. Am J Constr Build Mater 02(01):10–15. https://doi.org/10.11648/j.ajcbm.20180201.12
9. Bai X, Wang Q, Cheng S, Wang Y, Lou W (2019) Shaking table model test analysis of gymnasium building with large span. PEER Berkeley

10. Yin L, Ye Z, Shen G, Han, J (2011) Servo system of 6 DOF electro-hydraulic shaking table. Lecture notes in electrical engineering, pp 241–249. https://doi.org/10.1007/978-3-642-25899-2_33
11. Bathan MG, Baldovino MR, Ferrer JB, Yao BC, Manabat VB, Liza PF (2016) An electric shake table system for disaster and emergency preparedness training. Jurnal Teknologi 78(5):109–114. https://doi.org/10.11113/jt.v78.8521
12. Ohtani K, Ogawa N, Katayama T, Shibata H (2003) World's largest shaking table takes shapes in Japan (The Third Report). In: 17th international conference on structural mechanics in reactor technology (SMiRT17), Prague, Czech Republic. Paper K12-1
13. Nakashima N, Kawashima K, Ukon H, Kajiwara K (2008) Shake table experimental project on the seismic performance of bridges using E-defense. In: The 14th world conference on earthquake engineering, Beijing, China
14. Nagae T, Matsumori T, Shiohara H, Kabeyasawa V, Kono S, Nishiyama M, Moehle J, Wallace J, Sause R, Ghannoum W (2014) The 2010 E-defense shaking table test on four-story reinforced concrete and post-tensioned concrete buildings. In: 10th U.S. national conference on earthquake engineering (NCEE). Frontiers of Earthquake Engineering, Anchorage, Alaska
15. Brown S (2007). Seismic analysis and shake table modeling: using a shake table for building analysis. MS Thesis-University of Southern California

Behaviour of Different Lateral Stability Structural Systems for the Tall Steel Structures Under Wind Loads

Abhimanyu Pandey and R. K. Tripathi

Abstract The orientation of columns is one of the new trends that can be recognized in the current design of tall buildings. Diagrid structural systems are gaining popularity in design and construction of tall buildings. Diagrid has made its mark in the developed countries due to the features like aesthetic quality, structural efficiency and sustainability, but yet to be discovered in India. Introduction of tubular structures made its way for the diagrids. With the increase in population and limited availability of resources, the concept of sustainability plays a vital role in every aspect of life. Thus, a structural system, which can provide the solutions to the sustainability, is the demand we need to fulfil. In this paper, three different structural systems namely, diagrid, tubular and conventional rigid frame systems are analyzed and are compared on numerous parameters like top storey displacement, storey drift, shear lag, fundamental time period, structural steel mass usage and sustainability, etc.

Keywords Diagrid structures · Tubular structures · Sustainability · Tall steel structures · FEM analysis

1 Introduction

Tall buildings and towers have always been a fascination to the humankind. Structures like Mayan temples to the pyramids of Egypt represent a city's socio-economic power, prestige and the source of dignity of its people. At that time, tall buildings were not the necessity of the people. However, presently tall buildings are the result of drastic population growth, rapid urbanization and the limitation of land area availability. As per the requirement, the choice of different lateral stability structural systems is desirable for resisting the lateral loads coming on the structure. Lateral loads can be

A. Pandey (✉) · R. K. Tripathi
National Institute of Technology, Raipur, Chhattisgarh, India
e-mail: abhimanyu.pandey23@yahoo.com

R. K. Tripathi
e-mail: rktripathi.ce@nitrr.ac.in

© Springer Nature Singapore Pte Ltd. 2021

K. K. Pathak et al. (eds.), *Recent Trends in Civil Engineering*, Lecture Notes in Civil Engineering 77, https://doi.org/10.1007/978-981-15-5195-6_16

divided into earthquake load and wind load. In this paper, our concern is to carry out the analysis under wind load because as the height of the building increases, the fundamental time period of the building increases and the effect of earthquake load decreases. Lateral stability system of the structure is subdivided into two, interior structural systems and the exterior structural systems depending upon their position. Most widely used lateral load resisting systems are

- Rigid frames
- Shear wall systems
- Braced tube systems
- Outrigger systems and
- Tubular systems.

The age we are living in is an age of sustainable development. The need of the hour is to use that structural system for a building which promotes green economy and produces least carbon content to the environment [1]. Construction activities consume large amounts of steel every year due to the strength, formability and versatility of steel in numerous different applications [2]. Sustainable steel is at the core of a green economy. It has been more than a hundred years when the first diagrid structure was introduced in the world. However, the trend of its construction has just taken the boom. In 1896, Vladimir Sukhov (Russian engineer and mathematician) created the hyperboloid and introduced the diagrid structures. He designed a 350 m high hollow tower of hyperboloid shape having ring beams at certain intervals. The design emerged out as structurally efficient and easy to construct a tower for carrying a large gravity load at the top. Sukhov introduces the structural efficiency by reducing the material required and by providing enough stiffness to take lateral and gravity loads. Diagrid structures carry shear forces by axial action of diagonal members thereby minimizing the shear deformation [3]. The angle of the diagonal member plays a vital role in providing the stiffness to the structure. As the sine of diagonal angle increases, the vertical stiffness starts increasing and the lateral stiffness starts decreasing [4]. Moon [5] shows that the bending governs the design at the lower half of the building, and shear governs the upper half of the building.

Tubular structures have evolved from the conventional rigid jointed frame structures. Dr. Fazlur Khan is considered as the "father of tubular structures". He was the designer of the Sears Tower, the tallest building in the world from 1973 until 1998, and the 100-story John Hancock Centre. The design philosophy behind these types of structures is to place as much as possible load-carrying structural elements at the periphery of the building to maximize the flexural rigidity (inertia) of the cross section. These structures undergo a considerable amount of shear lag in the frame panel normal to the wind. The frame panel consists of closely spaced columns and deep beams. In these buildings, the strong bending direction of the column is aligned along the face of the building. The face of the building parallel to the wind acts as the web, and the face of the building perpendicular to the wind direction act as the flange. The most common types of tubular structures are

(1) Framed Tube, and
(2) Tube-in-Tube.

Tube-in-Tube is advancement over the framed tube structure as it resists higher lateral loads and reduces the shear lag effect.

2 Model Specifications

Modelling and analysis have been done in ETABS, finite element software. Following models have been designed and analyzed:

42-storey Diagrid building, 6-storey module (Fig. 1).

42-storey Tube-in-Tube building (Fig. 2).

42-storey Rigid Frame building (Fig. 3).

All the structural elements are made up of structural steel. The grade of structural steel used is Fe 345. The plan size of each building is kept same. The plan area of each building is 36 m × 36 m. The plan area of the core of diagrid and tubular building is 12 m × 12 m. The typical height of each storey is 3.6 m. The location considered for the design is Raipur, India. IS 875(part3):2015 [6] has been used for the calculation of along-wind and across wind. As per code, basic wind speed is taken as 39 m/sec.

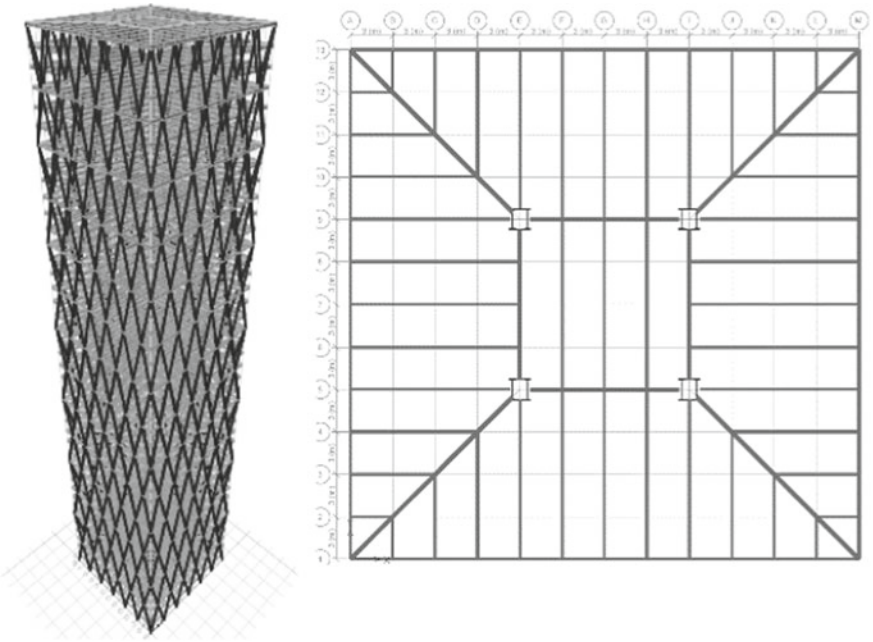

3D Model Plan View

Fig. 1 42-storey diagrid building (*Image source* ETABS)

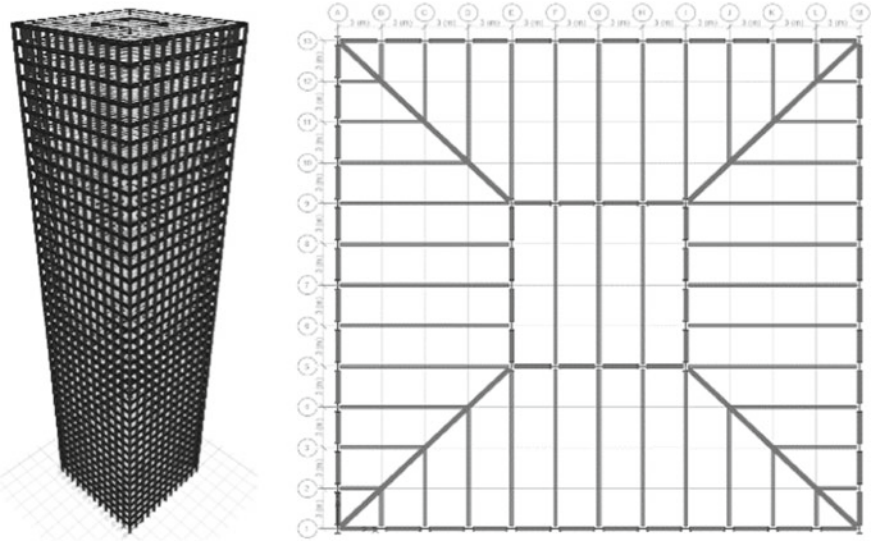

Fig. 2 42-storey tube-in-tube building (*Image source* ETABS)

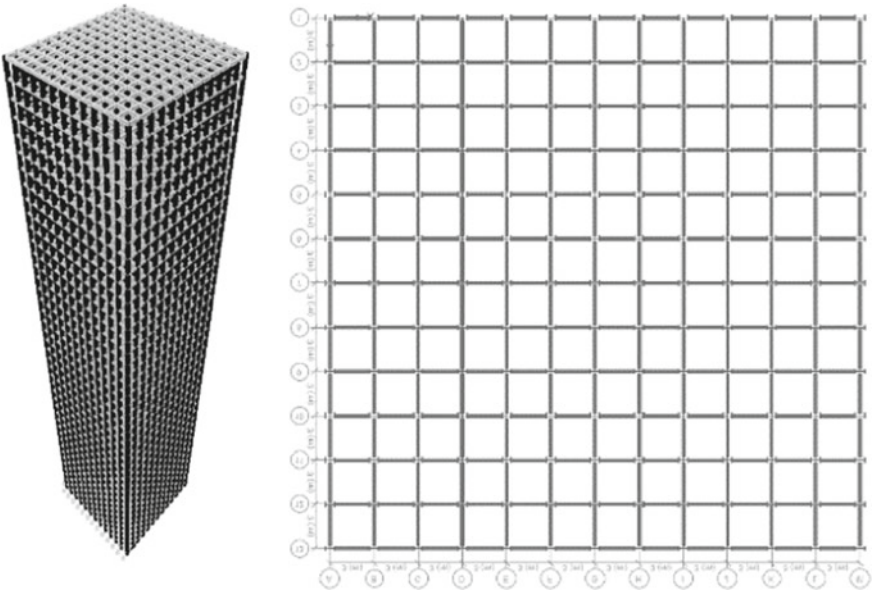

Fig. 3 42-storey conventional building (*Image source* ETABS)

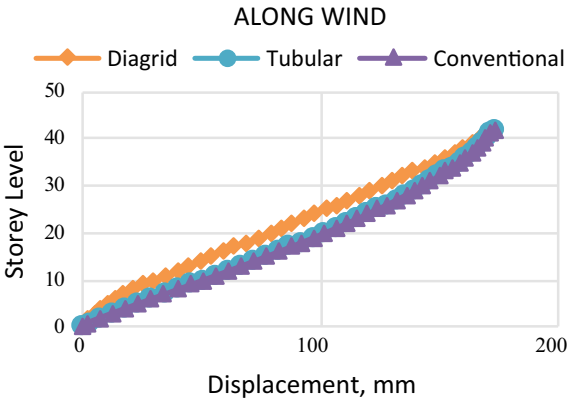

Fig. 4 Top storey displacement (Along-wind)

Terrain category 3 is considered for the design. The dead load and the imposed load coming on the floor is taken as 4.0 kN/m^2 and 3.0 kN/m^2, respectively. Indian codes have been used for the design and analysis of the buildings.

3 Results and Discussion

3.1 Top Story Displacement

As per clause 5.4.1 of IS 16700:2017 [7], maximum lateral drift shall be limited to H/500.

H/500 = 151200/500 = 302.4 mm. (where H—Total height of the building)

All the buildings are designed to have maximum top storey displacement of 173 mm due to the along-wind. Keeping it constant, all other parameters are compared to see the behaviour of different buildings. The top storey displacement of all the buildings due to across wind varies between 97 and 101.6 mm. This is shown in Figs. 4 and 5.

3.2 Storey Drift

As per clause 5.4.1 of IS 16700:2017 [7], for a single storey the drift limit may be relaxed to h_i/400 and for earthquake load (factored) combinations the drift shall be limited to h_i/250. As per clause 5.6.1 of IS 800:2007 [8], inter storey drift due to wind is limited to hi/300.

Therefore, maximum allowable storey drift is

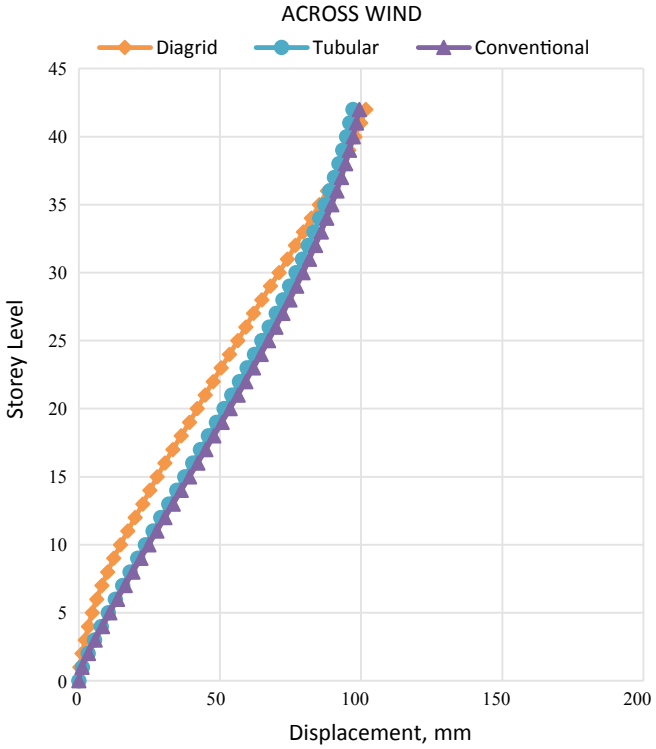

Fig. 5 Top storey displacement (Across wind)

$h_i/300 = 3.6/300 = 0.0120$, and

$h_i/400 = 3.6/400 = 0.0090$

(where h_i—Height of a storey of a building). Respective values are shown in Figs. 6 and 7.

3.3 Fundamental Time Period

As per, IS 16700:2017 [7], the fundamental translational natural period in any of the two horizontal plan directions, shall not exceed 8 s. The natural period of fundamental torsional mode of vibration shall not exceed 0.9 times the smaller of the natural periods of the fundamental translational modes of vibrations in each of the orthogonal directions in plan. As per, IS 875:2015(part 3) [6], time period is

For diagrid and tubular building:

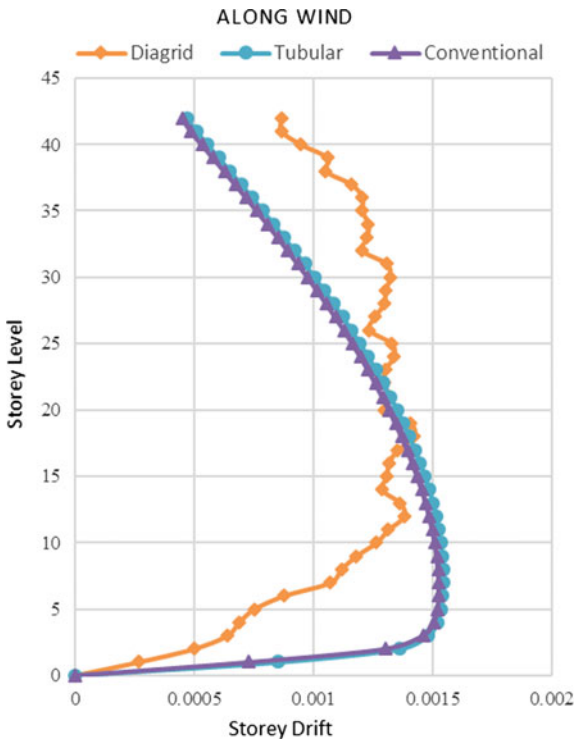

Fig. 6 Storey drift (Along-wind)

$$T = \frac{0.09h}{\sqrt{d}} = \frac{0.09 \times 151.2}{6} = 2.268 \text{ s.}$$

And, for conventional rigid frame building:

$T = 0.1 \times$ No. of storeys $= 0.1 \times 42 = 4.2$ s.

Respective values are shown in Fig. 8.

3.4 Structural Steel Mass Usage

About 43.89% of structural steel saving is observed in diagrid structures as compared to the tubular structures. And, about 41.90% of structural steel saving is observed in diagrid structures as compared to the conventional rigid frame structures. The structural steel mass usage has been shown in the Fig. 9. This structural steel usage is recorded for the condition of same top storey displacement due to along-wind in all the buildings.

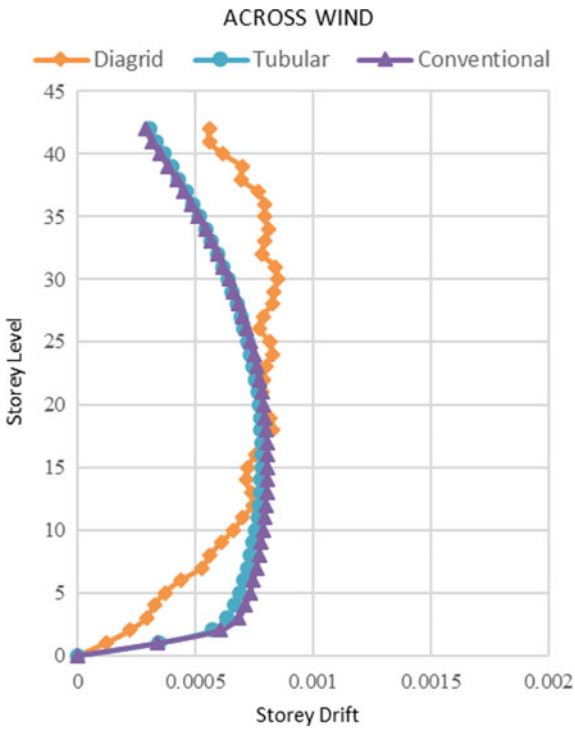

Fig. 7 Storey drift (Across wind)

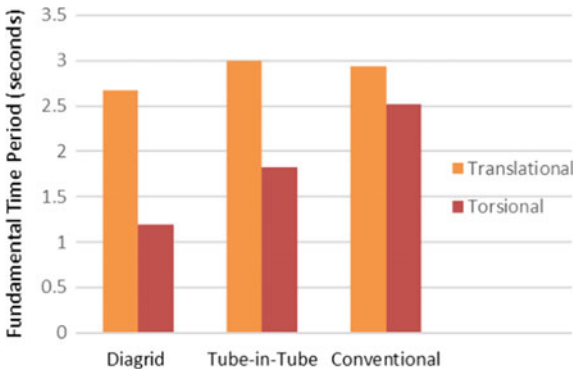

Fig. 8 Fundamental time period (in seconds)

3.5 Shear Lag

Shear lag is a phenomenon, which states the difference in the axial forces coming on the interior and the corner columns due to lateral loads acting on the building. The distance of columns on each face of the Conventional rigid frame and Tube-in-Tube buildings is 3 m c/c. And the distance of diagrids at the periphery is 6 m c/c. The beam

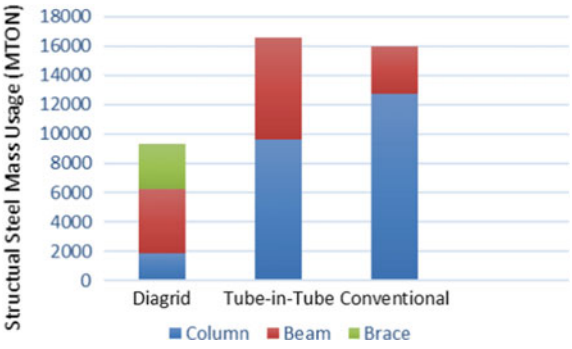

Fig. 9 Structural steel mass usage (in MTON)

theory assumes that a plane section remains plane after bending. This assumption is true only when the shear stiffness of the cross section either is infinite or if there is no shear force in the section. If the shear force exists, shear flow is developed across the flange and web faces (Leonard [9]). Due to the shear flow between the flange and the web of the box, the panels displace longitudinally in the way that the middle portion of the flange and web lag that of the portion closer to the corner of the building. This is the cause of shear lag in tubular and diagrid buildings. The variation has been shown for both the faces of the buildings (flange and web) under along-wind load below in Figs. 10 and 11:

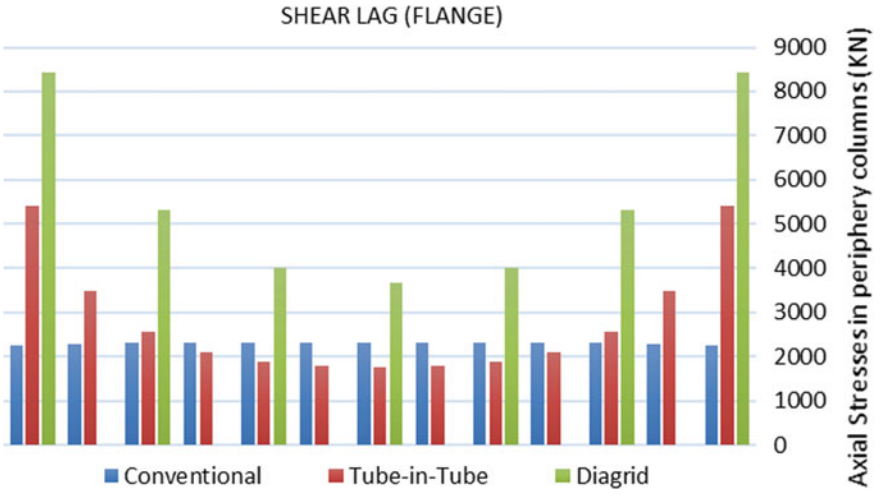

Fig. 10 Shear lag (flange plane)

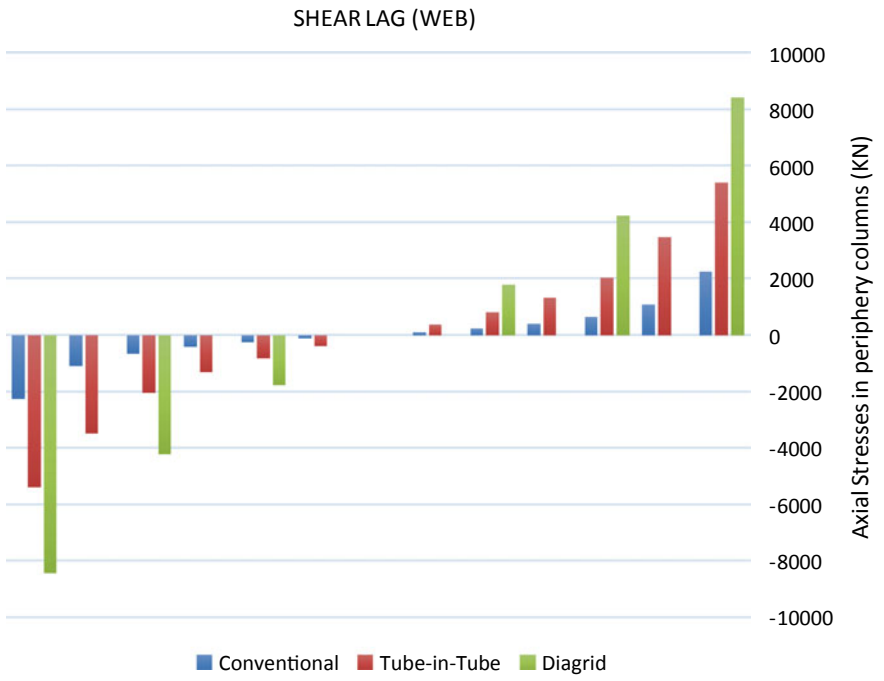

Fig. 11 Shear lag (web plane)

4 Conclusion

Steel is a very costly structural material. Hence, huge saving of structural steel brings the green economy to the project. In addition to it, the energy requirement becomes less, thereby emitting less carbon content to the environment. Hence, diagrid structures are sustainable in nature. About 43.89% of structural steel saving is observed in diagrid structures as compared to the tubular structures. And, about 41.90% of structural steel saving is observed in diagrid structures as compared to the conventional rigid frame structures. It is because of the triangular configuration of diagrid, which makes it stiffer than the other structural systems, and the lateral load taken by the other structural systems is by the bending action.

It has been observed that the shear lag on the both flange and web planes of the building is predominant in the diagrids and the tubular structures, whereas the shear lag is approximately negligible in case of conventional rigid frame.

The maximum allowable storey drift for 3.6 m typical height of storey is 0.0120, and the maximum storey drift coming in the building is 0.0017. Therefore, all the buildings are safe in storey drift. The drift values are very small because it is the ratio of relative displacement between any two adjacent storeys of a building and the height between those stories, and the relative displacement in any of the adjacent stories of the building is very less due to uniform stiffness and strength of the stories.

The fundamental torsional time period is within the limit of 0.9 times the smaller fundamental translational time period. Hence, torsion is not the predominant mode of vibration.

For same plan area, the maximum floor plan usage can be achieved in case of diagrid and tube-in-tube systems. However, structural steel mass usage is very high in case of tube-in-tube system. Therefore, the structural efficiency is the highest in diagrid structural system. Hence, we can say that among these three structural systems, diagrid system is the only sustainable choice for us for the height of 150 m high buildings.

References

1. Rafiei MH, Adeli H (2016) Sustainability in highrise building design and construction. Struct Des Tall Spec Build 25:643–658. https://doi.org/10.1002/tal.1276
2. Boake TM (2013) Diagrid structures: innovation and detailing. School of Architecture, University of Water bro, Canada
3. Moon K, Connor JJ, Fernandez JE (2007) Diagrid structural systems for tall buildings: characteristics and methodology for preliminary design. Struct Des Tall Spec Build 16:205–230. https://doi.org/10.1002/tal.311
4. Kim J, Lee Y (2012) Seismic performance evaluation of diagrid system buildings. Struct Des Tall Spec Build 21:736–749. https://doi.org/10.1002/tal.643
5. Kyoung Sun Moon (2008) Optimal grid geometry of diagrid structures for tall buildings. Archit Rev 51(3):239–251. https://doi.org/10.3763/asre.2008.5129
6. IS 875 (part 3):2015. Code of practice for design loads (other than earthquake) for buildings and structures
7. Indian Standard 16700:2017. Criteria for structural safety of tall concrete buildings
8. IS 800:2007. General construction in Steel-Code of practice
9. Leonard J (2007) Investigation of shear lag effect in high-rise buildings with diagrid system. Doctoral dissertation, Massachusetts Institute of Technology

To Compare ATC 40 and FEMA 440 Methods for Computation of Performance Point

Ankit Sandilya and Rajesh Kumar Tripathi

Abstract Nonlinear procedures of analysis have gained popularity nowadays. In this paper, two commonly used methods, one ATC 40 and other is FEMA 440 results are compared for regular as well as mass irregular structures for 4, 6 and 8 storey buildings in zone 5. The variation in the performance point by both the methods is noted and comparison has been done. The values of base shear at performance point obtained by FEMA 440EL came to be on higher side for both regular and mass irregular frames. Further, it is evident that if the mass irregularity goes to higher storey, the values at performance point go on increasing. SAP2000, a FEM-based software is used in this analysis.

Keywords Nonlinear analysis · Pushover analysis · ATC 40 · FEMA 440 · Performance point · Mass irregularity

1 Introduction

Pushover analysis nowadays is very common nonlinear analysis technique. It involves inelastic analysis of the structure considered, under a gradually increasing displacement or force vector, which represents the expected pattern of inertia forces or response displacement in the structure. It can track the formation, and plastic rotation of hinges in the structure, and hence can be of value in the design validation and verification. However, there are limitations involved with these methods also.

In this study, we have used SAP 2000. It defines material nonlinearity by two types: first is by defining concentrated yield at specified points. This method is appropriate for frame members, and the hinges are assigned at the member ends. Use of hinge overwrite command results in better output as it discretize members

A. Sandilya (✉) · R. K. Tripathi
National Institute of Technology, Raipur, Chhattisgarh, India
e-mail: akt9136@gmail.com

R. K. Tripathi
e-mail: rktripathi.ce@nitrr.ac.in

© Springer Nature Singapore Pte Ltd. 2021

K. K. Pathak et al. (eds.), *Recent Trends in Civil Engineering*, Lecture Notes in Civil Engineering 77, https://doi.org/10.1007/978-981-15-5195-6_17

to get convergence; Second is by using distributed plasticity. It is computationally expensive, and accuracy does not change much. Hence it is not used in this analysis.

In pushover analysis, we can control the response of structure by imposing force vector or by an imposed displacement vector. Both approaches have their limitation. In this paper, we have used displacement-controlled approach as it has the capability to follow the post-peak response of the system. Pushover Analysis (PA) is employed to obtain the capacity curve and by using capacity curves, we get the performance point of the structure. Performance point is described as the point where the capacity and demand curve of a structure intersects or simply say the point where the capacity of structure meets the demand or intersection of capacity and demand curve. Demand is defined based on site-specific requirements or by using Response Spectrum (RS) curves as defined in various national and international codes. Based on the acceptable performance point, we can design various components of the structure to an acceptable level of damage. Initiation of hinge and hinge propagation can be well traced using SAP2000.

1.1 Model

The advancement in the computational power has led to faster and more accurate results but still there is difficulty when we are analysing unsymmetrical structures/buildings. For this study, in plan symmetric buildings are considered. This leads to simplification of results, and the analysis will take less time.

Three bay frames having each bay of 5 m length in both x and y direction is considered. The plan dimension for every model is 15 m $\times$ 15 m (Fig. 1). All the materials and sections are designed in accordance with IS 456-2000 [1]. Seismic provisions are followed in accordance with IS 1893-2016 [2]. IS 13920 [3] is used

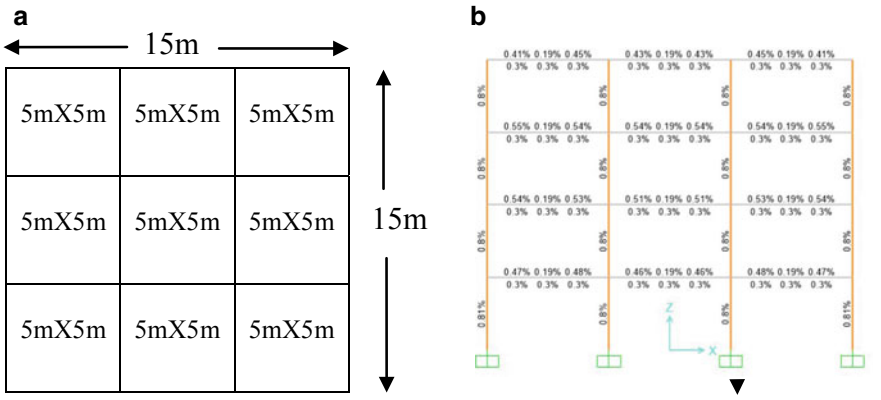

Fig. 1 **a** Plan of model; **b** Elevation of 4-storey type 2 building showing percentage reinforcement in beams and columns

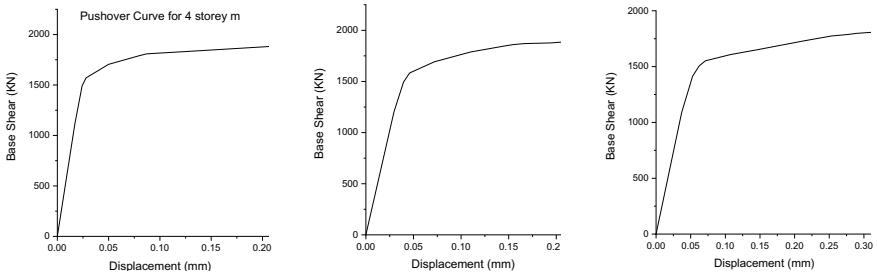

Fig. 2 **a–c** static pushover curve for 4 storey, 6 storey and 8 storey model type 1 building, respectively

for detailing purposes. Concrete used in columns is M40 and for beams is M30. Rebar of grade Fe415 is used.

For hinge definition, guidelines given in FEMA356 [4] and ASCE 41 [5] are followed. Hinges in both columns and beams are defined at relative distance of 0.05 and 0.95 from one of the ends. Column hinges are defined in accordance with Table 10-8 of ASCE41-13 [5] for flexure/shear failure condition and the degree of freedom is selected as P-M2-M3. Hinge in beams is defined as per Table 10-8 of ASCE41-13 for flexure (M3) failure condition (i.e. the strongest axis).

In model type 1, the beams and columns are uniform throughout. Dead load is imposed as SDL of magnitude 4 kN/m^2 and live load as 3 kN/m^2. Earthquake effect in both the directions is provided separately so that there is no effect of torsion. Hinge overwrite command is also used as it helps in discretising the hinges and results in the convergence. Model type 2, their sizes of columns and beams are varying throughout, maximum at lower and minimum at top. 8-storey, 6-storey and 4-storey building in Zone 5 is designed and analysed. Columns of size 500 mm × 500 mm and beams of size 500 mm × 300 mm have been used in model type 1 buildings. In model type 2 buildings, columns and beams have varying size. The maximum rebar percentage is 0.87% maximum.

Table 1 Performance point for various models used in type 1

	Method used by	Base shear (kN)	Deflection (mm)	Time period (s)
8 storey	ATC 40	1321.497	91.271	1.355
	FEM440 EL	1340.569	95.318	1.381
6 storey	ATC 40	1241.847	72.889	1.098
	FEM440 EL	1267.825	76.89	1.119
4 storey	ATC 40	1638.641	36.865	0.639
	FEM440 EL	1647.788	38.24	0.651

Table 2 Performance point for various models used in type 2

	Method used by	Base shear (kN)	Deflection (mm)	Time period (s)
8 storey	ATC 40	1553.912	72.744	1.352
	FEM440 EL	1559.091	76.065	1.381
6 storey	ATC 40	1620.508	54.914	0.993
	FEM440 EL	1628.356	56.774	1.009
4 storey	ATC 40	1627.369	37.348	0.656
	FEM440 EL	1633.55	38.357	0.664

Performance points for different storey buildings of model type 1, based on ATC 40 and FEMA 440EL is shown in Table 1 and for model type 2 is shown in Table 2 and Figs. 3 and 4.

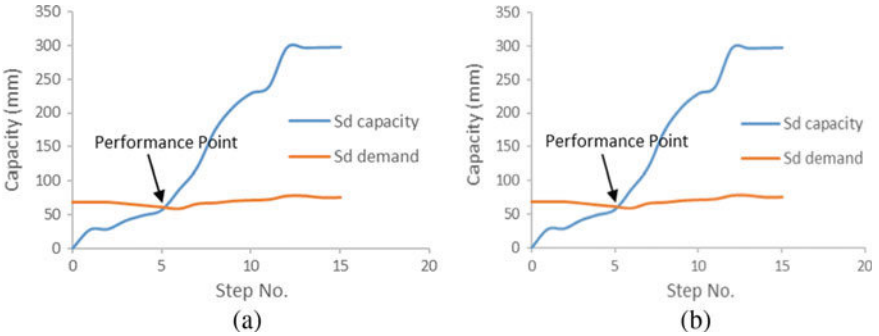

Fig. 3 Simple representation of capacity demand curve according to ATC 40 and FEMA 440 EL (Z5 8 Storey C0L500)

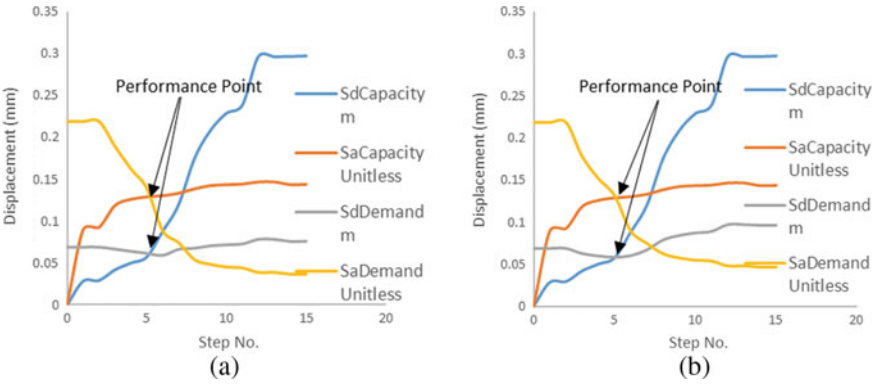

Fig. 4 **a** shows the procedure of performance evaluation of 8-storey building by FEMA 440 EL, and **b** shows the performance evaluation of 8-storey building, respectively, by ATC 40

The variation of performance points for different seismic zones as defined in IS 1893-2016 for 6-storey building of model type 2 is recorded in Table 3. Hinge formation in various stages for Zone 5 8-storey type 1 model is shown in Fig. 5 and for type 2 model is shown in Fig. 6. Variation of performance point for 6-storey building with respect to different mass arrangements defined is shown in Fig. 7.

The 'SaCapacityUnitless' in Fig. 4 represent the spectral acceleration for the capacity curve expressed as a fraction of the gravitational constant, g; 'SaDemandUnitless' represents the spectral acceleration for the single demand curve with variable damping expressed as a fraction of the gravitational constant, g. 'SdCapacity' represents the spectral displacement for the capacity curve, and 'SdDemand' represents the spectral displacement for the single demand curve with variable damping.

The maximum variation in the base shear values is about 2% for Zone 5 buildings. The variation in deflection values at performance point is about 20% but as the value is small and there is not much difference in hinge behaviour within that step, hence this variation does not have much impact in the performance evaluation and any of the two methods can be preferred.

Type 2 model performed satisfactorily when compared with type 1 model. Hence, it is recommended, wherever possible; decrease the size of columns with increase in number of storey by giving due care to the column-beam capacity ratio.

Table 3 Variation of performance points for different seismic zones as defined in IS 1893–2016 for 6-storey building of model type 2

	1st		1st and 3rd		1st, 3rd and 5th		1st and 5th	
Irregularity at floor	ATC 40	FEMA 440EL	ATC 40	FEMA 440EL	ATC 40	FEMA 440EL	ATC 40	FEMA 440EL
Base shear (KN)	1325.4	1342.39	1335.0	1343.89	1300.6	1308.5	1268.74	1290.03
Disp. (mm)	71.221	74.722	73.453	76.475	79.32	83.294	76.495	80.491
Time period (s)	1.065	1.088	1.143	1.167	1.265	1.296	1.199	1.224
	3rd and 5th floor		5th floor		3rd floor		No irregularity	
Irregularity at floor	ATC 40	FEMA 440EL	ATC 40	FEMA 440EL	ATC 40	FEMA 440EL	ATC 40	FEMA 440EL
Base shear (KN)	1240.38	1248.30	1211.252	1248.30	1272.97	1267.82	1241.85	1267.82
Disp. (mm)	80.713	85.162	77.833	82.383	75.078	76.89	72.889	76.89
Time period (s)	1.293	1.327	1.224	1.251	1.098	1.119	1.098	1.119

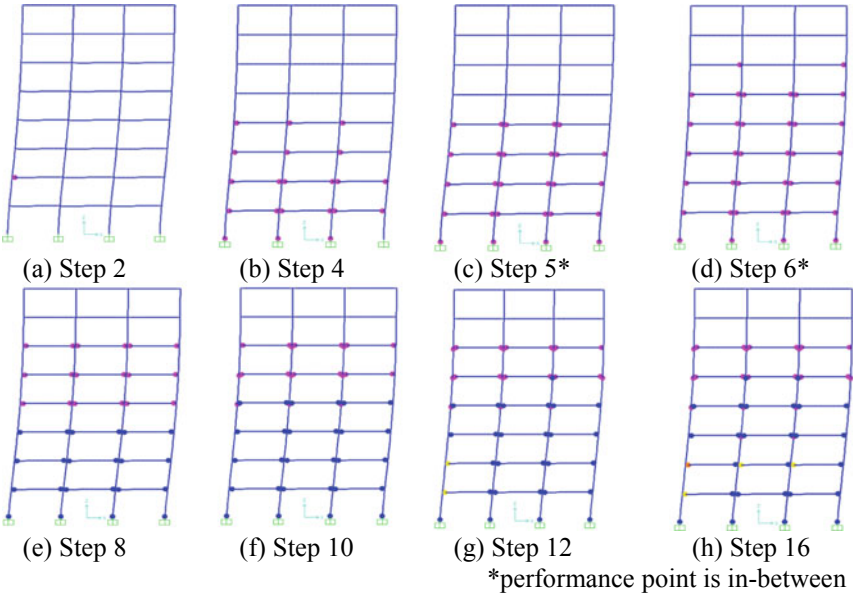

Fig. 5 Hinge formation in various stages for Zone 5 8-storey type 1 model

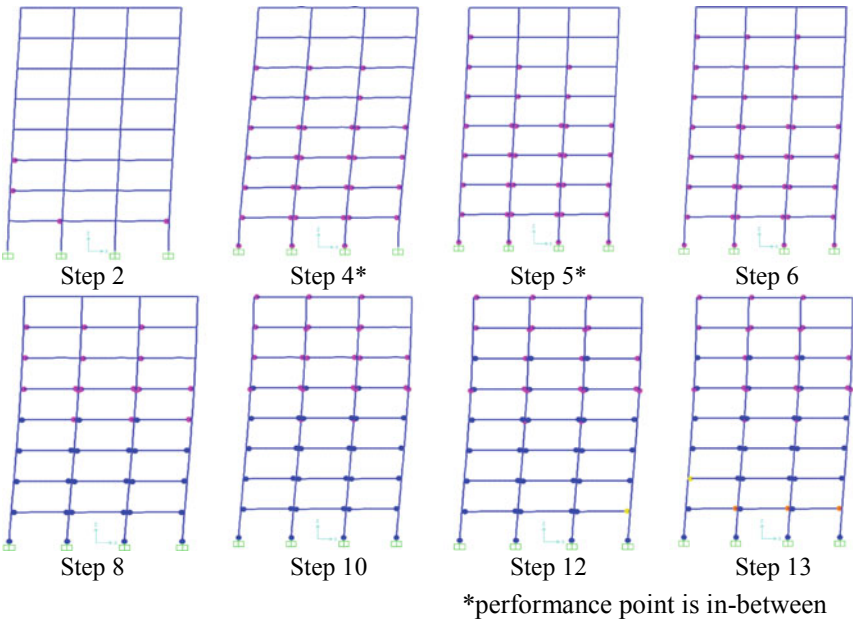

Fig. 6 Hinge formation in various stages for Zone 5 8-storey type 2 model

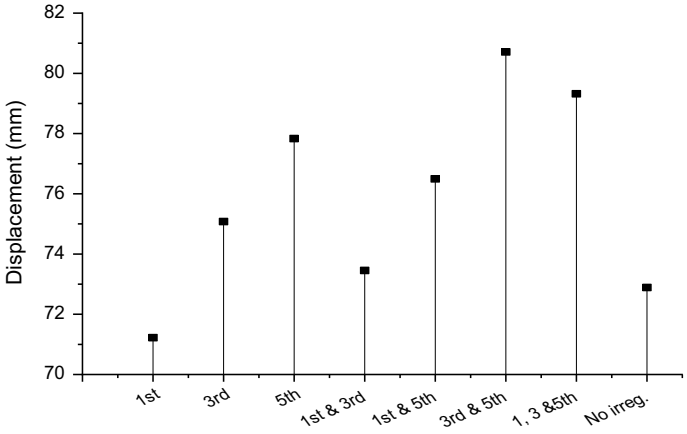

Fig. 7 Variation of performance point for 6-storey building with respect to different mass arrangements defined in Table 3

2 Conclusions

The results obtained by applying either FEMA 440EL or ATC 40 are comparable for Zone 5. However, the variation in base shear in the two cases is about 2.1%, FEMA 440 EL is always on higher side. Hence, we conclude that FEMA 440 EL provides conservative values of base shear at performance point.

In model type 1 buildings, the column size is similar throughout. By carefully monitoring the hinge formation in model type 1, upper storey does not form plastic hinges, and hence we can say that the upper stories do not take part in failure pattern. Hence, the failure of this type of structure is sudden and brittle type, which we certainly do not want as a structural designer. It is concluded from the above analysis that model type 1 buildings are over designed and by performing pushover analysis, economy and safety in the design can be achieved. As a result, a more reliable and sustainable structures can be formed.

The formation of hinges is only up to IO stage in all the cases until the performance point is reached. Even well after the performance point, there is no formation of mechanism in the structure; hence we can say that both model types satisfy the performance criteria as defined in FEMA356.

As there is irregularity in the mass of the structure/building, there is change in performance point. The variation of performance point with respect to increase in mass is proportional. If the irregularity is at higher storey, performance point increases as compared to when the irregularity in mass is at lower storey. The variation of performance point is plotted in Fig. 3 with respect to various models. It is interesting to note that when the irregularity is only in first storey, the performance point decreases.

References

1. Standard I (2000) Plain and reinforced concrete-code of practice. Bureau of Indian Standards, New Delhi
2. Standard I (1893) Criteria for earthquake resistant design of structures. Bureau of Indian Standards, Part, 1
3. BIS IS (2006) 13920-1993 (Part 1): Indian Standard code of practice for ductile detailing of reinforced concrete structures subjected to seismic forces, Bureau of Indian Standards, New Delhi, 1993
4. Council BSS (2000) Prestandard and commentary for the seismic rehabilitation of buildings. Report FEMA-356, Washington, DC
5. American Society of Civil Engineers (2014) Seismic Evaluation and Retrofit of Existing Buildings (ASCE/SEI 41-13) General Requirements; Chapter 2 Performance Objectives and Seismic Hazards; Chapter 3 Evaluations and Retrofit Requirements; Chapter 4 Tier 1 Screening; Chapter 5 Tier 2 Deficiency-Based Evaluation and Retrofit; Chapter 6 Tier 3 Systematic Evaluation and Retrofit; Chapter 7 Analysis Procedures and Acceptance Criteria; Chapter 8 Foundations and Geologic Sita Hazards; Chapter 9 Steel; Chapter 10 Concrete; Chapter 11 Masonry; Chapter .... American Society of Civil Engineers
6. Comartin CD, Niewiarowski RW, Rojahn C (1996) Seismic evaluation and retrofit of concrete buildings. Seismic Safety Commission, vol 1. State of California
7. FEMA A (2005) 440, Improvement of nonlinear static seismic analysis procedures. FEMA-440, Redwood City 7(9):11
8. Kalkan E, Kunnath SK (2007) Assessment of current nonlinear static procedures for seismic evaluation of buildings. Eng Struct 29(3):305–316
9. Hakim RA, Alama MS, Ashour SA (2014) Seismic assessment of RC building according to ATC 40, FEMA 356 and FEMA 440. Arabian J Sci Eng 39(11): 7691–7699

Non-linear Dynamic Analysis of a Multi-storey Building Subjected to Earthquakes

Arjit Verma, P. Pal, and Y. K. Gupta

Abstract During the last few decades, seismic analysis of multi-storey building has experienced notable growth. In the past years, multi-storey buildings were designed without considering any seismic excitation which is not reliable but later it was noticed that the nowadays multi-storey building is designed for some lateral loads like earthquake, wind, etc. When the dynamic load is considered for analysis, it performed significantly well than for gravity loading. In India, some states like situated in the seismically active Himalayan region in which evaluation of natural hazards due to seismic excitation is an important thing. In this paper, nonlinear dynamic analysis of a multi-storied RC building was carried out considering the different seismic intensities which occurred in seismically active state Uttarakhand. The building under consideration is modeled using finite element-based software SAP 2000 v.14.0.0. The response parameters used in the seismic analysis are time period, base shear, modal mass participation, lateral displacement, and storey drift. From the study, it is concluded that the time-history analysis method fortified the safety of multi-storey building when it is subjected to seismic excitations.

Keywords Gravity · Response · SAP2000 · Seismic

1 Introduction

The random ground motions are caused by earthquakes in all possible directions emerging from the epicenter. The horizontal shaking of ground occurs always along with the earthquake, whereas vertical ground motions are rare during earthquakes. The inertial forces were developed in building due to ground vibration when the building is resting on the soft soil. The phenomenon of reversal of stresses, i.e., tension may change to compression and vice versa in the structural component because the earthquake changes its directions abruptly. The high stresses generate in building due to the reversal phenomenon which lead to large distortion and yielding in structures

A. Verma (✉) · P. Pal · Y. K. Gupta
MNNIT Allahabad, Prayagraj, India
e-mail: arjit@mnnit.ac.in

© Springer Nature Singapore Pte Ltd. 2021

K. K. Pathak et al. (eds.), *Recent Trends in Civil Engineering*, Lecture Notes in Civil Engineering 77, https://doi.org/10.1007/978-981-15-5195-6_18

and due to this huge storey drift in the building occurs, which makes the structure insecure for the immigrants to habitat there. An extensive research has been carried out in the area of seismic studies on multi-storey building, and a few of them are presented herein. The behavior of multi-storey building with non-uniform dispersal of mass and stiffness is determined by Fernandez [1] in which he concluded that when storey stiffness is decreasing storey drift is increasing. Irregular buildings have higher modal masses as compared to the regular building for different seismic load conditions [2]. Nonlinear dynamic analysis was studied as a structural aspect by Esmaili [3] on high rise building situated in a high-risk zone of Tehran. The maximum base shear force in typical buildings of five and higher storeys during strong ground motions will be essentially unsophisticated by any degree of foundation and which is expected in normal building [4]. The comparative study was carried out by Ambrisi et al. [5] in which results are compared by pushover and inelastic dynamic analysis in terms of seismic responses of building. A twelve storey building under natural and artificial ground motion was studied by Mwafy and Elnashai [6] by static pushover and dynamic collapse analysis without SSI, and quoted that foundation is bound to move due to the flexibility of the supporting soil. The behavior of low-rise buildings is carried out with SSI under earthquake ground motion and shows that when considered SSI affect responses of the building may be increased mainly for low-rise rigid structure [7]. The seismic analysis of multi-storey building was carried for evaluation of seismic responses. There are various methods for seismic analysis based on external action, structural type, and behavior of structures and on that basis, methods are categorized as (i) Linear Static Analysis (ii) Nonlinear Static Analysis (iii) Linear Dynamic Analysis, and (iv) Nonlinear Dynamic Analysis. Among these methods, nonlinear dynamic analysis, i.e., time-history method is an organized tool to deal with the actual behavior of structures during earthquakes. This method is based on the direct numerical integration technique of the differential equations of motion in which elasto-plastic deformation of the structural element was considered [8]. The finite element analysis was carried out with SSI to study the behavior of cantilever retaining wall for earthquake frequency content ground motion by Cakir [8]. Many researchers perform the time-history analysis of multi-storey building using the Bhuj Earthquake, Imperial Valley Earthquake, and Kobe Earthquake, etc. but there is a very less study available on time history analysis under earthquake which occurs in Uttarakhand state in India. In this study, the responses of 6-storey regular RC buildings are investigated under different ground motions in terms of dynamic characteristics such as time period, modal mass participation, base shear, lateral displacement, and storey drift considering nonlinear time-history analysis. The present results are validated with the reported results, published in the open literature.

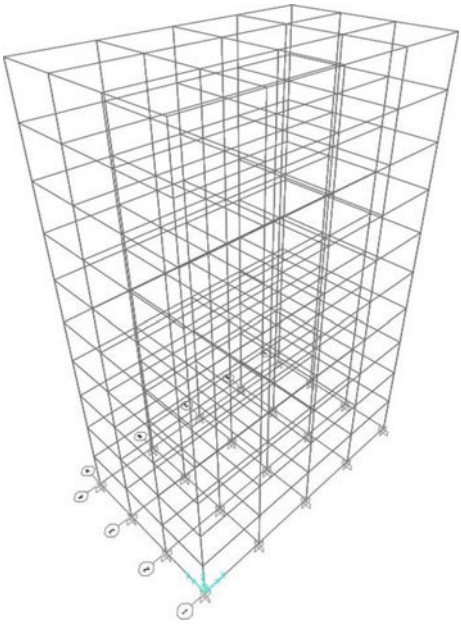

Fig. 1 3D model of the 10-storey building

2 Modeling and Validation

A 10-storey RC building model shown in Fig. 1 is used for validation. The similar model was presented by Farqaleet [8]. After modeling, nonlinear time-history analysis is performed using Imperial (El Centro) time-history. The value of the live load is 3.5 kN/m^2 and the dead load is 3.75 kN/m. The materials used are M25 concrete and Fe415 steel. The column and beam are 0.5 m × 0.5 m and 0.23 m × 0.45 m, respectively.

The present results are compared and found to be in close agreement with the results reported by Farqaleet [9]. Hence, the modeling procedure considered may be extended to further study.

3 Results and Discussion

The time-history analysis with nonlinearity is performed on 6-storey regular RC building, and two ground motions are considered. For the sake of simplicity, dimensions of beam and column are assumed as 230 mm × 450 mm and 300 mm × 400 mm, respectively. The height of the story is 3.1 m. The plan of a 6-storey RC building is 20 m × 15 m. The plan, elevation, and 3D model of 6-storied RC building are shown in Fig. 2, Fig. 3, Fig. 4, Fig. 5, and Fig. 6, respectively. The weight due to the dead load is 12 kN/m^2 on floors and 10 kN/m^2 on the roof. The live load is of 4 kN/m^2

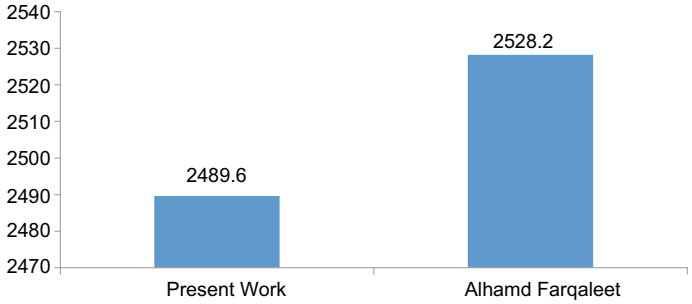

Fig. 2 Variation of maximum base shear

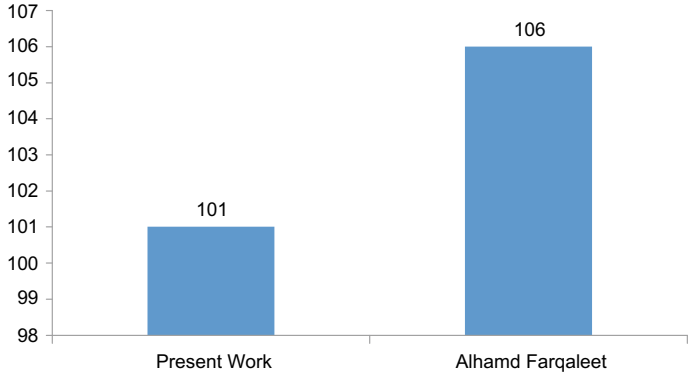

Fig. 3 Variation of roof displacement

Fig. 4 3D model of the building

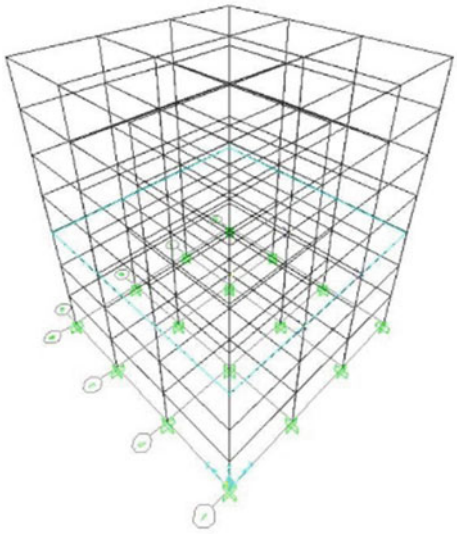

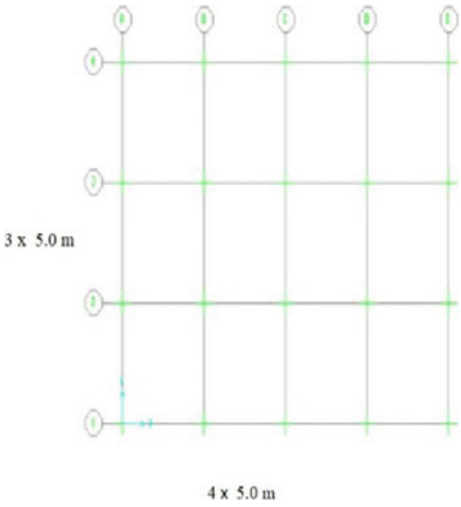

Fig. 5 Elevation of the building (X–Z)

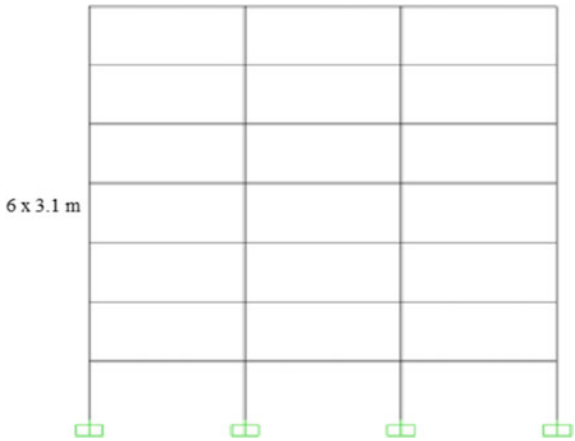

Fig. 6 Plan of the building (X–Y)

on floors and 1.5 kN/m^2 on the roof. For calculating the seismic weight, total dead load and 50% of the live load is considered as per IS code. The material properties of concrete (M20) and steel bar (Fe415) are taken as per IS code [10]. Slabs are modeled with SHELL element. This element has four nodes and six degrees of freedom at each node. Time-history analysis can be performed in SAP2000 [11] using the Direct Integration Method or Fourier Transformation Technique. In this study, the Direct Integration Method is used to perform the analysis. The Direct Integration Method fully integrates the equilibrium equations of motion for the structures subjected to dynamic loading. A series of time steps involving in analysis, which is comparatively small for loading duration.

Table 1 Ground motion records considered for the analysis

SL. no.	Ground motion	Magnitude Richter scale	PGA (g)	PGV (m/s)	Classification of frequency content
1	Uttarkashi	6.6	0.25	0.179	High
2	Chamoli	6.8	0.16	0.226	Low
3	IS 1893 (Part1): 2002[a]	–	1.0	1.040	Intermediate

[a]Time-history data of acceleration relevant to IS code [13]

The peak ground acceleration, peak ground velocity, peak ground displacement, frequency content, and duration are the main dynamic characteristics of the ground motion shown in Table 1. The ratio of PGA (g)/PGV (m/s) is denoted as frequency content, and the ground motion records are divided into three groups on the basis of frequency content [12]:

- High frequency content (PGA/PGV > 1.2)
- Intermediate frequency content (0.8 < PGA/PGV < 1.2)
- Low frequency content (PGA/PGV < 0.8)

3.1 Convergence Study

To evaluate the actual response of the building, more elements are required. A convergence study provides the size of the element required to achieve the minimum error in the evaluated results. In Fig. 7, results converge at the mesh size of 200 mm and

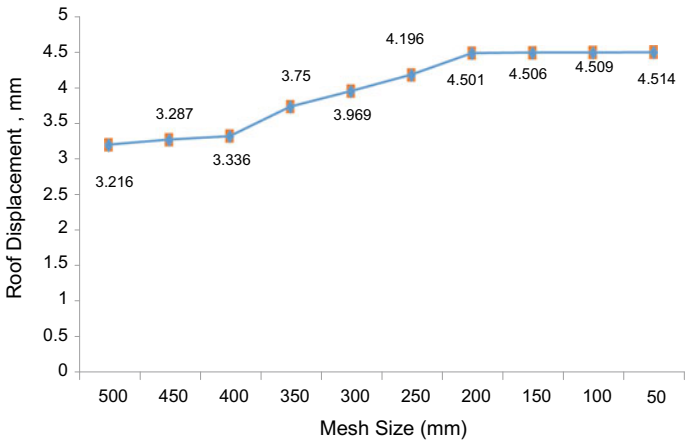

Fig. 7 Convergence study

after that, the percentage change in roof displacement value is around 0.1%. Hence the mesh size of 200 mm is adopted for discretizing the slab in the analysis.

3.2 Nonlinear Dynamic Analysis

The study of the dynamic behavior of the multi-storey building at several time steps is known as time-history analysis when the base of buildings is subjected to ground motion. In the analysis, the building is taken as multi-degree-of-freedom (MDOF) for modeling. The obtained results are tabulated and plotted in figures to observe the responses of the building.

Time Period. It plays an important role in estimating the lateral loads. The time period depends on mass and stiffness. Based on the time period, the behavior of buildings under lateral loads can be evaluated. However, it is difficult to determine the exact time period. Figures 8, 9, and 10 show the variation of the time period with all mode numbers for all ground motions considered in the study.

Modal Mass Participation. It gives the information about the particular mode that how much amount of system mass is participating in that mode with the help of Eigen values, and Eigen values can be calculated by time period. A mode with large effective mass is usually an important contributor to the system's response. According to IS code [13], the number of modes to be considered in such a way that minimum participation of the modal mass of all modes is at least 90%. Tables 2, 3, and 4 present the modal mass participation for ground motions.

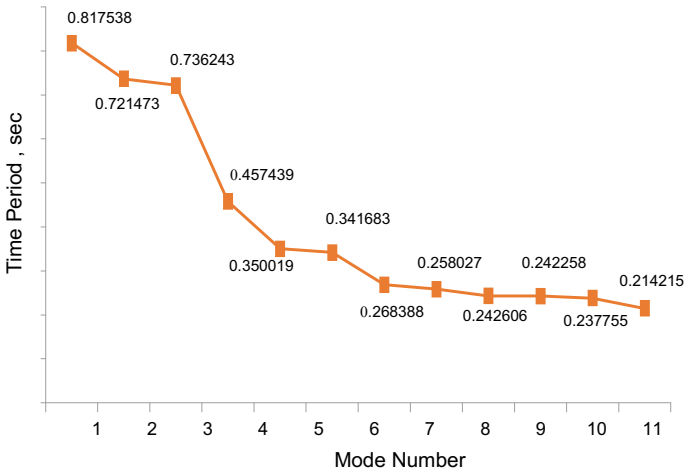

Fig. 8 Variation of time period (T) with mode number for Uttarkashi

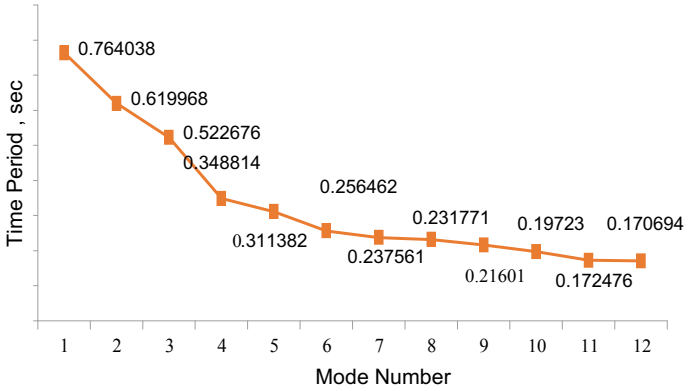

Fig. 9 Variation of time period (T) with mode number for Chamol

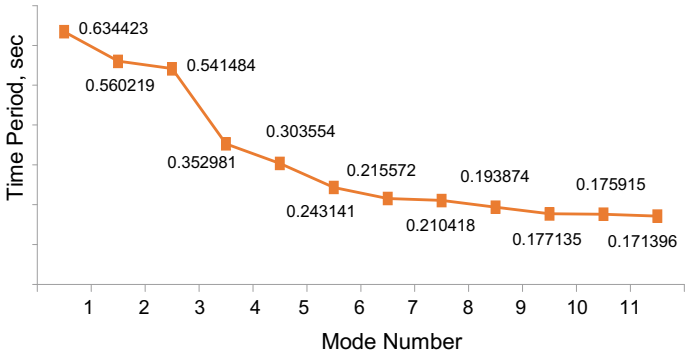

Fig. 10 Variation of time period (T) with mode number for IS-1893 (Part1): 2002

Table 2 Modal mass participation for Uttarkashi

Step number	Period sec	Mass participation	Sum
1	0.817538	8.080E-18	8.080E-18
2	0.736243	0.81186	0.81186
3	0.721473	6.654E-20	0.81186
4	0.457439	4.694E-18	0.81186
5	0.350019	2.805E-16	0.81186
6	0.341683	0.00099	0.81284
7	0.268388	5.909E-15	0.81284
8	0.258027	2.551E-15	0.81284
9	0.242606	2.269E-15	0.81284
10	0.242258	3.504E-17	0.81284
11	0.237755	0.09540	0.90824
12	0.214215	1.089E-16	0.90824

Table 3 Modal mass participation for Chamoli

Step number	Period sec	Mass participation	Sum
1	0.764038	1.613E-17	1.613E-17
2	0.619968	2.145E-19	1.634E-17
3	0.522676	0.82625	0.82625
4	0.348814	4.830E-17	0.82625
5	0.311382	9.436E-17	0.82625
6	0.256462	1.156E-16	0.82625
7	0.237561	0.00090	0.82715
8	0.231771	1.987E-17	0.82715
9	0.216010	1.275E-16	0.82715
10	0.197230	5.878E-15	0.82715
11	0.172476	4.215E-16	0.82715
12	0.170694	0.09571	0.92286

Table 4 Modal mass participation for IS 1893 (Part1): 2002

Step number	Period sec	Mass participation	Sum
1	0.634423	6.454E-17	6.454E-17
2	0.560219	1.617E-18	6.616E-17
3	0.541484	0.82843	0.82843
4	0.352981	2.448E-19	0.82843
5	0.303554	1.174E-15	0.82843
6	0.243141	0.00079	0.82922
7	0.215572	1.952E-15	0.82922
8	0.210418	1.717E-17	0.82922
9	0.193874	2.244E-16	0.82922
10	0.177135	0.09572	0.92494
11	0.175915	3.5E-15	0.92494
12	0.171396	1.399E-15	0.92494

The modes with a higher mass participation are the most important modes in the analysis and modes with a lower mass participation factor are minimal excitation; hence these modes may be ignored in the analysis.

Base Shear. It is the maximum presumed lateral force at the base of the multi-storey building due to any seismic activity. It directly depends on the input seismic acceleration. When the building is subjected to high seismic acceleration, its design base shear value is high which is not good for building. Figure 11 shows the maximum base shear values (kN) for ground motions.

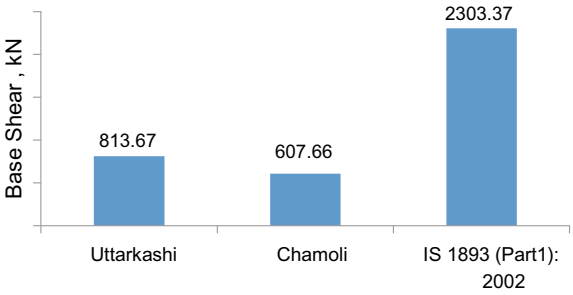

Fig. 11 Base shear for different ground motions

Table 5 Lateral displacement (mm) for different records

Floor	Uttarkashi	Chamoli	IS 1893 (Part1): 2002
1st	46.843	43.246	44.569
2nd	54.169	51.854	52.577
3rd	67.506	58.851	57.735
4th	80.039	75.137	73.156
5th	88.186	85.199	80.619
6th	96.416	86.698	82.813

Lateral Displacement. It is the absolute value of displacement of the storey under the action of the lateral forces. Larger the displacement, the less stiff is structure. Table 5 presents the lateral displacement for different ground motions.

Storey Drift. It is the inter-storey lateral displacement of one storey to the other storey below. In the design of partition wall, parameter storey drift is most significant. They must be designed as per IS code else partitions will be cracked. Table 6 presents the storey drift values for different ground motions. As per IS, due to the design lateral force the storey drift in any story shall not exceed 0.004 times the storey height. Hence, the maximal allowable storey drift $= 0.004 \times 18.6$ m $= 0.0744$ m $= 74$ mm.

Table 6 Storey drift (mm) values

Floor	Uttarkashi	Chamoli	IS 1893 (Part1): 2002
1st	19.601	18.688	19.424
2nd	7.326	8.608	8.008
3rd	13.377	6.997	5.158
4th	12.533	16.286	15.421
5th	7.947	10.062	7.463
6th	8.230	1.499	2.194

4 Conclusion

Based on the study carried out so far, the following conclusions are drawn.

1. The time period is gradually decreasing, which indicates an increase in stiffness.
2. The maximum time period is 0.817 s for high-frequency content ground motion and the minimum time period is 0.170 s for low-frequency content ground motion.
3. Modal participation is greater than 90% for all ground motion in which maximum participation is obtained for low-frequency content.
4. The number of modes that need to be essential for the study is 11 modes, 12 modes, & 10 modes for high, low, and intermediate frequency content, respectively.
5. The base shear is not dependent on the frequency content classification, whereas it depends upon the PGA.
6. The maximum value of base shear is 2303.37 kN for intermediate frequency content ground motion which has high PGA.
7. The maximum roof displacement is 96.416 mm for high-frequency content ground motion.
8. The maximum storey drift is 19.601 mm for high-frequency content which is in the permissible limit as per IS code.

References

1. Fernandez J (1983) Earthquake response analysis of buildings considering the effects of structural configuration. Bull Int Ins Seismol Earthq Eng 19:203–215
2. Wong CM, Tso WK (1994) Seismic loading for buildings with setbacks. Can J Civil Eng 21(5):863–871. https://doi.org/10.1139/194-092
3. Esmaili O (2008) Study of structural RC shear wall system in a 56-storey RC tall building. In: The 14th world conference on earthquake engineering, 12–17 October 2008
4. Meerit RG, Housner GW (1954) Effects of foundation compliance on earthquake stresses in multi-storey buildings. Bull Seismol Soc America 44(04):551–569
5. Ambrisi AD, Stefano MD, Tanganelli M (2009) Use of pushover analysis for predicting seismic response of irregular buildings: a case study. J Earthq Eng 13:1089–1100. https://doi.org/10.1080/13632460902898308
6. Mwafy M, Elnashai AS (2001) Static pushover versus dynamic collapse analysis of RC buildings. Eng Struct 23:407–424. https://doi.org/10.1016/s0141-0296(00)00068-7
7. Dutta SC, Bhattacharyaa K, Roy R (2004) Response of low-rise buildings under seismic ground excitation incorporating soil-structure interaction. Soil Dyn Earthq Eng (24):893–914. https://doi.org/10.1016/j.solidyn.2004.07.001
8. Cakir T (2013) Evaluation of the effect of earthquake frequency content on seismic behavior of cantiliver retaining wall including soil-structure interaction. Soil Dyn Earthq Eng 45:96–111. https://doi.org/10.1016/j/solidyn.2012.11.008
9. Farqaleet A (2016) Dynamic analysis of multi-storey RCC building. Int J Innov Res Technol 3:140–146
10. IS 456: 2000 Indian standard, Plain and reinforced concrete—code of practice, Bureau of Indian Standards, New Delhi

11. SAP2000 (2016) Analysis reference manual, Version 14.0.0. Computers and Structures Inc. (CSI), Berkeley, CA
12. Heidebrecht C, Lu CY (1988) Evaluation of the seismic response factor introduced in the 1985 edition of the national building code of Canada. Can J Civil Eng 15:332–338. https://doi.org/10.1139/118-053
13. IS 1893 (Part 1): 2016 Indian standard, Criteria for earthquake resistant design of structures, Bureau of Indian Standards, New Delhi

Finite Element Modeling of Precast Diaphragms Concrete and Their Connections

Raj Joshi, Astha Jhawar, Megharima Datta, Ashwin Parihar, and Ubaid L. Hanfee

Abstract The precast concrete building's structures are high superiority and speedy construction with the assurance of durability. In addition, there would be a reduction in site labor, formwork, and possible damage during earthquake. Probably due to lack of understanding of the basic nature of precast concrete during earthquake these could not get a place in India till recent past. In fact, with available tools and design philosophies designer of precast concrete structures can create a structure which will not only survive an earthquake but also will be subjected to a very little, if any, damage. The main objectives of this study work are the connections for different options of precast concrete floor unit in building situated in seismic zone for different aspect ratios and determine if precast concrete structures were more susceptible to earthquake damages, due to poor floor connections, to make the recommendations to Codal provision to improve the performance of these structural systems in future seismic events with the help of software.

Keywords Diaphragm connections · Precast concrete · Connections · Diaphragm

1 Introduction

Precast concrete during earthquake could not get a place in India till recent past. In fact, with available tools and design philosophies designer of precast concrete structures can create a structure which will not only survive an earthquake but also will be subjected to a very little, if any, damage. Desirable for this is the expertise and limit of tolerance in construction practice. A careful attention is also needed in conceptual design, detailed design, fabrication, transport, erection, jointing, and overall quality assurance. Another important issue to keep in mind is internal force paths in the different stages during construction. This research focuses on the role of diaphragm

R. Joshi (✉) · M. Datta · A. Parihar · U. L. Hanfee
Medi-Caps University, Indore, India
e-mail: rajjoshi2103@hotmail.com

A. Jhawar
MJP Government Polytechnic College, Khandwa, India

© Springer Nature Singapore Pte Ltd. 2021

K. K. Pathak et al. (eds.), *Recent Trends in Civil Engineering*, Lecture Notes in Civil Engineering 77, https://doi.org/10.1007/978-981-15-5195-6_19

and their connections for precast concrete structures within the lateral force resisting system. The main objectives of this technical Paper are To study the connections for different options of precast concrete floor unit in building situated in seismic zone for different aspect ratios. To determine, if precast concrete structures were more susceptible to earthquake damages, due to poor floor connections, to make the recommendations to Codal provision to improve the performance of these structural systems in future seismic events. To model the precast structure with the help of software [7], the future of precast concrete diaphragms needs to lay its focus on the inter-panel ductile detailing of connections. The success or failures of current design code across the globe on precast concrete diaphragms are to be studied in detail after an earthquake to further reinforce the trust on these recommendations. Experimental procedures with such detail should be structures, and Indian construction standard needs to be developed for their localized behavior. Inter-panel diaphragms being performed elsewhere in the world due to the increased use of precast structures must be suitably adapted to Indian conditions. These are certain challenges which need to be addressed in the time to come. Indian standards of construction do not provide significant importance to seismic design of precast construction. Some of the issues which need immediate attention in the Indian construction standards have been identified as mentioned below.

Indian standards provide guidelines for design and construction of precast concrete structures. No specific guidelines are provided for reinforcement and design of precast concrete floor slabs with lateral loads, i.e., seismic design of precast concrete diaphragms, especially for the hollow core slabs. Precast floor diaphragms are to be classified based on their construction and behavior requirements to provide an easy and suitable selection option to the designer [7].

No specific guidelines are provided for connection of precast concrete diaphragm with lateral loads, i.e., seismic design of precast concrete diaphragms connection.

Lateral loads on floor systems due to earthquakes and wind is an untouched topic in Indian standards, and there are no provisions for obtaining the diaphragm forces. The guidelines to obtain diaphragm forces from the base shear distributions need to be included in the Indian standards for precast construction. The Uniform Building Code provides these specifications as [6]

$$F_{px} \frac{F_t + \sum_{i=x}^{n} F_i}{\sum_{i=x}^{n} W_i} w_{px} \tag{1}$$

In G+3, manual design precast building connection provided were not appropriate due to which building were damaged. In present work modifications in the connections are suggested to high seismic forces. Detail drawing has been shown in the Figs. 1 and 2.

Further, a floor system is designed as a one-way or two-way slab with similar reinforcement following Indian standards, but diaphragms require dedicated chord,

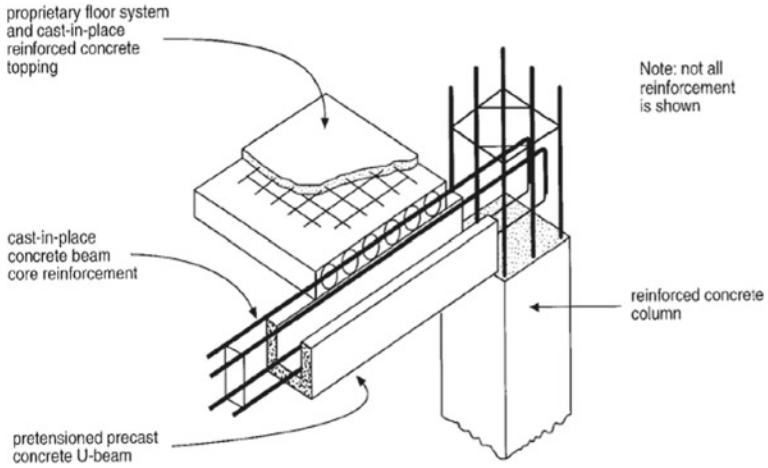

Fig. 1 Typical connections of beam, column, and slab [4, 5]

Fig. 2 Elevation of G+3

web, and collector reinforcements. There is a need to provide guidelines for these reinforcements adhering to the other similar requirements in the Indian standards for reinforced concrete construction. These requirements must be in coherence with the reinforcement guidelines provided in reinforced-concrete construction.

In high seismic zones only solid slab concrete panels are recommended, and their connection is permitted between ribs only. While the structural standards of practice across the world allow using composite or non-composite topping slab reinforced and detailed to provide for a complete transfer of forces to the lateral force resisting system. Such flexibility must be brought into the Indian standards to boost the use of precast concrete diaphragms in active seismic zones.

The absence of updates on precast concrete diaphragms Indian standards is partly due to the relative low magnitude of such construction being used in India. This also reflects by the relatively faster updates in the relevant construction standards in countries with high use of such construction practices. But with the infrastructure growing like never and the demands for faster, innovative, and safer construction options the doors to more numbers of such construction practices. In these regards, it is high time that Indian standards investigate the seismic design provisions of precast concrete floor system.

2 Analytical Studies

2.1 Diaphragm Action [3]

The function of a diaphragm is to receive and resist lateral loads by acting as a horizontal deep beam and transmit the loads to lateral-resisting elements which carry the lateral loads to the foundation. Thus, while the role of the precast/pre-stressed floor system is often considered as providing support for gravity loads acting out of the plane of the floor, it also plays a key role by providing strength and stiffness in the plane of the floor, by connecting the individual vertical elements to create the Lateral Force Resisting System (LFRS), and in the context of seismic design, transfers the inertial forces that develop in a seismic event so-called diaphragm action [1].

2.2 Structure Integrity [3]

The fundamental requirement of earthquake resistance is to provide a complete load path from any point in a structure to the foundation. The design must ensure that the building can sustain local damage without catastrophic failure. Structural integrity in the context of avoiding catastrophic collapse is normally obtained by using the fully tied solution incorporating full horizontal and vertical ties.

2.3 Precast Floor Systems

The selection of floor type depends upon factors related to the utility and form of the structure, availability, and the seismic zone. Each system has characteristics unique to its form that drive its diaphragm detailing. These characteristics depend on construction method and type of precast unit, as described below in detail.

3 Seismic Design Procedures

The design issues in precast diaphragm are the design of connections to get loads into the diaphragm, the strength and ductility of the slab system to transmit these loads to the lateral resisting elements, and the design of the connections required to unload the lateral forces from the diaphragm to the lateral resisting elements [2].

3.1 Design of Floor Diaphragm and Connections

See Figs. 3, 4, and 5.

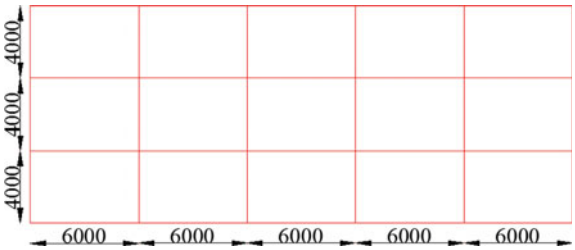

Fig. 3 Plan of G+3

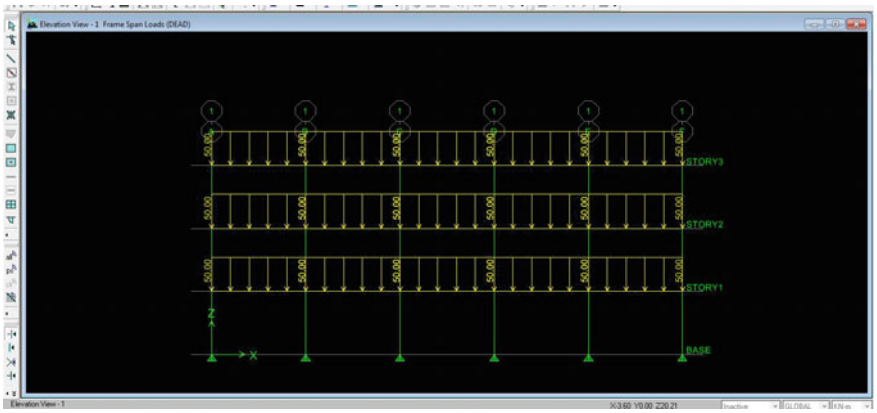

Fig. 4 Model in ETABS

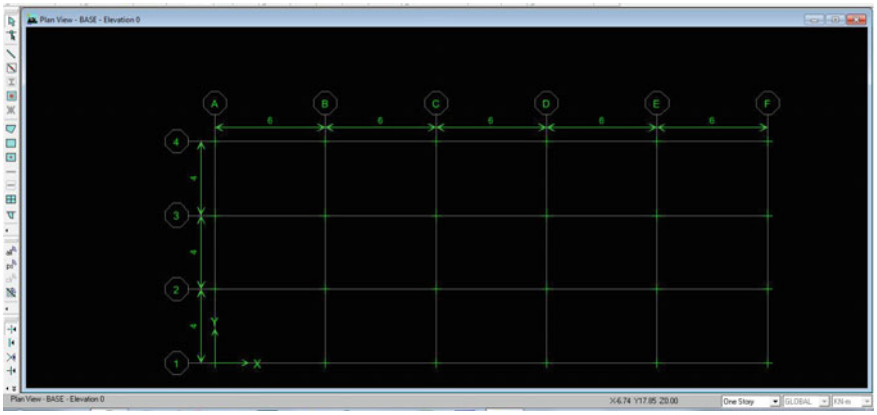

Fig. 5 Plan layout in ETABS

3.2 Design of a Hollow Core

Design of 200 mm Deep Hollow Core Slab [2]

Effective span − 4 m $= 4000$ mm
Total load 50 kN/m is distributed as $= 50\ \text{kN}/\text{m}/4$
Therefore w $= 12.5\ \text{kN}/\text{m}^2$
Therefore, the factor loads W $= 12.5\ \text{kN}/\text{m}^2 \times 1.5 = 18.75\ \text{kN}/\text{m}^2$
Moment for normal loading $= \text{wL}^2/8$
$= 12.5 \times 4^2/8 = 25\ \text{kNm}/\text{m}$
Factored as M_s $= 25 \times 1.2 = 30\ \text{kNm}/\text{m}$

Moment for factored loading $= \text{WL}^2/8$
$= 18.75 \times 4^2/8 = 37.5\ \text{kNm}/\text{m}$
Factored as M_u $= 37.5 \times 1.2 = 45\ \text{kNm}/\text{m}$

Now, design in shear

$$\begin{aligned} V_u &= \text{WL}/2 \\ &= 18.75 \times 4/2 \\ &= 37.5\ \text{kN}/\text{m} \times 1.2 \text{ (for unit width)} \\ &= 45\ \text{kN per unit.} \end{aligned}$$

Since the moment is $\text{M}_s = 30$ kNm, $\text{M}_u = 45$ kNm.

Therefore the % of steel provided will be 0.171% A_c (1200 × 200), i.e., 4 nos. of 12 mm bars (452.16 mm^2).

Design in Bearing

The effective bearing length is taken as the least of

1. The actual bearing length of the imposed member i.e. 1200 mm.
2. One half of (i) + 100 mm i.e. 1200/2 +100 mm = 700 mm
3. 600 mm.

which gives, effective bearing length = 600 mm.Also, Net bearing width = 75 -15 = 60 mm.

Therefore, the Bearing Stress
$= 45 \times 10^3/(600 \times 60)$
$= 1.25\,\text{N/mm}^2 < 0.4\,f_{cu} = 16\,\text{N/mm}^2$. Hence safe. (where $f_{cu} = 40\,\text{N/mm}^2$)

Design of Precast L-Beam

For M40 concrete the cover to reinforcement = 30 mm
Use b = 300 mm wide beam
Minimum up stand width (assuming 8 mm bars) $= 30 + (6 \times 8) + 30$
$= 108$ mm.

Slenderness Ratio Check

$$b_w > L/60$$
$$300 > 6000/60$$
$$300\text{ mm} > 100\text{ mm, hence safe.}$$

Or

$$\sqrt{L \times d/250} = \{(600 \times 550)/250\}^{1/2}$$
$$= 114.89 = 115\text{ mm.}$$

Using maximum possible up stand width $b_w = 165$ mm with 200 mm deep floor recess.

Maximum bending moment $= wl^2/8$

where w = 50 kN/m

Therefore,

The factored load $= 1.5 \times 50 = 75$ kN/m

Moment $(M_u) = 75 \times 6^2/8 = 337.5$ kNm

Shear $(V_u) = 75 \times 6/2 = 225$ kN

Flexural design for compression side, b = 165 mm, d = 550 mm, $M_u = 112.5$ kNm.

$$M_u = 0.87 f_y (P_t/100) \times \left[1 - 1.005 f_y \Big/ f_{ck} (P_t/100)\right] bd^2$$
$$= 0.87 \times 415 (P_t/100) \times [1 - 1.005415/40(P_t/100)]165 \times 550^2$$

On solving the quadratic equation, we get,

$$P_t = 0.671$$

Therefore,

$$A_{st} = 0.671 \times 165 \times 550 = 608.93 \text{ mm}^2$$
Hence 4 bars of 16 mm $\left(803.84 \text{ mm}^2\right)$.

Flexural design for tension side, b = 165 mm, d = 550 mm, M_u = 225 kNm.

$$M_u = 0.87 f_y (P_t/100) \times \left[1 - 1.005 f_y \Big/ f_{ck} (P_t/100)\right] bd^2$$
$$225 \times 10^6 = 0.87 \text{ x } 415 (P_t/100) \times [1 - 1.005415/40(P_t/100)]165 \times 550^2$$

On solving it we get

$$P_t = 1.47$$

Therefore,

$$A_{st} = 1.47 \times 165 \times 550 = 1338.5 \text{ mm}^2$$
Hence 7 bars of 16 mm $\left(1406.74 \text{ mm}^2\right)$.

Check for Deflection

See Fig. 6

$$L/d = 20$$
$$P_t = 1.47\%$$
$$F_s = 0.58 f_y A_{st} \text{ required}/A_{st} \text{ provided}$$
$$= 0.58 \times 415 \times 1338.5/1406.72$$
$$= 229 \text{ N}/\text{mm}^2$$

Modification factor for providing tensile steel-$F_1 = 0.98$, $F_2 = 1.15$, $F_3 = 1$

$$\text{Max L}/\text{d required} = F_1 \times F_2 \times F_3 \times \text{L}/\text{d}$$
$$= 0.98 \times 1.15 \times 1 \times 20 = 22.54$$
$$\text{L}/\text{d provided } 600/550 = 10.91 < 22.54, \text{ hence safe.}$$

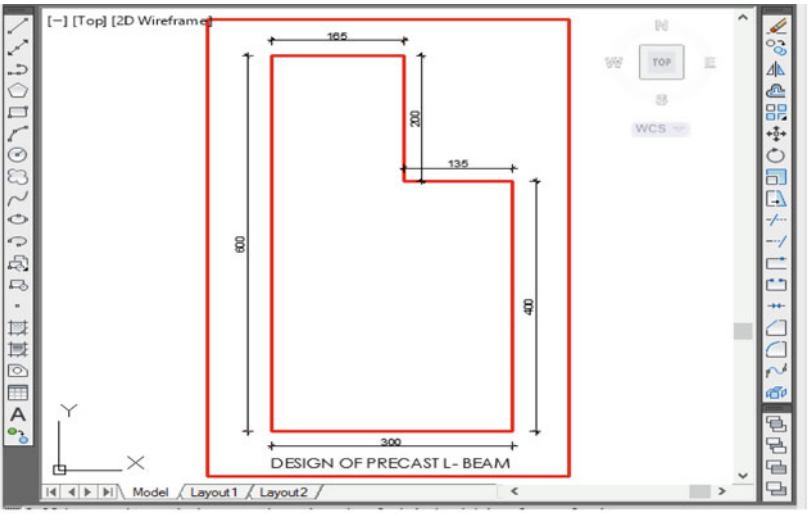

(a)

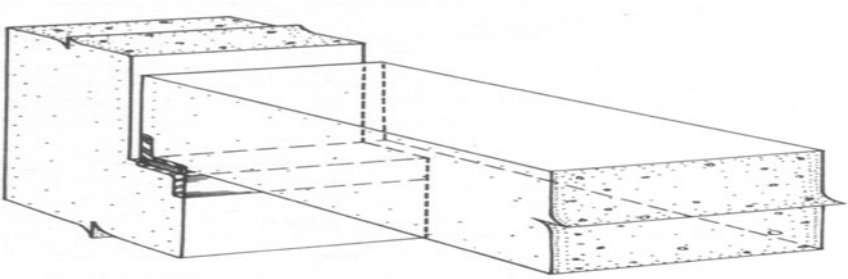

(b)

Fig. 6 **a** Beam connections (Section). **b** Beam connections (Isometric) [1]

Check for Shear

$V_u = 225$ kN

$T_v = V_u / bd = 225 \times 10^3 / 165 \times 550 = 2.47$ N/mm^2

$P_t = A_{st} / bd = 1406.7 \times 100 / 165 \times 550 = 1.55\%$

$T_c = 0.818$ N/mm^2 (Table 19 IS456)

T_c max $= 4$ N/mm^2

$T_c < T_V < T_c$ max

Hence, Shear reinforcement is to be designed.
Shear to be taken by steel reinforcement [2]

$$\begin{aligned} V_{US} &= V_U - T_C bd \\ &= 225 \times 10^3 - 0.818 \times 165 \times 550 \\ &= 150.76 \text{ kN} \end{aligned}$$

Using 2-legged, 8 mm vertical stirrups spacing S_v

$$\begin{aligned} V_{US} &= 0.87 f_y A_{sv} d / S_V \\ 150 \times 10^3 &= 0.87 \times 415 (2\pi / 4 \times 8^2) \times 550 / S_V \\ S_V &= 132.4 \text{ mm} \end{aligned}$$

Maximum spacing permitted = 0.75d = 0.75 × 550 = 412.5 mm or 300 mm whichever is less.

Hence provided $S_V = 140$ mm is enough.

Calculation of Tie Force

The basic horizontal tie force F_t is given by lesser of—$F_t = (20 + 4n)$ or 60 kN/m width

where n is the number of storey's including basement—$F_t = (20 + 4 \times 3) = 32$ kN/m

If the total characteristics dead (gk) + live loading (qk) is >7.5 kN/m^2 and or the distance (l_r) between the column or wall in the direction of the tie is greater than 5 m, the force is modified as the greater of

$$\begin{aligned} F_{t'} &= [(gk + qk)/7.5] \times [l_r/5] F_t \\ &= [(7.5 + 5)/7.5] = 1.66 \end{aligned}$$

If l_r is <5 m then $F_{t'} = 1.66 \times 32 = 53.33$ kN/m and ($l_r < 5$ m).

If l_r is >5 m then $F_{t'} = 533.3 \times l_r/5$ ($l_r > 5$)

4 Conclusion

The precast concrete building's structures are now worldwide accepted as an economic, structurally sound, and architecturally versatile form of construction. From literature, it is concluded that precast construction is continuously increasing and have become popular even in seismic sensitive country. An account of International practice on design and connection details of precast frame is presented. Brief description on precast concrete construction is studied and presented.

1. To achieve the objective of work, a parametric study of G + 6 storey building is attempted to understand and compare the modeling of precast concrete building with using different softwares. And, one manual design study is also presented in which the cause of failure of joints and suggested joints in G + 3 story building is

calculated and shown; design of floor diaphragm is also suggested for a building situated in seismic zone for different aspect ratios.

2. It is found that the precast concrete structures were more susceptible to earthquake damages. Hence, special attention must be given to them, and there is a burning need of Codal provisions and standards to withstand future seismic events.
3. Analysis and design of diaphragms in moderate to high rise structures required detailed modeling in dedicated programs like SAP2000, ETABS 9, etc. After performing such analysis, it is observed that several provisions related to precast concrete diaphragm analysis and design are unavailable or ambiguous in Indian structural standards. It is suggested to include guidelines for the procedure to be followed for the diaphragm analysis and the methodology for the diaphragm load distribution within the diaphragm. The reinforcement detailing for chord, web, and collector steel needs to be clarified, and their distinction from regular floor panels elements has to be pointed out. It is immediately required to address the connection philosophy and research .Experience shows that a combination of topping concrete and welded mechanical connectors proves effective in seismic loading.

References

1. ACI (2008) ACI: 318-2008 building code requirements for structural concrete and commentary, ACI Committee 318. American Concrete Institute, Farmington Hills, MI
2. BIS (2002) IS: 1893–2002 Indian standard criteria for earthquake resistant design of structures, Part I—general provisions and buildings. Bureau of Indian Standards, NewDelhi
3. Barkale M (2009) Seismic performances of precast concrete diaphragms and their connections. M.E Thesis, RGPV University, Bhopal, India
4. Cao L, Naito CJ (2007) Design of precast diaphragm chord connections for in-plane tension demands. J Struct Eng 133(11):1627–1635
5. D'Arcy T, Nasser, GD, Gosh SK (2003) Building code provisions for precast/pre-stressed concrete: a brief history. PCI J 116–124, November–December
6. Dhakal RP (2008) Exploring the feasibility of a floor system detached from seismic beams in moment resisting frame buildings. In: Conference Proceedings- 2008 NZSEE Conference-Poster Session, Paper 18. https://www.nzsee.org.nz/db/2008/Paper18.pdf
7. Englekirk RE (2003) Seismic design of reinforced and precast concrete buildings. Wiley, Hoboken, NJ

T-Beam Bridge Girder Analysis Using Finite Element Modeling for IRC Loading

Dhaker Rahul and U. K. Dewangan

Abstract T-beam slab deck bridge is the most common type of superstructure generally adopted in most of the highways in the country. Moving live load combinations are the critical loadings for which bridge deck needs to be analyzed. In this paper, T-beam slab bridge deck is modeled using finite element method by assuming it as a beam–plate model. In beam–plate model, the beam element is assembled in the plane of the plate element, so that the center of gravity of the beam coincides with the plate element. Live load for Class 70R wheeled vehicle, on a two-lane bridge is taken as per IRC: 6-2016. The analysis is performed as per IRC: 112-2011. The study on the three different cases of cross girder combinations is considered. The effect of number of cross girders is analyzed in order to reduce the maximum bending moment and deflection in longitudinal girders on the bridge deck model. A MATLAB code is developed for finite element modeling of T-beam slab deck bridge. The results of various combinations of loads for the maximum value of shear force, bending moment, and deflections are tabulated and plotted.

Keywords T-beam slab bridge · Beam–plate model · IRC loading · FEM analysis

1 Introduction

A T-beam slab bridge generally comprises longitudinal girders, cross girders, deck slab, and diaphragms at the ends. The longitudinal girders are usually spaced equally at 2–3 m and cross girders at 4–5 m along the span. The girders, slab, and diaphragms are casted monolithically so that T-beam action prevails, and torsional rigidity is introduced to the superstructure. Choosing the correct element for the analysis plays an important role in finite element analysis. As shear deformations are insignificant in girders, Euler beam element is acceptable [1]. For composite action, the number

D. Rahul (✉) · U. K. Dewangan
National Institute of Technology, Raipur 492010, India
e-mail: rahul.dhaker.543@gmail.com

U. K. Dewangan
e-mail: ukdewangan.ce@nitrr.ac.in

© Springer Nature Singapore Pte Ltd. 2021

K. K. Pathak et al. (eds.), *Recent Trends in Civil Engineering*, Lecture Notes in Civil Engineering 77, https://doi.org/10.1007/978-981-15-5195-6_20

of elements along the length of the bridge deck slab should be same as that for longitudinal girder [1]. Considering effective width of slab for composite action in T-section beams has significant influence on the capacity of the section [2]. Grid element is generally used in bridge analysis [3]. In this paper, Mindlin–Reissner plate element is chosen for modeling the deck slab in FEM, and the grid beam element is chosen for the modeling of girders in FEM, which provides torsional rigidity. This model gives an approach to analyze the bridge superstructure as two-dimensional analysis.

The actual T-beam system is modeled as a deck slab of constant depth and girder assembled at the mid plane of the slab. The depth of the equivalent beam is greater in actual dimension although the eccentricity in the modeling is neglected. The moment of inertia of the actual T-beam section should be equal to that of the idealized model [9]. The effective width of the flanges of the plate slab b_{eff} is considered as per IRC:112-2011 [5]. The simplest approach of formulation using direct method considers the distributed loads on an element. In the rectangular elements, the total load on the element is distributed and assigned as four equal magnitude of concentrated forces acting on the nodes [10].

In this paper, T-beam deck slab bridge is modeled using the finite element method while the live load is considered as per IRC: 6-2016 [4]. The live load travels in longitudinal direction which can occupy any position in transverse direction. A MATLAB program is developed for the above live load movement. By placing the IRC Class 70R load for the longitudinal and transverse travel combinations, the maximum bending moment is noted for the worst effect of maximum bending moment and deflections over the entire span. The effect of number of cross girders in span on deflection, bending moment, and shear forces of longitudinal girders are computed, and the results are plotted.

2 Modeling Technique

The slab is modeled as plate element, and girders are modeled as grid beam element. There is an eccentricity (e) between the centroid of slab element and centroid of beam element. It is acceptable to consider equivalent depth (D_{eq}) for beam element with the same moment of inertia of section with respect to the global center of gravity as shown in Fig. 1 [8].

2.1 Finite Element Model

A bridge superstructure is a hybrid structure that has several structural components such as deck, longitudinal girders, cross girders, etc. Therefore, the proper selection of finite elements plays a vital role in the finite element modeling. First, the modeling of bridge deck slab and girders is discussed separately. This is followed by

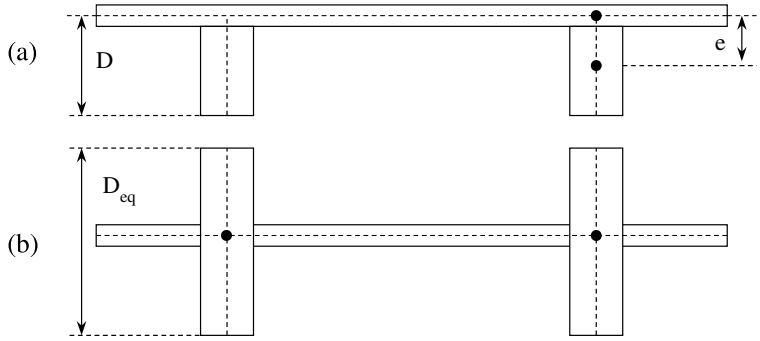

Fig. 1 FE model **a** Actual slab–beam deck. **b** Equivalent beam modeled centrically with slab

discussion and techniques involved to model the composite behavior of slab–beam structure. The analysis algorithm for numerical modeling is developed using the software MATLAB. This software provides extensive library of mathematical and plotting functions which makes the numerical modeling easier.

Modeling of Bridge Deck Slab. Mindlin–Reissner plate element with three degrees of freedom per node is chosen for the modeling of deck slab. The several assumptions of this theory are:

Only linear static analysis is considered.

Material is homogenous, isotropic, and linear elastic.

Deformations are small enough to use an infinitesimal deformation theory.

The Mindlin plate theory is used as it includes transverse shear deformations.

In linear Mindlin plate theory, the displacements $\{u, v, w\}$ at (x, y, z) are expressed as function of mid-plane deformations $\{w, \theta_x, \theta_y\}$ where w is vertical displacement, and θ_x and θ_y are rotations of normal as shown in Fig. 2. These rotations of normal remain straight even after deformation but do not remain perpendicular to mid plane; this permits shear deformation in the plates (particularly in thick plates).

The displacement field of plate is

$$a = \{w, \theta_x, \theta_y\}^T \tag{1}$$

The assumed displacement field for Mindlin plate is u (along x axis), v (along y axis), and w (along z axis) written as

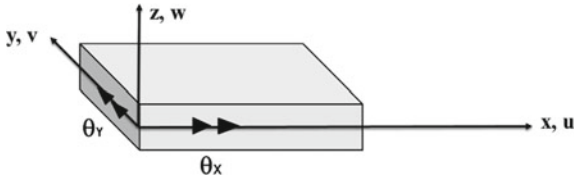

Fig. 2 Mindlin–Reissner plate element

$$\sigma_b = D_b \varepsilon_b \tag{2}$$

where

$$D_b = \frac{E}{\left(1-\nu^2\right)} \begin{bmatrix} 1 & 0 & 0 \\ 0 & 1 & 0 \\ 0 & 0 & \frac{1-\nu}{2} \end{bmatrix} \tag{3}$$

$$\sigma_s = D_s \varepsilon_s \tag{4}$$

where

$$D_s = \frac{E}{2(1+\nu)} \begin{bmatrix} 1 & 0 \\ 0 & 1 \end{bmatrix} \tag{5}$$

where subscript b is referred to bending and subscript s to shear part.

Quadrilateral (Four node) isoparametric element is discretized and the displacements within the element are given by

$$w = \sum_{i=1}^{4} N_i(\xi, \eta) w_i \tag{6}$$

$$\theta_x = \sum_{i=1}^{4} N_i(\xi, \eta)(\theta_x)_i \tag{7}$$

$$\theta_y = \sum_{i=1}^{4} N_i(\xi, \eta)(\theta_y)_i \tag{8}$$

where $N_i(\xi, \eta)$ are shape functions for four-noded Q4 element, and ξ and η are natural coordinates.

$$\begin{aligned} N1 &= \frac{1}{4}(1-\xi)(1-\eta) \\ N2 &= \frac{1}{4}(1+\xi)(1-\eta) \\ N3 &= \frac{1}{4}(1+\xi)(1+\eta) \\ N4 &= \frac{1}{4}(1-\xi)(1+\eta) \end{aligned} \tag{9}$$

Displacement matrix formulation for each element is given by

$$a^e = \left\{w_1, (\theta_x)_1, (\theta_y)_1 w_2, (\theta_x)_2, \left(\theta_y\right)_2 w_3, (\theta_x)_3, (\theta_y)_3 w_4, (\theta_x)_4, (\theta_y)_4\right\} \tag{10}$$

The element stiffness matrix in natural coordinates is written as

$$K^e = \frac{t^3}{12} \int_{-1-1}^{11} \left(B_b^e\right)^T \left(D_b^e\right)\left(B_b^e\right)|J|d\xi d + \alpha t \int_{-1-1}^{11} \left(B_s^e\right)^T \left(D_s^e\right)\left(B_s^e\right)|J|d\xi d\eta \tag{11}$$

Here, α is a shear correction factor and is equal to 5/6, and t is thickness of plate. Where J is Jacobian and written as

$$[J] = \begin{bmatrix} \frac{\partial N1}{\partial \xi} & \frac{\partial N2}{\partial \xi} & \frac{\partial N3}{\partial \xi} & \frac{\partial N4}{\partial \xi} \\ \frac{\partial N1}{\partial \eta} & \frac{\partial N2}{\partial \eta} & \frac{\partial N3}{\partial \eta} & \frac{\partial N4}{\partial \eta} \end{bmatrix} \begin{bmatrix} x1 & y1 \\ x2 & y2 \\ x3 & y3 \\ x4 & y4 \end{bmatrix} \tag{12}$$

The kinematic matrix B_b^e and B_s^e for bending and shear can be written as

$$B_b^e = \begin{bmatrix} 0 & \frac{\partial N1}{\partial x} & 0 & 0 & -\frac{\partial N2}{\partial x} & 0 & 0 & -\frac{\partial N3}{\partial x} & 0 & 0 & -\frac{\partial N4}{\partial x} & 0 \\ 0 & 0 & -\frac{\partial N1}{\partial y} & 0 & 0 & -\frac{\partial N2}{\partial y} & 0 & 0 & -\frac{\partial N3}{\partial y} & 0 & 0 & -\frac{\partial N4}{\partial y} \\ 0 & -\frac{\partial N1}{\partial y} & -\frac{\partial N1}{\partial x} & 0 & -\frac{\partial N2}{\partial y} & -\frac{\partial N2}{\partial x} & 0 & -\frac{\partial N3}{\partial y} & -\frac{\partial N3}{\partial x} & 0 & -\frac{\partial N4}{\partial y} & -\frac{\partial N4}{\partial x} \end{bmatrix} \tag{13}$$

$$B_b^e = \begin{bmatrix} \frac{\partial N1}{\partial x} & -N1 & 0 & \frac{\partial N2}{\partial x} & -N2 & 0 & \frac{\partial N3}{\partial x} & -N3 & 0 & \frac{\partial N4}{\partial x} & -N4 & 0 \\ \frac{\partial N1}{\partial y} & 0 & -N1 & \frac{\partial N2}{\partial y} & 0 & -N2 & \frac{\partial N3}{\partial y} & 0 & -N3 & \frac{\partial N4}{\partial y} & 0 & -N4 \end{bmatrix} \tag{14}$$

The element stiffness matrix is calculated by numerical integration of the equations shown above.

Numerical Integration. The Gauss quadrature integration rule is used for numerical integration. For bending part in stiffness matrix, 2 × 2 Gauss quadrature integration is used, and for shear part, 1 × 1 Gauss quadrature integration is used (This method is called as lower order/reduced integration for shear part to avoid shear locking) [7]. The Gauss quadrature integration is summarized below.

$$\int_{-1-1}^{11} f(\xi, \eta) d\xi d\eta = \sum_i \sum_j f\left(\xi_i, \eta_j\right) w_{ij} \tag{15}$$

where $f(\xi_i, \eta j)$ are function values and w_{ij} is weightage for sampling points.

Gaussian point locations for $n = 2$ in each direction are shown in Fig. 3, and for other values of n, weighting coefficients are given in Table 1.

where

$n =$ number of sampling points

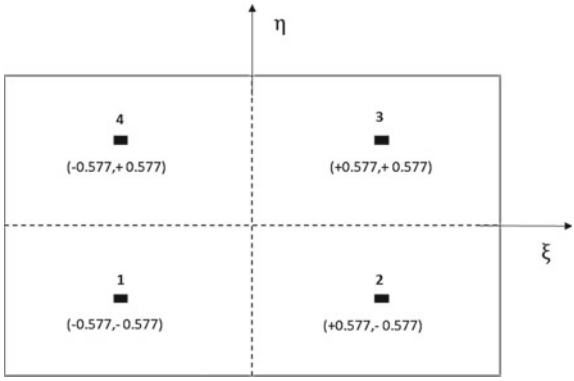

Fig. 3 Gaussian points location in element

Table 1 Gauss sampling points

n	ξ_i, η_j	w_{ij}
1	0.00	2.00
2	+0.57735	1.00
	−0.57735	1.00

$\xi_i, \eta_j =$ location of sampling points

$w_{ij} =$ weighting coefficients

The force vector is written as

$$F^e = \int_{-1}^{11}\int_{-1} PN|J|d\xi d\eta \tag{16}$$

where P is pressure force and N is vector of shape functions.

Now, each element stiffness and force matrix are added to the appropriate location (based on element position, nodal connectivity) to the global stiffness and force matrix. This process is called as assembly.

$$\sum_e k^e a^e = \sum_e F^e \tag{17}$$

Modeling of Bridge Girders. Bridge girders are modeled as grid beam line element as shown in Fig. 4 on which loads are applied perpendicular to the grid plane as compared to a 3D plane frame where loads are applied in plane. Both torsional and bending moment continuities exist at the node point as the elements of a grid are

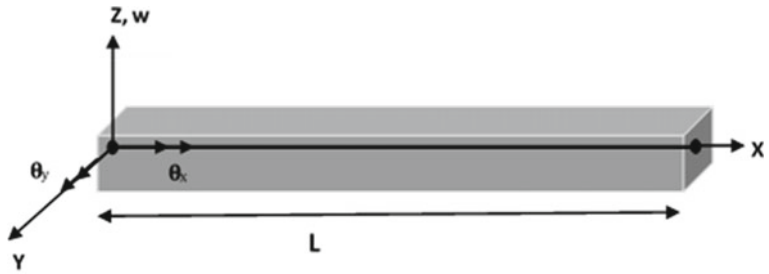

Fig. 4 Grid element with degree of freedom

assumed to be connected rigidly, such that angles between the elements connected at a node do not change. Grids are typically used for floors and bridge deck systems [6].

The local stiffness matrix for grid element is given by

$$K_e = \begin{bmatrix} \frac{12EI}{L^3} & 0 & \frac{6EI}{L^2} & -\frac{12EI}{L^3} & 0 & \frac{6EI}{L^2} \\ 0 & \frac{GJ}{L} & 0 & 0 & -\frac{GJ}{L} & 0 \\ \frac{6EI}{L^2} & 0 & \frac{4EI}{L} & -\frac{6EI}{L^2} & 0 & \frac{2EI}{L} \\ -\frac{12EI}{L^3} & 0 & -\frac{6EI}{L^2} & \frac{12EI}{L^3} & 0 & -\frac{6EI}{L^2} \\ 0 & -\frac{GJ}{L} & 0 & 0 & \frac{GJ}{L} & 0 \\ \frac{6EI}{L^2} & 0 & \frac{2EI}{L} & -\frac{6EI}{L^2} & 0 & \frac{4EI}{L} \end{bmatrix} \tag{18}$$

The transformation of element oriented in any random direction is discussed below, where θ is positive, taken anticlockwise from x to x' in the x–z plane as shown in Fig. 5.

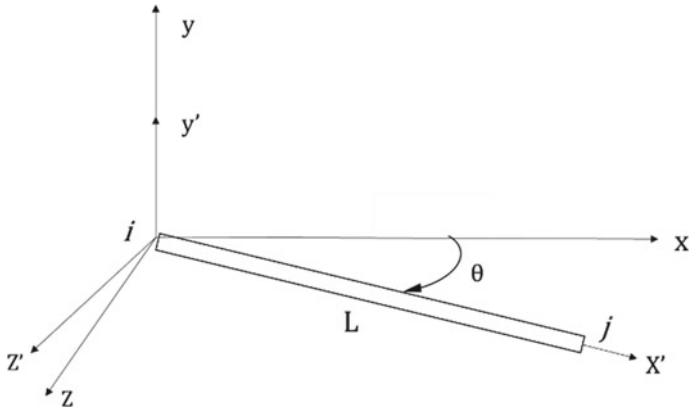

Fig. 5 Grid element oriented in the x–z plane

$$C = \cos\theta = \left(x_j - x_i\right)/L \quad \mathrm{S} = \sin\theta = \left(z_j - z_i\right)/L$$

where L is the length of element measured from node i to node j. The vertical deflection w does not change with respect to coordinate transformation ($y = y'$).

The transformation matrix of local to global degree of freedom for grid element is given by

$$T = \begin{bmatrix} 1 & 0 & 0 & 0 & 0 & 0 \\ 0 & C & S & 0 & 0 & 0 \\ 0 & -S & C & 0 & 0 & 0 \\ 0 & 0 & 0 & 1 & 0 & 0 \\ 0 & 0 & 0 & 0 & C & S \\ 0 & 0 & 0 & 0 & -S & C \end{bmatrix} \tag{19}$$

The global stiffness matrix for a grid element is given by

$$[K_G] = [T]^T [K_e][T] \tag{20}$$

3 T-Beam Slab Validation

Consider the centrally loaded, simply supported beam with T cross section of length 10 m, with load W, 1000 N, as shown in Fig. 6.

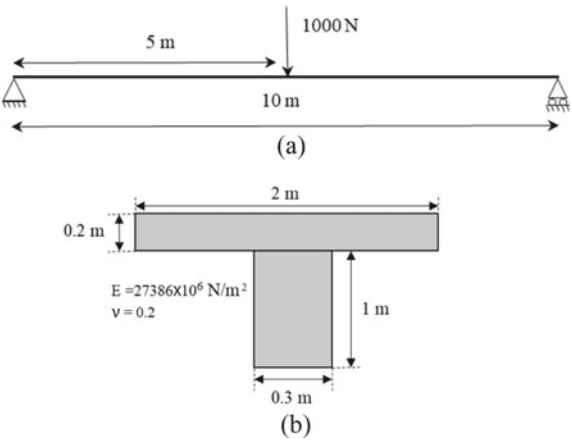

Fig. 6 T-beam problem. **a** Simply supported beam. **b** T-beam cross section

4 Hand Calculation—Theoretical Results

Maximum Bending moment $= \mathrm{Wb}/\mathrm{L}$
$= 1000 \times 5 \times 5/10$ Bending moment at supports $= 0$ Nm
$= 2500$ Nm

Shear force at left support $= \mathrm{Wb}/\mathrm{L}$
$= 1000 \times 5/10$
$= 500$ N

Shear force at right support $= -\mathrm{Wa}/\mathrm{L}$
$= -1000 \times 5/10$
$= -500$ N

$$\text{Area of cross section, } A = (0.2 \times 2) + (0.3 \times 1) = 0.7 \text{ m}^2$$

Centroid of section from bottom,

$$Y_c = ((0.3 \times 0.5) + (0.4 \times 1.1))/0.7 = 0.842857 \text{ m}$$

Moment of inertia about beam centroid,

$$I_c = I_{\text{top plate}} + I_{\text{rectangular beam}}$$
$$= \left[(1.1 - 0.8429)^2(0.4) + \left(2 \times 0.2^3/12\right)\right] + \left[(0.8429 - 0.1)^2(0.3) + \left(0.3 \times 1^3\right)/12\right]$$
$$= 0.0880 \text{ m}^4$$

The deflection at center of beam under point load for simply supported beam [11]:

$$Y = PL^3/48EI_c$$
$$= \left(1000 \times 10^3\right)/\left(48 \times 27386 \times 10^6 \times 0.0880\right)$$
$$= 0.0086424 \text{ mm}$$

The shear force and bending moment diagrams for hand calculation are shown in Fig. 7.

The bending moment and shear force obtained from MATLAB are tabulated in Table 2, and bending moment diagram, shear force diagram, and deflection curve are shown in Fig. 8.

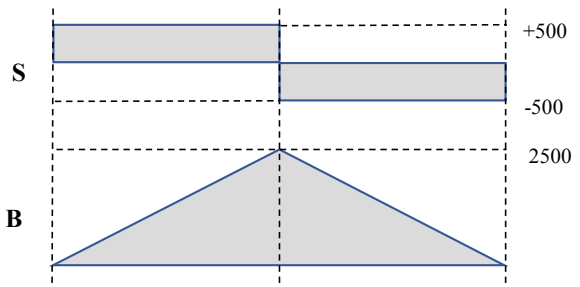

Fig. 7 Shear force (SF) diagram and bending moment (BM) diagram for beam

Table 2 Deflection results for validation of modeling

Resultants	Hand calculation	MATLAB
Bending moment	2500 Nm	2462.9 Nm
Shear force	500 N	495.67 N
Deflection	0.0086424 mm	0.00863918 mm

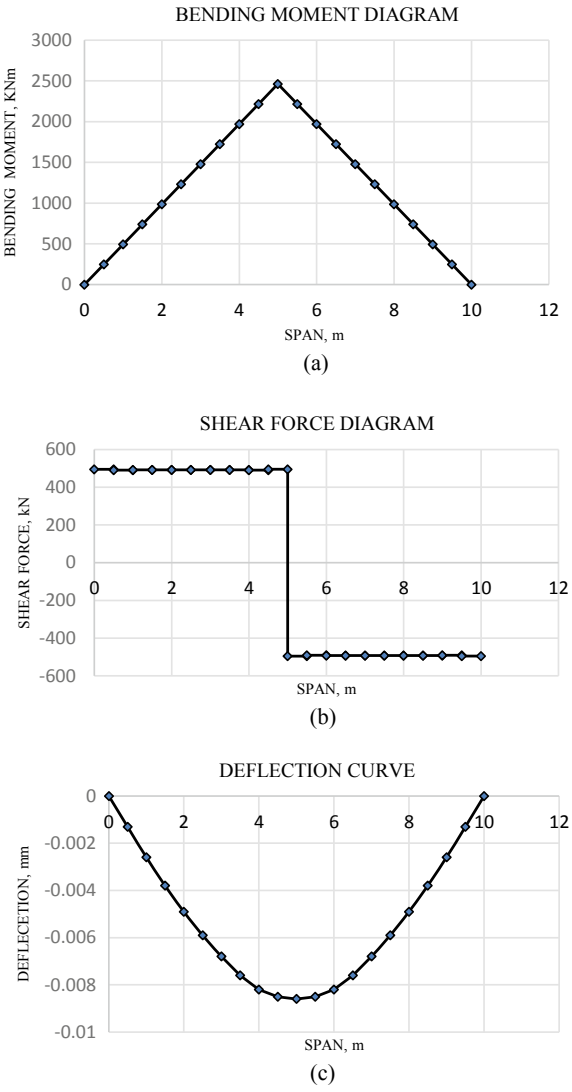

Fig. 8 FE results. **a** Bending moment diagram. **b** Shear force diagram. **c** Deflection curve

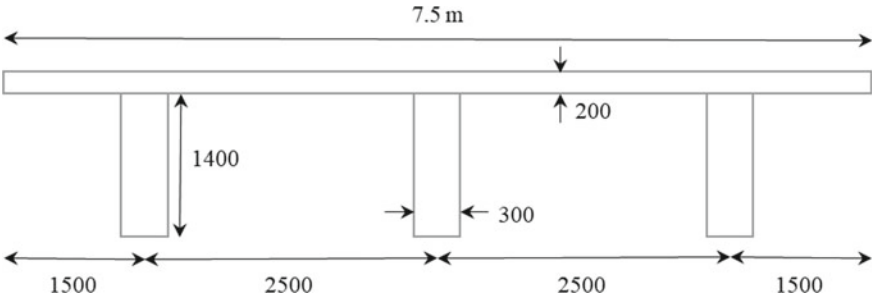

Fig. 9 Cross section of bridge deck

It is observed that the deflection obtained using MATLAB is accurately matched with deflection by hand calculations. MATLAB bending moment and shear force results are also in good agreement with result by hand calculations with only 1.484 and 0.866% differences.

5 Model Specifications

A simply supported bridge deck slab has three longitudinal girders having a span length of 16 m and carriageway width of 7.5 m as shown in Fig. 9. The width and depth of longitudinal girders is 0.3 m and 1.4 m, respectively. The center to center spacing between longitudinal girders is 2.5 m, and the cantilever portion is 1.5 m from the center of the outer girder. All cross girders and diaphragms are having same dimensions as longitudinal girders and are extended to full depth of longitudinal girders. M30 grade of concrete mix is taken. (Dead load is ignored.)

Poisson's ratio, = 0.2 (as per clause B3.1, Annexure B-3, IRC 112:2011) [5]

Case 1: Bridge deck with three longitudinal girders, diaphragms at both end, and 3 cross girders at equal spacing as shown in Fig. 10.

Case 2: Bridge deck with three longitudinal girders, diaphragms at both end, and 1 cross girder at center as shown in Fig. 11.

Case 3: Bridge deck with three longitudinal girders, diaphragms at both ends, and no cross girder as shown in Fig. 12.

6 Results

All the results are tabulated in Table 3, and shear force, bending moment, and deflection curves are shown in Figs. 13, 14, 15, and 16 which are generated by finite element analysis of simply supported bridge deck using a MATLAB programming code developed by the author.

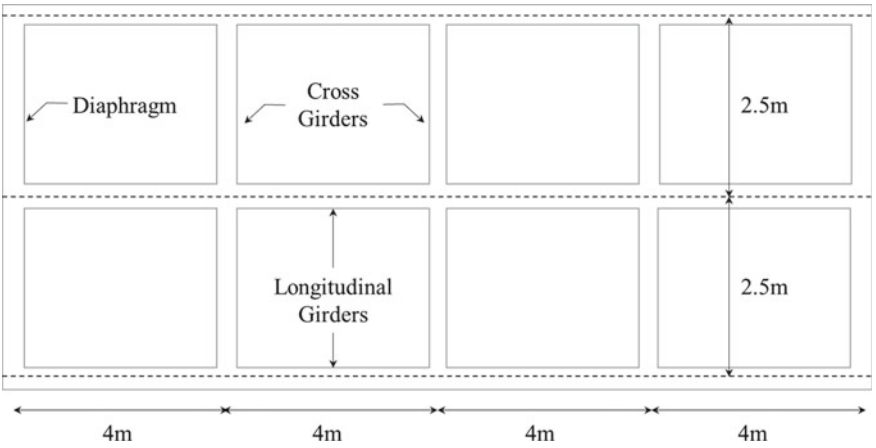

Fig. 10 Top view of bridge deck girder portion Case 1

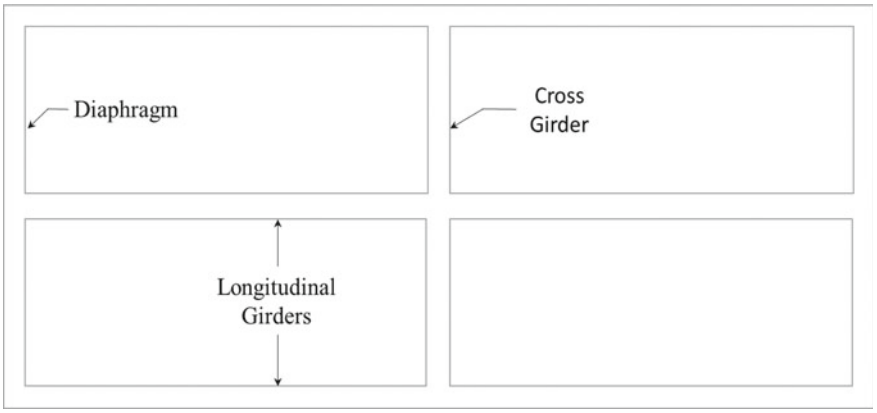

Fig. 11 Top view of bridge deck girder portion Case 2

7 Conclusions

In this paper, a T-beam deck slab bridge is modeled using the finite element. From the above results and plots, the following conclusions have been drawn:

1. Inner girder bending moments are lesser than outer girder when three longitudinal girders were considered.
2. The bending moment and deflections reduce with increase in number of cross girders. In the demonstration example, it was found that when a single cross girder in deck was provided.

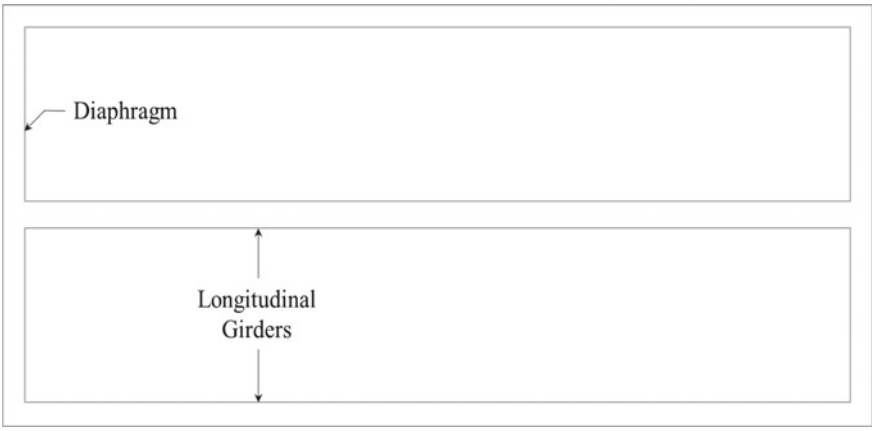

Fig. 12 Top view of bridge deck girder portion Case 3

Table 3 Maximum bending moment, shear force, and deflection in longitudinal girder for live load analysis of bridge deck due to Class 70R as per IRC 6: 2016

Case	Maximum bending moment (kNm)		Maximum shear force (kN)	Maximum deflection (mm)
	Outer	Inner		
Case 1	814.32	795.31	259.24	3.749
Case 2	861.07	772.12	282.68	3.81
Case 3	1067.4	940.2	324.34	4.739

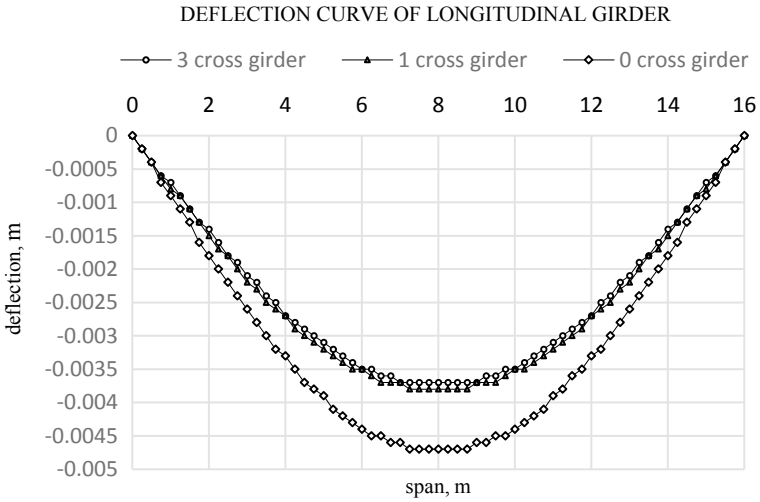

Fig. 13 Deflection of longitudinal girder for live load analysis

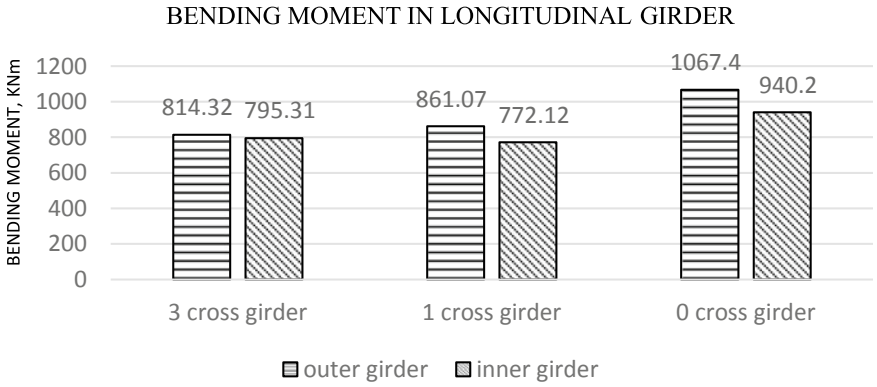

Fig. 14 Live load bending moments in longitudinal girders

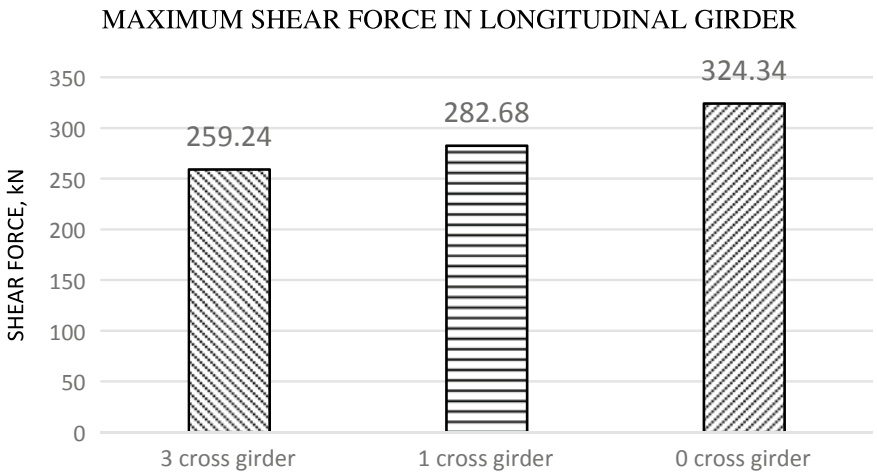

Fig. 15 Live load shear forces in longitudinal girders

3. That the maximum deflection at center was reduced by approximately 20%. While introducing 3 cross girders, deflections were reduced by approximately 21%.
4. That the maximum bending moment at center was reduced by approximately 19.33%. While introducing 3 cross girders, bending moment was reduced by approximately 24%.
5. That the maximum shear force was reduced by approximately 13%. While introducing 3 cross girders, shear force was reduced by approximately 21%.

Overall, it has been found that the introduction of cross girders has huge effect on bending moment and deflections of longitudinal girders. Cross girders play very crucial role in making the bridge superstructure economical.

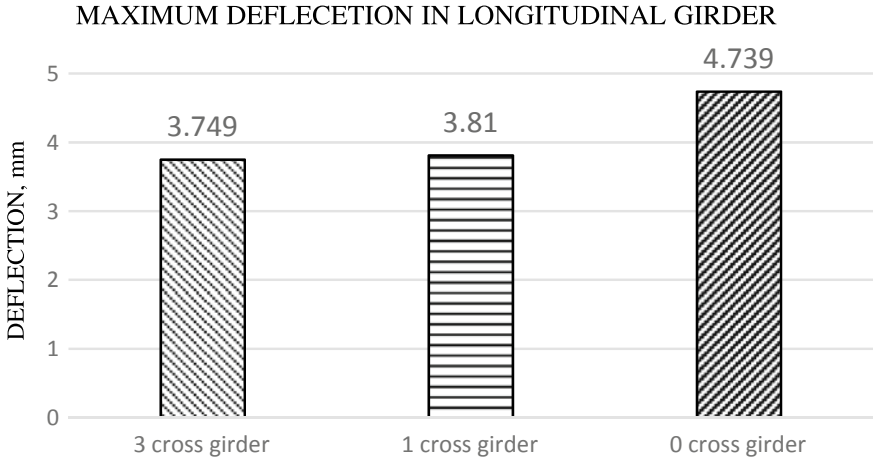

Fig. 16 Live load deflections in longitudinal girders for 3 cross girders, 1 cross girder, and 0 cross girder cases

References

1. Adams A, Galindez N, Hopper T, Murphy T, Ritchie P, Storlie V, Weisman J (2019) Manual for refined analysis in bridge design and evaluation (No. FHWA-HIF-18–046)
2. Ciesielczyk K, Szumigała M, Ścigałło J (2017) The numerical analysis of the effective flange width in T-section reinforced concrete beams. Procedia Eng 172:178–185
3. Fu CC, Wang S (2014) Computational analysis and design of bridge structures. CRC Press
4. IRC: 6-2016. Standard specifications and code of practice for road bridges section: II loads and load combinations
5. IRC:112-2011. Code of practice for concrete road bridges
6. Logan DL (2017) A first course in the finite element method. Cengage Learning
7. Oñate E (2013) Structural analysis with the finite element method. Linear statics: volume 2: Beams, plates and shells. Springer Science & Business Media
8. Reis AJ, Pedro JJO (2019) Bridge design: concepts and analysis. Wiley
9. Rombach GA (2011) Finite-element design of concrete structures: practical problems and their solution. Thomas Telford
10. Szilard R (2004) Theories and applications of plate analysis: classical, numerical and engineering methods. Wiley
11. Timoshenko S, Goodier J (1970) Theory of elasticity

Flexural Strengthening of Steel Structures with Fiber-Reinforced Polymers and Analysis Using ANSYS

Prabhudeva Gunthati and Mohit Jaiswal

Abstract Fiber-reinforced polymer has different material properties like higher strength, corrosion-resistant properties, and good durability. Fiber-reinforced polymer also has ability to restore decreased capacity of deteriorated structures. Moreover, most of the research has been conducted regarding applications of composites in concrete structures when it is compared to steel structures. It is said that tensile Young's modulus is lower than steel. Durability can be increased by wrapping the FRPs externally, thereby reducing the stresses of steel beam. The current research proposed the use of a new high modulus carbon fiber-reinforced polymer for strengthening of steel structures by applying laminates externally to the bottom flange of beam. Finite element modeling has been used for analysis to suggest some design guidelines. The experimental results obtained confirmed the effective enhancement in flexural capacity.

Keywords FE modeling · Flexural capacity · High modulus · Strengthening · CFRP

1 Introduction

For few years, structural strengthening has shown increased demand, due to decrease in cross section from corrosion formation and/or changes of the demand or certain uses of a structure. Several methods of strengthening of steel structures have few drawbacks such as machine requirements for erection, their behavior to fatigue including the prevention of corrosion. Fiber-reinforced polymer has different material properties like higher strength, corrosion-resistant properties, and good durability. Fiber-reinforced polymer also has ability to restore decreased capacity of deteriorated structures. The applications of CFRP are aerospace parts and marine structures, and the materials have expanded to wood, masonry, steel/concrete composite structures, and so on. Compared to the RC structures, there is less research conducted in the steel

P. Gunthati (✉) · M. Jaiswal
NIT Raipur, Raipur, CG, India
e-mail: madhuraja1996@gmail.com

© Springer Nature Singapore Pte Ltd. 2021

K. K. Pathak et al. (eds.), *Recent Trends in Civil Engineering*, Lecture Notes in Civil Engineering 77, https://doi.org/10.1007/978-981-15-5195-6_21

structure areas due to its lower modulus of elasticity compared to the steel. Later on, the new type of carbon fiber came into existence having elastic modulus higher than the steel. Also, the thickness should be considered in higher quantity when lower tensile modulus CFRP is preferred. Durability can be increased by wrapping the FRPs externally, thereby reducing the stresses in control beam.

The laminates of FRP are manufactured by pultrusion process or by wet layup process. There are different types of fiber based on material. Among them, carbon fiber has high strength and has brittle failure, and glass fiber has less strength compared to CFRP. So, glass fibers will be used while in case of ductility requirements. In this paper, both types of fibers are used to find the difference in their effects of enhancements. Some types of failures that govern the load capacity of fibers such as [8], which include: (a) in-plane bending failure (i.e., CFRP failure, concrete crushing); (b) lateral buckling; (c) debonding near the plate end (i.e., plate-end debonding); and (d) debonding far from the plate ends occurred due to cracks or concentrated yield in the steel beam like intermediate debonding. And the other failures are local buckling of compression flange and local buckling. In most of the cases, the common failure that has been seen is debonding of fibers. The current research is proposed by using a new high modulus CFRP for steel strengthening by applying laminates externally to the bottom flange of beam. Finite element modeling has been used for analysis to suggest some design guidelines. The experimental results obtained confirmed the effective enhancement in flexural capacity.

2 Research Background

Kamruzzaman et al. [3] the study has a discussion on research so far regarding fatigue response of FRP-strengthened steel structures. It was also included with research on techniques of surface treatment, adhesive curing, and support condition under cyclic loading besides fatigue behavior, crack propagation, and failure modes with FE modeling of the steel bridge girders and structural elements. It was observed that initial crack and its rate of growth has been reduced and that improves the fatigue life. In this study, the strips are anchored at the end so as to lower the local shear stress and peeling stress in between the interface [3].

Shaat et al. [5] paper, the effects of thicker strips and limitations while strengthening the structural elements are discussed. It was suggested that the thick strips must be avoided to avoid the failures on bonding. The techniques will be more suitable if the lateral supports have been given as in composite sections. Also, the prestressed CFRP plates had been applied in retrofitting of steel structural elements and found good response of fatigue. Epoxy must be applied between the carbon fiber and steel as there may be an issue of galvanic corrosion [5].

Narmashiri et al. [4] paper deals with numerical and experimental modeling of the composites like Carbon Fiber-Reinforced Polymer (CFRP), analysis on its failure, and structural response of the CFRP flexural strengthened steel I-beams. Some of the failure modes have been studied so as to avoid the failures in real practice.

Unstrengthened and 12 strengthened beams of different models based on the type of fiber and length are analyzed. A static ramped load is applied in the four-point experiment bending test. ANSYS FEM package is adopted for the simulation of the above performed tests in which the static non-linear analysis on 3D beam modeling is carried out. The outcomes are like the CFRP failure modes used in flexural strengthening of steel I-beams which consist of below point load splitting (BS), below point load debonding (BD), End Delamination (EDL), and End Debonding (ED). The strengthened beams show the varying behavior based on the specified strengthening parameters [4].

Teng et al. [7] paper provides information about the approach of FE modeling in predicting the bond failures especially on plate-end debonding. The behavior of interface will be depicted by introducing cohesive law into this approach. Mode 1 and 2 are the two different behaviors which depend on the normal stress and shear stress, and both modes will represent the bilinear traction–separation criteria. This approach has considered mixed modes cohesion law which performs under both Mode 1 and 2 loadings. Damage initiation will be defined by the quadratic strength criteria and the damage evolution based on the linear fracture energy criteria. Some of the experimental data done by previous researchers are considered to match the FE results which are found to be in good agreement. Using the proposed FE approach, the behavior of CFRP-strengthened steel beams is obtained, which indicates: (1) when the failure is governed due to plate-end debonding, the use of a CFRP plate with a higher elastic modulus and/or a larger thickness may lead to a lower ultimate load because plate-end debonding may then occur earlier; (2) plate-end debonding is likely to occur when a short CFRP plate is used, as anticipated; and (3) the failure mode might be changed to intermediate debonding or other failure modes such as compression flange when the longer plate is applied [7].

Altaee et al. [1] have done the study on web openings in the steel beams that lower the shear and flexural capacity. This paper deals with how the externally bonded CFRP played a role in strengthening of beams. Also, numerical modeling has been carried out on strengthened and unstrengthened beams which shows 7% increment in the shear strength with one layered ply of fiber on web of steel beam [1].

Teng et al. [6] have dealt with the critical part of the FRP strengthening and the study on types of adhesives, adhesive bonding, bond behavior, fatigue strengthening, retrofitting of thin-walled structures against local buckling, and strengthening of hollow or concrete-filled steel tubes through external FRP confining [6].

Shaat et al. [5] had used new CFRP of high modulus of elasticity in the increment of the strength of steel structures including the research on selection of resin in the process of wet layup of CFRP sheets. Some tests on monopole towers have shown 25% increment in stiffness in the range of elasticity compared to unstrengthened tower. They also did strengthen the composite beam like steel–concrete beam using different techniques.

Zhang and Tang [8] had dealt with the interfacial stresses prediction that governs the failure modes of debonding between the contact and target surfaces. This complete investigation had been done in finite element approach. They have mainly worked on simply supported beam elements with the applied UDL load as a wide research case.

In this study, five different FE models have been used assuming few things for deflections of beam, plate, and adhesive. These adopted finite models had been compared with one another and also with few analyzed outcomes at some sophisticated levels. It was confirmed that few assumptions had shown some impact on the stresses at interface and this indicated that the model combination of beam-spring-beam is not so complex which can be used in prediction of stresses at interface and failure due to debonding even in the complex structures like bonded plates. To determine the flexibility of beam-spring-beam model, the stresses at interface have been mentioned and detailed on the complex structural members like flat surface panel and curved surface panel. The outcomes will give us a valuable understanding about the capacity of the members strengthened [8].

Still, there exist some uncertainties regarding the long range response of this application; also this will bring clarification over the bond strength in composites and steel plate which is a critical part that governs the response. Another field in which the research should be carried out is the utilization of fiber-reinforced polymers on the steel with its impact under the water.

3 Modeling

The Steel beam is analyzed using FEM package ANSYS for simulation of strengthening of beams using fiber-reinforced polymers. The aim of finite element analysis is to create the behavior of the reality of engineering. This will lead to an accuracy of the analysis based on the element size used. These models constitute nodes, real constants, elements, material properties, boundary conditions, and the other features which help in representing the reality. ANSYS has a terminology in which the model will be generated by the creation of nodes and elements representing the volume and its connectivity of the real system.

In this FE modeling, the steel beam (I section) has been modeled and analyzed using non-linear static structural analysis. The elements are predefined in the FEM package among which the SHELL181 is used for Steel beam. This element can be used for analysis of thin and thick shell structures, and it has four nodes. Each node has six degrees of freedom, i.e., both translation and rotations in x, y, and z axes. Mostly, SHELL181 is chosen for layered applications of simulating composite models. In modeling composites, it works under Mindlin–Reissner shell theory which is also said to be first order shear deformation theory regarding the accuracy.

3.1 Cohesive Zone Modeling

To simulate the debonding of a thin plate (FRP), cohesive zone modeling can be adopted in the traction–separation behavior of interface. This tool is capable of interface delamination and debonding while the interface is a bonded contact using several

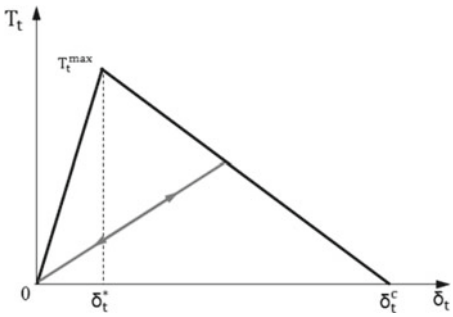

Fig. 1 Mode II bilinear CZM Law

contact algorithm methods. The following contact elements support debonding: CONTA171, CONTA172, CONTA173, CONTA174, CONTA175, CONTA176, and CONTA177.

In CZM, the inputs are the normal traction separation, shear separation, and maximum interfacial stress as the commands. Next step is to create the interface elements between steel beam and FRP layer with the suitable mesh size. As the debonding will be tangential, Mode II bilinear CZM law is considered. The Mode II-dominated bilinear CZM model has an assumption that the displacement jump is the factor that dominates the material separation at an interface, as shown in Fig. 1. The relation between tangential cohesive traction T_t and tangential displacement jump δ_t can be expressed as $T_t = K_t \delta_t (1 - D_t)$.

where T_t = Tangential cohesive traction.

δ_t = Tangential displacement jump.

D_t = Damage parameter.

K_t = Tangential cohesive stiffness.

3.2 Contact

In this modeling, we have used TARGE170 and CONTA174 to make an interface between the steel surface of bottom flange and FRP sheet. The behavior of contact is to be bonded (coefficient of friction being '0'). CONTA174 has some key options to be changed in shell–shell assembly such as contact detection and contact formulation theory. Among augmented Lagrange, penalty method, and Multi-point Constraint (MPC) method, multi-point constraint is chosen since the behavior of contact is bonded. It is a direct, efficient way of connecting surfaces of contact regions which are bonded. Large deformation effects are supported with MPC-based bonded contact. This method will support "nodes from contact surface" or "nodes to target surface". And TARGE170 should be modified to shell–shell assembly option.

3.3 Validation

Mesh Convergence. Mesh Convergence study is made to determine the best suited element size for the used shell element. Big element size is showing the large difference between the results compared to minimum element size. This larger difference is continued till the element size of 20 mm, and later, the minor difference in results indicates the mesh convergence, see Fig. 2. Hence, the element size of 20 mm has been chosen for the rest of the analysis.

Experimental Problem. The simply supported steel beam which was investigated by [2] has a total length of 1.2 m (having 1.1 m clear span length between the end supports), and a cross section of beam being 127 × 76 × 13UKB, the dimensions, and the boundary conditions of the steel beam are shown in Fig. 3. Grade 275 steel has been used with a tensile elastic modulus of 205 GPa. Given CFRP plates have a thickness of 3 mm, a width of 76 mm, a length of 500 mm, and an elastic modulus in the fiber direction of 212 GPa. Two 4 mm thick steel plate stiffeners were welded to each beam; one on each side of the web and mid-span to prevent the premature flange and web buckling.

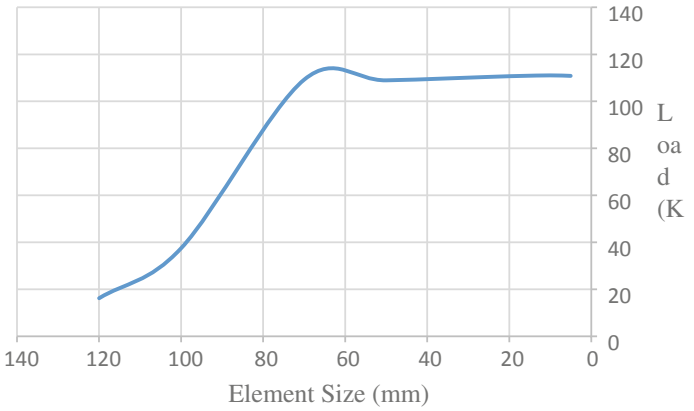

Fig. 2 Mesh convergence plot

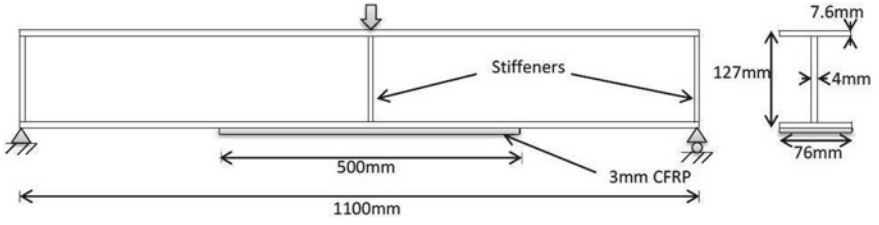

Fig. 3 Steel beam bending test (Strengthened bottom flange with CFRP) [1]

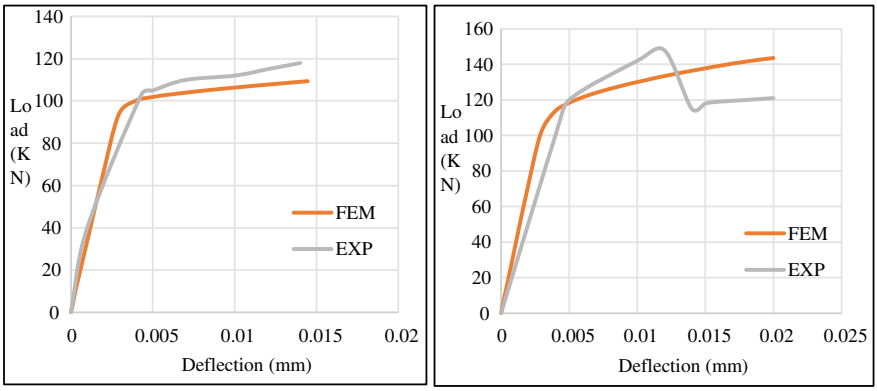

(a) Control beam (b) Strengthened Beam

Fig. 4 Load versus Deflection curve of (**a**) and (**b**)

For conducting the validation test, the experimental test and its results have been taken from the paper [7] and used for comparison. The below graphs show the comparison of experimental and FE modeling in ANSYS which indicates that the FE results are in good agreement with the experimental results. But there is some difference of 5% between them as shown in Fig. 4a and b. This will occur normally due to some reasons which effect the simulation in the software, or in rare cases, the experimental analysis may have minor errors while testing the specimen. Considering the above, the analysis method is further utilized for all models.

Materials Adopted in This Study. In order to enhance the strength of the steel, some kinds of FRP are used in this study like carbon and glass FRP. Among them, carbon fiber considered is of two types that vary in the properties based on their elastic modulus and the fabrication such as unidirectional and woven fibers. The Properties have been taken from the engineering data of ANSYS workbench as given in Table 1.

4 Results and Discussions

After analyzing the steel beam with pinned support at one end and roller support at other end under nodal displacement load as concentrated load, the following tables are the results obtained which indicates the difference of load capacity. When one layer is applied to the bottom flange of thickness 3 mm, it is found that the difference of effect of CFRP and GFRP is 12.5%. So, it is obvious that CFRP is preferred to GFRP. Unidirectional CFRP is providing more strength at 0° orientation compared to woven CFRP and whereas the woven fibers are dominating the others in 45° orientation, see Table 2. When unidirectional is to be used, prepreg CFRP is better than the normal and not preferable compared to high modulus carbon fiber. And the observation says

Table 1 Properties of different types of FRP used in this study

Properties	Epoxy carbon prepreg (Unidirectional)	Epoxy carbon high modulus (UD)	Epoxy carbon woven	Epoxy S-glass unidirectional (UD)
Density (kg/m^3)	1600	1540	1420	2000
EX (MPa)	2.12e5	3.5e5	6.1340e4	50,000
EY (MPa)	23,000	9450	6.1340e4	8000
EZ (MPa)	23,000	9450	6900	8000
PRXY	0.2	0.27	0.04	0.3
PRYZ	0.4	0.4	0.3	0.4
PRXZ	0.2	0.27	0.3	0.3
GXY (MPa)	9000	5500	19,500	5000
GYZ (MPa)	8214.3	3900	2700	3846.2
GXZ (MPa)	9000	5500	2700	5000

Table 2 Strength of the control and strengthened beam with one layer

Type of FRP	Orientation	Strength (kN)
Control beam	–	103.7
Epoxy carbon prepreg (Undirectional) (C1)	0	140.9
	90	111
	45	110.6
Epoxy carbon woven (C3)	0	116.4
	90	116.4
	45	137.2
Epoxy carbon high modulus (HM) (C4)	0	151.9
	90	119.2
	45	111.3
Epoxy S-glass UD (GFRP)	0	135.0
	90	121.2
	45	110.74

that nearly 35.8% increment is seen for single-layered normal unidirectional CFRP and 46.5% with high modulus carbon fiber. When the other orientations are taken, the increment is less compared to 0° laminate. If we observe the woven fiber, its alignment is combined in the two opposite directions. In other words, the tensile elastic modulus is being less than the unidirectional fibers. This kind of laminates when used shows good increment with 45° than the other directions, see Fig. 4.

After analyzing the beam externally bonded with different kinds of FRP, the strength and stiffness increment has been observed satisfactory for the zero-degree orientation. As shown in the above graph in Fig. 5, it is better to prefer zero oriented fibers for good results as it needs more load applied on it to reach rupture. Now, the

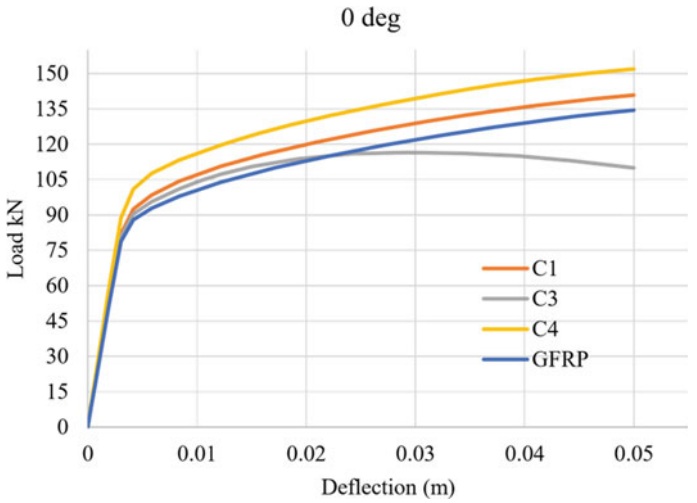

Fig. 5 Load versus Deflection for different fibers with 0° orientation

carbon fiber has higher modulus than a glass fiber that can give its maximum impact over strengthening of a plate or a member.

As shown in Fig. 6, woven fiber is different from unidirectional as it is fabricated in such a way that the strength in two perpendicular directions will be same. So, when it is applied to the member, it supports in resisting the deformations in that two perpendicular directions. And hence, it is observed that the increase of load carrying capacity is 30% with 45 orientation rather than 0 or 90°. This increment is less than the unidirectional fibers because it is less stiff and stronger than the unidirectional fibers in terms of tensile strength. Also, the woven fibers may get bent

Fig. 6 Load versus deflection for 45° orientation

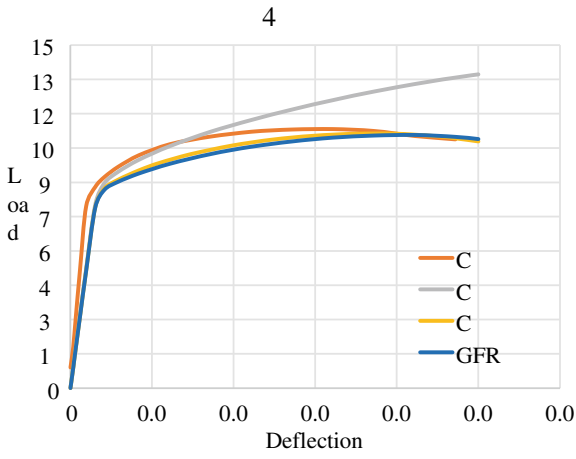

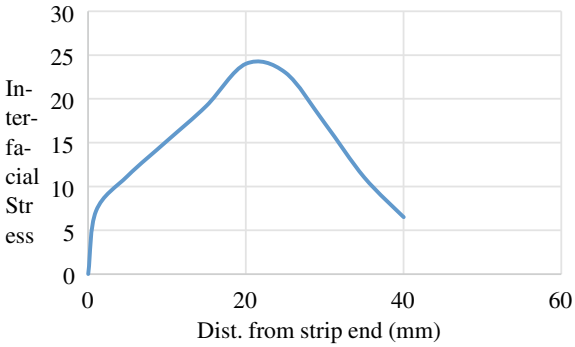

Fig. 7 Interfacial stress of the FRP

or straightened that reduces its stiffness and strength. And therefore, woven fibers could not contribute better than the unidirectional fibers in flexural strengthening.

The critical part in this technique is debonding, which means the failure at the interface between the beam and FRP laminate. This interface is modeled using INTER 205 element and cohesive zone modeling. When the strengthened beam is under loading for supposed bending condition, the laminate bonded to this beam tends to hold it to maintain the bonding. But at certain amount of load, the stresses at the interface will reach its maximum and fail showing the debonding at the plate ends, see Fig. 7. Hence, these interfacial stresses will be high at the plate ends and its middle. This behavior can be represented by a graph as shown in Fig. 8.

5 Conclusions

This paper is being concerned about the FE modeling in ANSYS on flexural strengthening of steel structures using different kinds of fibers and orientations. It discussed the FE approach in simulation of composites in ANSYS software which is useful for various analyses of structures with FRPs. The focus is primarily on finite element modeling and analyses used like non-linear analysis, contact, and debonding, etc.

As the direction of fiber is parallel to the beam (unidirectional), i.e., zero orientation, the increased load carrying capacity is 46.5% for high modulus CFRP and 35.8% for normal CFRP. It is just because of the greater strength of fiber strip in its axial direction (along the length of control beam) which supports the bottom flange of the beam in postponing the failure to a certain extent.

The woven fibers are different from unidirectional as it is fabricated in such a way that the strength in two perpendicular directions will be same. And this kind of alignment provides strength for 45° better than the other orientations. However, it could not contribute better than the unidirectional fibers in case of flexural strengthening as the fibers will experience the reduction in stiffness and strength.

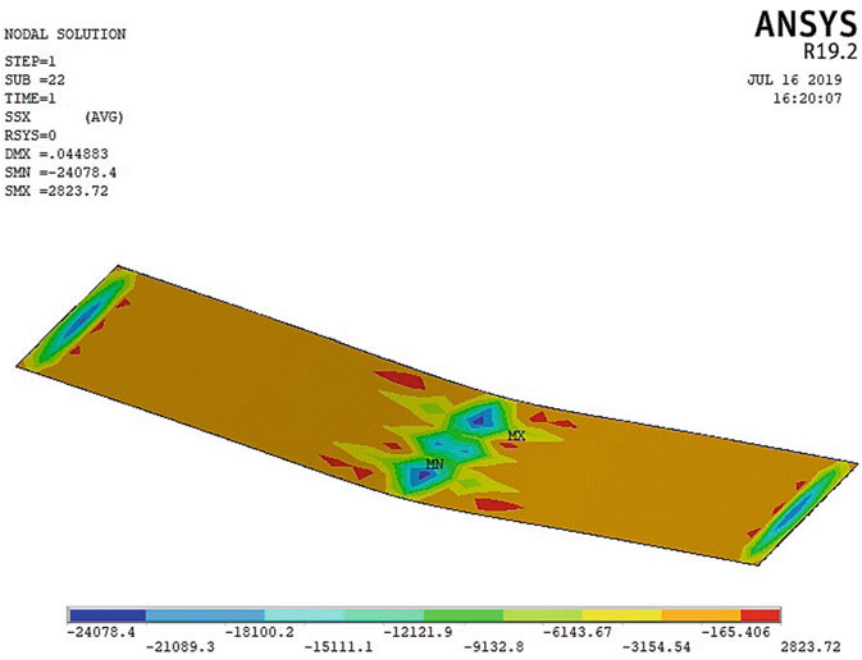

Fig. 8 Interfacial stress of the FRP

The comparison between CFRP and GFRP based on their mechanical properties says that CFRP has higher strength but shows brittle nature. And the difference in effect of CFRP and GFRP is found to be 12.5% being carbon fibers best suitable.

Acknowledgments The author would like to acknowledge the contribution and the support in this research: Dr. Mohit Jaiswal, The National Institute of Raipur, supervisor for guiding me through the concepts and modeling.

References

1. Altaee M, Cunningham L, Gillie M (2006) CFRP strengthening of steel beams with web openings
2. Deng, J, Lee MM (2007) Behaviour under static loading of metallic beams reinforced with a bonded CFRP plate. Composite Structures, 78(2):232–242. Chicago, https://doi.org/10.1016/j.compstruct.2005.09.004
3. Kamruzzaman M, Jumaat MZ, Ramli Sulong NH, Islam ABMS (2014) A review on strengthening steel beams using FRP under fatigue. Sci World J, August 2007. https://doi.org/10.1155/2014/702537
4. Narmashiri K, Ramli Sulong NH, Jumaat MZ (2012) Failure analysis and structural behaviour of CFRP strengthened steel I-beams. Constr Build Mater 30:1–9. https://doi.org/10.1016/j.conbuildmat.2011.11.009

5. Shaat A, Schnerch D, Fam A, Rizkalla S (2004) Retrofit of steel structures using fiber reinforced polymers (FRP): state-of-the-art. In: Transportation Research Board (TRB) 83rd annual meeting, no 919, CD-ROM (04-4063)
6. Teng JG, Yu T, Fernando D (2012) Strengthening of steel structures with fiber-reinforced polymer composites. J Constr Steel Res 78:131–143. https://doi.org/10.1016/j.jcsr.2012.06.011
7. Teng JG, Fernando D, Yu T (2015) Finite element modelling of debonding failures in steel beams flexurally strengthened with CFRP laminates. Eng Struct 86:213–224. https://doi.org/10.1016/j.engstruct.2015.01.003
8. Zhang L, Teng JG (2010) Finite element prediction of interfacial stresses in structural members bonded with a thin plate. Eng Struct 32(2):459–471. https://doi.org/10.1016/j.engstruct.2009.10.008

Study on Sensitivity of PZT Signatures for Damage Detection in RC Columns—A Numerical Study

Venkat Shivaram Yedlapati and Mallika Alapati

Abstract Structural health monitoring using EMI techniques have gained attention of the researchers in the past two decades. Damage detection in RC structural components in the form of cracks is important as it reduces the stiffness of structural members. Also, the occurrence of cracks in the near vicinity of the critical locations is a major issue which has to be addressed at the time of initial crack propagation. PZT sensors are effective in identifying the incipient damages locally. In the present paper, conductance signatures (real part of EMI signatures) are extracted from the smart RC column in healthy and damaged conditions (in the form of cracks) under different frequency ranges, i.e. 0–10 kHz and 0–300 kHz, and found that there is significant change in the conductance signatures by which the damage location and severity can be identified. The method also found to be effective in identifying the incipient damages in a low-frequency range of 0–10 kHz with well-defined changes in the EMI signature patterns.

Keywords EMI technique · PZT sensors · Healthy condition · Damaged condition · Conductance signatures

1 Introduction

The use of PZT sensors has gained lot of importance due to its varied benefits for the past two decades. Detection of the magnitude and the location of damage of the structure at the earliest possible plays a vital role in maintaining the structural health and helps to perform preventive measures. The piezoelectric material can convert the mechanical energy into electric energy and vice versa. They play the dual role as actuator as well as sensor. In the Electro-Mechanical Impedance (EMI) technique, the surface-bonded PZT patch is excited by passing alternating electric

V. S. Yedlapati (✉) · M. Alapati
VNR Vignana Jyothi Institute of Engineering and Technology, Hyderabad, India
e-mail: yvsram16@gmail.com

M. Alapati
e-mail: mallika_a@vnrvjiet.in

© Springer Nature Singapore Pte Ltd. 2021

K. K. Pathak et al. (eds.), *Recent Trends in Civil Engineering*, Lecture Notes in Civil Engineering 77, https://doi.org/10.1007/978-981-15-5195-6_22

voltage transversely. Then, the PZT acts as a thin bar subjected to axial vibrations longitudinally to the direction of the applied voltage. When the signatures of the healthy and damaged structures are compared, there will be deviation of mechanical impedances. Based on piezoelectric constituent relations, 1-D model [1] related to EM admittance signatures is given by

$$Y(\omega) = j\omega \frac{W_a l_a}{h_a}\left(\left(\bar{g}_{33}^{T} - d_{31}^{2}\bar{Y}^{E}\right) + \left(\frac{Z(\omega)}{Z(\omega) + Z_o(\omega)}\right) d_{31}^{2}\bar{Y}^{E}\left(\frac{\tan kl_a}{kl_a}\right)\right) \quad (1)$$

This equation further can be simplified by applying quasi-static approximation [1–3] as

$$Y = \omega \mathrm{j} \frac{W_a l_a}{h_a}\left[-\left(\varepsilon_{33}^{\bar{T}} \frac{Z}{Z + Z_o}\right) d_{32}^{2}\bar{Y}_{22}^{E}\right] \quad (2)$$

From the above equation, it is seen that admittance signatures are dependent on frequency of excitation and the PZT geometric parameters. In this paper, to study the PZT patch sensitivity to identify the location of damage in RC columns, coupled field finite element analysis of EMI technique is adopted.

2 Literature Review

Many researchers have done experimental and numerical studies on vibration-based EMI techniques for damage detection and on sensitivity of the patch for damage identification and classification. Some researchers have carried out simulation studies [4–6] for damage identification using EMI signatures. [7] utilized the dynamic characteristics of a structure for damage detection. Accelerometer sensors are used to locate the damages for various lengths along the length of a column experimentally in the field. Damage assessment due to fatigue loads using embedded PZT sensors in RC columns is studied by [8]. Authors conducted shake table tests on RC column for fatigue time history loading and proposed an expression to assess the remaining life of the structure. RMSD is the measure adopted by many researchers to quantify the damages in structures. However, due to errors in the collection of data, RMSD index sometimes doesn't provide true measure. [9] established relation between volume ratio-based and empirically based RMSD values using EMI technique to assess true damage. In some experimental studies [10], it is proved that EMI techniques using PZT sensors are promising techniques in detecting damages for FRP-retrofitted RC members also. Some authors have done studies on high frequency ranges experimentally and numerically for which the PZT sensors perform in a better manner, [11]. Many authors [1–3, 12–15] have done experimental and numerical studies on the sensitivity capabilities of EMI technique using PZT sensors. Sensitivity of the PZT sensors depends on the geometry and material properties of the host structure. But extensive research needs to be conducted on selection of frequency ranges for

different material types and structures. In the present work, changes in the EMI signatures are qualitatively analysed for the sensitivity diagnosis.

3 Numerical Study

For the present study, a smart cantilever RC column is considered. Coupled field finite element analysis is done on healthy and damaged cases using ANSYS^{TM}. The change in the conductance signatures are examined for a same patch location for all the cases considered (Table 1).

3.1 Geometry

Initially, a healthy cantilever RC column with dimensions 0.3 m × 0.45 m × 3 m is modelled in ANSYS^{TM}. A PZT patch with dimensions 0.01 m × 0.02 m cross section with a thickness of 0.002 m is surface bonded at 0.3 m from the fixed end to the RC column (Fig. 1). Column volume is discretized using solid 65 elements and PZT volume using solid five elements. Two element sizes are used in discretizing the column, i.e. 0.01 × 0.01 and 0.05 × 0.05. PZT is discretized by element size of 0.01 × 0.01. Damage is induced in the form of crack orthogonal to the polarization direction of the patch with 2 mm width and 5 mm depth along one dimension of the column, i.e. 300 mm length. Initially, the distance of the damage is 0.2 m from the patch. The same procedure is carried out for the remaining damage cases as mentioned in Table 1 (Fig. 2).

3.2 Properties

The properties of the RC column and PZT patch are stated in Tables 2, 3 and 4, respectively.

Table 1 Damage cases considered for the patch location at 0.3 m from fixed end

Case no.	1	2	3	4	5	6
Location of crack from fixed end (m)	Healthy column	0.5	1.0	1.5	2.0	2.5

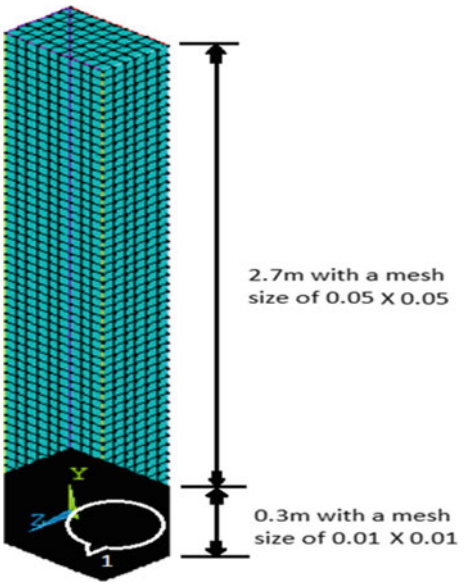

Fig. 1 ANSYS model of an RC column

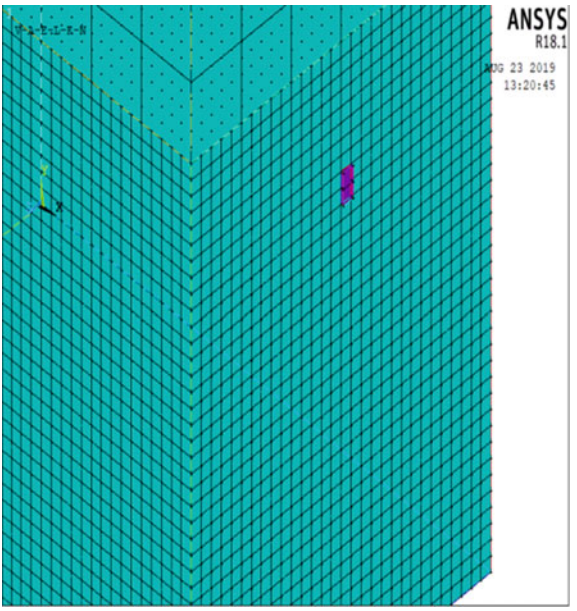

Fig. 2 zoomed view of RC column with a patch at 0.3 m

Table 2 Geometric and Material Properties of the cantilever RC column

Length (m)	Depth (m)	Breadth (m)	Elastic modulus (Pa)	Poisson's Ratio	Density (kg/m^3)
3	0.45	0.3	2.5×10^5	0.15	2500

Table 3 PZT Sensor geometric properties

Length (m)	Depth (m)	Width (m)	Density (kg/m^3)	Damping ratio
0.01	0.002	0.02	7800	0.005

Table 4 PZT Sensor material properties

Anisotropic properties ($\times 10^{-11}$) N/m^2		Relative permittivity/M		Piezoelectric properties ($\times 10^{-10}$) (C/m^2)	
D11	1.5	PERX	1977.4	K_{13}	−2.1
D12	0.45	PERY	1977.4	K_{23}	−2.1
D13	0.57	PERZ	2395.5	K_{33}	5.0
D22	1.5	–	–	K_{42}	5.8
D23	−0.57	–	–	K_{51}	5.8
D33	1.9	–	–	–	–
D44	3.9	–	–	–	–
D55	3.9	–	–	–	–
D66	4.94	–	–	–	–

3.3 Loads and Analysis

The RC Column is excited by applying an alternating voltage of 1 V to the PZT patch. Modal analysis and harmonic analysis are conducted for a frequency range of 0–10 kHz and 0–300 kHz.

4 Discussions of Results

4.1 Modal Analysis

Modal analysis is performed to extract natural frequencies of the smart RC column. The changes in the modal characteristics are almost negligible. As the natural frequency $\omega \alpha (EI/\rho AL^4)^{0.5}$, changes in the flexural rigidity and area of cross section for the damaged cases are not altered significantly resulting in the same values of frequencies.

4.2 Harmonic Analysis

As mentioned in Sect. 3.3, harmonic analysis is conducted, and the results are obtained. For case 1, i.e. smart column in healthy state under 1 V application through

PZT patch excitation for a frequency range of 0–10 kHz with a substep of 50 Hz, it is observed that significant peaks are attained at higher frequencies and in complex combined modes.

It is observed from Fig. 3 that there is significant increase in the peaks of the conductance signatures with the introduction of damage and maximum in the case of crack located in the near vicinity of the patch. As the damage location is varied away from the patch, the peak magnitudes have reduced which is clearly seen in Fig. 8. For a frequency range of 5500–7000 Hz, the changes are very clearly noticed.

A close look of the peaks at a resonant frequency of 6500 Hz shows that the peak amplitudes decrease with the increase in the distance of the damage from the patch as shown in Fig. 4. Close Study of other peaks also revealed the same trend which is not presented here for brevity.

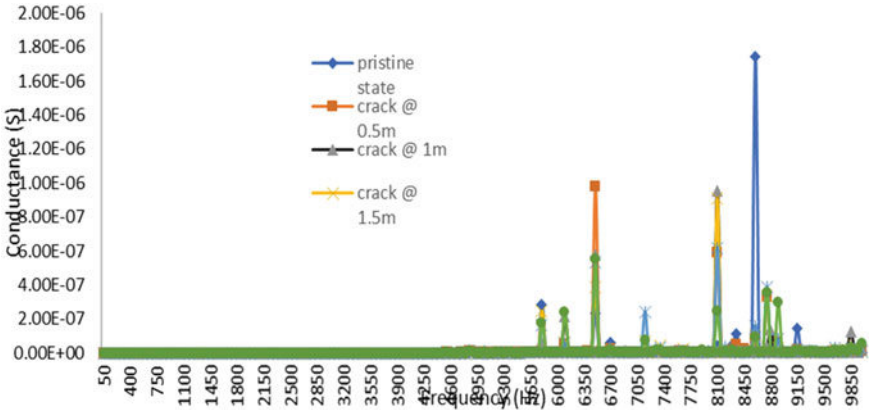

Fig. 3 Conductance signatures of all the cases considered in the RC column

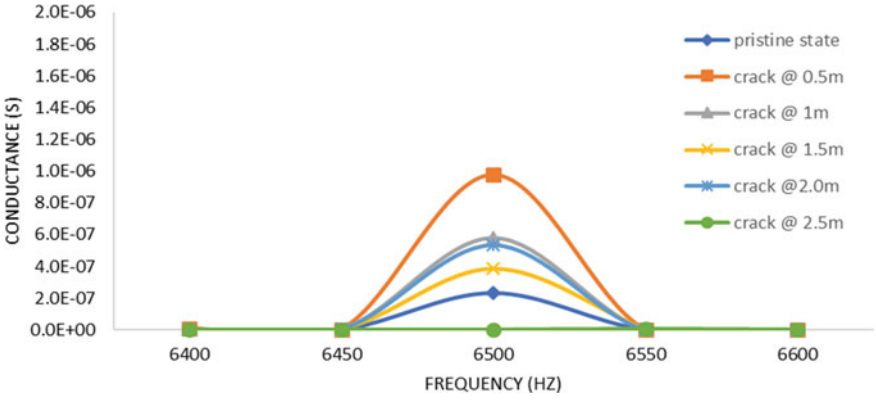

Fig. 4 Conductance signatures of all the damage cases between 5500 and 7000 Hz

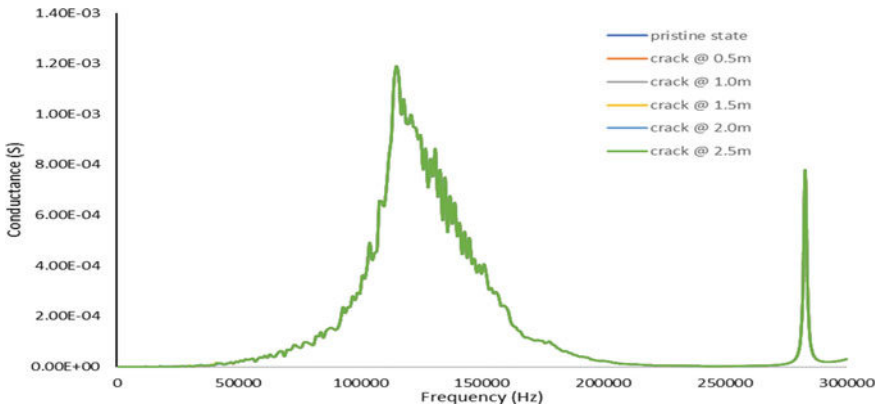

Fig. 5 Conductance signatures of all the cases between 0 and 300 kHz

From the above patterns in the conductance signatures, it is very clearly evident that sensitivity of the patch is effective within a range of 2000 mm from the damage location. However, for a frequency range of 0–10 kHz, change in the EMI signatures is prominently noticed. Authors conducted the studies for high frequency ranges, i.e. 0–300 kHz, for the same cases and found that there is no significant change in the peaks of the conductance signatures of all the damage cases as shown in Fig. 5.

5 Conclusions

In the present study, the sensitivity of the piezoelectric (PZT) patch for various damage distances is studied. The pattern changes in the conductance signatures in terms of peak amplitudes or shifts reveal the damage location and severity in the structural members. It is also observed that the selection of frequency range depends on the size and material properties of the structural members. In the present case, it is found for a frequency range of 5–10 kHz which showed the significant EMI peaks. As the damage location varied away from the patch, the peak amplitudes reduced. It is concluded that brief analysis of EMI signatures will serve as a diagnostic tool for structural health monitoring.

References

1. Liang C, Sun F, Rogers C (1994) Coupled electro-mechanical analysis of adaptive material systems—determination of the actuator power consumption and system energy transfer. J Intell Mater Syst Struct 5(1):12–20
2. Bhalla S (2004) A mechanical impedance approach for structural identification, health monitoring and non-destructive evaluation using piezo-impedance transducers. PhD Thesis,

Nanyang Technological University, Singapore
3. Giurgiutiu V, Zagrai AN (2002) Embedded self-sensing piezoelectric active sensors for on-line structural identification. Trans Am Soc Mech Eng J Vib Acoust 124(1):116–125
4. Naidu ASK, Pittala V (2018) Influence of piezoelectric parameters on admittance diagnostic signals for structural health monitoring: a numerical study. Int J Mater Struct Integr 12(4):316–338
5. Lim YY, Soh CK (2014) Towards more accurate numerical modeling of impedance based high frequency harmonic vibration. Smart Mater Struct 23(3):35017
6. Djemana M, Hrairi M (2016) Modelling and simulation of impedance-based damage monitoring of structures. Int J Simul Modell 15(3):395–408
7. Lyapina A, Shatilov Y (2016) Vibration-based damage detection of the reinforced concrete column. In: International conference on industrial engineering, ICIE, pp 1867–71
8. ul Huq M, Bhalla S, Naqvi T (2017) Fatigue damage assessment of RC column using PZT sensors. Procedia Eng 173:1223–1230
9. Fan S, Zhao S, Qi B, Kong Q et al (2018) Damage evaluation of concrete column under impact load using a piezoelectric-based EMI technique. Sensors 18:1591
10. Tzoura E (2015) Damage detection of reinforced concrete columns retrofitted with FRP jackets by using PZT sensors. Struct Monitor Mainten 2(2):165–180
11. Park G, Sohn H, Farrar CR, Inman DJ (2003) Overview of piezoelectric impedance-based health monitoring and path forward. Shock Vib Digest 35(6):451–463
12. Giurgiutiu V, Zagrai AN (2000) Characterization of piezoelectric wafer active sensors. J Intell Mater Syst Struct 11(12):959–976
13. Sowjanya J, Alapati M (2019) Influence of the patch location on damage detection of smart bar using EMI technique. i-manager's J Civil Eng 9(2):62–68
14. Tseng KK, Naidu ASK (2002) Non-parametric damage detection and characterization using smart Piezoceramic material. Smart Mater Struct 11(3):317–329
15. Park S, Ahmad S, Yun CB, Roh Y (2006) Multiple crack detection of concrete structures using impedance-based structural health monitoring techniques. Exp Mech 46:609–618

Experimental Studies on Flexural Behaviour of RC Beams Strengthened with High Performance Concrete Layer

Aravindkumar Harwalkar and Ashwini S. Ingale

Abstract This paper explains the effectiveness and the use of two different methods of flexural strengthening of reinforced concrete (RC) beams using high performance concrete (HPC) layer. A 50 mm thick layer/jacket of HPC was directly applied to the beam surface in two forms. In one form, strengthening is done only at the tension face. In the other form, U-shape HPC jacketing was done. A total number of six RC beams are tested under flexure. The different test parameters studied are crack pattern, load-deflection curves, first crack load and ultimate load. Results indicated a significant increase in the flexural strength of RC beams in both methods of strengthening. Beams strengthened in the form of U-shape jacketing showed a higher gain in strength.

Keywords High performance concrete · Flexural strengthening · RC beams · Crack pattern · U-Jacketing

1 Introduction

Strengthening of concrete structures is becoming an increased activity in construction works. Strengthening rather than replacing damaged RC members is sometimes a better choice since the strengthening procedure is faster and cost-effective. Available strengthening methods are based on the application of RC jackets of larger thickness. The effect of fibre-reinforced jackets of reduced thickness was studied by Martinola et al. [1]. The application of high performance fibre-reinforced jacket on an RC beam provided an increase in the ultimate load of 2.15 times that of conventional RC beams. Studies carried out by Chalioris and Pourzitidis [2] showed a significant increase in load-carrying capacity when RCC beams failed in shear, and are provided with jacketing of self-compacting concrete. Also the experimental study showed a

A. Harwalkar (✉) · A. S. Ingale
Department of Civil Engineering, PDA College of Engineering, Kalaburagi 585102, Karnataka, India
e-mail: harwalkar_ab@yahoo.co.in

A. S. Ingale
e-mail: ashwiniingale96@gmail.com

© Springer Nature Singapore Pte Ltd. 2021

K. K. Pathak et al. (eds.), *Recent Trends in Civil Engineering*, Lecture Notes in Civil Engineering 77, https://doi.org/10.1007/978-981-15-5195-6_23

slip between the control beam and the jacketing layer. Experimental studies carried out by Yang et al. [3] have shown better performance by RC Beams strengthened with a Layer of Expansive strain-hardening cement-based composite when compared with reference beams. The experiments conducted by Chalioris et al. [4] showed that strengthening of RC beams with reinforced self-compacting concrete layer is an effective method of strengthening. Monir et al. [5] conducted an investigation on the use of RC jackets to enhance the flexural results of RC beams and developed the mathematical model.

2 Scope

The current work compares the effect of two strengthening methods for RC beams subjected to bending. In the first method a high performance concrete (HPC) layer is glued to the tension face while in the second method HPC layer in the form of U-shape is bonded to the RC beams. The ultimate load, initial cracking load and cracking behaviour of strengthened beams are evaluated from the experimental results.

3 Methodology

3.1 Materials

OPC53 grade cement [6] is used throughout the investigation. Natural river sand satisfying the requirement of IS383-1970 [7] is used as fine aggregate for both M20 grade concrete and HPC. Coarse aggregates of nominal size 20 mm confirming to IS 383-1970 [7] are used for M20 grade concrete. Coarse aggregates of nominal size 12.5 mm are used for HPC.

Silica Fume and low calcium fly ash are used as pozzolanic admixtures for HPC. Crimped Steel fibres of 1.5% by weight of cementitious material having an aspect ratio of 80 are used for HPC. Addage Plast PCE840 is used as an ultra superplasticizer for the current study and the dosage of ultra superplasticizer is maintained at 2.5% by weight of cementitious material. MYK Bond Epoxy resin is used for bonding of the HPC layer to RC beams.

Fe 500 grade steel (10 mm and 8 mm diameter bars) conforming to IS 1786-1985 [8] is used as conventional reinforcement for RC beams.

3.2 Mix Proportion

M20 grade concrete: M20 grade concrete was used for casting RC beams. Mix proportions for M20 grade concrete are calculated using the codal [9] procedure. The mix proportions are given in Table 1.

HPC: In the current investigation, M80 grade concrete was used for the HPC layer. The mix design of HPC is carried out as per ACI 211.4R-93 [10] recommendations. Seven trial mixes are used. The final mix proportion which satisfied strength criteria for HPC (>80 MPa) is presented in Table 2.

3.3 Details of Specimens Used in the Work

All the specimen details are given in Table 3. The reinforcement details of reinforced concrete beams are shown in Table 4. The reinforcement design is carried out in order to ensure flexural failure. For two specimens, the HPC layer of 50 mm thickness was glued to the tension face using epoxy resin. For another two sets of specimens, 50 mm thick HPC layer is glued in the form of U-shape jacketing. A typical RC beam with HPC layer on the tension face and U-shape jacketing is shown in Figs. 1 and 2, respectively. Figure 3 represents the typical details of the RC beam.

Table 1 M20 grade concrete mix proportions

Ingredient	Weight in kg/m^3 of concrete
Cement	350
Coarse aggregate	1212.42
Fine aggregate	693.21
Water	197

Table 2 HPC mixture proportion

Material	Weight in kg/m^3 of concrete
Cement	800
Silica fume	150
Fly Ash	50
Fine aggregate	500
Coarse aggregate	730
Water + Ultra superplasticizer	258.65
Steel fibre	15

Table 3 Specimen details

Specimen type	Size of specimen (mm)	Test conducted	Number of specimens
Cubes	150 × 150 × 150	Compressive strength test for conventional concrete	03
Cubes	100 × 100 × 100	Compressive strength test for HPC	21 (seven trials) + 9 for final selected mix (3, 7, 28 days' results)
Plane concrete prism	75 × 100 × 500	(a) Flexural strength of conventional concrete (b) Flexural strength of HPC	03 03
RC beams	1500 × 150 × 230	Flexural strength test for four point loading:	02 02 02

3.4 Determination of Mechanical Properties

Compressive strength. The experimental test setup used for determining the compressive strength is as per the codal [11] provisions. Equation (1) is used for

Fig. 1 RC beam with HPC base layer

Fig. 2 Beam with HPC U-shape jacket (top view and side view)

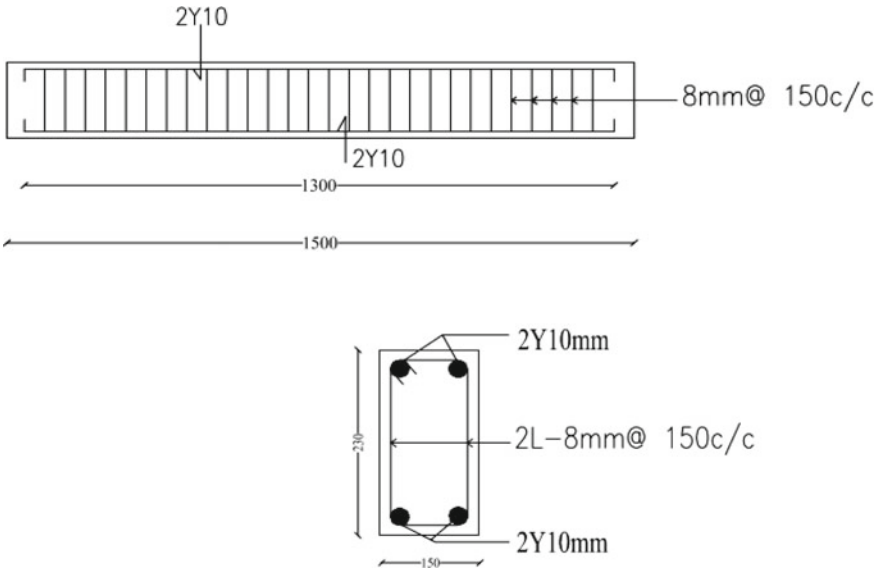

Fig. 3 RC beam details

calculating the cube compressive strength:

$$\text{Cube Compressive strength} = \frac{\text{load at failure}}{\text{area of cross section}} \text{ in N/mm}^2 \tag{1}$$

Bending strength. The bending strength of plain concrete prisms is calculated as per the codal provisions [11]. Equation (2) is used for calculating the bending strength.

$$\text{Bending strength} = \frac{\text{PL}}{\text{bd}^2} \tag{2}$$

P = load at failure
L = c/c distance between the supports
b = width of the prism
d = depth of the prism

Testing of RC beams. The testing of RC beams is done in a servo controlled loading frame of 1000kN capacity. Four-point loading arrangement was used thus creating a pure moment zone in the central one-third portion. The loading frame is equipped with load cell and LVDT for measuring the load and the central deflection, respectively. All the data was recorded through data acquisition system. Figure 4 shows the testing arrangement.

Table 4 Reinforcement Details of Beams

Series	Beam designation	Overall length in mm	Effective span in mm	Reinforcement details
Conventional RC beam	B11	1500	1300	2#10@ top and bottom, 2LVS-8 mm stirrups @150 mm c/c
	B12	1500	1300	2#10@ top and bottom, 2LVS-8 mm stirrups @150 mm c/c
RC beam with 50 mm thick HPC layer on tension face	B21	1500	1300	2#10@ top and bottom, 2LVS-8 mm stirrups @150 mm c/c
	B22	1500	1300	2#10@ top and bottom, 2LVS-8 mm stirrups @150 mm c/c
RC beam with 50 mm thick HPC U-shape jacket	B31	1500	1300	2#10@ top and bottom, 2LVS-8 mm stirrups @150 mm c/c
	B32	1500	1300	2#10@ top and bottom, 2LVS-8 mm stirrups @150 mm c/c

4 Results and Discussion

4.1 Compressive Strength Test

The results of the compressive strength test for M20 grade concrete are tabulated in Table 5 and the strength values for HPC are tabulated in Table 6. The relation of the cube compressive strength with age, up to 28 days for HPC, is shown in Fig. 5. From the results it can be observed that 62.2% of 28-day strength was obtained in 3 days and 79.1% of 28-day strength was obtained in 7 days for HPC. Total crushing type of failure was observed in case of M20 grade concrete cubes while in the case of HPC cubes, it failed mainly due to the development of crack. The typical failure pattern for conventional concrete and HPC cubes is shown in Figs. 6 and 7, respectively.

Fig. 4 Testing arrangement for RC beams

Table 5 28-day cube compressive strength values for M20 grade concrete

Specimen No.	Cube compressive strength N/mm^2	Average cube compressive strength N/mm^2
1	24.85	25.73
2	25.72	
3	26.59	

Table 6 Cube compressive strength values for HPC

Days	Cube compressive strength of concrete N/mm^2			Average cube compressive strength N/mm^2
3 days	54	55.42	55.91	55.11
7 days	69.65	70.14	70.63	70.14
28 days	87.79	88.29	89.76	88.62

4.2 Bending Strength

The 28-day bending strength test values of M20 grade concrete and HPC mix are tabulated in Tables 7 and 8, respectively.

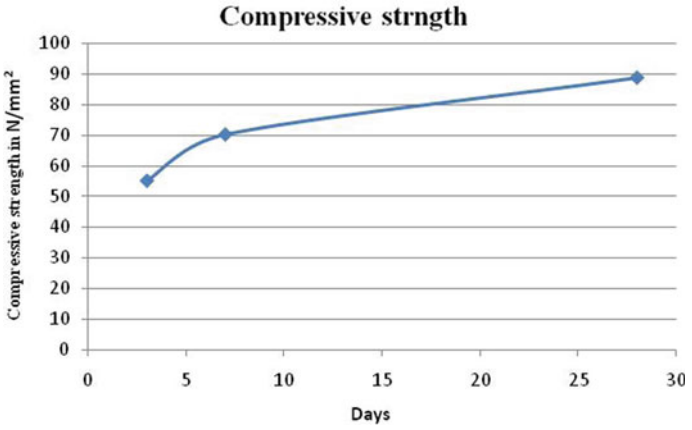

Fig. 5 Compressive strength versus age

Fig. 6 Failure pattern of cube M20 grade

The bending strength of M20 grade concrete is found to be 13% of cube compressive strength whereas the bending strength of HPC is found to be 7.5% of its compressive strength. Typical crack patterns of prisms of M20 grade concrete and HPC are shown in Figs. 8 and 9, respectively. It was observed that the failure of M20 grade concrete prisms is catastrophic whereas in case of failure of the HPC prisms, some three was time lapse for the extension of the crack.

Fig. 7 Failure pattern of HPC cube

Table 7 28-day bending strength values for M20 grade concrete

Specimen No.	28-day Bending strength in N/mm^2	Average bending strength N/mm^2
1	3.92	3.6
2	3.27	
3	3.59	

Table 8 28-day bending strength values for HPC

Specimen No.	28-day Bending strength in N/mm^2	Average bending strength in N/mm^2
1	6.54	6.65
2	6.21	
3	7.19	

4.3 Behaviour of RC Beams

Conventional RC beams. The total applied load versus mid-span deflection curves for conventional RC beams, B11 and B12, is shown in Fig. 10. The average initial crack load was 80KN. The failure of specimen B11 was due to the simultaneous extension of flexure and shear crack. In the other specimen, the failure was due to the extension of flexural crack up to the compression face. The crack widths for both the specimens vary between 2 mm and 4 mm. A typical failure pattern of these beams is shown in Fig. 11.

Fig. 8 Failure pattern of the prism of M20 grade concrete

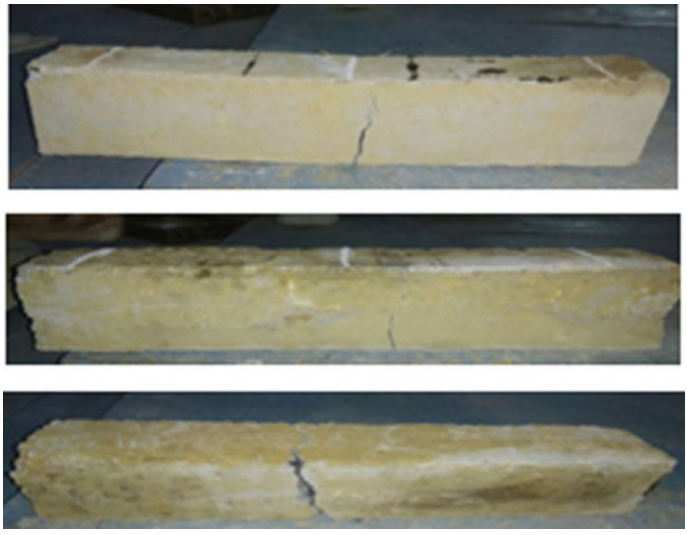

Fig. 9 Failure pattern of HPC prisms

RC Beam with HPC layer at base. The two RC beams (B21 and B22) strengthened with the HPC layer on the tension face exhibited a flexural failure. The load versus deflection curves of the two beams are shown in Fig. 12. The typical crack pattern of beams is shown in Fig. 13. Crack widths varied between 1 and 2 mm.

The first crack is observed on the HPC layer and then on the RC beam surface after traversing a horizontal distance along the interface. The HPC layer had an effect in delaying the growth of crack formation. And the percentage increase in ultimate

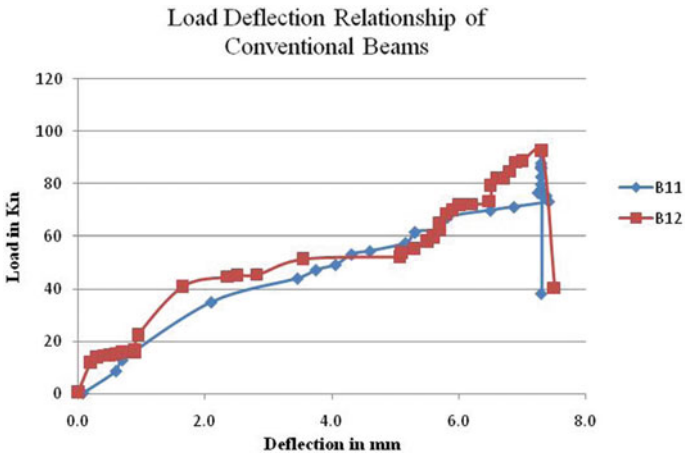

Fig. 10 Load versus deflection of conventional beam series

Fig. 11 Crack pattern for conventional beams

load-carrying capacity is 11.4% when compared with that of conventional beams and the percentage decrease in deflection is 45.9%.

RC Beams with U-Shape HPC jacket. The nature of failure of these beams (B31 and B32) was identical to that of RC beams strengthened on the tension face. Figure 14 represents the load versus deflection variation and the typical crack pattern is shown in Fig. 15.

The first crack load is observed on the HPC side face layer first and debonding of the HPC layer was not observed. In this set of beams, the mode of crack propagation was identical to that of beams B21 and B22. The ultimate load-carrying capacity of these beams is nearly twice the ultimate load value of conventional beams and the

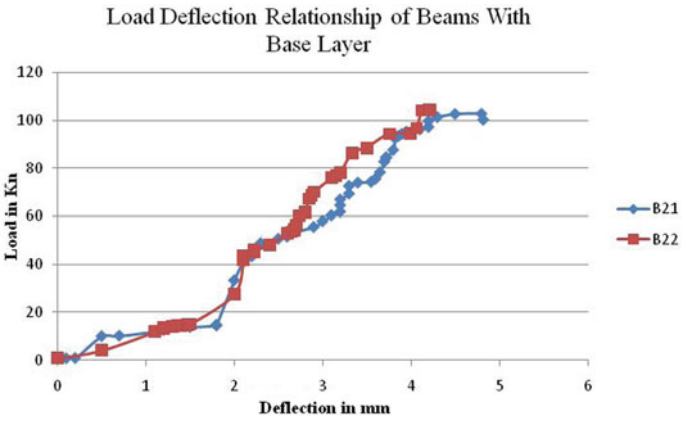

Fig. 12 Load versus deflection of RC beam with base layer series

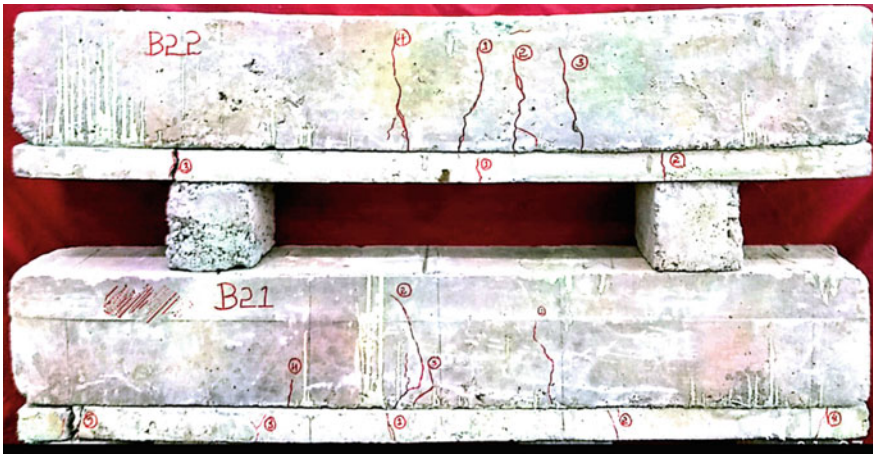

Fig. 13 Crack pattern for RC beam with base layer

percentage decrease in deflection is 67.6% when compared with that of conventional RC beams.

Comparison of behaviour of different RC beams. The values of ultimate load, load at first crack and deflection at ultimate load are presented in Table 9. Figure 16 shows the comparison of the behaviour of conventional reinforced concrete beams with that of strengthened RC beams. The beams with HPC jacket showed a flexural type of failure. The strengthened RC beams B21 and B22 having the same dimensions and strengthening HPC layer exhibited similar behaviour up to failure. Strengthening the

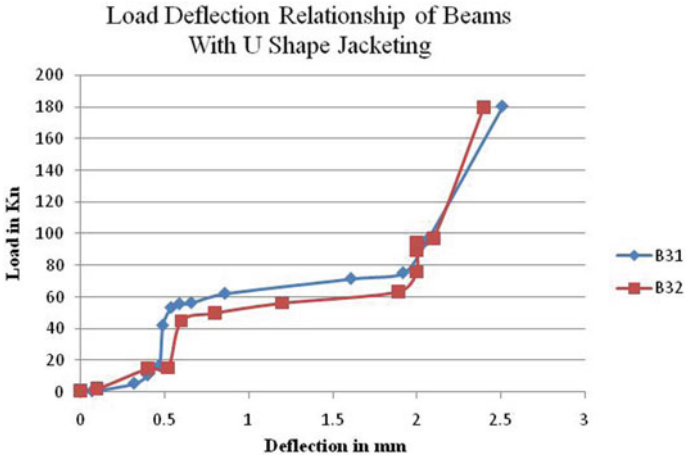

Fig. 14 Load versus deflection of beam with U-shape Jacket series

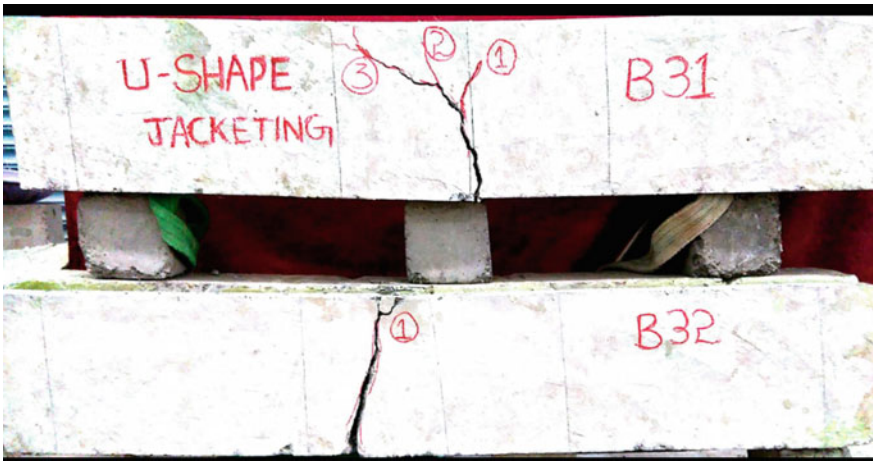

Fig. 15 Crack pattern for RC beam with U-shape jacketing

Table 9 Test Results of RC beams

Beam type	Average[a] First Crack Load (kN)	Average[a] Ultimate load (kN)	Average[a] Deflection (mm)
Convention beam	72.1	92.8	7.4
RC beam with HPC layer on tension side	95.2	103.4	4
RC beam with HPC U-shape jacketing	96.4	180.0	2.4

[a]Average value of two specimens

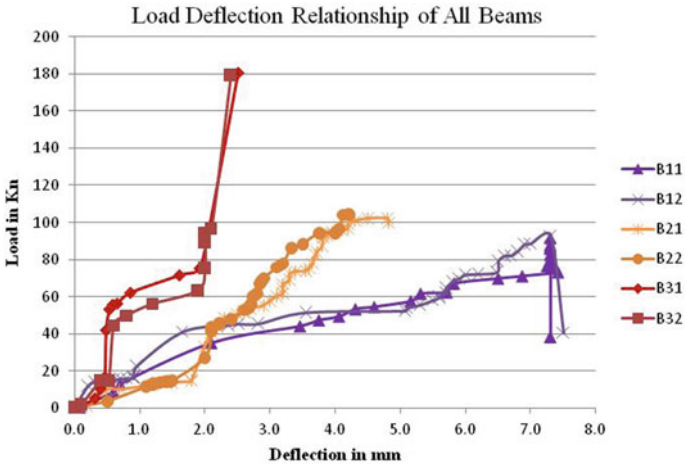

Fig. 16 Load–deflection curves for reinforced concrete beams

HPC layer increased the ultimate load-carrying capacity. The percentage increase in the first crack load for beams with HPC layer on the tension face and for U-type jacketing are 32 and 33.7, respectively. The ultimate load value increased by 94% for U-type jacketing while the percentage increase for beams with the HPC layer on the tension face was 11.4. The proposed techniques showed a decrease in the mid-span deflections at the ultimate load for both types of strengthening techniques thus showing the increase in stiffness values.

5 Conclusions

The experimental investigations have lead to the following conclusions:

1. High range water reducers and pozzolanic admixtures are essential to developing HPC mix having high strength. The HPC layer can be glued to the RC beams using epoxy for achieving monolithic action.
2. Percentage increase in ultimate load-carrying capacity for RC beams with U-shape jacket is 94% and the percentage decrease in deflection is 67.6% when compared with reference RC beam specimens.
3. The ultimate load-carrying capacity of reinforced concrete beams strengthened by the HPC layer on the tension face is 11.4% and the percentage decrease in deflection is 45.9% when compared with the corresponding value of reference RC beams.
4. HPC strengthening helps in delaying the crack formation and propagation.
5. The debonding phenomenon was not observed between the HPC layer and RC beams even up to the ultimate load.

Compliance with Ethical Standards.

- Authors have no conflict of interest.
- The current study did not involve human participants and/or animals.
- Authors hereby inform their consent for the submission of the paper.

References

1. Martinola G, Albertomeda, Plizzari GA, Zilarinaldi (2010) Strengthening and repair of RC beams with fiber reinforced concrete. Cement Concret Composit 32:731–739
2. Chalioris CE, Pourzitidis CN (2012) Rehabilitation of Shear-damaged reinforced concrete beams using self-compacting concrete jacketing. Int Schol Res Netw 2012, Article ID816107, 12 p
3. Yang HJ et al (2012) Flexural performance of reinforced concrete beams with a layer of expansive strain-hardening cement -based composite(SHCC) 15 WCEE LISBOA 2012 (5 p)
4. Chalioris CE et al(2013) Application of a reinforced self-compacting concrete jacket in damaged reinforced concrete beams under monotonic and repeated loading. J Eng 2013, Article ID 912983, 12 p
5. M. Monir Ajan Alhadid and Maged A. Youssef (2015) studied "Strengthening and Repair of Reinforced Concrete Beams Using Concrete Jackets**".**Conference on response of structures under extreme loading (6 pages)
6. IS 12269-1987, Specification for 53 grade ordinary Portland cement, New Delhi
7. IS 383:1970, Specification for coarse and fine aggregates from natural sources for concrete, Bureau of Indian Standard, New Delhi
8. IS 1786-1985, specification for high strength deformed steel bars and wires for concrete reinforcement, Bureau of Indian Standard, New Delhi
9. IS 10262:2009, Recommended guidelines for concrete mix design, Bureau of Indian Standard, New Delhi
10. ACI. Committee. 211 (211-4R-93.) "Guidelines for Selecting Proportions for High strength Concrete with Portland Cement and Fly Ash American concrete Institute, Detroit, Michigan
11. IS 516:1959, Method of test for strength of concrete, Bureau of Indian Standard, New Delhi

Health Monitoring of Civil Structures by Pulse Compression-Based Digital Frequency Modulated Thermography

J. A. Siddiqui and Sachin Patil

Abstract Strengthened solid structures such as reinforced concrete structures (RCS) have been broadly used in structural building due to their ideal properties like high-quality strength, toughness and adaptability. However, due to the presence of steel in the form of rebar in RCS, they are susceptible to premature corrosion which drastically reduces its durability. It is therefore important to detect this corrosion at an early stage to avoid fatal repercussions. However, it is generally not possible to detect this corrosion of rebar just by visual inspection. Active Thermography-based Nondestructive Testing (ATNDT) has emerged as one of the powerful techniques for this purpose and has seen a lot of advancements to improve its efficacy for monitoring of cracks and corrosion in rebar. One such advancement has been the use of Linear Frequency Modulated Thermography (LFMT). However, LFMT has limitations in the form of lower contrast of visibility of defects and depth detection capability. This paper introduces the use of Digital Frequency Modulated Thermography (DFMT) for RCS inspection. The results obtained from the Correlation images and Time Domain Phase Images clearly show the effectiveness of this approach in removing the drawbacks of LFMT for RCS inspection.

Keywords Digital frequency modulated thermograph · Reinforced concrete structures · Active thermograph-based nondestructive testing · Pulse compression correlation technique

1 Introduction

Active Thermography-based Nondestructive testing (ATNDT) has come into the picture as an effective technique for the investigation and assessment of deterioration of rebar in reinforced concrete structures due to its being a very swift, robust,

J. A. Siddiqui (✉) · S. Patil
Medi-Caps University, Indore, India
e-mail: junedsiddiqui5@gmail.com

S. Patil
e-mail: patilsachin4@gmail.com

© Springer Nature Singapore Pte Ltd. 2021

K. K. Pathak et al. (eds.), *Recent Trends in Civil Engineering*, Lecture Notes in Civil Engineering 77, https://doi.org/10.1007/978-981-15-5195-6_24

whole field and non-contact monitoring technique. This technique is very effective in civil engineering where constant inspection of structures is required to keep the danger levels in check. Moreover, since it is a nondestructive testing technique, it preserves the material under observation for future use after its inspection. Furthermore, it is a much more efficient technique as compared to the previously used NDT techniques used for RCS inspection like Ultrasonic testing and X-ray testing which are point-wise techniques and thus require a longer experimentation time. Active Thermography is a process that basically involves the use of an excitation signal in the form of a temperature profile over the object under inspection. This temperature profile deviates from its normal behavior in the presence of anomalies present in the interior of the structure as it changes the thermal properties of the object [1, 2].

For using ATNDT, mainly three different types of techniques namely Pulse Thermography, Lock-in Thermography and Pulse Phase Thermography were predominant in use over the last few years [3–5]. However, these methods have limitations like requirement of high peak power, longer experiment time, repetition, etc. To overcome these drawbacks of conventional thermography techniques, the use of Linear Frequency Modulated Thermography was proposed (LFMT) [6, 7]. However, this technique has limitations in the form of lower contrast of visibility of defects and depth detection capability because of less energy in the signal after its pulse compression. Due to this the corrosion present in rebar at deeper depths cannot be observed clearly.

To overcome this limitation, the use of Digital Frequency Modulated Thermography (DFMT) [8] is proposed which uses a digitalized version of the LFM signal. The advantage of using this technique is that since this signal has high energy after its pulse compression in the central peak, it gives a much better performance in rendering corrosion in rebar at much deeper depths and also with a much higher contrast as compared to the LFM signal. In this paper, a simulation study has been carried out for depicting the effectiveness of the above-proposed technique, i.e., DFMT for RCS inspection using a concrete structure with embedded mild steel (MS) rebar [9] deteriorated along its length utilizing a 3D numerical model of it. However, the main purpose of this study is to compare the DFMT technique with the LFMT technique by imposing the respective heat fluxes on the test material to analyze and compare the obtained maps of temporal thermal profile using Correlation and Time domain phase-based data-processing schemes [10, 11].

2 Theory and Data Analysis

In this work we have utilized two heat stimuli, the first one being LFM [12–14] heat stimulus shown in Fig. 1 which is described mathematically as a function of time as follows:

$$f(t) = Q_0 e^{j2\pi((f_1+kt)t)} \tag{1}$$

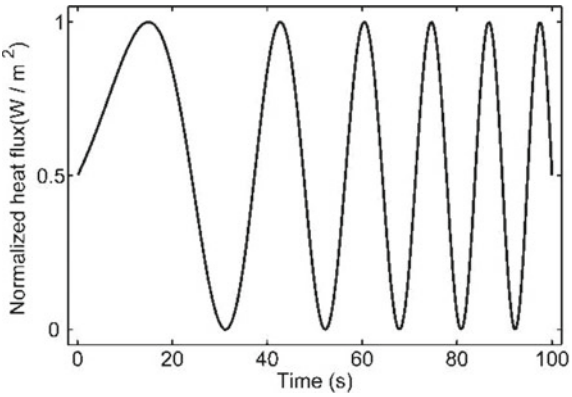

Fig. 1 LFM wave sweep from 0.01 to 0.1 Hz for 100 s

Here, f_1 is the starting base frequency, k is the sweep rate and Q_0 is modulated waveform intensity.

And second heat stimulus is DFM heat stimulus shown in Fig. 2 given by

$$f(t) = Q_0\left(\frac{2}{\pi}\sum_{n=-\infty}^{\infty} -1^n \frac{1}{2n+1} e^{j\varphi}\right) \tag{2}$$

Here,

$$\varphi = 2\pi(2n+1)((f_1 + kt)t) \tag{3}$$

And f_1 is the starting base frequency, k is the sweep rate and Q_0 is modulated waveform intensity.

These heat stimuli propagate in the interior of the test object and contribute toward the temperature deviation on the object surface at locations of an anomaly inside the object. The variation of the temperature response at any anomaly area is given by the

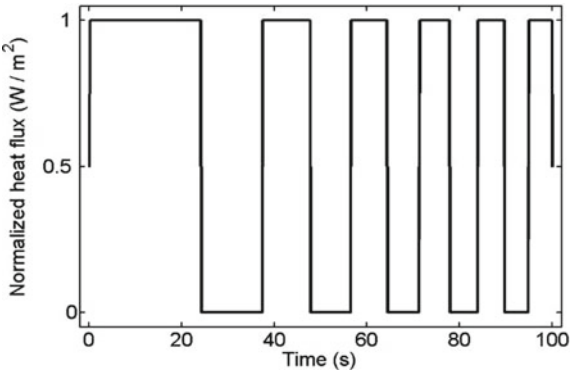

Fig. 2 DFM wave sweep from 0.01 to 0.1 Hz for 100 s

one-dimensional heat diffusion equation. However, in order to solve this equation we have considered that no heat source and heat sink are present inside the test sample. With this assumption, the equation can be given as follows [15]:

$$\frac{\partial^2 T(x,\omega)}{\partial x^2} - \sigma^2 T(x,\omega) = 0 \tag{4}$$

Here,

$$T(x,\omega) = T_1(x,\omega) - T_\infty \tag{5}$$

where $T(x, \omega)$ is the temperature response at a given spatial location x; T_∞ is ambient temperature; $T_1(x, \omega)$ is the Fourier domain temperature distribution for the same location in the presence of ambient temperature.

$$\sigma = \left(\frac{i\omega}{\alpha}\right)^{\frac{1}{2}} = (1+i)\sqrt{\omega/2\alpha} = \frac{(1+i)}{\mu} \tag{6}$$

σ is a complex wave component; which contains ω spectral angular frequencies, α is the thermal diffusivity of the sample and μ is thermal diffusion length.

To solve the one-dimensional equation, two boundary conditions are given below:

$$-k\frac{\partial T(x,\omega)}{\partial x}|_{x=0} = f(\omega) \tag{7}$$

$$-k\frac{\partial T(x,\omega)}{\partial x}|_{x=l} = 0 \tag{8}$$

where k represents the thermal conductivity of the given sample and f(ω) is the imposing heat flux f(t) in the frequency domain.

The acquired solution for the above conditions in the frequency domain for the test sample of thickness 'l' given as

$$T(x,\omega) = \frac{f(\omega)}{k\sigma}\left[\frac{e^{-2\sigma l}e^{\sigma x} + e^{-\sigma x}}{1 - e^{-2\sigma l}}\right] \tag{9}$$

This solution is utilized to obtain the depth penetration of heat flux in the given sample. The captured temporal thermal response R_T (x, τ) is further processed by utilizing Correlation and Time domain hase-based data-processing schemes as illustrated in Fig. 3.

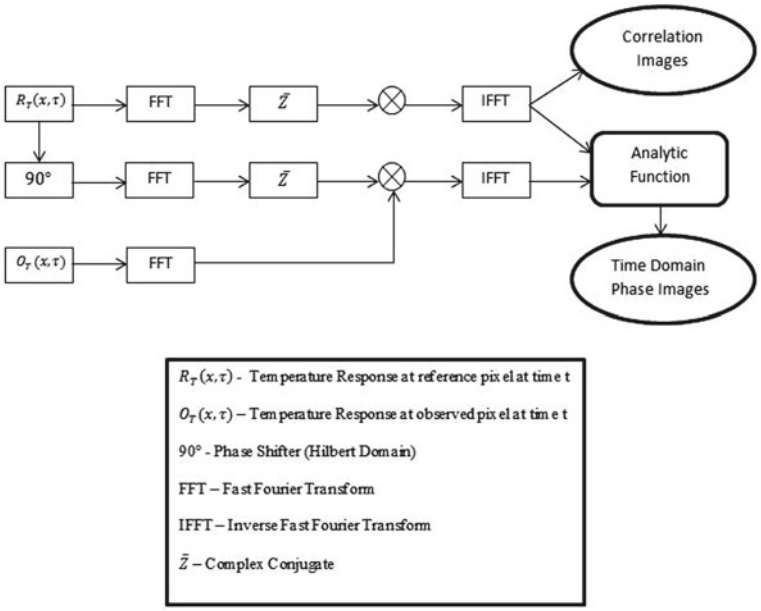

Fig. 3 Schematic of the procedure followed to acquire Time domain phase and Correlation images

2.1 Correlation Coefficient (CC) Image

In order to utilize the advantages of correlation technique in infrared thermography (IRT,) each pixel temperature profile is assumed to be a time series. These patterns include a temporal thermal response corresponding to the offset in excitation and the dynamic response. For acquiring a dynamic response, first the offset is expelled from each time series with the assistance of an appropriate data fitting procedure and then cross-correlation is performed between the temperature time series distributions of the picked reference pixel with the delayed version (time delayed) of the pixel over the sample. Difference in attenuation as well as the delay in temporal temperature responses provide the details about defective and non-defective regions which rely upon the thermal properties of the test sample. This captured temperature distribution can be recovered as follows:

$$\text{Correlation Coefficient}(CC) = IFFT\left\{R_T(x,\omega)^* O_T(x,\omega)\right\} \tag{10}$$

Here, $R_T(x,\omega)^*$ and $O_T(x,\omega)$ are the picked reference response and temporal temperature response at a given area in the frequency domain and '*' represents complex conjugate.

2.2 Time Domain Phase Approach

For implementation, the Fourier transform of temperature profile has been considered and then each observable temporal temperature profile $O_T(x, \omega)$ is correlated with an arbitrarily chosen non-defective temporal temperature profile $R_T(x, \omega)$. Along with that, correlation is taken between the temporal temperature profile $O_T(x, \omega)$ and its Hilbert-transformed version $\widehat{\mathrm{H}}(\omega)$. From this, the correlation coefficient image is acquired by taking the real part of the correlated data acquired through the reference temporal temperature profile which is in the same phase to it. However, the phase image is acquired by considering the real part of the reference temporal temperature profile as well as the real part of the Hilbert-transformed version of it. Further, inverse Fourier transform is taken to obtain the time domain phase. The time domain phase of any temperature profile is obtained as

$$\theta = \tan^{-1}\left(\frac{\mathrm{IFT}\left\{\widehat{\mathrm{H}}(\omega)^{*}\mathrm{O_T(x,\omega)}\right\}}{\mathrm{IFT}\left\{\mathrm{R_T(x,\omega)}^{*}\mathrm{O_T(x,\omega)}\right\}}\right) \tag{11}$$

where $R_T(x, \omega)$ and $O_T(x, \omega)$ are the Fourier transforms of the picked non-defective temporal temperature and temporal temperature profile at a given area, and '*' represents complex conjugate.

2.3 Criteria for Effective Detectability of Defects

For examining defect detection capabilities of various data-processing methods for various excitation heat fluxes, acquiring the signal-to-noise ratio (SNR) information of the given data has been considered as an effective quantifiable measure and is calculated using the following equation:

$$SNR_{(dB)} = 20\log\frac{\text{Mean of the defective area} - \text{Mean of the nondefective area}}{\text{Standrad deviation of the nondefective area}} \tag{12}$$

3 Specimen Details

The DFMT and LFMT techniques are conducted on the simulated 3D numerical model of a concrete beam which has a thickness of 15 *cm* and has been strengthened by a 4 cm thick MS rebar. The deteriorated length in the longitudinal direction of the beam varies as 2 cm, 3.5 cm and 4 cm. Furthermore, two mild steel rebars have

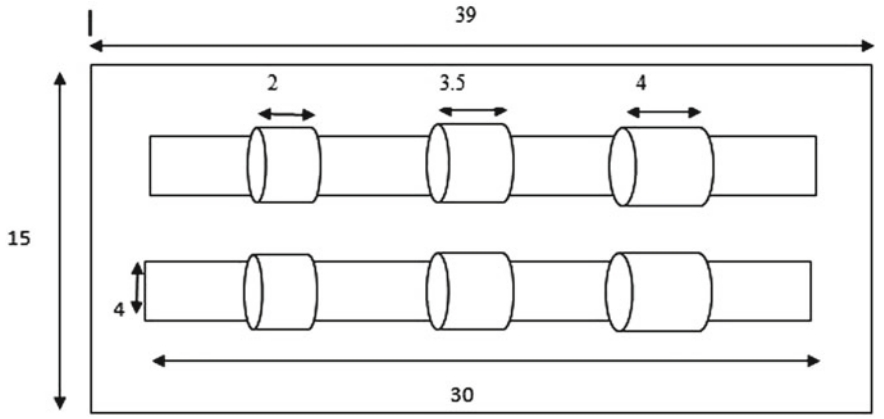

Fig. 4 Schematic layout of 3D numerical model of concrete structure (all dimensions are in cm)

Table 1 Values of properties of materials chosen to represent the characteristics of a mild steel structure

Material	Thermal conductivity k $\left[\frac{W}{m*K}\right]$	Heat capacity C_p $\left[\frac{J}{Kg*K}\right]$	Density D $\left[\frac{kg}{m^3}\right]$
Concrete	0.8	880	2300
Mild steel	60.5	434	7854
Iron oxide	12.5	650.6	5242

been placed 2.5 cm and 3 cm apart from the concrete beam surface. The schematic layout of the modeled concrete specimen is depicted in Fig. 4. Moreover, simulation parameters that were used for this simulation are summarized in Table 1.

4 Results and Discussions

To perform the present simulation, the heat transfer module of the COMSOL® Multiphysics version 4.2 is utilized. This simulation study has been conducted by using the heat fluxes of LFM and DFM which are imposed over the 3D numerical modeled concrete structure having a rusted rebar as shown in Fig. 4. Heat flux of 4 KW/m^2 with linearly modulated frequencies, i.e., 0.01–0.1 Hz for a duration of 100 s is utilized in this simulation. The acquired temporal thermal history over the simulated concrete model is considered as a data series which is recorded with a frame rate of 20 Hz. From this temporal thermal data, Correlation and Time domain phase images have been obtained by processing them according to the diagram shown previously in Fig. 3.

The correlation coefficient images and the time domain phase images got utilizing the Hilbert Transform approach for LFM are exhibited in Fig. 5a, b. However, DFM

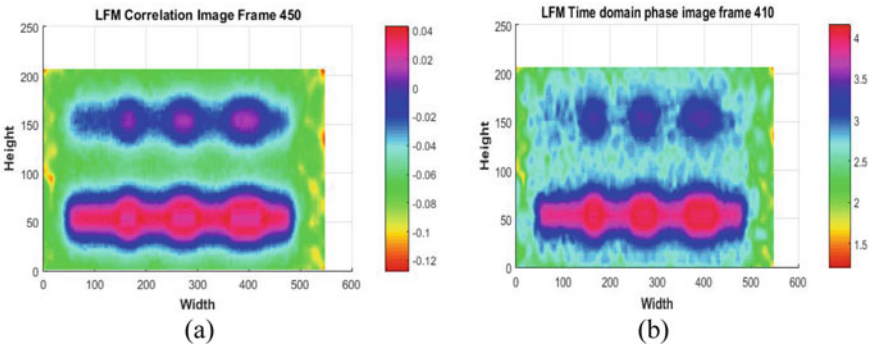

Fig. 5 Obtained LFM Correlation coefficient image at frame number 450 (**a**) and the Time domain phase image at frame number 410 (**b**)

in Fig. 6a, b provides much better contrast of the deeper as well as shallow corroded area as compared to that of the images obtained for LFM. This is maybe since DFM has a better Pulse compression ability as compared to LFM, i.e., it concentrates the vast majority energy in the main lobe after correlation.

Furthermore, the depth detection plot is generated using Correlation coefficient images in Fig. 7a, b for both DFM and LFM which on comparison clearly shows that DFM has a much better capability to render defects at deeper depths. This fact is also quantified by the SNR comparison plot for the corrosion length of 4 cm in the rebar depicted in Fig. 8 which evidently shows the high performance of DFM.

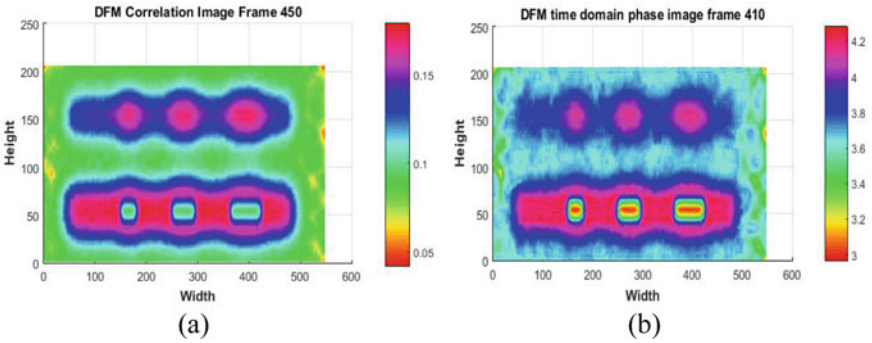

Fig. 6 Obtained DFM Correlation coefficient image at frame number 450 (**a**) and the Time domain phase image at frame number 410 (**b**)

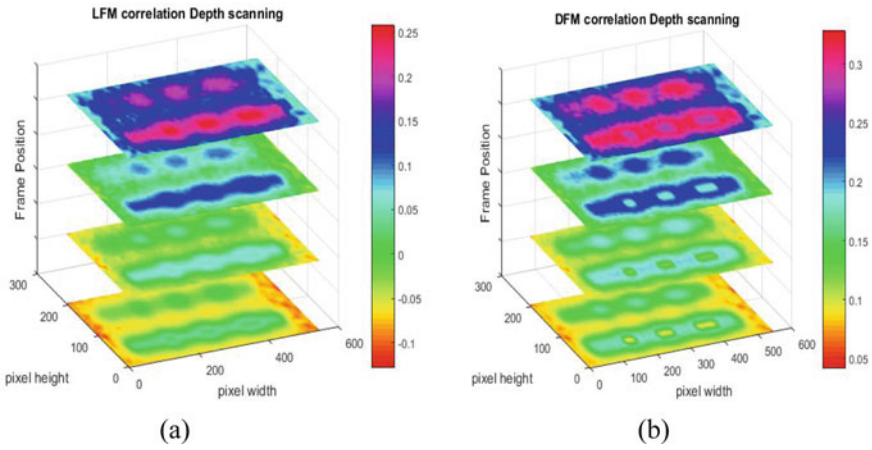

Fig. 7 Depth scanning performance using Correlation images for LFM (**a**) and DFM (**b**)

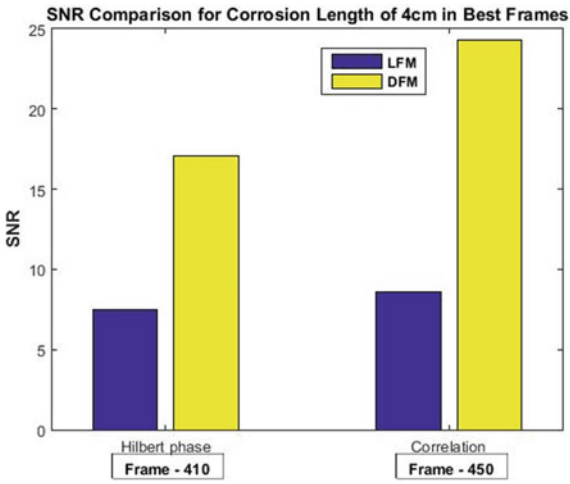

Fig. 8 SNR (dB) comparison for corrosion length of 4 cm in best frame

5 Conclusions

To summarize, this paper shows the effectiveness of the proposed pulse compression-based DFMT technique for the analysis of deteriorated rebar inside a concrete structure and its performance has also been compared with the earlier proposed LFMT technique. For effective post-processing, the utilization of Correlation and Time domain phase analysis schemes is performed in order to process the hidden corrosion and make the techniques more effective. The results obtained clearly illustrate that the DFM Correlation and Time domain phase images have a much higher contrast of visibility of defects as compared to LFM images for the same. Moreover, the depth

detection capability obtained from DFM is much better than LFM which can prove to be really helpful for the detection of corrosion at deeper depths [14].

References

1. Rosencwaig A (1982) Thermal wave imaging. Science 218:223–8, https://doi.org/10.1126/science.218.4569.223
2. Maldague XPV (2001) Theory and practice of infrared thermography for nondestructive testing. Wiley, New York. ISBN 978-0-471-18190-3
3. Wu D, Busse G (1998) Lock-in thermography for nondestructive evaluation of materials. Revue générale de thermique 37.8:693–703, https://doi.org/10.1016/S0035-3159(98)80047-0
4. Maldague X, Marinetti S (1996) Pulsed phase thermography. J Appl Phys 79:2694–2698. https://doi.org/10.1063/1.362662
5. Busse G, Wu D, Karpen W (1992) Thermal wave imaging with phase sensitive modulated thermography. J Appl Phys 71:3962–3965. https://doi.org/10.1063/1.351366
6. Dua G, Mulaveesala R, Siddiqui JA (2015) Effect of spectral shaping on defect detection in frequency modulated thermal wave imaging. J Opt 17(2):025604, 1–5, https://iopscience.iop.org/article/10.1088/2040-8978/17/2/025604
7. Mulaveesala R et al (2015) Testing and evaluation of concrete structures by thermal wave imaging. Thermosense: Thermal Infrared Appl XXXVII. Vol. 9485. International Society for Optics and Photonics, https://doi.org/10.1117/12.2176963
8. Mulaveesala R, SuneetTuli (2005) Digitized frequency modulated thermal wave imaging for nondestructive testing. Mater Eval 63(10), https://ndtlibrary.asnt.org/2005/ Digitized Frequency Modulated Thermal Wave Imaging for Nondestructive Testing
9. Mulaveesala R, Panda SSB, Mude RN, Amarnath M (2012) Non-destructive evaluation of concrete structures by non-stationary thermal wave imaging. Progress Electromagnetics Res Lett 32:39–48. https://doi.org/10.1117/12.919985
10. Arora V, Mulaveesala R, Siddiqui JA, Muniyappa A (2014) Hilbert transform-based pulse compression approach to infrared thermal wave imaging for sub-surface defect detection in steel material. Insight: Non-Destruct Test Condition Monit 56(10):550–552, https://doi.org/10.1784/insi.2014.56.10.550
11. Mulaveesala R, Siddiqui JA, Arora V, Muniyappa A (2014) Pulse compression approach to digitized frequency modulated infrared imaging for non-destructive testing of carbon fibre reinforced polymers. In: Proceedings of SPIE—The international society for optical engineering, 9105, 91050 M
12. Ghali VS, Mulaveesala R, Takei M (2011) Frequency-modulated thermal wave imaging for non-destructive testing of carbon fiber-reinforced plastic materials. Meas Sci Technol 22(10):104018. https://doi.org/10.1088/0957-0233/22/10/104018/meta
13. Mulaveesala R, Tuli S (2006) Theory of frequency modulated thermal wave imaging for nondestructive subsurface defect detection. Appl Phys Lett 89(19):191913
14. Mulaveesala R, Tuli S (2005) Implementation of frequency-modulated thermal wave imaging for non-destructive sub-surface defect detection. Insight: Non-Destruct Test Condition Monit 47(4):206–208(2005), https://doi.org/10.1784/insi.2010.52.9.475
15. Mandelis A (2001) Diffusion wave fields: mathematical methods and green functions. Springer, New York. https://doi.org/10.1007/978-1-4757-3548-2

Transportation Engineering

Application of Remotely Piloted Unmanned Aerial Vehicle in Construction Management

Tirth Patel, Vishal Suthar, and Naimish Bhatt

Abstract Construction projects may face challenges due to long project duration, uncertainties and big size. In recent times, remarkable research work has been done on automation of construction. Unmanned Aerial Vehicles are exponentially being utilized in various civil engineering areas like land surveying, crack detection, construction logistic management, highway asset management and site inspection. It is always difficult to monitor and track the status of a large construction site. However, unmanned aerial vehicles collect huge data of a construction project quickly. Remotely located large-scaled construction sites can be monitor by using advanced IT technology in a frequent manner. In this research endeavor, a drone has been used for construction monitoring of the G+6 building with the help of Pix4D software. This research proposed the unmanned aerial vehicle enabled site to automation building information modeling (BIM). Unmanned aerial vehicle-captured visual data can be utilized effectively with the help of Pix4Dbim. The robotic data collection during construction monitoring can provide enormous benefits to building information modeling.

Keywords Unmanned aerial vehicle · Building information modeling · Construction monitoring · Pix4d

T. Patel (✉)
Department of Civil Engineering, U.V. Patel College of Engineering, Ganpat University, Mehsana, India
e-mail: Tdpatel1610@gmail.com

V. Suthar
Construction Engineering and Management, U.V. Patel College of Engineering, Ganpat University, Mehsana, India

N. Bhatt
Department of Civil Engineering, Pandit Deendayal Petroleum University, Gandhinagar, India

© Springer Nature Singapore Pte Ltd. 2021

K. K. Pathak et al. (eds.), *Recent Trends in Civil Engineering*, Lecture Notes in Civil Engineering 77, https://doi.org/10.1007/978-981-15-5195-6_25

1 Introduction

The use of a drone in a construction site has exponentially developed in the previous couple of years. Unmanned Aerial vehicle/system (UAV/system) is described as any plane that operates without a pilot on board [1]. Today, Architecture Engineering Construction (AEC) industry utilizes drones for visually monitoring, controlling, safety management and building operation [2]. By a collection of pictures and video recordings, and utilizing programming alongside techniques that procedure the visual information into 3D model recordings and pictures, these stages as often as possible review building locales, construction monitoring, make reports for safety, and investigate existing structures, material stock, especially for difficult-to-achieve regions [3]. In conventional methods, the inspection for hard to reach places may result in injuries, increment of cost due to use of ladders, elevator and scaffolding on site and can cause the increased time for the work execution. UAV-based Inspection of the building site from an aerial perspective can expedite beneficial outcomes to a few portions; for instance, less time to inspect the construction site, the capacity to see more points of interest or to catch current conditions on the building site for resulting use [4]. The construction organizations have shown pretty less interest for the adoption of the latest technologies compared to others [5]. The construction industry can get numerous benefits from the advancement of information technology. It is crucial to compare the as-planned construction and actual construction; right now, traditional methods like manual site investigation report and visual investigation of particular construction stage are insufficient to grab the objective of the project. Due to advancement of technology, artificial intelligence can be the bridge for the UAV data and building information modeling.

The paradigm shift in the AEC industry can be seen after the implementation of building information modeling in a large scale and this remarkable transformation has created a positive impact on the construction industry [6]. This revolution changes the paper-based documentation process used in infrastructure construction and design; BIM will integrate the physical properties of building elements with different information in electronic form which includes time and cost [7]. It is known as n-dimensional (nD) modeling, where the virtual building model contains different dimensions of information [8]. For execution of the project, Microsoft project and Primavera used with manual construction progress update by personal site inspection, it is hard to monitor the construction of large-scaled construction site [1]. There are a lot studies that have been done for damage identification and land surveying [9]. The technical data, maintenance data, manufacturing data and cloud data are integrated into digital twin model [10]. The BIM model will be prepared to provide the platform for a common data exchange platform. Although, due to lack of appropriate use of UAV data with BIM, the effectiveness of drone use in construction is far to reach, UAV-enabled BIM development can leverage the integration of onsite data captured and BIM model and enable the effective decision-making process for construction monitoring [11]. Recently, researchers have explored the visual analytics from the reality captured data from UAV [12]. UAV is also able to locate

the workers, equipment's or any other construction object's geometric position with GPS. Any construction conflicts can be identified with the help of a drone. Thus, logistic management has greatly improved with UAV use.

The drone-enabled BIM-based construction monitoring can avail several benefits to the Indian AEC industry. In this investigation, a drone was utilized as an instrument for investigating potential advantages to construction monitoring and propose the framework of UAV-enabled building information modeling for construction monitoring.

1.1 Objective of Study

To study and optimize monitoring, inspection and project management at construction sites using by unmanned Arial Vehicles (UAVs) of their building sites. Any construction project should be complete within the stipulated time, budget with desired quality and safety. The introduction of drones in the construction industry changed the aspects of construction monitoring, with easy, cheap and especially quick data collection. The aerial photo/video of the project is transformed into a cloud model, which can help to take measurement and analysis of the proposed construction. The comparison between actual construction and planned construction can be done with the help of drone-based IT software.

2 Literature Review

In the beginning, UAVs were utilized in army operations, however greater these days, the capacity use of American engineering environments has won enormous interest within the discipline of civil engineering especially.

Unmanned Aerial System has been used inside the construction monitoring and maintenance of highways [13], bridge maintenance and condition assessment; building condition assessment, identification of damages and cracks, façade repairing or renovation and scanning of historic monuments [14]; 3D modeling for buildings reconstruction, photogrammetric programs [15]; consisting of extent size through using digital terrain model. In Highway Asset Management, drones also can contribute significantly to surveying without disrupting normal traffic. Kim et al. [16] made an algorithm to measure crack thickness and length using images taken from the drone (Fig. 1).

By UAV, it is quicker and efficient to locate the construction material, equipments and temporary structures on the construction site. For large construction sites, it is also possible to capture the material tracking, construction vehicle or equipment operation and construction progress [17]. Fang et al. [18] developed an algorithm to track the 3D movement of vehicles, concrete mixer and minivan by a drone. Total 169 photographs have been used for point densification. This algorithm can be a

Fig. 1 Delamination and crack detection using Infrared Camera [10]

solution for logistic management in the construction site by improving supply chain management.

A drone has been commonly equipped with a camera which will take the photos as well as videos for a specific location of infrastructures to locate structural cracks in it [14]. Drone application is also applicable for estimating the volume of sand with a 10% error. The drone is used widely in land surveying with efficacy. Land mapping surveying with aerial photography is definitely fruitful for the civil engineering field. By drone, highly accurate map with photogrammetric can be generated. The contour and topographic map can also be extracted with the help of Pix4D software [19]. The point densification and quality report also can be assessed for reliability of work. Drone-enabled BIM-based construction monitoring can avail several benefits to the Indian construction industry (Fig. 2).

In construction management area, there are significant research endeavors that have been done for image processing. Examples of such applications include productivity analysis [6], safety management [7], facility management and monitoring of construction [8]. Although, construction monitoring needs manual inputs, it is laborious and time-consuming to manually update with daily progress and it depends

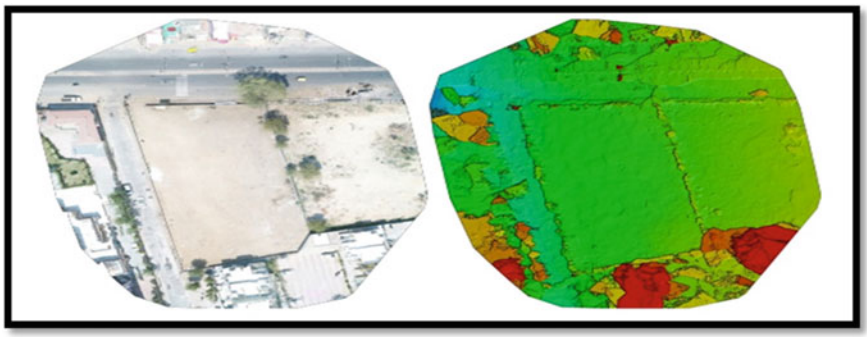

Fig. 2 Orthomosaic photo and Digital Surface Model (DSM)

on modeler capabilities. The automatic construction monitoring will revolutionize project management, which is yet to evolve with image procesing [20]. The IFC-based approach can be a revolution for automatic 4D BIM progress [21].

3 A Case Study of G+6 Building

The project of G+6 building has been selected for the drone-based construction monitoring. The drone has been piloted through a smart mobile. After the integration of a high-resolution camera, the project manager can achieve digital photographs of the different parts of the site quickly.

The flight plans for capturing the photographs have been created with the help of Pix4D Capture. It also assisted with the features like flight review and optimal data capture. Post flight, the image data has been shared with the Pix4d Cloud. Here flight plan can be viewed by the following photograph. After capturing images, Px4D mapping and ray cloud image processing lead the point cloud modeling of the building. Flight planning was set to 30 m above the ground. There are 81 photographs that have been captured by the drone from different views. After uploading the photographs, image processing step been performed by Pix4D. Then the report was generated to check the quality of the model (Figs. 3, 4, 5 and 6).

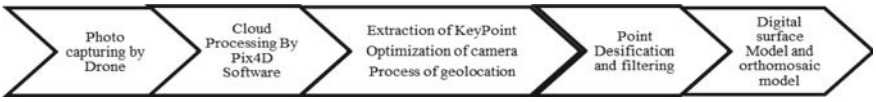

Fig. 3 Digital Surface modeling by Pix4D

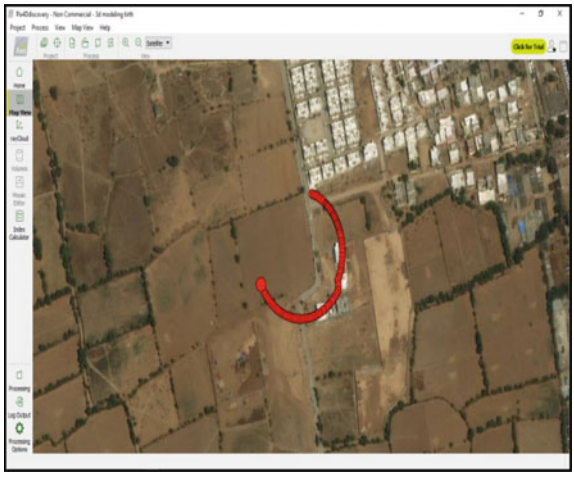

Fig. 4 Drone path denoted by red dotes

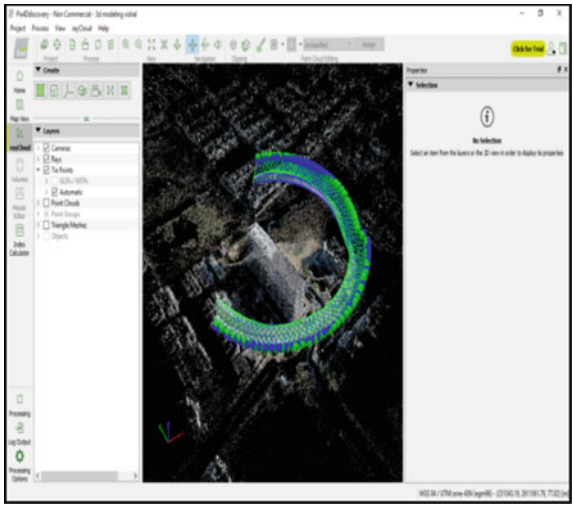

Fig. 5 Ray cloud image of Pix4D mapping

Fig. 6 Front view image captured by drone

Here, 81 out of 81 photographs have been calibrated,. It means the process of the problem is very good. In Fig. 7, the quality check model is described (Table 1).

In the next step, the dense point cloud has been done by Pix4D. The 3D mapping process involves the overlapping of thousands of common key points between images. Once the extraction of key points is performed, point densification and filtration are operated. Then, the 3D point cloud is developed and ground point can be added for accuracy and quality (Figs. 8 and 9).

Extracted key points on each group of images will be matched and overlapped in order to generate a 3D point cloud. The final model is shown in Fig. 10. This 3D cloud model is developed with a software called Pix4D. This cloud model can give better visualization and offer a great platform for measuring the dimension of building

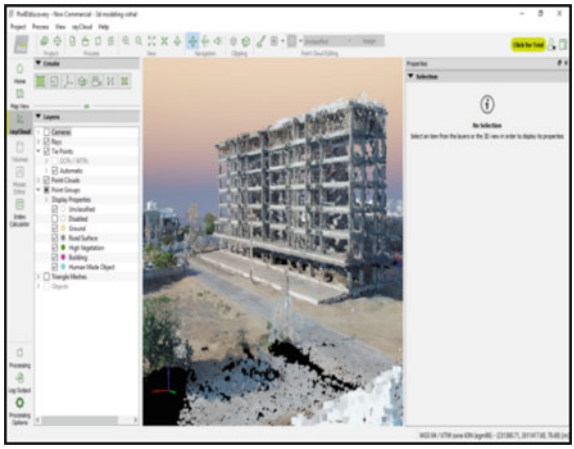

Fig. 7 3D generated model by Pix4D

Table 1 Quality check of model

Images	Median of 38486 key points per image
Data set	81 out of 81 images calibrated (100%), all images enabled
Camera Optimization	77% relative difference between initial and optimized internal camera parameters
Matching	Median of 23779. 9 matches per calibrated image
Georeferencing	Yes, no 3D GCP

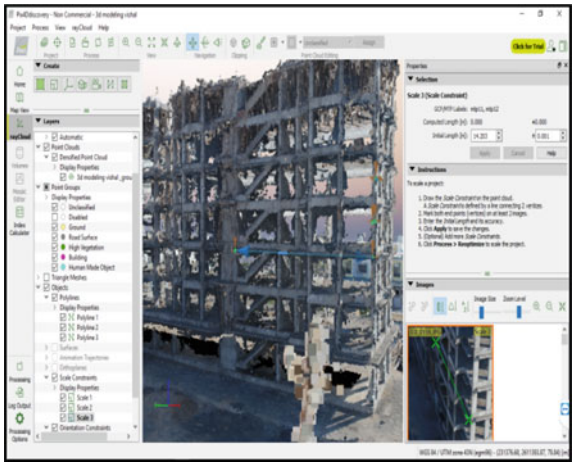

Fig. 8 Length of slab measurement

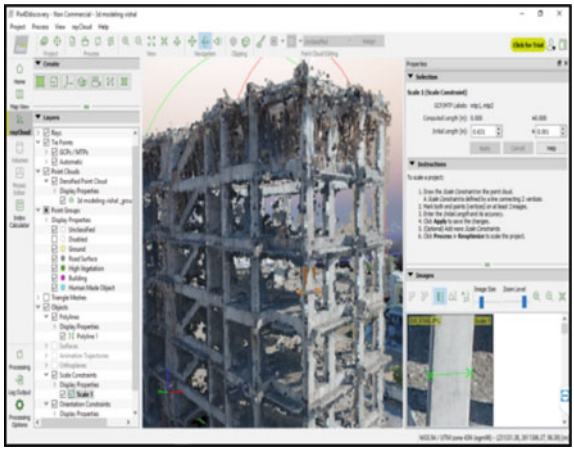

Fig. 9 Column width measurement

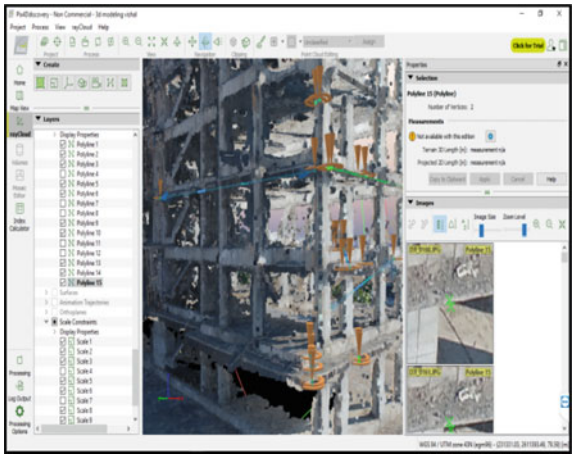

Fig. 10 Area of building measurement

elements to the construction manager. For visualization and analysis, this approach will greatly help engineers by a simple click on the 3D cloud model. The annotation, measurement and sharing of this data are quicker and easier. Even, this cloud model and images can be operated off-site. The photographs of actual construction progress will be overlaid on the timeline which can be seen and compared with planned construction (Figs. 11 and 12).

By means of sharing a link to the project, all project stakeholders can exchange and access the project information to visualize and examine the site from the drone-generated maps and 3D models. They may be able to extract powerful insights into the use of integrated equipment to measure the distance and make annotations, observe progress on a timeline, and compare the as-constructed with cad drawings. So, deviations can be recognized more quickly. Also, orthophotos can be compared with design drawings. So, construction mistakes can be identified at an early level of the

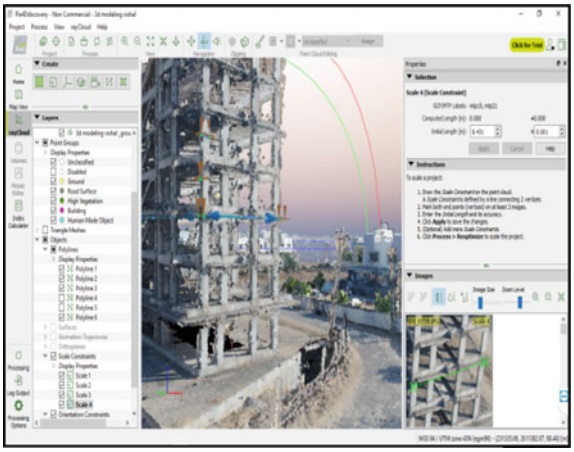

Fig. 11 Width of building measurement

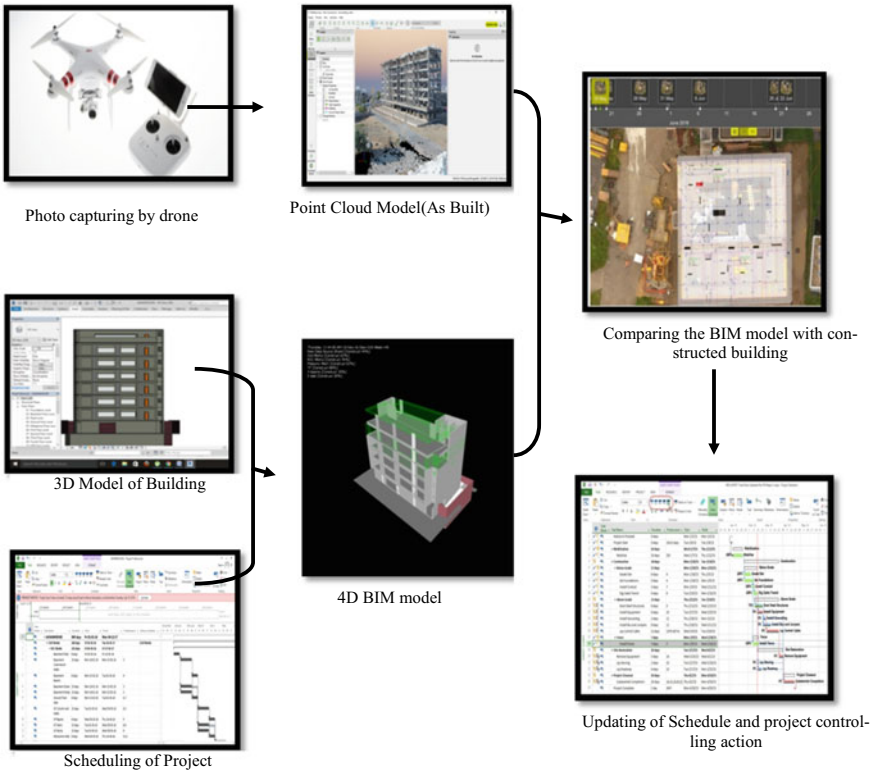

Fig. 12 Automated schedule updating

construction stage. Alternatively, scheduling can be retrieved from the BIM software, may be imported and compared with the planned progress to monitor the construction progress. The dimensions of the slab and column height, length and width have been calculated with the help of Pix4D. All dimensions have been taken as screenshots. Author has compared the data as per plan that was given and measure with using the man power at real time data and then measure the data with drone with using software at site real time data.

4 Conclusion

The application of drones can change the working pattern of construction monitoring in the construction industry due to high efficiency and automation in itself. In this research endeavor, construction monitoring has been done by a drone. The different features of PiX4D can play a significant role in the civil engineering field like surveying, earthwork estimation, logistic management, surveying for highway asset management, safety management and construction monitoring. In this case study, Pix4Dbim gave the visual idea of construction site progressing and construction monitoring. The project manager, owner or contractor can easily share the data of a construction site's progress efficiently and quickly by using UAV-enabled BIM for site execution. So, efficient project management led the desired goals of the project with the use of drones with Pix4D. Here, total 81 photographs have been taken by using the drone, then 3D model has been generated in Pix4D. Pix4Dbim can significantly track the project progress by adding scheduling. Here, the framework for UAV-enabled BIM is mentioned. The automatic 4D BIM updating is also going to be a significant research for the AEC industry, which will enhance project productivity by enabling the fast decision-making platform. The AEC industry can deliver project objectives in the region which is hard to achieve, with convenience and economy. Thus, the application of Drones for construction monitoring can add a new chapter in automation in the construction industry.

References

1. Themistocleous K, Neocleous K, Pilakoutas K, Hadjimitsis DG (2014) Damage assessment using advanced non-intrusive inspection methods: Integration of Space, UAV, GPR and Field Spectroscopy. In: Proceeding 2th international conference on remote sensing and Geoinformation of the environment. Vol 9229, Paphos, Cyprus
2. Brance P, Hudzietz SS (2011) An experimental evaluation Of 3d terrain mapping with an autonomous helicopter. In: Conference on unmanned aerial vehicle in Geomatics
3. Waslander S, Infrastructure inspection and monitoring using autonomous robotics, https://www.civil.uwaterloo.ca/snarasim/AutonomousInspectionMonitoring.html. Accessed 15 Jan 2018

4. Eschmann C, Kuo C-M, Kuo C-H, Boller C (2012) Unmanned aircraft systems for remote building inspection and monitoring. In: 6th European workshop on structural health monitoring, Dresden
5. Pix4D, "Pix4D," 2018. https://pix4d.com/industry/bim/. Accessed 28 Jan 2018
6. Siebert S, Teizer J (2014) Mobile 3D mapping for surveying earthwork projects using an Unmanned Aerial Vehicle (UAV) system. Autom Constr, 1–14
7. Ham Y, Han KK, Lin JJ, Golparvar-Fard M (2016) Visual monitoring of civil infrastructure systems via camera-equipped Unmanned Aerial Vehicles (UAVs): a review of related works. Visualizat Eng
8. Yang J, Park M-W, Vela PA, Golparvar-Fard M (2005) Construction performance monitoring via still images, time-lapse photos, and videostreams: Now, tomorrow, and the future. Adv Eng Inf
9. Herrmann M (2016) Unmanned aerial vehicles in construction: an overview of current and proposed rules. Construction Research Congress. San Juan, Puerto Rico
10. Liu Z, Meyendorf N, Mrad N (2018) The Role of data fusion in predictive MaintenanceUsing. In: AIP Conference
11. Puri A (2005) A survey of unmanned aerial vehicles (UAV) for traffic surveillance. In: Department of computer science and engineering, University of South Florida
12. Li Y, Liu C (2018) Applications of multirotor drone technologies in construction management. Int J Constr Manag, 1–13
13. Holt EA, Benham JM, Bigelow BF (2015) Emerging technologyin the construction industry: perceptions from construction industry professionals. In: ASEE Annual conference & exposition; Seattle, WA, USA
14. Bang S, Kim H, Kim H (2017) UAV-based automatic generation of high-resolution panorama at a construction site with a focus on preprocessing for image stitching. Autom Constr, 70–80
15. Hallermann N, Morgenthal G (2013) Unmanned aerial vehicles (UAV) for the assessment of existing structures. Int Assoc Bridge Struct Eng Zurich, Switzerland
16. Kim SC (2013) Automated construction progress measurement using a 4D building information modelling and 3D Data. Autom Constr Elsevier, 31:75–82
17. Yash TDP, Patel K (2018) Application of building information modeling in construction management with 5D modeling. J Emerg Technol Innov Res (JETIR) 5(8):668–665
18. Fang Y, Chen J, Cho Y (2016) A point cloud-vision hybrid approach for 3D location tracking of mobile construction assets. https://doi.org/10.22260/ISARC2016/0074
19. Succar B (2009) Building information modelling framework: A research and delivery foundation for industry stakeholders. Autom Constr (Elsevier), 357–375
20. Azhar S (2011) Building information modeling (BIM): trends, benefits, risks, and challenges forthe AEC industry. Leadersh Manag Eng (Am Soc Civil Eng), 11: 241–252
21. Hamledari H, Davari S, Azar ER, McCabe B (2018) UAV-enabled site-to-bim automation: aerial robotic- and computer vision-based development of as-built/as-Is BIMs and quality control. In: Construction research congress 20182018

Spatial Pavement Information System for Transportation Networks Based on Distress Features in Nagpur City Using RS and GIS

Y. B. Katpatal, Kaddak Harashal, and M. S. Mukesh

Abstract Preservation, maintenance and rehabilitation of pavements need continuous information through monitoring for their assessment. The deterioration rate of the pavement surfaces in developing countries like India is more due to a sudden rise in the automation industry which was not thought of during the planning stage of the road network. Increase in motorized vehicles has led to early failure of the roads which need to be properly maintained by carrying out the maintenance work to have a longer service life. Pavement Information System (PIS) is a valuable tool for evaluating the rapid deterioration of roads. PIS stores and compiles a large amount of data that are frequently collected on a timely basis. The new era of the pavement information system is utilizing the Remote Sensing and Geographical Information System. The present study analyzes the major pavements in Nagpur city. For these selected roads, the different types of distress conditions on the roads were collected and were represented on the high-resolution satellite map. From these data sets, a Spatial Pavement Information System (SPIS) was developed for Nagpur road network using ArcGIS software. The management system involved the development of distress indices which were calculated based on the frequency and types of distress. The different pavements were then prioritized based on distress indices for maintenance scheduling. This research paper provides a spatial method which helps prioritize pavements for maintenance and rehabilitation to improve Level of Service of the road.

Keywords Pavement information system · Pavement management system · Geographic information system · Rehabilitation of pavement

Y. B. Katpatal
Civil Engineering Department, Visvesvaraya National Institute of Technology, Nagpur, India

K. Harashal · M. S. Mukesh (✉)
Transportation Engineering, Visvesvaraya National Institute of Technology, Nagpur, India
e-mail: mukeshms060@gmail.com

© Springer Nature Singapore Pte Ltd. 2021

K. K. Pathak et al. (eds.), *Recent Trends in Civil Engineering*, Lecture Notes in Civil Engineering 77, https://doi.org/10.1007/978-981-15-5195-6_26

1 Introduction

The simplest indicator of the development of any nation is to have a properly designed and maintained road network. The gap between developed and developing countries can be bridged by developing the best possible transportation system. Transportation acts as a nervous system for the economic, industrial, social and cultural development of any country. The inadequate transportation facilities retard the process of socioeconomic development of a country. Transportation by road is the only mode which provides maximum service to the user. Road network in some cities in India does not retain its full-service life thereby reducing the riding comfort and even resulting in accidents and finally in the reduction in service level of roads.

Pavement information system is an integrated system used to store, edit, analyze, share and display information related to the pavement on a spatial scale [1]. PIS contains spatial information on the road network related to the road composition and present road condition. It is an important tool for road network maintenance and proper allocation of fund for a systematic process [2]. PIS is a management tool which can be implemented at different construction stages or the planning stages whose result can further be processed for refinement at the different management stages. The road maintenance at the proper time phrase reduces the maintenance cost and also increases the service life of the road [3].

Bhuyan [4] have differentiated different Level of Service (LOS) parameters. The present study evaluates LOS of Nagpur roads through proper characterization of pavements using analysis of distress features on them. By using spatial technology, the data obtained from field observations can be geographically represented and analyzed so that the problems of either flexible or rigid pavement can be minimized. Pavement Information System (PIS) is a tool which provides information regarding the pavement condition. GIS tool can be incorporated for the maintenance of pavements [5]. A Spatial Pavement Information System developed on the GIS platform can be used for preparing strategies for the development of maintenance activities. The involvement of GIS and RS aspects in PMS reduces the maintenance cost of the road and increases the failure life of the road network [6]. Remote Sensing (RS) and Geographical Information System (GIS) implementation in Maintenance Improvement Plans (MIPs) characterized the pavement distresses into different classes, including cracking, rutting and potholes [7]. Chang et al. [8] worked on Flexible Pavement maintenance by using Automated Road Analyser (ARAN) to set up Pavement Serviceability Index (PSI) and Structural Serviceability Index (SSI) which was used for the maintenance and rehabilitation strategies using Fuzzy logic theory.

The study aims to develop a pavement information system which gives full information regarding the failures in pavements and prioritization remediation strategies for pavement maintenance for the study area. Moreover, it explains all the data related to the failures on a timely basis. Analysis of data relating to the variability of pavement condition, pavement behavior, pavement characteristics, traffic loads, environmental characteristics, soil conditions and rideability provides actual quaintly and predict performance of pavement. But an attempt has not been made in the study to consider

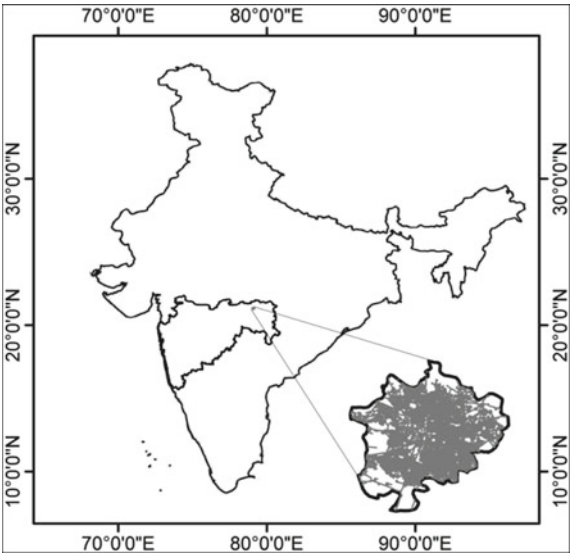

Fig. 1 The location of the study area, Nagpur city, along with digitized road network

the following factors as the papers concentrate on the maintenance of layover work in particular.

2 Study Area

The study has been conducted in Nagpur city which is centrally located in India (Fig. 1). The city is well connected with road network as it has three major National Highways (NH) and two Asian Highways (AH) running through the city. The road network of Nagpur city is radial and star patterned. It is observed that the majority of the road network in the city is flexible pavement which encounters more different types of distresses than the rigid pavement. In the study, major road links were considered which are spread throughout the city for the development of the PIS.

3 Methodology

Pavement maintenance strategies depend on nature and relevant characteristics of different distresses in the pavement. For proper maintenance and long-lasting life of pavement, it is necessary to know the extent of the failure, frequency of failure occurrence, initially faulty designing of pavement and all those reasons which are responsible for failure. The main methodology adopted in the study is shown in Fig. 2.

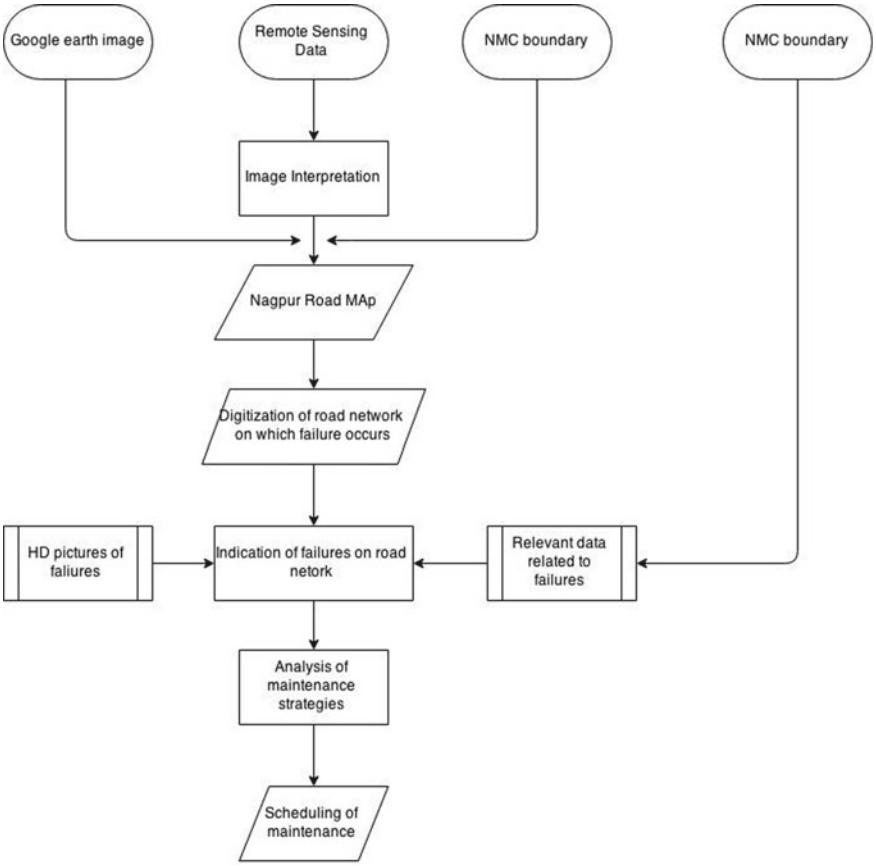

Fig. 2 Flowchart showing the methodology of the study

3.1 Selection of Road Network

For the development of PIS based on distress, the major road network located along the Nagpur city is considered. Figure 3 shows the location of the different road networks considered. For the modeling purpose, only NH4, NH7, NH69 and the Nagpur Inner Ring Road were taken into account during the study. The rate of deterioration of these roads was determined based on the distress in the road and the Level of Service (LOS) the road provides by the road was found based on the frequency of distress.

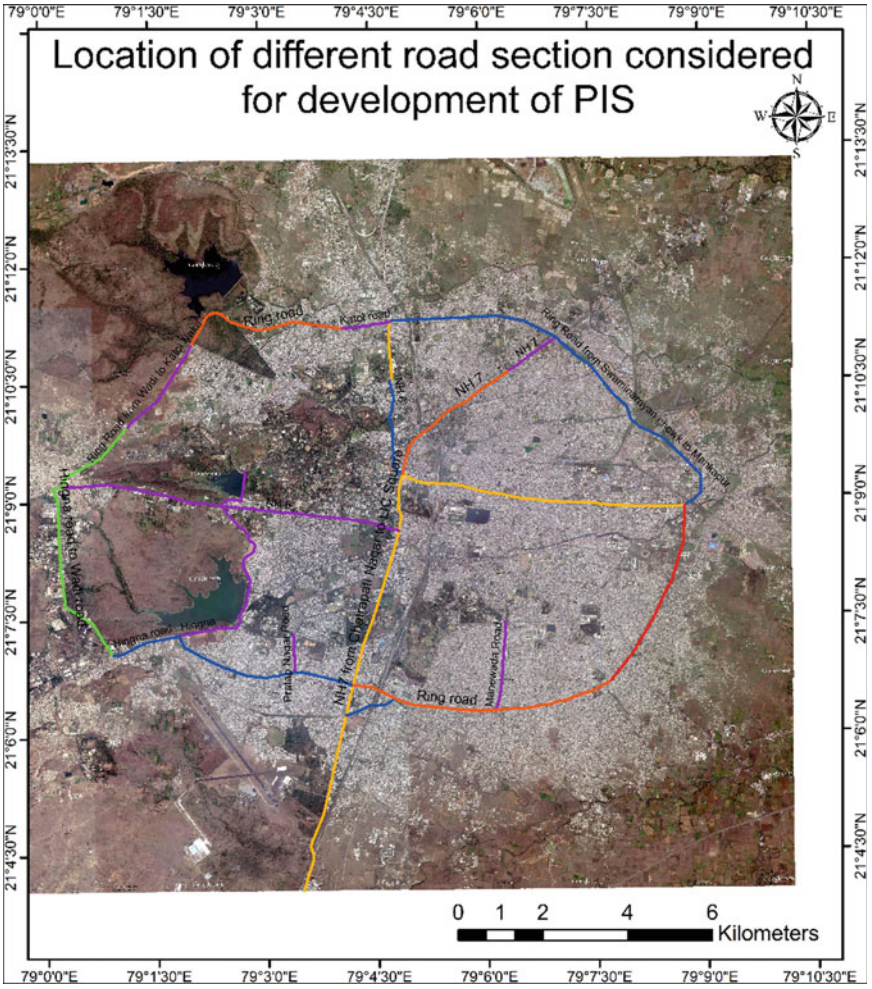

Fig. 3 The location of the road network considered for study along Nagpur city

3.2 Digitization of Road Network

For the study purpose, high-resolution IKONOS image of Nagpur city was used and the road network was digitized. The road network in the city was digitized and the information regarding the type of pavement and different pavement thickness, and the combination of the pavement were attached to the road segment based on the formation stretch whose data were obtained from the Nagpur Municipal Corporation (NMC). The analysis was done on the topology of the road network on functional roads which have a direct and essential impact on the overall maintenance and rehabilitation strategies of existing roads of Nagpur.

3.3 Level of Service

Level of Service (LOS) of a traffic facility is introduced in the study to assign the service provided by the road which is in relation to the vehicular flow. LOS is used to analyze the road network by considering the traffic flow and it determines the performance parameters like speed and density. In the study, the LOS of the roads has been defined based on the frequency of distress present in the road segment. The LOS defined in the study can be used as a multiplying factor for LOS of traffic capacity. The LOS defined for capacity does not take into account the condition of the road. Based on the frequency of distress present in the segment, the LOS is defined which is shown in (Fig. 4). As the frequency of distress increases, the service capacity of the road gets reduced significantly and LOS reduces considerably from A to F.

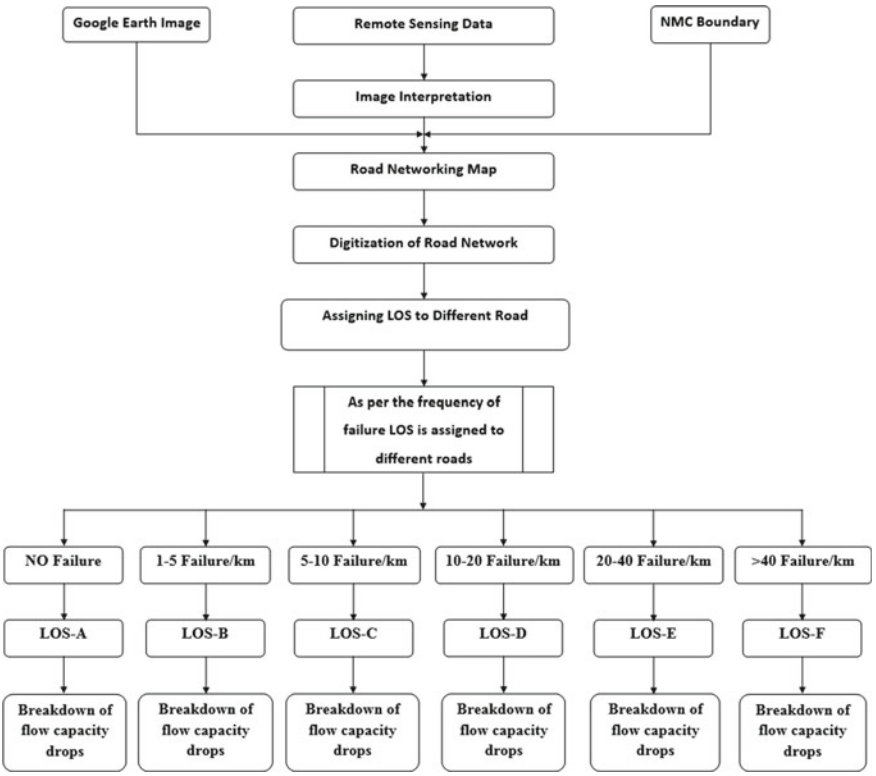

Fig. 4 Flowchart shows characterizing the roads of the study area to different LOS as per the frequency of failures

3.4 Qualitative Characterization of Pavements

With the application of Remote Sensing and GIS, the pavement can be characterized into various classes based on its quality. The quality parameters are differentiated by DN values obtained from handheld ground radiometer for different types of pavement conditions. The DN values in the selective wavelength of all the segments have been tabulated. Spectral Signature Curves have been plotted for segments of roads with varying surface conditions. In order to validate the observations on the satellite data, substantial ground data were found in order to relate the experimental findings along with the actual existing condition. The spectral signature curve technique is used to differentiate between the different types of roads and the distress features on the surface. Figure 5 clearly depicts that the rigid pavement has a higher DN value than that of the flexible pavement as the absorption in the rigid pavement is more. The small variation in the signature curve of the pavement type is observed which is due to the change in the composition of the road or might be the data collected at a different light intensity.

The DN value for the road in failure condition will be different from that of pavement without distress. Due to the presence of distress on the road, the absorbing of the road will be less thereby resulting in a lower DN value signature curve. Figure 6 shows the variation in the DN value for the road with distress and road without distress. It is evident from the figure that the road which has deteriorated has a lower value.

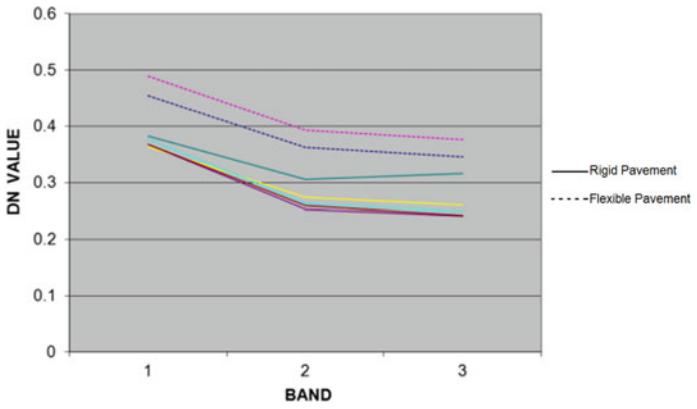

Fig. 5 Spatial Signature curve rigid and flexible pavement for different point samples

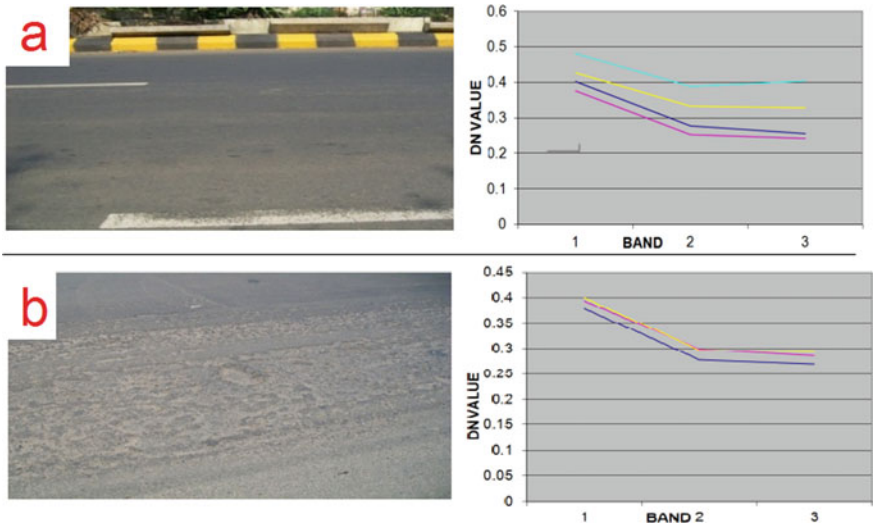

Fig. 6 Spatial signature curve for the flexible pavement for different points considered **a** Without Distress, **b** With Distress

3.5 Distress Index

In order to have timely maintenance of the road network, the distress index has been introduced in the study. The distress indices represent the intensity of the distress features over a road segment. The distress indices (Di) are calculated for each segment of the road network by considering the waited distress (Table 1) to the total number of distresses present in each segment (Eq. 1). The waited distresses were assigned to each type of distress based on the nature, cause and effect of distress on the road life and the road users. Even the nature of maintenance work and the cost of each distress

Table 1 Impact factor for different types of distresses

Sr. no.	Failure type	Impact of failure
1	Alligator cracking	5
2	Bleeding	5
3	Block failure	7
4	Edge cracking	3
5	Patch Failure	3
6	Potholes	9
7	Raveling	7
8	Rutting	7
9	Slab cracking	5
10	Transverse cracking	5

were considered for assigning the waited distress. Segment of the road network is confined to the length of stage-wise construction.

$$D_i = \frac{\Sigma(\text{number of failures} \times \text{Impact factor of that failure})}{\text{Length of road segment}} \quad (1)$$

4 Results and Discussions

The pavement distresses of the study roads were collected from the field study and the type of distress on the roads was geographically represented on the Nagpur city map (Fig. 7). From the field observation, the raveling, potholes and block failure are the major types of distress which are experienced on the Nagpur road.

Figure 8 gives the pictorial information on the type of distress at the locality. This type of information can be used for planning, designing or maintenance stage which gives information regarding the type of road, nature of failure, cause for failure and many more information regarding the road which can be attached to the road which conveys information in pictorial representation.

The pictorial information can be understood very easily than any other type of information. The figure gives the graphical representation on the LOS offered by the road to the users (Fig. 9). This type of information can be easily interpretive and helps in prioritizing the stage-wise maintenance work for the entire Nagpur city road network based on the condition of the road.

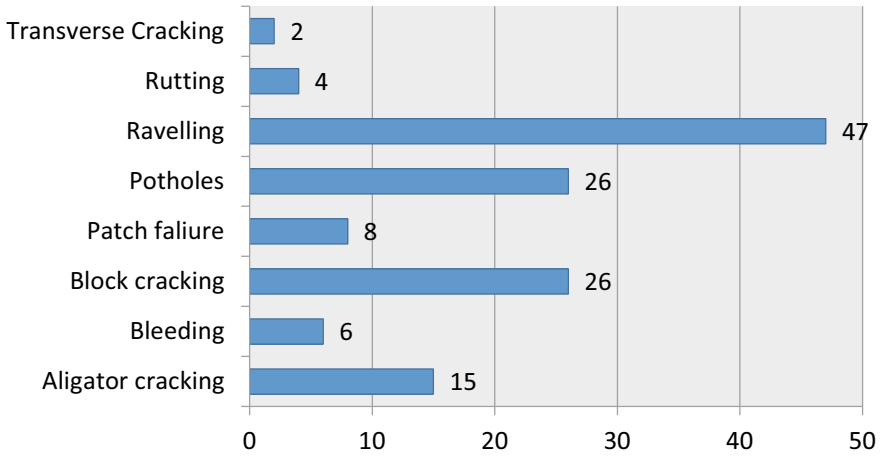

Fig. 7 Percentage distresses in the study area

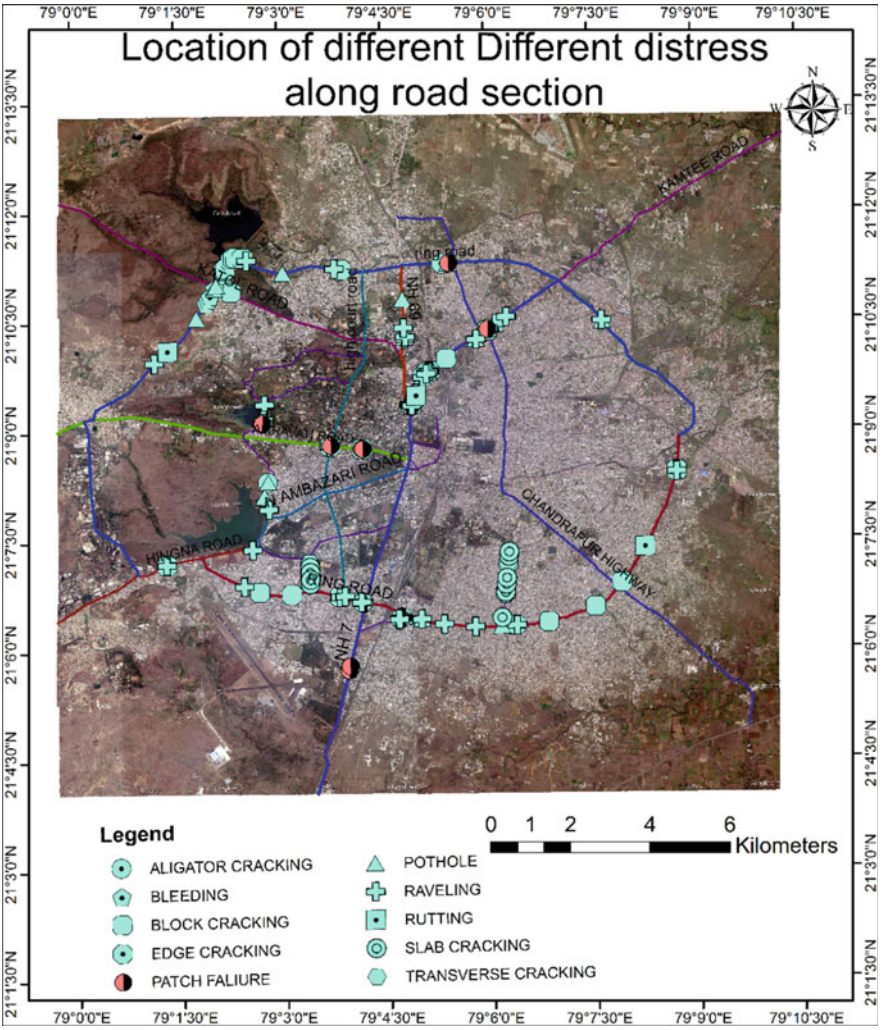

Fig. 8 The location of different distresses located along the road network

5 Conclusions

SPIS along with spatial tools like ArcGIS becomes a complete informative tool for a region whose data can be represented graphically. The pictorial information system makes it easy to interpret the data and the burden on the management system is reduced. PIS is a sophisticated tool to handle the periodic data of the road condition as it facilitates the integration and cooperation between the maintenance planning and decision-making mechanisms. ArcView software can build much better reports

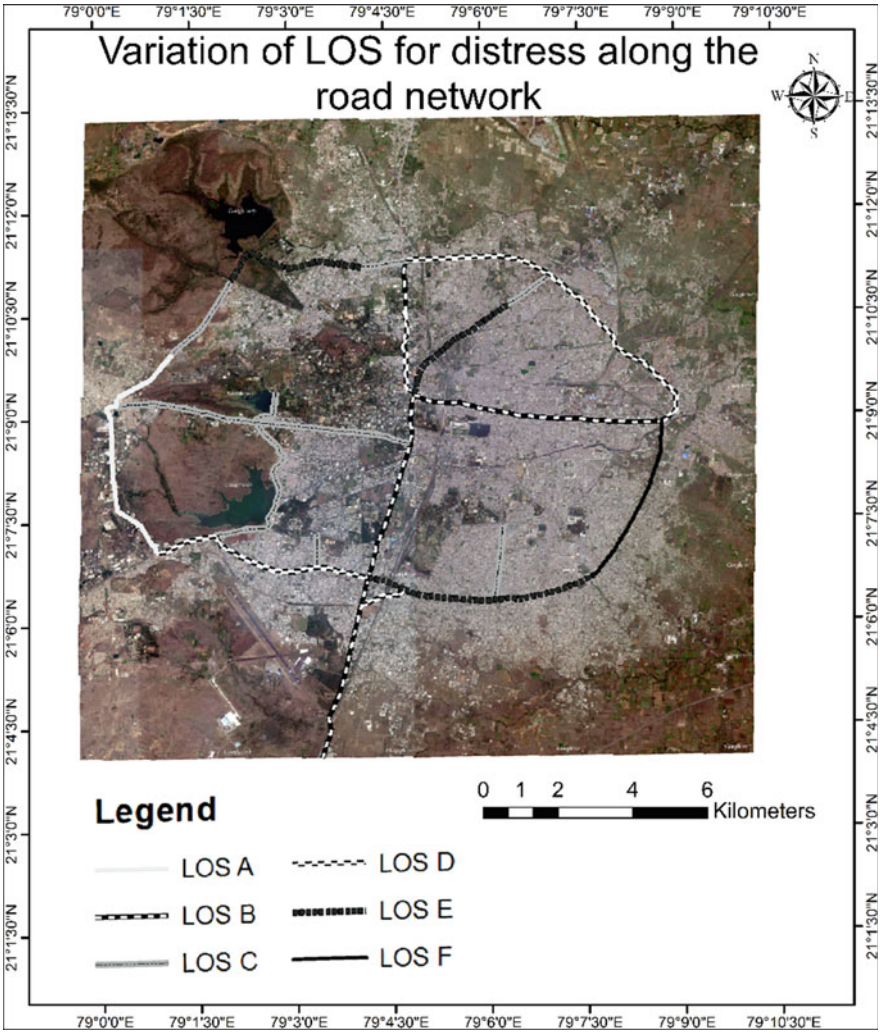

Fig. 9 The segmentation of major road network in PIS as per the frequency of failures/kilometer of the road

than can a pavement management program by itself. Attaching a spatial component makes the data much more readable and understandable. Thus, the integration of PIS with spatial technology is an ultimate tool in road network management.

References

1. Abkowitz M, Walsh S, Hauser E, Minor L (1990) Adaptation of geographic information systems to highway management. J Transp Eng 116(3):310–327
2. Ismail N, Ismail A, Atiq R (2009) An overview of expert systems in pavement management. Eur J Sci Res 30(1):99–111
3. Frangopol DM (2011) Life-cycle performance, management, and optimisation of structural systems under uncertainty: accomplishments and challenges. Struct Infrastruct Eng 7(6):389–413
4. Prasanta Kumar Bhuyan KK (2011) Defining level of service criteria of urban streets in Indian Context. Eur Transp
5. Ibraheem AT (2012) Applying geographic information system (GIS) for maintenance strategy selection. Engineering 4(1):44–54
6. Barry Waite and Alex Rocco. (2011) GIS and pavement management: a concrete relationship City of Carson, California. In: ESRI Conference
7. Asma Thamir Ibraheem DAR (2012) Applying geographic information system (GIS) for maintenance strategy selection. Engineering, 44–54
8. Chang JR, Hung CT, Lin JD (2005) Application of advanced computation on flexible pavement maintenance management system in Taiwan. National Central University, Taoyuan

Evaluation of Strength Development of Untreated and Treated Red Mud with Gypsum as a Road Construction Material

K. Sarath Chandra and S. Krishnaiah

Abstract The expense incurred in any treatment method of industrial waste is of major consideration to any manufacturer. The disposal of waste products is one of the major problems faced by the processing and manufacturing industries. Red mud is also a waste produced during the Bayer's process of extracting alumina from the bauxite. Red mud contains traces of radioactive elements and the disposal of it gives rise to air, water and soil pollution. 77 million tons of red mud is produced annually and it has turned into a major concern of environmentalists from all over the world. To reduce the problems incurred by red mud, it is necessary to harness this waste product into a susceptible construction material thereby diminishing the problems caused to the environment. This project work explores the reasonable usage for a specific red mud contingent on its durable property. The acquired sample is stabilized by adding gypsum which increases the strength by facilitating the pozzolanic action. In this project the gypsum content is varied from 2, 4, 6, 8 and 10% by a dry load of red mud. Initially, the basic index and engineering properties of the untreated red mud were studied which can be referred to when required while conducting the main test. Unconfined Compressive Strength (UCS) and California Bearing Ratio (CBR) tests were conducted for the stabilized samples and the results were compared between an untreated and treated red mud for finding the feasibility of it as a construction material.

Keywords Red mud · Gypsum · Index properties · Engineering properties · Road construction material

1 Introduction

Red mud (RM) is a highly alkaline material with a pH range of 10.5–13 in nature and is considered as a by-product obtained during the extraction of aluminum from Bauxite ore in Bayer's process . The main steps of the Bayer process include digestion,

K. Sarath Chandra (✉) · S. Krishnaiah
Jawaharlal Nehru Technological University, Anantapur, India
e-mail: sarathchandra.k@christuniversity.in

© Springer Nature Singapore Pte Ltd. 2021

K. K. Pathak et al. (eds.), *Recent Trends in Civil Engineering*, Lecture Notes in Civil Engineering 77, https://doi.org/10.1007/978-981-15-5195-6_27

clarification, precipitation and calcination to give smelting grade alumina which is the precursor to aluminum [1]. As the demand for aluminum continues to grow, the amount of RM production shows a proportional increase. Although the type of bauxite residue greatly influences the amount of RM produced, it tends to be seen that 0.3–2.5 huge amounts of RM is created per ton of alumina delivered [2]. As per the literature, there is a global production of 90 million tons of RM each year of which India accounts for 4.71 million tons/annum [3]. Due to the high-scale production of the alkaline material, most aluminum refineries find the disposal of RM quite problematic. RM is disposed of in dry or semi-dry form. The slurry usually has a solid concentration in the range of 30–60%.

When compounds of heavy metals and other toxic elements are present in an industrial effluent, they may bring about suppression of the biochemical self-purification of the sources where they are disposed. Red mud waste, which for the most part contains fine particles in the range from sand to residue estimate, is totally free from either quartz or earth-type mineral constituents. Strangely, in the nonappearance of either quartz or mud minerals in red mud waste, scientists have revealed that its pressure and versatility attributes are undifferentiated from clayey soils, and the frictional characteristics resemble that of sandy soils. Additionally, a significant number of its geotechnical properties were depicted to coordinate with those of clayey soils [4, 5]. Moreover, engineering properties, like compaction characteristics, consolidation, settlement limits, shear strength parameters, permeability, etc., of RM were strongly influenced by chemical and mineralogical characteristics [6]. The alkali seepage, airborne dust emissions, large disposal and the presence of trace amounts of heavy metals and radionuclide seepage into groundwater are common environmental problems associated with RM disposal.

Apart from the harmful impact on the environment, disposal of RM is also expensive due to the high investment necessary to construct and maintain the containment structures. Due to these very reasons, disposal of red mud has come to acquire much attention from researchers across the globe to find suitable disposal methods in the field on construction, materials, agriculture, water treatment, among many more. Due to the unbalanced quantity of production of RM, enormous amounts of red mud is being put away in impoundments or dumped into the saline waters of the sea [7]. The major industrial disaster faced by Hungary in 2010 where the wall of the reservoir failed made a revolutionary impact on the world. The reservoir walls collapsed spilling one million m^3 residue of highly caustic bauxite. The release led to 10 deaths and over 120 injuries. The land became highly polluted and contaminated the nearby Torna-Marcal River [8]. Different approaches have been developed to investigate the compatibility of this waste material with the environment. On account of fineness of this waste material, it will set quickly with a fixed proportion of mixing water for non-auxiliary applications. Non-calcinated red mud is utilized as mortars and even as cement in concrete[9].

The shortage of virgin materials is also the main reason for emphasizing many researchers on the utilization of different industrial waste in the construction industry [10]. But utilization of the waste materials directly will not attain the required construction standards in most of the cases [11], so it is very much needed to stabilize

the waste with any other suitable material which can increase the strength properties of the RM [12]. It has been shown from the literature that very less amount of work was done on the usage of RM when it is compared to the generation of waste annually. So in view of this, an attempt was made to settle the RM squander with the gypsum in different percentages starting from 2 to 10% upon the dry weight of the RM in this research work and tests were conducted to study the index and engineering properties of the untreated and gypsum-treated red mud waste.

2 Materials

2.1 Red Mud

Red mud was received from Hindalco, Belgaum, Karnataka for this research study. It was collected in dry state from an unused lake which has a minimum response of pozzolanic. To improve the strength of this RM and to use as a construction material in the construction of roads, it was stabilized with gypsum which imbibes the pozzolanic reaction in the RM and improves the strength. The geotechnical properties and chemical compositions of RM were presented as below. Table 1 presents the

Table 1 Physical and geotechnical properties of red mud

Property	Values
Specific gravity	2.85
pH	11.04
Liquid limit	39%
Plastic limit	28.5%
Sieve analysis	
Coefficient of uniformity (Cu)	0.67
Coefficient of curvature (Cc)	0.71
IS classification	Silt of low plasticity (i.e., ML)
Compaction test	
Optimum moisture content (OMC)	31.39%
Maximum dry density (MDD)	1.60 kg/m^3
California Bearing Ratio (CBR)	
Unsoaked and Soaked	5.28% and 4.17%
Cohesion	16.82 kPa
Angle of internal friction	22.8^o

Table 2 Chemical Composition of red mud in a powdered state by XRF analyzer

Sl. No.	Component	Result (%)	LLD
1	Fe_2O_3	44.3	0.0016
2	AI_2O_3	18.2	0.0194
3	SiO_2	14.5	0.0057
4	TiO_2	10.5	0.0098
5	Na_2O	9.29	0.295
6	CaO	1.11	0.0117
7	P_2O_5	0.738	0.0059
8	SO_3	0.373	0.0014
9	V_2O_5	0.354	0.0178
10	Cr_2O_3	0.177	0.0044
11	ZrO_2	0.132	<0.0001
12	K_2O	0.105	0.0176
13	Co_2O_3	0.103	0.0021
14	CI	0.0877	0.0015
15	MnO	0.0592	0.0037
16	CeO_2	0.0118	0.0015
17	CuO	0.0113	0.0010
18	SrO	0.0070	0.0002
19	La_2O_3	0.0069	0.0011
20	BaO	0.0058	0.0008
21	PbO	0.0052	0.0006
22	Y_2O_3	0.0051	0.0002
23	MoO_3	0.0041	0.0008
24	ThO_2	0.0033	0.0006
25	NiO	0.0031	0.0014
26	SnO_2	0.0017	0.0003
27	ZnO	0.0007	0.0006
28	Rb_2O	0.0003	0.0003

physical and geotechnical properties of red mud and Table 2 presents the chemical composition of red mud which was obtained by the XRF analyzer.

2.2 Gypsum

In Middle East, Asia and Africa, there are many places which have gypsum-contaminated soil called gypsiferous soil. Due to the presence of sulfur-rich minerals

Table 3 Combinations of gypsum and red mud

Sl. No.	Combination Type	Red mud (%)	Gypsum (%)
1	A	100	0
2	B	98	2
3	C	96	4
4	D	94	6
5	E	92	8
6	F	90	10

such as pyrite in the parent material, the origin of sulfate ions exist in the soil solution. The sulfur minerals are transformed into sulphuric acid which is calcareous soils due to weathering and oxidation and reacts with CaCO3 to form gypsum. Gypsum is normally a rock-like mineral which is found naturally under the earth's crust which is extracted, processed and used as plaster, then it is also used in man-made construction and decoration. The best source of calcium is gypsum and it is an important secondary plant nutrient. It is also a major balancing element in plants and soils. Gypsum is utilized to quicken the pozzolanic response between red mud and fly fiery remains.

3 Methodology

Every one of the tests performed was separated into two classifications: (i) To decide blends index properties (ii) To decide mixes properties of quality. Recorded properties are liquid limit, specific gravity, point of confinement of plastic, plasticity index and so on; the characteristics of strength are compaction test (OMC, MDD), UCS and CBR. By using density bottle, soil specific gravity was found according to IS 2720. Grain size analysis was determined by using sieve and hydrometer analysis according to IS 2720. According to the procedure stated in IS 2720, plastic and liquid limits are determined. By standard Proctor test compaction characteristics are determined according to IS 2720, and CBR tests were carried out according to the procedures in IS 2720. The UCS of the soil was determined in accordance with IS 2720. The index and engineering properties of untreated and treated red mud with gypsum were determined which indicates that red mud can be used as a material for construction. The combinations of gypsum and red mud in different percentages are mentioned in Table 3.

4 Results and Discussion

The results of the untreated RM and gypsum-treated RM were depicted in the below tables in the form of combinations. The index properties like specific gravity,

liquid and plastic limit of different mixtures of RM and gypsum were presented in Table 4 and the strength properties like compaction characteristics and unconfined compressive strength of RM and gypsum-treated RM were presented in Table 5.

The compaction characteristics like optimum moisture content (OMC), max dry density (MDD), unconfined compressive strength were determined for the treated and untreated mud along with gypsum.

Table 5 depicts that the OMC increases with the increase of gypsum content and at the same time MDD decreases with the increase of the gypsum percentage. It also shows that the value of UCS increased predominantly with the increase in the gypsum percentage and this resembles that by adding the gypsum it increments the quality properties of the RM.

Table 6 shows the CBR properties of untreated and treated RM samples in different combinations. The samples were prepared and tested as per IS: 2720 (Part 16). 1.25 mm/min strain rate is maintained to test all the CBR molds and the loads required for the penetration of 2.5 mm and 5.0 mm plungers are resolved according to the guidelines and are noted in the table. The CBR molds are soaked in water for 4 days to know the soaked values of CBR. It is the general tendency to account for the soaked CBR value. It is observed with the addition of gypsum the CBR value was increased tremendously and even the soaked CBR value also increases with gypsum addition. Improvement in CBR of both unsoaked and soaked can be identified with the help of F combinations. As the gypsum acts as a filler material when it comes in contact with RM in the microstructural level, the CRB percentage increases and the tendency of gypsum is to impart the strength upon curing which proves that the

Table 4 Index properties of different combinations of treated and untreated RM

Sl. No.	Combination	Specific gravity	Liquid limit (%)	Plastic limit (%)
1	A	2.64	39.00	28.50
2	B	2.14	42.56	32.41
3	C	2.34	44.35	33.42
4	D	2.42	45.35	33.69
5	E	2.39	48.12	34.82
6	F	2.28	49.22	36.28

Table 5 Engineering properties of untreated and treated red mud in different combinations

Sl. No.	Combination	OMC (%)	MDD (g/cc)	UCS (kN/m^2)
1	A	31.39	1.20	39.41
2	B	28.16	1.23	41.2
3	C	27.17	1.36	44.5
4	D	25.68	1.41	46.3
5	E	25.28	1.45	47.2
6	F	22.22	1.49	48.1

Table 6 CBR properties of untreated and treated red mud in different combinations

Sl. No.	Sample combination	Unsoaked		Soaked	
		2.5 mm	5 mm	2.5 mm	5 mm
1	A	5.62	5.69	1.24	1.31
2	B	5.84	5.91	1.61	1.72
3	C	6.35	6.44	2.11	2.26
4	D	6.13	7.47	2.63	2.67
5	E	7.11	8.80	3.50	3.47
6	F	13.33	13.87	5.69	5.87

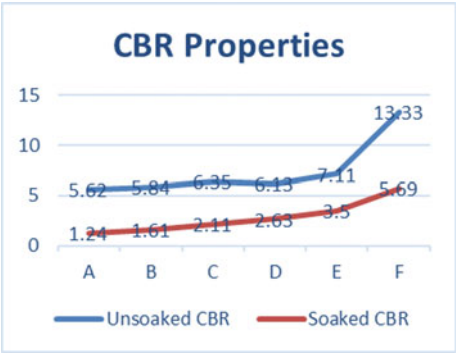

Fig. 1 Soaked and unsoaked CBR value comparison

soaking condition of all the samples have better CBR value and the trend of CBR improvement was clearly presented in Fig. 1.

5 Conclusions

Addition of gypsum to RM increases the maximum dry density and decreases the optimum moisture content. Detailed information regarding the OMC and MDD was studied with the various trails of standard compaction test which will enact the role of gypsum addition to the RM in dry density properties. More strength can be achieved if it undergoes more curing period. The UCS values also increase with the increase of gypsum as C-H-S gel form when gypsum comes in contact with the RM. The UCS values and MDD values show that the treated RM is suitable for the construction of roads when compared with the standards. As per the IRC the CBR value attained with the gypsum is most suitable for the construction of roads limiting to low volume roads. The value of CBR increases exponentially by gypsum addition.

References

1. Hind AR, Bhargavva SK, Grocott SC (1999) The surface chemistry of Bayers Process solids: A review. Colloids Surf A Physiochem Eng Asp
2. Cablik V (2007) Charecterization and applications of red mud from bauxite processing. Tech Rep
3. Patel S, Pal BK (2015) Current status of an industrial waste: red mud an overview. IJLTEMAS IV(VIII) ISSN 2278 – 2540
4. Gray DH, Somogyi F (1974) Engineering properties and dewatering characteristics of red mud tailings. DRDA Project 340364:100 p
5. Gray DH, Lin YK (1972) Engineering properties of compacted fly ash. J SMFE Proc ASCE 98:361–380
6. Parekh BK, Goldberger WM (1976) An assessment of technology for possible utilization of Bayer process muds. EPA-600/2–76-30 1:154 p
7. Brunori C, Cremisini C, Massanisso P, Pinto V, Torricelli L (2005) Reuse of a treated red mud bauxite waste: studies on environmental compatibility. J Hazard Mater 11(1):55–63
8. Renforth P, Mayes WM, Jarvis AP, Burke IT, Manning DAC, Griz K (2012) Contaminant mobility and carbon sequestration downstream of the Ajka (Hungary) red mud spill: the effects of gypsum dosing. Sci Total Environ Vol 421–422:253–259
9. Ribeiro DV, Labrinch JA, Morell MR (2011) Potential use of natural red mud as pozzolan for Portland cement. Mater Res 11(14)
10. Deelwal K, Dharavath K, Kulshreshtha M (2014) Stabilization of red mud by lime, gypsum and investigating its possible use as a geotechnical material in the civil construction. Int J Adv Eng Technol ISSN: 22311963 7(4)
11. Hanumanth Rao CHV, Ganapati Naidu P, Satyanayarana PVV, Adiseshu S (2012) Application of GGBS stabilized redmud in road construction. J Eng 2(8)
12. Pandey PK, Jawad Ali SM (2015) Soil improvement using red mud and fly ash. Glob J Eng Sci Res 1(2)

Strength Characteristics of Cement-Stabilized Recycled Asphaltic Pavement (RAP) for Pavement Applications

V. K. Vidyashree, K. H. Mamatha, and S. V. Dinesh

Abstract Good quality construction materials are on the verge of depletion in various parts of the world. It is essential to preserve the available natural resources for the future. This scenario forces the engineers toward recycling of the construction materials such as recycled asphaltic pavement, construction and demolition waste, and demands their reuse in construction. As these materials are already distressed, they are inferior compared to conventional natural construction materials. This poses a limitation for the use of such recycled materials in construction and only a small amount of recycled materials can be used in its original form. To overcome this limitation, admixtures such as cement, lime and fly ash can be added to the recycled materials for improving their mechanical properties making them more durable. In this study, one such recycled material obtained from pavements during its rehabilitation, reconstruction, maintenance, etc. over a period of time is considered for investigation. The strength of various RAP–conventional aggregate mixtures were characterized in terms of CBR, and its suitability for granular sub-base applications is evaluated based on minimum CBR criteria specified by the relevant standards. From the test results, it is observed that the addition of cement improves the strength of the mix. Based on the minimum strength criteria of GSB, cement content of up to 3% is found to replace up to 100% conventional GSB material providing eco-friendly and sustainable construction practice.

Keywords RAP · GSB · CBR · Service life · Pavement

1 Introduction

The construction of roadways involves a huge quantity of natural resources. Good quality construction materials are not available everywhere around the world. In order to minimize the adverse effects of quarrying on the environment and also, to preserve the available natural resources for the future, it is very much essential to

V. K. Vidyashree · K. H. Mamatha (✉) · S. V. Dinesh
Department of Civil Engineering, Siddaganga Institute of Technology, Tumakuru, India
e-mail: mamathakh@sit.ac.in

© Springer Nature Singapore Pte Ltd. 2021

K. K. Pathak et al. (eds.), *Recent Trends in Civil Engineering*, Lecture Notes in Civil Engineering 77, https://doi.org/10.1007/978-981-15-5195-6_28

recycle the distressed material and reuse wherever possible. In this connection, nowadays, the utilization of recycled asphaltic pavement (RAP) in construction activities is gaining popularity over the usage of conventional construction materials. However, the quantity of RAP production and utilization has no comparison [1]. The effective use of RAP is possible only when its strength characteristics are properly understood. 100% RAP material exhibits inferior mechanical properties such as density, unconfined compressive strength (UCS) and resilient modulus [2, 3]. Thus, RAP alone does not contribute to higher resistance to the applied load. In order to strengthen the RAP, it is necessary to add suitable admixtures such as cement, lime and fly ash. Limited research is available on the strength characteristics of RAP stabilized with various admixtures such as cement, lime and fly ash [1, 4–8]. Several studies in the literature examined the resilient modulus of RAP or RAP blends, which is a parameter used in the design of the thickness of the base course [9–12]. The maximum dry unit weight and UCS of RAP generally increase with the addition of virgin aggregates [13]. Several researchers investigated the influence of cement on the strength and stiffness of RAP for pavement applications [14–19]. However, these studies considered the use of a lower percentage of RAP to replace the conventional aggregates in the design mix, with a maximum replacement being 50%.

In this study, the strength of RAP under unstabilized and cement-stabilized conditions was evaluated in terms of CBR. The results were compared and analyzed for granular sub-base application and are reported. An attempt is made to replace higher percentages of conventional aggregates with RAP satisfying the strength requirements of granular sub-base (GSB) as specified by the prevailing standards.

2 Materials

In this study, RAP was collected from NH4, Savandurga, Tumakuru District, Karnataka. Conventional aggregates of size 40 mm down, 12.5 mm down and stone dust were collected from a local quarry located in Mydala, Tumakuru District, Karnataka. Initially, the RAP and aggregates were characterized for their physical and mechanical properties as per the procedures outlined in the prevailing Indian Standards (IS). The RAP was subjected to bitumen extraction followed by fractional distillation of the extract to determine the binder content present in the RAP and the binder content was found to be 2.36%. The properties of the extracted aggregates are tabulated in Table 1. Figure 1 shows the gradation curves of RAP and extracted aggregates. The properties of conventional aggregates along with the specifications of Ministry of Road Transport and Highways (MoRT&H) [20] are tabulated in Table 2. It is observed that the conventional aggregates satisfy the requirements of granular sub-base (GSB) specified by MoRT&H [20] guidelines. Further, individual gradation of all the three fractions was carried out as per IS 383 (2002) guidelines followed by combined gradation in order to meet the gradation requirements of GSB of grade 2 as specified by MoRT&H [20]. By trial and error, a design mix with 25% of 40 mm

Table 1 Properties of extracted aggregates

Property	Value
Specific gravity	
Fine aggregates	2.71
Coarse aggregates	2.61
Aggregate impact value (%)	22
Aggregate crushing value (%)	18
Combined indices (%)	23

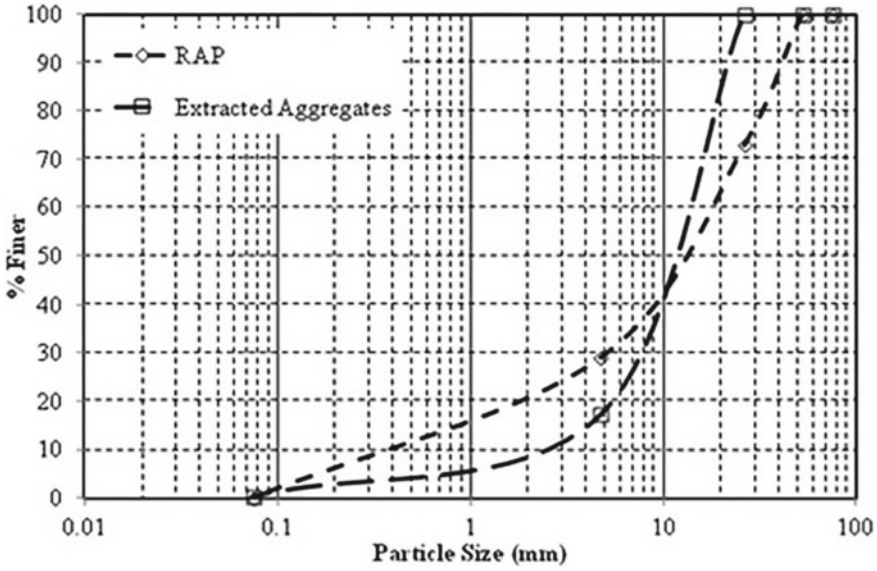

Fig. 1 Gradation curves of extracted aggregates and RAP

Table 2 Properties of conventional aggregates along with MoRT&H [20] specifications

Property	Aggregate fraction			MoRT&H [20] specifications
	40 mm down	12.5 mm down	Stone dust	
Specific gravity	2.63	2.62	2.68	2.5–3.2
Water absorption (%)	0.21	0.17	–	Max. 2%
Aggregate impact value (%)	26	26		Max. 30%
Aggregate crushing value (%)	25	25		Max. 30%
Los Angeles abrasion value (%)	27	27		Max. 40%
Combined indices (%)	30	30		Max. 35%

down, 27% of 12.5 mm down and 48% of stone dust was found to satisfy the requirements of grade 2 of GSB as per MoRT&H [20]. Figure 2 shows the gradation curve of the designed GSB mix confirming to grade 2 along with its upper and lower bound values as specified by MoRT&H [20]. The designed mixture possesses a maximum dry unit weight of 23kN/m3 and an optimum moisture content of 1.4% under modified Proctor condition. It possesses an unsoaked CBR of 45% and soaked CBR of 29% when compacted to its modified Proctor condition. In order to stabilize the RAP, ordinary Portland cement of grade 53 was used as a stabilizing agent. The physical properties of the cement along with the IS 269 [21] specifications are tabulated in Table 3.

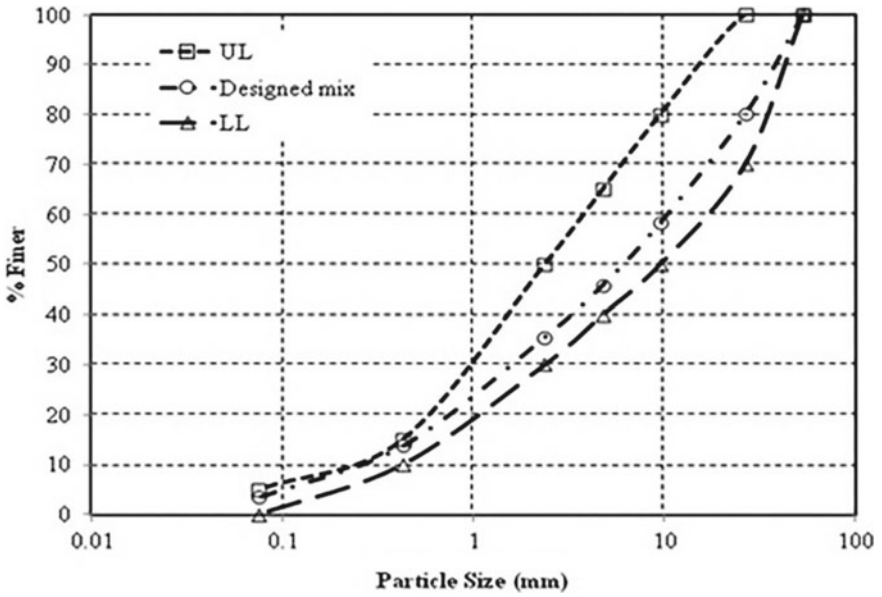

Fig. 2 Gradation curve of the designed GSB mix confirming to grade 2 along with its upper and lower bound values as specified by MoRT&H [20]. *UL—Upper limit, LL—Lower limit

Table 3 Properties of cement along with the IS 269 [21] specifications

Property	Value	IS 269 [21] Specifications
Specific gravity	3.11	3.15
Normal consistency (%)	29	30
Initial setting time (s)	95	Min. 30
Final setting time (s)	260	Max. 300

3 Design of Experiments

In this study, a series of compaction and CBR tests were carried out on RAP–conventional aggregate mixtures. The RAP content was varied from 0 to 100% with an increment of 20%. Under a cement-stabilized condition, the dosage of cement was varied from 0 to 4% with an increment of 1%. The cement-stabilized test specimens were kept in airtight bags and cured for 7 days. The CBR test specimens were tested under soaked conditions where they were soaked for a period of 96 h as per ASTM D 1883 [22]. Table 4 shows the design of experiments considered in this study. The mixtures were designated as % R + % C indicating the percentage of RAP + percentage of the conventional aggregate mix. For instance, a mix designated as 60% R + 40% C represents a mix consisting of 60% of RAP and 40% of the conventional aggregate mix.

Table 4 Design of experiments

Test	Composition of Mix (RAP + Conventional aggregate)	Cement content (%)	Curing period (days)	Test condition
Compaction test	100% R + 0% C	–	–	Modified proctor
	80% R + 20% C			
	60% R + 40% C			
	40% R + 60% C			
	20% R + 80% C			
	0% R + 100% C			
CBR	100% R + 0% C	–	–	Soaked
	80% R + 20% C			
	60% R + 40% C			
	40% R + 60% C			
	20% R + 80% C			
	0% R + 100% C			
	100% R + 0% C	1, 2, 3, 4	7	Soaked
	80% R + 20% C	1, 2, 3, 4		
	60% R + 40% C	1, 2, 3, 4		
	40% R + 60% C	1, 2, 3, 4		
	20% R + 80% C	1, 2, 3, 4		

4 Results and Discussions

A series of compaction and CBR tests were carried out. The test results were analyzed in terms of strength requirement of GSB as per MoRT&H [20] guidelines. The test results are presented and discussed in the following paragraphs.

Figure 3 shows the compaction curves of the RAP–conventional aggregate mixtures under unstabilized and modified Proctor condition. It was observed that with the increased RAP percentage in the mixture, the maximum dry unit weight reduced and optimum moisture content increased. This is attributed to the break-down of the RAP particles under the impact of the rammer leading to increased fines content in the mixture. With RAP content ranging from 0 to 100%, the dry unit weight of the mixture reduced from 23 to 18.8 kN/m^3 and the optimum moisture content increased from 1.4 to 3.8%.

Figure 4 shows the variation of CBR with RAP content in the mixture under soaked condition. It was observed that the CBR value reduced with an increase in the RAP content in the mixture. As the RAP material is inferior in comparison with the conventional GSB mixture, it is obvious that the strength decreases with an increase in the percentage of inferior material in the mixture. With the RAP content ranging from 0 to 100%, the CBR was found to reduce from 29 to 12%. As per MoRT&H [20] guidelines, the minimum CBR of GSB confirming to grade 2 is 25%. From the test results it is observed that the mixture with 20% of RAP satisfies the minimum CBR criteria as specified by MORT&H [20]. On the other hand, all other

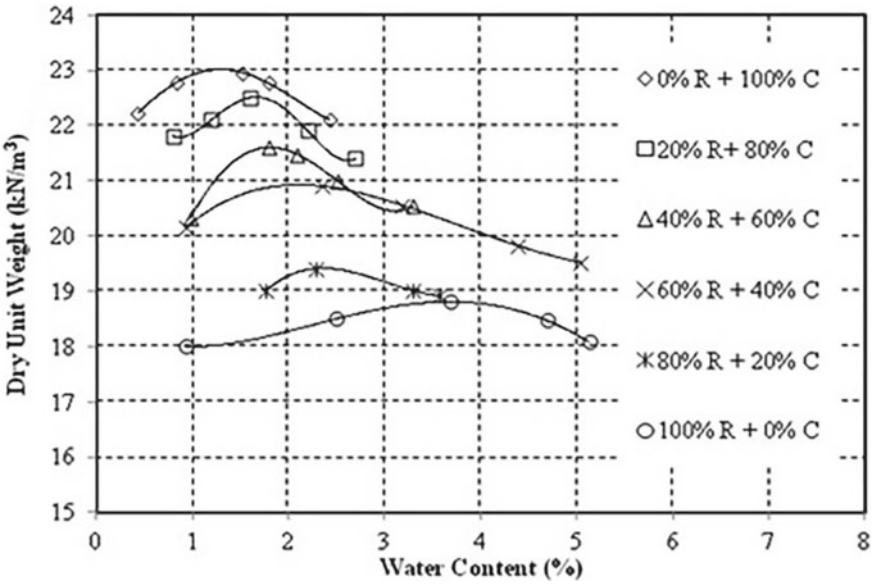

Fig. 3 Compaction curves of RAP–conventional aggregates mix under modified Proctor condition corresponding to unstabilized condition

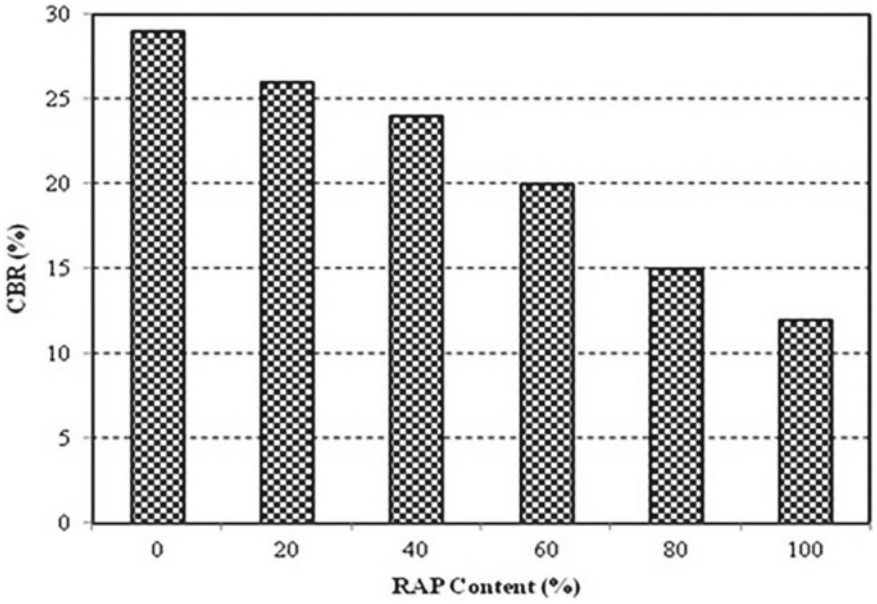

Fig. 4 Variation of CBR with RAP content in the mixture under soaked condition

mixtures were found to be not suitable for GSB application based on minimum strength criteria. Thus, under unstabilized condition, it is only possible to replace 20% of the conventional aggregates.

Figures 5 and 6 show the variation of CBR of 7-day cured cement-stabilized RAP–conventional aggregate mixtures with RAP content and cement content, respectively, under soaked condition. It is observed that the addition of cement had a positive impact on the strength of the RAP–aggregate mixture. It further increased with an increase in the cement content. In general, the mixtures with lower RAP contents possess higher CBR value irrespective of the dosage of cement. On this line, the mixture with 20% RAP possesses maximum strength and the mixture with 100% RAP possesses the least strength. Similarly, it is observed that the higher the cement content, the higher is the strength of the mixture irrespective of the mixture type. On this line, among the cement dosages considered in this study, the mixture with 1% cement possesses the least strength and the mixture with 4% cement possesses maximum strength. The increased CBR value with the addition of cement is attributed to the pozzolanic reactions involved leading to the formation of cementitious compounds. The CBR of the mixture with 20% of RAP increased from 26% (unstabilized) to 59% with cement content ranging from 0 to 4%. Similarly, CBR of the mixture with 100% RAP increased from 12% (unstabilized) to 35% with cement content ranging from 0 to 4%. For GSB application by considering the minimum strength criteria specified by MoRT&H [20], a cement content of 1% enables the replacement of up to 60% of conventional aggregates with RAP. Similarly, 2 and 3%

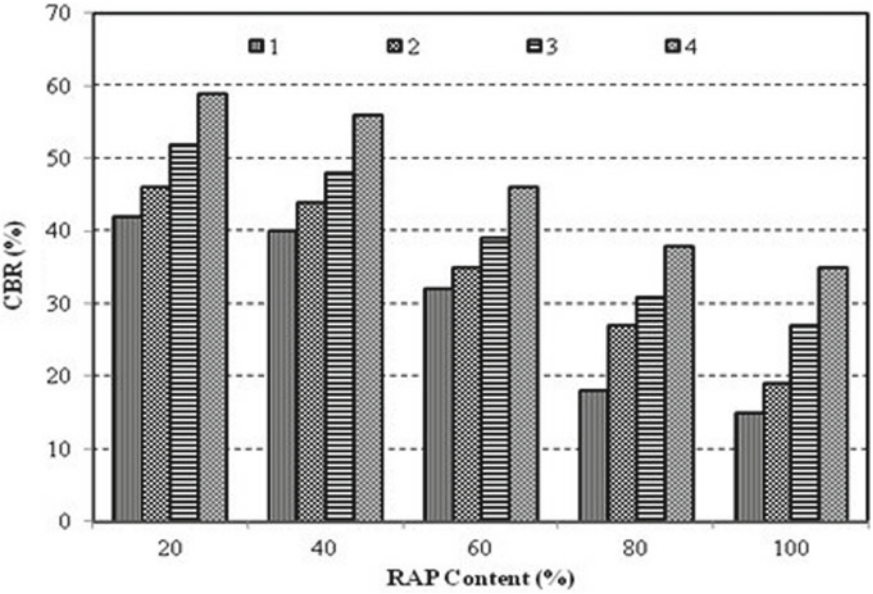

Fig. 5 Variation of CBR of 7-day cured cement-stabilized RAP–conventional aggregate mixtures with RAP content under soaked condition

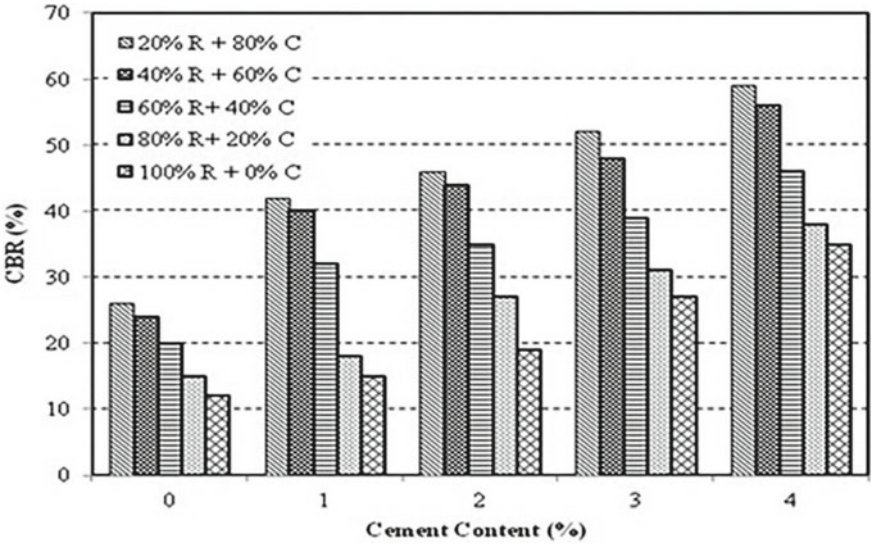

Fig. 6 Variation of CBR of 7-day cured cement-stabilized RAP–conventional aggregate mixtures with cement content under soaked condition

of cement enable the replacement of up to 80 and 100% of conventional aggregates with RAP. Thus, cement stabilization enables the utilization of higher percentage of RAP satisfying the minimum strength requirement as specified by MoRT&H [20] providing a sustainable solution for roadway construction.

5 Implementation

The GSB layer is mainly designed to serve as a drainage layer in pavements. The permeability of cement-stabilized RAP and/or RAP–conventional aggregate mixture is less in comparison with conventional GSB material. Therefore, in areas having medium rainfall, the cement-stabilized RAP or RAP–conventional aggregate mixture can be provided at the upper half of the GSB whereas the remaining lower half needs to be provided with the conventional GSB material to serve its drainage function on groundwater-level fluctuations. In low rainfall areas, the full depth of GSB can be replaced by cement-stabilized RAP or RAP–conventional aggregate mixture as the fluctuation in groundwater level is minimum in those areas. In general, the provision of RAP–aggregate mixture in GSB will increase the load-carrying capacity of the pavement section and reduce the overall stresses transferred to the subgrade leading to the increased service life of the pavement.

6 Conclusions

A series of CBR tests were carried out on unstabilized and cement-stabilized RAP–conventional aggregate mixtures for evaluating its suitability for GSB applications. Based on the test results and minimum strength of GSB as specified by MoRT&H (2013) guidelines, the following conclusions are drawn.

- Based on the minimum strength requirement of GSB, only 20% of a conventional aggregate mixture can be replaced by RAP under unstabilized condition.
- Cement stabilization is effective in improving the CBR of the RAP and/or RAP–conventional aggregate mixtures.
- In general, lower RAP content and higher cement content in the mixture yielded higher strength.
- Based on the minimum strength criteria, the cement content of up to 3% enables the use of RAP up to 100% for GSB applications.
- Higher percentage of RAP utilization under stabilized condition leads to more durable pavements leading to increased service life. Also, it forms a sustainable and eco-friendly alternative for conventional construction materials.

Acknowledgments The authors acknowledge the support provided by NR Crushers, Mydala, Tumakuru, Karnataka for providing the crushed aggregates for carrying out this study.

References

1. Saride S, Avirneni D, Javvadi SCP (2016) Utilization of reclaimed asphalt pavements in Indian low volume roads. J Mater Civ Eng 28(2):1–10
2. Li L, Benson CH, Edil TB, Hatipoglu B (2008) Sustainable construction case history: Fly ash stabilization of recycled asphalt pavement material. J Geotech Geol Eng 26(2):177–187
3. Arulrajah A, Piratheepan J, Disfani MM, Bo MW (2013) Resilient moduli response of recycled construction and demolition materials in pavement subbase applications. J Mater Civ Eng 1920–1928
4. Edil TB, Benson CH (2007) Demonstration of ash utilization in low volume roads. Report No. MN/RC-2007-12, Department of Transportation, St. Paul, MN
5. Deren Y, Nazarian S, Hoyos LR, Puppala AJ (2011) Evaluation and mix design of cement-treated base materials with high content of reclaimed asphalt pavement. Transportation Research Record 2212, Transportation Research Board, Washington, DC, pp 110–119
6. Curtis B, Haichert R, Podborochynski D, Colin W, Taylor B, Guenther D (2010) Cement stabilization of reclaimed asphalt pavement materials. In: Proceedings of transportation research board 89th annual meeting, Washington, DC
7. Albert M Bleakley and Paul J Cosentino (2013) Improving properties of reclaimed asphalt pavement for roadway base applications through blending and chemical stabilization. Transp Res Rec J Transp Res Board. No. 2335, Transportation Research Board of the National Academies, Washington, DC, pp 20–28
8. Saride S, Avirneni D, Javvadi SCP, Puppala AJ, Hoyos LR (2015) Evaluation of fly ash treated reclaimed asphalt pavement for base/subbase applications. Indian Geotech J 45(4):401–411
9. Alam TB, Abdelrahman M, Schram S (2010) Laboratory characterization of recycled asphalt pavement as a base layer. Int J Pavement Eng 11(2):123–131
10. Locander R (2009) Analysis of using reclaimed asphalt pavement (RAP) as a base course material. CDOT-2009-5, Colorado Department of Transportation, Denver
11. Kim W, Labuz JF, Dai S (2007) Resilient modulus of base course containing recycled asphalt pavement. Transp Res Rec J Transp Res Board. No. 2005, Transportation Research Board of the National Academies, Washington, DC, pp 27–35
12. Wu M (2011) Evaluation of high percentage recycled asphalt pavement as base course materials. MS thesis, Washington State University, Pullman
13. Taha R, Ali G, Basma A, Al-Turk O (2007) Evaluation of reclaimed asphalt pavement aggregate in road bases and subbases. Transp Res Rec 1652:264–269
14. Taha R, Al-Harthy A, Al-Shamsi K, Al-Zubeidi M (2002) Cement stabilization of reclaimed asphalt pavement aggregate for road bases and subbases. J Mater Civ Eng 14(3):239–245
15. Hoyos LR, Puppala AJ, Ordonez CA (2011) Characterization of cement-fiber-treated reclaimed asphalt pavement aggregates: preliminary investigation. J Mater Civ Eng 23(7):977–989
16. Puppala AJ, Hoyos LR, Potturi AK (2011) Resilient moduli response of moderately cement-treated reclaimed asphalt pavement aggregates. J Mater Civ Eng 23(7):990–998
17. Deren Y, Puppala AJ (2011) Evaluation and mix design of cement-treated base materials with high RAP content. In: Transportation research board 90th annual meeting, Transportation Research Board, Washington, DC
18. Tyson R, Icenogle PEI, Reech S (2011) Evaluation of cement and fly ash treated recycled asphalt pavement and aggregates for base construction. FHWA/LA.11/481, Louisiana Department of Transportation and Development, Baton Rouge, LA
19. Ebrahim A, Kootstra R, Tuncer BE, Benson CH (2012) Practical approach for designing flexible pavements using recycled roadway materials as base course. Road Mater Pavement Des 13(4):731–748
20. MoRT&H (2013) Ministry of road transport and highways: specifications for roads and bridges, 5th edn. Indian Roads Congress, New Delhi

21. IS 269 (2015) Methods of test for cement—mechanical and physical properties. Bureau of Indian Standards, New Delhi
22. ASTMD 1883 (2016) Standard test method for California bearing ratio (CBR) of laboratory compacted soils. ASTM International, West Conshohocken, PA

Feasibility of Recycled Tyre as Reinforcing Material for Pavements

B. N. Vinod Raj, K. H. Mamatha, and S. V. Dinesh

Abstract Rapid industrialization and urbanization lead to various forms of waste materials such as construction and demolition waste, industrial by-products, waste tyres, etc. In some cases, the disposal of waste materials is of prime concern and a few waste materials are hazardous to the environment. Such scenarios force engineers to recycle and reuse these waste materials in an effective way wherever possible. In this study, one such waste material produced from vehicles, i.e., waste tyres, is considered. An attempt is made to reinforce the model pavement section with the recycled tyre in the cellular grid form. Repeated load tests were carried out on unreinforced and reinforced model pavement sections. The test results indicated that the reinforcement significantly reduces the plastic settlement and the pressure transferred to the subgrade level providing long-lasting pavements.

Keywords Recycled tyre · Plastic settlement · Residual pressure · Service life

1 Introduction

Nowadays, infrastructure development is assuming greater importance and, in that, development of connectivity through a network of roadways is of prime concern. The construction of roads consumes a huge quantity of construction materials. Good quality materials are not available everywhere and if available, preservation of such materials for the future is important. At the same time, the roads cannot be constructed with the inferior materials as it leads to thicker pavement sections, shorter design life, etc. For effectively using these inferior materials in construction, it is essential to improve their properties. These days, the provision of reinforcement within the pavement section is being widely used over conventional ground improvement methods as the method is simple to execute, quick, etc. Many researchers in the past have investigated the effect of geosynthetic reinforcement on the pavement performance

B. N. Vinod Raj · K. H. Mamatha (✉) · S. V. Dinesh
Department of Civil Engineering, Siddaganga Institute of Technology, Tumakuru, India
e-mail: mamathakh@sit.ac.in

© Springer Nature Singapore Pte Ltd. 2021

K. K. Pathak et al. (eds.), *Recent Trends in Civil Engineering*, Lecture Notes in Civil Engineering 77, https://doi.org/10.1007/978-981-15-5195-6_29

[1–17] and they have been able to identify the benefits in terms of either reduced plastic deformation or reduced stresses at the top of subgrade.

In recent years, in India, there has been a tremendous increase in the number of vehicles. On a later date, this will lead to the generation of scrap tyres in large volumes which poses an increasing threat to the environment. To eliminate the adverse effects of such waste materials, it is intended to opt for the recycling of non-hazardous wastes. Waste tyres have excellent mechanical properties and they are non-biodegradable. The potential of using rubber from the worn-out tyres in various civil engineering projects has been studied for more than four decades. Waste tyres have been effectively used for partial replacement of aggregates in mortar and concrete [18, 19] to produce workable concrete for specific applications. Studies reported that mechanical properties such as compressive strength, flexural strength, tensile strength and dynamic modulus of elasticity of the cement-based products can be reduced by the addition of tyre particles thereby producing less brittle material [19–21]. The use of waste tyre in asphalt mixtures leads to better skid resistance, reduced fatigue cracking, improved rut resistance, improved tensile strength and toughness, longer pavement life and reduced maintenance cost compared with conventional mixtures [22–24].

In this study, an attempt is made to evaluate the feasibility of recycled tyre as reinforcing material for granular layer reinforcement in pavements. The performance of the pavement section was evaluated under unreinforced and recycled tyre reinforced conditions in terms of settlement, pressure at subgrade level and surface profile, and is reported.

2 Materials

In this study, black cotton soil and crushed aggregates were used for the construction of the prototype of the pavement section in the laboratory. Black cotton soil was collected from Harathikote near Chellakere, Chitradurga District, Karnataka. Crushed aggregates of size 40 mm down, 12.5 mm down and stone dust were collected from a quarry located in Mydala, Tumakuru, Karnataka. Initially, the soil and aggregates were tested for their physical and mechanical properties as per the relevant IS guidelines. Tables 1 and 2 show the properties of soil and aggregates along with the applicable specifications, respectively. The soil possesses 86% of fines, plasticity index of 42% and is classified as A-7-6 as per Highway Research Board (HRB) classification. It is observed that the soil fails to meet the criteria of subgrade soil as specified by Ministry of Road Transport and Highway Officials (MoRT&H) [25] and Indian Road Congress Special Publication (IRC SP) [26] and thus forming a weak subgrade. The aggregates were found to satisfy the requirements of base as specified by MoRT&H [25].

The aggregates were subjected to individual gradation followed by combined gradation in order to design a mix confirming to base course material of grade I as per MoRT&H [25] guidelines. By trial and error method, a mix with 36% of

Table 1 Properties of black cotton soil

Property	Result	Specification requirements
Specific gravity	2.7	–
Consistency limits (%)		
Liquid limit	74	<70% [25]
Plastic limit	32	–
Plasticity index	42	<45% [25]
Compaction characteristics (Standard Proctor test)		
Maximum dry unit weight (kN/m^3)	14.7	>16.5 kN/m^3 [25]
Optimum moisture content (%)	24	–
Free swell index (%)	80	<50% [25]
CBR (%)		
Unsoaked	6	–
Soaked	<2	>2% [26]

Table 2 Properties of aggregates

Property	Aggregates			Specification requirements [25]
	12.5 mm down	40 mm down	Stone dust	
Specific gravity	2.57	2.62	2.66	2.5–3.2
Aggregate crushing value (%)	17.8	–	–	<30%
Aggregate impact value (%)	24	–	–	<30%
Los Angeles abrasion (%)	28	31	–	<40%
Combined indices (%)	24	32	–	<35%
Water absorption	0.17	0.21	0.25	<2%

40 mm down aggregates, 28% of 12.5 mm down aggregates and 36% of stone dust were designed satisfying the gradation and plasticity requirements of MoRT&H [25]. The designed mix possesses a maximum dry unit weight of 24kN/m3 and 1.4% of optimum moisture content under modified Proctor condition. The mix possesses a CBR of 80% and 56%, respectively, under unsoaked and soaked test conditions.

For reinforcement, worn-out truck tyres were collected locally. The tyre was initially cut into strips of width 150 mm, length 1.5 m and thickness 2–4 mm. Figure 1 shows the preparation of recycled tyre strips. A cut was made up to the mid-height (i.e., 75 mm) of the strip at an interval of 150 mm along the length of the strip. For reinforcement, initially, a set of strips were arranged with the cut facing upwards with a spacing of 150 mm and then another set of strips having the cut facing downward

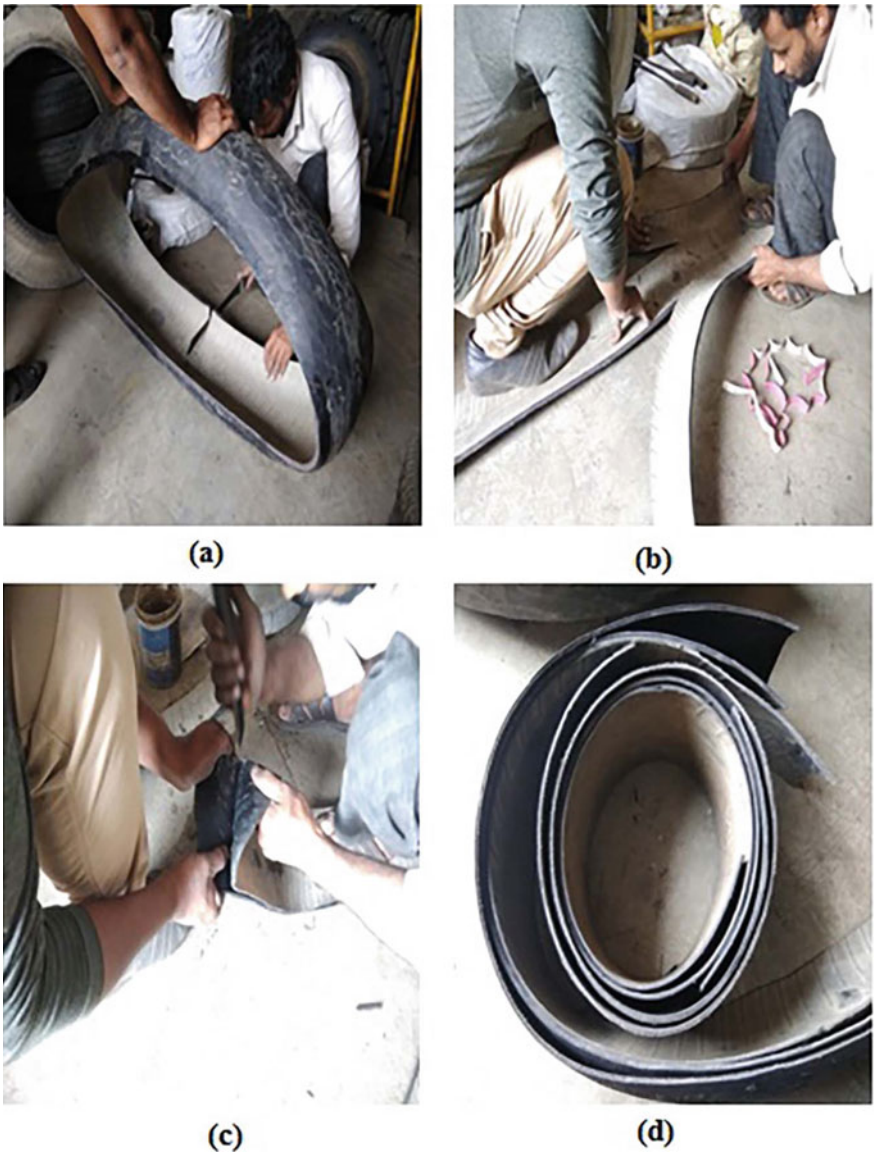

Fig. 1 Preparation of recycled tyre strips. **a** Cutting of tyre. **b** Making of strips. **c** Cutting into strips of required thickness. **d** Recycled tyre strips

Fig. 2 Recycled tyre reinforcement

was placed, thus forming a square grid having an aperture size of 150 mm. Figure 2 shows the recycled tyre reinforcement used in this study.

3 Pavement Design

Initially, pavement design was carried out as per the guidelines stated in IRC SP 72 [26]. For the pavement design, a soaked CBR of 2% and design traffic of 10,000–30,000 equivalent standard wheel load (ESWL) was considered. With these input data, the designed pavement consists of 100 mm of improved subgrade over the weak subgrade, 200 mm of granular base and 50 mm of unpaved surfacing. In order to evaluate the effect of recycled tyre reinforcement on the pavement, the improved subgrade was omitted. In this study, model pavements comprising 300 mm weak subgrade and 200 mm of base were considered under unreinforced and reinforced conditions. Figure 3 shows the typical pavement sections considered in this study.

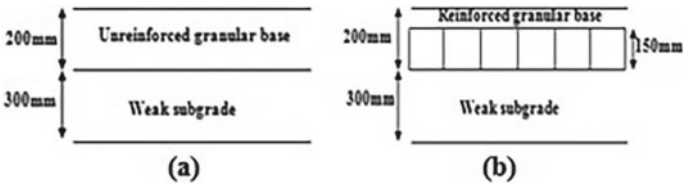

Fig. 3 Typical pavement section. **a** Unreinforced. **b** Reinforced

4 Construction of Model Pavement Section

The model pavement section was constructed in a steel tank having 2 m × 2 m × 2 m dimensions. A total of two pavement sections were constructed in this study and the details of the pavement composition are detailed under pavement design.

Initially, the steel tank was filled with sand with a relative density of greater than 85% up to a depth of 1 m. Over this sand bed, model pavement section having an area of 1.5 m × 1.5 m was constructed with the help of a steel frame having 1.5 m × 1.5 m × 0.3 m dimensions. The construction started with a weak subgrade of 300 mm thickness compacted corresponding to its standard Proctor conditions as recommended by MoRT&H [25] and the compaction was done manually using a rammer in three lifts of 100 mm each. When once the subgrade is compacted, relative compaction was evaluated through the core cutter method and a relative compaction of greater than 95% was considered as specified by MoRT&H [25]. Over the prepared subgrade, a granular base of 200 mm thickness was constructed in two lifts of 100 mm each and the compaction was carried out using a vibratory plate compactor. Figure 4 shows the vibratory plate compactor. The compactor consists of a square base plate of size 0.25 m and 10 mm thickness. The compactor facilitates compaction at four frequencies (i.e., 20, 40, 60 and 80 Hz) and the base material was compacted with 80 Hz frequency. When once the base layer is compacted, the relative compaction was evaluated through the sand replacement method and a relative compaction of greater than 98% was considered as specified by MoRT&H [25]. In the case of reinforced pavement section, the reinforcement was provided at the interface of the subgrade and base. The apertures were filled with the base course material and initial compaction was done using a tamping rod followed by vibratory plate compactor in order to achieve the desired relative compaction for the full depth of the base layer. After the construction of each layer, the steel frame was raised and the sides of the pavement section were filled by sand which is assumed to act as earthen shoulders. Figure 5 shows the pictorial view of the construction of the model pavement section.

Fig. 4 Vibratory plate compactor

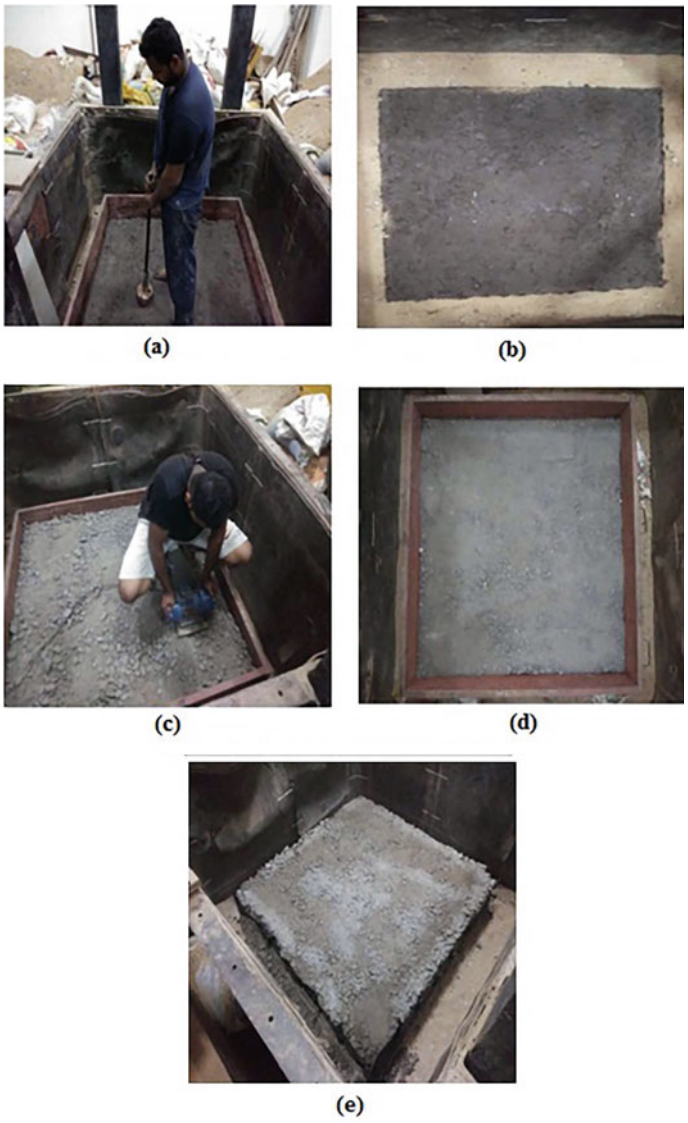

Fig. 5 Pictorial view of construction of model pavement section. **a** Compaction of subgrade. **b** Prepared subgrade. **c** Compaction of base. **d** Prepared base. **e** Recycled tyre reinforced base

5 Instrumentation

In this study, the pressure at the top of the subgrade was measured by means of pressure cells. The pressure cells were manufactured by Tokyo Sokki Kenkyujo Co. Ltd., Tokyo, Japan. A total of three pressure cells were used. Among the three

pressure cells, one pressure cell is of 1000 kPa capacity and was placed at the centre of the section. The remaining two pressure cells are of 200 kPa capacity and were placed at a distance of 30 cm and 45 cm from the centre on one side of the test section. At the top of the subgrade, a thin layer of fine sand was laid wherever the pressure cells were intended to be placed followed by one more thin layer of sand above the pressure cell. This was done in order to prevent the damage to pressure cells that can be caused during placement of base course material and compaction. The pressure cells were in turn connected to a data acquisition system which can facilitate the measurement of stresses. Figures 6 and 7 show the pressure cells placed over the prepared subgrade and data acquisition system, respectively.

Fig. 6 Pressure cells placed over prepared subgrade

Fig. 7 Data acquisition system

6 Test Setup and Procedure

A circular steel test plate of diameter 30 cm with a thickness of 25 mm was placed exactly at the centre of the base course layer laid. Over the test plate, a cylindrical steel column of 13.5 cm diameter and height 90 cm was placed to facilitate load transfer from proving ring to the test plate. Reaction support loading was adopted with a hydraulic jack of capacity 100 kN with a least count of 1 kN. A proving ring of 200 kN capacity with a least count of 0.1 kN was connected to the hydraulic jack. Digital dial gauges were used to record the settlement of the test plate and the surface profile of the test section. A total of six dial gauges were used. Four dial gauges were positioned on the test plate around its circumference. The remaining two dial gauges were positioned at a distance of 30 cm and 45 cm from the centre on one side of the test section. Initially, the dial gauges were set to zero followed by the application of a seating pressure of 0.7 kg/cm2 in accordance with IS 5249 [27] guidelines. In this study, the vehicular loading was simulated by haversine loading. A pressure of 560 kPa as per IRC 37 [28] guidelines was applied over the test plate. The dial gauge readings were recorded after loading, unloading and rest period which constitute one cycle of loading. Figure 8 shows the experimental setup.

7 Results and Discussions

Two repeated load tests were carried out. The following paragraphs present the test results in terms of settlement and pressure at the subgrade level.

7.1 Settlement

Figures 9, 10 and 11 show the comparison of total, plastic and elastic settlements of the unreinforced and reinforced model pavement sections. The test results indicated that the settlement accumulated with a number of load cycles irrespective of the test condition. However, the magnitude of settlement is lower in case of reinforced pavement section. The plastic settlement is predominant and it forms about more than 80% of total settlement in both the sections. It is observed that, at the end of 1000 loading cycles, the unreinforced pavement section showed a plastic settlement of 6.3 mm in case of unreinforced test section. Whereas, in case of reinforced pavement section, the settlement reduced significantly in about 200 load cycles in comparison with the unreinforced pavement section. The reinforced pavement section showed a plastic settlement of 3.6 mm at the end of 1000 load cycles and 5.1 mm at the end of 5000 load cycles. The effect of reinforcement on elastic behaviour is marginal. Therefore, the provision of recycled tyre within the pavement section results in

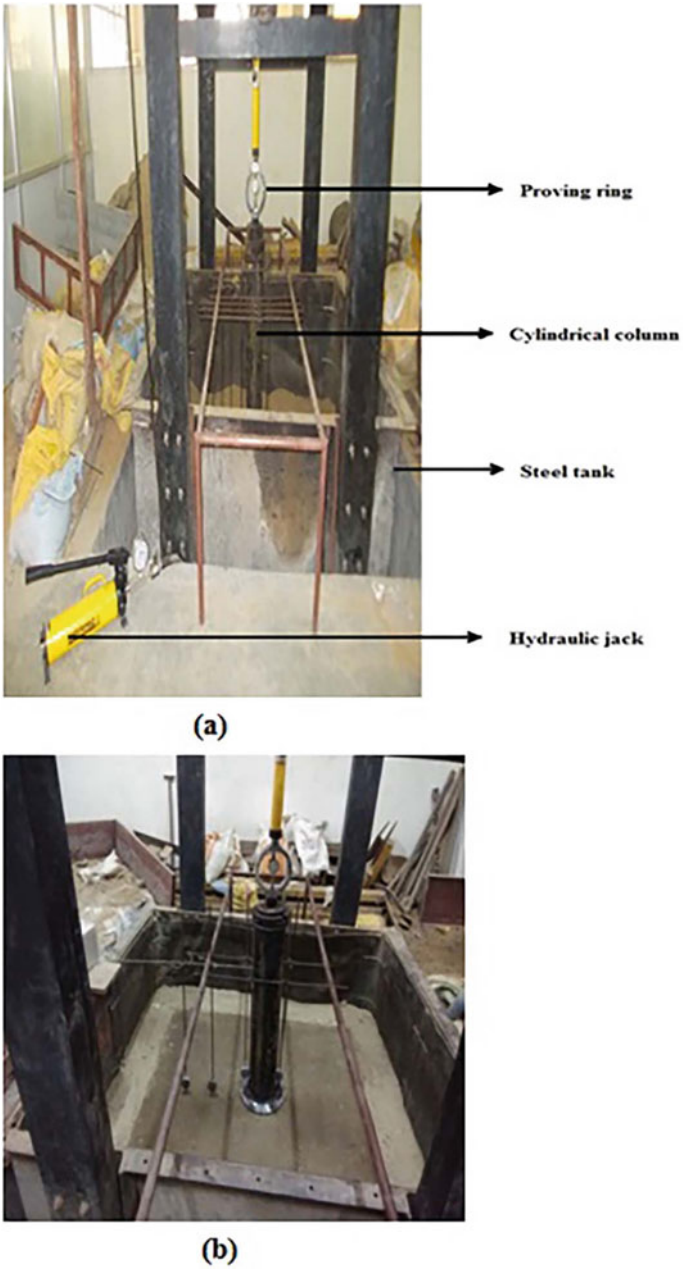

Fig. 8 Experimental setup. **a** Setup. **b** Close view of dial gauges

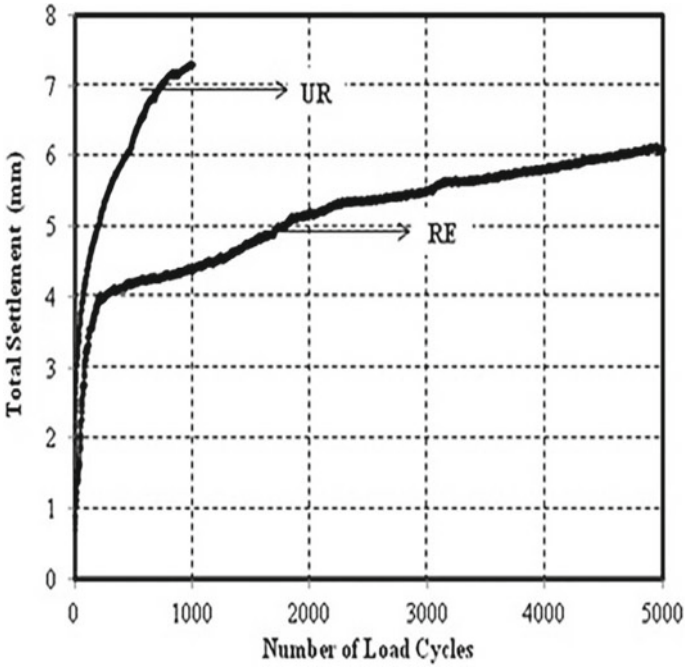

Fig. 9 Comparison of total settlement of unreinforced and reinforced model pavement sections

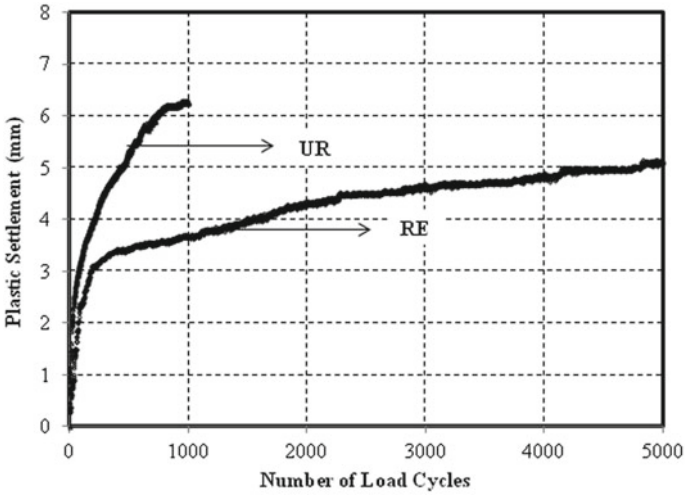

Fig. 10 Comparison of plastic settlement of unreinforced and reinforced model pavement sections

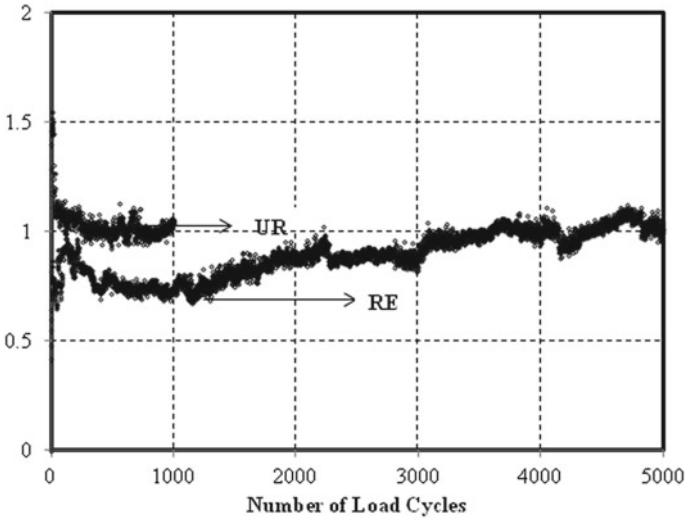

Fig. 11 Comparison of elastic settlement of unreinforced and reinforced model pavement sections

reduced settlement and thereby improves the service life of the pavement when compared to the unreinforced pavement section.

7.2 Surface Profile

Figure 12 shows the surface profile of both the test sections measured through dial gauges. As discussed under Settlement, the surface profile indicates the positive effect on the pavement behaviour in terms of settlement.

Figures 13 and 14 show the comparison of measured profiles of the subgrade and base course layer of unreinforced and reinforced pavement sections after terminating the test. At the end of 1000 load cycles, the subgrade of unreinforced pavement section indicated a settlement of 9.1 mm at the centre. Similarly, in case of reinforced pavement section, the subgrade indicated a settlement of 7.1 mm. The unreinforced and reinforced base indicated a settlement of 8.1 mm and 5.5 mm, respectively. It is evident from the settlement at the subgrade level that the load transferred to the subgrade is minimized in case of reinforced test section when compared with that of the unreinforced test section.

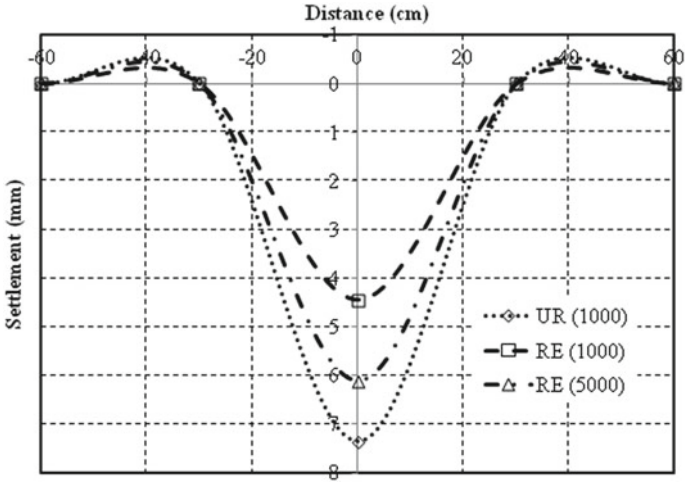

Fig. 12 Surface profile of the pavement sections

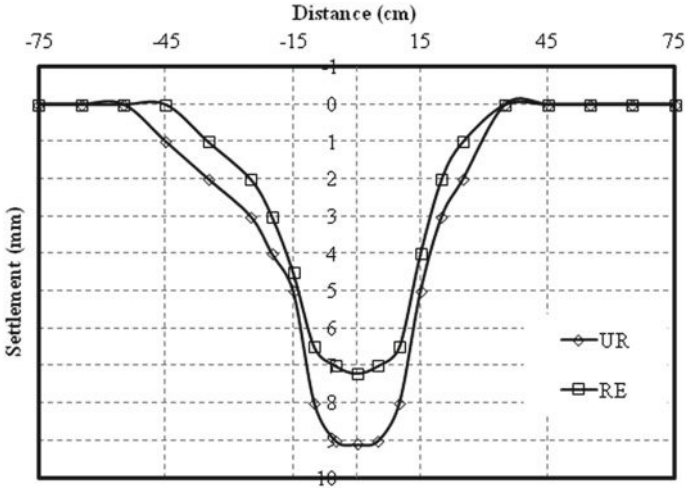

Fig. 13 Comparison of subgrade profile of unreinforced and reinforced test section after terminating the test

7.3 Pressure at the Subgrade Level

Figures 15, 16 and 17 show the comparison of net pressure, residual pressure and pressure due to loading at the subgrade level of unreinforced and reinforced pavement sections, respectively. It is observed that on loading a component, applied pressure gets accumulated at the subgrade level irrespective of the test condition. The magni-

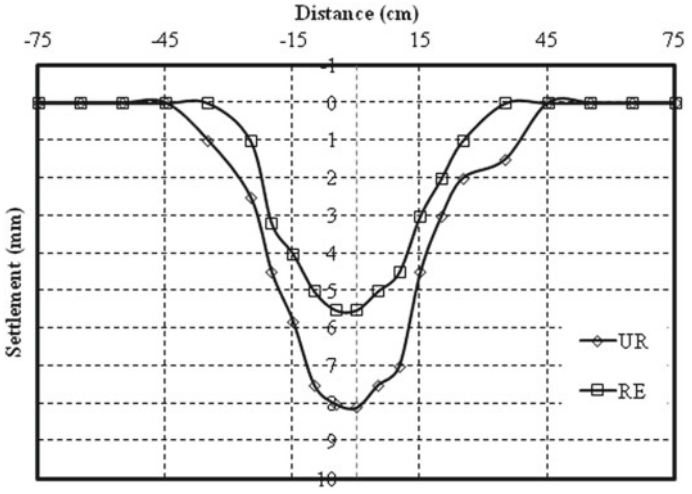

Fig. 14 Comparison of base course layer profile of unreinforced and reinforced test section after terminating the test

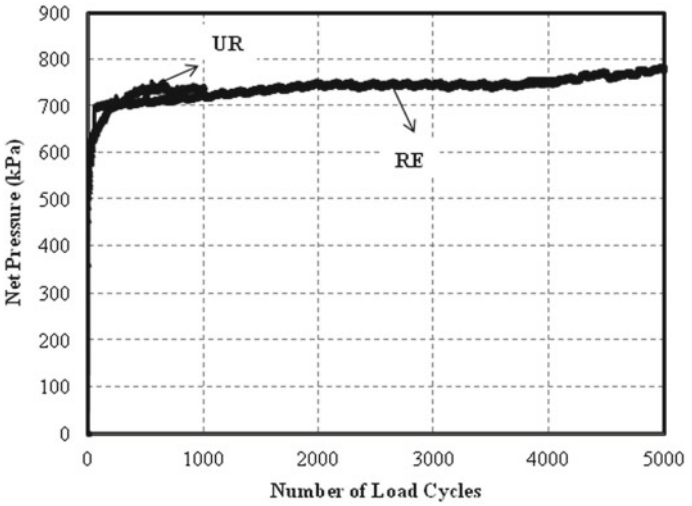

Fig. 15 Comparison of net pressure of unreinforced and reinforced pavement sections at the subgrade level

tude of this residual pressure increases with the number of load cycles and this effect is more pronounced in case of the unreinforced test section. The unreinforced test section indicated a residual pressure up to 380 kPa at the end of 1000 loading cycles. Whereas, in case of reinforced test section, the residual pressure remained at the

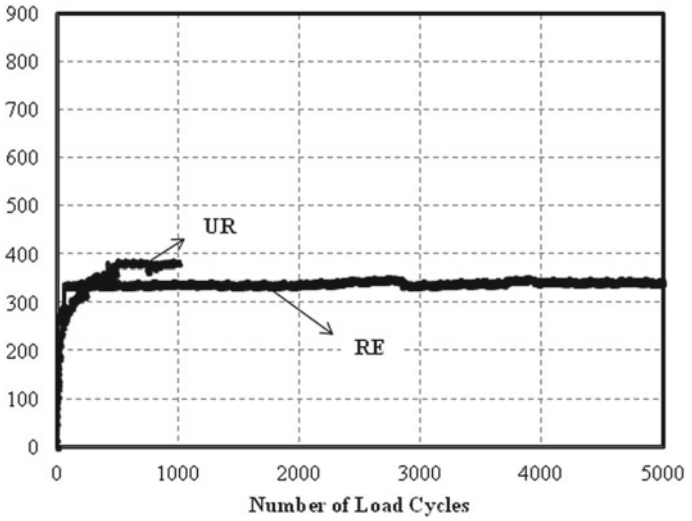

Fig. 16 Comparison of residual pressure of unreinforced and reinforced pavement sections at the subgrade level

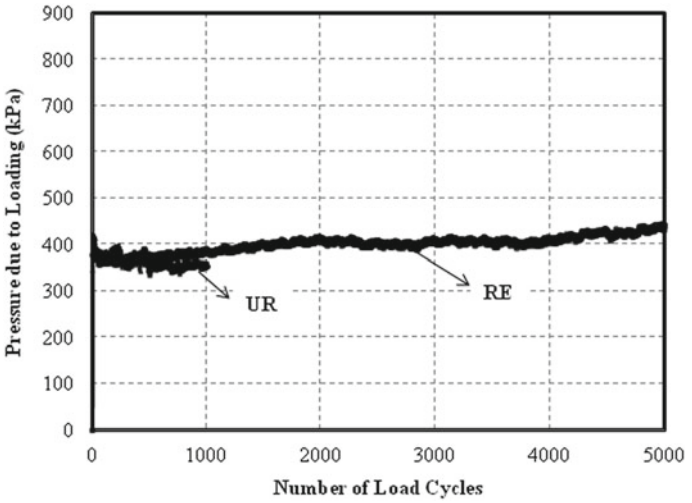

Fig. 17 Comparison of pressure due to loading of unreinforced and reinforced pavement sections at the subgrade level

level of 350 kPa up to 5000 load cycles. Out of 560 kPa of the applied pressure, the pressure due to loading ranged from 355–400 kPa (at the end of 1000 load cycles) and 400–420 kPa (5000 load cycles), respectively, in case of unreinforced and reinforced test sections.

8 Conclusions

Two repeated load tests were carried out on the model pavement sections in the laboratory. Recycled truck tyre was used as reinforcement in cellular grid form and its effectiveness on the pavement performance in comparison with the unreinforced pavement section was evaluated in terms of settlement, surface profile and pressure at the subgrade level. Based on the test results, the following conclusions were drawn.

- Recycled tyre reinforcement in the form of a cellular grid can be effectively used for reinforcing the pavement structure.
- The provision of recycled tyre reinforcement at the interface of subgrade and granular base reduced the plastic settlement significantly when compared with that of the unreinforced test section. The influence of reinforcement on the elastic behaviour of the test section is marginal.
- The reinforcement greatly improved the service life of the pavement section in comparison with the unreinforced test section.
- Recycled tyre reinforcement offers a sustainable, durable and eco-friendly solution for pavement construction.

References

1. Giroud JP, Noiray L (1981) Geotextile reinforced unpaved road design. J Geotech Eng 107(9):1233–1254
2. Lawson CR (1992) Some examples of separation geotextiles under road pavements. Proc Inst Civil Eng Transp 95:197–200
3. Al-Qadi IL, Brandon TL, Valentine RJ, Smith TE (1994) Laboratory evaluation of geosynthetic reinforced pavement sections. In: Transportation Research Board, No. 1439, 73rd Annual meeting, Washington, DC, pp 25–31
4. Ravi Shankar U, Suresha AN (2006) Strength behaviour of geogrid reinforced shedi soil subgrade and aggregate system. Road Mater Pavement Des 7(3):313–330
5. Tang X, Chehab GR, Palomino A (2008) Evaluation of geogrids for stabilizing weak pavement subgrade. Int J Pavement Eng 9(6):413–429
6. Madhavi Latha G, Nair AM, Hemalatha MS (2010) Performance of geosynthetics in unpaved roads. Int J Geotech Eng 4:151–164
7. Abu-Farsakh MY, Chen Q (2011) Evaluation of geogrid base reinforcement in flexible pavement using cyclic plate load test. Int J Pavement Eng 12(3):275–288
8. Al-Qadi IL, Dessouky SH, Kwon J, Tutumluer E (2012) Geogrid reinforced low volume flexible pavements: pavement response and geogrid optimal position. J Transp Eng 138:1083–1090
9. Tanyu F, Aydilek AH, Lau AW, Edil TB, Benson CH (2013) Laboratory evaluation of geocell reinforced gravel subbase over poor subgrades. Geosynth Int 20(2):47–61
10. Manjunath M, Mamatha KH, Dinesh SV (2014) Model studies on geocell reinforced unpaved roads under repeated traffic loading conditions. In: Proceedings of Indian geotechnical conference on geotechnics for inclusive development of India (GEOIND), Jawaharlal Nehru Technological University, Kakinada, India, pp 1149–1154
11. Rajagopal K, Chandramouli S, Parayil A, Iniyan K (2014) Studies on geosynthetic reinforced road pavement structures. Int J Geotech Eng 8(3):287–298

12. Saride S, Vijay KR, Gautam D, Madhav MR (2016) Performance evaluation of geocell reinforced granular subbase (GSB) layers through field trials. J Indian Roads Congr Paper No. 648, pp 249–257
13. Tang X, Palomino AM, Stoffels SM (2016) Permanent deformation behaviour of reinforced flexible pavements built on soft soil subgrade. Road Mater Pavement Des 17(2):311–327
14. Mamatha KH, Dinesh SV (2018) Evaluation of strain modulus and deformation characteristics of geosynthetic reinforced soil—aggregate system under repetitive loading. Int J Geotech Eng 12(6):546–555
15. Mamatha KH, Dinesh SV, Dattatreya JK (2018) Evaluation of flexural behaviour of geosynthetic reinforced unbound granular material beams. Road Mater Pavement Des. DOI: 10.1080/14680629.2017.142279
16. Mamatha KH, Dinesh SV, Swamy BC (2018c) Performance of geosynthetic reinforced model pavements under repetitive loading. Geotech Eng J SEAGS AGSSEA 49(4)
17. Mamatha KH, Dinesh SV (2019) Performance evaluation of geocell reinforced pavements. Int J Geotech Eng 13(3):277–286
18. Raghavan D, Huynh H, Ferraris CF (1998) Workability, mechanical properties and chemical stability of a recycled tire rubber-filled cementitious composite. J Mater Sci 33(7):1745–1752
19. Oikonomou N, Stefanidou M, Mavridou S (2006) Improvement of the bonding between rubber tire particles and cement paste in cement products. In: 15th Conference of the technical chamber of Greece, Alexandroupoli, Greece, 25–27 October (in Greek), pp 234–242
20. Pierce CE, Williams RJ (2004) Scrap tire rubber modified concrete: past, present and future. In: Proceedings of the international conference organized by the concrete and masonry research group, Kingston University-London. Limbachiya MC, Roberts JJ (eds) Sustainable waste management and recycling: used-post-consumer tyres, Thomas Telford, pp 1–16
21. Khaloo AR, Dehestani M, Rahmatabadi P (2008) Mechanical properties of concrete containing a high volume of tire-rubber particles. Waste Management
22. Khosla NP, Trogdon JT (1990) Use of ground rubber in asphalt paving mixtures. Technical Report, Department of Civil Engineering, North Carolina State University, Raleigh, NC, USA
23. Fedroff D, Ahmad S, Savas BZ (1996) Mechanical properties of concrete with ground waste tire rubber. Transp Res Board 1532:66–72
24. Khatib ZK, Bayomy FM (1999) Rubberized Portland cement concrete. J Mater Civil Eng 11(3):206–213
25. MoRT&H (2013) Ministry of road transport and highways: specifications for roads and bridges, 5th edn. Indian Roads Congress, New Delhi
26. IRC SP 72 (2015) Determination of dynamic properties of soil—method of test. Bureau of Indian Standards, New Delhi
27. IS 5249 (2006) Guidelines for the design of flexible pavements for low volume roads. Indian Roads Congress, New Delhi
28. IRC 37 (2018) Guidelines for the design of flexible pavements. Indian Roads Congress, New Delhi, p 2012

Partial Replacement of Moorum with Fly Ash in Embankment

Sagar D. Turkane and Sandeep K. Chouksey

Abstract The paper presents the geotechnical characteristics and slope stability analysis of moorum blended with fly ash for the construction of road embankments. The paper presents the geotechnical characteristics and slope stability analysis of moorum blended with fly ash for the construction of road embankments. An experimental investigation has been carried out on the moorum and moorum–fly ash mixes at various proportions of fly ash (i.e., 0%, 15%, 20%, 25%, and 30%) by dry weight of moorum. The index properties of moorum mixes and strength characteristics were evaluated by conducting Atterberg's limit, specific gravity, grain size analysis and compaction parameters, direct shear parameters, and California Bearing Ratio (CBR) test, respectively. The stability analysis of moorum embankment was performed using FLAC/Slope 7.0 (Fast Lagrangian Analysis of Continua/Slope version 7) software at a slope angle of 30° and various heights of 4.0, 5.0, and 6.0 m to determine Factor of Safety (FOS). The maximum FOS was obtained at 30% of fly ash mix in moorum with 6 m height of the embankment.

Keywords Stability analysis · Moorum · Fly ash · Embankment · FLAC/slope

1 Introduction

Soil may be considered a complex material obtained from the geological weathering process naturally. There are a variety of soils formed in nature based on their ways of formation. In soil engineering, some soils having good strength which are generally used for construction purposes. Sometimes locally available soil does not have adequate strength to bear the super-structural load. In such cases, the replacement of weak material by the strong material is in practice or giving the necessary treatment to the existing soil. As moorum is widely used in road subgrade as strong material

S. D. Turkane (✉) · S. K. Chouksey
Department of Civil Engineering, National Institute of Technology, Raipur 492010, India
e-mail: sagarturkane24@gmail.com

S. K. Chouksey
e-mail: schouksey.ce@nitrr.ac.in

© Springer Nature Singapore Pte Ltd. 2021

K. K. Pathak et al. (eds.), *Recent Trends in Civil Engineering*, Lecture Notes in Civil Engineering 77, https://doi.org/10.1007/978-981-15-5195-6_30

for load-bearing but the cost of moorum is high as compared to locally available material (soils). In addition, transportation cost of moorum to the construction site, which found to be uneconomical for uses in huge quantities. Hence, in a paper, experimental investigations have been carried out to check the stability of moorum fly ash mixes, so that the optimized percentage of moorum can be utilized with maximizing the fly ash utilization.

In India, the rate of combustion of coal is very high which produces a tremendous amount of coal ash (nearly 169.25 million metric tons) commonly known as fly ash. Where the relative utilization very less nearly 107.10 million metric tons, i.e., 63.28% [1]. Fly ash is categorized as either class C or F based on the available calcium oxide (CaO) present. According to the American Society for Testing Materials [2], fly ash can be classified as class C if the CaO content about 20% and a sum of SiO2, Al2O3 and Fe2O3 is less than 70%. If the sum of SiO2, Al2O3, and Fe2O3 is more than 70% then it can be classified as a class F. Fly ash has of serious impacts on the nature that suggests the need for proper consumption or disposal of fly ash and increase in fly ash utilization. The utilization of fly ash in the construction industry in the form of construction of embankments and structural fills and dykes is the most likely solution to the problem of the dumping or disposal of fly ash and also it helps to minimize the cost of construction or project [3]. The utilization of waste material is being given prime importance all over the world. The aim of this paper is to maximize the utilization of fly ash in geotechnical construction work, especially in road embankment. The moorum can be replaced with fly ash effectively is presented and reported. Several studies have been conducted for the use of fly ash in the stabilization of different types of soils [3–8]. Some of the research has been conducted in the utilization of fly ash in road pavement and embankment construction and its stability analysis using numerical modeling [6, 9–12].

2 Material and Method

2.1 Moorum

For the laboratory investigations, a locally available moorum was used, which collected at 2 m depth below ground level from NIT Raipur campus, Raipur, Chhattisgarh, India. The moorum preliminary allows drying for 2 days period. Its engineering and index properties are shown in Table 1.

2.2 Fly Ash

The fly ash is procured from NSPCL, Bhilai. The specific gravity (G) of the fly ash sample was 2.44 obtained by using a glass density bottle. The chemical compositions

Table 1 Basic properties of moorum

Sr. no	Properties	Value
1.	Color	Dark brown
2.	Specific gravity	2.72
3.	Liquid limit (%)	26.56
4.	Plastic limit (%)	19.5
5.	Coefficient of uniformity Cu	10
6.	Coefficient of curvature Cc	0.82
7.	IS classification of moorum	SP-SM
8.	MDD (kN/m3)	23.7
9.	OMC (%)	5.9

Table 2 Chemical compositions of fly ash

Constituents	Percentage Range (%)	Obtained values
Silica (SiO2)	49–67	63.78
Alumina (Al2O3)	16–29	24.44
Iron oxide (Fe2O3)	4–10	5.01
Calcium oxide (CaO)	1–4	1.94
Magnesium oxide (MgO)	0.2–2	0.48

of the fly ash sample are shown in Table 2. From Table 2, it can be observed that the sum of major oxides, i.e., SiO_2, Al_2O_3, Fe_2O_3 is more than 70%, hence the fly ash is Class F fly ash according to [2].

2.3 Moorum–Fly Ash Mixtures

Samples of moorum and moorum–fly ash mixes were prepared by mixing the desired proportions of potable water, moorum, and fly ash. The proportion of fly ash ranged from 0 to 30% by weight of dry moorum, while water content percentages ranged from 4 to 20%. The moorum–fly ash mixes were prepared by first thoroughly mixing predetermined quantities of dry moorum, and fly ash in a mixing tray to a uniform paste.

2.4 Numerical Modeling for Slope Stability

The slope stability analysis of embankment was performed using FLAC/Slope version Slope 7.0 developed by Itasca Consulting Group, Inc., The United States. The FLAC/Slope is a mini version of FLAC, which is mainly designed for the estimation of FOS of slope analysis. Numerical modeling using FLAC/Slope provides a quick and complete solution and locates the critical zones which help to take care against future difficulties [11].

2.5 Embankment Geometry

The slope stability analyses of moorum embankment and various proportions of fly ash–moorum embankments were carried out at a constant slope angle of 30° and at different embankment heights (i.e., 4.0, 5.0, and 6.0 m). The material properties used for analysis were shown in Table 3 and numerical analysis was performed in the FLAC/Slope for numerical modeling. Further, FOS for all the fly ash proportion were evaluated and reported. The typical geometry of the embankment slope shown in Fig. 1. The Shear Strain Rate contour (SSR) and failure pattern of the moorum embankment and moorum–fly ash composite embankment were observed to know the stability of the embankment.

3 Result and Discussion

In this study, the suitability of locally available moorum with a combination of fly ash for possible use in the road subgrade or embankment has been explored by conducting some laboratory tests. The compaction characteristics, DST, CBR value of moorum blended with fly ash, were investigated as per relevant IS codes. Also, slope stability of embankment was checked using software FLAC/Slope version 7.

Table 3 Materials properties at a various percentage of fly ash

Moorum (%)	FA (%)	MDD (kN/m3)	OMC (%)	Phi	C kpa
100	0	23.7	5.9	30.96	5
85	15	22.6	9.1	25.85	19
80	20	22.45	8	24.10	22
75	25	21.2	10.5	23.80	23
70	30	20.7	11.1	23	25

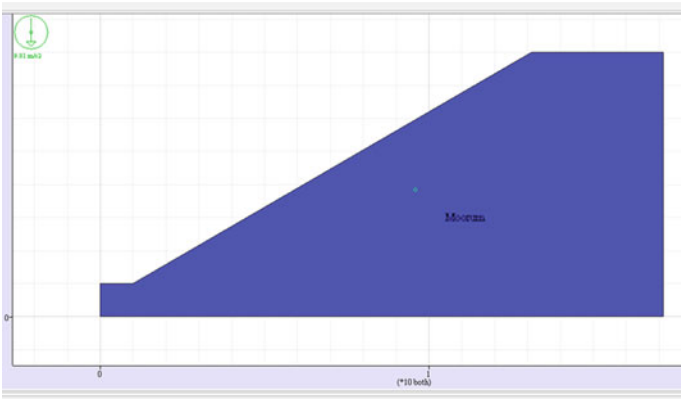

Fig. 1 Typical geometry of the embankment

Table 4 Atterberg's limit and specific gravity

Moorum (%)	FA (%)	Liquid limit	Plastic limit	Plasticity index	Cu	Cc	Class	Specific gravity
100	0	26.56	19.5	7.06	10.00	0.82	SP-SM	2.72
85	15	25.49	–	–	30.00	1.56	SW-SM	2.67
80	20	23.08	–	–	25.86	0.90	SP-SM	2.59
75	25	22.93	–	–	21.82	0.55	SP-SM	2.53
70	30	22.16	–	–	20.37	0.43	SP-SM	2.46

3.1 Atterberg's Limit and Specific Gravity

Atterberg limit is very useful for the characterization of moorum, which indicates the plastic nature of the moorum. The variations of liquid limit and plastic limit with varying percentages of fly ash are shown in Table 4. The specific gravity of various mixing parentage was estimated according to the IS: 2720 (Part 3)–1985. It can be seen that the addition of the fly ash with moorum reduces the specific gravity of the moorum mixes. The reason for the reduction of the specific gravity is due to the lightweight of fly ash.

3.2 Grain Size Analysis

The grain size distribution test was conducted as per IS 2720 (Part 4)–1985. Figure 2 shows the grain size distribution curve for moorum blended with fly ash at various proportions. The grain size distribution curve of moorum composite changes to poor gradation as silt and sand fractions increased whereas the clay fraction decreases

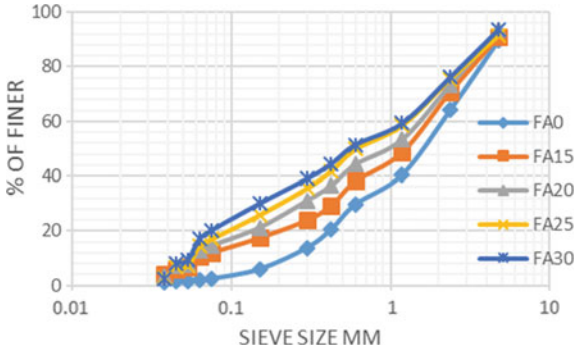

Fig. 2 Grain size distribution curve

with the addition of fly ash. Based on the grain size distribution curves, the value of Cu is 10 which is greater than 6 but the value of Cc is 0.82 which less than 1 so moorum falls in the poorly graded sand. The percentage of fines is less than 5% of the total mass of moorum, and therefore broadly moorum can be classified as a poorly graded sand with little silt content.

3.3 Compaction Parameters

The compaction test was carried out using modified proctor effort. Figure 3 shows the variation of the dry density–water content relationship of various moorum–fly ash mixes. As the laboratory results show the reduction in the maximum dry density with the addition of fly ash. The tendency of fly ash is less sensitive to the variation of water content than soil and it could be explained by the higher void content of fly ash. Normally, soils have air void content between 1 and 5% whereas fly ash has 5–15% at its maximum dry density [4]. The reduction of MDD is attributed to

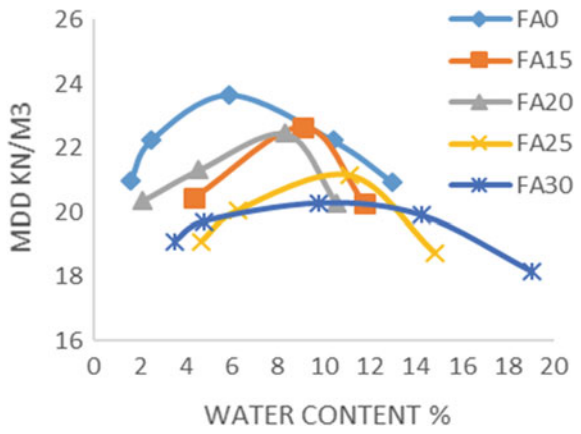

Fig. 3 Dry density–water content curve

the lower specific gravity of fly ash and the lack of certain fractions sizes particles for better packing. The percentage of air void content increases which reduces the density of moorum–fly ash mixes.

As per MoRT&H Report, the maximum dry density requirement up to 3 m height embankment should not be less than 15.2 kN/m3, from the experimental result MDD is 20.7 kN/m3 at 30% fly ash content of the moorum. Therefore, up to 30% of moorum can be saved with effective use of fly ash. Although the reduction in the dry density moorum fly ash mixes is found to be suitable for the sustainable construction of the embankment.

3.4 California Bearing Ratio (CBR)

For the design of the pavement, the CBR method is used widely. The CBR values of different proportionate mixes of fly ash and moorum were evaluated as per IS 2720, Part 16. The specimens were prepared to their respective MDD and OMC for unsoaked condition and respective value were evaluated (Fig. 4).

The results show plane moorum has a higher CBR value of 61.86%. This is mainly because moorum consists of all sizes of particles, which give better packing when placed at maximum dry density and corresponding water content, which provides frictional resistance to the penetration of the plunger and thus high values of CBR are obtained. The reduction in CBR at 15% fly ash is due to decreasing friction components as the increment of sandy-silty particles. A second peak at 20% of fly ash can be attributed to the better packing of different fractions [4]. There is a further reduction in the CBR value because of lack of a certain fraction of different sized particles and also due to particle size becomes uniform as the value of Cu is increasing indicating certain size particle increases.

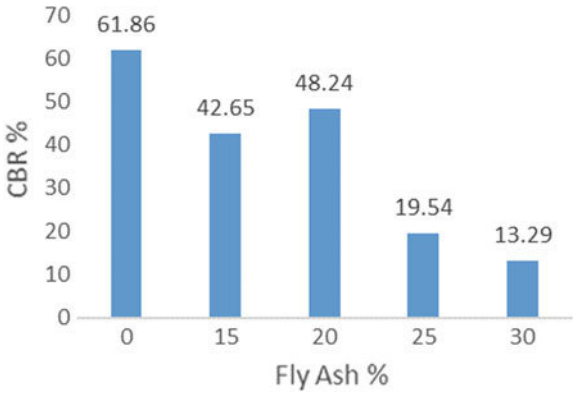

Fig. 4 CBR values for moorum-fly ash mixes

3.5 Direct Shear Parameters

The shear strength parameter, i.e., cohesion and angle of internal friction was calculated using a direct shear test. The samples of moorum–fly ash mixes were prepared for their respective MDD and OMC and tested. As there is an increase in the fly ash percentage the cohesion increases whereas the angle of internal friction decreases. Due to cementing and hardening property of the fly ash in the presence of moisture cohesion of moorum–fly ash increases [9], whereas weak bonding of moorum and fly ash particle angle of internal friction reduces.

3.6 Moorum Embankment Stability Analysis

The stability analyses were conducted for a slope angle of 30° and various slope heights of 4.0, 5.0, and 6.0. The result of the numerical analysis shows failure plane and shear strain rate contour of the moorum embankment and moorum–fly ash composite embankment at 30% fly ash (at 6.0 m height) are shown in Figs. 5 and 6, respectively. The stability analysis of all samples was evaluated and the FOS value is tabulated in Table 5.

The FOS variation under different proportions of fly ash and embankment heights are shown in Fig. 7. It can be observed that moorum embankment (FA0%) was stable

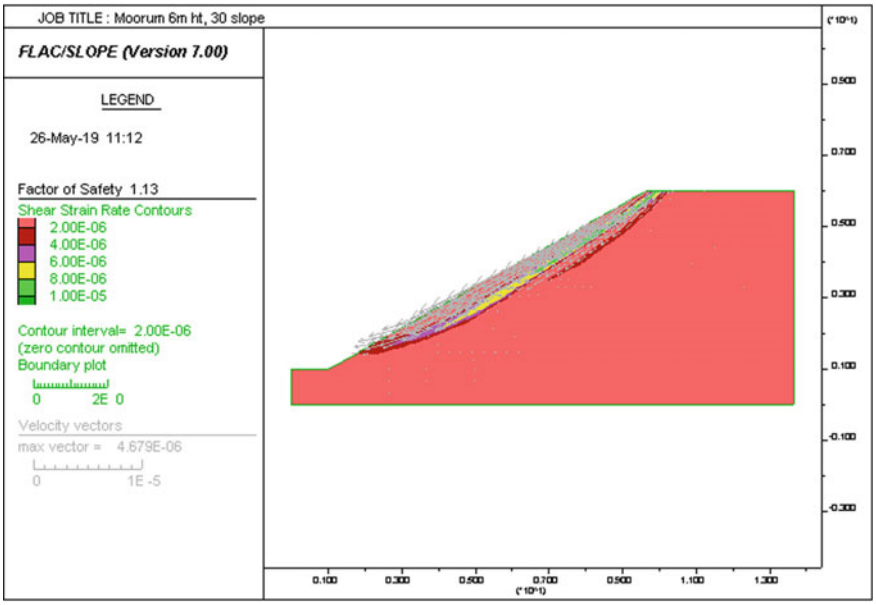

Fig. 5 Moorum embankment at 6 m height with a slope angle of 30°

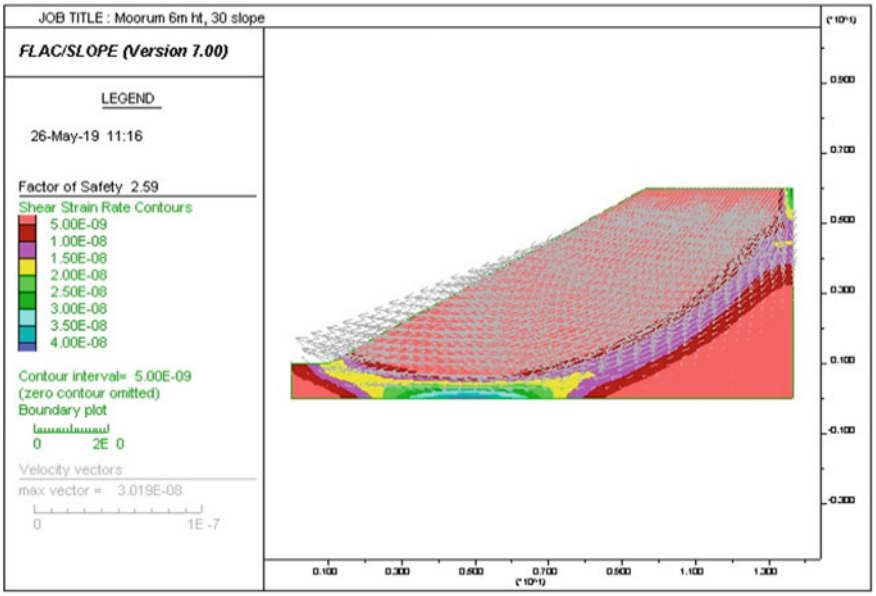

Fig. 6 Moorum–fly ash embankment of 30% fly ash at 6 m height with a slope angle of 30°

Table 5 variation of FOS under different geometries

Height (m)	4	5	6
FA0 (Moorum)	1.71	1.62	1.55
FA15	2.76	2.45	2.23
FA20	2.91	2.56	2.31
FA25	3.07	2.69	2.43
FA30	3.23	2.82	2.53

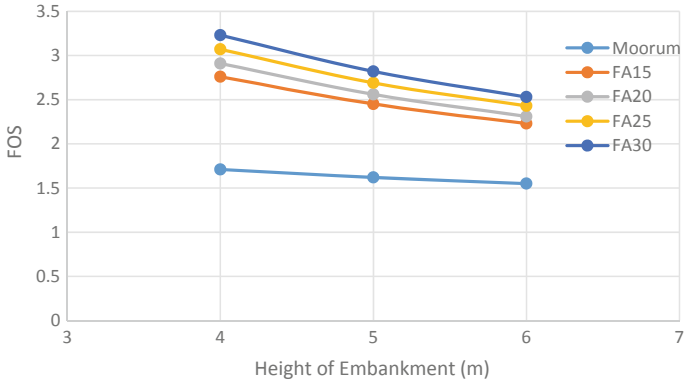

Fig. 7 FOS value under different height at a slope angle of 30°

up to 4.0 m height at a slope angle of 30° with a FOS of 1.7. With the addition of fly ash up to 30%, FOS increases, on further addition, FOS decreases. This may be due to the maximum shearing strength at 30% of fly ash content. The 30% fly ash addition in moorum embankment FOS reaches to 1.55 at a slope angle of 30° and height of embankment 6 m as per [13]. The minimum factor of safety is 1.4 at the end of construction. Thus, up to 30% of fly ash can be effectively used in the construction of moorum embankment that means up to 30% of moorum can be saved.

4 Conclusions

Based on the experimental results and numerical modeling for moorum–fly ash mixes soil, the following conclusions were drawn.

- The Atterberg's limit of moorum mixed fly ash changes as from plastic to non-plastic state with the addition of fly ash content.
- The maximum dry density of moorum fly ash mixes gets reduced with an increment of fly ash content. The 30% of fly ash shows the density of 20.7 kN/m3, which suitable for the construction of embankment up to 3 m height as per the guideline of MoRT&H.
- In the moorum, the addition of fly ash the cohesion of moorum increases with decreasing angle of internal friction due to hardening and cementation of fly ash.
- The maximum FOS of moorum fly ash composite embankment was at 30% fly ash with a height of embankment of 6 m can be constructed. Considering all the stability aspects of moorum–fly ash composite with the addition of 30% fly ash the disposal problem of fly ash can be sorted out by a certain amount in an eco-friendly manner also up to 30% of moorum can be saved.

Further study needs to be performed for the finding of the optimized angle of slope and proportion of fly ash with moorum and a maximum height of the embankment.

References

1. Central Electricity Authority: Fly ash generation at coal/ lignite based thermal power stations and its utilization in the country. Cent Electr Auth, no December, 1–63
2. ASTM C 618–05 (2012) Standard specification for coal fly ash and raw or calcined natural pozzolan for use in concrete, vol 1479, no 1
3. Ghosh A (2010) Compaction characteristics and bearing ratio of pond ash stabilized with lime and phosphogypsum. J Mater Civ Eng 22(4):343–351
4. Pandian NS (2004) Fly ash characterization with reference to geotechnical applications. J Indian Inst Sci 84:189–216
5. Bose B (2012) Geo-engineering properties of expansive soil stabilized with fly ash Electron J Geotech Eng 17 J(2004), 1339–1353
6. Martin JP, Collins RA, Browning JS, Biehl FJ, Members S (1991) properties and. use of fly ashes for embankments. J Energy Eng 116(2):71–86

7. Santos F, Li L, Li Y, Amini F (2011) Geotechnical properties of fly ash and soil mixtures for use in highway embankments. World Coal Ash Conf
8. Phani Kumar BR, and Sharma RS (2004) Effect of fly ash on engineering properties of expansive soils. J Geotech Geoenvironmental Eng 130(7), 764–767
9. Dewangan PK, Pradhan M, Ramtekkar GD (2016) Shear strength behaviour of fly ash mixed coal mine overburden dump material and stability assessment using numerical modelling. ARPN J Eng Appl Sci 11(1):615–628
10. Pradhan SP, Vishal V, Singh TN, Singh VK (2014) Optimisation of dump slope geometry Vis-à-vis flyash utilisation using numerical simulation. Am J Min Metall 2(1):1–7
11. Rajak TK, Yadu L, Pal, SK (2019a) Analysis of slope stability of fly ash stabilized soil slope, vol 13. Springer Nature Singapore
12. Rajak TK, Yadu L, Chouksey, SK (2019b) Strength characteristics and stability analysis of ground granulated blast furnace slag (GGBFS) stabilized coal mine overburden-pond ash mix. Geotech Geol Eng 0123456789, 2019
13. IRC:75-2015: Guidelines for the design of high embankments, vol NRC/ERB 11, no June,, pp. 44–64. India

Scour Around Bridge Abutments in Clay Bed

Anoop Kumar, B. N. Advith Ganesh, Shubham Vats, P. Sumanth, T. Gangadharaiah, and K. H. Mamatha

Abstract Most of the hydraulic failures of bridges occur due to the formation of the scour hole at the corner of the abutment and in front of the pier. When the scour hole is more, the grip length of the foundation of the abutment and pier reduces causing destabilization of the bridge as a whole. Scour studies around the abutments and pier in clay bed attracts more studies due to the swell–shrink characteristics of the soil. In this study, an attempt is made to conduct a series of scour studies for clayey soil with three densities, i.e. 1.15, 1.23 and 1.37 g/cc and four abutment sizes, i.e. 2, 3, 4 and 5 cm. Based on the test results, the effect of the width of abutment on the maximum scour depth at the end of 600 min of flow run was analysed. It is found that the maximum scour depth increases as the width of abutment increases and reduces as density increases. The rate of scour reduces with time and when the time parameter exceeds 4, it approaches to zero asymptotically.

Keywords Bridge · Scour depth · Abutment · Clay bed

1 Introduction

Many bridges are built in the river having clay bed. The hydraulic safety of these bridges depends on local scour depth. Local scour occurs due to river flow around abutments and piers. Several researchers have studied the scour depth caused around bridge piers and abutments for non-cohesive soils [1–10]. The cohesive soil consists primarily of fine-grained particles that exhibit cohesive properties that coalesce the individual particles to form a soil mass. The cohesion properties of soil are attributed mainly to clay mineralogy, clay content, compaction and liquidity index. Water is the main agent causing the cohesive forces between the clay particles of soil [11]. In an extensive study of bridge failure in the United States, it was reported that damage to bridges and highway from major regional floods in 1964 and 1972 amounted to about $100,000,000 per event. Similarly, Sutherland compiled a report of all

A. Kumar · B. N. A. Ganesh · S. Vats · P. Sumanth · T. Gangadharaiah · K. H. Mamatha (✉)
Department of Civil Engineering, Siddaganga Institute of Technology, Tumakuru, India
e-mail: mamathakh@sit.ac.in

© Springer Nature Singapore Pte Ltd. 2021

K. K. Pathak et al. (eds.), *Recent Trends in Civil Engineering*, Lecture Notes in Civil Engineering 77, https://doi.org/10.1007/978-981-15-5195-6_31

major bridge failures that occurred in New Zealand during the period 1960–1984 and found that 29 out of 100 were failed due to the scouring around abutments. Also, 6 out of 10 bridge failures that occurred in New Zealand during Cyclone Bola were related to abutment scour. Damages due to scour around abutments in bridges is predominating in comparison with other factors of damage [6]. In India, about 16% of the total land is covered with clayey soil. From the mineralogical analysis, it is evident that the proportion of montmorillonite is high in black cotton soil. A high degree of montmorillonite causes swelling and shrinkage, hence resulting in cracks. This makes it challenging to construct the bridges in the zones where black cotton soil is present. There are limited studies available on scour around bridge piers and abutments on river clay bed [11–15].

Therefore, in this study, clayey soil was considered and an attempt is made to assess the scour depth around abutments with a varied density of the clay bed and width of the abutment.

2 Materials

In this study, cohesive soil was used for preparing the bed. No other soil was mixed or blended tos this soil to keep it unadulterated. The soil was collected from Kalaburagi, Karnataka, India. Initially, the geotechnical properties of the soil were determined and all the tests were performed as per the relevant standards. The geotechnical properties of the soil are tabulated in Table 1. The soil possesses a plasticity index of 29%. It possesses a maximum dry density of 1.65 gm/cc and an optimum moisture content of 20%. The soil is classified as highly compressible clay with group symbol CH as per the unified soil classification system [16].

Table 1 Properties of cohesive sediment used

Property	Value
Specific gravity	2.74
Liquid limit (w_L)	68%
Plastic limit (w_p)	39%
Plasticity index (I_p)	29%
Fines content	73%
Maximum dry density ($\rho_{d\ max}$)	1.65 g/cc
Optimum moisture content (OMC)	20%

3 Experimental Setup

In this study, a flume of 20 m long, 0.6 m wide and 0.7 m deep was used for carrying out the experiments. The flume was slightly tilted with a constant slope of 1 in 1000 in order to facilitate the flow of water. A section of the flume was considered as test zone and is 2 m long, 0.6 m wide and 0.9 m deep. The test zone was positioned at a distance of 11 m from the inlet. The bed condition, abutment and scour depth of the experiment correspond to this test zone. Clear water was supplied to the flume with the help of two vertical submerged pumps from the sump and the same water was recirculated to minimize wastage. Water was first pumped to inlet stilling basin and then it flows through an arrangement of wire mesh screen and baffles for reducing the disturbance. A constant flow depth is maintained using a masonry arrangement at the end of the flume. A 90 V-notch was provided at the end of the flume to measure the discharge. The discharge into the flume was controlled using the valve mounted on the supply pipe. Four sizes of abutments having a thickness of 1 cm were used for the study and are shown in Table 2. Steel plates curved at edges, coated with primer and painted white in colour were used as abutments. The test zone has transparent fibre walls to view the flow of water and scouring process. Figure 1 shows the schematic representation of the experimental setup.

Table 2 Dimensions of abutment and material

Abutment material	Transverse dimension (B) (Perpendicular to stream) (cm)	Longitudinal dimension (L) (Streamwise length) (cm)
Steel plates coated with primer and white paint	5	1
	4	1
	3	1
	2	1

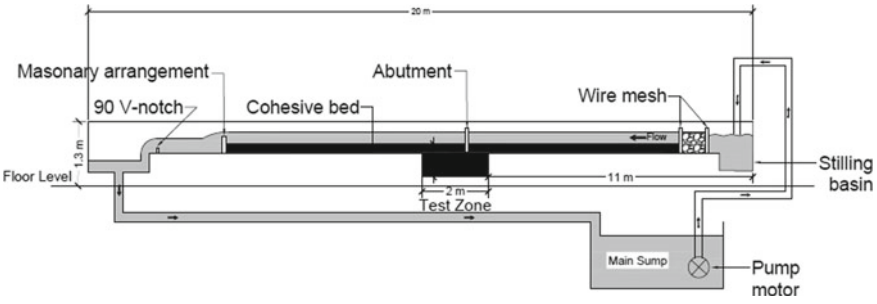

Fig. 1 Schematic representation of the experimental setup

4 Bed Preparation and Testing

Crushing machine was used to breakdown the lumps of the selected clayey soil of size (lumps) greater than 40 mm. 40 mm downsize lumps were broken down manually using the rammer. After crushing, the soil was sieved through 4.75 mm IS sieve. Soil retained on 4.75 mm IS sieve was further crushed unless and until it passes through 4.75 mm IS sieve. Crushed soil passing through 4.75 mm IS sieve was kept in oven for drying for about 24 h at 104 °C. Approximately, 500 kg of oven-dried soil was transferred into the test zone and was compacted manually in two layers. Extra care was taken for uniform compaction throughout the test zone. Ramesh [17] reported that the swelling of black cotton soil is maximum at the end of 24 h and remains constant for a further wetting period. In addition, the cohesion is fairly constant and less in magnitude up to a wetting period of 8–10 h. Beyond 10 h, cohesion increases up to about 48 h of wetting period and further wetting period results in stabilized cohesion. Thus, in this study, the water was allowed to flow for a period of 48 h. The wetting period was maintained to ensure proper swelling of bed and to check any leakage. After 48 h of wetting period, density was determined with the help of core cutter. Three samples were drawn from the saturated bed and the density was averaged to obtain the bulk density. Then, the scour study was carried out. In the same way, the bed was prepared afresh for the desired density. In this study, three dry densities under swollen conditions, i.e. 1.15, 1.23 and 1.37 g/cc were considered for investigation. Figures 2 and 3 show the prepared cohesive bed in the flume and abutments of varying widths, respectively.

After the desired wetting period, the discharge valve was gradually opened and water was allowed to run till the flow depth (y) $\geq$ 15 cm. Any undulations or depressions in the bed were levelled using a flat trowel without disturbing the density. Abutment was fixed firmly into the clay bed with the top of abutment well above the water. Scouring period is the time in which scour depth readings were taken from the start of scouring process. Scour depth was measured using two-degrees-of-freedom point gauge. In this study, the scour depth readings were noted down at an interval of 10, 20, 30, 45, 60, 90, 120, 150, 180, 210, 240, 270, 300, 360, 420, 480, 540 and 600 min from the start of the test. Scour depth was measured in the transverse direction at a distance of 0, 5, 10, 15 and 20 cm from the edge of the abutment.

5 Results and Discussions

An assessment of scour around abutment was carried out by using flume in the laboratory. The cohesive bed was prepared at three densities and four abutments were used. The test results are presented and discussed in the following paragraphs.

Table 3 indicates the scour depth at the end of 600 min of flow on clay bed having a density of 1.15, 1.23 and 1.37 g/cc for varying abutment sizes.

Fig. 2 Prepared cohesive bed in the flume

Figures 4, 5 and 6 show the variation of scour depth with time for all the abutments, respectively, for a density of 1.15, 1.23 and 1.37 g/cc. The scour around 2 cm wide abutment is insignificant irrespective of the bed densities considered. This is possibly due to the low strength of scouring vortex formed at the upstream edge of 2 cm wide abutment. It is observed that the scour increased with time up to 500 min and beyond 500 min, it is stabilized with the rate of scour being low for all the bed densities and abutments considered.

Figure 7 shows the variation of scour depth with the width of abutment and bed density. It is obvious that higher the density, higher will be the resistance to scour. The scour in the case of denser bed (among the three densities considered) is less in comparison with the loose bed. Among the three densities considered, the bed with 1.37 g/cc dry density offered higher resistance to scour irrespective of the width of abutment. The abutment of 3 cm width showed maximum scour for bed densities of 1.15 and 1.23 g/cc in comparison with other abutment sizes considered. Similarly, abutment of width 5 cm showed maximum scour for bed density of 1.37 g/cc in comparison with the other abutment sizes considered. However, the general trend was not found for scour depth with respect to abutment sizes.

Fig. 3 Abutments of varying widths

Table 3 Scour depth at the end of 600 min for different bed densities and abutments

Dry density of soil (g/cc)	Width of abutment (cm)	Depth of flow (cm)	Scour depth at the end of 600 min (cm)	Discharge (m^3/s)
1.15	5	16.76	2.95	0.0103
	4	17.75	2.85	0.0096
	3	18.00	3.06	0.0095
	2	18.28	0.11	0.0095
1.23	5	18.23	2.82	0.0095
	4	18.26	2.58	0.0095
	3	18.14	2.93	0.0095
	2	18.04	0.1	0.0096
1.37	5	16.76	2.69	0.0103
	4	18.39	2.38	0.0096
	3	18.09	2.28	0.0095
	2	18.36	0.02	0.0095

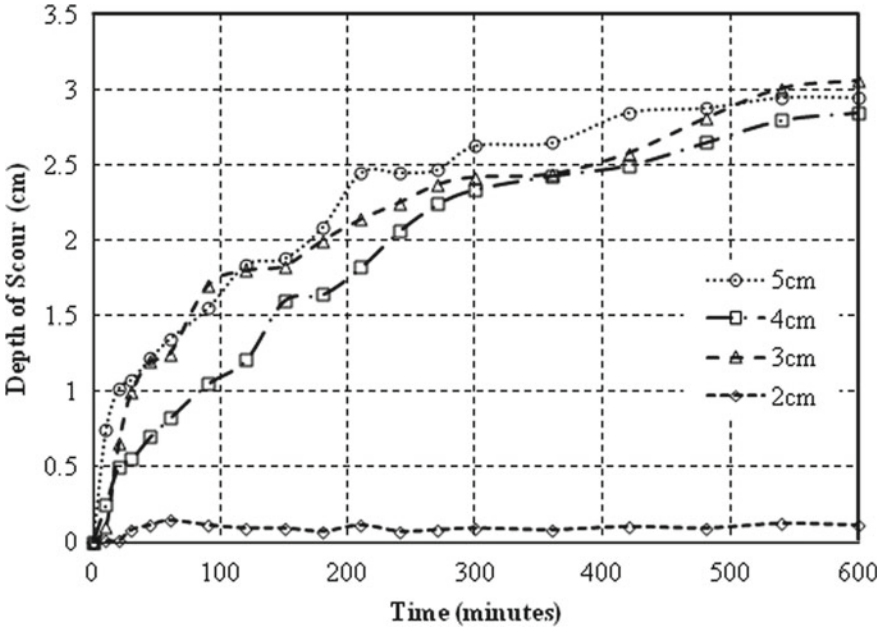

Fig. 4 Variation of depth of scour with time for bed density of 1.15 g/cc

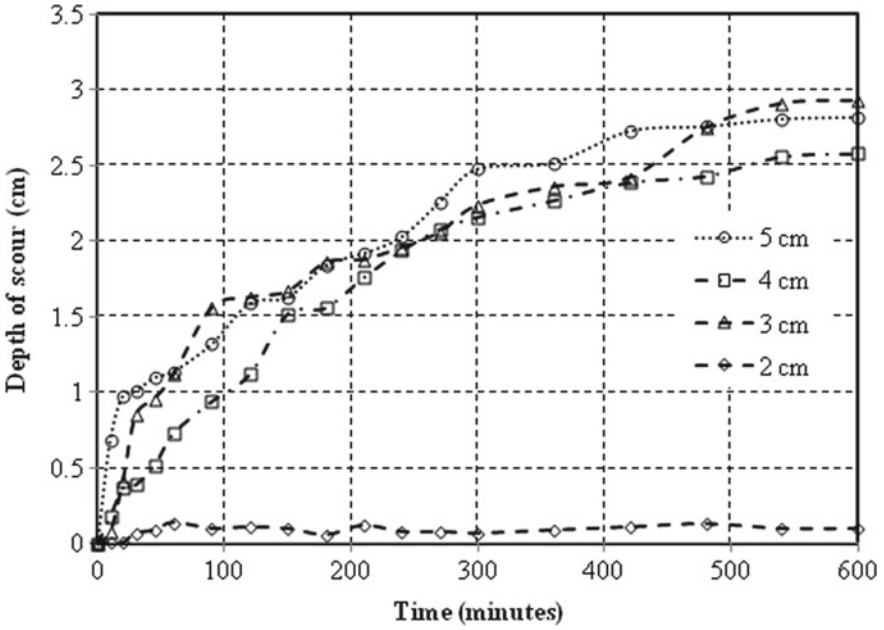

Fig. 5 Variation of depth of scour with time for bed density of 1.23 g/cc

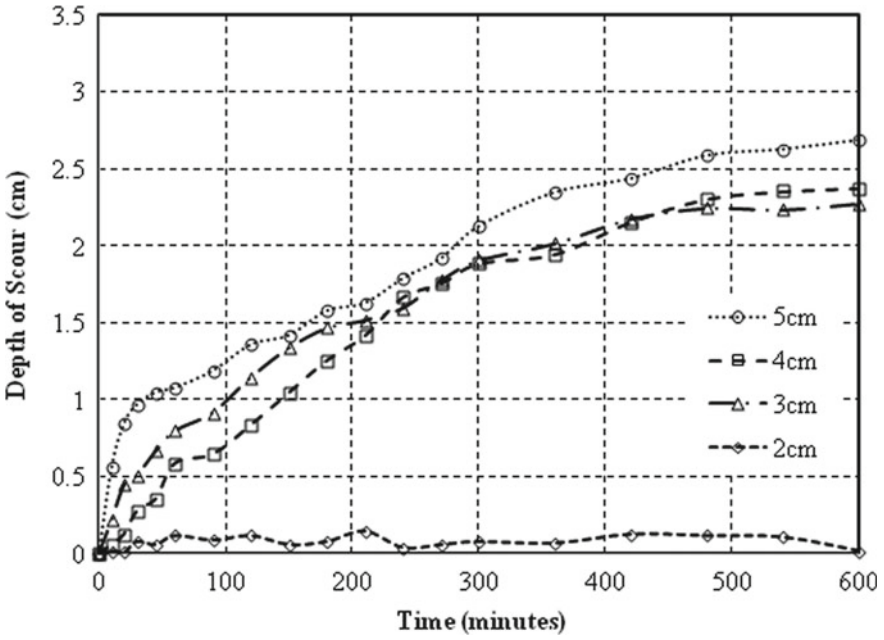

Fig. 6 Variation of depth of scour with time for bed density of 1.37 g/cc

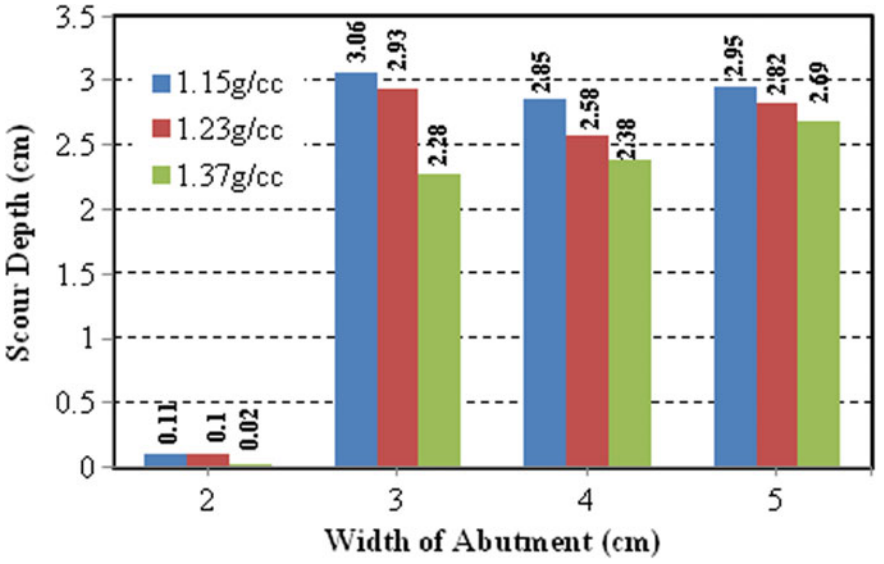

Fig. 7 Variation of the depth of scour with the width of abutment and bed density

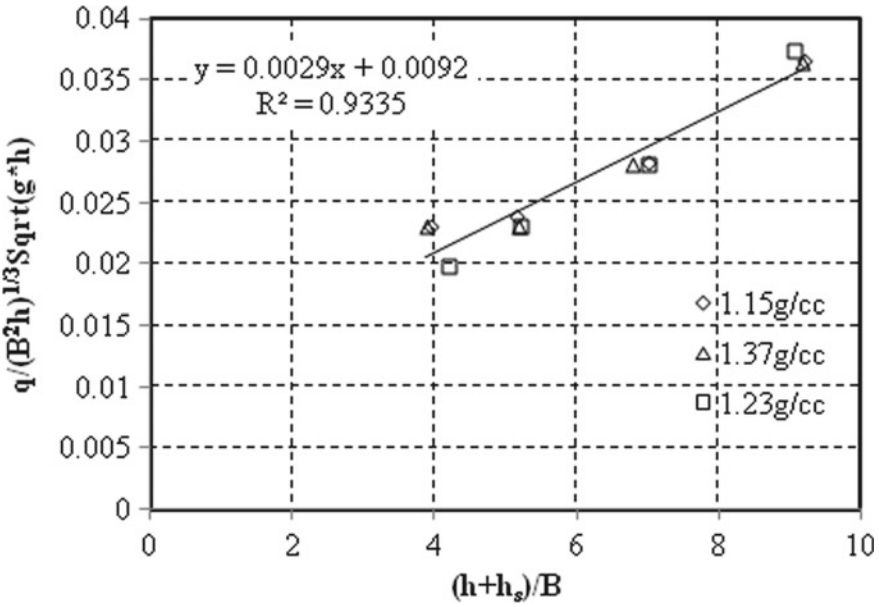

Fig. 8 Non-dimensional scour depth at the end of 600 min of flow

Non-dimensional scour depth measured from the free surface is represented as (h + h_s)/B and flow parameter (F_c) as q/$(B^2h)^{1/3}$Sqrt(g*h). The selection of length parameter $(B^2h)^{1/3}$ is similar to pier dimensions given by Veerappadevaru [18]. Figure 8 shows the variation of non-dimensional scour depth with flow parameter (F_c). It is found that the scour depth exhibited linear behaviour irrespective of the bed densities.

Non-dimensional scour depth and time are represented by $h_s/(B^2h)^{1/3}$ and $(q*t)/(B^2h)^{2/3}$, respectively. Figure 9 shows the variation of non-dimensional scour depth with non-dimensional time. It is observed that the variation of scour depth is linear in the initial period and then the rate of scour reduces irrespective of the bed density. As discussed earlier, the rate of scour is less in magnitude at higher density. When the scour depth is multiplied by density ratio (ρ_{soil}/ρ_w), the density effect is nullified and is shown in Fig. 10. This clearly indicates that the density plays a major role in scouring process and in turn cohesion of the soil. The relationship between non-dimensional scour depth and non-dimensional time is given Eq. (1).

$$\left(h_s/\left(B^2h\right)^{1/3}\right) * (\rho_s/\rho_w) = 0.121 * \ln\left((q*t)/\left(B^2h\right)^{2/3}\right) + 0.2448 \quad (1)$$

Figure 11 shows the variation of the rate of scour with time. The gradient of scour depth in terms of $h_s/(B^2h)^{1/3}*(\rho_s/\rho_w)$ varies inversely with time parameter $(q*t)/(B^2h)^{2/3}$. The equilibrium scour depends on the magnitude of discharge, width of the abutment, depth of flow and density ratio. It is observed that the rate of scour

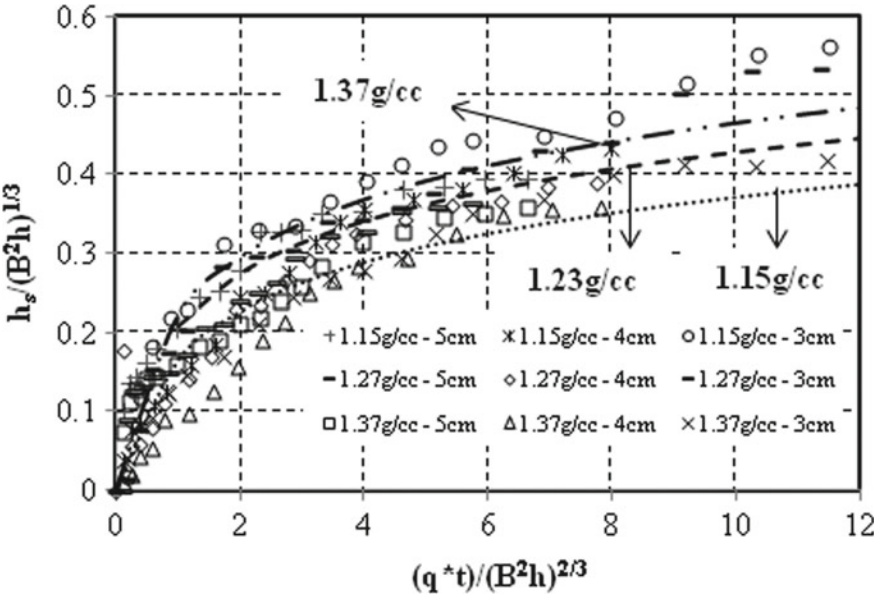

Fig. 9 Variation of non-dimensional scour depth with non-dimensional time

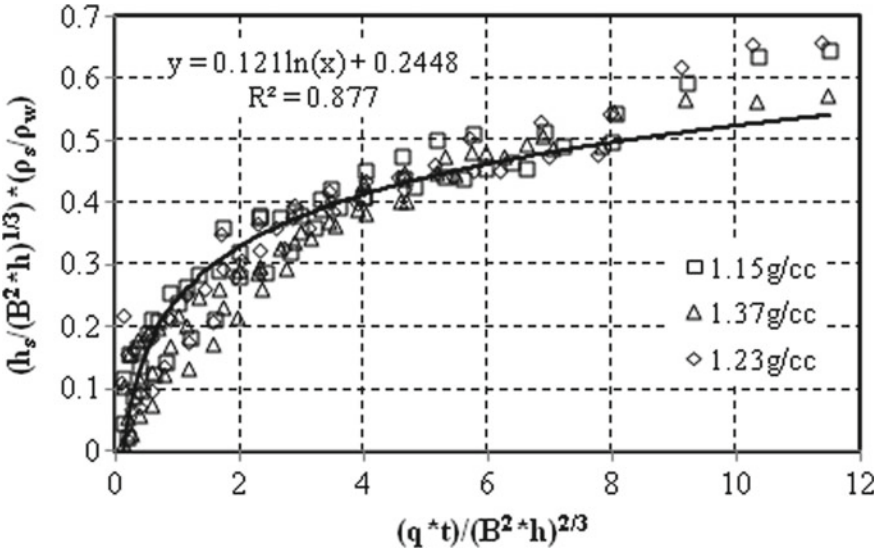

Fig. 10 Variation of dimensionless scour depth with dimensionless time after eliminating the effect of density

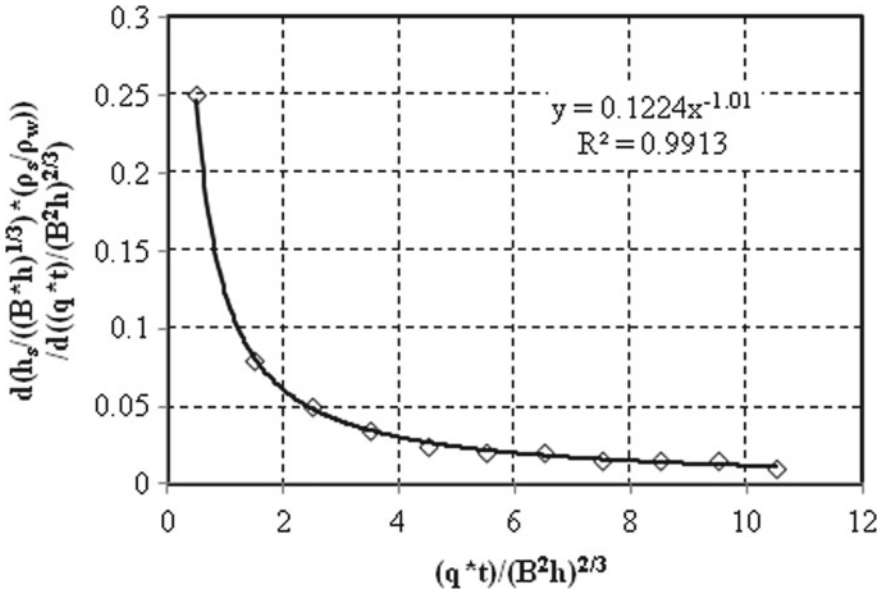

Fig. 11 Variation of the rate of scour with time

decreases rapidly with respect to time up to $(q*t)/(B^2*h)^{1/3} = 4$. Further increase in time parameter $(q*t)/(B^2*h)^{1/3}$ indicates a decrease in the rate of scour towards zero asymptotically. The relationship between the rate of scour and non-dimensional time is given by Eq. (2). Assuming equilibrium scour occurs when the rate of scour is 0.001, the magnitude of time at which equilibrium occurs is 131 as obtained from Eq. (2). Equilibrium scour depth in terms of $(h_s/(B^2h)^{1/3})*(\rho_s/\rho_w)$ is 0.8346 as obtained by Eq. (1).

$$\text{Rate of scour} = 0.1224 * \left((q * t)/\left(B^2 * h\right)^{1/3}\right)^{-1.01} \tag{2}$$

6 Conclusions

Scour around abutments was investigated through a series of flume tests with clayey bed under saturated conditions. Three densities for the bed and four abutments with a varied width were considered for the study. Based on the test results, the following conclusions are drawn.

- Scour depth around abutment in a cohesive bed is important to know the possibility of the depth of scour that may take place by knowing the flow properties, soil properties and geometry of the abutment.

- The scour depth increases with time linearly up to a time parameter of 1–1.5 and beyond this period, the rate of scour diminishes gradually.
- Density of the bed plays a significant role in the scoring process. The scour depth is more pronounced in beds with lower density and it reduces with increased density.
- The rate of scour reduces with time and when the time parameter exceeds 4, it approaches to zero asymptotically.

References

1. Coleman SE, Lauchlan CS, Melville BW (2003) Clear-water scour development at bridge abutments. J Hydraul Res 41(5):521–531
2. Dongol DMS (1994) Local scour at bridge abutments. Report no 544. School of Engineering, University of Auckland, Auckland, New Zealand
3. Lim SY (1997) Equilibrium clear-water scour around an abutment. J Hydraul Eng 123(3):237–243
4. Kouchakzadeh S, Townsend RD (1997) Maximum scour depth at bridge abutments terminating in the floodplain zone. Can J Civ Eng 24(6):996–1006
5. Kwan TF, Melville BW (1994) Local scour and flow measurements at bridge abutments. J Hydraul Res 32(5):661–673
6. Melville BW (1992) Local scour at bridge abutments. J Hydraul Eng 118(4):615–631
7. Tey CB (1984) Local scour at bridge abutments. Report no 329. School of Engineering, University of Auckland, Auckland, New Zealand
8. Oliveto G, Hager WH (2002) Temporal evolution of clear water pier and abutment scour. J Hydraul Eng 128(9):811–820
9. Melville BW (1997) Pier and abutment scour: integrated approach. J Hydraul Eng 123(2):125–136
10. Melville BW, Coleman SE (2000) Bridge scour. Water Resources Publications, Fort Collins CO
11. Mokhles M, Abou-Seida, Gamal H Elsaeed, Tarek M Mostafa and Elzahry F Elzahry (2012) Local scour at bridge abutments in cohesive soil. J Hydraul Res 50(2), 171–180
12. Abou-seida MM, Elsaeed GH, Mostafa TM, Elzahry EF (2012) Local scour at bridge abutments in cohesive soil. J Hydraul Res 50(2):171–180
13. Molinas A, Reiad-Yakoub NG (1999) Experimental study on scour around circular piers in cohesive soil. Publication no FHWA-RD-99-187, Federal Highway Administration, U.S. Department of Transportation, McLean, VA
14. Molinas A, Reiad-Yakoub NG, Jones S (1998) Effect of cohesion on abutment scour. In: Proceedings of International Conference on Water Resources Engineering, Reston VA, 1, pp 252–257
15. Reaid-Yakoub NG (1995) Effect of cohesion on bridge abutment scour. Ph.D. Thesis, Department of Civil Engineering, Colorado State University, Fort Collins, CO
16. ASTM2487 (2011) Standard practice for classification of soils for engineering purposes (Unified soil classification system)
17. Ramesh PS (2019) Erosion characteristics of stabilized clay beds. Ph.D. Thesis, Department of Civil Engineering, Visvesvaraya Technological University, Belagavi, Karnataka, India
18. Veerappadevaru G, Gangadharaiah T, Jagadeesh TR (2011) Grip length for bridge piers. ISH J Hydraul Eng 17(2):62–76

Analysis of Pedestrian Crossing Behavior at Uncontrolled Intersections

S. P. Niveditha and K. M. Mallesha

Abstract Increased vehicular population in second-tier urban areas and disobedience to the traffic laws by the road users (pedestrians and others) leads to a significant concern about the safety. This has become a very serious problem, unable to be controlled either by the enforcement or any means. In the present study, a city has been selected where the population is less than five lakhs but the substantial population of the vehicles and uncontrolled intersections are formed by adopting poor technical methods in town development. Eleven uncontrolled intersections were selected along the major arterial roads. The method adopted for data collection is a videography survey. The data collected were pedestrian volume, traffic volume, and the approaching speed of the vehicles. Also, the pedestrian characteristics were extracted to analyze the crossing behavior, gap acceptance, and critical gap. From the analysis, it is concluded that road geometry and traffic control device plays a significant role in pedestrian safety. In this analysis, while selecting the intersections, its formation, layout, and geometry are analyzed. Pedestrian crossing speed (15th percentile) was compared to the standard value 1.2 m/s and its relation between road geometry, pedestrian traffic control devices or signs, pedestrian characteristics, and traffic volume are analyzed. It is concluded that the 15th percentile speed of pedestrians did not meet the standard value 1.2 m/s in most of the intersections and male pedestrians crossing speed (1.39 m/s) is found to be higher when compared to crossing speed of female pedestrians (0.76 m/s). The critical gap is lesser for two-wheelers when compared to other classes of vehicles indicating that the size of the vehicles has a significant influence on gap acceptance, pedestrian crossing behavior, and critical gap.

Keywords Pedestrian characteristics · Gap acceptance · Critical gap · Pedestrian delay

S. P. Niveditha (✉) · K. M. Mallesha
Department of Civil Engineering, Siddaganga Institute of Technology, Tumakuru, Karnataka, India
e-mail: sp.niveditha10@gmail.com

© Springer Nature Singapore Pte Ltd. 2021

K. K. Pathak et al. (eds.), *Recent Trends in Civil Engineering*, Lecture Notes in Civil Engineering 77, https://doi.org/10.1007/978-981-15-5195-6_32

1 Introduction

In a country like India, rapid urbanization due to the migration of the people for different purposes has created several unattended problems. One among them is pedestrian safety, since there are several areas which are directly involved in a crash between the pedestrians and the vehicles due to the formation of uncontrolled intersections. In many cities, there are no crosswalks, pedestrian bridges, or pedestrian subways which are relatively a very serious concern from a safety point. The pedestrians during peak hours cross the roads wherever they desire and offer a serious risk ignoring all other problems. This is most vulnerable in the case of school-going children or aged people. Many such uncontrolled intersections have become the death traps due to the absence of traffic control and regulations of any nature.

Several studies were carried out to determine pedestrian risk at uncontrolled intersections. It was observed that minor the pedestrian safety margin larger the risk and also pedestrians gap acceptance for buses are more likely to run while crossing when compared to two-wheeler [1]. Pedestrians' crossing speed at signalized and non-signalized intersections were compared. It was found that pedestrians cross with higher speeds in unsignalized intersection [2]. By installing crosswalk, significant reduction in pedestrian waiting time and approaching vehicular speed is observed but it did not have a direct impact on pedestrian crossing behavior and gap duration [3]. The research outcome found that there is a higher acceptance gap on the six-lane roadway compared to two-lane undivided roadway. Male pedestrians have accepted a smaller gap compared to female pedestrians and older pedestrians. [4]. Road and geometric features like carriageway width, zebra crossing width, traffic features like traffic and pedestrian volume were identified to be significant in evaluating pedestrian risk [5]. Regression discontinuity evaluation and odds ratio indicate that at a pedestrian crossing there is a substantially higher risk of a pedestrian traffic accident after dark than at daylight. The likelihood of road traffic collisions after darkness was considerably greater for pedestrians aged 50 + and 30–49 compared to those aged under 18 at pelican and zebra crossings [6]. The results stated that, compared to female pedestrians, male pedestrians accept smaller gaps. The increase in the width of road and reduced traffic volume had led to lower gap acceptance time [7]. The audit results suggested that there was an absence of speed limit signage, faded crosswalks, synchronizing problems with traffic lighting and walk signs, and inadequate formal pedestrian crossings leading to dangerous crossings. An approach of framing pedestrian safety research and suggestions around the three "E's" worked well [8]. It is suggested that, wherever old pedestrians are dominant, 0.79 m/s crossing speed should be adopted for design purposes, otherwise 0.95 m/s may be used. Pedestrian crossing speeds also suggest that Indian pedestrians are slower than American and UK pedestrians [9]. The authors compared the equilibrium probability method and maximum likelihood method for calculating pedestrian critical gap at unsignalized intersections. It is found that the equilibrium probability method is more appropriate for the estimation of critical gap [10]. It is also concluded from the study that the pedestrian speed also increases with the increase in frictions encountered

by a pedestrian. Significant differences in pedestrian average speed were found with respect to pedestrian gender, age and flow conditions such as platoon movements or movements with baggage. As the age of pedestrians increases, the level of energy decreases and it adversely affects pedestrian speed [11]. Different methods of estimating critical gaps at unprotected mid-block crosswalks are done. It showed that there was a significant difference in the critical gap values estimated by considering and by not considering the pedestrians' behavioral characteristics [12]. The factors affecting gap acceptance are studied in detail. From the analysis, the variables such as vehicle speed change, age of pedestrian, and position of vehicle to the pedestrian start point are very much effective in gap acceptance of pedestrians [13]. The main objective of the present study is appraising and evaluating pedestrian crossing behavior at uncontrolled intersections in Tier-II cities.

2 Data Collection

The present study was restricted to Tier-II city, populated moderately around three lakhs, with quite an appreciable number of uncontrolled intersections on one of the major arterial roads, which was once NH-4 and now NH-206. It passes through the middle of the city, adjacent to the developed residential and commercial areas, followed the ribbon development as per the town planning theories. These intersections were selected on four-lane divided road. They are spaced at an interval ranging from 250 to 1000 m. Upon the identification of the intersections, the data collected were the following:

- The geometry, traffic, and pedestrian control devices and signs.
- Pedestrian volume and speed, traffic volume, approaching the speed of the vehicles.
- Pedestrian crossing behavior through video recording.

2.1 Geometry of the Intersection

The inventory of these intersections was carried out to record the existing geometric parameters, existence of any traffic control devices for both vehicles and pedestrians. The details are shown in Table 1.

2.2 Traffic Studies

The manual recording of traffic studies was carried out to collect the pedestrian volume, speed, vehicular volume, and approaching speed of both slow-moving and fast-moving vehicles toward the intersection. The pedestrian volume was collected

Table 1 Appraisal of Intersection

Intersection	Geometric parameters				Traffic control devices and pedestrian facilities				
	Width of crossing (m)	Type of intersection	Median opening (m)	Median width (m)	Zebra crossing	Traffic sign	Bus Stop	Speed breaker	Footpath
1	17.81	T-shape	23.50	1.20	✓	✓	✓	✓	–
2	20.00	T-shape	17.80	1.20	✓	–	✓	✓	–
3	15.00	T-shape	18.90	1.20	–	–	–	–	–
4	14.00	Oblique	56.30	1.10	–	–	–	–	–
5	22.54	T-shape	30.80	1.20	–	–	–	✓	–
6	13.00	Right angled	16.70	0.78	–	–	–	–	–
7	19.00	Right angled	22.26	1.04	–	–	–	–	–
8	19.00	T-shape	19.50	1.16	–	–	–	–	–
9	20.58	T-shape	21.01	0.98	✓	✓	✓	–	✓
10	20.56	T-shape	21.90	1.20	–	✓	✓	✓	✓
11	19.50	T-shape	16.80	1.15	–	–	–	–	✓

Table 2 Pedestrian volume, traffic volume, and approaching the vehicular speed

Intersection	Pedestrian volume (P/h)	15th Percentile pedestrian speed (m/s)	Traffic volume (PCU/h)	85th Percentile Speed (kmph)				
				Two-wheeler	Auto	Car	Bus	LCV
1	38	1.29	2145	32	28	38	29	31
2	289	1.04	1687	34	31	35	33	28
3	48	1.00	1254	28	29	34	38	36
4	88	0.91	986	29	26	30	27	24
5	87	1.26	758	25	23	23	21	21
6	88	0.80	1745	33	30	31	29	27
7	151	1.35	1268	36	26	36	28	35
8	141	1.13	1687	37	32	26	–	28
9	805	1.32	1256	34	34	36	32	36
10	322	1.38	1645	31	29	31	28	29
11	258	0.98	985	37	32	36	29	31

for one hour during peak hours in morning and evening. A similar procedure was adopted for traffic volume studies. The time of crossing the crosswalk by the pedestrians was completed at the same time. Sufficient samples were considered while arriving at the 15th percentile walking speed of various categories of pedestrians. The 15th percentile speed of the pedestrian, 85th percentile speed of the different types of the vehicles, pedestrian volume, and traffic volume details are shown in Table 2.

3 Videography Survey

The video recording was carried out at all intersections for a period of 60–90 min. The camera was set up at an elevated place for recording purposes. The pedestrian crossing behavior at these intersections was recorded. Thorough information such as crossing pattern, i.e., one step or two steps, age, gender, crossing in the platoon or single, gap acceptance, and gap rejection were observed and recorded. Sufficient samples were extracted from video recording and the data were used in a subsequent article for the analysis. Figure 1 shows the video frames of data extraction and Table 3 shows the details of data extracted from the videos.

Fig. 1 km player frames for data extraction

Table 3 Data extraction of Pedestrian characteristics (%)

Observed Data (%)	Intersections										
	1	2	3	4	5	6	7	8	9	10	11
Gender											
Male	64	60	52	64	78	48	49	57	69	55	59
Female	36	40	48	36	22	52	51	43	31	45	41
Age group											
Youth	48	53	34	26	38	78	31	12	15	30	31
Middle aged	35	26	42	62	55	11	63	57	54	44	42
Elders	16	20	24	12	7	11	6	31	31	25	28
Behavior											
Walk	94	93	74	92	97	89	91	98	95	95	93
Run	6	7	26	8	3	11	9	2	5	5	7
Group											
Alone	91	87	30	80	96	85	74	95	91	48	44
Platoon	9	13	70	20	4	15	25	5	9	52	56
Pattern											
One step	74	47	58	55	92	74	43	79	46	38	38
Two steps	26	53	42	45	8	26	56	21	54	62	62
Perpendicular	29	53	32	75	53	63	26	62	28	30	34
Oblique	43	13	34	10	42	19	50	19	46	49	52
Mixed	26	33	34	15	5.	18	24	19	26	21	13
Zebra crossing											
Yes	32	53	30	53	–	44	3	–	–	58	–
No	67	47	70	47	–	56	97	–	–	42	–

4 Analysis

The data collected at all 11 uncontrolled intersections were analyzed and the results were discussed. Various parameters such as inventory of the intersections, pedestrian volume, traffic volume, approaching speed of the vehicles, analysis of gap acceptance, critical gap, and pedestrian crossing behavior were discussed to evaluate pedestrian safety.

4.1 Crossing Width, Median Opening, and Its Width

The study was carried out on four-lane divided arterial road and the inventory showed wider variations in the width of the crossing. Figure 2 shows the minimum and maximum width of 13.00 m, 22.54 m, respectively. Figure 3 shows the variations in the crossing speed of the pedestrians with crossing width. The speed was considered between the curbs.

The crossing speed is 0.8 m/s for a width of 13.00 m, and slightly above by fifty percent for a greater width of 22.54 m. The important observation is totally distinct variation in pedestrian crossing speed at each pedestrian crossing, exhibiting the rise and fall. The linear model developed is given below.

$$v = 0.239 + 0.0490\,w\left(R^2 = 55.23\%,\ p = 0.009\right) \quad (1)$$

where v = Crossing speed (m/s), w = Crossing width (m)

The median opening did not play an important role in influencing the crossing speed of the pedestrians, but resulted in choosing the patterns of crossing such as perpendicular, oblique, mixed, one-step and two-step crossings. Figure 4 shows the variations in the median opening width measured longitudinally from nose to nose.

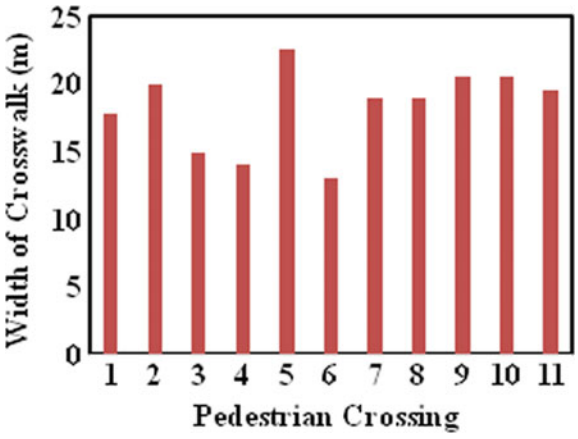

Fig. 2 Variation in width of crosswalk

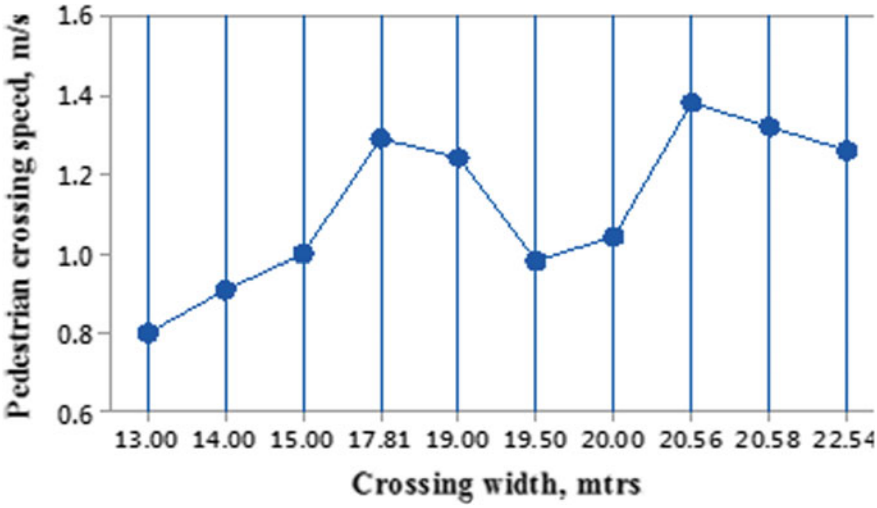

Fig. 3 Variation of crossing speed with crosswalk width

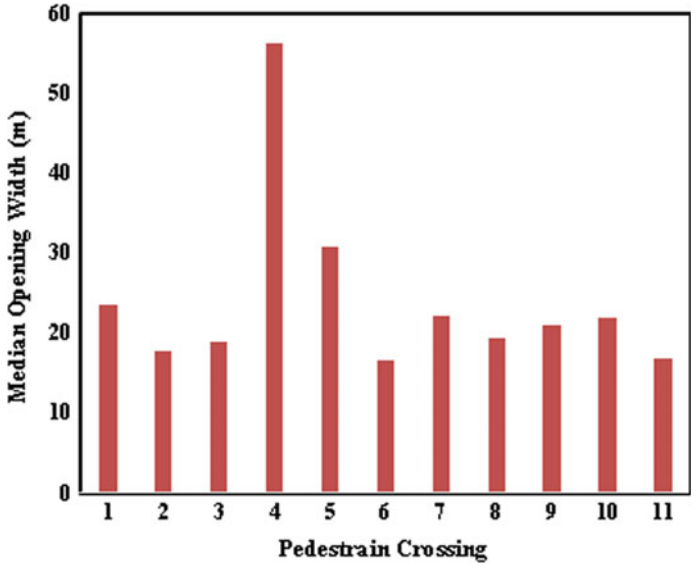

Fig. 4 Variation in median opening width

Width is minimum in case of 6th pedestrian crossing with a linear dimension of 16.70 m and resulted in a very low crossing speed of 0.8 m/s and as the same with respect to median width 0.78 m. The largest opening is 56.30 m, but still has a crossing speed of 0.91 m/s without any significant variations.

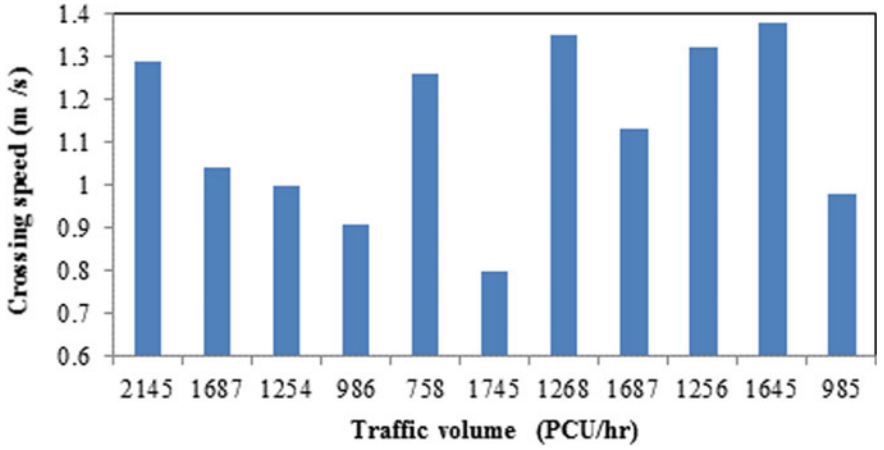

Fig. 5 Variation of pedestrian crossing speed based on traffic volume

4.2 Traffic Volume

The traffic flow was continuous since the intersections were uncontrolled. Figure 5 shows the variation of pedestrian crossing speed with respect to the traffic volume. In comparison to the standard design speed of 1.2 m/s, only five intersections whose traffic flow is in the range of 758–2145 PCU/h. The corresponding crossing speed was above the design standard, but in the remaining six intersections, the crossing speed is less than the design standard. No definite trend was predicted in this analysis.

4.3 Gender, Age, and Group Size

Table 4 provides the results of 15th percentile speed of males, females, and of different age groups. The statistical software Mintab 17 provided the 15th percentile crossing speeds after eliminating the outliers from a box plot analysis of more than one hundred samples. The field data collected did not represent any shy areas. The average crossing speed of the men was more than the standard design speed of 1.2 m/s [IRC:103 2002] ranging from 1.25 to 1.47 m/s in almost all eight locations. While analyzing the reasons it was the youth who preferred to cross in a hurry and even venture running. Another reason was the continuous movement of the vehicles. These results were obtained at the intersections which were moderately crowded. The reverse was in the case of females. The lowest crossing speed was 0.76 m/s and the maximum stood at 1.22 m/s in almost all the same number of intersections. Patience, physical ability could be reasons for these results.

At seven intersections, the crossing speed of the youths and middle-aged persons was more than standard design speed of 1.2 m/s, but in six intersections the crossing

Table 4 15th percentile crossing speed of pedestrians

Observed data	Intersections										
	1	2	3	4	5	6	7	8	9	10	11
Gender											
Male	1.39	1.12	1.47	0.91	1.28	0.92	1.35	1.13	1.35	1.25	1.00
Female	1.23	0.93	0.76	0.8	1.22	0.84	1.27	0.98	1.21	1.14	0.92
Age group											
Youth	1.47	1.21	1.34	0.94	1.37	1.08	1.55	1.17	1.39	1.29	0.97
Middle aged	1.30	1.21	1.31	0.91	1.25	0.94	1.39	1.11	1.35	1.23	1.01
Elders	1.28	1.07	1.21	0.84	1.20	0.76	1.27	0.95	1.29	1.15	0.83
Group											
Alone	1.34	1.16	1.42	0.92	1.26	0.80	1.46	1.15	1.44	1.24	1.00
Platoon	1.15	1.04	0.98	0.86	1.07	0.75	1.32	0.94	1.35	1.09	0.84

speed of elders was below the standard which is in the range of 0.76–1.20 m/s. While comparing the 15th percentile crossing speed of various pedestrian categories with other countries, it was observed that the crossing speed of youth in the UK was in the range of 1.32–1.72 m/s, but in the present study, it was between 0.97 and 1.47 m/s. Similarly, for elder persons, the crossing speed is between 1.11 and 1.16 m/s in the UK, while in the present study it stands between 0.76 and 1.28 m/s. For adults or middle-aged category, it is 1.3–1.51 m/s, while in this assessment it resulted between 0.91 and 1.35 m/s [9]. The overall analysis showed that the lower threshold value of crossing speed pedestrians in the UK is the maximum value in the present work. The length of the pace or strides which depend upon the race can be one of the valid reasons for such a huge variation. The other analysis focussed on pedestrian crossing speed in a group. The 15th percentile crossing speed of the pedestrians in single and in the group was also determined and analyzed. In single, the crossing speeds are nearer and above the standard value of 1.2 m/s in eight intersections, but fall short in three and far less when compared with the UK standards. The group was defined by more than two pedestrians crossing the crosswalk. The determination of crossing speed was limited only to a group, neglecting the age or gender. Except at one intersection, there was a considerable reduction of the crossing speed. The reduction in crossing speed was observed to be in the range of 4–37% when compared with a standard design value.

4.4 Gap Acceptance

The gap acceptance is a phenomenon described as an event of a conflict between the crossing pedestrian and the perpendicular moving vehicle. This is shown in Fig. 6. The vehicle position and speed gauged by a pedestrian in such a way that he or she

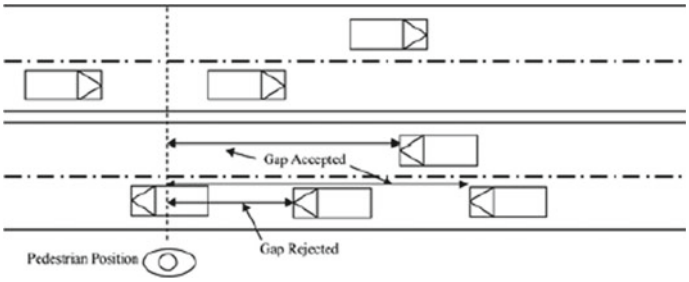

Fig. 6 Variation of pedestrian crossing speed based on traffic volume

Table 5 Gap acceptance at different locations

Pedestrian crossing	Mean	Standard deviation	Skewness
1	1.65	0.85	1.83
2	1.57	0.68	0.89
3	1.47	0.69	1.01
4	1.79	0.88	1.21
5	1.84	1.03	1.34
6	1.99	1.08	0.66
7	1.47	0.95	0.47
8	1.63	0.92	1.14
9	2.05	0.78	0.54
10	1.87	0.84	1.14
11	1.95	0.89	0.75

will cross the intersection, then the spatial distance between pedestrian and vehicle position is known as "gap accepted" or otherwise "gap rejected". The descriptive statistical analysis has been carried out to determine the gap acceptance mean, its standard deviation and skewness. The results are shown in Table 5.

In two locations gap acceptance observed was 1.47 s and in one location it was 2.05 s. The traffic volume was almost the same but there was little variation in crossing width of the intersections. But relatively the composition of the age group was significantly different between all three intersections. The lower gap accepted intersections had the youth and middle-aged group accounting to 76 and 89%, whereas the higher gap accepted intersection had a group composition of 69%. However, the gap acceptance was not discussed based on the land use pattern. The distributions were positively skewed indicating the avoidance of risk crossing. The minimum and maximum gap acceptance resulted in the pedestrians crossing risk at low and high stake.

4.5 *Critical Gaps*

The critical gap is another method of estimating or expressing the crossing time of the pedestrians. This gap would be determined by drawing the distribution curves between gap acceptance (F_a) and gap rejection (F_t). The intersection of curves (Fa) and (1-Ft) provides the critical gap value. The graphical method of determining the critical gap is shown in Fig. 7. The average critical gap at the selected intersection and vehicle class based critical gaps are shown in Table 6.

The critical gap at various intersections is compared and analyzed among themselves. The 7th intersection exhibited the lower value, 1.2 s critical gap, but a critical

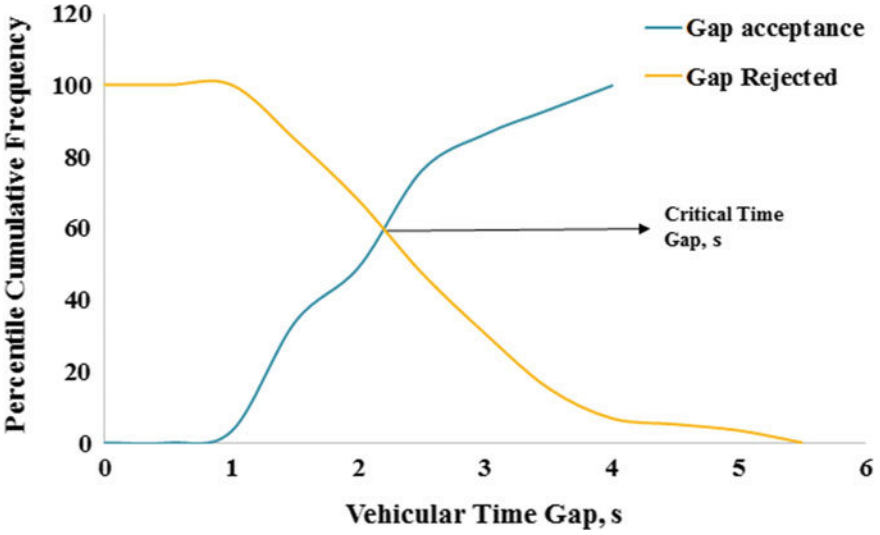

Fig. 7 Graphical method of determining the critical gap

Table 6 Critical gap at different intersections

Observed data	Intersections										
	1	2	3	4	5	6	7	8	9	10	11
Average critical gap (Global)	1.41	1.60	1.40	1.90	1.70	1.50	1.20	1.50	2.20	2.20	1.40
Vehicle-based critical gap											
Two-wheeler	1.52	1.48	1.45	1.68	1.44	1.47	1.42	1.39	1.65	1.62	1.41
Auto	1.68	1.72	1.54	1.75	1.58	1.65	1.62	1.58	1.84	1.75	1.57
Car	1.72	1.79	1.69	1.80	1.85	1.71	1.67	1.68	1.89	1.82	1.57
Bus	1.92	1.95	1.94	1.87	1.89	1.91	2.02	2.20	2.15	2.01	1.89
LCV	2.00	2.10	2.20	1.95	1.84	2.04	1.94	1.96	2.10	2.14	1.90

gap of 2.2 s stood highest at 9th and 10th intersection. Much emphasis was not explained about the land use pattern and hence significant evaluation was limited to discuss more on the results. But still there was a steep difference of 45%, indicating the pedestrians offering risk at more than six intersections. While analysing the critical gap for the vehicle class, the lowest and highest value was found to be 1.39 s and 1.68 s for two-wheelers, but the lowest value of other vehicles was 1.57 s and the maximum value was 2.2 s. There was a fall of 37% when compared to other class of the vehicles. There was quite an appreciable risk offering chance in case of two-wheelers than with other vehicles.

5 Conclusions

The present study assessed various factors involved and had an impact on the crossing behavior of the pedestrians at 11 uncontrolled intersections selected along the divided main corridor of the city. 15th percentile crossing speed of the pedestrians was compared with standard design value 1.2 m/s (IRC:103-1988 and HCM-2000). In this regard, the geometry of the road, pedestrian traffic control devices or signs, gender, age of the pedestrian, traffic volume were examined with pedestrian crossing speed. Besides, the analysis was also extended to estimate the critical gap acceptance of the pedestrians with various classes of vehicles. Based on the analysis and discussion carried out, the following conclusions were drawn.

- The crossing speed in most of the intersections was low in comparison to the standard design values (1.2 m/s), irrespective of its geometry and traffic control system.
- The crossing speed of the male pedestrians (1.39 m/s) is more than the female pedestrians (0.76 m/s) with no interference of intersection geometry.
- The crossing speed of the youths is greater than the middle aged and older (0.91 m/s and 0.76 m/s).
- The average crossing speed of the youths or older persons is lesser than the UK (1.32–1.72 m/s) and US (1.35–1.51 m/s) crossing speeds.
- The pedestrian's critical gap (method of expressing the intersection crossing time) is very low with two-wheelers when compared to other classes of the vehicles.

References

1. Ravishankar KVR, Nair PM (2018) Pedestrian risk analysis at uncontrolled mid-blocks and unsignalised intersections. J Traffic Transp Eng 5(2):137–147
2. Ramesh A, Ashritha K, Kumar M (2018) Development of model for pedestrian gap based on land use pattern at midblock location and estimation of delay at intersections. J Inst Eng (India): Ser A 99 (3), 413–422

3. Danaf M, Sabari A, Abou-Zeid M, Kyasi I (2018) Pedestrian–vehicular interactions in a mixed street environment. Int J Transp Res, 1–13
4. Raghuram Kadali B, Vedagiri P (2017) Evaluation of pedestrian accepted vehicle gaps with varied roadway width under mixed traffic conditions. Int J Transp Res, 1–10
5. Priyadarshini Priyanka, Mitra Sudeshna (2017) Investigating pedestrian risk factors leading to pedestrian fatalities in Kolkata city roads. Transp Develop Econ 18(6):287–301
6. Uttley Jim, Fotios Steve (2017) The effect of ambient light condition on road traffic collisions involving pedestrians on pedestrian crossings. Accid Anal Prev 108:189–200
7. Chandra S, Rastogi R, Das VR (2014) Descriptive and parametric analysis of pedestrian gap acceptance in mixed traffic conditions. KSCE J Civ Eng 18(1):284–293
8. Pollack KM, Gielen AC, Nasir M (2014) Investigating and improving pedestrian safety in an urban environment. Inj Epidemiol 1(11):189–200
9. Rastogi R, Chandra S, Vamsheedhar J, Das VR (2011) Parametric study of pedestrian speeds at midblock crossings. J Urban Plan Dev 137 (4), 381–189
10. Sahani R, Saipriya M, Bhuyan BK (2018) Application of gap acceptance concept to investigate crossing behavior of pedestrians at unsignalized intersections. Transp Dev Econ 4(15), 1–8
11. Laxman KK, Rastogi R, Chandra S (2010) Pedestrian flow characteristics in mixed traffic conditions. J Urban Plan Dev 136(1):23–33
12. Kadali RB, Perumal V (2016) Critical gap analysis based on pedestrian behaviour during peak hour traffic at unprotected midblock crosswalks. Asian Transp Stud 4(1):261–277
13. Boroujerdian AM, Nemati M (2016) Pedestrian gap acceptance logit model in unsignalized crosswalks conflict zone. Int J Transp Eng 4(2):87–96

Utilization of RAP in Flexible Pavements

Bhavana Suresh, K. H. Mamatha, and S. V. Dinesh

Abstract In modern days, life without the transportation industry is unimaginable. The roadways play a vital role in improving the economy of the country. As the roadways require necessary strengthening, rehabilitation or reconstruction depending on the severity of the damage caused to the structure during its service life, enormous quantity of RAP will be generated. It is essential to recycle and reuse the RAP generated in the pavement construction as it can help in preserving a large quantity of conventional construction materials. In this study, the strength characteristics of the bituminous mix with recycled binder or aggregates are compared with that of the conventional bituminous mix through laboratory investigation. The test result indicated that the recycled binder or aggregates can be effectively used in the bituminous mix satisfying the MoRT&H requirements up to a certain percentage. The recycled aggregates of up to 20% give maximum stability and ITS in comparison with conventional mix providing an eco-friendly, economical solution for the construction of pavements.

Keywords RAP · Recycling · Stability · ITS · TSR

1 Introduction

In recent years, the government is paying attention to the infrastructure development of the country and transportation sector is attracting a higher degree of interest owing to its positive influence on the economy of the country. The roadways or highways extend over thousands of kilometres and the construction of the same requires good quality construction materials like soil, aggregates, binder, etc., in large quantity. Once the pavements are constructed, they are open for traffic for the designed period. The pavements will be subjected to rehabilitation, maintenance and/or reconstruction depending on the extent of deterioration of the pavement materials during or at the

B. Suresh · K. H. Mamatha (✉) · S. V. Dinesh
Department of Civil Engineering, Siddaganga Institute of Technology, Tumakuru, India
e-mail: mamathakh@sit.ac.in

© Springer Nature Singapore Pte Ltd. 2021

K. K. Pathak et al. (eds.), *Recent Trends in Civil Engineering*, Lecture Notes in Civil Engineering 77, https://doi.org/10.1007/978-981-15-5195-6_33

end of its designed life. In this rehabilitation, maintenance and/or reconstruction process, large quantities of recycled asphaltic pavement (RAP) will be produced.

RAP is the removed and/or processed aggregate materials with an asphalt coating. Well-graded good quality aggregates along with asphalt coating can be obtained if the RAP is processed and screened properly [1]. Studies in the past have recommended the use of RAP for subgrade, GSB and base layer application [2–6]. The effect of RAP can be studied by separating the binder and aggregates and investigating the properties and their influence separately [7]. The strength characteristics of RAP depend on its age, asphalt content, temperature, etc. RAP is stiffer than the dense-graded aggregate base course. But, RAP has the greatest amount of permanent strain in comparison to recycled concrete aggregate and natural coarse aggregate which might be due to the breakdown of asphalt binder under loading. However, RAP exhibits creep behaviour under sustained loading which is attributed to the presence of asphalt coating and, therefore when it is intended to use RAP for base course applications, it is necessary to improve its strength by adding admixtures such as fly ash, cement, lime, etc.

In this study, an attempt is made to evaluate the influence of recycled binder or aggregate on the strength characteristics of the bituminous mixtures through a series of Marshall and indirect tensile strength tests.

2 Materials

In this study, RAP was collected from NH 4 situated near Savandurga, Karnataka. Conventional aggregates having a nominal mean aggregate size of 13.2 mm and stone dust of size 4.75 mm passing were collected from a nearby quarry located in Mydala, Tumakuru District, Karnataka and bitumen of grade VG30 was procured from FDL hot mix plant located in Madhugiri, Tumakuru District, Karnataka. The aggregates were grouped into four batches, namely, 20 mm down, 10 mm down, 6 mm down and 4.75 mm down. Initially, the conventional aggregates were tested for their physical and mechanical properties as per the relevant IS guidelines and the results are presented in Table 1 along with the permissible values recommended by the Ministry of Road Transportation and Highway Officials (MoRT&H) [8] for bituminous concrete (BC) layer. The test results indicated that the aggregates satisfy the specification requirements. Once the material is found suitable, individual gradation of all the four batches of aggregates was carried out. Using the results of individual gradation, combined gradation was exercised to satisfy the gradation requirements of bituminous concrete (BC) of grade II as specified by MoRT&H [8]. Table 2 shows the combined gradation results along with the upper and lower limits as specified by MoRT&H [8] for grade II. Figure 1 shows the gradation curve of the designed BC mix.

The conventional bitumen of grade VG30 was tested for its engineering properties as per the relevant IS guidelines. Table 3 shows the properties of VG30 bitumen. It is observed that the bitumen satisfies the specification requirements.

Table 1 Physical and mechanical properties of aggregates

Property	Result	MoRT&H [8] guidelines	Remarks
Specific gravity 20 mm down 10 mm down 6 mm down 4.75 mm down	2.66 2.64 2.65 2.68	2.5 – 3.2	Good
Aggregate impact value (%)	26	Max. 30%	Acceptable
Aggregate crushing value (%)	25	Max. 30%	Acceptable
Los angeles abrasion value (%)	27	Max. 40%	Acceptable
Combined indices (%)	30	Max. 35%	Acceptable
Water absorption (%)	0.17	Max. 2%	Good

The RAP was obtained through milling from the site and it was subjected to bitumen extraction in the laboratory using benzene through bitumen extractor and then the extracted bitumen was processed through fractional distillation by condensation. A total of ten trials were carried out for extraction and the average bitumen content was found to be 2.3%. The extracted aggregates were tested for their engineering properties and the test results are presented in Table 4.

3 Experimental Program

Initially, the optimum binder content was determined for the control mix, i.e. Mix 1. The binder was extracted from the RAP. The extracted binder and aggregates were stored separately. Then, the recycled binder or recycled aggregates were added into the mix in 10, 20, 30, 40 and 50% by weight of conventional binder or conventional aggregates. The mix where the conventional binder is replaced by recycled binder is designated as Mix 2 and the mix where conventional aggregates were replaced by recycled aggregates is designated as Mix 3. The Marshall properties and indirect tensile strength of all three mixes were evaluated. Table 5 shows the experimental program adopted along with the test condition and the number of samples tested. A total of three samples were prepared and tested for each condition and the average values are presented for analysis.

Table 2 Combined gradation for the designed BC mix of grade II as per MoRT&H [8]

IS Sieve Size (mm)	20 mm down		10 mm down		6 mm down		4.75 mm down		JMF	UL	LL
	% Passing	20%	% Passing	16%	% Passing	18%	% Passing	46%	100%		
19	100	20	100	16.0	100	18.0	100	46	100	100	100
13.2	35.2	7.04	100	16.0	100	18.0	100	46	87	100	79
9.5	2.1	0.42	92.2	14.8	100	18.0	100	46	79.2	88	70
4.75	0.8	0.16	81.1	13.0	21.1	3.8	100	46	62.9	71	53
2.36	0.0	0	0.0	0.0	0.0	0.0	99.61	45.8	45.8	58	42
1.18	0.0	0	0.0	0.0	0.0	0.0	84.51	38.9	38.9	48	34
0.600	0.0	0	0.0	0.0	0.0	0.0	68.12	31.3	31.3	38	26
0.300	0.0	0	0.0	0.0	0.0	0.0	49.51	22.8	22.8	28	18
0.150	0.0	0	0.0	0.0	0.0	0.0	29.73	13.7	13.7	20	12
0.075	0.0	0	0.0	0.0	0.0	0.0	13.12	6.0	6.0	10	4

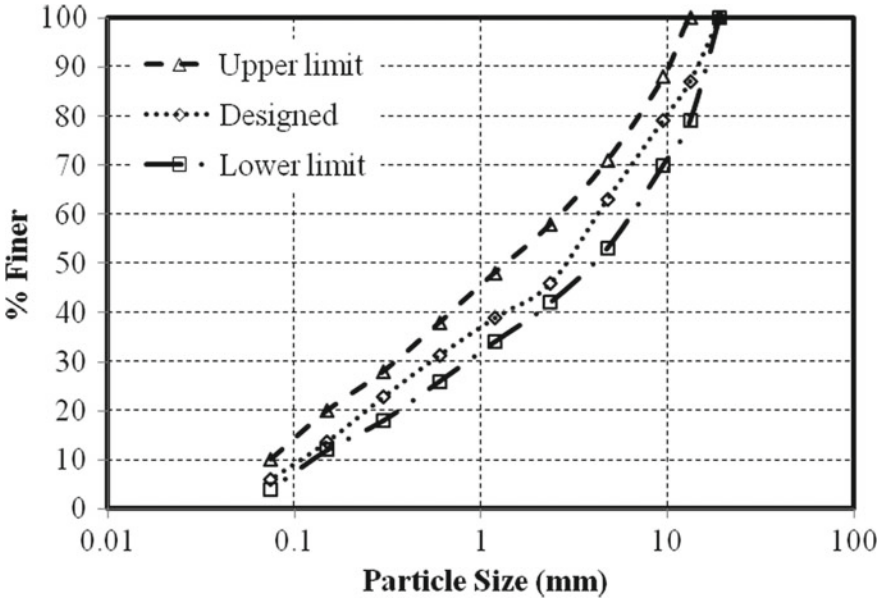

Fig. 1 Gradation curve of the designed BC mix

Table 3 Properties of VG30 binder

Property	Value	MoRT&H [8] guidelines	Remarks
Specific gravity	1.015	0.97–1.02	Acceptable
Ductility (cm)	69	Min. 40	Acceptable
Penetration (mm)	65	Min. 45	Acceptable
Flash point (°C)	240	Min. 220	Acceptable
Fire point (°C)	340	Min. 220	Acceptable

Table 4 Properties of RAP

Recycled aggregates	
Property	Value
Specific gravity	
Fine aggregates	2.64
Coarse aggregates	2.71
Aggregate impact value (%)	22
Aggregate crushing value (%)	18
Combined indices (%)	23

Table 5 Experimental program

Test	Mix designation	Mix composition	Binder content (%)	Recycled binder (%)	Recycled aggregates (%)	Test condition	Number of samples
Marshall properties	Mix 1	CA + CB	4, 4.5, 5, 5.5, 6, 6.5	–	–	–	6 * 3 = 18
	Mix 2	CA + CB + RB	5.1	10, 20, 30, 40, 50	–	–	5 * 3 = 15
	Mix 3	CA + RA + CB	5.1	–	10, 20, 30, 40, 50	–	5 * 3 = 15
Indirect tensile strength	Mix 1	CA + CB	5.1	–	–	Unconditioned	3
						Conditioned	3
	Mix 2	CA + CB + RB	5.1	10, 20, 30, 40, 50	–	Unconditioned	5 * 3 = 15
						Conditioned	5 * 3 = 15
	Mix 3	CA + RA + CB	5.1	–	10, 20, 30, 40, 50	Unconditioned	5 * 3 = 15
						Conditioned	5 * 3 = 15

*UC—Unconditioned, C—Conditioned

4 Results and Discussions

A series of Marshall and ITS tests were carried out on the three mixes and the results are presented and discussed in the following sections.

4.1 Marshall Properties

Marshall method of mix design was carried out as per ASTM D 1559-76 [9] and the mix properties (stability, flow, % air voids, % volume of bitumen, voids in mineral aggregate and voids filled with bitumen) were determined as per ASTM D 6926 [10] and ASTM D 6927 [11]. For the control mix design (i.e. Mix 1), binder content ranging from 4 to 6.5% with an increment of 0.5% was considered. The Marshall properties of Mix 1 are presented in Fig. 2. From the figure, the binder content corresponding to maximum stability, maximum bulk specific gravity and design air voids of 3.3% was found to be 5.2%, 5.1% and 5%, respectively. The average of these binder contents works out to be 5.1% and was considered as the optimum binder content.

For Mix 2 and Mix 3, the optimum binder content was retained at the same level. The Marshall properties of Mix 2 and Mix 3 in comparison with Mix 1 are presented in Fig. 3. Mix 2 and Mix 3 exhibited reduced stability and flow values with 10% of replacement. Mix 2 showed continuously decreasing trend in terms of stability of the mix with an increase in recycled binder content in the mix. Beyond 10%, Mix 3 showed increased stability of the mix and a further increase in recycled aggregates reduced the stability value and this reduced trend continues up to 50% replacement with recycled aggregates. Both the mixes exhibited reduced flow with 10% of replacement and thereby, the flow value increased with an increase in the recycled component in the mix. The increased stability of the mix with 20% of the recycled aggregates indicates the improved particle arrangement within the mix and thereby, exhibits the higher potential of the mix to reduce the compressive and tensile strains to be developed in the pavement.

4.2 Its

The moisture susceptibility of the mix under various conditions was determined through indirect tensile strength test. The indirect tensile strength (ITS) and tensile strength ratio (TSR) were evaluated for each test condition. Figures 4 and 5 show the variation of ITS and TSR of all the mixes considered. Mix 2 exhibited a reducing trend in terms of ITS and TSR with an increase in recycled binder content in the mix. Whereas, Mix 3 indicated slightly increased ITS and TSR values in comparison with Mix 1 up to 20% of recycled aggregates and beyond 20%, both ITS and TSR

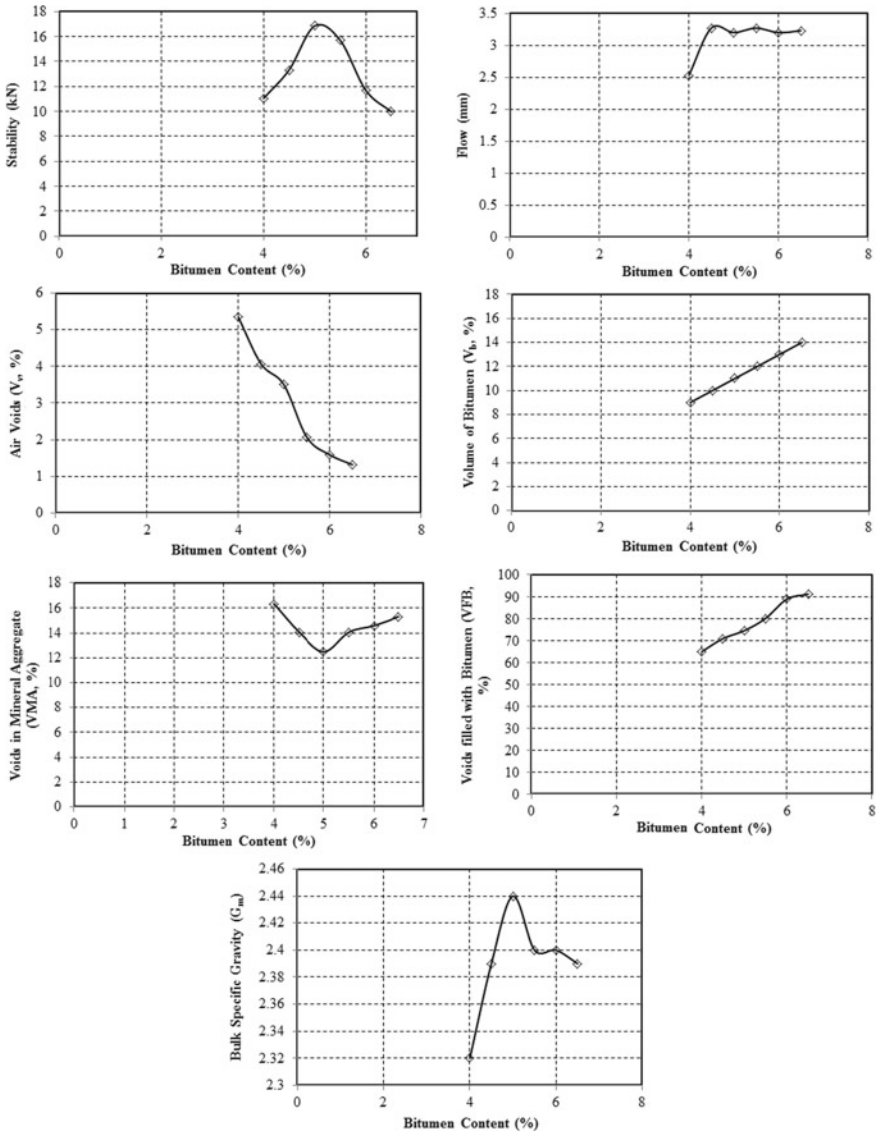

Fig. 2 Marshall properties of Mix 1

followed the reducing trend. This once again confirms the improved behaviour of the mix with 20% of recycled aggregates.

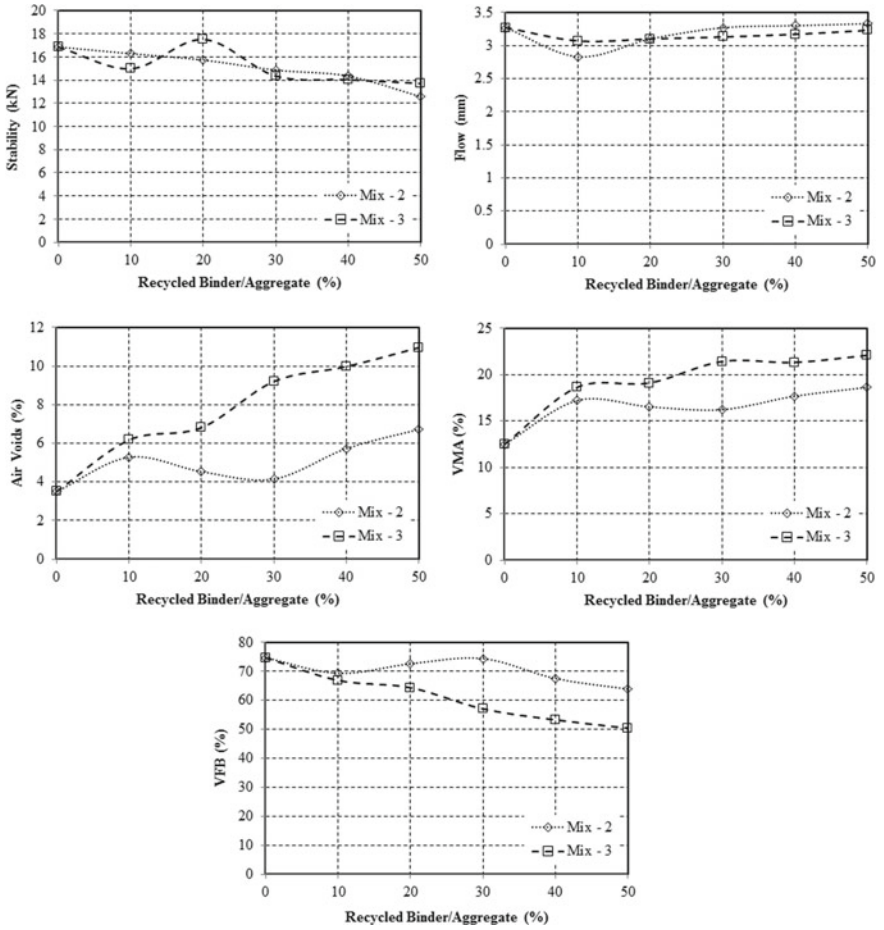

Fig. 3 Marshall properties of Mix 2 and Mix 3 in comparison with Mix 1

5 Conclusions

Based on the laboratory investigation carried out, the following conclusions were drawn.

- The partial replacement of conventional aggregates or binder with recycled aggregates or binder satisfies the MoRT&H requirements of the BC mix.
- The stability and ITS of the mix reduced with partial replacement with the recycled binder. Whereas, the partial replacement with recycled aggregates up to 20% yielded maximum stability and ITS values indicating better strength in comparison with the other two mixes.

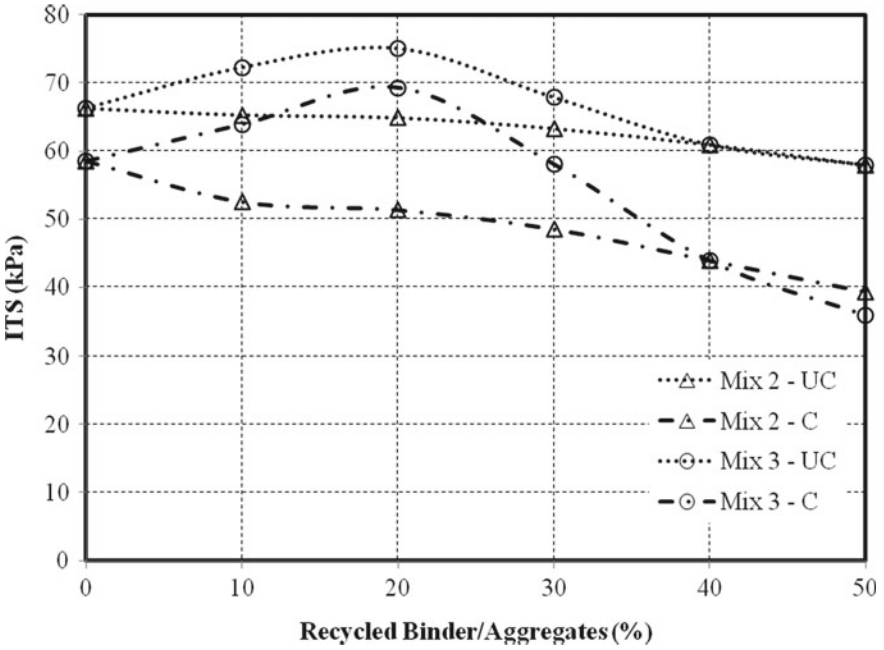

Fig. 4 Variation of ITS of the mixes under unconditioned and conditioned test condition

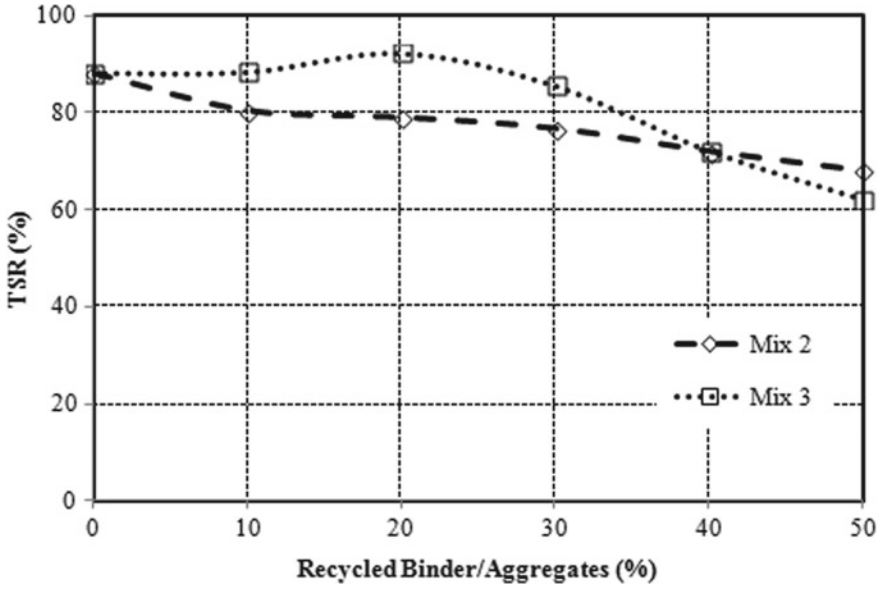

Fig. 5 Variation of TSR of the mixes

- It is possible to replace 20% of conventional aggregates with recycled aggregates with a positive impact on the performance of the mix and thus resulting in an economical and eco-friendly solution for pavement construction.

Acknowledgments The authors acknowledge the support provided by N R Crushers, Mydala, Tumakuru, Karnataka for providing the crushed aggregates for carrying out this study.

References

1. Saride S, Avirneni D, Javvadi SP (2016) Utilization of reclaimed asphalt pavements in Indian low volume roads. J Mater Civ Eng 28(2):1–10
2. Garg N, Thompson MR (1996) Lincoln avenue reclaimed asphalt pavement base project. Transportation Research Record 1525, Transportation Research Board, National Research Council, Washington DC, pp 115–123
3. Maher MH, Papp W (1997) Recycled asphalt as a base and subbase material. ASTM Special Publication 1275, ASTM, West Conshohocken, Pa, pp 42–53
4. Bennert T, Papp WJ, Maher A, Gucunski N (2000) Utilization of construction and demolition debris under traffic-type loading in base and subbase applications. Transportation Research Record: Journal of Transportation Research Board, No. 1714, Transportation Research Board, National Research Council, Washington DC, pp 33–39
5. Chinni A, Kuo S, Armaghani J, Duxbury J (2001) Test for recycled concrete aggregate in accelerated test track. J Transp Eng 127(6):486–492
6. Deniz D, Tutumluer E, Popovics JS (2010) Evaluation of Expansive characteristics of reclaimed asphalt pavement and virgin aggregate used as base materials. Transportation Research Record: Transportation Research Board, No. 2167, Transportation Research Board of the National Academies, Washington DC, pp 10–17
7. Kandhal PS, Foo KY (1997) Designing recycled hot mix asphalt mixtures using Superpave technology. Progress in Superpave (superior performing asphalt pavements): Evaluation and implementation, ASTM STP 1322, ASTM, West Conshohocken, PA
8. MoRT&H (2013) Ministry of road transport and highways: Specifications for roads and bridges. 5th Edition, Indian Roads Congress, New Delhi
9. ASTM D 1559-76 (2004) Standard practice for Marshall test procedure. ASTM International, West Conshohocken, PA
10. ASTM D 6926-16 (2016) Standard practice for preparation of asphalt mixture specimens using Marshall apparatus. ASTM International, West Conshohocken, PA
11. ASTM D 6927-15 (2015) Standard test method for Marshall stability and flow of asphalt mixtures. ASTM International, West Conshohocken, PA

Influence of Long-Term Laboratory Aging on Properties of Binder

S. Tejeshwini, B. Gowtham, K. H. Mamatha, S. V. Dinesh, and Anand Tadas

Abstract Aging of the binder is an important factor that affects the service life of flexible pavements. The main objective of the study is to evaluate the effect of long-term laboratory aging on binder. Normal oven aging in the laboratory at 85 °C for a varying period of 5, 6, 7, and 8 days was used to simulate the long-term field aging. Rheological characteristics of fresh VG-30 binder and laboratory aged binders were evaluated using a rheometer. Frequency sweep test and temperature sweep tests were conducted. Fourier Transforms Infrared Spectroscopy (FTIR) was employed to evaluate the effect of aging on the chemical composition of the binder. Scanning Electron Microscopy (SEM) was used to analyze the change in morphological characteristics of the binder with aging. The study demonstrated that the aging results in the reduction of fatigue cracking resistance of binders at low temperatures. Rutting resistance of binders increased with an increase in aging. FTIR results indicated that there is no significant change in the functional groups, the only difference was in the intensity of their peaks. Morphological changes in aged binders were well identified from SEM images.

Keywords Long-term aging · Rheology · Rutting · Fatigue

1 Introduction

Aging is one of the most important characteristics of bituminous binders that affects the service life of flexible pavement. It is evident that aging induces physical, chemical, and morphological changes in bitumen [1]. Aging causes hardening of bituminous binders which results in deterioration of pavements like low-temperature cracking, moisture damage, fatigue cracking, and hence reduces the service life of flexible pavements [2]. Bitumen aging occurs in two stages, namely, short-term aging

S. Tejeshwini · B. Gowtham · K. H. Mamatha (✉) · S. V. Dinesh
Department of Civil Engineering, Siddaganga Institute of Technology, Tumakuru, India
e-mail: mamathakh@sit.ac.in

A. Tadas
Malvern Panalytical, New Delhi, India

© Springer Nature Singapore Pte Ltd. 2021

K. K. Pathak et al. (eds.), *Recent Trends in Civil Engineering*, Lecture Notes in Civil Engineering 77, https://doi.org/10.1007/978-981-15-5195-6_34

and long-term aging. Short-term aging occurs at high temperatures during mixing, storage, and laying and long-term aging occurs at ambient temperature during in-service. Aging mechanisms include oxidation, evaporation, and physical hardening. Hardening is a reversible process and involves a change in rheological properties of bitumen without a change in its composition. Hardening is very slow at ambient temperature but it is rapid at low temperatures [3]. Oxidative aging is an irreversible mechanism that involves a chemical reaction between bitumen constituents and oxygen. Photooxidation and thermal oxidation are different reactions during the oxidation of bitumen. Different types of tests may be used to simulate field aging in the laboratory. Rolling Thin Film Oven Test (RTFOT) and Thin Film Oven Test (TFOT) are used to simulate short term aging at high temperatures in the laboratory. Pressure Aging Vessel (PAV) is used to simulate long-term aging in-service. During bitumen aging, saturates remain the same while the aromatics and resins decrease as they react with oxygen to form asphaltenes [4]. The dynamic viscosity and ductility can serve as important indicators of the aging status of the binder since dynamic viscosity represents binder hardness and ductility represents pavement performance in the field [5]. The rheological and conventional measurements from long-term field aged bitumen showed a low degree of age hardening. Hence, the equivalent laboratory aging durations are much shorter than being standardized [6]. Normal oven aging is considered as an alternative to simulate short-term and long-term aging of bitumen in the laboratory since it is cheap and readily available than RTFO and PAV equipment [7]. It is possible to study sulfoxides and carbonyls formation during aging and scanning electron microscopy (SEM) is useful to observe the changes in the bitumen microstructure [8]. It is possible to simulate short-term aging in the laboratory by aging the binder in the normal oven at 163 °C for 1–11 h and 3–4 days of normal oven aging at 85 °C would simulate 5–10 years of long-term aging [7].

Past studies focus on intermediate and high-temperature rheological properties of binders and only limited studies focused on low-temperature rheological properties [9]. Hence, there is a need to investigate the rheological properties of the binder at low temperature as fatigue properties of binders are highly affected at low temperatures. Most of the studies in the past have focused on laboratory aging using RTFO and PAV techniques [7]. But, these equipment are costly and are not readily available. Therefore, it is necessary to conduct a comprehensive study by employing normal oven aging which is cost-effective and readily available. Microstructural investigations using state-of-the-art equipment such as SEM need to be carried out for validating the aging phenomenon [1].

In this study, the effect of short-term and long-term aging on the characteristics of the binder is evaluated over a varied range of temperatures covering low to high temperatures by using a normal oven aging method. In addition, FTIR and SEM analysis were carried out to analyze the chemical and morphological changes on aging of binder. The test results were analyzed in terms of rheological and morphological characteristics and chemical composition of unaged and aged binder and are reported.

Table 1 Engineering properties of bitumen

Properties	Virgin binder (VG-30)				
	Penetration at 25 °C (1/10 mm)	Softening point (°C)	Ductility (cm)	Kinematic viscosity at 135 °C (c St)	Specific gravity
Results	68	50.2	73	450	1.01
MoRT&H [10] specification	≥45	≥47	≥50	≥350	0.99–1.02

2 Materials

VG-30 binder from Indian Oil Corporation Limited (IOCL), Chennai was used in the present investigation. Engineering properties of the bitumen considered are presented in Table 1 along with the Ministry of Road Transport and Highways (MoRT&H) [10] specifications.

3 Experimental Methods

3.1 Laboratory Aging

A circular plate of 140 mm diameter is taken and 10 gm of binder is poured such that it forms a uniform thickness of 650 μm. Then, the oven is preheated to 163 °C for 16 h and then bitumen sample is placed into the oven at 163 °C for 5 h to simulate short-term aging and then left in the oven for 24 h to achieve atmospheric temperature. The residue from short-term aging is then placed in the oven at 85 °C for varying periods from 5 to 8 days to simulate long-term aging of different periods.

3.2 Dynamic Shear Rheometer (DSR) Test

The frequency sweep and temperature sweep tests were conducted to evaluate the rheological performance of aged and fresh binder. 25 mm plate with a gap of 1 mm was used for testing fresh binder and 8 mm plate with a gap of 2 mm was used for testing aged binders. The test is conducted to determine the rheological indices like dynamic shear modulus (G^*) and phase angle (δ) which are used to evaluate the rutting factor ($G^*/\sin\delta$) and fatigue factor ($G^* \times \sin\delta$). Rutting factor gives a measure of anti-rutting performance and fatigue factor gives a measure of anti-fatigue performance of the binder. Frequency sweep test was conducted at varying

load frequencies from 0.2 to 30 Hz at a temperature of 48 °C. Temperature sweep test was performed at varying temperatures from 6 to 54 °C at a frequency of 10 rad/sec.

3.3 Fourier Transform Infrared Spectroscopy (FTIR)

Attenuated total reflection (ATR) mode of FTIR was used to identify the functional groups present in the bitumen. An infrared light is passed through the sample and the amount of light absorbed or transmitted is measured. The IR spectrum of transmittance versus wavenumber is obtained in the middle infrared region (400–4000 cm^{-1}).

3.4 Scanning Electron Microscopy (SEM)

SEM analysis was conducted to study the surface morphology and microstructure of bitumen binders. The test was conducted using Zeiss field emission scanning electron microscope (SEM). In this study, the SEM images were obtained with 1000 × magnification.

4 Results and Discussions

4.1 Dynamic Shear Rheometer (DSR) Test

Frequency Sweep Test. The change of rheological properties with oscillation frequency was examined for laboratory aged binders at an intermediate temperature of 48 °C and at varying frequencies from 0.2 to 30 Hz. The frequency of 10 Hz stimulates a speed of 60 kmph and frequency of 15 Hz stimulates a speed of 90 kmph [10]. The variation of rheological properties of 8 days oven-aged sample with a frequency is shown in Fig. 1. Dynamic viscosity (η') gives a measure of the binder hardness, which is calculated from the DSR measurements using the formula G″/ω [5], where G″ is loss modulus and ω is oscillation frequency. It is observed that the storage modulus increases with frequency but the dynamic viscosity decreases with frequency. Since storage modulus (G') represents the elastic portion, it is seen that the elastic component of the bitumen becomes stiffer with an increase in frequency. Dynamic viscosity of binder at a speed of 60 kmph was 1.031E + 07, which is 1.11 times higher than at a speed of 90 kmph. The decreased dynamic viscosity (η') indicates that the bitumen becomes thinner as the frequency increases. Dynamic viscosity of binder increases with an increase in aging.

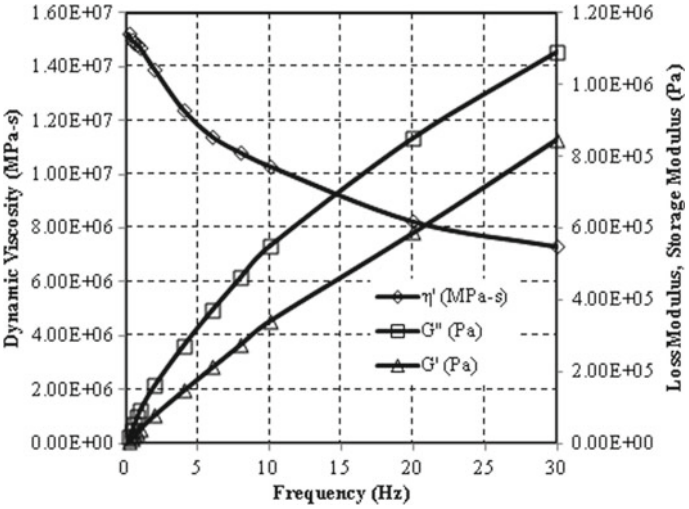

Fig. 1 Variation of η', G' and G″ with frequency at 48 °C

The variation of rutting factor (G*/sin δ) and fatigue factor (G* × sin δ) is shown in Fig. 2. The rutting factor (G*/sin δ) and fatigue factor (G* × sin δ) increased sharply at a frequency below 5 Hz and beyond 5 Hz, both the factors gradually increased with an increase in frequency. Thus, the rutting and fatigue resistance of the binder increases with an increase in aging. Rutting resistance of binders at a speed 90 kmph was 1.32 times higher than that at a speed of 60 kmph. The fatigue resistance of binder at a speed of 90 kmph was 1.27 times lower than that at a speed of 60 kmph.

The variation of complex modulus (G*) and phase angle (δ) with frequency is shown in Fig. 3. It is observed that the complex modulus increases and phase angle decreases with an increase in frequency. At frequencies less than 10 Hz, complex modulus increased sharply and beyond 10 Hz, it increased gradually. Thus, at higher frequency complex modulus is not highly affected by aging.

Temperature Sweep Test. The temperature sweep test was conducted on fresh VG-30 binder and laboratory-aged samples at a temperature varying from 6 to 54 °C with an interval of 6 °C. The results are summarized in Fig. 4. It is observed that the rutting factor is low for all the binders at a temperature greater than 30 °C but the values increased gradually with a decrease in temperature below 18 °C. The rutting factor increased with an increase in aging which shows that the rutting resistance of binder increases with an increase in aging. The increase in rutting resistance is considerably high at temperatures less than 30 °C.

The variation of fatigue factor with temperature is shown in Fig. 5. The fatigue resistance of the binder is highly affected at a temperature less than 30 °C. The fatigue factor of binder decreased with an increase in temperature. Thus, the fatigue resistance of binder is high at higher temperature. The fatigue factor of the binder

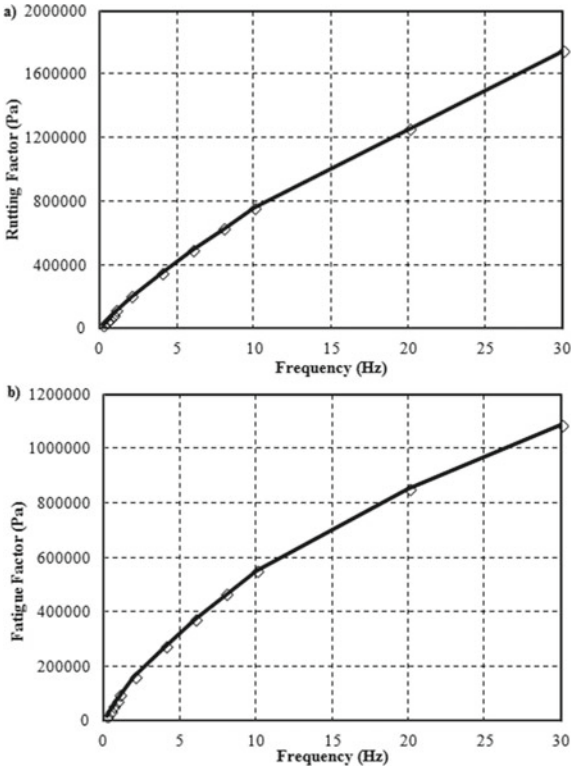

Fig. 2 Variation of **a** rutting factor **b** fatigue factor with frequency

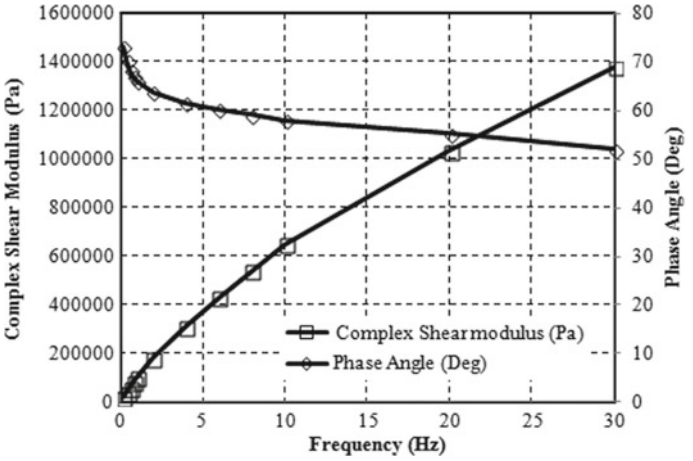

Fig. 3 Variation of complex modulus and phase angle with frequency at 48 °C

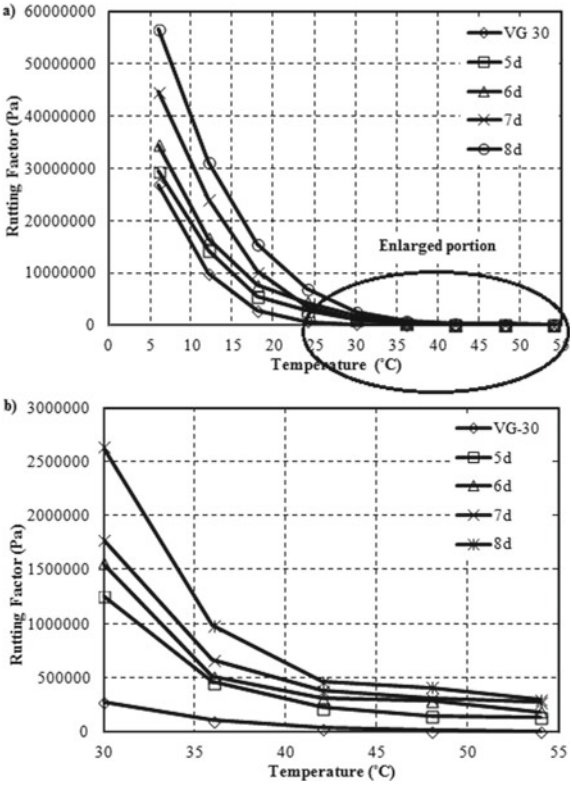

Fig. 4 Variation of **a** rutting factor with temperature **b** enlarged view

is low initially but with aging, fatigue factor increased showing decreased fatigue cracking resistance with increased aging.

The variation of complex modulus and phase angle with temperature is shown in Fig. 6. The rheological properties are highly affected at a temperature less than 30 °C. It is observed that the complex modulus of the binder decreased with an increase in temperature while it increased with an increase in aging. Increase in dynamic modulus indicates the improved resistance to external loading. The phase angle of binder increased with an increase in temperature while it decreased with an increase in aging. The decreased phase angle of aged samples shows that the aged binders had more elastic fractions than a fresh binder.

4.2 FTIR Spectra

The IR spectrum of fresh VG-30 and laboratory aged binders is shown in Fig. 7. The IR spectrum of VG-30 binder shows that the peaks are identified at 1016, 1375,

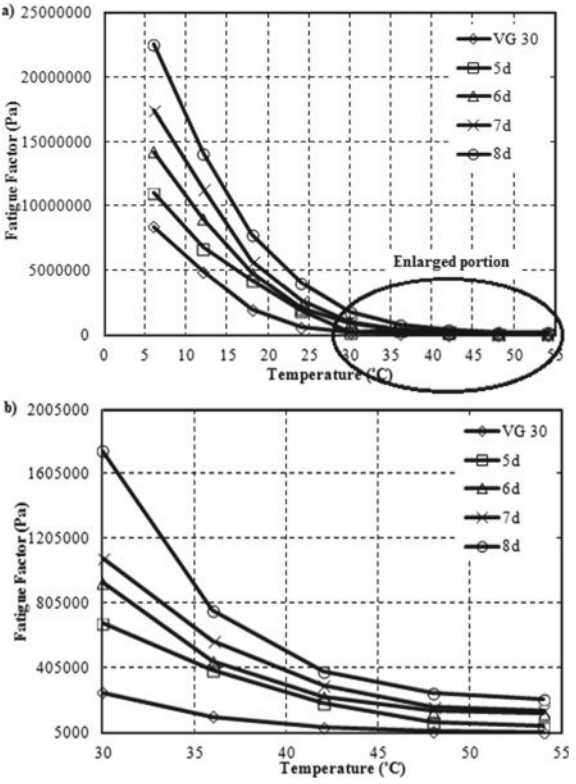

Fig. 5 Variation of **a** fatigue factor with temperature **b** enlarged view

1456, 2850 and 2919 cm^{-1}. The peaks at 2850 cm^{-1} and 2919 cm-1 indicate the presence of alkanes

The peaks at 2850 cm-1 and 2919 cm-1 indicate the presence of alkanes. The peaks at 1016 and 1375 cm^{-1} indicate C-F band and 1456 cm-1 indicate the presence of a saturated C-C band, which represents aromatics as the functional group. The IR spectrum shows that in laboratory-aged binders in addition to these functional groups the peaks were identified at 668 cm-1, 721 cm-1 and 2342.84 cm-1, which indicate the presence of alkanes and C $\equiv$ N band. Significant peaks are not identified at certain wavelength, which corresponds to functional groups like carboxylic acids, anhydrides, ketones and sulphoxides which play a significant role in the process of binder aging. It is evident that the aging would be higher as the aging duration increases. If the extent of binder aging is to be compared then ratios could be obtained between the peak heights at 1695 cm^{-1} (ketones) and 1455 cm^{-1} (saturated C-C band) [3]. In general, higher the ratio, higher is the rate of aging.

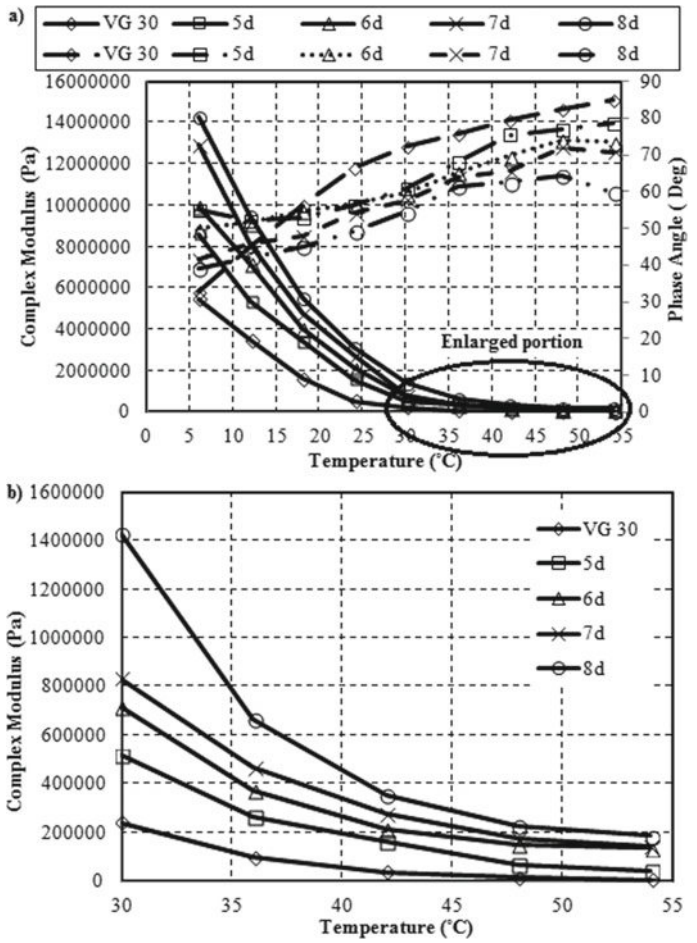

Fig. 6 Variation of **a** complex modulus and phase angle with temperature **b** enlarged view

4.3 SEM Analysis

SEM images of fresh and laboratory aged bitumen are shown in Fig. 8. From the images it is clear that before aging, fresh VG-30 binder showed no discontinuity and there exists a cloud formation. But, in aged samples, no such formation was observed. Individual particles were not identified in the fresh binder but in laboratory-aged binder, the particles were identified and their size decreased with an increase in aging which could be the effect of high temperature during aging which resulted in the interfacial bond deterioration of binder.

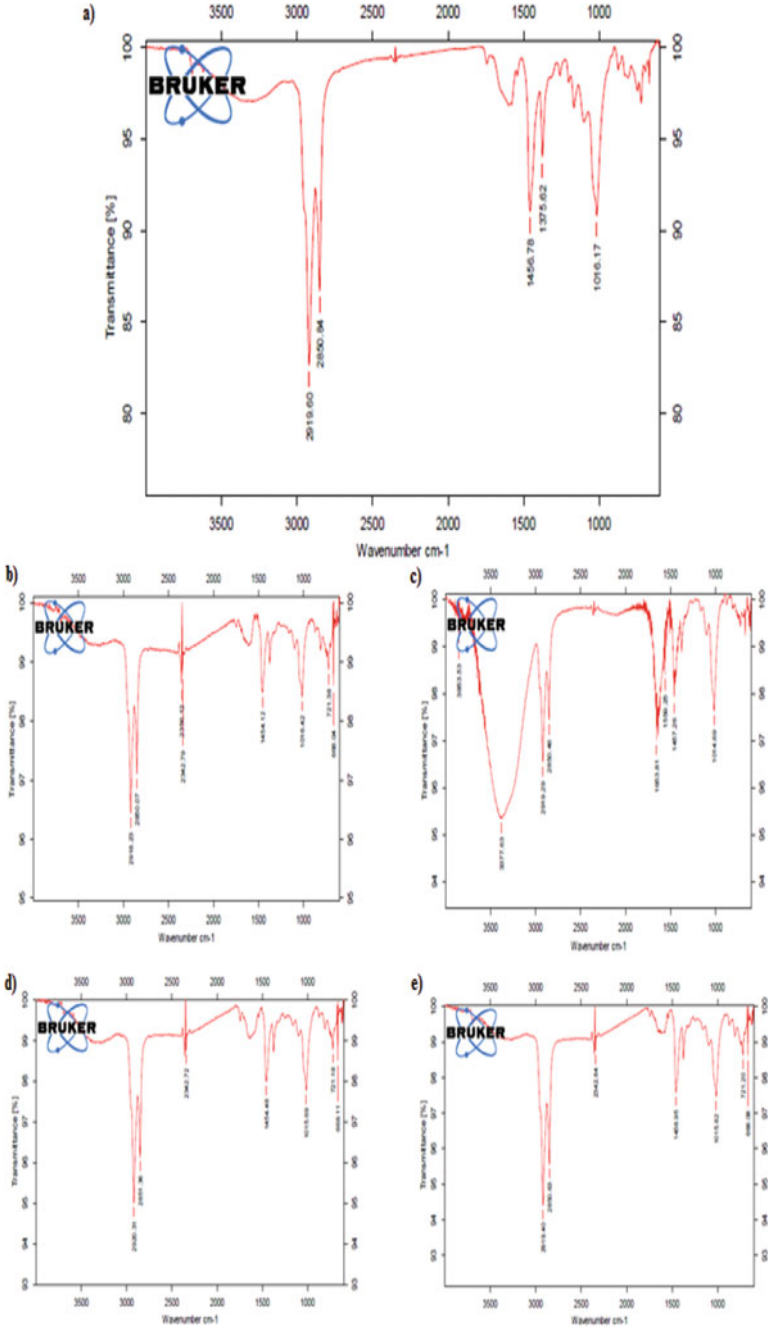

Fig. 7 IR spectrum of **a** Fresh VG-30 **b** 5 days oven-aged sample **c** 6 days oven-aged sample **d** 7 days oven-aged sample e) 8 days oven-aged sample

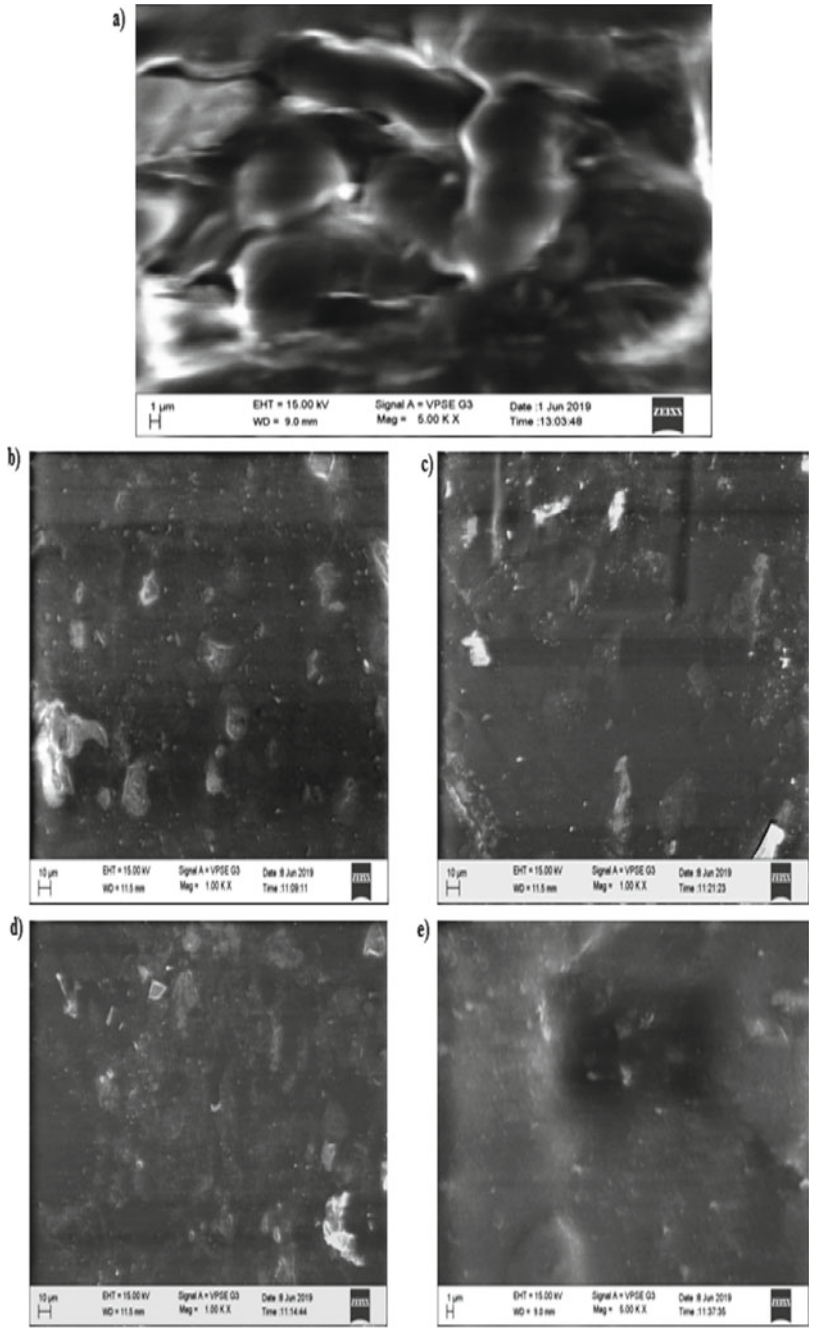

Fig. 8 SEM images of **a** Fresh VG-30 **b** 5 days oven-aged sample **c** 6 days oven-aged sample **d** 7 days oven-aged sample **e** 8 days oven-aged sample

5 Conclusions

This paper presents a comprehensive study to characterize the effect of long-term laboratory aging on binders using rheological, chemical, and morphological analysis. Based on the investigation carried out on fresh and laboratory-aged binders, the following conclusions are drawn.

- Dynamic viscosity decreases with an increase in frequency, i.e., dynamic viscosity decreases with an increase in traffic speed.
- Rutting resistance of binders increases with an increase in frequency. Rutting resistance of binders at 15 Hz (90 kmph) was 1.32 times higher than that at 10 Hz (60 kmph). The fatigue resistance of binder decreases with an increase in frequency (90 kmph). Fatigue resistance of binders at 15 Hz (90 kmph) was 1.27 times lower than that at 10 Hz (60 kmph). However, the rutting and fatigue factors were within the permissible values at 48 °C as the rutting factor was more than 2 kPa and fatigue factors were less than 5000 kPa.
- Complex modulus of binders increases gradually with an increase in frequency. Phase angle decreases sharply up to a frequency of 2 Hz, and thereafter it decreases linearly. This signifies that at any constant temperature, frequency (traffic speed) influences both phase angle and complex modulus.
- Rheology of bitumen is highly affected at lower temperatures (less than 30 °C) than at high temperatures. Rutting resistance of binders increased with aging and fatigue resistance of binders decreased with aging. Rutting resistance of binder was higher at a temperature less than 30 °C and fatigue resistance of binder decreased considerably below 30 °C. Therefore, pavement performance under aging is better in regions with high temperatures than in cold regions.
- FTIR spectrum of laboratory-aged binders did not show any additional peaks corresponding to functional groups which play a significant role in binder aging indicating that there was no change in the chemical composition of binder after aging. The only difference between the IR spectrum of aged and fresh binder was in the intensity of their peaks.
- SEM analysis showed that there is interfacial bond deterioration in binders which progresses with aging.
- Further, there is a need to compare the rheological properties of field aged binders with oven aged binders and thereby, validate field aging with laboratory aging.

References

1. Kambham BS, Vinayaka Ram V, Raju S (2019) Investigation of laboratory and field aging of bituminous concrete with and without anti-aging additives using FESEM and FTIR. Constr Build Mater 222:193–202
2. Lin J, Hong J, Liu J, Shaopeng W (2016) Investigation on physical and chemical parameters to predict long-term aging of asphalt binder. Constr Build Mater 122:753–759

3. Qin Q, Schabron JF, Boysen RB, Farrar MJ (2013) Field aging effect on chemistry and rheology of asphalt binders and rheological predictions for field aging. Fuel 121:86–94
4. Liu H, Hao P, Wang H, Adhikair S (2014) Effects of pysio-chemical factors on asphalt aging behaviour. J Mater Civ Eng 26(1):190–197
5. Wang Y, Wen Y, Zao K, Chong D, Wei J (2015) Connections between the rheological and chemical properties of long-term aged asphalt binders. J Mater Civ Eng 27:1–11
6. Lu X, Talon Y, Redelius P (2008) Aging of bituminous binders - Laboratory tests and field data. Proceedings of the 4th Eurasphalt and Eurobitume Congress, Copenhagen, Denmark
7. Behera PK, Singh AK, Amaranatha Reddy M (2013) An alternative method for short and long term aging for bitumen binders. Road Mater Pavement Design 14(2):445–457
8. Tauste R, Moreno-Navarro F, Sol-Sanchez M, Rubio-Gamez MC (2018) Understanding the bitumen aging phenomenon: a review. Constr Build Mater 192:593–609
9. Huang W, Wang D, He P, Long X, Tong B, Tian J, Yu P (2019) Rheological characteristics evaluation of bitumen composites containing rock asphalt and diatomite. Appl Sci, 1–13
10. Ministry of Road Transport and Highways (MORTH) (2013) Specifications for road and bridge works. 5th Revision, Indian Road Congress, New Delhi

Pavement Evaluation Using Falling Weight Deflectometer (FWD)

D. Nayana, K. H. Mamatha, S. V. Dinesh, and T. R. Lokesh

Abstract Pavements are the key elements for a country's infrastructure, and therefore its periodic evaluation, maintenance and rehabilitation activities are important. In the present study, a State Highway (SH) connecting Harihara to Honnalli, Karnataka was selected with a length of 40 km for evaluation. Road inventory survey, soil characterization and FWD studies were carried out along the selected stretch of the road. Functional evaluation was performed based on manual measurements and rated based on PCI values. The structural evaluation was performed using the modulus values obtained from Falling Weight Deflectometer (FWD). Pavement distresses were identified and maintenance measures were prioritized. Also, a comparison of CBR- and FWD-based modulus methods is also reported. It is concluded that insufficient thickness is the major reason for the failure which has to be corrected by considering overlay and strengthening measures.

Keywords FWD · PCI · Structural evaluation · Functional evaluation

1 Introduction

The road transport is the oldest and most widely used mode of transportation. In the economic growth and development of the country, transportation infrastructure plays a vital role. All structures fail at some point, but the life of the structure is extended by the maintenance and rehabilitation activities. The combined effects of traffic loading and the environment will cause every pavement, no matter how well it is being designed and constructed to deteriorate over time. The maintenance and rehabilitation activities of pavement structures have become increasingly important as pavements deteriorate with time and traffic operation. Pavement evaluation is a technique of assessing the condition of a pavement, both structurally and functionally from the

D. Nayana · K. H. Mamatha (✉) · S. V. Dinesh
Department of Civil Engineering, Siddaganga Institute of Technology, Tumakuru, India
e-mail: mamathakh@sit.ac.in

T. R. Lokesh
Infra Support Engineering Consultants Pvt. Ltd, Bengaluru, Karnataka, India

© Springer Nature Singapore Pte Ltd. 2021

K. K. Pathak et al. (eds.), *Recent Trends in Civil Engineering*, Lecture Notes in Civil Engineering 77, https://doi.org/10.1007/978-981-15-5195-6_35

point of view of strength and surface characteristics. Functional performance is the ability of the pavement to provide comfortable, safe and economical riding surface to the users. On the other hand, structural performance is related to the structural soundness of the structure or the load-carrying ability of the structure. The pavement evaluation is performed to determine the capacity of the pavement to sustain future traffic loading and is performed through destructive or non-destructive testing. A pavement evaluation is typically accomplished using non-destructive testing (NDT) equipment designed to measure the surface deflection of a pavement under a simulated wheel load.

Pavement deflection reflects its overall stiffness and strength of each layer. Roadbed form, material properties of each layer, construction quality, temperature, traffic load, weather conditions, testing equipment, etc. influence the deflection [1]. Pavement deflections are measured by the Falling Weight Deflectometer (FWD) and the Benkelman beam. FWD works under dynamic loading, which represents the moving load and Benkelman Beam Deflection (BBD) method works under static loading [2]. To evaluate the structural capacity of the pavement structure, FWD testing is more precise than BBD [3]. The deflection obtained from the FWD helps to calculate the modulus value of all the layers, strains, stiffness and remaining life of the pavement. The controlled construction quality, particularly in identifying the presence of weak material underlying the subgrade is made by conducting the FWD test on top of subgrade [4]. FWD is very expensive and not so common in India. Therefore, Benkelman beam and CBR-based methods are still in practice. In CBR-based method, the modulus of the granular layer is computed by the empirical relationship that depends on the thickness of the granular layer and modulus of subgrade. The presence of weak material in the granular layer cannot be factored and the pavement evaluation results in the wrong structural evaluation. As in the case of Benkelman beam, the static loading is applied and it does not reflect the dynamic method of traffic loading. In this connection, FWD is an improved methodology for computing the moduli of various pavement layers though it is expensive. The overlay thickness depends on the stiffness of the layer on which the overlay is laid [5]. Accurate prediction of the stiffness of the layer is important. As stiffness is a function of modulus, FWD is a better method for pavement evaluation. Therefore, there is a need to compare the pavement evaluation by CBR- and FWD-based methods for better understanding.

In the present study, a road stretch of 40 km length was chosen for investigation. Road inventory was carried out for the road stretch considered. In addition, pavement evaluation was carried out in terms of functional and structural evaluation. The structural evaluation was performed by obtaining modulus values using FWD. The modulus values obtained from CBR and FWD were compared and discussed.

2 Study Area

Road selected for the present study is a part of State Highways in Karnataka connecting two taluks. The length of the selected road stretch is 40 km and is a two-lane single carriageway road. The winter temperature of the region varies from 18 to 22 °C. The average precipitation is about 626 mm.

3 Field Studies

Over the selected stretch of 40 km, at every 500 m interval, the soil samples were collected, crust thickness was measured and FWD test was performed. The lengths having the same crust thickness were considered as homogeneous sections and further studies were carried out.

3.1 Pavement Condition Survey

The pavement condition survey was carried out by visual observation and manual measurement of the distress observed. The distress survey includes potholes, cracks, patching, ravelling, settlement and rutting as per standards. The details of the pavement condition survey are tabulated in Table 1 and schematically represented in Fig. 1. From the pavement condition survey, the predominant portion of the pavement was found to be in a good condition. The condition data helped to figure out the causes of distresses and some of which could be treated by considering non-structural treatments like sealing, slurry surfacing, cold planning, and replacement of unsound materials.

3.2 Soil Investigation

At the identified homogeneous sections, pits were dug at the edge of the pavement and excavated up to the bottom of the subgrade. At each of these pits, the existing crust thickness was recorded and soil samples from the subgrade were extracted. Measurement of crust thickness included measurement of thicknesses of all the layers and the details are presented in Table 2. The measured crust thickness varied from 325 to 515 mm.

The collected soil samples were tested for their grain size distribution, consistency limits, compaction characteristics under Proctor condition and strength characteristics in terms of CBR. All the tests were carried out as per the prevailing IS guidelines. The properties of subgrade soil along with the soil classification are tabulated

Table 1 Details of pavement condition survey

Existing chainage	Potholes (%)	Cracks (%)	Patching (%)	Ravelling (%)	Settlement/Upheaval (%)	Rutting (%)	Good condition (%)
116 + 500	3.13	11.25	3.13	3.75	6.88	3.13	31.25
121 + 000	0.00	0.00	7.13	0.00	0.00	0.00	7.13
126 + 000	0.00	6.50	0.00	0.00	0.00	0.00	6.50
131 + 000	5.63	5.63	8.75	6.88	0.00	0.00	26.88
136 + 000	1.88	6.88	0.00	5.63	0.00	0.00	14.38
140 + 500	10.00	8.13	10.00	10.00	0.00	2.50	40.63
145 + 000	12.50	5.00	8.13	2.50	0.00	0.00	28.13
150 + 000	0.00	0.00	0.00	0.00	0.00	0.00	0.00
156 + 500	0.00	0	0	0	0	0	0.00
Average condition	33.13	43.38	37.13	28.75	6.88	5.63	845.13
	4	5	4	3	1	1	83

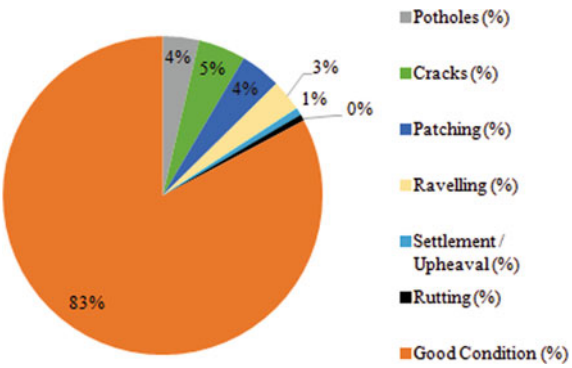

Fig. 1 Schematic representation of the existing pavement condition

Table 2 Details of the existing pavement crust thickness

Sl. No	Existing chainage	Pavement crust thickness (mm)			Total thickness (mm)
		Bituminous layer	Base	Sub-base	
1	116 + 500	65	120	220	405
2	121 + 000	60	125	220	405
3	126 + 000	75	150	200	425
4	131 + 000	75	150	200	425
5	136 + 000	60	150	110	320
6	140 + 500	65	140	125	330
7	145 + 000	75	150	100	325
8	150 + 000	75	150	100	325
9	156 + 500	65	150	300	515

in Table 3. CBR test specimens were prepared corresponding to Proctor condition with a relative density of 97% and tested under soaked conditions. The fines content range from 22.27 to 62.8% and the CBR value range from 5.83 to 18.58%.

4 FWD Test

FWD test was performed in accordance with IRC 115 [6] guidelines. FWD equipment used in this study consists of seven sensors positioned at a distance of 0 mm (D1), 200 mm (D2), 300 mm (D3), 450 mm (D4), 600 mm (D5), 900 mm (D6) and 1200 mm (D7). The instrument was initially calibrated for getting accurate and reproducible results. As the selected road is two-lane two-way single carriageway, deflection measurement is made along both outer wheel paths at a spacing of 500 mm. A standard axle load of 40 kN was applied to obtain dynamic deflection repeatedly and at each point, three sets of measurements were made. The deflection readings were recorded

Table 3 Properties of subgrade soil

Sl. No.	Existing chainage	Gravel (%)	Sand (%)	Silt & Clay (%)	LL (%)	PL (%)	PI (%)	MDD (gm/cc)	OMC (%)	HRB soil classification	Soaked CBR (%)
1	116 + 500	19.87	40.9	39.22	–	NP	–	2.02	9.2	A-4	14.65
2	121 + 000	18.42	36.54	45.04	–	NP	–	1.91	11.05	A-4	9.54
3	126 + 000	8.29	33.79	57.92	24	16	8	1.88	12.6	A-4	5.83
4	131 + 000	20.24	30.51	49.25	26	16	9	1.79	11.01	A-4	8.92
5	136 + 000	36.21	37.07	26.72	–	NP	–	2.03	9.1	A-2-4	14.24
6	140 + 500	27.37	34.05	38.58	27	17	11	1.98	11.01	A-6	8.98
7	145 + 000	5.51	31.69	62.8	30	19	11	1.84	13.2	A-6	6.25
8	150 + 000	30.14	33.25	36.61	27	18	9	1.78	13.25	A-4	10.58
9	156 + 500	46.65	31.08	22.27	24	18	6	2.1	7.2	A-2-4	18.58

through the FOV software. These deflections are normalized to 40 kN. Inputs such as radial distances at which deflections were measured, layer thicknesses, Poisson's ratio values of different layers, applied peak load and loading plate radius were used to back-calculate the elastic modulus of different layers of the existing pavement using KGPBACK, which is a specific version of BACKGA program developed by the Transportation Engineering Section of IIT, Kharagpur under the research scheme R-81 (2003) of the Ministry of Road Transport and Highways.

The back-calculated modulus of the bituminous layer obtained from the deflection survey conducted at a temperature T_2 was corrected to estimate the modulus corresponding to a temperature of 35 °C (T_1) using Eq. (1) as per IRC 115 [6].

$$E_{T1} = \lambda E_{T2} \tag{1}$$

where

λ = Temperature correction factor and is given by Eq. (2).

$$\lambda = \frac{1 - 0.238 \ln(\mathbf{T}1)}{1 - 0.238 \ln(\mathbf{T}2)} \tag{2}$$

Further, corrections for seasonal variations were made to obtain the final moduli values. Table 4 shows the normalized deflection and corrected moduli values. Low subgrade moduli values of 98.46, 98.46 and 103.6 MPa were observed at chainages 126 + 000, 145 + 000 and 150 + 000, respectively, where the deflections at the loading point were higher. This is due to the weaker subgrade condition. Among the chainages considered, chainage 140 + 500 was found to be the weaker section possessing the least subgrade modulus of 74.09 MPa.

5 Results and Discussions

5.1 Comparison Between FWD Moduli and CBR Moduli

The subgrade modulus values obtained from the FWD back-calculation were compared with that of the modulus values obtained from CBR through empirical relationships as suggested by IRC 37 [7] and the comparison is shown in Fig. 2.

At chainages with field CBR values of 8.98, 10.58 and 18.58%, the subgrade modulus obtained through FWD and CBR exhibited good comparison. On the other hand, at other chainages with other CBR values, the FWD modulus values showed greater variation in the order of greater than 100% in comparison with CBR based modulus. By considering the pattern of loading considered in CBR (static loading) and FWD (dynamic loading), modulus values determined from the FWD are more precise as the loading simulates traffic loading.

Table 4 Corrected normalized deflection and modulus values

Sl. No.	Chainage	Load (kN)	Normalized corrected deflections (mm)							Corrected FWD modulus (MPa)			Temp (°C)
			D1	D2	D3	D4	D5	D6	D7	Bituminous layer	Granular layer	Subgrade	
1	116 + 500	40	0.283	0.204	0.156	0.102	0.054	0.045	0.033	1207.02	323.65	232.59	30
2	121 + 000	40	0.226	0.165	0.138	0.105	0.07	0.061	0.041	1201.21	371.21	199.74	30
3	126 + 000	40	0.401	0.31	0.261	0.198	0.12	0.095	0.073	2188.97	275.75	103.60	43
4	131 + 000	40	0.358	0.256	0.196	0.128	0.064	0.053	0.038	2190.44	209.55	193.84	43
5	136 + 000	40	0.373	0.255	0.177	0.098	0.042	0.033	0.024	1560.83	145.43	235.16	36
6	140 + 500	40	0.185	0.112	0.077	0.044	0.02	0.015	0.007	1631.03	152.04	74.09	37
7	145 + 000	40	0.439	0.319	0.245	0.165	0.104	0.088	0.067	1634.31	367.32	98.46	37
8	150 + 000	40	0.436	0.322	0.255	0.177	0.091	0.069	0.043	1637.71	274.34	98.46	37
9	156 + 500	40	0.35	0.273	0.225	0.166	0.099	0.08	0.053	1815.85	285.030	126.95	40

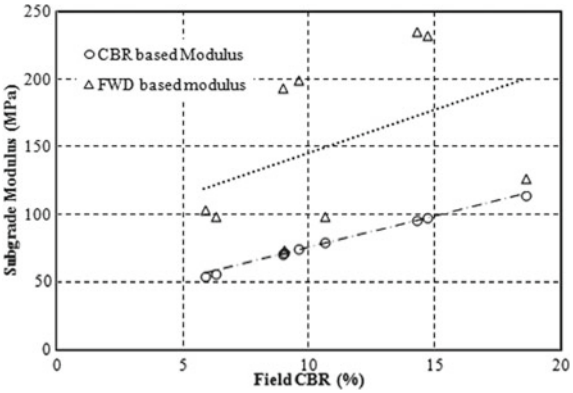

Fig. 2 Comparison CBR- and FWD-based subgrade modulus

5.2 Functional Evaluation

To understand the behaviour of pavements, functional and structural evaluation is generally performed. Functional performance is the ability of pavement to provide a comfortable, safe, economical riding surface to the road users. As long as the pavement is in a position to give satisfactory service to the road user in terms of a safe comfortable ride, the pavement continues to be in functionally acceptable condition. The functional performance of the pavement can be quantified in terms of either the present serviceability index (PSI), roughness, skid resistance or any other parameter that is related to the surface that could be related to the safety and comfort of the road users. Functional evaluation was carried out based on the rating of the Pavement Condition Index (PCI) and is presented in Table 5 covering the range of PCI and appropriate maintenance intervention to be adopted as suggested by Uday Kumar et al. [8]. As discussed in Table 4, the modulus values at the chainages 140 + 500 and 145 + 000 are very less and possess PCI values of 35 and 30, respectively, indicating the section as poor. Thus, strengthening of the section is to be considered as a part of maintenance.

Table 5 PCI value based rating along with maintenance measures [8]

Chainage	PCI value	Rating	Maintenance measures
116 + 500	85	Very good	Preventive
121 + 000	90	Very good	Preventive
126 + 000	88	Very good	Preventive
131 + 000	55	Fair	Overlay
136 + 000	75	Good	Resurfacing
140 + 500	35	Poor	Strengthening
145 + 000	30	Poor	Strengthening
150 + 000	100	Very good	Preventive
156 + 500	100	Very good	Preventive

5.3 Structural Evaluation

Structural performance is related to the structural soundness of the structure or the load-carrying ability of the structure. This is normally measured in terms of the structural response of the pavement when it is subjected to a load. Based on modulus values of FWD, the horizontal tensile strain at the bottom of the bituminous layer and vertical compressive strain at the top of the subgrade was determined using the IITPAVE tool. The obtained strain values were compared with the allowable strains determined from the rutting and fatigue models suggested by IRC 37 [7]. The locations having higher tensile strain or compressive strain than the allowable strains were considered as structurally failed in the respective mode of failure. If both the strains obtained through IITPAVE were greater than the allowable strains, the pavement is said to be failed completely. The determined strain values of the selected road are tabulated in Table 6. The IITPAVE strains at 140 + 500 were greater than that of the allowable strains indicating complete failure of the section both in fatigue and rutting mode. It is observed that the chainages 145 + 000 and 150 + 000 failed in rutting mode and the chainages 131 + 000 and 136 + 000 failed in fatigue mode.

Thickness corresponding to the obtained field CBR values and present traffic were computed using IRC 37 [7]. It is observed that the prevailing reason for pavement failure is the insufficient crust thickness and lower modulus values. The existing and required thickness of each layer for the present traffic is shown in Table 7.

Based on the above analysis, it is recommended to increase the thickness of the surface course for the sections those exhibited fatigue failure and strengthening for the sections those exhibited rutting failure or both modes of failures.

Table 6 Strains determined from IITPAVE and IRC 37 [7]

Chainage	FWD Modulus (MPa)			IIT PAVE current strains		IRC 37 [5] strains for current modulus		Failure mode
	Bituminous layer	Granular layer	Subgrade	ε_t (μs)	ε_v (μs)	ε_t (μs)	ε_v (μs)	
116 + 500	1207.02	323.65	232.59	249.30	360.50	392.89	694.42	Safe
121 + 000	1201.21	371.21	199.74	192.30	387.20	393.31	694.42	Safe
126 + 000	2188.97	275.75	103.60	292.60	533.00	344.76	694.42	Safe
131 + 000	2190.44	209.55	193.84	362.80	381.10	344.71	694.42	Fatigue
136 + 000	1560.83	145.43	235.16	521.40	563.30	371.34	694.42	Fatigue
140 + 500	1631.03	152.04	74.09	510.70	1205.00	367.76	694.42	Rutting and fatigue
145 + 000	1634.31	367.32	98.46	232.20	776.30	367.6	694.42	Rutting
150 + 000	1637.71	274.34	98.46	311.70	854.40	367.44	694.42	Rutting
156 + 500	1815.85	285.030	126.95	282.20	355.50	359.2	694.42	Safe

Table 7 Comparison of the existing and required crust thickness (mm)

Chainage	Existing bituminous layer	Required bituminous layer	Existing base layer	Required base layer	Existing sub-base layer	Required sub-base layer	Existing total thickness	Required total thickness
116 + 500	65	55	120	250	220	117	405	422
121 + 000	60	72	125	233	220	150	405	455
126 + 000	75	72	150	233	200	187	425	492
131 + 000	75	72	150	233	200	150	425	455
136 + 000	60	55	150	250	110	117	320	422
140 + 500	65	72	140	233	125	150	330	455
145 + 000	75	72	150	233	100	187	325	492
150 + 000	75	72	150	233	100	150	325	455
156 + 500	65	55	150	250	300	117	515	422

6 Conclusions

Field and laboratory studies were carried out for performing the pavement evaluation for the selected stretch of the road. Based on the analysis, the following conclusions are drawn.

- Based on PCI values, chainage 140 + 500, 145 + 000 need to be strengthened owing to the presence of weaker material.
- FWD moduli correspond to dynamic traffic loading and are more precise compared to CBR-based values. FWD based modulus values are in excess of 100% in comparison with the CBR based modulus values.
- Pavement sections having thinner bituminous layer thickness exhibited fatigue failure and those having thinner granular layer thickness exhibited rutting failure. The overall pavement thickness is less at chainage 140 + 500 and thus exhibited complete failure.
- At chainages 140 + 500, both the strains are greater than the allowable strains indicating a failure in both rutting and fatigue modes.
- Strengthening is recommended for the sections failed in rutting mode and overlay is suggested for the sections failed in fatigue mode.

References

1. Kim JR, Kang HB, Kim D, Park DS, Kim WJ (2007) Evaluation of in situ modulus of compacted subgrades using portable falling weight deflectometer and plate-bearing load test. J Mater Civ Eng 19(6):492–499
2. Murillo Feo CA, Bejarano Urrego LE (2013) Correlation between deflections measurements on flexible pavements obtained under static and dynamic load techniques. In: Proceedings of the 18th international conference on soil mechanics and geotechnical engineering Paris, pp 393–398
3. Zhou L, Wu Q, Ling J (2010) Comparison of FWD and Benkelman Beam in evaluation of pavement structure capacity. Paving materials and Pavement analysis, 405–411
4. Meles D, Yi Y, Bayat A (2016) Performance evaluation of highway embankment constructed from tire-derived aggregate using falling weight deflectometer tests. Transp Infrastruct Geotechnol 3:128–142
5. Jha V, Mehta Y, Byrne M, Manning F, Saridaki EJ (2009) Evaluation of pavement cracking performance in the state of Rhode Island using Falling Weight Deflectometer. IEEE Sensors Appl Symp, New Orleans, LA, USA
6. IRC 115 (2014) Guidelines for structural evaluation and strengthening of flexible road pavements using falling weight deflectometer (FWD) technique. Indian Roads Congress, New Delhi
7. IRC 37 (2018) Guidelines for the design of flexible pavements. 4th Revision, Indian Roads Congress, New Delhi
8. Udaykumar L, Vivian Robert R, Amarnath MS (2008) Ranking technique for prioritization of arterial and sub arterial roads for maintenance management. J Indian Road Congress, 41–52

Geotechnical Engineering

Design of Blanket by Adding Different Percentages of Soil

Hardev Singh

Abstract The paper discusses the analysis of a railway sub-blast blanket design mix using aggregates and sandy soil. Five-design mix with different proportions of aggregates and virgin soil is prepared as per RDSO guidelines, the property of soil used for the blanket mixes is the same in all the cases, and the effect soil on blanket mixes is studied.

Keywords Railways · Blanket · CBR · RDSO · Sub-ballast

1 Introduction

India is an emergent nation and the Indian Government declares a number of railway construction projects every year. Properties of soil and source of aggregates transition generally with respect to span along with the region. In some parts, the soil is available in large quantities as compared to the stone dust and aggregates. Thus, ahead of lay on soil subgrade, the detailed analysis to determine the nature of soil and aggregates is required.

To construct the railway track on a given site and to use of nearly obtainable soil to get economy in various layers such as subbase, subgrade, blanket, gradation of soil and aggregates needs to be done. In subgrade and subbase, only approved soil as per specification is used. However, in the blanket layer only aggregates of specified size are used. For blanket, the design is done with the help of RDSO guidelines in which 40 mm aggregates to stone dust is used.

Many projects like Eastern and Western Dedicated Freight Corridor Railway Project from Sanhewal to Pilkhani and Bathinda to Rajpura double lines have been declared by the government, and execution of these construction works have already been commenced recently. These jobs require a large quantity of blanket material for constructing a blanket layer. There is a shortage of stone dust/sand in the construction area due to the non-availability of quarries.

H. Singh (✉)
Department of Civil Engineering, Gurukul Vidyapeeth Institute of Engineering and Technology Punjab, Banur, India
e-mail: hdevz1@gmail.com

© Springer Nature Singapore Pte Ltd. 2021

K. K. Pathak et al. (eds.), *Recent Trends in Civil Engineering*, Lecture Notes in Civil Engineering 77, https://doi.org/10.1007/978-981-15-5195-6_36

An attempt has been made by the investigator to take advantage of this excess available earth in constructing a blanket layer by blending it with other blanket components. This may protect the environment and save costs. Effect of mixing local soil with blanket on gradation, modified Proctor test and California bearing ratios have been studied in this report.

2 Railway Guidelines for Design and Construction of Blanket

2.1 Blanket [1, 2]

Blanket is a layer that covers the entire width of the subgrade made of coarse-grained material between ballast and subgrade. This is also called as sub-ballast in different parts of the world in the railway system.

The important functions are the following:

1. It restricts subgrade damage from ballast.
2. It restrains the fouling of ballast by upward movement of fine particles of subgrade.
3. It also decreases the stresses to an allowable limit on the top of the subgrade.
4. It exfoliating moisture from ballast protect the subgrade. Subgrade also gets protected from climate variation and from erosion.
5. It also increases the bearing capacity by improving stiffness and attaining better distribution of loads' subgrade soil layer to avoid penetration of ballast into the subgrade.

2.2 Recommended Specification [1]

Specifications of the material for blanket layer over prepared subgrade should be such that it is a well-graded sandy gravel layer of adequate hardness. Particles size gradation curve should be more or less within the enveloping curves of blanket material and grading percentages within the range and should have following criteria satisfied (Fig. 1):

1. Cu > 7 and Cc between 1 and 3.
2. Fines (passing 75 microns): 3–10%.
3. Los Angeles Abrasion value <35%.
4. Minimum required soaked CBR value of 25 of the blanket material compacted at 100% of MD.

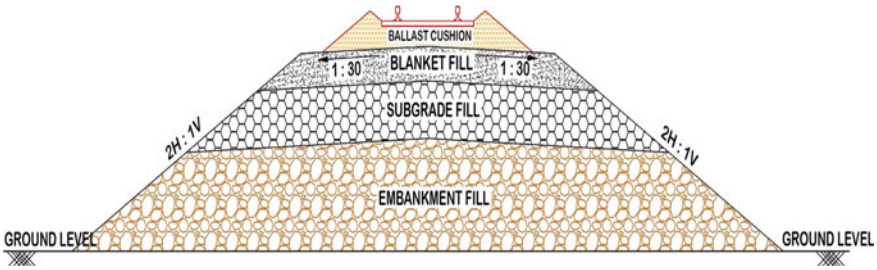

Fig. 1 Typical cross-section of single line railway track

Fig. 2 Material used

3 Experimental Work

3.1 Material Used

Aggregates: Aggregates of size varying from 40 mm to stone dust/crusher sand are taken from the Agampur Village, Shri Anandpur Sahib Tehsil, Rupnagar District, Punjab (Fig. 2).

Sandy Soil: The non-plastic soil is taken from Mandiala Khurd Village, Samrala Tehsil, Ludhiana District, where this soil is available in large quantities.

3.2 Blending of Ingredients

Sandy soil and aggregates are mixed together in each trial with a mix percentage from 20, 15, 12, 11, and 10 to 9%.

4 Methodology

Various tests are performed on the blanket mix are given below:

4.1 Atterberg's Limits[3, 4]

(IS 2720 part 5) is used to find out liquid limit, plastic limit, and plasticity index. Cone penetrometer test apparatus is used for finding the liquid limit. It is noted that the liquid limit, plastic limit, and plasticity index decreases from sandy soil to stone dust.

4.2 Aggregate Abrasion Value Test [1]

For aggregate abrasion value as per IS: 2386 Part 4 IS 460 using and RDSO GE-014. Los Angeles abrasion value of the sample taken is less than the maximum limit 35 due to which sample is accepted for blanket design mix.

4.3 Grading of Aggregates [1]

The aggregate shall conform to the grading given in Table 1 of RDSO GE-014.

From the table, it is seen that all mixes with or without soil having Uniformity Coefficient more than the minimum value 7 and 75 micron passing is also under the acceptable limit, that is, 10% but if analyzing Coefficient of Curvature, Cc value the only three blanket mixes Aggregates: Sandy soil 91:9, 90:10 and 100:0 are lies between 1 and 3% due to which only these mixes are selected for further investigation.

4.4 Modified Proctor Compaction Tests [1] for Max. Dry Density and Optimum Moisture Content as per RDSO GE-014

See (Table 2).

California bearing ratio tests [5]: **This test is performed to find soaked CBR** value as per RDSO GE-014 and IS 2720, Part-16, size of the mould used is 2250 ml capacity and blanket mix is compacted to 97% MDD with dynamical method taking the exact weight of the blanket mixture. After 96 h, soaking tests were performed

Table 1 Result table for all gradation for blanket

SN	Blanket material	Uniformity coefficient, Cu = D60/D10	Coefficient of curvature,Cc = (D30)2/D60XD10	75 micron passing
1	Aggregates : Sandy Soil :: 91:9	53.85	1.1	5.5
2	Aggregates : Sandy Soil :: 90:10	54.0	1.1	5.73
3	Aggregates : Sandy Soil :: 89:11	53.85	0.74	6.28
4	Aggregates : Sandy Soil :: 85:15	70	0.4	7.28
5	Aggregates : Sandy Soil :: 80:20	77.78	0.32	8.43
6	Aggregates : Sandy Soil :: 100:00	33.33	1.56	4.04
	Limits	>7%	1–3%	Max10%

Table 2 Modified proctor compaction tests results

SN	Type of Blanket	MDD in g/cc	OMC In % age
1	Aggregates: Sandy Soil :: 91:9	2.27	7.8
2	Aggregates : Sandy Soil :: 90:10	2.28	7.9
3	Aggregates : Sandy Soil :: 100:0	2.21	6.10

Table 3 CBR test (Soaked) results [5]

SN	Type of blanket mix	Soaked CBR values
1	Aggregates : Sandy Soil :: 91:9	135.50
2	Aggregates : Sandy Soil :: 90:10	138.80
3	Aggregates : Sandy Soil :: 100:0	160.38

for various blanket mixes with a ratio of aggregates: sandy soil :: 91:9, 90:10, 100:0 (Table 3).

4.5 Field Dry Density [3]

By Sand replacement method (IS 2720)

FDD test is performed on a test patch of mix aggregates: sandy soil :: 90:10 after passing through the vibratory roller compactor of weight 10MT 8 times and the

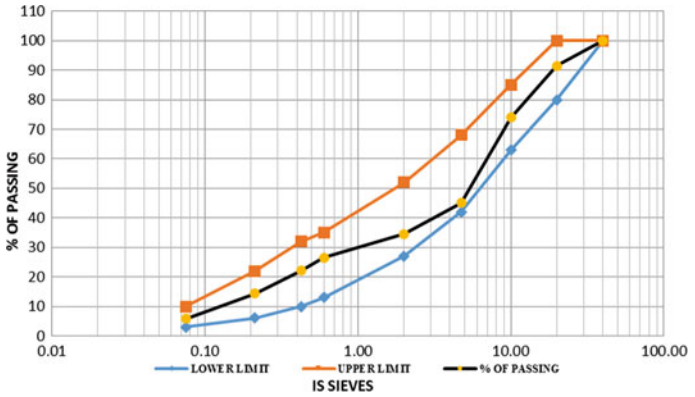

Fig. 3 Enveloping curves for blanket mix aggregates: soil is 90:10

following results are obtained (Fig. 3).

$$\text{FDD} = 100.2\%$$

Acceptance criteria as per GE-14 for blanket layer = 100%

5 Conclusions

Reduction in the liquid limit has been observed by 1.8% from sandy soil to stone dust.

Maximum dry density increases and optimum moisture content increases upon addition of sandy soil to aggregates.

Soaked CBR of blanket mix increases upon the addition of sandy soil. The maximum increase has been observed by 78% at the proportion of aggregates: sandy soil :: 90:10.

It is concluded that the proportion of aggregates: sandy soil:: 90:10 gives the most improved results and this proportion can be used for the construction of blanket as a two-layer structure as having passed the following criteria.

The observed soaked CBR value of 138.80 is more than the minimum required value of 25.

Observed Uniformity Coefficient Cu value of 53.85 is more than the minimum required value of 7% that is very well permitted.

Observed Coefficient of Curvature Cc value of 1.1 is lies between the ranges of requied value of 1–3%.

Observed 75 Micron Passing value of 5.73 is less than maximum required value of 10%.

Observed FDD value of 100.20% is more than the minimum required value of 100%

References

1. Research Design and Standard Organization (2009) Guidelines and Specifications for Design of Formation for Heavy Axle Load. RDSO/2007/GE:0014, Publication of Government of India, Ministry of Railway, Lucknow
2. Report No. GE-35 December, 2000 A State-of-the-Art Report on 'Provision of Blanket on Railway Formations' has been brought out by RDSO to describe historical developments of provision of blanket, design of blanket thickness and financial aspects of provision of blanket
3. IS: 2720 (Part 8) (1983) "Methods of Test for Soils", Part 8, Determination of Water Content—Dry Density Relation using Heavy Compaction (Second Revision)
4. IS: 2720 (Part 15) (1986) "Methods of Test for Soils", Part 15, Determination of Consolidation Properties (First Revision)
5. IS: 2720 (Part 16) (1987) "Methods of Test for Soils", Part 16, Laboratory Determination of CBR (Second Revision)

Challenges in Design and Construction of Pile Foundation in Non-liquefiable and Liquefiable Soil

M. K. Pradhan, G. R. Reddy, and K. Srinivas

Abstract Pile foundation is considered as a suitable and best foundation system at the site with the top stratum of soils possessing comparatively lower bearing capacity with respect to intended loads. It is also recommended at the site where soils possess susceptibly liquefaction potential (liquefaction prone site). In the present paper, it is studied various challenges encountered during the design and construction of pile foundations in non-liquefiable and liquefiable soils. It is also presented various suitable, appropriate, feasible and technically acceptable solutions adopted to overcome the same. In the present work, it is also investigated various suitable methodologies adopted for the construction of pile foundations considering site condition and size of projects. It is also briefed the engineering measures adopted at liquefaction prone site for pile foundation, ground improvements and liquefaction mitigation techniques. Various codes and their guidelines for construction, testing of pile foundation also briefed. It is observed, evaluation of various soil properties from the geotechnical investigation, evaluation of liquefaction potential of soil is very essential before selecting the appropriate pile foundation system and design the same in non-liquefiable and liquefiable soil. Suitable construction methodology also very essential to accomplish the execution of pile foundation safely, meeting desired quality and within the required time frame.

Keyword Pile foundations · Liquefaction of soil · Ground improvements · Bored cast in situ

M. K. Pradhan (✉)
Homi Bhabha National Institute (HBNI), Mumbai 400095, India
e-mail: mpradhan@barc.gov.in

G. R. Reddy · K. Srinivas
Bhabha Atomic Research Centre (BARC), Mumbai 400085, India

© Springer Nature Singapore Pte Ltd. 2021

K. K. Pathak et al. (eds.), *Recent Trends in Civil Engineering*, Lecture Notes in Civil Engineering 77, https://doi.org/10.1007/978-981-15-5195-6_37

1 Introduction

Foundation system is part of civil engineering structures to transfer the load to soil strata beneath it. The foundation system may be categorized as a shallow foundation or deep foundation based on its depth from the existing ground level. Shallow foundations are in the form of raft, strip, strap, etc. However, pile foundation and piers are of deep foundation categories. Selection of types of foundation depends mainly on soil types, soil profile and intended loads.

1.1 Applications of Pile Foundation

Pile foundations are more commonly used for civil engineering structures where the bearing capacity of the top layer soil is not sufficient. The top layer of soil is not capable to transfer intend loads to underlain soil layer without failure. Typical applications of pile foundations are as follows:

1. High-rise buildings, chimney/ stack, power transmission line tower.
2. Shoring system as shown in Fig. 1, offshore structures, retaining structures.
3. Underground structures/basement structures/ vault type structures.
4. Pier structures for the bridge.

Pile foundations are also the most suitable foundation system for a new structure, if it is constructed very close to existing structures without disturbing them. It is also more commonly recommended foundation system at collapsible types of soil.

The pile design and construction practice books by Tomlinson, Bowels are very useful for foundations design, construction and testing [1, 2]. In the available literature and textbooks, it can be seen that all the theories behind the analysis and design aspects about pile foundations. But during design stages and construction periods,

Fig. 1 Typical application of piles as shoring system for underground structure

various challenges and issues are anticipated in real life and as practical aspects. Details about challenges during pile design and construction, issues and its solutions are scarce in presently available technical papers.

In present work, it is studied various challenges encountered during planning, design and construction stages of pile foundations in non-liquefiable and liquefiable soils. It is also presented practical and feasible solutions adopted to overcome challenges and issues. The objective of the study is to identify real issues with the most feasible solutions which are very much useful to civil engineers, academicians and practitioners working in this area.

2 Design of Pile Foundation

Design of pile foundations is mainly based on types of soil and intended load. Based on soil conditions piles may be end bearing piles or friction piles. Foundations are designed subject to vertical (downward or upward), lateral and seismic loads. Accordingly, the load-transferring mechanism of pile foundation is considered. Design considerations also changed if soils at site susceptible to liquefy during an earthquake.

2.1 Pile Subject to Vertical Loads

Vertical load transfer may be of downward direction as in a normal building or upward direction as in case of transmission lines, RCC stacks (wind effects). Vertical load transferring mechanisms are basically transferring loads of superstructures either to surrounding soils through friction or to bottom layer through end bearing.

2.2 Pile Subject to Horizontal Loads

Sometimes pile foundations are subject to horizontal loads as in offshore application. Pile foundations are also used in basements types of the underground structure where soil fills in one side of piles but freestanding in the other side, it is subject to horizontal loads.

2.3 Pile Subject to Earthquake Loads

Pile foundations are also designed for earthquake loads or seismic loads along with various other loads similar to other civil engineering structures. Pile foundations are

subjected to inertial load from superstructures and kinematic load due to different or relative lateral movements of pile and surrounding soils during an earthquake.

2.4 Pile Foundation in Liquefiable Soil

Liquefaction is a phenomenon by which cohesionless soil (low to medium relative density) in saturated condition subjected to repeated cyclic load loses its stiffens and shear strength on account of increasing pore water pressure.

Influence of Liquefaction of Soil in Pile Design. Design philosophies for pile foundation located at non-liquefiable soil and liquefaction prone areas are not similar. During the liquefaction of soils, the frictional contribution of intermediate liquefied layer diminished hence its contribution towards bearing capacity that is not considered is shown in Fig. 2.

In case, if intermediate layer gets liquefied as per Japan Road Association (JRA), it is assumed that the top/crust non-liquefied layer pushed the piles with passive earth pressure [3]. Pile may behave as freestanding column resulting in buckling failure if the depth of intermediate liquefied layers is large as shown in Fig. 3.

Evaluation of Liquefaction Potential of Soil. Liquefaction of soil is an important phenomenon and having its detrimental effects on the pile foundation. Hence, liquefaction potential of soils must be evaluated before planning for execution of important civil engineering structures. The soils are considered as susceptible to liquefaction, if the factor of safety against liquefaction calculated as shown in Eq. 1., as proposed by Seed and Idriss [4] is less than unity [4]

$$\text{Factor of safety against liquefaction} = \frac{\text{Cyclic resiastance ratio (CRR)}}{\text{Cyclic stress ratio (CSR)}} \quad (1)$$

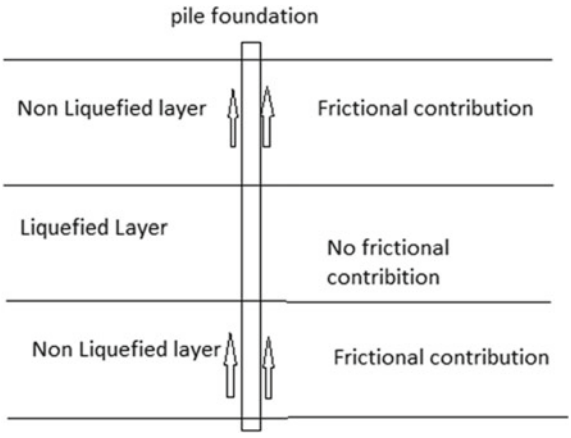

Fig. 2 Intermediate liquefied zone showing no frictional contribution

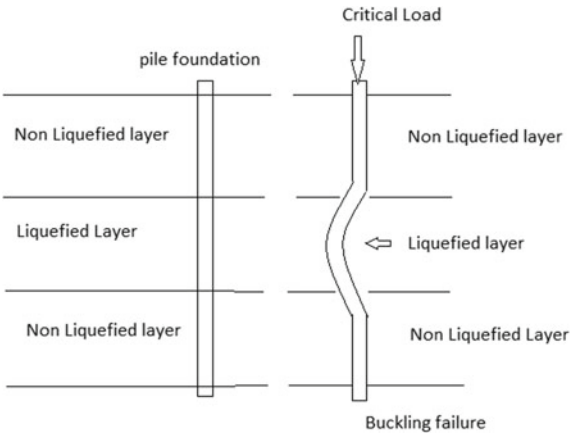

Fig. 3 Schematic diagram of buckling of pile foundation in liquefied zone

CSR and CRR are evaluated as Eqs. 2 and 3, respectively.

$$\text{Cyclic Resistance ratio (CRR)} = CRR_{7.5} \times K_m \times K_\alpha \times K_\sigma \tag{2}$$

where CRR7.5 is the cyclic resistance ratio obtained from Standard Penetration Test (SPT) for an earthquake of magnitude 7.5, Km is the magnitude scaling factor, Kα is the correction factor for sloping ground (generally assumed as unity), K_σ is the overburden correction factor.

$$\text{Cyclic Stress Ratio (CSR)} = 0.65 \times \frac{a_{\max}}{g} \times \frac{\sigma_{v0}}{\sigma_{v0}^{'}} \times r_d \tag{3}$$

where a_{max} is the peak horizontal ground acceleration at ground level generated by the earthquake, g is the acceleration due to gravity; σv0 is total vertical overburden stress, $\sigma_{v0}^{'}$ effective vertical overburden stress, r_d is the stress reduction coefficient. It can be seen from Eq. 3 that the depth of consideration layer also influences the cyclic stress ratio.

3 Construction of Pile Foundation

After the finalization of planning and design of the pile foundation, the next important stage is construction of pie foundations.

Fig. 4 Construction pile foundation by rotary drill methods

3.1 Methods of Construction

The RCC pile foundation may be of precast or bored cast in situ type. For design and construction of bored cast in situ pile foundation IS 2911 part 1 can be referred [5]. Bored cast in situ Reinforced Cement Concrete (RCC) pile construction can be executed by either conventional bailor and chisel methods or rotary drill method [1]. The method adopted depends upon the size of pile, size of projects, approach to the construction site, time limits to complete the projects and financial considerations.

Conventional Bailor and Chisel Method. In conventional bailor and chisel methods, the equipment and accessories such as bailor are made of cast iron, chisel tripod (6–9 m height), piling winch, hammer made of mild steel.

Rotary Drill Method. In this method, the rotary drill machine of suitable specifications is used as shown in Fig. 4. It is used in major projects where pile numbers are large and the time limit to complete the work is comparatively less.

3.2 Termination Criteria

During construction of pile foundation, types of soil or rock profile passing through is continuously monitored. Continues SPT tests are performed to assess the quality of soil encountered and samples are collected for visual observations to get ideas about types of soil reached. The rate of penetration also indicates how hard strata of soil or rock encountered. However, a more technical and quantitative way to decide the depth of pile depends upon the termination criteria of the pile foundation.

The termination criteria indicate the energy-absorbing capacity of soil strata under considerations depends upon the method adopted for pile construction.

Termination Criteria in Conventional and Bailor Chisel Method. Empirically termination depth is recommended if, 1MT weight chisel free falling from height of 1 m for 10 times penetrate less than 10 mm. In more technical and practical way, it is recommended as follows.

For bailor and chisel methods or conventional methods, energy-absorbing capacity of soil/rock is calculated as shown in Eq. 4.

$$\text{EnergyAbsorbing Capacity} = \frac{WhN\eta}{Ap} \tag{4}$$

where 'W' is the weight of chisel in Tone, 'h' is the height of fall in metre, 'N' is the number of falls, 'η' is the efficiency, 'A' is the pile cross-sectional area in m^2 and 'p' is the penetration measured in metres after N times of fall.

Termination Criteria in Rotary Drill Method. The termination criteria or the guidelines at which the piles are to be terminated for rotary drill methods is expressed as

$$\text{EnergyAbsorbing apacity} = \frac{2\pi NT}{Ap} \tag{5}$$

where 'N' is the number of rotations, 'T' is the torque applied in Tm, 'A' is the pile cross-sectional area in m^2 and 'p' is penetration in metres after N times of rotation. It is to be noted that the piles are further extended up to '4D' (D = diameter of pile) as socketing length beyond the termination level. The pile should be socketed and found in good rock only.

3.3 Challenges During Construction

If a pile foundation is recommended as a foundation system, the construction of pile foundation is very important and major activities in project execution. During construction of pile foundation various challenges may arise time to time enlisted as below.

1. Construction of new piles in the restricted area and near the existing structures.
2. Construction of new piles near the existing pile.
3. Setting the tripod at the exact pile location.
4. Locating exact positions of the pile during construction.
5. Maintaining vertically during pile construction.
6. Encounter of bulging of concrete and reinforcements of the existing nearby pile.
7. Slippage of chisel during boring.
8. Vertical side collapse during boring.

9. To get circular required pile from a chisel of the reduced section.
10. Placing long reinforcement cages.
11. Side collapse found after placing of reinforcements.
12. Concreting work in water by tremie methods.
13. Proper design mix of concrete.
14. Proper washing of borehole before casting.
15. Providing suitable concrete cover and maintaining its location.
16. Ensuring no air pocket caught in pile shaft while casting.
17. Evaluation of the extrapolated value of SPT to obtain the required bearing capacity.
18. Evaluation of liquefaction potential of soil.
19. Engineering solution if soils are prone to liquefaction.
20. Suitable methods of ground improvement.
21. Evaluation of the effectiveness of soil improvements.

Construction of New Pile in Restricted Area and Near Existing Structures. Sometimes, it is required to construct new pile foundation very close to the existing structures as shown in Fig. 5. Care must be taken to avoid any damage to existing structures during the construction of new pile foundations. The vibration levels during the execution of new piles should be within permissible limits of machines and equipment already in operation in the existing nearby structures.

Sometimes, it is required to construct a pile foundation in a restricted area without any approach to access for a rotary drill machine. Here bailor and chisel methods are only adopted with utmost care.

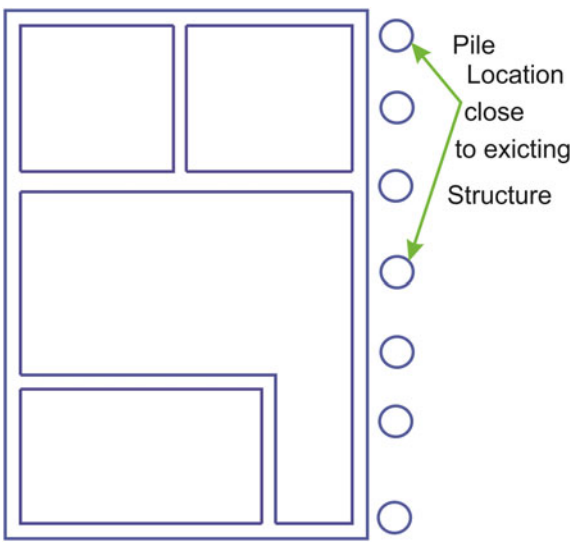

Fig. 5 New pile foundation location close to existing structures

Construction of New Pile Near the Existing Pile. New piles are constructed very close to the existing pile in case of a shoring system. It is very difficult to retain the side of new piles which are already loosened or got disturbed during the boring of previous piles. Sometimes, it starts collapsing heavily during boring activities of new piles. It is reported in several cases as a new pile filled 2–3 times due to heavy side collapse and start afresh after some time intervals.

Setting the Tripod at Exact Pile Location. The exact location of piles depends upon the accuracy of the centering of piling tripod during construction by bailor and chisel methods. During the construction of pile foundation, levelled and clean surfaces may not available. Still, efforts should be made to erect the tripod at its desired locations maintaining accuracy and adhering to safety standards as shown in Fig. 6.

Locating Exact Positions of Pile During Construction. The drawing of pile foundations with locations is prepared in the drawing office with the help of a computer and in very clean environments. But in actual practice during the construction of piles, the site becomes mud filled as shown in Fig. 7.

During boring activities water mixed with soil comes out of the boring holes. During concrete work by the tremie method, the water and mud flow out from the pile hole. Sometimes it becomes very difficult to find exact locations of the next scheduled pile resulting in a difference in exact pile location and tripod centre as shown in Fig. 8. Hence, permanent marking, viz., nailing, rod penetration helps to relocate the next pile's exact location.

Total stations can be used for locating the pile's location accurately during the pile construction. Each pile shall be identified with a reference number and proper record of boring, casting of concrete should be maintained date wise at the site.

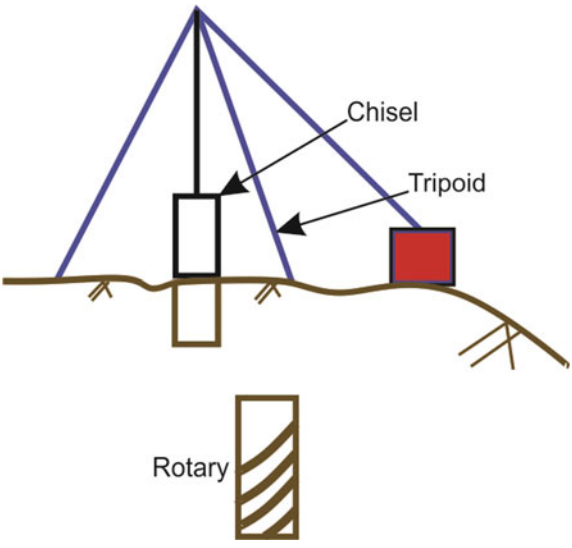

Fig. 6 Setting up a tripod in a levelled and desired location

Fig. 7 Identification of pile locations during pile construction

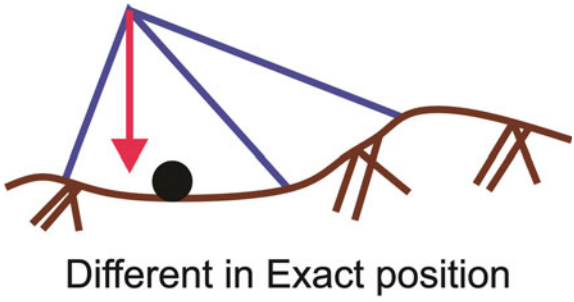

Fig. 8 Showing different pile locations and tripod centre position

Maintaining Verticality During Pile Construction. In design, it is assumed that the pile is to be constructed in a true vertical position and load-transferring mechanism is considered accordingly. Hence, it is very much required that the final pile position is maintained vertically or tilting within permissible limits. The permissible limits for deviation with respect to position and inclination/alignment shall conform to IS-2911 (Part I/Section 2) [5]. The maximum permissible deviation in alignment is 1.5%. Piles should not deviate more than 75 mm or 'Diameter/10' whichever is less from their positions at the working level. In the case of piles deviating beyond these limits, the piles should be replaced or supplemented by one or more additional piles.

As the boring of pile foundation is carried out by free fall of chisel and bailors, particularly in conventional methods it becomes very difficult to maintain the perfect vertical during construction. The chisels may move towards the soft soil during boring if soils in one direction are softer comparing to the other. If localized hard rock or stone is encountered in one direction of pile boreholes it may also result in piles bore leading towards one direction deviating verticality. Hence, verticality checking through plum bub at regular intervals are to be followed to avoid these problems. Advance instruments and techniques such as lasers are also used to measure the verticality of pile boreholes during construction. In regular practice if the boreholes

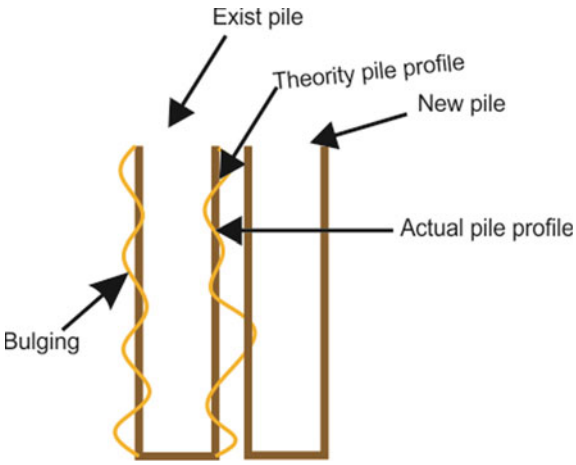

Fig. 9 Inside bulging of existing piles

are moving in one direction during boring, the borehole filled with stone boulders up to a certain height and boring is started once again.

Encounter of Bulging of Concrete and Reinforcements of Existing Nearby Pile. Sometimes piles are used as shoring systems as shown in Fig. 1. In such cases, piles are located very close to each other, and inside bulging of existing piles at certain depth may encounter during boring next nearby pile as shown in Fig. 9. Sometimes the reinforcements of previous piles also get entangled during boring a new pile.

Slippage of Chisel During Boring. During construction of pile foundation with the help of bailor and chisels method sometimes bailor and chisel may get slipped as shown in Fig. 10 and get choked and remain at greater depth. It becomes very difficult to remove the same from the boreholes. It is also reported that some timed it could not be removed. In such a case pile can be relocated near the existing pile location.

Vertical Side Collapse During Boring. During boring work for construction of piles vertical sided may collapse if the soil is not strong enough to self-stand, i.e. collapsible in nature. In such cases following measures are adopted.

Placing Cashing and Line. Metal steel cashing are generally provided at top layers of soil to retain the soil from collapse. Sometimes metallic liners are provided to

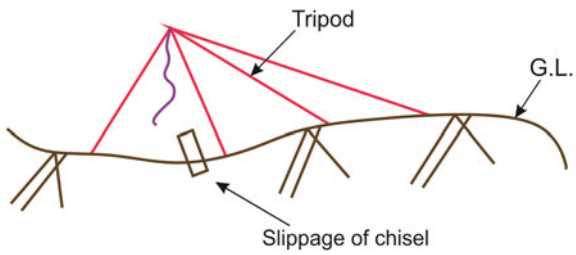

Fig. 10 Slippage of chisel during pile construction

Fig. 11 Metallic steel Cashing/Liner to prevent soil side collapse during pile construction

prevent the side collapse as shown in Fig. 11. The liners may be either of permanent types or are removed after concrete work.

Providing Bentonite Slurry: IS 2911: Part 4 [6]. Bentonite is also used to prevent the vertical surface from side collapse if soils are of a collapsible type. The bentonite suspension used in boreholes is basically a clay of montmorillonite group having exchangeable sodium cations. The action of bentonite in stabilizing the sides of boreholes during the construction of the pile foundation is primarily due to the thixotropic property of bentonite.

Achieve Circular Required Pile from A Chisel of Reduced Section. The bailors and chisels used for boring activities are smaller in diameter (D1) compared to the required pile diameter (D2) as shown in Fig. 12. However, the full diameter piles are created by the chisels and bailor only by free-falling and chiseling methods.

Placing of Long Reinforcement Cages. Reinforcements are provided in pile foundations as main vertical reinforcements and spiral secondary stirrup reinforcements as shown in Fig. 13. The lowering of reinforcements safely after preparation of cage is a very important activity in pile foundation construction.

Reinforcements Joint During Construction. The reinforcements that are commonly available are of length 11–12 m. However, sometimes pile foundations are constructed up to 40 m depth or even more. In such cases, reinforcement cages are to be lapped or extended to the desired length. The various methods adopted to extend reinforcement lengths are lap connecting, welding, mechanical couplers provision. It is also a big challenge to lower the very long reinforcement cages with available lowering equipment like a tripod or rotary drill machine safely as shown in Fig. 14. without disturbing the vertical side and preventing the side collapse.

Side Collapse Found After Placing of Reinforcements. Sometimes, it is experienced that the vertical side gets collapsed during the lowering of the reinforcement cages. Hence, it is always advisable to check the bottom levels by sounding methods after placing the reinforcement cages. It should be also checked after washing the mud from boreholes with water or bentonite circulation. If it is found that the measured

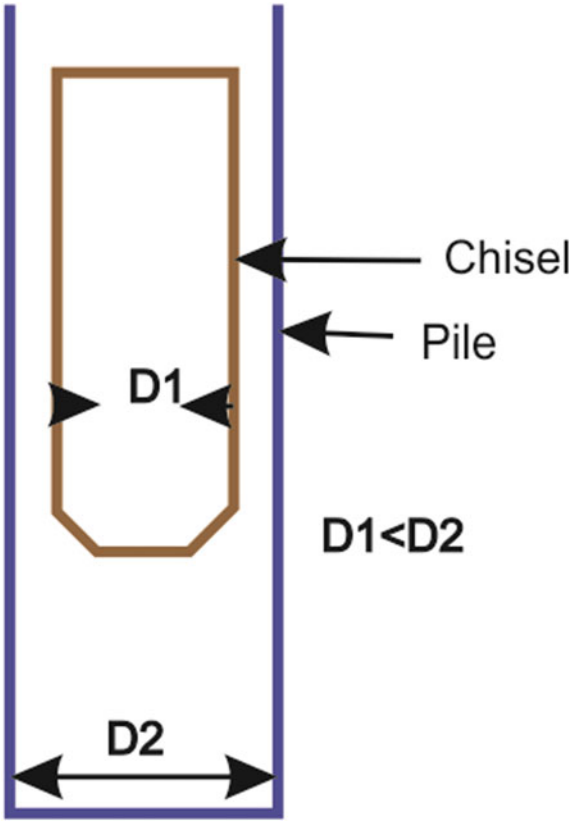

Fig. 12 Schematic diagram showing chisel diameter (D1) and pile diameter D2

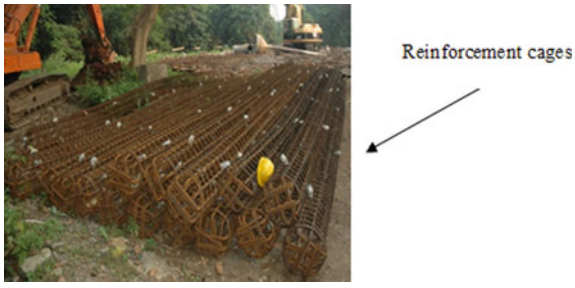

Fig. 13 Reinforcement cage for pile foundation

depth is less compared to the previously recorded depth it indicates side collapse. In such cases, the reinforcements cages are to be removed and boreholes are cleaned again. Then the reinforcements cages are placed systematically.

Concrete Work in Water by Tremie Methods. Entire concreting in pile bores is performed by the tremie method (IS:2911 Part I/Section 2) [5]. It is ensured that the volume of concrete poured in pile boreholes for construction of piles is more than

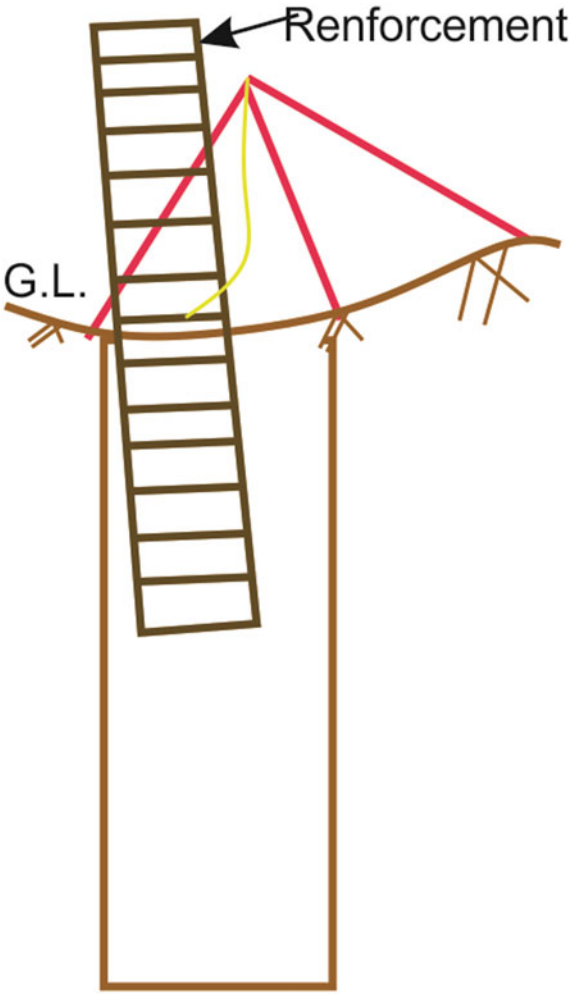

Fig. 14 Placing of long reinforcement cage during pile construction

or at least equal to the theoretically computed volume of pile shaft being cast. The temporary guide casing is withdrawn cautiously, after concreting is done up to the required level. While withdrawing the casing utmost care is taken so that concrete shall not be disturbed.

Proper Design Mix of Concrete. Concrete work of pile is performed by the tremie method as shown in Fig. 15. Hence, the proper design of concrete is a prerequisite and the design mix can be done as per the guidance of IS:20262-2019 [7]. Suitable chemical admixtures must be added to attain the required workability, retain the slumps up to the desired period. The admixtures shall conform to IS:9103 [8]. Concrete should meet the concrete specifications and guidelines recommended by IS456:2000 [9].

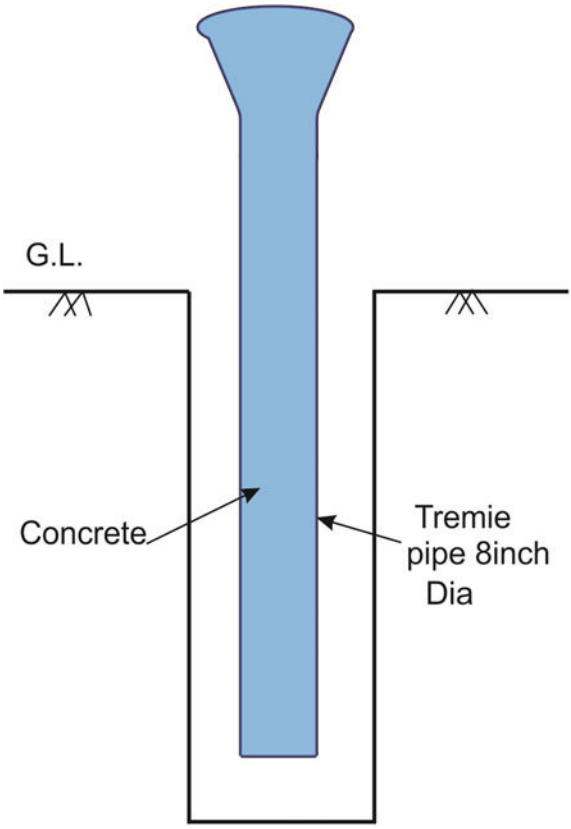

Fig. 15 Pile concreting with tremie methods

Providing Suitable Concrete Cover and Maintaining Its Location. As concrete is embedded in soil and ground water table with various chemical it is always susceptible to corrosion, chloride attack, sulphate attack, etc. Hence, it is required to cover the concrete. But the biggest challenge is the selection of suitable cover, its rigidity and chances to be position during mechanically lowering heavy mass of reinforcement. The concrete cover generally made of cement concrete/mortar or of plastic which is available in the market.

Extrapolated Value of SPT For Required Bearing Capacity. The general practice of assessments of the quality of soil/rock is the Standard Penetration Test (SPT). But after a certain depth, if hard rock is encountered then SPT will indicate the refusal. In that case SPT will be no more appropriate for evaluation and assessments. However, some researchers suggested to follow the extrapolated values of SPT as termination criteria, but its accuracy and performance may not be up to mark.

Evaluation of Liquefaction Potential of Soil. The liquefaction potential of the soils is evaluated from the test results of the geotechnical investigation. Various established methods are available based on SPT, Cone Penetration Test (CPT), shear wave

velocity test. Laboratory tests such as cyclic triaxial shear test also can be performed to assess the liquefaction potential of soils. Liquefaction potential evaluation is briefed in Sect. 2.2.

Engineering Solution of Pile Foundation in Liquefaction Soil. As it is observed that utmost care to be taken during design and construction stages for pile foundations located in liquefaction-prone areas. Due to the scarcity of important and valuable land, a site cannot be rejected merely because of liquefaction potential of soils. Engineering measures as briefed below can be adopted so that any valuable and well-located site is not rejected.

Engineering Solution 1: *Change in pile design.* This can be achieved by changing the design of pile foundations considering the liquefaction of soils. The length of the pile increased considerably as the intermediate liquefied layer is considered not contributing to any frictional resistance as briefed in Sect. 2.1. The diameter also gets increased to resist the buckling failure as the pile will behave as slender members when the confinements of surrounding soils are lost due to liquefaction of soils as presented in Sect. 2.1.

Engineering Solution 2: *Ground improvements/soil stabilizations.* Alternate engineering solution in case of liquefiable soils is performing ground improvements or soil stabilization with suitable methods to mitigate liquefaction potentials of soils. But it is very essential to select a suitable ground improving methods considering types of soils. There are various types of ground improvement techniques. Cement-based grouting, densification, permeation, etc. are a few of them.

4 Testing of Pile Foundations

Pile foundations tests are conducted to assess the performance of pile foundations. Pile tests are of either of initial tests performed on piles which are not the part of the main/parent structures or routine tests performed on piles which are part of the structures. Based on the direction of load application pile load tests are of vertical load tests or lateral load tests. Integrity tests are also performed to assess the quality of pile constructed or any necking is formed during the construction.

4.1 Problems/ Challenges During Pile Load Test

The various equipment and accessories used in pile load tests are dial gauges, pressure metres, ram, kentledge load, datum bars, etc. During the performance of pile testing, various challenges and issues may arise from time to time as given below.

1. Failure of dial gauges,
2. Leakage of hydraulic oil,

3. Puncture of pressure tube/pipe,
4. Toppling of kentledge loads during jack loading,
5. Side collapse of test pit,
6. Making the pile top perfectly smooth,
7. Main reinforcements cut to make smooth and perfectly horizontal piles.

5 Discussion and Conclusion

It is observed that the proper design is required of a pile foundation based on intended loads and types of soil that exists at the site. Detailed soil investigation should be performed for design, planning and execution of pile foundation. It is also observed that various challenges may arise from time to time during the design and construction of a pile foundation in non-liquefiable and liquefiable soils. All the issues and challenges are to be overcome successfully and safely by adopting suitable and feasible solutions as enumerated in present papers.

Acknowledgments The authors would like to thank Homi Bhabha National Institute (HBNI) and BARC, Mumbai, India for providing academic and research support.

References

1. Tomlinson M, Woodward J (2008) Pile design and construction practice, 5 edn
2. Bowles JE (1988) Foundation analysis and design. McGraw-Hill
3. JRA (1996) Seismic design specifications of highway bridges. Japan road association
4. Seed HB, Idriss IM (1971) Simplified procedures for evaluating soil liquefaction potential. J Soil Mech Found Div 97(9):1249–1273
5. Bureau of Indian Standard: IS 2911-part 1 Concrete pile Section 2 Bored cast in-situ piles. Design and construction of pile foundations-Code of practice
6. Bureau of Indian Standard: IS 2911 Part 4 "Code of practice for design and construction of pile foundations-Load test on piles"
7. Bureau of Indian Standard: IS 10262:2019, "Concrete mix Proportioning Guidelines
8. Bureau of Indian Standard: IS 9103: Specification for concrete admixtures Bure of Indian Standard
9. Bureau of Indian Standard: IS 456-2000 (Reaffirmed 2008) Plain and Reinforced Concrete - Code of Practice is an Indian Standard code of practice for general structural use of plain and reinforced concrete

Improvement of Clayey Subgrade by Using Ferro-Sand

Ambika Priyadarshini Mishra, Rupashree Ragini Sahoo, and Pradip Kumar Pradhan

Abstract Development of any country is always marked by its effective and efficient communication system. In a country like India, the roads connectivity through its rural section is of paramount significance. But the major drawback is the soil subgrade in these regions. The clayey soil poses a serious pitfall affecting the serviceability and durability of the soil subgrade. This study focuses majorly on the improvement of clayey subgrade by addition of ferro-sand, a by-product obtained from the extraction of copper. The ferro-sand is a waste product which is generated in huge amount. For every million tonnes of copper extracted, there are more than 2.2 million tonnes of ferro-sand generated. The utilization of this industrial waste for the stabilization of clayey subgrade is the objective of the paper. Standard Proctor's test, unconfined compressive strength test, direct shear test and California bearing ratio (CBR) test are performed on the virgin soil and the soil blended with ferro-sand. The ferro-sand is replaced in 10, 20, 30, 40% proportions by weight from the virgin soil. The standard Proctor's test emanates that the significant decrease of 38.22% in optimum moisture content (OMC) and an increase of 27.89% in maximum dry density (MDD) of the soil mix from the virgin soil. The virgin soil and the soil blends were examined for the unconfined compressive strength test and improvement of 193.16% is observed. Such improvement in strength was further improved by curing the soil mix for periods of 7, 14, 28 days. The direct shear test result shows that the cohesion of soil mix increases significantly from 26.87 to 51.68 kPa. Then these proportions of the soil blend are tested for both unsoaked and soaked CBR tests. The results show an increment of 4% in the unsoaked CBR value and 3.42% in the soaked CBR value. This significant improvement clearly shows that ferro-sand is adaptably suitable for the stabilization

A. P. Mishra (✉) · R. R. Sahoo · P. K. Pradhan
Department of Civil Engineering, Veer Surendra Sai University of Technology, Burla 768018, India
e-mail: priyadarshini1695@gmail.com

R. R. Sahoo
e-mail: rupashreesec@gmail.com

P. K. Pradhan
e-mail: pkpradhan1@yahoo.co.in

© Springer Nature Singapore Pte Ltd. 2021

K. K. Pathak et al. (eds.), *Recent Trends in Civil Engineering*, Lecture Notes in Civil Engineering 77, https://doi.org/10.1007/978-981-15-5195-6_38

of the clayey subgrade. Also, its properties resembling that of sand proposes its utilization as a replacement material for natural sand.

Keywords Ferro-Sand · Clayey soil · Pozzolanic reactions · Standard proctor test · California bearing ratio

1 Introduction

Roads are the lifelines of any civilization. The need for transportation and communication has been the basis of every major invention and discovery. The development of roads plays a pivotal role in the sustenance of the community. The roads are the linkages which reduce the gap between urban life and rural life. The increasing road network in the country is the prime indicator of its progress. The communication to the distant parts of the country is only possible through the roads. But the scarcity of feasible land reduces the durability of the constructed roads. The increasing demand for infrastructure in the urban civilization has degraded the possibility of land for the possibly good subgrade soil for pavement construction. The available land is so poor in pavement quality that the cost of road maintenance supersedes the cost of road construction. This has forced the civil engineers around the world to find alterations to deal with the problematic soils. This problem of swelling and shrinkage variation of soil can be addressed through soil stabilization. Stabilization of soils has been obtained as the most stable, economical and eco-friendly method as a solution to the problem. The soil stabilization process involves the analysis of the strength of the onsite soil and then suggesting ways and means to improve their strength by mixing various admixtures into the soil. Earlier lime, cement, bitumen, etc., have been used to stabilize the soil. Nowadays reutilization of the generated waste is in trend. This has paved way for the utilization of the waste generated from mining like blast furnace slag, copper slag, cement slag, etc. These wastes are produced in much higher quantity and are dumped in the environment leading to accumulation of waste in landfills and shortage in the dumping area for such waste. The waste if dumped in open will be the storehouse of filth resulting in many health hazards for the society. In the present study, we have considered ferro-sand, an industrial waste product, for the stabilization of such problematic soils. The ferro-sand has its properties similar to that of the medium sand. Also, it is non-toxic in nature thus immune to the leaching effect in the soils [1]. Thus mixing it with clayey soil will have eco-friendly benefits as compared to other stabilizing agents like cement, lime, chemical agents, etc. Many researches have been carried out on the utilization of ferro-sand also known as copper slag in the geotechnical front. It has been studied as an embankment fill material and also as a pavement construction material. In a study by Havangi, the local soils have been stabilized with copper slag and pond ash from a proportion of 25–75% to be used as a fill material. It was observed that in all these mixes, MDD increases and the OMC decreases progressively with the increment in the copper slag content. While the proportion mix of 75% copper slag

content had been proposed to be used in subgrade layer of the road pavement under construction in replacement of local soil [2]. In 2011, Lavanya studied the copper slag and confirmed through the grain size distribution that it is of coarser sand size particle. The specific gravity of the copper slag is 3.51 and it is non-plastic nature this can be due to the presence of a high amount of ferrous compounds in it. It had been suggested to use an optimum amount of about 30–50% for different problematic soils [3]. The mix of fly ash and copper slag has also been studied by many researchers. One such research proposes the implementation of 30% copper slag along with 70% fly ash as an optimum blend for the replacement of traditional subgrade materials like soils. There has been a significant amount of increase of 5.79% in the CBR value of such mix blend. The strength characteristics of such soils have also been very high as compared to the problematic soil subgrades [4]. Baraskar and Ahirwar studied the inclusion of copper slag in the black cotton soil. This soil being high plasticity clay is considered as hugely problematic soil for the soil subgrade during pavement construction. The CBR value of the copper slag and soil blend was also observed to increase 3 times for the same mix [5]. Further studies have experimented with the blending of copper slag with cement. The investigations have observed the stabilization of clayey soil with both cement and copper slag [8]. The ANN model has been created to study the impact of copper slag and cement stabilized soil on the elastic modulus of the soil [6]. The research has been conducted on the clayey subgrade with copper slag and another additive. The studies compare the strength of the soil subgrades but do not take into consideration the economical aspect of the study. Raj et al., in their study, explores the economical aspect of soil stabilized road with copper slag. There has been a significant amount of increase of 51.17% in the CBR value of the copper slag stabilized soil [7]. Thus, the present study explores the stabilization of clayey soil using only copper slag as an additive and studying the strength improvement of soil as a subgrade material. This helps in understanding of the properties of copper slag as stabilizing material and exploring its pozzolanic effect on the soil alone. The blending of the slag particles with the soil has a notable amount of effect on the appearance and physical attributes of the soil. The analysis of the studies performed, so far, restricts on the strength characteristics of the clayey soils and its improvement. The permeability and consolidation characteristics of the copper slag and soil blend have not been explored much. The copper slag being non-plastic in nature does not possess any strength of its own but when blended with the soil improves its strength and physical properties. The prospect of copper slag application in replacement of sand can be researched. The copper slag has geotechnical properties similar to that of the medium sand and thus has a significant potential to be utilized as a construction material. It can also be utilized as an alternative to natural sand in cushioning of sand drains. The geotechnical uses of this material have to be explored further. The waste generated by the industrialization should only be utilized in a sustainable and economical way otherwise the dumping of waste will create major safe disposal problem and utilization of it without considering the environmental impact will only degrade the environment further. Thus, careful and judicious utilization of the waste should be kept in view before utilization.

2 Materials and Methodology for Tests

2.1 Soft Clayey Soil

The virgin soil for the experiment had been acquired from the Brahmagiri locality of Puri District in Odisha. The area is a potential tourism hotspot under development by the State Tourism Department. The area boasts for its scenic beach view and the proposed site is the allotted area for the much-awaited Samukha project of the tourism department. But due to the deficiency of feasible construction area, the project has been on a standstill. The soil obtained for the study is a clayey soil from the coastal region. The similar kind of soil is also found near Morena, Bhind (Madhya Pradesh), Dholpur (Rajasthan) and Aurangabad (Maharastra), etc. The stabilization of such soils is important for the development of the region as well as it helps explore the possibilities of encountering such soils and providing feasible and economical solutions to it. The soil is fine-grained clay of high plasticity, high compressibility and low strength, thus can classified as soft clayey soil. According to the Unified Soil Classification System (USCS), the virgin soil has been classified as a CH soil. The soft clayey soil obtained was air-dried because of its high water content and then oven-dried for 24 h as per IS:2720 (Part 1)-1983 [9]. The dried soil sample in lumps was then pulverized into fine particles using a wooden mallet. The clayey soil is then sieved through the 425 μ sieve to check for any fine lumps. The physical and geotechnical properties of the soft clayey soil are given in Table 1.

2.2 Ferro-Sand

Ferro-sand is a by-product procured from smelting of copper which is composed mainly of iron oxide and silicate oxide compounds. The ferro-sand also known as copper slag had been rendered from HCL (Hindustan Copper Limited) in Ghatsila. Figure 1 clearly shows its appearance similar to that of coarse sand.

In India, about 150,000 million tonnes of ferro-sand is produced annually, which is dumped as a waste due to its low applicability in the industries. In the construction enterprise, not much study has been done on its reusability; hence, very low applicability of it is observed. It is an economic and feasible alternative towards the traditional stabilizers like lime, cement, etc. as it ensures improved stability of soil and reusability of the generated waste. Due to its resemblance with that of coarse sand, it can be a viable alternative of the sand, such as in the filling of embankments, foundations, backfills, etc. It does not produce a leaching effect on reacting with any harmful chemicals, thus can be safe and environment-friendly solution. Also, the natural source of sand can be utilized judiciously. After the extraction of copper from the ore, the oxides and sulphides of iron and copper combine covalently in the absence of silica, forming Cu–Fe–O–S phase. During this process of smelting, when the silica is included in the Cu–Fe–O–S phase, the silica combines with the oxides

Table 1 Physical characteristics and geotechnical properties of soft clayey soil and Ferro-Sand

Sl. No.	Material Properties		Virgin Soil	Ferro-Sand
1	Colour		Dark Brown	Greasy Black
2	Liquid Limit (%) (LL)		51.25	–
3	Plastic Limit (%) (PL)		18.71	–
4	Plasticity Index (PI)		32.54	–
5	Differential Free Swell Test (%)		50	Non-Swelling
6	Specific Gravity		2.53	3.16
7	Grain Size Distribution	Sand (%) Silt (%) Clay (%)	4.83 4.16 91.01	4.83 4.16 91.01
8	Swell Pressure Test (kN)		279.82	–
9	Classification		CH	SP
10	Maximum Dry Density (kN/m^3)		15.09	2.32
11	Optimum Moisture Content (%)		20.56	5.67
12	Unconfined Compressive Strength (kPa)		44.74	–
13	Cohesion (kPa)		26.87	0
14	Angle of Shearing Resistance (Φ)		25.64	40.76
15	CBR Test	Unsoaked Soaked	2.69 1.96	– –
16	pH		6.5	7.2

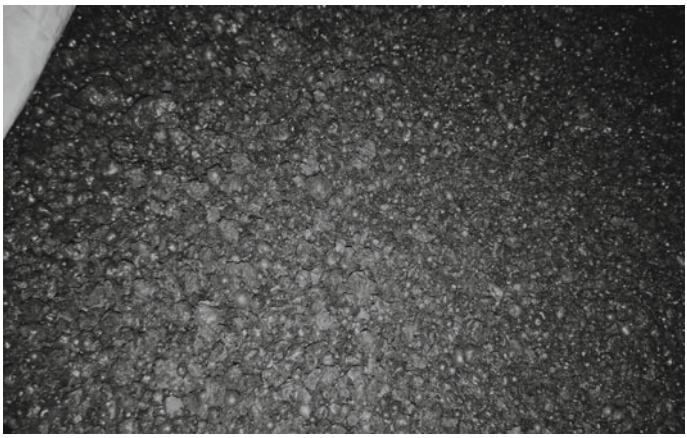

Fig. 1 Pictorial representation of Ferro-Sand from Ghatsila

and form strongly bonded silicate anions which group together to form the slag phase from the copper ore.

$$2FeO + 3SiO_2\ 2Fe^{2+} + Si_3O_8^{4-} \quad (1)$$

The ferro-sand produced is utilized for various purposes like sandblasting, cutting tools, cement production, etc. Thus, these free oxide compounds tend to react and a pozzolanic effect is observed when the ferro-sand blends with the soil. The pozzolanic effect tends to bind the soil particle with ferro-sand and densifies the mixture. The grain size distribution of the material was carried out as per IS: 2720 (Part 4)-1972. The geotechnical properties of ferro-sand are shown in Table 1.

2.3 Methodology

The oven-dried pulverized soil specimens were weighted and ferro-sand in proportions of 10, 20, 30 and 40% were replaced by weight of soil. The mixing was done in batches. Firstly, the soil sample was divided into ten parts and then the ferro-sand was divided into ten parts and each part was then mixed. Thereby, ensuring a uniform mix of the virgin soil and the ferro-sand. These soil blends were tested for OMC, MDD, UCS, cohesion intercept, angle of shearing resistance and the soaked and unsoaked CBRs of the soil. Thus, an optimum mix of soft clayey soil and ferro-sand was obtained.

Specimen Preparation for Standard Proctor Test. The light compaction test or the standard Proctor test was carried out to determine the OMC and MDD of the virgin soil and the soil blends. The standard Proctor test was conducted as per IS: 2720 (Part 7)-1983 [10], for determination of water content and dry density relation. The soil sample passing through 425-μ sieve was taken and weighed. The mix was prepared by replacing the ferro-sand in different proportions of 10, 20, 30 and 40% from the 2.5 kg soil sample for the standard Proctor test. The sample was then moistened with initial water content of 8% with the gradual increase in the moisture content of about 4%. This remoulded soil specimen was then compacted in the mould of volume 1000 cc in three separate layers, with each layer sustaining 25 blows with the help of a 2.6 kg weighing rammer dropping from a height of 310 mm. The rammer blows being uniformly distributed over each layer. The soil layer should be at 5 mm above the mould after the removal of the collar. The increase in the proportions of the ferro-sand should be with the replacement of the equal amount of soil from it. The soil sample should be collected after compaction to determine the water content of the mix blend. Thus, the dry density of the blend will determine the required compactive effort for the ferro-sand and soil proportions.

Specimen Preparation for Unconfined Compressive Strength Test. The UCS test is an unconsolidated–undrained (UU) test in which the compressive strength of the soil is obtained, without confinement. The UCS test was conducted as per IS: 2720

(Part 10)-1973 [11]. The preparation of the soil sample was done by light compaction of the dried soil sample at OMC of the soil sample and the mix proportions. Then the stainless tube of 3.7 mm diameter and 10.2 mm height was pushed into the mould by the rammer and cylindrical soil samples were extracted. The soil sample in the stainless tube was then pushed into the spilt mould and the cylindrical soil sample procured for the test. The soil sample was tested in a proving ring-type testing machine.

Specimen Preparation for Direct Shear Test. The DST is conducted to analyse the shear failure of the soil sample. The test results present the cohesion (c) and the angle of friction (Φ) of the soil samples which are important shear strength parameters of the soil. The soil sample is initially compacted in a 1000-cc mould at OMC. The steel frame of size 6 cm × 6 cm × 2.5 cm was inserted into the mould with compacted soil and the test sample is extracted. A constant normal load of (0.5, 1, 1.5 kg/cm^2) is applied for obtaining the value of C and Φ. The horizontal load is applied at a constant rate and incremented till failure point is reached. In the experimental study, the soil mix was placed in the shear box of 60 mm × 60 mm × 60 mm in unconsolidated undrained conditions as per IS: 2720 (Part 13)-1972. The loading rate was 0.002 mm/s for the tests. The proving ring readings at horizontal dial gauge intervals were noted. The soil mix proportions were also prepared and tested in the same procedure.

Specimen Preparation for California Bearing Ratio Test. The CBR test is performed for obtaining the ratio in percentage of the strength of the subbase soil with that of the strength of crushed stones. The test was conducted as per IS: 2720 (Part 16)-1983 [12]. Virgin soil of 5 kg was taken as test specimen. This 5 kg sample was again divided into ten equal proportions to be mixed with the ferro-sand mixes from 10 to 40% with an increment of 10%. The blend was then mixed thoroughly and compacted at OMC in a cylindrical mould of 150 mm diameter and 175 mm height. It was compacted in five distinct layers at MDD obtained from the standard Proctor test. Each layer was imparted 56 numbers of blows distributed evenly. The maximum dry density was obtained for the light compaction; hence, the compaction for the CBR has to be done as per the light compaction dry density value. The unsoaked specimen was tested and load penetration curve was obtained. For soaked specimen, the mould was kept in curing tank for 96 hrs prior to testing.

3 Results and Discussion

3.1 Effect of Ferro-Sand on Optimum Moisture Content and Maximum Dry Density

The OMC decreases with the replacement of soil with ferro-sand. The MDD increases with the replacement of virgin soil with ferro-sand up to 30% replacement and then

decreases gradually with the further addition of ferro-sand, as observed in Fig. 2. We can observe from Table 2 that with variation in proportions of ferro-sand, the MDD of the soil blend also differs with moisture content. This is because with the addition of heavier ferro-sand particles and the soil becomes coarser and denser in nature, thus the specific gravity of soil increases. This provides a denser packing to the soil and ferro-sand blend upon mixing. The dry density is indicative of the compactive effort required to have a closer packing. Thus, it increases with the increase in the ferro-sand proportion. The decrement in the optimum moisture content of the soil and ferro-sand blend is because there is a reduction in the interparticle repulsive forces when coarser ferro-sand particles are mixed with soil particles thus, void space reduces and the water content of the soil also reduces.

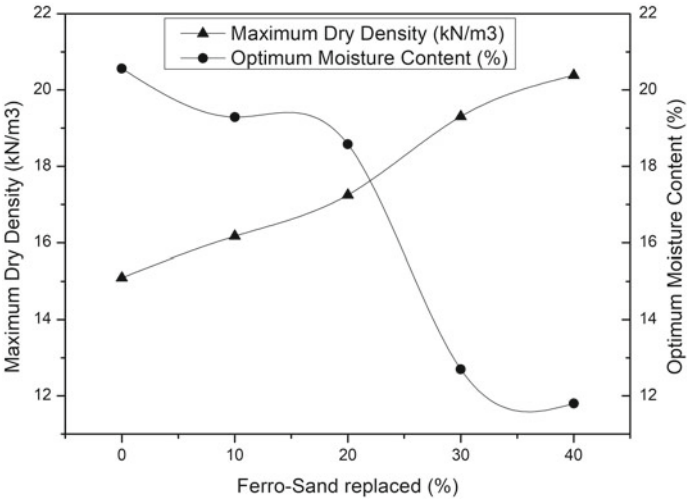

Fig. 2 Variation of maximum dry density and optimum moisture content with varying proportions of Ferro-Sand

Table 2 Effect of Ferro-Sand on the maximum dry density and optimum moisture content of the soft clayey soil

Sl. No.	Soil (%)	Ferro-Sand replaced (%)	MDD (kN/m^3)	OMC (%)
1	100	0	15.092	20.56
2	90	10	16.17	19.29
3	80	20	17.248	18.58
4	70	30	19.306	12.7
5	60	40	20.384	11.8

3.2 *Effect of Ferro-Sand on Unconfined Compressive Strength*

A notable increment in the UCS of the virgin soil is observed after the inclusion of ferro-sand into the soft clayey soil. The strength is maximum, i.e. 131.16 kPa, for 30% ferro-sand replaced and, thereafter, it goes on decreasing. This is observed because as the amount of granular ferro-sand increases and the soil particle becomes coarser in nature. Thus, the soil becomes less compressible. Due to pozzolanic nature of ferro-sand, the soil samples were cured for a duration of 7, 14, 28 days. The UCS increases when ferro-sand is mixed in different proportions. We observe the maximum increment in the strength of soil mix samples after 28 days of curing being 242.61 kPa, which is almost double the strength of soil without curing. The value of mix proportion is highest for 30% ferro-sand replaced with soil. The extracted sample is kept in desiccator for curing, to ensure the moisture content does not drop, by regular sprinkling of water. The curing of the soil sample is done to allow the ferro-sand to bond with the soil particle and form a homogenous mix that enhances the strength of the soil. We can also observe that the unconfined compressive strength value is highest, i.e. 205.64 kPa for 30% ferro-sand replaced soil after 14 days curing. The value is observed to increase in strength of 28% from 7 days curing. As it is observed from Table 3, the UCS test results of the soil sample tends to increase with the varying percentages of the ferro-sand and after its optimum state tends to decrease because the soil tends to become less compressible. The curing period of the soil samples helps in enhancing the strength of the soil mix because of the pozzolanic properties of the ferro-sand, as the ferro-sand particle binds with the soil particles and enhances its strength.

The increase in the percentage replacement of the soil with ferro-sand clearly shows in Fig. 3 that the strength of the soil blend increases. The 30% replacement of soil shows the maximum stability of the soil. This gain in the durability of the soil is because of the denser packing of the soil. With the pozzolanic action of the soil blend, the strength further increases to almost twice the strength of the soil blend without curing. The gradual decrease of the ferro-sand blend is because the higher proportion tends to bind the soil particle such that it cannot be compressed any further, thus is

Table 3 Effect of Ferro-Sand on the Unconfined Compressive Strength of the soft clayey soil

Sl. No.	Soil (%)	Ferro-Sand replaced (%)	UCS of soil (kPa)	UCS of soil mix (kPa) after 7 Days curing	UCS of soil mix (kPa) after 14 Days curing	UCS of soil mix (kPa) after 28 Days curing
1	100	0	44.74	44.74	44.74	44.74
2	90	10	77.29	96.03	109.34	121.44
3	80	20	107.01	132.6	153.41	170.99
4	70	30	131.16	160.52	205.64	242.61
5	60	40	101.39	126.48	155.76	188.44

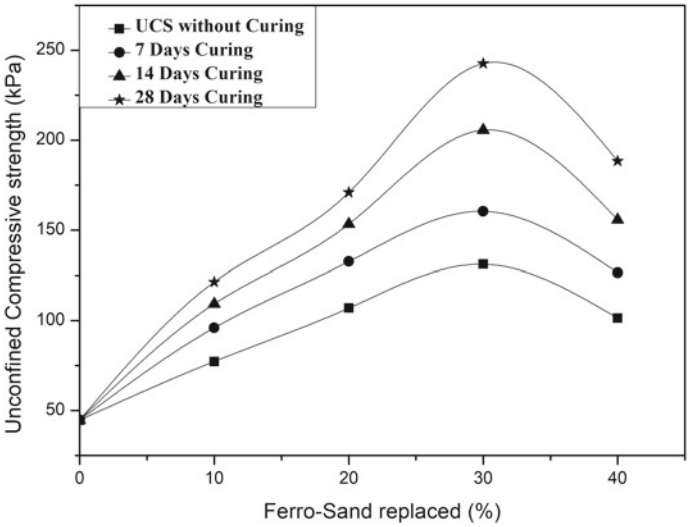

Fig. 3 Variation of Unconfined Compressive Strength of soft clayey soil with varying proportions of Ferro-Sand

not able to attain the strength required. After 28 days of moist curing, due to the pozzolanic effect, the strength gain in soil is maximum for 30% replacement with ferro-sand. This effect is similar to that of cement blended with soil, due to this effect the void space is reduced and the water contained in the diffused double layer of the surface of the clay particle is absorbed in the strength gaining process.

3.3 Effect of Ferro-Sand on Cohesion Intercept of Uncorrupted Soil and Angle of Shearing Resistance (Φ)

The shear strength of the blended soil sample is determined through the shear parameters. The unconsolidated–undrained test is conducted on the soil sample in confinement. This gives the peak value of the shear strength of the soil mix samples before failure. The improvement in strength of the soft clayey soil is due to the altering proportion the ferro-sand. The cohesion intercept of the ferro-sand blended soil increases, resulting in the enhancement of the shear strength of the soft clayey soil, as shown in Table 4.

The gain in the shear strength is gradual with sudden decrease in the 40% blend due to the coarser soil blend. The ferro-sand is coarser than the soft clayey soil and when mixed in 30% replacement it tends to make the soil sample coarser. The ferro-sand blended soil sample tends to gain shear strength because the granular ferro-sand particles offer resistance to shear force acting on the soil sample. Thus,

Table 4 Effect of Ferro-Sand on Cohesion Intercept and Angle of Shearing Resistance of the soft clayey soil

Sl. No.	Soil (%)	Ferro-Sand replaced (%)	Cohesion (kPa)	Angle of Shearing Resistance (°)
1	100	0	26.87	25.64
2	90	10	33.73	27.47
3	80	20	41.67	32.45
4	70	30	51.68	42.65
5	60	40	44.32	36.79

there is a considerable increment in the shearing resistance of the soft clayey soil. The cohesion intercept is indicates shear stability of the soil mix. The cohesion is highest for 30% ferro-sand, i.e. 51.68 kPa. The cohesion intercept increases up to 30% mix blend and then decreases, as observed in Fig. 4. The strength gain is of almost linear implying that the shear strength of the soil is in uniformity and increases constantly. The cohesive force between the soil particles and the ferro-sand increases because of the coarser ferro-sand tends to reduce the void space between the soil particles giving them a denser packing. Thus, the soil blend tends to resist the shear strength applied on the soil sample. The resistance further increases with the increase in the coarseness of the soil mix, but decreases when the mix proportion is increased. This is because the 40% ferro-sand replaced makes the soil coarser and the strength of the blend is weakened. The angle of shearing resistance (Φ) increases to 42.65° which is considerably greater than the angle of shearing resistance of 100% ferro-sand,

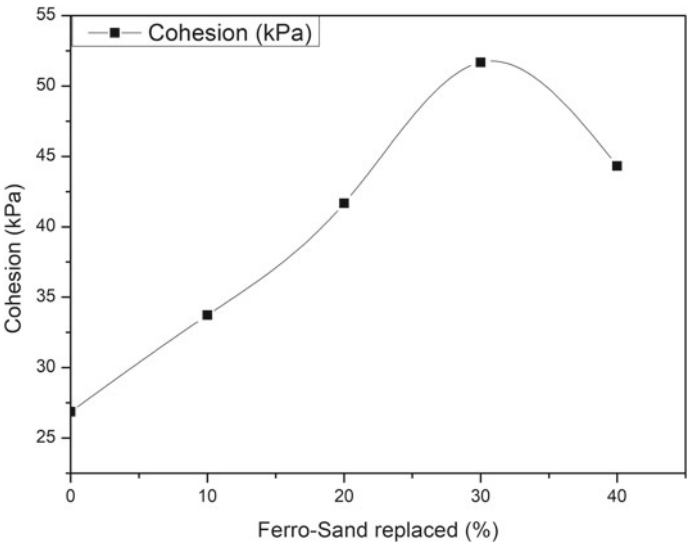

Fig. 4 Variation of Cohesion intercept with varying proportions of Ferro-Sand

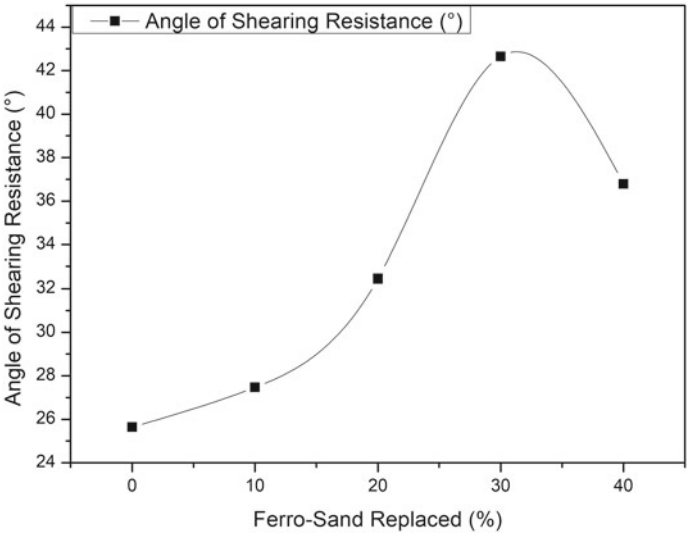

Fig. 5 Alteration of angle of shearing resistance with the varying proportions of Ferro-Sand

i.e. 40.76°. The further increase in the ferro-sand proportions decreases the shearing angle because the coarser ferro-sand particles tends to bind the soil into a denser packing which leads to the increase in the air voids which also decreases the shear strength of the soil blend as observed in Fig. 5. The maximum angle of friction is obtained for 30% ferro-sand blend. The soil mix is coarser and the ferro-sand binds with the soil due to the pozzolanic effect of it and increases its strength.

3.4 Effect of Ferro-Sand on California Bearing Ratio

The CBR value is the percentage ratio of the load exerted on the soil to the load exerted on the stone aggregate. The CBR value is crucial in construction of pavement, as it gives the strength of the subgrade, withstanding the load exerted on it. The CBR values of soaked soil mix samples is less than that of unsoaked soil mix samples. This is so because the soil is water cured for 4 days prior to the date of testing to analyse the blended soil sample in its drained state. We can observe that the CBR value of ferro-sand blended soft clayey soil increases from 2.69 to 6.69%, as shown in Table 5. This is because the coarser ferro-sand particles reduces the compressibility of the soil sample and gives a stabilized soil sample. The higher value of CBR after its optimum proportion is indicative that as the coarser particle increases, the CBR value also increases. The unsoaked CBR value is indicates the solidity of ferro-sand blended soil samples. The enhancing percentage of unsoaked CBR gives the strength of the subgrade without curing. The value of soaked CBR is observed to increase from 1.69 to 5.38%. The soaked CBR values give the field strength of the subgrade

Table 5 Effect of Ferro-Sand on the Soaked and Unsoaked California Bearing Ratio

Sl. No.	Soil (%)	Ferro-Sand replaced (%)	Soaked CBR (%)	Unsoaked CBR (%)
1	100	0	2.69	1.96
2	90	10	3.42	2.98
3	80	20	4.14	3.42
4	70	30	6.69	5.38
5	60	40	8.15	7.56

upon construction. The increasing soaked CBR value infers the subgrade strength of soil sample admixed with ferro-sand. The soil can be utilized for the construction of pavements with low to medium traffic load. This is so because the soil sample has been tested by the dry density value as per the standard Proctor test. The dry density value obtained by this method is of medium compressibility. Thus, the CBR values are also of low to medium compressibility. We can observe from Fig. 6 that the soaked CBR value is less than unsoaked CBR value because the draining of the soil leads to absorption of water into the air voids which makes the soil further compressible.

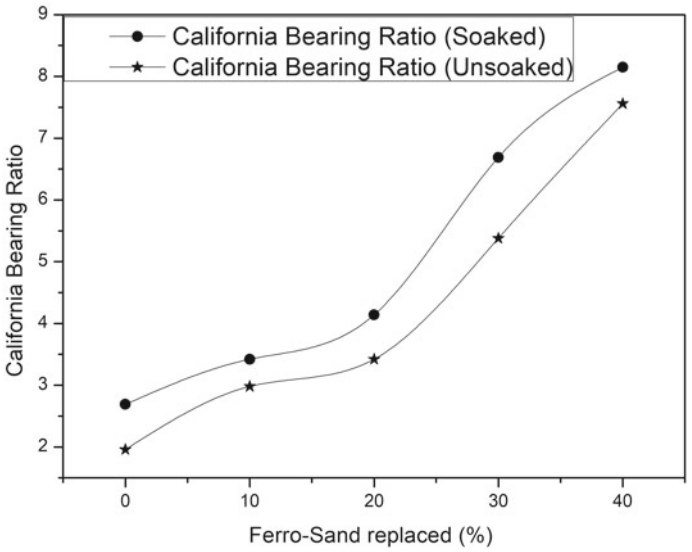

Fig. 6 Variation of Soaked and Unsoaked California Bearing Ratio with different proportions of Ferro-Sand

4 Conclusions

Stabilization of soft clayey soil mixed with ferro-sand was studied through an experimental investigation and the following conclusions are drawn.

- Replacement of virgin soil with ferro-sand in proportions from 0 to 40% with an increment of 10% has the benefits of a denser mix blend.
- The standard Proctor test results clearly indicates a considerable decrease of 42.06% in the OMC of the virgin soil and increment of 35.06% in the MDD of the soil mix samples which implies that the soil and ferro-sand blend form a denser packing.
- The UCS of the virgin soil after 28 days of moist curing increases to 242.61 kPa from 44.74 kPa with an improvement of 442.26 for 30% replacement of ferro-sand, thus inferring that the soil blend becomes incompressible in its nature.
- The moist curing of 28 days enhances the pozzolanic property of the soil by binding the coarser ferro-sand particles with the fine grained soil particles.
- The cohesion intercept increases from 26.87 to 51.68 kPa; thus, the angle of shearing resistance also increases from 25.64° to 42.65°. Thus, the shear strength of soft clayey soil improves with the inclusion of coarser ferro-sand particles into it.
- The soaked CBR of the soil blend increases from 1.96 to 5.38% indicating that the soil treated with ferro-sand can be utilized for the subgrade of the pavement.
- Thus, we can easily conclude that the optimum percentage of ferro-sand and soft clayey soil is 30:70.

Also, there is a potential for ferro-sand to be utilized as a geotechnical material in the near future. The physical properties of the ferro-sand strongly resemble that of sand so it can be utilized as a substituent for sand in the infrastructure sector, thus paving way for sustainable development of the nation through an eco-friendly approach.

References

1. Das BM, Tarquin AJ, Jones AD (1993) Geotechnical properties of a copper slag. Transp Res Record, 941
2. Gorai B, Jana RK, Premchand (2003) Characteristics and utilisation of copper slag-a review. Res Cons Rec 39:299, https://doi.org/10.1016/s0921-3449(02)00171-4
3. Havangi VG, Sinha AK, Mathur S, Prasad P (2008) Experimental study on the use of copper slag wastes in embankment and pavement construction. Symposium on engineering of ground & environmental Geotechnics (SEG 2), Hyderabad
4. Lavanya C, Sreerama Rao A, Darga Kumar N (2011) A review on utilization of copper slag in geotechnical applications. In: Proceedings of Indian geotechnical conference, December 15–17, Kochi (Paper No. H-212)
5. Patel S, Shahu JT, Senapati A (2012) Feasibility of Copper Slag–Fly Ash Mix as a road construction material. ACEE Int J Transp Urban Dev 2. https://doi.org/10.01.IJTUD.02.01.33

6. Baraskar T, Ahirwar SK (2014) Study on California Bearing Ratio of Black cotton soil using waste copper slag. IJSCER 3(4):45–56
7. Shahiri J, Ghasemi M (2017) Utilization of soil stabilization with cement and copper slag as subgrade materials in road embankment construction. Int J Trans Eng 5, https://doi.org/10.22119/IJTE.2017.45834
8. Raj S, Rai AK, Havanagi VG (2018) Suitability of stabilized copper slag and fly ash mix for road construction. World J Eng. https://doi.org/10.1108/WJE-08-2017-0220
9. IS: 2720 (Part 1) (1983) Methods of test for soils, Preparation of dry soil samples for various tests
10. IS: 2720 (Part 2) (1983) Methods of test for soils, Determination of water content of soil
11. IS: 2720 (Part 7)- 1983 Methods of test for soils, Determination of water content-dry density relation using light compaction
12. IS: 2720 (Part 16) (1983) Methods of test for soils, Laboratory determination of CBR

Soil Subgrade Stabilization Using Non-woven Polypropylene Geotextile

Ayush Mittal and Shalinee Shukla

Abstract Roads are the quintessential component for the social as well as economic upliftment of a country. Our country has a total road network of greater than 60 lakh kilometers of which 79% consists of rural roads. Around 20% of land area of our country is covered with the kind of soils having low shear strength and California bearing ratio (CBR) values. The pavement which is constructed over such soils deteriorates significantly under heavy wheel load which leads to substantial enhancement in maintenance and construction costs. To overcome such situations the soil reinforcement techniques have to be resorted to as replacement and removal of soil would lead to heavy economic liability. In this work, an attempt was made to study the effects of non-woven synthetic geotextile on the strength behavior of the soil. The geotextile was placed in single as well as multiple layers from the top of mold at different depths in soil subgrade and optimum moisture content (OMC), maximum dry density (MDD), soaked CBR, and unconfined compressive strength (UCS) values were determined experimentally. Multiple linear regression models were developed for predicting soaked CBR and UCS. Maximum improvement of 66% in CBR and 45% in UCS was reported when the soil sample was reinforced with double-layer geotextile (i.e., 25 mm and 50 mm).

Keywords Geotextile · Pavement · Stabilization · Strength · Subgrade

1 Introduction

To meet the demands of an increasing population, the engineers are compelled to use soft soils which were earlier not in use in order to set up more infrastructure projects. This brings the role of soil reinforcement (in form of bars, strips, sheets, fibers, and rods) technique into the picture. In India, 65% of freight traffic and 90% of

A. Mittal (✉)
REC Ambedkar Nagar, Ambedkar Nagar, Akbarpur 224122, U.P, India
e-mail: ayushmittalce0012@gmail.com

S. Shukla
MNNIT Allahabad, Prayagraj 211004, U.P, India

© Springer Nature Singapore Pte Ltd. 2021

K. K. Pathak et al. (eds.), *Recent Trends in Civil Engineering*, Lecture Notes in Civil Engineering 77, https://doi.org/10.1007/978-981-15-5195-6_39

passenger traffic passes through roads. To tackle such huge traffic, good quality roads are required. The performance of pavements depends mainly upon the subgrade soil properties since it serves as the foundation for pavement. The use of geosynthetic materials in soil is a physical method which is gaining acceptance worldwide because of saving in cost and time. The World Bank has made it mandatory to use geotextiles in construction projects funded by it [1]. The geotextiles improve performance by confinement/lateral restraint, tensioned membrane effect, and increased bearing capacity, leading to cost savings in costly sub-base and base aggregate materials.

The benefit of using non-woven polyester geotextile as reinforcement of different Egyptian soils and their effect on the reinforcement ratio of soils with geotextile materials were investigated by [2]. Significant improvement in reinforcement ratio of clayey soil reinforced with woven and non-woven geotextile, interfaced between unbound gravel and soft subgrade placed in an unpaved flexible pavement system utilizing the California Bearing Ratio (CBR) test was reported by [3]. Reference [4] studied the effect of geotextile on CBR and UCS values and found that maximum improvement occurs for single layer geotextile placement at 6 cm from the top of mold. Reference [5] concluded from visual observations that portion containing geotextile shows less undulation, cracks, and settlement compared to the unreinforced portion. Reference [6], on the basis of field trials, concluded that the use of geotextile improves the performance of pavement with reduced thickness of aggregate layer and frequency of maintenance required. Reference [7] concluded that as the number of reinforcing layers increases peak strength increases, failure takes place at greater strain and there is a smaller loss of post-peak strength. Reference [8] concluded that the use of geotextile increases permeability and it further improves with a layer of sand cushion but an increase in normal stress reduces permeability. Reference [9] concluded that use of geotextile in middle of sample reduces freeze–thaw effect by reducing the strength loss and taking water to deeper parts of soil as evidenced from tomography images. Reference [10] studied the effects of using geotextile on the CBR value of soils having different gradations. It was found that maximum improvement occurs for soil having more fine percent. Reference [11] studied and presented a gist on geosynthetic products and their standards. The study concluded that the effect of geosynthetic materials (with regard to reduction of base-course thickness) is up to 40% as compared with unreinforced section. In addition to the economical benefits, there are adequate environmental benefits associated with aggregate savings like reduced transportation by trucks, so lesser air pollution, lesser energy consumption, and lesser greenhouse gas (GHG) emissions.

In the present study, non-woven polypropylene geotextile was used as a reinforcing material in single and multiple layers at different depths for strength improvement of poor subgrade soil. Predictive models were formed for future estimation of CBR and UCS using StatPlus:mac LE software.

2 Materials Used

2.1 Soil

The soil sample used in this study was collected at Chakghat (25.04°N, 81.72°E), Rewa District, Madhya Pradesh, which is majorly covered by fine-grained soils. As the topmost soil is likely to contain organic matter, the trail pits of 1 m depth were dug below the ground level to collect the soil sample. The soil was air-dried and was pulverized with a wooden mallet. The pulverized soil was sieved through 4.75 mm sieve and was characterized by grain size analysis and Atterberg's limit tests. As per Indian standard classification system IS 1498 (1970), soil was classified as silt of high compressibility (MH). The various index and engineering properties of soil are shown in Table 1. The grain size distribution curve of soil is shown in Fig. 1.

Table 1 Chakghat soil characteristics

Property	Outcome
Atterberg's Limits	
(a) Liquid Limit (%)	52.20
(b) Plastic Limit (%)	34.88
(c) Shrinkage Limit (%)	18.85
(d) Plasticity Index (%)	17.32
Grain Size Distribution	
(a) Gravel (%)	2.95
(b) Sand (%)	6.46
(c) Silt (%)	64.67
(d) Clay (%)	25.92
Water Content (%)	8.75
Specific Gravity	2.69
Free Swell Index (%)	42.10
pH value	7.72
Optimum moisture content (%)	14.80
Maximum dry density (g/cc)	1.828
Unsoaked CBR (%)	7.32
Soaked CBR (%)	2.09
Swelling pressure (Kg/cm^2)	0.57
Unconfined compressive strength (kN/m^2)	128.63

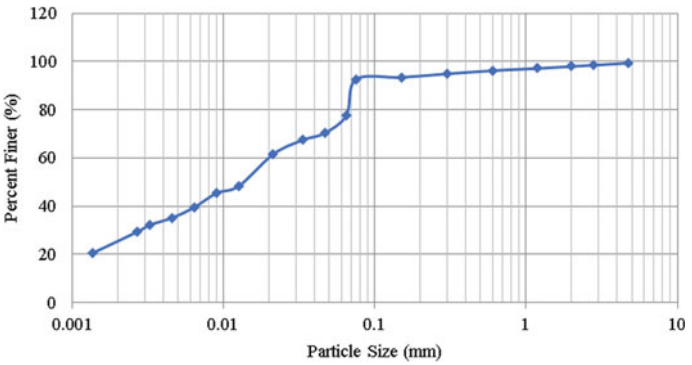

Fig. 1 Grain size distribution curve of the Chakghat soil

2.2 Geotextile

Non-woven polypropylene geotextile (PR 20) was used in the present study, which was selected from the list of materials accredited by the Indian Roads Congress. Figure 2 shows the non-woven geotextile. The different properties of (PR 20) geotextile are stated in Table 2.

Fig. 2 Non-Woven Polypropylene Geotextile (PR 20)

Table 2 Index properties of Non-woven Geotextile (PR 20)

Property	Unit	Provided by manufacturer	Tested in BTRA
Thickness at 2 kPa (ASTM D 5199)	mm	1.6	2.34
Physical Characteristics	–	Staple fiber needle-punched non-woven geotextile	–
Polymer	–	100% Polypropylene	–
UV Resistance (ASTM D 4355)	–	>70% of strength retention	–
Mass/Unit Area (ASTM D 5261)	g/m^2	200	223.1
Mechanical properties			
Wide width tensile strength (ASTM D 4595)	KN/m	11/13 [Machine Direction (MD)/Cross Machine Direction (CMD)]	13.94/19.77 (MD/CMD)
Tensile elongation (ASTM D 4595)	%	55/55 (MD/CMD)	59.8/58 (MD/CMD)
CBR puncture resistance (ASTM D 6241)	N	2050	2662
Grab tensile strength (ASTM D 4632)	N	720/770 (MD/CMD)	749/891 (MD/CMD)
Grab elongation (ASTM D4632)	%	60/60 (MD/CMD)	67.2/60.8 (MD/CMD)
Index puncture strength (ASTM D 4833)	N	420	552
Trapezoidal tear strength (ASTM D 4533)	N	320 (Weaker direction)	332 (Weaker direction)
Mullen bursting strength (ASTM D 3786)	kpa	2175	2629
Hydraulic properties			
Water flow normal to plane (50 mm Head) (ASTM D 4491)	$L/m^2/s$	80	–
Permeability (ASTM D 4491)	cm/s	0.26	–
Physical identification			
Color	–	White	White

3 Experimental Work

The tests performed on soil samples to determine the performance of the application of geotextile in different layers (single and multiple) in soil subgrade were heavy compaction, UCS, and soaked CBR. Heavy compaction test was performed as per IS

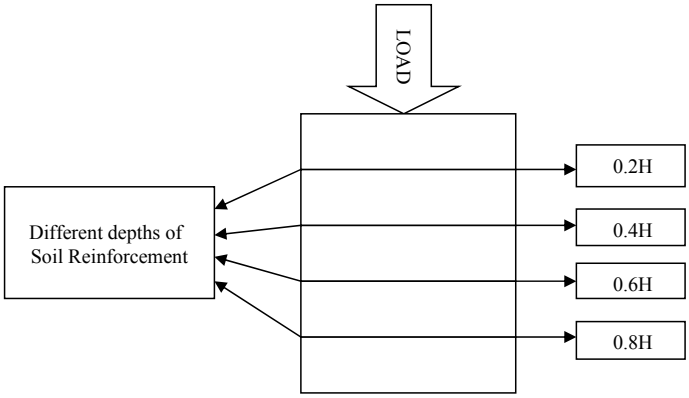

Fig. 3 Placement of Geotextile layers in the soil specimen

2720 (Part 8)-1983, CBR test was performed as per IS 2720 (Part 16)-1987, and UCS test was performed as per IS 2720 (Part 10)-1991. Figure 3 shows the positioning of various geotextile layers from the top of the specimen.

3.1 Heavy Compaction Test

The outcomes of OMC as well as MDD of the soil sample reinforced with non-woven geotextile are depicted in Table 3. It was found that MDD values for all reinforced cases were more as compared to unreinforced one with maximum of 1.918 g/cc for single layer of geotextile at 0.4 H depth and 1.958 g/cc for double layer of geotextile at 0.4 H and 0.6 H depths from top of the mold. This increase in MDD was because of closer packing of soil particles caused by confinement and bonding effect of

Table 3 Value of soil reinforced with Geotextile (OMC-MDD)

Position of Geotextile as from top of specimen	Depth of Geotextile as from top of mold	Experimental Outcomes (PR 20)	
		OMC (%)	MDD (g/cc)
Without Geotextile	Virgin Soil	14.80	1.828
25 mm	0.2H	15.20	1.876
50 mm	0.4H	15.00	1.918
75 mm	0.6H	15.60	1.878
100 mm	0.8H	14.40	1.906
25 mm and 50 mm	0.2H & 0.4H	13.50	1.922
25 mm and 75 mm	0.2H & 0.6H	13.80	1.908
50 mm and 75 mm	0.4H & 0.6H	12.00	1.958

Table 4 Value of soil reinforced with Geotextile (Soaked CBR)

Position of Geotextile as from top of specimen	Depth of Geotextile as from top of mold	Experimental outcomes (Soaked)	
		CBR (%) 2.5 mm	CBR (%) 5 mm
Without Geotextile (Unsoaked)	Virgin Soil	7.32	7.21
Without Geotextile (Soaked)	Virgin Soil	2.09	1.86
25 mm	0.2H	2.99	2.67
50 mm	0.4H	3.31	3.02
75 mm	0.6H	2.79	2.55
100 mm	0.8H	2.26	2.09
25 mm and 50 mm	0.2H & 0.4H	3.48	3.16
25 mm and 75 mm	0.2H & 0.6H	3.31	3.02
50 mm and 75 mm	0.4H & 0.6H	2.96	2.79

geotextile layer. The OMC for unreinforced specimen is 14.80% which changes to 15.20%, 15.00%, 15.60%, 14.40%, respectively, when the geotextile was placed in a single layer at depths of 0.2H, 0.4H, 0.6H, and 0.8H. This value further changed to 13.50%, 13.80%, and 12.00%, respectively, for double-layer geotextiles at 0.2H and 0.4H, 0.2H and 0.6H, and 0.4H and 0.6H depths from the top of the mold. This reduction in OMC in double-layer reinforcement is due to non-absorbance of water by geotextile layers.

3.2 CBR Test

The results of CBR for the specimen reinforced with as well as without geotextile are depicted in Table 4. The CBR value for unreinforced soil was 2.09% which changed to 2.99%, 3.31%, 2.79%, and 2.26%, respectively, when the geotextile was placed in a single layer at depths of 0.2H, 0.4H, 0.6H, and 0.8H. This value increased to 3.48%, 3.31%, and 2.96%, respectively, for double-layer geotextiles at 0.2H and 0.4H, 0.2H and 0.6H, and 0.4H and 0.6H depths from the top of the mold. This was because of a greater resistance offered by the geotextile to penetration of plunger in the top layers.

3.3 UCS Test

The results of compressive strength and failure strain for the soil specimen reinforced with as well as without geotextile are depicted in Table 5. Remarkable strength

Table 5 Value of soil reinforced with Geotextile (UCS and Failure Strain)

Position of Geotextile as from top of specimen	Depth of Geotextile as from top of mold	Experimental outcomes	
		UCS (KN/m^2)	Failure Strain (%)
Without Geotextile (mm)	Virgin Soil	128.63	4.02
25	0.2H	157.90	5.74
50	0.4H	173.30	6.89
75	0.6H	156.36	3.44
100	0.8H	143.76	2.29
25 and 50	0.2H & 0.4H	184.21	5.74
25 and 75	0.2H & 0.6H	180.04	5.17
50 and 75	0.4H & 0.6H	169.72	4.59

improvement was observed when the geotextile was placed in the upper layers of the soil subgrade as compared to the lower ones for both single- and double-layer reinforcement cases. This increase in UCS was attributed to surface friction, interlocking effect, and interception of failure plane within the specimen by the geotextile layer causing uniform stress distribution within the soil sample. Smaller post-peak strength loss and greater strain at failure are observed for all geotextile-reinforced specimens indicating more ductile behavior and improved rupture strength. The failure strain increased from 4.02% for unreinforced soil to a maximum value of 6.90% and 5.75%, respectively, for single- and double-layer geotextile-reinforced specimens. This was due to a greater flexibility of the geotextile as compared to the soil.

4 Statistical Analysis

The regression analysis can be said to be a statistical technique for modeling and investigating the relationship between variables. To obtain correlations of CBR and UCS with compaction characteristics (OMC & MDD) and various depths of geotextile (0.2H, 0.4H, 0.6H, 0.8H, 0.2H and 0.4H, 0.2H and 0.6H, 0.4H and 0.6H), regression analysis has been performed using StatPlus:mac LE software. Table 6 shows the model summary of CBR and UCS. Figures 4 and 5 show the plots of predicted and observed values of soake, d CBR and UCS respectively. Equations (1) to (2) formulated for geotextile reinforcement conditions are presented below:

Table 6 Model summary for soaked CBR and UCS

Test	R	R Square	Adjusted R Square	Prediction R Square	Standard Error (S)
CBR	0.981	0.963	0.914	0.724	0.146
UCS	0.980	0.961	0.909	0.794	5.682

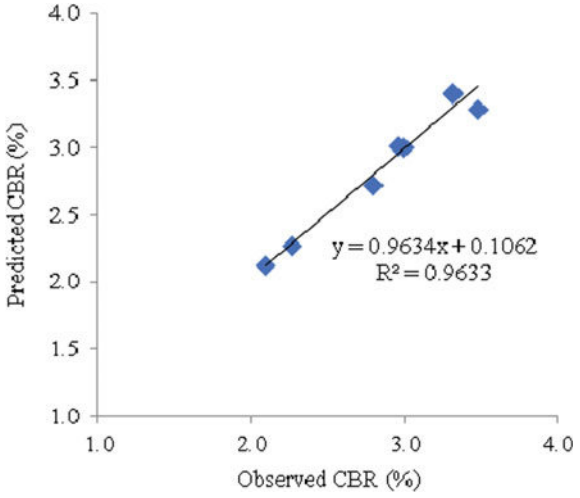

Fig. 4 Correlation between predicted and observed soaked CBR

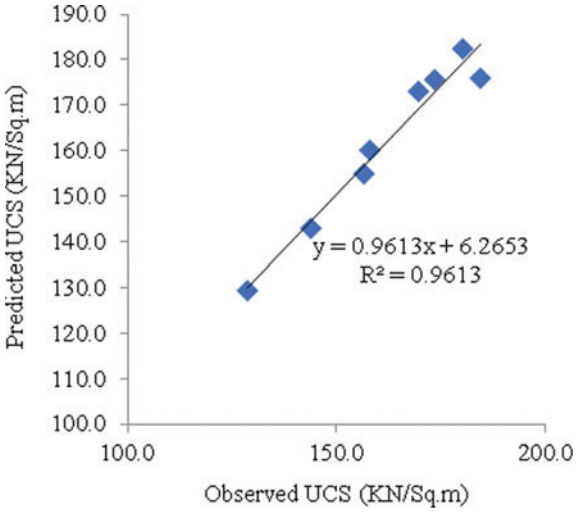

Fig. 5 Correlations between Predicted and Observed UCS

$$\text{Soaked CBR } (\%) = -41.379 + 0.590 \times OMC(\%) + 1.091 \times MDD\left(\frac{\text{KN}}{\text{m}^3}\right) - 0.011 \times \text{Single Layer Depth } (mm) + 0.008 \times \text{Double Layer Depth } (mm) \quad (1)$$

$$\text{UCS } \left(\text{KN}\Big/\text{m}^2\right) = -1,295.378 + 18.863 \times OMC(\%) + 62.657 \times MDD\left(\frac{\text{KN}}{\text{m}^3}\right) - 0.394 \times \text{Single Layer Depth } (mm) + 0.552 \times \text{Double Layer Depth } (mm) \quad (2)$$

5 Conclusion

The MDD value for all specimens with geotextile comes out to be greater than the unreinforced sample, with a larger improvement in double-layer application. This was due to the improved confinement and bonding effect of the geotextile layer on soil. With the increase in MDD, the value of OMC was decreasing which was more pronounced in double layers due to a reduction in void spaces. CBR value shows a maximum increase of 58% for single- (50 mm) and 66% for double-layer (25 mm and 50 mm) geotextiles as compared with virgin soil specimen. More improvement in CBR was seen in upper layers as compared to lower ones. This may be because of more resistance offered by geotextile to penetration when placed in the upper portion of soft subgrade. UCS value shows a maximum increase of 35% for single- (50 mm) and 45% for double-layer (25 mm and 50 mm) reinforcements in comparison to virgin soil. The increase in UCS value occurred due to confinement and surface friction effect provided by geotextile sheet.

The models developed will help in the future prediction of soaked CBR and UCS, thus eliminating the requirement of experimental analysis which is cumbersome, time-consuming, and costly. We could expect these models to explain 72.4% and 79.4% variability in predicting new observations for CBR and UCS, respectively.

For achieving maximum improvement in soil properties, the geotextile should be placed within a depth of 50 mm from top of mold. Thus, it can be concluded that the use of non-woven geotextile in pavement subgrade results in economical pavement design with reduced structural section. Hence, it saves costly sub-base and base aggregate materials and reduces frequent maintenance requirements.

References

1. Special Section Geosynthetics in Infrastructure. Indian Infrastructure, 63–76, July (2010)
2. Elshakankery MH, Almetwally AA, Tawfik KA (2013) Experimental study of Bearing Capacity for Egyptian soils reinforced by geo textiles. J Appl Sci Res 9:2378–2385
3. Kumar PS, Rajkumar R (2012) Effect of Geotextile on CBR strength of unpaved road with soft sub grade. EJGE 17:1355–1363
4. Sivapragasam C, Vanitha S, Arun VM, Sutharsanam S (2010) Study on synthetic Geotextiles for road pavements. IGC Mumbai Chapter & IIT Bombay, pp 255–258
5. Tailor RM, Desai MD, Shah NC (2011) Geotextile as reinforcement in flexible pavement for swelling subgrade. IGC Koch, pp 565–568
6. Viswanadham BVS, Satkalmi V (2008) Field trials with polypropylene woven geotextiles. In: First pan American geosynthetics conference and exhibition, Mexico, pp. 1112–1118
7. Noorzad R, Mirmoradi SH (2010) Laboratory evaluation of the behaviour of a geotextile reinforced clay. Geotextiles and Geomembranes 28:386–392 Elsevier
8. Raisinghani DV, Viswanadham BVS (2010) Evaluation of permeability characteristics of a geosynthetic-reinforced soil through laboratory tests. Geotextiles Geomembranes 28:579–588 Elsevier
9. Ghazavi M, Roustaei M (2013) Freeze-thaw performance of clayey soil reinforced with geotextile layer. Cold regions science and technology, Elsevier, 89:22–29

10. Naeini SA, Mirzakhanlari M (2008) The effect of geotextile and grading on the bearing ratio of granular soils. EJGE 13:1–10
11. Ingle GS, Bhosale SS (2013) Geo synthetic Reinforced Flexible Pavement: gateway of the sustainable pavement. Indian Highways 41:6–15

Assessment of Scaling Effects on Plugging of Driven Piles Using Image Analysis

G. Sreelakshmi, M. N. Asha, and S. Nandish

Abstract In recent years, open-ended steel pipe piles have been used in the foundations of urban and coastal structures such as long-span bridges, harbor terminals, and offshore wind power structures. It is found that pile capacity depends directly on pile dimensions and plugging phenomenon, especially in the case of open-ended driven piles. The present study investigates the effect of variation of pile cross sections and plugging behavior through image analysis. Three different scaling factors of 10, 5.7, and 4.5 are chosen for selecting pile dimensions and aluminum piles are modeled using Wood's scaling law. Later, modeled piles are subjected to impact loads replicating energy of standard penetration test (SPT) in sandy soil for different infill densities. The experimental process is captured through a digital camera and later images are analyzed through Geo PIV software to understand displacement behavior and strain path. It is found that, with an increase in pile diameter, there is a decrease in plugging and an increase in shear strain contour around the pile tip. It is also seen that shear strain concentration zones are developed around the annular area of a larger diameter pile tip region.

Keyword Plugging · Scaling factors · Standard penetration test · Strain path

1 Introduction

Open-ended driven piles are usually preferred in many of the deep foundation systems due to its ease of fabrication, drivability, and ease of handling conditions. Driven piles usually develop its capacity through end bearing resistance, frictional resistance, or

G. Sreelakshmi (✉)
VTU RRC, Department of Civil Engineering, CMR Institute of Technology, Bengaluru, India
e-mail: sreelakshmi.g@cmrit.ac.in

M. N. Asha · S. Nandish
Department of Civil Engineering, CMR Institute of Technology, Bengaluru, India
e-mail: asha.n@cmrit.ac.in

S. Nandish
e-mail: nandishshiratti@gmail.com

© Springer Nature Singapore Pte Ltd. 2021

K. K. Pathak et al. (eds.), *Recent Trends in Civil Engineering*, Lecture Notes in Civil Engineering 77, https://doi.org/10.1007/978-981-15-5195-6_40

combined end bearing and frictional resistances. When open-ended piles are driven in granular infills, a soil plug developed within pile–soil interface zone. With the increase in pile diameter, the soil plug developed undergoes a significant decrease in the volume inside the pile shaft region. It is seen that the driving resistance and the bearing capacity of driven piles are governed by this plugging effect.

2 Literature Survey

Several experimental studies have been carried out to investigate the plugging effect on hollow driven pile by researchers [1–4] and they stated that open-ended piles behave as closed pile under static loading. However, that the open-ended pile requires less installation effort than a closed-ended pile under the same soil conditions as the number of blows needed for driving in sand is lower for an open-ended pile than for a closed one [5]. But very few researchers [6] have investigated the scaling effects of driven and bored piles with embedment ratios in the sand bearing stratum. A formula for reduction factors for ultimate point resistance was developed for large diameter piles that estimated a decrease in pile resistance with increasing pile diameter and sand density near the pile point. The scaling effect of axially loaded open-ended piles in pulling and pushing conditions was studied. Results indicated that when pile diameter increased, there was a decrease in bearing capacity of the pile which was more pronounced in pushing than pulling conditions in denser media. It was also concluded that, with an increase in pile diameter, there was a decrease in a volume change of infill around the shaft region [7]. The effect of pile diameter on end bearing capacity of open-ended driven piles in sand was examined and sand plug density was measured. Finite element analysis was carried out to examine sand plug behavior and concluded that tip resistance reduced with an increase in pile diameter. This was mainly due to the result of non-development of stable arches (soil plug) in large diameters or because of the development of large soil displacements around the pile driving zone [8]. In recent years, many researchers have used image-based tool to visualize the displacement and deformation of infill materials in various geotechnical processes through digital image correlation. Some image-based methods are X-ray, stereophotogrammetric techniques, digital image correlation techniques (DIC), and computer-based image processing techniques which are applied to measure planar deformation fields in element and model test studies. PIV (particle image velocimetry) is one of the DIC techniques currently used in the field of civil engineering. GeoPIV software is a MATLAB based tool developed by [9] working on the principles of PIV. Plane strain model studies were carried in a tank of 1000 mm length and 745 mm depth and Geo PIV was used for analyzing images. It was concluded that the image analysis technique offered sufficient precision to measure pre-failure strains and offered flexibility to capture non-homogenous soil deformations [10]. Plane strain model fits well since strain components developed along horizontal and vertical components are only monitored during pile penetrations. Researchers [11] found that image-based deformation measurement is suited best for geotechnical applications and demonstrated

that enhanced measurement precision improves the clarity of the interpretation of all deformation modes, including rigid body displacements, rotations, and strains. Visualization of soil behavior helped to identify macroscopic failure mechanisms, provided stronger experimental support for geotechnical analysis, and to develop complex constitutive or discrete element models. The pile–soil interaction behavior on hollow and solid closed-end single pile and pile groups was investigated through image analysis. The surface heave developed around hollow pile under axisymmetric loading was more than solid pile due to lesser mass density of hollow pile than solid piles [12].

From the literature, it is observed that PIV technique has been used by researchers for investigating pile–soil interaction. Though image analysis can be used for measuring deformations, its potential toward estimating the plugging effect in piles has not been explored by any researcher. The main focus of the present study is to use the principles of particle image velocimetry, to estimate soil plug length in the hollow piles and analyze the deformation patterns at the pile–soil interface. A comparison of pile capacity with available methods is not presented in the current paper since work is concentrated toward investigating plug behavior through image analysis.

3 Methodology

Methodology adopted to ascertain the bearing capacity can be sequenced as follows:

- Characterization of infill material and estimation of its friction angle at different dry densities.
- Modeling of pile dimensions using scaling laws [13].
- Fabrication of steel tank in accordance with [14].
- Image acquisition using high-resolution digital camera and assess deformation profiles using Geo-PIV software.
- Assessment of pile drivability and soil plug length for different infill densities.

4 Experimental Work

Hollow open-ended piles are used for the experimental studies as it facilitates in capturing strain behavior at interface region as well as plug measurement along pile shaft through image analysis. The dimensions of the model pile and rammer have been determined by using the scaling law proposed by [12]. A factor of 1/10, 1/5.7, 1/4.5 are used for scaling length and $1/10^5$ has been used for scaling flexural rigidity. Aluminum half-section hollow piles of outer diameter and inner diameters, (12, 11.5 mm; 19, 18.5 mm; 32, 31.5 mm) (length to diameter ratios of 10), with open ends, has been used. Figure 1 shows the schematic sketch of pile cross section with pen markings at 1 cm interval.

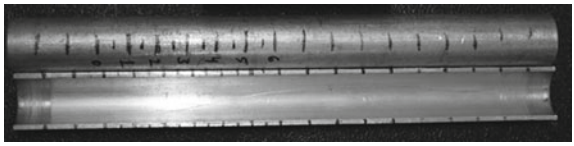

Fig. 1 Schematic sketch of pile cross section

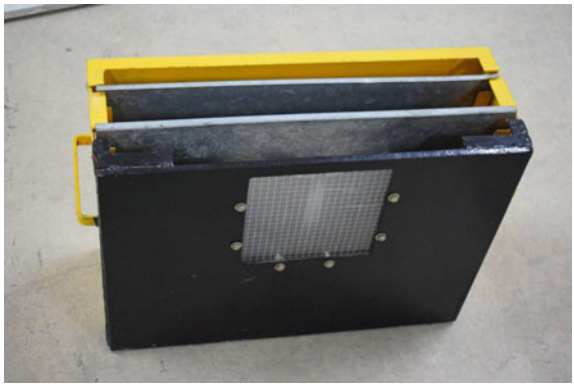

Fig. 2 Schematic sketch of steel chamber

The steel tank (Fig. 2) has dimensions 600 mm × 200 mm in plan and 450 mm depth [13] with perspex material with grid markings on one side/face (longer direction) with vertical partitions to replicate plane strain conditions.

Sandy soil with an average of less than 3.8 mm has been used as the infill material. The sand is deposited by pluviation method to achieve uniform density. Three different heights of fall had been used in the present study; viz., 5, 10, and 15 cm. Table 1 presents the physical properties of infill used in the experiment. In the present experimental study, hammer of masses 42.6 gm, 360 gm, and 760 gm falling from a height of 100 mm has been used to apply impact loads for driving the hollow piles. Figure 3 shows the standard penetration rammer model.

During pile driving, numbers of blows, soil plug length, and pile penetration depths are measured at every 15 mm for a total of 45 mm. The size of soil plugs and deformation around the pile during pile driving is captured with the help of high-resolution digital camera. When the pile is driven into the infill, a video is recorded,

Table 1 Physical properties of sand

Index property	Value
Coefficient of uniformity C_u	0.723
Coefficient of curvature C_c	7.64
Specific gravity G_s	2.584
Unit weight (28.3 cm) height of fall	14.2 kN/m^3
Unit weight (13.3 cm) height of fall	13.73 kN/m^3
Unit weight (5 cm) height of fall	12.75kN/m^3

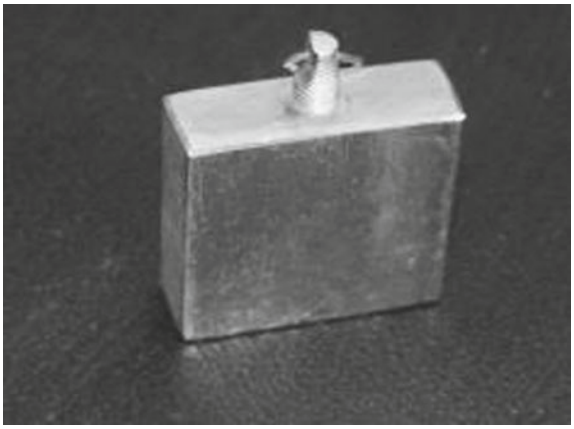

Fig. 3 Schematic sketch of standard penetration rammer model

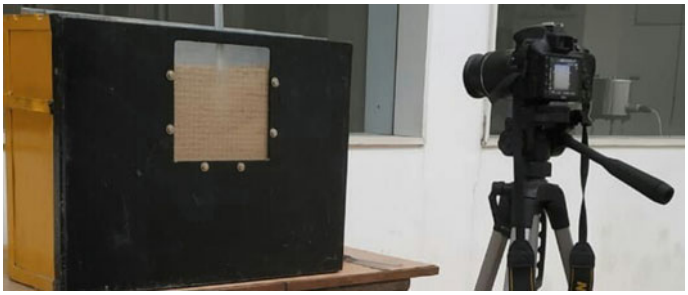

Fig. 4 Schematic sketch of experimental setup

and using an image grabber tool, still images at different microseconds are captured. Figure 4 shows the photograph of a detailed experimental test setup. The images are later analyzed using Geo-PIV software to capture the deformation profiles of the founded soil.

5 Results and Discussions

5.1 Effects of Scaling Factors on Soil Plugging Under Various Densities

The variations of soil plugging vs pile penetration are studied for three different scaling factors, viz. 10, 5.7, 4.5, and 12 mm, 19 mm, and 32 mm, respectively. Figure 5a, and 5b shows the variation of plugging behavior with respect to penetration

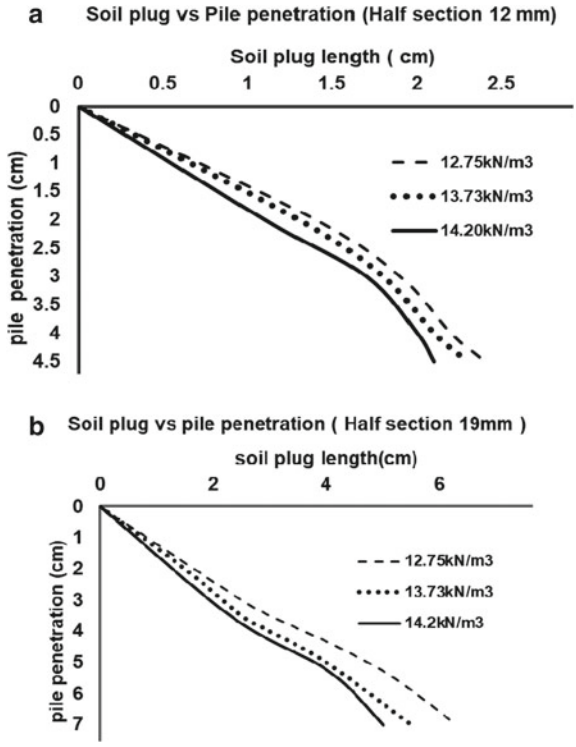

Fig. 5 **a** Variation of plugging for 12 mm with infill density, **b** variation of plugging for 19 mm with infill density

depth for 12 and 19 mm diameter half-section piles. Higher the density of the sand, higher will be the shear resistance offered by the sand and hence, more will be the resistance offered by the pile towards its deformation. From Figure. 5a, and 5b, it is seen that plug length is highest for loose sand and lowest for dense sands. When hollow pile is driven into the ground, the soil enters inside the pile in the initial stage of pile driving at very shallow depths which in later stage leads to densification of the sand at the pile tip. A similar behavior is seen in the case of a 32 mm pile also.

5.2 Effect of Scaling Factors on Shear Strain Contours Under Different Infill Densities

The shear strain development of the soil domain around hollow half pile section of 12 mm and 32 mm diameter under impact loading in three different densities (12.75 kN/m^3, 13.73 kN/m^3, 14.20 kN/m^3) are through obtained image analysis. Figure 6a, and 6b shows the comparison of shear strain contour for 12 mm diameter (scaling factor, $n = 10$) and 32 mm diameter (scaling factor, $n = 4.5$) for an infill density of 14.20 kN/m^3. From Fig. 6a, and 6b, it is observed that when the diameter of pile

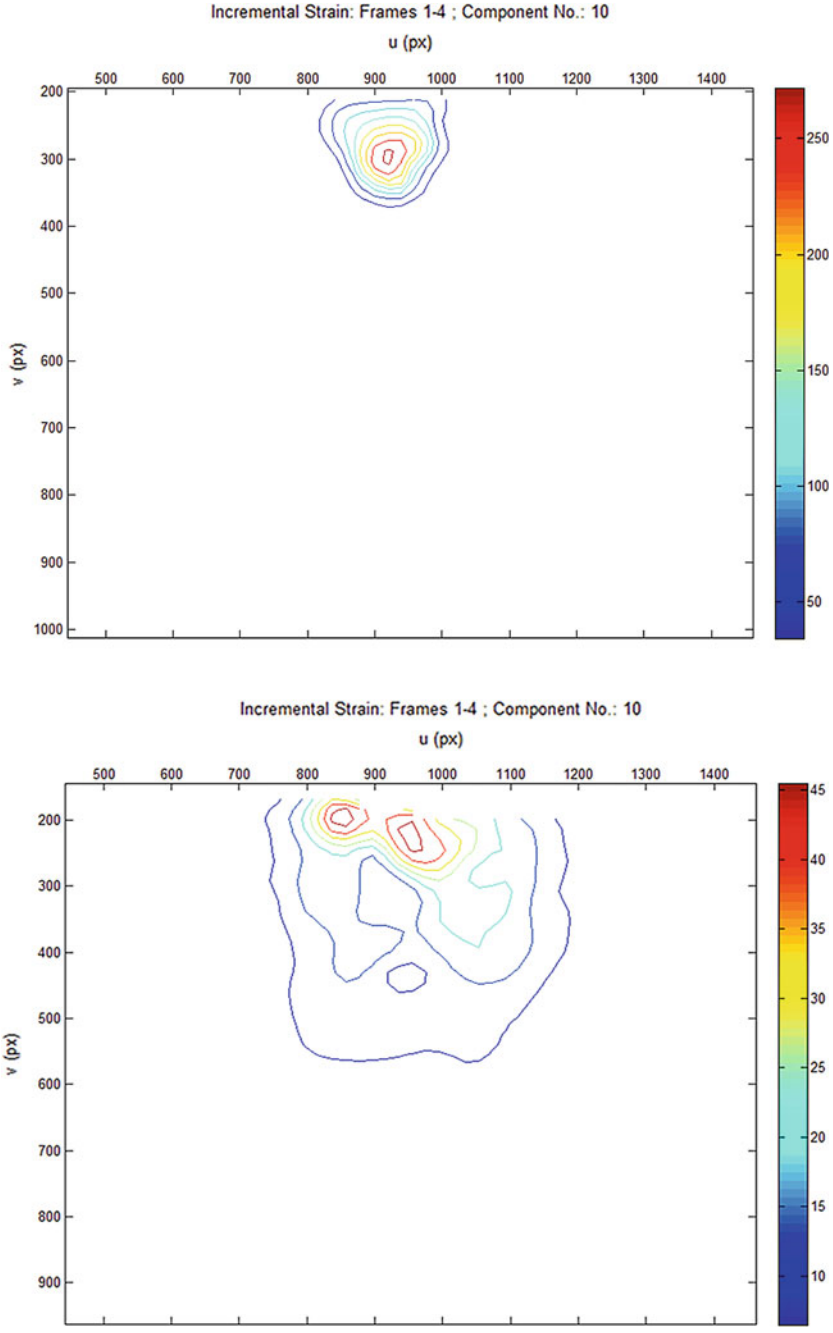

Fig. 6 **a** Variation of shear strain for 12 mm-diameter pile with infill density, **b** variation of shear strain for 32 mm-diameter pile with infill density

is increased there is an increase in the development of shear strain around pile with respect to its depth. This is evident from the gradation of red and dark blue color percentage which is increasing with respect to an increase in pile diameter.

The soil plug formed around pile reduced with respect to the increase in pile diameter which created less resistance to driving, leading to an increased area of influence of contour with respect to the density of infill. In the case of a 32 mm diameter pile, strain concentration zones are developed around the annular region, which is not evident in the case of 12 mm diameter pile wherein soil plug inhibits shear displacement of soil. Pile driving in any case will develop shear strains in the infill medium. However, for small diameter pile, the contours intercept. Whereas for large diameter piles, the contours did not intersect, which have resulted in shear strains around the pile annular region.

6 Conclusions

(a) Soil plug length decreases when there is an increase in infill density for all diameter piles.
(b) With an increase in diameter (scaling factors) there is an increase in shear band formation for both vertical and horizontal directions.
(c) Strain concentration zones are developed near the annular region for a large diameter pile (32 mm).

References

1. Brucy F, Meunier J, Nauroyn JF (1991) Behaviors of pile plug in sandy soils during and after driving. In: International proceedings of 23rd annual offshore technology conference, Houston, 1,145–154. https://doi.org/10.4043/6514-ms
2. Randolph MF, Leong EC, Houlsby GT (1991) One-dimensional analysis of soil plugs in pipe piles. Geotechnique 41(4):587–598. https://doi.org/10.1680/geot.1991.41.4.587
3. Raines RD, Ugaz OG, O'Neill MW (1992) Driving characteristics of open-toe piles in dense sand. ASCE J Geotech Eng 118(1): 72–88. https://doi.org/10.1061/(asce)0733-9410(1992)118:1(72)
4. Lehane BM, Gavin KG (2001) Base resistance of jacked pipe piles in sand. J Geotech Geoenviron Eng ASCE 127(6): 473–479. https://doi.org/10.1061/(asce)1090-0241(2001)127:6(473)
5. Szechy CH (1959) Tests with tubular piles. Acta Technica 24:181–219. https://doi.org/10.1139/cgj-2014-0041
6. George G (1983) Meyerhof: scale effects of ultimate pile capacity. J Geotech Eng 109:797–806. https://doi.org/10.1061/(asce)0733-9410(1983)109:6(797)
7. Tejchman A, Tejchman T (1994) Scale effect in pile model tests due to different pile and grain diameters. XIIII, CSMFE, New Delhi, India
8. Hight DW, Lawrence DM, Farquhar GB, Mulligan WE, GuE SS, Potts DM (1996) Evidence for scale effects in the end bearing capacity of open-ended piles in sand. In: Offshore technology conference annual OTC m Houston, TX, USA. https://doi.org/10.4043/7975-ms

9. Stanier SA, Blaber J, Take WA, White DJ (2015) Improved image-based deformation measurement for geotechnical applications. Can Geotech J 53:727–739. https://doi.org/10.1139/cgj-2015-0253
10. White DJ, Bolton MD (2004) Displacement and strain paths during plane-strain model pile installation in sand. Geotechnique 54(6): 375–397. https://doi.org/10.1680/geot.2004.54.6.375
11. Stanier SA, Blaber J, Take WA, White DJ (2015) Improved image-based deformation measurement for geotechnical applications. Can Geotech J 53(5): 727–739. https://doi.org/10.1139/cgj-2015-0253
12. Sreelakshmi G, Asha MN, Viswanath D (2017) Investigations on pile-soil interaction using image analysis. In: Proceedings of second Pan-American conference on unsaturated soils. November 12–15, 2017| Dallas, Texas, 466–476. https://doi.org/10.1061/9780784481684.047
13. Wood DM, Crew A, Taylor C (2002) Shaking table testing of geotechnical models. Int J Phys Model Geotech 1:1–13. https://doi.org/10.1680/ijpmg.2002.020101
14. Parkin AK, Lunne T (1982) Boundary effects in the laboratory calibration of a cone penetrometer for sand. In: Proceedings of 2nd European Symposium on penetration testing, Netherlands

Performance Evaluation of Bio-Stabilized Soils in Pavements

V. Divya and M. N. Asha

Abstract The method by which geotechnical properties of a soil is improved using enzymes is termed as bio-stabilization. This technique is found to have a low environmental impact as well as it is biodegradable. The present work involves the evaluation of the performance of bio-stabilized lateritic and black cotton soils in pavements. The experimental studies are conducted on three-volume proportions of the enzyme, namely 100, 150, and 200 ml/m^3. It was observed that the strength parameters exhibited high improvements in case of both the soils. The role of varying dosages and curing periods were also observed to be significant in achieving desirable properties. Further, an attempt is also made to study the feasibility of bio-stabilization in deciding the pavement thickness.

Keywords Bio-stabilization · Terrazyme · CBR · Laterite · Black cotton soil

1 Introduction

Ground improvement by mechanical or chemical means is widely adopted to stabilize soils for improving strength and durability. A number of chemical additives, both inorganic and organic, can be used to stabilize soils. Extensive research works have been carried out over the past decade in the field of ground improvement using stabilizers such as lime, cement, quarry dust [1], fly ash [2], construction demolition waste, plastics [3], etc. Recently, eco-friendly materials have been gaining importance due to its sustainable nature. Bio-Stabilization is one such method which helps to find natural treatments for ground improvements and the study cuts across multiple disciplines, namely Microbiology, Geochemistry, and Civil Engineering. This technique involves the application of microorganisms or enzymes to modify the

V. Divya (✉)
Department of Civil Engineering (VTU RC), CMR Institute of Technology, Bangalore, India
e-mail: divya.v@cmrit.ac.in

M. N. Asha
Department of Civil Engineering, CMR Institute of Technology, Bangalore, India
e-mail: asha.n@cmrit.ac.in

© Springer Nature Singapore Pte Ltd. 2021

K. K. Pathak et al. (eds.), *Recent Trends in Civil Engineering*, Lecture Notes in Civil Engineering 77, https://doi.org/10.1007/978-981-15-5195-6_41

performance characteristics of problematic or weak soils. Different microorganisms that can be used are facultative anaerobic bacteria, microaerophilic bacteria, anaerobic fermenting bacteria, anaerobic respiring bacteria, and obligate aerobic bacteria. Bio-enzymes are natural, non-toxic, non-flammable, non-corrosive liquid which is formulated from vegetable extracts and has the capacity to improve the soil stability [4]. It has been understood from the literature that treatment with bio-enzymes has a very low environmental impact and is economical in the long run since their effect is everlasting [5]. According to [6], the effect of soil bonding created by adhesion of extracellular polymers and enzymes and by charge interactions is mainly due to the presence of microorganisms. Bio-stabilized soil eliminates the risk of liquefaction and increase the stability of soil during landslides and earthquakes [4].

Enzymes can be extracted from plants and animals using suitable solvents. A field study on Terrazyme stabilized lateritic soil blended with sand was conducted by [5] and the results indicated a significant improvement in geotechnical properties such as unconfined compressive strength, CBR, and permeability. [7] studied the relevance of varying enzyme dosages on strength parameters of enzyme blended soil. It was inferred from their studies that curing plays a vital role during bio-modification of soil. It was summarized that biological stabilization is feasible in soil with a minimum clay content of 15% by [8]. The potential of bio-enzymes in controlling swelling nature of expansive soil was investigated and comprehended by [9]. The effect of enzyme on index and engineering properties of montmorillonite clay was explored by [10]. It was observed from literature that bio-enzymatic studies were carried out mostly in weaker soils and soils with some amount of cohesion. The suitability of air-dry curing and desiccators curing on enzyme-treated black cotton and red soils were studied by [11]. They observed from their results that air-dry curing was best suited for the modification of engineering properties enzyme-treated soils. The effect of three types of bio-enzymes on strength characteristics and consistency limits of treated soils was studied by [12] and confirmed the potential of bio-enzyme in achieving a denser packing of soil particles.

The current work aims at understanding the effectiveness of enzyme in altering the strength properties of two types of soils, namely lateritic soil and black cotton soil and hence estimates its contribution in pavement design. Laterite soil, which is used largely in many construction activities, loses its shear strength on saturation. Black cotton soil exhibits high swelling characteristics which renders it unsuitable for construction purpose. Comparative studies are proposed to understand the potential of enzyme in altering the strength characteristics of untreated soil such as compaction parameters and CBR and to evaluate/gauge its application as pavement subgrade.

2 Methodology

The methodology adopted in the present experimental study can be sequenced as follows:

Table 1 Properties of Lateritic and Black Cotton Soil

Property	Lateritic soil	Black cotton soil
Specific gravity	2.85	2.63
Liquid limit	45	65
Plastic limit	23	32
Plasticity Index	22	33
IS Soil classification	CI	CH
Maximum dry density, g/cc	1.76	1.499
Optimum moisture content, %	18.75	16.25
CBR, %	9.23	4.57

(a) Characterization of raw materials
(b) Enzyme dosages and curing periods
(c) Evaluation of mechanical properties of treated and untreated laterite and black cotton soils
(d) Discussions and conclusions.

3 Characterisation of Materials

3.1 Laterite Soil

The laterite soil used in the current study was taken from Mangalore District, at a depth of 1.5 m from the ground surface. The natural soil was kept in the oven for drying and then was used for making the samples for performing various laboratory tests. The index and engineering properties of laterite soil are given in Table 1.

3.2 Black Cotton Soil

The black cotton (BC) soil used in the experimental work was obtained from Yadgiri District, Karnataka. The BC soil was taken from a depth of 2 m from ground level and was oven-dried in the laboratory for the experimental investigations. The soil was classified as clay with high plasticity based on Atterberg's limits. Table 1 gives the geotechnical properties of the plain BC soil.

3.3 Terrazyme

The enzyme used in the present work is Terrazyme, which is dark brown in color with smell of molasses, obtained from vegetable extracts. It possesses a specific gravity of 1.00–1.09 and a boiling point of 212 °F (as provided by the supplier). The advantage of Terrazyme is that it is non-toxic in nature as well as completely soluble in water.

4 Enzyme Dosages and Curing Periods

Based on literature survey, three enzyme dosages fixed for the present experimental studies are Dosage 1 (100 ml/m^3), Dosage 2 (150 ml/m^3), and Dosage 3 (200 ml/m^3), respectively. The dosages were obtained by volume proportioning. The enzyme blended soils were kept for a period of 7 and 28 days in airtight containers for curing.

5 Results and Discussion

5.1 Compaction Parameters

Standard proctor compaction test as per IS specifications was conducted on treated and untreated lateritic and black cotton soils. Table 2 represents the variation in compaction characteristics of lateritic and BC soils, respectively. It is observed that with increase in enzyme dosage dry density increases marginally for both the soil types and there is a considerable decrease in optimum moisture content with increasing enzyme dosage. The addition of enzymes lubricates the flocculated soil and, hence, the soil moves to a denser packing. On comparing the two soils, it is observed that the reduction in optimum water content is more for lateritic soils (20%) in comparison to black cotton soil (6.5%). This is because in the case of black cotton soil, the water gets bound to the clay structure by virtue of its high electronegativity and it is difficult to break the diffused double layer in the presence of enzymes.

Table 2 Compaction parameters of Lateritic and Black Cotton Soil

Dosages	Lateritic soil		Black cotton soil	
	MDD, g/cc	OMC, %	MDD, g/cc	OMC, %
Plain soil	1.760	18.75	1.499	16.25
Dosage 1	1.761	16.00	1.521	16.00
Dosage 2	1.937	15.80	1.534	15.40
Dosage 3	2.020	15.00	1.540	15.20

This results in a lower dry density as well for the black cotton soil in comparison to lateritic soils.

5.2 Variation in Bearing Ratio

The California bearing ratio (CBR) test is penetration test meant for the evaluation of subgrade strength of roads and pavements. In the current study CBR test as per IS 2720-16 was conducted on enzyme blended soils of varying dosages. The treated samples were tested on 7 and 28 days curing period in unsoaked conditions. Figure 1 represents a typical load versus penetration graph for enzyme-treated laterite and black cotton soil.

The CBR values of blended lateritic and BC soils with different dosages of enzyme are presented in Table 3. It is observed that CBR value increases from 50 to 75% with increasing dosage and curing period in case of laterite soil, whereas the improvement is between 168 and 222% in BC soils. This highlights the fact the bio-enzyme stabilisation is suitable for weak soils with high clay content.

From the experimental results it can be inferred that enzyme treatment increases the strength of the pavement subgrade and hence can be successfully used in the

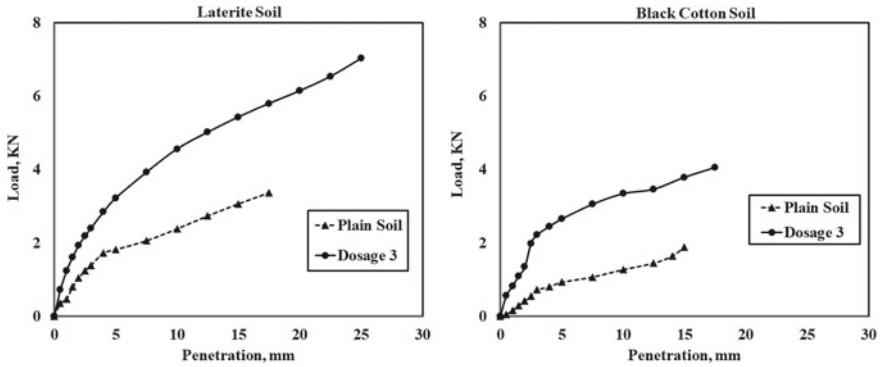

Fig. 1 Variation in load penetration values for treated laterite and BC Soil on 28 days curing period

Table 3 Variation in CBR values of treated Laterite and Black Cotton Soil

Dosages	Laterite soil		Black cotton soil	
	7 Days	28 Days	7 Days	28 Days
Plain soil	9.23	9.23	4.57	4.57
Dosage 1	10.48	13.88	11.30	12.24
Dosage 2	12.81	15.08	11.89	14.22
Dosage 3	13.39	16.22	12.56	14.72

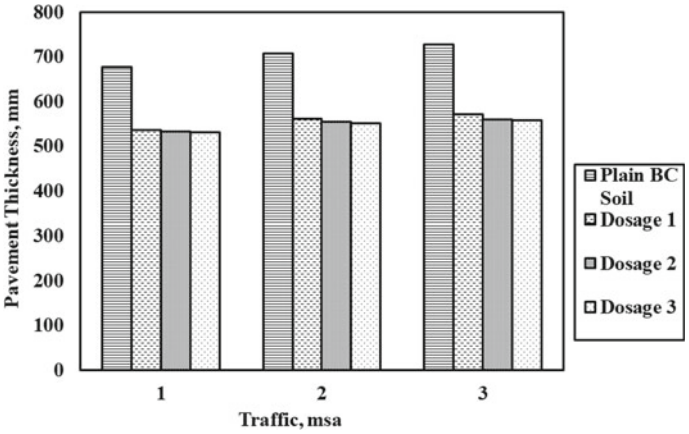

Fig. 2 Pavement thickness for enzyme treated BC Soil on 28 days curing period

design of thickness of flexible pavements. An attempt was made to estimate the thickness of a flexible pavement using IRC 37-2012 assuming bituminous surfacing with granular base and sub-base materials and enzyme blended soil subgrade for design traffic of 10, 20, and 30 msa, respectively. It is observed from Fig. 2 that the thickness of pavement to be provided decreases with increasing enzyme dosages in black cotton soil. Although the design traffic increases the comparative increase in thickness of the component layers are less. The percentage reduction in overall pavement thickness is of the order of 20–23% for the range of traffic and dosage considered.

6 Conclusions

Based on the experimental studies conducted the following conclusions can be arrived at:

1. Enzyme treatment is predominant in black cotton soil due to the presence of clayey particles. Terrazyme tends to reduce the thickness of the diffused double layer resulting in better bond development and thereby contributing to a higher strength achievement.
2. Curing periods play a significant role in appreciably improving the engineering properties of blended soils.
3. Soils blended with Terrazyme are found to be effective in improving the strength of the pavement subgrade. For laterite soil, the improvement in CBR value is 50–75%. On the other hand for a weak montmorillonite clay the improvement is in the order of 168–222%.

4. The percentage reduction of the overall pavement thickness is found to be in the order of 20–23. Hence, enzyme stabilization also helps in achieving a more economic design of pavement by decreasing the overall thickness of pavement.

References

1. Sridharan A, Soosan TG, Jose BT, Abraham BM (2006) Shear strength studies on soil-quarry dust mixtures. Geotech Geol Eng 24(5):1163–1179. https://doi.org/10.1007/s10706-005-1216-9
2. Kim B, Prezzi M, Salgado R (2005) Geotechnical properties of fly and bottom ash mixtures for use in highway embankments. J Geotech Geoenviron Eng 131(7):914–924. https://doi.org/10.1061/(ASCE)1090-0241(2005)131:7(914)
3. Khattab SA, Al-Mukhtar M, Fleureau JM (2007) Long-term stability characteristics of a lime-treated plastic soil. J Mater Civ Eng 19(4):358–366. https://doi.org/10.1061/(ASCE)0899-1561(2007)19:4(358)
4. Ivanov V, Chu J (2008) Applications of microorganisms to geotechnical engineering for bioclogging and biocementation of soil in situ. Rev Eniron Sci Biotechnol 7(2):139–153. https://doi.org/10.1007/s11157-007-9126-3
5. Shankar AU, Rai HK, Mithanthaya R (2009) Bio-enzyme stabilized lateritic soil as a highway material. In: Indian Roads Congress Journal, vol 70, no 2
6. Burns RG (1980) Microbial adhesion to soil surfaces: consequences for growth and enzyme activities. Microb Adhes Surf
7. Venkatasubramanian C, Dhinakaran G (2011) Effect of bio-enzymatic soil stabilization on unconfined compressive strength and california bearing ratio. J Eng Appl Sci 6(5):295–298. ISSN: 1816-949X
8. Shukla M, Bose S, Sikdar PK (2003) Bio-enzyme for stabilization of soil in road construction a cost-effective approach. In: Proceedings of the IRC seminar integrated development of rural and arterial road networks for socio-economic development
9. Naagesh S, Gangadhara S (2010) Swelling properties of bio-enzyme treated expansive soil. Int J Eng Stud 2:155–159. ISSN 0975-6469
10. Eujine GN, Somervell LT, Chandrakaran S, Sankar N (2014) Enzyme stabilization of high liquid limit clay. EJGE 19:6989–6995
11. Ramesh HN, Sagar SR (2015) Effect of drying on the strength properties of Terrazyme treated expansive and non-expansive soils. In: 50th Indian geotechnical conference, Pune, India
12. Khan TA, Taha MR (2015) Effect of three bioenzymes on compaction, consistency limits, and strength characteristics of a sedimentary residual soil. Adv Mater Sci Eng. Article ID 798965. https://doi.org/10.1155/2015/798965

Effect of Granular Pile Stiffness on Load Distribution for Piled Raft

Jitendra Kumar Sharma and Raksha Rani Sanadhya

Abstract Granular piles are a cost-effective technique of ground improvement which improves the load-carrying capacity, reduces the displacement of foundations built on the reinforced ground, and also a good alternative option of concrete pile. The reinforcement of ground becomes a necessity in many situations, where the soil is extremely weak or soft. The columns of granular material create an improved ground of lower compressibility and higher shear strength that of situ soil. Piles under the raft are designed to decreases the settlements and differential settlement of the soil. Raft, piles, and soil are three components of piled raft system through which the loads transfer to the subsoil. The present analysis is done to study the response of a floating granular piled raft based on the elastic continuum approach. The mathematical study is carried out for the comparative analysis of settlement of granular piled raft to rigid raft only and granular pile alone with variation of relative stiffness of GP, relative size of raft, and relative length of floating GP. The overall response of a granular pile with the rigid raft on top is presented in terms of settlement influence factor (SIF) for, viz. granular piled raft, rigid raft only, and pile alone. On the basis of findings, design charts are prepared to facilitate the design procedure.

Keywords Granular piled raft · Interfacial shear stress · Relative stiffness of granular pile · Relative size of raft · Relative length of floating granular pile

1 Introduction

Use of granular piles/stone columns is considered as one of the most flexible and cost-effective alternatives compared to other methods such as preloading, removal and replacement, thermal stabilization, dynamic compaction, ground freezing, etc. Granular piles are made of compacted sand or gravel installed in soft ground by

J. K. Sharma · R. R. Sanadhya (✉)
Department of Civil Engineering, Rajasthan Technical University, Kota, Rajasthan, India
e-mail: rrsanadhya.phd14@rtu.ac.in

J. K. Sharma
e-mail: jksharma@rtu.ac.in

© Springer Nature Singapore Pte Ltd. 2021

K. K. Pathak et al. (eds.), *Recent Trends in Civil Engineering*, Lecture Notes in Civil Engineering 77, https://doi.org/10.1007/978-981-15-5195-6_42

full displacement methods. Raft foundations are frequently used for tall buildings constructed on soft soil for distribution of load on a larger area. Piles beneath raft are designed to reduce the settlements and unequal displacement of the ground. Raft, piles, and soil are three components of piled raft system through which the loads transfer to the subsoil.

This study presents a simple analytical approach to investigate the behavior of floating granular piled raft foundation. The phenomenon of deformation and the interaction between two components of the composite ground by considering the similarity of vertical displacements along the interface of stone column and soil and the raft and the soil is used in the present analysis to evaluate the load distribution and the resulting settlements of the improved ground. The settlement of granular pile and soil elements and raft and soil elements are obtained by assuming the elastic deformations of granular pile, raft, and soil.

Analysis of a rigid raft over an incompressible pile was presented by Poulos [1]. Butterfield and Banerjee [2] analyzed group–pile cap interaction for the stiffness range of concrete and steel piles. Balaam and Booker [3] proposed a method to analyze displacement, moment, and shear distribution of evenly loaded rigid circular rafts founded on stone column improved soil by using a unit cell concept. Randolph [4] presented a simple analysis for an incompressible pile with a rigid raft depends on average factors for interaction between the raft and the pile.

Lee and Pande [5] presented an axisymmetric model to study the performance of circular footing over the stone column improved ground. The outcome of piled raft foundation over weak soil strengthened by short GP made of flexible materials was investigated by Liang et al. [6]. Madhav et al. [7] carried out the settlement analysis of a granular pile considering non-homogeneities in the deformation modulus as well as granular pile material. Consequence of lateral and moment loads on piled raft foundations in sand is given by conducting model tests by Sawada and Takemura [8]. Etezad et al. [9] purposed an analytical study to get the load-carrying capacity of expensive soil strengthen with stone columns underneath a rigid raft foundation.

Grover and Sharma [10] evaluated the vertical displacements of stiffened granular piles depends on the elastic continuum approach and find that with the rise in stiffness of GP, the displacement of a floating GP reduced. The effect of length of pile and alignment of pile on attained final load was evaluated by Elwakil and Azzam [11]. El-garhy and Elsawy [12] presented a method to investigate strip footing founded on a granular layer over expensive soil stabilized by floating granular or piles resting on bearing stratum. Gupta and Sharma [13] conduct a study of a non-homogeneous GP with non-linear behavior of modulus of elasticity for displacement analysis. Present paper focus on the numerical study of the sharing of load between the raft and granular pile with the variation of the comparative stiffness of GP, the comparative size of raft, and the comparative length of floating granular pile.

2 Analysis of Granular Piled Raft

Figure 1 shows a granular piled raft foundation carrying a load, P. The raft is rigid and of diameter, D. The granular pile is compressible with a constant of deformation or elasticity, E_{gp}; Poisson's ratio, ν_{gp}; diameter, d (=2a); and length, L. The nearby soft soil is characterized by it's the modulus of deformation, E_s, and Poisson's ratio, ν_s. The present analysis uses the continuum approach to determine the stress systems, shear stresses along with the pile, τ, and base pressure on the base of GP, p_b, along with the soil–GP interface and raft stresses, p_r, at the raft–soil interface, which accomplish the similarity of displacements along with the interfaces. For no slip at GP–soil interface, the GP and the raft settlements are equated to the soil settlements at the corresponding elements. The stresses and the soil displacements for GP and raft are evaluated depends on the interactions of raft on raft, raft on GP, GP on GP and GP on raft. The essential steps of the analysis are the evaluation of (a) Soil displacements, (b) GP and raft displacements, and (c) compatibility displacements.

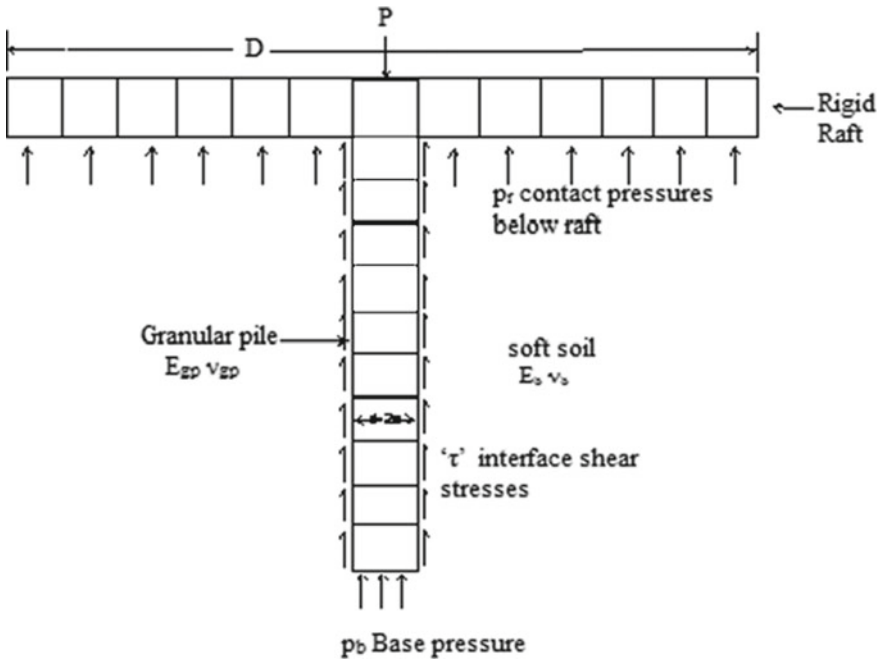

Fig. 1 Definition sketch

2.1 Soil Displacements

Soil Displacement at Granular pile nodes. Soil displacements along with GP–soil interface and along the raft–soft ground interface are evaluated at the mid-points on the side of each element by integrating Mindlin [14] and Boussinesq's expressions, respectively, respectively. The GP is divided into 'n' elements of length, ΔL (=L/n). Displacement along GP–soil interface are evaluated at the mid-point on the side of each element and at the center of the base by the integration of Mindlin and Boussinesq's expressions depends on the effect of the elemental stresses of GP and the raft stresses, respectively, in matrix form following Sharma [15].

$$\{\rho^{sp}\} = \left\{\frac{S^{sp}}{d}\right\} = [I_{pp}]\left\{\frac{\tau}{E_s}\right\} + [I_{pr}]\left\{\frac{p_r}{E_s}\right\} \tag{1}$$

where $\{S^{sp}\}$ and $\{r^{sp}\}$ are vertical and standardize vertical soil settlement vectors, respectively, $[I_{pp}] = (n + 1) \times (n + 1)$ of the displacement factor calculated by integrating Mindlin's equation (vertical settlement due to point load in interior of the semi-infinite elastic continuum) for the effect of GP elemental base pressure and shear stresses on settlements of nodes of pile elements, $[I_{pr}] = (n + 1) \times kr$, of the displacement factor calculated by integrating Boussinesq's equation (vertical settlements due to point load at surface) for the effect of raft, stresses on settlements of nodes of pile elements and $\{\tau\}$ and $\{p_r\}$—column matrix, $\{n + 1\}$ and $\{kr\}$, respectively.

Soil Displacement at Raft nodes. The raft is divided into 'kr' elements of equal area. Displacements along the raft–soil interface are evaluated at the node of each element by the integration of Mindlin and Boussinesq's expression depends on the effect of the elemental stresses of GP and the raft stresses. Corresponding soil displacement at raft node in matrix form is given by the following equation

$$\{\rho^{sr}\} = \left\{\frac{S^{sr}}{d}\right\} = [I_{rp}]\left\{\frac{\tau}{E_s}\right\} + [I_{rr}]\left\{\frac{p_r}{E_s}\right\} \tag{2}$$

where$\{S^{sr}\}$ and $\{\rho^{sr}\}$ are vertical and standardize vertical soil settlement vector, $[I_{rp}]$ $= kr \times (n + 1)$, respectively, whose displacement factor are evaluated by integrating Mindlin's equation considering the effect of GP elemental shear stresses on settlement of raft nodes $[I_{rr}] = (kr \times kr)$ of the displacement factor evaluated by integrating Boussinesq's equation for the effect of raft stresses on the settlements of raft nodes and $\{\tau\}$ and $\{p_r\}$—size of column matrix $\{n + 1\}$ and $\{kr\}$, respectively. Displacements for soil–raft nodes are calculated depend on the interaction of elemental stresses from raft and GP.

2.2 Pile Displacements

Settlements of node of granular pile are calculated depends on a relationship of stress and strain

$$\varepsilon_{\mathrm{v}} = \frac{\sigma_{\mathrm{v}}}{E_{gp}} \tag{3}$$

where ε_{v} is the direct/direct strains of an element, σ_{v} is the direct/direct stress on the element, and E_{gp} is the elasticity modulus of the GP.

Direct and shear stress relationship from consideration of equilibrium, the applied load, P, on GP is shared through base pressure, p_b, and shear stresses, τ, as

$$P = \sum_{j=1}^{j=n} \frac{\tau_j \pi d L}{n} + p_b \frac{\pi d^2}{4} \tag{4}$$

The average direct stress, σ_{vi}, on the element, 'i' is

$$\sigma_{\mathrm{v}i} = \frac{\sigma_{it} + \sigma_{ib}}{2} = p_b + \sum_{j=(i+1)}^{j=n} \frac{4(L/d)\tau_j}{n} + \frac{2(L/d)\tau_i}{n} \tag{5}$$

Relation between shear and direct stresses on pile nodes is presented in matrix as

$$\{\sigma_{\mathrm{v}}\} = [A]\ \{\tau\} \tag{6}$$

where $\{\tau\}$ and $\{\sigma_{\mathrm{v}}\}$ are the consecutive column matrices of shear and direct stresses on the pile nodes, size of both vectors is $(n + 1)$. Size of a matrix $[A]$ is $(n + 1) \times (n + 1)$.

$$[A] = \begin{bmatrix} \frac{2(L/d)}{n} & \frac{4(L/d)}{n} & \frac{4(L/d)}{n} & \frac{(L/d)}{n} & - & - & - & - & 1 \\ 0 & \frac{2(L/d)}{n} & \frac{4(L/d)}{n} & \frac{4(L/d)}{n} & - & - & - & - & 1 \\ 0 & 0 & \frac{2(L/d)}{n} & \frac{4(L/d)}{n} & - & - & - & - & 1 \\ & & & & & & & & \\ & & & & & & & & \\ & & & & & & & & \\ - & - & - & - & - & 0 & \frac{2(L/d)}{n} & \frac{4(L/d)}{n} & 1 \\ - & - & - & - & - & - & 0 & \frac{2(L/d)}{n} & 1 \\ - & - & - & - & - & - & 0 & 0 & 1 \end{bmatrix} \tag{7}$$

GP displacements of granular pile are evaluated depends on the method given by Garg and Sharma [16]. The vertical displacements at each node of granular pile

are calculated starting from top settlement of the granular pile, ρ_t by progressing downward considering the strain of each element successively. The settlement of the top element of GP is

$$\rho_1 = \frac{S_1}{d} = \rho_t - \varepsilon_{v1}\frac{\Delta z}{2d} \tag{8}$$

where ε_{v1} = direct strain of the first element of granular pile and $\Delta z = (L/n)$. S_1 and ρ_1 are the settlement and standardize settlement of the topmost node, respectively. Thus, the settlement, ρ_{ip}, of any element 'i' is derived as

$$\rho_i = \rho_t - \sum_{j=1}^{j=(i-1)} \varepsilon_{vj}\frac{\Delta z}{d} - \varepsilon_{vi}\frac{\Delta z}{2d} \tag{9}$$

where ε_{vi} and ε_{vj} are the direct strains of ith and jth elements, respectively.

Strain at the base to calculate the settlement at the pile base is,

$$\varepsilon_b = -\frac{\mathrm{d}S}{\mathrm{d}z} = \frac{p_b}{E_{gp}} \tag{10}$$

As suggested by Garg et al. [16], using finite difference method with unequal intervals of spacing, the above equation is

$$\frac{4S_{n-1} - 36S_n + 32S_{n+1}}{12(\Delta z/d)} = -\frac{p_b}{E_{gp}} \tag{11}$$

where S_{n-1}, S_n and S_{n+1} are settlements of nodes $n-1$, n, and $n+1$, respectively.

By putting the values of ρ_{n-1} and ρ_n from Eq. (9), and rearranging Eq. (11) gives

$$\rho_{n+1} = \rho_t - \sum_{j=1}^{j=m} \varepsilon_{vj}\frac{\Delta z}{d} - \sum_{j=m+1}^{j=(n-2)} \varepsilon_{vi}\frac{\Delta z}{d} - \frac{34}{32}\varepsilon_{v(n-1)}\frac{\Delta z}{d} - \frac{18}{32}\varepsilon_{vn}\frac{\Delta z}{d} - \frac{6}{32}\frac{(L/d)}{nK_{gp}}\frac{p_b}{E_s} \tag{12}$$

For the computation of ε_{vj}, ε_{vi}, and other ε_{vn}, and $\varepsilon_{v(n-1)}$, $K_{gp} = E_{gp}/E_s$ is taken.

Combining Eqs. (3) and (12), the vertical settlements of pile are given by

$$\left\{\rho^{ppv}\right\} = \rho_t\{1\} + [B]\left\{\frac{\sigma_v}{E_s}\right\} \tag{13}$$

where $[B]$ is matrix of sizes $(n+1) \times (n+1)$ and is given by

$$[B] = \frac{(L/d)}{nK_{gp}} \begin{bmatrix} -0.5 & 0 & 0 & 0 & - & - & - & - & 0 \\ -1 & -0.5 & 0 & 0 & - & - & - & - & 0 \\ -1 & -1 & -0.5 & 0 & - & - & - & - & - \\ - & - & - & - & - & - & - & - & - \\ & & & & & & & & \\ & & & & & & & & \\ -1 & -1 & -1 & - & - & - & - & -0.5 & 0 \\ -1 & -1 & -1 & - & - & - & -\frac{34}{32} & -\frac{18}{32} & -\frac{6}{32} \end{bmatrix} \tag{14}$$

By replacing the direct stresses by shear stresses using (Eq. 6)

$$\left\{\rho^{ppv}\right\} = \rho_t\{1\} + [C]\left\{\frac{\tau}{E_s}\right\} \tag{15}$$

where $[C] = (n+1) \times (n+1)$ matrix and given by $= [B]\,[A]$.

2.3 Raft Displacements

A raft is considered as rigid and, hence, displacements of raft nodes are all equal. The settlement of the top of the GP (ρ_t) is equal to raft displacement and expressed as

$$\left\{\rho^{r}\right\} = \rho_t\{1\} \tag{16}$$

where $\{\rho^r\}$ is the raft displacement vector of size 'kr'.

2.4 Condition of Compatibility

- Using compatibility of settlement of the GP and the soil,

$$\left\{\rho^{sp}\right\} = \left\{\rho^{ppv}\right\} \quad \text{or}$$

$$[AA]\left\{\frac{\tau}{E_s}\right\} + \left[I_{pr}\right]\left\{\frac{p_r}{E_s}\right\} = \rho_t\{1\} \tag{17}$$

  where $[AA] = [I_{pp}] - [C]$, of size $(n+1) \times (n+1)$
- Using compatibility of settlement of the raft and the soil,

$$\{\rho^{sr}\} = \{\rho^{r}\} \quad \text{or}$$
$$[I_{rp}]\left\{\frac{\tau}{E_s}\right\} + [I_{rr}]\left\{\frac{p_r}{E_s}\right\} = \rho_t\{1\} \tag{18}$$

By solving the Eqs. (17) and (18), standardize raft stresses and normalized interfacial shear stresses are evaluated. Further, the settlement at the top of partially stiffened GP–raft foundation is evaluated as

$$S^p = \frac{P}{E_s d} I_p \tag{19}$$

where Ip is the displacement factor.

3 Results and Discussion

Non-dimensional variables incorporated in the study are comparative length of GP, L/d = 10–40, comparative stiffness, K_{gp} of GP = 10–1000, comparative size, D/d of GP = 2–10, Poisson's ratio of soil, υ_s = 0.3–0.5, and Poisson's ratio of GP, υ_{gp} = 0.3–0.5. The effect of Poisson's ratios of surrounding soil and granular pile does not affect the results significantly. The usual range of K_{gp} for GP is 10–100, results are obtained for K_{gp} = 1000.

Figure 2 represents the deviation of standardize shear stresses, $\tau^* = \tau(\pi dL)/P$, with the standardize depth, $z_1 = z/L$ along with influence of comparative size of raft, D/d, for L/d = 10, υ_s = 0.5, and K_{gp} = 50 and 100. With the rise of comparative

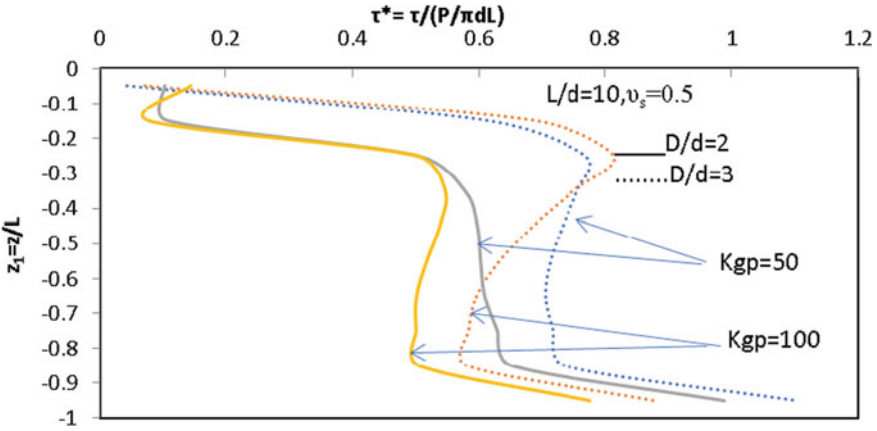

Fig. 2 Plot of standardize shear stresses, $\tau^* = \tau(\pi dL)/P$, with the standardize depth, $z_1 = z/L$—consideration of comparative size of raft, D/d, and comparative stiffness of GP, K_{gp}, on a GP–raft foundation (L/d = 10, υ_s = 0.5)

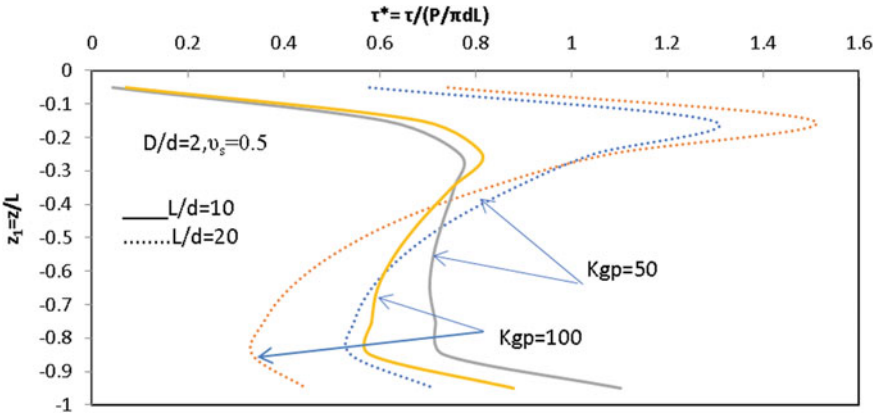

Fig. 3 Plot of standardize shear stresses, $\tau^* = \tau(\pi dL)/P$, with the standardize depth, $z_1 = z/L$—consideration of comparative length of GP, L/d, and comparative stiffness of GP, K_{gp}, on a GP–raft foundation ($D/d = 3$, $\upsilon_s = 0.5$)

stiffness of GP, K_{gp}, shear stresses reduce throughout the length of the pile except in the larger size of raft, $D/d = 3$, up to 30–40% length of pile shear stress increases. It can be well seen that the shear stresses are increased with increases in the comparative size of raft, D/d. Shear stress is rearrange distributed and move toward the bottom of the GP.

Figure 3 represents the variation of standardize shear stresses with total load on piled raft, $\tau^* = \tau(\pi dL)/P$, with the depth standardize with the length of pile i.e. $z_1 = z/L$ for $D/d = 2$, $\upsilon_s = 0.5$, $K_{gp} = 50$, 100 and with effect of comparative length of pile, L/d, on a granular piled raft. It is well seen that with an increment in comparative stiffness of granular pile, K_{gp}, the shear stresses increase up to the 30–40% the length of granular pile and decrease in the lower part of the pile. As the comparative length of GP increases from L/d = 10–20, the shear stresses in the upper length of pile increase for $K_{gp} = 50$, and for $z_1 = -0.15$ are 0.68 and 1.5, respectively, but, in the lower portion of granular pile, it can be decreased to 0.87–0.44 for $z_1 = -0.95$.

Figure 4 depicts the deviation of percentage baseload, $(P_b/P) \times 100$, pile load, $(P_p/P) \times 100$ and raft load, $(P_r/P) \times 100$ with comparative stiffness, K_{gp}, with the influence of comparative size of raft, D/d on a granular pile raft for $L/d = 10$ and $\upsilon_s = 0.5$. As can be expected, the percentage baseload of GP and pile load rises with rise of comparative stiffness of GP, K_{gp} and vice versa, raft load decreases. The base load and pile decreases with increases of comparative size of raft, D/d.

Variation of percentage baseload, $(P_b/P) \times 100$, pile load, $(P_p/P) \times 100$, and raft load, $(P_r/P) \times 100$ with comparative stiffness, K_{gp}, with the influence of comparative size of raft, D/d on a granular pile raft for $L/d = 10$ and $\upsilon_s = 0.5$ is depicted in Fig. 5. The percentage baseload of GP and raft load decreases with the increase in the comparative length of GP, L/d, and vice versa pile load increases. The baseload and pile load decreases with the increases in the comparative stiffness of GP, K_{gp}.

The variation of percentage raft load, $(P_r/P) \times 100$, with comparative stiffness of GP, K_{gp}, is depicted in Fig. 6 with the effect of the comparative size of raft, D/d, on

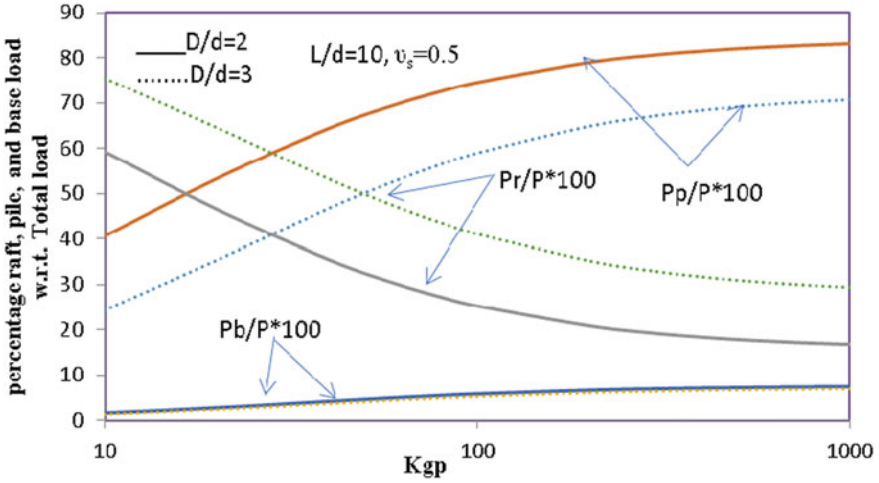

Fig. 4 Plot of percentage load of pile, base, and raft w.r.t. total load with the comparative stiffness of GP, K_{gp}—effect of comparative size of raft, D/d, on a GP–raft foundation ($L/d = 10$, $\upsilon_s = 0.5$)

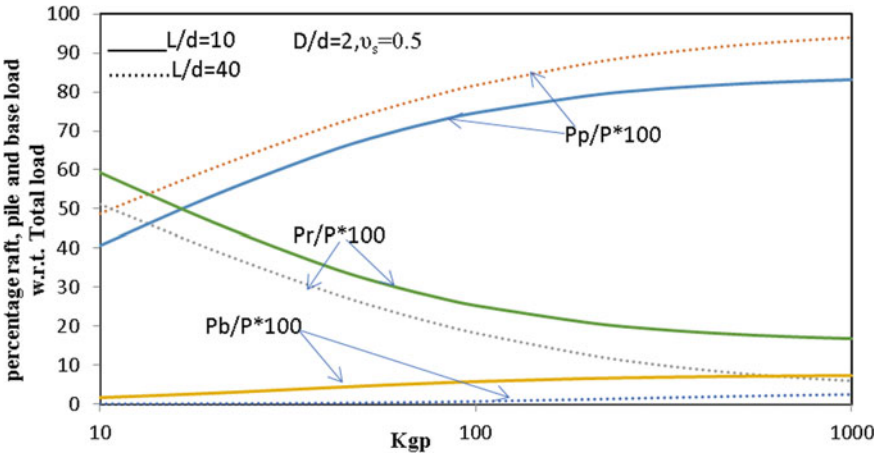

Fig. 5 Plot of percentage load w.r.t. total load with the comparative stiffness of GP, K_{gp}—consideration of comparative length of GP, L/d, on a GP–raft foundation ($D/d = 2$, $\upsilon_s = 0.5$)

a granular piled raft. The percentage raft load decreases with the rise in comparative stiffness of GP, K_{gp}. For $L/d = 10$, $\upsilon_s = 0.5$, $K_{gp} = 10$, and $D/d = 2$, 3, 5, 7, and 10 the values of percentage raft load are 59, 75, 87, 92, and 95, respectively. The percentage raft load rises from 59 to 95 for an increase in raft size, D/d, from 2 to 10.

Figure 7 depicts the deviation of percentage raft load, $(P_r/P) \times 100$, with compar-

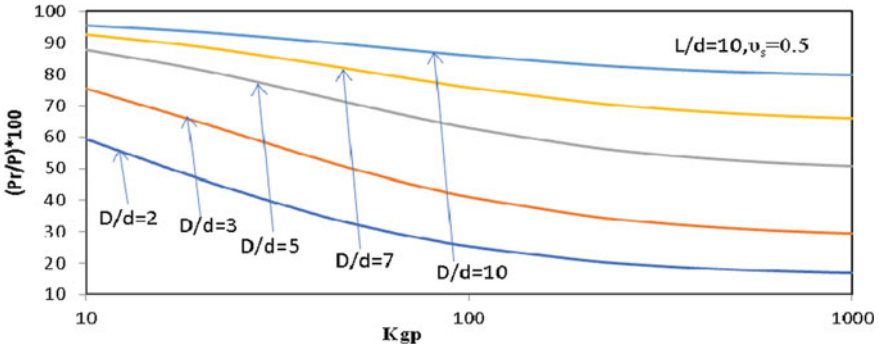

Fig. 6 Plot of percentage raft load, (P_r/P) * 100, with the comparative stiffness, K_{gp}—effect of comparative size of raft, D/d, on GP–raft foundation ($L/d = 10$, $\upsilon_s = 0.5$)

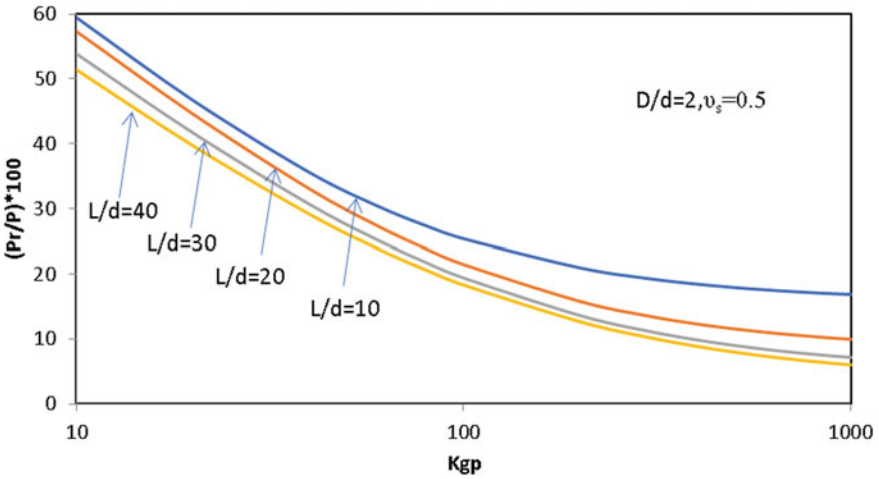

Fig. 7 Plot of percentage raft load, (P_r/P) * 100, with the comparative stiffness, K_{gp}—effect of comparative length of GP, L/d, on GP–raft foundation ($D/d = 2$, $\upsilon_s = 0.5$)

ative stiffness of GP, K_{gp}, is with the effect of the comparative length of GP, L/d, on a granular piled raft for $D/d = 2$, $\upsilon_s = 0.5$. The percentage raft load reduces with increment in comparative stiffness of GP, K_{gp}, and also with rise in comparative length of pile, L/d. For $D/d = 2$, $\upsilon_s = 0.5$, $K_{\text{gp}} = 10$, and $L/d = 10$, 20, 30, and 40 the % raft load are 59, 57, 53, and 51, respectively.

Figure 8 depicts the deviation of percentage pile load (P_p/P) with comparative stiffness of GP, K_{gp}, showing the influence of comparative length of pile, L/d. The % load shared by pile for $K_{gp} = 10$, $\upsilon_s = 0.5$, $D/d = 2$, and $L/d = 10$, 20, 30, and 40 are 40.6, 42.6, 46.0, and 48.7, respectively, implying that the percentage pile load rises with rise in comparative stiffness, K_{gp}. Pile load also increases with the increase in comparative length of granular pile, L/d.

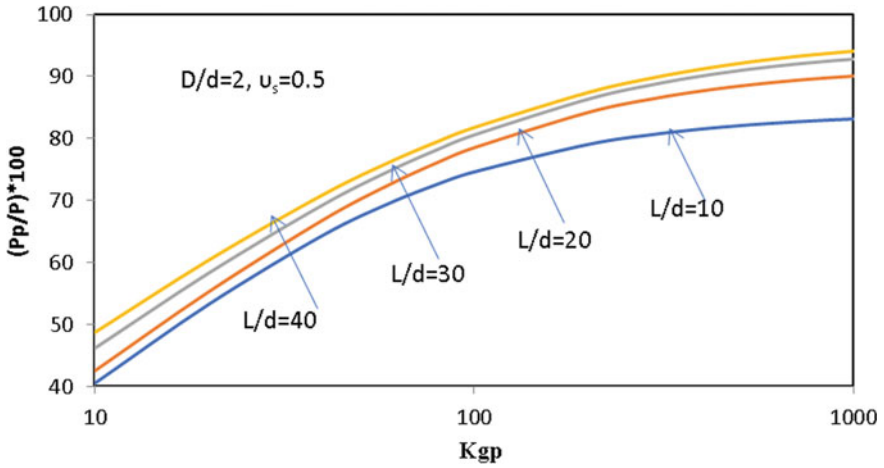

Fig. 8 Plot of percentage pile load, $(P_p/P) * 100$, with the comparative stiffness, K_{gp}—effect of comparative length of GP, L/d, on GP–raft foundation ($L/d = 10$, $\upsilon_s = 0.5$)

Variation of percentage pile load (P_p/P) transferred to the pile with comparative stiffness, K_{gp}, of GP showing the influence of comparative size of raft, D/d is depicting in Fig. 9. Load shared by pile rises with the increase of comparative stiffness of granular pile, K_{gp}. Percentage load shared by pile for $K_{gp} = 10$, $\upsilon_s = 0.5$, $L/d = 10$, and $D/d = 2$, 3, 5, 7, and 10 are 40.6, 24.4, 12.16, 7, and 4, respectively,

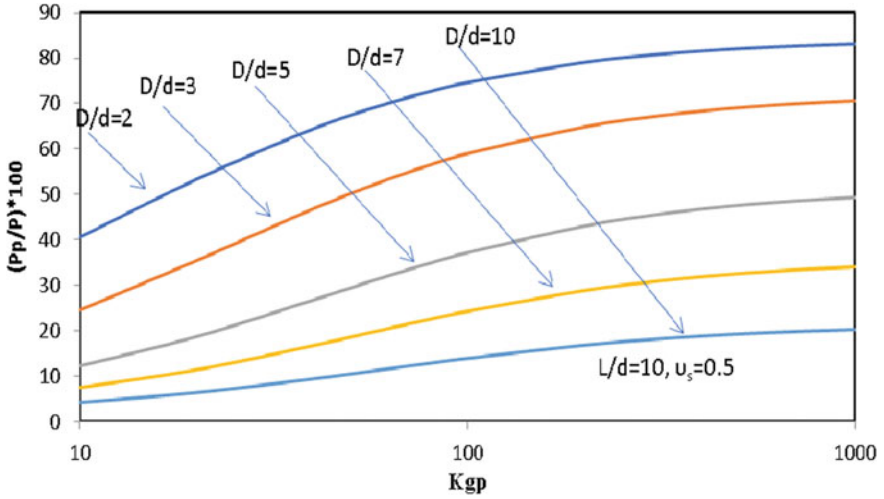

Fig. 9 Plot of percentage pile load, $(P_p/P) * 100$, with the comparative stiffness, K_{gp}—effect of comparative size of raft, D/d, on GP–raft foundation ($L/d = 10$, $\upsilon_s = 0.5$)

implying that the percentage pile load decreases with the increase in comparative size of raft, D/d.

Figure 10 depicts the deviation of percentage baseload $(P_b/P) \times 100$ with comparative stiffness, K_{gp}, with the influence of the comparative size of raft, D/d for $L/d = 10$, and $\upsilon_s = 0.5$. The percentage base load of the piled raft rises with the increment in comparative stiffness of GP, K_{gp}. The % load carried by the base of granular pile, (P_b/P) * 100 reduces with the increase in the comparative size of raft, D/d.

Figure 11 depicts the deviation of percentage baseload, $(P_b/P) \times 100$, with comparative stiffness, K_{gp}, with the influence of the comparative size of raft, D/d, on a granular piled raft for, $L/d = 10$ and $\upsilon_s = 0.5$. The percentage baseload improved

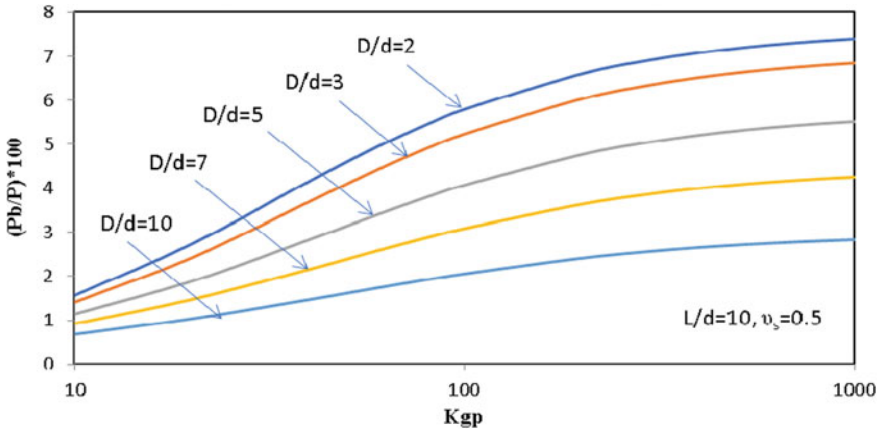

Fig. 10 Plot of percentage baseload, (P_b/P) * 100, with the comparative stiffness, K_{gp}—effect of comparative size of raft, D/d, on GP–raft foundation ($L/d = 10$, $\upsilon_s = 0.5$)

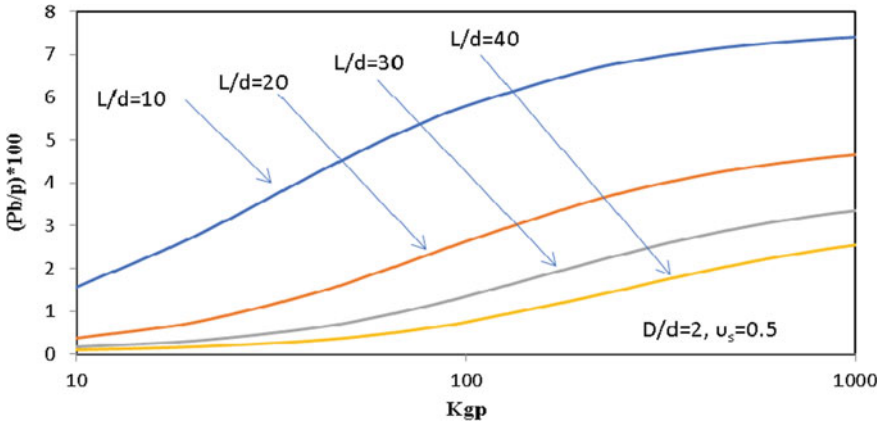

Fig. 11 Plot of percentage base load, (P_b/P) * 100, with the comparative stiffness, K_{gp}—effect of comparative length of GP, L/d, on GP–raft foundation ($L/d = 10$, $\upsilon_s = 0.5$)

with a rise in comparative stiffness of GP, K_{gp}, and reduces with a rise in the comparative pile length, L/d. For $L/d = 10$, $\upsilon_s = 0.5$, $K_{gp} = 100$, and $L/d = 10$, 20, 30, and 40 the values of % base loads are 5.7, 2.6, 1.3, and 0.74, respectively.

4 Conclusion

Depending on the elastic continuum approach, a pile settlement matrix is formulated in the current study. Following are the outcomes of this study:

- Regarding the rise of comparative stiffness of GP, K_{gp}, shear stresses reduces throughout the length of the pile except in the larger size of raft, $D/d = 3$, up to 30–40% length of pile shear stress increases.
- Standardized shear stresses for granular piled raft the comparative pile length increase from $L/d = 10$–20 the shear stresses at the top length of pile rises from 0.68 and 1.5 for $K_{gp} = 50$ at depth 1.5.
- The percentage base load of the piled raft rises with the improvement in comparative stiffness of GP, K_{gp} and reduces with the rise in the comparative length of the granular pile.
- The percentage baseload decreases from 5.7 to 0.74%, while the comparative length of the pile increases from 10 to 40.
- The percentage pile load rises with the rise in comparative stiffness of GP, K_{gp}, and vice versa percentage raft load decrease as it reflects true behavior of piled raft foundation system.
- As the comparative length of pile increases from $L/d = 10$ to 40, the percentage load on raft decreases from 25.39 to 18.25.
- Standardize geometric and strength parameters are used to prepare design charts to facilitate their wide range. To design a granular pile raft, these charts can be used by practicing engineers.

References

1. Poulos HG (1968) The influence of rigid pile cap on the settlement behaviour of an directly loaded pile: C.E. Trans Inst Eng Aust CE10(2):206–208
2. Butterfield R, Banerjee PK (1971) The problem of pile group-pile cap interaction: Geotech 21(2):135–142
3. Balaam NP, Booker JR (1981) Analysis of rigid rafts supported by granular piles. Int J Numer Anal Method Geomech 5:379–403
4. Randolph MF (1983) Design of piled raft foundations. In: Proceedings of international symposium on recent developments in laboratory and field tests and analysis of geotechnical problems, Bangkok, pp 525–537
5. Lee JS, Pande GN (1998) Analysis of stone-column reinforced foundations. Int J Numer Anal Meth Geomech 22:1001—1020

6. Liang FY, Chen LZ, Shi XG (2003) Numerical analysis of composite piled raft with cushion subjected to vertical load. Comput Geotech 30:443–453
7. Madhav MR, Sharma JK, Chandra S (2006) Analysis and settlement of a non-homogeneous granular pile. Indian Geotech J 36(3):249–271
8. Sawada K, Takemura J (2014) Centrifuge model tests on piled raft foundation in sand subjected. Jpn Geotechn Soc Soils Found 54:126–140
9. Etezad M, Hanna AM, Ayadat T (2015) Bearing capacity of a group of stone columns in soft soil. Int J Geomech 15(2):04014043. https://doi.org/10.1061/(asce)gm.1943-5622.0000393
10. Grover KS, Sharma JK, Madhav MR (2015) Settlement analysis of single granular pile with stiffened top. Int J Sci Eng Res 6(6):61–75
11. Elwakil AZ, Azzam WR (2016) Experimental and numerical study of piled raft system. Alex Eng J 55:547–560
12. E-G Elsawy (2017) Effect of different parameters on the behaviour of strip footing resting on weak soil improved by granular piles. Int J Geo-Eng 8:4. https://doi.org/10.1186/s40703-017-0042-2
13. Gupta P, Sharma JK (2018) Effect of nonlinear non-homogeneity of floating granular pile and soil on settlement. J Inst Eng (India): 1–11, series A
14. Mindlin RD (1936) Force at a point in the interior of a semi-infinite solid. Physics 7:195–202
15. Sharma JK (1999) Analysis and settlement of granular pile(s)—single, in group and with raft. A thesis submitted for the degree of Doctor of Philosophy to the Department of Civil Engineering, Indian Institute of Technology, Kanpur, India
16. Garg V, Sharma JK (2018) Analysis and settlement of partially stiffened single and group of two floating granular piles. Indian Geotechn J: 1–13. https://doi.org/10.1007/s40098-018-0321-7

Performance Evaluation of Expansive Soil Using Animal Bone Ash

Jitendra Kumar Sharma and Abdul Shahid Qureshi

Abstract There is a continuous search for improving the geotechnical properties of expansive soil economically due to non-availability of good construction sites for structures to build also to increase the strength of flexible pavements for efficiently withstand applied loads with a reduction in the thickness of pavements and improve the durability of pavements. The present study deals with the performance evaluation of expansive soil using animal bone ash (ABA). Significant changes are observed in mechanical and physical properties of expansive soil after adding ABA. The animal bones obtained from dead animals which are collected from an abattoir at Kota, Rajasthan. These animal bones are crushed and dried for 3 days in an open area. Then these crushed and dried bones are burnt in open air at uncontrolled temperature. The ashes obtained were cooled and sieved with 425-μm sieve to obtained ABA. This ABA was added in proportions of 2, 4, 6, and 8% by weight of samples to the soil to study the improvement in its properties. The local soil selected is highly plastic clay with a liquid limit of 51.68%, a plastic limit of 26.62%, and a plasticity index of 25.06%, which is not suitable for any construction activities purposes, needs stabilization. The results obtained on addition of ABA to the soil at different proportion reduces the plasticity of soil and soil convert from high plasticity clayey to intermediate plasticity and finally turned into low plasticity clayey. On addition of ABA to the soil at different proportions in soil samples reduces the water content and increases the dry density. For the addition of 6% of ABA with black cotton soil, the percentage increment in the value of CBR is more than 100% and beyond 6% of addition of ABA, the value of CBR decreases. The UCS value increases by increasing the percentage of ABA up to 6% and with the further increment in addition of ABA, the value of UCS also decreases. Thus, the optimum dose of ABA is found to be 6%. The value of swelling pressure for virgin black cotton soil is 1.38 kg/cm^2 and, after adding of 8% ABA, it decreases to 0.11 kg/cm^2. Thus, the percentage decrement in swelling pressure is 92.02%.

J. K. Sharma · A. S. Qureshi (✉)
Rajasthan Technical University, Kota, Rajasthan, India
e-mail: qureshishahid.qureshi5@gmail.com

J. K. Sharma
e-mail: jksharma@rtu.ac.in

© Springer Nature Singapore Pte Ltd. 2021

K. K. Pathak et al. (eds.), *Recent Trends in Civil Engineering*, Lecture Notes in Civil Engineering 77, https://doi.org/10.1007/978-981-15-5195-6_43

Keywords Animal bone ash · Black cotton soil · Stabilization soil · Atterberg's limit · California bearing ratio · Unconfined compressive strength

1 Introduction

A civil engineer faces many problems with soils and among them expansive soil is the most problematic one. Today, researchers are trying to develop different methods of utilizing and disposing of both agriculture and biological wastes products to reduce soil instability and making soil suitable for both agriculture and construction. The bearing capacity of soil is a very important aspect in consideration because the foundation of all structures has to be placed on or in soil.

Most failures of soil have been occurring due to poor shear strength. Every structure is supported either by soil or rock. Black cotton soil is highly expansive in nature and shows high potential for swelling and shrinking with seasonal moisture variation.

According to [1], they investigated the index properties of four soil samples in this research and find the maximum value of bone ash to increase the maximum value of California Bearing Ratio (CBR) in all four soil samples. The maximum value of bone ash to increase the value of CBR of all taken soil samples is 7%. In clay soil samples the maximum stabilization results were obtained. According to [2], they observed effect of mixing Rice Husk Ash (RHA) and found that due to lower specific gravity of RHA, the maximum dry density of mixture decreases after adding RHA and optimum moisture content increases because of pozzolanic action of rice husk ash and soil, which needs more water. The maximum value of unconfined compressive strength was 10% RHA content. According to [3], he investigated the index properties of black cotton soil; the sample was not suitable for construction purposes. The soil was highly plasticity clay, the value of unconfined compressive strength and CBR was low. Swelling pressure is very high so that the black cotton soil sample needs stabilization. Lime stabilized materials used to decrease the value of liquid limit, plastic limit, and plasticity index. The clay and lime materials provide the strength of soil samples and give a better result of UCS and CBR tests. The addition of lime gives the suitable index properties of soil sample. According to [4], they studied the effect of bone ash in kaolin stabilization of lateritic soil after using bone ash as an admixture. Lateritic soil gives the suitable value of CBR after adding 10% kaolin and 8% bone ash as admixture. The value of CBR increased up to 80.3% after adding 10% kaolin and 8% bone ash in lateritic Soil.

According to [5], they found in their study that the value of 2% coconut shell ash which is used to add in fired clay bricks for generating newly fired clay bricks. This can be manufactured on-site itself with the advantage of low cost and with semi-skilled labor and thus local economy will flourish. This introduces the natural agriculture waste material that can be used. According to [6], they investigated the geotechnical properties of the soil used in their research and enabled us to establish the effect of Chicken Bone Ash (CBA) on the CBR of soil. The maximum amount of CBA that would allow for an increase for CBR value is 6%. According to this

research, the maximum strength of soil is achieved with the help of 6% of CBA mixed into soil and reported through the unconfined compressive strength test. According to [7], they investigated the calcium phosphate was separated from animal's bones through the chemical process. The specimen was analyzed for components by using an X-ray fluorescence spectrometer. Different concentrations of hydrochloric and ammonia, a variation in pH value, and various parameters were analyzed of calcium phosphate productions. Results have shown that pH and ammonia concentration were the only factors that the maximum yield depends.

An attempt to stabilize or improve the index properties of the soil at the site with naturally available waste is the most economical solution to the problem. The present study incorporates the use of waste animal bones in soil improvement which otherwise takes a lot of time in degradation.

2 Methodology

The methodology adopted in the present experimental study can be sequenced as follows:

(a) Characterization of raw materials
(b) Evaluation of physical properties of treated and untreated expansive soils
(c) Discussions and conclusions
(d) Future scope.

3 Characterization of Materials

3.1 Black Cotton Soil

Expansive soil is used to study the engineering properties of expansive soil. It was taken from Borkhera area near Allen building construction site, 12 km from Rajasthan Technical University, District Kota, Rajasthan. Many tests have been conducted to determine the physical and mechanical properties of the expansive soil by IS specifications. The index properties of expansive soil are given in Table 1.

3.2 Animal's Bones and Wastes

There are a lot of abattoir houses in our country releasing animal wastes like animal bones, horns, and tissues, etc. Dead animal's bodies thrown at dumping yard as wastes. Animal bones decomposed after a long time. After finding the proper use of these wastes, these animal bodies need to collected separate places for getting useful

Table 1 Index properties of expansive soil

S. no.	Property	Value
1.	Liquid Limit (LL)	51.68%
2.	Plastic Limit (PL)	26.62%
3.	Plasticity Index (PI)	25.06%
4.	Soil classification	CH
5.	Specific gravity (G)	2.57
6.	Maximum dry density (d) g/cc	1.69
7.	O.M.C. (%)	18.67
8.	Free swell index (%)	48.23
9.	Unconfined compressive strength, KN/m^2	144.90
10.	Swelling pressure	1.38 kg/cm^2

Fig. 1 Animal's bones after crushing in small pieces

parts like bones and horns, etc. Figure 1 shown the animal bones after crushed and dried it for 3 days in an open area.

3.3 Animal Bone Ash

The animal bones, we used, are obtained from dead animals which are collected from an abattoir at Kota, Rajasthan. These crushed and dried bones were burnt in open air at uncontrolled temperature to obtained animal bone ash (ABA). The physical properties of ABA are given in Table 2. Figure 2 shown the burning process and ash particles of animal bones after burnt.

The mixture of clay and water contains cations (positively charged ions) around a clay particle which creates water film around clay particles and always adsorbed at the surface of clay that adsorbed water called double layer of clay. When the soil is swelling the size of double layer is increases. ABA reacts with double layer or adsorbed water of clay and reduces its thickness around clay particles due to which reduction in voids of particle occurs.

Table 2 Physical properties of ABA

S. no.	Properties	Values
1	Specific Gravity	3.10
2	Color	Gray
3	Melting Point	1670 °C
4	Bone Ash Formula	$Ca_5(OH)(PO_4)_3$
5	Calcium Oxide (CaO)	55.82%
6	Phosphorus pentoxide (P_2O_5)	42.38%
7	Magnesium Oxide (MgO)	1.41%
8	CO_2 + FeO + AlO + SiO_2	0.39%

Fig. 2 Ash particles of animal bones after burnt

4 Evaluation of Physical Properties of Treated and Untreated Expansive Soils

The evaluation of the effect of adding ABA on virgin black cotton soil based on its index properties is given in Table 1.

4.1 Specific Gravity (IS 2720 PART III, 1980)

The specific gravity is determined by the pycnometer test in laboratory. The specific gravity of black cotton soil and mix specimen is calculated and the result is given in Table 3.

Table 3 Specific gravity obtained for black cotton soil with various proportions of ABA

Particulars	Specific gravity
Black cotton soil	2.57
2% ABA + BCS	2.67
4% ABA + BCS	2.75
6% ABA + BCS	**2.87**
8% ABA + BCS	2.84

Specific gravity of expansive soil is 2.57 after adding ABA-specific gravity increases up to 6% ABA.

4.2 Consistency Limits-IS 2720 (PART 5)

Consistency limits are boundary condition at which its state changes by soil from one to another and liquid limit, plastic limit, and plasticity index fall under consistency limits. The value of liquid limit is 51.68%, plastic limit is 26.62%, and plasticity index is 25.06% of expansive soil. Table 4 shows values of consistency limits with ABA and graphical results are shown in Fig. 3.

Increasing the percentage of ABA in expansive soil, the resulting mixture turned gradually from highly plasticity clay (CH) to intermediate plasticity clay (CI) further increment in the percentage of ABA, it turned into low plasticity clay (CL).

Table 4 Consistency limits for black cotton soil with various proportions of ABA

Particulars	Liquid limit (%)	Plastic limit (%)	Plasticity index (%)	Specimen classification as per IS 1498(1970)
Black cotton soil	51.68	26.62	25.06	CH
2% ABA + BCS	44.01	22.49	21.52	CI
4% ABA + BCS	35.92	19.23	16.69	CI
6% ABA + BCS	30.91	17.22	13.69	CL
8% ABA + BCS	30.12	16.95	13.17	CL

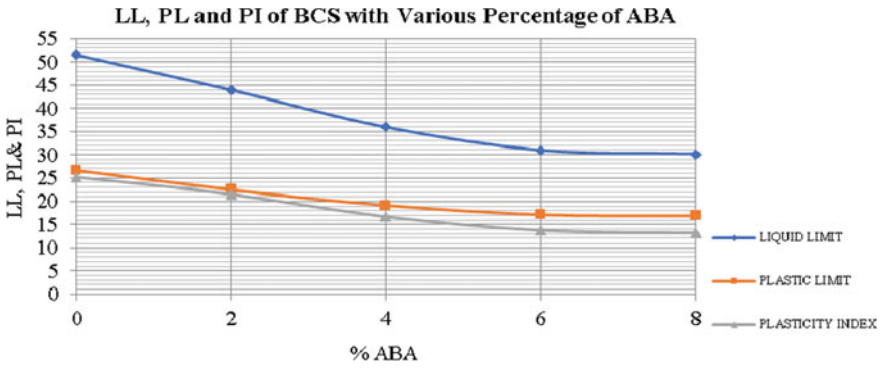

Fig. 3 Liquid limit, Plastic limit, and Plasticity index for black cotton soil with various proportions of ABA

4.3 Standard Proctor Test-IS 2720 (PART 7, 1980)

Standard Proctor test is done for black cotton soil with various proportions of ABA. OMC and MDD are calculated. The OMC and MDD of untreated soil are 18.67% and 1.69 gm/cm^3, respectively. The result of mix specimen is shown in Table 5.

The optimum moisture content is decreased and the maximum dry density is increased after adding various percentages of ABA. But after 6% of ABA the maximum dry density is decreased. Further increment of ABA, the value of dry density is decreased. The graphical representation of mix specimen is shown in Fig. 4.

Table 5 Standard proctor test results for black cotton soil with various proportions of ABA

Percentage of animal bones ash with BCS	MDD (gm/cm^3)	OMC (%)
Black cotton soil	1.69	18.67
2% ABA + BCS	1.75	17.72
4% ABA + BCS	1.78	16.77
6% ABA + BCS	1.80	15.12
8% ABA + BCS	1.79	14.92

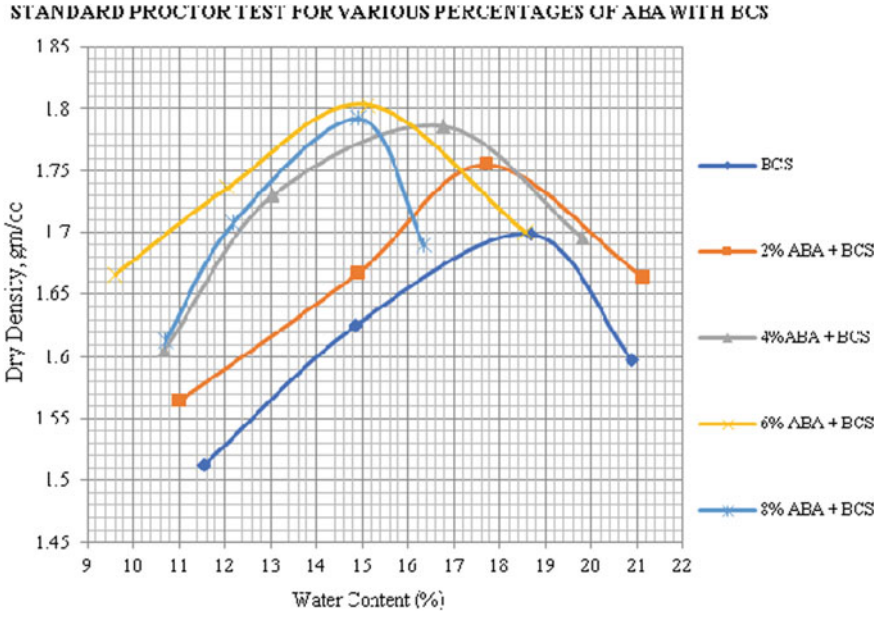

Fig. 4 Standard proctor test for black cotton soil with various proportions of ABA

4.4 *Unconfined Compressive Strength IS 2720 (PART 10, 1973)*

UCS of expansive soil was evaluated with different proportions of ABA. The test result is summarized in Table 6. And graphical representation is shown in Fig. 5, UCS value increases after increasing the value of ABA up to 6%. Further increment in the value of ABA in BCS the value of UCS decreases. The proportion of 6% of ABA with expansive soil shows maximum increment.

Table 6 Variations of UCS test results obtained for black cotton soil with various proportions of ABA

Test specimen	Unconfined Compressive Strength, q_u (KN/m^2)	Shear Strength, Cu (KN/m^2)	% Variation of compressive strength
Black cotton soil	144.9038	72.4519	–
2% ABA + BCS	168.1327	84.06635	16.03%
4% ABA + BCS	196.8922	98.4461	35.87%
6% ABA + BCS	241.1376	120.5688	66.41%
8% ABA + BCS	223.4395	111.71975	54.19%

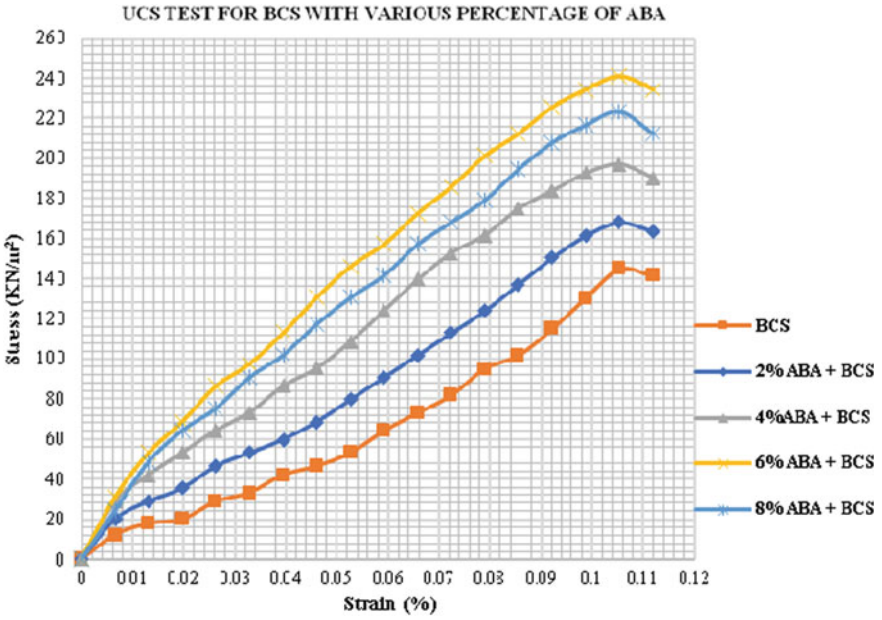

Fig. 5 UCS for black cotton soil with various proportions of ABA

4.5 *California Bearing Ratio (Soaked)—IS 2720 (Part 16, 1979)*

CBR test performed in laboratory in soaked condition for 4 days. The results are shown in Table 7.

From Table 7, the value of soaked CBR for black cotton soil specimen is 2.35%. ABA is mixed with black cotton soil in different proportions. When 6% ABA is added with black cotton soil, the CBR value is 4.86% which shows an increment of 106.80%, with the further increments of ABA, the value of CBR decreases. The graphical representation is shown in Fig. 6.

Table 7 CBR test (soaked) results obtained for black cotton soil with various proportions of ABA

Test Specimen	CBR value %	Increment (%)
Black cotton soil	2.35	
2% ABA + BCS	2.73	16.17
4% ABA + BCS	3.49	48.51
6% ABA + BCS	4.86	106.80
8% ABA + BCS	4.10	74.46

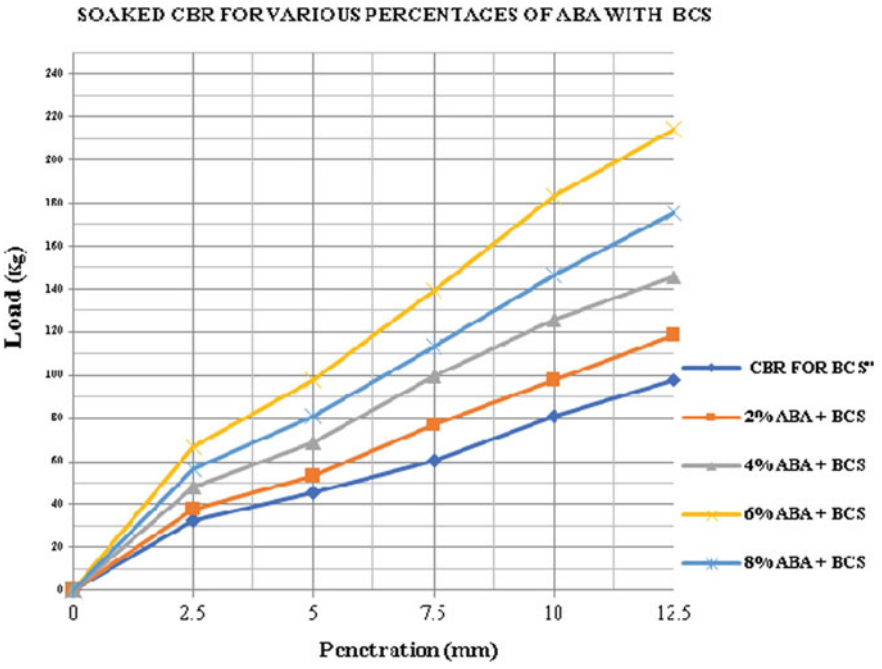

Fig. 6 CBR test (soaked) results obtained for black cotton soil with various proportions of ABA

4.6 California Bearing Ratio (Un-soaked)

CBR test performed in laboratory in un-soaked condition. The results are shown in Table 8.

From Table 8, it is observed that the value of un-soaked CBR for black cotton specimen is 6.53%. ABA is mixed with black cotton soil in different proportions. When 6% ABA is added with black cotton soil, the CBR value is 11.08% which shows an increment of 69.67%. With the further increment of ABA, the value of CBR decreases. The graphical representation is shown in Fig. 7.

Table 8 CBR test (unsoaked) results obtained for black cotton soil with various proportions of ABA

Test Specimen	CBR value %	Increment %
Black Cotton soil	6.53	–
2% ABA + BCS	8.81	35.06
4% ABA + BCS	9.49	45.32
6% ABA + BCS	11.08	69.67
8% ABA + BCS	10.25	56.96

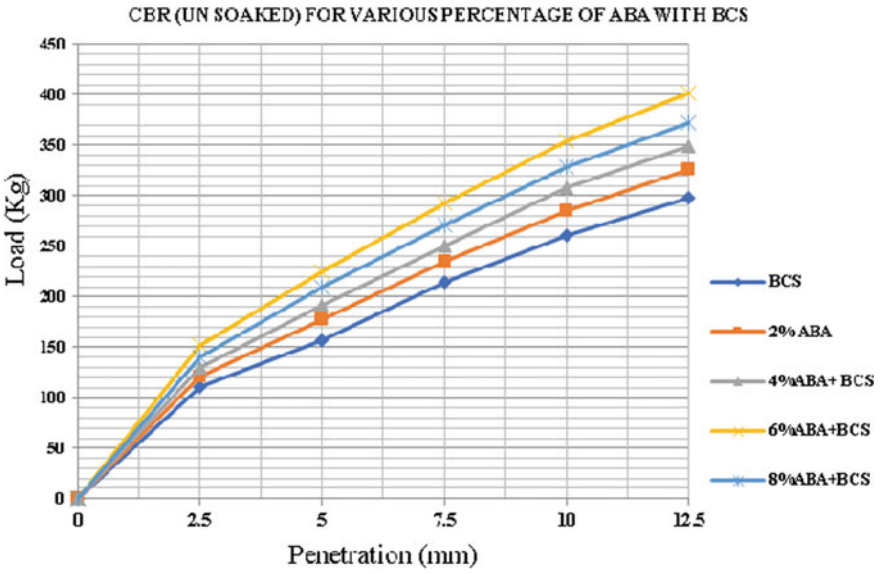

Fig. 7 CBR test (unsoaked) results obtained for black cotton soil with various proportions of ABA

Table 9 DFS results for black cotton soil with various proportions of ABA

Particulars	Swell index	Percent decrease	Degree of expansiveness
BCS	48.23	–	High
2% ABA + BCS	38.94	19.26	High
4% ABA + BCS	24.28	49.65	Moderate
6% ABA + BCS	14.34	70.26	Low
8% ABA + BCS	2.80	94.19	Low

4.7 Differential Free Swell–IS 2720 (PART 40, 1977)

The DFS is basically performed to check out the swelling percentage of black cotton soil in the case of ABA mix specimen. DFS is reducing after adding various percentages of ABA in black cotton soil.

From Table 9, it is observed that with increasing the percentage of ABA in expansive soil, the degree of expansiveness decreases. The value obtained for DFS 48.23% for Black cotton soil. The percentage decrement is 94.19% by adding 8% ABA.

4.8 Swelling Pressure—IS 2720 (PART 41, 1977)

The observations and calculation of swelling pressure for expansive soil and with different percentages of ABA were shown in Table 10. It is observed that the swelling pressure for expansive soil is 1.38 kg/cm^2.

Figure 8 shows the variation of swelling pressure with dial reading for Expansive soil and with different percentages of ABA. By varying the percentage of ABA in expansive soil and the increasing quantity of ABA in expansive soil the swelling pressure decreases to 0.11 kg/cm^2 and percentage decrement is 92.02%. Thus from the above it can be concluded that the swelling pressure decreases by increasing percentage of ABA in expansive soil.

Table 10 Swelling pressure results obtained for black cotton soil with various proportions of ABA

Test specimen %	Pressure (kg/cm^2)	Percentage decrease
Black cotton soil	1.38	–
2% ABA + BCS	0.80	42.02
4% ABA + BCS	0.42	69.56
6% ABA + BCS	0.23	83.33
8% ABA + BCS	0.11	92.02

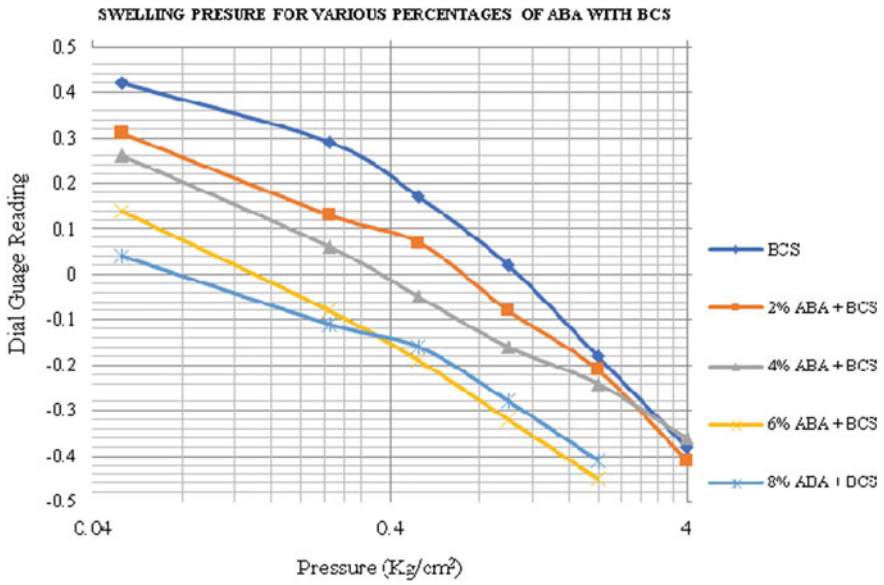

Fig. 8 Swelling pressure results obtained for black cotton soil with various proportions of ABA

5 Discussion and Conclusion

Based on the experimental investigations carried out and results obtained, following conclusion are drawn from the study

- The study reveals that with increasing the quantity of ABA in Black cotton soil, the resulting mixture turned gradually from highly plasticity clay (CH) to low plasticity clay (CL) according to Table 4.
- According to Table 5, Up to 6% of ABA adding in expansive soil, the MDD is increased and OMC is decreased. Further increment of ABA, the dry density is decreased.
- It is observed in Table 7, that on the addition of ABA in expansive soil the CBR values are greatly affected in both conditions (un-soaked and soaked). The CBR value (soaked) increases by about 106.80% on the addition of 6% of ABA with black cotton soil. Further addition of ABA percentage, the value of CBR decreases in both cases.
- On the other hand the CBR value (un-soaked) increases by about 69.67% on the addition of 6% of ABA with black cotton soil. Further addition of ABA percentage, the value of CBR (un-soaked) decreases in Table 8,
- The UCS value increases by increasing the percentage of ABA up to 6%. With the further increment of ABA, the value of UCS decreases. The percentage increment in the UCS value was found to 66.41% for mixing of 6% ABA in black cotton soil shown in Table 6.

- The value of swelling pressure for virgin black cotton soil is 1.38 kg/cm^2 and after adding 8% ABA; it decreases to 0.11 kg/cm^2. The percentage decrement of swelling pressure is 92.02%. Values are shown in Table 9.
- The differential free swell index of expansive soil used in the study is 48.23% and after adding 8% ABA the value of DFS is 2.80%. The percentage reduction in differential free swell index is in the order of 94.19%. The soil changes from very high swelling to very low swelling soil in Table 10.
- From the study it is revealed that the combination of 6% ABA with black cotton soil gives the best results for compaction, shear strength, and CBR. Hence the ABA proves to be a good stabilizing agent for expansive soil and it can be useful for various civil engineering constructions.

Future Scope

- Local fabrications of the furnace should be used for bone calcinations at a low cost. Local public are involved in bone ash production, the unemployment rate will be surely reduced and the standard of living will be surely improved.
- In the present paper the effect of inclusion of ABA has been studied the performance under axial load. It can be extended to study the performance under the tri-axial load.

References

1. Ayininuola GM, Denloye AO (2011) Influence of bone ash on soil California bearing ratio. J Emerg Trends Eng Appl Sci 9(5):55–67
2. Sarkar G, Islam R, Alamgir M (2012) Interpretation of rice husk ash on geotechnical properties of cohesive soil. Glob J Res Eng Civ Struct Eng 12(2):1–8
3. Mehta KS, Gaikwad KS (2014) Analysis of engineering properties of black cotton soil & stabilization using by lime. 4(4):59–63. ISSN : 2248-9622
4. Onyelowe KC (2016) Kaolin stabilization of Olokoro lateritic soil using bone ash as admixture. Int J Constr Res Civ Eng (IJCRCE) 2(1)
5. Fernando PR (2017) Mechanical and physical properties of fired clay brick partial doped with coconut shell ash. J Energy Nat Resour 6(5):58–63
6. Kumar V, Singh A, Garg P (2018) Stabilization of clayey soil using chicken bone ash. IJCRT 6(2). ISSN: 2320-2882
7. Ghuzaili SA, Jesil A, Saravanan AM (2019) Extraction of calcium phosphate from animal bones. Int J Eng Res Technol (IJERT) 8(01). ISSN: 2278-0181

Concrete Technology

High Performance Concrete Mixed with Combinations of Mineral Admixtures

Bhargav Reddy Isanaka, M. Abdul Akbar, P. Perumal, and R. Sai Priyanka

Abstract Concrete is a widely used construction material all over the world. However, the raw material resources used for making concrete are degrading day by day. This gives scope for researchers to experiment with new materials for replacement which will help to conserve natural resources and further limit environmental concern caused due to the extraction of materials and emission of carbon dioxide during the process of manufacturing. Moreover, a lot of modern-day constructions require the use of high-grade concrete, leading to the development of High Performance Concrete (HPC). Partial replacement of cement in HPC with fly ash, GGBS, metakaolin and silica fume presents an environmentally friendly way of dealing with increased construction demands. Although studies have been carried out on partial replacement of cement with mineral admixtures in HPC, the performance of the combination of mineral admixtures in HPC has received little to no attention. This paper deals with the study of compressive strength, tensile strength and durability of M40 grade concrete partial replacement of cement with combinations of different mineral admixtures. Three combinations of mineral admixtures namely a combination of fly ash and silica fume, fly ash and metakaolin, and fly ash and GGBS were used for the replacement of 15% of cement by weight. A comparison of strength and durability of different combinations are presented and discussed.

B. R. Isanaka (✉)
Indian Institute of Technology Jammu, Jagti, PO Nagrota, Jammu 181221, J & K, India
e-mail: isanaka.bhargav@gmail.com

M. A. Akbar · R. S. Priyanka
Madanapllle Institute of Technology & Science, Angallu, Madanapalle, Chittoor 517325, Andhra Pradesh, India
e-mail: maakbar83@yahoo.co.in

R. S. Priyanka
e-mail: saipriyanka1a8@gmail.com

P. Perumal
PSG Institute of Technology & Applied Research, Neelambur, Coimbatore 641062, Tamil Nadu, India
e-mail: cbeperumal53@gmail.com

© Springer Nature Singapore Pte Ltd. 2021

K. K. Pathak et al. (eds.), *Recent Trends in Civil Engineering*, Lecture Notes in Civil Engineering 77, https://doi.org/10.1007/978-981-15-5195-6_44

Keywords High performance concrete · Compressive strength · Mineral admixture · Silica fume · Fly ash · GGBS · Metakaolin

1 Introduction

Concrete as a building material has revolutionized the construction industry over the past decade. However, the large-scale use of cement for concrete constructions has led to the degradation of natural resources. This has intensified research activities on mineral admixtures as partial replacement of cement. Mineral admixtures in concrete are also known as supplementary cementing materials. Mineral admixtures are environmentally friendly as they reduce the emission of CO_2 in addition to improving the properties of concrete. Fly ash, Ground Granulated Blast Furnace Slag (GGBS), metakaolin, silica fume and rice husk ash are the major mineral admixtures used in construction. Fly ash is the by-product obtained from coal-based thermal power plants. Silica fume is obtained as a by-product from electric arc furnaces during the production of elemental silicon or alloys containing silicon; GGBS is a by-product obtained during the manufacturing process of pig iron. Metakaolin is a dehydroxylated form of clay mineral kaolinite which is manufactured from high purity kaolin clay by calcinations under high temperature (650–800 °C) [1]. The different mineral admixtures are shown in Fig. 1.

As per American Concrete Institute (ACI), HPC is defined as concrete which meets special performance and uniformity requirements that cannot always be achieved by using conventional materials and conventional methods of mixing, placing and curing. Since the 1990s, HPC has been very popular in the construction industry globally and it has taken its due place even in developing countries like India. Concrete of strengths ranging from 40 to 60 MPa has been used in the construction of tall buildings of metropolitan cities in India [2]. HPC is also employed in the construction of bridges and flyovers. A notable example of HPC in India is the construction of containment dome at the Kaiga power project. In this project, they have used M60 grade concrete with silica fume as one of the constituents [3].

Magudeaswaran et al. [4] studied the durability of HPC and observed a steady increase in water absorption with increase in the percentage of fly ash and silica

Fig. 1 Fly ash, metakaolin, silica fume, GGBS

fume. Workability aspects were studied by Perumal et al. [4] using GGBS as a replacement of cement without superplasticizer. Strength efficiencies using GGBS and high-volume fly ash (HVFH) were studied by Suvarna Latha et al. [5]. Jadhav [6] studied the strength characteristics of high performance concrete by using fly ash and silica fume. The influence of silica fume on conventional concrete is studied by Bhandari et al. [7] and Vinayak Awasare [8] presented the strength characteristics of concrete mixed with GGBS.

As HPC is typically used in special/large structures, the property of durability gains all the more importance to ensure the sustainability of the concrete structure. The effect of mineral admixtures on strength and durability properties have been explained [9–13]. Nabil M Al-Akhras [14] studied the effect of sulfate on the durability properties of concrete. After the specified 28 days of curing, the concrete specimens are immersed in sodium sulfate and chloride solution for a period of 90 days. The degree of chloride and sulfate attack was evaluated based on reduction in the compressive strength of cubes. Although the strength and durability aspects of concrete cubes mixed with mineral admixtures have been studied individually by researchers, the authors are yet to come across literature reporting studies reposted on the effect of a combination of admixtures. As it is the chemical reaction between the constituents that determine the property of concrete, it is important to understand the interaction of mineral admixtures.

The paper reports the results of a study on strength and durability of M40 grade HPC replaced with 15% of cement by weight with three combinations of mineral admixtures namely fly ash and GGBS, fly ash and metakaolin, and fly ash and silica fume. The experiment was repeated for two proportions in each combination. One set of experiments was carried out using equal proportions of mineral admixture (7.5% of each) and the second set of experiments were carried out with 5% of fly ash and 10% of other mineral admixtures.

2 Experimental Investigation

As per the guidelines of IS 516: 1959 [15], standard cubes are used for testing the compressive strength of concrete and cylinders are used to test their tensile strength. It is difficult to conduct a uniaxial tension test for concrete specimens. Split cylinder test and flexure test are indirect tests which are used to find the tensile strength. The method used for determining splitting tensile strength of concrete is as per IS 5816: 1999 [16].

2.1 Materials

The properties of materials used in the study are given in Table 1.

Table 1 Material properties

Material	Specific gravity	Fineness/Fineness modulus	Grade/Properties	Source
Cement	3.15	1%	53 OPC	KCP Cement
Fine aggregate	2.63	3.6	Zone II	Penna river, Nellore, AP
Coarse aggregate	2.72	8.25	Well graded	Ongole, AP
Fly ash	2.51	2%	Class F	AP Genco, Nellore
GGBS	2.85	1%	–	Astrra Chemicals, Chennai
Metakaolin	2.6	1%	–	
Silica fume	2.2	2%	–	

The specific gravity of cement and fly ash mentioned in Table 1 were the values specified by the manufacturer which was cross-verified by using density bottle in a laboratory. The specific gravity of fine aggregate and coarse aggregate used in the experiment (Table 1) was obtained by using a pycnometer in the laboratory. Fineness modulus was obtained from sieve analysis. For fine aggregates 1 kg of the sample was taken, and for coarse aggregates 5 kg was taken.

2.2 Mix Design of HPC

Mix design for HPC was carried out following the guidelines of Indian Standard Code, IS 10262: 2009 [17]. The design stipulations and the data considered for mix design are listed below.

Characteristic strength, f_{ck}	40 MPa
Maximum size of coarse aggregate	20 mm
Degree of quality control	Good
Type of exposure	Severe
Degree of workability	100 mm (Slump)
Target mean strength, f'_{ck}	$f_{ck} + 1.65S$, where S is the standard deviation 48.25 MPa

2.3 Mix Proportions

Using the guidelines of IS 10262: 2009 [13], a mix proportion of M40 grade HPC is finalized. After five trials, a cement content of 466 kg/m^3 and water–cement ratio of 0.39 were arrived at based on 28-day properties of compressive strength. The mix

Fig. 2 Cubes and cylinders after 28 days of curing

proportion was obtained without considering any addition or replacement of mineral admixture. The final mix proportion arrived at is 1:1.51:2.54:0.39 (Cement: Fine aggregate: Coarse aggregate: Water).

2.4 Preparation of HPC Mix

The quantities of all the required ingredients including mineral admixtures were taken by weigh batching, in their appropriate proportions. A minimum of three trial mixes was prepared for each of the combinations. It amounted to a total number of 168 cubes and cylinders. Figure 2 shows a set of cubes and cylinders that were subjected to 28 days of curing.

Workability of concrete was studied by conducting workability tests as per the standard procedures given in IS 1199: 1959 [10]. The table vibrator was used for compaction. Standard cube specimens of 150 mm and cylinders of 150 mm diameter and 300 mm height were cast using the procedure described in IS 516: 1959 [11].

2.5 Testing of Specimens

After 3 days, 7 days and 28 days of curing, the specimens were taken out of the curing tank. For durability, curing is done for the period of 90 days in chloride- and sulfate-contaminated water. The specimens were cured in water which was contaminated by 2% of HCl and 2% of $MgSo_4$ to determine chloride and sulfate attack on the concrete specimen. After allowing surface moisture to drain out, they were tested in compression testing machine to determine their compressive and tensile strengths. Crushing loads are noted, and the average compressive strength and tensile strength of specimens were calculated using Eqs. 1 and 2, respectively.

$$\text{Compressive strength} = {}^{P}/_{A} \tag{1}$$

$$\text{Tensile strength} = {}^{2P}/_{\pi DL} \tag{2}$$

where P is the crushing load of the specimen

A is the cross-sectional area of the specimen

D is the diameter of the cylindrical specimen

L is the length of the cylindrical specimen.

Strengths were calculated for an average of three specimens. The following symbols were used to identify each specimen during experimentation (also notable from Fig. 2).

C	Conventional concrete
M1	Combination of metakaolin (7.5%) + fly ash (7.5%)
M2	Combination of metakaolin (10%) + fly ash (5%)
S1	Combination of silica fume (7.5%) + fly ash (7.5%)
S2	Combination of silica fume (10%) + fly ash (5%)
G1	Combination of GGBS (7.5%) + fly ash (7.5%)
G2	Combination of GGBS (10%) + fly ash (5%)

3 Results and Discussion

The use of mineral admixtures or pozzolanic materials such as fly ash, GGBS, metakaolin and silica fume as partial replacement of cement in concrete results in the activation of binder reactions and mitigation of expansive reactions. This results in strength increase due to additional binder produced by the mineral admixtures when they react with lime and alkali present in concrete. The results of this study confirm the phenomenon as the strength of the mix with mineral admixtures results in a higher strength when compared with conventional concrete. The results of the analysis are given in Tables 2 and 3 which are plotted in Figs. 3, 4 and 5. The focus of this study is to determine the effect of combinations of mineral admixtures.

In this present study, the proportion of metakaolin was limited to 10% as it is known that if the proportion is increased compressive strength will decrease due to "dilution effect". The amount of metakaolin excess will react with calcium hydroxide resulting in a reduction of water–binder ratio. The difference of compressive and tensile strengths of different mixes compared with the base case (without any mineral admixtures) study is given in Table 4 along with the effect of sulfate and chloride attack on the specimen strengths.

Table 2 Slump, compressive strength and tensile strength test results

S. no.	Coding	Slump (mm)	Average compressive strength (N/mm^2)			Average tensile strength (N/mm^2)		
			3 days	7 days	28 days	3 days	7 days	28 days
1	C	105	29.18	34.44	45.22	1.71	2.01	4.59
2	M1	70	33.07	38.29	46.26	1.95	2.17	4.80
3	M2	65	35.77	39.59	48.88	2.11	2.36	4.91
4	S1	75	36.29	42.31	51.11	2.21	3.05	4.81
5	S2	70	40.81	44.07	55.18	2.25	3.13	4.98
6	G1	65	41.85	45.36	56.07	2.40	2.76	4.94
7	G2	60	42.77	47.10	58.29	2.57	2.89	5.09

Table 3 Compressive strength after chloride and sulfate attack

S. no.	Coding	Concrete without exposure (N/mm^2)	Concrete exposed to chloride attack (N/mm^2)	Concrete exposed to sulfate attack (N/mm^2)
1	C	45.22	42.57	40.20
2	M1	46.26	43.62	41.81
3	M2	48.88	46.18	43.62
4	S1	51.11	48.40	46.82
5	S2	55.18	51.56	49.98
6	G1	56.07	53.20	51.92
7	G2	58.29	55.48	53.16

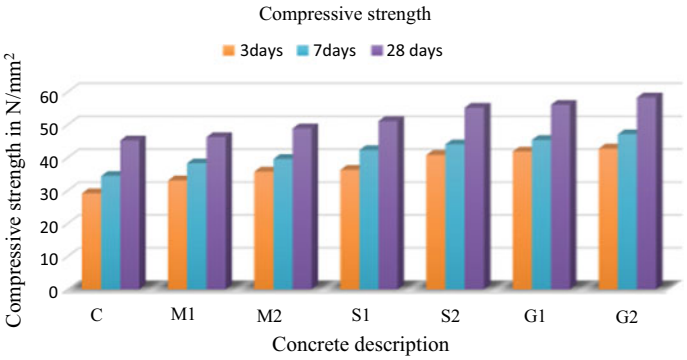

Fig. 3 Compressive strength test results

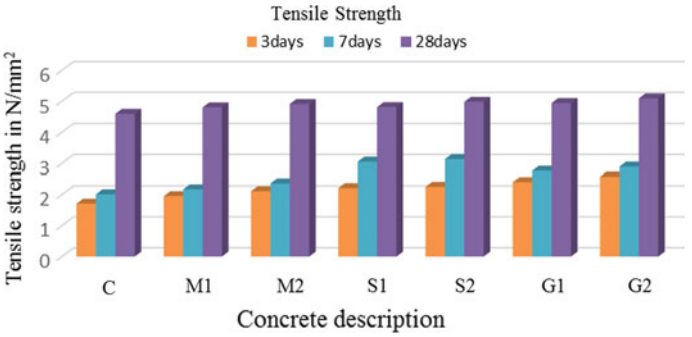

Fig. 4 Tensile strength test results

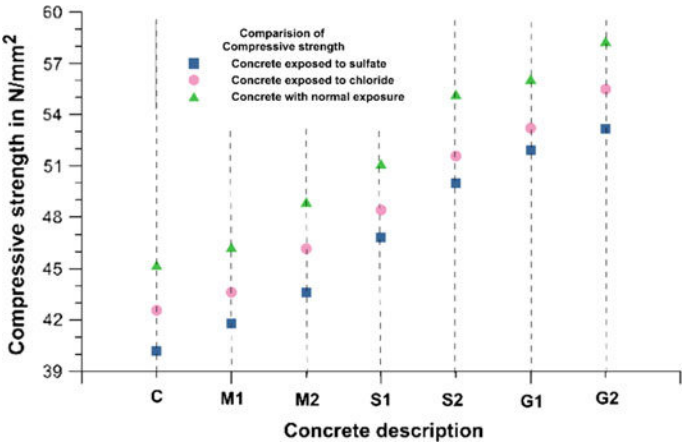

Fig. 5 Comparison of compressive strengths before and after exposure to chloride and sulfate

Table 4 Percentage change in strengths of concrete

S. no.	Coding	Percentage increase in		Percentage decrease in compressive strength after	
		Compressive strength	Tensile strength	Chloride attack	Sulfate attack
1	C	Base case		5.86	11.10
2	M1	4.52	6.75	5.70	9.61
3	M2	5.67	6.97	5.52	10.76
4	S1	12.20	4.79	5.30	8.39
5	S2	22.02	7.19	6.56	9.42
6	G1	23.40	6.97	5.11	8.80
7	G2	28.29	9.37	4.82	7.40

4 Conclusion

The study reports the results of strength and durability characteristics of M40 grade HPC replaced with 15% of cement by weight with three combinations of mineral admixtures, namely fly ash and GGBS, fly ash and metakaolin, and fly ash and silica fume. The experiment was repeated for two proportions in each combination.

From the test results, the following conclusions are made:

- In all three combinations of mineral admixtures, an improvement of mechanical properties was observed confirming earlier studies.
- Among the combinations, GGBS and fly ash combination (10% of GGBS + 5% of fly ash) gives the optimum percentage inflate on the compressive strength at 28 days by 28.29% when compared to conventional concrete.
- GGBS and fly ash combination (10% of GGBS + 5% of fly ash) is the optimum percentage enhancing the tensile strength at 28 days by 9.37% when compared to conventional concrete.
- All combinations enhanced the resistance to chloride and sulfate attack. For GGBS and fly ash combination (10% of GGBS + 5% of fly ash), compressive strength reduced by 4.82% and 7.40% for chloride and sulfate attack, respectively, which is less compared to the reduction of compressive strength of conventional concrete (5.86% for chloride attack and 11.10% for sulfate attack).

From the results, the mixture of GGBS and fly ash (10% of GGBS + 5% of fly ash) gives the best results from the aspect of both strength and durability.

References

1. Patil BB, Kumbhar PD (2012) Strength and durability of high-performance concrete incorporating High reactivity metakaolin. Int J Mod Eng Res 2(3):1099–1104
2. Ajay PS, Pradip DJ (2013) Strength appraisal of high-grade concrete by using high reactive metakaolin. Int J Innov Res Sci Eng Technol 2(3):657–663
3. Madudeaswaran P, Eswaeamoorthi P (2013) Experimental study on durability characteristics of high-performance concrete. Int J Eng Technol Adv Eng 3(1):507–510
4. Tamilarasan VS, Perumal P, Maheswaran N (2012) Workability studies on concrete with GGBS as a replacement material for cement with and without superplasticizer. Int J Adv Res Eng Technol 3(2):11–21
5. Latha KS, Seshagiri Rao MV, Reddy VS (2012) Estimation of GGBS and HVFA strength efficiencies in concrete with age. Int J Eng Adv Technol 2(2):221–225
6. Jadhav HS, Chavarekar RR (2013) Role of fly ash and silica fume on compressive strength characteristics of high-performance concrete. Int J Struct Civ Eng Res 2:32–39
7. Ghutke VS, Bhandari S (2014) Influence of silica fume on concrete. IOSR J Mech Civil Eng: 44–47
8. Awasare V, Nagendra MV (2015) Analysis of strength characteristics of GGBS concrete. Int J Adv Eng Technol: 82–84
9. Li LG, Zheng JY, Ng PL, Zhu J, Kwan AKH (2019) Cementing efficiencies and synergistic roles of silica fume and nano-silica in sulphate and chloride resistance of concrete. Constr Build Mater 223:965–975. https://doi.org/10.1016/j.conbuildmat.2019.07.241

10. Zhao Y, Gong J, Zhao S (2017) Experimental study on shrinkage of HPC containing fly ash and ground granulated blast-furnace slag. Constr Build Mater 155:145–153. https://doi.org/10.1016/j.conbuildmat.2017.07.020
11. Kumar A, Verma B, Nasrin T (2017) High performance concrete & its applications in civil engineering. Int J Adv Res Sci Eng 6:475–482
12. Wu S (2019) Application of mineral admixture in high performance concrete. Glob J Res Eng 19:33–36
13. Güneyisi E, Gesoğlu M, Karaoğlu S, Mermerdaş K (2012) Strength, permeability and shrinkage cracking of silica fume and metakaolin concretes. Constr Build Mater 34:120–130. https://doi.org/10.1016/j.conbuildmat.2012.02.017
14. Indian standard code of methods of sampling and analysis of concrete IS: 1199-1959. Bureau of Indian Standards, New Delhi
15. Indian standard code of methods of tests for strength of concrete, IS: 516-1959. Bureau of Indian Standards, New Delhi
16. Indian standard code of splitting tensile strength of concrete method of test, IS 5816-1999. Bureau of Indian Standards, New Delhi
17. Indian standard code of concrete mix proportioning—guidelines, IS: 10262-2009. Bureau of Indian Standards, New Delhi

Effect of Fly Ash as Replacement of Fine Aggregate on Strength Enhancement of Concrete

K. C. Panda, S. S. Samantaray, and S. Jena

Abstract In this study, class F fly ash (FA) is used as a partial replacement of fine aggregate on strength enhancement of concrete. Two series of concrete mixes are prepared. In the first series, fine aggregate is replaced with class F FA by weights such as 0, 10, 20, 30, 40 and 50% with varying w/c ratio to meet the required workability. In the second series, fine aggregate is replaced with class F FA by weights such as 10, 20, 30, 40 and 50% with constant w/c ratio (0.375) and the required workability was maintained by mixing the superplasticiser, i.e. Cera Hyperplast XR-W40. The design mix is carried out for M30 grade concrete. The workability of concrete is determined by slump test and hardened concrete properties such as compressive strength, split tensile strength and flexural strength are determined at 7, 28 and 90 days. The test result indicates that the compressive strength of concrete increases up to 30% replacement of fine aggregate with FA whereas for split and flexural strength, it increases up to 40% replacement of fine aggregate with FA.

Keywords Fly Ash (FA) · Compressive strength · Flexural strength · Split tensile strength · Concrete · Cementing efficiency

1 Introduction

Along with the rise in infrastructure development, the demand for sand is at its peak. River mining is the source of natural sand. But excessive mining of sand may cause uncalled harm to rivers' environment. The effects include the hardening of water, environment pollution, etc. In addition to that, the total effective cost of construction increases due to the very high cost of sand. All in all, an effective, eco-friendly, economic alternative that could successfully replace sand in concrete

K. C. Panda (✉)
Government College of Engineering, Kalahandi, Bhawanipatna, India
e-mail: kishoriit@gmail.com

S. S. Samantaray · S. Jena
Institute of Technical Education and Research, SOA (Deemed to be University), Bhubaneswar, India

© Springer Nature Singapore Pte Ltd. 2021

K. K. Pathak et al. (eds.), *Recent Trends in Civil Engineering*, Lecture Notes in Civil Engineering 77, https://doi.org/10.1007/978-981-15-5195-6_45

needs to be found out. Many standard codes of practice tell to use fly ash in the construction sector. Fossil fuel energy resources often produce fly ash as their by-product. Fly ash production has increased in recent years with the increasing usage of conventional energy sources. Unfortunately, above 60% of the produced fly ash is remaining unutilised causing several environmental issues like soil pollution by heavy metals, health problems, groundwater contamination and many more. Hence proper maintenance and innovative utilisation of fly ash is an alarming necessity. FA replaces both fine aggregate and cement perfectly. A number of studies have been reported on the use of class F FA. Siddique [1] presented a clear picture of the aftermath of replacement of fine aggregate with FA (class F) for concrete with w/c ratio value 0.47 from 7 to 365 days. Test results indicated that good upgradation in strength properties of plain concrete by the inclusion of class F FA for concrete as partial replacement of fine aggregate can be effectively used in a concrete structure. Rajamane et al. [2] predicted a formula for the compressive strength of concrete with FA as sand replacement material. This was purely established on the compressive strength of hardened concrete. The cementing efficiency factor (K) of FA was required when the amount of FA was partially more than that of sand that is replaced. The compressive strength of concrete was estimated by using the predicted formula for different proportions 20, 40 and 60% of sand replacement by FA. The w/b ratio was 0.35. It was concluded that concrete with FA as sand replacement material had higher strength than original control concrete and also the predicted formula was used to modify any basic concrete mix. The test results indicated that the strength of concrete which contains FA was more than that of cement concrete. Suggestions for modifying a concrete containing FA at desired sand replacement level were made in the paper and a prediction formula was evaluated to determine the compressive strength. It was observed that concrete containing FA as partial sand replacement material can enhance durability, refine the microstructure and is eco-friendlier. Raman et al. [3] experimentally investigated the applicability of quarry dust as a partial replacement for sand in HSC which contains rice husk ash (RHA). Yuksel et al. [4] investigated and concluded that non-grounded granulated blast-furnace slag (GBFS) and coal bottom ash (BA) can successfully replace sand in concrete. Rashad [5] researched the suitability of replacing fine aggregate by metakaolin (MK) up to 40%. Compressive strength, split tensile strength, unit weight density and abrasion test were studied by replacing sand partially by metakaolin (MK) at levels of 10, 20, 30, 40 and 50%. Panda et al. [6] studied the influence of partial replacement of fine aggregate with class F FA and without the addition of superplasticiser (SP) on compressive, flexural and split tensile strength of concrete and concluded that fine aggregate when replaced by 30% of class F FA gives higher compressive strength. Singh and Siddique [7] presented the potential use of coal bottom ash as fine aggregate in concrete and stated that the use of coal bottom ash in concrete will be eco-friendly and ecological since it helps in natural resource conservation. Aggarwal and Siddique [8] experimentally investigated how waste foundry sand and bottom ash in equal quantities as partial replacement of fine aggregate in various percentages (0–60%) affected concrete properties. The present study experimentally observed the pros and cons of fly ash as partial replacement

of fine aggregate material and without the addition of superplasticiser (SP) Cera Hyperplast XR-W40.

2 Experimental Programme

The experimental programme is divided into two stages. In the first stage, the materials used in the study such as cement (OPC 43), fine aggregate (sand), natural coarse aggregate (NCA) and fly ash (FA) and its physical and mechanical properties are established by experimentation. All materials are tested. In the second stage, concrete specimens with two series of concrete mixes are prepared. In the first series, fine aggregate is replaced with class F FA by weights such as 0, 10, 20, 30, 40 and 50% with varying w/c ratio to meet the required workability. In the second series, the fine aggregate is replaced with class F FA by weights such as 10, 20, 30, 40 and 50% with constant w/c ratio 0.375 and by changing superplasticiser to maintain the required workability. Finally the specimens are tested to know the compressive strength, flexural and split tensile strength of concrete.

2.1 Materials Used and Properties

Ordinary Portland Cement (OPC) 43 grade is used in this research. The physical properties of cement satisfying IS 8112:1989 [9] are listed in Table 1. Sand passing through IS 4.75 mm sieve and natural coarse aggregate passing through IS 20 mm sieve are used. The properties of fine aggregate and natural coarse aggregate satisfying IS 383-1970 [10] are presented in Table 2. In this study, class F FA was

Table 1 Physical properties of Ordinary Portland Cement (OPC 43 grade)

Characteristics	Experimental value (IS 8112:1989)
Normal consistency of cement (%)	34
Fineness of cement (m^2/kg)	330
Initial setting times of cement (min)	125
Final setting times of cement (min)	420
Specific gravity of cement	3.15
Compressive strength of cement (MPa) 3 days	30.05
7 days	45.75
28 days	52.39

Table 2 Physical properties of aggregates

Characteristics	Fine aggregate	Coarse aggregate
Abrasion value (%)	–	27.02
Crushing value (%)	–	28.70
Impact value (%)	–	24.00
Fineness modulus	3.48 (Zone1)	7.95
Water absorption (%)	0.30	0.10
Specific gravity	2.63	2.84
Bulk density (kg/m$^{3)}$	1568	1418

used supplied by NALCO, Angul, Odisha as shown in Fig. 1. The fine aggregate is replaced with class F FA having different percentages 10, 20, 30, 40 and 50%. The chemical composition of FA is presented in Table 3. Cera Hyperplast XR-W40 high-end superplasticiser is used.

Fig. 1 Fly Ash samples

Table 3 Chemical composition of FA

Oxides (%)	Average	Oxides (%)	Average
SiO_2	58.13	Na_2O	0.05
Al_2O_3	31.00	K_2O	0.90
Fe_2O_3	4.10	SO_3	0.12
CaO	0.60	P_2O_5	0.39
MgO	0.10	CI	0.011
LOI	2.90	TiO_2	1.63

2.2 Details of Concrete Mix

For M30 grade concrete mix, the technique used is mix design. The mix design as per standard specification IS 10262-1982 [11] helps in achieving the strength that is aimed, i.e. 39.9 MPa. The mix proportion is 1: 1.03: 2.37. The test for observing the compressive strength of the control specimen observed after 28 days of curing gives the value 56.25 MPa. High cement percentage in concrete leads to the higher compressive strength of control specimens. In this research, around eleven (11) concrete mixtures were prepared, out of which one mix was control mix with w/c ratio 0.375, five (5) mixes were made by replacing 10, 20, 30, 40 and 50% of fine aggregate with class F FA with varying w/c ratio and without superplasticiser. Therest five (5) concrete mixes were made by replacing 10, 20, 30, 40 and 50% of fine aggregate with class F FA with constant w/c ratio 0.375 and superplasticiser. M indicates concrete mix with 0% FA, i.e. conventional concrete. M1 indicates concrete mix with 10, 20, 30, 40 and 50% replacement of fine aggregate with class F FA and without superplasticiser with varying w/c ratio as per the requirement to get proper workability; M2 indicates concrete mix with 10, 20, 30, 40 and 50% replacement of fine aggregate with class F FA in addition to superplasticiser and w/c ratio 0.375. MS100F0 indicates 0% FA and 100% fine aggregate, M1S90F10 indicates 90% fine aggregate and 10% FA, M1S80F20 indicates 80% fine aggregate and 20% FA, M1S70F30 indicates 70% fine aggregate and 30% FA, M1S60F40 indicates 60% fine aggregate and 40% FA, and M1S50F50 indicates 50% fine aggregate and 50% FA. Concrete mix details and their identification is given in Table 4. The mix quantity details of M1, M2 are presented in Table 5. M1 mix is composed of different constituents like

Table 4 Concrete mix details with identification

Concrete mix details	Mix identity
Concrete mix (M and M1) without superplasticiser	
100% CA + 100% NFA + 0% FA + 0% SP + W/C 0.375	MS100F0
100% CA + 90% NFA + 10% FA + 0% SP + W/C 0.40	M1S90F10
100% CA + 80% NFA + 20% FA + 0% SP + W/C 0.42	M1S80F20
100% CA + 70% NFA + 30% FA + 0% SP + W/C 0.45	M1S70F30
100% CA + 60% NFA + 40% FA + 0% SP + W/C 0.48	M1S60F40
100% CA + 50% NFA + 50% FA + 0% SP + W/C 0.50	M1S50F50
Concrete mix M2 with superplasticiser	
100% CA + 90% NFA + 10% FA + 0.30% SP + W/C 0.375	M2S90F10
100% CA + 80% NFA + 20% FA + 0.40% SP + W/C 0.375	M2S80F20
100% CA + 70% NFA + 30% FA + 0.55% SP + W/C 0.375	M2S70F30
100% CA + 60% NFA + 40% FA + 0.80% SP + W/C 0.375	M2S60F40
100% CA + 50% NFA + 50% FA + 0.95% SP + W/C 0.375	M2S50F50

Table 5 Mix quantity details of different constituent per m^3 of concrete

Mix identity	Cement (kg)	Sand (kg)	Fly Ash (kg)	CA(kg)	Super plasticiser (kg)	Water (kg)	Slump (mm)
MS100F0	511.00	527.00	–	1209.27	–	191.6	35
M1S90F10	511.00	474.30	52.70	1209.27	–	204.4	25
M1S80F20	511.00	421.60	105.40	1209.27	–	214.6	18
M1S70F30	511.00	368.90	158.10	1209.27	–	230.0	15
M1S60F40	511.00	316.20	210.80	1209.27	–	245.3	12
M1S50F50	511.00	263.50	263.50	1209.27	–	255.5	15
M2S90F10	511.00	474.30	52.70	1209.27	1.53	191.6	30
M2S80F20	511.00	421.60	105.40	1209.27	2.04	191.6	20
M2S70F30	511.00	368.90	158.10	1209.27	2.81	191.6	28
M2S60F40	511.00	316.20	210.80	1209.27	4.09	191.6	24
M2S50F50	511.00	263.50	263.50	1209.27	4.85	191.6	30

cement, sand, FA, coarse aggregate and water. Similarly, M2 mix is composed of cement, sand, FA, coarse aggregate, superplasticiser and water.

2.3 Mixing and Casting

The fresh concrete test was conducted to know the workability of concrete. The fresh concrete such as a slump test was conducted for all concrete mixtures. The hardened properties of concrete specimens were conducted at 7, 28, and 90 days underwater at normal temperature and humidity conditions to know the mechanical properties of concrete, which include split tensile strength, compressive and flexural strength. The concrete cubes of size 150 × 150 × 150 mm were used for compressive strength, 100 mm diameter × 200 mm height cylinders for split tensile strength and 100 × 100 × 500 mm prisms for flexural strength. The setup for compressive strength, flexural strength and split tensile strength is shown in Fig. 2.

3 Experimental Results and Discussions

The workability of fresh concrete is measured by the slump test. The slump values of different mixes are presented in Table 5. The experiment shows that when only FA is used, the value of slump lied between 12 and 35 mm. But in the case of the concrete mix with FA and SP, the slump lied between 20 and 30 mm. The required workability was maintained below 40 mm slump for concrete mixes of both the series.

Fig. 2 Arrangement for compressive, flexural and split tensile strength

3.1 Compressive Strength

The compressive strength test results of FA without SP mixes (M1) and FA with SP mixes (M2) are presented in Table 6. Both the mixes show increment in compressive strength with an increase in curing time. It is noticed in M1 and M2 mixes that there is an increase in compressive strength when up to 30% fine aggregate is replaced by FA, after which it comparatively decreases. Lesser compressive strength

Table 6 Summary of compressive strength test results

Mix identification	7 days		28 days		90 days	
	Average compressive strength (MPa)	Difference in strength w.r.t control specimen (%) (MS100F0)	Average compressive strength (MPa)	Difference in strength w.r.t control specimen (%) (MS100F0)	Average compressive strength (MPa)	Difference in strength w.r.t control specimen (%) (MS100F0)
MS100F0	42.30	0	56.25	0	65.88	0
M1S90F10	44.73	5.74	59.50	5.77	67.50	2.46
M1S80F20	50.77	20.02	61.39	9.14	68.27	3.63
M1S70F30	51.00	20.57	62.35	10.84	69.50	5.49
M1S60F40	46.85	10.76	58.50	4.00	65.40	−0.73
M1S50F50	36.56	−13.57	48.48	−13.81	55.45	−15.84
M2S90F10	62.37	47.45	72.55	28.98	79.25	20.29
M2S80F20	65.55	54.96	75.45	34.13	82.15	24.70
M2S70F30	66.35	56.86	78.41	39.40	84.25	27.88
M2S60F40	61.30	44.92	72.45	28.80	78.25	18.78
M2S50F50	56.26	30.00	69.00	22.67	76.30	15.82

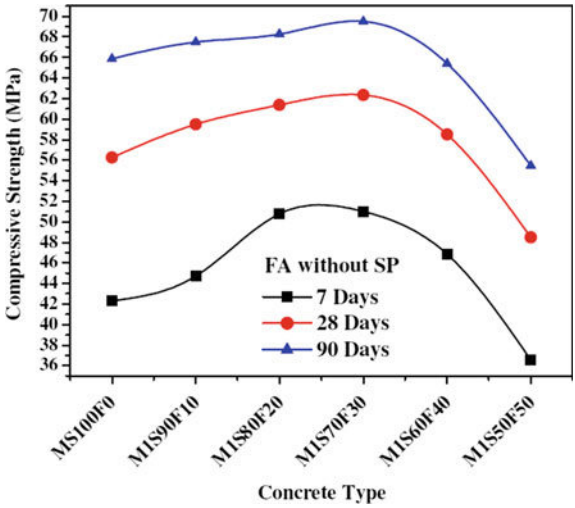

Fig. 3 Compressive strength versus concrete mix type (FA without SP)

of M1S50F50 in comparison to control specimen (MS100F0) is observed. The early age compressive strength enhancement of specimens M1S70F30 and M2S70F30 after 7 days in comparison to control specimen MS100F0 is 20.57% and 56.86%, respectively, whereas the strength enhancement after 28 and 90 days for specimens M1S70F30 and M2S70F30 is 10.84%, 5.49% and 39.40%, 27.88%, respectively. As age increases, the percentage enhancement of compressive strength decreases in comparison to the control mix. At all ages, more enhancement is observed in concrete mixes (M2) prepared with both FA and SP. The early age enhancement after 7 days of M2S70F30 mixes is 36.29% higher than M1S70F30 mixes. In M1S70F30, the w/c ratio used 0.45 whereas in M2S70F30, the w/c ratio was 0.375 with 0.55% of SP. The result indicates that initially the increment in compressive strength of M2 mixes is because of the presence of SP. The differences in compressive strength with respect to the type of concrete mix with FA and without SP for all SRR at different ages of curing is presented in Fig. 3. Similarly, the variation in compressive strength in comparison to concrete mix type with FA and with SP for all SRR at different ages of curing is presented in Fig. 4.

3.2 Flexural Strength

The summary of flexural strength results for FA without SP (M1) and FA with SP (M2) are presented in Table 7. Increases in flexural strength of all specimens of concrete mixes M1 and M2 are observed when up to 40% FA is used in place of fine aggregate and then there is a decrease in flexural strength. Early age flexural strength enhancement of specimens M1S60F40 and M2S60F40 observed after 7 days with respect to control specimen MS100F0 is 18.72% and 20.85%, respectively,

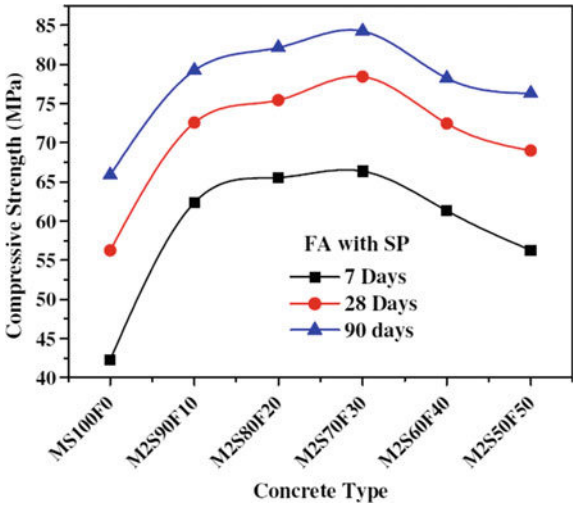

Fig. 4 Compressive strength versus concrete mix type (FA with SP)

Table 7 Summary of flexural strength test results

Mix identification	7 days		28 days		90 days	
	Average flexural strength (MPa)	Difference in strength w.r.t control specimen (%) (MS100F0)	Average flexural strength (MPa)	Difference in strength w.r.t control specimen (%) (MS100F0)	Average flexural strength (MPa)	Difference in strength w.r.t control specimen (%) (MS100F0)
MS100F0	4.70	0	6.25	0	6.80	0
M1S90F10	4.90	4.25	6.48	3.68	6.95	2.20
M1S80F20	5.20	10.64	6.75	8.00	7.12	2.45
M1S70F30	5.45	15.96	6.88	10.08	7.25	6.62
M1S60F40	5.58	18.72	7.08	13.28	7.31	7.50
M1S50F50	5.32	13.19	6.78	8.48	7.14	5.00
M2S90F10	5.25	11.70	6.85	9.60	7.35	8.09
M2S80F20	5.40	14.90	7.10	13.60	7.52	10.60
M2S70F30	5.55	18.09	7.28	16.48	7.68	12.94
M2S60F40	5.68	20.85	7.45	19.20	7.88	15.88
M2S50F50	5.32	13.19	7.20	15.20	7.62	12.06

whereas the strength enhancement after 28 and 90 days for specimens M1S60F40 and M2S60F40 is 13.28%, 7.50% and 19.20%, 15.88%, respectively. As curing time increases, the percentage enhancement of flexural strength decreases in comparison to the control mix. It is also noticed that the increment is more in concrete mixes prepared with both FA and SP (M2) as compared with FA and without SP (M1). The disparity in flexural strength with respect to concrete mix type with FA and

without SP for all SRR at different ages of curing is presented in Fig. 5. Similarly, the variation in flexural strength with respect to concrete mix type with FA and with SP for all SRR is presented in Fig. 6.

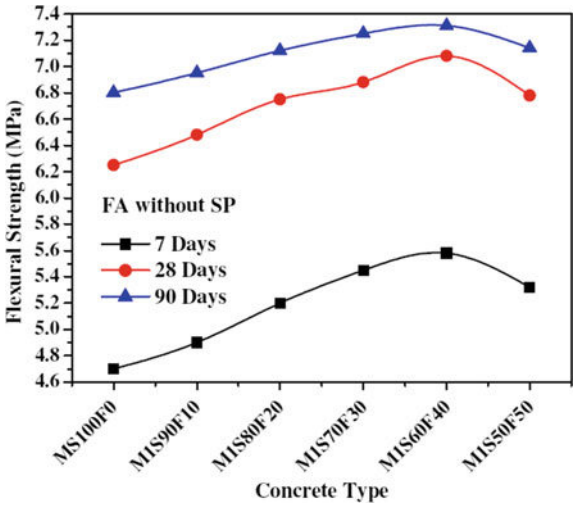

Fig. 5 Flexural strength versus concrete mix type (FA without SP)

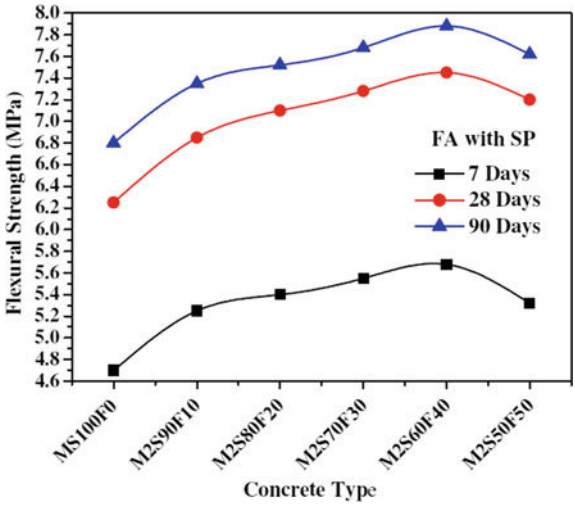

Fig. 6 Flexural strength versus concrete mix type (FA with SP)

Table 8 Summary of split tensile strength test results

Mix identification	7 Days		28 days		90 days	
	Average split tensile strength (MPa)	Difference in strength w.r.t control specimen (%) (MS100F0)	Average split tensile strength (MPa)	Difference in strength w.r.t control specimen (%) (MS100F0)	Average split tensile strength (MPa)	Difference in strength w.r.t control specimen (%) (MS100F0)
MS100F0	3.41	0	4.35	0	4.85	0
M1S90F10	3.51	2.93	4.45	2.29	4.98	2.68
M1S80F20	3.65	7.04	4.65	6.89	5.15	6.18
M1S70F30	3.78	10.85	4.85	11.49	5.28	8.86
M1S60F40	3.95	15.84	4.89	12.41	5.32	9.69
M1S50F50	3.82	12.02	4.70	8.04	5.18	6.80
M2S90F10	3.71	8.79	4.75	9.20	5.15	6.18
M2S80F20	3.85	12.90	4.84	11.49	5.28	8.86
M2S70F30	4.20	23.17	4.98	14.48	5.42	11.75
M2S60F40	4.25	24.63	5.15	18.39	5.51	13.61
M2S50F50	4.05	18.77	4.88	12.18	5.36	10.51

3.3 Split Tensile Strength

The summary of split tensile strength test results of concrete mixes (M1) FA without SP and (M2) FA with SP are furnished in Table 8. An increase in split tensile strength of mixes M1 and M2 is observed when up to 40% fine aggregate is replaced with FA and then there is a decrease in strength. Also, early age split tensile strength enhancement of specimens M1S60F40 and M2S60F40 is observed after 7 days in comparison to control specimen MS100F0, i.e. 15.84% and 24.63%, respectively, whereas the strength enhancement after 28 and 90 days for specimens M1S60F40 and M2S60F40 is 12.41%, 9.69% and 18.39%, 13.61%, respectively. As the age of curing increases, the percentage enhancement of strength with respect to corresponding control specimens decreases. The variation in split tensile strength with respect to concrete mix type with FA and without SP for all SRR at different ages of curing is furnished in Fig. 7. Similarly, variation in split tensile strength with respect to concrete mix type with FA and with SP for all SRR is presented in Fig. 8.

4 Concluding Remarks

In this paper, the outcomes of the concrete mixture containing fly ash as a replacement product of 50% fine aggregate and M30 grade concrete are shown. M30 grade concrete specimen and the concrete mix containing fine aggregate replacement up to

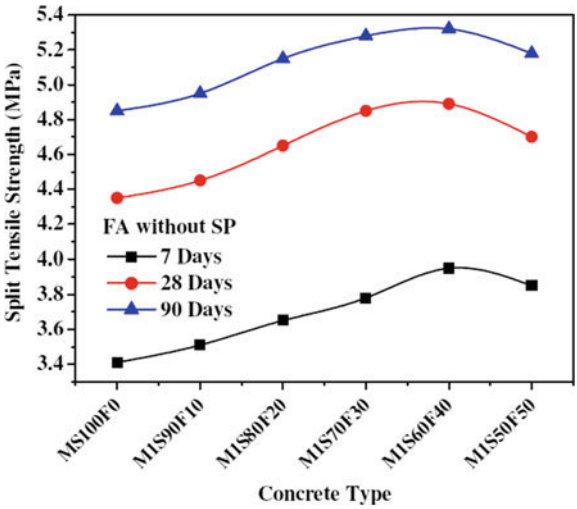

Fig. 7 Split tensile strength versus concrete mix type (FA without SP)

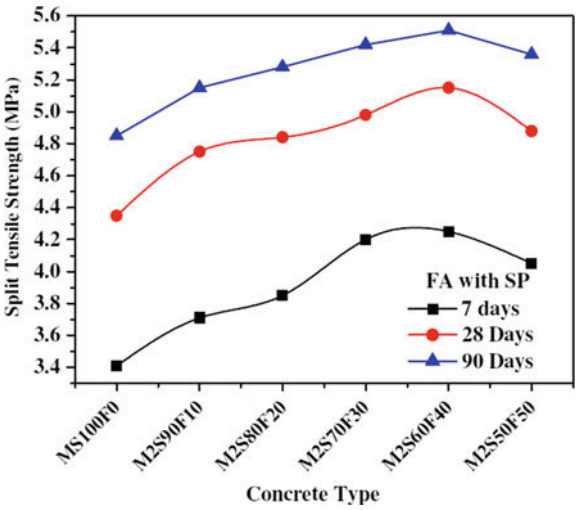

Fig. 8 Split tensile strength versus concrete mix type (FA with SP)

50% with fly ash are presented. The following conclusions are slowly based on the above outcomes.

- The workability of fresh concrete was controlled within a 40 mm slump for strength enhancement. It is seen that a concrete mix which contains only FA (without SP) gives slump results in between 12 and 35 mm and mix which contains both FA and SP gives slump results in between 20 and 30 mm.
- Performance of compressive strength of concrete mix prepared with FA and SP is better than concrete mix prepared with FA and without SP.

- At 30% replacement of fine aggregate with fly ash, i.e. 62.35 MPa for FA without SP and 78.41 MPa for FA with SP, the highest compressive strength is observed after 28 days of curing.
- Compressive strength is higher in the case of concrete with both FA and SP, i.e. 39.41% as compared to concrete prepared with FA and without SP, i.e. 10.84% after 28 days.
- As the age of curing increases, the percentage enhancement of compressive strength decreases with respect to the corresponding control specimen.
- The early age compressive strength of concrete prepared with FA and SP is higher as compared to concrete prepared with FA and without SP.
- The maximum flexural strength is observed at 40% replacement of fine aggregate with fly ash, i.e. 7.05 MPa for FA without SP and 7.45 MPa for FA with SP after 28 days of curing.
- The enhancement of flexural strength is higher for concrete prepared with FA and SP, i.e. 19.20% as compared to concrete prepared with FA and without SP, i.e. 13.28% after 28 days of curing.
- At 40% replacement of fine aggregate with fly ash, i.e. 4.89 MPa for FA without SP and 5.15 MPa for FA with SP after 28 days of curing, the test result produces the highest split tensile strength.
- The split tensile strength is higher for concrete containing FA and SP, i.e. 18.39% in comparison to concrete containing FA (without SP), i.e. 12.41% after 28 days of curing.
- The early age strength of FA-based concrete is enhanced by adding SP.
- The compressive strength result of concrete prepared by replacement of fine aggregate with FA up to 40% gives higher value than the control specimen at all ages.
- The split tensile strength and flexural strength of concrete prepared by replacement of fine aggregate with FA give higher value than the control specimen (without FA) at all ages.
- Maximum compressive strength is observed when 30% of fine aggregate is replaced with FA and lower strength is observed when 50% of fine aggregate is replaced with FA.

References

1. Siddique R (2003) Effect of fine aggregate replacement with Class-F Fly Ash on the mechanical properties of concrete. Cem Concr Res 33:539–547
2. Rajamane NP, Peter JA, Ambily PS (2007) Prediction of compressive strength of concrete with Fly Ash as sand replacement material. Cement Concr Compos 29:218–223
3. Raman SN, Ngo T, Mendis P, Mahmud HB (2011) High-strength rice husk ash concrete incorporating quarry dust as partial substitute for sand. Constr Build Mater 25:3123–3130
4. Yuksel I, Siddique R, Ozkan O (2011) Influence of high temperature on the properties of concretes made with industrial by-products as fine aggregate replacement. Constr Build Mater 25:967–972

5. Rashad AM (2013) A preliminary study on the effect of fine aggregate replacement with metakaolin on strength and abrasion resistance of concrete. Constr Build Mater 44:487–495
6. Panda KC, Samantaray SS, Mishra M (2014) Influence of fly ash as fine aggregate replacement material on mechanical properties of concrete. Int J Earth Sci Eng 7(4):603–607
7. Singh M, Siddique R (2014) Compressive strength, drying shrinkage and chemical resistance of concrete incorporating coal bottom ash as partial and total replacement of sand. Constr Build Mater 68:39–48
8. Aggarwal Y, Siddique R (2014) Microstructure and properties of concrete using bottom ash and waste foundry sand as partial replacement of fine aggregates. Constr Build Mater 54:210–223
9. IS 8112 (1989) Indian Standard 43 grade ordinary portland cement specification (First revision). Bureau of Indian Standards. New Delhi, India
10. IS: 383 (1970) Indian Standard specification for coarse and fine aggregates from natural sources for concrete (Second revision). Bureau of Indian Standards. New Delhi, India
11. IS: 10262 (1982) Recommended guidelines for concrete mix design. Bureau of Indian Standards. New Delhi, India

Bacterial Concrete for the Development of Sustainable Construction—A Review

S. Jena, B. Basa, and K. C. Panda

Abstract Concrete which is vastly utilized in building materials has its own disadvantages, one being the phenomenon of crack formation which allows the passage of water, CO_2 and other chemicals into the concrete. The incoming materials cause decrement in strength along with durability and ductility. These materials also have adverse effects on reinforcements. If the cracks are not healed as soon as they are formed, they might expand and become larger allowing passage of more amount of materials causing greater problems. That's why the best solution is to prevent the formation of cracks from the very beginning. Self-healing concrete provides one such solution. In self-healing concrete, the concrete material is capable of healing the cracks formed beforehand, on its own. Microbial actions help in this. The basic principle of self-healing concrete is the formation of calcium carbonate precipitate by bacterial action. This introduction of bacterial concrete paves the way to the production of more durable, sustainable, crack-free and more efficient concrete. The usage of bacteria in concrete justifies its name, microbial concrete or biological concrete (in short bio concrete). The bio concrete causes less pollution and is economic as well. This paper aims at defining bacterial concrete and its effects on concrete properties and describing its merits and few demerits.

Keywords Concrete · Strength · Durability · Self-healing · Bacteria

S. Jena (✉) · B. Basa
Institute of Technical Education and Research, SOA (Deemed to be University), Bhubaneswar, India
e-mail: sjena4203@gmail.com

B. Basa
e-mail: bidyadharbasa@soa.ac.in

K. C. Panda
Government College of Engineering, Kalahandi, Bhawanipatna, India
e-mail: kishoriit@gmail.com

© Springer Nature Singapore Pte Ltd. 2021

K. K. Pathak et al. (eds.), *Recent Trends in Civil Engineering*, Lecture Notes in Civil Engineering 77, https://doi.org/10.1007/978-981-15-5195-6_46

1 Introduction

In the recent era, concrete is the most utilized infrastructural material. As the ingredients for concrete are commonly available, it is easy to use it as a building material. Concrete is economically advantageous, can be equipped into the required shape and can withstand high temperature. Although the compressive strength of concrete is high, it has many drawbacks like it has low crack resistance, less tensile strength and less ductility. Fierce environmental factors along with consistent sustained pressure result in declination of self-life of concrete. While designing a concrete structure, strength and durability must be kept in mind. A major problem in concrete is the crack formation on its surface, which is due to the low tensile strength of concrete [1, 2]. Cracks in concrete lead to the reduction of strength and durability and make concrete sensitive to the deleterious environment [3]. Also cracks pave way to chloride attack, carbonate attack and sulphate attack, as a result of which corrosion of steel reinforcement and deterioration of concrete take place. The formation of crack is generally intercepted by manual examination and repairs by using synthetic fillers or cement [4]. But these repairs are not cost effective and not possible for deep cracks [5, 6]. Thus, emerging a favourable and inventive way to heal the cracks of concrete is the call of nature, i.e. self-healing concrete. Many self-healing techniques like adhesive-based, autogenous, bacteria-based and mineral admixtures based have been introduced [7]. Among these methods, bacteria-based self-healing of cracks is the most effective one [1–3, 5, 8–16].

Ureolytic bacteria was first time used as a healing agent by Gollapudi et al. (1995) for cracks which assists the enzymatic hydrolysis of urea to ammonia and carbon dioxide [9]. On the other hand, Ramakrishnan et al. (2001) first introduced the concept of utilizing microbiologically induced calcite ($CaCO_3$) precipitation [17]. When bacterial techniques were applied in fresh concrete, it produces calcite precipitation in the void of concrete which decreases the permeability and increases the strength of concrete. Deposition of calcite on the concrete specimen by the bacteria leads to the reduction of gas permeability and uptake of capillary water. Crystals of calcium carbonate deposition on the concrete specimen results in the decrease in water absorption up to 85%. Bacterial carbonate precipitation affects the durability of the concrete specimen with different porosity. Due to bacterial calcite precipitation, permeability and sorptivity of concrete decrease. Depending upon porosity, water absorption is reduced from 65 to 90% due to bacterial carbonate precipitation [18]. Due to the execution of the bacterial approach in concrete, the durability property of concrete has been improved effectively [10, 13, 19–21]. This research paper highlights about bacteria, its self-healing mechanism and crack remediation techniques along with various advantages and disadvantages of bacterial concrete on its various properties.

2 Bacteria, Its Growth and Reproduction

Bacteria are unique species having simple structure but large diversity. Bacteria is the plural form of bacterium. The plasma membrane of bacteria having all the properties acts as a cell membrane. It serves as the area of transport of protein and nutrients. Bacterial species were the first to evolve in non-oxygenic atmosphere. They are prokaryotes as they do not have membrane-bound cell organelles in their body.

In the case of prokaryotic unicellular organisms, reproduction and cell growth are two mutually inclusive events, i.e. reproduction takes place by means of cell growth. Cell growth is the most common method of asexual reproduction among unicellular organisms. The bacterial cells grow up to a certain amount by taking nutrients from their surrounding atmosphere and then the parent cell divides into two new daughter cells by binary fission. DNA, mesosomes and other cell organelles divide into two equal parts. Each cell is a duplicate of the other.

Bacteria can be cultured in a laboratory by using a suitable growth medium (solid or liquid). Culture means letting the bacteria grow and reproduce in a predetermined condition in a medium inside a laboratory. Agar plates are the most commonly used solid growth media which contain all required nutrients for bacterial growth. Selective nutrient medium is required for detecting specific organisms. Liquid mediums are helpful for the culture of enormous volumes of bacteria. Naturally, it becomes difficult for bacteria to grow and to do cell division in artificial conditions which becomes unsuitable for them, but the usage of gel or liquid media containing natural resources are quite helpful in speeding up their rate of cell division, i.e. they do not have to struggle for collecting nutrients, they get ready-made nutrients. There are four stages in which bacterial growth in a nutrient medium takes place. First, bacteria need to adapt to their new environment, which is a quite slow phase, as they require some time to comprehend the condition they are in. This phase is known as the lag phase, where the rate of growth is slow and bacterium prepares itself for the upcoming high growth rate. The second phase is the log phase. In this phase, bacteria take up the nutrient at a faster rate, and metabolism is done at a higher speed. The third phase is the stationary phase. Here, the growth curve becomes horizontal. Due to the heavy usage of nutrients, now the nutrient medium starts depleting. The cellular activity along with metabolism keeps on decreasing. The final phase is the death phase in which all of the nutrient media are finished and bacteria die due to lack of nutrients.

3 Self-healing Mechanism

The main purpose of self-healing concrete is that it should be able to sense when the damage just begins, so that it can properly utilize its healing properties. For treating the microcracks, the self-healing technique is genuinely a good approach. The mixture of bacteria in concrete results in forming a layer of hard calcite, which autogenously heals the concrete [8, 22].

As concrete has high alkalinity, the bacteria which are added to it should have the capability of surviving in such adverse conditions [23, 24]. The calcite precipitate formed by bacteria helps in filling the microcracks and acts as a binding material for sand and gravel [25]. The addition of microorganisms to concrete helps in increasing its durability. *Bacillus sphaericus* bacteria can form calcite precipitation in a very alkaline medium by the conversion of urea into ammonia and carbonate [14]. Concrete itself can fill the cracks which are lesser than 0.2 mm in size. It is the cracks having size more than 0.2 mm which need to be taken care of, as they create pathways for water and other chemicals into the concrete. In the case of self-healing concrete, once any crack is formed, it immediately leads to the activation of bacteria from its dormancy. The metabolic activities of bacteria lead to calcium carbonate precipitation, which in turn, forms a hard layer and blocks the concrete. After the cracks are completely blocked, the bacteria again enter the dormancy period. The bacteria act as a good source for self-healing concrete, and the process is known as Microbiologically Induced Calcium Carbonate Precipitation (MICP).

The underlying principle of bacterial concrete is the formation of calcium carbonate precipitation around particles to bind quite loosely attached particles that helps in the strengthening of concrete. Commonly, urease producing bacteria serve this purpose [26, 27].

1 mol of urea when hydrolysed gives rise to 1 mol of ammonia (NH_3) and 1 mol of carbamic acid (NH_2COOH) [28]. Further carbamic acid when reacts with water produces 1 mol of bicarbonate and 2 mol of ammonia. Bicarbonate gets reduced to bicarbonate ion and H^+ ion. Also, the 2 mol of ammonia when reacts with water give ammonium ion and OH^-. The last reaction results in an increase in pH, due to which the reaction shifts towards right producing more carbonate ions (law of mass action)

$$\begin{aligned} 2NH_3 + 2H_2O \leftrightarrow HCO_3^- + H^+ + 2NH_4^+ \\ + 2OH^- \leftrightarrow CO_3^{2-} + 2NH_4^+ + 2H_2O \end{aligned} \tag{1}$$

We know that the cell wall of bacteria is negatively charged. Therefore, it attracts Ca^{2+} cations from the surrounding environment. The previously deposited $CO_3{}^{2-}$ ions react with these Ca^{2+} ions forming $CaCO_3$ precipitation at the cell wall which acts as the site for nucleation.

$$\text{Cell} - Ca_2^+ + CO_3^{2-} \rightarrow \text{Cell} - CaCO_3 \downarrow \tag{2}$$

The amount of deposited or non-reacted lime particles determines the potential of the concrete for self-healing.

4 Effect on Mechanical Properties of Concrete

4.1 Setting Time

In MICP process, bacteria are induced in the concrete mixture by replacing water with cultured bacteria along with nutrient medium [29]. Sometimes a decrease in hydration of cement is observed [30]. This may be due to the various minerals or constituents of the nutrient medium and various carbon and nitrogen sources. The frequently used Yeast extract as a part of the nutrient medium retards the hydration process [16, 31]. Calcium chloride, which is used to increase the calcite precipitation, accelerates the hydration of cement [32]. But it affects the durability of steel reinforcement for which it can't be used in concrete. Calcium nitrate which is used as the calcium source also accelerates the hydration process [33]. In general, setting time reduces when calcium lactate is used and increases when calcium nitrate and calcium formate are used [34, 35]. The main focus of the research being the decrement of the overall cost of materials and production of an economic biological concrete system, the chemical should be chosen in such a way that there is less migration of them causing the addition of chemicals from time to time, which in turn might be able to reduce the cost related to the purchase of chemicals.

4.2 Compressive Strength

Compressive strength plays a vital role in determining the durability of concrete. Hence, research in bio concrete is an essential field from the application point of view. When bacteria species are injected into concrete and mortar, it shows a significant increase in the compressive strength of concrete. By using bacterial sample Bacillus sp CT-5, the author observed that bacterial specimen gives strength of 31Mpa and compressive strength increases about 36% with respect to concrete without bacteria after 28 days of curing [26]. In the concrete containing Bacillus Sphaericus, increase in compressive strength of 30.76, 46.15 and 32.21% at 3, 7 and 28 days occurs. Split tensile strength increases by 13.75, 14.28 and 18.35% in a period of 3, 7 and 28 days, respectively [36]. Bacillus subtilis bacteria was introduced in concrete by using various bio influenced self-healing technique such as carrier compound namely lightweight aggregate and graphite nano platelets. By using carrier compound lightweight aggregate, there is an increase of 12% of compressive strength as compared to concrete without bacteria and by using graphite nano platelets, there is 9.8% increase in compressive strength as compared to concrete without bacteria [2]. Bacillus Haloduransstrain KG1 was used along with replacing Cement Kiln Dust with cement from 0 to 20%. With 10% CKD, 7.15 and 26.6% increase in strength at 28 and 91 days of test was observed [37]. By using Bacillus cereus 38% and by Bacillus pasturii 29% increase in compressive strength takes place after 28 days curing [38]. Bacillus Subtilis JC3 was used with a cell concentration of 10^4,10^5,10^6

and 10^7 cells per ml. The highest strength was achieved by cell concentration 10^5 cells/ml, which gives 23% increase in strength after 28 days of curing [39]. Addition of bacteria Bacillus Subtilis JC3 leads to an increase in the compressive strength by 13.93% at a curing period of 28 days whereas in the case of split tensile strength, there is an increase in strength by 12.60% at 28 days [40]. By adding B. Subtilis, the compressive strength of the structure increases about 23% at a curing period of 28 days for ordinary concrete when compared to controlled concrete [41]. Both dead and live bacterial cells of B. Pasturii were used with different cell concentrations and found that the live cells having a smaller number of cells per ml, if allowed to grow for a longer period, increase the compressive strength of cement mortar. As per the results, a marginal increase of up to 10% of compressive strength was observed by adding B. Pasturii [23].

Shewanella species was used with 10–10^7 cells/ml concentration and the highest strength, i.e. 25% increase in strength in comparison to control concrete was achieved with cell concentration of 10^5 cells/ml [42]. In the case of Bacillus cohnii, a change in the ongoing process was observed. In this case, the highest strength increment of 49.18% was observed with a concentration of 10^7 cells/ml [43]. Also in the case of Bacillus subtilis, the highest strength is observed in 10^5cells/ml concentration [44]. In fly ash based concrete, Sporoscarcina pasteurii was used with concentration of 10^3, 10^5 and 10^7 cells/ml and the highest increment of compressive strength, i.e. 22% is observed with 10^5 cell/ml bacterial concentration [20]. A similar result is observed in the case of AKKR5 where there is 10% increment in compressive strength as compared to control concrete with 10^5 cell/ml concentration [45]. In the case of Bacillus megaterium, the highest strength was observed with cell concentration of 30×10^5 cfu/ml [46]. With Bacillus aerius, the highest strength is achieved with the cell concentration of 10^5 cells/ml. There is an increase in compressive strength by 11.8% in bacterial concrete compared to control with 10% dosage of RHA [47]. From literature, it is observed that for the highest value of compressive strength, the optimum cell concentration should be in between 10^5 and 10^7 cells/ml. Different bacteria with their optimum cell concentration for best compressive strength are shown in Fig. 1. In addition to all the studies, the authors would like to present the results of their ongoing studies involving two bacteria, i.e. Bacillus subtilis and Bacillus cohnii. The study shows that by using Bacillus subtilis with 10^5 cells/ml, the highest strength is achieved, i.e. 66.7 Mpa, which is similar to the value mentioned for obtaining the best strength in the previous literature. In the case of Bacillus cohnii bacterial species, the highest strength of 60.7 Mpa is achieved with cell concentration of 10^5 cells/ml, which was not the case in the previous literature, since there, the strength was the highest when cell concentration was 10^7 cells/ml. Graphical comparison between present work and existing literature is furnished in Figs. 2 and 3.

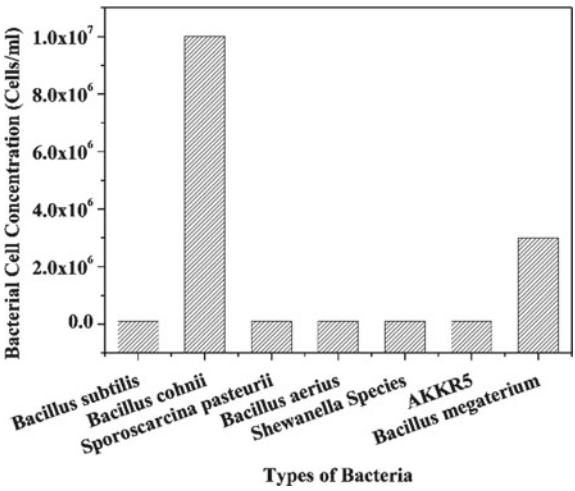

Fig. 1 Various types of bacteria with optimum cell concentration for the highest compressive strength

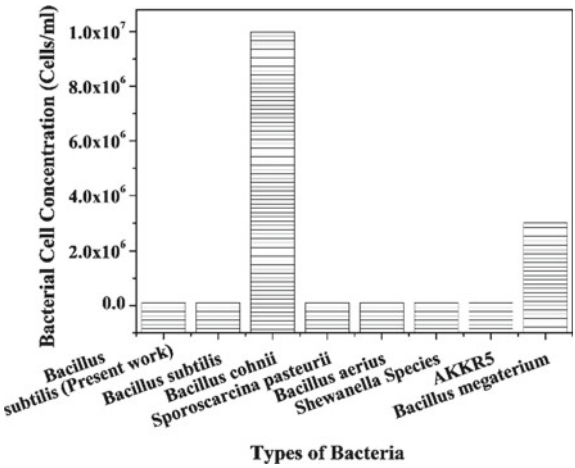

Fig. 2 Comparison of present work containing *Bacillus subtilis* with previous literature

4.3 Reduction in Permeability

Permeability is one of the key features by which the durability of concrete is affected. Concrete having a very high amount of permeability results in the percolation of water and pollutants, which affects the concrete durability along with integrity. Hence, low permeability is a must for having a long activity period. Using bacterial concrete helps in decreasing the permeability of concrete. Since the calcite precipitation because of bacterial concrete mainly occurs at the surface of concrete, it acts as the covering system that helps in covering the pores [48]. Figures 4 and 5 show the SEM image where calcite is deposited on the concrete surface which in turn blocks the pores and decreases permeability. Carbonation test (surface treatment) results in decrement in

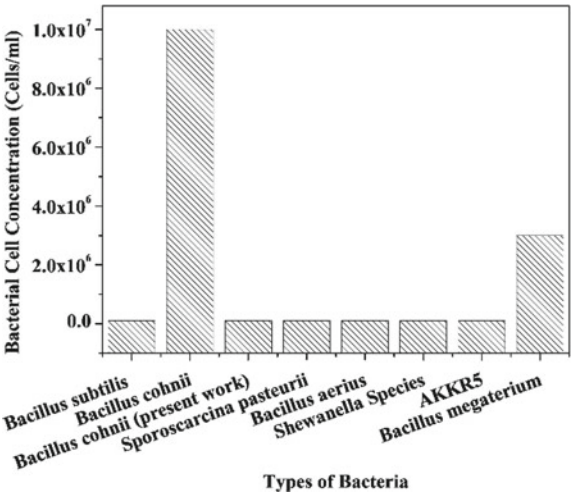

Fig. 3 Comparison of present work containing *Bacillus cohnii* with previous literature

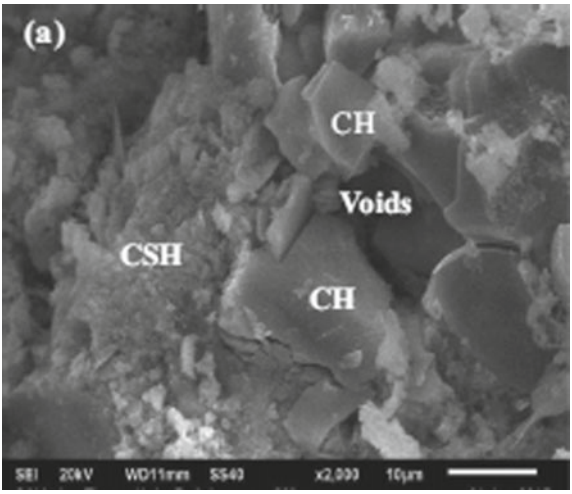

Fig. 4 SEM of concrete without bacteria [56]

gas permeability which leads to a method of examining the permeability because it is known that decrease in gas permeability which further leads to increment in resistance for carbonation and chloride entry. An increment in resistance of concrete for alkali, drying shrinkage, freeze thaw attack by addition of bacterial cells was observed. The impact of calcite precipitation on permeability was a part of the study, who used S. *Sphaericus* and reported a significant amount of decrement in concrete permeability [13]. Research has been done on the effects of *Bacillus pasteurii* bacteria on the permeability of concrete and observed a significant reduction in permeability of water in cement cubes incorporated with the bacterial species [49]. It also observed the same effects when they used *Sporosarcina pasteurii* in concrete cubes. Many

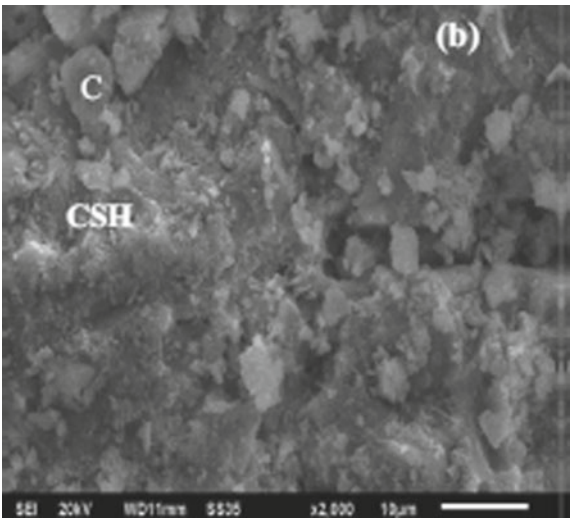

Fig. 5 SEM of concrete with bacteria [56]

believe that this reduction in water permeability of concrete specimen with bacteria content is due to the calcite deposition in the voids of concrete [26]. When concrete specimens were treated with *Bacillus* sp. CT-5, they showed reduction up to six times in water absorption of concrete in comparison to control specimen [50]. When the effect of *Sporosarcina pasteurii* was studied on concrete with fly ash, it showed reduction up to 8 times in chloride permeability. This might be possible because of the deposition of calcite in concrete. When mortar specimens were incorporated with *Bacillus sphaericus* spores that are hydrogel encapsulated, the permeability reduces up to 68% [51]. Concrete with fly ash content incorporated with bacteria showed a decrement in water absorption up to four times. As bacteria concentration increases, the capacity for absorption of water decreases. When bacteria contain 10^5 cells/ml bacterial concentration, then the reduction in water absorption is maximum. Overall with respect to the control specimen, there is a decrease in water absorption in the presence of bacteria [52]. The deposition of a layer of calcium carbonate on the surface and inside the pores of the concrete specimens resulted in a decrease in water absorption. When the quantity of carbonation is higher in concrete containing bacteria, the surface reaction causes an increment in resistance to chloride attack, which in turn helps in decreasing the permeability along with porosity [53–55].

5 Crack Remediation

By using bacteria in concrete, the main focus revolves around healing of cracks in concrete with the help of calcium carbonate deposited by microbial action. Ramachandran et al. used S. pasteurii bacteria along with calcium chloride and urea solution to repair the cracks successfully [10]. Sporoscarcina pasteurii was used

with calcium chloride and nutrient medium to seal the cracks [57]. L. sphaericus was used by incorporating in silica gel matrix along with nutrients and calcium sources to seal the cracks. It was observed that in comparison to the control mix, crack was healed by using the bacteria [14].

Jonkers et al. were the first ones to include Bacillus cohnii endospores in cement stone so that it would induce calcium carbonate precipitates [8]. Wiktor and Jonkers again used the same species of bacteria to infuse lightweight coarse aggregates into the concrete to protect the bacteria. L. phaericus endospores were used in a mixture of concrete and it was noticed that cracks of size up to 970 μm were sealed up automatically by bacterial specimens, whereas cracks up to size 250 μm could be healed by nonbacterial specimens. A decrease in water permeability of concrete (apparently 10 times less) indicated that the cracks were autogenously healed by the bacterial specimens [16]. Bacillus subtilis with highest cell concentration, i.e. 10^7 cells/ml heals the crack more efficiently. It is observed that with higher bacterial cell concentration, the cracks healed effectively in comparison to lower cell concentration [58]. Crack healing with different cell concentrations of bacteria is shown in Fig. 6. Encouraging results have been witnessed, but there is still scope for the development of reliable and cost-friendly concrete specimen for self-healing concrete [59].

6 Drawback

Even though bacterial concrete is useful in reducing the repairing cost of concrete that might become enlarged with the course of time, the total cost in forming the concrete mixture is almost 28% more than conventional concrete [46, 49, 50]. There is no concrete design that makes sure of 100% performance of bacterial concrete. The right amount of bacteria and the perfect type keeps changing from time to time [46, 51, 52]. Some bacteria like Shewanella species, Leuconostoc mesenteroides, Pseudomonas aeruginosa, Escherichia coli, Acinetobacter species, etc. are harmful to human health as they cause various diseases [53]. So, there is a common belief among people that if they live in a bacterial filled environment, it will have adverse effects on their health. But bacteria species like *Bacillus pasteurii, Bacillus sphaericus and Bacillus lentus* are effectively used in concrete because they do not affect the health of human [46–60].

7 Conclusion

In recent times, self-healing concrete is the talk of the town because of its biological techniques. Calcium carbonate precipitation by microorganisms is the perfect solution to the problem of crack formation in concrete. The metabolic reactions occurring inside of microorganisms such as photosynthesis, urea hydrolysis and sulphate-reduction cause all-round development in concrete quality as they produce calcium

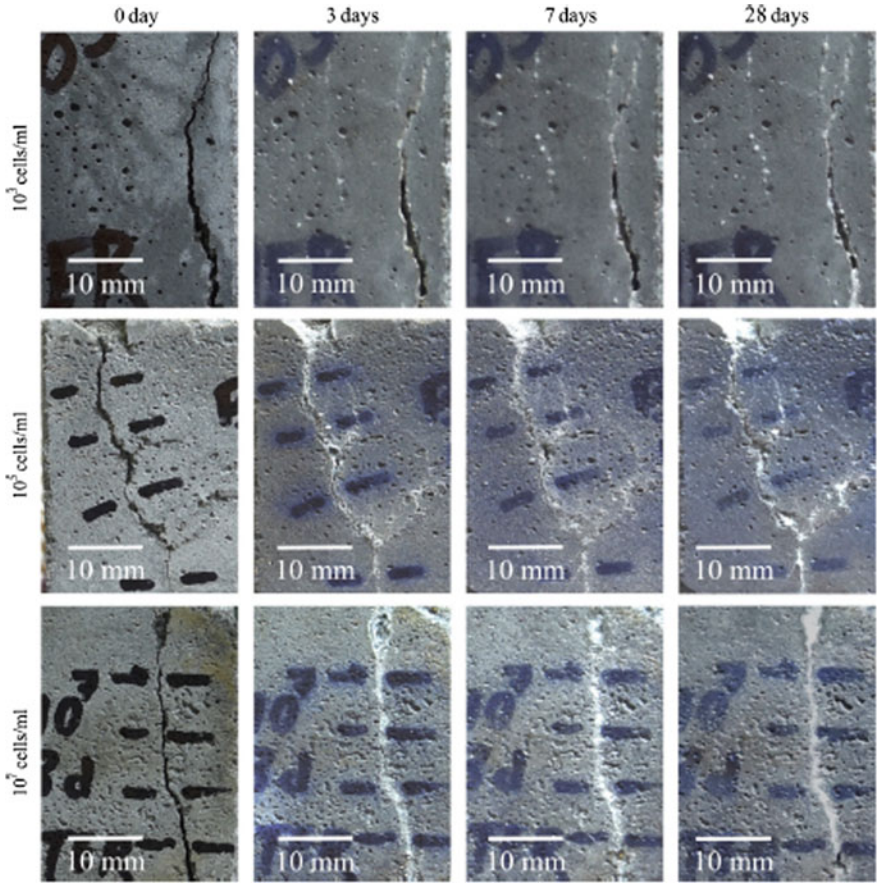

Fig. 6 Crack healing with different bacterial cell concentrations [58]

carbonate precipitate as the byproduct. Self-healing concrete which contains bacteria positively affects different kinds of attributes like durability, self-life strength, permeability and water and chloride absorption. Researchers have found that the utilization of biotechnology in self-healing concrete enhances the durability along with strength and decreases the permeability of concrete. There is a common belief that a bacteria filled environment negatively affects their health and causes diseases. It is hoped that in future, people will understand the value of using self-healing bio concrete and realize its importance and start using it widely as a substitute for conventional concrete. Moreover, the usage of self-healing concrete is a reassuring method for having better quality infrastructure.

References

1. Wiktor V, Jonkers HM (2011) Quantification of crack-healing in novel bacteria based self-healing concrete. Cem Concr Compos 33(7):763–770
2. Khaliq W, Ehsan MB (2016) Crack healing in concrete using various bio influenced self-healing techniques. Constr Build Mater 102:349–357
3. Jonkers HM, Schlangen E (2007) Crack repair by concrete-immobilized bacteria. In: Proceedings of the first international conference on self-healing materials, pp 18–20
4. Neville AM (1996) Properties of concrete. Pearson Higher Education, 4th edn. Prentice Hall, New Jersey
5. Wang J, Tittelboom KV, Belie NDe, Verstraete W (2012) Use of silica gel or polyurethane immobilized bacteria for self-healing concrete. Constr Build Mater 26(1):532–540
6. Muhammad NZ, Shafaghat A, Keyvanfar A, Majid MZA, Ghoshal S, Yasouj SEM, Ganiyu AA, Kouchaksaraei MS, Kamyab H, Taheri MM (2016) Tests and methods of evaluating the self-healing efficiency of concrete: a review. Constr Build Mater 112:1123–1132
7. Huang H, Ye G (2014) A review on self-healing in reinforced concrete structures in view of serving conditions. In: 3rd international conference on service life design for infrastructure, Zhuhai, China, 15–17 October 2014
8. Jonkers HM, Thijssen A, Muyzer G, Copuroglu O, Schlangen E (2010) Application of bacteria as self-healing agent for the development of sustainable concrete. Ecol Eng 36(2):230–235
9. Gollapudi U, Knutson C, Bang S, Islam M (1995) A new method for controlling leaching through permeable channels. Chemosphere 30(4):695–705
10. Ramachandran SK, Ramakrishnan V, Bang SS (2001) Remediation of concrete using micro-organisms. ACI Mater J 98(1):3–9
11. Bang SS, Galinat JK, Ramakrishnan V (2001) Calcite precipitation induced by polyurethane-immobilized Bacillus pasteurii. Enzyme Microb Technol 28(4):404–409
12. Dick J, De Windt W, De Graef B, Saveyn H, Van der Meeren P, DeBelie N, Verstraete W (2006) Bio-deposition of a calcium carbonate layer on degraded limestone by Bacillus species. Biodegradation, 17(4):357–367
13. De Muynck W, Debrouwer D, De Belie N, Verstraete W (2008) Bacterial carbonate precipitation improves the durability of cementitious materials. Cem Concr Res 38(7):1005–1014
14. Tittelboom KV, De Belie N, De Muynck W, Verstraete W (2010) Use of bacteria to repair cracks in concrete. Cem Concr Res 40(1):157–166
15. Wiktor V, Jonkers H (2015) Field performance of bacteria-based repair system: pilot study in a parking garage. Case Stud Constr Mater 2:11–17
16. Wang J, Soens H, Verstraete W, De Belie N (2014) Self-healing concrete by use of microencapsulated bacterial spores. Cem Concr Res 56:139–152
17. Ramakrishnan V, Ramesh K P, Bang SS (2001) Bacterial concrete. In: Smart materials and MEM, international society for optics and photonics, pp 168–176
18. De Muynck W, Cox K, De Belie N, Verstraete W (2008) Bacterial carbonate precipitation as an alternative surface treatment for concrete. Constr Build Mater 22:875–885
19. Rodriguez NC, Rodriguez GM, Chekroun KB, Gonzalez MT (2003) Conservation of ornamental stone by Myxococcus xanthus induced carbonate biomineralization. Appl Environ Microbiol 69:2182–2193
20. Chahal N, Siddique R, Rajo A (2012) Influence of bacteria on the compressive strength, water absorption and rapid chloride permeability of fly ash concrete. Constr Build Mater 28:351–356
21. Qiu J, Qin D, Teng S, Yang E (2014) Surface treatment of recycled concrete aggregates through microbial carbonate precipitation. Constr Build Mater 57:144–150
22. Pei R, Liu J, Wang S, Yang M (2013) Use of bacterial cell walls to improve the mechanical performance of concrete. Cem Concr Compos 39:122–130
23. Siddique R, Kaur N (2011) Effect of ureolytic bacteria on concrete properties. Constr Build Mater 25(10):3791–3801
24. Ersan YC, Bravo da Silva F, Boon N, Verstraete W, De Belie N (2015) Screening of bacteria and concrete compatible protection materials. Constr Build Mater 88:196–203

25. Kaur N, Reddy MS, Mukherjee A (2012) Improvement in strength properties of ash bricks by bacterial calcite. Ecol Eng 39:31–35
26. Achal V, Mukherjee A, Reddy MS (2011) Microbial concrete—a way to enhance the durability of building structures. J Mater Civil Eng 23:730–734
27. Dhami NK, Mukherjee A, Reddy MS (2012) Biofilm and microbial applications in biomineralized concrete. In: Seto J (ed) Advanced topics in biomineralization. InTech Publishers, pp 137–164
28. Burne RA, Chen RE (2000) Bacterial ureases in infectious diseases. Microbes Infect 2:533–542
29. Claus GW (1988) Understanding microbes: a laboratory textbook for microbiology. W. H. Freeman
30. Basaran Z (2013) Biomineralization of cement based materials: inoculation of vegetative cells. The University of Texas at Austin, Austin
31. Bundur Z, Kirisits M, Ferron R (2015) Biomineralized cement-based materials: impact of inoculating vegetative bacterial cells on hydration and strength. Cem Concr Res 67:237–245
32. Ramachandran V (1996) Concrete admixtures handbook, 2nd edn. William Andrew Inc., Norwich
33. Chikh N, Cheikh-Zouaoui M, Aggoun S, Duval R (2008) Effects of calcium nitrate and triisopropanolamine on the setting and strength evolution of Portland cement pastes. Mater Struct 41(1):31–36
34. Luo M, Qian C (2016) Influences of bacteria-based self-healing agents on cementitious materials hydration kinetics and compressive strength. Constr Build Mater 121:659–663
35. Zhang Y, Guo HX, Cheng XH, Caco CA, Ca CA (2015) Role of calcium sources in the strength and microstructure of microbial mortar. Constr Build Mater 77:160–167
36. Gavimath CC, Mali BM, Hooli VR, Mallpur JD, Patil AB, Gaddi DP, Tenikar CR, Ravishankear BE (2012) Potential application of bacteria to improve the strength of cement concrete. Int J Adv Biotechnol Res 3:541–544
37. Kunal Siddique R, Rajor A (2014) Influence of bacterial treated cement kiln dust on the properties of concrete. Constr Build Mater 52:42–51
38. Maheswaran S, Dasuru SS, Murthy ARC, Bhuvaneswari B, Kumar VR, Palani GS, Iyer NR, Krishnamoorthy S, Sandhya S (2014) Strength improvement studies using a new type wild strain Bacillus Cereus on cement mortar. Curr Sci 106:50–57
39. Rao MVS, Reddy VS, Hafsa M, Veena P, Anusha P (2013) Bioengineered concrete—A sustainable self healing construction material. Res J Eng Sci 2(6):45–51
40. Reddy SP, Rao MVS, Aparna P, Sasikala CH (2010) Performance of ordinary grade bacteria (Bacillus Substilis) concrete. Int J Earth Sci Eng 3:116–124
41. Reddy SV, Satya AK, Rao SMV, Azmutunnisa M (2012) A biological approach to enhance strength and durability in concrete structure. Int J Adv Eng Technol 4:392–399
42. Ghosh P, Mandal S, Chattopadhyay BD, Pal S (2005) Use of microorganism to improve the strength of cement mortar. Cem Concr Res 35:1980–1983
43. Kumari C, Das B, Jayabalan R, Davis R, Sarkar P (2017) Effect of nonureolytic bacteria on engineering properties of cement mortar. J Mater Civ Eng 10:1943–5533. https://doi.org/10.1061/(ASCE)MT.1943-5533.0001828
44. Sarkar M, Adak D, Tamang A, Chattopadhyay B, Mandal S (2015) Genetically-enriched microbe-facilitated self-healing concrete—a sustainable material for a new generation of construction technology. RSC Adv 5:105363–105371. https://doi.org/10.1039/C5RA20858K
45. Siddique R, Nanda V, Kunal (2016) Influence of bacteria on compressive strength and permeation properties of concrete made with cement baghouse filter dust. Constr Build Mater 106:461–469
46. Andalib R, Majid MZA, Hussin MW, Ponraj M, Keyvanfar A, Mirza J, Lee HS (2016) Optimum concentration of Bacillus megaterium for strengthening structural concrete. Constr Build Mater 118:180–193
47. Siddique R, Singh K, Kunal M, Singh VC, Rajor A (2016) Properties of bacterial rice husk ash concrete. Constr Build Mater 121:112–119

48. Achal V, Mukherjee A, Basu PC, Reddy MS (2009) Lactose mother liquor as an alternative nutrient source for microbial concrete production by Sporosarcina pasteurii. J Int Microb Biotechnol 36:433–438
49. Ramakrishnan V, Bang SS, Deo KS (1998) A novel technique for repairing cracks in high performance concrete using bacteria. In: Proceedings of international conference on high performance high strength concrete, Perth, Australia, pp 597–618
50. Achal V, Mukherjee A, Reddy MS (2011) Effect of calcifying bacteria on permeation properties of concrete structures. J Int Microb Biotechnol 38:1229–1234
51. Cwirzen A, Penttala V (2005) Aggregate–cement paste transition zone properties affecting the salt–frost damage of high-performance concretes. Cem Concr Res 35:671–679
52. Igarashi SI, Watanabe A, Kawamura M (2005) Evaluation of capillary pore size characteristics in high-strength concrete at early ages. Cem Concr Res 35:513–519
53. Khan MI (2003) Isoresponses for strength, permeability and porosity of high performance mortar. Build Environ 38:1051–1056
54. Toutanji HA, Bayasi Z (1999) Effect of curing procedures on properties of silica fume concrete. Cem Concr Res 29:497–501
55. Ramezanianpour AA, Malhotra VM (1995) Effect of curing on the compressive strength, resistance to chloride-ion penetration and porosity of concretes incorporating slag, fly ash or silica fume. Cement Concr Compos 17:125–133
56. Siddique R, Jameel A, Singh M, Hunek DB, Kunal Mokhtar AA, Belarbi R, Rajor A (2017) Effect of bacteria on strength, permeation characteristics and micro-structure of silica fume concrete. Constr Build Mater 142:92–100
57. Bang S, Lippert J, Yerra U, Mulukutla SRV (2010) Microbial calcite, a bio-based smart nanomaterial in concrete remediation. Int J Smart Nano Mater 1(1):28–39
58. Mondal S, Ghosh AD (2018) Investigation into the optimal bacterial concentration for compressive strength enhancement of microbial concrete. Constr Build Mater 183:202–214
59. Silva F, Boon N, De Belie N, Verstraete W (2015) Industrial application of biological self-healing concrete: challenges and economic feasibility. J Commer Biotechnol 21(1):31–38
60. Sarkar M, Alam N, Chaudhuri B, Chattopadhyay B, Mandal S (2015) Development of an improved E. coli bacterial strain for green and sustainable concrete technology. RSC Adv 5:32175–32182. https://doi.org/10.1039/C5RA02979A

Effect of Aggregate Ratio Using Non-pozzolanic Mineral Filler Waste on the Property of Self Compacted Concrete

V. C. Panchal and G. R. Vesmawala

Abstract The presence of different filler materials in the SCC mixture is a major change in Self-Compacting Concrete (SCC) compared to ordinary concrete. The use of filler materials in SCC improves workability and reduces cement content. In the existing work, an investigational study has been carried out by using two filler waste materials, Marble Powder (MP) and Lime Powder (LP), to increase the fresh and hardened property of SCC. Different tests were performed using three replacement levels of 0, 10, and 15% of cement along with fine aggregate to the total aggregate ratio, ranging from 0.50, 0.54, and 0.56 to evaluate the fresh and hardened property of SCC. M30 concrete was designed and investigated for the same parameters with the use of LP and MP as non-pozzolanic fillers in SCC. The presence of filler types and content has a significant influence on flow behavior and the better deformability obtained in SCC samples. The test results show that fine aggregate to the total aggregate ratio has substantially affected the fresh and hardened property of SCC in the presence of filler materials. The compressive strength at a higher fine aggregate to the total aggregate ratio (0.56) and higher replacement (15%) decreases compared to 0.50 and 0.54 ratios of the same replacement. Also at 0.54 coarse aggregates to fine aggregate ratio, medium content of coarse aggregate and presence of filler provide better lubrication and enhance flowability, passing ability, segregation, and bleeding resistance. All samples of M30 concrete have satisfied workability criteria. The results are well matched with the SCC guideline (EFNARK 2005).

Keywords Self-Compacting Concrete (SCC) · Mineral filler waste · Fine aggregate to the total aggregate ratio (S/a)

V. C. Panchal (✉) · G. R. Vesmawala
Applied Mechanics Department, SVNIT, Surat, India
e-mail: vinodpanchal11@yahoo.com

G. R. Vesmawala
e-mail: grv22@yahoo.com

© Springer Nature Singapore Pte Ltd. 2021

K. K. Pathak et al. (eds.), *Recent Trends in Civil Engineering*, Lecture Notes in Civil Engineering 77, https://doi.org/10.1007/978-981-15-5195-6_47

1 Introduction

1.1 Material Property

Self-Compacting Concrete (SCC) is used in the construction sector for the last three decades. In this time period, a number of research works have been explained with regards to its application, different mix designs, pump-ability, long-term strength, rheology, and performance of the SCC. Before 1990, not so much importance was given to engineering properties of the material and its skeletal performance. Recently, a large amount of research has been dedicated to the mechanical properties of SCC [1]. Investigation plans frequently include data on design strength, Young's modulus, and durability properties, even though the main attention keeps on other features of concrete as stated above. Previously, some researchers [2, 3] have carried out a survey and presented data on the properties of SCC based on literature.

As SCC usually contained large amounts of fine aggregate and powder content compared to conventional concrete, the paste content is higher too to make the coarse aggregate float in the mix [1, 4]. A common cement and addition of filler contents for SCC mixtures are situated in the range of 360–630 kg/m^3. In most of the cases, the total paste quantity of SCC mixes is higher than that of a vibrated concrete mix, which may have its outcome on flowability, passing ability, and durability property.

2 Materials and Method

2.1 Materials Property

In existing experimental work, Ordinary Portland Cement 53 grade, which meets Indian standard 12269 (53 grade) and ASTM C150 [5, 6] specification, is used. From ancient time, marble stone has been utilized as a building material. The disposal of micro-fine powder produced by marble industries is the principal problem in the present environment. In the present experimental work, locally available marble powder of specific gravity 2.50 and fineness less than 125 μm is used to prepare an SCC mix design. Figure 1 shows the particle size distribution for LP and MP. Limestone powder is considered as daily goods and adopted as a construction material. Additionally, it's a sedimentary rock formed by inorganic leftovers, such as skeletons or shells of animals that compressed for a very long time. Calcium carbonate (CaCO3) is the principal component found in limestone, and also it may contain manganese, iron, and magnesium shown in Table 1.

The specific gravity of lime powder was 2.40 used for SCC. River sand available nearby of specific gravity 2.63 and fineness modulus 2.92 conform to IS 383-12269 [5]. The specific gravity of coarse aggregate is obtained using a wire basket method in accordance with ASTM C127 [7], and fine aggregate conforming to Zone

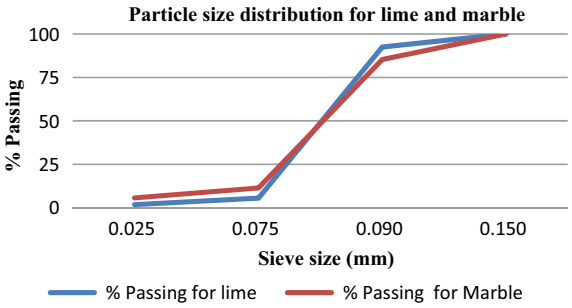

Fig. 1 Particle size distribution for lime and marble powder

Table 1 Chemical composition of cement and mineral filler LP and MP

Component (%)	Cement (%)	LP (%)	MP (%)
SiO_2	20.86	4.25	1.18
Al_2O_3	4.64	0.89	0.85
Fe_2O_3	2.40	0.49	0.04
CaO	62.45	95.65	89.12
SO_3	2.12	1.35	0.65
Loss on ignition	1.35	1.24	2.15

II is utilized. A maximum 16 mm size clean and crushed coarse aggregate stone of specific gravity 2.66 is used. The superplasticizer (1.5% by weight of powder content) of commercially available brand of slightly dark yellow color, volumetric mass 1.07 kg/L, and solid content 31% is employed to reduce water demand in SCC. The viscosity modifying agent is required to avoid segregation or bleeding for the SCC mixes; in the present experimental investigation, 0.20% by weight of the powder is used. For mixing and curing of the concrete sample, potable water is used of a temperature 28 ± 1 °C.

2.2 Earlier Mix Design Method

Since inception, researchers [8–12] have suggested for designing SCCs statistical base methods, particle packing models, regression analysis base, and rheology-based methods. Okamura [8] has carried out a study on the compatibility of superplasticizer and suggested SCC mix design methods followed by trial mixes on the paste and mortar as shown in Fig. 2. The final product should be tested for slump flow, bleeding resistance, segregation, passing, and filling ability for the SCC mix.

Hu et al. [9] have suggested the rheometer-based method, which described the fresh rheological concrete properties and also presented a software-based mathematical model to optimize the aggregate to binder composition. Based on a higher fines method, Su et al. [10] introduced a mix design methodology, in which the required

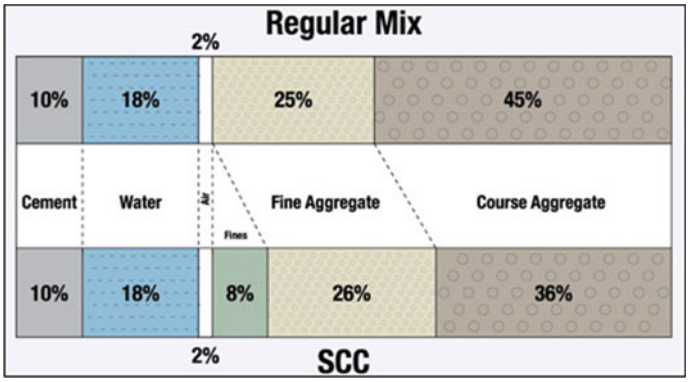

Fig. 2 Design model of SCC. *Source* Okamura Ozawa, K., Ouchi, (2000)

quantity of coarse aggregates was calculated first. As per [11] design methodology, the paste fills the voids between these aggregates to ensure concrete workability and other properties of SCC.

In the present research work, the optimal packing factor (range of 1.05–1.15) used to determine the quantity of fine and coarse aggregate of the mix and the volume of paste and powder content is fixed in the range of 310–370 and 360–500 kg/m^3, respectively. To get medium compressive strength of M30 SCC mix, potable water in the range of 160–200 L/m^3 is used. The SCC mix generally comprises a higher amount of powder and 30–37% coarse aggregate content, which makes the paste more flowable and decreases the wall effect. This procedure improves the workability of the SCC mix and decreases the quantity of binder required. Like Okamura [12], Dinakar [13] has presented a method based on the high strength design of SCC using fly ash. First, Marsh cone is used to find the optimum dosage of superplasticizer for filler and binder. Next, the mini-slump test is used to determine optimum filler dosage for proper paste formation with stipulated water to cement ratio (w/c). The coarse and fine aggregate proportions were calculated based on the least void content of the aggregate frame. At last, an optimum fine aggregate to the total aggregate ratio of the concrete mix and paste volume was tested. However, the concept of the mix design methodology, material properties, and available research to date does not recommend any particular procedure for obtaining SCC of specific strength to date, unlike conventional vibrated concrete [14].

2.3 Method and Mix Design

The mix design methodology is a significant parameter in the SCC. Except for Nan-Su method [15], till date, no specific mix design procedure is regulated to get a proportion of the ingredients of a particular grade in SCC. The mix design proportioning

was performed for SCC with target compressive strength 30 MPa in fulfillment of EFNARC and a new mix design methodology by Nan-Su [13, 15]. This method gives the details of the mix design procedure to get target strength that will be gained after 28 days of water curing, apart from other mix design methods like the Okamura and EFNARC [13]. For laboratory trials, the initial mix was prepared by keeping the water to binder ratio 0.43, powder content between 360 and 600 kg/m^3, water content 150–210 kg/m^3, and fine aggregate to the total aggregate ratio (S/a) 0.50, 0.54, and 0.56 as per guideline. The mix proportion is illustrated in Table 2, which indicates a different replacement of cement by 0, 10, and 15% by two fillers in SCC.

The experimental program aimed to investigate the fresh and hardened property of SCC, additionally comparing these different mixes with normal SCC without filler. Three different SCC groups A, B, and C were prepared and cast by having S/a ratio 0.50, 0.54, and 0.56, respectively. Table 2 represents the three different percentages of LP (0, 10, 15) and MP (0, 10, 15) as a substitute for cement with different combination with fine aggregate to total aggregate (S/a) ratio of 0.50, 0.54, and 0.56 prepared in the laboratory. All the tests for fresh and hardened properties of concrete were conducted as per EFNARC guidelines [13] for SCC.

3 Test Results and Discussion

3.1 Compatibility Test

Mini-Slump Cone Test. It has been noticed from several trials that all groups of superplasticizers with different types of a binder have not been explained in the same degree of advancement in fluidity. In addition, the cement is very perplexing; involving many factors like the composition of cement, fineness, and type of cement, [16, 17]. Therefore, to initiate the flow of the mix, a retained water powder ratio of the paste (*Bp*) was determined for the design of filler paste composition. If the workability of plastic concrete in a fresh state is not obtained as per standard guideline, it can be hard to transport, place, and compact it properly. The workability characteristic of SCC, therefore, becomes immensely important [18]. For mini-slump cone test [19], 450 g cement and 150 g filler are used to prepare a standard paste keeping water to powder ratio by volume 1.0, 1.1, and 1.2 with selected powder composition of LP and MP. The dosage matching to 175 ± 10 mm without bleeding of filler paste was known as the optimum dosage as shown in Fig. 3. The intercept on the y-axis (water to powder ratio) is designated as the *Bp* value for filler.

The value of βp has been obtained as 0.96 water/powder ratio (volume), at which water content is just sufficient to initiate flow and it's called the retain water ratio of powder (*Bp*) as shown in Fig. 3. To decide the superplasticizer doses for the SCC concrete mix, the Marsh Cone test is performed, with 1.0 kg of cement and 400 ml of water with prescribed superplasticizer doses of 1.0, 1.2, 1.4, 1.5, and 1.6% by weight of cement taken to prepare paste. The time elapses for a consistent free

Table 2 Mix design of different S/a ratios of SCC

Mix proportioning = M30 (kg/m^3), Water cement ratio = 0.43, C.A = Course Aggregate									
F.A = Fine Aggregate, LP = Lime Powder, MP = Marble Powder, S/a = Fine aggregate to total aggregate ratio									
Group and S/a ratio	Mix Type	Cement	F.A	C.A	Water	LP	MP	Slump flow (mm)	L- Box value (mm)
A (0.50)	SCC0	412.00	924.00	852.50	178.50	0.00	0.00	480	0.95
	SCC10	370.80	924.00	852.50	178.50	20.60	20.60	605	0.89
	SCC15	354.43	924.00	852.50	178.50	30.90	30.90	610	0.85
B (0.54)	SCC0	409.50	997.92	784.30	177.70	0.00	0.00	545	0.90
	SCC10	369.00	997.92	784.30	177.70	20.48	20.48	640	0.85
	SCC15	351.64	997.92	784.30	177.70	30.71	30.71	690	0.87
C (0.56)	SCC0	408.21	1034.88	750.20	176.80	0.00	0.00	475	0.98
	SCC10	367.71	1034.88	750.20	176.80	20.41	20.41	460	0.97
	SCC15	350.36	1034.88	750.20	176.80	30.62	30.62	425	1.0

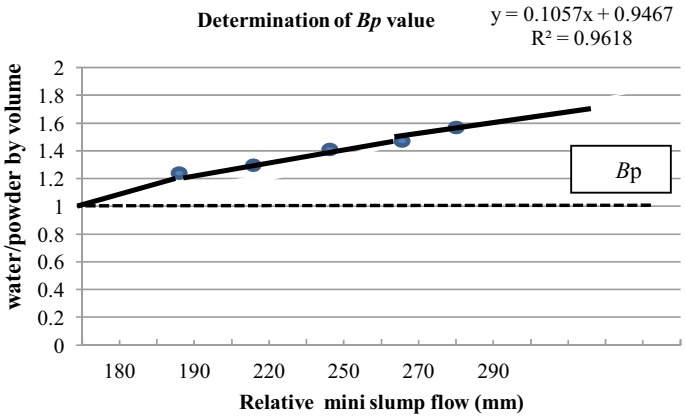

Fig. 3 Mini-slump spread test value

Fig. 4 Mini-slump flow test and flow measurement

flow of paste through the cone have been recorded for different mixes. The doses of superplasticizer at the minimum time with the constant free flow have been chosen and obtained a value of 1.5% by weight of cement. Figures 3 and 4 give the value and flow of mortar mixes through Mini-slump. The optimum value found out for superplasticizer doses is 1.5% by weight of powder content.

3.2 Slump Flow Test and L-Box Test

Figure 5 and Table 2 represented slump spread mean diameter value for mixes of SCC.

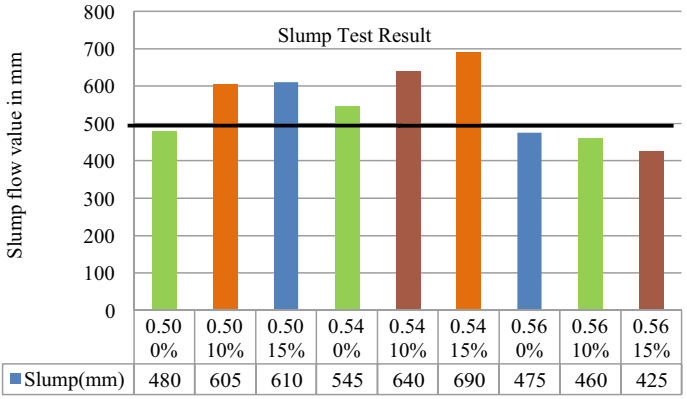

Fig. 5 Result of slump flow test of SCC

The full line indicates the limit of flow under which the mix has a higher viscosity and cannot move without external force. The spread time in seconds (T) can be determined when the original shape of a cone flow by its gravity force and form a largely "Pizza-like" layer for SCC [20]. The shorter the time t_{500}, higher will be the flow rate of SCC during placement. Researchers have classified the spread of slump flow into four parts; between 400 and 500, 500 and 600, 600 and 700, and 700 and 800 mm [19, 20].

Usually, the SCC mixture having a spread-flow value between 400 and 500 mm would be considered as very sticky and can't move easily. After 500 mm and up to nearby 600 mm spread of SCC mix, the mass changes its zone from paste to semi-liquid and develops its fluidity [21]. Slum flow is the mean of two diameters of spread flow taken by the spread to reach 500 mm. The spread diameter of the mix above 550 mm clearly shows a transformation in viscosity of SCC mix and conversion to improve additional fluidity. From the visual observations during this test, no 'laitance' or 'halo' of fine mortar was found in the bulk of the concrete mix. As time passed, the flow of the slump has stretched from 400 to 600 mm.

The mixture viscosity would be projected to be fine. The mixer would move easily because of its own self pressure and presence of micro filler in the mix. For group A (0.50), the normal SCC sample without filler exhibited a lower slump value of 480 mm compared to 10% and 15% replacement filler sample by value 605 mm and 610 mm, respectively. It could be due to a higher quantity of coarse aggregate and the absence of micro filler material in the mix, resulting in the lower value of slump spread. It is observed in the reference mix of group B (0.54) that the presence of filler materials provides sufficient fluidity to coarse aggregate to float in the mix, resulting in a higher value of spread 640 and 690 mm. While in group C (0.56) of higher S/a ratio, it was observed that the fine aggregate and filler particle would interface with each other during flow and cause blocking near the circle 500 mm; as a result, the spread value reduces by 10% and 15% to 500 mm and 540 mm, respectively. From all experimental slump spread value, it is concluded that the group B (0.54)

Fig. 6 Slump flow test and L-Box test of SCC

has satisfactory results with flow values 545, 640, and 690 mm, so it satisfied SF1 to SF2 criteria of SCC.

The L-box test was performed to measure the filling and passing ability of the SCC mix. A 15 L of SCC mix is prepared and tested. Initially, concrete is filled in a vertical L-Box up to a top-level and later allowed to release by its own pressure through three vertical bars. After the flow of concrete when it comes to rest, the height of the concrete was measured at the slope end and near the vertical L section. The ratio of elevation was calculated from all measurements of different concrete mixes shown in Table 2 and Fig. 6. The effect of filler on the SCC0 mix in the three groups A, B, and C, the calculated value of the L-Box obtained 0.95, 0.90, and 0.98, respectively. From the visual observation, it could be understood that the sample with 0% filler sets very quickly and requires more time to reach the end of a section of the apparatus. This could be due to a higher content of cement and thus it increases the viscosity of non-filler (0%) concrete mixes. The fillers in the mix provide lubrication and balance the setting time.

In the case of group B, from the visual observation, the balance between the coarse aggregate contents and paste matrix have seen. As a result, the vertical section to the horizontal section, the flow of the mix was continuous through the reinforcement. Nguyen et al. [22] have primarily reported, when the gate of L-box lifted, the flow governed by the effect of its self-gravity force. When the gate gently raised, the dynamic energy has expanded to cover the gate lifting span, depending on the skill of the worker and the speed of the lifting gate. The concrete tends to flow gradually toward the end of the plate. From the obtained value, one could say that fillers improve the flowability and passing ability of the mix. For 10% and 15% replacement, the obtained value of the ratio was within accepted levels of 0.85–1 except group C (closer to 1) satisfied the criteria of SCC guideline.

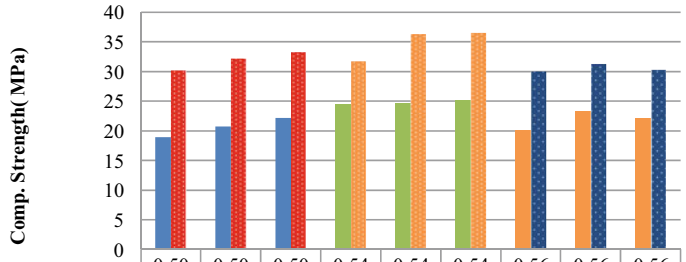

	0.50 0%	0.50 10%	0.50 15%	0.54 0%	0.54 10%	0.54 15%	0.56 0%	0.56 10%	0.56 15%
7 days (Mpa)	18.97	20.78	22.15	24.52	24.59	25.08	20.08	23.26	22.22
28 days(Mpa)	30.18	32.21	33.32	31.78	36.33	36.56	30.05	31.34	30.26

Fig. 7 Compressive strength results of SCC

3.3 Compressive Strength Test

The development of compressive strength for 7 and 28 days of curing time for nine different filler and non-filler SCCs is shown in Fig. 7.

Experimental results show that there was a continuous strength development in each group compared to the normal non-filler mix. Figure 7 shows, for groups A, B, and C, the rate of strength increases with the increase in the amount of filler compared to non- filler samples (0%) in all three cases. In group B (0.54), strength was higher at 10 and 15% filler replacement compared to other concrete samples. Losses in strength have been observed in group C (0.56) compared to group B (0.54), for 0, 10, and 15% replacement in SCC with an extent of 1.73, 4.99, and 6.30 MPa, respectively. That was due to reduction in coarse aggregate content from 852.50, 784.30, and 750.20 kg in groups A, B, and C, respectively, that causes less interlocking between the coarse aggregate. From these results, one can say that there is no significant variation between group A (0.52) and group C (0.56). It observed that replacing cement by LP and MP improves the strength to some extent; however, at a higher replacement level (0.15) and a ratio (0.56), the development of strength decreases. Similar results were discussed by Singh et a. [23]. The SCC containing LP and MP exhibits better performance, particularly in group B (0.54) due to the presence of micro filler, moderate content of the coarse aggregate, and proper combination of S/a ratio. The non-pozzolanic filler improves and constructs densely the microstructure of the paste matrix and transition zone.

3.4 Sorptivity Test

Sorptivity is measured and defined as a liquid force exerted through capillarity by the pore structure to absorb the water from the homogeneous material. $Ca(OH)_2$ solution

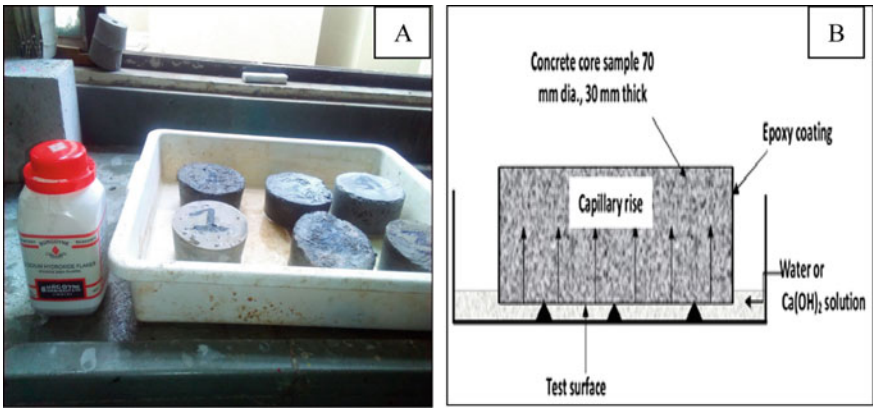

Fig. 8 Sorptivity test specimen immersed in $Ca(OH)_2$ solution. *Source* Topçu, I. B. et al. (2009)

is used as the test fluid. The test of Sorptivity (S) is performed for concrete mix SCC samples according to ASTM C 1585-04 [24]. The test specimens are immersed for 56 days curing. Figure 8 shows the specimen of size 100 mm diameter × 50 mm height kept in a tray after drying in an oven at a temperature of 100 ± 10. Air-dried specimen is immersed in liquid $Ca(OH)_2$ solution. The liquid level is kept 2–5 mm above the base of the specimen. The bottom surface is exposed to water and the remaining surfaces are sealed with a waterproof coating. The quantity of solution rise by capillary action for 30-min interval is measured by scaling the samples on a pan balance. The water outside the samples is cleaned off with a moistened cloth, and each measuring process is finished within 30 s. For one dimensional flow of liquid, the relation between the rate of absorption and Sorptivity is given by

$$I = (S)t^{0.5} \tag{1}$$

where I is the total water absorption by sample per unit area of penetration, S is the Sorptivity in mm, and t is the time taken in minutes. Figure 8 and Table 3 show test specimens with 0% replacement in all three cases 0.50, 0.54, and 0.56 exhibited higher absorption 0.085, 0.062, and 0.095, respectively, compared to 10% and 15% replacement. This may be due to the absence of a micro filler in the mortar mix. This leads to a porous inner cell of concrete mix. While the range of Sorptivity in other cases lies in the range of 0.045–0.076. The reality is that an SCC mix has a more uniform structure and fill most of the pores in the core portion of SCC. As a result, it produces a compacter Interfacial Transition Zone (ITZ) in correspondence to a filler-free SCC of related strength. It could be one of the causes of its low Sorptivity [25]. From the above reason, the effect of micro-fine powder material in association with VMA may develop microstructure and decrease the water penetration of SCC. The values of Sorptivity of all the samples were in the permissible range of 0.045–0.095 [24, 25].

Table 3 Sorptivity test value

Mix type	Dry weight (g)	Wet weight (g)	56 days sorptivity value (10^{-3}mm/min$^{0.5}$)
SCC0-050	859.50	870.23	0.085
SCC10-050	845.64	852.65	0.047
SCC15-050	864.32	871.10	0.045
SCC0-054	878.68	887.60	0.062
SCC10-054	865.64	879.41	0.048
SCC15-054	854.32	870.33	0.054
SCC0-056	868.68	894.37	0.095
SCC10-056	844.45	863.34	0.083
SCC15-056	871.54	878.08	0.076

4 Conclusion

From the finding of experimental and analytical investigation for different filler concrete mixes of SCC, the following conclusion can be made:

- From the use of these three different S/a ratios, the presence of filler LP and MP provides sufficient fluidity to a mass of matrix up to 10% replacement; since LP is made up of fossilized particles, it is porous and is soluble in water, resulting in a higher value of spread in 0.50 and 0.54 ratios. So these two fillers can replace successfully in SCC.
- In a reference mix B (0.54), the presence of filler materials provides adequate fluidity to coarse aggregate content to float in the mix. As a result, it enhances flow, provides higher segregation resistance, and stabilizes the mix. For further replacement, SCC samples of 0.54 ratios can be investigated.
- In the SCC mix, a replacement up to 15% of LP and MP with an aggregate ratio of 0.50 and 0.54 has a higher compressive strength, segregation resistance, and absorption resistance related to 0.56 ratios.
- For group C (0.56) of 15% replacement, the compressive strength decreases compared to 0.50 ratio of the equal replacement, and it may be due to the lowering of coarse aggregate content and higher amount of fine aggregate. Hence, it could not develop microstructure and weakens the bonding of coarse and fine aggregate skeleton.
- The micro filling ability of these two mineral fillers in SCC helps to construct a more homogeneous structure and fills most of the pore in the core portion of SCC. Hence, it developed higher resistance against the capillary action of water, produced a denser microstructure, and Interfacial Transition Zone (ITZ) in related to a filler-free SCC of equal strength may be the one cause of its low value of Sorptivity and higher strength.

References

1. Khayat KH, De Schutter G (2014) Mechanical properties of self-compacting concrete—state of art review
2. Assie S, Escadeillas G, Waller V (2007) Estimates of self compacting concrete 'potential durability'. Constr Build Mater 21(10):1909–1917. https://doi.org/10.1016/j.conbuildmat.2006.06.034
3. Belaidi ASE, Azzouz L, Kadri E, Kenai S (2012) Effect of natural pozzolana and marble powder on the properties of self-compacting concrete. Constr Build Mater 31:251–257. https://doi.org/10.1016/j.cemconcomp.20011.12.109
4. Dinakar P, Babu KG, Santhanam M (2008) Durability properties of high volume fly ash self compacting concretes. Cement Concr Compos 30(10):880–886. https://doi.org/10.1016/j.cemconcomp.2008.06.011
5. IS: 12269 (2013) Ordinary Portland Cement, 53 grade-specification (First revision). Bureau of Indian Standards (March)
6. ASTM International (2011) ASTM C 150 Standard Specification for Portland Cement. Test. https://doi.org/10.1002/jbm.b.31853
7. ASTM (2001) ASTM C127-01: Standard test method for density, relative density (Specific gravity), and absorption of coarse aggregate. ASTM Int. https://doi.org/10.1520/C0127-12.1
8. Okamura Ozawa K, Ouchi M, Okamura H, Ozawa K, Ouchi M (2000) Self compacting concrete. Struct Concr 1(1):3–17. https://doi.org/10.1680/stco.2000.1
9. Hu C, Larrard F De, Sedran T, Boulay C, Bosd F, Mat C-LN, Loiter S (1996) Validation of BTRHEOM, the new rheometer for soft-to-fluid concrete. Mater Struct/Matriaux Constr 29(December):620–631
10. Su N, Hsu K-C, Chai H-W (2001) A simple mix design of self compacting concrete. Cem Concr Res 31(12):1999–1807. https://doi.org/10.1016/S0008-8846(01)00566-X
11. Khatib JM (2009) Performance of self compacting concrete containing fly ash. Constr Build Mater 22(9):1963–1971
12. Okamura H, Ozawa K (1996) Self-Compacting High Performance Concrete. Struct Eng Int. https://doi.org/10.2749/101686696780496292
13. Dinakar P, Babu KG, Santhanam M (2008b) Mechanical properties of high-volume fly ash self-compacting concrete mixtures. Structural concrete 9(2):109–116
14. Su N, Miao B (2003) A new method for the mix design of medium strength flowing concrete with low cement content. Cement Concr Compos 25(2):215–222. https://doi.org/10.1016/S0958-9465(02)00013-6
15. Bennenk HW (2005) The European guidelines for self-compacting concrete specification, production and use II "The European Guidelines for Self Compacting Concrete"
16. Desnerck P, Van Itterbeeck P, Boel V, Craey, De Schutter G (2011) Survey of the mechanical properties of self-compacting concrete: 20 years of research, pp 4–11
17. Van Der Vurst F, Desnerck P, Peirs J, De Schutter G (2014) Shape factors of self-compacting concrete specimens subjected to uniaxial loading. Cement Concr Compos 54:62–69. https://doi.org/10.1016/j.cemconcomp.2014.05.009
18. Ouchi M, Aki S, Osterberg T, Hallberg S-E, Lwin M (2003) Applications of self-compacting concrete in Japan, Europe and the United States. Fed Highw Adm: 1–20. https://doi.org/10.1024/0301-1526.32.1.54
19. Topçu IB, Bilir T, Uygunoğlu T (2009) Effect of waste marble dust content as filler on properties of self-compacting concrete. Constr Build Mater. https://doi.org/10.1016/j.conbuildmat.2008.09.007
20. Schutter GD, Gibbs J, Domone P, Bartos PJ (2008) Self-compacting concrete. Whittles Publishing, Dunbeath, Scotland, UK
21. Safawi MI, Iwaki I, Miura T (2005) A study on the applicability of vibration in fresh high fluidity concrete. Cem Concr Res 35(9):1834–1845. https://doi.org/10.1016/j.cemconres.2004.10.031

22. Nguyen TLH, Roussel N, Coussot P (2006) Correlation between L-box test and rheological parameters of a homogeneous yield stress fluid. Cem Concr Res 36(10):1789–1796. https://doi.org/10.1016/j.cemconres.2006.05.001
23. Singh M, Srivastava A, Bhunia D (2017) An investigation on effect of partial replacement of cement by waste marble slurry. Constr Build Mater 134:471–488. https://doi.org/10.1016/j.conbuildmat.2016.12.155
24. ASTM C_1585 (2004) Standard test method for measurement of rate of absorption of water by hydraulic-cement concretes. ASTM Int
25. Zhu W, Bartos PJM (N.d.) Permeation properties of self-compacting concrete. https://doi.org/10.1016/S0008-8846(02)01090-6

Strength and Drying Shrinkage of High Strength Self-Consolidating Concrete

V. A. Shruthi, Ranjitha B. Tangadagi, K. G. Shwetha, R. Nagendra, C. Ranganath, Bharathi Ganesh, and C. L. Mahesh Kumar

Abstract The present study highlights on the strength and drying shrinkage behavior of High Strength Self-Consolidating Concrete (HSSCC) mixes, are studied through experimental investigation. HSSCC mixes of M60, M80 and M100 are produced using Ground Granulated Blast Furnace Slag (GGBFS) and Alccofine as mineral admixtures. The IS 10262-2019 was adopted to design the mixes of HSSCC. The HSSCC are evaluated using tests on Slump flow, T_{500} slump flow, V funnel and L Box test. The strength parameters such as compressive strength and split tensile strength at period of moist curing are evaluated. For each mix proportion of HSSCC, three prism specimens of 75 × 75 × 150 mm were cast for drying shrinkage measurement and three cubes of 150 mm size were cast for water permeability measurement. The results have shown that shrinkage strain of HSSCC increases with the increases with powder content increases in the mix. Total powder content increases in the

V. A. Shruthi (✉) · R. B. Tangadagi · K. G. Shwetha · B. Ganesh · C. L. Mahesh Kumar
Department of Civil Engineering, Nitte Meenakshi Institute of Technology, Bangalore, India
e-mail: shruthiva95@gmail.com

R. B. Tangadagi
e-mail: ranjithatangadagi@gmail.com

K. G. Shwetha
e-mail: shwetha.kg@nmit.ac.in

B. Ganesh
e-mail: bharathi.gan11@gmail.com

C. L. Mahesh Kumar
e-mail: maheshkumar.cl@nmit.ac.in

R. B. Tangadagi
Department of Civil Engineering, GITAM University, Bangalore, India

R. Nagendra
INAE-DVP at Nitte Meenakshi Institute of Technology, Stedrant Technoclinic Private Limited, Bangalore, India
e-mail: r.nagendra@stedrant.com

C. Ranganath
Stedrant Technoclinic Private Limited, Bangalore, India
e-mail: chimbiliranganath@gmail.com

© Springer Nature Singapore Pte Ltd. 2021

K. K. Pathak et al. (eds.), *Recent Trends in Civil Engineering*, Lecture Notes in Civil Engineering 77, https://doi.org/10.1007/978-981-15-5195-6_48

mix and shrinkage strain of concrete mixes was found to increase with time up to around 28 days and beyond which no appreciable increase was observed. The shrinkage result was in the range of 300–600 microstrain. As powder content in the mix increases, the depth of water penetration in specimens was found to reduce.

Keywords High Strength Self-Consolidating Concrete · Supplementary Cementitious Materials · Workability · Durability · Drying shrinkage

1 Introduction

In the present world, Concrete is the most commonly used construction material. Many research are carried out to reduce and minimize the effect of CO_2 on the environment and many new alternative materials are used up to improve and achieve environmental friendly, cost-effective concrete with improved strength and durability characteristics. High Strength Concrete (HSC) is a cement-based matrix, which is normally referred to as having 28 days cube compressive strength in the range of 60–80 MPa or higher than that [1–3]. Self-Consolidating Concrete (SCC) is a highly flowable concrete that spreads into the form uniformly which does not require any mechanical vibrations [4].

The strength of concrete in tension is much lesser than that of compressive strength. When tensile stresses reach the tension strength, then microcracks will develop, these cracks spread and may cause damages to the structure. In concrete structures, the presence of cracks is one of the utmost objectionable defects. Cracking of concrete is partially due to drying shrinkage [5, 6] which affects the durability, shorten the service life and increase the maintenance cost of the structure.

Through literature survey data, it is obtained that a variety of test procedures are employed for several experiments and specimens for the estimation of strength parameters and shrinkage performance for different types of concrete mixtures. In many of the studies, cement is replaced by alternative materials like fly ash, GGBS, Silica fume, and metakaolin by varied proportions of percentage to determine the shrinkage properties of the mix. Many researchers have predicted various shrinkage models [7–9] and compared with experimental shrinkage values to check the accuracy of the models. A high rate of shrinkage was observed in high strength concrete and self-compacting concrete than normal strength concrete, and it is observed that increase in water–cement ratio and cement content increases shrinkage [10, 11].

2 Research Significance

The objectives of this work are to develop a high strength self-consolidating concrete and to investigate strength, drying shrinkage and water permeability properties using alternative cement replacement materials like Ground Granulated Blast Furnace Slag and Alccofine.

Table 1 Mix proportions of HSSCC for 1 m^3 of concrete in kg (kg/m^3)

Grade of concrete	Total cementitious material	OPC(kg)	GGBFS(kg)	Alccofine(kg)	W/C ratio	FA(kg)	CA(kg)	SP(lts)
M 60	600 (100%)	430 (71.67%)	150 (25%)	20 (3.33%)	0.30	882	744	2.44
M 80	625 (100%)	439 (70.20%)	156 (25%)	30 (4.80%)	0.28	877	739	3.13
M 100	650 (100%)	438 (67.31%)	162 (25%)	50 (7.69%)	0.26	873	736	3.25

Note FA-Fine Aggregates, *CA*-Coarse Aggregates, *SP*-Superplasticizer

3 Experimental Work

3.1 Materials and Mix Design

In the present work, Ordinary Portland Cement (OPC) of 53 Grade is used, Manufactured sand (M-sand) is used as fine Aggregate, Coarse Aggregates of maximum size of 12.5 mm and Potable water are used for preparing a HSSCC along with Ground Granulated Blast Furnace Slag (GGBFS) and Alccofine as mineral admixture [12], and a new generation Poly-Carboxylated Ether(PCE) based superplasticizer as per IS 9103:1999 [13] are used.

As per IS 10262: 2019 [14] procedure, three mixes were designed for M60, M80, and M100 grades of HSSCC mixes to investigate the workability, strength, drying shrinkage and permeability properties. The summary of the design mixes is shown in Table 1.

3.2 Test Methods

The fresh properties are evaluated by Slump flow, T_{500} time, V funnel flow time, and L Box test according to IS 1199 (Part6) : 2018 [15] procedure. The cube specimens of 150 mm and six cylinders of 150D × 300H were cast to determine the compressive strength and split tensile strength of hardened concrete, as per the procedure of IS 516 : 1959 [16]. Drying shrinkage of concrete is measured using dial gage in shrinkage apparatus as shown in Fig. 3 as per IS 1199 : 1959 [18]. The cube specimens are used to determine water permeability of concrete as per DIN 1048 : 1991 [17] and permeability setup is shown in Fig. 4.

Test for drying shrinkage was carried out on 75 × 75 × 150 mm sized prism specimens. For each proportion, three prism specimens were cast and are immersed in water for 3 days after demolding. The first measurement of length (L_1) was taken immediately after being taken out from the water at 3 days using a digital dial gage.

Table 2 Fresh properties of HSSCC mixes

Fresh properties	Grade of concrete		
	M 60	M 80	M 100
Slump flow (mm)	670	720	730
T_{500} flow time (s)	5.5	5.1	5.0
V funnel test (s)	9.5	9.2	8.3
L Box test (H2/H1 ratio)	0.81	0.85	0.90

Then, the specimens are dried in an oven at (50 ± 1) °C, at 17% Relative Humidity for 44 h. The specimen is removed from the oven and air dried for 4 h and the dry reading is taken at 7 days. Then, the above procedure is repeated and 7, 14, 28, and 56 days of dry measurement (L_2) are taken, for various specimens. The change in length (ΔL) is calculated by the difference between the final and initial reading. Then, the shrinkage strain was calculated by dividing a change in length by original length (L) according to IS 1199 : 1959 [18].

4 Results and Discussions

4.1 Properties of Fresh Concrete Mixes

The flowability, passing ability and filling ability of HSSCC are evaluated by the following test methods: Slump flow, T_{500} time, V funnel time, and L Box test according to IS 1199 (Part6) : 2018 [15]. The range of slump flow diameter is kept around 650–750 mm, T_{500} duration is less than 7 s, V funnel flow time is between 6.3 and 33 s, and the ratio H_2/H_1 is kept within 0.7–0.97 throughout the study. Improved workability properties were observed. The fresh properties of HSSCC results are shown in Table 2 and Fig. 1a, b, c, d.

4.2 Properties of Hardened Concrete Mixes

The hardened properties are measured for different grades of HSSCC mixes such as Compressive strength and split tensile strength as per IS 516 : 1959 [16]. The cube compressive strength of different mixes of HSSCC by partial replacement of cement with GGBFS and Alccofine is evaluated and calculated for curing periods of 3, 7, and 28 days and the results are shown in Table 3 and Fig. 2a (Figs. 3 and 4).

The split tensile strength is determined for various grades of concrete using a cylindrical specimen for a curing period of 7 and 28 days. At 28 days. The tensile strength of HSSCC mixes ranged from 5 to 8 MPa. The results are presented in Table 3 and Fig. 2b.

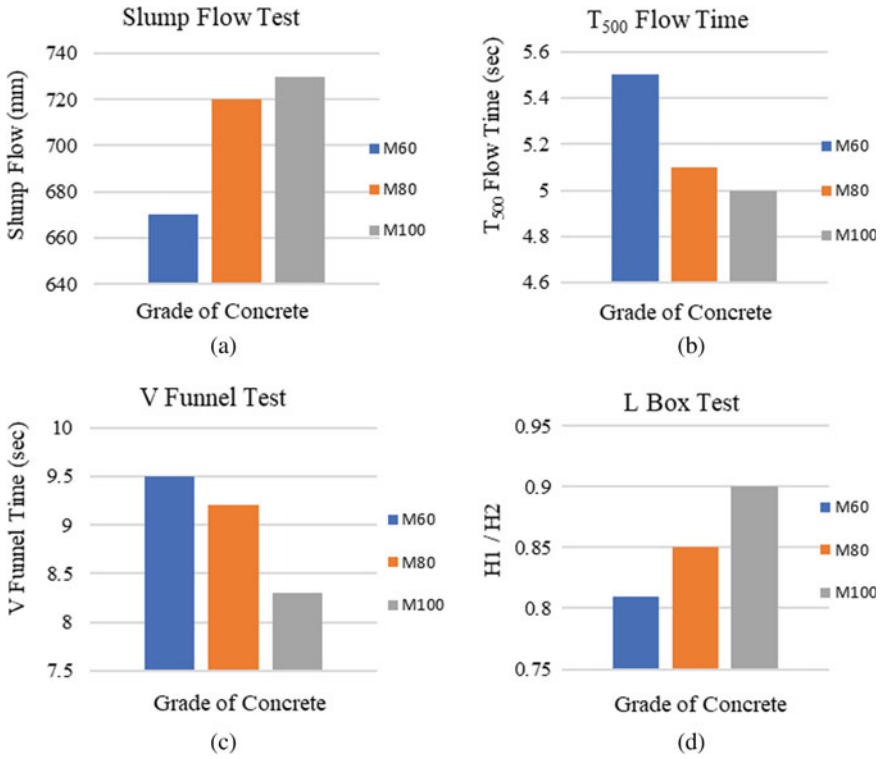

Fig. 1 Fresh properties of HSSCC **a** Slump Flow test Results, **b** T500 Flow Time Results, **c** V Funnel Flow Time, and **d** L Box Blocking Ratio

Table 3 Cube compressive strength and split tensile strength

Grade of concrete	Compressive strength of concrete (N/mm^2)			Split tensile strength of concrete (N/mm^2)	
	3 days	7 days	28 days	7 days	28 days
M 60	35.3	46.9	68.9	3.97	5.62
M 80	44.5	59.3	88.5	4.35	6.44
M 100	54.0	71.4	107.4	5.09	7.29

4.3 Durability Properties

Drying Shrinkage. The effect of shrinkage strain on M60, M80 and M100 grades of concrete is determined at 25 ± 2 °C temperature and 17% Relative Humidity by replacing cement content with Alccofine and GGBFS according to IS 1199 : 1959 [18] procedure. The length change of the specimens is obtained, and shrinkage strain is evaluated for different grades of concrete mixes. The results of the shrinkage strain

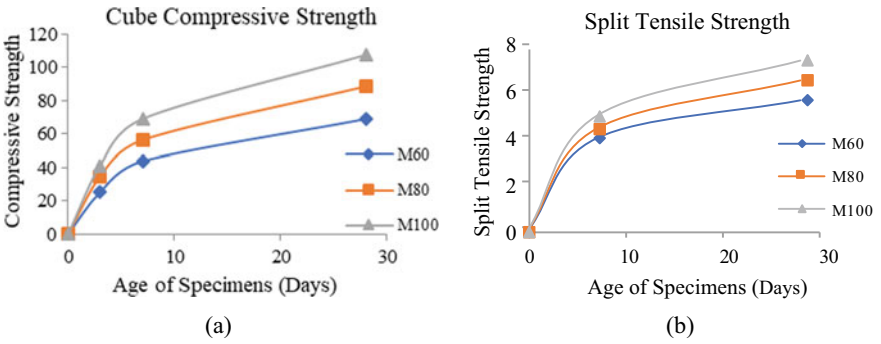

Fig. 2 Hardened properties of HSSCC **a** compressive strength **b** split tensile strength

Fig. 3 Shrinkage measurement

are presented in Table 4 and shrinkage strain versus time of drying was shown in Fig. 5.

Water Permeability. Permeability of concrete is determined as per the procedure of DIN 1048 (Part 5) : 1991 [17] for different grades of concrete M60, M80 and M100, partially replacing fine particle with ultra-fine particles. The permeability test measures the amount of water penetrated into the concrete under exerting pressure. The amount of penetration of concrete is given in Table 5 and shown in Fig. 6.

Fig. 4 Permeability setup

5 Conclusions

Based on the work conducted and test results, the following conclusions may be drawn:

1. The workability properties of the concrete mixes are found to increase with an increase in the cementitious content due to the presence of more finer particle content.
2. Target compressive strength was achieved at 28 days of moist curing period. The Split tensile strength at 28 days of moist curing achieved slightly lesser than 10% of cube compressive strength values. This may be due to higher pozzolanic material content, tensile strength may be at prolonged curing period.
3. Shrinkage Strain of HSSCC increases as total powder content increases in the mix. This may be due to evaporation of moisture content in the capillary pores of the paste which leads to shrinkage of the mix.
4. Shrinkage Strain of all concrete mixes was found to increase with time up to around 28 days and beyond which no appreciable increase was recorded.
5. As powder content in the mix increases, the depth of water penetration in specimens was found to reduce. This is due to the particle packing effect.
6. The durability of concrete was found to improve with higher powder content which is evident from water permeability and shrinkage values.

Table 4 Test results of shrinkage of concrete with length of specimen, L = 150 mm

Sl. No.	Grade of concrete	Change in length (ΔL) in mm					Shrinkage strain (ΔL/L) × 10^{-6}				
		7 days	14 days	28 days	56 days	90 days	7 days	14 days	28 days	56 days	90 days
1	M 60	0.037	0.060	0.075	0.080	0.084	246.6	399.9	500.0	533.3	560.0
2	M 80	0.033	0.055	0.073	0.078	0.082	220.0	366.6	486.9	520.0	546.6
3	M 00	0.024	0.047	0.068	0.076	0.079	160.0	313.3	453.3	506.6	526.6

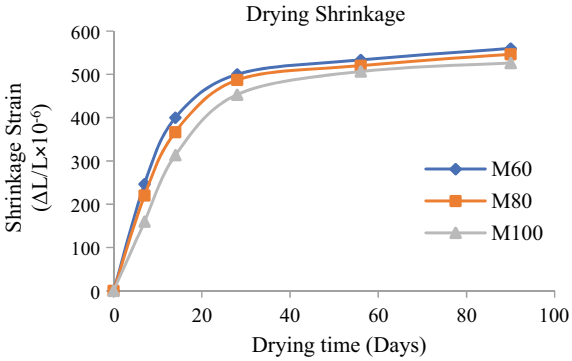

Fig. 5 Drying shrinkage of HSSCC

Table 5 Permeability of HSSCC mixes

Sl. No.	Grade of Concrete	Permeability (mm)	Maximum limit (Morth 2013)
1	M 60	13	Should not be more than 25 mm
2	M 80	11	
3	M 100	9	

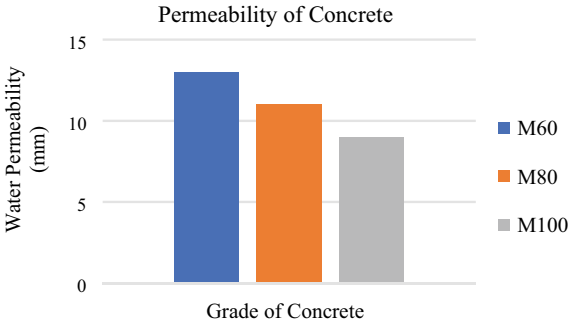

Fig. 6 Water permeability of HSSCC

Acknowledgements The authors wish to thank to Stedrant Technoclinic Pvt. Ltd. Bangalore for providing all the testing facilities at their NABL accredited laboratories and also Dr. R Nagendra, Senior Director-Technical, for his guidance throught the project work. The authors acknowledge Nitte Meenakshi Institute of Technology for providing an opportunity to carry out this reseach work.

References

1. Gupta SM et al (2006) Shrinkage of high strength concrete. Asian J Civ Eng (Build Hous) Res Gate 7(2):183–194. https://www.researchgate.net/publication/237464365

2. Shetty MS (2008) Concrete technology—theory and practice, 6th edn. S. Chand & Company Ltd., Ram Nagar, New Delhi
3. Neville AM (2002) Properties of concrete, 5th edn. Pearson Education Limited, England
4. Guneyisi Erhan et al (2010) Strength and drying shrinkage properties of self-compacting concretes incorporating multi system blended mineral admixtures. Constr Build Mater, Elsevier 24:1878–1887. https://doi.org/10.1016/j.conbuildmat.2010.04.015
5. Ghezal AF et al (2014) Restrained shrinkage cracking of self-consolidating concrete. J Mater Civil Eng ASCE. https://doi.org/10.1061/(ASCE)MT.1943-5533.0001239
6. Turcry P et al (2006) Cracking tendency of self compacting concrete subjected to restrained shrinkage: experimental study and modeling. J Mater Civil Eng ASCE 18:46–54. https://doi.org/10.1061/(asce)0899-1561(2006)18:1(46)
7. Lomboy Gilson et al (2011) Shrinkage and fracture properties of semi flowable self-consolidating concrete. J Mater Civ Eng ASCE. https://doi.org/10.1061/(ASCE)MT.1943-5533.0000249
8. Albert, Kwan KH et al (2013) Shrinkage of high-strength concrete and high flowability concrete. HKIE Trans, Taylor and Francis 17(3):25–33. http://dx.doi.org/10.1080/1023697X.2010.10668201
9. Barr B et al (2003) Shrinkage of concrete stored in natural environments. Cem Concr Compos, Elsevier 25:19–29
10. Bao-guo MA et al (2007) Drying shrinkage of cement-based materials under conditions of constant temperature and varying humidity. J China Univ Min Technol, Science Direct 17(3):0428–0431
11. Han MC et al (2018) Mixture and material factors affecting the strength and shrinkage of high-performance concrete. J Asian Arch Build Eng, Taylor and Francis 5(1):145–151. https://doi.org/10.3130/jaabe.5.145
12. IS 16714 : 2018 Grand granulated blast furnace slag for use in cement, mortar and concrete—specifications. Bureau of Indian Standards, New Delhi
13. IS 9103 : 1999 Concrete admixtures—specification. Bureau of Indian Standards, New Delhi
14. IS 10262 : 2019 Concrete mix proportioning—guidelines. Bureau of Indian Standards, New Delhi
15. IS 1199 : 2018 Fresh concrete—methods of sampling, testing and analysis. Bureau of Indian Standards, New Delhi
16. IS 516 : 1959 Methods of tests for strength of concrete. Bureau of Indian Standards, New Delhi
17. DIN 1048 : 1991 Testing concrete (Part 5). Bureau of Indian Standards, German Standards
18. IS 1199 : 1959 Methods of sampling and analysis of concrete. Bureau of Indian Standards, New Delhi

Creep Characteristics of High Strength Self Compacting Concrete

Ranjitha B. Tangadagi, V. A. Shruthi, Bharathi Ganesh, M. V. Vasudev, R. Nagendra, and C. Ranganath

Abstract The Self Compacting Concrete (SCC) is a type of concrete that gets compacted under its own weight. The present paper is an experimental investigation on the strength and creep characteristics of different mixes of High Strength Self Compacting Concrete (HSSCC). HSSCC mixes were prepared using Ground Granulated Blast Furnace Slag (GGBFS) and Alccofine as mineral admixtures. Trial mixes were carried out for three different grades namely M 60, M 80 and M 100. The rheology of mixes was obtained by varying both water–binder ratio and the dosage of superplasticizer. The properties of fresh HSSCC such as flowability, passing ability and filling ability were evaluated as per EFNARC 2005 with tests on Slump Flow, T_{500} Slump, V Funnel Flow Time and L Box. The cube specimens of 150 mm side were cast and cured as per the standard codal procedures. The compressive strength of the mixes at a curing period of 28 days was assessed as per IS 516:1959 (reaff. 2013), recorded and analysed. The cylindrical specimens of 150 mm dia. and 300 mm height were cast to measure creep as a durability parameter of HSSCC. From the analysis of results, it was observed that the workability and strength of mixes get enhanced due

R. B. Tangadagi (✉)
Department of Civil Engineering, GITAM University, Bangalore, India
e-mail: ranjithatangadagi@gmail.com

R. B. Tangadagi · V. A. Shruthi · B. Ganesh · M. V. Vasudev
Department of Civil Engineering, Nitte Meenakshi Institute of Technology, Bangalore, India
e-mail: shruthiva95@gmail.com

B. Ganesh
e-mail: bharathi.gan11@gmail.com

M. V. Vasudev
e-mail: mvvasudev.mv@gmail.com

R. Nagendra
Department of Civil Engineering, INAE-DVP at Nitte Meenakshi Institute of Technology, Stedrant Technoclinic Pvt. Ltd., Bangalore, India
e-mail: r.nagendra@stedrant.com

C. Ranganath
Stedrant Technoclinic Private Limited, Bangalore, India
e-mail: ranganath.chimbili@stedrant.com

© Springer Nature Singapore Pte Ltd. 2021

K. K. Pathak et al. (eds.), *Recent Trends in Civil Engineering*, Lecture Notes in Civil Engineering 77, https://doi.org/10.1007/978-981-15-5195-6_49

to the presence of GGBFS and Alccofine as mineral admixtures. The resistance to creep strain of HSSCC, in comparison with that of normal SCC, is found to increase with the increase in the grade of HSSCC (from M 60 to M 80 and from M 80 to M 100). The range of creep strain obtained varied from 450 microstrain M 100 to 1350 microstrain M 60. Hence it may be rationally concluded that the addition of GGBFS and Alccofine in concrete increases the durability (creep characteristics) of HSSCC.

Keywords High strength self compacting concrete · Ground granulated blast furnace slag · Alccofine · Rheology · Compressive strength · Creep

1 Introduction

Self Compacting Concrete (SCC), an innovative product developed by Professor Hajime Okamura and Professor Ozawa (1980), is gaining popularity and evolving fast in the field of Civil Engineering. The need for the development of SCC was to address the lack of availability of skilled labour and also to reduce the noise of compaction during construction. Concrete being one of the most extensively used construction materials in the world, the emphasis of the research was on the reduction of consumption of cement in RC constructions because a tone of CO2 is released into the atmosphere for every tonne production of cement. Parallelly, recommending the usage of a finer particle in concrete to enhance the packing density of concrete, which in turn enhances the durability. The improvement in the durability of concrete may be due to the formation of extra gel by secondary hydration due to pozzolanic materials [1]. The addition of Supplementary Cementitious Materials (SCM) such as GGBFS, Silica fumes, fly ash, rice husk ash, etc. has dual benefits of reducing the industrial wastes and also adding value to building materials. Alccofine also known as Ultrafine GGBFS is a processed product of GGBFS. High Strength Concrete has compressive strengths in the range of 60 MPa to 80 MPa and higher. Concrete with compressive strength more than 100 MPa is known as Ultrahigh Performance Concrete (UHPC) [2]. The product HSSCC is gaining popularity due to the reduced size of structural elements and hence the reduction in overall self-weight of the structure.

2 Research Significance

The HSSCC is a technology in use in many of the advanced countries and developing countries. Few published literature highlights the use of SCMs in HSSCC. However, literature on the use of alternative micro and nano-cementitious materials [3] as SCM in HSSCC and assessment of creep characteristics [4] are scanty. Hence, the present work is taken up to develop a HSSCC with GGBFS and Alccofine as SCM

to investigate the effect on strength and also durability characteristics of HSSCC through creep of concrete.

3 Experimental Work

The present experimental investigation consists of collection of materials, assessment of characteristics of the materials as per relevant codes of practice, designing the mix as per IS 10262:2019 [5] and freezing the design mix after conducting extensive trials. The fresh properties of HSSCC mixes are assessed, specimens are cast, cured at ambient temperature to assess strength and creep characteristics of HSSCC. The details are provided as follows.

3.1 Materials Used and Mix Design

In this work, for the preparation of various mixes, Ordinary Portland Cement (OPC) of 53 Grade tested as per IS 4031:1996 [6], conforming to the requirements of IS 269:2015 [7] GGBFS and Alccofine as mineral admixture [8], Manufactured Sand (M-Sand) as fine Aggregates, confirmed to zone II as per IS 383-2016 [9], 12.5 mm sized well-graded Coarse Aggregates and Potable water from the laboratory were used for preparing a HSSCC mixes. The Poly Carboxylate Ethers (PCE) based new generation superplasticizer was used as chemical admixture [10].

Mix design was carried out as per IS 10262:2019 [5], for M 60, M 80 and M 100 grades of concrete. The design mix for HSSCC mixes was arrived after extensive trials to investigate the workability, compressive strength and creep characteristics of HSSCC with cement content, GGBFS and Alccofine content as variables in the mixes [11]. The weigh batching design mixes are provided in Table 1. The dosage of admixture was varied to get the required rheology of mixes; variation of dosage was within the specified dosage in ml/kg of cement/cementitious content.

3.2 Test Methods

The fresh properties evaluated by Slump Flow, T_{500} slump, V Funnel flow time and L Box tests were as per IS 1199 (Part6): 2018 [12]. Cube specimens of 150 × 150 × 150 mm and cylinders of 150 mm dia. × 300 mm height were cast to determine the compressive strength as per IS 516:1959 [13] and creep of HSSCC strain as per ASTM C-512 [14] procedure.

Table 1 Mix Proportions of HSSCC in kg/m^3

Sl.No	Grades of HSSCC	Materials in kg/m^3				W/C ratio	FA	CA	SP
		Total cementitious content	Cement	GGBFS	Alccofine				
1	M 60	600	406	174	20	0.30	861	753	2.44
		100%	67.66%	29%	3.33%				
2	M 80	625	414	181	30	0.28	852	746	3.13
		100%	66.24%	29%	4.80%				
3	M 100	650	412	188	50	0.26	840	735	3.25
		100%	63.38%	29%	7.69%				

Note FA—Fine Aggregate, CA—Coarse Aggregate, SP—Superplasticizer

Table 2 Fresh Properties of HSSCC mixes

Fresh Properties	Grades of HSSCC			Specification as per EFNARC 2005
	M 60	M 80	M 100	
Slump flow (mm)	680	730	750	600–750
T_{500} Slump (sec)	5.2	4.6	4.3	3.5–6.0
V Funnel (sec)	9.0	8.8	8.1	3.0–12.0
L Box test (H2/H1 ratio)	0.87	0.89	0.92	0.8–1.0

4 Test Results and Discussions

The test results and discussions are as follows.

4.1 Properties of Fresh HSSCC

The fresh properties of HSSCC mixes of M 60, M 80 and M 100 grades such as flowability, passing ability and filling ability of HSSCC were assessed by Slump flow, T_{500} slump, V funnel and L Box test as per IS 1199 (Part6): 2018 [12] procedure. The range of slump flow diameter was around 650–750 mm; T_{500} duration was less than 7 sec; V funnel flow time for different mixes ranged from 8.1 sec. to 9.0 sec. The Blocking ratio (H_2/H_1) was 0.87, 0.89 and 0.92 for M 60, M 80 and M 100 grades respectively indicating the resistance to the flowability of HSSCC. The results of the properties of fresh HSSCC obtained during the study are shown in Table 2.

- The slump flow was found increased with an increase in the cementitious content. Reduced time of flow from 5.2 sec. for 600 kg/m^3 to 4.3 sec. at 650 kg/m^3 may be attributed to the increased cementitious content as well as nanoparticles of GGBFS namely Alccofine of spherical shape, which might have reduced the inter particle friction.
- Similar behaviour of improved flow properties was observed in slump flow and V funnel test as well. However, the blocking ratio is lesser than unity for all the three grades of HSSCC, indicating the resistance of passing ability.
- Rheological properties of HSSCC mixes measured are within the specified values as per EFNARC 2005 [15].

4.2 Properties of Hardened Concrete Mixes

The Compressive strength, the main property of hardened HSSCC, needed to be conducted and linked to all other properties of concrete, was assessed as per IS 516-1959 [13]. The cube compressive strength of different HSSCC grades was evaluated at a curing period of 28 days [16], and the results are presented in Table 3 and analysed

Table 3 Cube Compressive Strength of HSSCC Mixes

Grade of Concrete	Compressive Strength of Concrete (N/mm^2) at a Curing period of 28 days	Normalized Strength
M 60	64.60	1.00
M 80	84.87	1.31
M 100	103.57	1.60

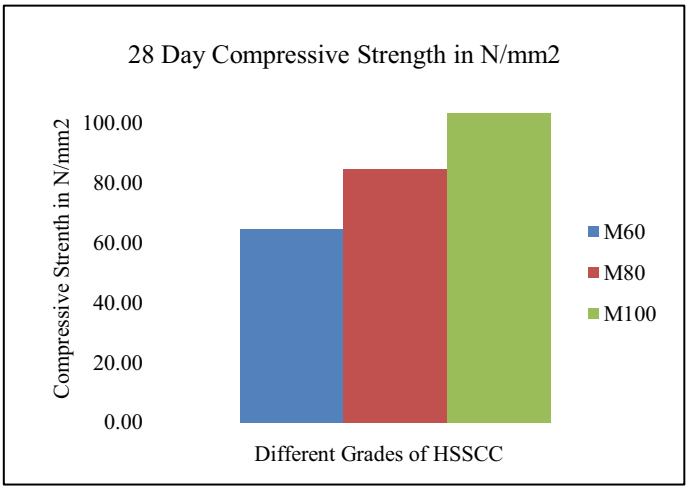

Fig. 1 Hardened Properties of HSSCC—Compressive Strength

in Fig. 1.

- The increase in strength of nearly 60% is observed for M 100 grade in which 4.34% of cementitious content was replaced with Alccofine and 29% of both the mixes was GGBFS. The contribution of Alccofine to the increased strength is clearly highlighted.
- Similarly, when the cementitious content of M 80 grade is replaced with nearly 1.5% Alccofine, the increased strength is 30% in mixes, where GGBFS content was 29% in both the mixes.

4.3 Creep as Durability Property

The concrete deforms when the load is applied continuously for longer period on a RC structural member, i.e. under sustained stress with time, showing an increase in strain along with certain changes that affect the durability of the structure and is termed as Creep [17, 18].

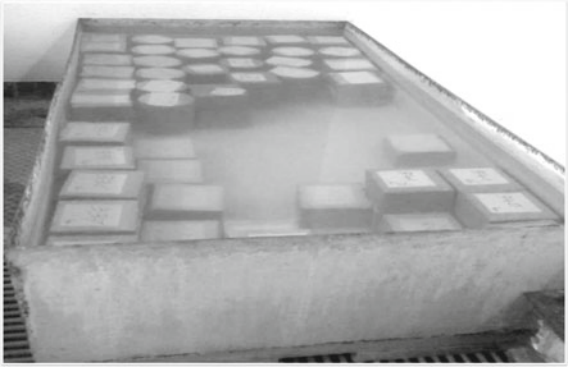

Fig. 2 Specimens under Water Curing

To determine the creep, the load-induced time-dependent strain is measured at controlled stress condition at a selected age of concrete for a specimen, under an arbitrary set of controlled environmental condition [19]. The standard test method for creep determination of concrete is carried out as per ASTM C 512-87 [14].

The cylindrical specimens were cured (Fig. 2) for 28 days after demoulding. The effect of creep strain on M 60, M 80 and M 100 grades of concrete was determined at a controlled temperature of 25 ± 2 ºC temperature and 50 ± 2% relative humidity. Deformations of the specimens of different grades of concrete under sustained load were assessed in terms of creep strain, using Demec gauge at regular intervals, starting from the instant of loading, immediately after loading, next after 2 h and then after 6 h of loading. Readings are continued to record every day for a week, every week until the end of 1 month and every month until the end of 3 months (Table 4). The total load-induced strain for a particular age and corresponding sustained stress were used to calculate the amount of creep [19]. Each creep strain calculated is an average of strain measured with three Demec gauges placed on the same plane. Creep strain versus age of loading is plotted (Fig. 3) and analysed (Fig. 4).

From the analysis of data of creep of mixes of HSSCC, it is observed that the shape of the plot of Creep Strain with Time for HSSCC mixes is identical in profile to those of normal SCC.

- Stress is proportional to Strain within the elastic limit up to almost three days and beyond which the shape of the curve is parabolic. It is almost approaching a constant value with time.
- It is observed from the results that higher the grade of concrete, the lower is the creep value and vice versa. Nearly 4% reduction in strain on day one to 6% reduction on 90th day was observed for M 80 grade when expressed in terms of that of M 60 grade, and the reduction observed is 11% and 13% at day one and 90th day, respectively for M 80 grade, showing that the stiffness of the mix increases as the cementitious content of the mix is increased. This may be because of increased packing density of HSSCC due to the presence of finer particles or mix composed of different sized particles of cementitious materials which in turn fill the finer voids in concrete.

Table 4 Test Results of Creep Strain

Age in days	Micro strain ($\times 10^{-6}$) for Different grades of HSSCC			Normalized micro strain ($\times 10^{-6}$) values in terms of that of M 60 HSSCC		
	M 60	M 80	M 100	M 60	M 80	M 100
1	505	485	452	1.000	0.960	0.895
2	822	785	773	1.000	0.955	0.940
3	853	817	812	1.000	0.958	0.952
4	868	843	820	1.000	0.971	0.945
5	883	853	835	1.000	0.966	0.946
6	895	862	848	1.000	0.963	0.947
7	910	874	867	1.000	0.960	0.953
14	945	888	902	1.000	0.940	0.954
21	985	977	957	1.000	0.992	0.972
28	1047	993	988	1.000	0.948	0.944
30	1065	1023	1005	1.000	0.961	0.944
60	1223	1155	1160	1.000	0.944	0.948
90	1342	1270	1173	1.000	0.946	0.874

Fig. 3 Creep Test Setup

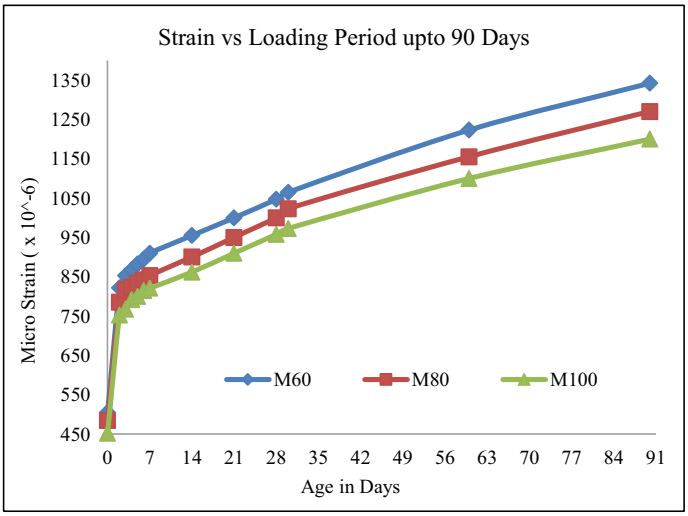

Fig. 4 Variation of Creep Strain with Time—HSSCC Mixes

- The present investigation triggers an interest to study the fire resistance of HSSCC as reduced void content is detrimental to fire rating of concrete and also it may lead to bursting of concrete [20].

5 Conclusions

From the discussions on test results of rheology of different mixes of HSSCC, compressive strength and creep behaviour, the following rational conclusions may be drawn.

1. The presence of GGBFS and Alccofine as mineral admixtures in SCC improves the rheology of SCC mixes.
2. Compressive strength of HSSCC mixes (with 29% GGBFS) increases significantly: 30% increase in the strength was recorded for a replacement of cementitious content with 1.5% Alccofine, and 60% increase was recorded for a replacement of cementitious content with 4.33% Alccofine.
3. Higher the grade of concrete, the lower is the creep value and vice versa. There is a reduction of nearly 6% and 11% creep for M 80 and M 100 grades, respectively in comparision with M 60 grade. This shows that the stiffness of the HSSCC increases with increase in the cementitious content.
4. The fire resistance of HSSCC mixes with higher finer particle content is to be studied as the concrete with lowered void content may lead to bursting of concrete at elevated temperature.

Acknowledgements The authors wish to thank Stedrant Technoclinic Pvt. Ltd. Bangalore for providing all the testing facilities at their NABL accredited laboratories and also Dr. R Nagendra, Senior Director-Technical, (INAE - Distinguished Visiting Professor at Nitte Meenakshi Institute of Technology, Bangalore) for his guidance throughout the project work. The authors acknowledge the permission granted by Malnad College of Engineering and also Nitte Meenakshi Institute of Technology to use their laboratory to carry out this research work.

References

1. Kapoor K et al (2018) Evaluating the durability properties of Self Compacting Concrete made with coarse and fine recycled concrete aggregates. Taylor and Francis, ISSN: 1964–8189, pp 2116–7214. https://doi.org/10.1080/19648189.2018.1506825
2. Ganesh B, Ramesh MN, Santhosh M, Manoj V, Sharada Bhai H (2018) Rheology of ultra high performance self compacting concrete – UHPSCC, themes of the conference: proceedings of innovative materials for better construction, innovative world of concrete (IWC). In: Proceedings of international conference "INNOVATIONS IN CONCRETE—To Meet Housing And Infrastructure Challenges" 19th–22nd September 2018, pp 38–45
3. Mohan A, Mini KM (2018) Strength and durability studies of SCC incorporating silica fume and ultrafine GGBS. Constr Build Mater 171:919–928. http://doi.org/10.1016/j.conbuildmat.2018.03.186
4. Mazloom M (2007) Estimating long-term creep and shrinkage of high strength concrete. Cem Concr Compos 30:316–326. https://doi.org/10.1016/j.cemconcomp.2007.09.006
5. IS 10262:2019, "Concrete Mix Proportioning—Guidelines". Bureau of Indian Standards, New Delhi
6. IS 4031:1996, "Method of Physical tests for Hydraulic Cement". Bureau of Indian Standards, New Delhi
7. IS 269:2015, "Ordinary Portland Cement- Specification". Bureau of Indian Standards, New Delhi
8. IS 16714:2018, "Grand Granulated Blast Furnace Slag for use in Cement, Mortar and Concrete-Specifications". Bureau of Indian Standards, New Delhi
9. IS 383:2016, "Specification for Coarse and Fine Aggregates from Natural Source for concrete". Bureau of Indian Standards, New Delhi
10. IS 9103:1999, "Concrete Admixtures- Specification". Bureau of Indian Standards, New Delhi
11. Felekogolu B et al (2007) Effect of water/cement ratio on the fresh and Hardened properties of self-compacting concrete. Build Env Elsevier 42:1795–1802. https://doi.org/10.1016/j.buildenv.2006.01.012
12. IS 1199:2018, "Fresh Concrete- Methods of Sampling, Testing and Analysis". Bureau of Indian Standards, New Delhi
13. IS 516:1959, "Methods of tests for strength of concrete". Bureau of Indian Standards, New Delhi
14. ASTM (American Society for Testing and materials) "Standard Test Method for Creep of Concrete in Compression". ASTM C 512–587, West Conshohocken, United States
15. EFNARC-2005 "The European guidelines for Self-Compacting Concrete specification production and use"
16. Boukendakdji O et al (2012) Effects of granulated blast, furnace slag and superplasticizer type on the fresh properties and compressive strength of self compacting concrete. Cem Concr Compos 34:583–590. https://doi.org/10.1016/j.cemconcomp.2011.08.013
17. Shariq M et al (2016) Creep and drying shrinkage of concrete containing GGBFS. Cem Concr Compos 68:35–45. https://doi.org/10.1016/j.cemconcomp.2016.02.004

18. Chern J-C et al (2011) The influence of loading age on long-term drying creep of concrete. J Chinese Ins Eng 11(2):113–120. https://doi.org/10.1080/02533839.1988.9677048
19. Su L et al (2017) Experimental investigation of fundamental behaviour of concrete creep, Constr Build Mater 152:250–258. https://doi.org/10.1016/j.conbuildmat.2017.06.162
20. Helal MA, Heiza KM (2011) Effect of fire and high temperature on the properties of self compacted concrete. In: Ye L, Feng P, Yue Q (eds) Advances in FRP composites in civil engineering. Springer, Berlin, Heidelberg

Effects of Cigarette Butts in Fly Ash Cement Bricks

Chaitanya Mishra, Aayush Verma, Aditya Ratra, Ankit Jain, Anuj Agrawal, Anuj Dodeja, and Anuj Dubey

Abstract Cigarette butts are more than just pesky litter, their filters contain heavy metals, and since they take many years to break down, that gives these metals plenty of time to leach into the soil and water. It has become a big environmental threat. Using fly ash and cigarette butts and developing cement bricks with the help of these was the idea that was taken up as an innovative concept. The fly ash cement bricks with cigarette butts (FCBCB) were studied; different useful properties and prospects of the material were investigated; as a new building material, the FCBCB has shown very good plasticity and low water absorption characteristics.

Keywords Cigarette butts · Fly ash · Cement bricks

1 Introduction

There are many waste materials that are developing an alarming effect on the environment. Among these plastics, carbon dioxide gas and cigarette butts [5] are few of the names of such types of waste materials.

About 6 trillion cigarette butts [8] are produced every year leading to the creation of about 1.2 trillion tonnes of cigarette butt. Estimates report an increase of 50% by 2025 [9].

Cigarette butts being lightweight and little in size are easily carried away by wind and rain, from the ground, through the street drains and the storm drainage network, these flow to the lakes, rivers and sea. These cigarette butts carry a lot of poisonous chemicals like arsenic, acetone, lead, benzopyrene, toluene, butane, etc. Cigarette butts carry more than 165 chemicals. These chemicals are a huge threat to the marine life [7]. Many reports have highlighted that tobacco litter caused malnutrition, starvation and thereby causing the death of marine animals [2] and shorebirds. The effect of nicotine has been found severe even in dogs.

C. Mishra (✉) · A. Verma · A. Ratra · A. Jain · A. Agrawal · A. Dodeja · A. Dubey
Medi-Caps University, Indore, MP, India
e-mail: chaitanya_95212@rediffmail.com; chaitanya.mishra@medicaps.ac.in

© Springer Nature Singapore Pte Ltd. 2021

K. K. Pathak et al. (eds.), *Recent Trends in Civil Engineering*, Lecture Notes in Civil Engineering 77, https://doi.org/10.1007/978-981-15-5195-6_50

The treatment of cigarette butts waste is very complex. Hence, it not very easy to deal with it.

Various efforts [1, 4] are being made like incineration and using these in the construction industry like lightweight fired clay bricks [6].

Fly ash is a waste product of the power plant industry. About 72% of India's power plants are coal based. The combustion of coal produces CO_2 and ash. Now this fly ash is also used in the construction industry.

As the clay bricks production in India contributes to 49 million tonnes of CO_2 which is quite significant. As per ongoing practices in India, each million clay bricks consume about 200 tonnes of coal (or other fuel) and emit about 270 tonnes of CO_2.

All these lead to the development of the concept of using fly ash [3] and cigarette butts in cement bricks, thereby using waste materials and developing lightweight unfired fly ash cement bricks with cigarette butts(FCBCB).

2 Methodology

2.1 Materials

For the construction of Fly ash cement bricks, the following constituting materials were used:

(i) Ordinary Portland cement
(ii) Fly Ash
(iii) Stone dust
(iv) Cigarette Butts (refer Fig. 1)
(v) Water

For the construction of fly ash cement bricks (FCB), the materials were used in the following proportions (Table 1).

The amount of water added is 650 ml according to workability.

For the construction of fly ash cement bricks with cigarette butts (FCBCB), the materials were used in the following proportions (Table 2).

The amount of water added is 634 ml and extra water required due to water absorption of butts is 146 ml. The total water is 780 ml according to workability.

For the construction of cement fly ash bricks with cigarette butts (FCBCB), the materials were used in the following proportions (Table 3).

The amount of water added is 617.5 ml and extra water required due to water absorption of butts is 292 ml. The total water is 909.5 ml according to workability.

For the construction of cement fly ash bricks with cigarette butts (FCBCB), the materials were used in the following proportions (Table 4).

The amount of water added is 602 ml and extra water required due to water absorption of butts is 435 ml. The total water is 1040 ml according to workability.

Fig. 1 Cigarette butts

Table 1 Proportions for FCB

Materials	Percentage used	Weight (in gm)
Fly Ash	50	1250
Stone Dust	38	950
Cement	12	300
TOTAL	100	2500

Table 2 Proportions for FCBCB (with 2.5% CB)

Materials	Percentage used	Weight(in gm)
Fly Ash	48.75	1218.75
Stone Dust	37.05	926.25
Cement	11.7	292.5
Cigarette butts	2.5	62.5
TOTAL	100	2500

Table 3 Proportions for FCBCB (with 5% CB)

Materials	Percentage used	Weight(in gm)
Fly Ash	47.5	1187.5
Stone Dust	36.1	902.5
Cement	11.4	285
Cigarette butts	5	125
TOTAL	100	2500

Table 4 Proportions for FCBCB (with 7.5% CB)

Materials	Percentage used	Weight(in gm)
Fly Ash	46.25	1156.25
Stone Dust	35.15	878.75
Cement	11.1	277.5
Cigarette butts	7.5	187.5
TOTAL	100	2500

Table 5 Proportions for FCBCB (with 10% CB)

Materials	Percentage used	Weight(in gm)
Fly Ash	45	1125
Stone Dust	34.2	855
Cement	10.8	270
Cigarette butts	10	250
TOTAL	100	2500

For the construction of cement fly ash bricks with cigarette butts (CB), the materials were used in the following proportions (Table 5).

The amount of water added is 585 ml and extra water required due to water absorption of butts is 584 ml. The total water is 1169 ml according to workability.

For each category, three samples were prepared.

3 Method

Pre-defined proportions of constituent materials were properly mixed in a dry state (refer Fig. 2). Water was added and the whole mix was again mixed properly (refer Fig. 3). This wet mix was well placed in moulds of size 19.8X9.8X9 cm in three layers with proper compaction through the temping rod. Bricks were removed from moulds after 24 h (Refer Fig. 4). These samples were cured for 28 days (Refer Fig. 5).

Fig. 2 Dry mixing of materials

4 Observations

Different properties of the fly ash cement bricks(FCB) and fly ash cigarette butts(CB) cement bricks(FCBCB) were observed (Refer Figs. 6, 7, 8).

4.1 Determination of Density of Cigarette Butts

Weight of single cigarette butt = 0.15gm
Volume of single cigarette butt = 0.615 cc

4.2 Determination of Water Absorption of Cigarette Butts

Weight of dry cigarette butt = 0.15 gm
Weight of wet cigarette butt (after 24 h of immersion in water) = 0.50 gm

Fig. 3 Wet mixing of materials. (This Fig. is depicting the images of persons (Mr. Aditya Ratra, Mr. Aayush Verma, Mr. Ankit Jain and Mr. Anuj Dodeja) who are authors of the chapter and their consent for revealing their identity has been taken.)

5 Sieve Analysis of Fly Ash

Percentage passing through 90 Micron sieve = 17%

5.1 Determination of Density of FCB and FCBCB

See Table 6.

5.2 Determination of Failure Load in Compression Testing Machine

See Table 7.

Fig. 4 Brick sample after 24 h

6 Results

Based on the observations, the following results were arrived at.

6.1 Density of Cigarette Butts

Weight of single cigarette butt = 0.15gm
Volume of single cigarette butt = 0.615 cc
Therefore, density of cigarette butts = (0.15/0.61) = 0.244gm/cc

6.2 Water Absorption of Cigarette Butts

Weight of dry cigarette butt = 0.15 gm
Weight of wet cigarette butt (after 24 h of immersion in water) = 0.50 gm

Fig. 5 Brick samples after 28 days curing

Fig. 6 Testing of specimen. (This Fig. is depicting the images of persons (Mr. Aditya Ratra, Mr. Anuj Dubey, Mr. Anuj Dodeja who are authors of the chapter and Mr. Arun Gupta, Lab Technician) and their consent for revealing their identity has been taken.)

Fig. 7 Testing on UTM. (This Fig. is depicting the images of persons (Mr. Harish Vyas and Mr. Arun Gupta, both are Lab Technicians) and their consent for revealing their identity has been taken.)

Fig. 8 Failure pattern of specimen

Table 6 Weight of Bricks

Type of brick	Weight(in Kg)
Fly ash cement bricks (CB)	2.952
Fly ash cigarette butts cement bricks (FCBCB) with 2.5% replacement	2.72
Fly ash cigarette butts cement bricks (FCBCB) with 5% replacement	2.573
Fly ash cigarette butts cement bricks (FCBCB) with 7.5% replacement	2.254
Fly ash cigarette butts cement bricks (FCBCB) with 10% replacement	2.115

Table 7 Failure Load of bricks

Type of brick	Load (in kN)
Fly ash cement bricks (CB)	58.2
Fly ash cigarette butts cement bricks (FCBCB) with 2.5% replacement	29.3
Fly ash cigarette butts cement bricks (FCBCB) with 5% replacement	33
Fly ash cigarette butts cement bricks (FCBCB) with 7.5% replacement	27.75
Fly ash cigarette butts cement bricks (FCBCB) with 10% replacement	14

Therefore, water absorption = (0.5−0.15)/0.15*100 = 233.33%

6.3 Density of FCB and FCBCB

Therefore, the percentage decrease in density between FCB and FCBCB can be tabulated as follows (Tables 8, 9 and 10).

Table 8 Density of bricks

Type of brick	Weight (in Kg)	Density (in kg/m3) = Wt./(19.8*9.8*9)*109
Fly ash cement bricks (CB)	2.952	1690.37
Fly ash cigarette butts cement bricks (FCBCB) with 2.5% replacement	2.72	1557.52
Fly ash cigarette butts cement bricks (FCBCB) with 5% replacement	2.573	1473.35
Fly ash cigarette butts cement bricks (FCBCB) with 7.5% replacement	2.254	1290.68
Fly ash cigarette butts cement bricks (FCBCB) with 10% replacement	2.115	1211.09

Table 9 % decrease in Density of FCBCB bricks

Type of brick	Density (in kg/m3)	Variation in Density (in %) from FCB
Fly ash cigarette butts cement bricks (FCBCB) with 2.5% replacement	1557.52	(1690.37–1557.52)/1690.37*100 = 7.86
Fly ash cigarette butts cement bricks (FCBCB) with 5% replacement	1473.35	(1690.37–1473.35)/1690.37*100 = 12.83
Fly ash cigarette butts cement bricks (FCBCB) with 7.5% replacement	1290.68	(1690.37–1290.68)/1690.37*100 = 23.64
Fly ash cigarette butts cement bricks (FCBCB) with 10% replacement	1211.09	(1690.37–1211.09)/1690.37*100 = 28.35

Table 10 Compressive stress of bricks

Type of brick	Load (in kN)	Compressive stress (in N/mm2)
Fly ash cement bricks(CB)	58.2	3
Fly ash cigarette butts cement bricks (FCBCB) with 2.5% replacement	29.3	1.51
Fly ash cigarette butts cement bricks (FCBCB) with 5% replacement	33	1.7
Fly ash cigarette butts cement bricks (FCBCB) with 7.5% replacement	27.75	1.43
Fly ash cigarette butts cement bricks (FCBCB) with 10% replacement	14	0.72

6.4 Compressive Stress

7 Conclusions

Based on observations made and results arrived at, the following conclusions were derived:

1. The increased percentage of cigarette butts in the range from 2.5 to 10% helps in decreasing the density of FCBCB from 7.8 to 28.3%.
2. The compressive stress for FCBCB is about 50% lesser than that of FCB which leads to its use as a non-structural member.
3. The use of 10% cigarette butts leads to very much reduction in compressive stress. Hence, this much use of cigarette butt is not advisable.
4. The water absorption percentage is below 10%, after 24 h which is well within the limits.
5. It is advisable to use cigarette butts at 7.5% proportion which has provided better results in the range under study.
6. Crack failure patterns showed initially the presence of small length vertical cracks at failure load. Thereafter cracks did not lead to brittle failure, testing on universal

testing machine (UTM) indicated that there was a lot of plastic behaviour by FCBCB, even till end sample did not collapsed in pieces. This indicated that FCBCB gives more than enough warning before failure.

7. As FCBCB is made up of cigarette butts and fly ash which are waste materials; therefore, it is an eco-friendly product. Due to the reduced density of bricks, the dead load will decrease and thereby lead to an economical design.

References

1. Kae Long Lin (2006) Feasibility study of using brick made from municipal solid waste incinerator fly ash slag. J Hazardous Mater B137:1810–1816
2. Nicole C, Hackendahl DVM, Collin W Sereda (2004) DVM, the dangers of nicotine ingestion in dogs veterinary medicine March, 218–222
3. Obada Kayali (April 2005) High performance bricks from fly ash, world of coal ash, Lexington Kentucky USA
4. Sohrab V, Ali AY (2003) The use of polystyrene in light weight brick production. Iranian Polym J 12(4):323
5. Dietrich H, Iise H (1997) The changing cigarette. J Toxicol Env Health 50(4)
6. Abdul Kadir A, Mohajerani A (2008) Possible utilization of cigarette butts in light weight fired clay bricks. Int Schol Sci Res Innovat 2(9):137–141
7. http://www.beachapedia.org/cigarette_butt_litter
8. http://www.buttlitteringtrust.org (2007 April 10), about butt litter (online available)
9. World Academy of Science (2008) Eng Technol Int Civil Env Eng 2(9)

Influence of Copper Slag Properties on Behaviour of Cement Mortars and Concrete

D. Arpitha and C. Rajasekaran

Abstract The promotion of green infrastructure as an alternative to traditional concrete, known as grey infrastructure, is not as benign as many people think. In this concern, many alternative materials have been kept in place as a solution for the problems faced by the construction industry. The knowledge of understanding the basic property of a material is significant as the characteristics cannot be directly assumed that it can be compared to FA while mixing concrete. In this work, Copper Slag (CS) is used as a partial replacement for Fine Aggregate (FA), and a major focus is to understand the behaviour of the material based on its particle size, texture shape and surface characteristics as it decides the quality of concrete. Also, the importance of optimizing water/cement ratio (w/c) and dosage of Superplasticizer (SP) is a major consideration in this work which has a great impact on workability and strength parameter as it affects durability performance of concrete. Marsh cone test to decide optimum SP was carried out for PCE-based SP and Portland Pozzolana Cement (PPC). Optimal w/c ratio was decided based on the trials carried out using flow test for mortars, and mortar cubes were prepared and tested for 3, 7 and 28 days compressive test. In order to check the behaviour of CS in concrete, cubes were prepared and subjected to compressive strength for 7, 28 and 90 days based on the ideal water–cement ratio (w/c) and SP obtained from various trials conducted to achieve required workability and strength. Test results revealed that CS mortars and concrete exhibited higher strength than the control mix. The chemical reaction between the cement matrixes, incorporation of CS and SP for optimized w/c and dosage of SP not only enhanced the strength but also provided the required workability though CS has less water absorption capacity.

Keywords Copper slag · Superplasticizer · Workability · Strength

D. Arpitha (✉) · C. Rajasekaran
Department of Civil Engineering, National Institute of Technology Karnataka, Surathkal 575025, India
e-mail: arpithad.cv16f04@nitk.edu.in

C. Rajasekaran
e-mail: bcrajasekaran@nitk.edu.in

© Springer Nature Singapore Pte Ltd. 2021

K. K. Pathak et al. (eds.), *Recent Trends in Civil Engineering*, Lecture Notes in Civil Engineering 77, https://doi.org/10.1007/978-981-15-5195-6_51

1 Introduction

Developed nations that appreciate an inheritance of many years of infrastructure investment are attempting new approaches. Since their urban areas and populaces are developing gradually, their essential concern is presently basically to keep up and improve what is already set up and make it progressively feasible. In a few cases, issues emerge when social orders accept that their very own inclinations ought to be the standards that administer others. A portion of the focuses concerned about this point are the preferences of developed nations on what the focal point of infrastructure improvement ought to be are now and then implemented through hard instruments.

There is sound reason for some of the explanations that developed nations have thought of to tackle their pressing environmental issues. The budget spending plans for research of the rich nations are ordinarily bigger than those of developing nations, they will in general figure out what subjects are looked into and from what point of view. Great infrastructure turns into a driver for the engine of the financial development of the economy. With the development in the field of infrastructure, a few new difficulties have arisen in different forms like alternative techniques in construction, selecting alternative materials to beat the shortage and lessening the expenditure and mechanization and utilizing most recent present-day equipment and techniques. Cost variety of normal sand utilized as fine aggregate in concrete expanded the expense of development in the past decade. Alternative materials to be utilized as fine aggregate to decrease the burden on nature are being broadly investigated everywhere throughout the world and looking to the quantum of prerequisites, quality and properties, there has been a worldwide accord on the materials. In such manner, copper slag which is created as a result during the extraction of copper is being utilized as halfway swap for fine aggregate. Processed air-cooled and granulated copper slag have a number of positive mechanical properties for aggregate use, including great adequacy for features like soundness, advantage of resistance for abrasion and good strength properties [1]. Concrete is composed of 70% volume of fine and coarse aggregates. Utilization of CS as a replacement for aggregates will reduce the disposal problem as from the environmental point of view CS is a safe industry waste material as suggested by the different standards like United States Environmental Protection Agency and United Nations (UN) Basel Convention ruled CS as non-hazardous waste on the Transboundary Movement of Hazardous Wastes and their Disposal [2]. In corner to mechanical properties of concrete, the axial compressive strength perished with the rise of blasted CS content. Concrete mixes with replacements of above 40% showed the highest decline in compressive strength. All concrete mixes with blasted CS achieved results of compressive strength higher than the control mix. This showed that the total or partial replacement of natural FA for this industrial waste may be possible for structural concretes considering the strength aspects in addition to adequate disposal of this waste [3]. The compressive strength of concrete containing CS has shown better performance in sulphate condition when compared to control specimens. Deteriorative ettringite formation was observed in concrete during microstructure studies in control specimens whereas, in

case of CS concrete, these deteriorative crystals were not found which showed that concrete with CS has resistance for sulphate attack [4]. The use of CS as a partial replacement for FA in concrete improved the strength and durability properties in case of High strength Concrete; attaining the same workability through the action of SP will become important to meet the workability and consistency in order to produce high strength concrete mix [5]. Higher compressive strength was achieved for cement mortars for different replacement ratios of CS, compared to control mix, and flexure strength of concrete was comparable to control mix up to 50% partial replacement of CS for FA, but there was a decrease in strength with the increase in CS content. Reduction in surface water absorption was noticed up to 40% CS replacement level and decrease in the volume of permeable voids was observed up to 50% FA replaced by CS concrete. This showed that CS concrete has a better potential for partial replacement for sand [6].

2 Materials

2.1 Binder

Portland Pozzolana Cement (PPC) conforming to IS: 1489-1991 having a specific gravity of 2.98 was used.

2.2 Fine Aggregate (FA)

Locally accessible river sand that was sourced from Gurupura River, Dakshina Kannada, India was used as FA. FA confirms to Zone II of IS: 383-2016. CS was supplied from Sterlite Industry, Tamil Nadu. Physical properties of FA and CS are mentioned in Table 1.

Table 1 Physical properties of FA and CS

Sl. No.	Description	River sand	CS
1	Specific gravity	2.6	3.65
2	Water absorption, %	0.2	0.10
3	Fineness modulus	3.59	3.8

2.3 Superplasticizer (SP)

Poly Carboxylate Ether (PCE) based SP: Master Glenium sky 8233 confirming to ASTM C494 Type F En934-2 T3.1/3.2, IS9103:1999, IS2645:2003 was supplied by BASF.

2.4 Coarse Aggregate

Crushed granite of 20 mm maximum size and retained on IS: 480 sieves have been used as coarse aggregate. Two different sized coarse aggregates were used; 55% of aggregates are 20 mm passing 16 mm retained and 45% coarse aggregate 16 mm passing and 12.5 mm retained sieve were used having a water absorption of 1%. The sieve analysis of combined aggregates conforms to the specifications of IS: 383-1970 (Reaffirmed 2007) for graded aggregates having a specific gravity of 2.74 and fineness modulus of 4.16.

3 Experimental Program

With the purpose to study the influence on the use of CS, mortar mixes were prepared and subjected to a compressive test in the laboratory. The steps mentioned below recap the program that was followed.

- Marsh cone test was carried out to determine the ideal dosage of SP required to design the cement mortar and concrete mix.
- Mortar cubes were prepared for 1:3 cement sand ratio for 0.6% dosage of SP and w/c ratio of 0.45 were fixed after carrying out trials in marsh cone test. Specimens were cured and then tested at the age 3, 7 and 28 days for compressive strength. The average of three values provided the strength of concrete (Table 2).
- Various trials were carried out to achieve the workability for 75 mm–100 mm by varying w/c. From the trial test, the design mix for conventional concrete mixes and concrete with replacement of FA by CS for 0 and 50% was decided for ideal w/c of 0.35. Guidance of the IS: 10262:2000 was followed in the preliminary design of these mixes.

Table 2 Mix proportions

% of replacement of slag	Cement (kgs)	FA (kgs)	CA (kgs)	CS (kgs)	Water (kgs)	Admixture (kgs)
0%	410.51	650	1268.62	0.00	143.68	2.46
50%	410.51	325	1268.62	456.25	143.68	2.46

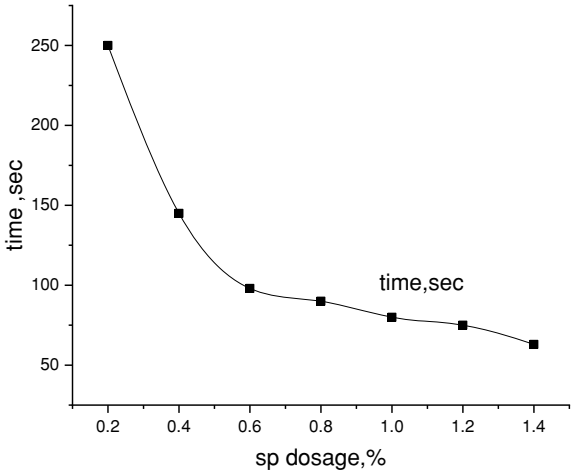

Fig. 1 Marsh cone test

- Concrete cubes of 150 mm side length were prepared and cured and then tested at the age of 7, 28 and 90 days for compressive strength. The average of three values provided the strength of concrete.

4 Results and Discussion

4.1 Marsh Cone Test

Mortar blender was used to prepare cement slurry of 1L for w/c of 0.35. SP dosage was varied from 0.2–2%. Time of flow was recorded and a graph was plotted in order to determine the dosage of SP (Fig. 1).

4.2 Cement Mortars

The optimum dosage of SP and w/c was decided based on the flow values after conducting flow test trials. The flow values were restricted until the cohesive mix was obtained. Since water absorption of aggregates varies, w/c ratio also got varied and the cohesive mix was obtained for the same dosage of SP that matches the results obtained from marsh cone test. Mortar cubes were subjected to compressive test, and mix containing CS showed higher strength when compared to mortars with 0% replacement of FA. The reaction in the matrix between PPC with SP added to the strength of mortars as it enhanced the formation of C-S-H gel in case of 50% replaced FA by CS. Since CS absorbs less water when compared to FA, the water demand by these aggregates is comparatively lesser which would be a major parameter for

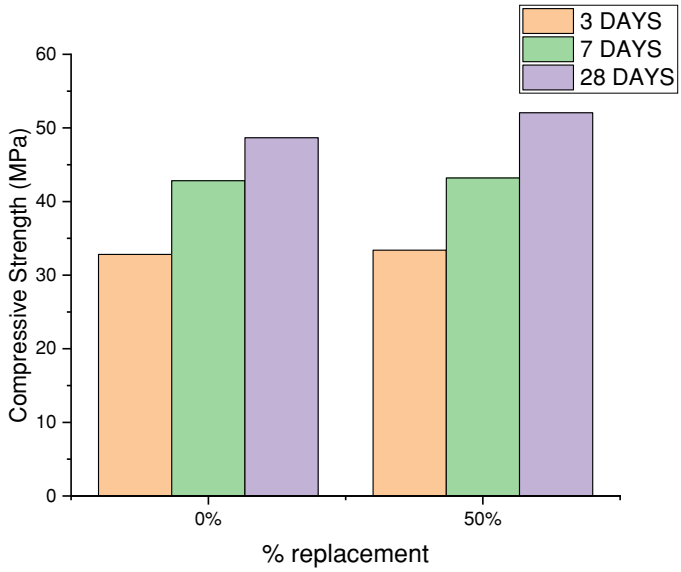

Fig. 2 Compressive strength of mortar

strength gain mortars. This noteworthy increment in the workability because of the low water retention attributes of CS contrasted to FA, where the more free water retains in the mortar mix after hydration [1]. The glassy surface and very nearly zero water absorption of the CS are the reasons for such behaviour. The particle shape of CS enhanced the interaction between CS and cement matrix along with PCE. The compressive strength results for 0% FA and 50% replaced FA by CS increased due to the positive effect of PCE which increased the workability and scattering of cement grains. However, IS: 383-2016 restricts the usage of CS for a maximum of up to 50% replacement for FA (Fig. 2).

4.3 CS Concrete

CS concrete showed a rise in the compressive strength in Fig. 3 when compared with 0% replaced FA concrete. The growth in strength of CS concrete was about 10% more compared to the original value as CS particles are granular in shape. This also results in an increase in the water content with the increase in CS replacement as the absorption capacity is less for CS granules which is because of the glossy texture. If the water in the mix enhances with the increase in CS percentage, this will affect the properties of concrete by an increase in the porosity due to improper compaction and poor hydration of the cement paste which leads to separation of concrete constituents.

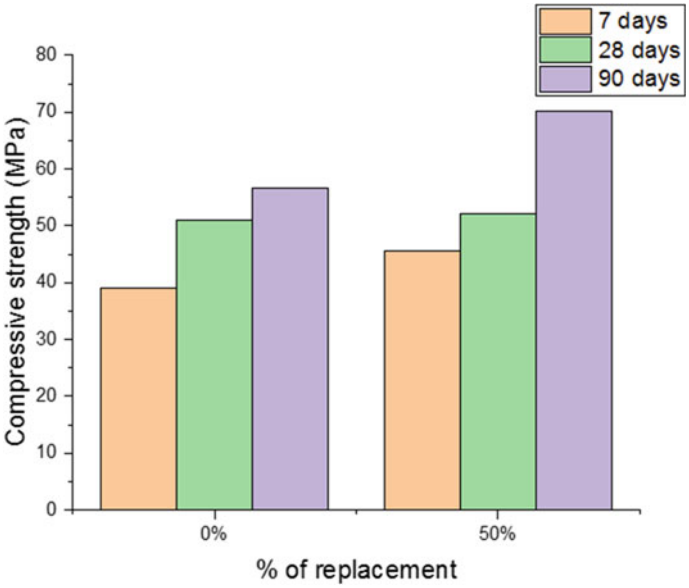

Fig. 3 Compressive strength of concrete

This will result in the decline of concrete performance if the percentage of replacement of CS content exceeds beyond 50% [4]. In turn, the reduction in the water content of the mixes might have reduced free water available in the concrete mix which results in less porosity and improved compressive strength. Also from past literature, it is witnessed that compressive strength of concrete increases when CS is replaced up to 50% beyond which compressive strength reduces due to an increase in free water available in the mix in excess that will be required for the hydration process of cement matrix along with proper compaction of concrete during its fresh state.

5 Microstructure Study

Scanning Electron Microscopy (SEM) was carried out for raw copper slag to understand its behaviour in concrete. These particles showed that the strength of concrete got increased was mainly because of the physical characteristics of CS. CS has better compressibility than FA which reduces the stress concentration and tries to hold the concrete mix. In Fig. 4, it can be observed that CS has angular shape edges that increase the cohesion of the concrete matrix. The abrasion properties associated with its rough surface texture, natural sand can enhance the cohesion between coarse aggregates and cement paste. Despite this, the abrasion property of sand weakens over time because of years of weathering [7]. On the contrary, the improved cohesion

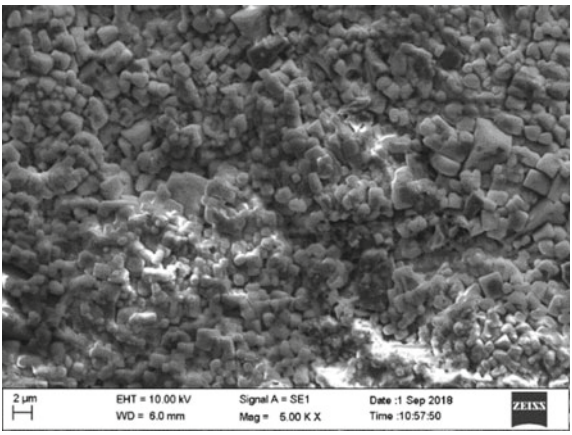

Fig. 4 SEM image of raw copper slag

due to sharp, angular edges and the better compressibility of the copper slag particles [7, 8] compensate the adverse effect of sand to some extent and result in improved compressive strength. But the glassy surface on CS particle reduces the absorption properties and affects the cohesion as it allows excess of water in concrete that may result in bleeding with the increase in the CS substitution in the mix. As a result, there will be an increase in the voids content and capillary pores which decreases the quality of the concrete. Therefore, the strength of concrete with lesser CS replacement can be enhanced by the optimistic effect of CS by limiting the usage by up to 50%.

6 Conclusions

1. Partial replacement of FA by CS has tried to solve the problem of disposal for industries and has provided solutions for the construction industry to overcome the issues of scarcity of river sand.
2. New researches on alternatives for FA has made the construction industry alert to seek and understand the knowledge on the behaviour of new materials first so as to avoid the blind concept that all materials have same characteristics as similar to FA in order to improve the quality of concrete.
3. In this work, it can be inferred that water absorption of CS aggregates has played a vital role to understand the behaviour of CS in mortars and concrete which helped to decide the maximum percentage of replacement recommended to achieve better strength.
4. The chemical reaction between the cement matrix and SP along with CS improved the microstructure of concrete which resulted in the enhancement of strength.

5. Usage of CS restricted for 50% is appreciable as better results can be yielded when compared to control mix as beyond which reduction in strength was observed in previous studies due to an increase in free water availability in the mix with the increase in CS percentage.
6. Also, above 50% replacement increases the voids and capillary pores in the matrix as absorption rate increases in CS concrete mixture.
7. Therefore, it is recommended that up to 40–50% (by weight of sand) of copper slag can be used as a replacement for fine aggregates in order to obtain a concrete with good strength and durability requirements.
8. The variance in the strength development between cement mortars and concrete may be due to the bonding among the particles within the cement paste. Addition of coarse aggregates in concrete mixtures would contribute to the different behaviour observed for the same mixture in mortars and concrete. The increased porosity in concrete deteriorates the bond between the concrete components, which helps to determine the strength factors of concrete.
9. The less water absorption of CS reduces the permeability which can withstand the effect of aggressive environment.
10. Optimizing w/c ratio and SP dosage not only improves the strength of the mortars but also takes care of the durability as leaching of CS can be avoided and the free water available in the mix gets reduced as w/c gets reduced with the usage of SP. This helps to block the pores and avoids the chemical attacks on concrete.

References

1. Bipra Gorai RK, Jana Premchand (2003) Characteristics and utilisation of copper slag/a review. Res Con Rec 39:299–313
2. Shia Caijun, Meyer Christian, Behnoode Ali (2008) Utilization of copper slag in cement and concrete. Resour Conserv Recy 52:1115–1120
3. Dos Anjos MAG, Sales ATC, Andrade N (2017) Blasted copper slag as fine aggregate in Portland cement concrete. J Env Manage 196:607–613
4. Najimi M, Sobhani J, Pourkhorshidi AR (2011) Durability of copper slag contained concrete exposed to sulfate attack. Constr Build Mater 25:1895–1905
5. Al-Jabri KS, Hisada M, Al-Saidy AH, Al-Oraimi SK (2009) Performance of high strength concrete made with copper slag as a fine aggregate. Constr Build Mater 23(6):2132–2140
6. Al-Jabri KS, Al-Saidy AH, Taha R (2011) Effect of copper slag as a fine aggregate on the properties of cement mortars and concrete. Constr Build Mater 25(2):933–938
7. Wu W, Zhang W (2010) G Ma (2010) Optimum content of copper slag as a fine aggregate in high strength concrete. Mater Design J 31(6):2878–2883
8. Wu W, Zhang W, Ma G (2010) Mechanical properties of copper slag reinforced concrete under dynamic compression. Constr Build Mater 24(6):910–917

Monitoring Methods of Concrete from Early Age Strength Gain of Concrete: A Review

Tripti Sonker, Anupam Rawat, and Rakesh Kumar

Abstract The concrete is the most used man-made construction materials. Early age structural failures were observed all over the world. This is due to a low rate of strength gain at an early age. The paper deals with early age strength gain in the process of hydration and monitoring change in a cementitious material change in water–cement ratio and strength gain during the curing period. Wave propagation technique, wave reflection factor, ultrasonic pulse velocity, and EMI technique are sensitive enough to see the change in the parameters. These techniques may be used for damage detection in the existing structures as well as the indicator of strength gain process of newly constructed structures.

Keywords Concrete · Early age strength · Piezoelectric material · Ultrasonic wave velocity · Wave reflection factor · Electromechanical impedance technique

1 Introduction

Concrete is a word of Latin origin based on hydraulic cement a material that is hardened under water. Concrete is man-made material; man cannot use any material in such a tremendous quantity except water. As it is known globally, the consumption of concrete exhibited the country's growth in terms of infrastructural establishment or industrial growth. In the present scenario, a new establishment is not only required, but a smart establishment is recommended for anticipating the structural behavior. Concrete accommodates cement, coarse aggregate, fine aggregate, water, and admixture. The process of hydration gets started, the moment at which cement is blended with water. Hydration process involves the strengthening mechanism of concrete in

T. Sonker (✉) · A. Rawat · R. Kumar
Civil Engineering Department, MNNIT Allahabad, Prayagraj, India
e-mail: rce1605@mnnit.ac.in

A. Rawat
e-mail: anupam@mnnit.ac.in

R. Kumar
e-mail: rkpat@mnnit.ac.in

© Springer Nature Singapore Pte Ltd. 2021

K. K. Pathak et al. (eds.), *Recent Trends in Civil Engineering*, Lecture Notes in Civil Engineering 77, https://doi.org/10.1007/978-981-15-5195-6_52

which it exhibits the different stages of concrete from fluid to transition to a hardened state where they loosen their plasticity and acquire stiffness or strength. Durability refers to a structure having a life span in their service period. Concrete's performance gets affected by physical and environmental conditions. Therefore, it is mandatory to monitor the early age (0–48 h) strength gain of infrastructure to prevent failures of structures during construction and savior to socioeconomic loss [1].

The water–cement ratio, degree of cement hydration (curing conditions), aggregate size, compaction, and admixture play a vital role in influencing the strength of concrete. Compressive testing is the primary test to conduct for knowing its concrete strength properties. Properties of concrete are a function of various parameters, that is, time, temperature, humidity, and curing. So in order to perform assessment tests on concrete, specific guidelines (that is I.S. Code 456) are to be followed according to standards. Test is performed for two main reasons that are quality control and conformity. Testing is done with respect to the comparison with some standard value, which will give assurance of the quality of concrete. In the case of concrete, compressive strength plays a vital role in order to give an assurance of the product because it will directly measure the strength of concrete and easy to calibrate [2]. Nowadays, the collapse of constructing infrastructure is due to insufficient development of strength gain of concrete or the lack of monitoring of the structures. Here, in this paper, various non-destructive techniques are discussed for assessment of early age strength gain of concrete.

2 Literature Review

There are various methods for the monitoring of concrete strengthening processes and continuous structural health monitoring of concrete. Tests can be divided into mechanical tests to destruction and non-destruction testing (NDT). The destructive test usually involves a core test and a load test. In destructive testing samples are cut down from the existing structure for assessing the health and strength of the structure. Destructive testing contributes exact, precise, and authentic data regarding structures' condition and performance. These methods have certain limitations like it is not suitable for the existing old structure. To overcome the limitations of destructive testing, NDT methods were introduced [3]. NDT bestowed the suitability for the checkup of the real-life structure without damaging. NDT has many benefits because it will not cause destruction which is leading to re-testing of the real-life structure several times in their life span. NDT will provide ease to monitoring the change in the structure that will enhance the safety of the occupants as well as structures either new constructing one or existing ones. NDT is a comparatively cost-effective technique for mass concrete and large infrastructure, but it required further processing of obtained data from the structure. Early age concrete and hardened concrete both will be assessed by the NDT technique, not only in the laboratory but also in real-life structures.

The setting of concrete refers to the end of workability and hardening leads to strengthening and stiffening of the material. So in order to acquire the readiness of concrete and their early age gain of strength various techniques are used.

2.1 Ultrasonic Pulse Wave

Ultrasonic pulse wave velocity recording machine and software have been developed by Reinhardt et al. for continuous monitoring of the setting and hardening of concrete. The results of age of the mortar (hours) versus velocity (m/s) curves have clearly depicted the variation of w/c ratio, addition of various admixtures. The initial and final setting of mortar, age of mortar versus velocity observed through the curves (Fig. 1) [4].

The initiation of setting time showed, by the point of the first maximum in the curvature of velocity versus age plot [5]. Similarly, High-Performance Concrete (HPC) was measured with reference to setting time of HPC mix having different w/c ratios along with replacement of fly ash or without fly ash (Fig. 2). The author studied the setting characteristics of HPC via two alternative methods, which are waveforms and UPVs.

From the UPV evolution curve (Fig. 3), Step-I is the same for all four different concrete mixes that are: OPC concrete, OPC mortar, Fly ash mortar, and Fly ash concrete. Step-II represents a sharp increment of rapid hydration of cement, Step-III reveals stable growth due to the completion of hydration [6].

The wave transmission method in which the compression wave (p wave) have to measure the velocity, relative energy and frequency of content cement mortar, which

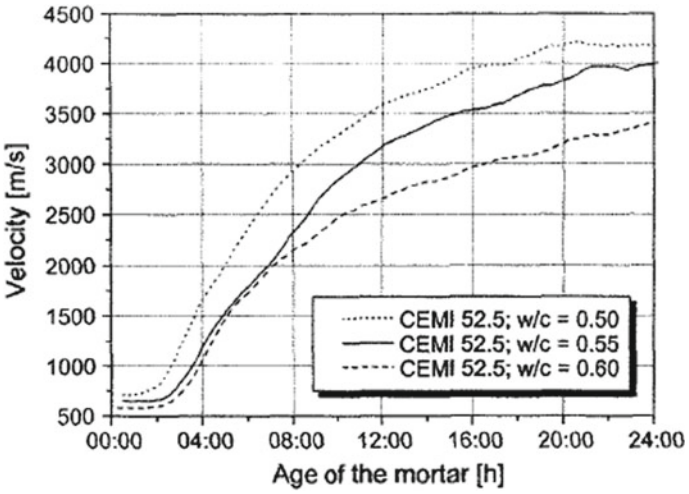

Fig. 1 Wave propagation velocity versus age of mortar with three w/c ratios

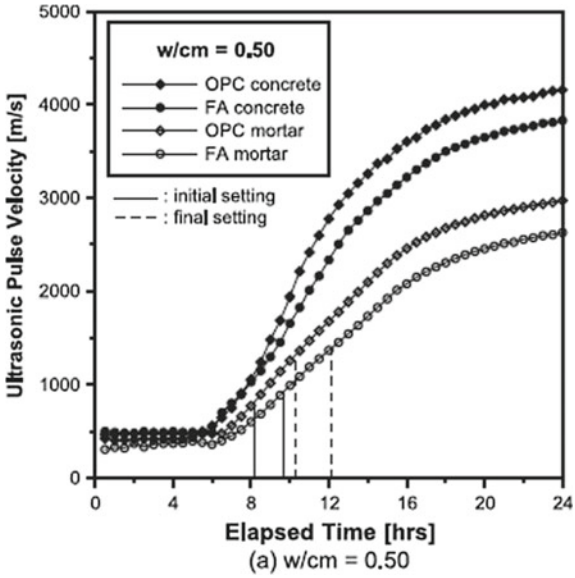

Fig. 2 Evolution of UPV of mortar and concrete specimens [6]

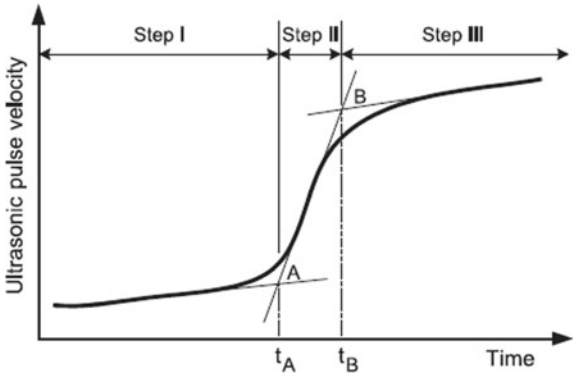

Fig. 3 UPV evolution curve [6]

is sensitive for the hydration process w/c ratio, quantity and quality of admixture and type of cement also. In wave reflection method, shear wave (*s* wave) transmitted through ultrasonic transducer, which is based on travel of shear wave in medium calibrated in terms of reflection loss. The results is further verified by the release of adiabatic heat and shrinkage of concrete. In order to continuous monitoring of the hydration process when it transforms in liquid state to solid that is cement acquire some stiffness on getting hardened. The reflection coefficient method is capable of acquiring the parameter such as the compressive strength, elastic moduli and degree of hydration [7].

2.2 Wave Reflection Factor (WRF)

Another term is Wave Reflection Factor (WRF) that was implemented on one-sided surface of structures, which is useful (like pavement and bridge decks) for evaluating the rate of strengthening process when hydration occurred. The WRF was measured in terms of the quantity of incident wave energy to reflected wave energy at the interface of two dissimilar materials. The author deals with three different types of mix design for casting the slab having four quarters, 3 core test samples are cut down from the slab and the left quarter has the WRF measurement setup. In Table 1, mix design is shown and the WRF measurement setup is shown in Fig. 4.

Table 1 Concrete mixture designations and mixture compositions [8]

Mixture constituent	PCCP	AA	AAA
Coarse aggregate, lb.	1905	1830	1896
Fine aggregate, lb.	1145	1217	1265
Water, lb.	233	201	262
Cement, lb.	395	620	521
Fly ash (Class F), lb.	169	–	140
Silica fume slurry, lb.	–	–	79
Air-entraining agent, ml	198	217	231
High-range water reducer, ml	675	–	5284

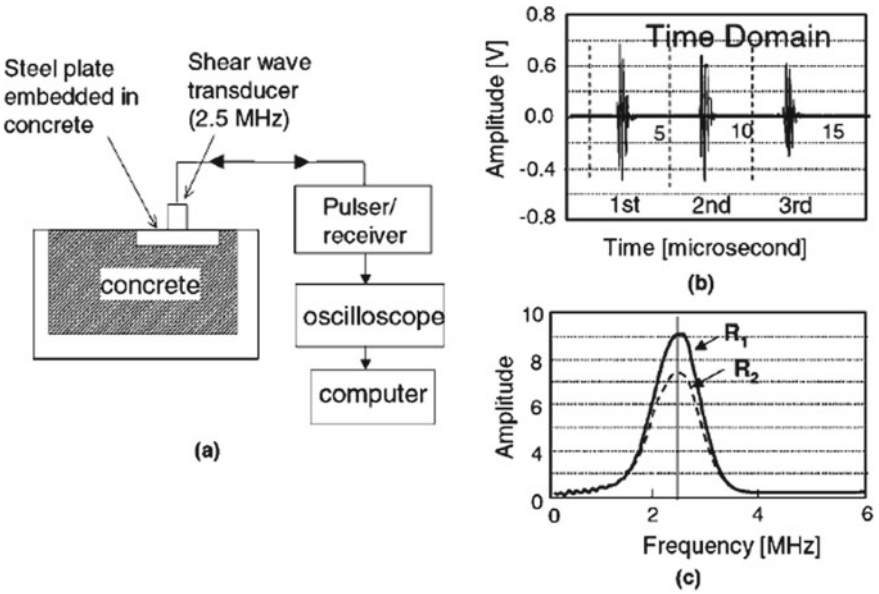

Fig. 4 **a** Experimental setup for WRF measurements and **b** and **c** Pictogram [8]

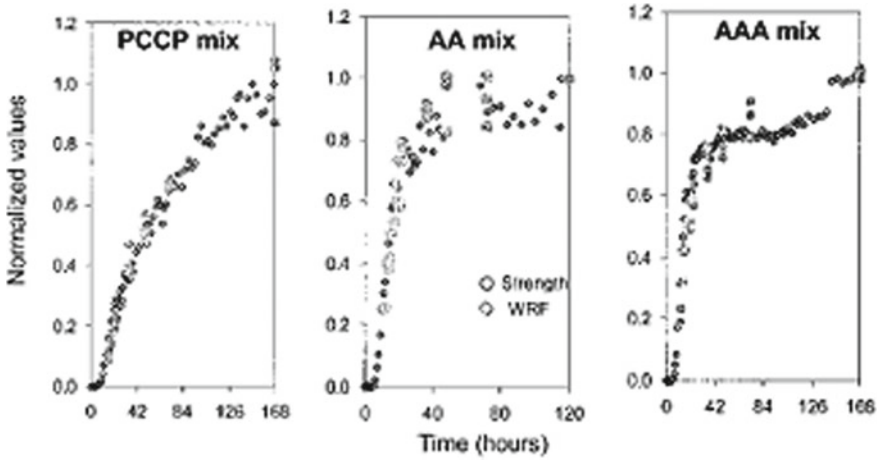

Fig. 5 Comparisons of results of WRF measurement and compressive strength results with respective concentration [8]

The close variation observed from the compressive strength result and WRF measurements is shown in Fig. 5 [8].

2.3 Wave Propagation Technique

Considering the early age strengthening of concrete in wave propagation method, using embedded PZT transducer. Smart aggregate terminology used by Gu et al. for embedded PZT in their two different techniques:

Hydration heat based monitoring. Hydration of concrete was an exothermic reaction, when the quantity of water decreased heat of liberation is getting lowered. Thermocouples were used to monitor the curing temperature inside the block.

Physical property based monitoring. The physical properties of concrete (medium) change with the time, and hence it will affect the wave velocity or attenuation of the ultrasonic waves. Smart aggregate, that is, embedded piezo-ceramic material is used as both sensor and actuators. The test setup for the experiment is shown in Fig. 6 including function generator, oscilloscope amplifier, and sample with two embedded PZT sensors.

In Fig. 7, it is shown that the harmonic amplitude decreased more rapidly within the first week of the hydration process. Later on, after 7 days the drop in amplitude is slower. The compressive strength testing of concrete is obtained from the experiments; and the correlation has been developed in between the compressive strength test results with the amplitude of the sensor's signal via fuzzy pattern that has been

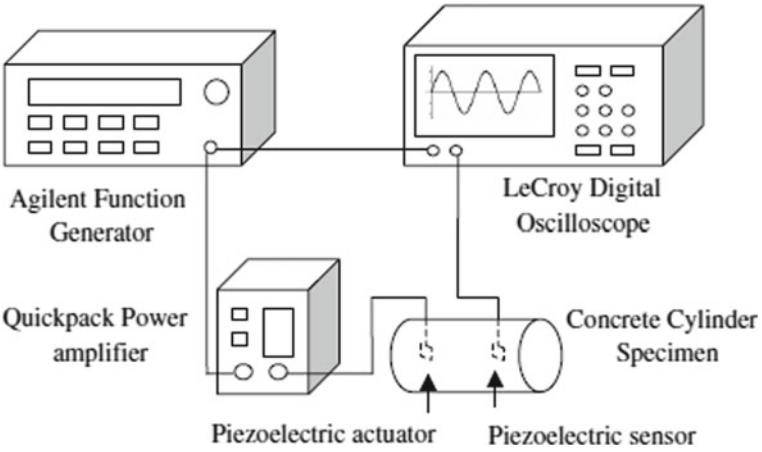

Fig. 6 Experimental setup for the early age strength monitoring of the concrete specimen [9]

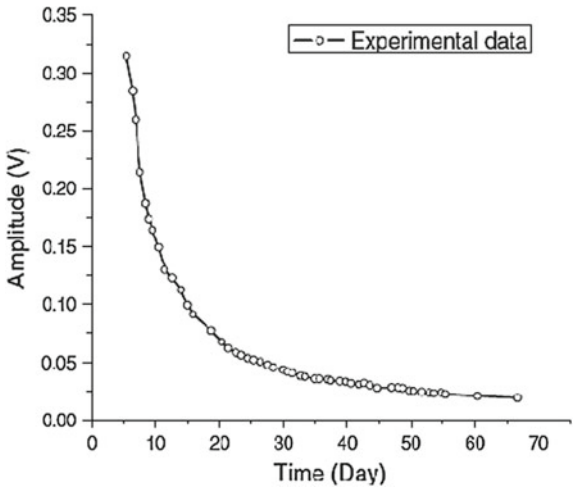

Fig. 7 Amplitude versus time for mortar specimen 1–10 kHz harmonic excitation [9]

drawn(in Fig. 8), which is based on the experimental data training of fuzzy logics. Along with this trained fuzzy pattern, it will also consider the shrinkage strain effect for vast infrastructure (Water Dam) [9].

The very early age (0–20 h) concrete hydration characters have to be monitored in three different stages of hydration of concrete, that is, fluid stages, transition, and hardened stages. In which the concept of second-generation smart aggregates has been used by sandwiching a PZT patch in between two marble rocks and used as SMART Aggregates (SA). Two smart aggregates were fixed to rebars before casting of the beam at a distance of 50.8 mm, through function generator sinusoidal waves are generated from one signal and responses are collected from other smart aggregates.

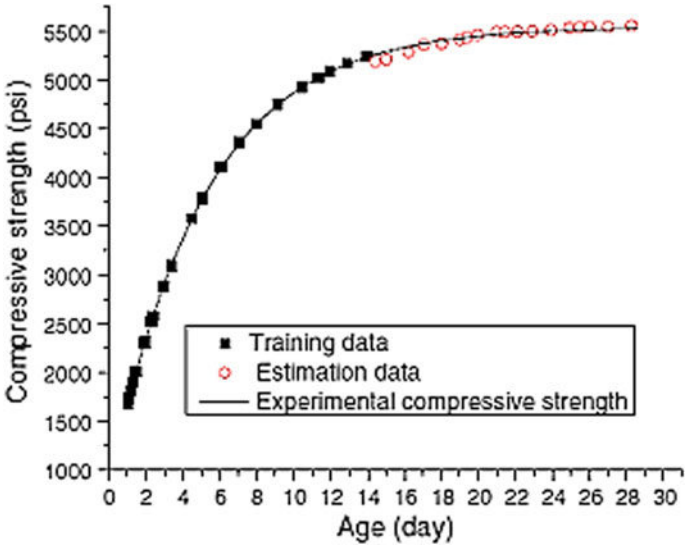

Fig. 8 The comparison of the experiment' compressive strength with the estimated compressive strength [9]

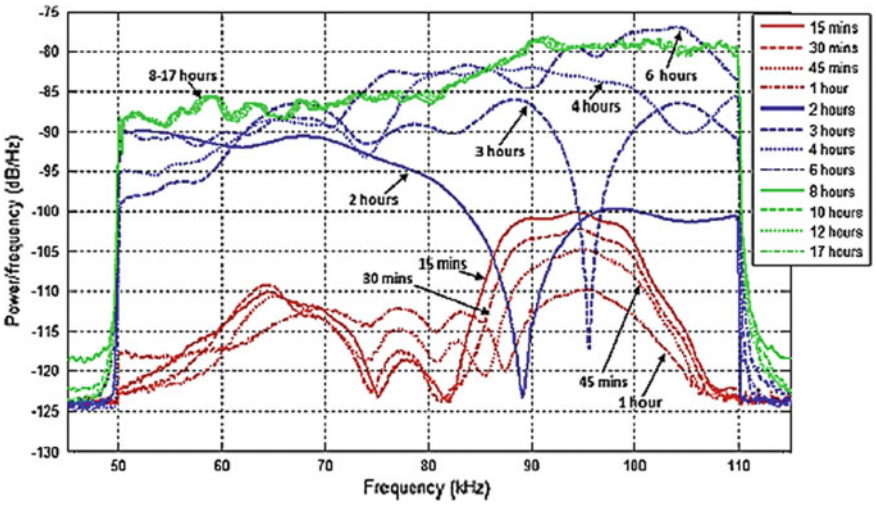

Fig. 9 The sensor's response signal from constant frequency sine wave excitation (90 and 100 kHz) [10]

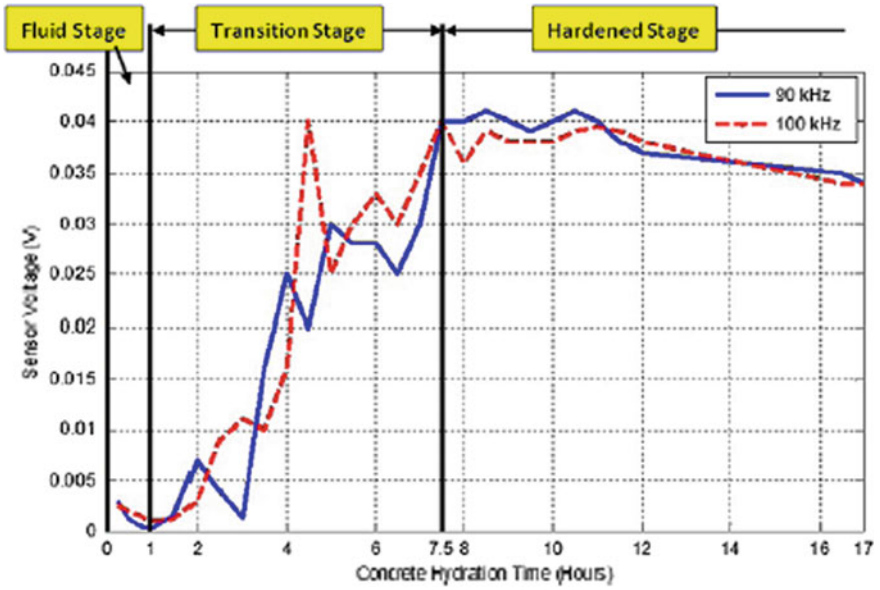

Fig. 10 Frequency domain signal response during the concrete hydration [10]

The collected signal response was plotted with both time domain and frequency domain (Fig. 10) during various stages of hydration of concrete with respect to two types of signal; one was swept sine wave another one was constant frequency sine wave (Fig. 9) [10].

The stress wave transmission characteristics in cement and mortar (from 8 to 50 h) under curing state have been monitored using embedded piezoelectric transducers termed as 'Smart Aggregate'. The author has taken 3 samples of cement and mortar mix with varying different w/c ratios (Table 2).

Power Spectral Density function (PSD) shows the strength of the variations (energy) as a function of frequency. The results obtained have a clear demarcation of different w/c ratios of different samples and the presence of coarse aggregate in the plots. The lowest w/c ratio has been given maximum change or higher rate of change of the in peaks. PSD is increasing with an increasing number of curing days from day 1 to day 9.

The bar chart (Fig. 11) showed an increase of resonant frequency with respect to

Table 2 Concrete mix samples [11]

Specimen	Materials		
	Sand	Coarse aggregate	Water/cement ratio
SC1	1.19	2.02	0.40
SC2	1.19	2.02	0.48
SM2	1.19	–	0.48

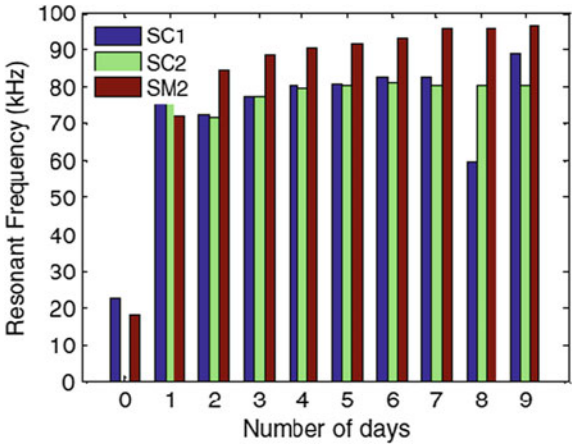

Fig. 11 Resonant frequency of all specimens versus days from 0 to 9 days [11]

no. of hours and no. of days because of the stiffening of the structure. Along with that the total power received (in dBm) (Fig. 12) from sensors of all samples for the first 20 h and for the first 9 days from the hydration day.

Recently in 2017, Kong further introduced the concept shear and compression waves, shear wave travels parallel to the plan of PZT patch while the compression waves are produced perpendicular to the PZT patch. In the experiments, a pair of smart aggregates were used for monitoring of very early age (0–48 h) strength of cement. After analyzing both *P*- and *S*- wave results, *S* wave is more sensitive in the initial phase from 0 to 8 h while *P* wave is more appropriate for the hardened stage after 8 h. The magnitude of the resonant peak is increased when cement is hydrated [11].

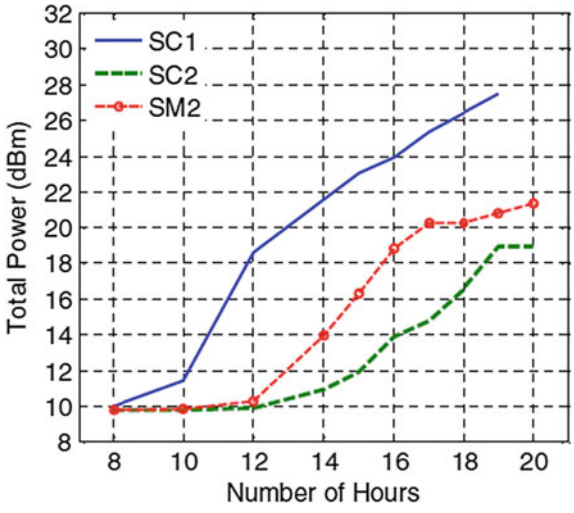

Fig. 12 Total power (in dBm) received for the sensors of all specimens for the first 30 h [11]

Principle wave propagation method. The principle behind the early age strength monitoring of concrete is based on the wave propagation method. The wave equation is given below.

$$\frac{\partial^2 u}{\partial x^2} = \frac{1}{c_b^2}\frac{\partial^2 u}{\partial t^2}\left(c_b^2 = {}^{E}/_{\rho}\right) \tag{1}$$

In the above equation displacement of an element is denoted by u and Young's Elastic Modulus is denoted by E and density of the material is denoted by ρ. The average of power p of harmonic response over a period can be expressed as

$$p = {}^{EA^2\omega^2}/_{2c_b} = {}^{\sqrt{E\rho}A^2\omega^2}/_{2} \tag{2}$$

In Eq. (2), harmonic amplitude is represented by A while the angular frequency is shown by ω. Eq. (2) can be rewritten as

$$A = \left(\frac{1}{\omega}\right)\left(\frac{4p^2}{E\rho}\right)^{\frac{1}{4}} \tag{3}$$

From Eq. (3), the harmonic amplitude A is inversely proportional to Young's modulus E of the medium. Throughout the early age strength gain process when concrete gets hardened and stiffens Young's modulus E increases. Hence, if of Young's modulus increases, reduction in harmonic amplitude will occur or vice versa. The harmonic amplitude gets affected by the compressive strength of concrete via status of Young's modulus E.

2.4 Electro-Mechanical Impedance Technique (EMI Technique)

Wave propagation technique is used for monitoring the strength gain of the concrete structure. Similarly, the EMI technique is based on impedance-based monitoring of the structure using PZT sensors. Liang et al. [12] have firstly introduced the impedance-based measurement of the structures. The dynamic response of active material, i.e., PZT was determined by the impedance approach method. It attributes the physical interaction between actuators and host structures [12].

Bhalla et al. have discussed the technicalities of the EMI technique at its ground level and introduced a new model based on the PZT–structure interaction and checking the effectiveness of the damage characteristics on frame-type-reinforced concrete structure. The PZT is highly sensitive to minor or even hairline cracks. A statistical technique (RMSD) is used to quantify the change in the behavior of signatures patterns. For checking the correctness of the proposed model, the implementation of this EMI technique will be verified by two experiments. One is demonstrated

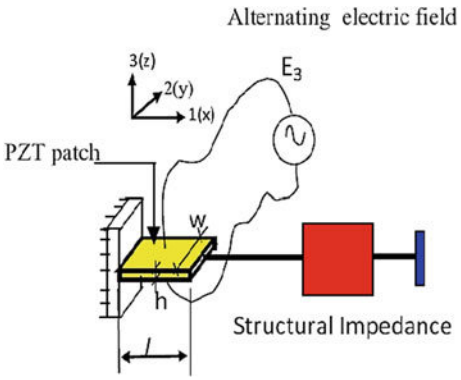

Fig. 13 1D structural impedance model [13]

on the lab-sized aerospace structure and another one is a prototype of reinforced concrete bridge under destructive loading. Damage patterns will be clearly identified in both the experiments. Also, 2D formulation can minimize the hardship of calculation or identifying the numerical values of unknown parameters. To simplifying impedance-based models, an impedance of the structure is correlated with electrical admittance of PZT via 2D coupling in between them to evaluate the admittance from the equation (4). Thus, the model is connecting the Liang et al. 1D impedance model (1994) (in Fig. 13) and the Zhou et al. 2D model (1995) [13–15].

Bhalla and Soh derived the following expression for the complex electrical admittance of the PZT–structure interaction model by introducing the concept of the effective mechanical impedance as follows:

$$\begin{aligned}\overline{Y} &= G + Bj \\ &= 4\omega j \frac{l^2}{h}\left[\overline{\varepsilon_{33}^{T}} - \frac{2d_{31}^2\overline{Y^E}}{(1-\nu)} + \frac{2d_{31}^2\overline{Y^E}}{(1-\nu)}\left(\frac{Z_{a,eff}}{Z_{s,eff}+Z_{a,eff}}\right)\bar{T}\right]\end{aligned} \tag{4}$$

where $\overline{Y}$ = complex admittance (inverse of electric impedance).

G = conductance, B = susceptance, ω = angular frequency, l = half-length of the PZT patch and h = thickness. j is $\sqrt{-1}$.

d_{31} = piezoelectric strain coefficient, $\bar{Y}^E = Y^E(1+\eta j)$ is the complex Young's modulus of the PZT patch (at constant electric field) $\bar{\varepsilon}_{33}^T = \varepsilon_{33}^T(1-\delta j)$ is the complex electric permittivity of the PZT patch (at constant stress field), υ = Poisson's ratio and κ is the wavenumber. η and δ denote the mechanical loss factor and the dielectric loss factor of the PZT patch.

$Z_{a,\text{eff}}$ is the effective mechanical impedance of PZT patch, $Z_{s,\text{eff}}$ is the impedance of the host structure, which incorporates the effect of mass, stiffness, damping, and boundary condition.

EMI technique is used for damage detection earlier, later on, it was utilized for early age monitoring of concrete. In 2008, Shin et al. have made an effort to extend the EMI sensing technique which was used for strength gain monitoring of early

age concrete, in which casting of concrete in three groups and three different curing conditions and PZT patch is attached as free and perfectly fixed. Strength gain of concrete is a process of hydration that causes stiffening of material with passage of time. Hydration causes changes in mechanical properties which changes impedance. Signatures pattern of the concrete shift towards right and downward as curing age increased. Shifting of conductance versus age curve exhibits the additional stiffening due to the strength gain of concrete. This verifies that the EMI sensing technique is used for the strength gain of concrete [16].

The internal bonding between steel-reinforced bar and concrete was estimated via EMI technique through conductance signature by Tawie et al. in 2010. EMI methods can successfully evaluate the gradual internal bonding between steel and concrete. If the curing temperature is getting low, it will affect the rate of frequency shift (Fig. 14), because it is assumed due to delayed setting and the strength gain of concrete. In the case of compaction, a lower amount of frequency shift is demonstrated by the poorly compacted specimen [17].

EMI signature pattern depicts the variation of horizontal shift, that is, signatures are shifting toward rightward corresponding to an increase of curing period. The effect of main parameters such as water to cement ratio and cement content, which affects the strengthening of concrete are verified by EMI spectra. To overlook for overall variation in EMI signatures during the entire process, data can be further processed via statistical techniques like RMSD, MAPD, and CCD which are mostly used in SHM of structure for damage indices as well as early age strength gain process. The statics metrics such as the RMSD, MAPD, and CCD was found to be a reliable indicator [18]. The rightward shift of the resonant spectrum frequency exhibits the stiffening and strengthening of the concrete after the hydration process (Fig. 15) [19].

Similarly, the acquired signature from PZT of concrete cubes at distinct age of time and gets correlated with compressive strength of concrete including in terms

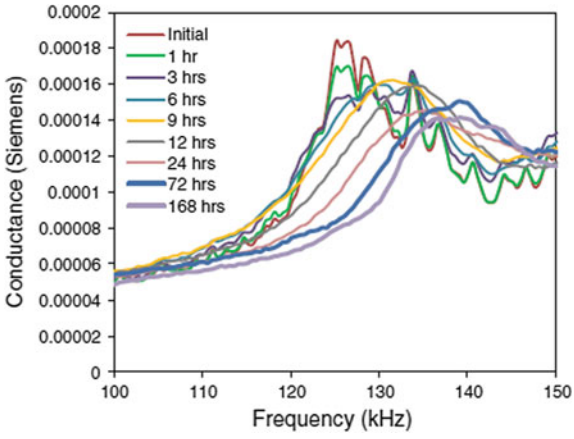

Fig. 14 Conductance spectra at different curing times (w/c ratio = 0.40 T = 20 °C) [17]

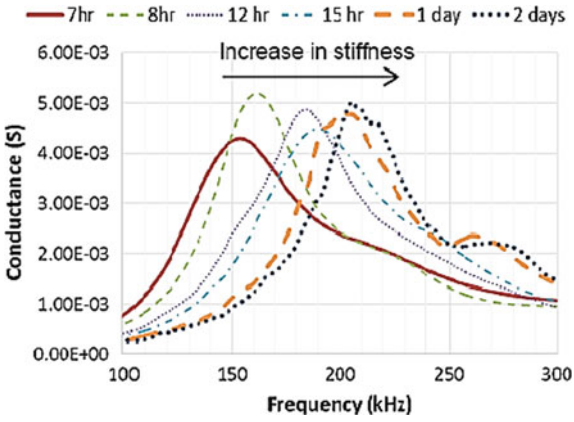

Fig. 15 Conductance signatures versus frequency acquired from patch *R* (room condition) in the frequency range of 100–300 kHz [19]

of statistical indexes such as RMSD and MAPD. The strength gain pattern is exceptionally well correlated with RMSD and MAPD indexes. The fitting curves are the empirical curves based on experimental data. The obtained admittance signature inferred that the growth of compressive strength will be dependent on an increase in resonant frequency. In the process of further evaluation, the correlation between the compressive strength of concrete in ages and the electrical admittance of the PZT transducer embedded into concrete, RMSD, and MAPD indexes were introduced [20].

Recently in 2017, Bhalla et al. acquired the baseline admittance signature from LCR meter for all 6 cylinders immediately within 1 h of casting and monitoring was continued till 28 days to track the hydration process shown in Fig. 16. Long-term monitoring (refers to day 1–day 28) and short-term monitoring (from initial

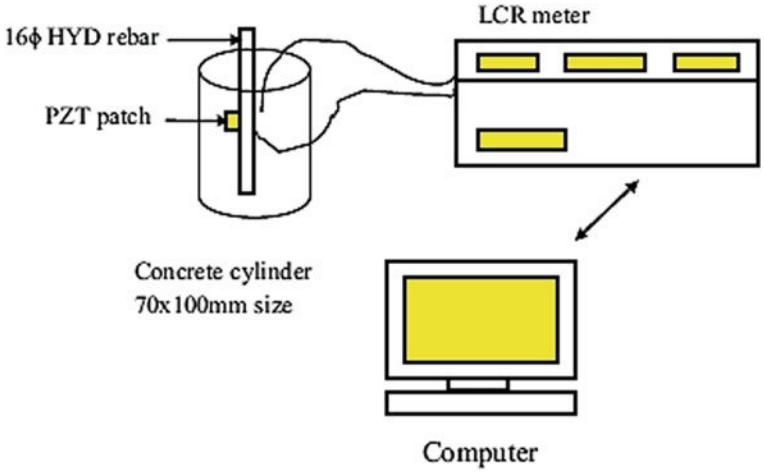

Fig. 16 Experimental setup [21]

setting to final setting, approx. 1–12 h) have been done by analyzing conductance and susceptance signatures from free and bonded PZT patches. Also, repeatability of PZT conductance signatures, perfect bond for PZT patch, PZT patch condition was determined via susceptance plot versus frequency. The author introduced a non-dimensional parameter to monitor the early age of concrete, using EMI admittance signature. From the observation, it was found that damping (c) decreased consistently up to 3rd day, while the variation in stiffness (k) values increasing throughout the monitoring period. Hence, while monitoring the strength gain of concrete, k is more consistent and sensitive than c [21]. A new concept of smart probe is introduced instead of surface-bonded PZT on the host structure. The aluminum beam is used for the surface to bond to the PZT patch, which is embedded in the host structure partially termed as a smart probe. The analytical and theoretical models have been developed for identifying the dynamic modulus of the mortar by utilizing the experimental data from the smart probe. Adding on smart probe to EMI technique will enhance their features and used for commercialization of the techniques for the future purpose [22]. The authors have tried different ways of implementing the EMI method by using series and parallel connections of the sensors to identify the strength gain pattern as well as damage diagnosis. They have discussed in detail various aspects of the EMI techniques which will be an implication on aluminum plate, concrete beam, shear wall, and 15 cm cube [23–25].

3 Experimentation

For the verification of the EMI method standard concrete cube was cast in the lab. After one hour, recording of signatures for corresponding strength gain for 1st day and 1st week of M25 grade concrete started. The test setup was arranged in the lab on standard experimentation conditions (Fig. 17 and Table 3).

The reinforced concrete sample is formed in the mold of 15 cm cube for the experiment. The signature pattern for early age strength gain pattern for 1-day plot and 1-week plot is acquired. In the graph, the no. of hours depicted after casting, respectively, forms the 1st to 5th hour. As concrete hardens rapidly at early age, hence gain in strength corresponding age is shown. Shifting of peaks is depicted in the Fig. 21, which is indicating the strength gain in concrete with time (Fig. 18).

As concrete rapidly gains strength during its 1st week, variations of peaks in the first few days within a week are quite noticeable in a signature pattern. As it is known earlier form destructive testing, approximately 67% of the strength was achieved by concrete in 7 days of casting. Assessment of the EMI signature in different frequency ranges in their hydration process after casting process is as follows.

30–110 kHz. Figure 19 represents the EMI signature of the low-frequency band. From the fig., it is clear that there is very little change in the signature pattern. In the next hour change in the signature is double than the previous one. After that, the experiment was continued for the 5th hour. Concrete cube gains strength at a higher rate in the 2nd to the 3rd hour.

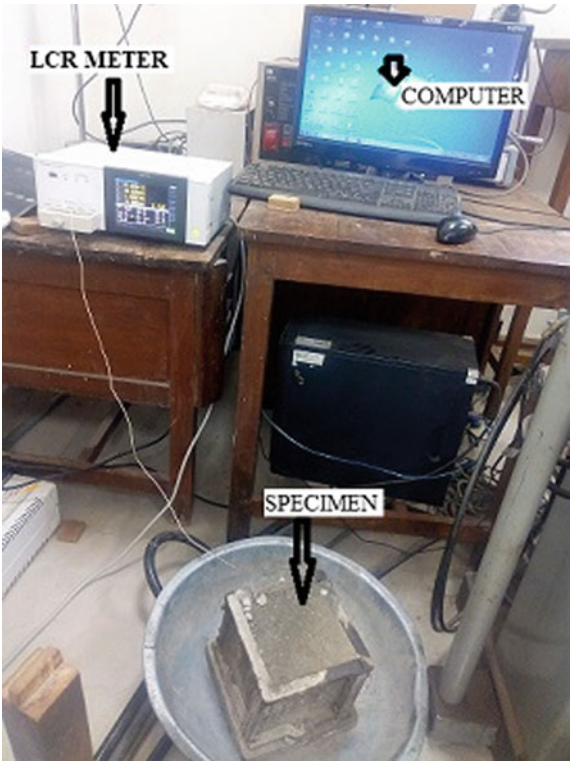

Fig. 17 Experimental setup

Table 3 Material selection for Experiment

Material	Quantity
Cement	350 kg/cm^3
w/c ratio	0.4
water	149 kg/cm^3
Coarse aggregate	
20 mm	766.23 kg/cm^3
10 mm	510.8 kg/cm^3
Fine aggregate	712.95 kg/cm^3
Superplasticizer	1%

110–260 kHz. Figure 20 represents the EMI signature of the medium frequency band. From the fig., it is clear that maximum change occurs in this frequency range of signature from the 1st to the 2nd hour. In the next hour, the change in the signature is double the previous one.

260–350 kHz. Figure 21 represents the EMI signature of the high-frequency band form. This region has also depicted the least variation of peaks.

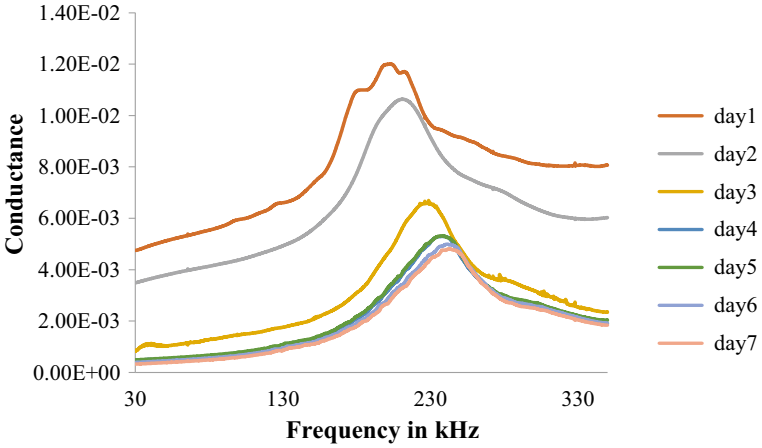

Fig. 18 Weekly variation of conductance versus frequency

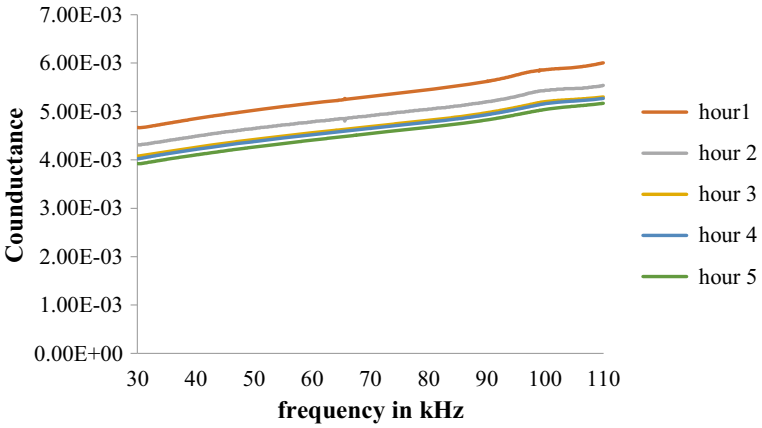

Fig. 19 30–110 kHz hourly variation of conductance

It is concluded from the frequency variation that low-frequency range is less sensitive for the detection of strength gain for the standard cube. While the 110–260 kHz frequency range is more susceptible to identifying the variation in peaks. The high-frequency range is also not as much as receptive like medium range for such a small sample of 15 cm concrete cube. The shifts of peaks are demarcation of the change in stiffness which further belongs to gain in strength.

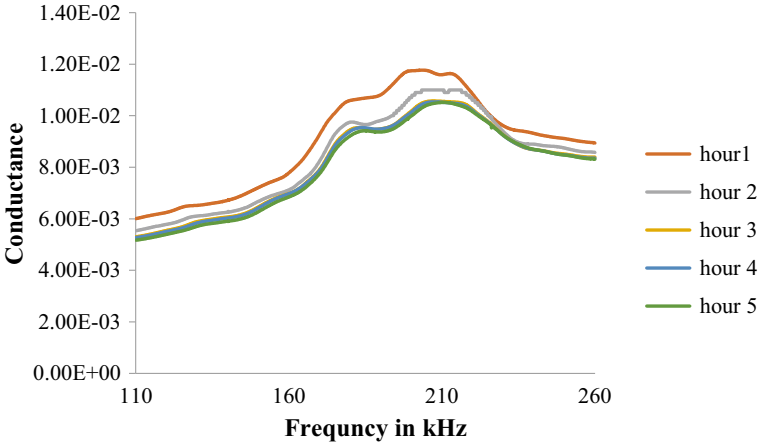

Fig. 20 110–260 kHz hourly variation of conductance

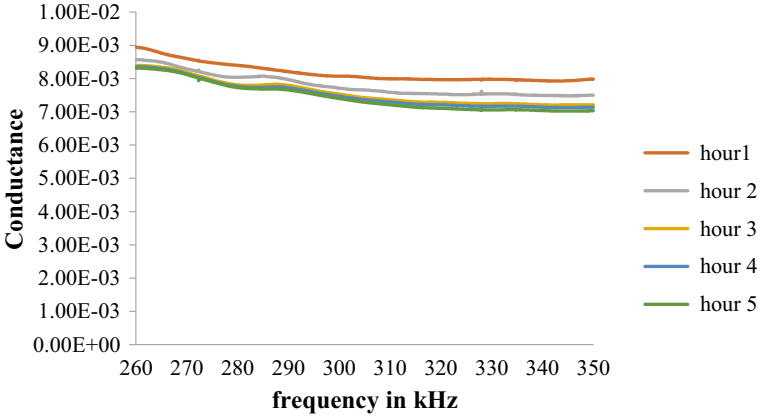

Fig. 21 260–350 kHz hourly variation of conductance

4 Discussion and Conclusion

In the present scenario, the strength of the concrete materials is measured from two prospectives: early age strength (3rd, 7th, and 28th day's strength) and ultimate strength of the material. In the present time demand for early strength gain of concrete is increased. To avoid the catastrophic failure of the structure at the time of construction, it is necessary to monitor the structural health in their early age period. So here in this article there is a detailed discussion about various methodologies for early age strength monitoring. UPV is a traditional and old method for monitoring the concrete in terms of velocity of the ultrasonic pulse, which determines the quality of concrete [IS 13311-1(1992)]. As discussed earlier, the piezo-ceramic material (PZT

patch) is used as an actuator and sensor both. In the same way, they have a multi-utility function and used in various methods, i.e., wave propagation, wave reflection factor, ultrasonic pulse, and electromechanical impedance technique. In the context of early-age strength monitoring via PZT patch, embedded as smart aggregate, is capable of acquiring structure information. Hence, it behaves as an actuator, when it is vibrating the structure and act as a sensor, when it collects the data from the structure. Hence, PZT have dual property to behave in different ways according to work like actuator and as well as sensors both. Acquired data (conductance and susceptance signature) is an indicator of structural condition (equivalent stiffness and damping). The techniques discussed here, given some satisfactory results on lab-scale samples. EMI method is a frequency-dependent method. So the appropriate frequency range for the sample should be selected. For small samples, the medium frequency range offers better signature variation as compared to the low- and high-frequency range. However, it is also necessary to develop a standardized theoretical modal of EMI to implement for commercial purposes.

Acknowledgment **My Springer—A Service for Springer Authors and Editors**: I don't require any special service like mention in guideline from Springer. Please accept my sincere regards to Springer for publishing and acknowledging my work.

Ethics and Permissions According to my knowledge, there is no need of any permission to be required.

References

1. Mehta PK, Monteiro PJM (2006) Concrete microstructure, properties, and materials, 3rd edn. McGraw-Hill, New York
2. Neville AM (1996) Properties of concrete, 5th edn. Pearson, Harlow
3. Karaiskos G, Deraemaeker A, Aggelis DG, Van Hemelrijck D (2015) Monitoring of concrete structures using the ultrasonic pulse velocity method. Smart Mater Struct 24:113001. https://doi.org/10.1088/0964-1726/24/11/113001
4. Reinhardt HW, Große CU, Herb AT (2000) Ultrasonic monitoring of setting and hardening of cement mortar—a new device. Mater Struct 33(9):581–583. https://doi.org/10.1007/BF02480539
5. Reinhardt HW, Grosse CU (2004) Continuous monitoring of setting and hardening of mortar and concrete. Constr Build Mater 18:145–154. https://doi.org/10.1016/j.conbuildmat.2003.10.002
6. Lee HK, Lee KM, Kim YH, Yim H, Bae DB (2004) Ultrasonic in-situ monitoring of setting process of high-performance concrete. Cem Concr Res 34(4):631–640. https://doi.org/10.3390/ma9040294
7. Voigt T (2005) Comparison of ultrasonic wave transmission and reflection measurements with *P*- and *S*-waves on early age mortar and concrete. Mater Struct 38:729–738. https://doi.org/10.1088/0964-1726/22/8/085025
8. Subramaniam KV, Mohsen JP, Shaw CK, Shah SP (2002) Ultrasonic technique for monitoring concrete strength gain at early age. ACI Mater J 99(5):2002
9. Gu H, Song G, Dhonde H, Mo YL, Yan S (2006) Concrete early-age strength monitoring using embedded piezoelectric transducers. Smart Mater Struct 15:1837–1845. https://doi.org/10.1088/0964-1726/15/6/038

10. Kong Q, Hou S, Ji Q, Mo YL, Song G (2013) Very early age concrete hydration characterization monitoring using piezoceramic based smart aggregates. Smart Mater Struct 22:085025. https://doi.org/10.1088/0964-1726/22/8/085025
11. Kong Q, Song G (2017) A comparative study of the very early age cement hydration monitoring using compressive and shear mode smart aggregates. IEEE Sens J 17:256–260. https://doi.org/10.1109/jsen.2016.2624799
12. Liang C, Sun FP, Rogers CA (1994) An impedance method for dynamic analysis of active material systems. J Vib Acoust 116:120–128. https://doi.org/10.1177/1045389X9700800405
13. Bhalla S, Soh CK (2004) Structural health monitoring by piezo-impedance transducers. i: modeling. J Aerosp Eng 17:154–165
14. Bhalla S, Soh CK (2004) High frequency piezoelectric signatures for diagnosis of seismic/blast induced structural damages. NDT E Int 37:23–33. https://doi.org/10.1016/j.ndteint.2003.07.001
15. Bhalla S, Soh CK (2004) Structural health monitoring by piezo-impedance transducers. ii: applications. J Aerosp Eng 17:166–175
16. Shin SW, Qureshi AR, Lee J (2008) Piezoelectric sensor based nondestructive active monitoring of strength gain in concrete. Smart Mater Struct 17:1–8. https://doi.org/10.1088/0964-1726/17/5/055002
17. Tawie R, Lee HK (2010) Monitoring the strength development in concrete by EMI sensing technique. Constr Build Mater 24:1746–1753. https://doi.org/10.1016/j.conbuildmat.2010.02.014
18. Tawie R, Lee HK (2010) Piezoelectric-based non-destructive monitoring of hydration of reinforced concrete as an indicator of bond development at the steel-concrete interface. Cem Concr Res 40:1697–1703. https://doi.org/10.1016/j.cemconres.2010.08.011
19. Lim YY (2014) Monitoring of concrete hydration using electromechanical impedance technique. In: 23rd australasian. conference on the mechanics of structures and materials, vol II, no 9–12, pp 1155–1160
20. Wang D, Zhu H (2011) Monitoring of the strength gain of concrete using embedded PZT impedance transducer. Constr Build Mater 25:3703–3708. https://doi.org/10.1016/j.conbuildmat.2011.04.020
21. Talakokula V, Bhalla S, Gupta A (2018) Monitoring early hydration of reinforced concrete structures using structural parameters identified by piezo sensors via electromechanical impedance technique. Mech Syst Signal Process 99:129–141. https://doi.org/10.1016/j.ymssp.2017.05.042
22. Xubin Lu CKS, Lim Yee Yan (2017) A novel electromechanical impedance—based model for strength development monitoring of cementitious materials. Struct Heal Monit 17:902–918. https://doi.org/10.1177/1475921717725028
23. Bharathi Priya C, Jothi Saravanan T, Balamonica K, Gopalakrishnan N, Rao ARM (2018) EMI based monitoring of early-age characteristics of concrete and comparison of serial/parallel multi-sensing technique. Constr Build Mater 191:1268–1284. https://doi.org/10.1016/j.conbuildmat.2018.10.079
24. Jothi Saravanan T, Balamonica K, Bharathi Priya C, Gopalakrishnan N, Murthy SGN (2015) Non-destructive piezo electric based monitoring of strength gain in concrete using smart aggregate. In: International symposium on non-destructive testing in civil engineering. Germany, pp 15–17
25. Jothi Saravanan T, Balamonica K, Bharathi Priya C, Gopalakrishnan N, Murthy SGN (2017) Piezoelectric EMI-based monitoring of early strength gain in concrete and damage detection in structural components. J Infrastruct Syst 23:1–15. https://doi.org/10.1061/(ASCE)IS.1943-555X.0000386

An Experimental Study on Strength Development in Concrete by Incorporating Rice Husk Ash as Replacement to Cement with Recycled Aggregate for Low Volume Roads

D. Sai Bharadwaj and Adepu Ramesh

Abstract Use of the Natural Aggregate (NA) in cement concrete mixture is resulting in depletion of natural resource and incidence to global warming. In the present work, an assessment was carried to understand the effect of Recycled Aggregate (RA) and Rice Husk Ash (RHA) when blended cement in concrete mix. During first stage of study, RA was partially replaced with NA at interval 0, 50, 75, and 100%, and in second stage of study RHA was introduced as a substitute for cement at interval 6, 9, 12, and 15%. Mixes were prepared to understand the effect of mechanical properties when partially replaced with RA and RHA as a cement substitute at 7 and 28 days age of concrete. The chemical properties of RHA mix were analyzed using XRD and SEM. The chemical test results explain that the fines of RHA are important for homogeneity and the morphology of RHA was also discussed. The experimental results explain that the concrete suitability is governed with the incorporation of RA and RHA in cement. However the optimum content RA of (50%) and RHA of 6% in concrete mix stabilizes the requirement of sustainable cement concrete pavement from industry perspective which will be the need for low volume roads.

Keywords Rice husk ash · Recycled aggregate · Compressive strength · Flexural strength

1 Introduction

The fact that an infrastructure facility helps in development and improves economy is often constructed with cement concrete.Natural aggregates (NA) occupies the major protion in preparation of concrete mix, however, the use of NA results in depletion of natural resources and this can be improved with the use of waste or recycled aggregate

D. Sai Bharadwaj · A. Ramesh (✉)
Department of Civil Engineering, VNR Vignana Jyothi Institute of Engineering and Technology, Hyderabad, India
e-mail: ramesh_a@vnrvjiet.in

D. Sai Bharadwaj
e-mail: saibharadwaj982@gmail.com

© Springer Nature Singapore Pte Ltd. 2021

K. K. Pathak et al. (eds.), *Recent Trends in Civil Engineering*, Lecture Notes in Civil Engineering 77, https://doi.org/10.1007/978-981-15-5195-6_53

[1–3]. RA possesses a relatively lower density and slightly increases percentage in water absorption because cement motor has adhesion with aggregate [4, 5]. The mechanical property was enhanced with the use of RA for 25% replacement in NA for concrete mix [6, 7]. . Up to the 20% replacement of RHA with cement the optimum levels of strength and durability properties are obtained and slightly decreases beyond that [8, 9]. The rice husk ash contains a high quantity of silicon oxide, and it is proved to be of good workability [10].

1.1 Research Significance

The literature review explains that RA was used in properties of cement concrete mix. Mechanical and chemical properties were studied to apprehend the use of RA. Limited studies were into the use of RHA and RA in combined. An attempt is made to explore chemical and mechanical properties of concrete mix when prepared with RA and RHA. Further the usefulness of these results shall be applied in construction industry when paved on low volume roads.

1.2 Objective

Following are the major objectives planned to meet the development of the concrete mix of RHA.

- To assess the characteristics of cement concrete pavement with the partial replacement of coarse recycled aggregate at different proportions.
- To analyze the classified proportions of RHA when added in cement concrete pavement and prepared at optimum RA.
- To study mechanical properties of mix combination and compared for its effectiveness.

2 Materials and Experimental Program

2.1 Materials

Cement used as Ordinary Portland Cement (OPC) of 53 grade. The cement's physical properties are arrived from laboratory test and satisfies IS: 269-2015 [11] . The test results are summarized in Table 1.

Aggregate. Natural aggregate collected from local quarry was used in the study. The RA was collected from the construction and demolishes waste was further

Table 1 Physical properties of cement

Cement type	Grade of cement	Specific gravity	Soundness (mm)	Fineness (%)	Consistency (%)	Initial time setting (min)	Final time setting (min)
OPC	53	3.05	4.5	5	3	30	600
Code limits	–	<3.14	<10	<10	26–33	30	600

Table 2 Properties of natural aggregate and recycled aggregate

Property type	NA	RA
Specific gravity	2.631	2.612
Crushing value (%)	26	30
Impact value (%)	20	25
Water absorption	0.55	0.60
Elongation index (%)	5.495	6.569
Flakiness index	15.082	20.520
Apparent sp. gravity	2.655	2.637
Bulk density kg/m^3	1645.2	1360
Moisture content (%)	4	7.5

processed for jaw crusher. The physical properties of RA and NA were performed in the laboratory [12] and were summarized Table 2.

The physical properties of RA exhibit absorption of water that is more and has lesser relative density as compared with NA. This is due to the fact that recycled aggregate has higher porosity and hence possess lower density.

Rice husk ash. The residual RHA was collected from the rice mill at Mahbubnagar district, Telangana state. RHA prepared by the rice husk is burnt at a temperature of 500–600 °C in the ball mill as presented in Fig. 1. The chemical composition of

Fig. 1 RHA used in the study

Table 3 Chemical combination of RHA

Component	RHA
SiO_2	93.68
MgO	0.60
CaO	1.10
Al_2O_3	0.42
Fe_2O_3	0.36
Na_2O	0.26
K_2O	1.05
SO_3	1.26
Physical property	
Specific gravity	2.06

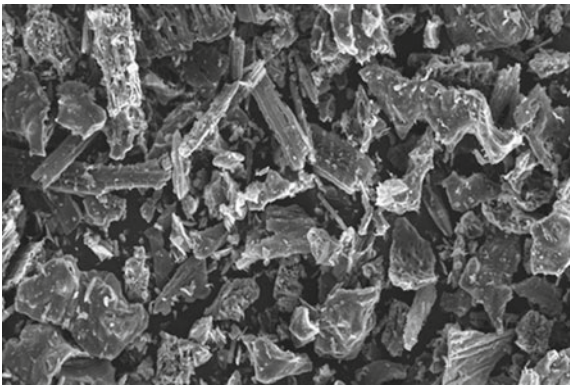

Fig. 2 Morphology structure of RHA

RHA is attributed to EDS and summarized in Table 3. RHA consists of amorphous silica oxide and partial crystalline silica as obtained through morphology analysis and is depicted in Figs. 2 and 3.

2.2 Mix Proportions

In the preparation of the control mix the quantities of different materials were used and are tabulated in Table 4. The mix proportion of equivalent methods [13] was used for the preparation of the mixture containing the RA and RHA. Before preparing the concrete mix the material should be saturated dried and is summarized in Table 5.

The workability of each mix preparation was determined as outlined in ASTM C 143. The three numbers of identical samples were casted for each set of mix.

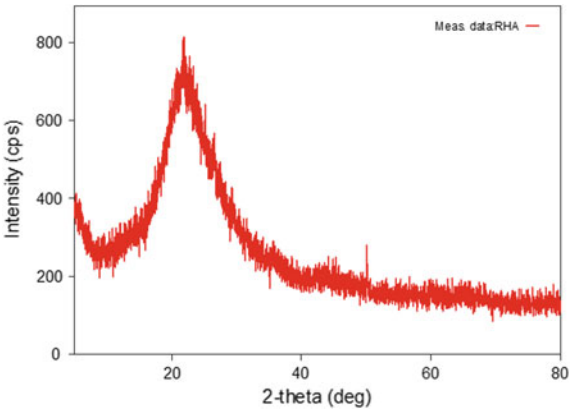

Fig. 3 X-ray diffraction (100 μm) of RHA

Table 4 Control mix proportion

Mix notation	Cement (kg/m^3)	FA (kg/m^3)	NA (kg/m^3)	Water (kg/m^3)	Admixture (kg/m^3)
RA0%, RHA 0%	370	756	1107	148	7

Table 5 Modified Mix proportions (RA and RHA) (kg/m^3)

Mix proportion	Portland cement (Kg)	RHA (Kg)	Fine aggregate (Kg)	Coarse aggregate (NA) (Kg)	Coarse aggregate (RA) (Kg)
RA50%, RHA6%	348	22	743	545	545
RA50%, RHA9%	337	33	743	545	545
RA50%, RHA12%	326	44	743	545	545
RA50%, RHA15%	315	55	743	545	545

2.3 Test Program

Compressive Strength. In accordance with IS 516-1959 [14], the compressive strength of concrete is determined, 100 mm size cubes were casted for three trials, and samples are cured for period of 7, 28 days of age.

Split Tensile Strength test. The dimension of concrete tensile strength is 100 mm diameter for 150 mm height size cylinders are casted for three trials and tested as per the guidelines of IS 5816-1999 [15] at the maturing period of 7, 28 days.

Flexural Strength test. To conduct flexural test, 500 × 100 × 100 mm size beams were casted for two trials as per the guidelines of ASTM C293 [16]. It was conducted for a curing period of 7, 28 days.

Scanning Electron Microscopy (SEM). SEM is an electron microscope that focuses across the specimen as an electron of beam interacts with it through scanning. ASTM C1723—16 is the guidelines for the process of the SEM test, at 28 days of curing period after compressive test.

X-Ray Powder Diffraction (XRD). XRD analysis was conducted to study the composition of concrete mixes and materials used in it. The test was performed in accordance with ASTM C1365—18 after 28 days of curing period.

3 Results and Discussions

The study is performed in two stages. In the first phase, the study was partial replacement of RA in NA at different proportions 0, 50, 75, and 100%. In the second phase, the study of RHA was induced as a substitution for cement at different proportions 6, 9, 12, and 15%. The mechanical properties were analyzed, and the results are used to determine the optimum value of RA and RHA.

3.1 The Mechanical Property Indices

Replacement of Recycled Aggregate With Natural Aggregate. *Compressive Strength.* Compression strength for different combinations of concrete mix was performed in accordance with IS 516-1959. Table 6 and Fig. 4 summarizes compressive strength of concrete mix prepared with RA at different proportions 0, 50, 75, and 100% for 7, 28 days.

Split Tensile Strength. Tensile strength was performed for different mix combinations as outlined in IS: 5816-1999. The size of the specimen is 100 mm diameter and 150 mm height was placed between two plates and applied for the compressive load. The failure load is used to analyze the tensile strength and are presented in figure 5 and table 7.

Table 6 Compressive strength test results for RA

Replacement percentage	Compressive strength (MPa)	
	7 days	28 days
0	20.60	31.70
50	**18.89**	**29.37**
75	16.20	26.41
100	15.06	24.56

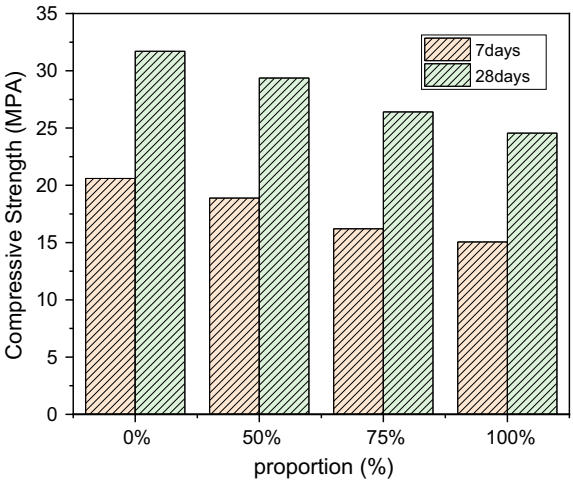

Fig. 4 Compressive strength ages @ 7, 28 days

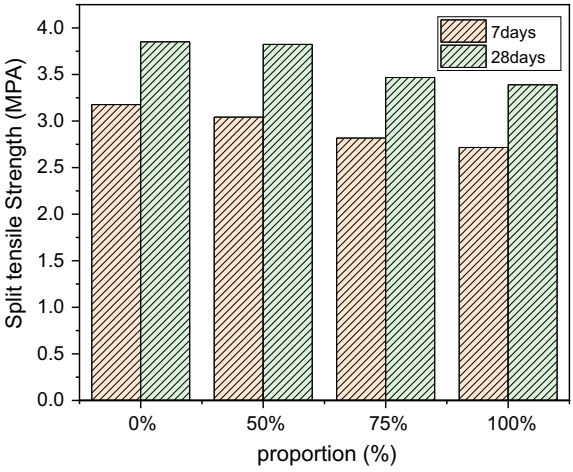

Fig. 5 Tensile strength for different proportions of RA @ 7, 28 days of age

Table 7 Tensile strength properties for different RA proportions

Replacement percentage (%)	Tensile strength (MPa)	
	7 days	28 days
0	3.177	3.851
50	**3.042**	**3.823**
75	2.817	3.467
100	2.716	3.389

Three trials were performed for each mix combination. Mix prepared with the NA and optimum RA has the compressive strength of 31.70 and 29.37 MPa and the Tensile strength of 3.851 and 3.823 MPa at 28 days age of concrete. It was observed that maximum strength attains at 50% replacement.

Inclusion of Rice Husk Ash in Optimum Recycled Aggregate Mix. *Compressive Strength.* The analysis of compression strength for different combinations of the concrete mixture was performed as outlined in IS 516-1959. Compressive strength test results of RHA at 6, 9, 12, and 15% for 7, 28 days is summarized in Table 8 and Fig. 6.

Spilt Tensile Strength. Tensile strength was performed for different mix combinations of RHA for concrete mix. The test of different concrete mixes was determined by using a size of the specimen as 150 × 300 mm. It was placed between the two plates and compressive load was applied, where the specimen breaks due to low tensile strength as shown in figure 7. The test results are presented in table 9 and figure 8.

Flexural strength. A three-point load test was conducted for different mixes. The specimen of size 500 × 100 × 100 mm was casted and tested. It was noticed that beyond 6% of RHA in concrete mix, the flexural strength showed a declined trend. The test results are presented in Table 10 and Fig. 9.

Table 8 Compressive strength test results for RHA

RHA inclusion (%)	Compressive strength (MPa)	
	7 days	28 days
6	20.2	30.3
9	18.5	29.32
12	18	28.82
15	17.0	28.20

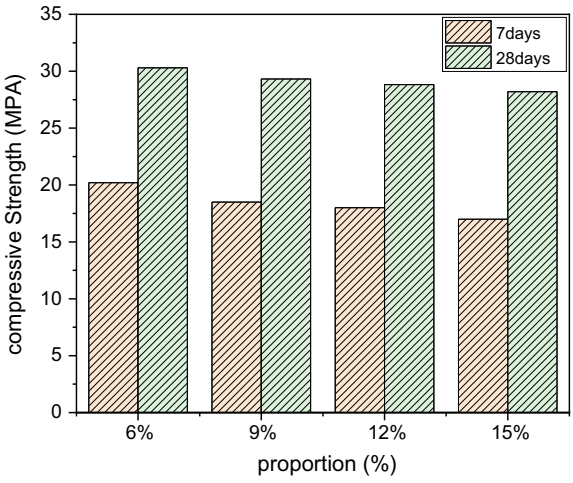

Fig. 6 Compressive strength of RHA mixes at 7 and 28 days of age

Fig. 7 Tensile test for sample prepared

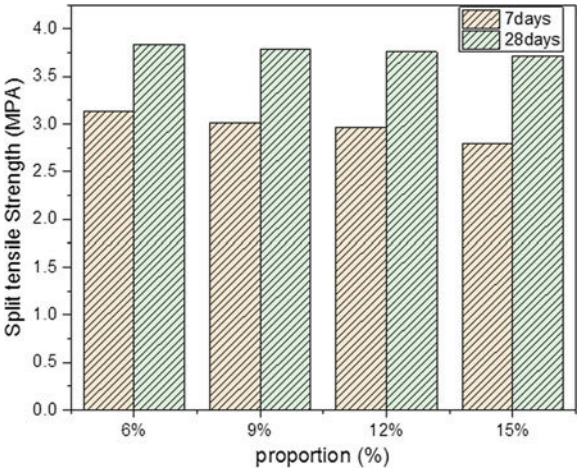

Fig. 8 Tensile strength of RHA concrete at 7 and 28 days of age

Table 9 Tensile strength for RHA mixes

RHA inclusion (%)	Tensile strength (MPa)	
	7 days	28 days
6	3.14	3.84
9	3.01	3.79
12	2.97	3.76
15	2.80	3.72

Table 10 Flexural strength test results for RHA mixes

RHA inclusion (%)	Flexural strength (N/mm^2)	
	7 days	28 days
6	3.0	4.4
9	2.4	4.1
12	2.0	4.0
15	1.8	3.8

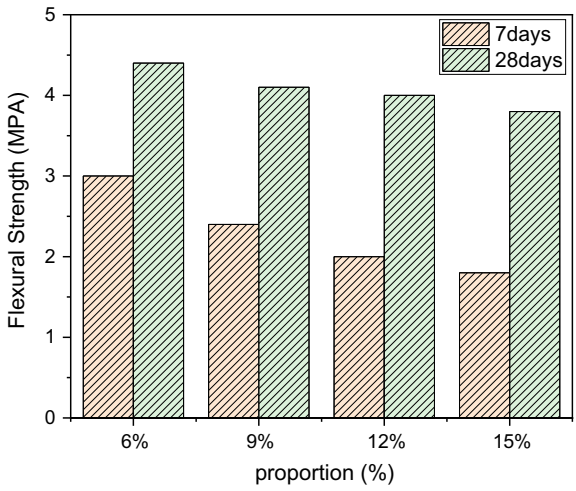

Fig. 9 Flexural strength of RHAconcrete mixes at 7 and 28 days of age

Scanning Electron Microscope (SEM). The micrographs of SEM and EDS images of blended RHA mixture at 6, 9, 12 and 15% are presented in Fig. 10. It is associated with an electron microscope that targets across a specimen through scanning its interaction with an electron beam. The micrograph shows the clear unfold of the Ca silica gel over the concrete. From Fig. 10(a), 6% of RHA inclusion has shown less micro pores in concrete, and the C-S-H gel is the reason for the improvement in mechanical properties. From figure10(d), 15% RHA replacement in concrete mix has shown seperation of bond structure.

X-Ray Diffraction. The X-Ray powder optical phenomenon was performed to investigate the elements and material employed in the concrete combine. The XRD pattern of RHA shows that the RHA consists of most amorphous silicon dioxide and partial crystalline silica presented in it. Specimen with sizable amount of mixture particles contains quartz that results in the intensive *Si* peaks and are shown in Fig. 11.

4 Conclusion

In this study, the results of laboratory perform to investigate the quality of RA in RHA concrete mix. Hardness properties were performed on RHA concrete mixture. Influence of RHA supplementary material for cement attains positive results for concrete combine.

- From the mechanical properties, it is noticed that Compressive Strength and Tensile Strength of RA mixes is marginally less compared to fresh concrete. However, it satisfies the M25 grade requirements for concrete.
- When compared with the fresh concrete the addition of RHA in concrete mix has improved the Compressive Strength, Tensile Strength, and Flexural Strength.

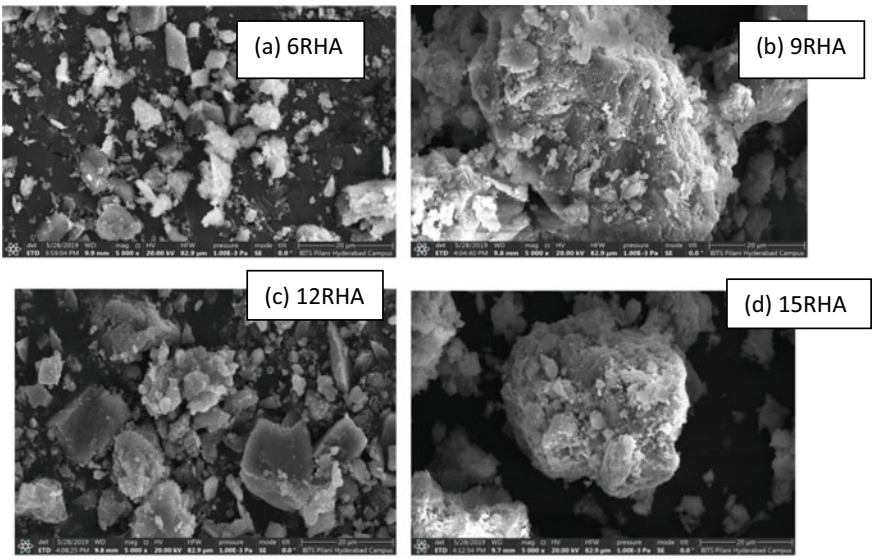

(a)

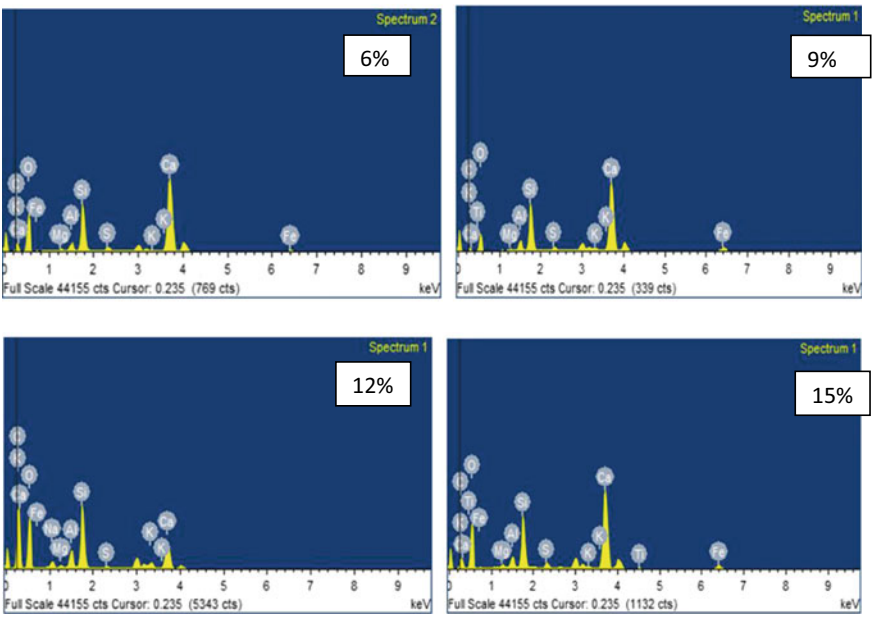

(b)

Fig. 10 **a** SEM Micrographs of various mixes of RHA. **b** EDS image of the RHA mixes

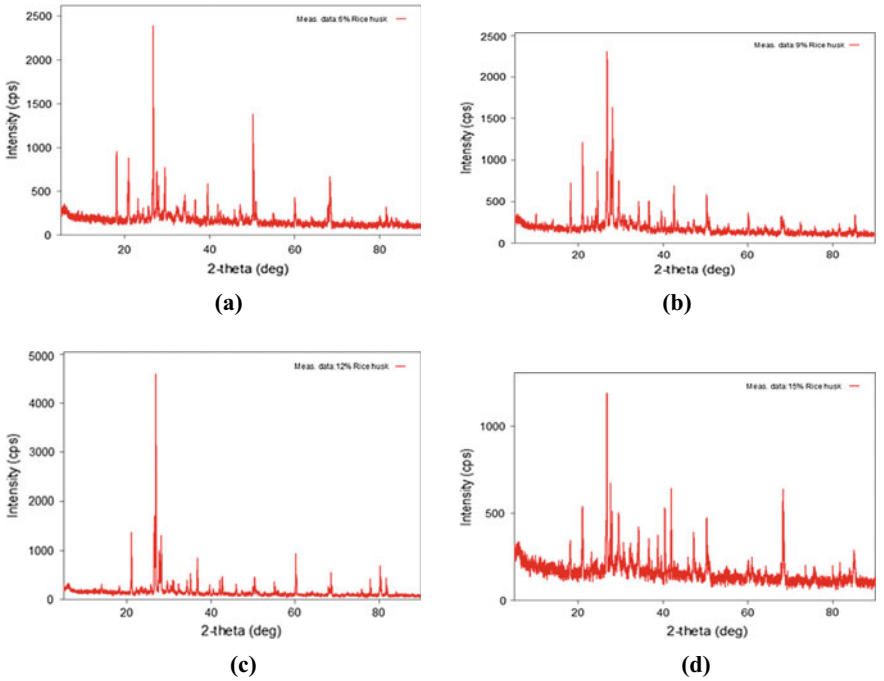

Fig. 11 **a** 6% RHA. **b** 9% RHA. **c** 12% RHA. **d** 15% RHA

This is because of the development of C-S-H gel and improvement of *Si* in RHA mix.

From the study the optimum Recycled aggregate of 50% and 6% RHA has proven moreover the mechanical and chemical indices which can be used for construction of sustainable pavements in construction of low volume roads.

Remarks

I got the appropriate permissions from authorities of rice mill and local quarry for collecting "Rice husk ash"' and "natural aggregate", respectively.

References

1. Ganesan K, Rajagopal K, Thangavel K (2008) Rice husk ash blended cement: Assessment of optimal level of replacement for strength and permeability properties of concrete. Constr Build Mater 22:1675–1683
2. Chao-Lung Hwang, Le Anh-Tuan Bui, Chun-Tsun Chen (2011) Effect of rice husk ash on the strength and durability characteristics of concrete. Constr Build Mater 25:3768–3772

3. Zareeia Seyed Alireza, Ameri Farshad, Dorostkar Farzan, Ahmadi Mojtaba (2017) Rice husk ash as a partial replacement of cement in high strength concrete containing micro silica: Evaluating durability and mechanical properties. Case Stud Constr Mater 7:73–81
4. Kishore R, Bhikshma, V. Jeevana Prakash P (2011) Study on strength characteristics of high strength rice husk ash concrete. Procedia Eng 14:2666–2672
5. Thomas C, Setién J, Polanco JA, Alaejos P, Sánchez de Juan P (2013) Durability of recycled aggregate concrete. Constr Build Mater 40:1054–1065
6. Van Tuan Nguyen, Ye Guang, van Breugel Klaas, Fraaij Alex LA, Dai Bui Danh (2011) The study of using rice husk ash to produce ultra high performance concrete. Constr Build Mater 25:2030–2035
7. Rahal Khaldoun (2007) Mechanical properties of concrete with recycled coarse aggregate. Build Environ 42:407–415
8. Thomas Job, Thaickavil Nassif Nazeer, Wilson PM (2018) Strength and durability of concrete containing recycled concrete aggregates. J Build Eng 19:349–365
9. Tabsh SW, Abdelfatah AS (2009) Influence of recycled concrete aggregates on strength properties of concrete. Constr Build Mater 1163–1167
10. Behera Monalisa, Bhattacharyya SK, Minocha AK, Deoliya R, Maiti S (2014) Recycled aggregate from C&D waste & its use in concrete—a breakthrough towards sustainability in construction sector: a review. Constr Build Mater 68:501–516
11. IS 12269-2013 ordinary portland cement, 53 grade—specification (first revision)
12. IS 2386 (part 1, 2,3)—1963 methods of test for aggregates for concrete
13. IS 10262—2009 Indian standard concrete mix proportioning—guidelines (first revision)
14. IS 516—959 Indian standard methods of tests for strength of concrete
15. IS 5816-1999 Splitting tensile strength of concrete—method of test (first revision)
16. ASTM C293 Standard test method for flexural strength of concrete

Influence of Partial Replacement of Cement by Industrial Wastes on Properties of Concrete

Nikhil Kumar Verma

Abstract With express increase in the demand of high rise structure with high strength concrete in construction industry, led to enhance the cement consumption. The cement production consumes large energy and liberates CO_2 during manufacturing of cement and concrete, resulting to environmental imbalance. Researchers are putting their untiring effort to conserve energy and control the environmental degradation, an attempt has been made to reduce the cement consumption by partially replacing it with pozzolanic materials. In the present study, attempt has been made to evaluate the strength properties of high strength concrete made of cement mixed with green and pozzolanic material like "Fly Ash and Silica Fume". Using partial replacement method, in portland cement concrete, the percentage of fly ash adopted is 0, 10, and 20% and percentage of silica fume adopted is 0, 5, 10, and 15% for each percentage of fly ash replacement. Polycarboxylate Ether based Superplasticizer is used for desired workability with water to binder ratio as 0.3. Twelve different concrete mixes are prepared with ordinary portland cement, silica fume, and fly ash. Specimens are put to curing for 7, 28, and 90 days. Different properties such as workability, cube compressive strength, split tensile strength are investigated for the concrete. From the various test it is concluded that the nature of strength gain in the above concrete with fly ash and silica fume is in conformity with concrete made with OPC only. The optimum content of fly ash and silica was found to be 0 and 10% for 7 and 28 days cube compressive strength, but for 90 days strength, optimum content is observed to be 10 and 10% of fly ash and silica, respectively. Thus, increase in strength properties for the above shown values as compared to that of normal concrete are significantly good.

Keywords Fly ash · Silica fume · Concrete

N. K. Verma (✉)
Guru Ghasidas Vishwavidyalaya, Bilaspur, India
e-mail: nikhilvermanit@gmail.com

© Springer Nature Singapore Pte Ltd. 2021

K. K. Pathak et al. (eds.), *Recent Trends in Civil Engineering*, Lecture Notes in Civil Engineering 77, https://doi.org/10.1007/978-981-15-5195-6_54

1 Introduction

Concrete is one of the bizarre material in the earth. There is no disbelief that concrete will become a most important construction material in the future with the expansion of humanoid society. But, the expansion of modern concrete industry also contributes too many ecological problems such as pollution, waste dumping, emission of hazardous gases, diminution of natural resources, etc. In the present scenario portland cement and some complementary cementitious materials are cheapest binders which help in improving the performance of concrete. Apart from all the binders, manufacturing of portland cement is very energy exhaustive and also produces CO_2 in large quantities. Hence to keep the place of concrete in the dominant materials, the concrete industry needs to be shifted toward "sustainability". For the sustainable development of the whole society, the future concrete will not only be stronger, also it should be industrialized in such a manner that it satisfies the socioeconomic needs at the minimum ecological impact. Use of various industrial wastes and by-products in concrete is one of the foremost contribution of the concrete industry to the sustainable growth of human society. As we already know that the by-products and wastes from various industries lead to many ecological trouble around the world. Many countries of the world encouraging recycling of waste and restricting hazardous waste dumping, also implement tax on landfill but still it is a severe ecological issue in the world. Fly Ash (FA) and Silica Fume (SF) are the by-products of industries in which most of the concrete researcher are working. FA and SF have some exceptional desirable properties which OPC is not able to produce when used individually. By the use of Supplementary Cementious Materials (SCMs), such as SF and FA not only produce concrete but High Strength Concrete (HSC) can also be produced. HSC is a concrete which made with proper materials, combined according to a selected mix design; properly mixed, transported, placed, consolidated, and cured so that the resulting concrete will give an excellent strength in the structure in which it is placed and with the loads to which it will be subjected for its design. Current study helps to identify the influence of FA and SF on various mechanical properties of HSC by partial replacement of OPC. The partial replacement of OPC with SCMs also helps OPC manufacturing plants to reduce the emission of greenhouse gases (CO_2), also helps to reduce the cost of waste disposal. This work will also help in increasing and accelerating management procedure in the initial, current, and future construction program of any infrastructure projects.

2 Literature Review

2.1 High Strength Concrete

Compressive strength more prominent than 6000 psi or 42 MPa of cylinder after 28 days is commonly perceived as high strength concrete. This value was given by American Concrete Institute (ACI) in 1984, however isn't yet fixed, on the grounds that ACI perceives that the meaning of high strength changes with geographical factor [1]. Concrete can never be made sustainable since it depends on non-inexhaustible mineral resources. Nonetheless, the sustainability of the concrete can be increased by supplementing or replacing concrete with strengthening, establishing material dependent on modern industrial waste materials like slag and fly ash. Bigger measure of fly ash can be utilized if adversity in early quality is balanced by better crushing or uncommon pounding (mechanical initiation) or quickening agents [2]. High performance concrete can be planned to give streamlined execution attributes for a given stacking and presentation condition alongside the prerequisite of coat, service life, and durability. The accomplishment of high performance concrete requires more consideration on suitable mix design, production, placing, and curing of concrete. For each of these activities controlling parameters ought to be accomplished by concrete producer for a situation that a structure needs to confront [3].

2.2 Utilization of Silica Fumes in HSC

Silica Fumes (SF) is an incredibly responsive pozzolana material. It is by-product got from the production of silicon or ferrosilicon. It is removed from the vent gases from electric bend furnaces. SF molecules are fine with molecule measures around multiple times smaller than those of normal size of OPC particles. It is dandified powder. The standard details of silica fumes are characterized in ASTM-1240. It is regularly utilized effectively as a replacement up to 5–12% by mass of absolute cementitious materials. It may be utilized effectively for the structure where high strength is required or fundamentally decreased porousness to water is the significant concern. Exceptional systems are required to be incorporated for handling, placing, and curing concrete with these fine SF particles. Cube compressive strength at 23 days old, 0, 30, and 70% replacement accomplished 54, 63, and 64 MPa, respectively. Concrete mixes (30 and 70%) showed better execution than the OPC concrete in seawater accessible to tidal zone. The pore size distribution of both high strength concrete was finer at 6 months was reduced around three times contrasted with OPC concrete [4]. Mullick [5] Proposed ternary mixes of OPC with 10% Silica Fume and 45% granulated slag invigorates 69.5 MPa at 28 days. When relieved at 38 °C, a blend of 32.5% OPC, 60.5% slag, and 7% Silica Fume was found to bring about compressive strength of 50 MPa at 48 h. Total of 22.5 kg Silica Fume to 300 kg concrete and 350 kg fly ash blends of Self-Compacting Concrete (SCC) produce

high strength early (21 MPa at 3 days and 45 MPa at 28 days) alongside increment in cohesiveness. The greatest compressive strength at 28 day is 60 MPa at 15% SF replacement level with Water/Cement (W/C) proportion of 0.30, and 35 MPa is the lowest compressive strength got at 5% SF replacement level at a W/C proportion of 0.40 [6]. When contrasted with other blends the reduction in weight and compressive strength percentage was established to lose by 2.23 and 7.69 when the cement was replaced by 10% of SF. An increment of 40% in the normal consistency was observed, when there is increment in the percentage of SF from 0 to 20%. The ideal 7 and 28 days compressive strength and flexural strength have been found in the scope of 10–15% SF replacement [7]. It is proposed SF consolidation in concrete outcome in critical improvement in the tensile strength of concrete, alongside the compressive strength. Increment in split tensile strength found by 15% SF replacement is practically irrelevant, though sizeable gains in flexural tensile strength observed even up to 25% replacement [8]. Under the quickened testing conditions, agglomerated SF was reduced in expansion when utilized as a 5% replacement of reactive sand. At the point when a similar sand was replaced by 5% of sintered SF aggregates, there is significant increment in expansion [9]. A 10% replacement of Portland concrete by Silica Fume gave a more prominent aggregate hydration heat and more noteworthy compressive strength than the suggested concrete at all stages. Despite what might be expected when the SF content increments up to 30%, the weakening impact decreases these enhancements [10].

2.3 Utilization of Fly Ash in HSC

Fly ash is one of the by-product produced by the ignition of coal. Fly ash is mainly produced by the coal operated thermal power plants. By replacing portland cement with fly ash during the manufacturing of cement reduces the greenhouse gas, as one ton of CO_2 is produced during the manufacturing of one ton of portland cement, whereas zero CO_2 is produced using the existing fly ash. New fly ash generation, i.e., the consumption of coal generates around twenty to thirty tons of CO_2 for every ton of fly ash. To accomplish a manageable improvement of the concrete industry, the utilization of pozzolanic and cementations by-products should be enhanced [11]. Many research and field examinations on concrete containing fly ash had shown phenomenal mechanical and durability properties. Anyway the pozzolanic response of fly ash being a moderate procedure, its commitment toward the quality advancement happens just at last ages. Because of the round state of fly ash particles, it also increases the workability while decreasing water content. Mehta [12] Took Class F fly ash to replace OPC, and replaces OPC about 15–60% by fly ash and maintained Water/Binder (W/B) proportion to about 0.30–0.40. At 28 days 25–30% replacement accomplished good compressive strength, thermal cracking and splitting, and salt resistance. It is utilized for over 50% FA for practical advancement. IS 1489:1969 for PPC was presented in India, the addition of fly ash was restricted to just 10–25%, and now in IS 1489: 1991 the point of confinement of fly ash addition in PPC is

15–30%. This Research and Development work was completed in Quality Control Department of Cement Manufacturing Company Limited, Meghalaya, India in the lab scale, to know the effect of higher inclusion of fly ash beyond BIS restriction (up to half), with different clinker quality, fineness and Indian standards IS 1489:1991 for PPC. At 0, 40, 42, 45, 47, 50% replacement of FA, they discovered 28-days compressive strength as 69, 58, 58, 52, 52, 48 MPa, respectively [13]. Donald [14] add 0%, 30%, 40% and 50% FA and maintains W/B ratios 0.35, 0.40 and 0.50. At 28 days, FA at inclusion levels of 30%, 40%, and 50% has somewhat lower compressive strength, higher permeability, and higher carbonation rates, respectively, than concrete with 0% FA. Increment in W/B proportion diminishes compressive strength, increases permeability, and expands carbonation rates [14]. M30 grade concrete was produced by utilizing FA at 50% cement replacement level. A slump of 100 mm was to be accomplished for the workability. After 28 days strength values were same and at later stages high strength was exhibited by High Volumes of Fly Ash in Concrete (HVFAC). The flexural strength was seen as higher for HVFAC. HVFAC demonstrated exceptionally low chloride penetrability and low water absorption and decreased water permeability as compared to OPC-based concrete. The abrasion value of HVFAC was seen as imperceptibly better contrasted with OPC-based concrete [15]. The extents of fly ash in concrete can fluctuate from 30 to 80% for different grades of concrete. It is seen that at later age strength of concrete having over 40% replacement of cement by fly ash endures unfavorably however W/B ratio is generally decreased. For concrete with less than 40% replacement of cement, the characteristics compressive strength at 28 days is on higher side. While, concrete with 40% replacement of cement, the 28 days compressive strength is at par with that of OPC [16]. Class C kind of FA is utilized to deliver high-performance concrete. Lime is responding during curing process, the early strength gain in 3–7 days is less compared to normal OPC but toward the finish of 28 days the compressive strength quality is more than the target compressive strength. Optimal strength gets replacement of cement with FA up to 20–25%. Within 7 days about 70–80% compressive gain is achieved. Replacing cement with FA gives comprehensive arrangement and practical way for concrete with no extra expense [17]. Compressive strength would decrease slowly with increase in FA up to 0–60%. Class C and Class F type FA have same compressive quality following 7 days. Warm water curing shows low compressive strength as compared to accelerating curing. The Class C type FA acquires more strength with replacement of 40% contrast with Class F type FA while Class F type FA acquires more strength contrast with Class C type FA with substitution of 60% FA. The swap of 40% FA for Class C and Class F invigorates good strength with later ages and it was financially contrasted with others [18]. The compressive strength and flexural strength of concrete blends were increased with replacement of sand by FA was 34% and 24%, respectively. By replacing sand with FA compressive strength increases also cost reduces by replacement of sand with FA [19].

2.4 Mix Design of HSC

The mix design as per IS10262:2009 is in line with ACI. Use of supplementary materials such as chemicals and mineral admixture are applicable as per IS456:2003 for durability requirement with all types of exposure. Also Ready Mix Concrete (RMC) can be designed. The code illustrates this with an M40 concrete with and without FA. A typical mix design (first mix) for commonly used M20 grade is illustrated based on the properties of the ingredients using the new BIS and ACI methods. In ACI method fine aggregate content is higher compared to new BIS method. In BIS method coarse aggregate is higher. Therefore more workability will be achieved in ACI method. Also, it would lead to increase in strength as fine aggregate fills the voids [20]. Existing IS codes are appropriate for design of concrete elements for HVFAC. Significant perceptions on IS 3812 (Part I and II): 2003 specification for ingredients or elements of FA are [21]

(a) IS codes force restriction of 35% on the most extreme utilization of FA in PPC however there exists no confinement on the amount of FA in concrete mix if in site mixing is done separately.
(b) HVFAC ought to be produced in mechanized batching plant or RMC plant under essential quality control. Target strength for creating HVFAC or any concrete mix delivered by automated mixer need not be fixed at compressive strength plus 1.65 times standard deviation. A conservative estimate of target strength is 1.2 times and characteristics strength for mix not leaner grade M30.
(c) No code is available on mixing method of HVFAC. Only some papers suggest that mixing methods affect the quality of HVFAC and other types of concrete mixes.

Similar to that of OPC in concrete, the mineral admixture like FA and Ground Granulated Blast Furnace Slag (GGBS) help in the strength gain at 28 days. This supports the perceptions made by an autonomous methodology utilizing summed up Abrams Law for multi-component cementing materials. The relationship would thus be able to be utilized for choosing water cementitious materials proportion for the target of 28 days compressive strength of concrete containing fly ash or GGBS and a superplasticizer. This relationship anyway can't be utilized for extremely high compressive strength concrete, i.e., for concrete having 28 days compressive strength above 80 MPa utilizing SF and Polycarboxylate (PC)-based superplasticizer, the preliminary mix approach is best for choosing mix proportion for such high strength concrete [22]. Solid blend configuration is the way toward picking reasonable elements of concrete and deciding their relative amounts with the object of delivering ash economically as conceivable concrete of certain base properties prominently workability, strength,

and durability. It ought to be clarified that a definite assurance of mix ratio by methods for table or computer is commonly non-conceivable. The primary target of the investigation was to design M25 concrete and to find the compressive strength by mix design as per the different codes such as IS10262-1982, IS 10262-2009 [23], ACI strategy and Department of Environment's Design (DOE) methods, we presume that in over four techniques least cement is utilized in DOE method and it invigorates required compressive strength of concrete economically [24].

3 Proposed Experimental Work

3.1 Different Phases of Experimental Work

i. Determination of physical properties of natural coarse aggregate, fine aggregate, and cement which are to be used in experimental work.
ii. Concrete mix design based on the results obtained in the first phase and as per IS 10262-2009 [23]. The design mix is done for M65 grade of concrete shown in Table 1.
iii. Based on second phase of mix design casting of cylinders and cubes specimens are done. All the specimens are casted manually and follow the IS 1199-1959 [25].
iv. Testing of the mechanical properties of the specimens like compressive strength of cubes and split tensile strength of cylinders [26].

Table 1 Mix design proportion for M65 concrete for 1 m^3 of concrete

Cement (kg)	Fine aggregate (kg)	Coarse aggregate (kg)		W/C ratio	Admixture (superplasticizer %) as per IS 9103-1999 [28]
		20–10 mm	10–4.75 mm		
635	610	640	315	0.30	1.10

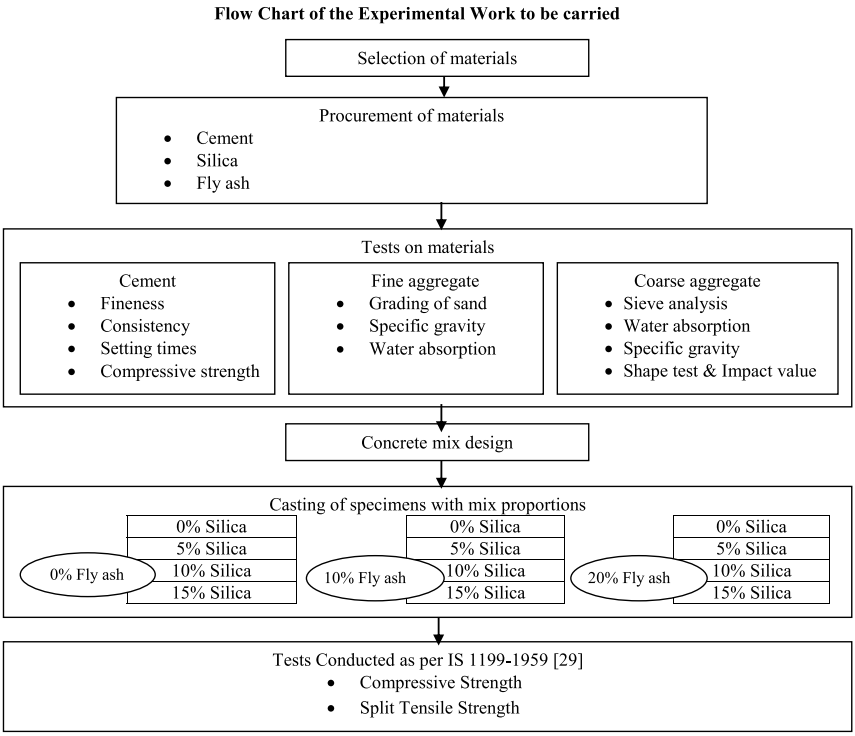

4 Experimental Results and Analysis

4.1 Test on Cement

See Table 2.

4.2 Tests on Fine Aggregate

See Table 3.

4.3 Tests on Coarse Aggregate

See Table 4.

Table 2 Tests and results of cement

Sr. no.	Test	IS reference	Experimental values		Suggested values as per IS specifications
1.	Fineness of cement (%)	IS: 4031(PART3)-1988 IS 12269:2013 [29]	8		>/10
2.	Normal consistency (%)	IS: 4031(PART 4)-1988	32		26–33
3.	Initial setting time (min.)	IS: 4031(Part 5)-1988 IS 12269:2013 [29]	45		30–60
4.	Final setting time (min.)	IS: 4031(Part 5)-1988 IS 12269:2013 [29]	435		≤600
5.	Compressive strength (N/mm^2)	IS:4031 (Part-6) 1988 IS 12269:2013 [29]	3 days	29.93	27
			7 days	39.46	37
			28 days	55.1	53

Table 3 Tests and results of fine aggregate

Sr. no.	Test	Reference	Experimental values		Suggested values as per IS specifications
1	Sieve analysis of fine aggregate	IS 383 1970 [30]	Fineness modulus	3.16	–
			Zone	II	
2.	Specific gravity of sand	IS 2386 (Part-III)1963 [31]	2.81		2.6–3.0

Table 4 Tests and results of coarse aggregate

Sr. no.	Test	Reference	Experimental values		Suggested values as per IS specifications
1	Sieve analysis of coarse aggregate	IS: 383-1970	Size	20 mm	–
			Grading	Single sized	
2.	Water absorption	IS 2386 (Part-III)1963 [31]	0.25%		0.6 per unit by weight
3.	Specific gravity	IS 2386 (Part-III)1963 [31]	2.64		2.6–3.0
4.	Flakiness index	IS: 2386 Part 1 1963	20.49		<30
5.	Elongation index	IS: 2386 Part 1 1963	22.75		<45
6.	Impact value	IS: 2386 Part 4 1963	9.94		Exceptionally strong

Table 5 Properties of silica fume

Properties	Conclusion
State	Amorphous-sub-micron powder
Color	Grey to medium grey powder
Specific gravity	2.10–2.40
Solubility	Insoluble
Bulk density-densified	650–700 kg/m^3

Table 6 Specification of silica fume

Specifications	
Particular	Typical values
SiO_2 (%)	92
Moisture (%)	0.8
Loss On Ignition (LOI)	2.5
Retained on 45μ sieve (%)	2
7 days pozzolanic activity index (%)	115
Specific surface area m^2/gm	20

4.4 Properties and Specifications of Silica Fumes

See Tables 5 and 6.

4.5 Mix Design for M65

The mix design of concrete with varying percentage of cement, fly ash, and silica fume is shown in Table 7.

4.6 Compressive Strength

The compressive strength is the important test out of all the tests which gives an idea about all the characteristics of concrete. Compressive strength test was performed on normal concrete as per method specified by BIS (IS: 516 1959) [27] on different curing periods, i.e., 7, 28, and 90 days shown in Tables 8, 9, and 10, respectively.

The observations from the above Figs. 1 and 2 are discussed below.

At 7 days the variation in compressive strength of concrete by partial replacement of cement with FA (0, 10, and 20%) and SF (0, 5, 10, and 15%) is observed that by increasing the percentage partial replacement of cement with FA there is a decrease in the strength, but because of the SF replacement increasing trend was shown in the

Table 7 Design mix with cement, FA, and SF

Mix	Cement		Fly ash		Silica fume		Water	$\frac{W}{B}$	Superplasticizer		Fine aggregate	Coarse aggregate	
	%	kg/m^3	%	kg/m^3	%	kg/m^3	kg/m^3		%	kg/m^3	kg/m^3	20–10 mm	10–4.75 mm
												kg/m^3	kg/m^3
A	100	635	0	0	0	0	190	0.3	1.10	7	610	640	315
B	95	605	0	0	5	32	190	0.3	1.30	8.25	610	640	315
C	90	572	0	0	10	64	190	0.3	1.50	9.52	610	640	315
D	85	540	0	0	15	96	190	0.3	1.75	11.1	610	640	315
E	90	572	10	64	0	0	190	0.3	1.00	6.35	610	640	315
F	85	540	10	64	5	32	190	0.3	1.20	7.62	610	640	315
G	80	508	10	64	10	64	190	0.3	1.35	8.57	610	640	315
H	75	477	10	64	15	96	190	0.3	1.55	9.85	610	640	315
I	80	508	20	127	0	0	190	0.3	0.95	6.04	610	640	315
J	75	477	20	127	5	32	190	0.3	1.15	7.30	610	640	315
K	70	445	20	127	10	64	190	0.3	1.30	8.25	610	640	315
L	65	413	20	127	15	96	190	0.3	1.45	9.20	610	640	315

Table 8 Cube compressive strength at 7 days for different FA and SF contents

Mix	Fly ash (%)	Silica fume (%)	Cement (%)	Compressive load (KN)	Compressive strength (MPa)
A	0	0	100	1035	46.00
B		5	95	1085	48.22
C		10	90	1160	51.56
D		15	85	1075	47.78
E	10	0	90	1000	44.44
F		5	85	1070	47.56
G		10	80	1140	50.67
H		15	75	1010	44.89
I	20	0	80	890	39.56
J		5	75	930	41.33
K		10	70	1000	44.44
L		15	65	910	40.44

Table 9 Cube compressive strength at 28 days for different FA and SF contents

Mix	Fly ash (FA %)	Silica fume (SF %)	Cement (%)	Compressive load (KN)	Compressive strength (MPa)
A	0	0	100	1540	68.44
B		5	95	1610	71.56
C		10	90	1700	75.56
D		15	85	1595	70.89
E	10	0	90	1410	62.67
F		5	85	1560	69.33
G		10	80	1620	72
H		15	75	1360	60.44
I	20	0	80	1310	58.22
J		5	75	1390	61.78
K		10	70	1510	67.11
L		15	65	1400	62.22

strength till 10% and then there is decrement in strength due to further addition of SF fume for all % of SF. The optimum strength was obtained at 0% FA and 10% SF replacement. At this replacement percentage increase is 12.086% as compared to that of control one.

The observations from the above Figs. 3 and 4 are discussed below.

At 28 days the variation in compressive strength of concrete show the same trend as that of 7 days, i.e., the variation in compressive strength of concrete by partial replacement of cement with FA (0, 10, and 20%) and SF (0, 5, 10, and 15%) is

Table 10 Cube compressive strength at 90 days for different FA and SF contents

Mix	Fly ash (FA %)	Silica fume (SF %)	Cement (%)	Compressive load (KN)	Compressive strength (MPa)
A	0	0	100	1570	69.78
B		5	95	1670	74.22
C		10	90	1780	79.11
D		15	85	1630	72.44
E	10	0	90	1575	70
F		5	85	1685	74.89
G		10	80	1790	79.56
H		15	75	1600	71.11
I	20	0	80	1540	68.44
J		5	75	1590	70.67
K		10	70	1740	77.33
L		15	65	1580	70.22

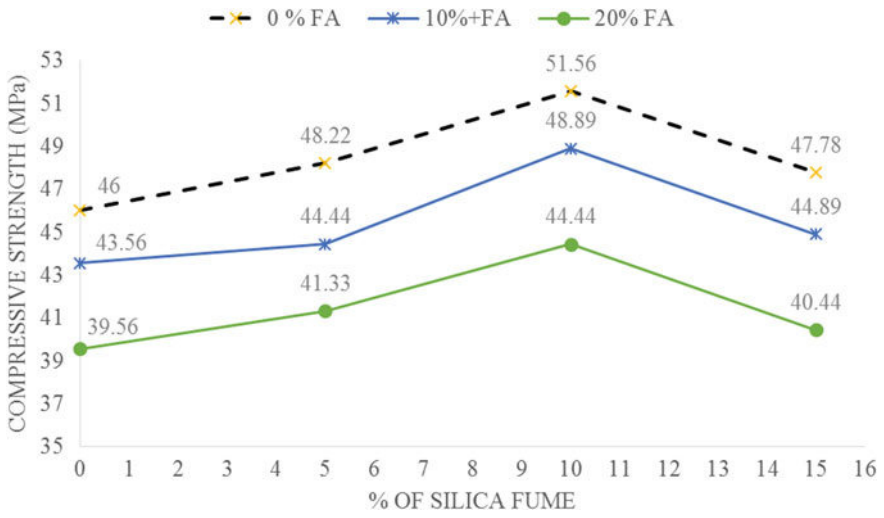

Fig. 1 Variation in compressive strength of HSC at 7 days with different SF and FA contents

observed that by increasing the percentage partial replacement of cement with FA there is a decrease in the strength, but because of the SF partial replacement increasing trend was shown in the strength till 10% and then there is decrement in strength due to further addition of SF for all % of SF. The optimum strength was obtained at 0% FA and 10% SF partial replacement. At this partial replacement percentage increase is 10.40%.

The observations from the above Figs. 5 and 6 are discussed below.

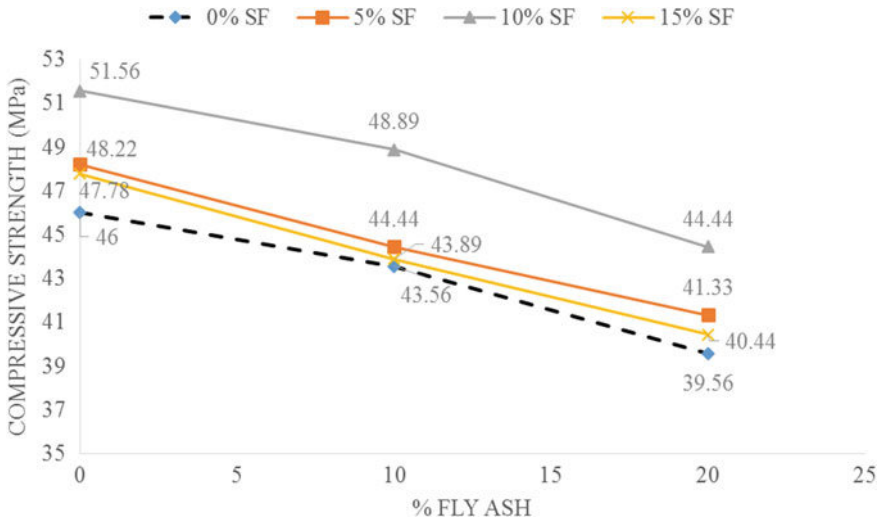

Fig. 2 Variation in compressive strength of HSC at 7 days with different FA and SF contents

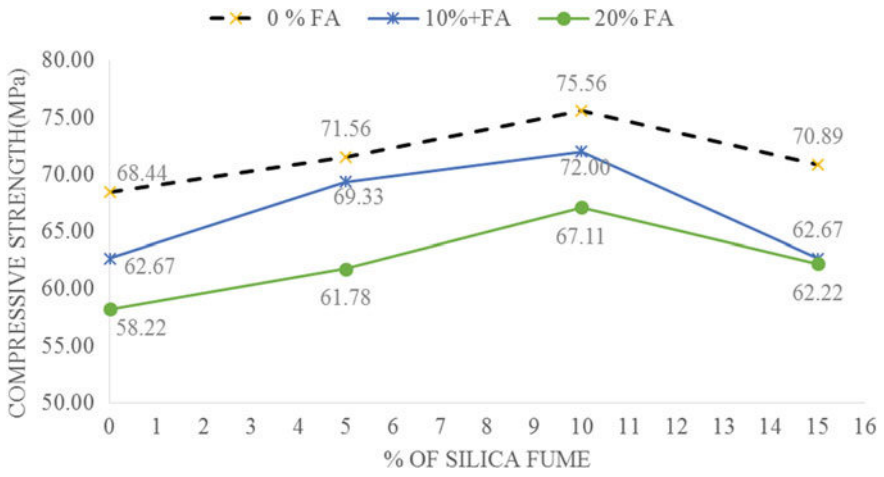

Fig. 3 Variation in compressive strength of HSC at 28 days with different SF and FA content

At 90 days a different trend is observed in the variation of compressive strength when compared to that of 7 days and 28 days. The variation in compressive strength of concrete by partial replacement of cement with FA (0, 10, and 20%) and SF (0, 5, 10, and 15%) is observed that by increasing the percentage partial replacement of cement with FA there is first increase in the strength and then decrease, but because of the SF partial replacement, increasing trend was shown in the strength till 10% and then there is decrement in strength due to further addition of SF for all % of SF.

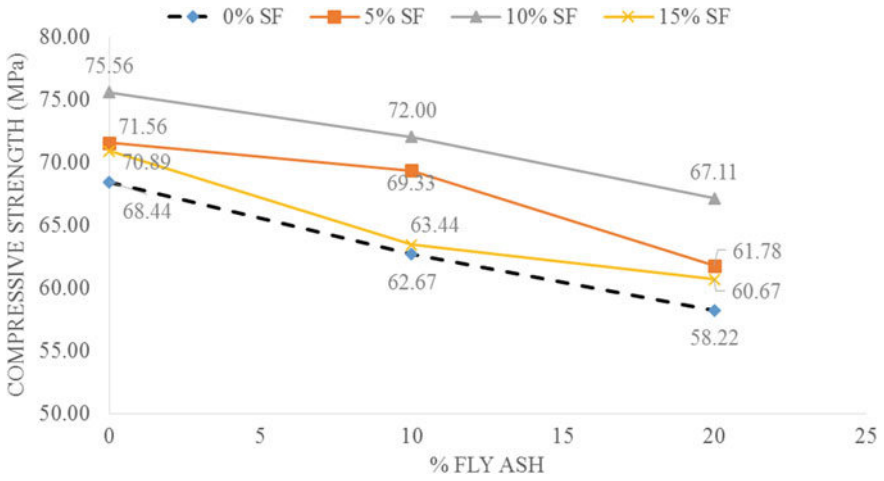

Fig. 4 Variation in compressive strength of HSC at 28 days with different FA and SF contents

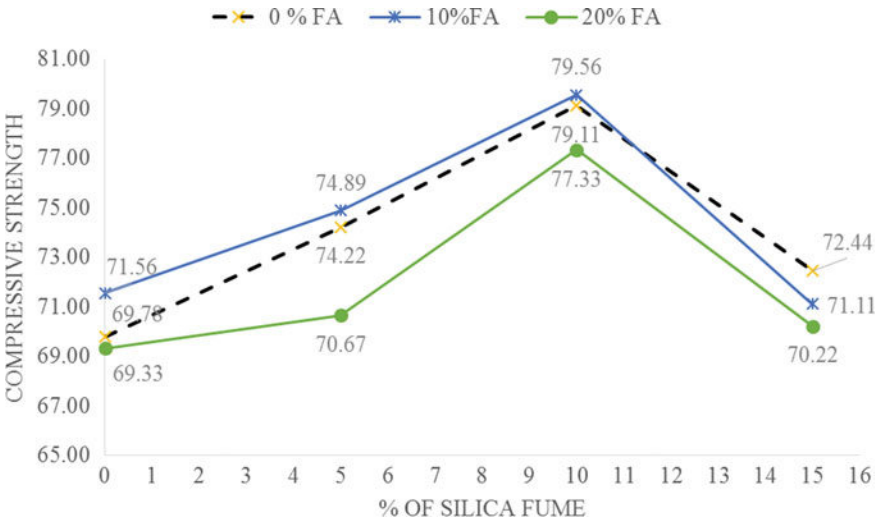

Fig. 5 Variation in compressive strength of HSC at 90 days with different SF and FA contents

It is further observed that the compressive strength showed an increasing trend for all percentage partial replacement of FA till 10% but optimum value is obtained at 10% FA and 10% SF partial replacement. At this partial replacement the percentage increase is 14.01%. The maximum value of cube compressive strength is found to be 79.56 MPa while control one is having only 69.78 MPa.

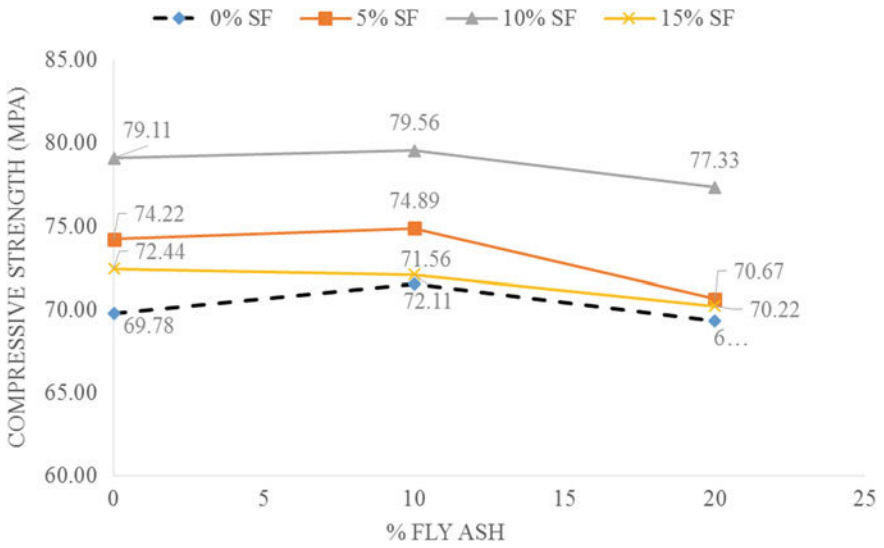

Fig. 6 Variation in compressive strength of HSC at 90 days with different FA and SF content

4.7 Split Tensile Strength

The other important property of concrete is split tensile strength. The concrete is very weak in tension due to its brittle nature. Thus, it is necessary to determine the tensile strength of concrete. The split tensile strength is performed on normal concrete with all twelve different mixes after 7 days, 28 days, and 90 days curing as per specifications given by BIS (IS: 516 1959) [27] and average results are presented in Tables 11, 12, and 13, respectively. The graphical comparison of these strengths is shown.

The observations from the above Fig. 7 are discussed below.

At 7 days the variation in split tensile strength of concrete by partial replacement of cement with FA (0, 10, and 20%) and SF (0, 5, 10, and 15%) is observed that by increasing the percentage partial replacement of cement with FA there is a decrease in the strength, but because of the SF partial replacement increasing trend is shown in the strength till 10% and then there is decrement in strength due to further addition of SF for all % of SF. The optimum strength is obtained at 0% FA and 10% SF partial replacement. At this partial replacement percentage increase is 11.26%.

The observations from the above figure Fig. 8 are discussed below.

At 28 days the variation in split tensile strength of concrete show the same trend as that of 7 days, i.e., the variation in split tensile strength of concrete by partial replacement of cement with FA (0, 10, and 20%) and SF (0, 5, 10, 15%) is observed that by increasing the percentage partial replacement of cement with FA there is a decrease in the strength, but because of the SF partial replacement increasing trend was shown in the strength till 10% and then there is decrement in strength due to

Table 11 Split tensile strength after 7 days curing

Mix	Fly ash (FA %)	Silica fume (SF %)	Cement (%)	Split tensile load (KN)	Split tensile strength (MPa)
A	0	0	100	270	3.82
B		5	95	285	4.03
C		10	90	300	4.25
D		15	85	260	3.68
E	10	0	90	255	3.61
F		5	85	270	3.82
G		10	80	290	4.10
H		15	75	255	3.61
I	20	0	80	240	3.40
J		5	75	250	3.54
K		10	70	270	3.82
L		15	65	240	3.40

Table 12 Split tensile strength of cylinders after 28 days curing

Mix	Fly ash (FA %)	Silica fume (SF %)	Cement (%)	Split tensile load (KN)	Split tensile strength (MPa)
A	0	0	100	410	5.8
B		5	95	430	6.09
C		10	90	445	6.3
D		15	85	405	5.73
E	10	0	90	380	5.38
F		5	85	420	5.94
G		10	80	435	6.16
H		15	75	370	5.24
I	20	0	80	345	4.88
J		5	75	360	5.1
K		10	70	410	5.8
L		15	65	365	5.17

further addition of SF for all % of SF. The optimum strength is obtained at 0% FA and 10% SF replacement. At this partial replacement percentage increase is 8.62%.

The observations from the above Fig. 9 are discussed below.

At 90 days, a different trend is observed in the variation of split tensile strength when compared to that of 7 days and 28 days. The variation in split tensile strength of concrete by partial replacement of cement with FA (0, 10, and 20%) and SF (0, 5, 10, and 15%) is observed that by increasing the percentage partial replacement of cement with FA there is first increase in the strength and then decrease, but because of

Table 13 Split tensile strength of cylinders after 90 days curing

Mix	Fly ash (FA %)	Silica fume (SF %)	Cement (%)	Split tensile load (KN)	Split tensile strength (MPa)
A	0	0	100	415	5.87
B		5	95	450	6.37
C		10	90	470	6.65
D		15	85	420	5.94
E	10	0	90	425	6.02
F		5	85	480	6.79
G		10	80	490	6.94
H		15	75	430	6.09
I	20	0	80	400	5.66
J		5	75	440	6.23
K		10	70	460	6.51
L		15	65	390	5.52

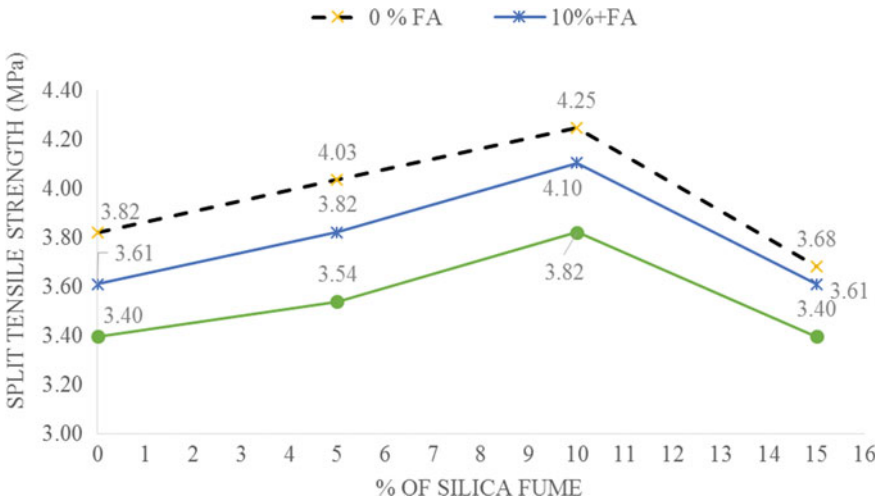

Fig. 7 Cylinder split tensile strength at 7 days

the SF partial replacement, increasing trend is shown in the strength till 10% SF and then there is decrement in strength due to further addition of SF for all % of SF. It is observed that the split tensile strength showed an increasing trend for all percentage partial replacement of FA till 10% but optimum value is obtained at 10% FA and 10% SF partial replacement. At this partial replacement the percentage increase is 18.23% than that of control mix.

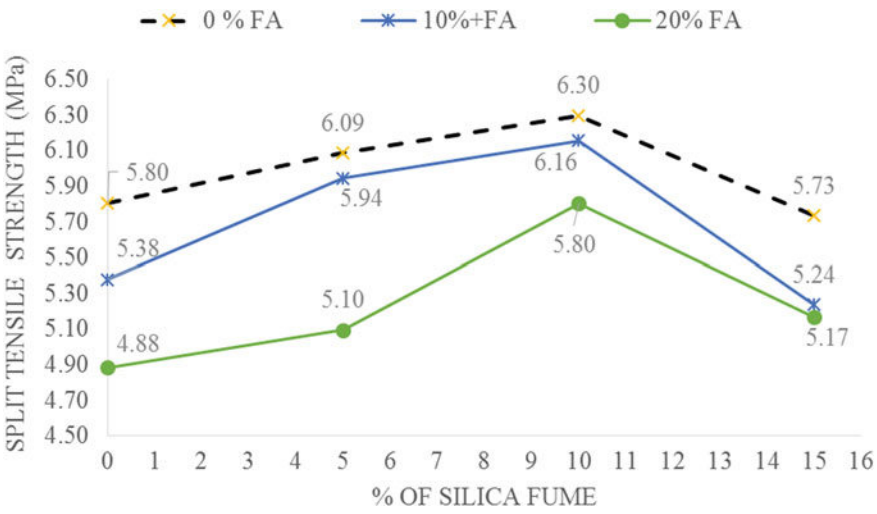

Fig. 8 Cylinder split tensile strength at 28 days

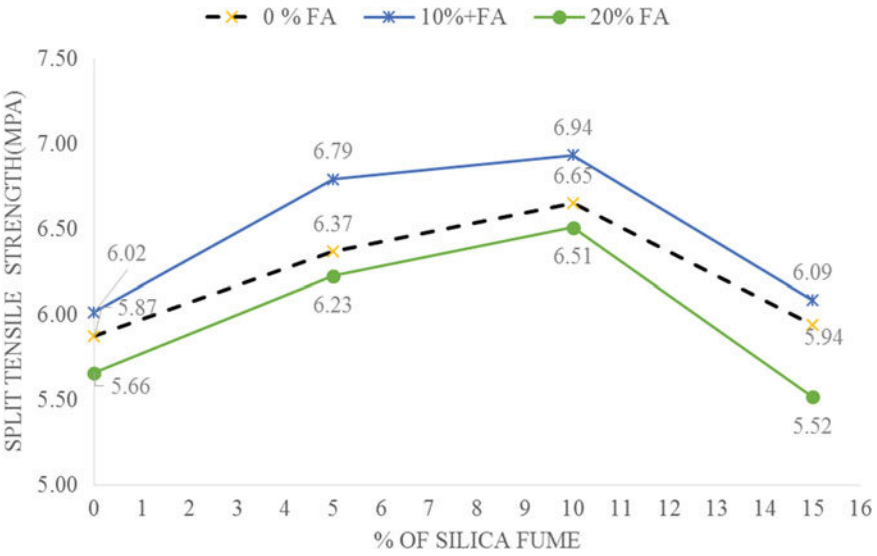

Fig. 9 Split tensile strength at 90 days

5 Conclusions

The physical and mechanical properties of different materials in the experimental program are studied and the different properties of concrete were studied. Based on the results and discussion elaborated in preceding units, the following can be concluded in nutshell:

i. On increasing the percentage partial replacement of cement with FA (0, 10, and 20%), there is decrease in the compressive and split tensile strength of concrete at 7 and 28 days.
ii. There is an increase in compressive and split tensile strength of concrete for all partial replacement of cement with FA at 90 days.
iii. At 10% partial replacement of cement with FA at 90 days, the percentage increase in compressive and split tensile strength of concrete is 2.55% and 2.55%, respectively.
iv. By increasing the percentage partial replacement of cement with SF (0, 5, 10%), there is increase in the compressive and split tensile strength of concrete at 7, 28, and 90 days up to 10%.
v. Further increase in the % partial replacement of cement with SF, i.e., beyond 10%, there is decrease in the compressive and split tensile strength of concrete at 7, 28, and 90 days.
vi. The optimum values for compressive and split tensile strength are obtained at 0% FA and 10% SF at 7 and 28 days for cement partial replacement with FA and SF.
vii. At 90 days, the optimum values for compressive and split tensile strength are obtained by partial replacing cement with 10% FA and 10% SF.
viii. At 90 days, the percentage increase for compressive and split tensile strength is 14.01% and 18.22%, respectively.

References

1. State-of-the-Art Report on High- Strength Concrete (1992) ACI 363R-92, ACI Committee 363 Report, American Concrete Institute, Detroit
2. Harald J (2012) How to make concrete more sustainable. ICI J 13(1):28–39
3. Vatsal P, Niraj S (2013) A survey of high performance concrete developments in civil engineering field. Open J Civ Eng 3(2):69–79
4. Memona, AH, Radin SS, Zainc MFM (2002) Effects of mineral and chemical admixtures on high-strength concrete in seawater. Cem Concr J
5. Mullick AK (2007) Performance of concrete with binary and ternary cement blends. ICJ J
6. Muhamad I (2009) Effect of mineral admixtures on high strength concrete made with locally available materials. Jordan J Civ Eng 3
7. Amudhavalli NK, Jeena M (2012) Effect of silica fume on strength and durability parameters of concrete. Int J Eng Sci Emerg Technol 3(1):28–35
8. Bhanja S, Sengupta B (2004) Influence of silica fume on the tensile strength of concrete. Cem Concr Res 35:743–747

9. Juenger MCG, Ostertag CP (2004) Alkali–silica reactivity of large silica fume-derived particles. Cem Concr Res 34
10. Kadri EH, Roger D (2009) Hydration heat kinetics of concrete with silica fume. Constr Build Mater 23:3388–3392
11. Malhotra VM, Mehta PK (1996) Pozzolanic and cementitious materials. Overseas Publishers, pp 191
12. Mehta PK (2003) High-performance, high-volume fly ash concrete for sustainable development. J Concr Int 3
13. Roongta U, Dewangan D, Dr. Usha D (2004) Addition of fly-ash beyond BIS limit in portland pozzolana cement. R&D Work Cleaner Environment
14. Donald B (2006) The durability of concrete containing high levels of fly ash. The University of New Brunswick
15. Gopalakrishnan S, (2005) Demonstration of utilizing high volume fly ash based concrete for structural applications. Structural Engineering Research Centre, Chennai
16. Vanita A (2008) Concrete durability through high volume fly ash concrete. Research Scholar, CED, NIT, Haryana, India
17. Gandage AS, Kalantri A, Dixit B (2010) Study of the properties of concrete with processed fly ash. ACECON 607–613
18. Bala MS, Mohan GG, Santhi AS (2010) Behaviour of class C and class F fly ash in high volume fly ash concrete. ACECON 639–644
19. Pofale AD, Deo SV (2010) Replacement of natural sand by fly ash in concrete. ACECON 657–665
20. Nataraja MC, Das L (2010) Concrete mix proportioning as per IS 10262:2009-comparison with IS 10262:1982 and ACI 211.1-91. The Indian Concr J 84(10):64–70
21. Basu PC, Saraswati S (2006) Are existing IS codes suitable for engineering of HVFAC?. The Indian Conc J 80(10):17–21
22. Maiti SC, Agarwal RK (2006) Concrete mix proportioning. The Indian Concr J 80(12):23–26
23. Indian standard code of practice for, "Concrete mix proportioning – Guidelines" IS 10262 – 2009, Bureau of Indian Standards, New Delhi
24. Sinha Deepa A (2002) Comparative mechanical properties of ternary blended concrete. Indian J Res 1:65–69
25. Indian standard code of practice for, "Methods of sampling and analysis of concrete", IS 1199 – 1959, Bureau of Indian Standards, New Delhi
26. Shetty MS (2009) Concrete technology. S. Chand & company Limited, New Delhi
27. Indian standard code of practice for, "Methods of tests for strength of concrete", IS 516 – 1959, Bureau of Indian Standards, New Delhi
28. Indian standard code of practice for, "Concrete admixtures—specification", IS 9103 – 1999, Bureau of Indian Standards, New Delhi
29. Indian standard code of practice for, "Specification for 53 grade ordinary Portland cement", IS 12269 - 2013, Bureau of Indian Standards, New Delhi
30. Indian standard code of practice for, "Specification for coarse and fine aggregates from natural sources for concrete", IS 383 – 1970, Bureau of Indian Standards, New Delhi
31. Indian standard code of practice for, "Methods of test for aggregates for concrete", IS 2386 (Part III)—1963, Bureau of Indian Standards, New Delhi

Water Resource Engineering

Bathymetric Mapping for Shallow Water Using Landsat 8 via Artificial Neural Network Technique

Arun Patel, S. K. Katiyar, and Vishnu Prasad

Abstract Bathymetric measurement using remote sensing can be replaced by the conventional technique which reduces the cost and labor required for bathymetric measurement. It can also overcome the complications in provision required during spatial and temporal depth estimates. But to obtain bathymetric information from multispectral satellite imagery using remote sensing techniques requires many corrections such as atmospheric, bottom albedo water and bottom reflectance, attenuation coefficient, and concentration of suspended solid constituents such as organic and inorganic, etc. Sometimes it is practically impossible to apply such correction to imagery because of non availability of field data. Therefore, there is a need to have faster and practical approach to hand the complex relationship between satellite reflectance and water depth for finding bathymetric measurement. The methodology based on Artificial Neural Network (ANN) is very simple to derive bathymetric maps in shallow water via reflectance's value of imagery and sample depth measurement. ANN techniques used simple approach for deriving of the depth estimation possibility, without refining image reflectance value in the depth causing scattering from environmental parameters such as type of vegetation and bottom material available. In this paper, the best linear or non-linear mathematical models to be fitted for bathymetric application are applied on Upper Lake Bhopal using Landsat 8. For this, the best fitting curve, linear with single and multi band, polynomial fit for first, second and higher degree, ratio and exponential-based algorithm, and ANN models were tried. The main conclusions are ANN model have produced lowest pass, chi-square test, and RMSE value as compared to other models.

Keywords Bathymetric · Remote sensing · Spectral reflectance · Depth · ANN

A. Patel (✉)
Department of Civil Engineering, Vedica Institute of Technology, RKDF University, Bhopal, India
e-mail: arunpatel123@gmail.com

S. K. Katiyar · V. Prasad
Department of Civil Engineering, M.A.N.I.T-Bhopal, Bhopal, India

© Springer Nature Singapore Pte Ltd. 2021

K. K. Pathak et al. (eds.), *Recent Trends in Civil Engineering*, Lecture Notes in Civil Engineering 77, https://doi.org/10.1007/978-981-15-5195-6_55

1 Introduction

A bathymetric monitoring of water resources is essential for its existence. If continuous monitoring is not done, it increases the silt deposited rate which declines in life period of reservoir. Therefore monitoring based on bathymetric is significant for the existence of water resources [1, 2]. Due to external agent changes are fast in water bed therefore bathymetric maps are often difficult to obtain, unavailable, or outdated. The conventional method of bathymetric survey using shipboard-based echo-sounders is very time consuming, labors and not cost effective for continuous monitoring [3, 4]. Many researchers have demonstrated the power of successful usage of remotely based Air/Spaceborne sensor for bathymetric surveying [5, 6]. In bathymetry survey using remotely sensed data, several remote sensing methods have been applied either to measure water depths directly or indirectly to estimate water depths through water surface movements using depth inversion modeling.

Some important researches have suggested to linear or non-linear model for determining the bathymetry under different conditions. Polcyn and Lyzenga [7] have used empirical-based model (non-linear model), applied on the ERTS Multispectral Scanner (MSS) (Single band)-based linear mode of the signal is directly proportional to the radiance at the detector. Author concluded that MSS band 4 (0.5–0.6 μm) has better penetration as compared to band 5 (0.6–0.7 μm), band 6 (0.7–0.8 μm) band 7 (0.8–1.1 μm). Lyzenga [4] had used empirical-based model (non-linear model) for determination of bathymetric information. In this method regression-based approach was used to find the log of the ratio between two spectral bands (555 and 670 nm). It is applied on Landsat MultiSpectral Scanner, and selection of band depends upon the bottom type. This model has higher depth determination as compared to ratio basis algorithm in which maximum penetration for the band 4 (0.4–0.5 μm) and band 5 (0.5–0.6 μm) are as deep as 25 m and 6 m, respectively. This is due to a close relationship that exists between remote sensing reflectance and water depth, using a single band reflectance for water bodies of uniform bottom reflectance and optical properties are even throughout. If the optical properties are not uniform, multiple bands must be used to derive bathymetric depth. This method is simple to use and able to find variances in water depth only when there is homogenous bottom material. Tripathi et al. [8] have used linear regression model single band1 (IRS-1C LISS-III) for bathymetric mapping. Significant conclusion was that depth estimation could produce up to a reasonable accuracy $R2 = 0.97$, and correction for turbidity of the water was also taken into account while determining depth. Dierssen et al. [9] used the second-order polynomial empirical model based on seafloor reflectance, and radiative transfer modeling was applied on the high-resolution hyperspectral imager for determination of depth information. In this research work, high resolution with wavelength varies with 555 and 670 nm was used and accuracy of $R2 = 0.97$ was achieved but it is a site-specific relationship. Stumpf et al. [10] had proposed a ratio model (non-linear model) for estimation of depth. Author has suggested that modification in the bottom albedo should affect both spectral bands equally, but the modification in attenuation with depth will be greater than the alteration attributable

to bottom albedo so that the ratio between two bands should remain comparable over different substrates at the similar depth. The outcomes of author's work had demonstrated that the ratio tranform is suitable for clear water, retrieve depth in >25 m and shows greater stability for different areas. But in linear transform it does not distinguish depths of 15 m and is more subjected to variability across the study area. Ozcelik and Arisoy [1] had used ANN's non-linear analysis on two imageries such as ASTER three-band images and Quick bird pan sharpen image. Significant conclusion was that there are great advantages of ANN-based model, because it helps to solve the complex relationship between reflectance value and depth without considering other correction over the image such as bottom reflectance's and vegetation, etc. Application of ANN model could decrease spatial and repetitive depth measurement requirements in bathymetric mapping. Patel et al. [2] had used ANN-based non-linear model that was applied on the Lower Lake Bhopal using LISS-IV for determination of the temporal changes which occurred in the Lower Lake Bhopal. Literature review made above reveals that various authors had used different remote sensing satellite imageries, and a diverse linear/non-linear model was used for bathymetric applications. For processing satellite imageries, various corrections such as atmospheric, bottom albedo water and bottom reflectance, attenuation coefficient, and concentration of suspended solid constituents such as organic (Chlorophyll) and inorganic (Dissolved Organic Carbon), etc. were applied over it for obtaining depth information. Selection of linear or non-linear models was based on the imagery and other conditions. These models are sometimes impractical to apply under different conditions for bathymetric determination. From the above literature reviews, few authors such as Ozcelik and Arisoy [1] and Patel et al. [2] had worked on the non-linear model (ANN techniques) for bathymetric application. So it had wide scope of investigation of application of ANN-based model for handling the complex relationship between reflectance value of image and water depth. The advantage of ANN-based modeling is that no heavy correction is needed to apply on imagery for simulation of depth. In the present research work, an attempt has been made to determine the best linear/non-linear model fitted for Upper Lake Bhopal. For this the best fitting curve, linear with single and multi band, polynomial fit first, second and higher degree, ratio algorithm developed by Stumpf [10], and ANN models were tried for bathymetric determination.

2 Study Area and Data Resources

Bhopal city is also known as "City of Lakes", which is capital of state of Madhya Pradesh, India, situated at 23°11′30.44° N latitude and 77°27′59 E longitude with an average elevation of 523 m above mean sea level. The upper lake is main lake of Bhopal situated in the midst of Vindhyachals and is an important source of drinking water (almost 35%) for Bhopal city. Ministry of Environment and Forests, New Delhi have given Upper and Lower lake status of Wetland of National importance. These lakes are fighting for their survival because of great environmental stress due

Table 1 Morphometric features of the Upper Lake Bhopal [13]

S.no.	Morphometric features	Upper Lake
1.	Period of construction	Eleventh century
2.	Catchment area	361 km^2
3.	Submergence area at FTL	30.72 km^2
4.	Storage capacity	101.5 M.Cum.
5.	Maximum depth	117.5 m
6.	Sewage wastewater inflow	5.381 M/day
7.	Total silt lad from catchment area	036 M cum/Annum

to pollution from various sources, eutrophication, silting, organic matter inputs, and human encroachment [11]. Morphometric features of Upper lake Bhopal [12] is given in Table 1.

3 Data Used

In this research work, Landsat 8 image is obtained from United States Geological Survey (USGS); and for investigation using seven bands, spatial property of these bands is shown in Table 2; and date of acquisition is May 12, 2013. Water depth is collected by Differential GPS (DGPS) and ecoshouner, horizontal position of the vessel during Hydrographic Surveying (HS) is fixed by using DGPS, which is widely used nowadays. GPS can produce height information into many datum formats but the most desirable model format is WGS 84.

Table 2 Spatial and spectral resolution of Landsat 8

S.no	Band		Spectral band (μm)	Spatial resolution (m)
1	Band 2	Blue	0.45–0.51	30
2	Band 3	Green	0.53–0.59	30
3	Band 4	Red	0.64–0.67	30
4	Band 5	Near Infrared (NIR)	0.85–0.88	30
5	Band 6	Short-Wave Infrared (SWIR) 1	1.57–1.65	30
6	Band 7	Short-Wave Infrared (SWIR) 2	2.11–2.29	30
7	Band 8	Cirrus	1.36–1.38	30
8	Band 9	Panchromatic	0.50–0.68	15

4 Theoretical Background

4.1 Radiometric Correction Methods for Landsat 8 Imagery

Landsat 8 data is provided by the USGS EROS Center. It is standard data which consists of quantized and calibrated scaled Digital Numbers (DN) representing multispectral image data. Operational Land Imager (OLI) and Thermal Infrared Sensor (TIRS) are sensors used to acquire Landsat 8 imagery. It is 16-bit unsigned data in integer format and it also provided metadata file (MTL file) which contains radiometric coefficient that is used to rescale Top Of Atmosphere (TOA) reflectance/radiance value of spatial/non-spatial feature value. Conversion of DN values to TOA reflectance (Eq. 1) and Correction for the sun angle (Eq. 2) are as follows [14].

$$\rho\lambda' = M_\rho Q_{\text{cal}} + A_\rho \tag{1}$$

where $\rho\lambda$ = TOA planetary reflectance, without correction for solar angle, M_ρ = Band-specific multiplicative rescaling factor from the metadata (REFLECTANCE_ MULT_BAND_x, where x is the band number), A_ρ = Band-specific additive rescaling factor from the metadata (REFLECTANCE_ ADD_ BAND _x, where x is the band number), Q_{cal} = Quantized and calibrated standard product pixel values (DN)

$$\rho\lambda = \frac{\rho\lambda'}{\cos(\theta_{\text{sz}})} = \frac{\rho\lambda'}{\sin(\theta_{\text{SE}})} \tag{2}$$

where $\rho\lambda'$ = TOA planetary reflectance, θ_{SE} = Local sun elevation angle. The scene center sun elevation angle in degrees is provided in the metadata (SUN_ELEVATION), θ_{SZ} = Local solar zenith angle; $\theta_{\text{SZ}} = 90 - \theta_{\text{SE}}$.

5 Methodology

Bathymetric study should be carried out with synchronous satellite pass. The time difference between the contour map and satellite data should not be high. Therefore, synchronous to satellite pass removes the bias association which removes the temporal changes. For determination of bathymetric using remote sensing, step by step process is as follows:

1. Distributed points were in form of lines collected by HS, and the line patterns are chosen in middle of the lake in order to show the variation of underwater terrain. These points were collected in altitude, longitudes, and ellipsoidal height water depth. Depths recorded in the field by the echo sounder were corrected to

obtain depth with respect to mean sea level. To obtain the corrected depth tidal variations and echo sounder immersion were taken into consideration (Fig. 1) [8]. For observing of tidal variations in Bhopal Lake, gauge station readings were taken every hour basis for two days. On these bases, the variation of tidal was recorded and corrected depth to mean sea level (msl) was determined as follows:

$$d = d_c + d_1 + d_2 \tag{3}$$

where d = Corrected depth; d_c = correction for the immersion of echo sounder in the lake, d_1 = depth from the echo sounder to the sea bed, and d_2 = correction for tidal variation.

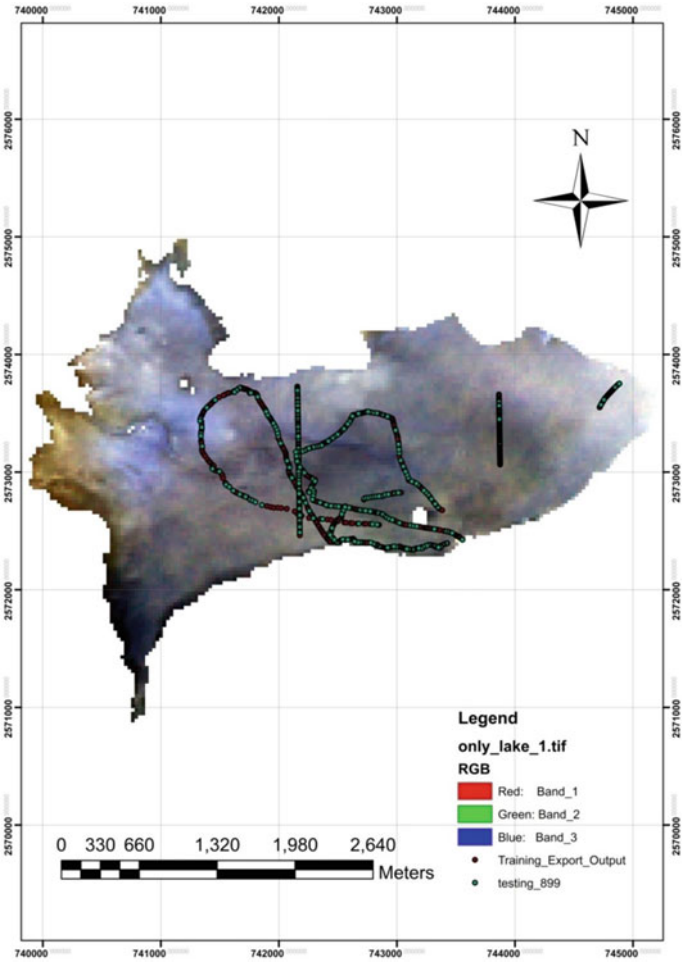

Fig. 1 Landsat_8 of Upper Lake Bhopal and DGPS samples points superimposing

2. A synchronous satellite pass Landsat 8 imagery of May 12, 2013 is downloaded from the website of USGS explore. After downloading which are already geo-references and applying radiometric correction on it and making it free from atmospheric and other parameters. Panchromatic band in the Landsat 8 is used for the fusion with the other bands, in order to have advantage of spatial resolution of panchromatic image and spectral resolution of multispectral image. Table 2 Spectral and spatial resolution of Landsat 8 is used for bathymetric measurement. Remaining seven bands were used for bathymetric measurement application.
3. The water depth points have superimposed on the Landsat 8 imagery as shown in Fig. 1. Extracting the spectral reflectance values of seven visible bands and its corresponding depths after superimposing the sample points over satellite imagery is used for bathymetric modeling.
4. This reflectance's value of 7-visible bands (X_1 to X_7 details are given in Table 2) of Landsat 8 and corresponding depth was used for bathymetric measurements. For finding the relationship between reflectance's value and depth of water dividing these samples, into training and testing data, samples points about 1347 numbers and 337 numbers were taken as training and testing, respectively, for mathematical model creation.
5. Some important linear and non-linear model were applied in order to correlate depth with reflectance's values for the determination of bathymetric model. To determine the best fitting curve, linear with single and multi band, polynomial fit first, second and higher degree regression analysis were tried and ratio algorithm developed by Stumpf (2003) was also applied to it.
6. The bathymetric extraction analysis using ANN model developed in MATLAB is given below [15].

    - The structure of the artificial network is first defined by the comment function feedforward backpropagation (*newff*), activation functions are chosen as Gradient descent backpropagation (*traingd*), Levenberg-Marquardt backpropagation (*trainlm*), BFGS quasi-Newton backpropagation (*trainbfg),* Resilient backpropagation (*trainrp*), etc. The random weights and biases are initialized with comment *initnw*.
    - The training algorithm with user defines parameters like error goal, maximum number of epochs (iterations), etc., which are defined.
    - Randomly assigning weights to the first layer as an input.
    - The first layer has weights coming from the input. Other subsequent layers have weights based on the previous layers.
    - The training algorithm is run.
    - Next step is to simulate the output date of the ANN with the measured input date and to compare its efficiency.
    - Final validation is carried out with independent data.

For analysis purpose various combinations of internal parameters, i.e., number of bands, data partitioning approach, data pre/post-processing, error goal to minimum, number of hidden layers to be used, number of neurons in each hidden layer, type of

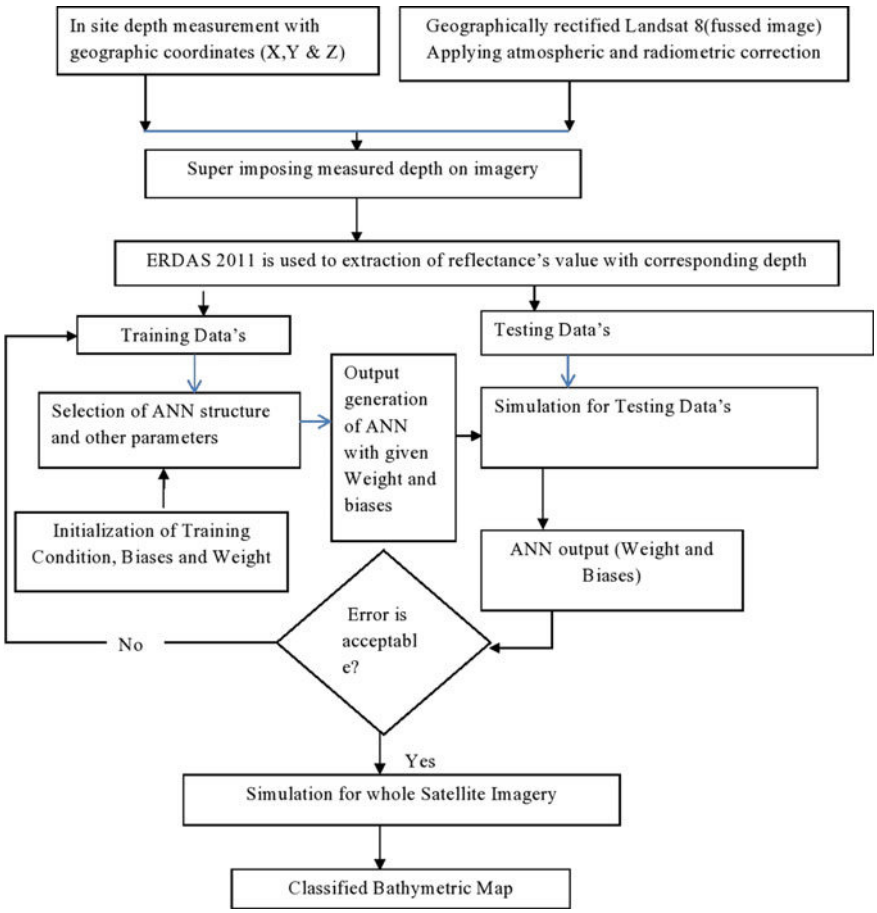

Fig. 2 Steps involved in bathymetric mapping using ANN

transfer function is to be used, etc., were adopted. Sequence of experiment process is adopted as followed by inflow chart as shown in Fig. 2.

7. Various statistical tests such as chi-test were used for evaluation of the results.

6 Result and Discussion

Bathymetric study should be carried out with synchronous satellite pass which means the time difference between the contour map and satellite data should not be high. Therefore, synchronous to satellite pass removes the bias association which removes the temporal changes. For this reason, landsat 8 imagery of data May 12, 2013, freely available on website of USGS explore and bathymetric survey has carried on May 10, 2013 as shown in data resources. For preprocessing of Landsat 8 imagery

all radiometric and atmospheric correction is applied and for removing the effect of land area and clouds, Boolean filter is used for water bodies. For removal of noise, scattering effects, and other problems, Gaussian 5 × 5 filters are used from the imagery. All raster and vector data collected from field and obtain from satellite data is transform into same projection system (UTM 43 North hemisphere, WGS84 datum) of filtered image and depth measurements. The depth samples are divided into training and testing data samples, about 1347 number of points were taken as training and 337 number of points were taken as testing as shown in Fig. 1.

Results obtained by applying some important linear and non-linear transformations were applied in order to correlate depth with reflectance's values for determination of bathymetric model. The results obtained after fitting curve, linear with single and multi band, polynomial fit first, second, higher degree regression analysis, ratio algorithm developed by Stumpf (2003) and other exponentials model developed by various authors were tried, and the statistical parameters of the models were shown in Table 3. From above statistical analysis of the models, it is clear from Table 3 as once we increase the number of parameters such as number of bands and models (linear and non-linear), RMSE decreases with increase by number of bands and by applying nonlinear model as shown in Table 3. This is because the information

Table 3 Various models used and its statistical parameters

Model	Description of models		R^2	RMSE
1	Linear regression model using single band (blue band) with depth [8]	$Z = a_0{*}X_1 + a_1$	0.019	1.65
2	Multiple linear regression model using two bands (blue and green band) [2]	$Z = a_0 + a_1{*}X_1 + a_2{*}X_2$	0.09	1.58
3	Multiple non-linear (polynomial) regression model using two bands [2]	$Z = a_0 + a_1{*}X_1 + a_2{*}X_2 + a_3{*}X_1^2 + a_4{*}X_1{*}X_2 + a_5{*}X_1^3 + a_6{*}X_1^2{*}X_2$	0.15	1.54
4	Ratio algorithm [10]	$Z = m_i \frac{(\ln(nR_W(\lambda_i)))}{(\ln(nR_W(\lambda_j)))} - m_0$	0.18	1.48
5	Multiple linear regression analysis using seven bands [9]	$Z = a_0 + a_1{*}X_1 + a_2{*}X_2 + a_3{*}X_3 + a_4{*}X_4 + a_5{*}X_5 + a_6{*}X_6 + a_7{*}X_7$	0.39	1.38
6	Exponential function [16]	$R = r * e^{-2k} + c * \left(1 - e^{-\mathrm{kz}}\right)$	0.015	8.54
7	Exponential function [17]	$L_{\delta Z} = L_{0\delta} * e^{-e_\theta Z}$	0.005	12.18

$a_0, a_1, a_2, a_3, a_4, a_5, a_6, a_7$ are coefficients of relations; Z is depth; m_i is a tunable constant to scale the ratio to depth; n is a constant to ensure the ratio remains positive under all values; R_w is observed reflectance of blue band ($R_w(\lambda_i)$) and green Band ($R_w(\lambda_j)$) and m_0 is the offset for a depth of Z = 0; $X_1, X_2, X_3, X_4, X_5, X_6, X_7$ all seven bands of Landsat 8 from Table 2. R = Reflectance of the water body, r = bottom reflectance, k = Sum of absorption coefficient of water and backscattering coefficient of water C = backscattering coefficient of water $L_{\delta Z}$, = Radiance which under the sea surface depth is Z, $L_{0\delta}$ = Water surface downwell radiance, e_θ = Attenuation coefficient of water, Z = Depth of water

stored in each band and good non-linear model is helpful for solving the bathymetric problem using Landsat 8 in shallow water. There is a need to have such a non-linear model which can handle non-linear relationship with greater accuracy. Therefore using ANN model-based approach handled complex non-linear relationship between depth and reflectance value of satellite imagery.

6.1 Model 8: ANN Model

For solving complex world problems which are non-linear and complex in nature, ANN-based approach has produced reliable and practical solution to it. For bathymetric application based on remote sensing, reflectance's values of water body in imagery play a vital role. There are various environmental factors which affect reflectance's values such as type bottom material and flora underwater. ANN-based approach use reflectance's values directly without applying much correction to above mention factors under water [1]. There are various neural network, among them Feedforward Backprojection Algorithm (FFBPA) has produced better result. Basic structure of FFBPA is shown in Fig. 3, where m, n, and y are, respectively, node, input layer, and output layer; $w[1, \ldots, m)$ = weight of input layer; $w[1, \ldots, n)$ = weight of hidden layer; let bin are the biases; $X[1, \ldots, m]$ is input vector (reflectance from mth band); $Y(x)$ is the expected output vector (water depth). For generation the samples are divided into training and testing data samples, about 1347 number of points were taken as training and further these input samples are divided into training, testing, and validation points. For formation of the model consider 70% of data for training, 20% of data testing, and 10% of data as validation points. Apart from these data, which is not taken in model formation, 337 numbers of points were taken a testing.

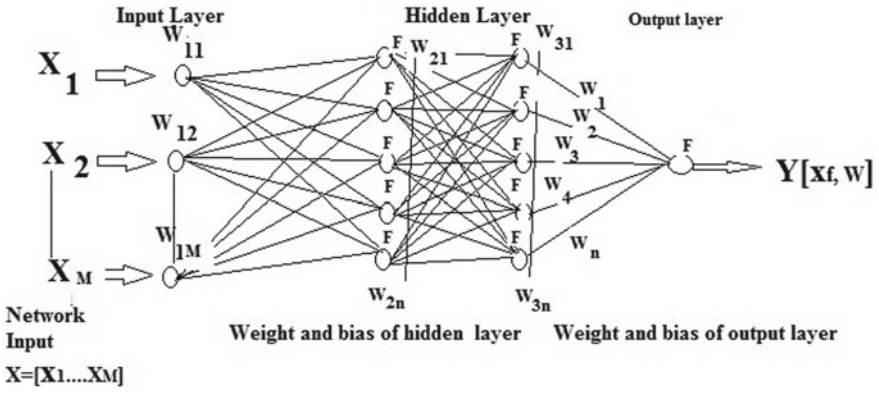

Fig. 3 A general ANN architecture used in depth estimations [1]

There are two important steps involved in model preparation. First step includes the selection of parameter such as number inputs/output for model, model architecture, etc. The spectral reflectances of the bands and in situ depth measurements are basic input for ANN model. The spectral reflectance should be processed before using as input in ANN model. It should be processed as geometric rectification, radiometric correction (high-pass filters), and scaling/rescaling of the model inputs and outputs. Second step involved the selection of structure ANN. Many authors have investigated on input/output data constrained by some factorial problem which involved in choosing the number of input and output factors based on requirement for ANN model architecture [18]. In multi-layer ANN, the number of nodes input is based on the number of input spectral bands and for output layer the number is one since there is only one output (water depth). There is no hard and fast method to determine the number/nodes inner layer and neuron from nodes to have best performance ANN models, some author had experiment with performed many investigations to determining it [19]. Determination of optimum number of hidden layers and neurons for each hidden layers for ANN structure is done experimentally because they are function of expected intelligence [20]. It had suggested by many authors that the use of single hidden layer can be very powerful to solve non-linear complex problem [21]. Experimental parameters as shown in Table 4 are obtained from result of train and test data after training, testing, and validation process of ANN model. It is observed that the best computational for training Feedforward Backpropagation (FFBPA) networks with Levenberg–Marquardt (lm) algorithm maximum and minimum the MSE and efficient of regression are given in Table 5 and graphical results are shown in Figs. 4 and 5.

It is found that in such an analysis there are many parameters like quality of input/output data, network structure, and training algorithm are the most important factors because network parameter is limited. Post regression analysis and its

Table 4 Parameters used in neural network generation

Type of neural network	Feedforward backpropagation
Number of hidden layers	1
Number of hidden neuron	10
Number of epochs	1000
Assign weight/bias	Random
Weight learning function	LM-Algorithm
Transfer function of layer in hidden layer	Tan-sigmoid
Transfer function of layer in output layer	Pure linear

Table 5 Best performances under the given parameters

S. no	Band	Type of ANN network	MSE (m)	R
1	ANN model	FFBP	0.75	0.90

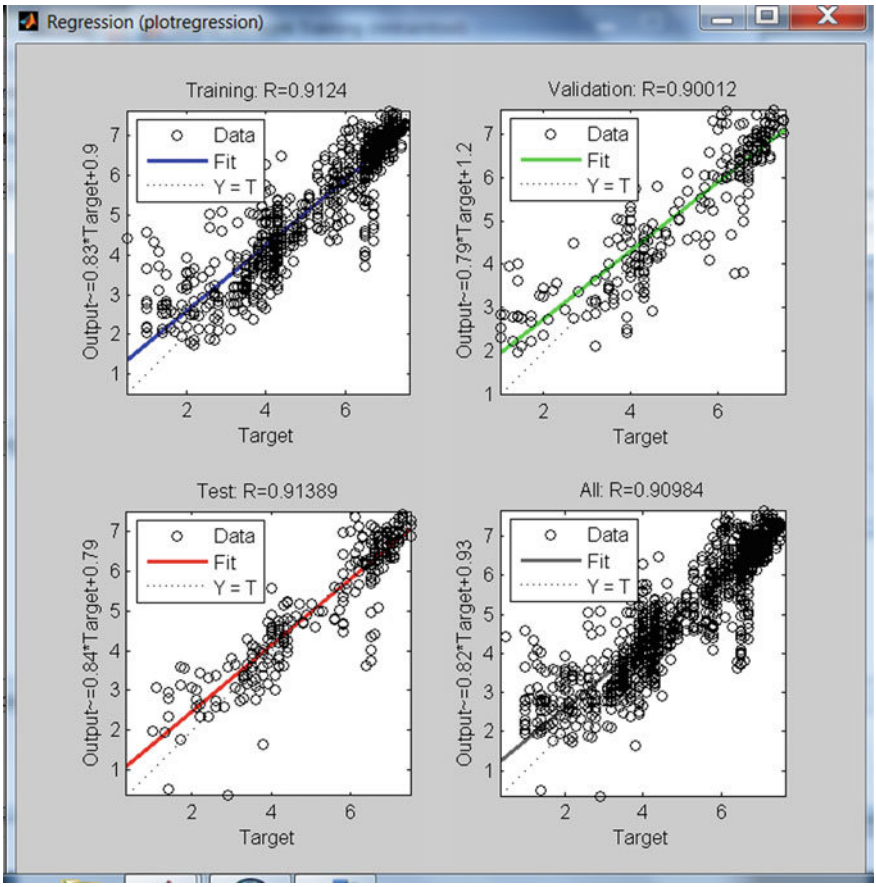

Fig. 4 Plot regression of training, testing, and validation data by ANN in matlab

comparison of the output at each bus show that output obtained after running several times were sufficiently accurate if well-organized training is conducted to reduce the redundancy and normalizing the inputs as well as outputs [21].

Results obtained by network training sample are considered to be satisfactory, due to many constrain in the location and its distribution data collection over the area. It is very good if data is well distributed over the area. The data used such as spectral resolution and distribution of sample points for generating model effect the model generation. The size and quality of the imager used to generate model are very important due to the following factors, i.e., variation in bottom material, pollution, and vegetation are major sources of affecting the reflectance of water column. For building an appropriate model, the input data chosen should be representative and concurrent. It is assumed that the bathymetric changes are slight or homogenous on the references points. However, these changes in water bodies should not be abrupt between the date of acquired image and depth measurements [1, 2].

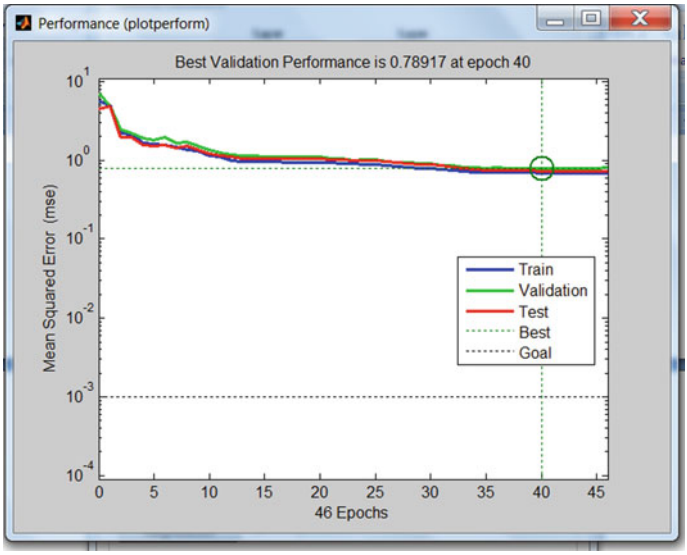

Fig. 5 Best validation performances of ANN model

6.2 Classification Accuracy of Imagery Using Models

From below-classified contour maps generated after applying, these models in the imagery and classification of depth predicted by the models are shown in Fig. 6a–h. The contour map generated most précises by ANN model (Fig. 6h) is more accurate as compared to other models because maximum depth contour variation during bathymetric survey of upper lake is 0–10 m and variation of contour line in contour map.

6.3 Validation of Models and Discussion

Bathymetric classified image using six different models and models were validated using 337 test point are shown in Fig. 1. Parameters of the above models were calculated with the help of 1347 nos of water depth sounding points of known location. Goodness of fit of above models was tested using chi-square test of the different models are given in Table 6. In chi-square test, critical values from the tables are 379.74 for degree of freedom 336. The model-8 (ANN Model) has produced lowest pass chi-square test value, RMSE among the other model, and it is also low as compared to other models. Therefore ANN model for Upper lake Bhopal is preferred for depth determination.

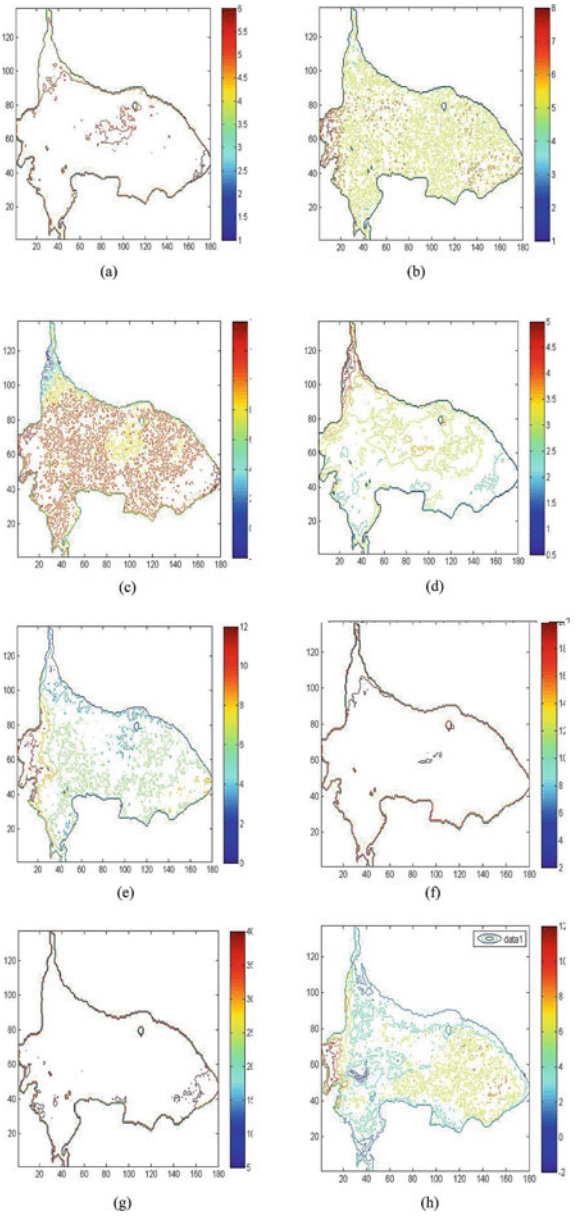

Fig. 6 **a–h** Classified bathymetric contour maps in meters by different models **a** linear single-band regression **b** linear regression double band **c** multi-polynomial using double-band regression **d** ratio bands method (Stumpf 2003) **e** multi linear using seven-band linear regression **f** exponential model developed by Yoshitani and Tushino [16] for shallow water **g** exponential model developed by Yi and Li [17] for shallow water **h** ANN modeling

Table 6 Validation results of various models

S. no	Type of model	Model description	Chi-square test
1	Model 1	Linear regression model using single band (blue band) with depth [8]	672.26
2	Model 2	Multiple linear regression model using two bands (blue and green band) [2]	552.03
3	Model 3	Multiple non-linear (polynomial) regression model using two bands [2]	528.66
4	Model 4	Ratio algorithm [10]	807.38
5	Model 5	Multiple linear regression analysis using seven bands [9]	514.33
6	Model 6	Exponential model [16]	2603.06
7	Model 7	Exponential model [17]	2619.06
8	Model 8	ANN Model	52.58

6.4 Discussion

Landsat 8 imagery spatial resolution of 30 m can be used for bathymetric mapping. It is applied on Upper Lake Bhopal, satisfactory result are obtained for very shallow-water areas that had lower reflectance than deep water, therefore the linear transform could not give better result [10]. Due to the presence of dense algae or seagrass cover over a shallow water area they are less reflective than deep water; Investigation was carried out in shallow area where patches of algae were found that is why it does not give proper bathymetric information at corner area in any of the models. So the linear transformation is unable to solve the problem of the low-albedo issue; solution this problem has been proposed by Hengel and Spitizer [18]. Hengel and Spitizer [18] suggest that tuning is required to the patch as well, whereas the ratio method requires only two parameters: m_0 and m_1. However, due to the presence of high noise in the water, the ratio transform has limitations relative to the linear transform, particularly in an increased level of noise. The ratio solution is simple to implement, and it requires tuning which can be achieved with a handful of accurate soundings and correction applied to image. In case multi-band regression analysis fails to identify the changing material and vegetation of the water body, it makes problematic to use regression using multi-band analysis [1]. Identifying the non-linear and complex relationship occurs between image reflectance's and depth. Therefore, there is wide scope to use ANN model-based approach which should be capable of solving both the problems.

Significant features of the ANN methodology are as follows:

- The environmental elements such as type of bottom material and vegetation are the important parameters that contribute to estimation of depth using reflectance values of imagery. ANN-based modeling does not consider such environmental factors while analysis.

- Apart from environmental factors there are other multi-parameter relationships that occur between multispectral reflectance from the various spectral bands and water depth. It can be easily solved using ANN.
- It doesn't require the spatial and repetitive depth measurement.
- Due to free from various corrections to be applied, this makes ANN method more consistent and practically applicable among the researcher for bathymetric.

7 Conclusions

The following conclusions are drawn from the above investigation:

1. The important parameter for bathymetric map generation is technique adopted for water depth measurement. This method should be accurate and reliable to produce practical solutions for bathymetric measurement.
2. The result obtained using Landsat 8 data of 30 m resolution were applied on the Upper Lake Bhopal, due to its non-linear relationship with spectral reflectances of bands and water depth. Many regression-based models based on single-, double-, and multi-bands, and ratio-based algorithm were applied. It has failed to produce desired results due to change in bottom type, pollution, vegetation, and resolution of imagery. ANN model based on FFBPA provided a better result as compared to other models because of its capability of handling non-linear relationships. ANN model are structure free and have capability to handle non-linear relationships of spectral reflectances of bands and water depth, without applying heavy environmental correction to imagery.
3. ANN model have the highest coefficient of correlation, and it also produced lowest pass, chi-square test, and RMSE value among the other models.

Acknowledgments The authors are grateful to Mr. Vivek Bansal and its entire team of PAN India Consultants Pvt Ltd. Gurgaon122015 for their cooperation in rendering equipment and technical support and necessary help in conducting the bathymetric survey.

References

1. Ozcelik C, Arisoy Y (2010) Remote sensing of water depths in shallow waters via artificial neural networks. Estuar, Coast Shelf Sci, Elsevier, PP 89–96
2. Patel A, Katiyar SK, Prasad V (2016) Bathymetric mapping of Bhopal City Lower Lake IRS-P6:Liss-4 imagery using artificial neural network. J Indian Soc Remote Sens, Springer, 1–10. https://doi.org/10.1007/s12524-015-0523-8
3. Leu L, Change H (2005) Remote sensing in detecting the water depths and bed load of shallow waters and their changes. Ocean Eng 32:1174–1198
4. Lyzenga DR (1978) Passive remote sensing techniques for mapping water depth and bottom features. Appl Opt 17(3):379–383

5. Benny AH, Dawson GJ (1983) Satellite imagery as an aid to bathymetric charting in the red sea. Cartographic J 20(1):5–16
6. Ibrahim M, Seeni M, Samsudin A, Mohamad Y (1990) Bathymetry in clear waters from Landsat-5 Satellite Data. In: Proceeding of ACRS 1992, GIS development, pp 1–4
7. Polcyn FC, Lyzenga DR (1979) Landsat bathymetric mapping by multispectral processing. In: Proceedings of thirteenth international symposium on remote sensing of environment. ISPRS, Ann Arbor, MI, pp 1269–1276
8. Tripathi NK, Rao AM (2002) Bathymetric mapping in Kakinada Bay, India, using IRS-1D LISS-III data. Int J Remote Sens, Taylor and Francis 23(6):1013–1025
9. Dierssen HM, Zimmerman RC, Leathers RA, Downes TV, Davis CO (2003) Ocean color remote sensing of seagrass and bathymetry in the Bahamas Banks by high-resolution airborne imagery. Limnol Oceanogr 48:444–455
10. Stumpf RP, Holderied K, Sinclair M (2003) Determination of water depth with high resolution satellite imagery over variable bottom types. Limnol Oceanogr 48:547–556. http://dx.doi.org/10.4319/lo.2003.48.1_part_2.0547
11. Kulshrestha SK (1988) Review of studies on Bhopal Lakes. In: Proceeding, past, present and future of Bhopal Lakes, pp 11–22
12. Misra SM, Pani S, Bajpai A, Bajpai AK (2001) Assessment of trophic status by using Nygaard Index with special reference to Bhoj Wetland. Poll Res 20(2):1–7
13. Gupta SL (2007) Preliminary survey of Upper Lake, Bhopal in rainy season with reference to Algal Flora. In: Proceedings of Taal 2007: the 12th world lake conference. Bhopal, pp 2031–2032
14. USGS (2019) Landsat mission: using the USGS Landsat Level-1 data product. https://www.usgs.gov/land-resources/nli/landsat/using-usgs-landsat-level-1-data-product. Accessed 11 Jul 2019
15. Mark HB, Martin TH, Howard BD (2015) Neural network toolbox-user guide MatLab. https://www.mathworks.com/help/pdf_doc/nnet/nnet_ug.pdf.Accessed 27 Sep 2016
16. Yoshitani J, Tushino Y (1988) Water depth estimation based on attenuation and bottom reflectance. In: Proceedings of the ninth Asian conference on remote sensing. Bangkok, Thailand, p F-9–1
17. Yi G, Li T (1988) The ocean information contents of remotely sensed image and the acquisition of water depth message. In: Proceedings of the ninth Asian conference on remote sensing. Bangkok, Thailand, p F-3-1
18. Hengel WV, Spitizer D (1991) Multi-temporal water depth mapping by means of Landsat TM. Int J Remote Sens 12(4):703–712
19. Freeman JA, Skapura DM (1991) Neural networks algorithm application and programming techniques. Addison-Wesley publishing company Inc. ISBN-0-201-51376-5
20. Goyal S, Goyal GK (2011) Cascade and feedforward backpropagation artificial neural network models for prediction of sensory quality of instant coffee flavoured sterilized drink. Can J Artif Intell, Mach Learn Pattern Recognit 2(6):78–82
21. Uma K, Potdar RM (2011) Matlab based artificial neural network model for prediction of melt down temperature in steel making matlab based artificial neural network model for prediction of melt down temperature in steel making. IJEMS 2(4):229–232

Land Suitability Assessment for Agriculture Using Analytical Hierarchy Process and Weighted Overlay Analysis in ArcGIS ModelBuilder

Ayush Tiwari and Sunil Ajmera

Abstract In this study, we utilize the concept of Analytical Hierarchy Process (AHP) and the functionalities of ArcGIS ModelBuilder towards a multiparametric classification of land regimes of Dewas District of Madhya Pradesh, based on their aptitude for agriculture. The study follows FAO's land suitability criteria and uses data from Landsat-8 OLI+ (NDVI, NDWI, Land Use/Land Cover), ASTER-GDEM V2 (Elevation, Slope, Drainage), ISRIC Soilgrid (Soil Characteristics), OpenStreetMaps (road/river/well proximity) and India WRIS (Groundwater Depth). The methodology involves defining the evaluation criteria, creating Pairwise Comparison Matrix (PWCM), assigning relative degree of importance to the 18 chosen parameters, preparing raster maps, performing Weighted Overlay Analysis (WOA) in ArcGIS ModelBuilder to generate the land suitability map and comparing it to the land use/land cover map. The results help us identify the potentials and constraints of land parcels for agriculture, designating 17.8% (1,24,970 ha) area as highly suitable, 57.3% (4,02,294 ha) area as moderately suitable and 24.9% (1,74,818 ha) area as marginally suitable. The suitability analysis can help build justified land use policies and devise logical agrarian management strategies by recommending agricultural exclusivity in highly suitable areas.

Keywords AHP · Weighted overlay analysis · Pairwise comparison matrix · ModelBuilder · Landsat-8 OLI+

A. Tiwari (✉)
Indian Institute of Technology Indore, Discipline of Civil Engineering, Khandwa Road, Simrol, Madhya Pradesh, India
e-mail: ayushtiwari@iiti.ac.in

S. Ajmera
Department of Civil Engineering and Applied Mechanics, Shri Govindram Seksaria Institute of Technology and Science, 23, Park Road, Indore, Madhya Pradesh, India
e-mail: sbajmera@gmail.com

© Springer Nature Singapore Pte Ltd. 2021

K. K. Pathak et al. (eds.), *Recent Trends in Civil Engineering*, Lecture Notes in Civil Engineering 77, https://doi.org/10.1007/978-981-15-5195-6_56

1 Introduction

India possesses 2.4% of world's geographical area, 4% of world's renewable water resources and holds 18% of world's population [1]. India's total food grain production during 1999–2000 was 208MT, during 2006–2007 it was 209.2 MT and it needs to be raised to 350 MT by 2050 [2, 3] to feed the expected population of 1390M. On the contrary, since 1995–1996, the average size land holding has decreased from 1.41 hectares to 1.15 hectares which accounts for a decrease in cultivable land at the rate of 30,000 ha/year. With an increase in population, decrease in percentage of farmers and with problems like drought and floods in various states, one can fathom the seriousness of the issue [4].

Madhya Pradesh (M.P.) is the second largest state of India. Its population growth rate is 20.4%, higher than that of India (17.6%) [5]. According to Directorate of Census Operation of M.P., District Dewas has tenth largest urban population and fourteenth largest urban area of M.P. [6]. Lowering groundwater levels, excessive fluoride content in groundwater, late commencing and erratic rainfall are regular scenes in Dewas. According to Central Ground Water Board's Aquifer Mapping Report, only 50% of district's net sown area is actually irrigated [7]. According to District Census Handbook, Dewas (2011), there has been 19.53% increase in its population between 2001 and 2011 [8]. The rate and the extent of urbanization in Dewas may challenge its agriculture scene in future.

A land regime once urbanized cannot be reclaimed again for agriculture. Post urbanization, agriculture can only be practiced on what is left open, irrespective of its appropriateness. Wastelands in India assume 67 Mha of the land use pattern, out of this cultivable wasteland constitute 20%. Clearly, there is a mismatch between land aptitude and land use. Land use should be in conjunction with its inherent capability to achieve long sustained agricultural productivity. In order to increase crop output and achieve food security, crops must be grown in areas where they are best suited. To generate the maximum agricultural production, land regimes must be utilized in an environmentally compassionate, socially justified and economically feasible manner. It is often observed that the land is either overused or underused or improperly used without examining its potential and constraints for that intended purpose. In order to increase/maintain the productivity per land unit, crops must be grown in areas where they are best suited. Remote Sensing and GIS-based Land Suitability Assessments (LSAs) should be performed before every major land-use-related decision to assure respectable use of natural resources and to control any unsustainable shifts and transformations.

LSA is an inter-disciplinary approach defined by FAO [9] as 'The analysis of land performance when used for a specified purpose, involving the execution and interpretation of anatomization-based surveys and studies of land forms, soils, vegetation, climate and other characteristics of land in order to identify and make a comparison of promising kinds of land use in terms of suitability to the objectives of the evaluation'. Land is categorized into spatially distributed agriculture potential zones based on soil and terrain characteristics and hydroclimatic constraints [10].

Through Analytical Hierarchy Process (AHP), dissimilar inputs from these parameters are combined and processed to form a single index of evaluation [11, 12]. AHP can integrate huge amount of heterogeneous data and deduce the relative weights of the parameters [13–15] facilitating the selection of best alternative amongst multiple options [16]. In this study, we combine the concept of AHP with geospatial modelling and create a decision support system to classify the district's land regimes and identify the potential land parcels for agriculture. In order to stop conversion of agriculture land for non-agricultural purposes, the government has formulated the National Policy for Farmers 2007 (NPF 2007) [17] and the National Rehabilitation and Resettlement Policy 2007 (NRRP 2007) [18]. The present study aims to make the implementation of these policies easier and more accurate.

2 Study Area

Dewas lies between 20°17′N and 23°20′N latitude and 75°54′E and 77°08′E longitude, falling under Survey of India Toposheets 46M, 46N, 55A, 55B and 55F and UTM zone WGS1984 43N [19]. Dewas covers an area of 7020.84 km^2 with a population of 1,563,715 [8]. It is situated at an altitude of 555.5 m above mean sea level. It falls under Agro-Ecological Sub-Region 5.2 (hot semi-arid moist eco-region) [20]. The district has six administrative blocks: Tonk Khurd, Dewas, Sonkach, Kannod, Khategaon and Bagli as shown in Fig. 1. There are three national highways (NH-3, NH-86, NH-59A). The average annual rainfall is 1083 mm. Narmada, Kali Sindh and Kshipra are the three main rivers. There are four physiographic regions, such as Dewas Plateau, Vindhyan Range, Kali Sindh Basin and Middle Narmada Valley. Hydrogeology is largely Basalt. Black cotton soil is the major soil type. Groundwater contains alkaline earth–bicarbonate. There are two major drainage basins: The Ganga (North) and The Narmada (South). Groundwater is 'alkaline earth–bicarbonate (Sangemini)' and accounts for 82% of irrigation. The principal crops are soya bean, wheat, groundnut and cotton [21].

3 Methodology

3.1 Preparation of Parameter Maps

The District Administrative Boundary shapefile is obtained from DivaGIS [22]. The units of the parameters are shown separately in Table 4. All the maps are projected (geometric correction) to World Geodetic System (WGS) 1984 datum and Universal Transverse Mercator (UTM) Zone 43N (Fig. 2).

The digital elevation model given in Fig. 3 is prepared using ASTER GDEM V2 product [23] for 21 January 2018. The DEM is a [1 × 1] degree tile and has a spatial

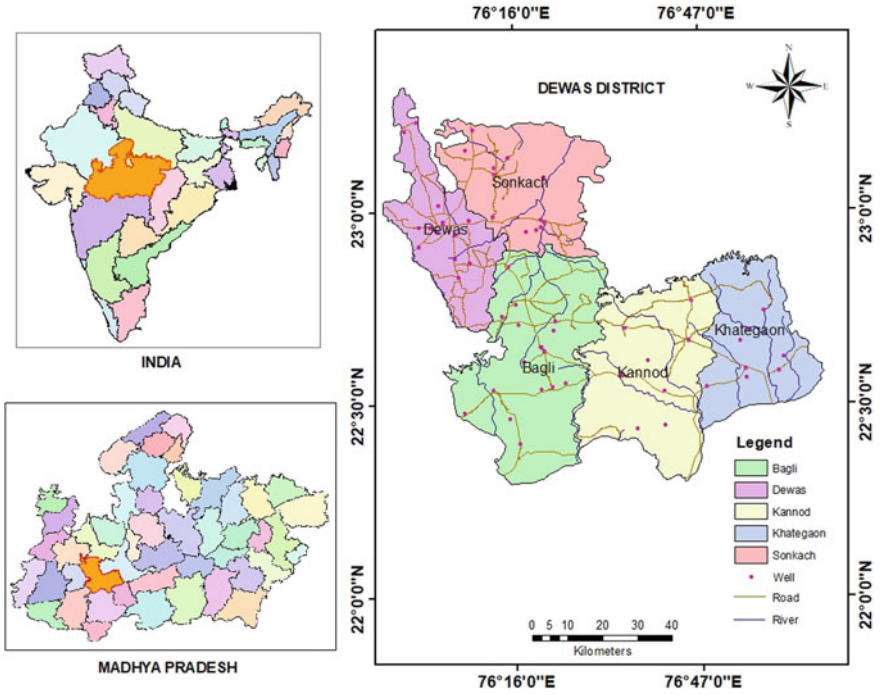

Fig. 1 Study area

resolution of 30 m. The slope map given in Fig. 4 is derived from the DEM using 'Slope' Spatial Analyst tool.

The drainage density map is prepared using 'ArcHydro Tools' extension [24] for ArcGIS. Consecutive terrain processing operations, fill sink < flow direction < flow accumulation < stream definition < stream segmentation < stream order, are performed on the DEM to obtain the drainage map given in Fig. 5. 'Line Density' tool is applied on the drainage map to obtain drainage density map given in Fig. 6. Efficient drainage prevents cases of waterlogging or excessive infiltration.

The multi-temporal (*MTL.txt) Landsat-8 OLI+ image for 26 February 2018 (Path: 146/Row: 44) given in Fig. 7 obtained from USGS Earth Explorer [25] is subjected to automatic cloud detection and haze removal (radiometric correction) using PCI Geomatica. Iso-cluster unsupervised classification is performed in ArcGIS to prepare the land use/land cover map given in Fig. 8 which is then verified from Google Earth [26].

Net Differential Vegetation Index (NDVI). Map shown in Fig. 9 is prepared from Landsat-8 Band-4 and Band-5 in 'Raster Calculator' as shown in Eq. 1.

$$(\text{Band}_5 - \text{Band}_4) \big/ (\text{Band}_5 + \text{Band}_4) \tag{1}$$

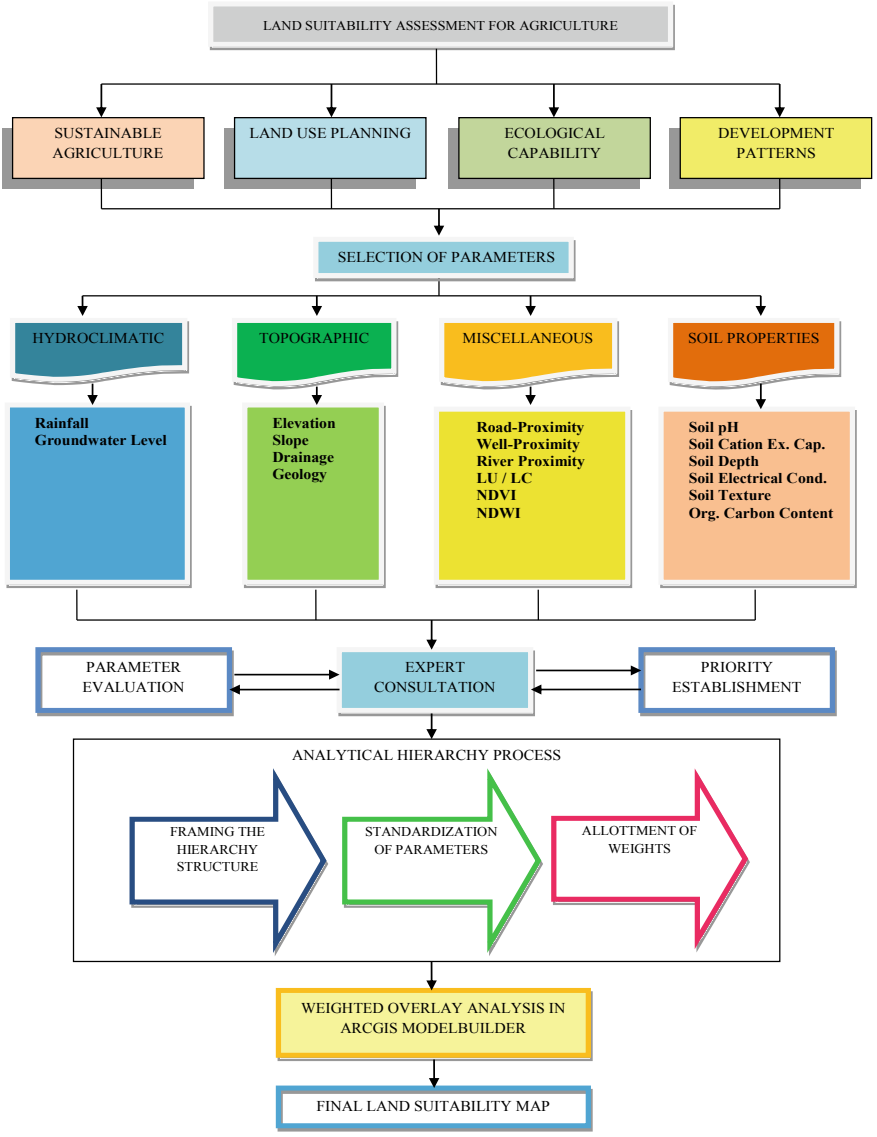

Fig. 2 Flow chart of land suitability assessment methodology

NDVI is used for estimating vegetation health from remote sensing data. NDVI is a numerical indicator that uses red and NIR bands of the electromagnetic spectrum to detect the regions of live green vegetation (regions with greener vegetation are good for agriculture practices). According to USGS's band designations for Landsat-8 OLI+ satellite image given in Table 1, healthy vegetation (chlorophyll) reflects near-infrared light and absorbs red light.

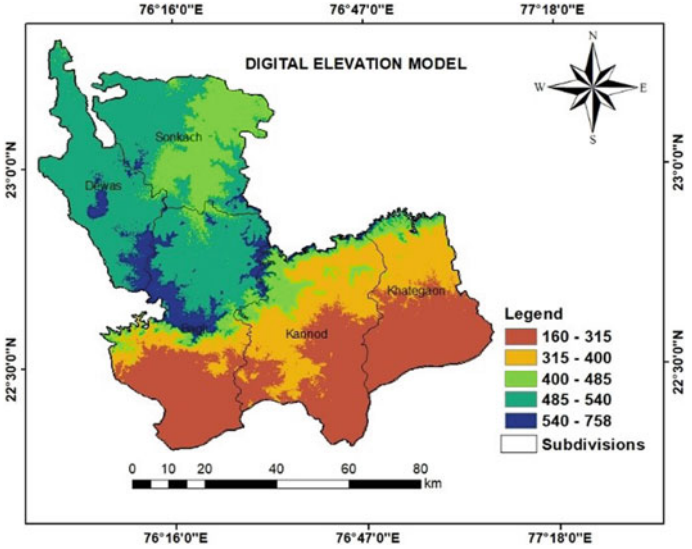

Fig. 3 Digital elevation model

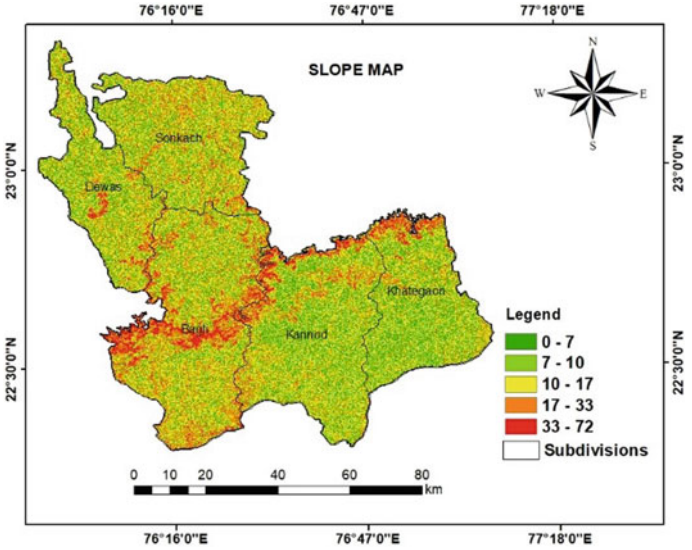

Fig. 4 Slope map

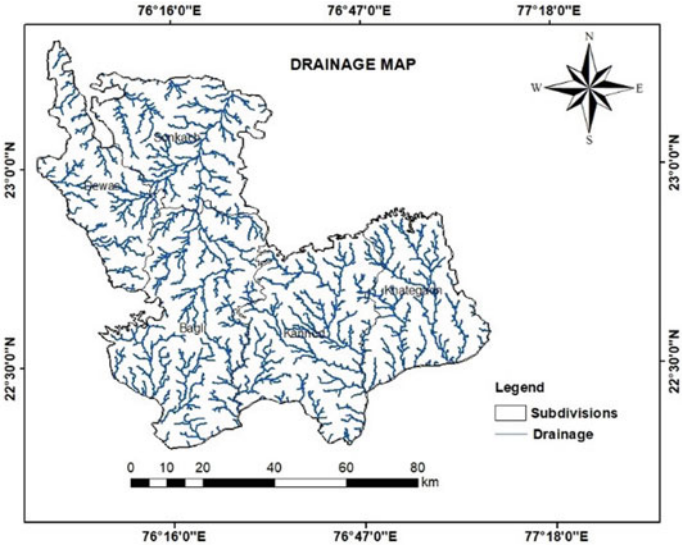

Fig. 5 Drainage map

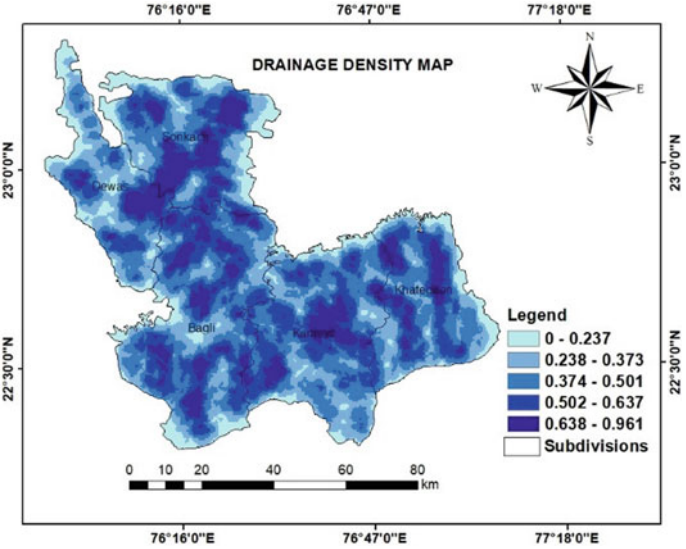

Fig. 6 Drainage density map

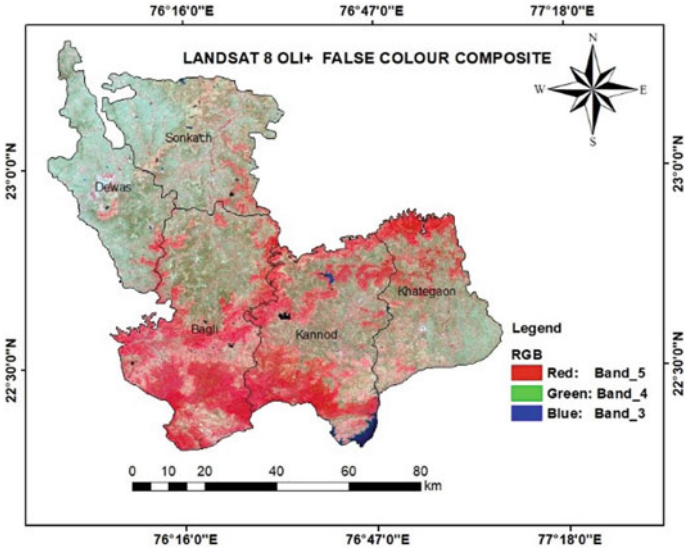

Fig. 7 Landsat-8 OLI+ FCC image

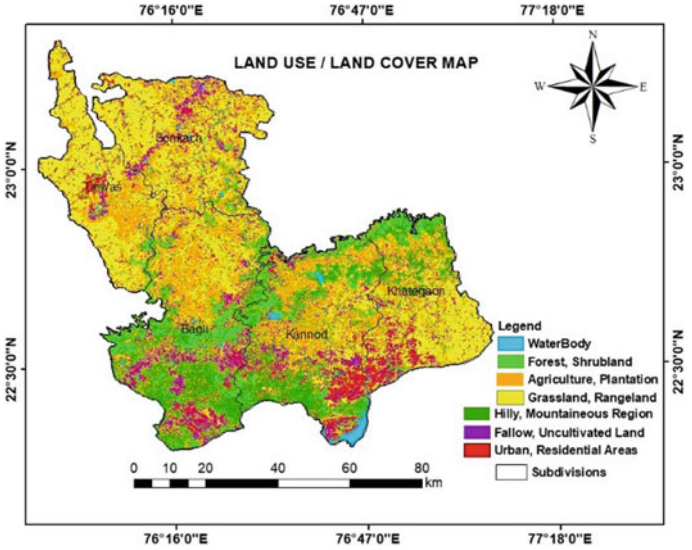

Fig. 8 Land use/land cover map

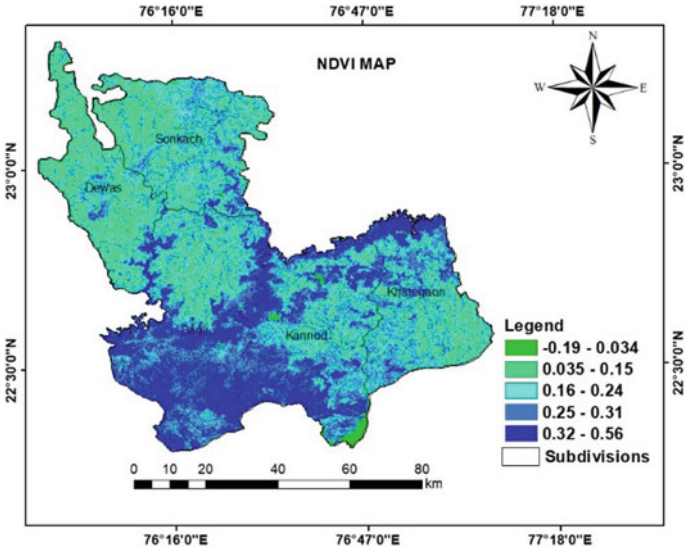

Fig. 9 NDVI map

Table 1 Band designations for Landsat-8 OLI+ satellite

No.	Band number	Wavelength (μm)	Use
1.	Band-4 (red)	0.636–0.673	Focuses on biomass content and shorelines
2.	Band-5 (near-infrared NIR)	0.851–0.879	Discriminates moisture content of soil and vegetation; penetrates thin clouds
3.	Band-6 (shortwave infrared SWIR) 1	1.566–1.651	Improved moisture content of soil and vegetation and thin cloud penetration

Source USGS Earth Explorer [27]

Normalized Difference Water Index (NDWI). Map shown in Fig. 10 is prepared from Landsat-8 Band-5 and Band-6 in 'Raster Calculator' as shown in Eq. 2

$$(\text{Band}_6 - \text{Band}_5) \big/ (\text{Band}_6 + \text{Band}_5) \tag{2}$$

NDWI detects the changes in liquid water content of spongy mesophyll of vegetation canopies. SWIR shows changes in the water content of mesophyll, whereas NIR shows changes in leaf internal structure and its dry matter content, and hence the equation.

The road proximity map shown in Fig. 11 is developed from the road network shapefile using 'Euclidean Distance' Spatial Analyst Tool. The road network shows

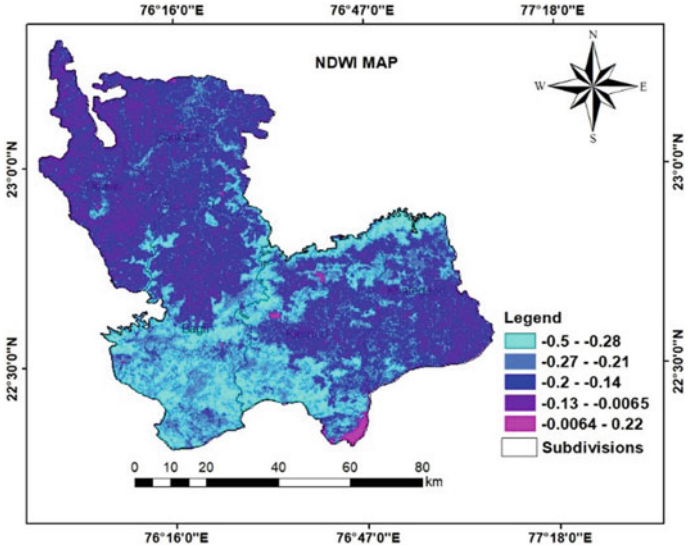

Fig. 10 NDWI map

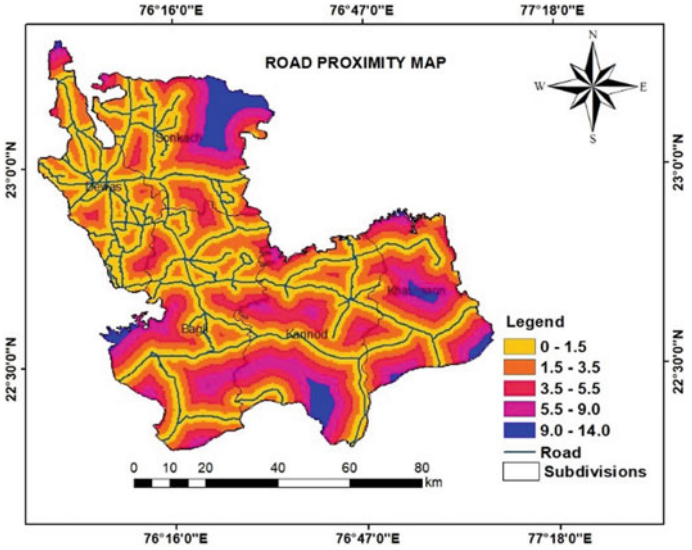

Fig. 11 Road proximity map

a line layer of road systems like national highways, state highways and major roads. The river proximity map shown in Fig. 12 and well proximity map shown in Fig. 13 are prepared in the same manner and show a line layer of river systems (Narmada, Kali Sindh and Kshipra) and a point layer of wells, respectively. The road shapefile and

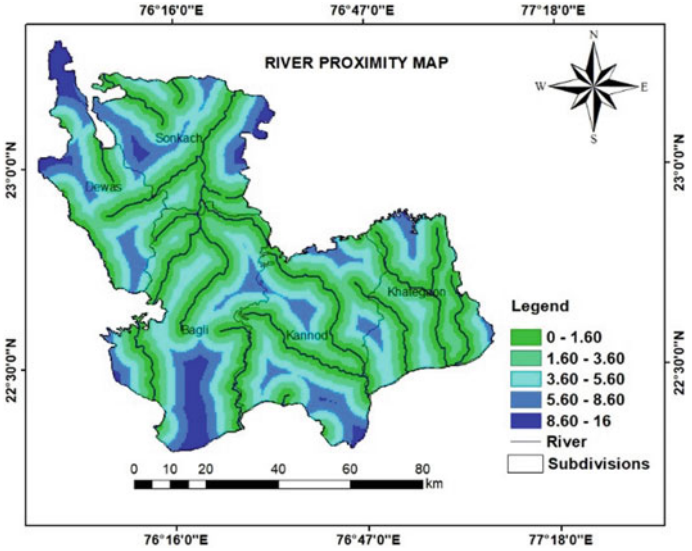

Fig. 12 River proximity map

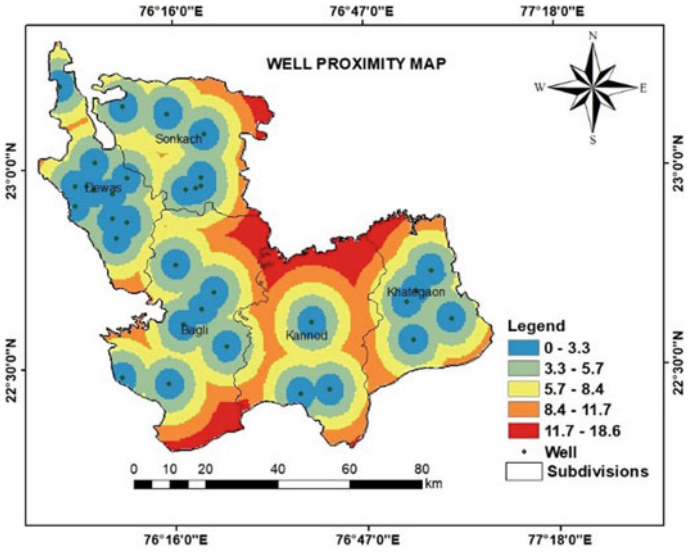

Fig. 13 Well proximity map

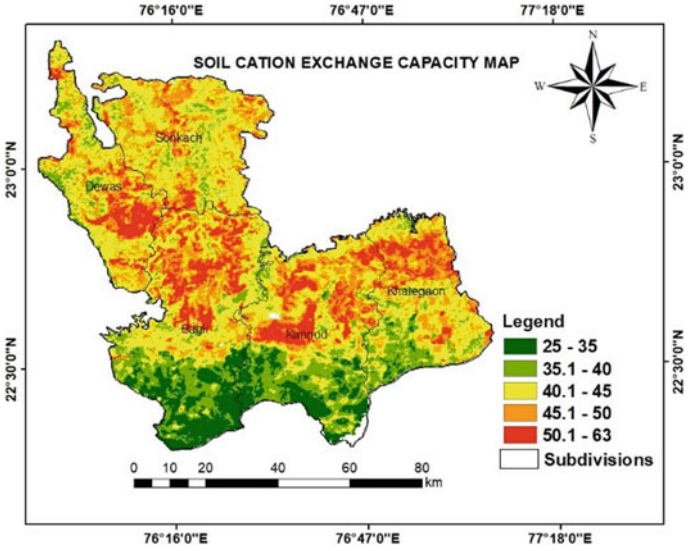

Fig. 14 Soil cation exchange capacity map

river shapefile are obtained from *OpenStreetMap* via *Geofabrik* [28]. The proximity maps are verified from 1:50,000 Survey of India (SOI) Toposheets (46M, 46N, 55A, 55B and 55F) [29].

Soil Cation Exchange Capacity (CEC) map shown in Fig. 14, Soil Organic Carbon Content (OCC) map shown in Fig. 15, Soil pH map shown in Fig. 16 and Soil Depth map shown in Fig. 17 were available from ISRIC SoilGrids [30]. CEC is the measure of negatively charged content present in soil that holds ions like calcium (Ca2+), magnesium (Mg2+) and potassium (K+) through electrostatic forces and stops them from being leached down the soil profile. It is the nutrient retention capacity of the roots [31].

OCC is a direct measure of soil fertility. OCC affects water holding capacity, nutrient availability and maintains soil structure. Soil pH is the degree of acidity/alkalinity of soil. For majority of crops, the optimal range of pH is from 5.8 to 6.8. Crops rarely survive extreme pH environments. Soil depth basically depends on the nature of the parent material on which soils were formed. For a well-drained friable soil, the maximum root depth of crops can be 200 cm. Lower depth of soil restricts plant rooting, hinders overall growth and ultimately the yield.

Soil Electrical Conductivity (EC) map shown in Fig. 18 is prepared using the remote sensing data of 202 soil sampling sites obtained from KrishiKosh [32]. The data is imported into ArcGIS as a point shapefile, followed by subjection to Inverse Distance Weighted (IDW) Interpolation tool. EC is a direct measure of salinity of soil. Plants are detrimentally affected, both physically and chemically, by excess salts in some soils and by high levels of exchangeable sodium in others. EC depends on the amount of moisture held by soil particles [33].

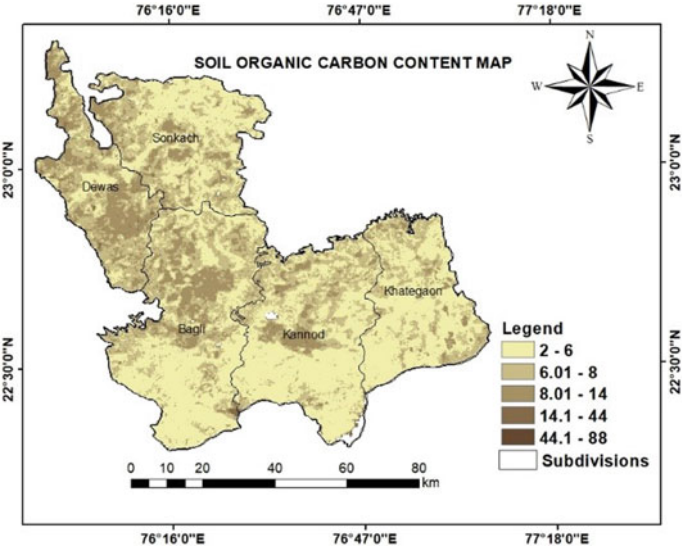

Fig. 15 Organic soil carbon content map

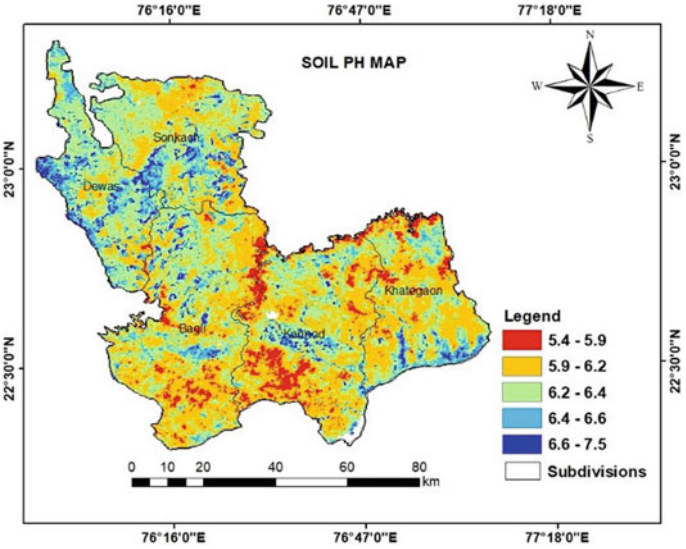

Fig. 16 Soil pH map

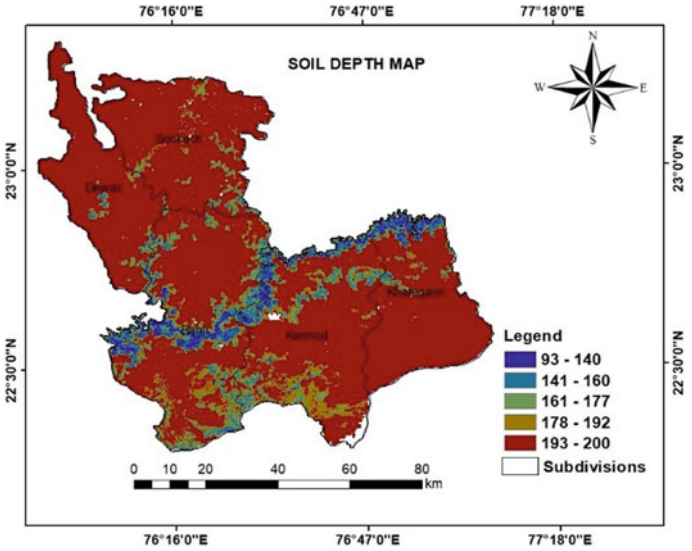

Fig. 17 Soil depth map

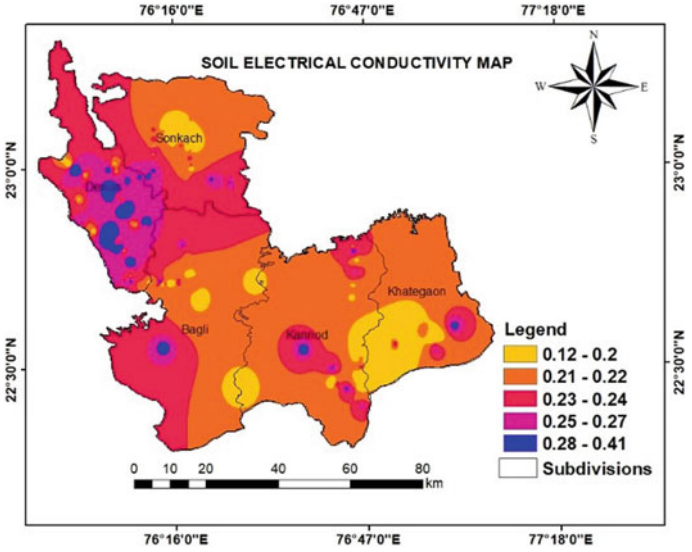

Fig. 18 Soil electrical conductivity map

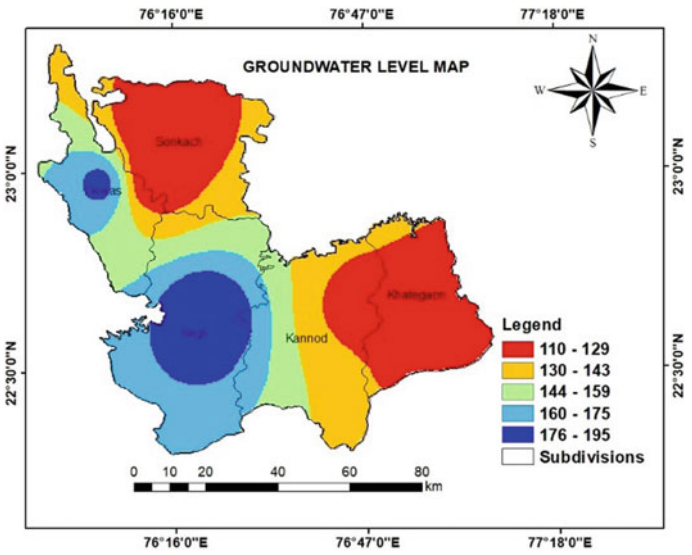

Fig. 19 Groundwater level map

The location of wells and groundwater level data are obtained from India-WRIS [34] and CGWB's Aquifer Mapping Report [7]. A point shapefile containing the coordinates of the wells and their respective water level depths is created. The groundwater depth map given in Fig. 19 is prepared using IDW tool. The annual average rainfall map given in Fig. 20 is prepared in the same manner using rainfall data (2004–2014) from Global Weather Data for SWAT [35].

The soil texture map given in Fig. 21 is prepared in QGIS Desktop 2.18 using 'Soil Texture' plug-in [36]. Soil texture is determined by the relative proportions of sand (0.05–2 mm), silt (0.002–0.05 mm) and clay (<0.002 mm) [37]. The inputs of sand map and clay map are given and the output is generated based on the rules of soil texture triangle. The geology map given in Fig. 22 is digitized from its photo image [7] using ArcScan tool and converted to raster format using 'Polyline to Raster' conversion tool.

3.2 Analytical Hierarchy Process

To assign a relative degree of importance (weight) to every parameter based on a fundamental scale [14], AHP priority calculator is used [38]. The scale ranges from 1 (equal significance) to 9 (extreme significance) as shown in Table 2. Comparisons are performed for different pairings of 18 parameters using Pairwise Comparison Matrix (PWCM) as shown in Table 3. The total number of pairwise comparisons is calculated as shown in Eq. 3:

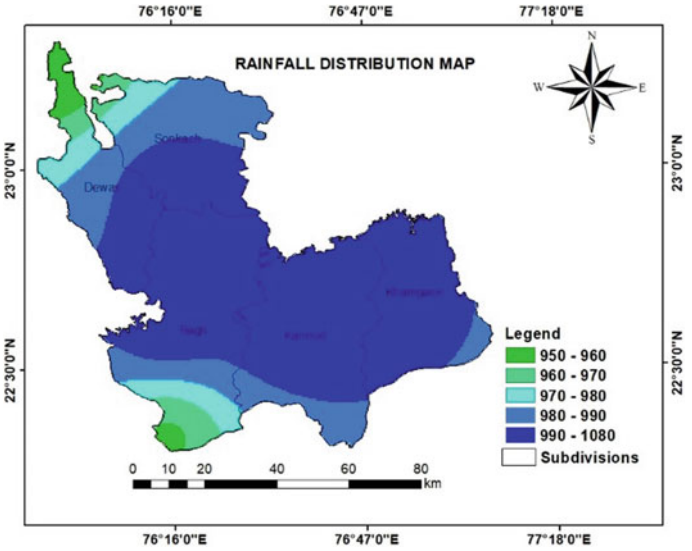

Fig. 20 Annual rainfall distribution map

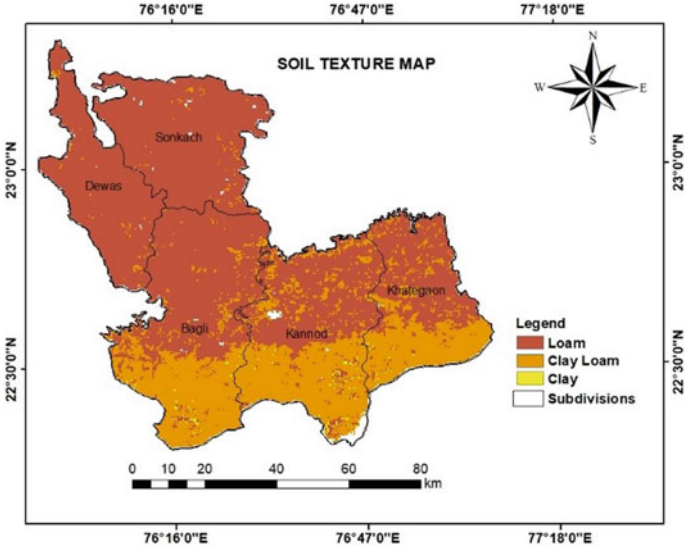

Fig. 21 Soil texture map

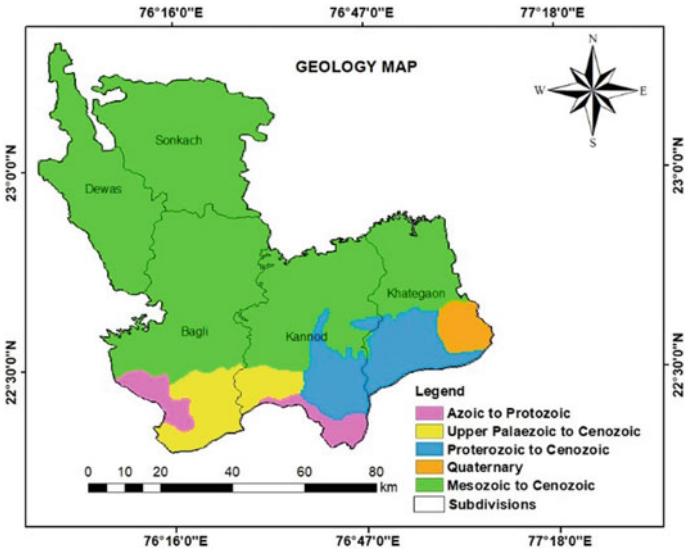

Fig. 22 Geology map

Table 2 The fundamental scale for pairwise comparison matrix [14]

Rank	Definition	Explanation
1	Equal importance	Two criteria enrich equally to the objective criteria
3	Low importance of one over another	Judgments and experience slightly favour one criterion over another
5	Strong or essential importance	Judgments and experience strongly favour
7	Established importance	A criterion is strongly favoured (dominance established in practice)
9	Absolute or high importance	The evidence favouring one criterion over another is of the highest probable order of affirmation
2, 4, 6, 8	Intermediate values between two adjacent importance or judgements	When adjustment is needed

$$\mathrm{PC} = (n(n-1)/2) \tag{3}$$

where 'n' is the number of parameters. Hence, for $n = 18$, PC = 153. Consistency ratio, an indicator of the degree of consistency/efficiency of AHP analysis, is calculated as shown in Eq. 4:

$$\mathrm{CR} = \left(\mathrm{CI}/\mathrm{RI}\right) \tag{4}$$

Table 3 Pairwise comparison matrix for AHP-MCDM

Para.	E	S	L	VI	GW	O	R	T	C	EC	WI	PH	GEO	DR	ROP	RIP	SD	WEP
E	1	1	2	2	3	3	4	4	5	5	6	6	7	7	8	8	9	9
S	1	1	2	2	3	3	4	4	5	5	6	6	7	7	8	8	9	9
L	1/2	1/2	1	2	2	3	3	4	4	5	5	6	6	7	7	8	8	9
VI	1/2	1/2	1/2	1	2	2	3	3	4	4	5	5	6	6	7	7	8	8
GW	1/3	1/3	1/2	1/2	1	2	2	3	3	4	4	5	5	6	6	7	7	8
O	1/3	1/3	1/3	1/2	1/2	1	2	2	3	3	4	4	5	5	6	6	7	7
R	1/4	1/4	1/3	1/3	1/2	1/2	1	2	2	3	3	4	4	5	5	6	6	7
T	1/4	1/4	1/4	1/3	1/3	1/2	1/2	1	2	2	3	3	4	4	5	5	6	6
C	1/5	1/5	1/4	1/4	1/3	1/3	1/2	1/2	1	2	2	3	3	4	4	5	5	6
EC	1/5	1/5	1/5	1/4	1/4	1/3	1/3	1/2	1/2	1	2	2	3	3	4	4	5	5
WI	1/6	1/6	1/5	1/5	1/4	1/4	1/3	1/3	1/2	1/2	1	2	2	3	3	4	4	5
PH	1/6	1/6	1/6	1/5	1/5	1/4	1/4	1/3	1/3	1/2	1/2	1	2	2	3	3	4	4
GEO	1/7	1/7	1/6	1/6	1/5	1/5	1/4	1/4	1/3	1/3	1/2	1/2	1	2	2	3	3	4
DR	1/7	1/7	1/7	1/6	1/6	1/5	1/5	1/4	1/4	1/3	1/3	1/2	1/2	1	2	2	3	3
ROP	1/8	1/8	1/7	1/7	1/6	1/6	1/5	1/5	1/4	1/4	1/3	1/3	1/2	1/2	1	2	2	3
RIP	1/8	1/8	1/8	1/7	1/7	1/6	1/6	1/5	1/5	1/4	1/4	1/3	1/3	1/2	1/2	1	2	2
SD	1/9	1/9	1/8	1/8	1/7	1/7	1/6	1/6	1/5	1/5	1/4	1/4	1/3	1/3	1/2	1/2	1	2
WEP	1/9	1/9	1/9	1/8	1/8	1/7	1/7	1/6	1/6	1/5	1/5	1/4	1/4	1/3	1/3	1/2	½	1

Where E is elevation, S is slope, L is land use/land cover, VI is NDVI, GW is groundwater level, O is organic carbon content, R is annual average rainfall, T is texture, C is cation exchange capacity of soil, EC is electrical conductivity of soil, WI is NDWI, GEO is geology, DR is drainage density, ROP is road proximity, RIP is river proximity, SD is soil depth up to bedrock, WEP is well proximity

Table 4 Average RI for corresponding matrix size [14, 43, 44]

n	1	2	3	4	5	6	7	8	9	10	11	12	13	14	15
RI	0	0	0.58	0.90	1.12	1.24	1.32	1.41	1.45	1.49	1.51	1.48	1.56	1.57	1.59
n	16	17	18	19	20	21	22	23	24	25	26	27	28	29	30
RI	1.60	1.61	1.62	1.63	1.63	1.64	1.65	1.65	1.66	1.66	1.67	1.67	1.67	1.68	1.68

where RI is the random index. RI depends on the order of the matrix as shown in Table 4 [13]. For $n = 18$, RI is 1.62 [14]. CI is the consistency index. It is expressed as shown in Eq. 5:

$$\mathrm{CI} = (\lambda_{\max} - n) \big/ (n - 1) \tag{5}$$

where '$\lambda_{\max}$' is the principle eigenvector and 'n' is the order of the matrix [12]. If CR < 0.10, it means that an acceptable level of consistency is achieved [13], the weights calculated are meaningful and valid [39]. In this case, CR is 0.04. The synthesized matrix is shown in Table 5. The ranking of parameters is given in Table 6. The results of AHP analysis are given in Table 7.

AHP-MCE calculates the 'weight' of every parameter by calculating the eigenvalue corresponding to the highest eigenvector of the matrix and normalizing the sum of all the parameters to unity [40, 41]. In this case, eigenvector solution is obtained after six iterations. The weights, hence, computed from AHP analysis are converted into percent for further processing in Weighted Overlay Analysis (WOA) in ArcGIS ModelBuilder. ModelBuilder is a dynamic, interactive and heavily customizable geoprocessing application of ArcGIS. It is used for data integration and data analysis. It can be regarded as a visual programming language for generating workflows. ModelBuilder is used to create, edit and manage custom-based models for a diverse stream of applications. Models are automated GIS workflows that string together sequences of geoprocessing tools that need GIS data as the initial input [42].

3.3 Weighted Overlay Analysis

Reclassification/Standardization: Initially, all the parameters have diverse and dissimilar units. Standardization converts the measurement to uniform units [39] for further processing in WOA. The parameters lose their dimensions [45]. The subcriteria are brought to a common suitability scale ranging from 1 to 10 as shown in Table 8 in order to eliminate their inherent vagueness.

Overlaying: The reclassified raster layers are overlaid by multiplying the values of their sub-criteria by their corresponding weight value [40] as shown in Eq. 6. The combined weight of all input maps should be

Table 5 Synthesized matrix for AHP-MCDM

Para.	E	S	L	VI	GW	O	R	T	C	EC	WI	PH	GEO	DR	ROP	RIP	SD	WEP
E	0.177	0.177	0.235	0.192	0.21	0.174	0.181	0.154	0.157	0.136	0.138	0.122	0.123	0.109	0.11	0.1	0.1	0.091
S	0.177	0.177	0.235	0.192	0.21	0.174	0.181	0.154	0.157	0.136	0.138	0.122	0.123	0.109	0.11	0.1	0.1	0.091
L	0.088	0.088	0.117	0.192	0.14	0.174	0.136	0.154	0.126	0.136	0.115	0.122	0.105	0.109	0.096	0.1	0.089	0.091
VI	0.088	0.088	0.058	0.096	0.14	0.116	0.136	0.115	0.126	0.109	0.115	0.101	0.105	0.094	0.096	0.087	0.089	0.081
GW	0.058	0.058	0.058	0.048	0.07	0.116	0.09	0.115	0.094	0.109	0.092	0.101	0.087	0.094	0.082	0.087	0.078	0.081
O	0.058	0.058	0.038	0.048	0.035	0.058	0.09	0.077	0.094	0.082	0.092	0.081	0.087	0.078	0.082	0.075	0.078	0.071
R	0.044	0.044	0.038	0.031	0.035	0.029	0.045	0.077	0.063	0.082	0.069	0.081	0.07	0.078	0.069	0.075	0.067	0.071
T	0.044	0.044	0.029	0.031	0.023	0.029	0.022	0.038	0.063	0.054	0.069	0.061	0.07	0.062	0.069	0.062	0.067	0.061
C	0.035	0.035	0.029	0.024	0.023	0.019	0.022	0.019	0.031	0.054	0.046	0.061	0.052	0.062	0.055	0.062	0.055	0.061
EC	0.035	0.035	0.023	0.024	0.017	0.019	0.014	0.019	0.015	0.027	0.046	0.04	0.052	0.047	0.055	0.05	0.055	0.051
WI	0.028	0.028	0.023	0.019	0.017	0.014	0.014	0.012	0.015	0.013	0.023	0.04	0.035	0.047	0.041	0.05	0.044	0.051
PH	0.028	0.028	0.018	0.019	0.014	0.014	0.011	0.012	0.01	0.013	0.011	0.02	0.035	0.031	0.041	0.037	0.044	0.04
GEO	0.024	0.024	0.018	0.015	0.014	0.011	0.011	0.009	0.01	0.009	0.011	0.01	0.017	0.031	0.027	0.037	0.033	0.04
DR	0.024	0.024	0.016	0.015	0.011	0.011	0.009	0.009	0.007	0.009	0.007	0.01	0.008	0.015	0.027	0.025	0.033	0.03
ROP	0.021	0.021	0.016	0.013	0.011	0.009	0.009	0.007	0.007	0.006	0.007	0.006	0.008	0.007	0.013	0.025	0.022	0.03
RIP	0.021	0.021	0.014	0.013	0.009	0.009	0.007	0.007	0.006	0.006	0.005	0.006	0.005	0.007	0.006	0.012	0.022	0.02
SD	0.019	0.019	0.014	0.011	0.009	0.008	0.007	0.006	0.006	0.005	0.005	0.005	0.005	0.005	0.006	0.006	0.011	0.02
WEP	0.019	0.019	0.012	0.011	0.008	0.008	0.006	0.006	0.005	0.005	0.004	0.005	0.004	0.005	0.004	0.006	0.005	0.01

Table 6 Ranking of parameters

Parameter	Weight	Rank
Elevation	15.2	1
Slope	15.2	2
Land use/land cover	12.5	3
NDVI	10.5	4
Groundwater	8.6	5
Organic carbon content	7.2	6
Rainfall	5.9	7
Soil texture	4.9	8
Cation exchange capacity	4.0	9
Electrical conductivity	3.3	10
NDWI	2.7	11
Soil pH	2.3	12
Geology	1.9	13
Drainage density	1.6	14
Road proximity	1.3	15
River proximity	1.1	16
Soil depth	0.9	17
Well proximity	0.8	18

Table 7 Results of AHP analysis

Number of parameters	18
Number of pairwise comparisons	153
Consistency ratio	4.4%
Principal eigenvalue	19.218
Eigenvector solution	6 iterations
Delta	4.5E−8

$$\mathrm{LSS} = \sum_{i=1}^{n} W_i X_i \tag{6}$$

where LSS = l and suitability score, W_i = weight of the suitability parameter, X_i = score of the sub-criteria of the suitability parameter, n = number of suitability parameters.

Addition: All the resulting cell values are finally added. The area falling under each suitability class is determined using 'Zonal Geometry as Table' Spatial Analyst Tool.

Table 8 Weights of main criteria and scores of sub-criteria

No.	Cri.	Wt.	Sub-criteria	Unit	Sc.	No.	Cri.	Wt.	Sub-criteria	Unit	Sc.
1.	E	15.2	160–315	m	10	10.	EC	3.3	0.12–0.2	dS/m	2
			315–400		6				0.21–0.22		4
			400–485		4				0.23–0.24		6
			485–540		2				0.25–0.27		8
			540–758		1				0.28–0.41		10
2.	S	15.1	0–7	%	10	11.	WI	2.7	−0.5–0.28	N/A	2
			7–10		8				−0.27–0.21		4
			10–17		6				−0.2–0.14		6
			17–33		4				−0.13–0.0665		8
			33–72		2				−0.0064–0.22		10
3.	L	12.5	Water body	m	0	12.	PH	2.3	5.4–5.9	N/A	7
			Agriculture land		10				5.9 – 6.2		10
			Grassland, Rangeland		7				6.2–6.4		9
			Hills, mountains		1				6.4–6.6		5
			Forest		3				6.6–7.5		5
			Fallow, uncultivated land		10						
			Urban areas		0						
4.	VI	10.5	−0.19–0.034	N/A	2	13.	GEO	1.9	Azoic to Protozoic	N/A	2
			0.035–0.15		4				Upper Paleozoic to Cenozoic		5
			0.16–0.24		6				Proterozoic to Cenozoic		6
			0.25–0.31		8				Quaternary		9

(continued)

Table 8 (continued)

No.	Cri.	Wt.	Sub-criteria	Unit	Sc.	No.	Cri.	Wt.	Sub-criteria	Unit	Sc.
			0.32–0.56		10				Mesozoic to Cenozoic		10
5	GW	8.6	110–129	m	2	14.	DR	1.6	0–0.237	km^2	10
			130–143		4				0.238–0.373		8
			144–159		6				0.374– 0.50		6
			160–175		8				0.502–0.637		4
			176–195		10				0.638–0.961		2
6.	O	7.2	2–6	g/kg	1	15.	ROP	1.3	0–1.5	km	10
			6.01–8		3				1.5 – 3.5		8
			8.01–14		5				3.5–5.5		6
			14.1–44		7				5.5–9.0		4
			44.1–88		10				9.0–14.0		2
7.	R	5.9	950–960	mm	1	16.	RIP	1.1	0–1.60	km	10
			960–970		3				1.60–3.60		8
			970–980		5				3.60–5.60		6
			980–990		7				5.60–8.60		4
			990–1080		10				8.60–16.0		2
8.	T	4.9	Loam	N/A	10	17.	SD	0.9	93–140	m	2
			Clay loam		7				141–160		5
			Silt loam		5				161–177		6
			Water		0				178–182		9
			Silt		1				193–200		10

(continued)

Table 8 (continued)

No.	Cri.	Wt.	Sub-criteria	Unit	Sc.	No.	Cri.	Wt.	Sub-criteria	Unit	Sc.
9.	C	4.0	25–35	cmolc per kg	2	18.	WEP	0.8	0–3.3	km	10
			35.1–40		4				3.3–5.7		8
			40.1–45		6				5.7–8.4		6
			45.1–50		8				8.4–11.7		4
			50.1–63		10				11.7–18.6		2

4 Results and Discussions

The land suitability assessment model is given in Fig. 23. The final land suitability map for agriculture is given in Fig. 24. The analysis designates 17.8% (1,24,970 ha) area as highly suitable, 57.3% (4,02,294 ha) area as moderately suitable and 24.9% (1,74,818 ha) area as marginally suitable for agriculture. A niche-based multiparametric LSA was performed in accordance with FAO (1976). The assessment faced internal variability and complexity with abundance of highly localized features. Weighted overlay analysis allowed strategic delineation of suitability regimes by integrating the diverse spatial layers encompassing 18 different environmental themes, terrain specifics and hydroclimatic vistas. The relative degree of importance between parameters was realized after considering the subjective opinions of farmers and local experts which made the results more original at grassroot level. The study benefitted from online availability of remote sensing data.

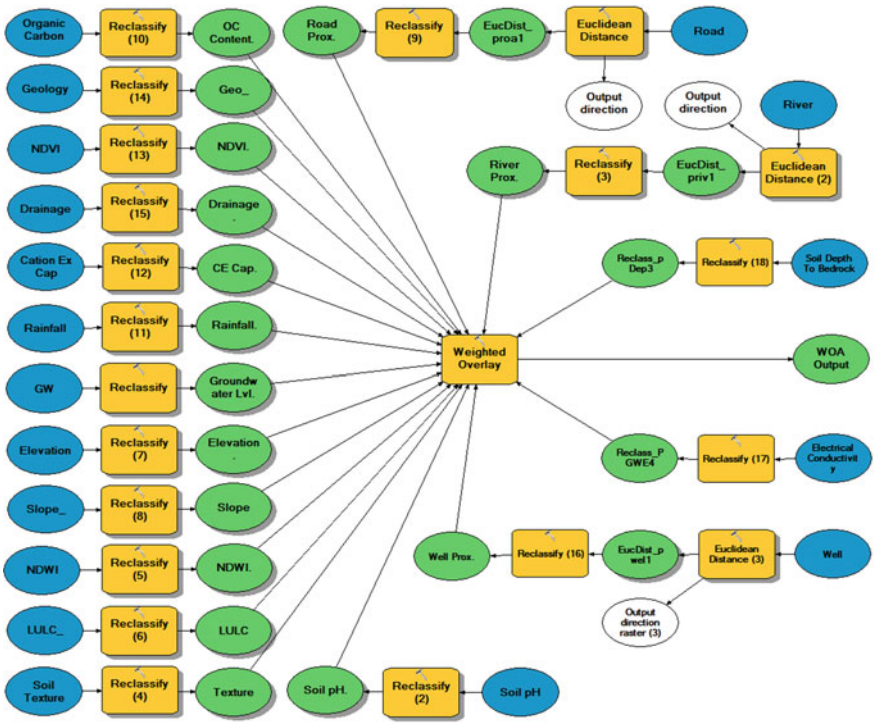

Fig. 23 Land suitability assessment model

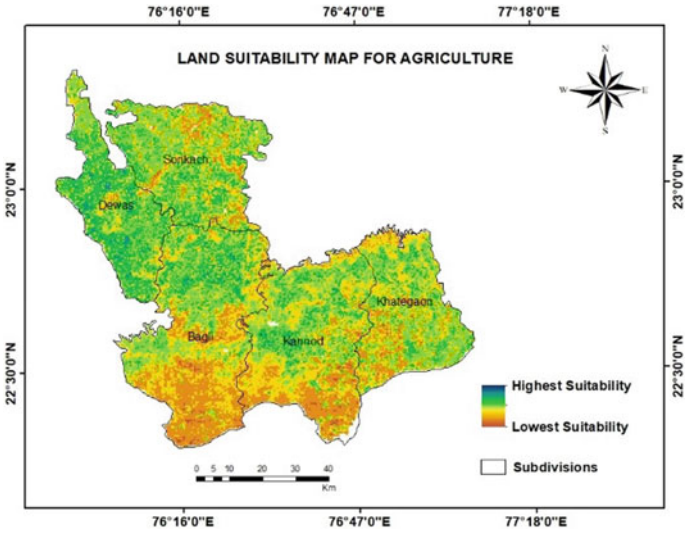

Fig. 24 Land suitability map for agriculture

5 Conclusion

The aim of this research was to create a comprehensive guideline integrating AHP with ArcGIS ModelBuilder that can classify the district into land parcels based on their suitability for agriculture. In highly suitable areas, large-scale agriculture can be practiced and appreciable production can be expected. In moderately suitable areas, irrigation method should be chosen carefully and soil management must be performed. In marginally suitable areas, farming will be risky and should be limited. The results of this study help us identify the inherent potentials and constraints of land for agriculture whilst accounting for the rigidity of the existing land use pattern.

Acknowledgments The authors are grateful to Mr. Sagar Patni (Graduate Assistant, Herbert Wertheim College of Engineering, University of Florida) for his useful insights on the content and formatting aspects of the paper.

References

1. Kumar A, Dubey OP, Ghosh, SK (2014) GIS based irrigation water management. 3
2. Natural Resources Census. NRSA/LULC/1:250K/2008-03. National Land Use and Land Cover Mapping Using Multi-Temporal AWiFS Data. National Remote Sensing Agency, Department of Space, Govt. of India
3. National Water Policy (2012) Ministry of water resources, government of India, New Delhi. http://mowr.gov.in/sites/default/files/NWP2012Eng6495132651_1.pdf

4. Indiatimes. With 30 K Hectares Cultivable Land Decreasing Per Year, Food Surplus India Might Become Food Deficient in Future. https://www.indiatimes.com/news/india/with-population-on-the-rise-and-agricultural-land-shrinking-india-might-become-food-deficient-254964.html
5. Urban Development Sector Profile, Department of Industry Policy and Promotion, Government of M.P
6. Trends in Urbanization. Directorate of Census Operation Madhya Pradesh. http://censusmp.nic.in/censusmp/All-PDF/3Trendsinurbanization21.12.2011.pdf
7. Government of India, Ministry of Water Resources, River Development and Ganga Rejuvenation, Central Ground Water Board, Aquifer Mapping Report (2015–16), Dewas District, Madhya Pradesh, North Central Region, Bhopal, August, 2016. https://cgwb.gov.in/AQM/NAQUIM_REPORT/MP/DEWAS.pdf
8. District Census Handbook, Dewas (2011) Census of India. Government of India http://censusindia.gov.in/2011census/dchb/2320_PART_B_DCHB_DEWAS.pdf
9. FAO (1976) A framework for land evaluation, Soil Bulletin 32. Food and agriculture organization of the United Nations. http://www.fao.org/docrep/t0715e/t0715e06.htm
10. Bandyopadhyay S, Jaiswal RK, Hegde VS, Jayaraman V (2009) Assessment of land suitability potentials for agriculture using a remote sensing and GIS based approach. Int J Remote Sens 4(879–895)
11. Aldababseh A, Temimi M, Maghelal P, Branch O, Wulfmeyer V (2018) Multi-criteria evaluation of irrigated agriculture suitability to achieve food security in an arid environment. Sustainability 10(3):803
12. Saaty RW (1987) The analytic hierarchy process—what it is and how it is used. Mathematical modelling 9(3–5):161–176
13. Saaty TL (1977) A scaling method for priorities in hierarchical structures. J Math Psychol 15:234–281
14. Saaty TL (1980) The analytic hierarchy process: planning, priority setting, resource allocation. McGraw Hill International, New York
15. Saaty TL, Vargas LG (1991) Prediction, projection, and forecasting: applications of the analytic hierarchy process in economics, finance, politics, games, and sports, Kluwer Academic Publishers
16. Jankowski P (1995) Integrating geographical information systems and multiple criteria decision-making methods. Int J Geogr Inf Syst
17. National Policy for Farmers (2007) Department of Agriculture & Cooperation. Ministry of Agriculture. Government of India. http://agricoop.nic.in/sites/default/files/npff2007%20%281%29.pdf
18. National Rehabilitation and Resettlement Policy (2007) Ministry of Rural Development. Government of India. http://dolr.gov.in/sites/default/files/National%20Rehabilitation%20%26%20Resettlement%20Policy%2C%202007.pdf
19. Alan Morton. UTM Grid Zones of the World. http://www.dmap.co.uk/utmworld.htm
20. Sarkar A (2008) Geo-spatial approach in soil and climatic data analysis for agro-climatic suitability assessment of major crops in rainfed agroecosystem, Indian Institute of Remote Sensing (IIRS), Agriculture and Soils Division, Master of Science, Andhra University, Dehradun, India
21. Central Research Institute for Dryland Agriculture. Indian Council of Agricultural Research. Agriculture Contingency Plan for District Dewas. http://www.crida.in/CP2012/statewiseplans/madhya%20pradesh/MP5-Dewas-26.6.2012.pdf
22. DivaGIS. http://www.diva-gis.org/Data
23. Advanced Space Thermal Emission Radiometer Global Digital Elevation Model Version 2 (ASTER GDEM V2). National Aeronautics and Space Administration Land Processes Distributed Active Archive Center (NASA LP-DAAC). https://gdex.cr.usgs.gov/gdex/
24. ArcHydro Tools for ArcGIS 10.x. http://downloads.esri.com/archydro/archydro/Setup/
25. United States Geological Survey Earth Explorer. https://earthexplorer.usgs.gov/
26. Google Earth. https://www.google.com/intl/en_in/earth/
27. United States Geological Survey Earth Explorer. Frequently Asked Questions. https://www.usgs.gov/faqs/what-are-best-landsat-spectral-bands-use-my-research?qtnews_science_products=0#qt-news_science_products

28. OpenStreetMap. Geofabrik. https://download.geofabrik.de/asia/india.html
29. Survey of India. Department of Science and Technology. Government of India. http://soinakshe.uk.gov.in/
30. International Soil Reference and Information Centre. Soilgrids. https://soilgrids.org/
31. Permaculture Research Institute. Permaculture News. https://permaculturenews.org/2016/10/19/soils-cation-exchange-capacity-effect-soil-fertility/
32. KrishiKosh. An Institutional Repository of Indian National Agricultural Research System. http://krishikosh.egranth.ac.in/
33. Nevada Climate Change Portal. http://sensor.nevada.edu/NCCP/Education/Clark%20Activities/Articles/Electric%20Conductivity%20of%20Soil.aspx
34. India-Water Resources Information System. http://www.india-wris.nrsc.gov.in/
35. National Centers for Environmental Prediction. Climate Forecast System Reanalysis. Global Weather Data for SWAT. https://globalweather.tamu.edu/
36. QGIS Python Plugins Repository. Soil Texture. https://plugins.qgis.org/plugins/SoilTexture/
37. University of Rhode Island. Rhode Island Stormwater Solutions. Importance of Soil Texture. https://web.uri.edu/riss/files/Importance-of-Soil-Texture.doc
38. Business Performance Management Singapore. AHP Online System—AHP-OS. AHP Priority Calculator. Klaus D. Goepel. https://bpmsg.com/academic/ahp.php
39. Lee GK, Chan EH (2008) The analytic hierarchy process (AHP) approach for assessment of urban renewal proposals. Soc Indic Res 89(1):155–168
40. Effat HA, Hassan OA (2013) Designing and evaluation of three alternatives highway routes using the Analytical Hierarchy Process and the least-cost path analysis, application in Sinai Peninsula. Egypt. Egypt J Remote Sens Space Sci 16(2):141–151. https://doi.org/10.1016/j.ejrs.2013.08.001
41. Pramanik MK (2016) Site suitability analysis for agricultural land use of Darjeeling district using AHP and GIS techniques. Model Earth Syst Environ 2(2):56
42. A quick tour of ModelBuilder. https://desktop.arcgis.com/en/arcmap/10.3/analyze/modelbuilder/a-quick-tour-of-modelbuilder.htm
43. Chang CW, Wu CR, Lin CT, Chen HC (2007) An application of AHP and sensitivity analysis for selecting the best slicing machine. Comput Ind Eng 52(2):296–307
44. Alonso JA, Lamata MT (2006) Consistency in the analytic hierarchy process: a new approach. Int. J. Uncertainty Fuzziness Knowl Based Syst 14(04):445–459
45. Cengiz T, Akbulak C (2009) Application of analytical hierarchy process and geographic information systems in land-use suitability evaluation: a case study of Dümrek village (Çanakkale, Turkey). Int J Sustain Dev World Ecol 16(4):286–294. https://doi.org/10.1080/13504500903106634

Dynamic Analysis of Tunnels in Western Ghats of Indian Peninsula: Effect of Shape and Weathering

Mohammad Zaid and M. Rehan Sadique

Abstract The rapid urbanization in the twentieth century has increased the demand of a smart transportation system for the movement of goods and services. The geotechnical structures required the proper study, analysis and application of theoretical, analytical and numerical model(s) from the stability, safety and sustainability aspect. In the present research work, the stability analysis of different tunnel shapes for four different earthquake zones using the finite element analysis has been carried out. The Mohr–Coulomb material constitutive model has been implemented for the elasto-plastic behaviour of the basalt rock mass using 2D plane strain modelling. Three different shapes of tunnel, circular, horseshoe and arch, under four earthquakes of different magnitudes have been considered (i.e. 4.6, 5.6, 6.5 and 7.4 M). The present study suggested that arch-shaped tunnel is stable in all earthquake zones while the horseshoe-shaped tunnel is the most unstable. The effect of depth of overburden has been also considered for each case by varying the overburden depth in three intervals (5, 10 and 17.5 m). The study further reveals that with the increase in depth of overburden, the stability of the tunnel increases. It is also suggested that the weathering of rock has a significant effect on the deformations in tunnels which may in turn increase the instability of tunnel.

Keywords Basalt · Tunnel · Rock · Mohr–Coulomb · Earthquake

1 Introduction

Improvement of transportation infrastructure in urban areas for the transport of goods and mass rapid transit has increased the research interest in the study of tunnels [1–3]. Amorosi and Boldini carried out the study of the dynamic behaviour of the circular tunnel in clayey soil using the finite element method [4]. The authors further concluded that a seismic event can produce a substantial modification of loads acting

M. Zaid (✉) · M. Rehan Sadique
Department of Civil Engineering, ZHCET, Aligarh Muslim University, Aligarh, UP, India
e-mail: mohammadzaid1@zhcet.ac.in

© Springer Nature Singapore Pte Ltd. 2021

K. K. Pathak et al. (eds.), *Recent Trends in Civil Engineering*, Lecture Notes in Civil Engineering 77, https://doi.org/10.1007/978-981-15-5195-6_57

in the lining. Yu et al. studied the longitudinal seismic response of tunnel liner using an analytical approach [5].

The shape of the tunnel plays a pivotal role when deformation study is carried out. Several researchers have studied the effect of tunnel shape on the stability of the tunnel [6–11]. Augarde and Burd described the finite element for the deformations in case of the shallow tunnel and concluded that a thin layer of the continuum may be used for modelling a tunnel lining for soil–structure interaction problems [12]. Chungsik Yoo studied the longitudinal reinforced face of the tunnel using finite element analysis and concluded that the face deformations can be reduced by the application of longitudinal pipes as face reinforcement [13].

Nevertheless, authors have not found any open literature dealing with the effect of weathering of a rock mass on the behaviour of the tunnel. In the present study, weathering effect of rock, the mass has been incorporated with different opening shapes, different magnitude seismic loadings and varying depth of tunnels. The present paper provides a comparative study by considering four different stages of weathering for three different shapes of tunnels, i.e. circular-shaped tunnel, arch-shaped tunnel and horseshoe-shaped tunnel. These cases have been analysed under four different magnitude earthquake loadings. The effect of depth of overburden has also been considered for each case by varying the overburden depth in three intervals, i.e. 5, 10 and 17.5 m.

2 Numerical Model

The dynamic analysis has been carried out for the 2D plane strain model of 42 m $\times$ 42 m size using finite element software Abaqus/Dynamic. Arch-shaped, circular-shaped and horseshoe-shaped tunnels are drawn having a 7 m diameter, and thickness of tunnel lining has been taken as 120 mm. The three depths of overburden, 5, 10, and 17.5 m, are considered to compare the effect of overburden depth under different (4.6, 5.6, 6.5 and 7.4 M) magnitudes of earthquakes for different stages of rock mass weathering (fresh basalt, slightly weathered, medium weathered and highly weathered basalt). The CPE3R-three-noded plane strain linear triangular element with reduced integration and hourglass control element type has been used for meshing the model. 500 m of overburden due to the already present rock mass has been taken into account in the form of pressure at the top line of the model. The infinite boundary condition has been adopted at the side faces of the tunnel model [14]. The CINPE4, a four-noded linear infinite quadrilateral element, was used for the infinite boundary condition meshing. 1.5 m mesh size has been used for meshing the rock mass and 0.1 m for meshing the tunnel lining (Fig. 1).

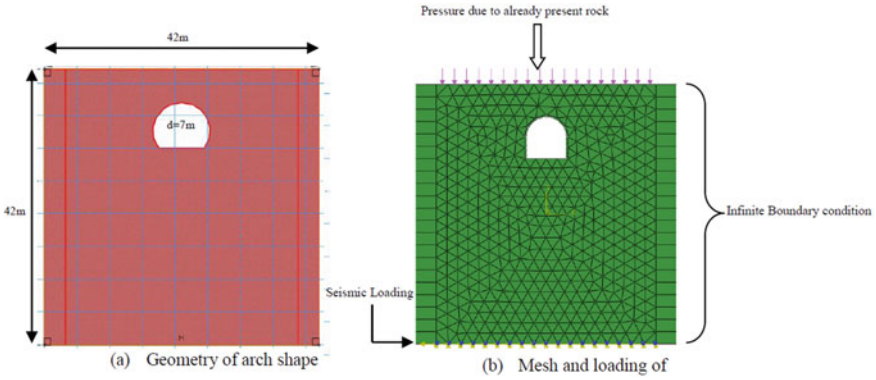

Fig. 1 The geometry of tunnel and meshed model

3 Input Properties

The Mohr–Coulomb model of elasto-plastic material has been considered for the behaviour of the rockmass. Various properties of different rockmass taken in the present study are shown in Table 1 [15–21]. The different weathering stages considered in the present study are fresh basalt (W_0), slightly weathered basalt (W_1), medium weathered basalt (W_2) and highly weathered basalt (W_3).

3.1 Analysis

The model was prepared using Abaqus/CAE and boundary conditions were applied. The vertical sides of the model were restrained in position by creating infinite boundary conditions. The earthquake loading has been applied at the base of the model in the form of the acceleration-time history of different earthquakes. The acceleration versus time history plot is shown in Fig. 2.

Table 1 Properties of different weathering stages [22]

Rockmass	Modulus of elasticity (GPa)	Poisson's ratio (ν)	Density (kg/m^3)	Friction angle (°)	Dilation angle (°)	Cohesion (MPa)
Basalt (W_0)	46.50	0.186	2960	63.38	12	26.25
Basalt (W_1)	20.60	0.260	2740	53.71	12	18.50
Basalt (W_2)	02.80	0.272	2470	33.33	04	08.08
Basalt (W_3)	00.60	0.272	1820	43.87	00	01.64
Concrete	31.6	0.15	2400			

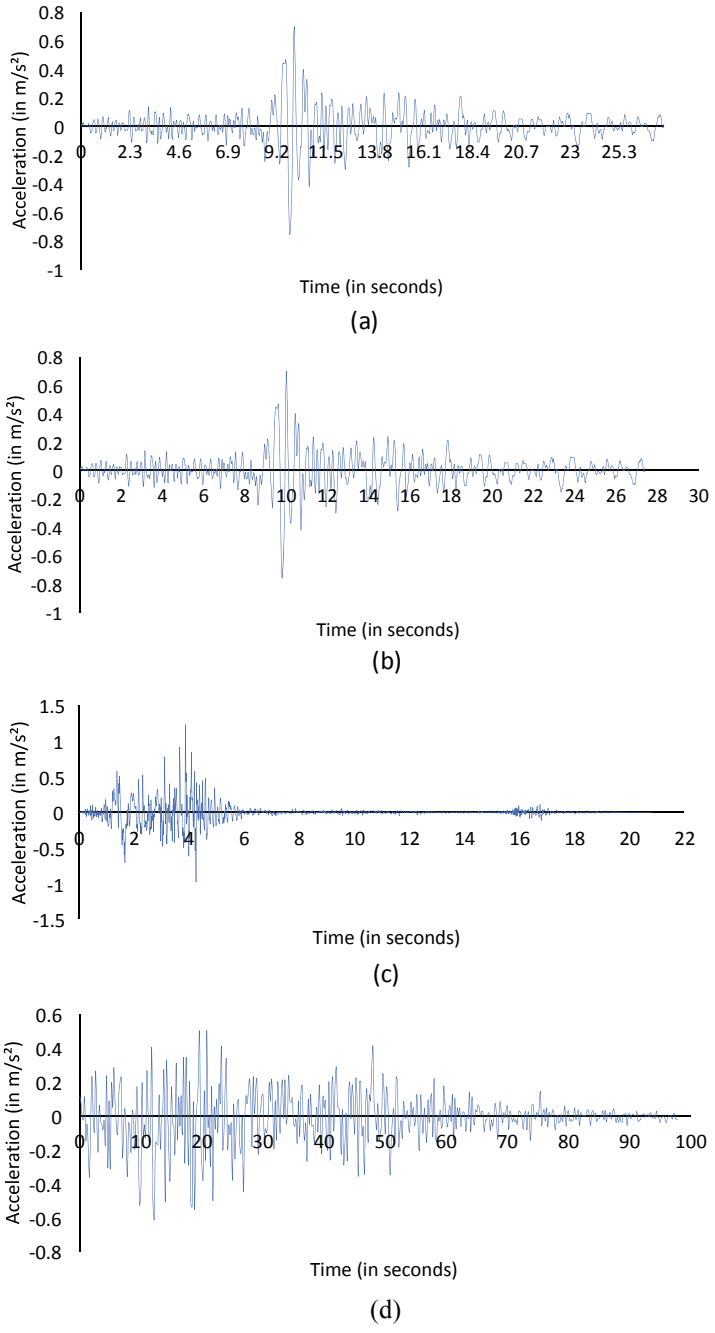

Fig. 2 Acceleration-time history of **a** 4.6 M, **b** 5.6 M, **c** 6.5 M and **d** 7.4 M magnitude of earthquake [23]

4 Results and Discussion

In the present paper, different shapes of the tunnel are analysed under different earthquake conditions. The weathering of the basalt rock has also been considered. The four weathering stages of basalt rock adopted in the present paper are; fresh basalt (W_0), slightly weathered basalt (W_1), medium weathered basalt (W_2) and highly weathered basalt (W_3). The depth variation has also been taken into account. There are three depths of overburden 5, 10 and 17.5 m adopted in the present analysis. The finite element software Abaqus/Explicit has been adopted for the present study. The paper focuses on the comparison of the stability of different shapes in different magnitudes of earthquakes.

The comparison of the depth of overburden has been shown in Table 2. It can be seen from the table that with the increase in the depth of overburden the deformation decreases. For the 4.6 M magnitude of the earthquake, a 5% decrease in deformation has been observed for the increase in depth of overburden from 5 m to 10 m.

For an increase in depth of overburden from 10 to 17.5 m, a 3.5% decrease in deformation has been observed. Similarly, for the 5.6 M magnitude of the earthquake, an increase in depth of overburden from 5 to 10 m and 10 to 17.5 m shows 12 and 1% decrease in the values of deformations, respectively. And for the 6.5 M magnitude of the earthquake, 16 and 3% decrease in the value of deformation has been observed for the similar increase in depth of overburden. Lastly, for 7.4 M magnitude, 28 and 8% decrease in the value of deformation has been observed for the increase in the depth of overburden from 5 m to 10 m and 10 m to 17.5 m, respectively.

The deformation has been plotted against each weathering stage for comparing the depth of overburden in Fig. 3 for the arch-shaped tunnel. This shows that weathering has a significant effect on deformation. Also, as the depth of overburden increases the deformation of the tunnel decreases. Figure 3 shows the results for 4.6 M of earthquake for different shapes of the tunnel.

The graph shows that as the weathering stage of a basalt rock increases, it results in an increase in deformation at each depth of overburden. Also, as the depth of overburden increases, the deformation reduces as the situation results to lead towards the lithostatic condition.

Table 3 shows the comparison of different shapes of tunnels considered in the present study. It is noted that in the case of fresh basalt (W_0), an arch-shaped tunnel is the safest and the horseshoe-shaped tunnel is most unstable. Similar is the case with slightly weathered basalt (W_1). But, as the weathering of rock increases, a circular-shaped tunnel becomes the safest and the arch-shaped tunnel is the most unstable tunnel.

Table 2 Deformation for arch-shaped tunnel for medium weathered (W_2) basalt rock at right springer of tunnel

Magnitude of an earthquake	4.6 M			5.6 M			6.5 M			7.4 M		
Depth of overburden	17.5 m	10 m	5 m	17.5 m	10 m	5 m	17.5 m	10 m	5 m	17.5 m	10 m	5 m
Deformation	0.057 m	0.059 m	0.062 m	0.216 m	0.228 m	0.257 m	0.3 m	0.335 m	0.389 m	0.861 m	0.934 m	1.196 m

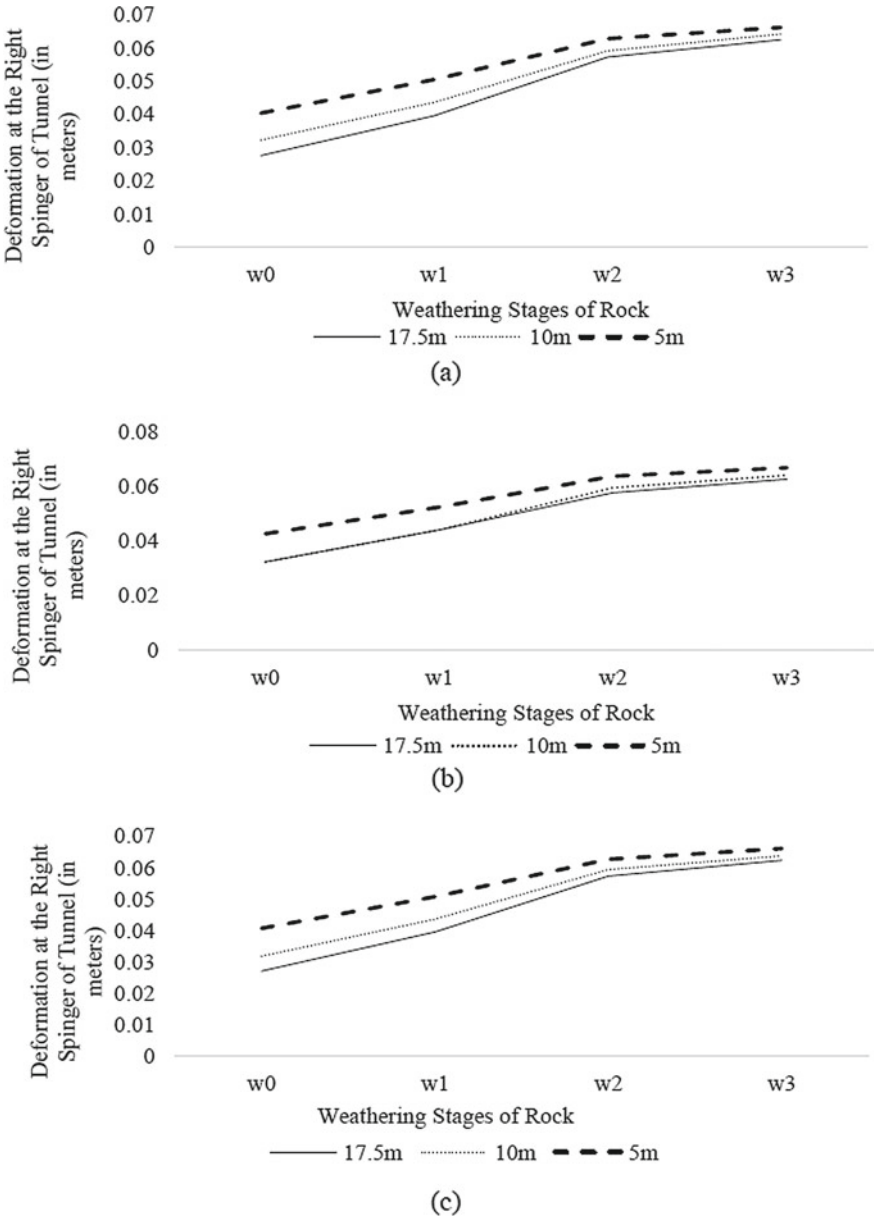

Fig. 3 Comparison of depths for different stages of weathering for **a** arch-shaped tunnel, **b** circular-shaped tunnel and **c** horseshoe tunnel under 4.6 M earthquake loading

Table 3 Comparison of tunnel shape for the 5 m depth of overburden under 7.4 M earthquake loading for different stages of weathering

Weathering stages of rock	W_0			W_1			W_2			W_3		
Shape of tunnel	Circular	Arch	Horseshoe	Circular	Arch	Horseshoe	Circular	Arch	Horseshoe	Circular	Arch	Horseshoe
Deformation	0.173 m	0.264 m	0.308 m	0.206 m	0.353 m	0.363 m	0.646 m	1.196 m	0.780 m	0.921 m	1.339 m	1.335 m

The magnitude of an earthquake similar to or equal to the 7.4 M makes the comparison clearer, as shown in Fig. 4. In this case, the arch-shaped tunnel is most stable at every depth of overburden. The horseshoe-shaped tunnel has maximum deformation, and thus it is the most unstable shape of a tunnel.

Figure 5 shows a graph for the comparison of the magnitude of an earthquake for the horseshoe shape of the earthquake at 5, 10 and 17.5 m of overburden depth. The magnitude of the 4.6 M earthquake has the least deformation and the 7.4 M magnitude of earthquake has maximum deformation. Figure 5 has been plotted for horseshoe-shaped tunnel, irrespective of shape; the deformation pattern is similar for all shapes of tunnels.

Table 4 shows the comparison between different magnitudes of earthquakes for the deformation readings taken at the right springer of the tunnel. For fresh basalt rock (W_0), it can be noted that an increase of the magnitude of the earthquake from 4.6 to 5.6 M increases the deformation by 27, 33% for an increase in magnitude from 5.6 to 6.5 M and 7.4% increase for 6.5 to 7.4 M increase in the magnitude of the earthquake.

5 Conclusion

A two-dimensional finite element analysis has been performed to study the behaviour of rock tunnels considering weathering effects. Few important observations may be concluded as follows:

- As the weathering stage of a basalt rock increases, due to a loss in structural strength, it results in an increase of deformation in the rock tunnel at each depth of overburden.
- As the depth of overburden increases, the deformation in the rock tunnel reduces. It is may be due to the development of a lithostatic condition.
- In the case of fresh basalt (W_0), arch-shaped tunnel is the safest and the horseshoe-shaped tunnel is most unstable, similarly for slightly weathered basalt (W_1).
- As the weathering of rock increases, circular-shaped tunnel becomes the safest and the arch-shaped tunnel is the most unstable tunnel.
- In case of an earthquake of a magnitude of 7.4 M, the arch-shaped tunnels are most stable at every depth of overburden and the horseshoe-shaped tunnels have maximum deformation, and thus it is the most unstable shape of a tunnel.
- Deformation increases with an increase in the magnitude of the earthquake.

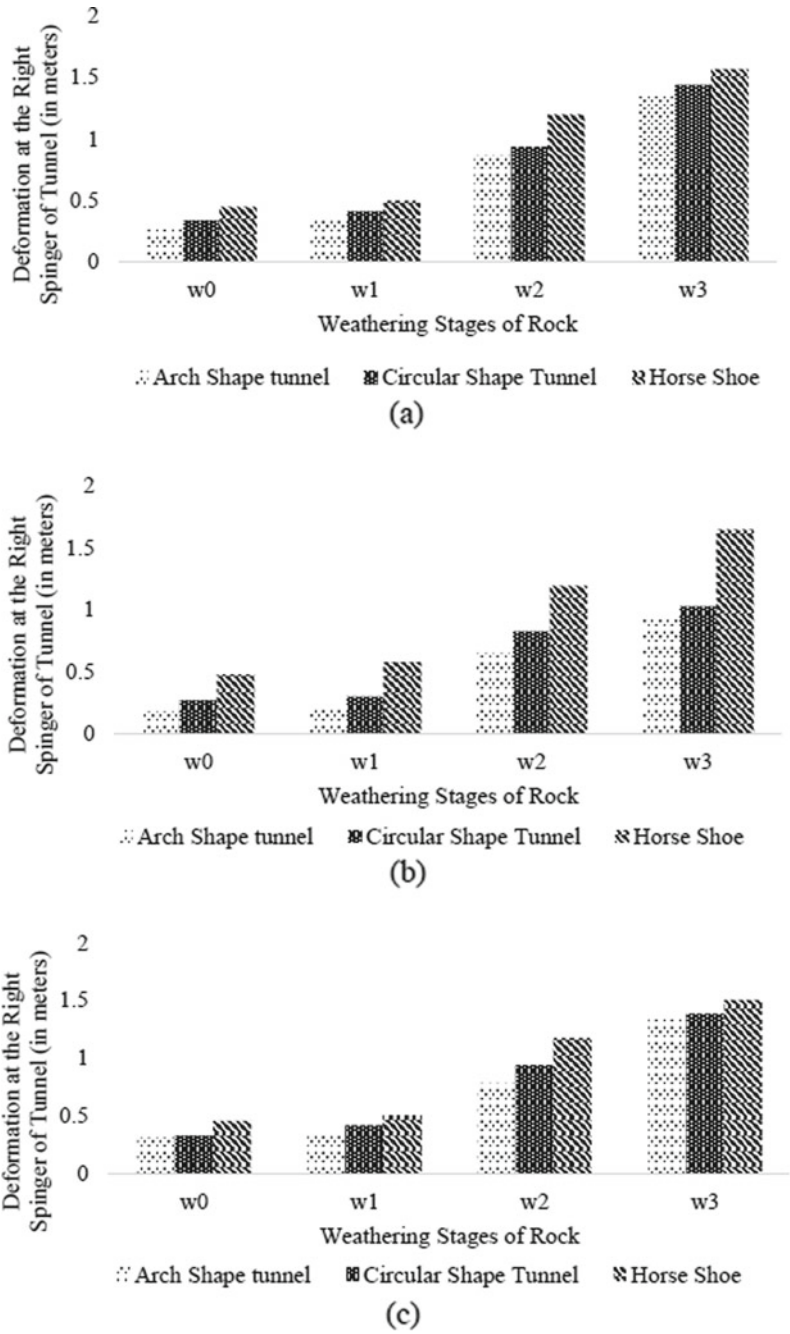

Fig. 4 Comparison of shapes of the tunnel in different stages of weathering for **a** 5 m, **b** 10 m and **c** 17.5 m under 7.4 M earthquake loading

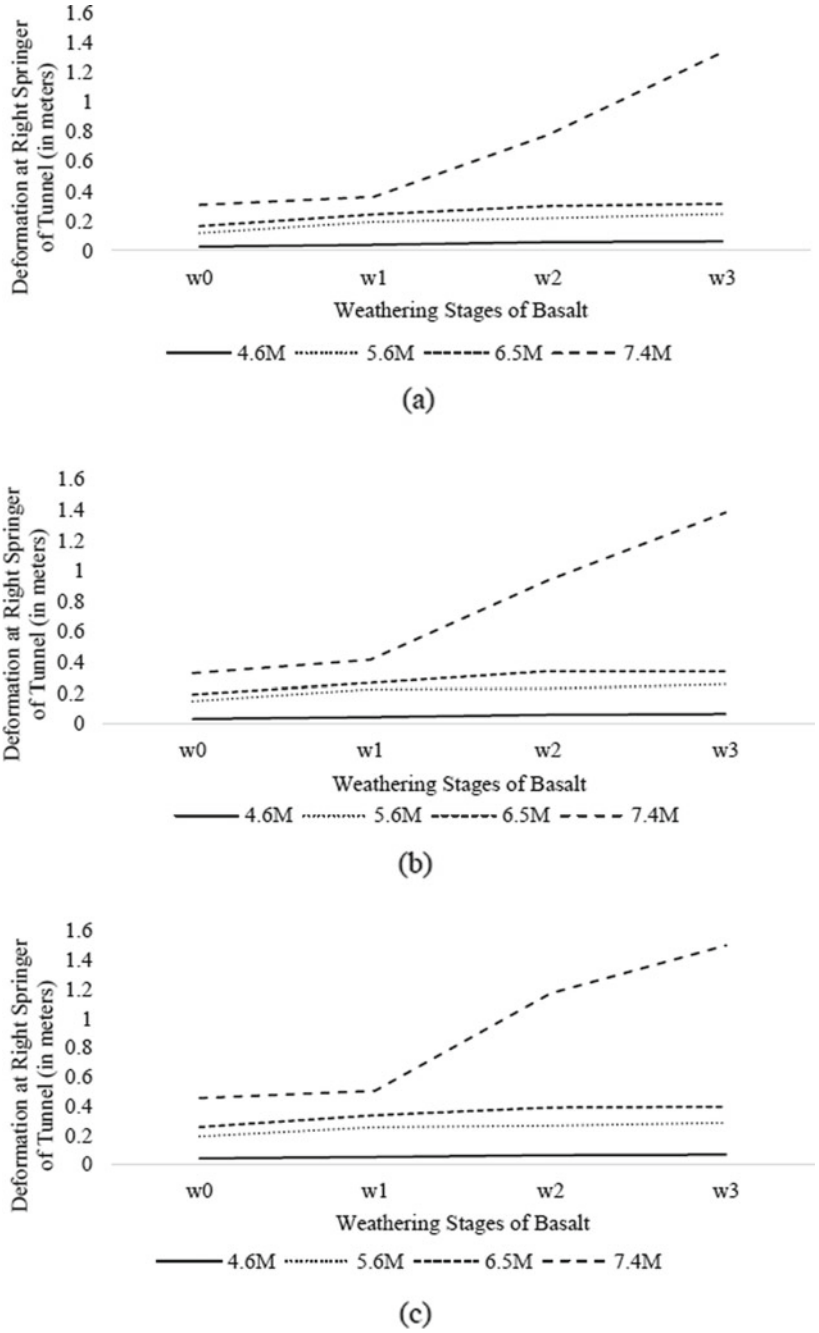

Fig. 5 Comparison of deformation under the different magnitudes of the earthquake in different stages of weathering for **a** 5 m, **b** 10 m and **c** 17.5 m of depth for the horseshoe-shaped tunnel

Table 4 Deformation comparison under the different magnitudes of earthquakes for circular-shaped tunnel at a 5 m depth of overburden (in metres)

Weathering stages	W_0				W_1				W_2				W_3			
Magnitude of an earthquake	4.6 M	5.6 M	6.5 M	7.4 M	4.6 M	5.6 M	6.5 M	7.4 M	4.6 M	5.6 M	6.5 M	7.4 M	4.6 M	5.6 M	6.5 M	7.4 M
Deformation at right springer of tunnel (in metres)	0.032	0.121	0.161	0.173	0.044	0.201	0.244	0.206	0.057	0.215	0.302	0.646	0.062	0.241	0.306	0.921

References

1. Mishra S, Rao KS, Gupta NK, Kumar A (2017) Damage to shallow tunnels under static and dynamic loading. Procedia Eng 173:1322–1329
2. Zhang ZX, Liu C, Huang X, Kwok CY, Teng L (2016) Three-dimensional finite-element analysis on ground responses during twin-tunnel construction using the URUP method. Tunn Undergr Sp Technol 58:133–146
3. Kargar AR, Rahmannejad R, Hajabasi MA (2014) A semi-analytical elastic solution for stress field of lined non-circular tunnels at great depth using complex variable method. Int J Solids Struct 51:1475–1482
4. Amorosi A, Boldini D (2009) Numerical modelling of the transverse dynamic behaviour of circular tunnels in clayey soils. Soil Dyn Earthq Eng 29(6):1059–1072
5. Yu H et al (2018) Analytical solution for longitudinal seismic response of tunnel liners with sharp stiffness transition. Tunn Undergr Sp Technol 77:103–114
6. Banerjee SK, Chakraborty D (2018) Stability analysis of a circular tunnel underneath a fully liquefied soil layer. Tun Undergr Sp Technol 78:84–94
7. Ng CWW, Fong KY, Liu HL (2018) The effects of existing horseshoe-shaped tunnel sizes on circular crossing tunnel interactions: three-dimensional numerical analyses. Tunn Undergr Sp Technol 77:68–79
8. Athar MF, Zaid M, Sadique MR (2019) Stability of different shapes of tunnels in weathering stages of basalt. In: Proceedings of national conference on advances in structural technology. CoAST2019, pp 320–327
9. Chen HL, Xia ZC, Zhou JN, Fan HL, Jin FN (2013) Dynamic responses of underground arch structures subjected to conventional blast loads: curvature effects. Arch Civ Mech Eng 13:322–333
10. Dancygier AN, Karinski YS, Chacha A (2016) A model to assess the response of an arched roof of a lined tunnel. Tunn Undergr Sp Technol 56:211–225
11. Lai J, Fan H, Liu B, Liu T (2011) Analysis of seismic response of shallow large section multi-arch tunnel. Adv Control Eng Inf Sci 15:2–6
12. Augarde CER, Burd HJ (2001) Three-dimensional finite element analysis of lined tunnels. Int J Numer Anal Methods Geomech 25:243–262
13. Yoo C (2002) Finite-element analysis of tunnel face reinforced by longitudinal pipes. Comput Geotech 29:73–94
14. Naqvi MW, Zaid M, Sadique R, Alam MM (2017) Dynamic analysis of rock tunnels Considering joint dip angle: a finite element approach. In: 13th international conference on vibration problems
15. Zaid M, Sadique MR (2019) Effect of Joint Orientation and Weathering on Static Stability of Rock Slope Having. In: 7th Indian young geotechnical engineers conference—7IYGEC 2019 15–16 March 2019, NIT Silchar, Assam, India SILCHAR
16. Zaid M, Talib A, Rehan Sadique Md (2018)Stability analysis of rock slope having transmission tower. IJRECE 6
17. Gahoi A, Zaid M, Mishra S, Rao KS (2017) Numerical analysis of the tunnels subjected to impact loading. In: 7th India Rock Conference IndoRock
18. Zaid M, Mishra S, Rao KS (2018) Finite element analysis of static loading on urban tunnels. In: Indian Geotechnical Conference 2018 (IGC-2018)
19. Zaid M, Khan MA, Sadique MR (2019) Dynamic response of weathered jointed rock slope having the transmission tower. Proc Nat Conf Adv Struct Technol 1:414–422
20. Zaid M, Talib A, Sadique MR (2018) Effect of joint orientation on the seismic stability of rock slope with transmission tower. In: Indian Geotechnical Conference 2018 (IGC-2018)

21. Mishra S, Rao S, Gupta NK (2016) Effect of different loading conditions on tunnel lining in soft rocks. In: ISRM International Symposium–EUROCK 2016, 29–31 August, Ürgüp, Turkey
22. Gupta AS, Rao KS (1998) Index properties of weathered rocks: inter-relationships and applicability. Bull Eng Geol Environ 57:161–172
23. Systems, C. of O. for S.-M. O. Strong Motion Virtual Data Center (VDC) (2018) https://strongmotioncenter.org/vdc/scripts/default.plx. Accessed 15th October 2018

Trend Analysis and Rainfall Variability of Monthly Rainfall in Sheonath River Basin, Chhattisgarh

Shashikant Verma, A. D. Prasad, and Mani Kant Verma

Abstract Hydrological effects comprise the changes in soil use to comprehend the mechanisms of future climate and land use. The significant temporal trend was identified in this study as being performed monthly, seasonal time scales using rainfall data from 39 monitoring stations throughout the Sheonath Basin, subdivided into five effective weighted stations by the creation of Thiessen polygon over Sheonath River Basin in Chhattisgarh State for the period of 1980–2012. Hydro-meteorological factors are evaluated using a combined trend detection technique. The findings show a substantial downward trend at 5% significance level, an average of −0.10 mm per year for all five monitoring stations for the month of March, May, September, October, December, January, and February similar to June, July, August, April, and November reveal the upward trend at 5% significance level, an average of 0.12 mm per year. While the trend continues in various phases such as winter and pre-monsoon seasons, the trend is considerably declining an average of −0.041 and −0.009 mm per year, respectively, for all five monitoring stations and post-monsoon periods; simga, andhayakore, and patharidih monitoring stations represent a downward trend at an average of −0.0084 mm per year. The variability of rainfall has resulted to the conclusion that the amount of rainfall variability decreases by 5.56% compared to the average annual rainfall variability in the Rajnandgaon, Durg, and Kawardha Districts during the Kharif season, and the rainfall variability decreases by 93.14%, 93.88%, and 93.34% compared to the annual average rainfall variability in the Rajnandgaon, Durg, and Kawardha Districts during the rabi season, respectively. Therefore, there is a need for improvement in the eastern zone.

Keywords Trend detection · Rainfall · Kendall tau statistics · Theil–sen slope estimator · Rainfall variability · Rain-fed crop yield

S. Verma (✉) · A. D. Prasad (✉) · M. K. Verma
National Institute of Technology Raipur, Raipur 492001, India
e-mail: shashiv50@gmail.com

A. D. Prasad
e-mail: adprasadiit@gmail.com

M. K. Verma
e-mail: manikverma.ce@nitrr.ac.in

© Springer Nature Singapore Pte Ltd. 2021

K. K. Pathak et al. (eds.), *Recent Trends in Civil Engineering*, Lecture Notes in Civil Engineering 77, https://doi.org/10.1007/978-981-15-5195-6_58

1 Introduction

Water is a natural resource and its availability is a major problem for any venture being planned, developed, and managed. Indian farming focuses primarily on rainfall distribution and allocation. Rainfall distribution is the primary variable in the preparation and governance of water resource activities such as agricultural production, water requirement alterations, irrigation, and reservoir activities [1]. The climate change is related to distinct parameters of hydro-meteorology behavior relative to two distinct phases. Variability in climate is not a very short-term technique. A noticeable change in the climate takes years or centuries [2]. The temperature variations and the irregular rainfall first appear in the picture when the term climate changes are coined. Because of poor adjustment strategies and a very large population, this can contribute to serious damaging conditions from the perspective of India [3]. Intensive flooding and severe drought in distinct regions of the country can concurrently prevail [4]. Extensive human interventions will further accelerate this. But the issue to be studied is that, whether it is a drought or flood, an important effect on these parts will be the variability in precipitation [5]. In India, owing to the southwest monsoon, that is, June–September precipitation, it counts for rainfall. Also, in view of the rise in temperature, rainfall is expected to rise in certain parts of the globe in favor of such climate change. A number of researches worked on trend analysis of rainfall in different geographical locations of India. Non-parametric and linear regression test approaches were used in most of the researches to identify trends. In this study, we used non-parametric techniques because World Meteorological Organization (WMO) suggests it is free from any type of distribution and robust against outliers to detect important monotonous upward and downward trends for distinct climatological and hydrological time scales [4].

2 Study Area and Data Used

Sheonath (also called Seonath) is located in Chhattisgarh region plains of India. This basin extends from 20°16′ to 22°41′N latitude to 80°25′ to 82°35′E longitude. A large part of the Upper Mahanadi Valley is occupied by the basin [6]. Sheonath is Mahanadi River's longest tributary, spanning a length of 380 km. It originates near the village of Panabaras in the district of Rajnandgaon, Chhattisgarh, 624 meters above sea level. The main tributaries are Arpa, Tandula, Agar, Kharun, Maniyari, and Hamp [5]. The basin's area is 30,560 km^2. The watershed topography is basically flat. The Sheonath Basin has a tropical wet and dry environment; from March to June, temperatures can be highly warm, though moderate throughout the year. The watershed receives an average precipitation of 1150 mm per year with a large proportion contributing to the rainy season from June to early October, followed by the post-monsoon period from October to December and gathered daily rainfall

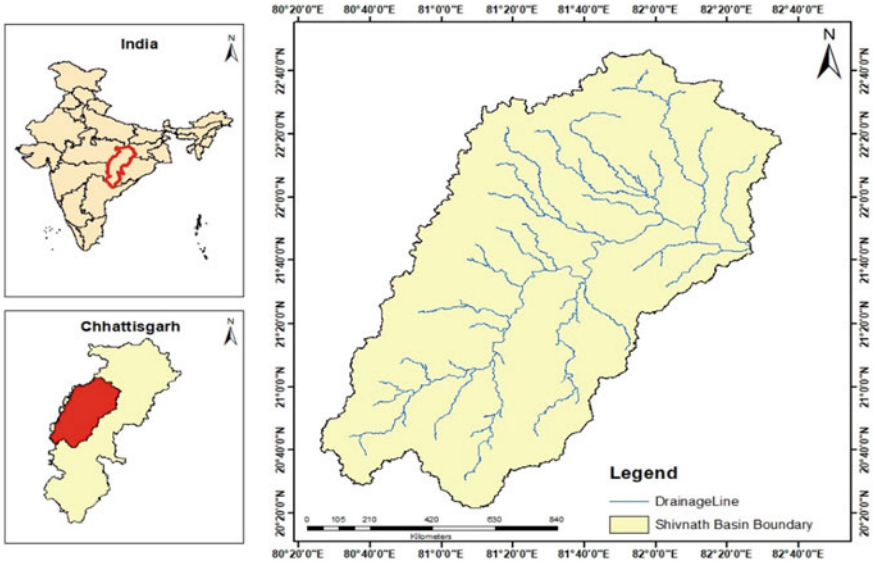

Fig. 1 Sheonath River Basin

information for 39 meteorological stations across the Sheonath River Basin to evaluate space and time variation for a span of 30 years (from 1980 to 2010). The five stations, namely, Simga Jondhra, Patharidih, Kotni, and Andhiyakore are the Central Water Commission (CWC) stations used in this study. Location map of the Sheonath River Basin is shown in Fig. 1.

2.1 Data Used

The various sets of data have been used were the study course of Chhattisgarh State. The basic data, which were collected and used during the entire works, are soil physiography, soil type, soil depth, DEM, precipitation, temperature, length of growing period, land use/land cover, available water capacity (AWC), and administrative boundary. All the data were collected by visiting respective areas of the concerned state. The maps relating to Chhattisgarh's soil resources are collected as first information and second most important parameters such as rainfall and temperature are collected from different meteorological stations of Chhattisgarh.

2.2 Rainfall Variability

The degree to which the quantity of rainfall changes across a region or over time is a significant feature of the climate of a region called rainfall variability in climatology and meteorology [7]. Analysis of rainfall is crucial for any area in terms of crop planning. To maintain crop yield in the rain-fed scenario at important concentrations, planning, and management of rain-fed crops in combination with frequent rainfall patterns in the area is essential. For rain-fed crop planning, surveys of rainfall, in particular, offer more data about its variability and probability assessment. Among the climatic elements, rainfall is the most important single factor by climatic analyzer and farmers which determines rainfall on the different time scale and daily rainfall plays an important role in weather phenomena in tropical countries and helps to determine the hydrological and agriculture land use potential investigation. Further, accurate knowledge of agro-climate conditions is critical to the effective planning of crops in any specific area [6]. This sort of knowledge is more significant in a rain-fed area where crop production depends on climatic parameter and monsoon incoherence. The distribution of rainfall in the rain-fed area is, therefore, a significant determinant of crop yield [8]. In this context, it is necessary to collect, analyze, and examine the region's historical weather data in order to characterize the region's agricultural climate.

2.3 Annual Average Rainfall

The Chhattisgarh State has been divided into five major categories such as very high rainfall zone (1600 mm), high rainfall (1500–1600 mm), medium rainfall (1400–1500 mm), low rainfall (1300–1400 mm), and very low rainfall (rainfall < 1300 mm) [6]. The spatial distribution of rainfall indicates that the southeastern Baster Region comprising some parts of Dantewada and Jagdalpur, the southern portion of the southern mountains, some parts of Sarguja and most parts of Jashpur and northwestern part of Chhattisgarh, some parts of Janjgir, Raipur, Mahasamund and most parts of Raigarh perceive high to very high precipitation. The reason is that monsoon's onset is quite early in this part of the country, not in other areas of the country, so monsoon remains active in this portion for a longer period [9]. Due to the undulating area, another region that contributes to high rainfall may be dense forest cover and orographic rainfall industry. Medium rainfall is received throughout Bijapur District and parts of Dantewada, Narayanpur, Koriya, Jagdalpur, Bilaspur, Korba, Sarguja, Janjgir, Mahasamund, Raigarh, and Raipur. The position and region of the stations in the basin are shown on the Thiessen polygon map in Fig. 2 (Table 1).

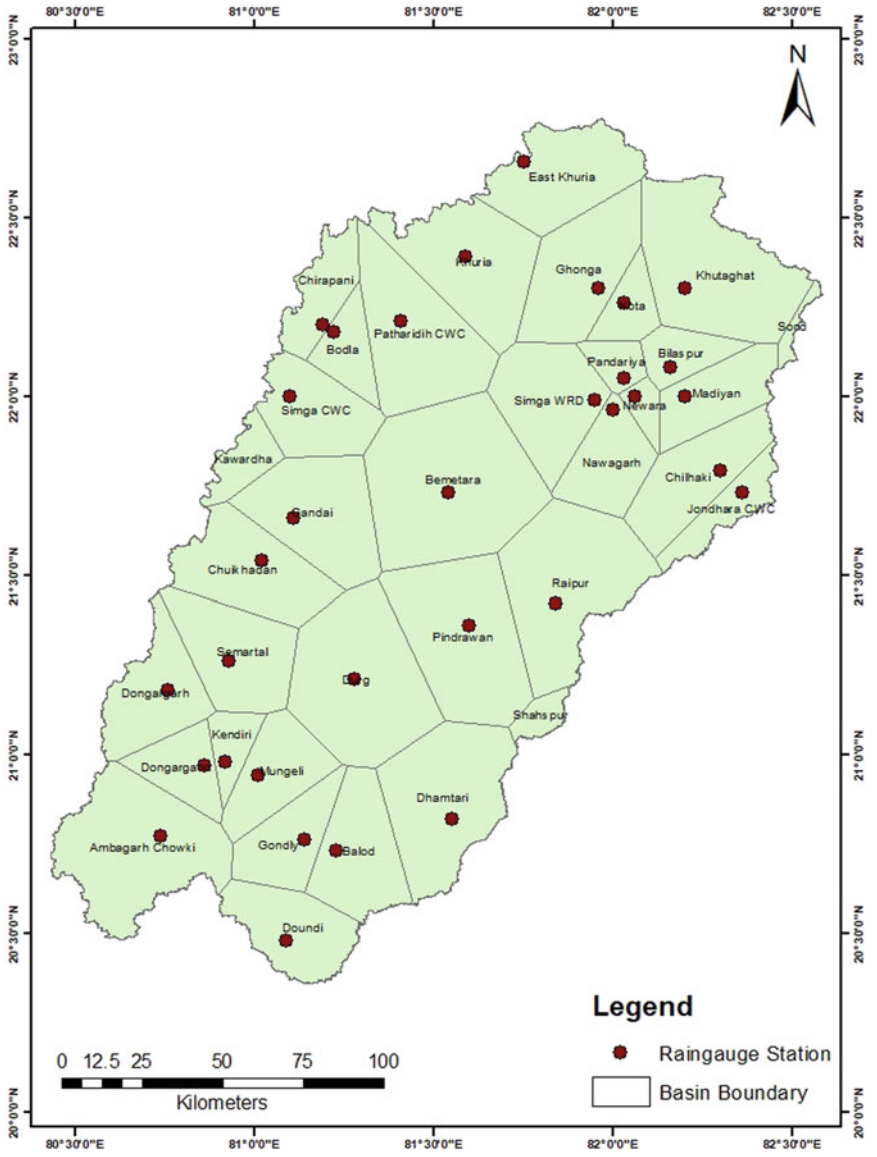

Fig. 2 Thiessen polygon of Sheonath River Basin

3 Methodology

In this study, daily rainfall data is used to generate monthly and seasonal time series for investigating spatiotemporal changes in rainfall pattern. Ideally, rainfall data used

Table 1 List of rain gauge stations

Rain gauge station	Location	Thiessen polygon area (km^2)
Ambagarh Chowki	(20.77N, 80.74E)	1298.78
Andhyakore CWC	(21.82N, 81.60E)	364.88
Balod	(20.73N, 81.23E)	934.39
Bemetara	(21.73N, 81.54E)	537.71
Bilaspur	(22.08N 82.16E)	1185.89
Bodla	(22.18N, 81.22E)	114.63
Chirapani	(22.20N, 81.19E)	1030.25
Chilhaki	(21.7N, 82.30E)	547.10
Chuikhadan	(21.54N, 81.02E)	1167.67
Dhamtari	(20.82N, 81.55E)	1158.84
Dongargaon	(20.97N, 80.86 E)	622.85
Doundi	(20.48N, 81.09E)	976.89
Dongargarh	(21.18N, 80.76E)	789.88
Durg	(21.21N, 81.28E)	1574.88
Ghonga	(22.30N, 81.86E)	684.03
Gandai	(21.66N, 81.11E)	1562.45
Gondly	(20.76N, 81.14E)	641.39
Jondhara CWC	(21.73N, 82.36E)	490.28
Kawardha	(21.90N, 80.93E)	630.16
Kendiri	(20.98N, 80.92E)	563.02
Kharkhara	(19.97N, 80.94E)	924.55
Khuria	(22.39N, 81.59E)	1519.24
Khutaghat	(22.30N, 82.20E)	1523.80
Kota	(21.26N, 82.03E)	382.00
Kotni CWC	(21.93N, 80.24E)	229.80
Madiyan	(22.00N, 82.20E)	386.26
Mungeli	(20.94N, 81.01E)	1114.24
Nawagarh	(21.96N, 82.00E)	689.73
Newara	(21.00N, 82.06E)	1050.78
Pandariya	(22.05N, 82.03E)	881.23
Patharidih CWC	(22.21N, 81.41E)	552.49
Pindrawan	(22.36N, 81.60E)	610.78
Raipur	(21.42N, 81.84E)	394.21
Semartal	(21.26N, 80.93E)	432.25
Shahspur	(21.00N, 82.00E)	667.41
Simga CWC	(22.00N, 81.10E)	291.54

(continued)

Table 1 (continued)

Rain gauge station	Location	Thiessen polygon area (km^2)
Simga WRD	(21.99N, 81.95E)	590.47
Sond	(22.00N, 82 72E)	931.62
Surhi (Palemeta)	(20.98N, 82.07E)	472.04

to investigate patterns of precipitation should be affected by climatic and atmospheric conditions. Trend analysis was carried out using non-parametric methods as shown in Fig. 3 and flowchart for study of rainfall variability is shown in Fig. 4, respectively.

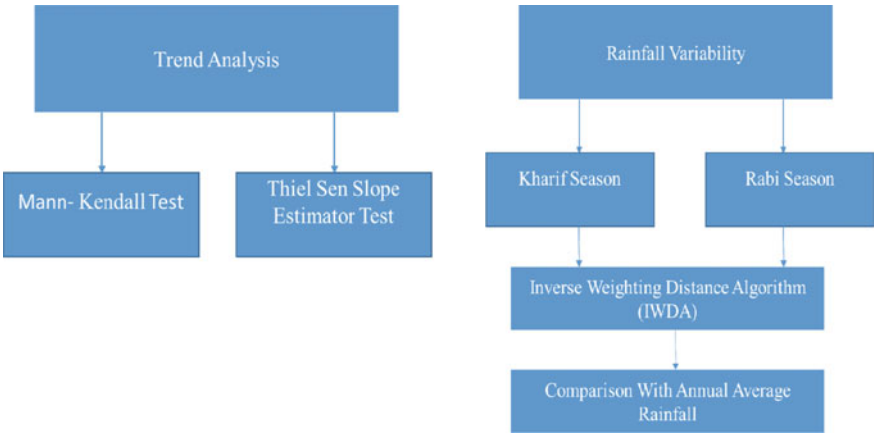

Fig. 3 Methodology

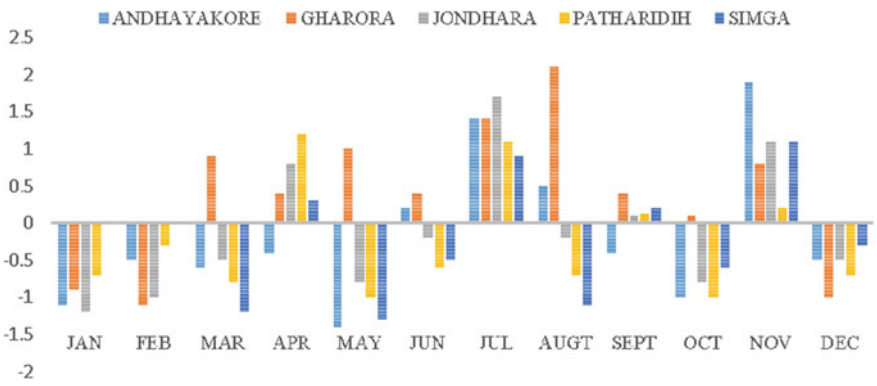

Fig. 4 Mann–Kendall (Zmk) statistics from 1980 to 2012 for monthly time scale

3.1 Study of Time Series

A time series is a set of statistics, generally gathered at periodic intervals (monthly average rainfall, annual rainfall temperature) and happens, of course, in many fields of application (such as temperature, rainfall, precipitation) [10, 11]. Analysis of the time series method predates those for particular stochastic processes and Markov chains [12]. The purpose of analyzing time series is describing and summarizing data and meetings from time series to low-dimensional model and predicting future predictions.

3.2 Rainfall Variability

Rainfall Variability During Kharif Season. The maximum rainfall occurred in the Kharif season from July to September months of the year. As shown in the table, the average annual rainfall was divided into five categories as shown in Table 2. During Kharif season, the spatial distribution of rainfall is shown in the eastern part of northern hills zone comprising headquarters of Jashpur District and its surrounding area. Due to hilly region, onset of monsoon is early and also active during Kharif season, made to get maximum rainfall in this season.

Rainfall Variability During Rabi Season. As mentioned above, the highest precipitation during the Rabi season varies from 80 mm to 160 mm. Most of the plains of Chhattisgarh, southern mountains, and the southern portion of the plateau of Baster fall under very low rainfall, (<85 mm), and the average annual rainfall has been divided into five categories as shown in Table 3.

Table 2 Rainfall during Kharif season [13]

S. no.	Category	Rainfall in (mm)
1.	Very high	(>1525)
2.	High	1450−1525
3.	Medium	1375−1525
4.	Low	1300−1375
5.	Very low	(<1300)

Table 3 Rainfall during Rabi season [13]

S. no.	Category	Rainfall in (mm)
1.	Very high	(>160)
2.	High	130−160
3.	Medium	100−130
4.	Low	85–100
5.	Very low	(<85)

3.3 Trend Analysis

It is the most common statistical method used to explore the hydro-climatic time scale temporal change [14]. The current research utilizes a non-parametric test (such as Mann–Kendall and Theil–Sen Slope) experiment to evaluate trend identification. A non-parametric test is considered as it is robust against outliers and distribution-free [15].

4 An Analytical Method for Trend Analysis

4.1 Quantification of Trend Significance by MK Test

The aim of the Mann–Kendall (MK) experiment is to statistically evaluate whether the interest variable over time series has a monotonous upward or descending tendency [16]. A monotonous upward (downward) trend involves constantly growing (decreasing) factors over time, but sometimes the trend may or may not be linear. This method does not require any assumption (i.e., distribution-free) and frequently known as the tau statistics of the Kendall, which has been widely used in climatological time series testing for randomness against the trend [17]. The sample size should not be less than four in the statistics of the MK test. It is the most frequently used for analyzing climate and hydrological time scales to detect a trend [18].

The test is based on statistical S as described below in Eq. 1:

$$S = \sum_{j=1}^{N-1} \sum_{j=j+1}^{N} \operatorname{sgn}\left(x_j - x_i\right) \tag{1}$$

where N is the data point number in the given time series, x_i and x_j are the data values at the time scales i and j, respectively, as shown in Eq. 2

$$\delta = \left(x_j - x_i\right) \tag{2}$$

$$\operatorname{sgn}(\delta) = \begin{cases} 1 & \text{if } \delta > 0 \\ 0 & \text{if } \delta = 1 \\ -1 & \text{if } \delta < 0 \end{cases} \tag{3}$$

In Eq. 3, the mean and variance of the S statistics are assumed to be independent and identically distributed [19] and $E(S) = 0$, therefore

$$\operatorname{Var}(S) = \frac{N \cdot (N-1) \cdot (2N+5) - \sum_{k=1}^{n} tk \cdot (tk-1) \cdot (2tk+5)}{18} \tag{4}$$

$$Z = \begin{cases} \dfrac{s-1}{\sqrt{\text{var}(s)}} & \text{if } S > 0, 0 \text{ if } S = 0, \\ \dfrac{S+1}{\sqrt{\text{var}(s)}} & \text{if } S > 0 \end{cases} \tag{5}$$

Here, if the value of $|Z| > Z^*$ then in a two-tailed test, it rejects the null hypothesis of no trend at 5% of the significance level (the trend is significant) [15].

4.2 Theil–Sen Slope Estimator

Theil–Sen slope is useful to estimate the change in the magnitude of a linear trend and has been most commonly used to identify the magnitude of the hydro-meteorological time series. If there is a linear trend, a straightforward non-parametric method is developed by Sen [20]. Here, the full information group's slope (T_i) is calculated which is given below in Eq. 6 [6]:

$$T = \frac{x_j - x_k}{j - k} \text{ for } i = 1, 2, 3, 4 \ldots N \tag{6}$$

where, at time j and k ($j > k$), respectively, the data sizes are x_j and x_k. The slope estimator's median Q_i is depicted in Eq. 7 as

$$Q_i = \begin{cases} \dfrac{TN+1}{2}, & N \text{ is odd}, \\ \dfrac{1}{2}\left(\dfrac{TN}{2} + \dfrac{Tn+2}{2}\right), & N \text{ is even} \end{cases} \tag{7}$$

The increasing trend is depicted by a positive Q_i value, and an adverse valuation in the specified time series is a descending trend.

4.3 Inverse Weighting Distance Algorithm (IWDA)

It is a sort of deterministic technique with a known point for multivariate interpolation [21]. The allocated values to unidentified points are determined using a weighted average of available values at recognized points. The weighted average encouraged this sort of technique [22]. Because when allocated weights, it transferred each known point to the reverse range. A distinct commercial GIS software setting is the most commonly used and available IDW technique [23].

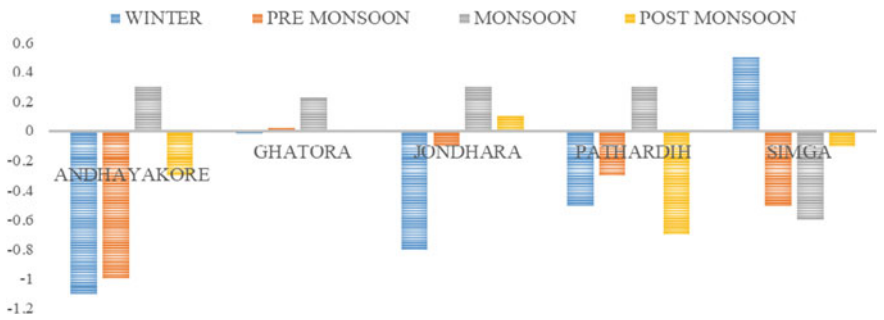

Fig. 5 Mann–Kendall (Zmk) statistics from 1980 to 2012 for seasonal time scale

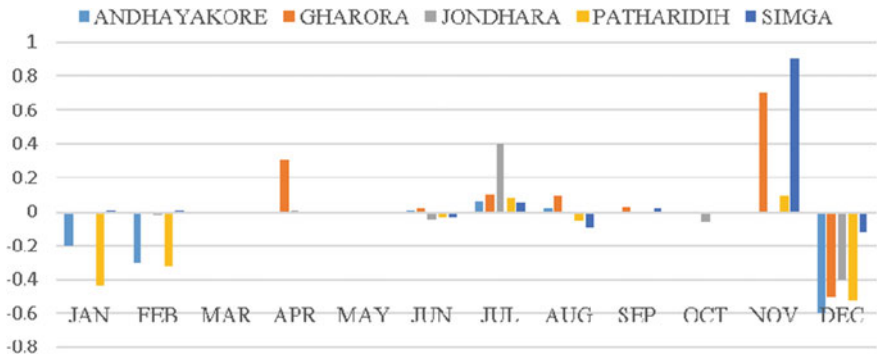

Fig. 6 Sen slope (Q_i) statistics from 1980 to 2012 for monthly time scale

5 Results and Discussion

5.1 Trend Analysis

See Figs. 5, 6 and 7. See Tables 4 and 5.

6 Conclusion

To deal with the ever-changing circumstances, climate change is very preliminary. The trend analysis is performed for the Chhattisgarh State's Sheonath River Basin from 1980 to 2012 monthly rainfall and data is analyzed using non-parametric approaches like a Mann–Kendall and Theil–Sen slope estimator. In this study, the findings show a substantial downward trend at 5% significance level, an average of − 0.10 mm per year for all the five monitoring stations and the amount of rainfall variability decreases by 5.56% compared to the annual average rainfall during the Kharif

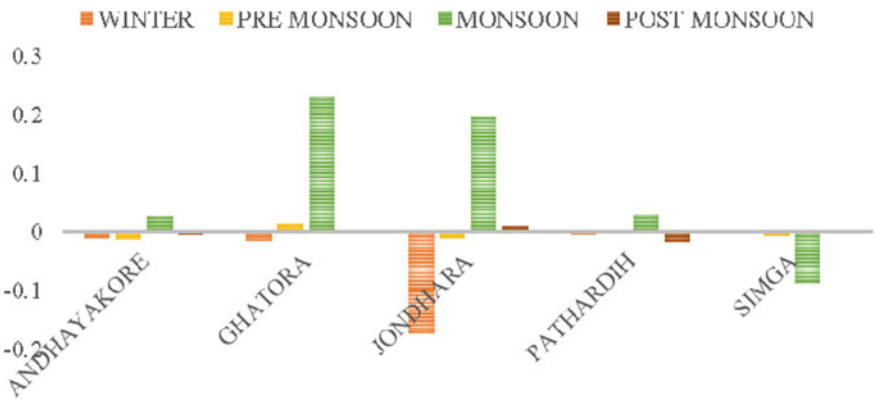

Fig. 7 Sen slope (Q_i) statistics from 1980 to 2012 for seasonal time scale

Table 4 Mann–Kendall (Zmk) statistics from 1980 to 2012 for monthly time scale

Month	Rain gauge stations				
	Andhayakore	Ghatora	Jondhara	Pathardih	Simga
January	−1.10	−0.90*	−1.20*	−0.70*	0.01
February	−0.50*	−1.10*	−1.0*	−0.30*	0.00
March	−0.60*	0.90*	−0.50*	−0.80*	−1.20*
April	−0.40*	0.40**	0.80*	1.20	0.30
May	−1.40*	1.00**	−0.80*	−1.00*	−1.30*
June	0.20	0.40**	−0.20*	−0.60*	−0.50*
July	1.40	1.40**	1.70	1.10	0.90
August	0.50	2.10**	−0.20*	−0.70*	−1.10*
September	−0.40*	0.40**	0.10	0.13	0.20
October	−1.0*	0.10**	−0.80*	−1.00*	−0.60*
November	1.90	0.80**	1.10	0.20	1.10
December	−0.50*	−1.00**	−0.50*	−0.70*	−0.30*
Winter	−1.10	−0.01	−0.80	−0.50	0.50
Pre-monsoon	−1.00	0.01	−0.10	−0.30	−0.50
Monsoon	0.30	0.22	0.30	0.30	−0.60
Post-monsoon	−0.30	0.00	0.10	−0.70	−0.10

The positive statistics of (Zmk) data reflects the increasing trend and an adverse statistic is a declining or decreasing trend in the given time series, and the * sign also indicates the significant decreasing trend and * * indicates the significant increasing trend at 5% significance level

Table 5 Sen slope (Q_i) statistics from 1980 to 2012 for monthly time scale

Month	Rain gauge stations				
	Andhayakore	Ghatora	Jondhara	Pathardih	Simga
January	−0.201	−0.001	−0.012	−0.431	0.01
February	−0.301	−0.001	−0.024	−0.321	0.01
March	−0.000	0.001	−0.009	−0.001	−0.002
April	0.000	0.300	0.011	0.002	0.000
May	−0.005	0.001	−0.015	−0.003	−0.009
June	0.008	0.022	−0.049	−0.031	−0.034
July	0.064	0.104	0.398	0.080	0.052
August	0.025	0.092	−0.001	−0.052	−0.094
September	−0.013	0.027	0.006	0.003	0.021
October	−0.015	−0.002	−0.059	−0.018	−0.006
November	0.000	0.701	0.006	0.101	0.901
December	−0.601	−0.500	−0.400	−0.521	−0.121
Winter	−0.011	−0.015	−0.173	−0.004	−0.006
Pre-monsoon	−0.013	−0.016	−0.010	−0.002	−0.007
Monsoon	0.028	0.229	0.197	0.030	−0.087
Post-monsoon	−0.005	0.004	0.011	−0.018	−0.002

Q_i's positive value represents the increasing trend and a negative value reflects a declining or decreasing trend in the specified time series

season, and the rainfall variability decreases 93.14, 93.88, and 93.34% compared to the annual average rainfall in the Rajnandgaon, Durg, and Kawardha Districts during the Rabi season, respectively. This study demonstrates that understanding of changes in the pattern of rainfall and their periodic assessment could be useful for hydrologist management and irrigation planning to make more effective use of the water of the area and appropriate decision on crop patterns as well as crop suitability.

References

1. Chakraborty S, Pandey RP, Chaube UC, Mishra SK (2013) Trend and variability analysis of rainfall series at Seonath River Basin, Chhattisgarh (India). J Appl Sci Eng Res 2(4):425–434. https://doi.org/10.6088/ijaser.020400005
2. Swain S (2014) Impact of climate variability over Mahanadi river basin. Int J Eng Res Technol 3(7):938–43. ISSN: 2278-0181
3. Mudelsee M (2018) Trend analysis of climate time series: a review of methods. Earth Sci Rev. https://doi.org/10.1016/j.earscirev.2018.12.005
4. Gosain AK, Rao S, Basuray D (2006) Climate change impact assessment on hydrology of Indian river basins. Curr Sci 90(3):346–353
5. Katz RW, Brown BG (1992) Extreme events in a changing climate: variability is more important than averages. Clim Change 21(3):289–302. https://doi.org/10.1007/BF00139728

6. Parthasarathy B, Dhar ON (1975) Trend analysis of annual Indian rainfall. Hydrol Sci Bull 20(2):257–260
7. Guhathakurta P, Rajeevan M (2008) Trends in the rainfall pattern over India. Int J Climatol: A J Royal Meteorol Soc 28(11):1453–1469. https://doi.org/10.1002/joc.1640
8. Choudhury A, Jones J (2014) Crop yield prediction using time series models. J Econ Econ Educ Res 15(3):53
9. Hipel KW, McLeod AI (1994) Time series modelling of water resources and environmental systems, vol 45. Elsevier
10. Adhikari R, Agrawal RK, (2013) An introductory study on time series modeling and forecasting. arXiv preprint arXiv:1302.6613
11. Longobardi A, Villani P (2010) Trend analysis of annual and seasonal rainfall time series in the Mediterranean area. Int J Climatol 30(10):1538–1546. https://doi.org/10.1002/joc.2001
12. Verma MK, Verma MK, Swain S (2016) Statistical analysis of precipitation over Seonath river basin, Chhattisgarh, India. Int J Appl Eng Res 11(4):2417–2423
13. Bhelawe S, Chaudhary JL, Nain AS, Singh R, Khavse R, Chandrawanshi SK (2014) Rainfall variability in Chhattisgarh State using GIS. Curr World Environ 9(2):519
14. Adarsh S, Janga Reddy M (2015) Trend analysis of rainfall in four meteorological subdivisions of southern India using nonparametric methods and discrete wavelet transforms. Int J Climatol 35(6):1107–1124. https://doi.org/10.1002/joc.4042
15. Potvin C, Roff DA (1993) Distribution-free and robust statistical methods: viable alternatives to parametric statistics. Ecology 74(6):1617–1628. https://doi.org/10.2307/1939920
16. Hirsch RM, Slack JR (1984) A nonparametric trend test for seasonal data with serial dependence. Water Resour Res 20(6):727–732. https://doi.org/10.1029/WR020i006p00727
17. Zhang X, Harvey KD, Hogg WD, Yuzyk TR (2001) Trends in Canadian streamflow. Water Resour Res 37(4):987–998. https://doi.org/10.1029/2000WR900357
18. Zhang Q, Liu C, Xu CY, Xu Y, Jiang T (2006) Observed trends of annual maximum water level and streamflow during past 130 years in the Yangtze River basin, China. J hydrol 324(1–4):255–265. https://doi.org/10.1016/j.jhydrol.2005.09.023
19. Kendall MG (1975) Rank correlation measures. Charles Griffin, London 202:15
20. Sen PK (1968) Estimates of the regression coefficient based on Kendall's tau. J Am Stat Assoc 63(324):1379–1389
21. Lu GY, Wong DW (2008) An adaptive inverse-distance weighting spatial interpolation technique. Comput Geosci 34(9):1044–1055. https://doi.org/10.1016/j.cageo.2007.07.010
22. Lam N-S (1983) Spatial interpolation methods: a review. Am Cartogr 2:729–749. https://doi.org/10.1559/152304083783914958
23. Burrough PA (1986) Principles of geographical information systems for land resources assessment. Oxford University Press, New York, NY

Performance Evaluation of Pench Command Area of Maharashtra, India Using Spatial Approach

Digambar S. Londhe, Y. B. Katpatal, and Garima Newar

Abstract Scientific planning requires information about the irrigation projects. The surface water and groundwater sources support the irrigation purpose in India which requires regular monitoring to generate feedbacks regarding the optimum utilization of the water resources as well as the efficiency of the schemes. In this study, effect of irrigation has been evaluated based on variations in crop density in temporal and spatial scale from NDVI obtained from MODIS (moderate resolution imaging spectroradiometer) for the years 2006–2016. For this study, Pench command area of Vidarbha Region of Maharashtra was digitized along with their canal network; LULC map was generated indicating agricultural lands. By using the NDVI images for the different seasons of cultivation, crop density was determined. The entire command area was classified into varying crop density classes. Area of coverage of each class was then studied and later correlated with the water released for irrigation through the canal system. The study corroborates the use of the spatial technologies of remote sensing and geographical information system for generating vital information required for command area performance evaluation and further organization of the information for futuristic management of the agricultural land and water resources.

Keywords Kharif · Rabi · NDVI · Irrigation · GIS

1 Introduction

Indian economy is largely dependent on agriculture and most of the agricultural activity relies on monsoon. Inconsistent distribution of rainfall and inadequate land and water management practices result in water scarcity problems in most of the sub-humid regions in India. Prolonged dry spells and the resulting agricultural drought are very common in the rain-fed agricultural lands in such areas. This non-uniform nature

D. S. Londhe (✉) · G. Newar
Department of Civil Engineering, Visvesvaraya National Institute of Technology, Nagpur, India
e-mail: digambarlondhe@students.vnit.ac.in

Y. B. Katpatal
Water Resource Engineering, Visvesvaraya National Institute of Technology, Nagpur, India

© Springer Nature Singapore Pte Ltd. 2021

K. K. Pathak et al. (eds.), *Recent Trends in Civil Engineering*, Lecture Notes in Civil Engineering 77, https://doi.org/10.1007/978-981-15-5195-6_59

of rainfall makes irrigation a necessity in most parts of India. Vidarbha Region of Maharashtra, which forms a part of Central India, receives moderate rains from mid-June to mid-September. But, the crop seasons extend from mid-June to mid-October (Kharif), mid-October to mid-February (Rabi), and in some regions in March and April. Thus, irrigation is essential in this area. Khan et al. [1] in their paper concludes that there will be a fall in water resource availability from 72% in 1995 to 62% by 2020 globally, and from 87 to 73% in developing countries alone. Ashofteh et al. [2] in their report, "Impacts of Climate Change on the Conflict between Water Resources and Agricultural Water Use" concluded that the crops under changing climatic conditions will have larger irrigation requirements.

The growth and health of crops of a region directly depend on the availability of irrigation facilities. The NDVI (normalized difference vegetation index) provides us with a measure of greenness of vegetation by using remote sensing and is related to various properties of vegetation including its growth and productivity [3]. Different long-term changes in our surroundings such as photosynthetic activities [4], vegetation density [5], and deforestation [6] can be analyzed from NDVI time series. Monitoring seasonal changes in vegetation activity and crop phenology over wide areas is essential for many applications, such as estimation of net primary production [7] and supporting decisions about water supply [8].

For an efficient irrigation system, the foremost requirement is proper planning that aims at optimum utilization of available water, from rainfall as well as water stored in the reservoir supplementing the agricultural activities in the nearby commands. To achieve this, every year various irrigation departments across the nation prepare irrigation planning report. And, even after such an efficient and substantial planning, it is observed that the irrigation efficiency may not be as expected. Various factors affect the irrigation scenario. Hence, the ultimate objective of better crop production is affected. Thus, an efficient and quick monitoring mechanism becomes essential. To assess the performance of irrigation system of a command area by spatial techniques, a measure of density of crop and crop health can be considered as an effective parameter. The advancement in satellite technology in terms of spatial, temporal, spectral, and radiometric resolutions successfully leads to more specific and intensified research on agriculture [9]. Automatic assessment of spatial–temporal cropping pattern and extent at multi-scale (community level, regional level, and global level) has been a challenge to researchers.

Remotely sensed data and GIS techniques are gaining popularity as an effective way to monitor crop health and other climatic and physiographic factors. Any variation from the existing or expected pattern of crop growth can be studied and impact of various other factors on the same can be analyzed. Brian and Stephen [10, 11] in their study of crop mapping used time series MODIS 250 m NDVI data to evaluate the applicability of time series MODIS 250 m normalized difference vegetation index (NDVI) data for large-area crop-related LULC (land use/land cover) mapping and concluded that the series of MODIS NDVI-derived crop maps generally had classification accuracies greater than 80%.

This study is focused on monitoring of crop density by means of time series analysis with vegetation indices and also to measure the change in agricultural area

due to availability of canal system and to identify a trend for crop density in the selected command area with regard to irrigation facilities available.

In this study, it has been aimed to evaluate the performance of a command area, irrigated majorly by canal system, by using remote sensing and GIS for the period 2006–2016 in different crop seasons. A time series analysis is conducted by using freely available NDVI data to study the crop growth and use of simple yet effective GIS techniques to supplement the analysis. LULC maps are generated to understand the extent of agriculture land. Also, an attempt has been made for a proper understanding about ENSO conditions and rainfall variations, which, in turn affects the crops in the study area, and will provide the capability to successfully improve and manage agriculture.

2 Materials and Data Used

2.1 Study Area

Figure 1 shows the location map of the study area considered for the present study, i.e., Pench command area. This area is located in the Nagpur Division, Vidarbha Region of Maharashtra. Pench is located in the districts of Nagpur and Bhandara with its area of 1891 km^2. Pench Major Irrigation Project was established in the year 1989 and three storage reservoirs, Totladoh, Navegaon Khairy, and Khindsi, were created by the construction of dams for the purpose of irrigation and power generation.

The climate is typical seasonal monsoon type with maximum and minimum temperatures as 490 °C during summer and 50 °C during winter, respectively. Ecological sub-region is hot dry to moist sub-humid type. The soil present is pre-dominantly black cotton and lithology is almost homogenous basalt. Average rainfall range is 800–1200 mm most of which is experienced during mid-June to mid-October, which also marks the major cultivation season.

2.2 Data Used

MODIS NDVI Time Series Data. For assessment of crop density as a response to irrigation facility available in the study area, a time series analysis was conducted using NDVI images for the period 2006–2016. The analysis was done for all the three major crop seasons, namely, Kharif, Rabi, and Hot Weather (Fig. 2).

NDVI values vary with the absorption of red light by plant chlorophyll and the reflection of infrared radiation from water-filled leaf cells [12]. MODIS NDVI data are collected for the period 2004–2016. MOD13Q1 datasets were obtained with spatial resolution of 250 m and temporal resolution of 16 days. The NDVI is the

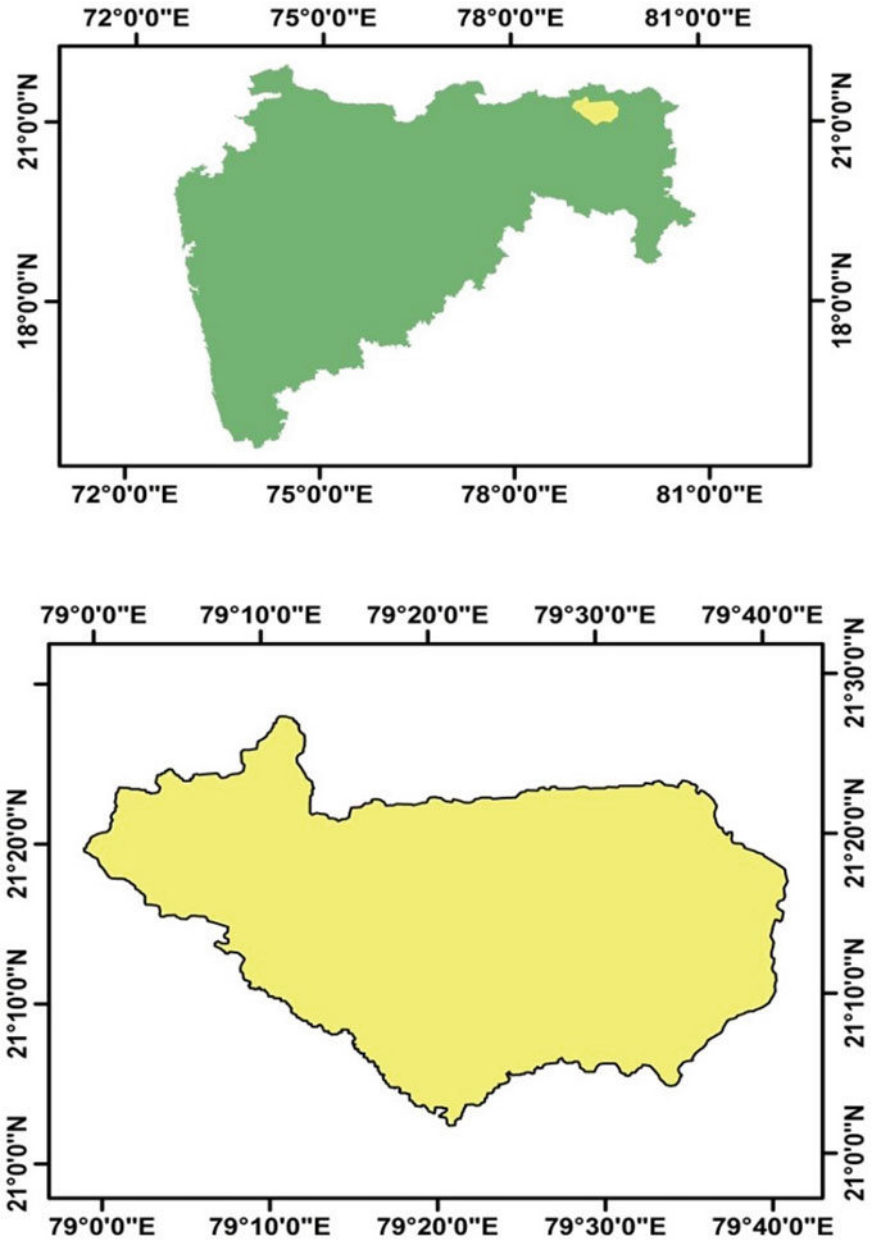

Fig. 1 Location map of Pench command area

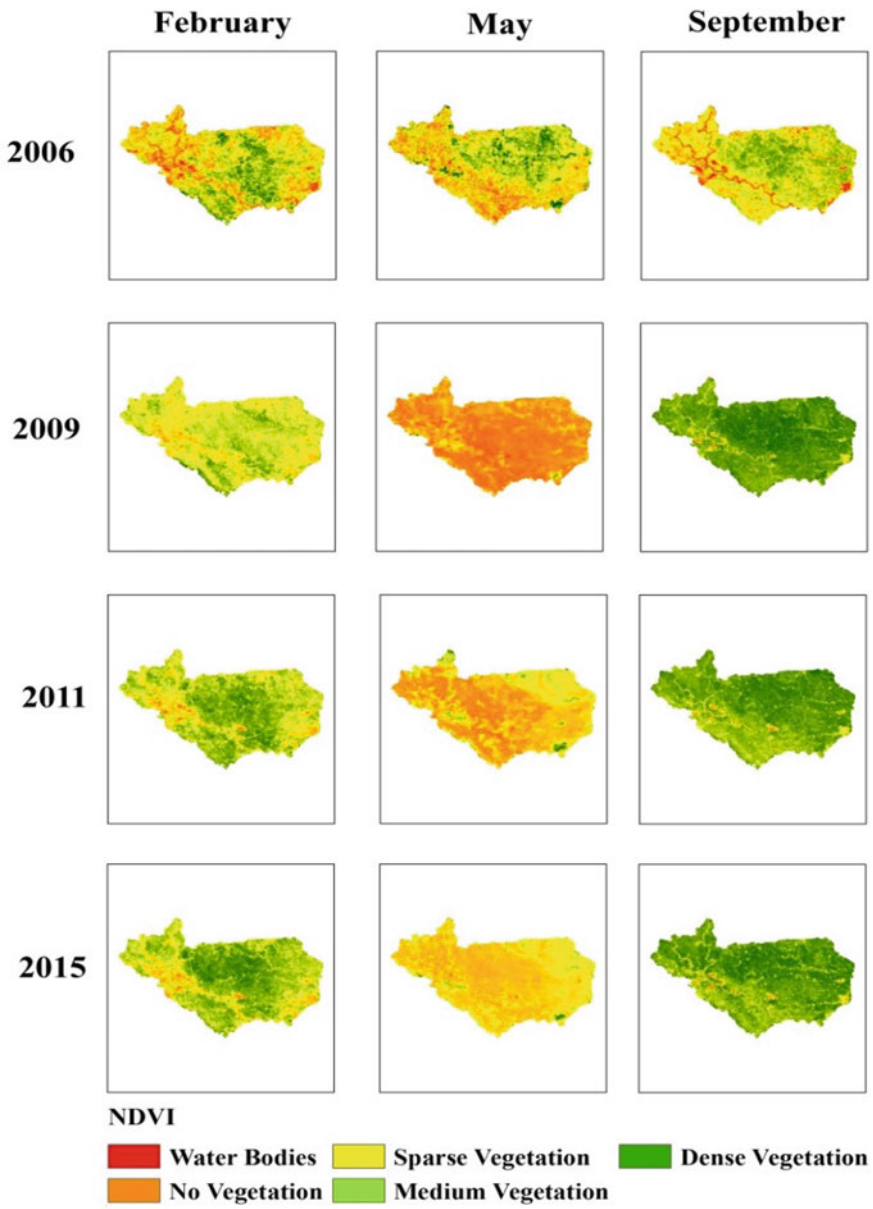

Fig. 2 NDVI variation within the study area

Table 1 NDVI Classification and their classes

Class	NDVI range
Water bodies	<0.1
No vegetation	0.1–0.3
Sparse vegetation	0.3–0.5
Medium vegetation	0.5–0.7
Dense vegetation	>0.7

Table 2 Average annual rainfall in "mm" in Pench command area

Year	Average annual rainfall in "mm"
2005	1544.2
2006	1070.9
2007	1082.1
2008	919.2
2009	1009.6
2010	1270.2
2011	1043.1
2012	1039.6
2013	1479.1
2014	784.5
2015	1104.2
2016	864.8

index, which gives the information about the actual situation and growth of the vegetation and crop condition. NDVI value varies between −1 and +1 and classified into five classes as given in Table 1. Annual minimum NDVI occurred in the month of May and annual maximum NDVI occurred in September. Based on the NDVI value, the surface conditions are classified between five classes.

NDVI also depends on the temperature and rainfall. Maximum rainfall occurs in the month of August, and therefore the vegetation index is the maximum in the month of September since the growth of the vegetation is increasing. Also, in April and May, the temperature is maximum, and hence vegetation decreases; therefore, NDVI value is less in May.

Variation in the NDVI values, hence, is based on temperature, precipitation, available moisture, type of the crop or vegetation, and growing stage of the vegetation [13].

Rainfall Data. Rainfall data is collected from the website of Rainfall Recording and Analysis, Department of Agriculture Maharashtra State [14]. Actual yearly average rainfall data is collected for the period 2006–2016 for all the Talukas of Nagpur and Bhandara Districts. Then mean annual rainfall was found out for Pench command area in Table 2.

A point shape file is created depicting all the rain gauge sites in and around the Pench commands. Average annual rainfall is attached in the attribute table. Then, Thiessen polygons were created around each rain gauge site and extent was set as the study area boundary. Area of each polygon is determined using calculate geometry option.

Figure 3 shows the decreasing trend of the rainfall within the study area. Even though the trend is decreasing, the rainfall graph clearly indicates the fluctuations in the rainfall for every 2–3 years. This trend may be because of the different ENSO events and climatic phases such as El Niño and La Niña.

Irrigation Canal Network Map. Figure 4 shows the extent of canal system present in the study area overlaid on the Google Earth image of recent period. The

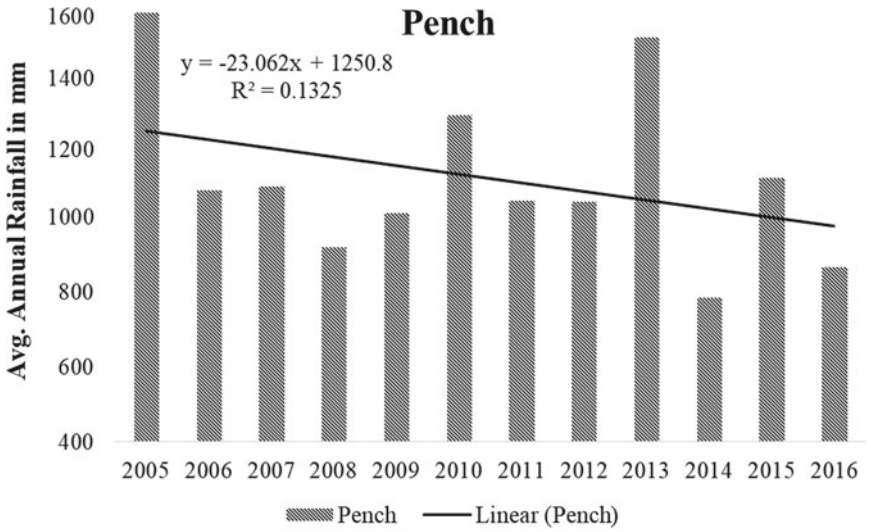

Fig. 3 Trend of rainfall in command area

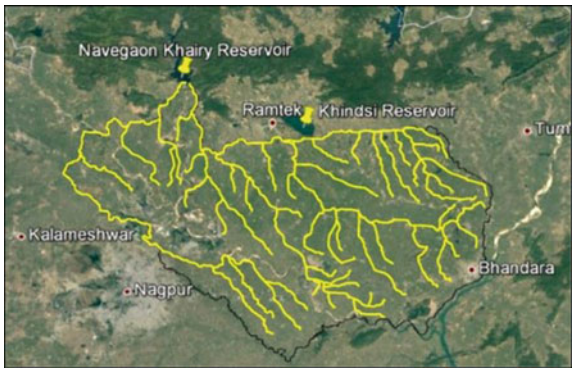

Fig. 4 Google Earth image of Pench command area showing the canal network

major canals, i.e., LBC and RBC, taking off from the reservoirs, branch canals, and distributaries have been shown.

3 Methodology

The methodology consists of determining the area of cultivated land in different crop seasons, density of crops grown, and availability of water for irrigation through canal network. The impact of irrigation through canals on crop growth within the selected command areas has been studied. An assessment of crop health has been done by time series analysis using NDVI images. Figure 5 shows the overall methodology adopted in the analysis. Overall methodology is broadly divided into four sub-parts which are explained in this section.

3.1 Analysis of Land Use/Land Cover

Land use/land cover images of scale 1:250,000 were downloaded from ISRO Bhuvan portal [15]. LULC maps were generated for the years 2006–2014 using ArcMap software by raster-based supervised classification. The image is classified into eight different classes. The total area of all the classes is calculated using image processing technique in ArcMap. Then the statistical analysis of all the classes is calculated and comparison is done for the years 2006 and 2014.

3.2 Analysis of Water Released in Canal Irrigation

The total water released for the command area was collected from the Water Resource Department, Maharashtra State. Based on the collected data, the graph for the release

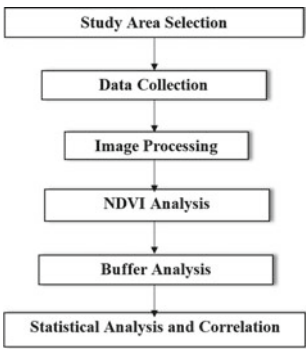

Fig. 5 Overall methodology adopted in the analysis

of water for different seasons is plotted. Also, the graph of the number of days of operation for release of water represents the condition and total area covered with crop throughout the study area during 2006–2016. The total irrigated area assessed by irrigation department is also plotted which represents the increasing trend from 2006 to 2016. Overall methodology is shown in Fig. 5.

3.3 NDVI Analysis

For assessment of density of vegetation within the command area, a time series analysis with vegetation indices is done using NDVI images. NDVI images are a product of MODIS sensor of Earth Observatory Satellites of NASA. In the analysis carried out for the NDVI, the Zonal Statistics tool in ArcMap is used to extract the pixel-wise NDVI values throughout the image. To study the crop condition in the each season, based on the NDVI range, the image is classified into four classes as no crop, less dense crop, moderate dense crop, and very dense crop. Then the statistical analysis is carried out for the NDVI values for different seasons in the year which shows the variation in the mean NDVI values is presented in the graphical form.

3.4 Buffer Analysis

Buffer zones of 500, 1000, and 1500 m were generated on either side of the main canals and distributaries of Pench command area and were then dissolved to get a single vector polygon feature.

These buffer zones were then used to clip NDVI images to study adjacency of dense crop class to the canal network. The largest sized buffer served another purpose of taking into account the impact of irrigation through minor canals and field channels as these were almost 1–2 km in length and were not digitized keeping in view the scope of present study.

3.5 Statistical Analysis

The data obtained by NDVI time series analysis in the form of tables of NDVI values and area were then used to find out mean NDVI value of each crop density class and area of coverage of that class, respectively. Plots were made for the period 2006–2016 for both command areas and linear correlation was done between area of crop coverage and water release for respective crop seasons. The trends were identified and studied.

4 Results and Discussion

For an efficient irrigation system, the foremost requirement is proper planning that aims at optimum utilization of available water, from rainfall as well as water stored in the reservoir supplementing the agricultural activities in the nearby commands. To achieve this, every year various irrigation departments across the nation prepare irrigation planning report. And, even after such an efficient and substantial planning, it is observed that the irrigation efficiency may not be as fulfilled and various factors affect the irrigation scenarios during the year. Hence, the ultimate objective of getting better crop production is affected. Thus, an efficient and quick monitoring mechanism becomes essential. To assess the performance of irrigation system of a command area by spatial techniques, a measure of density of crop and crop health can be considered as an effective parameter.

To fulfill the objectives considered for the study, NDVI images, LULC images, and rainfall data are processed with ArcMap 10.1 software. Then, buffer analysis, trend analysis, and correlation analysis are done. The results obtained are discussed in this section.

4.1 Comparison of Land Use/Land Cover Classification

The LULC maps are generated for the study areas for the period 2006–2014. The supervised classification is carried out in ArcGIS 10.1 by collecting the training samples from the raster image. The comparison of the LULC maps is done by calculating the total area of each class within the study area. LULC map is shown in Fig. 6.

Comparison of LULC classes is elaborated with the help of graphical representation as shown in Fig. 7. The result shows that areas of all the LULC classes are decreased except double/triple crop class. Area of Rabi crop is largely decreased in 2014 as compared to 2006, whereas double/triple crop is largely increased in 2014 which shows that the area of Rabi crop is replaced by the double/triple crop in 2014. Same results, i.e., maximum area of Rabi crop which is replaced by double/triple crop is shown in Fig. 5 which compares the LULC in 2006 and 2014.

If the only two scenarios of area of vegetation and area of no vegetation are compared in the study area, the change in the area is explained in Table 3. This gives the information that the area of vegetation is increased by 5.128% in 2014 and that of area of no vegetation is decreased by 30.752% in 2014. This result shows that the irrigation capacity and management of irrigation water is preferably better in 2014 than 2006 in the Pench command area.

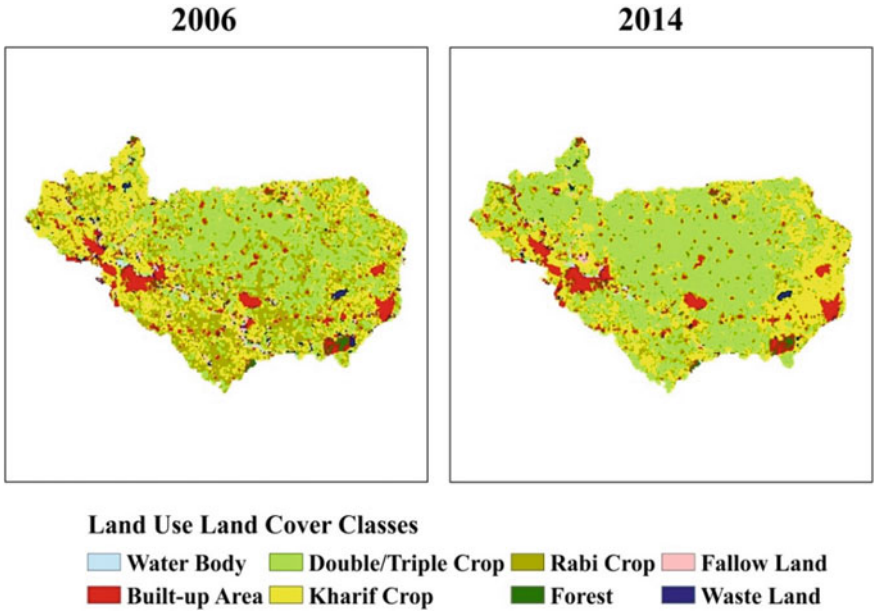

Fig. 6 LULC map of Pench command area for the years 2006 and 2014

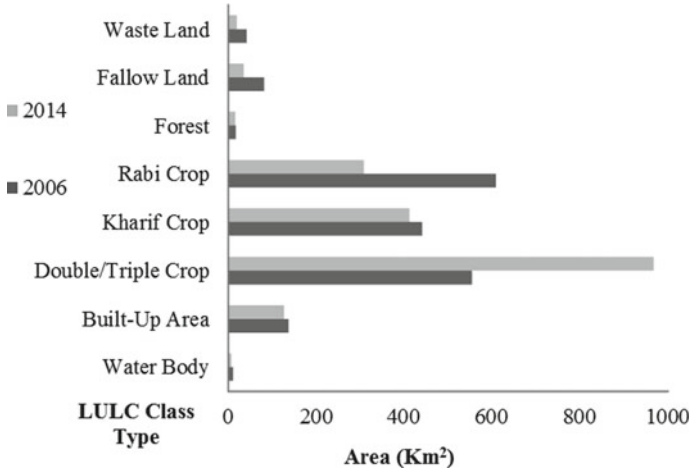

Fig. 7 Comparison of LULC classes in Pench for the years 2006 and 2014

Table 3 Comparison between coverage of area of vegetation and no vegetation classes. All units in sq. kms

Class	2006	2014	Change in %
Area of vegetation	1620.301	1703.073	+5.128
Area of no vegetation	271.639	188.104	−30.752

4.2 Water Releases for Canal Irrigation

Graphical representation of water released in the canals for irrigation for Pench command area is shown in Fig. 8. The total annual releases along with releases in different crop seasons, i.e., Kharif, Rabi, and Hot Weather are plotted for the period 2006–2016.

It is observed that the release of water in Kharif season increased than that in Rabi season showing the increasing dependence of Kharif crops on surface irrigation from the year 2012 to 2016. It may be inferred that double season crop cultivation increased in Pench. Also, years 2008–2009 and 2015–2016 show minimum annual releases. This is due to insufficient monsoon rainfall and decreased storage in the reservoirs. The decrement in release of water in Rabi season may be because of the less amount of water available in the reservoirs for that period. The availability of water is mainly affected by the amount of precipitation in that year and other losses of water.

Release of water in canals may also be affected by the canal operations in number of days done in that year. Figure 9 shows that the season-wise total number of days of canal irrigation operation within Pench command area has been done. There is drastic change in the year 2009 which is shown in Fig. 9. This is because the lowest rainfall occurred in the year 2008 and hence amount of water is very less for the supply for irrigation purpose.

Figure 10 shows the total area assessed as irrigated land by the irrigation department of Maharashtra State for the period 2006–2016. This shows an increasing trend for command area considered for study. Hence, it may be inferred that irrigation facilities improved within the commands. This data includes area irrigated by canals, wells and nallas, river lifts and reservoir lifts in all the crop seasons, Kharif, Rabi, and Hot Weather.

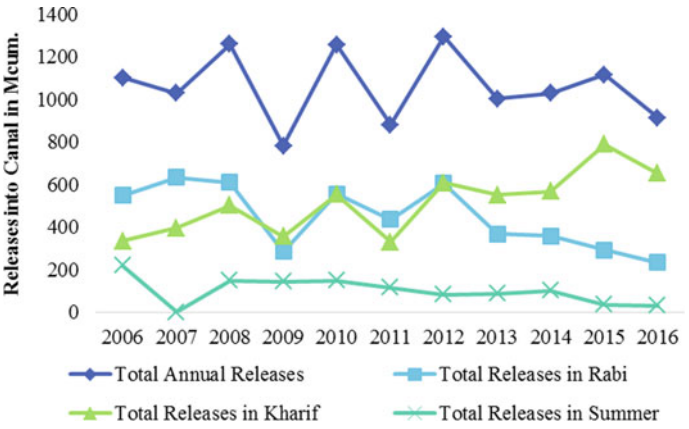

Fig. 8 Irrigation water releases into canals for Pench area

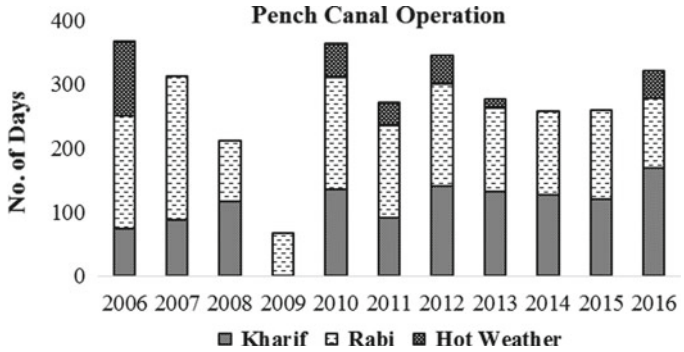

Fig. 9 Total no. of days of canal irrigation within Pench area

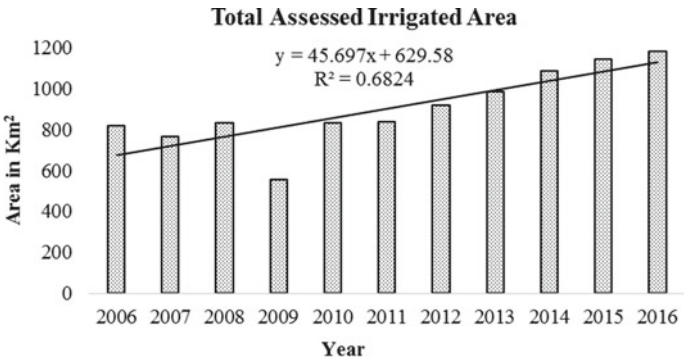

Fig. 10 Total irrigated area assessed by the irrigation department

4.3 NDVI-Based Crop Classification

For the present study, all the NDVI images from 2006 to 2016 were studied. Then, images affected by clouds and other noises were excluded from the study as applying techniques for removal of cloud interference and any other sorts were out of scope of the present study. Hence, images for the month of June, July, and August were discarded in the process.

The images were then categorized based on the major cultivation seasons, i.e., Kharif, Rabi, and Hot Weather. Images for the month of September and October were considered as Kharif images. For Rabi, the images of December, January, February, and March have been considered. April and May have been selected for hot weather crop images.

NDVI gives a measure of greenness of vegetation. A crop is considered to have maximum greenness during its flowering period when it has attained full growth of the leaf structure. Hence, out of all the images available for each crop season, we considered images of September, February, and April, respectively, for the final

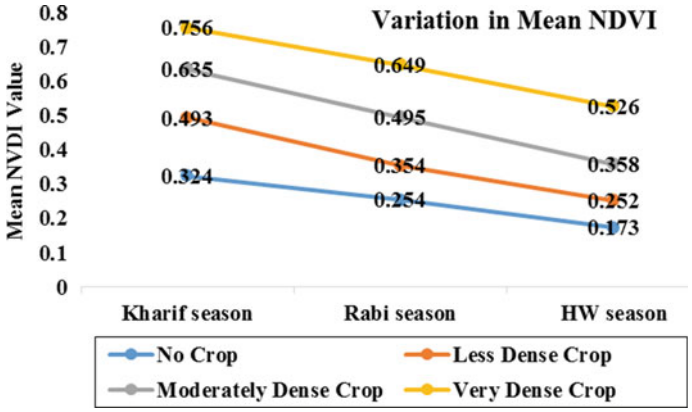

Fig. 11 Irrigation water releases into canals for Pench area

Table 4 Crop classification for the commands based on NDVI values

Class	NDVI-based crop classes			
Crop season	No crop	Less dense crop	Moderately dense crop	Very dense crop
Kharif season	<0.40	0.40–0.55	0.55–0.70	>0.70
Rabi season	<0.30	0.30–0.40	0.40–0.60	>0.60
Hot Weather season	<0.20	0.20–0.30	0.30–0.50	>0.50

analysis. This data was also synced with the general crop calendar of major Kharif and Rabi crops grown in the areas under study.

Based on the NDVI values and by help of LULC map, the entire command area was classified into four classes as follows: (1) No Crop, (2) Less Dense Crop, (3) Moderately Dense Crop, and (4) Very Dense Crop. The range of NDVI classes was fixed and is different for different seasons. This is done to account for the fact that each kind of crop has a specific spectral response, and hence a unique NDVI value range. Different crops are grown in different crop seasons. The threshold value for No Crop class for Kharif season was highest at 0.4 and it was least in summer season.

Figure 11 is a graphical representation of variation of mean NDVI for different classes in the major growing seasons. In Kharif season, i.e., monsoon crops mean NDVI for very dense class is more than 0.75 which represents good cultivation, and hence better crop yield. The mean NDVI for No Crop class is only 0.17 for summer season as given in Table 4.

4.4 Buffer Analysis of Canal Network within Command Area

Figure 12 shows a comparison between the crop scenario in Pench for the years

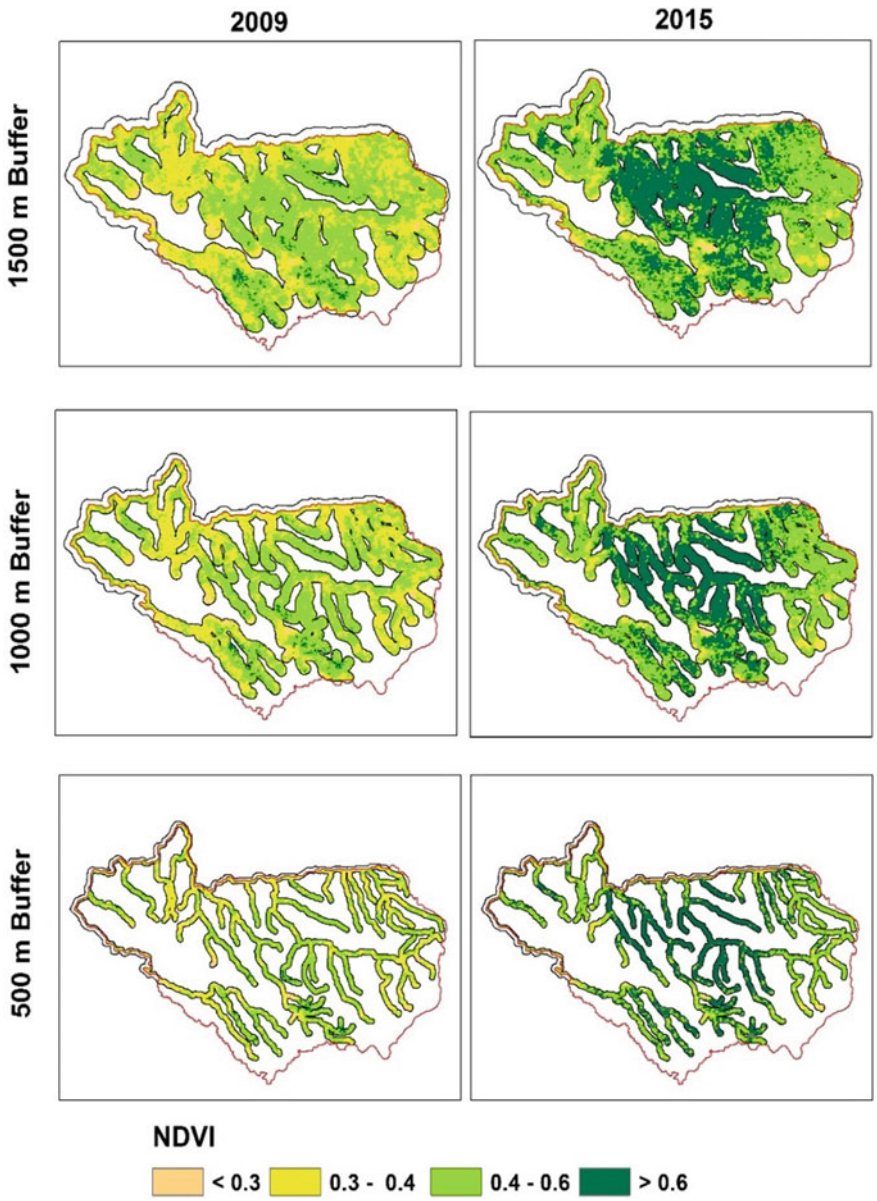

Fig. 12 Crop scenario in buffer zones of Pench in Rabi season

2009 and 2015 for Rabi crop season. Various previous researchers have implied a decreased vegetation activity for the El Nino ENSO event. This is also evident for the year 2009 as dense crop class is negligibly present. But the year 2015 shows very satisfactory crop cultivation with maximum area in the buffers showing a very dense crop class. As Pench hardly receives any winter rains, this increased agriculture activity can be said to be an effect of canal irrigation.

Figure 13 shows summer crop cultivation for the years 2009 and 2015, respectively. The April month of 2009 does not show a good cultivation within the command, even around the canals in 1500 m buffer. In case of 2015, almost all the areas inside buffer have moderate density of crops. Even the La Nina year 2009 shows maximum coverage of less dense crop, although the left bank canal area shows some moderate dense crop coverage. The year 2015 has a far better condition for summer crops. But, releases for these years in Hot Weather season hardly differed. Hence, this can be due to more use of groundwater for irrigation.

4.5 Statistical Analysis

Table 5 shows correlation matrix created for water release through canals for irrigation and area of dense crop coverage. Water releases for months of December, January, and February were correlated with areas of February month to find out the dependency of Rabi cultivation on canal irrigation. This was done for the full command area and 1500 m buffer zones for Pench command area.

5 Conclusions

Remote sensing can determine vegetation distribution and occurrence, and also how various factors influence it. As the availability of time series data of high-resolution satellite products is restricted, MODIS is one of the best options for time series analysis. In the present study, MODIS data is found to be beneficial in characterizing the crop classes based on NDVI index over space and time, which can be very helpful for the determination of cropping pattern, and thus proper planning and management of irrigation water. In addition, the digitization of canal network and LULC map generation through ArcGIS are found to be very convenient. The vegetation cover within the commands increased from 85.6 to 90.1% in Pench between the years 2006 and 2014. Rainfall analysis shows that during the period of study, 2006–2016, rainfall in the command area had a decreasing trend.

It is observed that the NDVI values for different LULC classes vary with respect to the season; highest NDVIs are found in monsoon and lowest during the summers. Maximum area of coverage of very dense type of crop is observed during the Kharif season. Buffer analysis proved to be very effective in identifying the fact that dense vegetation occurrence is the maximum within the buffer zones, in proximity to the

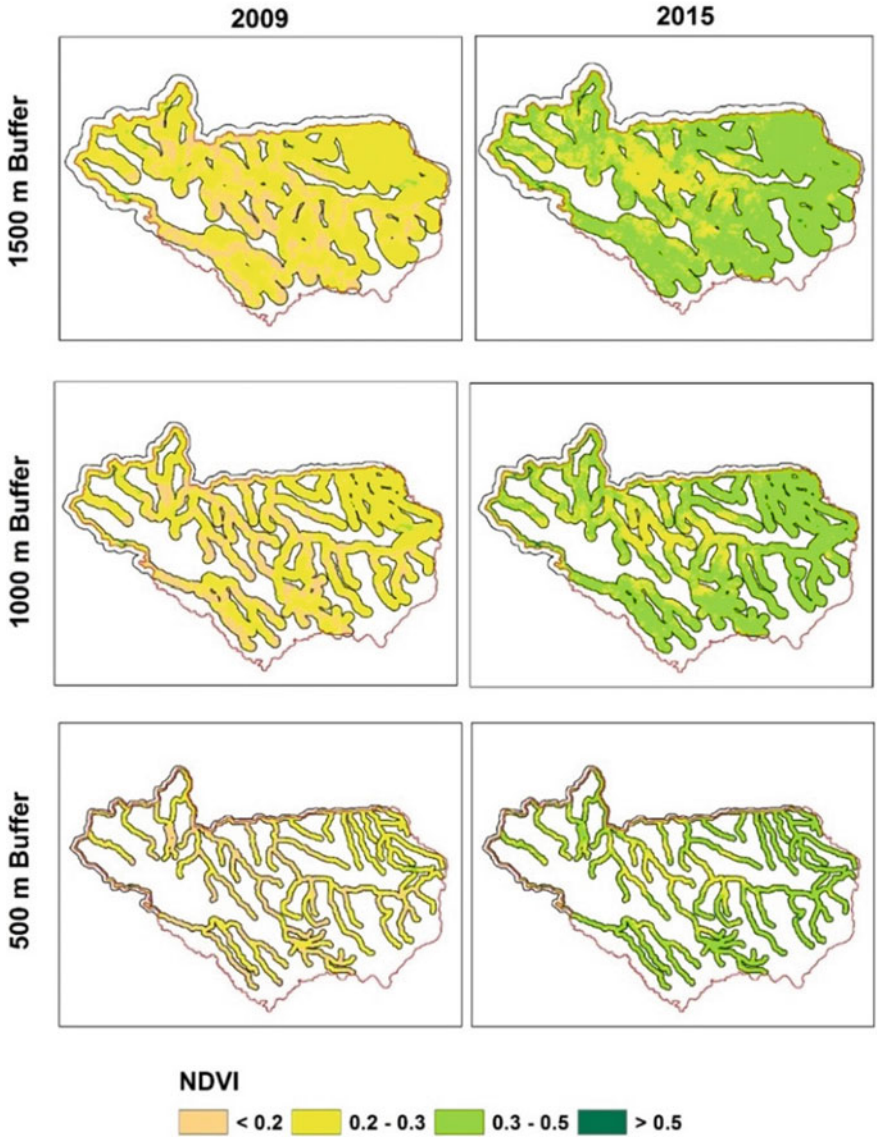

Fig. 13 Crop scenario in buffer zones of Pench in April month

canals. For the results of correlation carried out for the overall area, the linear correlation matrix showed lower levels of correlation in most of the cases. Also, NDVI values vary with crop type, difference in growing period, lengths of crop period, climate, etc. Therefore, a similar methodology can be adopted for crop-wise analysis, and the results can be more accurate by using very high-resolution satellite images. The NDVI values can be further related with irrigation scheduling pattern

Table 5 Correlation matrix for water releases and dense crop coverage for the whole Pench command area and 1500 m buffer area in the commands for the years 2006–2016

Linear correlation matrix of area and water releases into canal for irrigation from 2006 to 2016				
	For entire Pench command area		For 1500 m buffer in Pench command area	
	Water releases in December, January, and February	Water releases in March and April	Water releases in December, January, and February	Water releases in March and April
Very dense crop area	0.3521	0.7973	0.3212	0.8102
Moderately dense crop area	0.4162	0.3540	0.4213	0.3731
Very dense and moderately dense crop area combined	0.5674	0.3679	0.7214	0.3903

Similarly, water releases in the months of March and April were correlated with area of April month to find out impact of canal irrigation supplies on summer crops. Results showed a better correlation in this case. Thus, the extensive canal system has a lot of effect on the agricultural activities of Pench. The combined very dense and moderately dense classes showed highest correlation

practiced in Maharashtra and a better understanding of irrigation system management can be obtained. This work can be extended to evaluate the efficiency of irrigation scheduling method. It is also possible to find out an optimum irrigation scheduling method for this region having maximum crop production with minimum irrigation facilities. The study shows new vistas for application of remote sensing and GIS in water management within command areas.

References

1. Khan S, Tariq R, Yuanlai C, Blackwell J (2006) Can irrigation be sustainable? Agric Water Manag 80(1–3):87–99
2. Ashofteh PS, Bozorg-Haddad O, Loáiciga HA (2017) Impacts of climate change on the conflict between water resources and agricultural water use. J Irrig Drain Eng 143(4)
3. Gamon J, Field C, Goulden M, Griffin K, Hartley A, Joel G, Valentini R (1995) Relationships between NDVI, canopy structure, and photosynthesis in three Californian vegetation types. Ecol Appl 5(1):28–41
4. Myneni RB, Hall FG, Sellers PJ, Marshak AL (1995) The interpretation of spectral vegetation indexes. IEEE Trans Geosci Remote Sens 33(2):481–486
5. DeFries R, Hansen M, Townshend J (1995) Global discrimination of land cover types from metrics derived from AVHRR pathfinder data. Remote Sens Environ 54(3):209–222
6. Hudak Andrew T, Wessman Carol A (2000) Deforestation in Mwanza district, Malawi, from 1981 to 1992, as determined from Landsat MSS imagery. J Appl Geogr 20(2)

7. Kimball J, McDonald K, Running S, Frolking S (2004) Satellite radar remote sensing of seasonal growing seasons for boreal and subalpine evergreen forests. Remote Sens Environ 90:243–258
8. Digkuhn M, Gal P (1996) Effect of drainage date on yield and dry matter partitioning in irrigated rice. Field Crops Res 46:117–126
9. Mondal S, Jeganathan C, Sinha NK, Rajan H, Roy T, Kumar P (2014) Extracting seasonal cropping patterns using multi-temporal vegetation indices from IRS LISS-III data in Muzaffarpur district of Bihar, India. Egypt J Remote Sens Space Sci 17(2):123–134
10. Wardlow Brian D, Egbert Stephen L, Kastens Jude H (2006). Analysis of time-series MODIS 250 m vegetation index data for crop classification in the U.S. Central Great Plains. Remote Sens Environ 108
11. Wardlow Brian D, Egbert Stephen L (2008) Large-area crop mapping using time-series MODIS 250 m NDVI data: an assessment for the U.S. Central Great Plains. Remote Sens Environ 112
12. Kumar T, Koteswararao K, Barbosa H, Prabha Jothi E (2013). Studies on spatial pattern of NDVI over India and its relationship with rainfall, air temperature, soil moisture adequacy and ENSO. Geofizika. 30:1–18
13. Rishma C, Katpatal YB (2016) Variability in rainfall and vegetation density as a response to ENSO events: a case study in Venna River Basin of Central India. J Agrometeorol 18(2):300–305
14. Department of Agriculture, Maharashtra State. http://maharain.gov.in
15. National Remote Sensing Centre.http://bhuvan.nrsc.gov.in/data/download/index.php

Regional Frequency Analysis Using L-Moment Methodology—A Review

Ramgopal T. Sahu, Mani Kant Verma, and Ishtiyaq Ahmad

Abstract In order to carry out hydrological and climatological characteristics of a region that is far apart or completely isolated which goes away from the gauging network, and on other hand it becomes a part of watershed or catchment area under consideration for the purpose of any hydraulic structure analysis. This can be resolved by means of regionalization technique using some statistical methods. Different techniques together with L-moments introduced by Hosking and Wallis [24] are being utilized by many researchers and hydrologists in their research work. The researchers have applied the L-Moment methodology to almost every extreme event, viz., extreme rainfall, low flow, flood and drought. The regionalization or RFA tends to compensate for the lack of data for ungauged watershed or catchments. The purpose of this paper is to describe regionalization procedure for hydrological and climatological assessment of ungauged watershed.

Keywords Regionalization · RFA · L-Moment · Distributions · Parameters

1 Introduction

Information about rainfall is generally derived from precipitation measured at gauging stations on watersheds. Proper gauging records are relatively Inadequate (i.e. in India for every 500 km^2 there is 1 rain-gauge station). Inadequate data records cannot provide direct answers to many of the practical questions in the planning and management of water resources. Water resources engineers and Hydrologists often face these challenges in watershed planning, design of dam safety assessments, hydraulic structures and hydropower development. Project evaluation based on economic as well as hydrologic with respect to water resource also helps to determine return period for which rainfall frequency analysis holds an important role.

R. T. Sahu (✉) · M. K. Verma · I. Ahmad
Civil Engineering Department, National Institute of Technology - Raipur, Raipur, India
e-mail: ramgopal_sahu@yahoo.com

© Springer Nature Singapore Pte Ltd. 2021

K. K. Pathak et al. (eds.), *Recent Trends in Civil Engineering*, Lecture Notes in Civil Engineering 77, https://doi.org/10.1007/978-981-15-5195-6_60

The past or conventional technique for delineating regions are based on geographically contiguous area, i.e. based on political/Administrative/physiographic boundaries, but such regions may not have a finite relationship with the variable affecting or influencing the extreme rainfall. In spite of these developments, the regions may not be homogeneous in rainfall. Even for reporting forecast related information (Precipitation) and other estimates at temporal scale, IMD uses meteorological subdivisions which are again political boundaries. At present, there are 36 subdivisions and these increase as new political state emerges. Several studies state that India is large enough to be homogeneous [39]. Non-homogeneity was observed among MSDs in rainfall frequency distribution [46]. Some even suggested a shearing of information between sites within MSDs so as to maintain similarity in rainfall characteristics [49]. Five summer monsoon rainfall homogeneous regions were delineated for India based on grouping MSDs [41]. Recently found that the 5SMR is to be non-homogeneous in frequency distribution [47].

Regionalization can be defined as the process of dividing the area into a similar segment called regions; one of the transparent examples of regionalization is the division of country into states. The goal of the regionalization technique can be described as identifying watersheds that are similar enough to transfer the hydrological data of the site with other sites. Numbers of techniques for regionalizing hydro-climatic variables were used such as drought, flood, rainfall, evapo-transpiration and streamflow, which include (i) spatial interpolation, (ii) spatial maximum likelihood estimation approach (SMLE), (iii) Bayesian spatial modelling approach, (iv) regression analysis based approach, (v) regional rainfall frequency analysis.

In spatial interpolation based regional frequency analysis approach, extreme rainfall data is subjected to a frequency distribution corresponding to each gauging station, and local estimates or parameters of rainfall quantiles of projected return periods are spatially interpolated. As it requires sufficient station data for interpolation, hence it may not be applicable for ungauged or sparsely gauged areas. Also it requires a prior assessment of the type of frequency distribution of dataset and parameter estimation at the gauged location before interpolation and as such this form of pre-assumption may be inappropriate when accessible data records are brief.

For large geographical areas where spatial variation in distribution parameter is uneven, generally expect large errors when applied to areas such as Indian subcontinents [38, 43].

In regional frequency analysis based SMLE approach which is an enhancement of spatial interpolation approach, using predictor variables, i.e. spatial covariates, the highest probability estimates of GEV distribution parameters of extreme rainfall are modelled as smooth functions in space, which forms the basis for target region to estimate GEV distribution parameters and quantile estimates of extreme rainfall [38, 43]. Bayesian spatial modelling approach based RFA which is an improvement over SMLE approach is used when complicated spatial patterns of GEV distribution parameters are enough, as such cannot be precisely modelled by simple regression techniques [38, 43, 52]. Bayesian spatial modelling and SMLE approach also requires prior assessment of the type of frequency distribution of extreme rainfall similar to spatial interpolation approach.

In regional frequency analysis based regression analysis approach, a regression relationship among physiographic and climatic characteristics, i.e. predictors and moments of extreme rainfall, i.e. predictants is developed. Moments of the target sites are thus estimated using those relationships. Parameters of regional frequency distribution, i.e. shape, scale and location are computed using those moments which forms the base for quantile estimation of target sites. The regression relationship can only be robust if sufficient station data is available, and similar to spatial interpolation approach it also faces sampling effect due to the nonavailability of data records or short data.

Classification of regional rainfall frequency analysis are of two different types, (1) "Regionalization—identification of a homogeneous region comprising locations having rainfall characteristics similar to those of the target ungauged/sparsely gauged site" [43, 52] and PUB (Prediction of Ungauged Basins) in which a relationship is established between physiographic, climate characteristics and hydrological characteristics (e.g. drought, flood, low flow) of gauged basins and in order to predict the hydrological features, this relationship is applied to ungauged basins. These methods include multi-variable statistics such as Principal Component Analyses, Cluster Analysis, Hierarchical Cluster and Region of Influence, Regression and Canonical Correlation Analysis; (2) Pooled Frequency Analysis or Regional Frequency Analysis is the Second type of regionalization technique. In which numbers of techniques have been suggested for regional frequency analysis using regional homogeneity theory, most of them tend to define homogeneous areas, select appropriate parent distribution and estimate parameters for the chosen distribution. The L-moments technique was commonly used by scientists and hydrologists among various techniques for regional frequency analysis [33].

The conventional practice of identifying geographical contagious region based on political, climate, physiographic and/or administrative boundaries, delineation based on such properties/characteristics will not ensure any statistical homogeneity in rainfall; the contagious geographical regions are such that the characteristics of extreme rainfall may vary significantly. To overcome such implications development of effective regionalization approach includes (i) Hierarchical approach, (ii) PCA, (iii) ROI, (iv) Cluster analysis. Previously elementary linkage analysis and alternate correlation analysis based regionalization approach were used to delineate homogeneous region which were based on the concept of correlation between time-series precipitation data with all the possible pairs of rain gauges. The approach begins with identifying the highest or weakest correlation pairs, respectively, to form seed point and then to form surrounding or coherent zones gauges whose correlation is significantly positive with respect to seed point are identified and assigned in decreasing order of correlation. The approach was applied to form (2–9) coherent zones in Karnataka state [13], 31 zones in India w.r.t SMR variation [14] and further India was delineated into 26 and 20 zones using annual with south-west monsoon and annual with north-east monsoon, respectively [45].

A hierarchical approach is specifically used for accounting spatial variations in moments of extreme rainfall data [2]. "It is based on the hypothesis that higher order

moments (e.g. skewness and kurtosis) of extreme rainfall data do not display significant spatial variability over a larger area than the relatively lower order moments (variance), which in turn are assumed to vary more smoothly over space than the first-order moment" [43]. "As a consequence, data from more (less) sites is used for target site frequency analysis to estimate distribution parameters that are higher (lower) order moments functions." [43]. If the moment's spatial variation is uneven along with sampling effect, quantile estimates of rainfall for target location obtained with the application of hierarchical approach will result in a large error.

In a principal component analysis based regionalization approach, components from rainfall inter-station covariance or correlation matrix are extracted and patterns of the components are analyzed for grouping homogeneous coherent regions with respect to their rainfall variability [15]. This can be done either by plotting rotated and/or unrotated PC loadings on study area map or represent the stations in 2D plane as points. Extreme rainfall regional quantile estimates are obtained based on (1) regional regression relationship fitted between PCs and parameters of regional frequency distribution [55] and (2) regional growth curve constructed for each of the delineated RFA. Demarcating regions increase when large number of sites along with large number of principal components account for total variance of the study area. In India, Gangetic plains and sub-Himalayan regions were delineated into four rainfall homogeneous regions based on monthly and seasonal time scale to analyze summer monsoon rainfall of monthly and seasonal of 90 stations during 1871–1984 [51]. India was further divided into 10 homogeneous sequentially coherent rainfall regions by applying PCA using sequential sewing of station to SMR over 200 stations from 1901 to 1980 [25]. Ten of the six coherent regions were found definitely heterogeneous and three were possibly heterogeneous based on $1^\circ \times 1^\circ$ gridded rainfall dataset when tested for homogeneity in SMR frequency distribution.

Region of Influence based regionalization approach is designed to estimate regional quantiles of extreme hydro-meteorological events by forming site-specific regions, to address the concern about strictly contiguous region by considering a zone of transition between adjacent climatic regions to provide smooth transition [8, 12, 54]. "Approach that considers each target site to have its own region consisting of sites, whose distance to the target site in a weighted multidimensional space of predictors does not exceed a chosen threshold value" [43].

Cluster analysis recently obtained a good identity for regional frequency analysis with the accessibility of data on various predictors of extreme rainfall and the development of powerful computing resources [35, 56]. Different or range of multivariate statistical processes which are helpful for the investigation, interpretation and classification of big datasets into comparable groups or clusters that may or may not overlap are generically named as Cluster analysis [44]. Partitional clustering and hierarchical techniques were conventionally used as extreme rainfall frequency analysis which in turn produces hard clusters where every site is assigned to only one cluster. In actual real scenario, casual factor, i.e. predictor variables which affect the extreme rainfall resemble sites (partly or wholly). A fuzzy clustering technique accounts such a phenomenon where every site can belong to more than one region or cluster at a time [43]. Nine regions that were homogeneous in annual rainfall were

framed by applying cluster ensemble algorithms to IMD gridded rainfall datasets (1° × 1°) over a period 1951–2003 [1].

In Spectral analysis based regionalization approach the gauges that show low spectral variability are grouped together to form regions; recently, Monte-Carlo simulation procedure are developed to assess regions' spectral homogeneity. The application is applied to a group of 14MDs in central and north-western part of India which was declared to be homogeneous Indian monsoon (HIM) region [40] and was found to be spectrally non-homogeneous [5].

The implementation of rainfall frequency analysis is hindered by inadequate information and observation units when estimating the occurrences of large return periods. At-site rainfall frequency analysis can be defined as an assessment in which only records of rainfall from the specific locations are used. Generally, a regional analysis will have to be performed if data on rainfall from a group of similar watersheds is used. Regional analysis or Regionalization tends to compensate the deficiency of temporal data; therefore, rainfall regionalization needs to be employed in order to extend rainfall information to areas where gauge stations are not available.

Using the standard statistical concept, the probability distribution of an observed dataset is summarized with the help of its moments. Equating the sample moments with the fitted distribution is commonly used to predict the parameters by adding a parametric distribution to a dataset; the moment based statistical techniques are not always reliable. It becomes difficult for the third or higher order moments to describe the shape of a distribution. The results obtained from sample moments of a small sample size differ markedly from the probability distribution from where the sample was drawn [22].

2 L-Moments Concept

For summarizing the conceptual distribution of an observed dataset, L-moment is employed which is a replacement system for exploring the structure of the probability. L-moment statistics are widely used in Regional Analysis Program. L-moment statistics are utilized for examining heterogeneity/homogeneity of proposed regions; for computing sample statistics of data at individual sites; goodness-of-fit tests to find appropriate probability distributions; and parameters of the selected parent distribution.

"The name came from the linear combinations of order statistics" [24]. The conventional product-moment replaced by L-moment is an improved statistic to describe the shape of probabilities and parameter estimation, especially for environmental data for which the sample sizes are generally small. Hosking and Wallis [24] "defined L-moments as linear functions of (PWM) probability-weighted moments." The L-moment statistics are

- Mean (Location) $= \lambda_1$
- (τ_2) L-Cv (Scale): $\tau_2 = \lambda_2/\lambda_1$

- (τ_3) L-Skewness: $\tau_3 = \lambda_3/\lambda_2$
- (τ_4) L-Kurtosis: $\tau_4 = \lambda_4/\lambda_2$
- Where: λ_2 = Scale, λ_3 = Skewness, λ_4 = Kurtosis.
- $\lambda_1 = \beta_0$
- $\lambda_2 = 2\beta_1 - \beta_0$
- $\lambda_3 = 6\beta_{2\text{-}6}\beta_2 + \beta_0$
- $\lambda_4 = 20\beta_{3\text{-}3}0\beta_2 + 12\beta_1 - \beta_0$.

Definition of L-moment ratios: λ_1 is a central tendency, $\tau_2 = \lambda_2/\lambda_1$ L-Coefficient of variation (LCV) also called dispersion and scale measure, the ratio λ_3/λ_2 represent τ_3 L-Coefficient of skewness (L-CS) or skewness measure, and the ratio λ_4/λ_2 represent τ_4 L-Coefficient of kurtosis (L-CK) or kurtosis measure.

"Probability Weighted Moments (PWM) is defined as $\beta_r = E\left\{x[F(x)]^r\right\}$" [16].

"Where $F(x)$ is the (CDF) cumulative distribution functions of X, and β_r is rth-order PWM." PWMs based initial four L-moments are calculated as above.

Where the data ($X_{1:n}$) *arranged in chronological order (1–n).*

- $\beta_0 = n^{-1}\sum_{j=1}^{n} X_j$
- $\beta_1 = n^{-1}\sum_{j=2}^{n} X_j \dfrac{(j-1)}{(n-1)}$
- $\beta_2 = n^{-1}\sum_{j=3}^{n} X_j \dfrac{(j-1)(j-2)}{(n-1)(n-2)}$
- $\beta_3 = n^{-1}\sum_{j=4}^{n} X_j \dfrac{(j-1)(j-2)(j-3)}{(n-1)(n-2)(n-3)}$.

2.1 Moment Ratio Diagrams (MRDs)

The MRDs tool is helpful to discriminate against alternative distribution functions and to select an appropriate parent probability distribution. τ_3 and τ_4 relation is described by [21]. For the appropriate choice of parametric distribution, the highest probability distribution must meet the mean sample points. The heterogeneity of a region can also be inspected by the use of MRDs and for goodness-of-fit tests, moment ratio diagrams are always preferred. [18] suggested GPA distribution appears to be the best distribution as indicated by MRDs for the entire Luanhe basin of Hebei China.

For effective regional frequency analysis, the ratios of L-CV and L-skewness, i.e. L-moment ratio is the main component in computing quantile estimates of selected regions; L-C_V and L-skewness are the measure variance and asymmetry, respectively,

Table 1 Relative magnitude range for L-CV

$0.000 < \|\text{L-Cv}\| \leq 0.025$	Minimum variance often found in controlled manufacturing processes
$0.025 < \|\text{L-Cv}\| < 0.075$	Minor variance
$0.075 < \|\text{L-Cv}\| < 0.150$	Moderate variance
$0.150 < \|\text{L-Cv}\| < 0.400$	Large variance—often found when skewness is large
$0.400 < \|\text{L-Cv}\|$	Very large variance—often found when skewness is very large

Table 2 Relative magnitude range for L-Skewness

When L-skewness is 0.0	Its distribution is symmetry
$0.000 < \|\text{L-skewness}\| \leq 0.050$	Skewness is minor
$0.050 < \|\text{L-skewness}\| \leq 0.150$	Skewness is moderate
$0.150 < \|\text{L-skewness}\| \leq 0.300$	Skewness is large
$0.300 < \|\text{L-skewness}\|$	Very large skewness, outlier prone or "volatile" distributions

and is dimensionless; L-Skewness ranges from $0 \leq |\text{L-Skewness}| < 1$ for a distribution or sample data and L-C_V ranges from $0 \leq \text{L-}C_V < 1$ for distribution or sample data that has only positive values. The L-C_V can only have negative values if at-site mean is negative. Tables 1 and 2 list range for relative magnitude of L-Coefficient of variance and skewness.

2.2 Impact on Regional Growth Curve Due to Changes in L-Skewness and L-C_V

"A homogeneous region(s) that meets the requirements that all sites within a region can be defined by a single probability distribution with common distribution parameters, once the site information is rescaled by their at-site mean, the non-dimensional rescaled probability distribution is termed a regional growth curve" [23].

The homogeneity criteria, i.e. having the same values of L-moment ratios correspond to all the sites in the region, which in turn also helps how the variation in L-Skewness and L-C_V influence regional growth curve [37]. "An instance of how changes in L-CV and L-Skewness impact the shape of the regional growth curve was created for the Generalized Extreme Value distribution, the result indicates that if L-CV varies for a set L-Skewness value, the slope of the regional growth curve will be influenced" [23].

Similarly, the shape of the regional growth curve is also affected by varying L-Skewness. The upper tail of the regional growth curve is affected by positive rises in the magnitude of L-skewness. Probability distributions are often "unstable" along with positive large L-skewness and also have big quantile values for the upper tail. Negative rises in L-skewness, on the other side, influence the lower tail of the regional

growth curve. While describing how quantile are influenced by changing magnitude of L-Skewness and L-CV, the above conduct should be taken into account [37].

3 Regional Frequency Analysis Methodology

To identify a suitable group of sites, RFA is carried out in four significant stages (1) Data Screening: L-moment along with sample L-moment ratios used to create a discordancy that recognizes sites that are notably unique compared to others. (2) Identification of homogeneous regions: this is an important process of RFA where L-moment defines the set of sites that fulfils the requirements of regional homogeneity. In testing a region's heterogeneity, L-moments can be utilized to create summary statistics. (3) Selection of frequency distribution: (*Z*-statistical test) Regional average L-moments statistics or L-moment ratio diagram can be utilized for testing correlation among candidate distribution and observed data. (4) Parameter Estimation: L-moments are utilized to appraise parameters of the selected parent distribution. [28] used AMT (Mean annual maximum temperature) "coherent-basin" approach using L-moments methodology for regional frequency analysis of Colombia basin. [27] used L-Moments methodology for regional frequency analysis of North Brahmaputra Region of India.

Moreover, precipitation statistics are to be affected by different climatic factors such as orographic effects, oceanic proximity and rainforest environments. To depict homogeneous regions, the importance of spatial variability of extreme characteristics using L-moment-based statistical tests of homogeneity is proposed [2]. "L-moment based goodness-of-fit tests is used for identification of the regional distribution within each homogeneous region" [23]. "Goodness-of-fit test based L-moments are more robust than classical single-site goodness-of-fit test since they use regional rather than single-site data to discriminate between parent distributions" [2]. A hierarchical method for estimating parameters of an appropriate regional parent distribution in which L-skewness and L-kurtosis (higher order L-moments) are predicted over larger areas than mean and L coefficient of variation (lower order L-moments). The hierarchical method is important in order to demonstrate the precision of estimating design floods, particularly at sites with short record lengths: [2].

Cluster Analysis is a standard multivariate statistical analysis used to part the observed datasets into groups or form cluster based on greater similarity, such that each cluster contains the least variance, i.e. smallest dissimilarity. Ward's minimum variance method and dissimilarity squared Euclidean distance were used to measure maximum similarity and dissimilarity of the groupings. [18] suggested regional rainfall frequency function and spatial rainfall regions of Luhane Basin of Hebei China. [31] CA together with region of Influence is used to estimate peak flood with specific return period of Namak Lake Basin of Iran. Malekinezhad and Zare-Garizi [17] used it for regional rainfall frequency analysis for Golestan province of Iran. [42] used it to check trends in precipitation for Pranhita catchment in Godavari Basin. [43]

used GFCM based cluster analysis for regionalization and regional flood frequency analysis of India.

Principal Component Analysis is used to transform the original dataset to a newly uncorrelated dataset known as principal component. The first component captures as many variations as possible in the original dataset, while the second component captures uncorrelated maximum variability captured by second component and so on. [33] suggested along with CA to find the spatial variation of extreme dry events for Isfahan Province of Iran. [48] PCA together with Cluster Analysis (CA) and Discriminant Analysis (DA) was used to estimate stream-flow parameters at each gauged catchment in Alabama, Georgia and Mississippi.

Method of Moments is a procedure for building parameter estimators by coordinating the sample moments with the distribution moments. MOM is a moderately simple technique yet its assessments are normally lower in quality and are commonly not productive for distributions with parameters (3 or more) because in case of small samples higher order moments are relatively highly biased. [34] used to estimate maximum flood discharge at Malakkara and Neeleswaram River in Pampa and Periyar River Basins.

SPI Standardized Precipitation Index is a reference index representing the chance of occurrence of rainfall amount with respect to the rainfall climatology for a long period of time at certain geographical location. Negative SPI indicates insufficient rainfall, on the other hand, positive SPI represents surplus rainfall. The magnitude of negative SPI is generally used to classify the Intensity of drought event, such that the seriousness of an event increases with the increase of negative SPI. For example, an extremely dry condition can be classified if the negative SPI is greater than 2. The Area under Dryness (AUD) was analyzed for persistence of drought, drought spread and drought frequency in India [30].

Method of Maximum Likelihood is a parameter estimation technique and is an efficient method because it has desirable properties such as invariance property and asymptotically unbiasedness, consistency, efficiency and sufficiency in the large sample size estimation of complex probability density functions. [36] used (POT) Peak over Threshold together with (AM) Annual Maximum flood series for regional frequency analysis of Tel basin of Mahanadi River system, India.

Index Flood technique uses the information of gauged catchments to assess a regional relationship from which the flood extents of different return periods for ungauged catchments can be assessed. After creating an effective relationship between different variables including mean peak annual flood, catchment area and return period it turns out to be simple to design heavy hydraulic structures at regions where information is scarcely available or available not at all. Ejigu Eregno [11] used it for regional frequency analysis of Didessa sub-basin of South-Western Ethiopia. [29] used it for flood frequency analysis of Sabarmati River Basin, Gujarat. [50] used it to compute the quantiles using regional dataset so as to obtain the design events and at-site quantiles with greater reliability of Pakistan monsoon region. Parida et al. [6] used to compute the regional parameters, the growth curve and hence the quantiles of India's hydro-meteorological subzone 3a Mahi-Sabarmati River Basins. Basu and Srinivas [7] used to evaluate the performance of CIF, LIF and two variants of PIF to

estimate the flood quantiles of ungauged basin using Monte Carlo simulation experiments for Indiana watersheds in U.S. Dad and Benabdesselam [9] used to improve the estimated quality of AMD precipitation of northeastern area of Algeria.

3.1 Discordant Sites Identification

It is a common practice for proposed homogeneous regions to estimate (Di) discordance for all sites during the process of gathering [23]. The measure of discordance is used to identify locations whose L-moment ratios differ from the L-moment ratios of the sites of the region. Sites whose discordance measurement exceeds 3 are regarded to be inconsistent with the general conduct of the proposed site grouping. The discordance measure has two aspects for their use, first, the data screening method in which the discordance measure is used to detect doubtful datasets where discordant behaviour issues may be caused by data quality. Another is regional analysis. Here, if the proposed region is identified as heterogeneous with respect to high H1value, i.e. heterogeneity measure, to understand the cause of heterogeneity the physical characteristics of discordant sites may be necessary and helpful in deciding the strategy expected to produce a homogeneous region.

To identify the unusual sites, the L-moment based Discordancy measure (Di) is defined as

$$D_i = \frac{1}{3}(u_i - \bar{u})^T S^{-1}(u_i - \bar{u})$$

$$S = (N_S - 1)^{-1} \sum_{i=1}^{N_S} (u_i - \bar{u})(u_i - \bar{u})^T$$

$$\bar{u} = N_S^{-1} \sum_{i=1}^{N_S} \mathrm{u_i}$$

where u_i is the vector of L-moments, LCv, L-Cs and L-C_k, for site i, $\bar{u}$ is the group average, A is the covariance matrix of the sample and the T indicates transposition of a matrix or vector.

The total no of sites is N_S. If Di value exceeds 3 the site is considered as discordant.

The Di statistic for 1 among 17 stations of the Luanhe Basin of Hebei China was found to exceed the critical value [18]. Six gauging sites of Didessa sub-basin of South-Western Ethiopia were in the range of 0.23–1.48 which lies within the critical range hence all gauging sites are suitable for RFA [11]. Isfahan Province of Iran has 31 gauging stations among which only one station was discordant having value Di = 3.46 [33]. The discordancy calculated for 7gauging station lies within the critical region having value Di = 1.92 for Mirim-Sao Goncalo basin, Brazilian territory and Uruguay [10]. Forty-seven gauging stations were in Golestan Province of Iran

among which 4 stations were found to be discordant [17]. Pranhita catchment in the Godavari Basin has 131 gauging stations and found Di to be within the critical range Di < 3 [42]. The measure of Di = 1.648 among 6 gauging sites lies within the threshold region for meteorological sub-division 4 of India [4]. Twelve gauging sites were tested and found Di = 2.10 suggested no sites were discordant for Mahi-Sabarmati River Basins [6]. India's North Brahmaputra region's Di of 13 gauging sites was 2.757, hence all the sites were suitable for RFA [27]. Di-Statistics was tested on 58 gauging sites of north-eastern area of Algeria and it was found within the critical value Di < 3 and the value was in the range of 0.59–2.65 [9].

Discordant sites found in the data screening process. During the data screening process, the datasets found to be hailed as discordant should be assessed by examining time-series graphics and the probability-plot to find if one or more information whose magnitude differs uniquely from the common conduct of dataset. Once the discordant values are found, the site records are examined and an assessment will be made to determine whether the values are the consequence of some data entry or recording error, error in the assessment method or valid values. This can be done by comparing the values with the neighbor sites.

Site or sites that are recognized as discordant do not necessarily indicate that the site will not belong to the proposed group of sites. In fact, it says that more study is required to justify the cause of discordant in order to decide whether to maintain the doubtful site with the proposed grouping of sites; to transfer the site to another group of sites; or to remove the site from all analyses entirely. The datasets should not eliminate large or small outliers. At some sites, large or small outliers are expected to result in large samples from multiple sites. The outliers are a very important sign for the frequency of occurrence of high or low values and the phenomenon of natural variability. The validation of high or low values is the real issue. Keep the valid data and remove the erroneous data.

Mann-Kendall trend test is a nonparametric test used to check stationarity and to identify a trend in time-series datasets, even if the data series includes seasonal component. It was first proposed by [32] and was later studied by [26] which was further improved by [19, 20] who allowed taking seasonality into consideration [4, 10, 17, 30, 53]. Kwiatkowski-Phillips-Schmidt-Shin test (KPSS) is used to analyze observed datasets to check the null hypothesis for their stationarity and was used for the Colombian basin [28]. Factor Analysis (FA) was utilized to reduce and summarize the spatial variation of data of Nalak Lake basin of Iran [31]. Autocorrelation of lag-1 to lag-5 was used to test the independence, and for spatial independence Moran's I was used [17]. To analyze Area under Dryness (AUD) derived from SPI, Durbin–Watson D test was used to analyze the presence of autocorrelation for India: [30]. Statistical clustering along with AHC technique was used to divide the data into cluster and sub-cluster and to classify the dataset into homogeneous regions Iterative Self Organizing Data Analysis Technique clustering algorithm (ISODATA) along with spatial interpolation of data using (ANUDEM) Digital Elevation Model Algorithm was used for Pranhita catchment in Godavari Basin [42]. Serial correlation coefficients of lag 1, lag 5 and lag 10 checks were used to check independence of the time-series data [4, 53]. Ljung-Box Q-statistic, Kendall's tau test, and Mann–Whitney

Table 3 Possible action to discordant sites identified at regional analysis

Heterogeneity range	Possible actions
$H_1 \leq 2$	There is no reason to reassign a discordant site until a particular site is prompted with a large discordance magnitude with respect to the mean
$2 < H_1 \leq 3$	In such cases, Judgment is to take whether to reassign the doubtful site to different regions to enhance the homogeneity of the present group of sites or to accept it as homogeneous region.
$3 < H_1$	This case is likely heterogeneous. More study is required to justify the discordancy to make a decision on doubtful site whether to keep along with the proposed grouping of sites or not

Source [23]

test were used to check stationarity and independency of AMR series datasets of the Pakistan monsoon region [50].

Discordant sites found during regional analyses. For rejecting or accepting any site amongst a group of sites or a proposed region, the heterogeneity measure (H_1) is the primary indicator. The secondary indicator is discordance measure which is used to justify whether to shift a doubtful site to another region. Table 3 shows some necessary activities that need to take if discordant site is found.

The entire Luhane Basin of Hebei China was not homogeneous as the H_1 was larger than the critical value of $H_1 < 1$ [18]. For the Namak Lake Basin of Iran, the H_1 value of 21 sites was 3.29, more than $H_1 < 1$, thus the entire region was not homogeneous [31]. 4-parameter Kappa distribution using JAVA which indicates $H = -0.185886$ is within $H_1 < 1$ for meteorological sub-division 4 of India [4]. $H_1 = 0.68$ was estimated which agrees $H_1 < 1$ for India's hydro-meteorological subzone 3a Mahi-Sabarmati River Basins [6]. 245 regions were tested for homogeneity out of which 71 were accepted as homogeneous, 61 were possibly heterogeneous and rest of them was defiantly heterogeneous for Indiana watersheds in U.S. [7]. [27] made homogeneity test for 13 gauging sites and found to exceed the criteria of $H_1 < 1$, which was $H_1 = 3.68$, on excluding three discordant sites the H_1 becomes 0.48 for 10 sites of North Brahmaputra region of India.

3.2 Heterogeneity Measure

According to [23], "the heterogeneity computation of a proposed region is accomplished by correlating the magnitude of site-to-site variability of the L-moment ratios with respect to the level of variability in a homogeneous region, H_1, H_2 and H_3 are the heterogeneity measures for L-moment ratios of L-CV, L-Skewness, and L-Kurtosis, respectively." It has been discovered that the H1 measure for the observed variability (L-CV) has high discriminatory power and is, therefore, more helpful. In addition, the high natural variability in H2 and H3 sample values for L-skewness and L-kurtosis has outcomes in low discriminatory power. Hence, the H_1 measure of heterogeneity

to determine the variability of L-CV in at-site values becomes the de facto to describe the heterogeneity level of a proposed region.

Heterogeneity H1 Computation, for the proposed sites of the region, "a weighted average regional value of L-CV (L-CVR) is predicted from the L-CV sample values, where the weights refer to the length of the record. A weighted-average standard deviation is then calculated for the at-site L-CV values (VLCv). A four-parameter Kappa distribution is then fitted using the weighted-average regional values of the L-moment ratios for the group of sites. 500 computer simulations are then conducted using the fitted four-parameter Kappa distribution, where each simulation has the same number of sites and record lengths as that of the proposed region. The mean (μ_v) and standard deviation σ_v are computed of the 500 samples of the standard deviation of the at-site samples of L-CV" [23]. H_1 is then computed as

$$H_1 = \frac{V_{\mathrm{LC}_v} - \mu_v}{\sigma_v} \tag{1}$$

With the observed L-moment ratios, if the H_1 value is zero, the expected value of a homogeneous region is similar to that of site-to-site variability of a region, fitted by a four-parameter Kappa distribution. The expected value of a homogeneous region is higher than the site-to-site variability of at-site L-CV values then the H_1 indicates positive values and large H_1 values indicating likely or possible heterogeneity (see Table 4). On the other hand, if a homogeneous region's expected value is lower than the at-site L-CV values of site-to-site variability, then H_1 becomes negative and the region is marked as acceptably homogenous.

[23] originally proposed H_1 value as 1.0 for describing any proposed region to be acceptably homogeneous. Using Monte Carlo experiments with samples from known distributions, the above criterion depends on the statistical notion of sampling characteristics for L-CV. More often, from the difficulties in a recording of data and the accurate measurement cause extra variability in L-CV. The human efforts in managing and collecting the data may cause a variety of supplementary data quality issues. The research up to date indicates that $H_1 = 2.0$ is a good choice which creates a line between likely heterogeneous and likely homogeneous. Table 4 lists some regulations for accepting any proposed homogeneous regions. Changing the limit value of H_1 in Table 4 may be justified for examining certain phenomena that depend on the magnitude of variability conferred on test sample data for data

Table 4 Regulation for rejection/acceptance of a proposed region

Heterogeneity measure	Decision
$H_1 < 2$	Acceptably homogeneous
$2 < H_1 < 3$	Possibly heterogeneous, minor reassignment could be beneficial
$3 < H_1$	Definitely heterogeneous, drastic site reassignment is required

Source [23]

precision and contemplation of quality control. Lower estimates of H_1 could be used to some extent for environmental data where information recording and management are sensibly highly accurate and where extensive data quality control is conceivable. "A region is said to be acceptably homogenous when $H < 1$, possibly heterogeneous when $1 \leq H < 2$ and definitely heterogeneous when $H \geq 2$."

Hierarchical Ward's method was used for (CA) cluster analysis of Luhane Basin and recognized 7 groups on the basis of pseudo t_2 and pseudo R_2 statistics [18]. Ward's method for (CA) cluster analysis and Region of Influence was used for the Namak Lake Basin of Iran and found 3 groups [31]. Amongst 974, 277 stations were used for RFA process and were identified as 15 homogeneous regions for Colombia Basin [28]. For peninsular Malaysia based on storm event and geographical location four (4) regions were identified [3]. The entire region of Didessa sub-basin of South-Western Ethiopia was considered to be homogeneous as the H-statistics results were within the critical range [11]. Higher order L-moments and lower order L-moments were used to identify the homogeneity amongst regions and sub-regions of Canada [2]. The H_1, H_2 and H_3 were 0.41, 0.83 and −0.46, respectively, suggesting that Isfahan Province of Iran was acceptable homogeneous [33]. The regions for Mirim-Sao GoncaloBbasin consists of 7 sub-basin which were homogeneous as the H-statistics $H < 1$ of Brazilian territory and in Uruguay [10]. Pranhita catchments in Godavari Basins were divided into 3 groups using AHC method of statistical clustering and were homogeneous $H_1 < 1$ [42].

4 Goodness-of-Fit Measure

The goodness-of-fit test was introduced to find parent probability distribution which is close to the weighted average regional values of L-Kurtosis and L-Skewness for the proposed group of sites [23]. Test visualization is carried out by drawing a graph between observed regional values of L-Skewness and L-Kurtosis of the proposed region and defining the value of L-Kurtosis matches close to the regional value of L-Kurtosis. "The Z statistic has the form of goodness of fit and has approximately a standard Normal distribution."

The goodness-of-fit test is as

$$Z^{\mathrm{DIST}} = \frac{\tau_4^{DIST} - \bar{\tau}_4 + \beta_4}{\sigma_4}$$

$$\sigma_4 = \left[(N_{\mathrm{sim}} - 1)^{-1} \left\{ \sum_{m=1}^{N_{\mathrm{sim}}} \left(\tau_4^{(m)} - \bar{\tau}_4 \right)^2 - N_{\mathrm{sim}} \beta_4^2 \right\} \right]^{\frac{1}{2}}$$

$$\beta_4 = N_{\mathrm{sim}}^{-1} \sum_{m=1}^{N_{\mathrm{sim}}} \left(\tau_4^{(m)} - \bar{\tau}_4 \right)$$

Where "Dist" indicates candidate distribution, $\bar{\tau}_4$ indicates average L-kurtosis value, i.e. from observed data, β_4 indicates bias (for regional average sample L-Kurtosis) and τ_4^{DIST} indicates average L-Kurtosis value for a fitted distribution computed from a simulation. "A given distribution is declared as good fit if $|Z^{Dist}| \leq 1.64$ and if more than one distribution meets all the goodness-of-fit-test criteria, the preferred distribution will be the one with the minimum $|Z^{Dist}|$ value also the acceptance of the distribution, i.e. hypothesized corresponds to criteria at a confidence level of 90%" [24]. $|Z^{Dist}|$—Statistics were used as GOF test [2, 4, 6, 9, 11, 17, 18, 27, 28, 31, 33, 53]. (Δ) Mean percentage difference, the R_2 coefficient of determination and CVRMSE coefficient of variation of root mean square error, indices were used as GOF to differentiate two sets of IDF Curves of Peninsular Malaysia [3]. The overall GOF test for every distribution was done by ranking all the tests such as RMSE, RRMSE, PPCC, MADI as per their magnitude for Nigeria [37]. Non-parametric Anderson–Darling test was used as a GOF test for Mirim-Sao Goncalo Basin of Brazilian territory and in Uruguay [10]. Chi-square and Kolmogorov–Smirnov test was used as GOF test at Malakkara and Neeleswaram River in Pampa and Periyar River Basins [34]. Kolmogorov–Smirnov test was used as a GOF test for India [43]. AD test, KS test, and Chi-Square test were used as GOF test for Tel basin for Mahanadi river system, India [36].

Candidate Distributions. In Regional frequency analysis, for observed dataset, only one frequency distribution is to be fitted among several groups of sites. Moreover, no true or single distribution is applied to every site of a grouping when a region is slightly heterogeneous. In such cases the objective is not to find the true distribution, but to find a distribution that produces accurate quantile estimates. There is number of distribution families which can become candidate for a regional dataset. The candidate suitability can be ascertained by testing their ability to generate highlights of data relevant to some random applications. The strong recognizable evidence of the prevalent regional distributions within each region is the representation of homogeneous regions. A region can be classified as homogeneous if appropriate proof can be drawn such that the information at various sites of the region is drawn from the same parent distribution [31]. Amongst 7groups, G1 and G2 with GPA distribution and groups G3, G4, G5, G6 and G7 with GEV distributions were the best parent distributions of Luhane Basin of Hebei China [18]. [31] found GEV distribution amongst 3 groups the closest fit parent distribution for Namak Lake Basin of Iran. For Colombian Basin amongst 15 regions, 8 regions fit GLO, 3_GNO, 4_GEV [28]. The GEV distribution for AMS intensities with storm durations of 1, 2, 3, 4, 6, 8, 10, 12, 16 and 24 h for Peninsular Malaysia region: [3]. The GEV distribution was the best-fit parent distribution [2, 6, 9–11, 27, 29, 34]. For Isfahan Province of Iran GLOG distribution was the best-fit distribution: [33]. Return period below 25 years GPA was the best fit and above GLO and GEV in that order be used as best-fit probability distribution for Nigeria [37]. The GEV distribution was the best-fit parent distribution tested using D-index statistics at Malakkara and Neeleswaram Rivers [34]. Based on Chi-Square, L-moments ratio diagram and ZDIST statistics LN3 was selected as the best-fit distribution for meteorological sub-division 4 of India [4]. GEV, GLO and GNO were the best-fit probability distributions identified

for RFA of AMER were predominantly in order of their frequency, and for most of the regions it was not common across all the durations for India [43]. Amongst two datasets GPA showed best result for AM datasets, whereas LN (3P) showed best result for POT datasets followed by GPA for Tel basin for Mahanadi River system, India [36]. GEV was the best fit for low return periods and GNO for high return periods in monsoon climatic region of Pakistan [50]. Three regions were identified for which GNO was the best-fit for region-I, GLO for region-II and GEV for region-III of Hanjiang River Basin, China [53].

Distributions in L-Moment Regional Analysis Program consists of seven distributions for fitting the regional dataset. The major portion of L-Moment Ratio Diagrams is covered by these seven distributions and found to be useful in exploring environmental data. Distributions along with their shape parameter are as follows:

- (GNO) Generalized Normal
- (P3) Pearson Type-3
- (KAP) Kappa distribution
- Special Case of Kappa Distribution
- (GLO) Generalized Logistic, with ($h = -1$) shape parameter
- (GEV) Generalized Extreme Value, with ($h = 0$) shape parameter
- Gaucho, with ($h = +0.5$) shape parameter
- (GPA) Generalized Pareto, with ($h = +1$) shape parameter.

4.1 Parameter Estimation Using L-Moments

The parameters of the identified parent probability distributions function were estimated using L-moment with respect to their respective equations as shown in Table 5, where K, ξ and α are shape, location and scale parameter, respectively. [30] used FORTRAN subroutine to compute parameters of Pearson Type III distribution for India.

4.2 Performance Evaluation of Fitted Distribution Function

Adequacy or acceptability of a probability distribution function fitted to a dataset is evaluated using the goodness-of-fit measure. These methods are Relative Root Mean Square Error (RRMSE), Root Mean Square Error (RMSE), Probability Plot Correlation Coefficient (PPCC) and Mean Absolute Deviation Index (MADI). Here RMSE, RRMSE and MADI methods judge the fitted distribution by summarizing the deviation of observed data and predicted data subjected to a site, while correlation amongst the corresponding fitted quantiles obtained from plotting position and ordered observations is done by PPCC. The above test results ascertain how efficiently a selected distribution fits the regional dataset and hence choose the one from

Table 5 Quantile function and parameter estimation using L-moment

Distributions	Quantile function	Parameter estimates
GEV	$X(F) = \xi + \frac{\alpha}{K}\{1 - (-\ln F)^K\}$	$\alpha = \frac{l_2 K}{\Gamma(1+K)\Gamma(1-2^{-K})}$ $\xi = l_1 + \frac{\alpha(\Gamma(1+K)-1)}{K}$ $K = 7.8590C + 2.9554C^2$ $C = \frac{2}{3+\tau_3} - \frac{\ln 2}{\ln 3}$
GLO	$X(F) = \xi + \frac{\alpha}{K}\left\{1 - \left(\frac{1-F}{F}\right)^K\right\}$	$\alpha = \frac{l_2}{\Gamma(1+K)\Gamma(1-K)}$ $\xi = l_1 + \frac{(l_2-\alpha)}{K}$ $K = -\tau_3$
GPA	$X(F) = \xi + \frac{\alpha}{K}\{1 - (1-F)^K\}$	$\alpha = l_2[(K+1)(K+2)]$ $\xi = l_1 - l_2(K-2)$ $K = \frac{4}{\tau_3+1} - 3$
GNO	$X(F) = \xi + X(F) =$ $\xi + \frac{\alpha}{K}[1 - \exp(-K\emptyset^{-1}(F))]$	$\alpha = \frac{l_2 K e^{-K^2/2}}{\left[1-2\emptyset\left(-K/\sqrt{2}\right)\right]}$ $\xi = l_1 - \frac{\alpha}{K}\left(1 - e^{K^2/2}\right)$ $K = -\tau_3 \frac{E_0+E_1(\tau_3)^2+E_2(\tau_3)^4+E_3(\tau_3)^6}{1+F_1(\tau_3)^2+F_2(\tau_3)^4+F_3(\tau_3)^6}$
PE3	$K_T\sqrt{\alpha^2 K}X(F) = K_T\sqrt{\alpha^2 K}$	$\alpha = l_2\frac{\sqrt{\pi}\Gamma(K)}{\Gamma(K+0.5)}$, $\xi = l_1 - K\alpha$ $K = \frac{1+0.2906z}{z+0.1882z^2+0.59567z^3}$ $z = 3\pi(\tau_3)^2$ for $0 < \lvert\tau_3\rvert < 1/3$ $K = \frac{0.36067z-0.59567z^2+0.25361z^3}{1-2.78861z+2.56096z^2-0.77045z^3}$ $z = 1 - \lvert\tau_3\rvert$ for $1/3 <= \lvert\tau_3\rvert < 1$

Source [7, 37]

candidate distributions that best fits the observed dataset. The Bais and (RMSE) root-mean-square error was computed to check adequacy of fitted distribution of Canada [2]. [37] suggested RMSE, PPCC, RRMSE and MADI to check the acceptability of parent distribution. Malekinezhad and Zare-Garizi [17] applied Bias, RMSE and 90% error bounds to test adequacy of a fitted distribution for Golestan Province of Iran. [43] used R-bias, R-RMSE and AR-bias for performance measure, effectiveness of the regions as well as ROI's were checked using leave-one-out cross-validation (LOOCV) procedure for India. Basu and Srinivas [7] used R-bias, AR-bias and R-RMSE for performance measure and LOOCV procedure to check the effectiveness of CIF, LIF and two variants of PIF procedure in estimating the quantiles for un-gauges sites of Indiana watersheds in U.S. Dad and Benabdesselam [9] suggested RMSE and relative bias to check the adequacy of the fitted distribution of north-eastern area of Algeria. BIAS, RRMSE and A-BIAS were used for adequacy check for Pakistan

monsoon region [50]. (RMSE) was used to check adequacy of Hanjiang River Basin, China [53].

4.3 Estimation of Quantiles

The initial four L-moments attached to each station from the set of stations qualifying the homogeneity and discordance measurements were divided by their respective λ1 values to make them dimensionless. To acquire the standard regional L-moment estimates $\left(\lambda_r^R\right)$ weighted values of above dimensionless L-moments are utilized. Without using the regional homogeneity criteria, frequency estimates of gauged and ungauged watersheds were matched.

$$\lambda_r^R = \frac{\sum_{i=1}^{N} n_i \lambda_r^{(i)}}{\sum_{i=1}^{N} n_i}$$

where (i) indicate a station
λ_r^R = standardized regional L-moment of order
$\lambda_r^{(i)}$ = standardized L-moments of order r
n_i = years of data
N = no of homogeneous stations

For a Gauged Site, λ_1 is the average observed values, which is multiplied with the regional values to obtain λ_1, λ_2, λ_3, λ_4, τ_3 and τ_4 values. [22] gave a relationship between the L-moments and parameters for some selected distributions, Using this relationship parameters for the best-fit distribution are computed (identified by GOF test). The standardized quantiles for a given return period at proposed regions and also at other gauging network stations were estimated. The same is graphically represented by plotting average standardized value against the respective return periods. Similarly the other return periods are also marked with their plotting points and joined together to form a curve called a regional growth curve.

For an Ungauged Site, a relationship between the physiographic characteristics of a catchment and (λ_1) the average observed values of the gauged sites is developed, the same is utilized for computing (λ_1), i.e. the average observed values of an ungauged site. The product of (λ_1) and standardized quantile obtained from regional growth curve to obtain the quantile estimate.

5 Conclusion

Results based on studies carried out by many researchers on Regionalization and Regional frequency analysis are as follows.

Regionalization and regional frequency analysis of any hydro-climatological characteristics should avoid geographical contiguous region (area). Homogeneous rainfall region formation with soft or transition boundaries should have the prime objective. Studies on IMD meteorological subdivisions have suggested being heterogeneous in nature with respect to precipitation, which is considered for reporting precipitation related forecasts. India is large enough to be considered as homogeneous in nature. As initial principal components are not accessible to account significant percent of the total variation shared by station, hence PCA is considered not being the best possible choice for delineating summer monsoon rainfall regions in India. At most common factor analysis overcomes the short-comes of PCA and accounts for specific variance related to local forcing that is responsible for affecting or influencing the rainfall variability. CA-based regionalization appears to be effective in interpretation, classification and investigation of big datasets of casual factors influencing the rainfall or other Principal Components of PCA. Conventional regionalization techniques for region delineation won't be appropriate when the area or region is sparsely or ungauged and even the data record length is short. The regional frequency analysis was created effectively using L-moments methods. Regional function moreover has considerable improvements by using multi-parameter Probability Distribution Functions rather than Conventional Two-parameter Probability Distribution Functions; Furthermore, for identified homogeneous region L-moment provides appropriate statistics adjustment; substantive validation procedure; huge predictive capacity; simple to use and requires only one description variable, implementing to practical flood risk management and engineering projects is easy. Application to L-moments and L-moment ratios are wide and helpful in estimating distribution parameter and selection of best-fit distribution as well as statistical characterization of hydrological data. Despite the probability distribution from where the observation is drawn, the shape, scale and location are unbiased estimators of L-moments ratios. Particularly for high skewed samples the conventional product-moment ratios exhibit higher bias compared to L-moment ratio estimators such as L-CV, L-CS and L-CK. The ratio estimators of coefficient of variation Cv and skewness Cs have bounds that depend on size of the samples, on the other hand L-moment ratio estimators L-CV and L-CK do not have such bounds.

The application of L-moment approach together with Cluster Analysis (CA) is highly suggested for different climatic and geographical regions to demonstrate the connection between rainfall distribution function and rainfall regimes. Regional frequency analysis based L-moment can significantly be employed to area or region with no rainfall station to find Intensity Duration Frequency (IDF) curves. To forecast the future rainfall projection along with climate change scenarios using the relationship between LSAPV (Large Scale Atmospheric Predictors Variables) and rainfall data (historical).

Acknowledgments The Authors are grateful to institute (National Institute of Technology—Raipur) and individuals (Staff and Person) who are directly or indirectly supported to complete the paper.

References

1. Ahuja S, Dhanya CT (2012) Regionalization of rainfall using RCDA cluster ensemble algorithm in India. J Softw Eng Appl 5:568–573. https://doi.org/10.4236/jsea.2012.58065
2. Alila Y (1999) A hierarchical approach for the regionalization of precipitation annual maxima in Canada. J Geophys Res 104(D24):31645–31655. https://doi.org/10.1029/1999jd900764
3. Ariff NM, Jemain AA, Abu Bakar MA (2016) Regionalization of IDF curves with L moments for storm events. Int J Math Comput Sci 10(5). https://doi.org/10.5281/zenodo.1123891
4. Devi A, Parthasarthi C (2013) Extreme rainfall frequency analysis for meteorological subdivision 4 of India using L-moments. Int J Civ Environ Eng 7(12). https://doi.org/10.5281/zenodo.1336128
5. Azad S, Vignesh TS, Narasimha R (2010) Periodicities in Indian monsoon rainfall over spectrally homogeneous regions. Int J Climatol 30(15):2289–2298. https://doi.org/10.1002/joc.2045
6. Parida BP, Kachroo RK, Shrestha DB (1998) Regional flood frequency analysis of Mahi-Sabarmati Basin (Subzone 3a) using index flood procedure with L-moments. Water Resour Manag 12:1–12. https://doi.org/10.1023/A:1007970800408
7. Basu B, Srinivas VV (2016) Evaluation of the index-flood approach related regional frequency analysis procedures. J Hydrol Eng (ASCE) 21(1):04015052. https://doi.org/10.1061/(ASCE)HE.1943-5584.0001264
8. Burn DH (1990) Evaluation of regional flood frequency analysis with a region of influence approach. Water Resour Res 26(10):2257–2265. https://doi.org/10.1029/WR026i010p02257
9. Dad S., Benabdesselam T. 2018. Regional frequency analysis of extreme precipitation in northeastern Algeria. Journal of Water and Land Development. No. 39 p. 27–37. https://doi.org/10.2478/jwld-2018-0056, https://doi.org/10.2478/jwld-2018-0056
10. Felício C, Samuel B, Marcelle Martins V, Maíra Martim de M, Leo Fernandes Á, Carlos Rogério de M (2017) Hydrological regionalization of maximum stream flows using an approach based on L-moments. RBRH 22:e27. Epub March 13, 2017. https://dx.doi.org/10.1590/2318-0331.021720160064
11. Ejigu Eregno F (2014) Regional flood frequency analysis using l-moment in the tributaries of upper Blue Nile River, South-Western Ethiopia. Merit Res J Eng Pure Appl Sci 2(2):012–021
12. Gaal L, Kysely J, Szolgay J (2008) Region-of-influence approach to frequency analysis of heavy precipitation in Slovakia. Hydrol Earth Syst Sci 12(3):825–839. https://doi.org/10.5194/hess-12-825-2008
13. Gadgil S (1988) Gowri R and Yadumani, Coherent rainfall zones: case study for Karnataka. Proc Indian Acad Sci (Earth and Planetary Sciences) 97(1):63–79. https://doi.org/10.1007/BF02861628
14. Gadgil S, Yadumani, Joshi NV (1993) Coherent rainfall zones of the Indian region. Int J Climatol 13:547–566. https://doi.org/10.1002/joc.3370130506
15. Garcia-Marin AP, Ayuso-Munoz JL, Taguas-Ruiz EV, Estevez J (2011) A regional analysis of the annual maximum daily rainfall in the province of Malaga (southern Spain) using the principal component analysis. Water Environ J 25(4):522–531. https://doi.org/10.1111/j.1747-6593.2011.00251.x
16. Greenwood JA, Landwehr JM, Matalas NC, Wallis JR (1979) Probability weighted moments: definition and relation to parameters of several distributions expressable in inverse form. Water Resour Res 15:1049–1054. https://doi.org/10.1029/wr015i005p01049
17. Malekinezhad H, Zare-Garizi A (2014) Regional frequency analysis of daily rainfall extremes using L-moments approach. Atmósfera 27(4):411–427. https://doi.org/10.1016/S0187-6236(14)70039-6
18. Hassan BGH, Ping F (2012) Regional rainfall frequency analysis for the Luanhe Basin—by using L-moments and cluster techniques. ICESD APCBEE Procedia 1(2012):126–135. https://doi.org/10.1016/j.apcbee.2012.03.021

19. Hirsch R, Slack RJ, & Smith R. (1982). Techniques of Trend Analysis for Monthly Water Quality Data. Water Resources Research. 18. 107–121. https://doi.org/10.1029/wr018i001p00107
20. Hirsch R, Slack RJ (1984). Non-parametric trend test for seasonal data with serial dependence. Water Resour Res 20:727–732. https://doi.org/10.1029/wr020i006p00727
21. Hosking JRM, Wallis JR, Wood EF (1985) Estimation of the generalized extreme-value distribution by the method of probability-weighted moments. Technometrics 27:3, 251–261. https://doi.org/10.1080/00401706.1985.10488049
22. Hosking JRM (1990) L-moments: analysis and estimation of distributions using Linear combinations of order statistics. J R Statist Soc B 52(1):105–124. https://www.jstor.org/stable/2345653
23. Hosking JRM, Wallis JR (1993) Some statistics useful in regional frequency analysis. Water Resour Res 29(2):271–281. https://doi.org/10.1029/92WR01980
24. Hosking JRM, Wallis JR (1997) Regional frequency analysis. In: An approach based on L-moments. Cambridge University Press, Cambridge, New York, Melbourne, 224 pp
25. Iyengar RN, Basak P (1994) Regionalization of Indian monsoon rainfall and long-term variability signals. Int J Climatol 14(10):1095–1114
26. Kendall MG (1975) Rank correlation methods. Charles Griffin, London
27. Kumar R, Chatterjee C (2005) Regional flood frequency analysis using L-moments for north Barhamputra region of India. J Hydrol Eng ASCE, 1084–0699. https://doi.org/10.1061/(ASCE)1084-0699(2005)10:1(1)
28. Nunez-Galeano L, Giraldo-Osorio JD (2016) Adaptation of the L-moments method for the regionalization for maximum annual temperatures in Colombia. Ing Univ 20(2):373–389. http://dx.doi.org/10.11144/Javeriana.iyu20-2.almr
29. Modi M, Mitra A (2017) Regional flood frequency analysis: a case study of Sabarmati River Basin. Int J Eng Sci Inven (IJESI) 6.7:55–65
30. Kumar MN, Murthy CS, Sesha Sai MVR, Roy PS Spatiotemporal analysis of meteorological drought variability in the indian region using standardized precipitation index. National Remote Sensing Centre, Hyderabad, 500625, India
31. Malekinezhad H, Nachtnebel HP, Klik A (2011) Regionalization approach for extreme flood analysis using L-moments. J Agr Sci Tech 13:1183–1196
32. Mann HB (1945) Nonparametric tests against trend. Econometrica 13:245–259. http://dx.doi.org/10.2307/1907187
33. Modarres R (2009) Regional dry spells frequency analysis by L-Moment and multivariate analysis. Water Resour Manage 24:2365–2380
34. Vivekanandan N (2015) Flood frequency analysis using a method of moments and L-moments of probability distributions. Cogent Eng 2:1018704. http://dx.doi.org/10.1080/23311916.2015.1018704
35. Ngongondo CS, Alemaw B, Xu C, Chirwa T, Tallaksen LM (2011) Regional frequency analysis of rainfall extremes in southern Malawi using the index rainfall and L-moment approaches. Stoch Environ Res Risk Assess 25(7):939–955. https://doi.org/10.1007/s00477-011-0480-x
36. Guru N, Jha R (2015) Flood frequency analysis of tel Basin of Mahanadi River system, India using annual maximum and POT flood data. Aquatic Procedia 4. https://doi.org/10.1016/j.aqpro.2015.02.057
37. Izinyon OC, Ehiorobo JO (2014) L-moments approach for flood frequency analysis of River Okhuwan in Benin-Owena River Basin in Nigeria. Nigerian J Technol (Nijotech) 33(1):10–18. http://dx.doi.org/10.4314/njt.v33i1.2
38. Panthou G, Vischel T, Lebel T, Blanchet J, Quantin G, Ali A (2012) Extreme rainfall in West Africa: regional modeling. Water Resour Res 48(8):W08501. https://doi.org/10.1029/2012wr012052
39. Parthasarathy B (1984) Interannual and long-term variability of Indian summer monsoon rainfall. Proc Indian Acad Sci (Earth and Planetary Sciences) 93(4):371–385. https://doi.org/10.1007/BF02843255

40. Parthasarathy B, Kumar RK, Munot AA (1993) Homogeneous Indian monsoon rainfall: variability and prediction. Proc Indian Acad Sci (Earth and Planetary Sciences) 102(1):121–155. https://doi.org/10.1007/BF02839187
41. Parthasarathy B, Munot AA, Kothwale DR (1995) Monthly and seasonal rainfall series for all-India homogeneous regions and meteorological subdivision: 1871–1994. Research report No. RR-065, Indian Institute of Tropical Meteorology, Pune
42. Bothale R, Katpatal Y (2014) Spatial and statistical clustering based regionalization of precipitation and trend identification in Pranhita Catchment, India. IJIRSET 3(5), ISSN: 2319-8753
43. Bharath R, Srinivas VV (2015) Regionalization of extreme rainfall in India. Int J Climatol 35:1142–1156. https://doi.org/10.1002/joc.4044
44. Rao AR, Srinivas VV (2008) Regionalization of Watersheds—an approach based on cluster analysis, vol 58. Water Science and Technology Library, Springer, New York, NY
45. Saikranthi K, Rao TN, Rajeevan M, Rao SVB (2013) Identification and validation of homogeneous rainfall zones in India using correlation analysis. J Hydrometeorol 14(1):304–317. https://doi.org/10.1175/jhm-d-12-071.1
46. Satyanarayana P, Srinivas VV (2011) Regionalization of precipitation in data-sparse areas using large scale atmospheric variables—a fuzzy clustering approach. J Hydrol 405(3–4):462–473. http://dx.doi.org/10.1016/j.jhydrol.2011.05.044
47. Satyanarayana P, Srinivas VV (2008) Regional frequency analysis of precipitation using large-scale atmospheric variables. J Geophys Res Atmos 113:D24110. https://doi.org/10.1029/2008jd010412
48. Chiang S-M, Tsay T-K, Nix SJ (2002) Hydrologic regionalization of Watersheds: methodology development. J Water Resour Plann Manage 128:1(3). https://doi.org/10.1061/(ASCE)0733-9496(2002)128:1(3)
49. Shukla J (1987) Interannual variability of monsoons. In: Fein JS, Stephens PL (eds) Monsoons. Wiley and Sons, New York, Chapter 14, pp 399–464
50. Shahzadi A (2013) A review: regional frequency analysis of AMR in the monsoon region of Pakistan using L-Moments. Int J Adv Stat Probab 1(3):97–101. http://dx.doi.org/10.18187/pjsor.v9i1.461
51. Singh KK, Singh SV (1996) Space time variation and regionalization of seasonal and monthly summer monsoon rainfall of the sub-Himalayan region and Gangetic plains of India. Clim Res 6(3):251–262. https://www.jstor.org/stable/24864562
52. Srinivas V (2013) Regionalization of precipitation in India—a review. J Indian Inst Sci 93:153–162
53. Hao W, Hao Z, Yuan F, Ju Q, Hao J (2019) Regional frequency analysis of precipitation extremes and its spatio-temporal patterns in the Hanjiang River Basin, China. Atmosphere 10:130. https://doi.org/10.3390/atmos10030130
54. Wallis JR, Schaefer MG, Barker BL, Taylor GH (2007) Regional precipitation-frequency analysis and spatial mapping for 24-hour and 2-hour durations for Washington State. Hydrol. Earth Syst Sci 11(1):415–442. https://doi.org/10.5194/hess-11-415-2007
55. Wotling G, Bouvier CH, Danloux J, Fritsch JM (2000) Regionalization of extreme precipitation distribution using the principal components of the topographical environment. J Hydrol 233(1–4):86–101. https://doi.org/10.1016/s0022-1694(00)00232-8
56. Yang T, Shao Q, Hao ZC, Chen X, Zhang Z, Xu CY, Sun L (2010) Regional frequency analysis and Spatio-temporal pattern characterization of rainfall extremes in the Pearl River basin, China. J Hydrol 380(3–4):386–405. https://doi.org/10.1016/j.jhydrol.2009.11.013

Fluctuation of Pressure Due to Bends in Venturimeter

S. Masalvad Shravankumar, Rallapalli Alice Grace, Kaveti S. Venkatesh, Ruthika Gujjula, and Anjali Gujjari

Abstract Venturi meter is a device used to measure the discharge of the flow of fluids in closed conduit. This device works on Bernoulli's principle which states, "An increase in the speed of the fluid particle occurs when simultaneously with the decrease in pressure or decrease in fluid's potential energy." It consists of a converging section, a throat and a diverging section. Velocity increases with the decrease in the cross-sectional area and pressure. In this paper, the variations in pressure due to various bends applied after the diverging portion is depicted and is compared with the formal venturi meter mounted into a straight pipe. The diameter of the pipe is taken as 20 mm, converging angle is 11°, diverging angle is 6°, length and diameter of the throat portion are 20 mm and 10 mm. The results indicated the shape, size, and orientation of the pipe after the venturi meter. These parameters affect the performance of the venturi meter in the calculation of the coefficient of discharge. A detailed analysis was carried by computational fluid analysis by ANSYS software to know the pressure variations along the venturi meter, and also the velocity vectors along the length of the pipe.

Keywords Venturi meter · Pressure distribution · Velocity dispersal · Simple bend · U-bend · Acute bend · Obtuse bend

1 Introduction

Precise flow measurement is required in few industries (say medical industry, aeronautical engineering, spaces sciences, etc.) lest it should become a hazard at the end of the day. The coefficient of discharge for venturimeter meter is 0.98. In essence, the actual flow rate is 0.98 times the theoretical flow rate [1]. As the body of any venturimeter meter is designed according to the streamlines of fluid particles, unlike in the case of orifice meter, venturimeter meter finds its applications in various industries (like aviation, automotive, medical, chemical and petrochemical industries, etc.).

S. M. Shravankumar (✉) · R. A. Grace · K. S. Venkatesh · R. Gujjula · A. Gujjari
Sreenidhi Institute of Science and Technology, Hyderabad 501301, India
e-mail: shravankumarsm@sreenidhi.edu.in

© Springer Nature Singapore Pte Ltd. 2021

K. K. Pathak et al. (eds.), *Recent Trends in Civil Engineering*, Lecture Notes in Civil Engineering 77, https://doi.org/10.1007/978-981-15-5195-6_61

Venturimeter meter follows Bernoulli's principle which articulates that velocity is directly proportional to the decrease in pressure [1]. However, the piping is different in industries, (unlike in preliminary laboratories where only simple horizontal pipes with venturimeter meter are found), as the pipes contain twists, turns, curves, and bends, which may affect the pressure and velocity distributions along the pipe. The paper aims to find out pressure distribution and velocity distribution along the length of pipe, due to bends and other peripheral fittings and its effects on the flow rate and performance of the venturimeter meter [2].

2 Theory and Observations

2.1 Venturimeter Meter in a Straight Pipe

Consider a fluid flowing in a straight pipe with certain velocity and pressure. If a venturimeter meter is fixed amidst the pipe, then the pressure at the converging section is found to be reducing until the throat. At the throat, the pressure almost comes down to zero [3]. After the fluid particles come to an end of the throat portion, pressure starts increasing drastically; in essence, pressure increases abruptly.

On the other hand, velocity has its role entirely opposite as that of pressure. Velocity reaches its maximum point at the throat and velocity reduces to at the diverging portion because of the increase in the cross-sectional area [4] (Figs. 1 and 2).

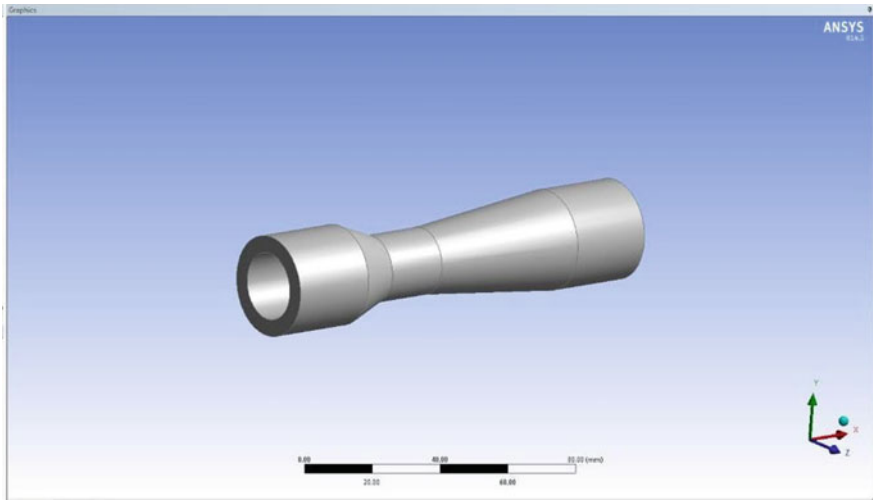

Fig. 1 Venturimeter simulation in ANSYS

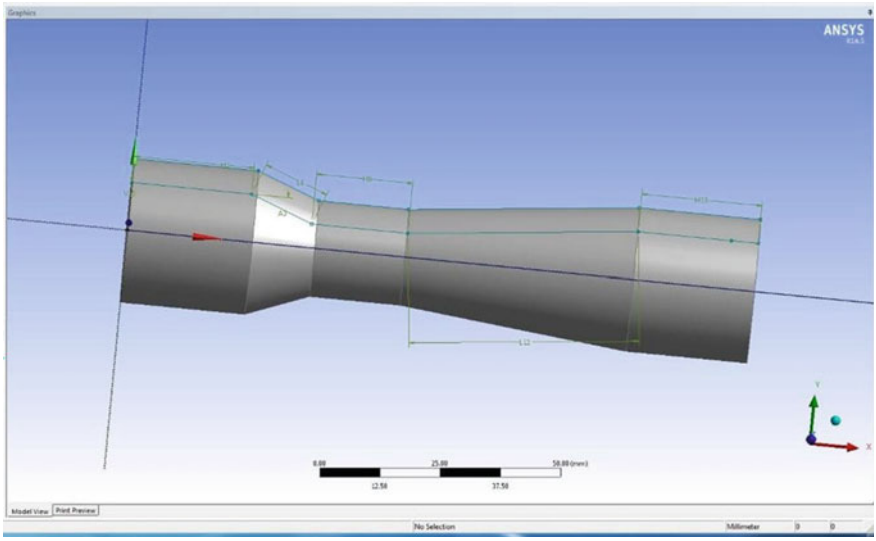

Fig. 2 Converging and diverging sections of venturimeter

2.2 Venturimeter with a Bend (50 mm Radius) After Diverging Portion

The fluid flow at the converging section experiences the reduction of pressure due to decrease in the cross-sectional area, at the throat section due to minimum cross-sectional area the velocity is maximum and due to this difference in pressure and velocity it is possible to measure the coefficient of discharge, but the effect of the various installations provided after Venturimeter affect the pressure gradient formed at the diverging, converging, and throat section. The tabulation explains the pressure differences occurring at various sections of Venturimeter, comparing pressure distributions for straight pipe and for the bend pipe (Figs. 3, 4, 5, 6, 7).

The continued increase in potential energy at the bend enunciated by the pressure contour at the bend due to the impact of fluid on the walls of the pipe, this effects the pressure distribution at the throat section which will affect the performance of the Venturimeter in calculating the coefficient of discharge [5]. The pressure developed is localized mostly due to the impact of the fluid on the walls of the pipe; at the bend, the pressure is found to be maximum (at the farther end from the center), i.e., 4.78e+04 N/mm^2 due to which the flow velocity reduces drastically and further the fluid continues the flow due to the impact and pressure difference created, and also the velocity at the converging portion is 1.06e+03 and shoots up to 2.32e+03 at the throat and then gradually reduces as the fluid travels from the throat through the diverging portion and at the bend then velocity is 6.79e+02 m/s. Due to the bend provided after the diverging section of the Venturimeter the pressure at the throat increases by 10,000 times. Due to such undue pressure development, the pressure

Fig. 3 Contours of static pressure

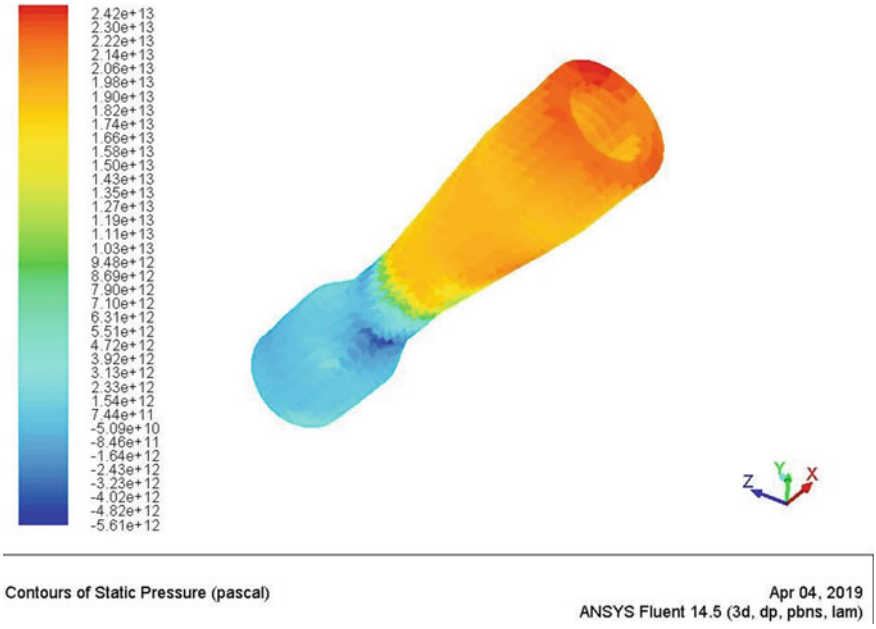

Fig. 4 Contours of static pressure

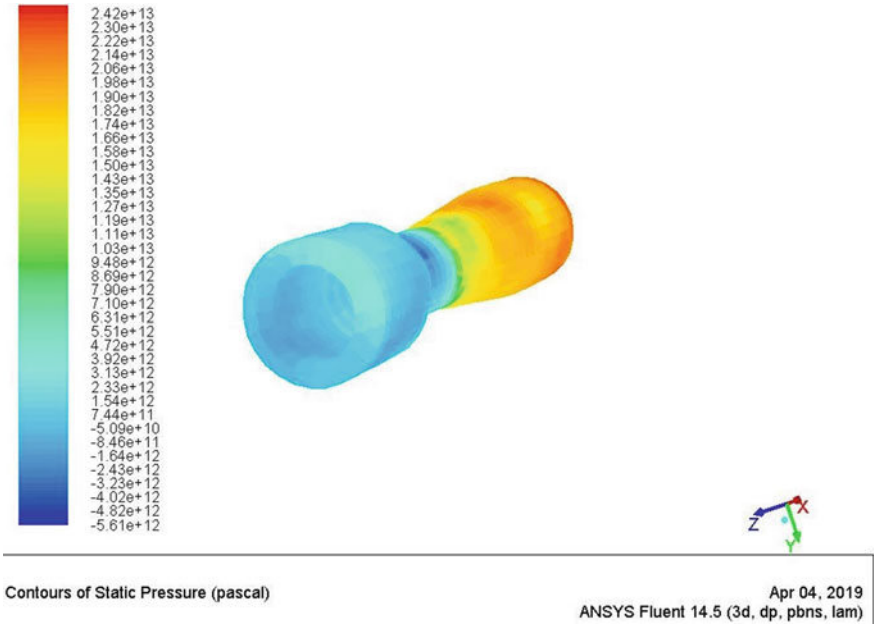

Fig. 5 Contours of static pressure

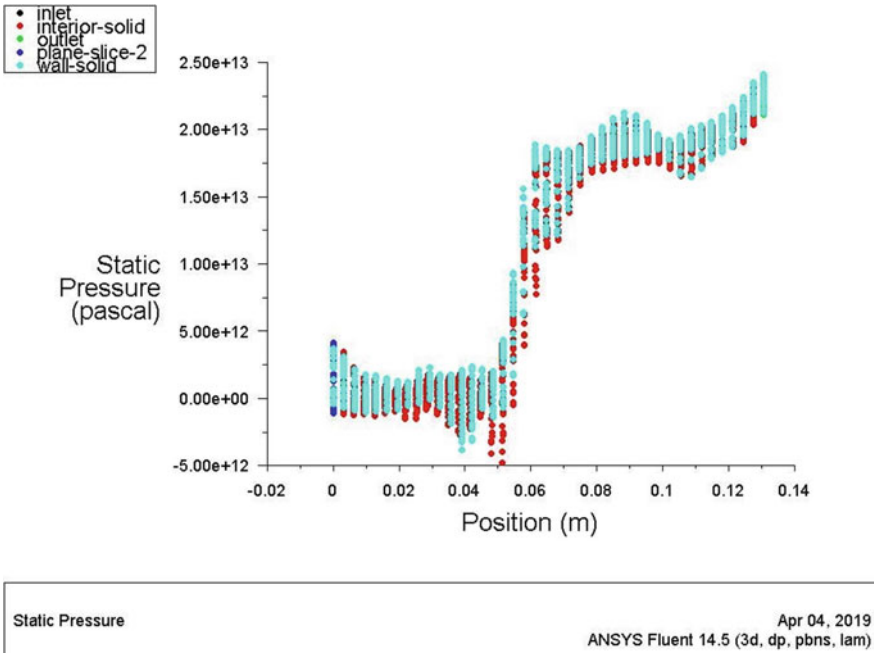

Fig. 6 Static pressure variation along venturimeter

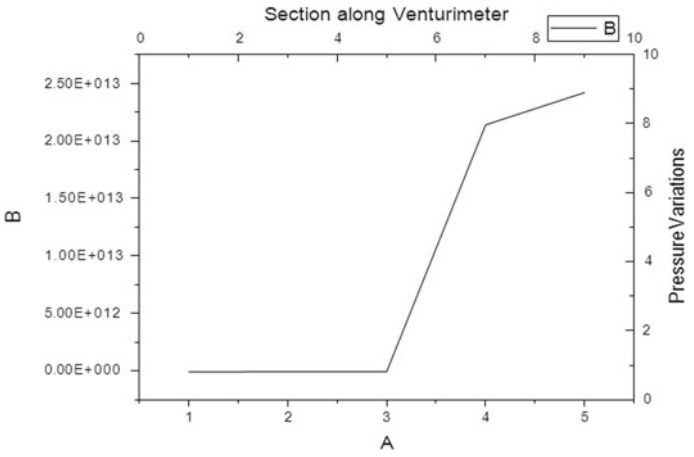

Fig. 7 Pressure variation along venturimeter

gradient varies and the velocity of flow at the throat and converging section varies with the pressure distribution and reduces the efficiency of the Venturimeter (Fig. 8 and 9, Table 1).

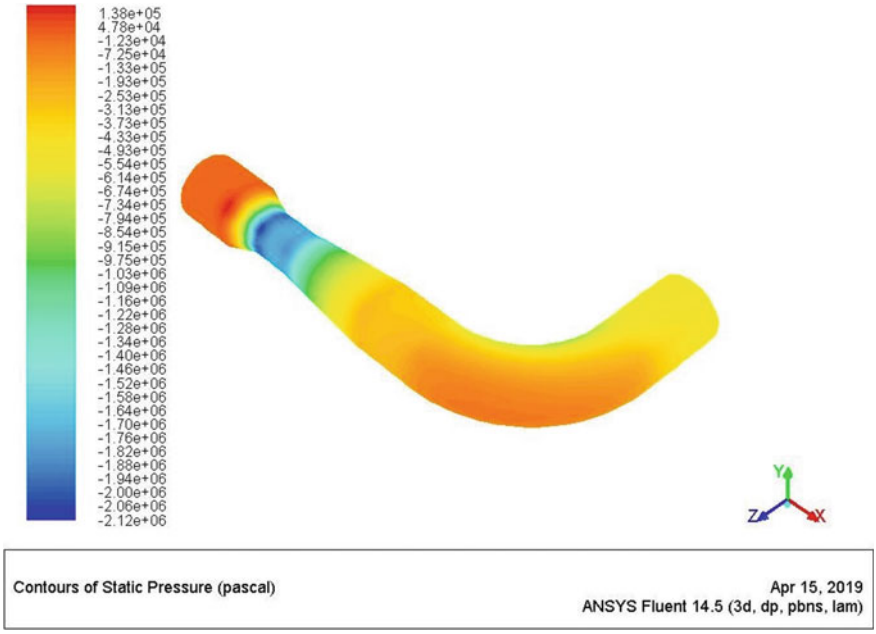

Fig. 8 Contours of Static pressure with pipe bend

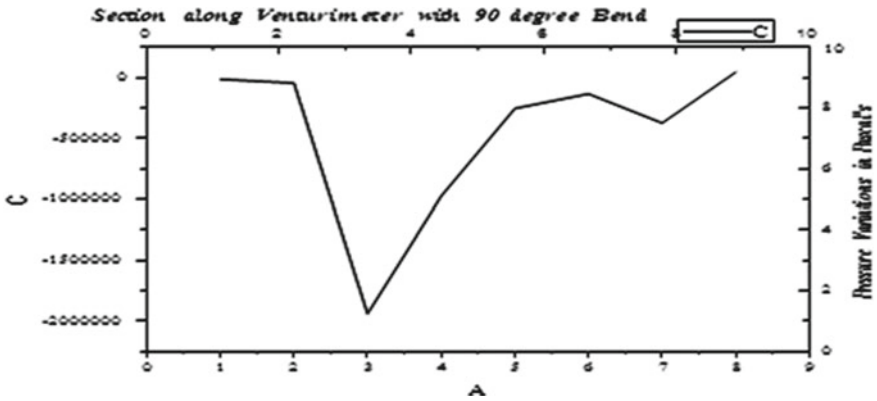

Fig. 9 Pressure variation along venturimeter with 90° bend

Table 1 Comparison of pressure distribution between venturimeter fitted with straight pipe and venturimeter fitted with bend

Position		Straight pipe (N/mm^2)	Pipe with bend (N/mm^2)	Remarks
Before converging	1	−8.46e+10	−1.23e+04	Pressure increase
Converging portion	2	−5.09e+10	−4.33e+04	Pressure increase
Throat	3	−5.61e+10	−1.94e+06	Pressure increase
Diverging portion	4	2.14e+13	−9.75e+05	Pressure decrease
After diverging portion	5	2.42e+13	−2.53e+05	Pressure decrease
Before the bend	6	–	−1.33e+05	–
At the bend (nearer end from the center)	7	–	−3.73e+05	–
At the bend (farther end from the center)	8	–	4.78e+04	–

2.3 Venturimeter with a U-Bend After Diverging Portion

Fluid enters the converging portion with high pressure and attains lower pressure (as compared to the initial pressure) from the converging portion to the throat. When the fluid enters the diverging portion, the pressure starts shooting up unto to the bend.

Now, a U-bend has been applied after the diverging section: first bend with 50 mm radius and second bend with 25 mm radius. Comparing the pressure distributions at various points (Fig. 10).

It is observed that the pressure is increased by 10^4 Pa in the U-bend pipe, at the throat when compared with the venturimeter meter with no bend. Pressure shoots up at the 2nd bend of the pipe. It varies from 3.77e+05 to 5.09e+05 Pa (nearer to farther

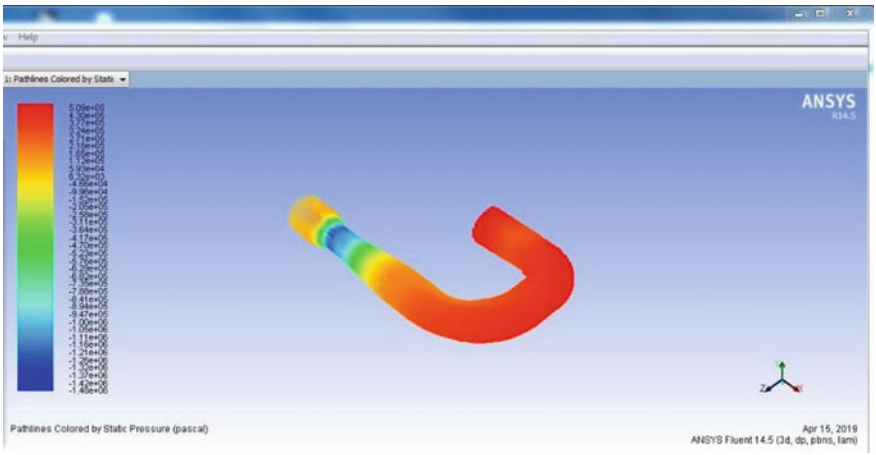

Fig. 10 Contours static pressure with U-bend

end from the center), while velocity in that portion of the pipe remains almost 0 m/s (Fig. 11, Tables 2 and 3).

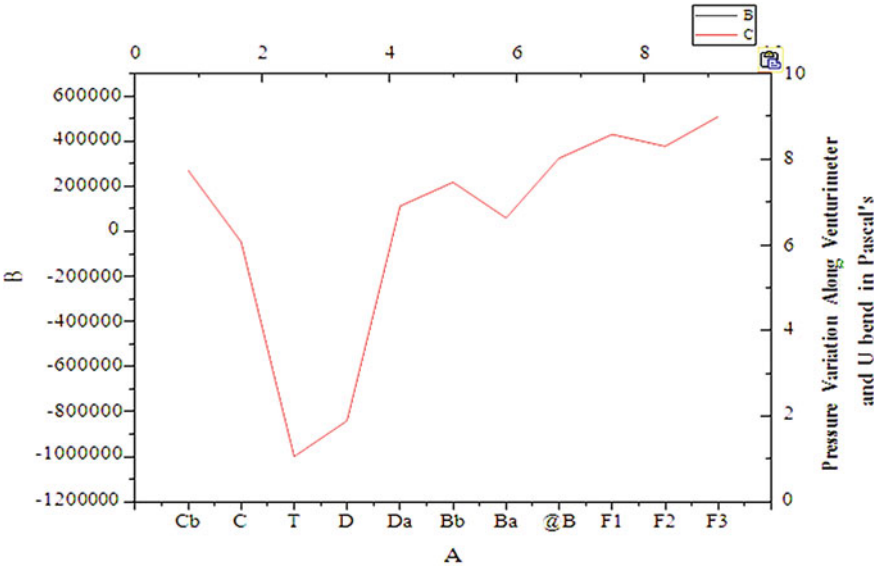

Fig. 11 Pressure variation along venturimeter and U bend

Table 2 Comparison of pressure distribution between venturimeter fitted with straight pipe, venturimeter fitted with bend and venturimeter fitted with U-bend

Point	Straight pipe	Pipe with single bend	Pipe with U-bend
Before converging	−8.46e+10	−1.23e+04	2.71e+05
Converging portion	−5.09e+10	−4.33e+04	−4.66e+04
Throat	−5.61e+10	−1.94e+06	−1.00e+06
Diverging portion	2.14e+13	−9.75e+05	−8.41e+05
After diverging	2.42e+13	−2.53e+05	1.12e+05
Before bend	–	−1.33e+05	2.18e+05
At the bend (nearer to the center)	–	−3.73e+05	5.93e+04
At the bend (farther to the center)	–	4.78e+04	3.24e+05
After bend	–	−5.54e+05	4.3e+05
Second bend (nearer to the center)	–	–	3.77e+05
Second bend (farther to the center)	–	–	5.09e+05

Table 3 Comparison of pressure distribution between venturimeter fitted with 45° bend, venturimeter fitted with 90° bend, and venturimeter fitted with U-bend

Position	Pipe with 90° bend	Pipe with U-bend	Pipe with 45° bend
Before converging	−1.23e+04	2.71e+05	4.50e+02
At the converging portion	−4.33e+04	−4.66e+04	3.78e+02
At the throat	−1.94e+06	−1e+06	-9.04e+01
At the diverging portion	−9.75e+05	−8.41e+05	8.97e+01
After diverging	−2.53e+05	1.12e+05	3.06e+02
At the bend (nearer end)	−1.33e+05	2.18e+05	1.26e+02
At the bend (farther end)	−3.73e+05	5.93e+04	3.42e+02

2.4 Venturimeter with a 135° Bend After the Diverging Portion

Fluid, with high pressure, enters the converging portion (as in other cases) and attains lower pressure at the converging portion unto the throat. And from the throat, pressure gradually increases and reaches a higher level of pressure (lower than the initial pressure) at the 45° bend. Pressure at the farther end of the bend is observed to be greater than that of the nearer end. However, the velocity distribution is exactly opposite to that of the pressure distribution.

Following is the table comparing the results of the 3 bends on pressure distributions:

Based on the observations made, the pressure in the venturimeter meter, with 45° pipe bend, at the throat is 10^4 times greater than that of the U-bend and 10^5 times than that of the 90° bend.

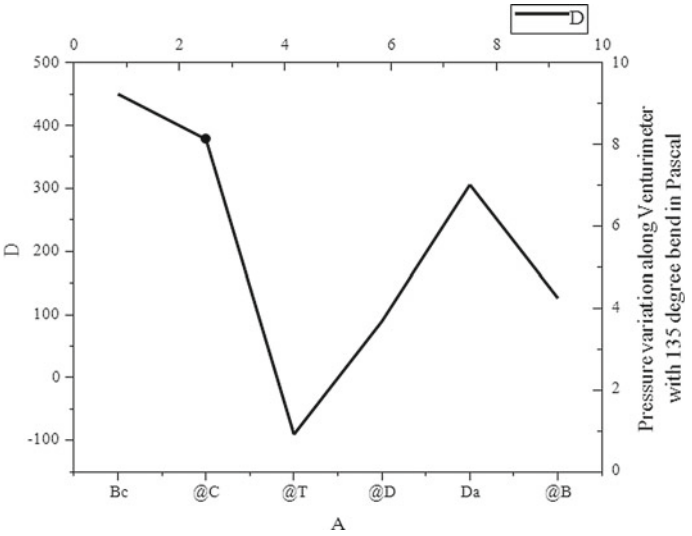

Fig. 12 Pressure variation along venturimeter with 135° bend

Sections along Venturimeter connected with 135° bend (Fig. 12).

2.5 Venturimeter Meter with an Obtuse Bend After the Diverging Portion

Fluid enters the converging portion with high pressure and reduces until the throat (velocity distribution is opposite to the pressure distribution). Fluid particles after coming out of the throat attain a higher pressure (lower than the initial pressure). If an obtuse bend (135°) is applied after the diverging portion, the pressure almost seems unaffected and remains based on the observations made, pressure at the throat is observed to be increased by 10 times than that of acute bend (45°) (Fig. 13).

On the other hand, velocity is found to be lesser after the diverging portion and remains constant to the bend and to an extent after it (Figs. 14 and 15, Table 4).

3 Conclusions

The extensive usage of Venturimeter in diverse industrial applications makes the instrument more unique, but the connections following the Venturimeter are making an impact in the fluid flow measurements [5]. The following are the observations

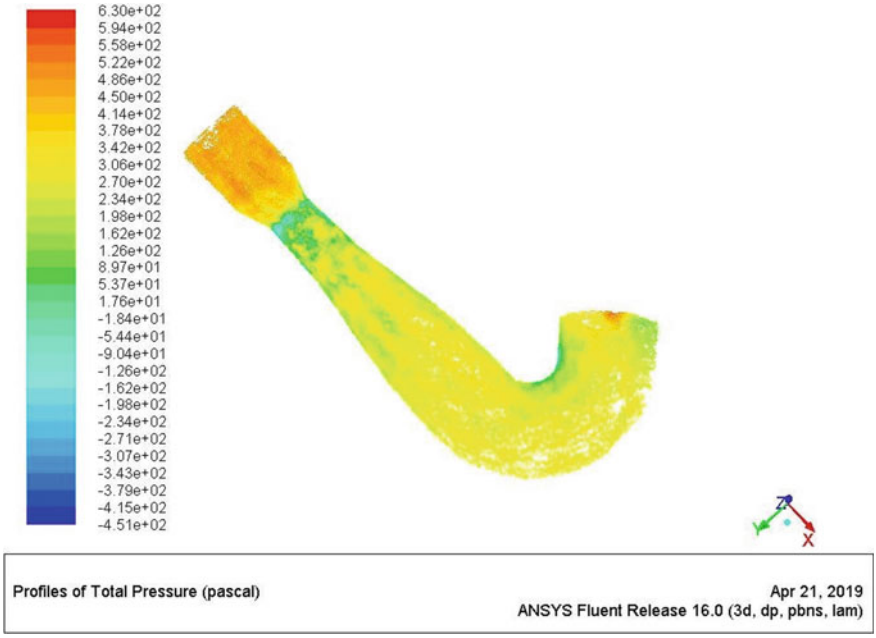

Fig. 13 Venturimeter with an acute bend

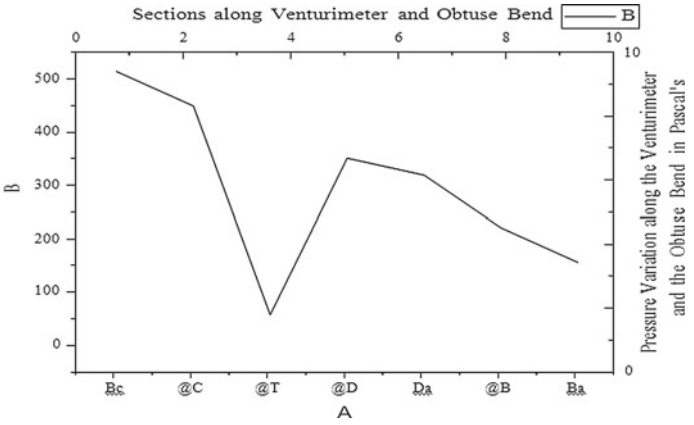

Fig. 14 Pressure variation along venturimeter and obtuse bend

made by analyzing Venturimeter connecting it to different types of typical possible bends used in industries for various applications.

According to Bernoulli's principle, there is standard pressure variation along the length of the pipe [6]. At the throat section, the pressure decreases allowing for increase in velocity, further gradually allowing the pressure to augment by increasing

Fig. 15 Venturimeter with 135° bend

Table 4 Comparison of pressure distribution between venturimeter fitted with 90° bend venturimeter fitted with 45° bend, venturimeter fitted with obtuse bend and venturimeter fitted with U-bend

Position	Pipe with 90° bend	Pipe with U-bend	Pipe with 45° bend	Pipe with obtuse bend
Before converging	−1.23e+04	2.71e+05	4.50e+02	4.64e+02
At the converging portion	−4.33e+04	−4.66e+04	3.78e+02	3.99e+02
At the throat	1.94e+06	−1.00e+06	−9.40e+01	7.77e+00
At the diverging portion	−9.75e+05	−8.41e+05	8.97e+01	3.01e+02
After diverging	−2.53e+05	1.12e+05	3.06e+02	2.69e+02
At the bend (nearer end)	−1.33e+05	2.18e+05	1.26e+02	1.71e+02
At the bend (farther end)	−3.73e+05	5.93e+04	3.42e+02	1.06e+02

the cross section of the diverging section of the Venturimeter. But due different end connections the standard variation in Venturimeter is affected and will reduce the efficiency in the discharge measurement [7]. The analysis done through ANSYS CFX 14.5 illustrates the effect of various such connections; the paper highlights the importance of various attachments

1. For the single bend (90° bend), pressure at the throat is found out to be 3×10^3 times the pressure at the throat for Venturimeter without a bend.
2. Pressure in the throat for the straight pipe. For the U-bend pipe, pressure at the throat is 2×10^3 times the
3. For the acute bend (45° bend), pressure in the throat is found out to be 10^9 times the standard pressure.
4. For the obtuse bend (135° bend), pressure in the throat is observed to be 10^{10} times the standard pressure.
5. So, it can be concluded that the pressure at the throat increases if the above sequence of bends is applied after the divergent. Contrarily, velocity keeps on decreasing at the throat for the same sequence.

Although in laboratories, the venturimeter meters are used in a straight pipe, the scenario is not the same in all the cases in real-time applications. Venturimeter finds their roles in several industries in numerous ways (not all with straight pipes). Below are some of the industrial applications of Venturimeter:

- For water treatment, the pipe network is of 1000s of kilometers, the pipe geometry after the Venturimeter installations has to be taken care of or else a bulked and induced pressure will get added to the result thus reducing the efficiency of the pipe flow.
- In today's scenario of sustainable development and water security playing a major role in achieving many of the Millennium development Goal's the paper emphasis on the importance of flow rate measurement in water supply industries [8].
- Many lift irrigation schemes have been on the anvil if the measurements are not done efficiently, then there would be a lot of wastages and hence they reduce the sole purpose of lift irrigation schemes (Fig. 16).

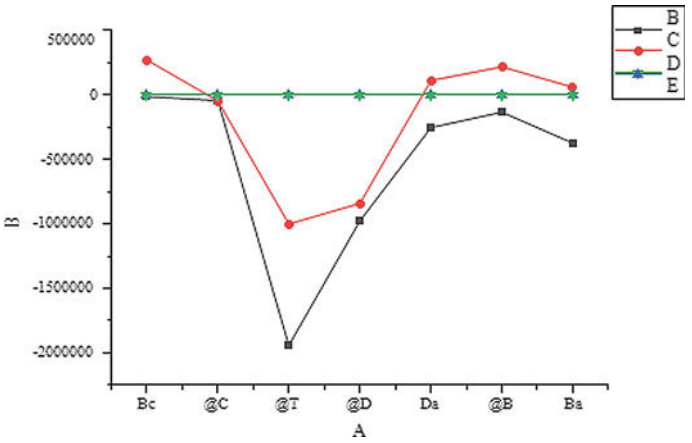

Fig. 16 Pressure variation in pipes with different outlets. Legend: B: Pipe with 90° bend, C: pipe with U-bend, D: pipe with 45° bend, E: pipe with obtuse bend

References

1. Elperin T, Fominykh A, Klochko M (2002) Performance of a venturi meter in gas–liquid flow in the presence of dissolved gases. Flow Meas Instrum 13:13–16
2. Kumar J, Singh J, Kansal H, Narula GS, Singh P (2014) CFD Analysis of flow through Venturi. Int J Res Mech Eng Technol 4(2):214–217
3. Tamhankar N, Pandhare A, Joglekar A, Bansode V (2014) Experimental and CFD analysis of flow through venturimeter to determine the coefficient of discharge. Int J Latest Trends Eng Technol 3(4):194–200
4. Kumar P, San SM (2014) CFD study of the effect of venturi convergent and divergent angles on low pressure wet gas metering. J Appl Sci 14(22):3036–3045
5. Huang X, Li G, Wang M (2009) IFIP international federation for information processing, volume 294. Computer and computing technologies in agriculture II, vol 2, pp 805–815
6. Bharani S, Mishra R, Singh SN, Seshadri V (1999) Performance characteristics of an eccentric venturimeter with elongated throat for flow rate measurement of solid-liquid flows. Indian J Eng Mater Sci 6:119–124
7. Hari Vijay P, Subrahmanyam V (2014). CFD simulation on different geometries of venturimeter. Int J Res Eng Technol 3(7):456–463
8. Karthik MS, Seshadri V (2014) Prediction of viscous coefficient of venturi meter under non ISO standard conditions. Int J Res Eng Technol 3(7):456–464

UV/Fe^{+3} Photolysis Process Optimization Using Response Surface Methodology for Decolorization of Reactive Red 120 Dye Simulated Wastewater

Bhatt Dhruv and Makwana Abhipsa

Abstract Decolorization of synthetic azo Reactive Red 120 (RR120) dye wastewater via UV/Fe^{+3} process was investigated. A preliminary study was conducted to understand the effect of various process variables like oxidant dose Fe^{+3} (0.25–2.75 mM)), initial dye concentration (100–200 mg/L), time (0–35 min), initial pH (1–11) on the decolorization of RR120. Response surface methodology (RSM) was employed to assess individual and interactive effects of critical process parameters on treatment performance in terms of colour removal efficiency. The photo-degradation of RR120 was investigated in a laboratory-scale batch photo-reactor equipped with low-pressure mercury lamp. Optimized process conditions for UV/Fe^{+3} treatment of RR120 suggested by RSM are Fe^{3+} = 2.35 mM, pH = 3.6, Initial dye concentration = 170 mg/L and reaction time = 55 min. Under these conditions, 92% colour removal was actually observed which is found to be very close to prediction given by fitted model. Treatment cost of UV/Fe^{+3} process was ~4 Rs/L.

Keywords RR120 · Fe^{+3} · Response surface methodology · Photolysis

1 Introduction

R–N=N–R′ functional group is the main structure of azo dyes; an organic compound, where R′ and R are commonly aryl. C–N=N–C link is commonly contained by azo dyes. Food, fabrics and leather item manufacturing involves azo dye usage. Azo pigments of azo dyes remain insoluble in solvents and even in water. Large types of azo dyes dominate the dye market [1] like reactive, metal-based, substantive or dispersed. Substantive dye usage is predominantly done for textile material based on cellulose like cotton. Non-electrostatics forces govern dye bonding. The number of azo bond also governs another type of azo dye. This study focuses on non-hydrolyzed reactive red 120 (RR120) dye which is anionic, bi-functional, di-azo reactive dye,

B. Dhruv · M. Abhipsa (✉)
Civil Engineering Department, Faculty of Technology & Engineering, The Maharaja Sayajirao University of Baroda, Baroda 390002, Gujarat, India
e-mail: abhipsamakwana78@gmail.com

© Springer Nature Singapore Pte Ltd. 2021

K. K. Pathak et al. (eds.), *Recent Trends in Civil Engineering*, Lecture Notes in Civil Engineering 77, https://doi.org/10.1007/978-981-15-5195-6_62

which is commonly manufactured and used in textile and dye industries. It contains two azo groups (–N=N–) and hence difficult to degrade biologically.

Stringent rules for effluent disposal and risk associated to environment force to treat non-toxic and toxic pollutants, dyes, inorganic of nitrate phosphate and sulphate along with heavy metals. Physicochemical, biological and chemical treatments were conventional treatments for dye decolorization in earlier years [1, 2], while electrochemical treatments and advanced oxidation processes can be considered as emerging technologies being applied now-a-days [1]. Phase separation is the only phenomena that take place in physical process; hence pollutant separation takes place from one state to another. Pre-requisite of chemical process is the requirement for chemical and shortcoming of the same is due to higher sludge production.

Biological processes short fall when employed for complex organics, but advanced oxidation processes seem to be efficient when compared with physical, chemical or biological processes. Complete oxidation is not a need for chemical process, while biological process needs reduction in toxicity [3]. End product through oxidation has four classifications: (i) structural revision in the base compound due to primary degradation; (ii) structural revision along with toxicity reduction in the base compound; (iii) mineralization or inorganic CO_2 production from organic carbon due to complete degradation; (iv) structural reformation of base compound into other more toxic intermediates due to objectionable degradation or fusing of base compound.

AOPs use •OH radicals as a strong oxidant for destruction of compound which cannot be degraded by other usual oxidants line ozone, oxygen or chlorine.

Understanding the effects of UV/Fe^{+3} treatment variables on RR120 decolorization and optimization of the treatment using RSM are the two objectives of this study.

2 Materials and Methodology

2.1 Materials

Model Azo Dye: Reactive Red 120. RR120 (Reactive red 120) dye molecular weight is 1469.34 g/moL having $C_{44}H_{24}Cl_2N_{14}Na_6O_{20}S_6$ molecular structure obtained in fine powdered form from ALPHA Industries, Ahmadabad, Gujarat, India as a gift sample. Figure 1 reports the chemical structure of RR120 dye. Table 1 narrates characteristics of RR120 dye.

Experimental Setup. Acrylic material batch reactor equipped with magnetic stirring operated at room temperature to conduct UV/Fe^{+3} based experimental runs (Fig. 2a). Figure 2b shows arrangement of UV tubes.

30 cm × 10 cm × 10 cm size reactor is equipped with 8″ long two UV tubes with 11 W nominal output and 253.4 nm emission band. Treated samples were taken from outlet valve. 1 L synthetic dye solution of desired dye concentration was magnetically stirred at 100 RPM.

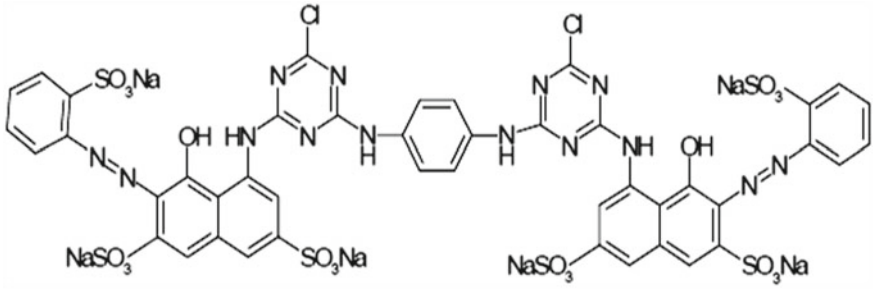

Fig. 1 Molecular structure of reactive red 120

Table 1 Characteristics of Reactive Red 120 [1]

Chemical class	Anionic, bi-functional, di-azo reactive dye
Molecular formula	$C_{44}H_{24}Cl_2N_{14}Na_6O_{20}S_6$
Molecular weight	1469.34 g/mol
Solubility in water	>100 g/L at 25 °C
λ_{max}	535 nm

Influence of treatment parameters like initial dye concentration, initial pH, oxidation time and oxidant dose were investigated. Treated samples were taken from outlet valve and analyzed for dye decolorization.

2.2 Methodology

Preparation of Dye Solution. Accurate amount of solid dye was dissolved in distilled water to obtain dye stock solution and then refrigerated in air-tight glass container. Experimental runs were performed at fixed dye concentrations; these concentrations were obtained on diluting certain amount of stock solution in distilled water.

Calculation of Cost. For treating 1 L RR120 simulated dye wastewater under optimized condition, required quantities of $FeCl_3$ (10% w/v) and H_2SO_4 (98%) were 1.128 g and 1.028 ml, respectively. Cost of $FeCl_3$ and H_2SO_4 are1.5 Rs/g and 0.035 Rs/ml, respectively. Hence, total chemical cost = (1.128 g × 1.5 Rs/g) + (1.02 ml × 0.035 Rs/ml) = 1.728 Rs. Electricity cost of 1kWh is 4.65 Rs. (as per MGVCL, Gujarat, India). Two UV lamps of 11 W each and magnetic stirrer of 480 W were used for 55 min. Hence, total electricity cost = [(11 × 2) W × 0.92 h × 0.001 × 4.65 Rs/kWh] + [480 W × 0.92 h × 0.001 × 4.65 Rs/kWh] = 2.144 Rs.

RSM Design and Data Analysis. The Box–Behnken design (BBD) with response surface methodology (RSM) was used to investigate the effect of the four variables, namely, initial dye concentration (100–200 mg/L), initial pH (3–7), dose of Fe^{+3} (0.25–2.75 mM) and treatment time (15–75 min).

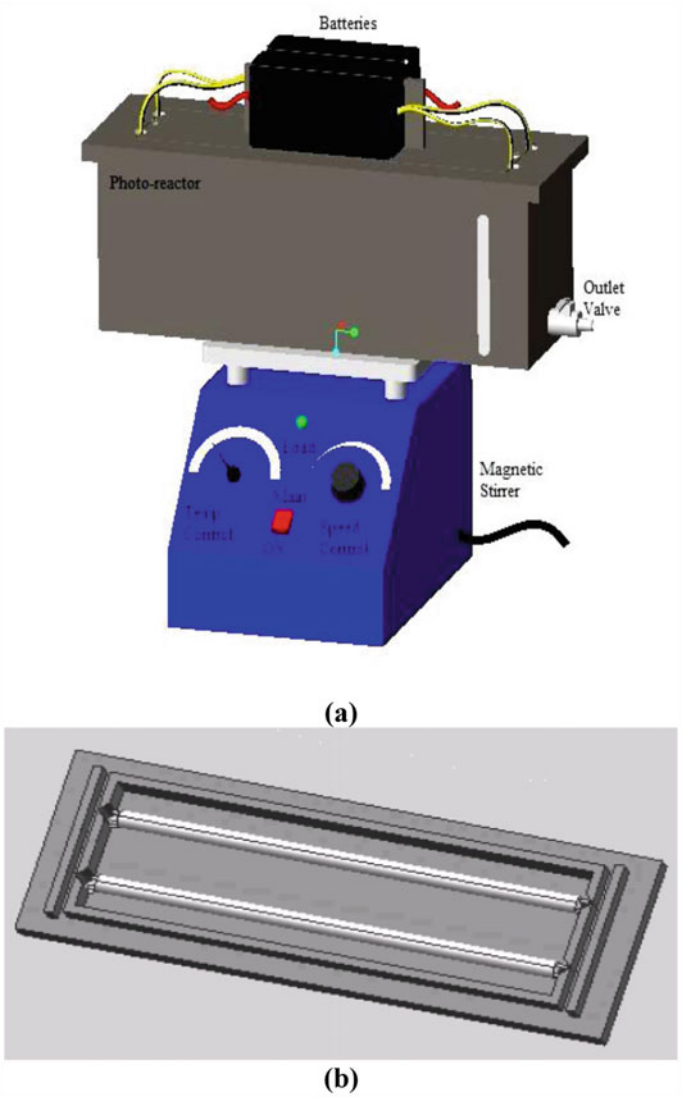

Fig. 2 **a** Schematic of experimental setup **b** assembly of UV tubes for photolysis

Optimization of treatment parameters, namely, initial pH (3–7), Fe^{+3} dose (0.25–2.75 mM), oxidation time (15–75 min) and dye concentration (100–200 mg/L) was carried using the Box–Behnken design (BBD) with response surface methodology (RSM).

The BBD is a cost-effective, efficient and rotatable quadratic design where factor combinations are at the midpoints of the edges and at the centre [4, 5].

Table 2 Experimental levels and range of the independent variables for UV/Fe^{+3} process

Experimental range and levels of the independent variables		Coded factor level		
Variable	Factors	−1	0	1
Initial dye (mg/L)	x_1	100	150	200
pH	x_2	3	5	7
Fe^{+3} dose (mM)	x_3	0.25	1.5	2.75
Time (min)	x_4	15	45	75

Model adequacy check and experimental errors estimation can be done through centre points.

The effluent dye concentration and % decolorization were taken as the response parameters. Finalization of range of treatment variables for designing experimental matrix was based on the understanding developed through preliminary runs. Table 2 represents parameters' range and their levels. Table 3 reports BBD factorial design with 5 replicates of centre point. Design Expert 8.0 software was employed to calculate effect of all four treatment parameters and also to analyze and fit second-order polynomial model.

3 Results and Discussion

Primarily, dye degradation was carried alone using Fe^{+3} in absence of UV and using UV but in the absence of any oxidant; both study showed very little and slow rate decolorization. However, decolorization became faster when both degrading agencies were (UV + Fe^{+3}) taken together. Kalsoom [6] has reported similar trend of AOPs. Hence, primary objective of this study was to understand the effect of various process conditions under One-Factor-At-a-Time (OFAT) approach.

3.1 Effect of PH

Influence of solution pH was analyzed by varying solution's pH from 1 to 11 as shown in Fig. 3 keeping dye concentration at 100 mg/L with 0.5 mM dose of Fe^{+3} for 15 min time. UV + Fe^{+3} worked better under acidic condition. Neamtu [2] reports similar trend and explained that different species of Fe(III) ions will be formed under different pH of solutions and all species have their light absorptive behaviour, but with different absorption quantum yield (Table 4).

The influence of solution pH was analyzed by varying solution's pH from 1 to 11 as shown in Fig. 3 keeping dye concentration at 100 mg/L with 0.5 mM dose of Fe^{+3} for 15 min time. UV + Fe^{+3} worked better under acidic condition. Neamtu [2] reports

Table 3 RSM design matrix for UV/Fe^{+3} process

Std run order	Process variables			
	Initial dye (mg/L)	Initial pH	Fe^{+3} dose (mM)	Time (min)
1	100	3	1.5	45
2	200	3	1.5	45
3	100	7	1.5	45
4	200	7	1.5	45
5	150	5	0.25	15
6	150	5	2.75	15
7	150	5	0.25	75
8	150	5	2.75	75
9	100	5	1.5	15
10	200	5	1.5	15
11	100	5	1.5	75
12	200	5	1.5	75
13	150	3	0.25	45
14	150	7	0.25	45
15	150	3	2.75	45
16	150	7	2.75	45
17	100	5	0.25	45
18	200	5	0.25	45
19	100	5	2.75	45
20	200	5	2.75	45
21	150	3	1.5	15
22	150	7	1.5	15
23	150	3	1.5	75
24	150	7	1.5	75
25	150	5	1.5	45
26	150	5	1.5	45
27	150	5	1.5	45
28	150	5	1.5	45
29	150	5	1.5	45

similar trend and explained that different species of Fe(III) ions will be formed under different pH of solutions and all species have their light absorptive behaviour, but with different absorption quantum yield (Table 4). Ferric ion at pH < 3 exists in soluble form and absorbs light at about 300 nm wavelength which is attributed to the presence of ferric ion. It has been documented that Fe^{3+} hydrolyze in water-based solution and forms different Fe(III) species which can be divided into three classes, i.e. low-molecular weight hydroxo complexes ($Fe(OH)^{2+}$, $Fe(OH)_2^+$, $Fe_2(OH)_2^{4+}$ etc.);

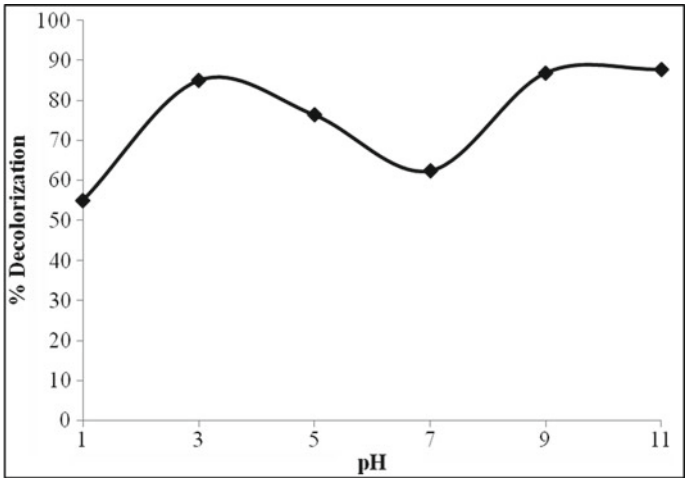

Fig. 3 Effect of pH for UV/Fe^{+3} process (initial dye concentration = 100 mg/L, Fe^{+3} dose = 0.5 mM, time = 15 min)

Table 4 Hydrated Fe(III) species in solution, as a function of pH [2]

Fe^{+3} species	pH range
$Fe(H_2O)_6^{+3}$	1–2
$Fe(OH)(H_2O)_5^{+2}$	2–3
$Fe(OH)_2(H_2O)_4^{+}$	3–4

hydrolytic polymer ($(Fe)_n(OH)_m(H_2O)^{+}_{(3n-m)}$) and precipitated oxides (amorphous $Fe(OH)_3$, FeOOH and Fe_2O_3) [7].

As decreased pH, amount of $Fe(OH)^{2+}$ may also decrease, which could be the reason for lower efficiency of RR120 degradation at pH 1 than that at pH 3. Increase in pH beyond 3 showed lesser efficiency, which might be due to the precipitation of other ferric hydroxides ($Fe(OH)_3$), as it was reported earlier that ferric hydroxide colloids formed favourably at pH > 3 [8].

Among these species, hydroxo compounds like $Fe(OH)_2^{+}$, $Fe(OH)^{2+}$, $Fe_2(OH)_2^{4+}$, etc. have special photochemical properties and so that they can be photo reduced to produce ferrous (Fe^{2+}) ions and hydroxyl radicals (•OH). $Fe(OH)^{2+}$ has been found to be the most efficient specie for the photo-production of •OH radicals in acidic solutions [8]. Hence, results indicated maximum % decolorization at pH = 3 (~86%). The basic reaction of UV + Fe^{+3} would be

$$Fe(OH)^{2+} + h\nu \rightarrow Fe^{2+} + \bullet OH \quad (1)$$

The speciation of ferric ion at certain pH is strongly dependent upon the ferric ion concentration. At pH > 3 ferric ion starts forming precipitates of ferric hydroxides ($Fe(OH)_3$) which are insoluble in water. Thus, the overall degradation mechanism

can be represented as under

$$Fe^{3+} + H_2O \rightarrow Fe(OH)^{2+} + H^+ \quad (2)$$

$$Fe(OH)^{2+} + h\nu \rightarrow Fe^{2+} + \bullet OH \quad (3)$$

$$RR120 + \bullet OH \rightarrow \text{Mineralization products} \quad (4)$$

Firstly, ferric ion hydrolyzed to form $Fe(OH)^{2+}$, a dominant photo-reactive specie in the pH range of 2.5-3. Then $Fe(OH)^{2+}$ photo reduced to form ferrous (Fe^{2+}) ions along with hydroxyl radicals (•OH) as given in reaction under UV-C light irradiation. Hydroxyl radicals on being strong oxidizing agent further oxidized RR120 up to mineralized product.

When the experiment was carried out at pH > 3, i.e. at pH 9 and 11 in the presence of 0.5 mM Fe^{3+}, two important things were observed, one is the formation of iron precipitates and the other is the higher % decolorization of RR120. So, it was assumed that RR120 has been adsorbed on iron precipitates. Thus, higher % decolorization was shown at alkaline pH. Also, previously it was reported that at pH > 3 and in the presence of ferric ion observed reduction of organic matter could be governed by adsorption phenomenon; authors reported that precipitates of ferric hydroxides could have acted as an adsorbent in this case [8]. So, in the present study also the disappearance of RR120 colour may lead to adsorption of RR120 on precipitates of ferric hydroxide. To confirm that the pH of the mixture was decreased to 7 and it was observed that at neutral to slightly alkaline pH, mixture was again turned to initial colour which is due to desorption of RR120. Hence it was confirmed that RR120 has been adsorbed on $Fe(OH)_3$ precipitates.

3.2 *Effect of Fe^{+3} Dose*

Fifteen min oxidation was carried for 100 mg/L RR120 dye decolorization at 5 pH with varying Fe^{+3} dose from 0.25 to 2.75 mM to understand the influence of Fe^{+3} dose (Fig. 4). Increase in decolorization was observed with increase in Fe^{+3} dose up to 1.5 mM beyond which reduction in efficiency has been reported due to an increase in $Fe(OH)_3$ precipitates and reduction in Fe^{+2} species. When the experiment was carried out in the presence of Fe^{3+} > 1.5 mM, immediate formation of precipitates has been observed. Hence, all other experiments were carried out with 1.5 mM ferric ion concentration.

Application of Fe^{3+} concentration beyond certain dose and at fixed carbon load can retard the efficiency of process due to free radical scavenging effect due to overdosing of Fe^{3+}/Fe^{2+} concentrations [9].

$$Fe^{2+} + \bullet OH \rightarrow Fe^{3+} + OH^-,\ k = 3.0 \times 10^8 M^{-1}s^{-1} \quad (5)$$

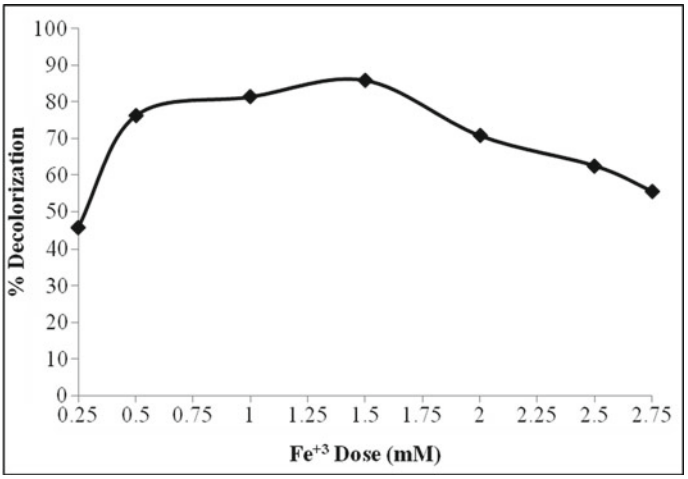

Fig. 4 Effect of Fe^{+3} dose for UV/Fe^{+3} process (pH = 5, time = 15 min, dye concentration = 100 mg/L)

Giroto [10] had also reported negative influence due to overdosing of Fe^{+2}. On the contrary, higher dose of Fe^{+3} with higher COD or pollution develops good removal efficiency. Means for any particular pollution load, there would be certain fixed dose of Fe^{+2}/Fe^{+3}. Like for our case maximum 85% degradation was obtained at 1.5 mM Fe^{+3} dose and above its efficiency was observed to be decreasing due to free radical scavenging.

3.3 Effect of Time and Initial Dye Concentration

Time and dye load influence were investigated on varying time from 0 to 35 min for three difference dye load (100, 150 and 200 mg/L) at 5 pH with 1.5 mM Fe^{+3} dose (Fig. 5). Efficiency and time were found to be directly proportional to each other. % decolorization increased with time and reduces with initial dye concentration. Time required and organic loading are found to be inversely related when focused to achieve particular efficiency. Either time required would be more or dye concentration would be lower to achieve focused decolorization. After 35 min decolorization for 100, 150 and 200 mg/L dye concentrations were observed to be ~99%, ~98% and ~70%, respectively. Literature also reports that photolysis process reaction rates are very much high due to increase in reactant concentration during initial few minutes [2].

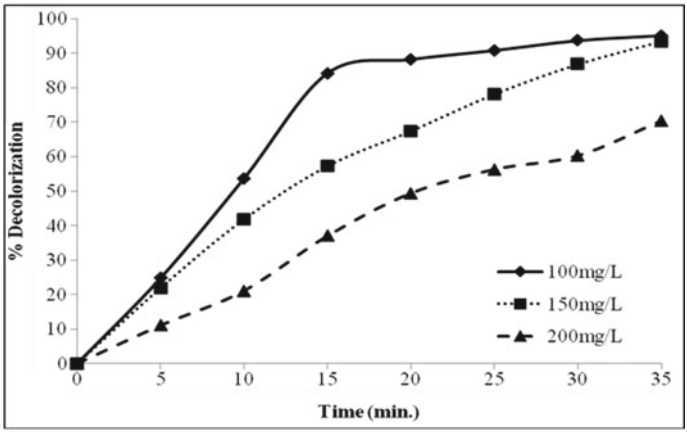

Fig. 5 Effect of time and dye concentration for UV/Fe^{+3} process (pH = 5, Fe^{+3} dose = 1.5 mM)

3.4 Process Optimization

Response surface methodology was adopted to understand influence of pH, dye concentration, time and Fe^{+3} dose on focused photolysis. RSM also helps to establish the importance of main effect, interaction effect and quadratic effect of these targeted treatment parameters.

Looking to the finding given in Figs. 3, 4 and 5, experimental runs were conducted at initial pH 3, 5 and 7 for duration from 15 to 75 min on 100 to 200 mg/L dye concentration with Fe^{+3} dose varying from 0.25 to 2.75 mM. Table 5 shows a combination of various experimental conditions suggested by BBD along with actual and predicted final dye concentration and decolorization efficiency.

3.5 Model Development and Its Validation

BBD suggested 29 runs with 5 central points (std. run no. 25–29) (Table 5). Equations (6) and (7) are proposed quadratic models developed using actual final dye concentration and % decolorization.

Responses		**Proposed Quadratic Model**	
Effluent Dye Concentration (mg/L)	=	$1.12 + 28.25x_1 + 12.72x_2 - 20.35x_3 - 27.83x_4 + 5.81x_1x_2 - 8.45x_1x_3 - 20.43x_1x_4 + 8.52x_3x_4 + 19.04x_1^2 + 16.36x_2^2 + 18.57x_3^2 + 25.10x_4^2$	(6)
% Decolorization	=	$99.24 - 11.16x_1 - 8.50x_2 + 13.53x_3 + 17.91x_4 + 8.01x_1x_4 - 5.63x_3x_4 - 9.02x_1^2 - 11.29x_2^2 - 12.55x_3^2 - 16.68x_4^2$	(7)

Predicted final dye concentration and % decolorization fits well all statistical requirements of ANOVA. Tables 6 and 7 report all vitals of ANOVA for both developed models and included model-terms. As per Fisher test value of "Prob >

Table 5 Design matrix with actual and predicted values for UV/Fe^{+3} process

Std run order	Process variables				Responses			
	Dye concentration (mg/L)	Initial pH	Fe^{+3} dose (mM)	Time (min)	Actual final dye concentration (mg/L)	Actual % decolorization	Predicted final dye concentration (mg/L)	Predicted % decolorization
1	100	3	1.5	45	2.96	97.02	1.36	98.59
2	200	3	1.5	45	41.33	79.24	46.23	76.26
3	100	7	1.5	45	19.08	80.60	15.18	81.60
4	200	7	1.5	45	80.71	59.29	83.30	59.27
5	150	5	0.25	15	102.24	31.23	101.48	32.95
6	150	5	2.75	15	44.80	69.54	43.74	71.26
7	150	5	0.25	75	26.73	81.96	28.78	80.02
8	150	5	2.75	75	3.37	97.74	5.12	95.82
9	100	5	1.5	15	20.20	79.35	24.40	74.80
10	200	5	1.5	15	125.20	36.65	121.77	36.45
11	100	5	1.5	75	1.94	98.00	9.61	94.60
12	200	5	1.5	75	25.20	87.35	25.24	88.29
13	150	3	0.25	45	41.63	71.92	43.67	70.38
14	150	7	0.25	45	66.53	55.37	69.12	53.38
15	150	3	2.75	45	1.84	98.77	2.97	97.43
16	150	7	2.75	45	25.71	82.76	28.42	80.44
17	100	5	0.25	45	25.92	73.73	22.38	75.31
18	200	5	0.25	45	98.16	50.82	95.77	52.98
19	100	5	2.75	45	1.43	98.56	−1.43	102.36

(continued)

Table 5 (continued)

Std run order	Process variables				Responses			
	Dye concentration (mg/L)	Initial pH	Fe^{+3} dose (mM)	Time (min)	Actual final dye concentration (mg/L)	Actual % decolorization	Predicted final dye concentration (mg/L)	Predicted % decolorization
20	200	5	2.75	45	39.90	79.98	38.18	80.03
21	150	3	1.5	15	57.55	61.16	57.69	61.85
22	150	7	1.5	15	82.24	44.26	83.13	44.86
23	150	3	1.5	75	8.67	94.08	2.02	97.67
24	150	7	1.5	75	32.35	77.96	27.47	80.68
25	150	5	1.5	45	1.22	99.18	1.12	99.24
26	150	5	1.5	45	1.43	99.04	1.12	99.24
27	150	5	1.5	45	0.92	99.38	1.12	99.24
28	150	5	1.5	45	1.12	99.25	1.12	99.24
29	150	5	1.5	45	0.92	99.38	1.116	99.24

Table 6 Analysis of variance (ANOVA) table (partial sum of squares-Type-III) for effluent dye concentration (y_1) for UV/Fe^{+3} process

Source	Sum of squares	df	Mean square	F value	p-value Prob > F	
Model	34966.96	12	2913.91	176.94	<0.0001	Significant
x_1-Initial dye concentration	9575.62	1	9575.62	581.46	<0.0001	
x_2-Initial pH	1942.09	1	1942.09	117.93	<0.0001	
x_3-Fe^{+3} dose	4969.47	1	4969.47	301.76	<0.0001	
x_4-Time	9295.22	1	9295.22	564.43	<0.0001	
x_1x_2	135.26	1	135.26	8.21	0.0112	
x_1x_3	285.27	1	285.27	17.32	0.0007	
x_1x_4	1670.36	1	1670.36	101.43	<0.0001	
x_3x_4	290.36	1	290.36	17.63	0.0007	
x_1^2	2351.37	1	2351.37	142.78	<0.0001	
x_2^2	1736.53	1	1736.53	105.45	<0.0001	
x_3^2	2236.11	1	2236.11	135.78	<0.0001	
x_4^2	4086.39	1	4086.39	248.14	<0.0001	
Residual	263.49	16	16.47			

Table 7 Analysis of variance (ANOVA) table (partial sum of squares-Type-III) for % decolorization (y_2) for UV/Fe^{+3} process

Source	Sum of squares	df	Mean square	F value	p-value prob > F	
Model	11576.9	10	1157.69	180.57	<0.0001	Significant
x_1-Initial dye concentration	1495.66	1	1495.66	233.28	<0.0001	
x_2-Initial pH	866.15	1	866.15	135.1	<0.0001	
x_3-Fe^{+3} dose	2195.38	1	2195.38	342.42	<0.0001	
x_4-Time	3848.86	1	3848.86	600.32	<0.0001	
x_1x_4	256.64	1	256.64	40.03	<0.0001	
x_3x_4	126.79	1	126.79	19.78	0.0003	
x_1^2	528.01	1	528.01	82.35	<0.0001	
x_2^2	826.76	1	826.76	128.95	<0.0001	
x_3^2	1021.19	1	1021.19	159.28	<0.0001	
x_4^2	1805.71	1	1805.71	281.64	<0.0001	
Residual	115.4	18	6.41			

Table 8 Statistical criteria (responses in coded form) for UV/Fe^{+3} process

Responses	R^2	Adj R^2	Pre R^2	AP	SD	CV	Press	Mean
Effluent dye concentration (mg/L)	0.9925	0.9869	0.9657	45.344	4.06	11.99	1207.27	33.83
% Decolorization	0.9901	0.9846	0.9638	44.514	2.53	3.22	423.15	78.74

F" lesser than 0.0500, makes model or model-term significant [11]. Model-term with "Prob > *F*" value more than 0.1 can be statistically insignificant [11]. Equations (6) and (7) were developed after neglecting such insignificant model-terms. Both suggested models gave *p*-value less than 0.05, which ensures 95% confidence interval of prediction.

R^2 being the coefficient of determination (should be nearly 1.0) tells us about overall efficiency of the proposed model. R^2 values for both the models were very near to 1.0 which make sure a good correlation between predicted and actual responses. Difference between R^2 and R^2_{adjusted} should be less than 0.15. When they differ much, indication for insignificant terms inclusion in model is there [11]. Prediction efficiency for new responses can be ensured through R^2_{adjusted}, it should be in close agreement with R^2 [12]. R^2, R^2_{adjusted} and R^2_{adjusted} fall within the statistical requirements (Table 8). Adequate precision (AP) can be defined as the ratio of the range of the predicted values of the design points to the average standard deviation of all predicted response and should be greater than 4 for a good model [13]. Both models satisfy these criteria.

Model reproducibility can be defined by coefficient of variance, which is the ratio of the standard error to the mean value of the observed response. CV lesser than 10% makes model reproducible [14], and CV value for % decolorization was well below 10%, and for effluent dye concentration it was slightly above 10%. Predicted and actual values of dye concentration and % decolorization are very much in agreement (Fig. 6), which makes both the quadratic models given in Eqs. (6) and (7) reliable within the studied range of experimental conditions. Figures 7 and 8 report 3D surface of interaction effects of certain two process parameters on effluent dye concentration and % decolorization, respectively.

Figure 7a represents interaction of time and dye on effluent dye concentration at 3.6 pH and Fe^{+3} dose of 2.35 mM. Surface plot depicts that lower dye, the rate of decreasing effluent dye is higher than that of at higher dye. At initial few minutes of treatment, lower initial dye is enough for complete mineralization of RR120 while for highest initial dye (200 mg/L) or as initial dye increases, the effluent dye increases rapidly. On the other hand, at higher treatment time, rate of decreasing effluent dye at higher initial dye is high. Figure 7b represents interaction of Fe^{+3} dose with initial dye on effluent dye at pH 3.6 and 55 min of treatment time. Surface plot depicts that less Fe^{+3} dose is not sufficient for complete mineralization of RR120 while at higher dose of Fe^{+3}, the rate of decreasing effluent dye is high also at higher initial dye.

Figure 7c represents interaction of pH and initial dye concentration on effluent dye concentration at Fe^{+3} dose of 2.35 mM and 55 min of treatment time. Surface

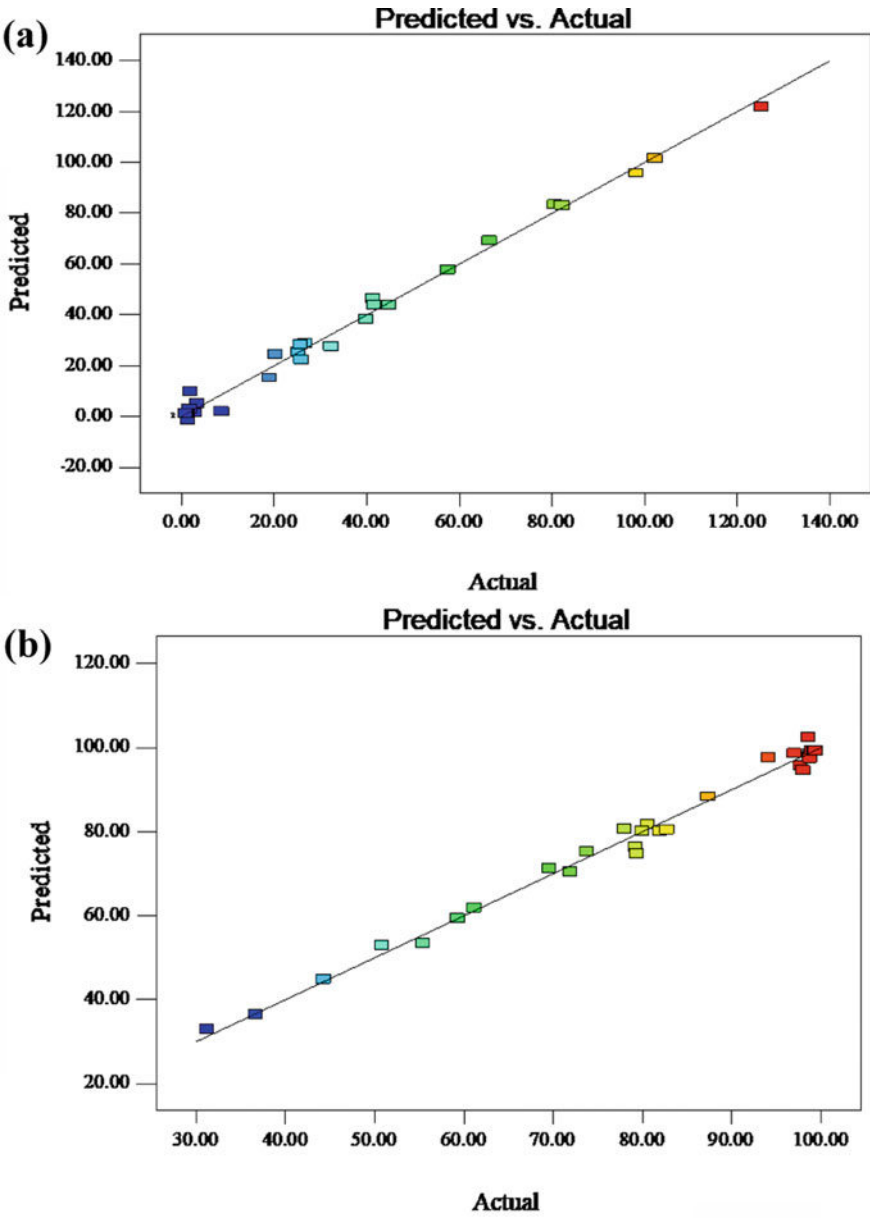

Fig. 6 Predicted versus actual values for **a** effluent dye concentration and **b** % decolorization, for UV/Fe^{+3} process

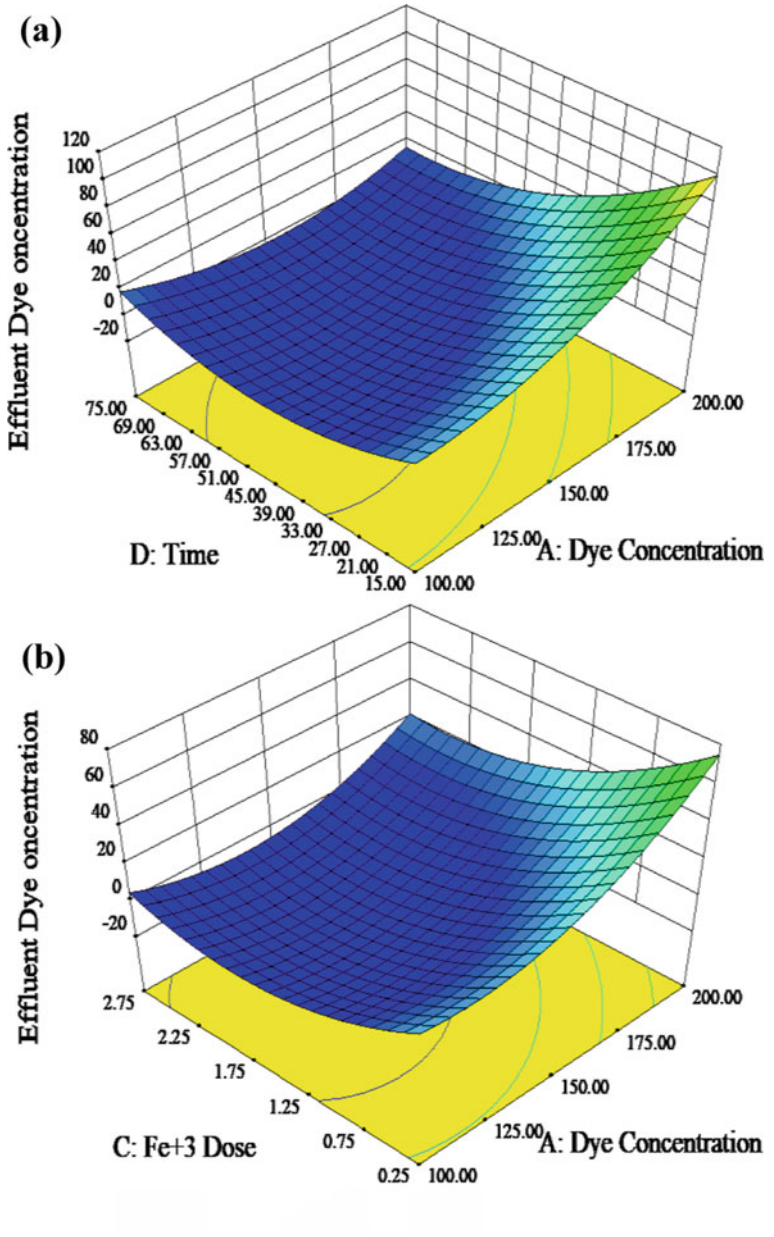

Fig. 7 Surface plots for effluent dye **a** time and initial dye at pH 3.6 and Fe^{+3} dose 2.35 mM **b** Fe^{+3} dose and dye at pH 3.6 and time of 55 min. **c** pH and dye at Fe^{+3} dose of 2.35 mM and time of 55 min and **d** Fe^{+3} dose and time at pH 3.6 and initial dye 170 mg/L, for UV/Fe^{+3} process

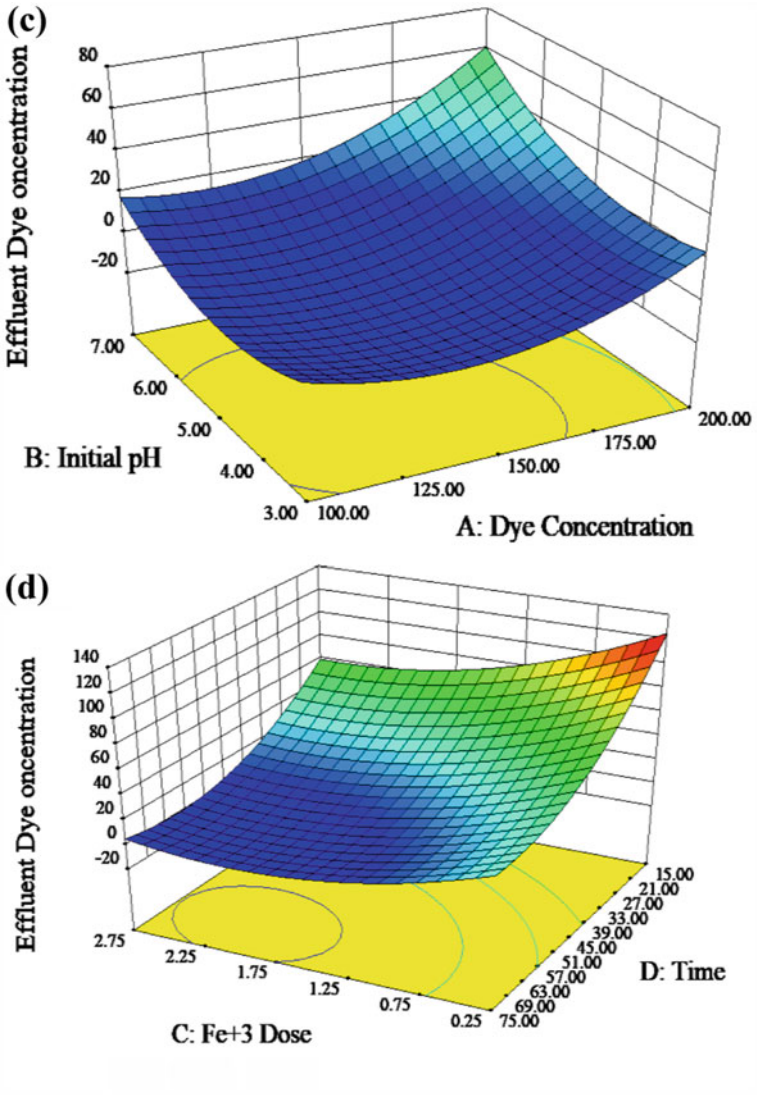

Fig. 8 Surface plots for % decolorization **a** time and initial dye at Fe^{+3} dose of 2.35 mM and pH 3.6 and **b** Fe^{+3} dose and time at pH 3.6 and initial dye of 170 mg/L, for UV/Fe^{+3} process

plot depicts that the rate of decreasing effluent dye concentration at lower initial dye concentration is high, while at higher initial dye concentration it is low. At lower pH values, the rate of decreasing effluent dye concentration is high while it is low at higher pH values. Figure 7d represents interaction of Fe^{+3} dose and time on effluent dye level at pH 3.6 and initial dye of 170 mg/L. Surface plot depicts that the lower Fe^{+3} dose is not sufficient for complete mineralization of RR120 in less time, while

Table 9 Optimum conditions for effluent dye concentration and % decolorization

	pH	Fe^{+3} (mM)	Dye concentration (mg/L)	Time (min)	Effluent dye concentration (mg/L)	% Decolorization	Desirability
Predicted	3.6	2.35	170	55	0	100	1.0
Observed	~3.6	2.35	170	55	13.8775	91.7725	

at higher treatment time it is found to be enough. The rate of decreasing effluent dye concentration is high with higher treatment time and Fe^{+3} Dose.

Figure 8a represents interaction of time and initial dye on % decolorization at 3.6 pH and Fe^{+3} dose of 2.35 mM. Surface plot depicts that at higher treatment time, effect of initial dye concentration is insignificant, while at lower treatment time the rate of % decolorization is high. At lesser initial dye, % decolorization is less, while it is high at higher initial dye concentration. Figure 8b represents interaction effect of Fe^{+3} and time on % decolorization at pH 3.6 and initial dye concentration of 170 mg/L. Surface plot depicts that less Fe^{+3} dose is not sufficient for complete mineralization of RR120 for lesser treatment time. At lesser treatment time, the rate of % decolorization is slow as compared to that of that at higher time.

RSM involves multiple response optimization through converting them in single by uniting all individual responses into a composite function succeeded by optimization of the same [15]. RSM uses desirability function for optimization which converts all response to separate desirability function (d) and then they all are combined in the form of composite desirability function (D) an arithmetic mean [15]. Preferably to be equal to 1 but should be very near to 1. Table 9 reports optimum conditions given by model along with predicted and actual responses under the same.

4 Conclusion

Based on preliminary studies, it has been reported that acidic pH (around 3) as well as alkaline (>9) were found to be effective. Further, it has also been observed that increase in Fe^{+3} dose increased removal up to 1.5 mM beyond which reduction in removal had been reported due to free radical scavenging effect of excessive concentrations of Fe^{+3}/Fe^{+2}. Increase in dye concentration has inverse effect on removal efficiency while time showed direct effect on the same.

Optimized conditions of UV/Fe^{+3} treatment for RR120 as per RSM study are Fe^{+3} = 2.35 mM, pH = 3.6, Initial dye concentration = 170 mg/L, and reaction time = 55 min. Under these conditions, 92% colour removal was actually reported which fitted prediction of the model well. Cost analysis was done for treatment of 1L wastewater and approximate operating cost of UV/Fe^{+3} processes was estimated to be ~4 Rs/L.

References

1. Neamtu M, Simmiceanu I, Yediler A, Kettrup A (2002) Kinetics of decolourization and mineralization of reactive azo dyes in aqueous solution by the UV/H_2O_2 oxidation. Dyes Pigm 53:93–99. https://doi.org/10.1016/S0143-7208(02)00012-8
2. Neamtu M, Simmiceanu I, Yediler A, Kettrup A (2003) Oxidation of commercial reactive azo dye aqueous solutions by the photo-fenton and fenton-like processes. J Photochem Photobiol, A 161:87–93. https://doi.org/10.1016/S1010-6030(03)00270-3
3. Metcalf & Eddy Inc (1991) Wastewater engineering: treatment disposal and reuse. New York, McGraw-Hill
4. Bezerra MA, Santelli RE, Oliveiraa EP, Villar LS, EscaleiraL A (2008) Response surface methodology (RSM) as a tool foroptimization in analytical chemistry. Talanta 76:965–977. https://doi.org/10.1016/j.talanta.2008.05.019
5. Makwana AR, Mansoor MA (2016) Continuous electrocoagulation process for the post-treatment of anaerobically treated municipal wastewater Process Saf Environ. I02:724–733. https://doi.org/10.1016/j.psep.2016.06.005
6. Kalsoom U, Salman Ashraf S, Meetani MA, Rauf MA, Bhatti HN (2012) Degradation and kinetics of H_2O_2 assisted photochemical oxidation of Remazol Turquoise Blue. Chem Eng J 200–202:373–379. https://doi.org/10.1016/j.cej.2012.06.058
7. Feng W, Deng N (2000) Photochemistry of hydrolytic iron (III) species and photoinduced degradation of organic compounds. A minireview. Chemosphere 41:1137–1147. https://doi.org/10.1016/s0045-6535(00)00024-2
8. Lam SW, Chiang K, Lim TM, Amal R, Low GKC (2005) The role of ferric ion in the photochemical and photocatalytic oxidation of resorcinol. J Catal 234:292–299. https://doi.org/10.1016/j.jcat.2005.06.014
9. Arslan-Alaton I, Kabdash I, Hanbaba D, Kuybu E (2008) Electrocoagulation of a real reactive dyebath effluent using aluminium and stainless steel electrodes. J Hazard Mater 150:166–173. https://doi.org/10.1016/j.jphotochem.2008.11.019
10. Giroto JA, Guardani R, Teixeira ACSC, Nascimento CAO (2006) Study on the Photo-fenton degradation of polyvinyl alcohol in aqueous solution Chem. Eng Process 45:523–532. https://doi.org/10.1016/j.cep.2005.12.001
11. Montgomery DC (2010) Design and analysis of experiments, 7th ed. Wiley India Pvt. Ltd., New Delhi
12. Myers RH, Montgomery DC, Anderson-Cook CM (2009) Response surface methodology: process and product optimization using designed experiments, 2nd ed. Wiley, New York
13. Anderson MJ, Whitcomb PJ (2005) RSM simplified. Productivity Press, New York, USA. https://doi.org/10.1201/9781315382326
14. Ghafari S, Aziz HA, Hasnain MI, Zinatizadeh AK (2009) Application of response surface methodology (RSM) to optimize coagulation flocculation treatment of leachate using poly aluminum chloride (PAC) and alum. J Hazard Mater 163:650–656. https://doi.org/10.1016/j.jhazmat.2008.07.090
15. Costa NR, Lourenco J, Pereira ZL (2011) Desirability function approach: a review and performance evaluation in adverse condition. Chemom Intell Lab Syst 107:234–244. https://doi.org/10.1016/j.chemolab.2011.04.004

Relative Wave Run-Up Parameter Prediction of Emerged Semicircular Breakwater

Suman Kundapura, Subba Rao, and Vittal Hegde Arkal

Abstract Relative wave run-up parameter (R_u/H_i) on breakwaters is a vital component in fixing the elevation of the breakwater crest. In the present study, several soft computing methods has been employed to predict the wave run-up on the emerged seaside perforated semicircular breakwater for the prevailing Arabian sea wave climate, off Mangaluru coast in India. Unlike the mathematical modeling techniques, the soft computing tools have no complexity involved about understanding the nature of underlying process and prediction consumes less time when proper physical model data is available. The soft computing methods like artificial neural network (ANN), adaptive neuro fuzzy inference system (ANFIS), genetic algorithm based adaptive neuro fuzzy inference system (GA-ANFIS) and particle swarm based adaptive neuro fuzzy inference system (PSO-ANFIS) are the four models employed in the study. The ANN predicted well for the set architecture of (5-7-1). The ANFIS is used to predict the wave run-up on semicircular breakwater models using the hybrid efficiency of fuzzy logic and neural network. An initial FIS is generated for input variables by mapping the input-output data; the training is done using ANN; and the objective of GA and PSO is set to find the best FIS, reducing the root mean square error in the prediction of wave run-up. The most influencing input parameters (H_i/gT^2, d/gT^2, S/D, h_s/d, R/H_i) are taken in non-dimensional form. The data required has been acquired from the physical model experiments conducted in the Marine structures laboratory of National Institute of Technology Karnataka (NITK), Surathkal, India. The GA-ANFIS prediction of wave run-up is found to be better than that of ANFIS prediction in terms of Correlation coefficient (R), Root mean square error (RMSE), Nash sutcliffe efficiency (NSE), Bias and Scatter index (SI). However, among the four models developed the ANN prediction outperformed the other three considered models with a higher $R = 0.9467$.

Keywords Relative wave run-up · ANN · ANFIS · GA-ANFIS · PSO-ANFIS

S. Kundapura (✉) · S. Rao · V. H. Arkal
Department of Applied Mechanics and Hydraulics, National Institute of Technology Karnataka, Surathkal, Mangaluru 575025, India
e-mail: sumankundapura@yahoo.com

© Springer Nature Singapore Pte Ltd. 2021

K. K. Pathak et al. (eds.), *Recent Trends in Civil Engineering*, Lecture Notes in Civil Engineering 77, https://doi.org/10.1007/978-981-15-5195-6_63

1 Introduction

Wave run-up level on breakwaters is defined as the maximum water-surface distance measured vertically from the still water level. Wave run-up is one of the most important physical process which is studied to design the crest level of semicircular breakwaters or as an indicator of possible overtopping or wave transmission. Run-up is important in fixing the crest elevation for non-overtopping condition. It mainly depends on the structure shape, roughness, porosity, depth of water at the structure toe, bottom slope in front of the structure, and incident wave characteristics (CEM, 2001). Run-up is an important factor to be considered for stability of structure as run-up level influences the inflow of water into the structure and the elevation of water level within the structure core, causing differential hydrostatic pressures.

As per the studies of Le Mehaute et al. [25] the relative run-up R_u/H was a function of slope of the structure (tan α), the relative depth $2\pi d/L$ or k_d, the wave steepness H/L, where α is the structure or beach slope, d is the depth of water, L is the incident wave length, and H is the incident wave height. His observations were that for a given H/L and d/L values, the R_u/H tended to increase as the slope decreased up to the point where the waves begin to break. The R_u/H of breaking waves decreased as the slope continued to decrease. For non-breaking waves, the R_u/H increased with the wave steepness. Whereas, for breaking waves, the relative run-up decreased with the increase in wave steepness. The findings of Sollitt and Debok [31] was that for a given wave period, T and steepness, shallow water produced more run up and also increased with the increase in wave steepness and wave period. Dhinakaran [10] compared the fully perforated SBW results with impermeable SBW results of Sri Krishna Priya et al. [30] and seaside perforated results of Dhinakaran et al. [11] to study the effect of perforation and influence of' water depth. Also, the influence of different rubble mound heights for a constant water depth $d = 0.54$ m, on hydrodynamic characteristics like reflection coefficient, transmission coefficient, and run-up were studied. They studied the variation of R_u/H_i with h_w/L for different percentage of perforations for $h_w/h_t = 0.6$, 0.7 and 0.8 for a constant $h_r/h_t = 0.18$ for regular waves. They found R_u/H_i decreased with the increase in h_w/L, reason being lesser period waves most of the energy is lost due to reflection and the R_u/H_i was found to decrease. The R_u/H_i was found to decrease with the increase in h_w/h_t; this shows the effect of curvature on run-up as larger structure area is exposed to the waves where energy is dissipated. Their study shows the influence of percentage perforations up to 17% on R_u/H_i, which decreased as there is transmission. Though the design of the crest involves the estimation of the run up in the laboratory in some instances, it was observed of the underestimation of wave run-up for rubble mound structures by the physical model tests [12, 32]. In practice, the exponential models are used for determining dimensionless 2% wave run-up ($R_{u2\%}/H_s$) of concrete armor units exposed to irregular waves [1]. Several studies have been carried out to find the wave run-ups for random seas [22, 24, 26]. Erdik et al. [13] predicted maximum wave runup on rubble mound structures by ANN. The author attempts to predict the $R_{u2\%}/H_s$ to determine the crest level of coastal structures. The relative run-up was

found to increase with the increase in *S*/*D* ratio for a seaside perforated SBW Hegde et al. [18]. The M5′ model tree prediction [5] of wave run-up on rock slopes using Van der Meer experimental data was found to be better than the Van der Meer and Stam formula, Kingston and Murphy [22] formula and Erdik et al. TS Fuzzy method [13].

Although the physical model usage cannot be completely ruled out the application of several soft computing tools either individual or hybrid for the prediction of breakwater parameters has been carried out in the past [3, 7, 9, 13–15, 17, 20, 23, 27, 33–36]. The AI integration into coastal modeling can be seen in the review of Chau [8]. ANFIS has been widely used in prediction problems in coastal engineering. ANFIS outperformed ANN models in predicting wave transmission (K_t) for a horizontally interlaced multilayer moored floating pipe breakwater [29]. ANFIS outperformed ANN models in predicting K_r for a quarter circular breakwater [29]. Zanaganeh et al. [35] developed a GA-ANFIS hybrid model predicted the significant wave height and the peak spectral period in Lake Michigan better than ANFIS models and SPM method.

Over the past decades, researchers have predicted the performance of various types of breakwaters using the soft computing techniques. However, there is a lack of research on the relative wave run-up parameter studies on caissons like semicircular breakwaters. Hence, the objective of this paper is the estimation of relative wave run-up parameter of semicircular breakwaters using different soft computing techniques like ANN, ANFIS, GA-ANFIS, and PSO-ANFIS. A conventional method of data segregation of 70:30 is applied to the entire randomized dataset. The robustness of the model is assessed by the error metrics like the correlation coefficient, root mean squared error, Nash Sutcliffe efficiency, bias, and scatter index.

2 Soft Computing Models

2.1 Employment of ANN, ANFIS, and PSO-ANFIS Model

In ANN a Feed Forward Back Propagation Neural Network (FFBPNN) with a single hidden layer is used for training the input-output data sets using Levenberg-Marquardt algorithm with transfer functions like ‘tansig’ (hidden layer) and ‘purelin’ (output layer). The neurons in this hidden layer is found by trial and error. The best architecture is thus chosen.

Further, the application of ANFIS model using the Fuzzy c-means clustering [4] has been employed in the current study. The rule-based learning happens here after the inputs are converted into fuzzy membership functions to arrive at output [2]. Application of two optimization techniques is carried out in the present study, i.e., Particle swarm optimization (PSO) and Genetic algorithm (GA) [6]. Particle swarm optimization a metaheuristic method [21] which uses the swarm intelligence to arrive at optimal solution. Here the PSO has been combined with ANFIS to reduce

the RMSE of the prediction. The detailed working of the ANN, ANFIS, PSO-ANFIS can be seen in my previous publication. The details of PSO variants is found in work of Imran et al. [19].

2.2 Genetic Algorithm

Genetic algorithm (GA) is heuristic inspired by Charles Darwin's theory of natural evolution. In GA, by the natural selection, the fittest individuals are selected from a population for reproduction to produce the offspring of the next generation. So fittest parents produce better offspring, and hence the chances of surviving are better. Three main phases involved in genetic algorithm are:

Selection. Initially, a set of individuals which is called a population (data variables) is chosen from the entire dataset. Each individual is a solution to the problem to be solved. A fitness function determines how fit an individual is and gives a fitness score to each individual. Selection of a pair of individual (chromosomes) with highest fitness scores is done to pass on their genes to the next generation. Among the several existing operators, to choose the best individuals for the next generation, the roulette wheel selection method has been employed in the current study. Followed by the most significant phase, is the crossover in genetic algorithm.

Crossover. Crossover in genetic algorithm combines the genes of two parents to form new offspring for the next generation. This could be done by single point crossover, two point crossover or k point crossover method. Here a single point crossover is employed in which a point is randomly picked on both parents' chromosomes and designated as a 'crossover point.' The bits to the right of the crossover point are swapped between the two parent chromosomes resulting in two offspring's. Each carries some genetic information from parents and is further added to the new population.

Mutation. In some of these new offspring formed, their genes can be subjected to a mutation with a low random probability. To prevent premature convergence and to maintain diversity within the population, the mutation will occur. If the population has converged, then, the algorithm terminates wherein; any further produced offspring is not significantly different from the previous generation. Thus the GA provides a set of solutions to the given problem.

Hybrid GA-ANFIS model The fuzzy c-means clustering parameters on which the fuzzy rules of ANFIS depends are determined by trial and error. To arrive at the optimal values is attempted by employing genetic algorithm (GA). In GA-ANFIS model, the clustering parameters are optimized using GA and ANFIS is called within the GA for the fitness value evaluation of every possible candidate solution generated by GA. The objective function of the genetic algorithm as in Eq. 1, is to reduce the RMSE of the ANFIS model prediction of resulting final FIS whose rules are controlled by FCM. Here the parameters of an FIS designed for mapping input values to targets are optimized by GA-ANFIS model, thus reducing training prediction error. Stopping criteria being either the set maximum number of iterations reached

or minimum improvement between two consecutive iterations not exceeding 0.01. Further, with the optimized trained model, the testing is done. The methodology of GA-ANFIS is shown in Fig. 1 [16].

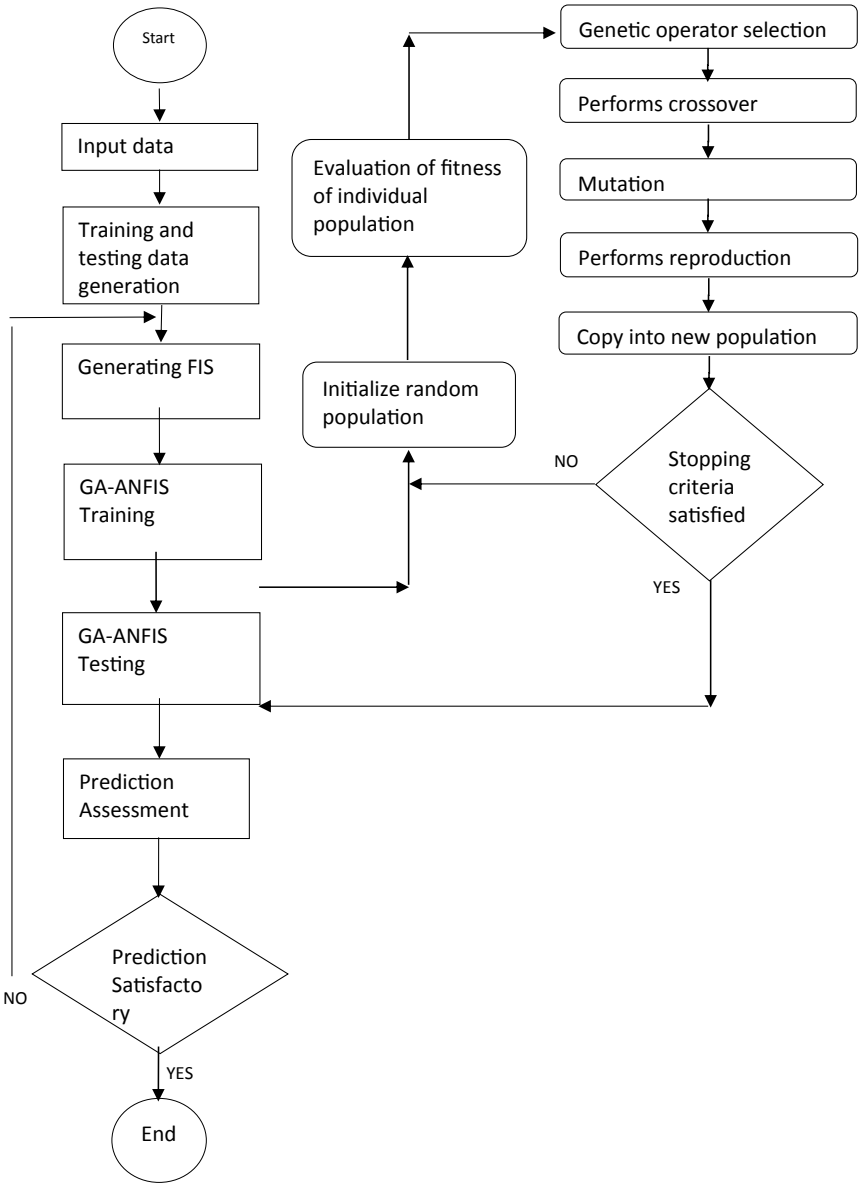

Fig. 1 GA-ANFIS model

$$\text{MinRMSE}_{\text{train}} = \sqrt{\frac{1}{N}\sum_{i=1}^{N}(O_i - P_i)^2} \tag{1}$$

3 Results and Discussion

In the current study the prediction of relative wave run-up parameter is done for non-dimensional input parameters, i.e., H_i/gT^2, d/gT^2, S/D, h_s/d and R/H_i obtained from dimensional analysis using Buckingham's π-theorem. The data segregation was done as 70% for training and 30% for testing respectively, and the corresponding prediction is undertaken. The prediction of relative wave run-up parameter by using ANN, ANFIS, GA-ANFIS, and PSO-ANFIS was carried out successfully. The ANN with a single hidden layer consisting of 7 neurons in it predicted the R_u/H_i very well with higher $R = 0.9467$, with least RMSE = 0.0874, higher NSE = 0.8694, SI = 20.41 whereas there is a positive bias of 0.0343. The ANFIS model predicted R_u/H_i did not improve the ANN model results hence needed further improvement. Two hybrid models were developed i.e. GA-ANFIS and PSO-ANFIS. The optimization techniques GA and PSO were individually clubbed to ANFIS and prediction were compared. The optimal parameters for each algorithm used in the study is tabulated in Table 1. The performance of each model is presented in Table 2, and it is found that GA

Table 1 Optimal parameters of different models

Model	Parameters	Values
ANN	Number of neurons	7
	Epochs	50
ANFIS	Partition matrix	2
	Minimum improvement factor	0.001
	Maximum iterations	25
	Number of clusters	9
GA-ANFIS	Population size	30
	Number of generations	7000
	Crossover rate	0.7
	Mutation rate	0.4
	Selection pressure	8
PSO-ANFIS	Number of iterations	1000
	Number of Particles	80
	Inertia weight	0.4
	Cognitive acceleration C_1	2
	Social acceleration C_2	2

Table 2 Relative wave runup parameter prediction performance of different soft computing models for 750 data points

Input form	Error metrics	Soft computing models							
		ANN		ANFIS (FUZZY C-MEANS CLUSTERING)		GA-ANFIS		PSO-ANFIS	
		Train	Test	Train	Test	Train	Test	Train	Test
Non-dimensional	R	0.9662	0.9467	0.9227	0.9026	0.9718	0.9149	0.9249	0.9107
	RMSE	0.0652	0.0874	0.0975	0.1162	0.0595	0.1032	0.0961	0.1336
	NSE	0.9334	0.8694	0.8513	0.7690	0.9444	0.8178	0.8555	0.6950
	SI	12.94	20.41	19.34	27.15	11.82	24.12	19.07	31.20
	BIAS	0.0013	0.0343	-2.167E-09	0.0495	0.0293	-0.0002	0.0002	0.0827

and PSO improved the ANFIS model result. However the hybrid methods consumed time when the population size and number of iterations were increased. The Fig. 2 shows the scatter plot of predicted versus actual values of relative wave run-up parameter for individual model. And Fig. 3 shows the comparison of best prediction of each employed model in the prediction of relative wave run-up parameter (R_u/H_i) with actual values.

From the Table 2, as seen the NSE of GA-ANFIS model being 81% was higher compared to ANFIS and PSO-ANFIS models with a very small underestimation of values being negatively biased. Also, the $R = 0.9149$ of GA-ANFIS was better than the ANFIS and PSO-ANFIS models. The scatter index of GA-ANFIS being 24.12 was better than 27.15 (ANFIS) and 31.20 (PSO-ANFIS). Hence the application of GA to ANFIS improved the training of the ANFIS model and hence a better prediction was possible, reducing the root mean square error. However, among the four models employed the ANN model best predicted the R_u/H_i value.

4 Conclusions

The estimation of relative wave run-up parameter (R_u/H_i) is vital for the design of the crest of the breakwater. An approach to predict the relative wave run-up parameter (R_u/H_i) on emerged semicircular breakwater has been carried out in the present study. The study presents four different soft computing models, i.e., ANN, ANFIS, GA-ANFIS, and PSO-ANFIS, for estimating the R_u/H_i parameter for non-dimensional input parameters. It is found that GA-ANFIS with $R = 0.9149$ has slightly improved the prediction of ANFIS model with $R = 0.9026$ however, ANN predictions outperformed the other three models with the $R = 0.9467$.

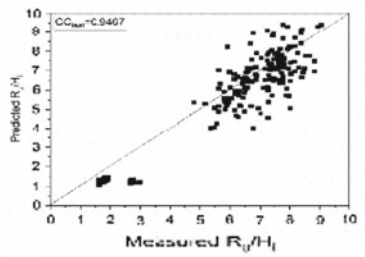

(a) ANN Model

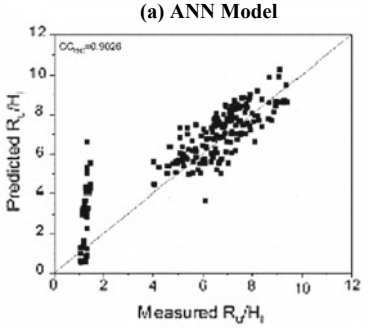

(b) ANFIS Model

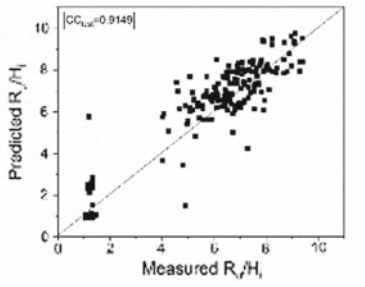

(c) GA -ANFIS model

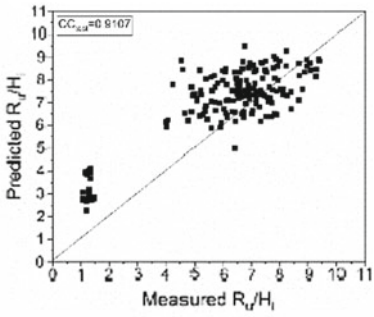

(d) PSO -ANFIS model

Fig. 2 Scatter plot of predicted versus actual values of relative wave run-up parameter for different models

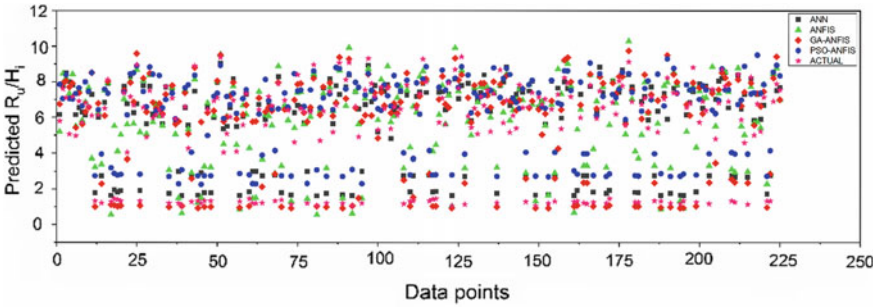

Fig. 3 Comparison of R_u/H_i prediction performance of ANN, ANFIS, GA-ANFIS, PSO-ANFIS models

Acknowledgments The authors are grateful to the Director, National Institute of Technology Karnataka, Surathkal, India, for the support and encouragement provided by them and for the permission to publish.

Appendix

R_u/H_i	Relative wave runup parameter
H_i/gT^2	Incident wave steepness parameter
d/gT^2	Depth parameter
S/D	Ratio of spacing to diameter of perforations
R/H_i	Relative caisson radius
h_s/d	Relative structure height

References

1. Allsop NWH, Hettiarachchi SSL (1988) Reflections form coastal structures. Proceedings of 21st Conference on Coastal Engineering Malaga ASCE New York
2. Azamathulla HM, Ghani AA (2011) ANFIS-based approach for predicting the scour depth at culvert outlets. J Pipeline Syst Eng Pract 2(1):35–40. https://doi.org/10.1061/(ASCE)PS.1949-1204.0000066
3. Balas CE, Koç ML, Tür R (2010) Artificial neural networks based on principal component analysis, fuzzy systems and fuzzy neural networks for preliminary design of rubble mound breakwaters. Appl Ocean Res 32(4):425–433
4. Bezdek JC (1981) Pattern recognition with fuzzy objective function algorithms. Advanced applications in pattern recognition ISBN 0-306-40671-3 New York NY: Kluwer Academic Publishers

5. Bonakdar L, Etemad-Shahidi A (2010) Predicting wave run-up on rubble-mound structures using M5 model tree. Ocean Engg. https://doi.org/10.1016/j.oceaneng.2010.09.015
6. Castillo O, Rubio E, Soria J, Naredo E (2012) Optimization of the fuzzy c-means algorithm using evolutionary methods. Eng Lett 20(1):61–67
7. Castro A, Pinto FT, Iglesias G (2011) Artificial intelligence applied to plane wave reflection at submerged breakwaters. J Hydraul Res 49(4):465–472. https://doi.org/10.1080/00221686.2011.568197
8. Chau K (2006) A review on the integration of artificial intelligence into coastal modeling. 80:47–57
9. Deo MC (2010) Artificial neural networks in coastal and ocean engineering. 39:589–596
10. Dhinakaran G, Sundar V, Sundaravadivelu R, Graw KU (2002) Dynamic pressures and forces exerted on impermeable and seaside perforated semicircular breakwaters due to regular waves. Ocean Eng 29(15):1981–2004
11. Dhinakaran G, (2012) Hydrodynamic characteristics of Semicircular breakwaters. Advances in environmental research (17)
12. Van de Walle B, De Rouck J, Troch P, Geeraerts J, Frigaard P (2005) Wave run-up on rubble breakwaters: Spectral effects. Proc Inst Civ Eng Marit Eng 158:59–67
13. Erdik T, Savci ME, Şen Z (2009) Artificial neural networks for predicting maximum wave runup on rubble mound structures. Expert Syst Appl 36(3):6403–6408
14. Garrido JM, Medina JR (2012) New neural network derived empirical formulas for estimating wave reflection on Jarlan-type breakwaters. Coast Eng 62:9–18. https://doi.org/10.1016/j.coastal.eng.2011.12.003
15. Goyal R, Singh K, Hegde AV (2014) Quarter circular breakwater: prediction and artificial neural network. Mar Technol Soc J 48(February):1–7
16. Habibi E, Salehi M, Yadegarfar G, Taheri A, (2018) Optimization of the ANFIS using a genetic algorithm for physical work rate classification, Int J Occup Saf Ergon 0(0): 1–8
17. Harish N, Mandal S, Rao S, Patil SG (2015) Particle swarm optimization based support vector machine for damage level prediction of non-reshaped berm breakwater. Appl Soft Comput 27:313–321
18. Hegde AV, Ganesh C, Kumar V (2010) Hydrodynamic performance characteristics of semicircular breakwater wave run-up and run-down. ISH J Hydraul Eng. 16(Supp 1)
19. Imran M, Hashim R, Khalid NEA (2013) An overview of particle swarm optimization variants. Procedia Eng 53(1):491–496. https://doi.org/10.1016/j.proeng.2013.02.063
20. Jabbari E, Talebi O (2011) Using Artificial Neural Networks for estimation of scour at the head of vertical wall breakwater. J Coast Res 64:521–526
21. Kennedy J, Eberhart R (1995) Particle Swarm Optimization. Proceedings of the IEEE International Conference on Neural Networks 4:1942–1948
22. Kingston K, Murphy J, (1996) Thematic report: wave runup/ rundown. MAST II Report
23. Kuntoji G, Rao M, Rao S (2018) Prediction of wave transmission over the submerged reef of tandem breakwater using PSO-SVM and PSO-ANN techniques. ISH J Hydraul Eng. https://doi.org/10.1080/09715010.2018.1482796
24. Losada MA, Curto GLA (1981) Flow characteristics on rough permeable slopes under wave action. Coastal Eng 4:187–206
25. Mehaute LB, Koh RC, Hwang LS, (1968) Synthesis on wave runup. J.W.W.H. Proc ASCE 94(WW1):77–92
26. Mase H, Kosho K, Nagahashi S (2001) Wave runup of random waves on a small circular pier on sloping seabed. J WATERW PORT C-ASCE 127(4):192–199
27. Patil SG, Mandal S, Hegde AV, Alavandar S (2011) Neuro-fuzzy based approach for wave transmission prediction of horizontally interlaced multilayer moored floating pipe breakwater. Ocean Eng. Elsevier 38(1):186–196
28. Patil SG, Mandal S, Hegde AV (2012) Genetic algorithm based support vector machine regression in predicting wave transmission of horizontally interlaced multi-layer moored floating pipe breakwater. Adv Eng Softw, Elsevier Ltd 45(1):203–212

29. Raju B, Hegde AV, Chandrashekar O (2015) Computational intelligence on hydrodynamic performance characteristics of emerged perforated quarter circle breakwater. Procedia Eng Elsevier B.V. 116(1):118–124
30. Sri Krishna Priya M, Roopsekhar K A, Sundar V, Sundaravadivelu R, Graw K U, Susanne K (2000) Hydrodynamic pressures on semicircular breakwaters. In: Proceedings of the 4th international conference on hydroscience and engineering, Seoul, South Korea
31. Sollitt CK, Debok DH (1976) Large scale model tests of placed stone breakwaters. In: Proceedings of 15th Conference on Coastal Engineering, Honolulu, Hawaii, vol 3. ASCE, New York, pp 2572–2588
32. Van de Walle BJ (2003) Wave Run-up on Rubble Mound Breakwaters. Ph.D. thesis, University of Gent
33. Yagci O, Mercan DE, Cigizoglu HK, Kabdasli MS (2005) Artificial intelligence methods in breakwater damage ratio estimation. Ocean Eng 32(17–18):2088–2106
34. Zanaganeh M, Mousavi SJ, Farshad A, Shahidi E (2009) Engineering applications of artificial intelligence a hybrid genetic algorithm—adaptive network-based fuzzy inference system in prediction of wave parameters. Eng Appl Artif Intell 22(8):1194–1202. Elsevier. https://doi.org/10.1016/j.engappai.2009.04.009
35. Zanuttigh B, Mizar S, Briganti R (2013) A neural network for the prediction of wave reflection from coastal and harbor structures. Coast Eng 80:49–67
36. Zahmatkesh I, Soleimani B, Kadkhodaie A, Golalzadeh A (2017) Journal of petroleum science and engineering estimation of DSI log parameters from conventional well log data using a hybrid particle swarm optimization—adaptive neuro-fuzzy inference system. J Pet Sci Eng 157:842–859. https://doi.org/10.1016/j.petrol.2017.08.002

Study of Pavement Unevenness Using Sensor-Based Smartphone Software

Mandeep Kaur Arora, Mahesh Ram Patel, and Abhyuday Titiksh

Abstract Pavement surface monitoring has been a challenging activity historically in transport infrastructure management. Many researches have proposed a solution to check and control the pavement profile automatically. Mostly heavy sensors are employed in vehicles, like bump integrator or other class-1 profilers, resulting in an expensive measure. In developing countries detection of pavement irregularities also focuses on use of Merlin Cycle. This paper is based on monitoring a specific road surface using Merlin Cycle and Android-based smartphone mounted on a motor vehicle, that is, bike at a varying condition of speed and type of bike used. The overall architecture consists of the integration of a smartphone application (ROADROID), a georeferenced database system, a visualization front-end (MS EXCEL) and a regression analysis software (SPSS, i.e. Statistical Package for Social Sciences). Pavement quality is summarized through roughness parameters (i.e. estimated international roughness index (EIRI) and calculated international roughness index (CIRI)) computed using in-built accelerometer and global positioning system (GSM) technique on mobile devices. The roughness values captured were wholly transmitted in a back-end geographic information system that gave the value of road condition in terms of international roughness index (IRI). Then comparison of the two values obtained from two sources, that is, Merlin Cycle and smartphone application was done, and a correlation and regression analysis was also done using SPSS software.

Keywords Smartphone application · Software · IRI · Merlin · Motor bike · Correlation and regression

M. K. Arora (✉) · M. R. Patel
Shri Shankaracharya Group of Institution, Bhilai, Chhattisgarh 490020, India
e-mail: mandeepsoniarora@gmail.com

M. R. Patel
e-mail: mahesh.mrp999@gmail.com

A. Titiksh
Visvesvaraya National Institute of Technology, Nagpur, Maharashtra 440010, India
e-mail: abhyuday.t@ssgi.edu.in

© Springer Nature Singapore Pte Ltd. 2021

K. K. Pathak et al. (eds.), *Recent Trends in Civil Engineering*, Lecture Notes in Civil Engineering 77, https://doi.org/10.1007/978-981-15-5195-6_64

1 Introduction

Developing countries like India have shown an enormous increase in its road network since last century. According to the data of Annual Report 2015, around 100,000 km of roads has been built in last 15 years in India. As soon as the new roads have been developing, there is a major challenge of maintaining the old roads. Moreover, the freshly laid roads are also getting patches of holes in it because of uncertain climate change, use of less durable building materials and cheap technologies for construction.

Potholes have been provably responsible for causing serious hazards and also lead to vehicular damage. Such damaged roads also lead to lowering of highest possible traffic speed causing more congestion, higher fuel consumption, and finally causing pollution. Some tests have concluded that the alteration in road roughness parameter and the fluctuating speed of the vehicle can significantly decrease heartbeat of the driver which impact driver's response significantly [1]. There is a need of characterizing roughness of the pavement profile so that a proper check of ride comfort as well as safety can be achieved.

IRI is a roughness measurement unit, represented as cumulative vertical distance travel in unit horizontal length. It stands for international roughness index, expressed in mm/km, or in./mi. It describes road roughness used for evaluation and management of road system. It is reproducible, stable, and applicable for every terrain. IRI measuring devices are categorized into following classes on the basis of its accuracy:

- Type 1 profiler—these give exact profile with high precision;
- Type 2 profiler—these are the non-biased type of profilers, e.g., Merlin;
- Type 3 profiler—these are the response-type devices with 80% accurate results, e.g., smartphone apps;
- Type 4 profiler—these are the least accurate profiler based on subjective ratings.

IRI is correlated with the following variables:

- Pavement characteristic (a statistical quantity)
- Vertical vibration (pavement quality)
- Tire load (safety and control ability) [2].

Historically, there has been various equipment and techniques for determining pavement quality. One of such equipment is a towed fifth wheel bump integrator that is very popular in developing countries like India. Its composition is same as quarter car model dynamically, where the spring system supports the upper part and the wheel helps to protect against unexpected excitations, but this is really a tedious and expensive technique and the instrument is too heavy to handle. Similarly, dipstick can be used for determining IRI and also for measuring road roughness, but cracks cannot be sensed through it. While Merlin Cycle works on the speed of a cycle towed by hand, so the data collection is again a time-taking phenomenon. Conclusion is that every profiler has its certain limitations.

One of the emerging technologies to find IRI is based on Android-based smartphone applications. Smartphones are the mobile applications equipped with the technologies like global positioning system (GPS), sensor, gyroscope, data collection and storing potentiality, image-capturing potentialities, and fast processability. These features enable it to be used as a pavement surface classification instrument. In this paper, the variation of the roughness value, that is, IRI value obtained using smartphone at a varying speed and vehicle type is being discussed and correlated. The standard value of IRI is obtained using standard profiler, that is Merlin equipment, and comparison is made.

2 Literature Review

Many research works have been done in pavement profiling since nineteenth century. Most of those techniques proved to be reliable in estimating unevenness. Some of the research works related to pavement profiling are summarized below.

2.1 Literature Review on Profiling Parameters

Michael W. Sayers, Thomas D. Gillespie, and Cesar A. V. Queiroz (1986) characterized the pavement unevenness in a universal, consistent, and relevant manner and evaluated standard indices based on the geometric characteristics, road simulation, vehicular characteristics, and spectral analysis of the roughness recorder output. Response-type pavement unevenness measurement system based on vehicle simulation was used to calibrate profile [3].

Michael W. Sayers (1998) wrote a little book of profiling for understanding and determining road profile. In this book three basic questions were answered, that is, (1) How profilers are used? (2) How it helps? (3) How we can reduce errors? He described three basic parameters of a profiler, that is, a certain elevation, a height with respect to that elevation, and a horizontal length, where rod and level were defined as static profiler and dipstick as a dynamic profiler. He proposed the use of power spectral density (PSD) function as a high-speed profiling system, which is based on the classification of voltage, and applied the same mathematical function for profile measurement. He also elaborated that longitudinal acceleration and vertical vibration experienced by the rider while moving in a high seat vehicle like truck is higher than that experienced by the rider of a passenger car due to road roughness leading to a situation of discomfort.

Peter Mucka and Johan Granlund (2012) dealt with estimating the effect of the contents of the wavelength on IRI. It was found that the IRI corresponding to a velocity of 20 kmph is twice sensitive to velocity of 80 kmph for a local obstacle [4].

Peter Mucka (2016) proposed velocity-related IRI limit curves. He observed the large range of RMS values on the basis of vibrational response corresponding to an IRI value and quantified comfort level and safety of the ride along with the dynamic pressure [5].

2.2 Literature Review on Different Profiling Techniques

M. A. Cundill (1991) devised a simple low-cost pavement roughness data measuring machine, that is, MERLIN, which stands for a machine for evaluating roughness using low-cost instrumentation. This device has been well correlated with the pavement roughness data measuring machine known as bump integrator. Also the roughness output obtained is correlated to get the roughness value in terms of IRI (m/km).

Oldrich Kropac and Peter Mucka (2009) proposed an indicator defining about the pavement unevenness on the basis of the response of the vehicle on vertical vibration caused by the waviness of the pavement profile. Also they proposed modified IRI values which are affected by speed, and assessment of subjective rating methods [6].

Manish Paul and Rumi Sutradhar (2014) derived a generalized equation to get the values of IRI using bump integrator at any speed corresponding to 32 kmph speed by using SPSS software [7].

$$(\mathrm{BI})_{32} = 0.956(\mathrm{BI})V + 0.842V - 25.544 \left(R^2 = 0.958\right) \quad (1)$$

Marwan Hafez, Khaled Ksaibati, and Richard Anderson-Sprecher (2016) used statistical technique and old PMS data and then developed uni-variable regression multiple accusation. It was concluded that by the use of historical data, a good estimation of pavement data can be obtained [8].

2.3 Literature Review on Smartphone-Based Profiling Technology

Kasun De Zoysa, Kasun Chamath, Keppitiyagama chamath (2007) designed a road surface observing system which worked on a sensor-based network Bus Net. Bus Net is an ideal approach to monitor data network using a public transport because public transport uses the road that we want to monitor and the most economical attempt for monitoring road condition [9].

Shahidul Islam, William G. Buttlar, Roberto G. Aldunate, and William R. Vavrik (2014) collected IRI values at two test sites using smartphone technology and validated those values with the help of values of standard inertial profiler. They found that in 37 out of 40 tests, values were within 15% of the standard results. A linear correlation can bring the close result which can be implemented, if required [10].

Trevor Hanson, Coady Cameron, and Eric Hildebrand (2014) calculated IRI values from different smartphones to compare the value of IRI by varying type of device, vehicular speed, type of vehicle, and also mounting arrangement with respect to a class-1 profiler.

They concluded that significant factor causing variation in IRI values are type of smartphone used, mounting arrangement, and type of vehicle [11].

Rajiv Kumar, Abhijit Mukherjee, and V.P. Singh (2016) performed crowd sourcing, that is, distributed smartphones to the people for gathering road roughness parameter; used a fuzzy system and characterized the roughness parameter; presented road surface condition on web mapping service platform by different patterns of surface classes; and the roads were monitored visually for justification of the smartphone technology [12].

3 Objective and Scope

It is already concluded above that the emerging smartphone technologies determine pavement profile in a very short time. So, the objective of this paper was to detect pavement unevenness of a certain test section using smartphone application and correlating the obtained IRI values with the most reliable value of IRI obtained using a standard equipment at the same section. The smartphone values were determined at a varying condition of speed and type of bike used to understand the variation in IRI values with the respective variations. The standard equipment used was a type-2 profiler, that is, Merlin Cycle.

4 Methodology

In this paper, before performing any experiment, some basic components of the experiment need to be understood well. Following are the basic requirements:

4.1 System Architecture

System of pavement roughness data analysis consists of the following parameters:

Smartphone: Smartphone embedded with Android OS > 5.0 is to be taken, so in this paper MOTO G^5 Android version 8.1.0 had been taken as a smartphone platform.

Smartphone Application: ROADROID mobile application as shown in Fig. 1 installed in smartphone with the following features in it:

- Analyze vehicle vibration in 100–200 Hz

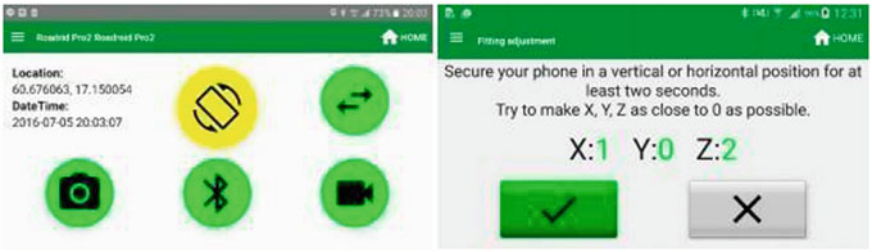

Fig. 1 ROADROID application installed in smartphone

- Calculate two IRI values, that is, calculated IRI (CIRI) and estimated IRI (EIRI) and GPS
- Sensitivity and segment length adjustment
- Degree of accuracy 80% of type-1 IRI measuring equipment
- ROADROID is a type-3 IRI measurement equipment, that is, a response-type survey system
- EIRI value is calculated from quarter car formula
- CIRI value uses a smothering filter, hence reported as the required IRI [13].

Vehicle: In this study, two motor bikes have been selected for performing experimental study. One of them is shown in Fig. 2 (Table 1).

Survey Speed: A constant speed needs to be maintained as the speed considerably affects the vertical vibration. In this paper, two speeds were maintained and values had been recorded in 25 and 30 kmph speed.

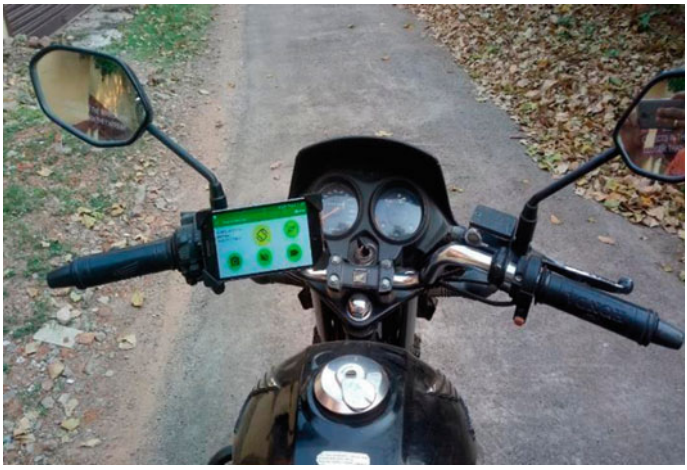

Fig. 2 Image of the smartphone mounted on bike

Table 1 Profile of test vehicle

S. no.	Vehicle type	Engine type	Chassis type	Front-suspension	Rear-suspension
(1)	Honda LIVO	110 cm^3	Diamond	Telescopic fork	Spring loaded hydraulic type
(2)	Honda CB Shine	125 cm^3	Diamond	Telescopic fork	Spring loaded hydraulic type

Test Section: Since Merlin equipment was available in NIT Raipur campus; therefore, a 400 m test section was taken from NIT Raipur campus, as shown in Fig. 3.

Software: Using SPSS software, data obtained from experimental results are represented graphically and a correlation between different observations is made. A snapshot is shown in Fig. 4 [14].

Mounting Arrangement: A stable mount is necessary to get an accurate profile and vertical vibrations.

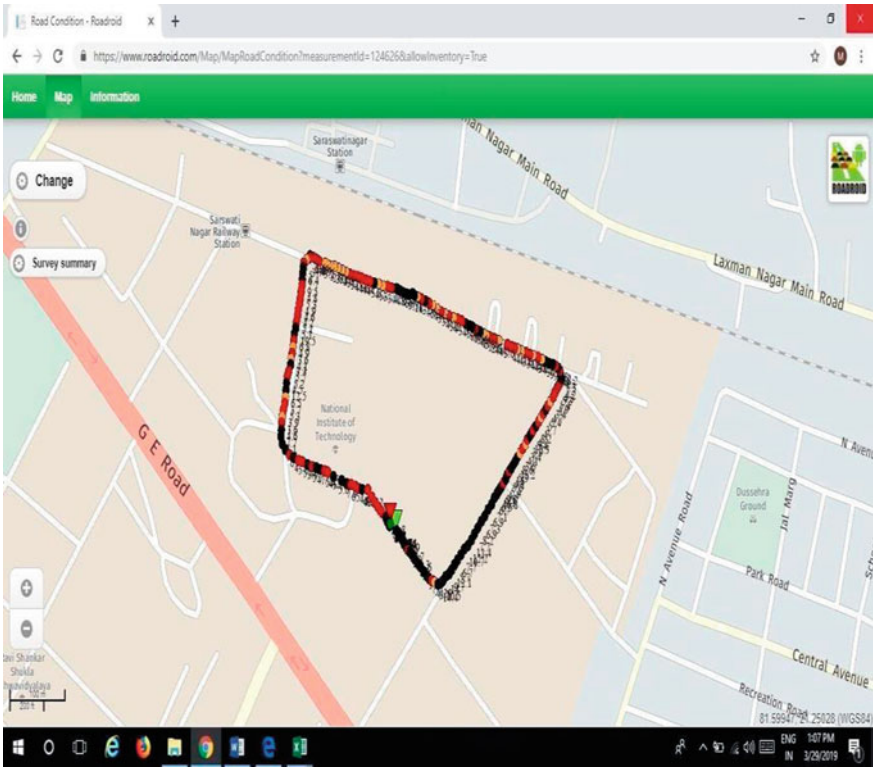

Fig. 3 Test section snapshot taken by using Google Map

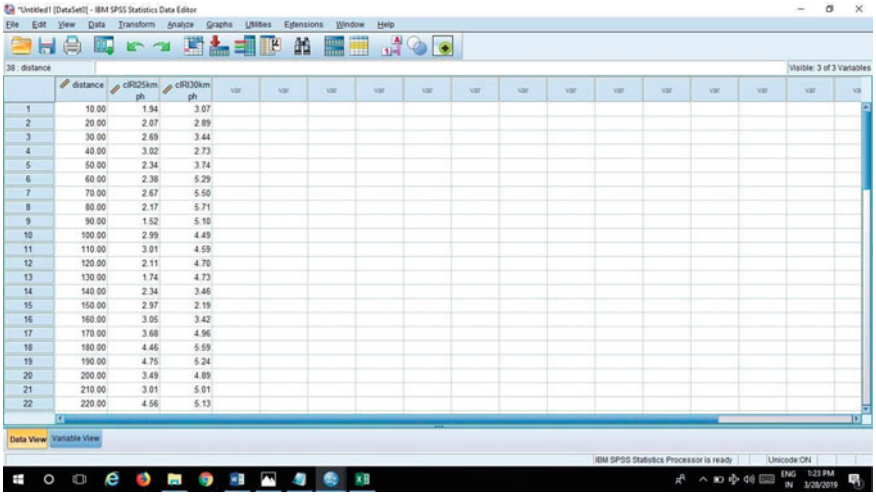

	distance	clRI25kmph	clRI30kmph
1	10.00	1.94	3.07
2	20.00	2.07	2.89
3	30.00	2.69	3.44
4	40.00	3.02	2.73
5	50.00	2.34	3.74
6	60.00	2.38	5.29
7	70.00	2.67	5.50
8	80.00	2.17	5.71
9	90.00	1.52	5.10
10	100.00	2.99	4.49
11	110.00	3.01	4.59
12	120.00	2.11	4.70
13	130.00	1.74	4.73
14	140.00	2.34	3.46
15	150.00	2.97	2.19
16	160.00	3.05	3.42
17	170.00	3.68	4.96
18	180.00	4.46	5.59
19	190.00	4.75	5.24
20	200.00	3.49	4.89
21	210.00	3.01	5.01
22	220.00	4.56	5.13

Fig. 4 Data view in SPSS software (snapshot)

Merlin Equipment: It is a class-2 profiler which gives accurate IRI value. MERLIN stands for machine for evaluating roughness using low-cost instrumentation. It consists of a graph paper in which displacements are plotted as a histogram. A working equipment has been shown in Fig. 5. In this equipment, the probe is connected to an arm such that it is moving close to the probe. To the next side of the arm, a pointer is attached such that 1 mm movement of the probe moves the pointer by 1 cm over the prepared data chart. The chart consists of column divided into 5 mm boxes [15].

Fig. 5 Merlin equipment while working (author Mandeep Kaur Arora along with co-author Mahesh Ram Patel recording data)

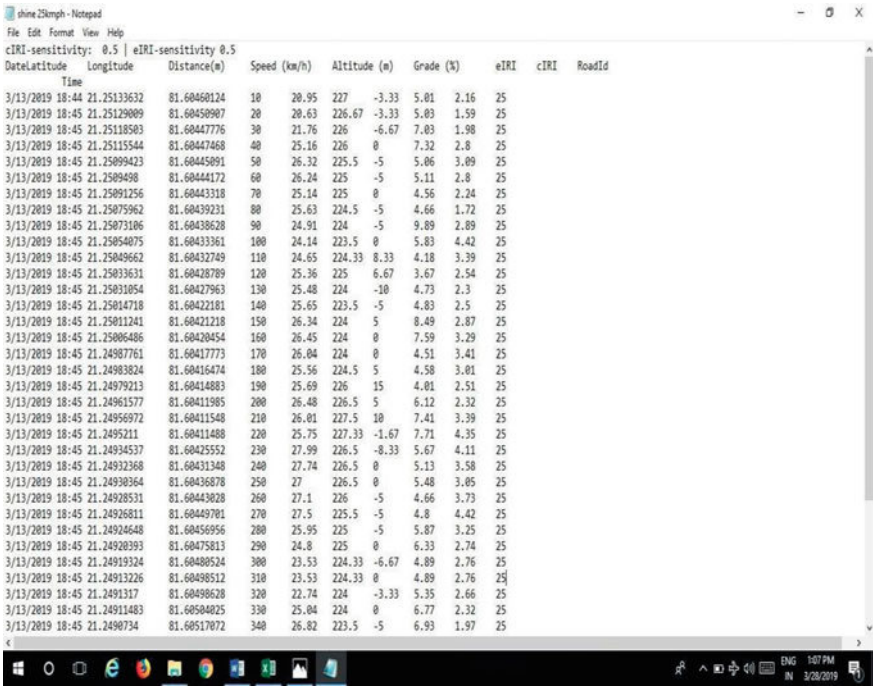

shine 25kmph - Notepad

File Edit Format View Help

cIRI-sensitivity: 0.5 | eIRI-sensitivity 0.5

DateLatitude Time	Longitude	Distance(m)	Speed (km/h)	Altitude (m)	Grade (%)		eIRI	cIRI	RoadId
3/13/2019 18:44	21.25133632	81.60460124	10	20.95	227	-3.33	5.01	2.16	25
3/13/2019 18:45	21.25129009	81.60450907	20	20.63	226.67	-3.33	5.03	1.59	25
3/13/2019 18:45	21.25118503	81.60447776	30	21.76	226	-6.67	7.03	1.98	25
3/13/2019 18:45	21.25115544	81.60447468	40	25.16	226	0	7.32	2.8	25
3/13/2019 18:45	21.25099423	81.60445091	50	26.32	225.5	-5	5.06	3.09	25
3/13/2019 18:45	21.2509498	81.60444172	60	26.24	225	-5	5.11	2.8	25
3/13/2019 18:45	21.25091256	81.60443318	70	25.14	225	0	4.56	2.24	25
3/13/2019 18:45	21.25075962	81.60439231	80	25.63	224.5	-5	4.66	1.72	25
3/13/2019 18:45	21.25073106	81.60438628	90	24.91	224	-5	9.89	2.89	25
3/13/2019 18:45	21.25054075	81.60433361	100	24.14	223.5	0	5.83	4.42	25
3/13/2019 18:45	21.25049662	81.60432749	110	24.65	224.33	8.33	4.18	3.39	25
3/13/2019 18:45	21.25033631	81.60428789	120	25.36	225	6.67	3.67	2.54	25
3/13/2019 18:45	21.25031054	81.60427963	130	25.48	224	-10	4.73	2.3	25
3/13/2019 18:45	21.25014718	81.60422181	140	25.65	223.5	-5	4.83	2.5	25
3/13/2019 18:45	21.25011241	81.60421218	150	26.34	224	5	8.49	2.87	25
3/13/2019 18:45	21.25006486	81.60420454	160	26.45	224	0	7.59	3.29	25
3/13/2019 18:45	21.24987761	81.60417773	170	26.04	224	0	4.51	3.41	25
3/13/2019 18:45	21.24983824	81.60416474	180	25.56	224.5	5	4.58	3.01	25
3/13/2019 18:45	21.24979213	81.60414883	190	25.69	226	15	4.01	2.51	25
3/13/2019 18:45	21.24961577	81.60411985	200	26.48	226.5	5	6.12	2.32	25
3/13/2019 18:45	21.24956972	81.60411548	210	26.01	227.5	10	7.41	3.39	25
3/13/2019 18:45	21.2495211	81.60411488	220	25.75	227.33	-1.67	7.71	4.35	25
3/13/2019 18:45	21.24934537	81.60425552	230	27.99	226.5	-8.33	5.67	4.11	25
3/13/2019 18:45	21.24932368	81.60431348	240	27.74	226.5	0	5.13	3.58	25
3/13/2019 18:45	21.24930364	81.60436878	250	27	226.5	0	5.48	3.05	25
3/13/2019 18:45	21.24928531	81.60443028	260	27.1	226	-5	4.66	3.73	25
3/13/2019 18:45	21.24926811	81.60449701	270	27.5	225.5	-5	4.8	4.42	25
3/13/2019 18:45	21.24924648	81.60456956	280	25.95	225	-5	5.87	3.25	25
3/13/2019 18:45	21.24920393	81.60475813	290	24.8	225	0	6.33	2.74	25
3/13/2019 18:45	21.24919324	81.60480524	300	23.53	224.33	-6.67	4.89	2.76	25
3/13/2019 18:45	21.24913226	81.60498512	310	23.53	224.33	0	4.89	2.76	25
3/13/2019 18:45	21.2491317	81.60498628	320	22.74	224	-3.33	5.35	2.66	25
3/13/2019 18:45	21.24911483	81.60504025	330	25.04	224	0	6.77	2.32	25
3/13/2019 18:45	21.2490734	81.60517072	340	26.82	223.5	-5	6.93	1.97	25

ENG IN 1:07 PM 3/28/2019

Fig. 6 A snapshot of downloaded aggregated file (obtained through smartphone application)

4.2 Data Collection

Using Smartphone App: This was the first step of pavement roughness measurement in this paper. As shown in Fig. 2, the smartphone, that is MOTO G[5], was stably mount in the handle of the bike. Such a fixing was done so that there was no self-movement of the smartphone. Bike was ridden at a constant speed and the recording of the values was carried out in smartphone app simultaneously. In this experiment two values of speed, that is 25 and 30 kmph, were taken for recording values. Recording was done in both of the bikes separately, one at a time. Specifications related to application, smartphone, and motor bike are already mentioned in the above section. Finally, the readings were uploaded from the application which was opened further by logging in ROADROID website for getting the readings in terms of IRI.

Using MERLIN Equipment: To measure roughness of road using MERLIN equipment, 200 observations were made. Each observation was taken by resting the machine on road when the wheel was in stable position and the probe, stabilizer, and back end foot in contact with the pavement. Then the pointer was recorded in the graph and a tally box with a cross-sign in the respective column is shown in Fig. 7, to keep an observation of the records. Then the handle was elevated such that the wheel

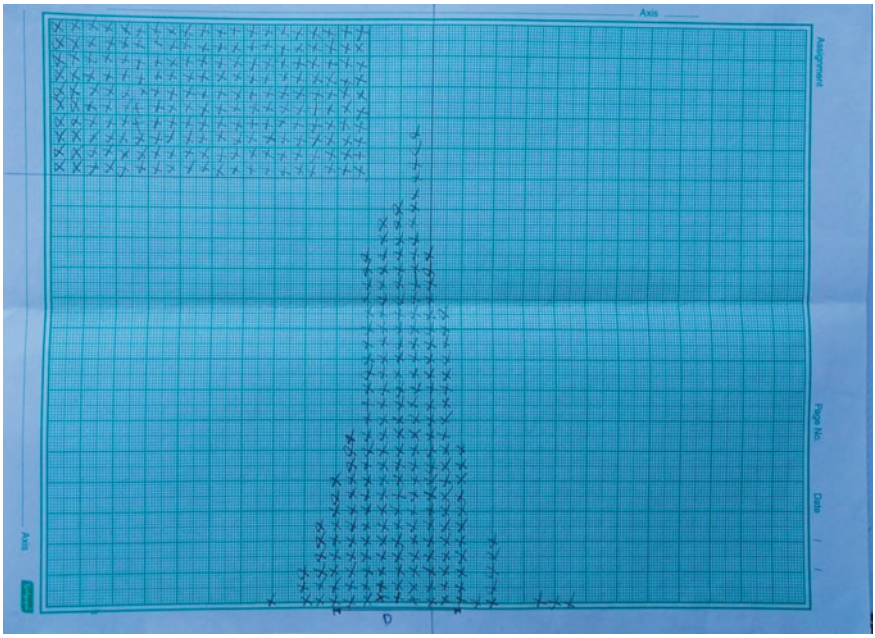

Fig. 7 Chart obtained from Merlin equipment

was only in contact with the pavement surface and then was taken ahead for the next normal position and the same procedure was repeated. After 200 observations were made, chart was removed from the MERLIN.

4.3 Data Analysis

Smartphone Data: The downloaded data are available in .txt format, as shown in Fig. 6. The readings corresponding to CIRI were exported to SPSS software and average IRI was calculated and also a graphical representation of the roughness was plotted as shown in Fig. 9. Further, there was also a correlation and regression analysis made between two values of IRI corresponding to 25 and 30 kmph speed, using SPSS software.

MERLIN Data: The chart obtained after the experiment was observed and the position from the both sides of the chart after 10th cross was marked. The distance between the two cross was measured in mm and calculated as D mm, that is, 45 mm in this experiment. This value was the roughness in terms of MERLIN scale. Then pavement unevenness in terms of IRI was obtained with the help of this relation

$$\text{IRI} = 0.593 + 0.0471D \tag{2}$$

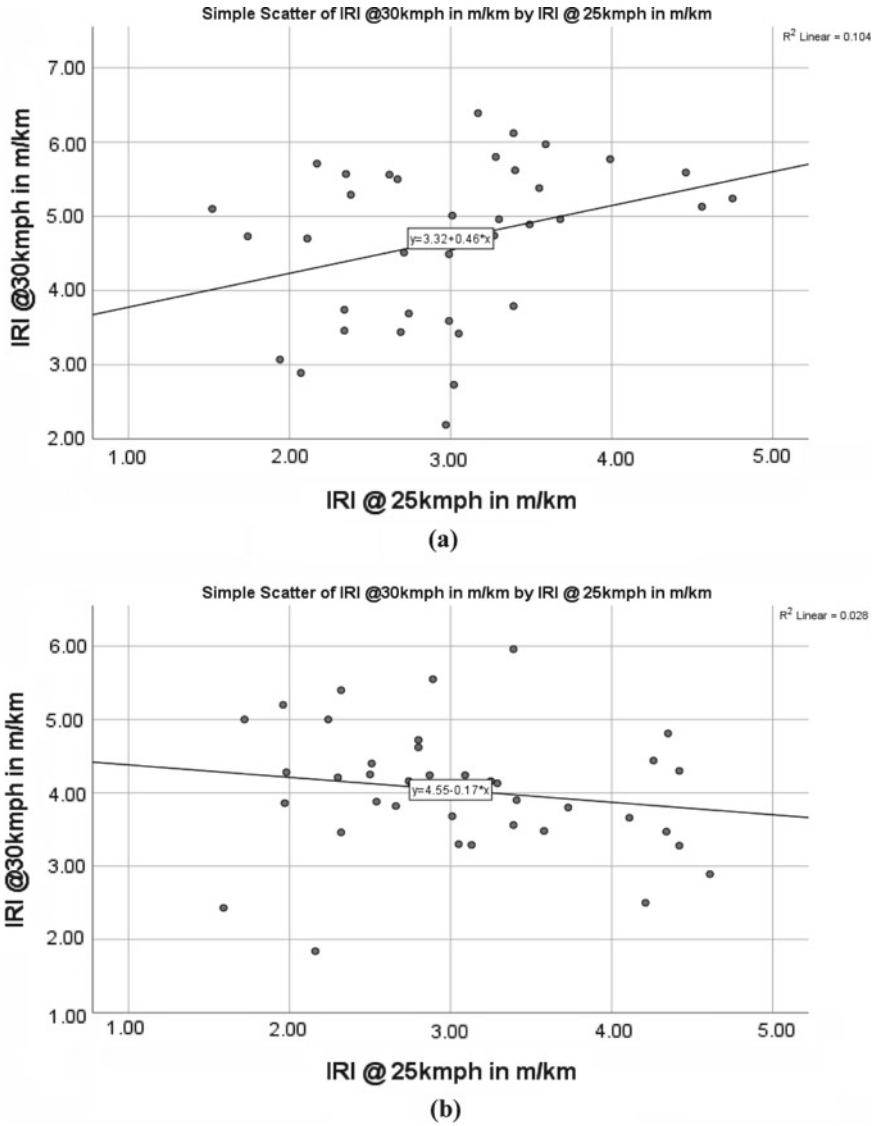

Fig. 8 **a** Correlation in IRI values in Honda LIVO. **b** Correlation in Honda CB Shine

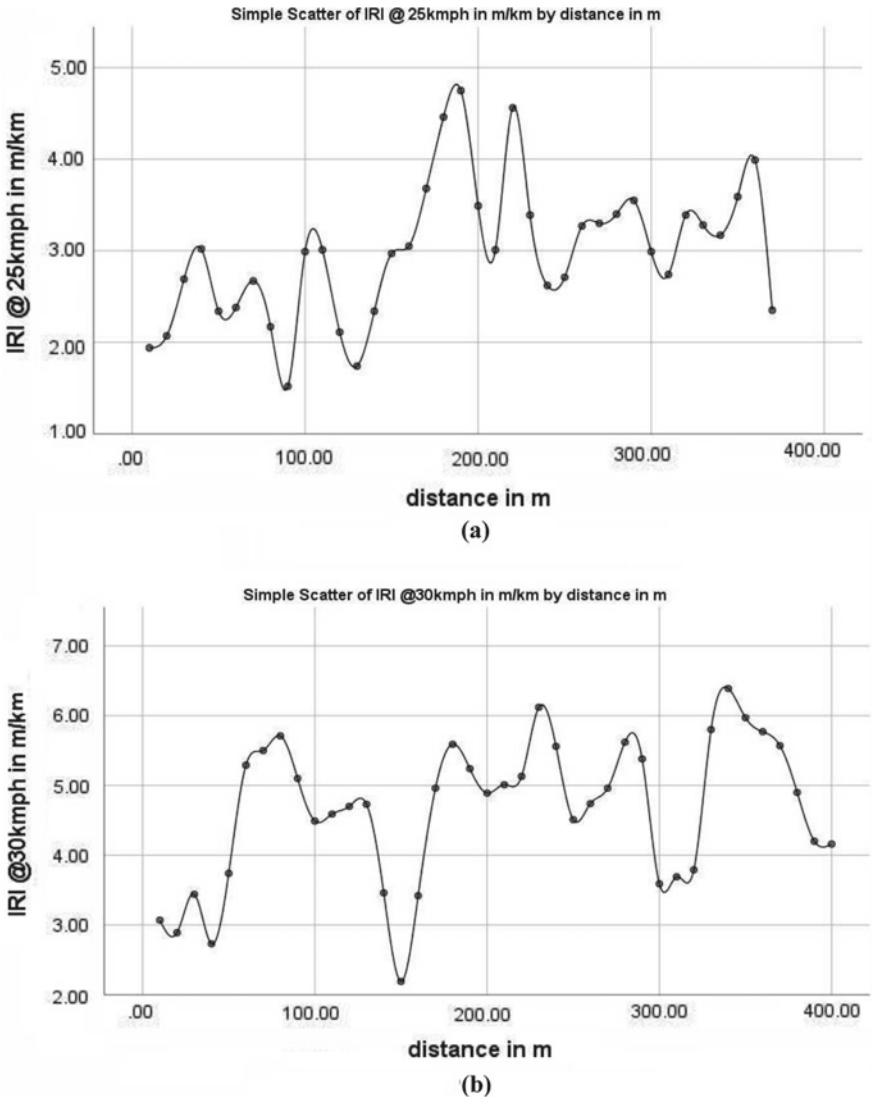

Fig. 9 **a** IRI versus distance @25 kmph speed in Honda LIVO. **b** IRI versus distance @30 kmph speed in Honda LIVO. **c** IRI versus distance @25 kmph speed in Honda CB Shine. **d** IRI versus distance @30 kmph in Honda CB Shine

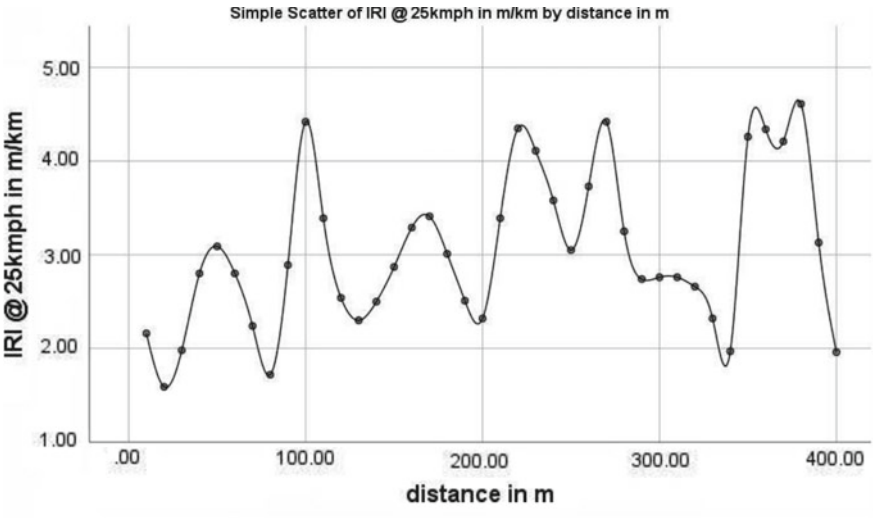

(c)

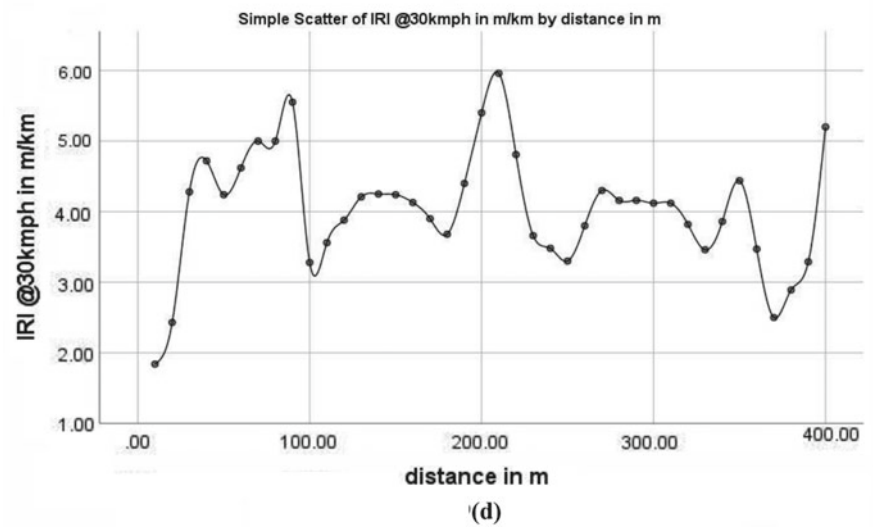

(d)

Fig. 9 (continued)

5 Flow Chart

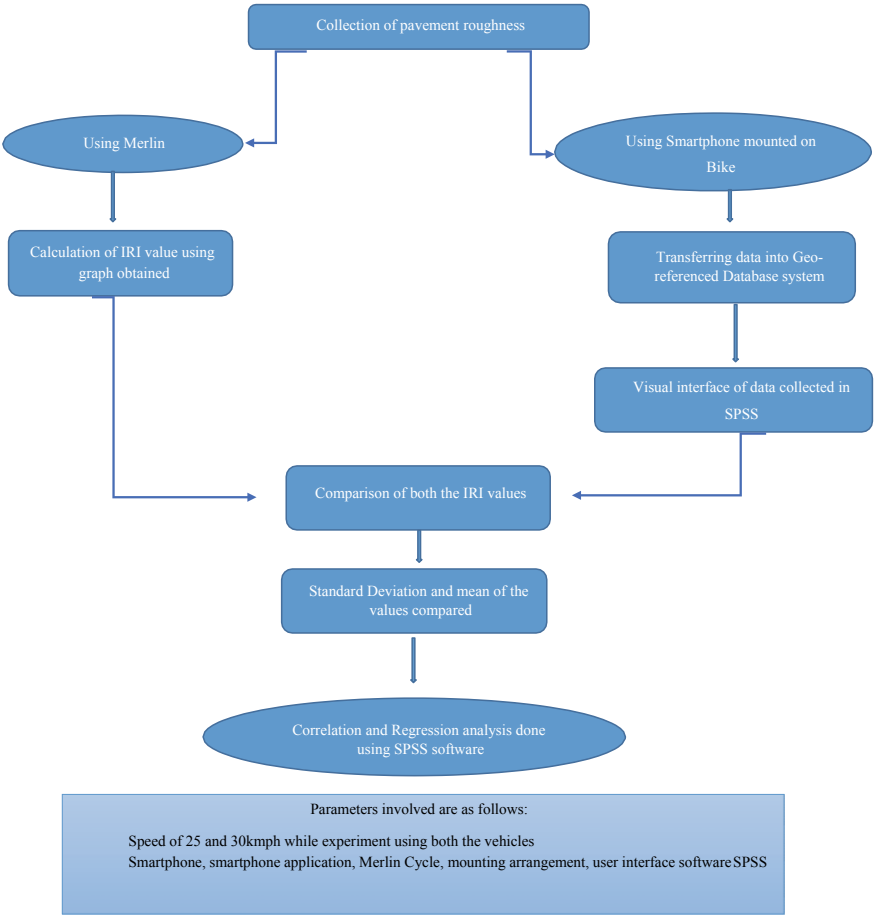

6 Results and Discussion

6.1 Merlin

The standard value of IRI obtained from Merlin equipment was 2.7125 m/km.

Table 2 Variation in IRI value by varying speed and vehicle type

S. no.	Device type	Vehicle type	Speed in km/h	Average IRI in m/km	Number of observations in 400 m length	% Difference from Profiler
(1)	Moto G[5]	Honda LIVO	25	2.9330	40	8.129
(2)	Moto G[5]	Honda LIVO	30	4.6647	40	71.970
(3)	Moto G[5]	Honda CB Shine	25	3.0032	40	10.717
(4)	Moto G[5]	Honda CB Shine	30	4.0352	40	48.763

6.2 Smartphone and Software

The test results demonstrate that there is a significant variation in average IRI value obtained when the speed is increased. Following are the results corresponding to both the bikes:

Honda LIVO: In this bike, the value of IRI obtained @25 kmph speed was 2.9330 m/km, which was close to the standard value, that is, within 10% of the standard value. However, the values @30 kmph speed was 4.6647 m/km, which was highly deviated from the standard IRI, that is, differ by 71.97% from standard IRI.

Honda CB Shine: In this bike, the value of IRI obtained @25 kmph speed was 3.0032 m/km, which was again close to the standard value, that is, within 10% of the standard value. However, the values @30 kmph speed was 4.0352 m/km, which was once again highly deviated from the standard IRI, that is, differ by 48.763% from standard IRI.

This can be seen that the variation in vehicle type does not significantly impact because the suspension type and chassis type are almost similar in both the cases. Only variation is in engine of the vehicle, which is not causing large variation in values (Table 2).

6.3 Correlation and Regression Analysis

Using SPSS software, there was a correlation and regression analysis established between IRI values obtained @25 kmph values with that of 30 kmph values, such that 25 kmph values were the independent variable x and 30 kmph values were dependent variable y. Positive value of correlation represented in Table 3 of Honda LIVO bike represents an increase in difference of IRI value with increase in speed.

Standard deviation is 0.986. The required relation is

Table 3 Correlation in IRI values @25 and 30 kmph speed obtained from Honda LIVO

		Correlations	
		IRI @30 kmph in m/km	IRI @25 kmph in m/km
Pearson correlation	IRI @30 kmph in m/km	1.000	0.322
	IRI @25 kmph in m/km	0.322	1.000
Sig. (1-tailed)	IRI @30 kmph in m/km	–	0.026
	IRI @25 kmph in m/km	0.26	–
N	IRI @30 kmph in m/km	37	37
	IRI @25 kmph in m/km	37	37

$$y = 3.32 + 0.46x \tag{3}$$

However, a negative correlation shown in Table 4 was found in Honda CB Shine values, which represents that on increasing value of speed in this bike, the difference in IRI value decreases. Standard deviation is 0.987. The required relation is

$$y = 4.55 - 0.17x \tag{4}$$

Figure 8 shows the correlation in both the vehicles. Figure 10 shows the histogram. Figure 11 shows the normal *P*–*P* plot of regression standardized residual.

Table 4 Correlation in IRI values @25 and 30 kmph speed obtained from Honda CB Shine

		Correlations	
		IRI @30 kmph in m/km	IRI @25 kmph in m/km
Pearson correlation	IRI @30 kmph in m/km	1.000	−0.167
	IRI @25 kmph in m/km	−0.167	1.000
Sig. (1-tailed)	IRI @30 kmph in m/km	–	0.151
	IRI @25 kmph in m/km	0.151	–
N	IRI @30 kmph in m/km	40	40
	IRI @25 kmph in m/km	40	40

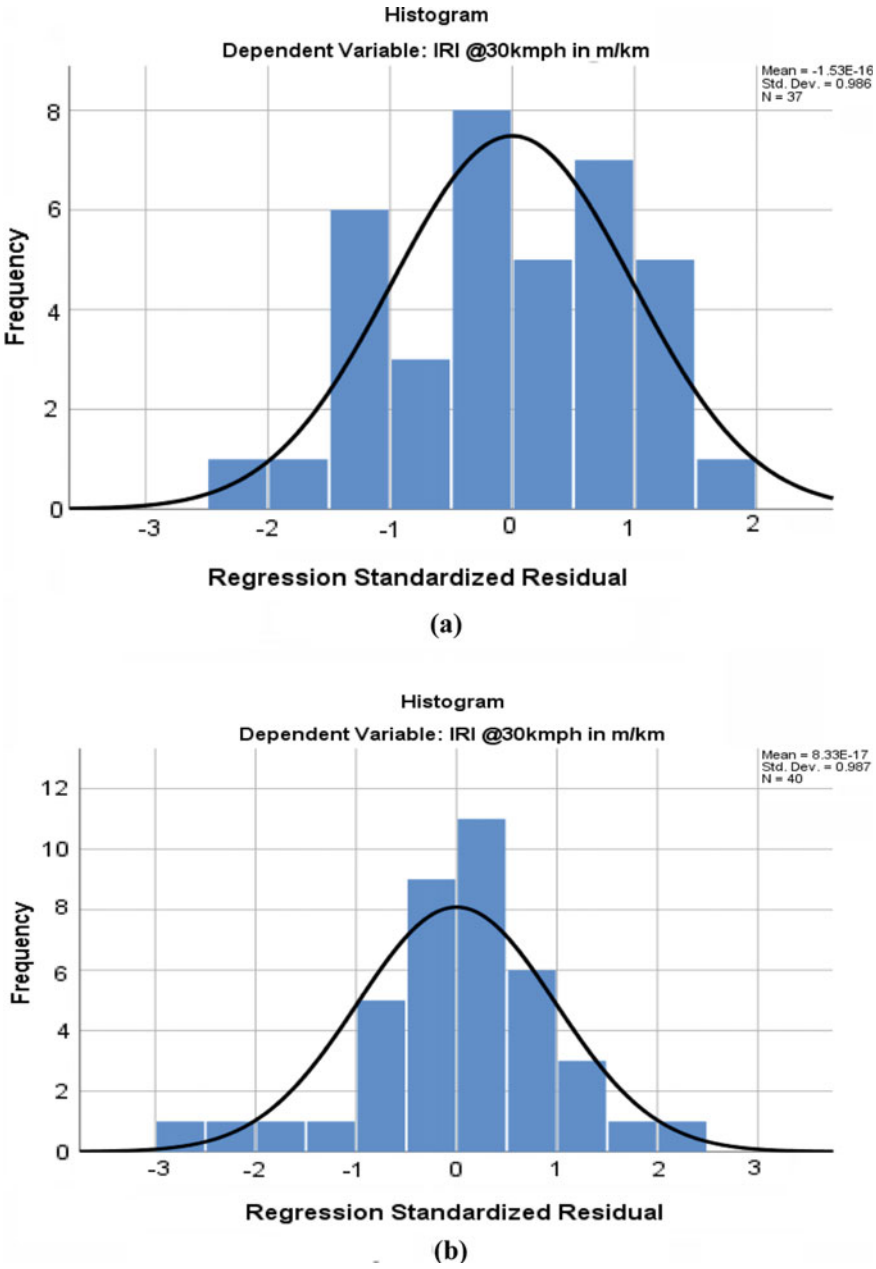

Fig. 10 **a** Histogram in Honda LIVO. **b** Histogram in Honda CB Shine

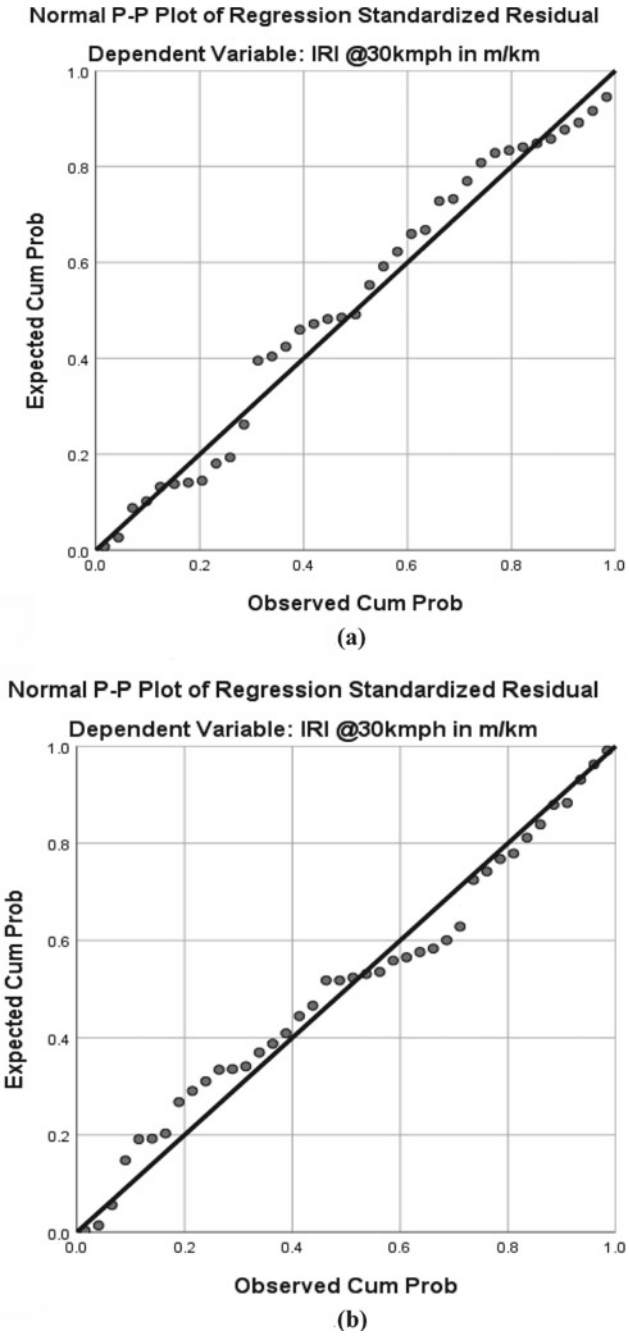

Fig. 11 **a** Normal *P–P* plot of regression standardized residual in Honda LIVO. **b** Normal *P–P* plot of regression standardized residual in Honda LIVO

7 Conclusion

This paper demonstrated the capability of a smartphone to measure pavement profile with the help of its in-built feature accelerometer. Use of a smartphone app, that is ROADROID, visual interface system, that is MS Excel, correlation and regression analysis software, that is SPSS, has enabled accelerometer feature of a smartphone to give a comparable pavement surface unevenness measurement. In this paper, two motor bikes, Honda CB Shine and Honda LIVO, were used with a suitable mount fixed in it to give a platform to smartphone, that is, Moto G^5 for measuring values of IRI in a 400 m stretch of road. The values were recorded at a varying speed of 25 and 30 kmph in both the motor bikes. For the validation of obtained results, a standard profiler, that is Merlin Equipment, was used to record the pavement unevenness value in terms of IRI. IRI value obtained through Merlin equipment was 2.7125 m/km. IRI value obtained through smartphone was within 10% of this value when measurement was made @25 kmph, whereas measurement made @30 kmph gave a significant difference in IRI value, that is about 48 and 72%, respectively, in both the vehicles. A comparison of these values yielded the following conclusion:

- It has been assured that the pavement profile is easily obtainable with the help of smartphone equipped accelerometer technique.
- Higher value of speed gives higher value of IRI, because of higher vertical vibration
- Varying motor vehicle of same kind does not significantly cause the variation in IRI, if the suspension system is not varying
- In Honda LIVO bike, with increase in speed, difference in IRI value also increases.
- However, in Honda CB Shine with increase in speed, difference in IRI value decreases.
- More accurate profile of pavement is obtained @25 kmph speed
- IRI value obtained @ 30 kmph speed in Honda LIVO can be approximated to IRI value of 25 kmph by using relation $y = 3.32 + 0.46x$
- IRI value obtained @ 30 kmph speed in Honda CB Shine can be approximated to IRI value of 25 kmph by using relation $y = 4.55 - 0.17x$
- IRI value obtained from smartphone app is generally higher than the standard equipment because of the engine vibration of vehicle.

Acknowledgments This study was supported by National Institute of Technology, Raipur. The author acknowledges the support of Dr. Sunny Deol G for providing Merlin equipment. The author would also like to thank Vikas Kumar Reddy, Ashish Rathore and Gaurav Pandey for their assistance in collecting experimental data. Finally, for the vote of thanks, the author refers to the viewers for their valuable comments on this paper.

Future Scope Further investigations can be made to get the effect of varying suspension type of the vehicles, mounting arrangement, pavement surface type, and so on, on the IRI values.

References

1. Jinxi Z, Du Y, Su R (2011) Investigating the relationship between pavement roughness and heart-rate variability by road driving test. In: Proceedings of the 3rd international conference on road safety and simulation, Washington, DC, USA
2. Sayers MW (1998) The little book of profiling: basic information about measuring and interpreting road profiles
3. Sayers MW (1986) The international road roughness experiment: establishing correlation and a calibration standard for measurements
4. Múčka P, Granlund J (2012) Is the road quality still better? J Transp Eng 138(12):1520–1529
5. Peter M (2016) Road roughness limit values based on measured vehicle vibration. J Infrastruct Syst 23(2):04016029
6. Kropáč O, Múčka P (2009) Alternative single-number indicator of longitudinal road unevenness. Cana J Civ Eng 36(3):389–401
7. Pal M, Sutradhar R (2014) Pavement roughness prediction systems: a bump integrator approach world academy of science, engineering and technology. Int J Civil Environ Struct Constr Archit Eng 8(12):1258–1261
8. Hafez M, Ksaibati K, Anderson-Sprecher R (2016) Utilizing statistical techniques in estimating uncollected pavement- condition data. J Transp Eng 142(12):04016065
9. Kasun DZ, Keppitiyagama C, Seneviratne GP, Shihan WWAT (2007) A public transport system based sensor network for road surface condition monitoring. In: Proceedings of the 2007 workshop on networked systems for developing regions. ACM, p 9
10. Shahidul I, Buttlar WG, Aldunate RG, Vavrik WR (2014) Use of cellphone application to measure pavement roughness. In: T&DI congress 2014: planes, trains, and automobiles. pp 553–563
11. Hanson T, Cameron C, Hildebrand E (2014) Evaluation of low-cost consumer-level mobile phone technology for measuring international roughness index (IRI) values. Can J Civ Eng 41(9):819–827
12. Rajiv K, Mukherjee A, Singh VP (2016) Community sensor network for monitoring road roughness using smartphones. J Comput Civ Eng 31(3):04016059
13. Android Application "Roadroid Pro2 Pro2_v2.4.1", available at the website http://www.roadroid.com/home/app
14. Regression analysis software SPSS (Statistical Package for Social Sciences)
15. Cundill MA (1991) MERLIN-a low-cost machine for measuring road roughness in developing countries. Transp Res Rec 1291:106–112
16. Alessandroni G, et al (2014) Smartroadsense: collaborative road surface condition monitoring. Proceedings of the UBICOMM-2014. IARIA, pp 210–215
17. Bruscella B, Rouillard V, Sek M (1999) Analysis of road surface profiles. J Transp Eng 125(1):55–59

Detection of Flood Hazard Using QGIS

Shivani Soni and A. D. Prasad

Abstract Flash floods result in significant damage to the society and economics of a particular country. These are serious issues in built-up areas, where the drainage network is weak and unable to survive a heavy flood event. Knowledge of the areas which are vulnerable to flood risk is mandatory to apply techniques to reduce the risk. Identifying flood is difficult in basins which are not gauged. The present study aims to define a manageable procedure for a delineation of flood plain areas. There are many tools for detecting the flood hazards areas effectively and economically like FLO-2D Integration tool, Flood Risk tool, Geomorphic Flood Area Plugin, and QGIS with HEC RAS. The QGIS tool, Geomorphic Flood Index (GFI), is the worthiest tool to identify flood vulnerable areas if the areas are large and data-deficient. In terms of data and calculating cost, this tool provides good accuracies with low requirements.

Keywords Floods · Risk · Delineation · QGIS

1 Introduction

Flood is a very complex phenomenon and flood events are different according to their frequency and nature of the occurrence. A flood is the high flow of rivers, streams which overhead the natural and artificial bank of rivers [1]. The occurrence of floods is a natural phenomenon and population has to face it right from the beginning. India is a monsoon-driven country, so maximum flooding occurs in the monsoon season. It is a globally extensive hazard [2]. Floods may originate in many ways; usually, there are lots of influencing factors in the bottom of the valley and offshore areas. Their effect on the environment depends upon the occurrence of magnitude and frequency of flood.

S. Soni · A. D. Prasad (✉)
Civil Engineering Department, National Institute of Technology Raipur, Raipur 492001, India
e-mail: adprasadiit@gmail.com

S. Soni
e-mail: shivani.soni975@gmail.com

© Springer Nature Singapore Pte Ltd. 2021

K. K. Pathak et al. (eds.), *Recent Trends in Civil Engineering*, Lecture Notes in Civil Engineering 77, https://doi.org/10.1007/978-981-15-5195-6_65

The United Nations (UN) noted that 'a flood is a serious disturbance of the economics, society, materials, and environment losses which exceed the ability of lack of resources' (UN 1992). By considering past years' impacts of floods, it may be categorized as either 'sudden impact' (floods, earthquakes, tropical storms, volcanic eruptions, etc.), 'slow-impact' (drought, famine), or 'epidemic diseases' (cholera, measles, plague, etc.) [3].

About 15–20% of rainwater is usually converted as surface runoff in rivers. The remaining water immerses into the ground and meets groundwater or return to the atmosphere through transpiration and evaporation from plants. The amount of rainfall–runoff runs between 2 and 25% with differences in various factors like climate, slope, soil and rock type, and vegetation. Continuous rainfall can soak the land and the atmosphere which can further lead to floods as runoff with 100% of rainfall.

For the relief from these flood events, immediate action is taken on time and by accurate information on the extent by a flood event [4]. Flood event originates when a large amount of water is flowing in natural streams, in channels or sea, and extend their limits of geographic feature and sheltered waterway into areas, where water cannot drain satisfactorily. A flood occurs due to excessive rainfall with no warning, hence resulting in the overspill of lakes, dams, and rivers, which originate huge damage on human, infrastructure, and living things [5].

This study will focus on reviewing the existing literature on the use of QGIS Tool in flood disaster management. The study includes types, causes and socioeconomic impact, and effects of flooding and techniques of mitigating flood hazards in the following sections.

1.1 River Flood

River flood is the main type of natural disaster. It originates when rivers are filling with water above their maximum limits. The surplus water is now overflowed on the bank of rivers and other protection barriers and runs into low-elevation areas. River floods are responsible for the loss of life, infrastructure, and economy of the country. There are no seasons for river flooding, it can occur during any season, but the most common interval for occurring flood is in heavy rainfall in the monsoon and, sometimes, snowmelt. According to Rupinder, 2008, a flood that is moving in a constant part of rivers is a natural and unavoidable part of life. During heavy rains from a cyclone or tropical systems, rainwater passes through steep gradients may cause river flooding and submergence.

1.2 Coastal Flood

Coastal flooding occurs when generally low-elevation land is flooded by seawater. Wind storms and cyclones develop a low-pressure system that causes coastal flooding.

The volcanic activity and earthquake create waves that caused a coastal flood. Tropical storms or cyclones are the main reasons for this type of flooding. According to Rupinder, 2008, extraction of groundwater from coastal areas can result in the collapse of land causing the risk of flooding.

1.3 Urban Flood

The main causes of flooding in urban areas are flash floods, coastal floods, or river floods, but there is also one type of flooding which is urban flooding [6]. Urban flooding is caused due to the absence of a good drainage system. When the city's sewage system and the draining canal are not having adequate capacity to drain away from the high intensity of rainfall, flooding occurs. If the land is converted to urban areas having roads, buildings, and infrastructure, land loses its capability to absorb water [7].

1.4 Flash Flood

A flash flood is caused by the sudden and heavy rainfall that occurs with no warning. If rainfall occurs relatively high at a small period, flooding occurs [8]. Flash Floods can be originated by many influencing factors but are mostly due to high rainfall from thunderstorms. The occurrence of a flash flood can be due to dam or levee breaches, etc. To determine flash flooding, several influencing factors such as the intensity of the rainfall, the location, and distribution of the rainfall, the land use and topography, vegetation types and growth/density, soil type, and soil water content are responsible [9]. Urban areas are also susceptible to flooding in a short period; rainfall is the main source of urban flooding. In urban areas having impervious layers, water cannot drain off quickly and so flows to low-elevation areas. Flash flooding is very dangerous as water is fast moving while flowing.

2 Identification of Flood Hazard Areas

The identification of flood hazard areas is used to verify the areas exposed to the flood. Identification of flood hazard areas is derived with the help of past data of rivers, previous floods, and topographical data. The factors of risk, particularly development plans, are also needed for effective zoning. For planning a counteractive strategy in creating a flood hazard map, proper managerial units are to be accurate, quick, and cost-effective. Aerial photographs and satellite images of pre- and post-flood events are required for any flood management strategy. By using the data, a hypothetical map is generated for a 10-year flood, a 50-year flood, and a 100-year flood. Additionally,

Table 1 List of various hazard map-producing organizations

S. no.	Agency	Map developed
1	Central water commission (CWC)	Flood atlas of India
2	Building materials and technology promotion council (BMTPC)	Vulnerability atlas of India
3	National atlas and thematic mapping organization (NATMO)	Natural hazard map of India

for the identification of areas that is vulnerable to flood, scale models are constructed. Such models only work if they are timely recorded with flood events.

Various guidelines have been prepared to enable the stakeholder's agencies and implementers to identify the critical flood-affected area, so that the risk can be minimized. National Disaster Management Authority (NDMA) is the principal body to make and implement any plan for disaster management. Table 1 shows the list of various organizations which develop different hazard maps for Indian rainfall conditions.

Imageries of satellites such as IRS, LANDSAT, ERS, and RADARSAT have been used to monitor flood occurrences. For higher accuracy of flood monitoring, WiFS data from IRC-1C and 1D are good at geographical scale. The evaluation of flood hazards is done by combining geographical, hydrological, and environmental information.

3 Quantum GIS Tools

Quantum GIS (also known as QGIS) is a freely available desktop geographic information system (GIS) that is used for analyzing spatial data. It is compatible with both raster and vector data. Raster data are based on pixel; on the other hand, vector data are stored as either point, or line, or polygon feature. QGIS supports various formats such as shapefiles, coverage, personal geodatabases, dxf, Map Info, Post GIS. Web services, including Web Map Service (WMS) and Web Feature Service, are also supported to allow the use of data from external sources. QGIS is combined with other GIS Package such as Map server, GRASS GIS, and Post GIS. QGIS capabilities are increased by adding plug-ins written in Python or C++.

3.1 FLO-2D Tool

FLO-2D is a very intensive, inexpensive, and simple flood modeling tool. This model is beneficial for simulating high-intensity urban flooding and contains extensive details including storm drainage. FLO-2D gives information in terms of

volume conservation, speed, and numerical stability. This plug-in is very helpful for simulating flood created from heavy rainfall.

3.2 Flood Risk Tool

The GIS tool called FloodRisk benefits the delineation of risk maps based on an approach that aims to improve the efficacy of flood risk map overcoming the limits of expert-drive qualitative approach (produce errors in comparative ranking of risk areas) in supplying the knowledge base that allow to analyze costs and benefits of potential mitigation measures [10]. This plug-in is based on a framework based on 2D inundation modeling with different return periods, as input, and identified how structural and non-structural measures can significantly decrease the cost of floods for households [11].

3.3 Geomorphic Flood Index

The QGIS tool [12], Geomorphic Flood Index (GFI) [13], is the worthiest tool to identify flood vulnerable areas, if the areas are large and data-deficient. In terms of data and calculating cost, this tool provides good accuracies with low requirements. This index is defined as the ratio of water depth in the river basin closest to the points under study areas (calculated using hydraulic scaling) and the difference in elevation between these two points.

4 Methodology of GFI Tools

The GFI tool divides the results into two groups in which, firstly, area which is prone and, secondly, the area which is not flood-prone [14]. The mentioned index is:

$$\text{Ln}\ (\text{hr}/H) \tag{1}$$

where

hr—Water level in the nearest element of river network.
H—Elevation difference between these two points.

$$\text{hr} = \text{Ar}^2 \tag{2}$$

where

hr—Water level in the nearest element of river network.
Ar—Drainage Network.

For generating flood hazard map, an Ordered Weighted Averaging (OWA) works on multi-criteria evaluation. The result depends on the weights assigned for a particular criterion. These weights are assigned according to their greater influence over another. The criteria values are associated with the changes in order weight. They are allocated to attribute values according to different situations in decreasing pattern. Now, the re-ordering process is done to provide ordered value with particular weighted attribute values.

The first weight value is allocated according to the highest weighted attribute values for each location, the second-order weight to the second highest values, and so on. In the raster data model, all pixels receive the same assigned factor weight.

In case of OWA method, weight value of each and every layer has to be assigned. This weight value is multiplied by the input layer, then adding all layers to create the final output map and choosing "SAGA geo algorithm" from the processing tools and click on "Grid Analysis." Now, the output map name is set and OWA method is completed [15].

The flood index is modified to flood maps by applying a threshold value "τ". This parameter is used to validate and compare the flood map obtained by using software with the standard flood maps. By this comparison, the following presentation is evaluated: the rates of true positives (TP), false positives (FP), true negatives (TN), and false negatives (FN). The threshold values are differentiating between the areas which are flooded or not flooded for a particular basin. These values are used to identify flooded areas covering large area basins.

5 Current Challenges, Possible Solution, and Future Approach

The overall objective of this activity is to provide a simplified procedure or method which is able to provide reliable flood susceptibility map in data-deficient areas. Geomorphic flood tool is a plug-in in QGIS and it is very helpful in the recognition of flood-affected areas on data-poor environment. This DEM-based procedure plug-in needs a flood hazard map for understanding the areas affected by flood events. The accuracy is totally depending on standard and resolution of DEM. For accurate flood plain extent, there is a need of providing a high-resolution DEM and a detailed flood hazards map for validation. This method is very useful when limited data are available.

6 Conclusion

The QGIS-based tool is very useful to provide a preliminary and an efficient delineation with low cost, reduced computational time, and with fewer data requirements.

For any ungauged basin areas, GFA tools have more advantages over other tools for zoning of flood hazard areas. The recognition identification of flood-prone areas is done by GFA tool that has various applications in geomorphological and hydrological communities. Proceeding with this tool is particularly helpful for the evaluation of risk zone over a large area. With the identification of flood hazard area, it is an important information for helping/supporting and to take proper mitigation measures against flooding impacts on human lives, infrastructure, and economics of the district.

References

1. Rostvedt JO (1968) Summary of floods in the United States during 1960: US geological survey water-supply paper 1790–B, 147 p 1972. Summary of floods in the United States during, 1970–1978. https://pubs.usgs.gov/wsp/1970b/report.pdf
2. Domeneghetti A, Carisi F, Castellarin A, Brath A (2015) Evolution of flood risk over large areas: quantitative assessment for the Po river. J Hydrol 527:809–823. https://doi.org/10.1016/j.jhydrol.2015.05.043
3. Getahun YS, Gebre SL (2015) Flood hazard assessment and mapping of flood inundation area of the Awash River Basin in Ethiopia using GIS and HEC-GeoRAS/HEC-RAS model. J Civil Environ Eng 5(4):1. https://doi.org/10.4172/2165-784X.1000179
4. Merz B, Kreibich H, Schwarze R, Thieken A (2010) Review article" assessment of economic flood damage". Nat Hazards Earth Syst Sci 10(8):1697–1724. https://doi.org/10.5194/nhess-10-1697-2010
5. https://damsafety.org/sites/default/files/files/DamsSectorConsequenceEstimation_LossOfLife.pdf
6. Tinsanchali T (2011) Urban flood risk management. program of civil and environment engineering
7. Rafiq F, Ahmed S, Ahmad S, Khan AA (2016) Urban floods in India. Int J Sci Eng Res 7(1):721–734. ISSN 2229-5518
8. Dhillon RK (2008) Flood damage assessment and identification of safe routes for evacuation using a micro-level approach in part of Birupa river basin, Orissa, India. https://www.iirs.gov.in/iirs/sites/default/files/StudentThesis/rupinder.pdf
9. Collier CG (2007) Flash flood forecasting: What are the limits of predictability? Q J R Meteorol Soc 133(622):3–23. https://doi.org/10.1002/qj.29
10. Albano R, Mancusi L, Abbate A (2017) Improving flood risk analysis for effectively supporting the implementation of flood risk management plans: the case study of "Serio" Valley. Environ Sci Policy 75:158–172. https://doi.org/10.1016/j.envsci.2017.05.017
11. Kale VS (2003) Geomorphic effects of monsoon floods on Indian rivers. In: Flood Problem and Management in South Asia, pp 65–84. https://doi.org/10.1007/978-94-017-0137-23
12. Mancusi L, Albano R, Sole A (2015) Flood Risk: a QGIS plugin for flood consequences estimation. Geomat Workbooks. https://doi.org/10.13140/RG.2.1.4215.7846
13. Samela C, Troy TJ, Manfreda S (2017) Geomorphic classifiers for flood-prone areas delineation for data-scarce environments, Adv Water Res 102:13–28. http://dx.doi.org/10.1016/j.advwatres.2017.01.007
14. Samela C, Albano R, Sole A, Manfreda S (2018) A GIS tool for cost-effective delineation of flood-prone areas. Comput Environ Urban Syst 70:43–52. https://doi.org/10.1016/j.compenvurbsys.2018.01.013
15. Zabihi H, Alizadeh M, Kibet Langat P, Karami M, Shahabi H, Ahmad A, Nor Said M, Lee S (2019) GIS multi-criteria analysis by ordered weighted averaging (OWA): toward an integrated citrus management strategy. Sustain 11:1009. https://doi.org/10.3390/su11041009

Comprehensive Study on Foamed Bitumen

Shweta Mandloi, Sarvesh Kumrawat, and Vinay Deulkar

Abstract For many decades, bitumen has been with success utilized in asphalt concrete to pave roads. Despite continuous enhancements to bitumen production processes, combine style, and pavement style, there square measure limits to the extent that bitumen will surmount the challenge. Fast wear and tear caused by serious traffic and harsh climates square measure taking a toll. Additionally, there square measure increasing demands for quieter and safer roads. In Asian countries, regarding 90th of roads square measure bitumen paved. Pavement trade has developed chop-chop everywhere the planet throughout the previous few decades, particularly in developing countries. Following the speedy development, augmented traffic load, higher traffic volume, and too little maintenance junction rectifier to several severe distresses (e.g., rutting and cracking) of road surfaces. The tough reality was difficult a lot on bitumen quality. Considering these issues, it's seen that exploitation plain bitumen isn't adequate nowadays, because of an increase in distress so considering the requirement of modification of bitumen; foaming of bitumen is additionally a step toward the modification of bitumen.

Keywords Foamed bitumen · Modified bitumen · Characteristics · Test results

S. Mandloi (✉)
Medi-Caps University, Indore, Madhya Pradesh, India
e-mail: shwetamandloi79@gmail.com

S. Kumrawat · V. Deulkar
JIT Borawan Khargone, Khargone, Madhya Pradesh, India
e-mail: Sarveshkumrawat29@gmail.com

V. Deulkar
e-mail: deulkarvinay@gmail.com

© Springer Nature Singapore Pte Ltd. 2021

K. K. Pathak et al. (eds.), *Recent Trends in Civil Engineering*, Lecture Notes in Civil Engineering 77, https://doi.org/10.1007/978-981-15-5195-6_66

1 Introduction

1.1 Foamed Modified Bitumen

Foamed asphalt may be a mixture of aggregates (stone and soil) and foamed bitumen. The bitumen is foamed by the Associate in Nursing innovative method, harnessing the sometimes undesirable reaction that happens once hot bitumen is contaminated with water.

Foamed asphalt combine refers to a mixture of pavement construction aggregates and foamed bitumen. Foamed bitumen is created by a method within which water is injected into the recent bitumen leading to spontaneous foaming. Water on contact with hot bitumen is vapor, that is treed in thousands of little bitumen bubbles. Incorporating foamed bitumen into the aggregates produces foamed asphalt mix [1].

In order to combine bitumen with road-building aggregates, initial it's required to significantly scale back the consistency of the cold arduous binder bitumen [2]. Historically, this was done by heating the bitumen and admixture it with heated aggregates to supply hot combine asphalt. Alternative ways of reducing the bitumen consistence embrace dissolving the bitumen in solvents and emulsification. Within the foam state the bitumen includes a terribly giant area and intensely low consistency making it ideal for admixture with aggregates.

The very basic concept behind the foaming of the bitumen by adding cold water in hot bitumen is shown diagrammatically in the following Fig. 1.

In the foamed state, the bitumen is ideal for mixing with fine aggregates, which increases workability [3]. In the foamed state, bitumen has a very large surface area and an extremely low viscosity. This increases the surface tension which reduces water percolation, and also increases fatigue and rut resistance [3].

1.2 Foamed Bitumen Apparatus

A device for producing small-scale batches foamed bitumen. The device has a first pressurized, holding chamber for heating bitumen to a selected temperature, a second pressurized, holding chamber for heating bitumen additive (e.g., a foaming agent or chemical additive) to a selected temperature, and various conduits and valves as needed for delivering heated and pressurized bitumen with a heated and pressurized additive to a mixing chamber having a selected volume to produce foamed bitumen. A method of producing foamed bitumen, the method comprising the steps of:

1. Heating bitumen to a selected temperature in a first holding chamber,
2. Heating additive to a selected temperature in a second holding chamber,
3. Pressurizing the bitumen to selected air pressure inside first holding chamber,
4. Pressurizing the additive to selected air pressure inside second holding chamber,

Fig. 1 Foaming of bitumen

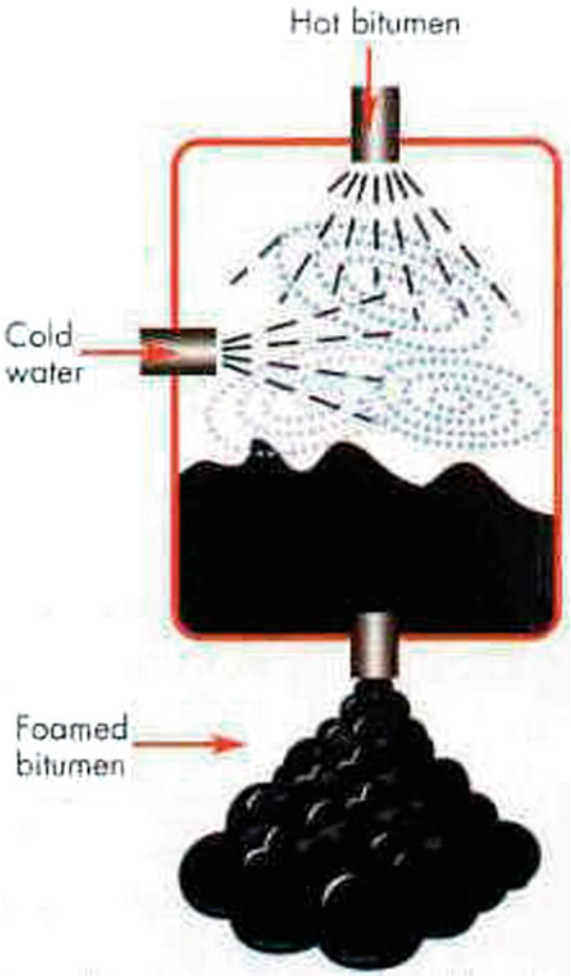

5. Mixing the heated and pressurized bitumen with the heated and pressurized additive in a mixing chamber having a selected volume to form a foamed bitumen and collecting the foamed bitumen in a container.

Due to the half-life period of foamed bitumen, it has to be mixed and laid fast; therefore, the setup consists of a mixer to help lay the foam layer faster and continuously [4].

2 Methodology

As, in foreign countries, cement and lime are used as filler materials but, in India, the most common filler material used is stone dust, so the same stone dust as a filler material along with foamed bitumen and road construction aggregates as per IRC grading for surface course layer is been used.

All the tests have been conducted according to the IRC specifications so that the result will be feasible in India and Indian conditions. The IRC: 37-2012 has been used for conforming to the specification given for the flexible pavement construction in India [5].

As this foamed bitumen asphalt method is being practiced in foreign countries for pavement construction and also for soil stabilization, we wanted to check whether it is feasible in India, since the boundary conditions are different and the method of construction is also different [6].

3 Materials

1. Aggregates
2. Stone dust
3. Bitumen (60–70 grade)
4. Water.

Aggregates used were according to the IRC grading for surface course as follows in Tables 1 and 2.

Table 1 Grading of aggregates for surface coarse

Size	% lesser than	Wt lesser than 10 kg sample (kg)	Weight (kg)
12.5 mm	100	10	1
1 mm	90	9	2.5
4.75 mm	65	6.5	2.25
2.36 mm	42.5	4.5	1
600 μ	23.5	2.35	0.55
300 μ	18	1.8	0.4
150 μ	12	1.2	0.5
75 μ	7	0.7	0.7

Table 2 Penetration value test results

Reading no.	Pure bitumen	Foamed bitumen
1	71	66
2	65	63
3	64	60
Average	66.66	63

3.1 Preparation of Samples

The foamed bitumen has been prepared by the traditional method by heating bitumen on electric coil heater up to temperature 150–180 °C and spraying water (2.5% by weight of bitumen) on it along with diesel as a foaming agent.

Bitumen grade—60–70
Heating apparatus—Electric oven
Water—Sprayed using a spray bottle.

Foamed bitumen is used for further experimental purposes. This prepared foam of bitumen is to be handled carefully and mixed with the aggregates in its foamed state; because in the foamed state, the viscosity of the bitumen is very less and, due to expansion, it becomes very easy to mix with less quantity and also good coating of the aggregates is achieved as shown in Fig. 2.

Fig. 2 Sample of foamed bitumen

3.2 Material Properties

The foaming properties are characterized by two terms: Expansion ratio and half-life.

Expansion Ratio—The ratio of the maximum volume of foamed bitumen compared to the volume of unfoamed or conventional bitumen [7].
Half-Life—The time taken for the volume of foamed bitumen to settle to half of the maximum volume achieved due to foaming.

Sufficient expansion ratio and half-life characteristics must be present to ensure adequate coating of the fine particles by bitumen. [7]

Only the foaming water can be changed readily to improve foaming characteristics. Testing indicates that the best foaming properties are usually achieved with a water content of 2.5%. The relation is shown by the graph in Fig. 3.

4 Tests Performed

1. Penetration test
2. Ductility test
3. Softening point test
4. Marshall stability test.

By these tests, characteristics of plain bitumen and foam bitumen have been compared.

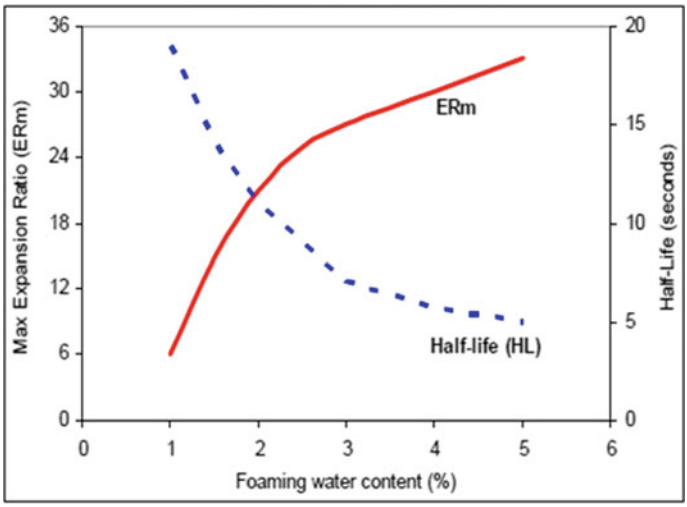

Fig. 3 Half-life and expansion ratio

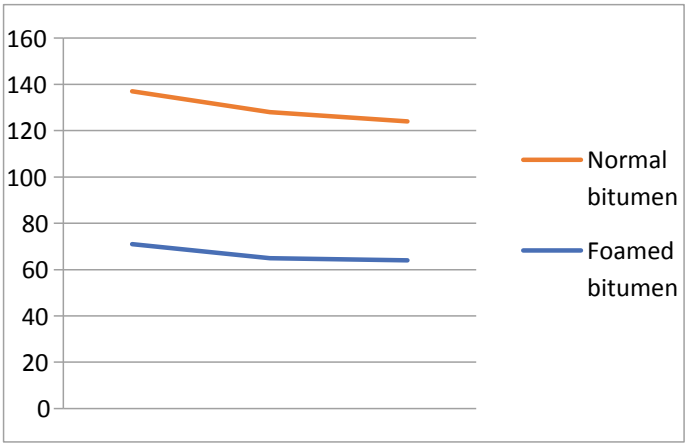

Fig. 4 Penetration graph

5 Results and Discussions

5.1 Penetration Test

Penetration indicates the consistency of bitumen. From penetration test on pure bitumen and foam bitumen, it is found that the penetration value is reduced, since foam bitumen has higher stiffness and it gets harder. Higher values of penetration indicate softer consistency [8]. Due to the foaming of bitumen, as the penetration value decreases, the consistency increases. In warmer regions, lower penetration grades are preferred to avoid softening of bitumen. Therefore, foaming can be considered beneficial. Penetration value for pure bitumen is 66.66 and for foamed bitumen is 63 as in Table 2 and the graph is shown in Fig. 4.

5.2 Ductility Test

In flexible pavement design, it is necessary that binder should form a thin ductile film around aggregates, so that the physical interlocking of aggregate is improved. From the test results, it is found that ductility or the stretching ability of the bitumen is increased due to foaming [4]. Therefore, it is beneficial to avoid cracking of flexible pavement due to repeated traffic load and it provides impervious pavement surface. The result of ductility for pure bitumen is 90 and for foamed bitumen is 108 in Table 3 and chart of differences as in Fig. 5.

Table 3 Ductility test results

Parameter	Pure bitumen	Foamed bitumen
Ductility value (Cm)	90	108

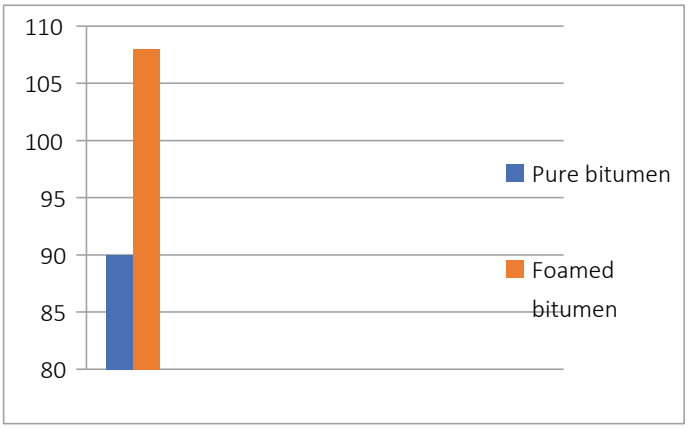

Fig. 5 Ductility graph

Table 4 Softening point test result

Parameter	Pure bitumen	Foamed bitumen
Softning point value (°C)	45	53

5.3 Softening Point Test

Softening purpose indicates the temperature at that binder possesses identical viscousness. Hydrocarbon material doesn't have a freezing point. Rather, the modification of state from solid to liquid is gradual over a good vary of temperature. Softening purpose encompasses an explicit significance for materials to be used as joint and crack fillers. Higher softening purpose ensures that they will not flow throughout service. Higher the softening purpose, lesser the temperature condition [2]. Hydrocarbon with higher softening purpose is most popular in hotter places. The softening purpose for pure hydrocarbon is 45 and for foamed hydrocarbon is 53 in Table 4 and the chart is shown in Fig. 6.

5.4 Marshal Test

Strength is measured in terms of stability, which is the resistance to the plastic deformation of bituminous concrete. After foaming of the bitumen, the mixture becomes stiffer as it can be seen by a decreased penetration value and high softening

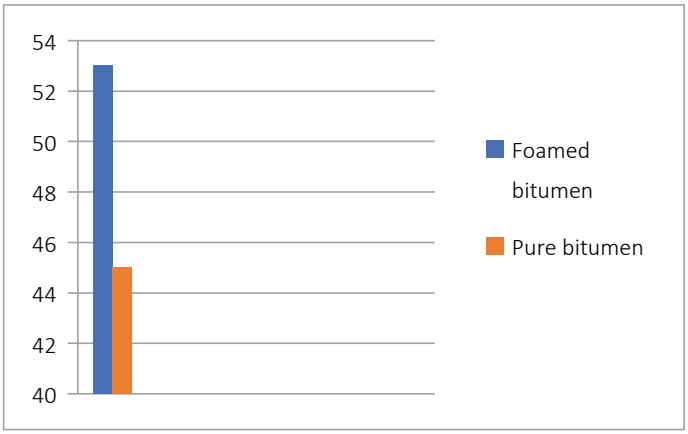

Fig. 6 Softening chart

point, resulting in higher stability values [9]. As the stability of the bituminous concrete increases, its strength increases.

Flexibility is measured in terms of flow value, which is the measure of the deflection of the cylindrical specimen of bituminous concrete. Ideally, the flow value should be as minimum as possible. The deflection is an important criterion while judging pavement performance [9]. After foaming of the bitumen as the mixture becomes stiffer, the flow valve decreases indicating more resistance to deflection.

For an ideal sample, the stability value should be higher and the flow value should be lower. Both the values, stability and flow, were as required showing a positive result after foaming of the bitumen. Stability and flow values were found for bituminous concrete made with pure bitumen and recycled aggregates. Since the aggregates were recycled, it previously had certain bitumen content. The recycled aggregates showed higher stability values and lower flow values as compared to Combination 1 (Pure Bitumen and Fresh Aggregates). From the test results, it can be stated that, in general, the use of recycled aggregates is a good option helping to save use of fresh aggregates and reducing the binder content. For combination 1, stability varies from 13.90 to 14.35 and flow from 4.2 to 3.66 which is normal and, for combination 2, stability varies from 17.54 to 19.14 and flow from 3.4 to 2.2 which is acceptable, and it is discussed in Tables 5 and 6, respectively, and graph of the variation in stability and flow in Figs. 7, 8 and 9.

Table 5 Combination (1) pure bitumen and fresh aggregate

Sample no.	Stability (Kn)	Flow (Mm)
1	13.90	4.2
2	13.85	3.35
3	14.35	3.66

Table 6 Combination (2) foamed bitumen and fresh aggregate

Sample no.	Stability (Kn)	Floe (Mm)
1	17.54	3.4
2	18.32	3.3
3	19.14	2.2

Fig. 7 Marshal apparatus

6 Conclusions

On the basis of the study performed and test results on foamed bitumen, we can conclude the following points,

1. Based upon the laboratory foaming experiment, 2.5% water content was selected as the optimum foaming water content, along with a temperature of 170 °C and 60–70 grade bitumen, to produce the foam bitumen whose expansion ratio was 2.5–3 times that of the original and half-life was around 10 s.
2. The addition of foamed bitumen significantly improved the performance of the pavements.
3. From penetration test on foam bitumen, it is found that the penetration value is reduced, since foam bitumen has higher stiffness and it gets harder. Due to

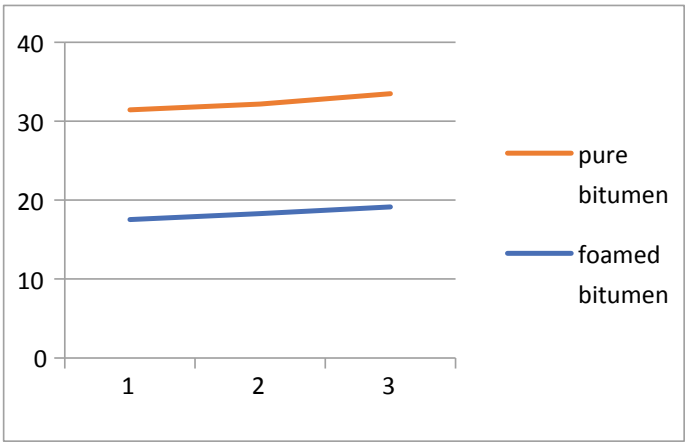

Fig. 8 Stability curve

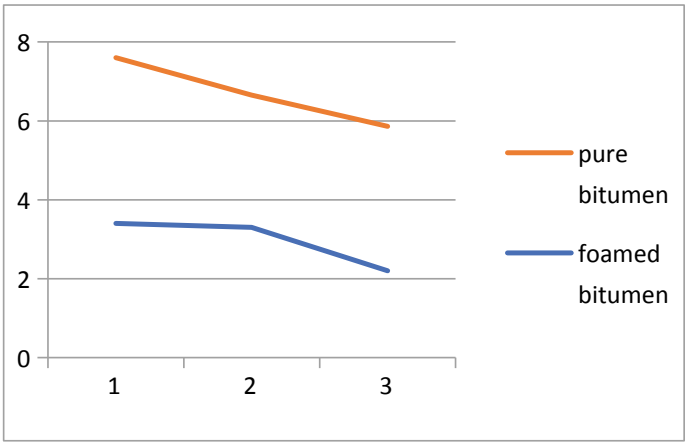

Fig. 9 Flow curve

the foaming of bitumen, as the penetration value decreases, the consistency increases. In warmer regions, lower penetration grades are preferred to avoid the softening of bitumen.

4. Ductility or the stretching ability of the bitumen is increased due to foaming.
5. Foam bitumen had a higher softening point. It can be successfully used as joint and crack fillers. Higher softening point ensures that they will not flow during service. Bitumen with a higher softening point is preferred in warmer places.
6. After foaming of bitumen, there is better adhesion in between bitumen and aggregates, thereby reducing water susceptibility.

7. Pavement behaves in a ductile manner and shows a good performance even in presence of water.
8. The foamed bituminous concrete showed higher stability (strength) values and lower flow (deflection) values which is very desirable as compared to conventional bituminous concrete.
9. The foamed bituminous concrete made using recycled aggregates showed highest stability values and low flow values as compared to all combinations.
10. Recycled aggregates can be successfully used and foam bitumen can be used as a technique of full depth reclamation (FDR).
11. The technique of foamed bitumen can be successfully used where there is hot climate, road failure due to water susceptibility. It can be used in India, as there are similar exposure conditions.

References

1. Ramanujam JM, Jones JD (2000) Characterisation of foam bitumen stabilisation. Road Syst Eng Technol Forum
2. Alabaster D, Patrick J, Arampamoorthy H (2013) A Gonzalez have done study on the design of stabilised pavements in New Zealand. New Zealand Transport Agency research report 498
3. Huan Y, Siripun K, Jitsangiam P, Nikraz H (2010) A preliminary study on foamed bitumen stabilisation for Western Australian pavements. Sci Res Essays 5(23):3687–3700
4. Bejjenki A (2015) Performance of bituminous mixes with modified binders. SSRG Int J Civil Eng (SSRG-IJCE) 2(3)
5. Browne (2011) A Foamed bitumen stabilisation in New Zealand. Hiway Stabilizers New Zealand Ltd
6. Muthen KM (1999) Foamed asphalt mixes. CSIR Transportek, Contract Report CR-98/077
7. Kendall M, Baker B, Evans P, Ramanujam J (2000) Foamed bitumen stabilisation
8. Ruenkrairergsa T (2004) Engineering properties of foam bitumen mixtures in Thailand. In: Proceedings of the 8th conference on asphalt pavements for Southern Africa (CAPSA'04)
9. Ramanujam J, Janosevic M (2009) Design, construction and performance of insitu foamed bitumen stabilised pavements. Queensland Roads Edition No 7

Water Lettuce for the Improvement of River Water Quality in Pune Metropolitan Area

Jayeshkumar Maheshkumar Bhagwat, Veruval Devadas, and Bharati V. Mahajan

Abstract The concentration of population in the metropolitan areas is a trend globally. The growth and development of human settlements are always aligned to natural resources. Indian metropolitan areas are also following similar trends. Rapid urbanization had caused losses to natural resources. It is important to develop ways to reduce the losses caused to natural resources. River is one of the prime natural resources. Effective wastewater management can play a vital role in the process of improving the rivers. Indian metropolitan areas are exposed to certain issues with the river water quality improvement. Inadequate wastewater management capacity, inefficiently installed capacity, lack of recovery cost, etc., are some of the crucial issues. In this paper, the Pawana River of Pune Metropolitan Region is considered for the study. Water lettuce, which is grown in the River Pawana is potentially used to improve river water quality. Context-specific parameters were considered for the purpose of the study. A prototype of the proposed system was modeled. Results based on the laboratory experiment were derived. Experimental results associated with the study were documented and ways to mainstream use of water lettuce in the wastewater management of Pune Metropolitan Area were proposed.

Keywords Water lettuce · River water quality · Urbanization · Wastewater management

1 Introduction

River water improvement is a prime concern globally. In developing countries, constant efforts are made to rejuvenate the rivers. Prevention of runoff with pollutants, research related to new technologies and policy formulations, creation of a favorable atmosphere for the aquatic species, and sustainable utilization of rivers

J. M. Bhagwat (✉) · V. Devadas
Indian Institute of Technology, Roorkee, India
e-mail: jayeshmaheshbhagwat@gmail.com

B. V. Mahajan
JSPM's Rajarshi Shahu College of Engineering, Pune, India

© Springer Nature Singapore Pte Ltd. 2021

K. K. Pathak et al. (eds.), *Recent Trends in Civil Engineering*, Lecture Notes in Civil Engineering 77, https://doi.org/10.1007/978-981-15-5195-6_67

are some of the prime interventions attempted in this regard [1]. Water improvement primarily focuses on the use of high energy-driven technologies. The growing concern for energy motivates researchers to incorporate low energy-driven mechanisms to improve river water quality. Urbanization had led rivers to a degraded situation in terms of water quality [2]. The irreversible losses caused to the quality of water had reduced the aquatic life in rivers and the river-based economies in the cities are at risk of livelihood loss, fishing is one such economic activity [3–5].

This work concentrates on improvising the quality of water in the River Pawana. The 1991 economic reforms, contributed to a boom in industrial activities of the various cities of India [6]. In this period, the suburban areas of Pune Metropolitan Area emerged as the industrial centers along with an important education center of India [7, 8]. The growth of industrial activities and associated unplanned concentration of people in the suburban areas resulted in the deterioration of river water quality of rivers Pawana, Mula, Mutha, and Indrayani of Pune Metropolitan Area [9]. It is extremely necessary to check the river water quality for the promotion of sustainable urbanization in Pune Metropolitan Area. The aim of this work is to improve the quality of water in the River Pawana by employing a model with water lettuce. The objectives of the work are to reduce the nutrient content of wastewater discharged in the river and to study the model designed for the improvement of wastewater in the Pawana River. The scope of the work is limited to the study the parameters like pH, hardness, turbidity, conductivity, Dissolved Oxygen (DO), Biochemical Oxygen Demand (BOD), Chemical Oxygen Demand (COD), total solids, total nitrogen, total phosphorus, potassium, lead, and iron is studied in this work.

1.1 Pimpri-Chinchwad and the Pawana River

Pimpri-Chinchwad is located 18.62°N and 73.79°E in the Indian state of Maharashtra. It is one of the major industrial centers in Pune Metropolitan Area. The population of the city is 17.30 lakhs, and the area is 171 km^2. [10]. The population density of the city is 9770 per km^2. [11]. Pimpri-Chinchwad is one of the industrial cities in India, located 530 m above sea level [12]. The settlement was evolved from a group of villages along the rivers like Pawana, Indrayani, and Mula. It is more important to understand that the city has well-established automobile and aligned industries. The city flourished due to the presence of adequate resources like cheap manpower, water, electricity, and favorable infrastructure for the growth of industries.

Pawana is an important river originating in the Western Ghats of the Indian peninsula. The Pawana River is 50 km in length,14.3 km of its flow is within the limits of the Pimpri-Chinchwad city, and it is presented in Fig. 1. The industrial development is plotted on the map in Fig. 1. The river flowing through the city of Pimpri-Chinchwad is Pawana, the river flowing south to the River Pawana is the River Mula. This area is responsible for the major environmental damages caused to the river [13]. In this

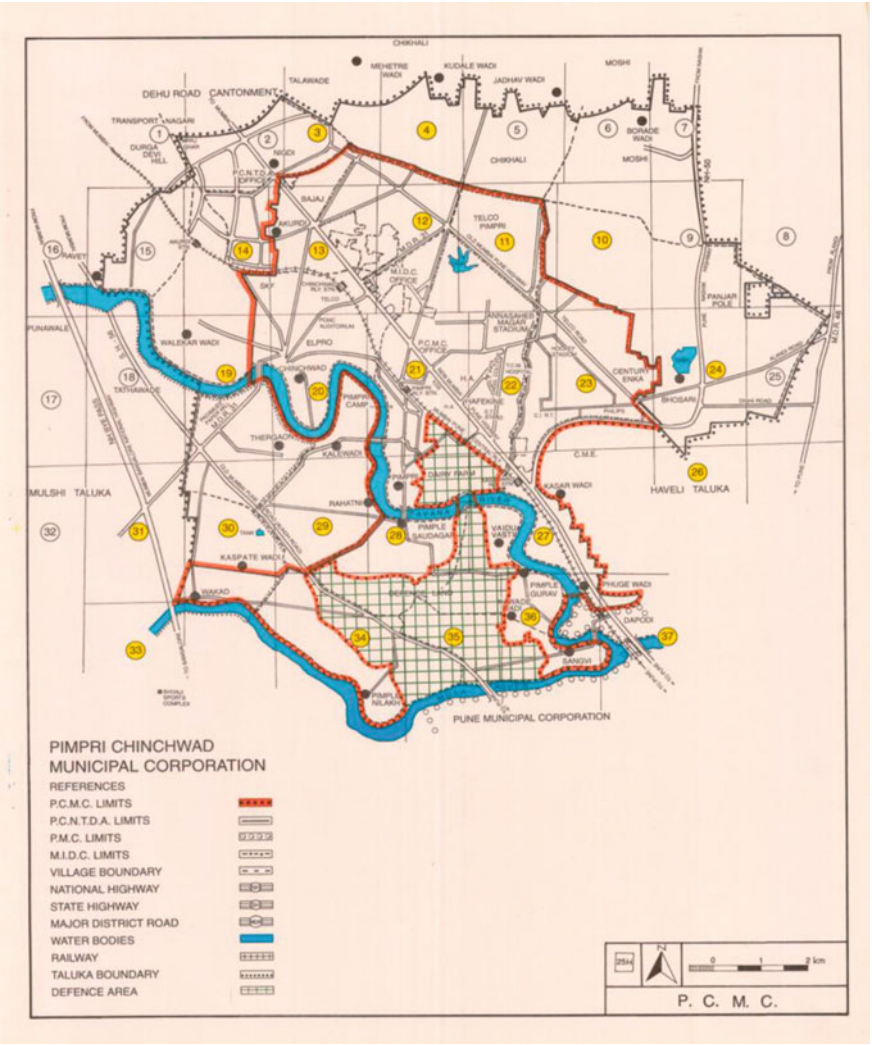

Fig. 1 Pimpri-Chinchwad ward map and the Pawana river flow as per development plan: 2016. *Source* Development plan for Pimpri-Chinchwad—2016

paper, the words river water and wastewater are used interchangeably since the quality of water in the Pawana River is degraded, as per the number of studies. The river also passes through other suburban areas like Dehu, Dapodi before the confluence with the Mula River.

2 Literature Study

Water lettuce is a free-floating plant. It can grow up to 15 cm in height and 30 cm in width. The plants are linked with each other by the thread-like structure. Water lettuce is primarily found in Africa, Asia, and equatorial America. Water lettuce spreads quickly and develops a green cover over the entire water body [14]. Water lettuce is less explored in terms of water quality improvement but water hyacinth is used by various researchers to show the impact on wastewater quality. Nutrient-rich wastewater purification is researched by using aquatic plants. The samples are tested at inlet and outlet is tested using the detention tanks. The parameters like COD, potassium, total nitrogen, DO, and transparency were considered for the research. It was concluded by this study that water hyacinth was effectively used in the treatment wastewater [15]. Cost-effectiveness of improvement of wastewater using water hyacinth, water lettuce, and vetiver grass is conducted by the researchers. The parameters like TSS, DO, conductivity, hardness, BOD, COD, nitrogen, phosphorous, and heavy metals were used for the study, which showed positive results in improving wastewater quality [16]. The potential use of water hyacinth, Pistia, and Azolla for municipal waste treatment was undertaken by the researchers. Satisfactory removal of total dissolved solids (TDS), fecal coliform, BOD, COD was attempted by the researchers. The research was carried out by considering certain parameters and others were unaccounted in these earlier researches [17]. Constructed wetlands were used to reduce various polluting parameters. An important observation noted by this study is that underground water pollution was reduced using water lettuce [18].

Physicochemical assessment of the Pawana River in 2005 and 2013 shows that water quality has degraded. Wastewater generated from small-scale industries and untreated waste from planned settlements is primarily responsible for water quality degradation [19]. Heavy metal is an important determinant in the assessment of the quality of river water [20]. It was observed that various aquatic plants like water hyacinth, Pistia, Azolla, etc., were used for the improvement of water quality. Water lettuce could hold a possibility to improve the river water quality in the aquatic systems. The use of water lettuce will be utilized in this work in order to develop a new approach to improve river water quality.

3 Methodology

The reconnaissance survey was conducted along the banks of the River Pawana within the limits of the Pimpri-Chinchwad City. The intrusions are the points from where wastewater is released in the river. Intrusion points were identified based on factors like discharge, accessibility, and uniform distribution along the stretch of the river. The intrusions with adequate discharge, more accessibility, adequately spaced apart were considered for the collection of samples. The discharge at the selected intrusions was measured based on the discharge, the model with detention tank is developed.

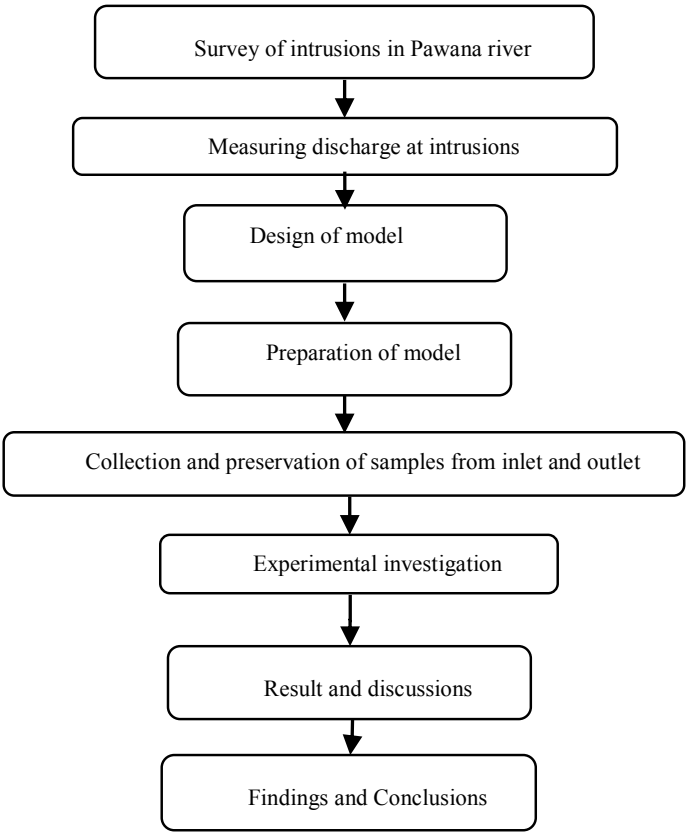

Fig. 2 Methodology *Source* Authors

The samples were collected and preserved at inlet and outlet of the detention tank in the model. A suitable experimental investigation was carried out on the predefined parameters. The results of the experiments were analyzed, discussed, and conclusions were drawn. The methodology used in this study is provided in Fig. 2.

3.1 Method and Process

In this work, an in-depth study of the research conducted in various parts of the world was reviewed. This resulted in the development of a methodology employed in this work. The discharge, which is the flow of wastewater into the river was determined using the surveys employed at ten different intrusions in the river within the limits of Pimpri-Chinchwad City. The samples were collected from four locations out of the ten intrusions. In the process, in order to observe the combined result of the sample

at the four locations, a mix of samples at all the four sampling locations was used as a fifth sample for the study.

3.2 Determination of Discharge

The discharge at ten different intrusions along the length of the river was determined by field survey. The reconnaissance survey was employed in order to find the number of intrusions. It was observed that ten intrusions exist in the stretch of river within the city limits. The total discharge was determined using the formula,

$$Q = V/t \tag{1}$$

where

Q = Discharge (m^3/s)
V = Volume (m^3)
t = time (s).

The treated wastewater which is released in the river is not considered for calculation of discharge. The reason being, such water will facilitate the improvement of river water quality. The discharge at ten identified intrusions is presented in Tables 1 and 2.

The volume of wastewater discharged in the River Pawana, except the treated wastewater is 4.4 MLD.

Table 1 Discharge at intrusion (part A) (m/s^3)

Time	Dhaneshwar Bridge	Dhaneshwar Mahadev Mandir	Keshav Nagar, Chinchwad	Kalewadi Bridge, JNNURM Colony	Tapkir Mala, Pimpri
8 am	1.3×10^{-3}	3.1×10^{-3}	1.5×10^{-3}	30.0×10^{-3}	3.2×10^{-3}
10 am	1.7×10^{-3}	3.7×10^{-3}	1.75×10^{-3}	30.0×10^{-3}	3.1×10^{-3}
12 pm	2.8×10^{-3}	3.6×10^{-3}	0.9×10^{-3}	29.0×10^{-3}	1.9×10^{-3}
5 pm	1.6×10^{-3}	0.52×10^{-3}	0.25×10^{-3}	5.0×10^{-3}	1.2×10^{-3}
7 pm	1.3×10^{-3}	1.1×10^{-3}	0.37×10^{-3}	17.0×10^{-3}	1.6×10^{-3}
Average	1.74×10^{-3}	2.40×10^{-3}	0.96×10^{-3}	22.2×10^{-3}	2.2×10^{-3}

Source Authors

Table 2 Discharge at intrusion (part B) (m/s^3)

Time	Pimple Saudagar (Jalkumbh)	Pimple Saudagar (Seeta plaza)	Pimple Gurav (Srushti Chowk)	Sangavi Mosque	Bopodi Mosque
8 am	8.13×10^{-3}	2.33×10^{-3}	1.25×10^{-3}	2.17×10^{-3}	9.09×10^{-3}
10 am	9.35×10^{-3}	2.64×10^{-3}	1.44×10^{-3}	2.89×10^{-3}	7.69×10^{-3}
12 pm	7.42×10^{-3}	4.37×10^{-3}	1.16×10^{-3}	4.29×10^{-3}	7.57×10^{-3}
5 pm	6.91×10^{-3}	1.89×10^{-3}	1.19×10^{-3}	1.89×10^{-3}	3.20×10^{-3}
7 pm	7.55×10^{-3}	2.18×10^{-3}	1.33×10^{-3}	2.42×10^{-3}	4.80×10^{-3}
Average	7.89×10^{-3}	2.67×10^{-3}	1.36×10^{-3}	2.75×10^{-3}	6.47×10^{-3}

Source Authors

3.3 Determination of Detention Time

We have taken a 14.3 km (Thergaon Boat Club to Bopodi) stretch of river. The area velocity method was employed to calculate the velocity of water. The calculated velocity and distance of 14.3 km was used to determine the detention time. The formula associated with area–velocity method is as follows:

$$Q = A \cdot v \tag{2}$$

where

Q = discharge
A = cross-sectional area
$v = d/t$, velocity = distance/time.

The detention time calculated is 4 h and 20 min. This implies that the time required for improvement of 4.4 MLD wastewater will be 4 h and 20 min. These are the basis for the design of the detention tank used for the work.

3.4 Design of Tank

In the model, a tank of the capacity of 175 L having the dimension 88 cm × 45 cm × 45 cm was used. The detention time necessary for the wastewater improvement is maintained by providing a zigzag flow, using baffle walls. The zigzag flow is regulated by providing holes on alternate baffles at 1 cm from the top and 1 cm from

Table 3 Components and specifications of the model

Sr. No.	Component	Specification
1	Dimension of tank	88 cm × 45 cm × 45 cm
2	Baffle walls	Three number of acrylic sheets with thickness 8 mm and places 22 cm apart in the tank
3	Inlet and outlet	These are provided at diagonally opposite sides of the tank with a level difference of 5 cm
4	Drainage valves	Provided for washing and cleaning purposes.
5	Detention period	4 h 20 min
6	Inlet tank	An inlet tank is provided with a plastic pipe connection
7	Deflection resistance net	An iron net is provided at the top to resist the deflection in the tank

Source Authors

the bottom of the baffle walls. The inlet is provided at 5 cm from the top and outlet at 10 cm from the top on the diagonally opposite side of the tank to maintain the desired flow. The specifications of the model are as follows (Table 3).

3.5 Sampling

The sampling was done at four selected intrusions and one sample was a mixture of all the previous four samples. The water lettuce was transplanted with equal density on the surface of water collected from the Pawana River. Adequate provision was made to transfer the wastewater from the intrusions to the model employed for the work (Figs. 3 and 4).

The sample was taken by filling the inlet tank with 118-L wastewater. In the tank, 1.5-kg water lettuce was maintained, for attaining an equal density of the plants. The wastewater was allowed to flow through the tank for a detention period of 4 h and 20 min. The samples in the quantity of 2 L were taken at the inlet and outlet of the tank and transferred to the laboratory for further experimental investigation. Adequate precautions were taken to preserve the sample before taking to the laboratory. Safety measures were taken by the persons involved in taking the samples from the river. This includes the use of hand gloves, washing of hands before and after the sample is taken using soap, and the use of masks if required. It the process of transplantation of water lettuce from the river to the model, adequate precaution was taken to make the plants adaptable to the atmosphere in which the model is established. To establish the model, an adequately shaded area was selected after investigation.

Fig. 3 Model preparation and execution [Identity of persons in the Fig. 1 (from left) Jayeshkumar Maheshkumar Bhagwat, Vikrant S. Thakur, Mayur G. Ubhe, Pradip D. Pawar, Tushar S. Sarade, Jayeshkumar Maheshkumar Bhagwat, and Vikrant S. Thakur] *Source* Authors

3.6 Laboratory Test

The samples collected from the model and tested in the laboratory. The tests conducted in this work are as follows:

1. pH
2. TDS
3. Hardness
4. Conductivity
5. Alkalinity
6. Total solids
7. DO
8. BOD
9. COD
10. Lead

Fig. 4 Sample collection at different intrusions. [Identity of persons in the Fig. 1. In sample 1. Jayeshkumar Maheshkumar Bhagwat. In sample 2. (from left) Ujjwala Chavhan, Tushar S. Sarade, Vikrant S. Thakur, Swati Kurvade, and Ranjana Gore. In Sample 3. (from left) Ujjawala Chavhan, and Pradip D. Pawar, sample 4. (from left) Pradip D. Pawar, and Mayur G. Ubhe.] *Source* Authors

11. Nitrate
12. Iron
13. Total phosphorus.

4 Results

The experiments required for the selected parameters were employed and results were drawn for future discussions. The removal or reduction in the specific parameter was documented.

4.1 pH

Rapid photosynthesis process by the algae and water lettuce in the tank consumes CO_2 faster than it can be replaced by bacterial respiration. The algae and water lettuce

Table 4 pH values obtained after an experimental investigation

Sampling at	Inlet	Outlet
Morya gosavi temple	8	7.25
Kalewadi	7.23	7
New sangvi	7.94	7.42
Bopadi	7.5	7.65
All intrusion mix	6.95	7.42

Source Authors

Table 5 Total dissolved solids (TDS) values obtained after an experimental investigation

Sampling at	Inlet (mg/l)	Outlet (mg/l)	Removal (%)
Morya gosavi temple	164	144	12.19
Kalewadi	297	201	32.32
New sangvi	339	273	19.47
Bopadi	302	398	–
All intrusion mix	132	356	–

Source Authors

fix the resulting CO_2, and the hydroxyl ions accumulate, this results in the rise of pH value near 8. This phenomenon could be clearly observed in the results at the outlet as provided in Table 4.

4.2 Total Dissolved Solids (TDS)

TDS test measures all suspended solids which may or may not pass through the filter. It is the number of particles that are dissolved in water. The amount of TDS in rivers ranges from 100 to 20,000 mg/l. The dissolved solids containing chemicals, such as nitrogen and phosphorus, which are apparently removed by water lettuce in our experimental investigations are provided in Table 5.

4.3 Hardness

Hardness is a chemical parameter of wastewater that represents the total concentration of Ca^{++} and Mg^{++} ions. Calcium ions consist of 2/3 of hardness and 1/3 of total hardness [21]. The results obtained from the experiments employed as provided in Table 6, reduces hardness for certain samples but the reduction is insufficient to be considered and draw conclusions.

Table 6 Hardness values obtained after an experimental investigation

Sampling at	Inlet (mg/l)	Outlet (mg/l)	Reduction (%)
Morya gosavi temple	130	125	3.85
Kalewadi	204	150	26.47
New sangvi	215	260	–
Bopadi	243	280	–
All intrusion mix	105	205	–

Source Authors

Table 7 Conductivity values obtained after an experimental investigation

Sampling at	Inlet (μmho/cm)	Outlet (μmho/cm)
Morya gosavi temple	130	125
Kalewadi	204	150
New sangvi	215	260
Bopadi	243	280
All intrusion mix	105	205

Source Authors

4.4 Conductivity

Conductivity measures the ability of the aqueous solution to carry an electric current. The conductivity of domestic sewage wastewater ranges from 50 to 1500 μmho/cm [22]. The conductivity of wastewater indicates the quantity of dissolved inorganic present in water. Wastewater has a normal range of conductivity associated with the dissolved solids in the concentration in wastewater. It was observed in this work that dissolved solids decrease apparently, and hence conductivity decreases, as provided in Table 7.

4.5 Alkalinity

Alkalinity is a measure of the substances in water that have "acid-neutralizing" ability. Alkalinity indicates a solution's power to react with acid and buffer its pH—i.e., the power to keep its pH from changing [23]. The pH value measures the strength of acid and alkalinity measures the ability to neutralized acid. Alkalinity provides a buffering capacity to the aqueous system. The higher the alkalinity, the higher is the buffering capacity against pH changes [24]. In this work, it was observed, as provided in Table 8, that increment in alkalinity is observed at two locations.

Table 8 Alkalinity values obtained after an experimental investigation

Sampling at	Inlet (mg/l)	Outlet (mg/l)	Increment (%)
Morya gosavi temple	360	280	–
Kalewadi	72	56	–
New sangvi	196	244	24.49
Bopadi	188	232	23.40
All intrusion mix	84	148	76.19

Source Authors

Table 9 Total solids values obtained after an experimental investigation

Sampling at	Inlet (mg/l)	Outlet (mg/l)	Removal (%)
Morya gosavi temple	200	180	10
Kalewadi	667	574	13.94
New sangvi	600	320	46.67
Bopadi	442	394	10.86
All intrusion mix	620	467	24.67

Source Authors

4.6 Total Solid

In the model employed for the work, it was observed that if a suitable detention time is provided, the solids get settled due to self-weight and accumulate at the bottom of the model. It is observed that the percentage of removal ranges from 10 to 46% as provided in Table 9.

4.7 Dissolved Oxygen

Water lettuce required Nitrogen (N), Phosphorus (P), and Potassium (K) for their growth. Water lettuce is very efficient in absorbing nutrient from the wastewater [25]. It is observed that there is a reduction in N, P, and K. The reduction in organic matter results in the increase in DO. The results provided in Table 10 show that the increase in DO is in the range of 10–46%.

Table 10 Dissolved oxygen (DO) values obtained after an experimental investigation

Sampling at	Inlet (mg/l)	Outlet (mg/l)
Morya gosavi temple	2.57	2.08
Kalewadi	2.6	1.99
New sangvi	6.12	5.53
Bopadi	6.85	7.86
All intrusion mix	4.16	6.11

Source Authors

Table 11 Biochemical oxygen demand (BOD) values obtained after an experimental investigation

Sampling at	Inlet (mg/l)	Outlet (mg/l)	Reduction (%)
Morya gosavi temple	10	11	–
Kalewadi	9	6	33.33
New sangvi	17	9	47.05
Bopadi	13	6	53.85
All intrusion mix	6	3	50

Source Authors

4.8 Biochemical Oxygen Demand (BOD)

It is observed that organic matter, i.e., N, P, and K in wastewater is used by water lettuce. The N, P, and K values reduce, so the requirement for BOD is also reduced [26]. In this work, the reduction in BOD is in the range of 33–54% as provided in Table 11.

4.9 Chemical Oxygen Demand

COD is the oxygen required by inorganic matter, such as iron. The rhizo-degradation of COD in the rhizosphere is brought about by the bioactivity between plant roots and microbes [27]. In this work, it was observed that iron decreases from the range of 50–100%. The reduction is observed in the inorganic matter as provided in Table 12, COD also reduces in the range of 40–50%.

4.10 Potassium

Aquatic plants use the potassium in the wastewater for their growth and development. The presence of potassium is due to various reasons; the presence and decomposition

Table 12 Chemical oxygen demand (COD) values obtained after an experimental investigation

Sampling at	Inlet (mg/l)	Outlet (mg/l)	Reduction (%)
Morya gosavi temple	63	66	–
Kalewadi	53	31	41.5
New sangvi	101	51	49.5
Bopadi	70	38	45.71
All intrusion mix	38	19	50

Source Authors

Table 13 Potassium values obtained after an experimental investigation

Sampling at	Inlet (mg/l)	Outlet (mg/l)	Reduction (%)
Morya gosavi temple	14	11	21.43
Kalewadi	31	16	48.39
New sangvi	35	11	68.57
Bopadi	36	32	11.11
All intrusion mix	17	14	17.65

Source Authors

of aquatic plants are one of the important reasons [28]. The reduction of potassium, as provided in Table 13, ranges from 10 to 68%.

4.11 Total Nitrogen

Nitrogen is present in wastewater due to similar reasons as the presence of potassium [28]. The removal of nitrogen by employing the model is 9–70% as provided in Table 14.

Table 14 Total nitrogen values obtained after an experimental investigation

Sampling at	Inlet (mg/l)	Outlet (mg/l)	Removal (%)
Morya gosavi temple	1.68	1.87	–
Kalewadi	2.05	1.87	8.78
New sangvi	18	5.51	69.38
Bopadi	10	7.65	23.5
All intrusion mix	2.89	1.86	35.64

Source Authors

Table 15 Iron values obtained after an experimental investigation

Sampling at	Inlet (mg/l)	Outlet (mg/l)	Removal (%)
Morya gosavi temple	0.151	0.023	84.76
Kalewadi	0.558	0.118	78.85
New sangvi	4.25	0.07	98.35
Bopadi	1.457	3.302	–
All intrusion mix	0.138	0.07	49.27

Source Authors

4.12 Iron

Water lettuce is a bioaccumulator as they accumulate contaminants, i.e., heavy metals in their tissues [29]. The results in the case of the removal of iron content in the wastewater are significant as provided in Table 15 and ranges vary from 49.23 to 98.35%.

4.13 Phosphate

Phosphate is present in wastewater. Aquatic plants use and store phosphate as per the requirement. The amount of phosphate is due to the presence and decomposition of aquatic vegetation. Phosphate decreases significantly in wastewater as this is an effective nutrient for water lettuce for the growth as provided in Table 16 and the range of removal is in the range of 54–93%.

Table 16 Phosphate values obtained after an experimental investigation

Sampling at	Inlet (mg/l)	Outlet (mg/l)	Removal (%)
Morya gosavi temple	1.384	0.1	92.77
Kalewadi	4.526	1.448	68
New sangvi	4.756	0.804	83.12
Bopadi	3.18	1.326	58.38
All intrusion mix	1.64	0.752	54.15

Source Authors

4.14 Analysis of Results

Wastewater released into the rivers is required to attain a set of quality parameters [30]. This work studies the parameters pertaining to river water improvement and establishes the facts about river water improvement using water lettuce. It is important to note that parameters like pH, total solids, BOD, COD, potassium, total nitrogen, iron, and phosphate showed a significant improvement. On the contrary, DO, alkalinity, hardness, TDS, and conductivity show optimistic results with less significance. The pH value is the indicator of the acidic, basic, or neutral nature of the sample. The process of photosynthesis consumes CO_2, the basis for the rise in pH is the faster replacement of CO_2 by bacterial respiration followed by fixation of resulting CO_2 and the hydroxyl ions [31]. The TDS are removed using this work [32]. The removal was observed in the initial stretch of the river due to the absence of TDS propelling industries like metal plating, electrical, and automobile [33]. Hardness in water results in scaling, if used for industrial purposes like boilers. It increases the cost of energy consumed during the process of heat exchange [34]. In this work, hardness assessment results were insignificant to be considered. Conductivity is a determinant of wastewater quality primarily in the coastal areas, the River Pawana and the adjoined area is considerably spaced from the coastal area. Conductivity showed significant results in terms of river water improvement [35]. The absence of conductivity impacting industries in the city is the expected reason for the samples with permissible conductivity.

In the case of alkalinity, an increment was observed at two different locations. The reason for this could be the presence of industrial activities which generate dissolved salts as a by-product or waste in the downstream side of the river [36]. Total solids are a result of the existence of the carbonates bicarbonates, chlorides, minerals, and organic silt. It is effectively removed from the samples under investigation due to the detention time provided by the model employed in this work. Oxygen for river water must be above 2 mg/l. [37]. The presence of oxygen in the water could be primarily enhanced by employing aeration. In this work, notable improvement of dissolved oxygen is attained. The reason lies in the reduction of organic matter in the water due to the absorption by water lettuce, i.e., DO content had increased due to the decrease in organic matter [25]. BOD is related to organic matter, i.e., N, P, and K contents in the wastewater [26]. In this work, a considerable amount of reduction of organic matter was observed; this is the premise for the reduction in the BOD in the samples under test. In the case of COD, the oxygen required for inorganic matter is determined. Researchers also proved that organic matter is a responsible factor for COD increase [38]. In this work, a considerable reduction of COD is documented. It is observed that K, P, and N are present in the sample due to the decomposition caused by the biotic elements in the river [28]. The K, P, and N contents are effectively reduced using water lettuce. It is significant to note the reduction of iron in the samples under investigation. Researchers noted that water lettuce is a bioaccumulator. A bioaccumulator possesses the characteristics of

accumulating contaminants in their tissues [38]. The same mechanism applied for heavy metals like iron and reduction is observed in the samples under investigation.

In this work, it is observed that, in certain parameters, the results are violating the expected outcomes. The reason which could be encountered for this is the manual errors, while sample collection and experimentation. The work was undertaken during the period of December 2015–August 2016.

5 Conclusion

In this work, we developed and employed a model for the study, the improvement of Pawana River water quality by using water lettuce. In this work, 13 different parameters related to wastewater were considered for experimentation. The parameters like pH, total solids, biochemical oxygen demand (BOD), chemical oxygen demand (COD), potassium, total nitrogen, iron, and phosphate show significant results in terms of improvement of the Pawana River water quality. The other parameters like dissolved oxygen (DO), alkalinity, hardness, total dissolved solids (TDS), and conductivity show optimistic results comparatively with less significance. Thus, it could be concluded that water lettuce shows a significant impact on the improvement of river water quality in the case of Pawana River in Pune Metropolitan Area.

6 Future Scope

In this age of rapid urbanization, it is becoming a challenging task for researchers to find context-specific solutions to the problems in the urban system. The model prepared could be replicated on the river bed of Pawana at the suitable intrusion and the result could be analyzed. The number of samples could be increased in order to enhance the reliability of the results. Water lettuce could be coupled with other aquatic plants like vetiver grass, water hyacinth, etc., and studies could be conducted as per the requirement of the context. The factors like storm water drainage could be considered while designing the detention tank.

Acknowledgments and Permissions This work was funded by the Board of College and University Development, Savitribai Phule Pune University, Pune (India). The authors wish to thank the Board of College and University Development (BCUD), JSPM's Rajarshi Shahu College of Engineering, Savitribai Phule Pune University, Pune (India) and Indian Institute of Technology, Roorkee (India), for the support and assistance for this work. The authors would also thank Mayur G. Ubhe, Pradip D. Pawar, Tushar S. Sarade, Vikrant S. Thakur, Swati Kurvade, Ujjwala Chavhan, Ranjana Gore, and Shweta Bembade for their contribution toward this work.

We have taken permission from the local governing authorities to collect the samples from the river body. We have also taken permission from Mayur G. Ubhe, Pradip D. Pawar, Tushar S. Sarade, Vikrant S. Thakur, Swati Kurvade, Ujjwala Chavhan, Ranjana Gore, and Shweta Bembade for using they photographs in the research paper.

References

1. MoWR.: Annual Report: 2017–18 (2018). http://mowr.gov.in/sites/default/files/Annual_Report_MoWR_2017-18.pdf. Accessed 10 May 2019
2. Guppy L, Anderson K (2017) Water crisis report. United Nations University Institute for Water, Environment and Health, Hamilton, Canada. https://inweh.unu.edu/wp-content/uploads/2017/11/Global-Water-Crisis-The-Facts.pdf. Accessed 25 Apr 2019
3. Opperman JJ, Orr S, Baleta H, Dailey M, Garrick D, Goichot M, McCoy A, Morgan A, Turley L, Vermeulen A (2018) Valuing rivers: how the diverse benefits of healthy rivers underpin economies. http://awsassets.panda.org/downloads/wwf_valuing_rivers__final_.pdf. Accessed 28 Apr 2019
4. UNICEF, FAO and SaciWATERs: water in India: situation and prospects. http://www.indiaenvironmentportal.org.in/files/file/water%20in%20india.pdf. Accessed 15 Apr 2019
5. United Nations Human Settlements Programme (UN-HABITAT) (2003) Water and sanitation in the world's cities local action for global goals. https://unhabitat.org/wp-content/uploads/2016/01/Water%20and%20Sanitation%20in%20the%20World%E2%80%99s%20Cities%20Local%20Action%20for%20Global%20Goals%20.pdf. Accessed 17 Apr 2019
6. Tripathi S (2018) Do economic reforms promote urbanization in India?. Munich Personal RePEc Archive. https://mpra.ub.uni-muenchen.de/86591/. Accessed 13 Apr 2019
7. Butsch C, Kumar S, Wagner P, Kroll M, Kantakumar L, Bharucha E, Schneider K, Kraas F (2017) Growing "Smart"? urbanization processes in the Pune urban agglomeration. Sustainability 9:2335
8. Chadchan J, Shankar R (2012) An analysis of urban growth trends in the post-economic reforms period in India. Int J Sustain Built Environ 1:36–49
9. Hui R, Wescoat J (2018) Visualizing peri-urban and rurban water conditions in Pune district, Maharashtra, India. Geoforum
10. Census: District census handbook (2011) Directorate of census operations. New Delhi. http://censusindia.gov.in/2011census/dchb/2725_PART_B_DCHB_%20PUNE.pdf. Accessed 22 Apr 2019
11. Pimpri Chinchwad Municipal Corporation (2014) System of assisting residents and tourists through helpline information (SARATH). Pimpri Chinchwad Municipal Corporation, Pimpri Chinchwad
12. Pimpri-Chinchwad Municipal Corporation (2000) Draft development plan-2021. Tata Consultancy Services, Pune
13. Kendre L, Gawande S, Pawar A (2017) Study of physico-chemical characteristics of Pavana river: review. Int J Eng Res 6:216
14. Wang J, Fu G, Li W, Shi Y, Pang J, Wang Q, Lü W, Liu C, Liu J (2018) The effects of two free-floating plants (*Eichhornia crassipes* and *Pistia stratiotes*) on the burrow morphology and water quality characteristics of pond loach (*Misgurnus anguillicaudatus*) habitat. Aquac Fish 3:22–29
15. Lu J, Fu Z, Yin Z (2008) Performance of a water hyacinth (*Eichhornia crassipes*) system in the treatment of wastewater from a duck farm and the effects of using water hyacinth as duck feed. J Environ Sci 20:513–519
16. Gupta P, Roy S, Mahindrakar BA (2012) Treatment of water using water hyacinth, water lettuce and vetiver grass—a review. Resourc Environ 2:202–215
17. Deshmukh A, Bandela N, Chavan J, Nalawade P (2011) Studies on potential use of water hyacinth, *Pistia* and *Azolla* for municipal waste water treatment. Ind J Appl Res 3:226–228
18. Gupta P, Roy S, Mahindrakar A (2012) Treatment of water using water hyacinth, water lettuce and vetiver grass—a review. Resourc Environ 2:202–215
19. Jain N, Shrivastava R (2014) Comparative review of physicochemical assessment of Pavana river. IOSR J Environ Sci Toxicol Food Technol 8:25–30
20. Hussain J, Husain I, Arif M, Gupta N (2017) Studies on heavy metal contamination in Godavari river basin. Appl Water Sci 7:4539–4548

21. Tahvildari K, Jafari MJ, Sharif A, Nazarpoor P (2016) Remove water Hardness from water and wastewater by using magnetic field. J Curr Res Sci 237–239
22. Gautam S Guide manual: water and wastewater analysis. http://cpcb.nic.in/openpdffile.php?id=UmVwb3J0RmlsZXMvMjA0XzE1MjQ2NTA4OTNfbWVkaWFwaG90bzEyODI3LnBkZg==
23. Boyd C, Tucker C, Viriyatum R (2011) Interpretation of pH, acidity, and alkalinity in aquaculture and fisheries. North Am J Aquac 73:403–408
24. Ibanez J (2008) Environmental chemistry. Springer, New York
25. Eddiwan K, Fawani E, Janatul Magwa R (2018) Growth and N and P absorption capability of *Pistia stratiotes* cultured in the inorganic fertilizer enriched media. Int J Mar Biol Res. 3:1–9
26. Shah M, Hashmi H, Ali A, Ghumman A (2014) Performance assessment of aquatic macrophytes for treatment of municipal wastewater. J Environ Health Sci Eng 12:106
27. Boyles W The science of chemical oxygen demand. https://www.hach.com/asset-get.download.jsa?id=7639984471
28. Little E (1979) Handbook of utilization of aquatic plants. Food and Agriculture Organization of the United Nations, Rome
29. Lu Q, He Z, Graetz D, Stoffella P, Yang X (2011) Uptake and distribution of metals by water lettuce (*Pistia stratiotes* L.). Environ Sci Pollut Res 18:978–986
30. Manual on sewerage and sewage treatment systems—2013: central public health & environmental engineering organisation (CPHEEO), Govt of India. http://cpheeo.gov.in/cms/manual-on-sewerage-and-sewage-treatment.php
31. Luklema L (1969) Factors affecting pH change in alkaline waste water treatment—I. Water Res 3:913–930
32. Ali N, Mo K, Kim M (2012) A case study on the relationship between conductivity and dissolved solids to evaluate the potential for reuse of reclaimed industrial wastewater. KSCE J Civil Eng 16:708–713
33. Basha C, Ghosh P, Gajalakshmi G (2008) Total dissolved solids removal by electrochemical ion exchange (EIX) process. Electrochim Acta 54:474–483
34. Chen Y, Fan R, An D, Cheng Y, Tan H (2016) Water softening by induced crystallization in fluidized bed. J Environ Sci 50:109–116
35. De Sousa D, Mozeto A, Carneiro R, Fadini P (2014) Electrical conductivity and emerging contaminant as markers of surface freshwater contamination by wastewater. Sci Total Environ 484:19–26
36. Triphati N How to maintain alkalinity in wastewater. https://sciencing.com/maintain-alkalinity-wastewater-8740862.html
37. Dissolved oxygen measurement in wastewater treatment. https://www.emerson.com/documents/automation/application-data-sheet-dissolved-oxygen-measurement-in-wastewater-treatment-rosemount-en-68468.pdf
38. Lee Y, Kang C (2010) Causes of COD increases in Gwangyang Bay, South Korea. J Environ Monit 12:1537

Non-parametric Trend of Drought and Its Future Applicability: A Case Study of Sagar Station

A. Vishwakarma, M. K. Choudhary, and M. S. Chauhan

Abstract Drought is a dominant factor for major deficiency of water, especially for agriculture. This study deals to understand the changing pattern of key climatic variables along with the PET and understanding the drought status of Sagar District, Madhya Pradesh, India, which is also a part of Bundelkhand; a severe drought-affected region of Madhya Pradesh and Uttar Pradesh. Water resources clearly affected due to the change in temperature and rainfall patterns. Hence, the increase in temperature would result in higher evapotranspiration rate and higher need for agricultural water requirement. To achieve the rainfall pattern, trends in monthly, annual, and seasonal rainfall time series from 1977 to 2010 have been examined by Mann–Kendall test and Sen's slope for Sagar District. There is a negative trend of rainfall seen in the month of August with Sen's slope value as −5.65 mm/year. PET evaluated using the Hargreaves method for Sagar Station using minimum and maximum temperature data of duration 1989–2013. Trend analysis of drought has been assessed by using the same method used for rainfall trends. Two drought indices, SPI and RDI, are used for the study area. A *T*-test is performed for yearly values of SPI and RDI (1989–2013) and statistical significance is checked for the mean values.

Keywords DrinC: drought indices calculator · PET: potential evapotranspiration · RDI: reconnaissance drought index · SPI: standardized precipitation index

1 Introduction

A drought index is a single-number value utilized for showing the extremity of drought, and those indices broadly classified under four major parts as meteorological, agricultural, hydrological, and socioeconomic droughts [1]. Sagar has a long-standing history of drought but the frequency and extremity of drought have risen over earlier decades. It makes it more important to see the trend of drought whether it is increasing or decreasing. The current study deals to know about drought events

A. Vishwakarma (✉) · M. K. Choudhary · M. S. Chauhan
Department of Civil Engineering, Maulana Azad National Institute of Technology, Bhopal, India
e-mail: ankur18vishwa@gmail.com

© Springer Nature Singapore Pte Ltd. 2021

K. K. Pathak et al. (eds.), *Recent Trends in Civil Engineering*, Lecture Notes in Civil Engineering 77, https://doi.org/10.1007/978-981-15-5195-6_68

and their trend on various time scales as well as the trend of responsible key meteorological variables. It has also tested the accuracy of indices whether they fit for prediction of the future scenario of drought or not.

2 Study Area and Data

Sagar District is a divisional headquarter of Sagar Division of Madhya Pradesh in India, which is located between 23.10″ and 24.27″ North (Latitude) and 78.4″and 79.2″ East (Longitude). It is situated upon a spur of the Vindhya Range and 1,758 feet above sea level of Madhya Pradesh (Fig. 1). Sagar District has a population density of 147 per km^2. It splits into 7 tahsils and 11 blocks [2].

Daily rainfall data of Sagar Station (1977–2013) were used for this study. The data have been collected from the Department of Water Resources, Sagar (MP).

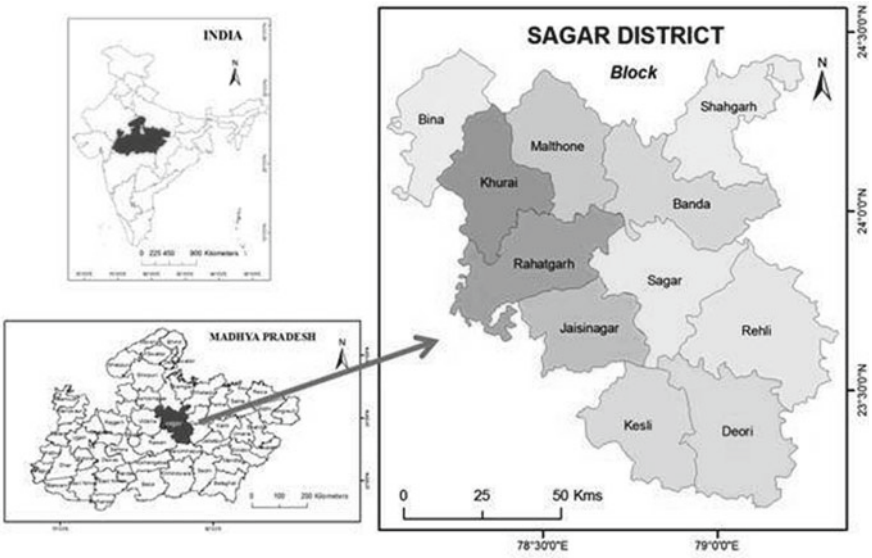

Fig. 1 Location of Sagar District in Madhya Pradesh, India [2]

3 Methodology

3.1 Trend and Variability Analyses

Trend analysis is a technique of predicting future scenarios by utilizing historical results. In this study, the first approach is to find non-parametric trends using the Mann–Kendall test and the next is to find the magnitude and the way of change using Sen's slope estimator [3]. The increasing/decreasing trends have been analyzed using the normalized test statistics value (Z). The positive value of Z shows an increasing trend, while a negative value indicates a diminishing trend. The slope of the trend represents the rate of change and its direction annually.

3.2 Assessment of Drought

DrinC (Drought Indices Calculator) model is used to evaluate two drought indices, SPI and RDI [4]. SPI calculation uses only rainfall data [5], while RDI uses both rainfall and temperature data, which makes it more effective as two meteorological elements are involved here [6].

3.3 T-Test

A *t*-test is a type of probabilistic statistic used to define if there is a notable difference among the means of two groups, those may be related to certain characteristics. It is used as a hypothesis testing tool. If the hypothesis is accepted, there will be no significant difference in concerned groups [7]. The purpose of this test is to see the applicability of SPI and RDI values simultaneously for future projection, while there will be no significant difference seen in their yearly values.

4 Results

4.1 Rainfall Trend

Trend result of 33 years precipitation data of Sagar station at 95% significant level is shown in Table 1.

Hence, from the given table, there is no trend seen in rainfall annually as well as seasonally for Sagar Station, because the Z-Value doesn't come in 95% significance

Table 1 Precipitation trend and Sen's slope

S. no.	Rainfall (mm)	*Z*-value	Sen's slope (β)
1.	Annual	−0.29	−2.028
2.	Summer	1.00	0.465
3.	Monsoon	−0.57	−4.009
4.	Winter	0.33	0.860
5.	Spring	−1.42	−0.831

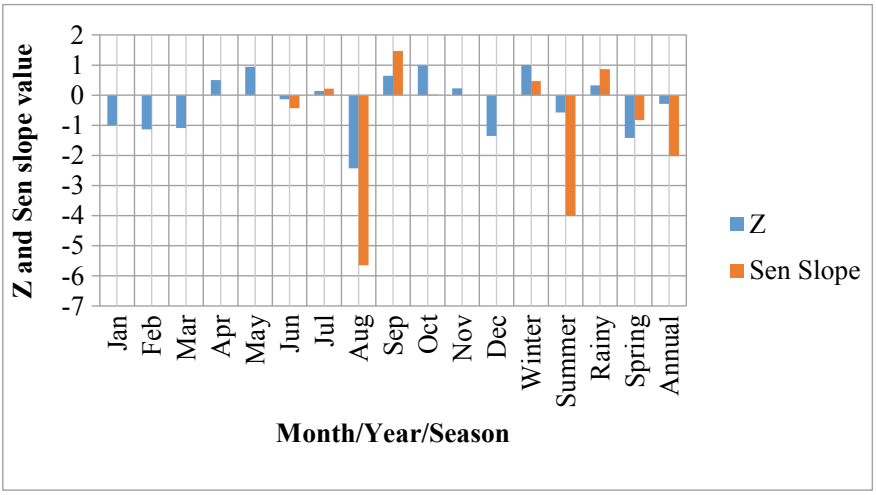

Fig. 2 Rainfall trend over 33 years of Sagar station (1977–2009)

level. There is a negative trend seen in the month of August with Sen's slope value as −5.65 ($Z < -1.96$) which can be seen in Fig. 2.

5 Drought Indices Trend

Monthly SPI and RDI values of 25 years for Sagar Station can be seen on the basis of their severity level in the chart shown in Fig. 3.

From the above calculation, severe drought can be seen in the year of 2001–2002 and 2006–2007 for Sagar Station during 1989–2013. As per the Mann–Kendall trend analysis, there is no trend seen of drought (SPI as well as RDI) for any of the time scale (monthly, yearly, and seasonally) for Sagar Station.

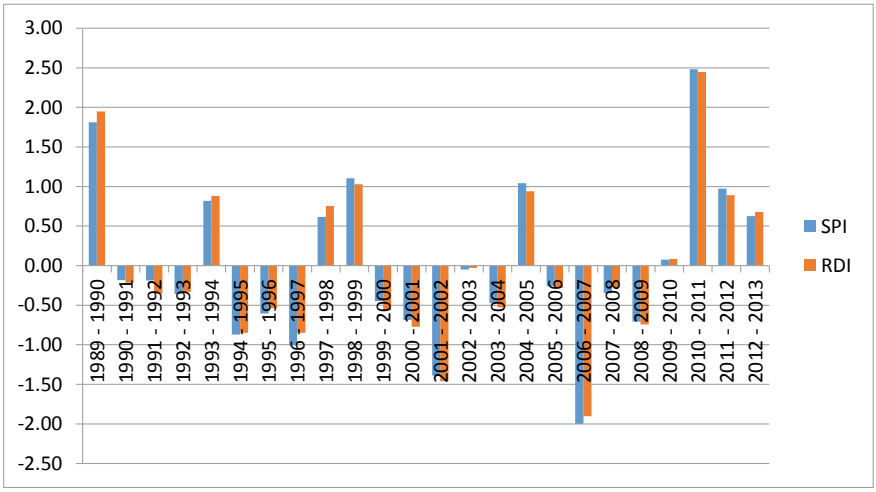

Fig. 3 Yearly trend of SPI and RDI

Table 2 Paired SPI and RDI for means

	Variable 1 (SPI)	Variable 2 (RDI)
Mean	−0.0012	−0.0016
Variance	1.0432	1.0431
Observations	24	24
Pearson correlation	0.9964	
Hypothesized mean difference	0.00	
Df (Degree of freedom)	23	
t Stat	0.0185	
$P(T <= t)$ one-tail	0.4927	
t Critical one-tail	1.7139	
$P(T <= t)$ two-tail	0.9854	
t Critical two-tail	2.0687	

5.1 T-Test for Mean

Performing t-test for yearly values of SPI and RDI (1989–2013) and their statistical significance are checked for their means. Both indices show a higher correlation as well as hypothesis accepted at *p*-value (probability value) of 5% for both one-tail and two-tail tests (Table 2). It concludes that SPI and RDI values show very similar yearly results and can be used simultaneously for future projections.

6 Conclusions

There is a negative trend of rainfall seen in the month of August for Sagar Station and no trend seen for other months as well as for any season. Even there is no trend found for SPI and RDI indices monthly, seasonal, and yearly. Hence, there is no trend of drought for Sagar Station. It makes mandatory to improve our study by predicting drought using the climate change model, those can clear a better picture of future drought for the study region, especially for severe drought-prone zones so that mitigation strategies can be preceded on time. To achieve this, SPI and RDI should be used parallelly as SPI only depends on rainfall, while RDI on rainfall as well as temperature so that the effect of both rainfall and temperature would be reflected.

As the *t*-test shows high similarity in SPI and RDI values, both can be performed for future prediction of drought in the absence of a significant trend.

References

1. Sridhar L, Guhathakurta P, Hatwar HR, Pai DS (2010) Districtwise drought climatology of the southwest monsoon season over india based on standardized precipitation index (SPI) DS pai
2. Som KS, Mishra RP (2018) Impact of family welfare programme on fertility and its socio-economic determinants in Sagar district. Int J Res Geogr (IJRG) 47–60
3. Mondal A, Kundu S, Mukhopadhyay A (2012) Rainfall trend analysis by Mann-Kendall test: a case study of north-eastern part of Cuttack district, Orissa. Int J Geol Earth Environ Sci 2(1):70–78
4. Tigkas D, Vangelis H, Tsakiris G (2015) DrinC: a software for drought analysis based on drought indices. Earth Sci Inf 8(3):697–709
5. McKee TB, Doesken NJ, Kleist J (1993) The relationship of drought frequency and duration to time scales. In: Proceedings of the 8th Conference on Applied Climatology, vol 17, no 22. pp 179–183
6. Tsakiris G, Vangelis H (2005) Establishing a drought index incorporating evapotranspiration. Eur Water 9(10):3–11
7. Feng YC, Huang YC, Ma XM (2017) The application of Student's t-test in internal quality control of clinical laboratory. Front Lab Med 1(3):125–128

Effect of Dam Reservoir Interaction on Response of Dam Subjected to Dynamic Load

Pooja D. Girme and Manisha V. Waghmare

Abstract Gravity dams are solid structures that maintain their stability against design loads due to their geometric shape, mass, and material strength. In access to the static water pressure, the dam undergoes dynamic forces from the reservoir when the system is subjected to earthquake ground motion. When the structure and the fluid are placed alongside and affected by the same base acceleration, fluid, and structure interaction problem becomes important and it causes changes in responses of both of these parts. The available literature review shows that most of the analysis work is done to study the dynamic effect on dams but reservoir dam structure interaction is neglected. The Eulerian approach has been adopted to investigate the dynamic behavior and the interaction phenomenon of the dam–reservoir system. The structures are modeled and analyzed using ANSYS WORKBENCH R.16 Software. The response of the dam structure subjected to excitation of the Koyna earthquake, 1967, is studied. An arbitrary section of gravity dam has been chosen for the extensive analysis such that it is an economic section and satisfies all the conditions and requirements of stability. The results of maximum hydrodynamic pressure, pressure contour, crest displacement; stresses are obtained by time history analysis for the Koyna earthquake, 1967, using ANSYS. The results obtained demonstrate that the dam reservoir interaction is significantly affected by the reservoir filled capacity when subjected to earthquake response.

Keywords Dam–reservoir interaction (DSI) · Concrete dam · ANSYS · Fluent

P. D. Girme (✉) · M. V. Waghmare
Department of Civil Engineering, AISSMS COE, Pune 411001, India
e-mail: girmepooja111@gmail.com

M. V. Waghmare
e-mail: mvwaghmare@aissmscoe.com

© Springer Nature Singapore Pte Ltd. 2021

K. K. Pathak et al. (eds.), *Recent Trends in Civil Engineering*, Lecture Notes in Civil Engineering 77, https://doi.org/10.1007/978-981-15-5195-6_69

1 Introduction

A concrete gravity dam is a submerged structure with complicated geometry and complex behavior under seismic conditions. The issues of seismic safety of dams have been looked at with special attention in various parts of the world in recent years. It has become a major factor in the planning and designing of new dams proposed to be built in seismic regions and for safety evaluation of existing dams in these regions. The analysis of concrete dams, including earthquakes, forces tend to several difficulties to evaluate the dam's dynamic stress, the result of the dam–reservoir system interaction, and the assessment of the impact regarding the parameters involved. It is presumed to retain the water stored in the reservoir and to resist the unpredictable earthquakes without unacceptable damages in seismic prone areas. When an earthquake occurs and reservoir level dangerously fluctuates the stresses may exceed the calculated values leading to failure of the dam. In addition to the static water pressure, the dam is subjected to dynamic forces from the reservoir when the system is subjected to earthquake ground motion. The magnitude of this additional hydrodynamic force is quite significant and may lead to crack initiation and propagation in the dam even under a moderately strong seismic event. When a dam or any other structure with water is subjected to an earthquake, one of the dynamic loads will be hydrodynamic pressure. In dam–reservoir interaction problem, the reservoir, and the dam do not vibrate separately, but they act together in a coupled way under external excitations. The pressures at the dam–reservoir interface due to the reservoir will affect the response of the dam.

Many researchers have worked on the static and dynamic behavior of dams considering dam–reservoir–foundation interaction using different water modeling approaches. H.M. Westergaard carried out the first hydrodynamic analysis on the dam–reservoir system. Especially, the concept of added mass was introduced for the incompressible water reservoir. [1] work has given a comprehensive study of the damped forced motion of a gravity dam during horizontal ground motions. In the occurring of a major earthquake, it is recognized that the structure will be stressed beyond its elastic limit and thus a significant structural damage may occur. [2] used FEM for analyzing the two-dimensional (2D) response of reservoir–dam systems subjected to horizontal ground motion. P. [3] presented the analysis of concrete gravity dams, accounting the dynamic effects of stored water and flexible foundation rock, to the transverse (horizontal) and vertical components of earthquake ground motion. [4] has developed a numerical scheme to deal with arbitrary geometries of the reservoir of arch dams. Effects of water compressibility, flexibility of the dam, energy radiation in infinite reservoir, and vertical ground motion contributions are studied. [5] extended the method for the earthquake analysis of concrete gravity dams, including the dynamic effects of the impounded water and the flexible foundation rock. [6] continued the work in linear response of a concrete gravity dam monolith to harmonic horizontal or vertical ground motion, for a range of the important system parameters that characterize the properties of the dam, foundation rock,

impounded water, and reservoir bottom materials. [5] simplified the analysis procedure to include the effects of dam–foundation rock interaction and reservoir bottom sediments, in addition to the effects of dam–water interaction and water compressibility included in the earlier procedure. The gravity dam–water–foundation system including the physical and mechanical properties of the sediment at the reservoir bottom is modeled [7]. [8] in his study performed the 2D analysis of a gravity dam–reservoir system using both the Eulerian and Lagrangian techniques, the effects of the variation of fluid compressibility on the model behavior were first determined. [9] The nonlinear seismic fracture response of concrete gravity dams is performed, and the dam–reservoir interaction is accounted for in the time domain analysis using the staggered solution technique. [10] performed the numerical simulation of the displacement response history of a real-life system to a known earthquake excitation using the FEM and specially developed interface elements have been employed to model the discontinuities of the structure. [11] presented a numerical algorithm for the dynamic analysis of a concrete dam in the area of an infinite reservoir with the use of damage mechanics including fluid–structure interaction. The time-dependent degradation of concrete owing to environmental factors and mechanical loading in terms of isotropic damage index is considered. [11] presented a dynamic analysis of the Koyna dam excited to the koyna earthquake to determine the aging effect on the behavior of concrete gravity dams. The performance of an aged dam with a known percentage of isotropic or orthotropic damage due to seismic excitation is studied. [12] performed a study about the comparison of coupled and decoupled modal approaches in seismic analysis for concrete gravity dams. [13] identified the factors that influence significantly the three-dimensional (3D) analysis of arch dam. Heydari and Mansoori discussed on dam–reservoir interaction modeling approaches using different finite element software's considering dynamics earthquake loads. [14] addressed the problems being involved in the dynamic interaction of solids (structure and foundation) with a liquid (water). Response of a structure subjected to seismic excitations is accounted. [15] developed an efficient approach for the hydrodynamic analysis of dam–reservoir systems. A dynamic velocity flow and pressure have been considered with the approach of two-way coupling partitioned method for the weak and strong coupled systems in ANSYS FEA software. [16] presented an analytical solution for a fluid–structure system regarding dam–water system. [17] compared the two methods and made sure the reality that the finite element is more reasoned than stiff mass body limit equilibrium method for analyzing the stability of concrete gravity dam. [18] analyzed the effect of the nonlinear dynamic behavior of the Oued el Fodda concrete dam and both cases near- and far-fault ground motion is taken into account. [15] Numerical results are obtained on the hypothetical models for the close and open-spillways concrete gravity dam. The partitioned two-way coupling method is applied to the dynamic velocity flow and pressure using the ANSYS FEA software. [19] carried out seismic analysis of concrete dam with concern to foundation effects and considering the dam interaction effect with bed Lake and lake. [20] FEM was used to model the water–dam structure using utilizing ANSYS code. The dam–water–foundation soil system using added mass and Lagrangian approaches is

investigated. An ANSYS-based finite element formulation was developed for static structural analysis of gravity dams.

From literature review, it is observed that the fluid–structure interaction is one of the problems which have been the subject of many researchers for decades. Finite element techniques for the linear elastic analysis of the responses of concrete gravity dams to earthquake excitations are well accepted in the literature and they are very often used in practice. Dynamic response of concrete gravity dams using different water modeling approaches: Westergard, Lagrange, and Euler approaches are studied. Comparative analysis between various analytical methods and software has been used for the analysis of dam subjected to the dynamic load. The available literature review shows that most of the analysis work is done to study the dynamic effect on dams but reservoir–dam–structure interaction is neglected. Comparative study of 3D plain stress and 3D plain strain dam–reservoir modeling is not studied. Clearly, analysis to include accurately the effects of dam–reservoir interaction on the seismic response of concrete gravity dams is needed.

The present study is based on analyzing the effect of dam–reservoir interaction on the response of structure subjected to dynamic load. The aim of the current work is to examine the modeling effect of dam structure and reservoir due to the dynamic response. The Eulerian approach has been adopted to investigate the dynamic behavior and the interaction phenomenon of the dam–reservoir system. The structures are modeled and analyzed using ANSYS WORKBENCH R.16 Software. The response of the dam structure subjected to excitation of the Koyna earthquake, 1967, is studied. The dam–reservoir system is analyzed for 2D (Plane Stress) and 3D (Plane Strain) modeling for reservoir full condition. The time history analysis is carried out for the dam length of 1 m as well as with dam length of 800 m with and without FSI.

1.1 Fluid–Structure Interaction

Fluid–structure interaction, FSI, can be recorded as the coupling of fluid mechanics and structure mechanics. FSI problems include the classical multi-physics feature which occur in many engineering applications such as aerodynamics, wave propagation, wind turbines, bio-engineering, offshore structures, and bridges. FSI or multi-physics problems can be solved with either experimental or numerical simulations. The advance on Computational Fluid Dynamics (CFD) and Computational Structure Dynamics (CSD) has let the numerical simulations of FSI to be performed rapidly. The distressing on the concrete dam are caused by several parameters, that are compressibility of the impounded water, the various dynamic interactions which can be incorporated in the general term “dam–reservoir interaction,” the effect of surface (sloshing) waves, and the selection of an appropriate upstream boundary condition to represent the infinite extent of the reservoir in the upstream direction. FSI applications require a combination of fluid dynamics and structure mechanics

control. Fluid flow exerts hydrodynamic forces on a structure and deforms or translates the structure. Flow due to fluid can also newly change thermal stresses within the structure. Deformed or translated structure exerts velocity to the water surface and changes its shape and thus changes the fluid flow. In order to evaluate FSI problems, three approaches have been developed in the past: the added mass approach; the Eulerian approach and the Lagrangian approach.

1.2 Eulerian Formulation

Euler approach is used on large scale in the FEA for dams considering FSI. In this approach, the structure and fluid motions are conveyed with displacements and pressures, respectively. Structure and fluid moves combinable found on FSI. Hence, specific interface equations must be identified. In the Eulerian approach, the analysis of a fluid–structure (dam–reservoir) has been based on the substructure has been an abstract idea in which fluid and structure are treated as two substructures. Hydrodynamic pressures in the reservoir are available from the solution of the wave equation, which is obtained for the fluid, for the suitable boundary conditions. It is presumed that the motion of the fluid takes place only due to the excitation at the FSI, and there are no surface waves on the free surface. When we focus on Eulerian approach, the displacements are the changeable in the structure and the pressures are the variables in the fluid; hence, a high configuration computer program is necessary to obtain the solution of the coupled systems.

1.3 Plane Stress Condition (2D Problems)

This is a state of stress when all the stresses act in a single plane, i.e., the direct as well as shear stresses perpendicular to the plane are zero. Generally, thin structural members loaded in their plane are considered to be in plane stress condition. Plane stress analysis is performed for structures loaded in their plane such as plates. Only a unit thickness of these structures is considered for analysis because all unit thicknesses except near the ends of the structure behave identically. A thin planer structure having uniform thickness and loading within the plane of structure (x–y plane) are shown in Fig. 1.

Plane stress: $\sigma_X = \tau_{YZ} = \tau_{ZX} = 0 (\varepsilon_Z \neq 0)$.

1.4 Plane Strain Condition (3D Problems)

If there are no strains out of the plane, i.e., the strains perpendicular to the plane being considered, or any components, therefore, are all zero, then this condition is called the

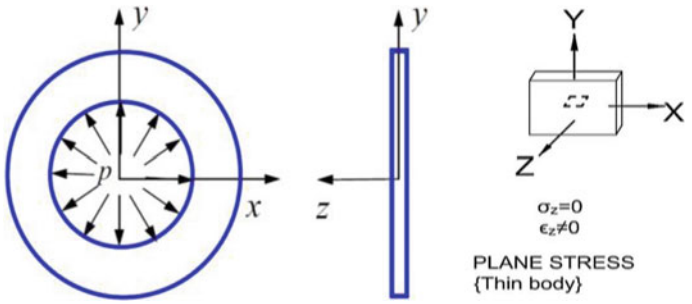

Fig. 1 Plane stress problem

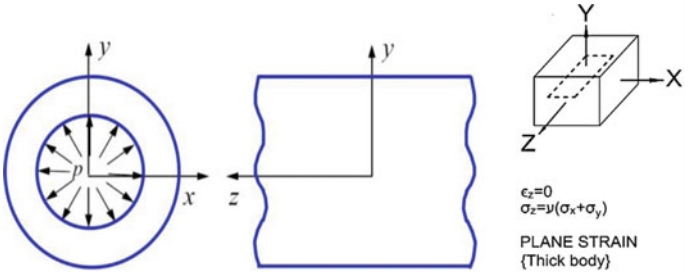

Fig. 2 Plane strain problem

plane strain condition This happens in long bodies with constant cross-sectional area and loads acting in x or y directions only with a constant value along the z-direction. Plane strain analysis is performed generally for long structures subjected to constant load along their length such as dams, culverts, etc. A uniform long structure with a cross section at transverse loading along its length (z-direction) is shown in Fig. 2.

Plain strain: $\varepsilon_Z = \gamma_{YZ} = \gamma_{ZX} = 0(\sigma_Z \neq 0)$.

2 Modeling and Assumptions

In the present study, results of a FEA of a reservoir–gravity dam system by using ANSYS Release 16.0.1 are presented. An arbitrary section of gravity dam has been selected for the analysis such that section is economic and assures all the conditions and requirements of stability. For the study, properties of the the Koyna dam are considered as given in Table 1 taken from research paper by Indrani Gogoi A and Damodar Maity (2005). In the dam body, the concrete is assumed homogeneous and isotropic. The water is considered as incompressible and in viscous flow. Fluid domain is modeled into a finite one using reservoir length $L = H$, in which H is the reservoir depth as shown in Fig. 3. The dam bottom condition is assumed completely

Table 1 Material properties

Material	Parameters	Values
Concrete	Mass density	2400 kg/m^3
	Modulus of elasticity	31500 MPa
	Poisson's ratio	0.235
Water	Unit weight of water	10 kN/m^3
	Acoustic wave velocity of water	1438.7 m/s

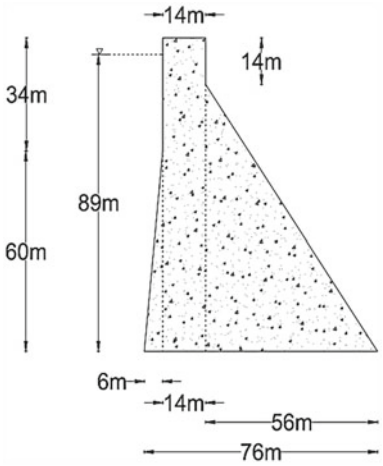

Fig. 3 Geometrical details of the gravity dam

fixed. While modeling, dam structure is modeled with fluent as water up to the reservoir level and, thereafter, as air up to freeboard. The dimensions of the dam are given in Figs. 3 and 4.

The structure (gravity dam) is assumed to be linear elastic and is analyzed by plane strain formulation. The water contained in the reservoir is considered an incompressible in viscous fluid. Surface gravity waves as well as reservoir bottom absorption effects are neglected. The selected FEM of the dam–reservoir system is modeled using Eulerian approach as shown in Fig. 5. The solid dam is discretized by using plane finite elements and the reservoir water is discretized by using fluid finite elements as presented in Fig. 5. The Koyna earthquake acceleration, 1967, as shown in Fig. 6 is applied (Fig. 7).

3 Analysis

In this analysis, interaction between dam and reservoir was considered and system foundation is considered to be fixed and dam interaction with soil is ignored. Here, the gravity dam section is modeled as 2D plain strain models as well as 3D models

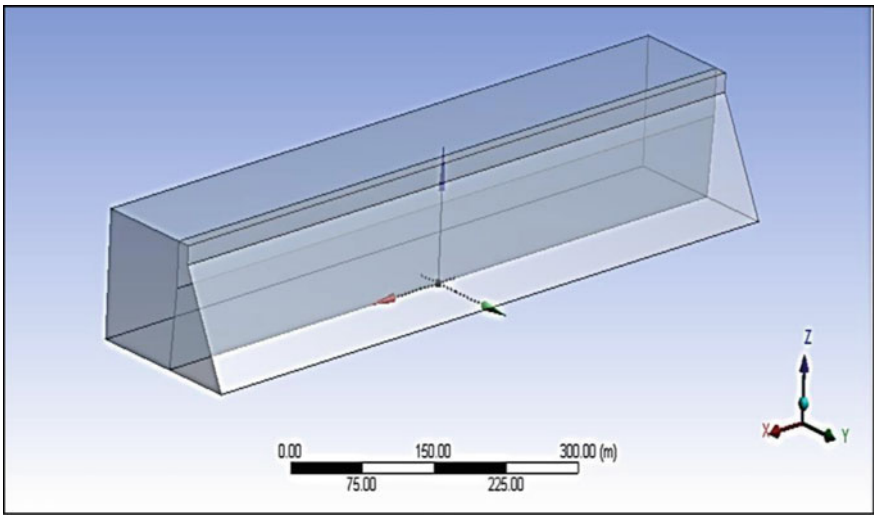

Fig. 4 Modeling of the gravity dam and reservoir

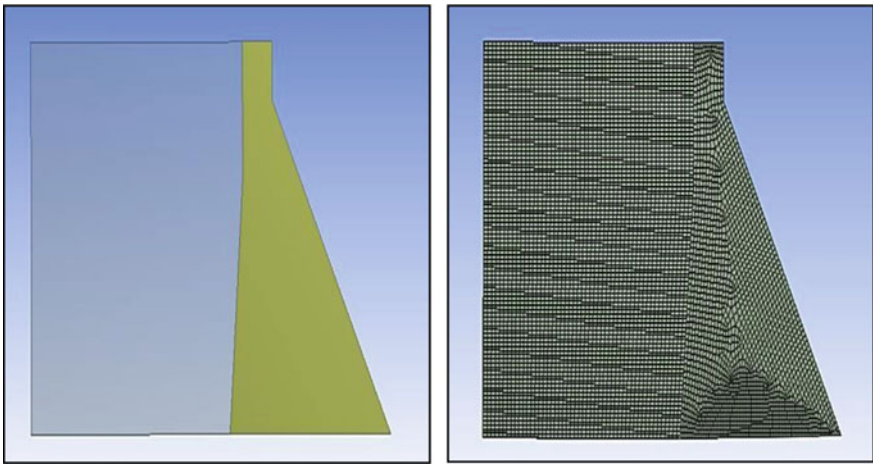

Fig. 5 Finite element model and meshing of the dam using Eulerian approach

Fluid domain is modeled into a finite one using reservoir length $L = H$, in which H is the reservoir depth. Analysis is done considering dam–reservoir interaction effect; therefore, the reservoir water is modeled and analyzed using Ansys CFD. While modeling the reservoir, fluent is modeled up to total height of dam, reservoir is modeled up to water height, and then air is considered throughout freeboard. The pressure results given by the fluent analysis are imported into the load case of structural analysis. 2D and 3D models is modeled and analyzed for gravity dam with

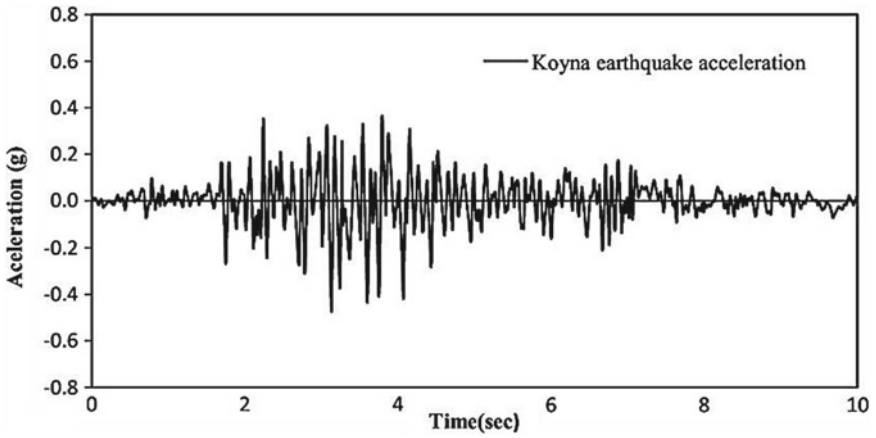

Fig. 6 Horizontal acceleration record of the Koyna earthquake

full reservoir level, i.e., 89 m. Loads applied in the analysis consist of self-weight of the dam, hydrostatic water pressure, and uplift forces. Other normal loads such as silt pressure, wave pressure, vertical water loading, and thermal loads are not considered as their effect will be small on the dam behavior. The reservoir system is firstly analyzed for the Koyna earthquake acceleration data using ANSYS FLUENT and the pressure obtained on outlet of modeled reservoir is imported as a force on the face of wall.

4 Results

The hydrodynamic pressure on a rigid caused by horizontal earthquake acceleration over a length L, of the base of the fluid domain of constant depth is shown in Figs. 8 and 9. The results of 2D and 3D analyses of dam considering dam–reservoir interaction effect for reservoir full condition are as given below in Figs. 10 and 11. Figures 10 and 11 include the contour patterns of response quantities occurred on the dam due to the dynamic analysis considering dam–reservoir interaction. Due to the effect of dam–reservoir interaction, the pressure of 0.4137 MPa for 2D modeling and 0.7183 MPa for 3D modeling, is created at the reservoir outlet which is transferred on dam wall. The results of 2D and 3D analyses of dam neglecting dam–reservoir interaction effect for reservoir full condition are as given below in Figs. 12 and 13.

Water pressures due to dynamic effect are generated by horizontal motions of the vertical upstream face of the dam and by vertical motions of the horizontal bottom of the reservoir. Maximum principal stress, maximum shear stress, equivalent stress, and normal stress obtained are higher at heel of the dam in both the cases. For 2D case as well as 3D, the results obtained seen that the maximum deformation at the top of

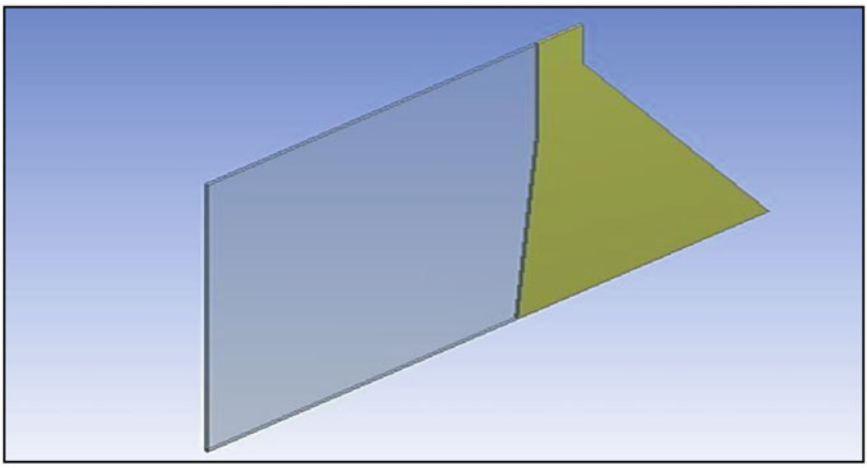

a) Dam with 1 m length

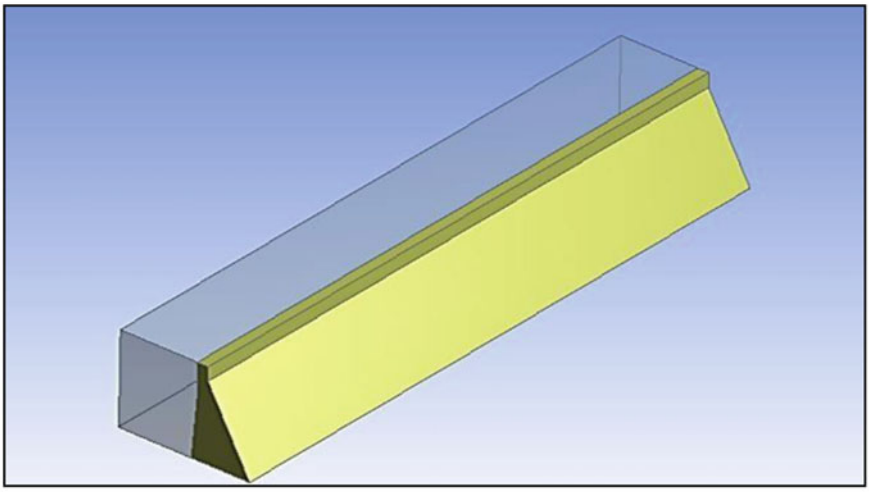

b) Dam with 800 m length

Fig. 7 2D and 3D Finite element models of the dam

dam is greater; this is due to the hydrodynamic pressure induced due to dam–reservoir interaction. Comparing the results of 2D with 3D, the deformation obtained in 3D is more, and also the deformation pattern along the dam length can be seen. The maximum pressure exerted on dam is at coordinates (50, 6, 68.81) m and (−37.4, 0.2705, 2.712) m for 3D modeling as seen in Fig. 9. Here, along the length maximum interaction, pressure is at midspan of length toward base of dam. It is seen that the interaction pressure is maximum at the midspan of dam very near to the base of dam;

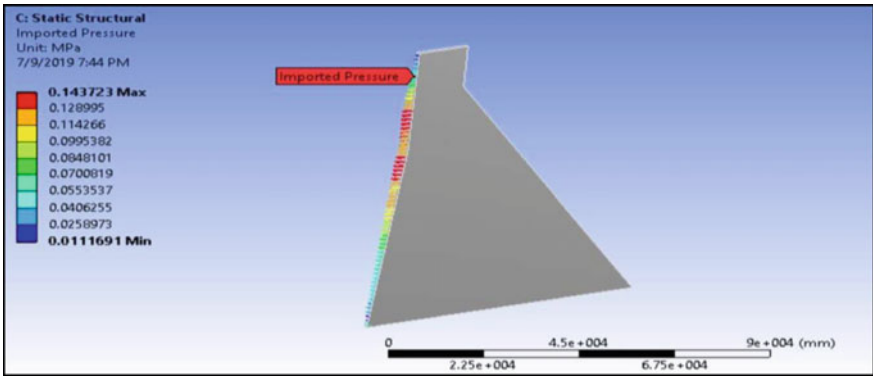

Fig. 8 Pressure values imported on 2D dam model with full reservoir level ($H_W = 89$ m)

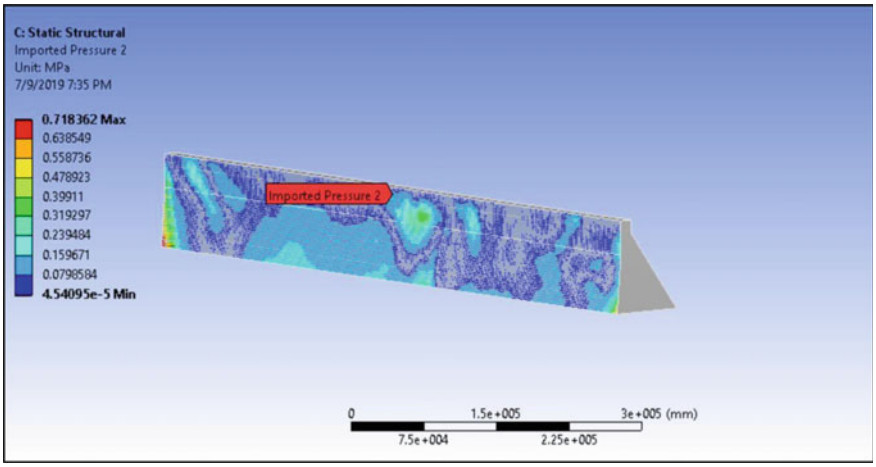

Fig. 9 Pressure values imported on 3D dam model with full reservoir level ($H_W = 89$ m)

this is because the hydrodynamic pressure is maximum at the base and decreases as the reservoir height increases, whereas maximum stresses are obtained at the heel of the dam. After consideration of interaction effect, the response quantities are increased as shown in Table 2. As fluid placed alongside of dam body and affected by base acceleration, the magnitude of additional hydrodynamic forces due to effect of dam–reservoir interaction is comparatively less than without the dam–reservoir interaction effect. The variation of deformation is along the height of dam that is from base to crest because as the reservoir water level increases the pressure acting increases. Dam–reservoir interaction affects the maximum values of response quantities. This is because as the water stored in the dam increases, for the acceleration applied, the interaction of reservoir increases, and thus the pressure on dam face increases due to which the response quantities obtaining high values can be seen.

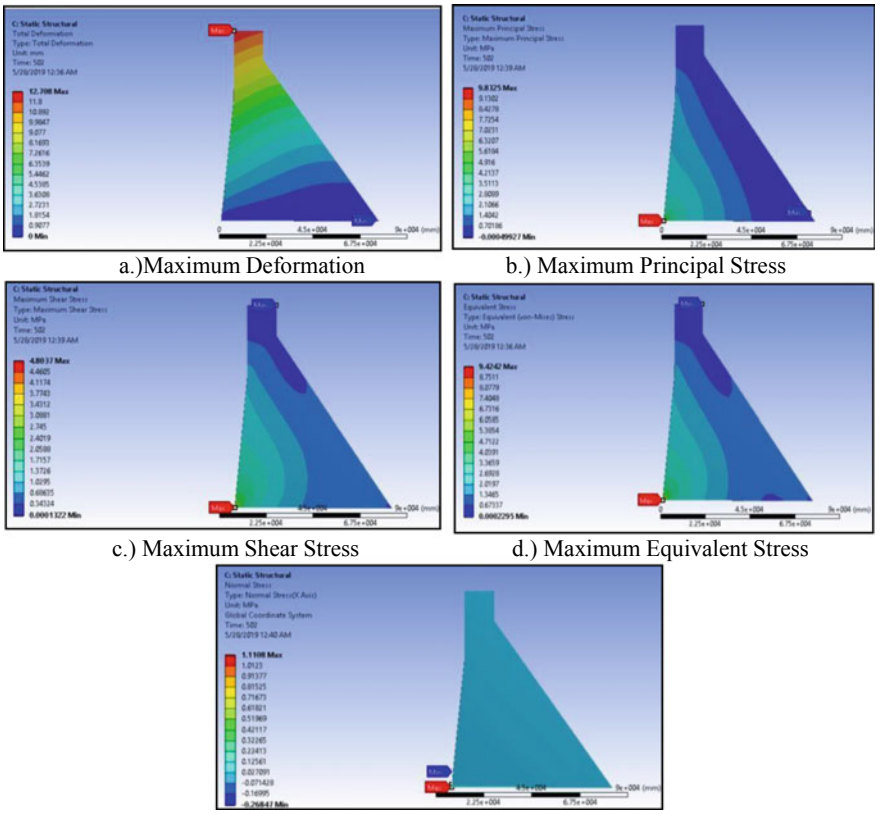

a.)Maximum Deformation b.) Maximum Principal Stress

c.) Maximum Shear Stress d.) Maximum Equivalent Stress

e.) Normal Stress

Fig. 10 Response quantities for 2D analysis with Dam–reservoir interaction ($H_W = 89$)

The existence of water, assumed to be incompressible, provides an additional hydrodynamic pressure. Therefore, due to the added pressure, the deformation obtained considering dam–reservoir interaction effect is far more than neglecting the interaction effect, whereas 3D analysis without dam–reservoir interaction affect gives less values of response quantities than analysis with dam–reservoir interaction effect.

5 Conclusions

The hydrodynamic pressure exerted on the upstream face of the dam, crest displacement, and stresses react significantly to the coupled fluid–structure system. With respect to the feasibility of ANSYS feature in simulating the coupled dam–reservoir interaction effects on gravity dam seismic response, it proves to be appropriate enough. Summing up the results, dynamic analysis indicates that most of maximum

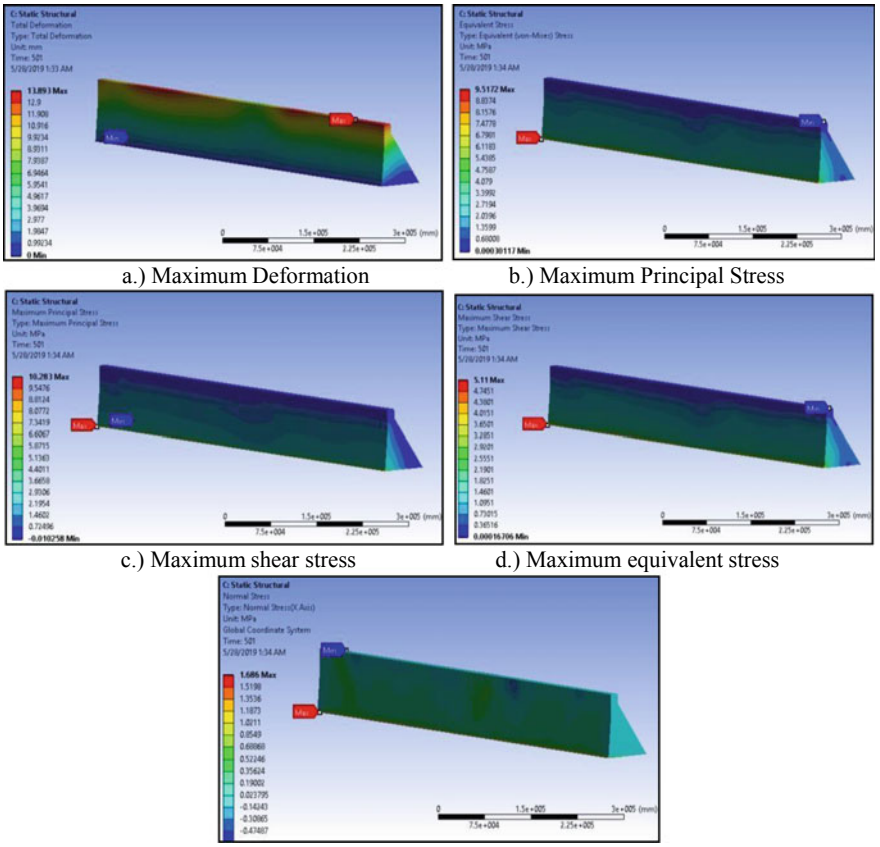

Fig. 11 Response quantities for 3D analysis with Dam–reservoir interaction ($H_W = 89$ m)

responses occur at time 4 s and all maximum stress responses occur at the dam heel. Results indicate that the dam heel is subjected to stresses that vary from compression to tension.

Accordingly, the following conclusions are drawn:

1. Results of dynamic analysis reveal that taking into account dam–reservoir interaction in analysis significantly affects the response of the gravity dam at its heel where maximum responses induce with respect to responses at dam toe.
2. The earthquake acceleration leads to added hydrodynamic pressure exerted due to the interaction effect which is imported on 1-m strip of the dam face, this gives the effect of dam–reservoir interaction but critical section along the length of dam cannot be identified precisely.
3. Plane strain analysis (3D modeling) gives variation of response quantities along the length of dam. Coordinates of maximum hydrodynamic (interaction) pressure can be obtained. For analyzing the effect of interaction (plane stress), 2D analysis

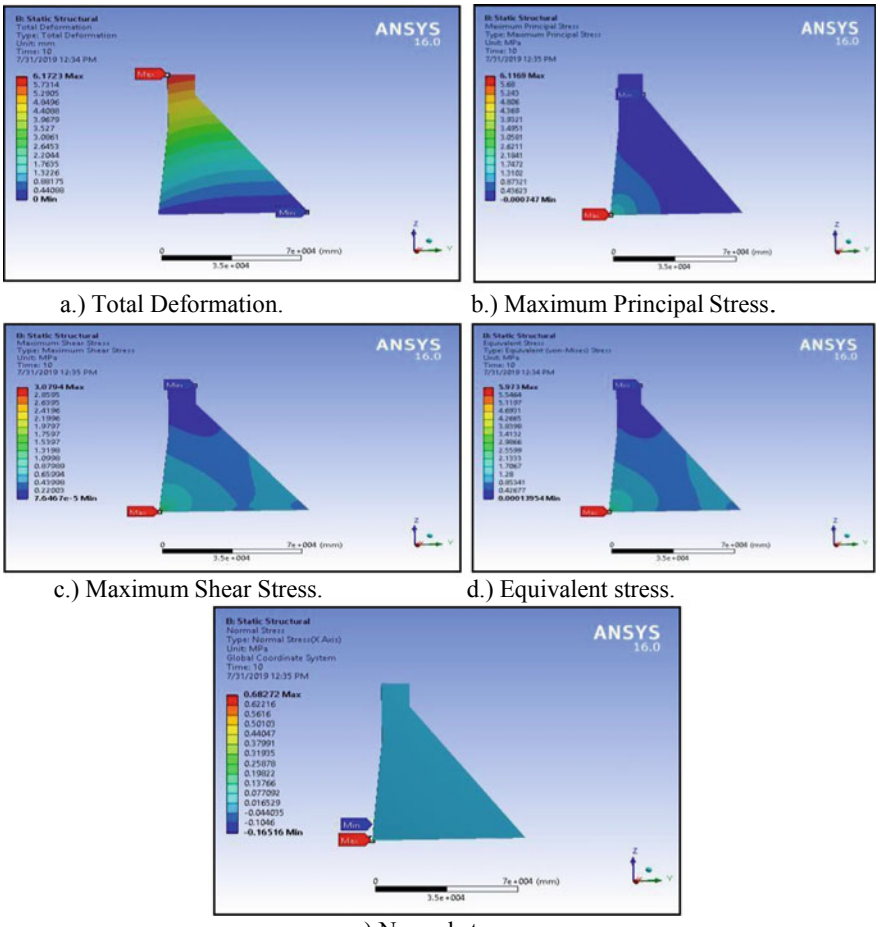

Fig. 12 Response quantities for 2D analysis without Dam–reservoir interaction ($H_W = 89$ m)

is sufficient but, if the critical section due to added hydrodynamic pressure is to be identified for further design of appurtenant structures. we need to model dam as plane strain (3D) model.

4. Dynamic finite element analysis considering dam–reservoir interaction, which is the most exhaustive and expensive of all analyses, can be avoided by the use of the 2D modeling of dam. 3D modeling requires more time and higher configuration computer system which increases the computational cost.
5. The responses obtained considering dam–reservoir interaction with 3D modeling are higher up to 10% than those with 2D modeling. As there is a noticeable increase in maximum deformation compared with stresses, to study the effect of fluid structure interaction specifically on deformation of concrete gravity dam, 3D

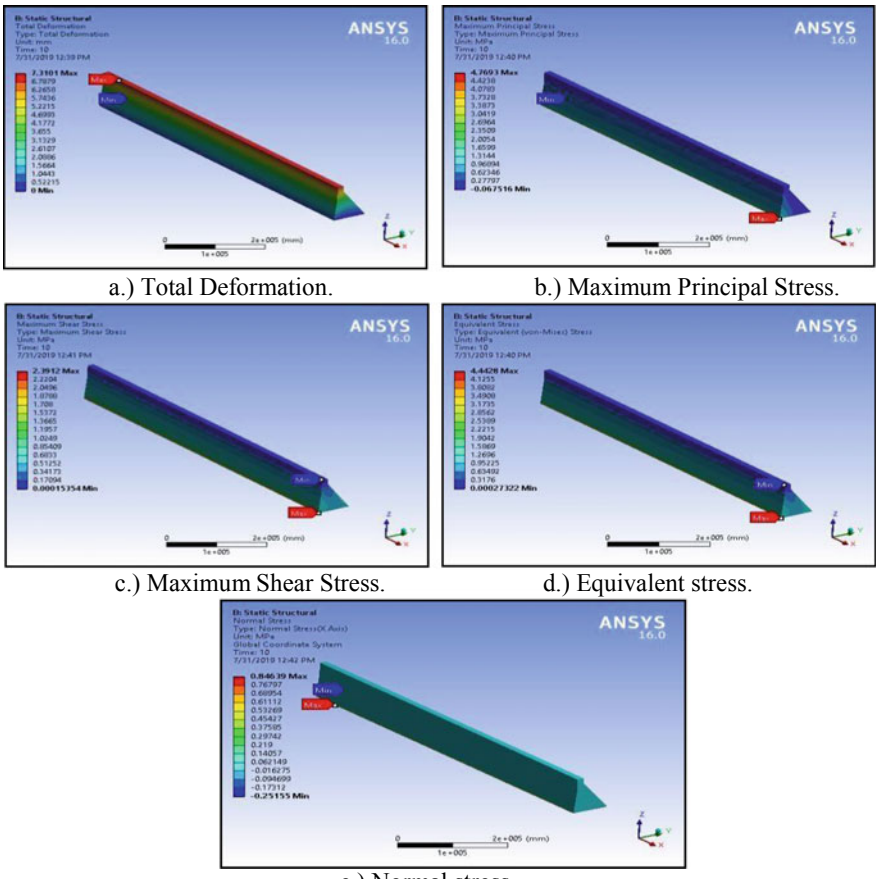

Fig. 13 Response quantities for 3D analysis without Dam–reservoir interaction ($H_W = 89$)

modeling is necessary. However, if the analysis is concerned only for maximum stresses on dam body, 2D (plane stress) modeling is adequate.

Table 2 Results for reservoir filled capacity with and without Dam–reservoir interaction effect

Responses obtained for full reservoir capacity.						
	Response quantities $H_W = 89$ m	Maximum deformation (mm)	Maximum principal stress (MPa)	Maximum shear stress (MPa)	Maximum equivalent Stress (MPa)	Normal stress (MPa)
3D	Considering DSI effect	13.893	10.283	5.11	9.517	1.686
	Neglecting DSI effect	7.310	4.769	2.391	4.442	0.846
	Percentage increased	47.38%	53.62%	53.20%	53.32%	49.84%
2D	Considering DSI effect	12.708	9.832	4.803	9.424	1.110
	Neglecting DSI effect	6.172	6.116	3.079	5.973	0.682
	Percentage increased	51.43%	37.79%	35.89%	36.61%	38.55%

References

1. Nath B (1971) Coupled hydrodynamic response of a gravity dam. Proc Inst Civil Eng 48:245–257
2. Saini SS, Bettess P, Zienkiewicz OC (1978) Coupled hydrodynamic response of concrete gravity dams using finite and infinite elements. Int J Earthquake Eng Struct Dyn 6:363–374
3. Chakrabarti P, Chopra AK (1972) Earthquake analysis of concrete gravity dams interaction including dam-water-foundation rock. In: Earthquake engineering research center, Report No. EERC/ UCB 72-6. University of California, Berkeley
4. Hall JF, Chopra AK (1982) Hydrodynamic effects in the dynamic response of concrete gravity dams. Earthquake Eng Struct Dynam 10:333–345
5. Fenves G, Chopra AK (1985) Simplified earthquake analysis of concrete gravity dams. J Struct Eng 113:1688–1708
6. Fenves G, Chopra AK (1985) Simplified earthquake analysis of concrete gravity dams: separate hydrodynamic and foundation interaction effects. J Mechan Eng 111:715–735
7. Valliappan S, Zhao Chongbin (1992) Dynamic response of concrete gravity dams including dam-water-foundation interaction. Int J Numer Anal Meth Geomech 16:79–99
8. Calayir Y, Dumanoglu AA, Bayraktar A (1996) Earthquake analysis of gravity dam-reservoir systems using the Eulerian and Lagrangian approaches. Comput Struct 59(5):877–890
9. Ghaemian M, Ghobarah A (1999) Nonlinear seismic response of concrete gravity dams with dam– reservoir interaction. Eng Struct 21:306–315
10. Asteris PG, Tzamtzis AD (2003) Nonlinear seismic response analysis of realistic gravity dam-reservoir systems. Int J Nonlinear Sci Numer Simul 4:329–338
11. Indrani Gogoi A, Maity D (2005) Seismic safety of aged concrete gravity dams considering fluid-structure interaction. J Earthquake Eng 9:637–656
12. Sani AA, Lotfi V (2007) Analysis of dam–reservoir interaction by employing the modified-efficient fluid hyper-element. WIT Trans Built Environ 92:1743–3509
13. Chopra AK (2008) Earthquake analysis of arch dams: Factors to be considered. In: The 14th world conference on earthquake engineering, October 12–17. Beijing, China
14. Rodriguez J, Crespo MJ, Lacoma LM (2012) Fluid-structure interaction in civil engineering structures. SIMULIA Commun Conf

15. Lim1 WZ, Xiao RY, Chin CS (2012) A comparison of fluid-structure interaction methods for a simple numerical analysis of concrete gravity-dam
16. Keivani A, Shooshtari A (2012) Analytical solution for a fluid-structure interaction problem in comparison with finite element solution. 15 WCEE Lisboa 2012
17. Wen Z, Zhou J (2012) Stability analysis of concrete gravity Dam. Appl Mech Mater 238:252–255
18. Hebbouche A, Bensaibi M, Mroueh H (2012) Behavior of concrete dam under seismic load. 15 WCEE Lisboa 2012
19. Mehdipour B (2013) Effect of foundation on seismic behavior of concrete dam considering the interaction of dam—reservoir. J Basic Appl Sci Res 3(5):13–20
20. Zeydan BA (2015) Hydrodynamic analysis of concrete gravity dams subjected to ground motion. Research Gate, Conference paper

A Small-Scale Study for the Treatment of Grey Wastewater Through Free Surface Constructed Wetlands Using Water Hyacinth Plant

Anudeep Nema, Dhaneesh K. H, Kunwar D. Yadav, and Robin A. Christian

Abstract This study was carried out to analyze the treatment efficiency of water hyacinth constructed wetland system with greywater. Greywater was collected from Boys' Hostel in SVNIT campus for constructed wetland reactor. Parameters such as pH, conductivity, BOD_3, COD, TS, TSS, TDS and TKN were analyzed. This study was observed in two phases. Water hyacinth wetland system operated in continuous mode with 3 retention time 1, 2 and 3 day. In continuous system, water hyacinth wetland system operated for 5 days with each different retention time. From the results of the continuous system, it can be concluded that the water hyacinth wetland system will work efficiently for a retention time of 2 days with high removal of BOD_3 and COD of 88.55% and 79.20%, respectively. TDS reduced by 56.76% in a continuous system, whereas, TS reduction occurred only by 14.03% in wetland operated with 2-day retention time. After the treatment conductivity, pH, TS, TSS, and TKN of greywater increased when operated in continuous modes as water hyacinth reintroduces nutrients to greywater. During the continuous operation of the water hyacinth wetland system, plant biomass also analysed and observed for its growth. Water hyacinth increased by 61.83% by mass after the treatment. This shows the high greywater-suitability of water hyacinth for its growth.

Keywords Greywater · Constructed wetlands · Water hyacinth · Surface flow · Continuous system · Small-scale study

A. Nema (✉) · D. K. H · K. D. Yadav · R. A. Christian
Civil Engineering Department, Sardar Vallabhbhai National Institute of Technology (SVNIT), Surat, Gujarat, India
e-mail: anudeepneman@gmail.com

© Springer Nature Singapore Pte Ltd. 2021

K. K. Pathak et al. (eds.), *Recent Trends in Civil Engineering*, Lecture Notes in Civil Engineering 77, https://doi.org/10.1007/978-981-15-5195-6_70

1 Introduction

Freshwater is a viable natural resource that has been depleting rapidly with time due to mismanagement of human activities and increasing in population. Water scarcity is a global problem and if not solved will imbalance the whole environment [1]. As the population and prosperity of the world are growing; water demand is increased and multiplying without the chance of increasing supply. The increasing demand for this finite and invaluable resource has motivated new freshwater management techniques, including innovative wastewater recycling techniques. Reducing the needs for freshwater can be achieved by reusing wastewater. An average person typically produces 150–250 L of domestic wastewater per day, and greywater accounts for up to 75% of wastewater. Greywater is very less polluted and easy to treat within decentralized system such as send filters, constructed wetland, trickling filters bio-reactor and coagulation.

Most constructed wetlands around the world are still primarily used to treat municipal and domestic wastewaters. However, the treatment of greywater, diffrent types of industrial, agricultural wastewaters, stormwater runoff and landfill leachate has recently come in trend. Despite the suspicion of many civil engineers and water authorities, constructed wetlands have been widely accepted around the world and have become a suitable solution for wastewater treatment. Constructed wetlands (CW) are engineered wastewater treatment systems that encompass a plurality of treatment modules including biological, chemical and physical processes, which are all to processes occurring in natural treatment wetlands. Bacterial metabolism, accumulation and plant uptake interaction with each other plays a crucial role in the removal of pollutants in constructed wetland [2]. Algae and bacteria remove impurities by natural processes in facultative ponds [3, 4]. Also, the most dominant feature of constructed wetland is its vegetation which also acts as an important biotic factor in the majority of treatment processes [5].

The aim of the study is to evaluate water hyacinth that can be used for the treatment of greywater with a constructed wetland system. In Surat, the Vapi river is covered with water hyacinth in the majority of areas and creates problems in pumping and irrigation. Hence, clearing water hyacinth required a huge amount of money that can be regained by using it beneficially. Using a low cost constructed wetland system with water hyacinth, that can implement a new system with beneficially use water hyacinth and greywater for non-potable applications.

2 Methodology

2.1 Water Hyacinth and Gravel

Water hyacinth collected from the pond near Bhagwan Mahavir College of Engineering, which is 2 km away from the SVNIT campus (Fig. 1). Collected water

Fig. 1 **a** Water hyacinth pond near VIP road, Surat **b** Location of pond

hyacinth had an average height of 15 cm. Collected water hyacinth was carefully washed with tap water without doing damage to roots. These plants were acclimatized for greywater by increasing the percentage of greywater (50, 60, 70, 80, 90 and 100%) into the water for 30 days.

Gravels were sieved, analyzed as per ASTM and were thoroughly washed with tap water to remove the deposited impurities peel off from the surface. The grain size distribution ranges from 20–40 mm. Gravels were provided in the outlet area of the reactor for avoiding the entry of dead plants, leaves and roots and also to minimize the disturbance during sample collection.

2.2 Feeding Tank and Constructed Wetland Reactor

Feeding tank and the reactor were made by cutting half of a rectangular tank of 300 L capacity. One part of the plastic/PVC rectangular tank was used as a feeding tank. Feeding tank had the capacity of 130 L with dimensions of 120 cm × 40 cm × 35 cm (L × W × H) and an effective height of 25 cm. Feeding tank has one outlet pipe at the bottom of the tank to feed greywater to the reactor. The reactor was made of the remaining half part of the plastic/PVC rectangular tank. The reactor had a capacity of 130 L and had the same dimensions as the feeding tank. It had a void volume of 115 L in the presence of vegetation and other internals were used to form a shallow pond system. It had 2 outlets; one located at bottom of the tank for taking sample and another located at height of 18 cm from the bottom for maintaining the water level to a fixed height.

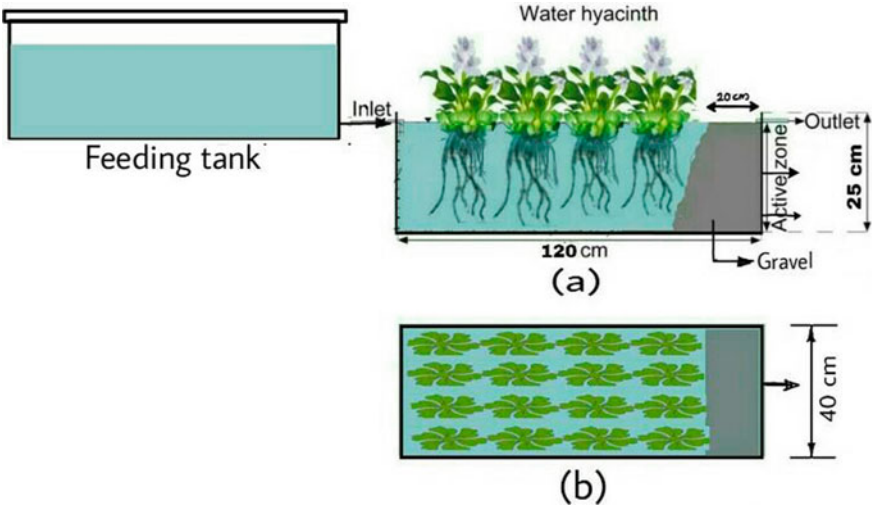

Fig. 2 Schematic diagram of the constructed wetland setup: **a** Cross-section view; **b** Plan view

2.3 Operational Procedure

The laboratory-scale setup was divided into two parts. Feeding tank and constructed wetland reactor schematic diagram are shown in Fig. 2. The water hyacinth (*Eichhornia crassipes*) plants were placed in the reactor at the initial stage of the plantation to give full coverage of 171–172 plants/m^2 [6–9]. The surface area of the reactor comes around 0.35 m^2. For this area, 60 plants are used in a constructed wetland system in continue run. The input and output management was performed according to standard practices. In the outlet of the reactor provides the gravel layer of 20 cm depth with size ranging from 20 to 40 mm provided, as shown in Fig. 2. Raw greywater was fed manually into a feeding tank and after by gravitational flow greywater transferred to the wetland.

2.4 Greywater Sampling and Analysis

The treated greywater was collected from a constructed wetland daily for performance evaluation to observe the variation in the treatment efficiency wetland in each day operation. All samples were analyzed for water quality parameters like pH, electrical conductivity (EC), BOD_3, COD, Total suspended solids (TSS), Total dissolved solids (TDS) and Total Kjeldahl Nitrogen (TKN) according to the standard method (APHA 2012).

3 Results and Discussion

3.1 Variation in One Day Retention Time

Initial pH value was 8.06 ± 0.43, and after treatment, pH value decreased to 7.87 ± 0.28. Conductivity was 0.89 ± 0.05 mS/cm in the initial stage of treatment, and it increased to 1.00 ± 0.02 mS/cm after treatment. Initial BOD_3 was 90.27 ± 0.55 mg/L and was reduced to 23.38 ± 5.90 mg/L and also initial COD of greywater was 137.33 ± 7.02 mg/L and was reduced to 49.20 ± 14.39 mg/L after treatment with 1-day RT. Valipour et al. (2015) show that after treatment TS reduced from 457.00 ± 67.58 mg/L to 451.40 ± 51.20 mg/L and TSS increased from 151.00 ± 32.60 mg/L to 174.60 ± 26.20 mg/L. TDS value decreased from 306.00 ± 39.95 mg/L to 276.80 ± 28.80 mg/L after treatment, but TKN value increased from 3.39 ± 1.47 mg/L to 6.62 ± 1.39 mg/L). Figure 3 shows the variation of greywater characteristics in initial and treated greywater.

During this study, the pH of the sample does not change significantly from the initial value, and conductivity also has only a slight increase from the initial value. Initial conductivity was 0.89 mS/cm, and it varies close to 1 mS/cm during the 1-day RT operation of continuous system. The temperature of the sample varies with respect to the ambient temperature variation. Initial BOD_3 of the sample was 90.27 mg/L and treated greywater reduced BOD_3 values ranging between 20.30 and 30.30 mg/L. During 5 days of operation, on 3rd-day maximum removal of BOD_3 of 81.16% was observed. Initial COD of the sample was 137.33 mg/L. The observed COD of the treated sample was shown in Fig. 3. During the operation of a continuous system with 1-day RT, COD removal efficiency was observed in the range of 53.39–76.69%. Maximum removal obtained in the 2nd day of operation of the reactor was 76.69%.

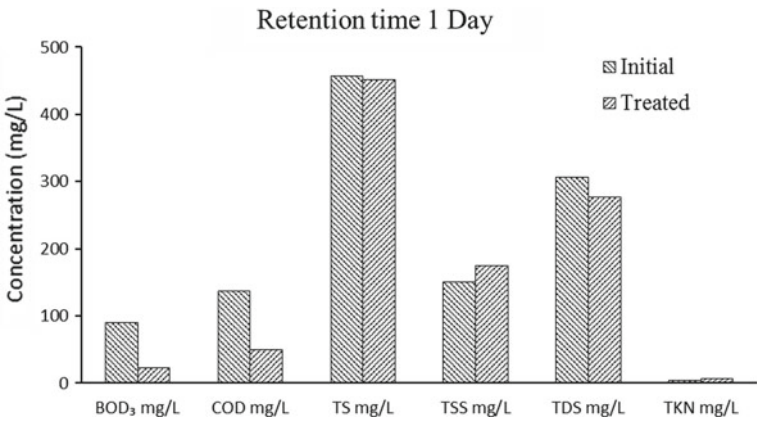

Fig. 3 Characteristics of initial and treated greywater (BOD_3, COD, TS, TSS, TDS) in 1-day retention time

TS removal was very low in the 5 days of the operation period; maximum removal obtained was 8.31% on the 5th day of operation period. Initially first day of operation, TS removal was not obtained in the treated greywater. TSS removal was not observed during 5 days of operation. TDS and TS removal were very less up to 18.95% and 8.31%, respectively. On the 1st day of operation, TDS removal was not obtained and from 2nd day onwards removal was obtained in the treated greywater ranging from 6.53 to 18.95%. The maximum removal of TDS was observed on the 5th day of operation of the reactor with a removal efficiency of 18.95%. Mean variation of influent greywater and effluent after treatment for various parameters are shown in Fig. 3.

TKN of the initial sample was 3.39 mg/L, and after treatment, TKN value increased from the initial value. Treated greywater had TKN in the range of 5–7.70 mg/L. Increased TSS and TKN were observed from the initial values, and 1-day RT did not show any removal in operation period. TKN increment was due to the organic nitrogen component that was reintroduced into the water from ecosystem decomposition processes [8]. In a previous study, raw sewage treating with water hyacinth showed 31% removal of TKN after treatment [6]. However, this study showed that water hyacinth not suitable for TKN removal from the greywater.

3.2 Variation in Two-Day Retention Time

In this study, Initial pH value was 7.91 ± 0.42 and it increased to 8.67 ± 0.11 after treatment. Conductivity was 0.91 ± 0.02 mS/cm in the beginning and it was increased to 0.94 ± 0.03 mS/cm after treatment. Initial BOD_3 was 83.45 ± 10.54 mg/L reduced after treatment with 2-day RT to 9.32 ± 1.21 mg/L. Initial COD was 134.00 ± 5.66 mg/L reduced to 28.80 ± 12.13 mg/L after treatment with 2-day RT. After treatment TS reduced from 383.50 ± 16.26 mg/L to 380.00 ± 51.87 mg/L and TSS increased from 170.50 ± 20.51 mg/L to 253.60 ± 42.46 mg/L [6]. TDS value was decreased from 213.00 ± 4.24 mg/L to 126.40 ± 10.24 mg/L after treatment but TKN value was increased from 3.82 ± 1.80 mg/L to 7.64 ± 2.55 mg/L [7].

Initial BOD_3 of the sample was 83.45 mg/L and the treated sample showed reduced BOD_3 in the range of 8–10.30 mg/L. During 5 days of operation maximum BOD_3 removal was 90.41% that was observed on the 2nd day of operation. On each day, the operation of the system had a small variation in the treated quality of water. Initial COD of the sample was 134 mg/L. During the operation of continuous system with 2-day, RT COD removal efficiency was observed in the range of 64.18–88.06% in the 5 days of operation period. The maximum removal of COD, observed on the 4th day of operation of the reactor, was 88.06%.

Initial TS of the sample was 383.50 mg/L and after treatment, it increased to 392 mg/L within 24 h TDS of treated greywater was gradually decreasing during the 5-day operation period. During wetland working with 2-day retention time, TDS removal attained considerably throughout 5 days of operation period. On the 1st day of operation TDS removal was observed to be 40.85%. The removal efficiency

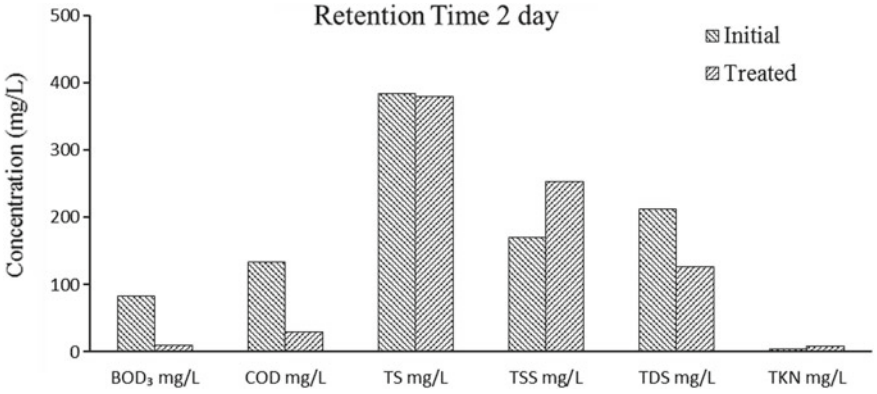

Fig. 4 Characteristics of initial and treated greywater (BOD_3, COD, TS, TSS, TDS) in 2-day retention time

of TDS obtained in the treated greywater ranged between 35.21 and 48.36%. The maximum removal of TDS was obtained on the 3rd day of operation of the reactor with a removal efficiency of 48.36%.

TKN of the initial sample was 3.82 mg/L and after treatment, its value started increasing. Treated greywater had TKN values in the range of 5.09–10.18 mg/L. TS, TSS and TKN removal was not achieved in the 5 days of operation period with 2-day RT. The TKN increment was due to the organic nitrogen component that was reintroduced into the water from ecosystem decomposition processes [8]. The reactor operating with 2-day RT shows good removal efficiency in BOD_3, COD and TDS. Figure 4 shows the variation of greywater characteristics along with different operation periods keeping RT as 2 days.

3.3 Variation in 3-Day Retention Time

Initial pH value was 8.01 ± 0.06 and increased to 8.68 ± 0.82 after treatment. Conductivity was 0.93 ± 0.04 mS/cm in the beginning and increased to 1.18 ± 0.15 mS/cm after treatment. Initial BOD_3 of 70.50 ± 7.78 mg/L reduced to 18.32 ± 8.40 mg/L. Initial COD, which was 144.00 ± 5.66 mg/L came down to 41.60 ± 6.69 mg/L after treatment with 3-day RT.

On the 2nd day of operation, maximum removal of BOD_3 of 85.39% was observed. On each day, the operation of the system had small variations in the treated quality of water. Initial COD of the sample was 144 mg/L. During the operation of the continuous system with 3-day RT in the 5 days of operation, the removal efficiency of COD was in the range of 66.67–77.78%. The maximum removal of COD, observed on the 2nd day of operation of the reactor, was 77.78%. Initial TS of the sample was 485.50 mg/L and after treatment, it decreased to 408 mg/L within 24 h. The maximum

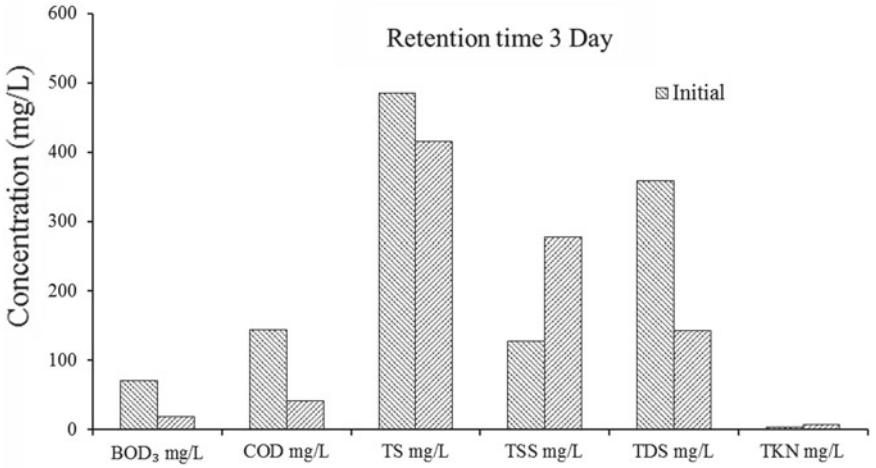

Fig. 5 Characteristics of initial and treated greywater (BOD_3, COD, TS, TSS, TDS) in 3-day retention time

removal obtained was 19.46% on the 5th day of operation of the reactor. On the first day of operation, TS removal efficiency was 15.76%. TS removal efficiency ranged between 10.20 and 19.46%. TDS of treated greywater was found to be decreasing during the 5-day operation period. TDS removal efficiency was 52.56%, and from the 2nd day onwards the removal efficiency gradually increased from 45.51 to 61.54%. The maximum removal of TDS was observed on the 5th day of operation of the reactor with a removal efficiency of 61.54%.

TKN of the initial sample was 3.82 mg/L. In 3-day RT, treated sample TKN concentration was higher than the initial concentration; which was due to organic nitrogen as explain privious sections. TKN increased by 30-50 % in all observed RT. TS removal was very low (up to 19.46%) and TSS and TKN were found to be increasing from the initial value and not showing any removal on operation period of 5 days with 3-day RT. The reactor operating with 3-day RT showed good removal efficiency in BOD_3, COD and TDS. TS removal was observed but with low efficiency. Figure 5 shows the variation of characteristics of greywater treated with 3-day retention time with an operation period of 5 days.

3.4 Mass Variation of Water Hyacinth

In this study change in biomass was carried out by selecting 5 plants and further total biomass was calculated for 60 plants. Plants were selected randomly, and separation analysis was done for root, stem and leaves. Change in biomass was carried out by weighing the different parts of plants. After weighing calculated total mass growth of plants in the reactor during this continuous system operation considering total plants

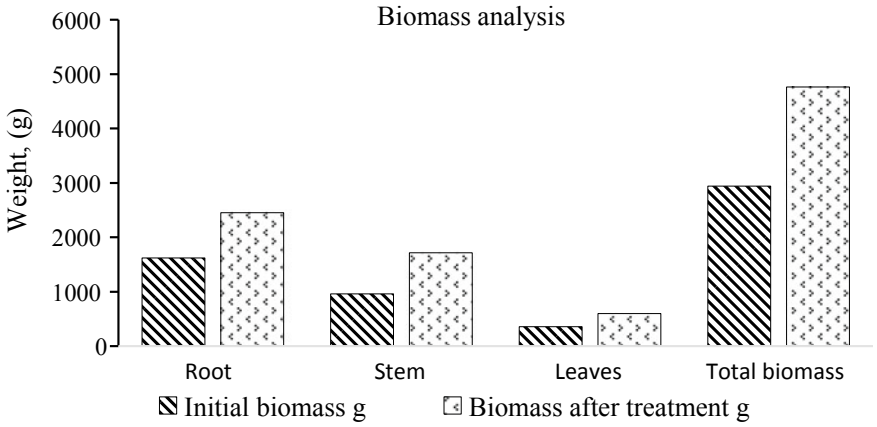

Fig. 6 Biomass production in a continuous process of treatment

used in the reactor. The change in the mass of plants is obtained by weighing each part of the plants separately after treatment. A continuous run of wetland system took 3 weeks for completing constructed wetland operation in three different retention times.

This analysis gave an idea about plant mass growth during the treatment and suitability of greywater with water hyacinth growth. Figure 6 shows the mass variation plant after the treatment process. It was observed that the weight of plant increased to 61.83%, 51.459% and 77.85% in plant root and stem, respectively, leaves weight increased to 65.67%. Maximum growth of biomass was observed in the stem than roots and leaves. Initial biomass of 2944.08 g of 60 plants was increased to 4764.48 g after treatment process.

4 Conclusions

Greywater has a great potential to be reused due to its availability and the low concentration of pollutants in it when compared to combined household wastewater. Greywater reuse is a useful measure for saving water at the domestic level. In this study, water hyacinth was used for the treatment of greywater with a constructed wetland system. Constructed wetland performs well in removing BOD_3 and COD. From the results of a continuous system, it can be concluded that the water hyacinth wetland system will work efficiently for a retention time of 2 days with high removal of BOD_3 and COD (88.55% and 79.20%, respectively). TDS reduced by 56.76% in a continuous system, whereas, TS reduction occurred only by 14.03% in wetland operated with 2-day retention time. Conductivity, pH, TS, TSS, and TKN of greywater were observed to increase from the initial values after treatment because of the presence of plant parts and their decomposition. In continuous system wetland

works effectively with a retention time of 1 day, 2 day and 3 day in the removal of BOD_3, COD and TDS, but the maximum removal was observed when wetland works with 2-day retention time. Water hyacinth increased by 61.83% by mass after the treatment. This shows the high greywater-suitability of water hyacinth for its growth.

References

1. Liu J, Liu Q, Yang H (2016) Assessing water scarcity by simultaneously considering environmental flow requirements, water quantity, and water quality. Ecol Indic 60:434–441. https://doi.org/10.1016/j.ecolind.2015.07.019
2. Osem Y, Chen Y, Levinson D, Hadar Y (2007) The effects of plant roots on microbial community structure in aerated wastewater-treatment reactors. Ecol Eng 29:133–142. https://doi.org/10.1016/j.ecoleng.2006.06.003
3. Abdel-Raouf N, Al-Homaidan AA, Ibraheem IBM (2012) Microalgae and wastewater treatment. Saudi J Biol Sci 19:257–275. https://doi.org/10.1016/j.sjbs.2012.04.005
4. Abdel-Shafy HI, El-Khateeb MA, Regelsberger M, El-Sheikh R, Shehata M (2009) Integrated system for the treatment of blackwater and greywater via UASB and constructed wetland in Egypt. Desalin Water Treat 8:272–278. https://doi.org/10.5004/dwt.2009.788
5. Dhote S, Dixit S (2009) Water quality improvement through macrophytes—a review. Environ Monit Assess 152:149–153. https://doi.org/10.1007/s10661-008-0303-9
6. Valipour A, Raman VK, Ahn YH (2015) Effectiveness of domestic wastewater treatment using a Bio-hedge water hyacinth wetland system. Water 7:329–347. https://doi.org/10.3390/w7010329
7. DeBusk TA, Reddy KR, Hayes TD, Schwegler B.R. Jr. (1989) Performance of a pilot-scale water hyacinth-based secondary treatment system. J. Water Pollut. Control Fed. 61:1217–1224. https://doi.org/10.2307/25043735
8. Diaz P (2016) Constructed wetlands and water hyacinth macrophyte as a tool for wastewater treatment: a review. J Adv Civ Eng 2:1–8. https://doi.org/10.18831/djcivil.org/2016011001
9. Ingole NW, Bhole AG (2002) Utilization of water hyacinth relevant in water treatment and resource recovery with special reference to India. J Water Supply Res Technol AQUA 51:283–295. https://doi.org/10.2166/aqua.2002.0025

Real-Time Flood Analysis Using Artificial Neural Network

Vijendra Kumar and S. M. Yadav

Abstract Floods are natural disasters that affect the likelihood of occurrence. Forecasting and predicting floods have a significant role to play in ensuring that mitigation, adequate planning, and management can be carried out in advance. The Artificial Neural Network (ANN) is one of the techniques by which rapid forecasting and prediction can be carried out. In the present study, ANN has been used to simulate real-time floods in the lower Tapi basin. Data from the upstream gauging station of the reservoir, the inflow of the reservoir, and the downstream gauging site were simulated for three different events. The Feed–Forward network, the Levenberg Marquardt learning rule, and the Sigmoidal Axon transfer function are used in the models. Developed models have a correlation coefficient value close to one. The findings acquired from these models are satisfactory and the predicted flood discharge of the ANN is consistent with the observed values.

Keywords Flood · Forecasting · Prediction · Artificial neural network · Hidden layer · Feed-forward network

1 Introduction

Floods are one of the natural disasters that give rise to the likelihood of occurrence in a given time period. There have been many destructive floods in India in recent years. Few of them are Mumbai flood in the Mithi River (2005) with roughly 1,094 deaths, Surat flood in the Tapi River (2006) with roughly 300 deaths, Bihar flood in the Kosi River (2008) affected more than 2.3 million people and roughly 434 deaths, Cloud bursting in the Uttarakhand River (2013) with roughly 5,700 suspected dead, The Jammu and Kashmir flood (2014) caused almost 277 deaths in India and about

V. Kumar (✉) · S. M. Yadav
Civil Engineering Department, Sardar Vallabhbhai National Institute of Technology, Surat, Gujarat, India
e-mail: vij100000@gmail.com

S. M. Yadav
e-mail: shivnam27@gmail.com

© Springer Nature Singapore Pte Ltd. 2021

K. K. Pathak et al. (eds.), *Recent Trends in Civil Engineering*, Lecture Notes in Civil Engineering 77, https://doi.org/10.1007/978-981-15-5195-6_71

280 deaths in Pakistan, the Chennai flood (2015) killed more than 500 people and estimated losses of Rs 200 billion, and the Assam flood (2016) affected 1.8 million people and 28 deaths. Forecasting and predicting the river stage and discharge play a crucial role in flood management and prevention. Conventional models involve a wide range of information such as topography map, rainfall, runoff, river system and profile, soil characteristics [1].

In order to overcome the limitation of the conversion method, various researchers used the Artificial Neural Network (ANN) as an effective and simple method for forecasting and predicting floods. The ANN is capable of self-learning, self-organization, self-adaptation, and fault tolerance [2]. The ANN has been used for flood forecasting such as [3–12], for flood predictions [13–15]. [11] studied flood forecasting in multiple sections of the Barak River. [16] researched river stage prediction using wavelet packet decomposition and data-driven models for the Nakdong river basin, South Korea. [17] compared feed forward back-propagation and radial base function for the Johor river. [10] used the neural network to predict peak discharge and peak time from a single rainfall pattern, and [18] used artificial intelligence to predict and forecast streamflow.

Thirumalaiah and Deo [3] research demonstrated the application of the neural network to the real-time forecasting of hourly flood runoff and the daily river stage, as well as the forecasting of rainfall in India. The Neural Network has been used efficiently to determine the forecasting of the River Stage [8, 19]. [6] used a neural network combined with a fuzzy and genetic algorithm for flood forecasting. [2] studied the flood forecasting using Artificial Neural Network for Dadu River, China. [20] used a social-based neural network algorithm to prepare a flood routing model. [21] researched the flash flood forecast for the Tamsui River.

In this research, the flood forecasting of the lower Tapi River was analyzed using the Artificial Neural Network. Data from the upstream gauging station of the reservoir, the inflow of the reservoir, and the downstream gauging site were simulated for three different events. The Feed–Forward network, the Levenberg Marquardt learning rule, and the Sigmoidal Axon transfer function are used in the models.

2 Study Area and Data Collection

The Tapi River is the second largest west flowing interstate river. The Tapi basin lies in the northernmost part of Deccan Plateau, between 72°33′E to 78°17′E longitudes and 20°09′N to 22°0′N latitudes approximately. It covers a large area in the state of Maharashtra and other parts of the state of Madhya Pradesh and Gujarat. Figure 1 shows the catchment of the Tapi basin. The Tapi River drains an area of 65,145 km^2, of which nearly 80 percent (51,504 km^2) is located in Maharashtra state, 9804 km^2 in Madhya Pradesh, and 3837 km^2 in Gujarat [22]. The total length of this west-flowing river is 724 m. The entire Tapi basin is divided into three sub-basins, namely the upper Tapi basin up to Hathnur (29,430 km^2), the middle Tapi basin from Hathnur

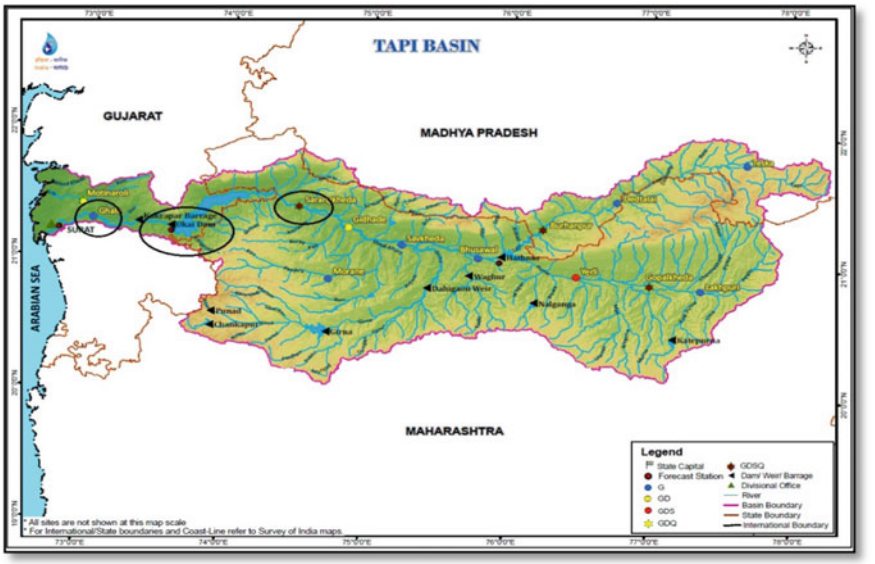

Fig. 1 Catchment of the Tapi Basin [25]

to Ukai Gauging (25,320 km^2), and the lower Tapi Basin from Ukai to the Arabian Sea. Silent features of the Tapi River are shown in Table 1.

In this study, a real-time flood analysis was conducted in the lower and middle parts of the Tapi Basin with the help of ANN. Tapi River has its mouth in the Arabian Sea near Surat city. The River reach between Ukai Dam to its mouth is 123 km and has a carrying capacity is 16990 m^3/s [23]. The river regime in Surat city has a capacity of 8495 m^3/s within the banks. Major floods occurred in the Tapi River in years 1727, 1776, 1782, 1829, 1837, 1872, 1944, 1959, 1968, and 1970. Out of this, the 1968 flood was the worst catastrophe with 42,500 m^3/s of discharge. The floods have a direct effect on the people of Surat city. As a result, a dam was built at a

Table 1 Silent features of Tapi River

Sl. no.	Features	
1.	Average rainfall	820.70 mm
2.	Highest elevation	1556 m
3.	Area	65145 km^2
4.	Highest dam	Ukai
5.	Number of irrigation projects	Major-13, Medium-68
6.	Number of sub-basin	2
7.	Number of watersheds	100
8.	Number of villages	9443

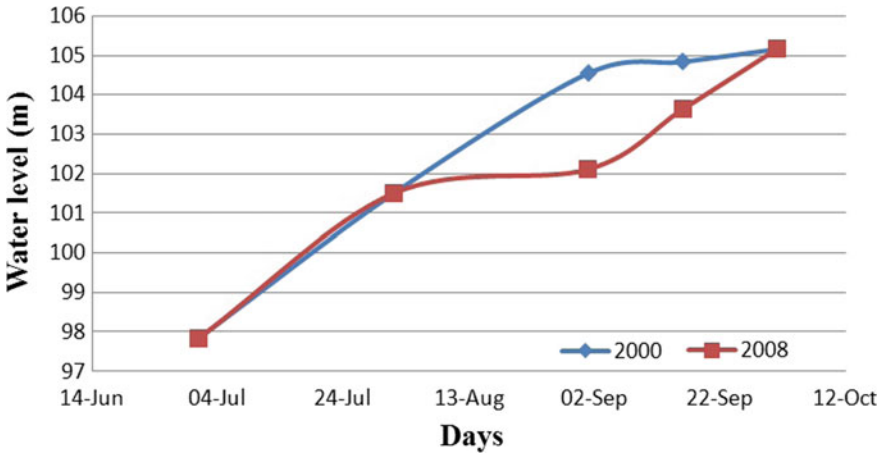

Fig. 2 Rule curve for 2000 and 2008

distance of 123 km from its mouth in 1972. So, the flood intensity can be decreased and operated. After the construction of the Ukai dam, floods occurred in 1994, 1998, 2006, and 2013. Figure 2 shows the Ukai's dam rule curve from July to October, 2000 and 2008. Rule curve helps in the proper operation of the reservoir to keep the water level of the reservoir at a specified time.

In order to establish an understanding of the inflows into the reservoir and how the releases from the dam affect the downstream side of the dam, the gauging stations are chosen. Sarangkheda gauging station approx. 107 km upstream of the Ukai dam, gauging at the Ukai reservoir and at downstream Ghala station approx. 45 km are the three chosen stations. Figure 3 indicates the line diagram of the study region where all the stations are located. The Nehru Bridge plays a significant role in the warning scheme whenever there is a chance of flooding in the Tapi River. The siren is blown based on Nehru Bridge level. When the level of the river increases to 7.5 m, the siren blows continually for one minute. Second, when the river level rises to 8.5 m, i.e., warning level, the siren blows in an interval of half a minute. When the level of the river increases to 9.5 m, i.e., danger level, the siren is blown intermittently for two minutes.

Daily flood discharges during 1998 September; 2006 August and 2013 August were collected from the Surat Irrigation Department and the Gandhinagar Central Water Commission for the Sarangheda Gauging Station, the Ukai Reservoir, and the

Fig. 3 Line diagram of the study area

Ghala Gauge Station. Real-time flood hydrographs for 1998, 2006, and 2013 were simulated using the Artificial Neural Network.

3 Development of Artificial Neural Network Models

The Artificial Neural Network (ANN) has been used for forecasting in many areas of engineering. ANN are extremely simplified biological neural network mathematical models. An ANN is a network of distributed parallel information processing systems connecting an input vector to an output vector. It comprises of a number of components of information processing called neurons, divided into layers. ANN can be split into two types, based on the layer link patterns and neuron arrangement [24].

(1) Feed-Forward Networks,
(2) Feed-Back (Recurrent) Networks.

Feed-forward networks generate a number of output signals from an input set. The required transformation input–output is generally determined by externally supervised system parameter adjustment. Here the input data flows only through the network from one layer to another. Figure 4 shows a characteristic feed-forward network.

The input values are fed into input nodes in a feed-forward network which, after multiplying by a weight, passes them on the hidden layer nodes. A hidden layer node adds the weighted input obtained from each input node, associates it with a bias, and then transfers a nonlinear transfer function to the result. The output nodes perform the same procedure as a hidden node. The network is first trained before its application to any problem, where the target output is compared to the network output at each output node and the difference (error) is minimized by adjusting the weights and biases through training algorithms. The three variations of feed-forward networks are perceptron, multilayer perceptrons (MLPs), and radial-based function networks [24].

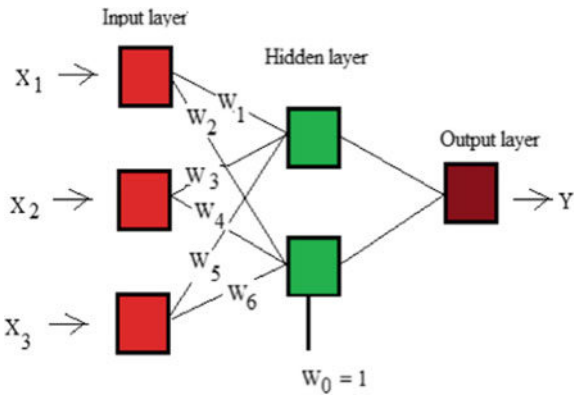

Fig. 4 A feed-forward neural network [24]

Table 2 Details of the data used

Flood event	No. of data	Month	Peak discharge m^3/s		
			Sarangkheda	Ukai	Ghala
1998	30	September	21292	20054	22500
2006	31	August	23044	26764	31230
2013	31	August	9027	12475	8447

The flood data for 1998, 2006, and 2013 were used to create ANN-based flood hydrograph models using MATLAB. The flood hydrograph was prepared to demonstrate the response of the discharge versus time. Details on the data for the three locations are given in Table 2. These models were developed using the Feed–Foreword network, the Levenberg Marquardt learning rule, and the Sigmoidal Axon transfer function. The model used 70% of the data for training, 15% of the data for testing, and 15% of the data for validation.

4 Results and Discussions

From the accessible flood data, nine models were created using ANN. The resulting graphs are displayed in Figs. 5, 6 and 7. Figure 5a–c show the actual versus predicted inflow for the 1998 flood event created using ANN having hidden layer 10, respectively, for Sarangkheda, Ukai, and Ghala. Models have been named M1, M4, and M7. Figure 6a–c show the actual versus predicted inflow for the 2006 flood event created using ANN for Sarangkheda gauge station, Ukai reservoir, and Ghala gauge station using hidden layer 10. Models have been named M2, M5, and M8. Figure 7a–c show the actual versus predicted inflow for the 2013 flood event developed using ANN for Sarangkheda gauge station, Ukai reservoir, and Ghala gauge station. For the Sarangkheda gauging station and the Ukai reservoir, 10 hidden layers were used and 15 hidden layers was used for the Ghala gauging station. The models were named M3, M6, and M9. All models show a nice correspondence with the actual value. It is noted that the predicted models are close to the actual data.

The correlation coefficient was produced to assess the efficiency of the model. The correlation coefficient for M1 to M9 is shown in Table 3. Compared to all models, the M3 model has a slightly lower correlation coefficient.

5 1998 Flood Event

Figure 8 shows the actual inflow of the 1998 flood hydrograph compared to the predicted inflow of the ANN for all the gauging stations. Heavy rainfall was observed in the upstream Sarangkheda and Ukai catchment areas with a high inflow of short

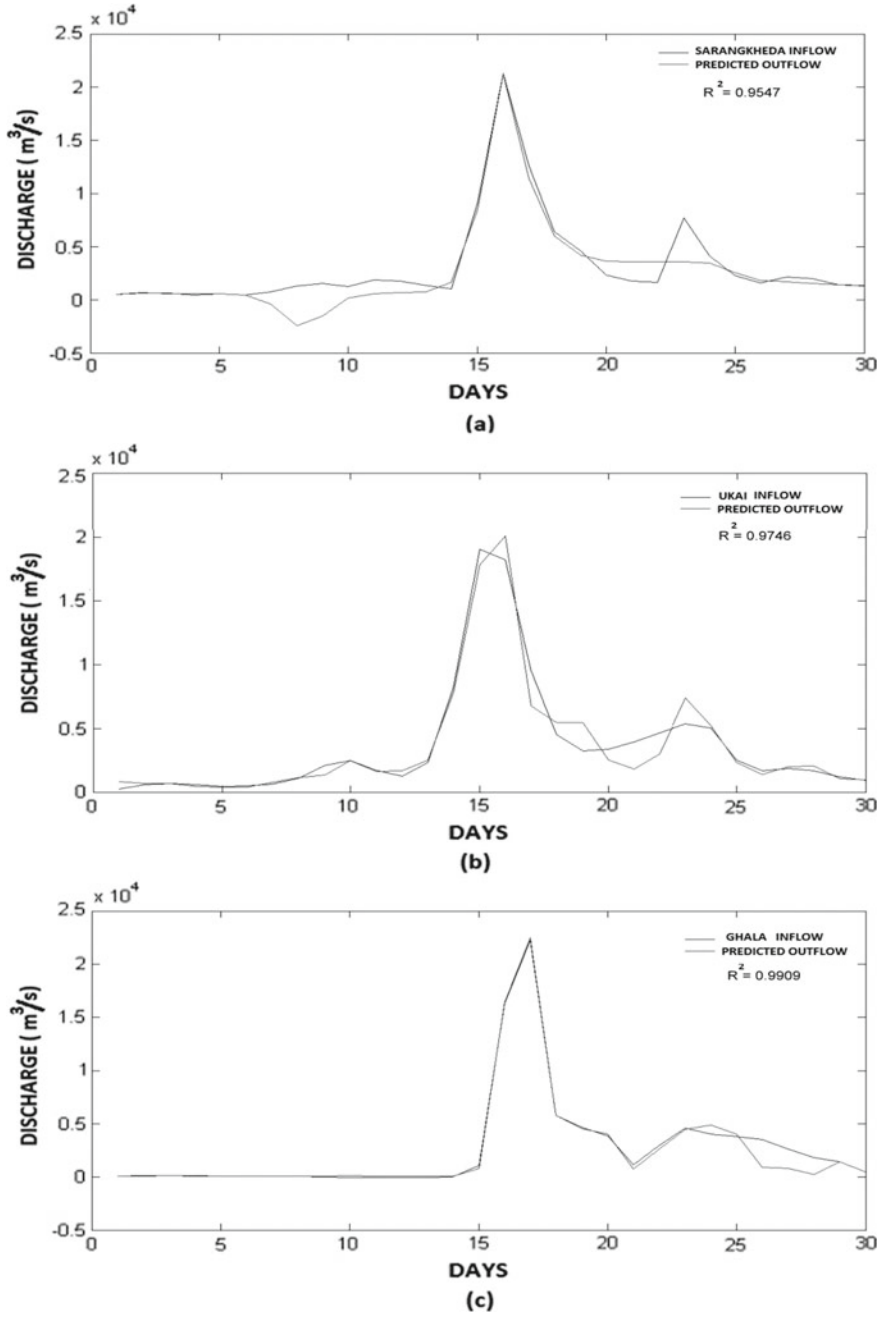

Fig. 5 **a** 1998 actual inflow versus predicted inflow for Sarangkheda (M1); **b**1998 actual inflow versus predicted inflow for Ukai (M4); **c**1998 actual inflow versus predicted inflow for Ghala (M7)

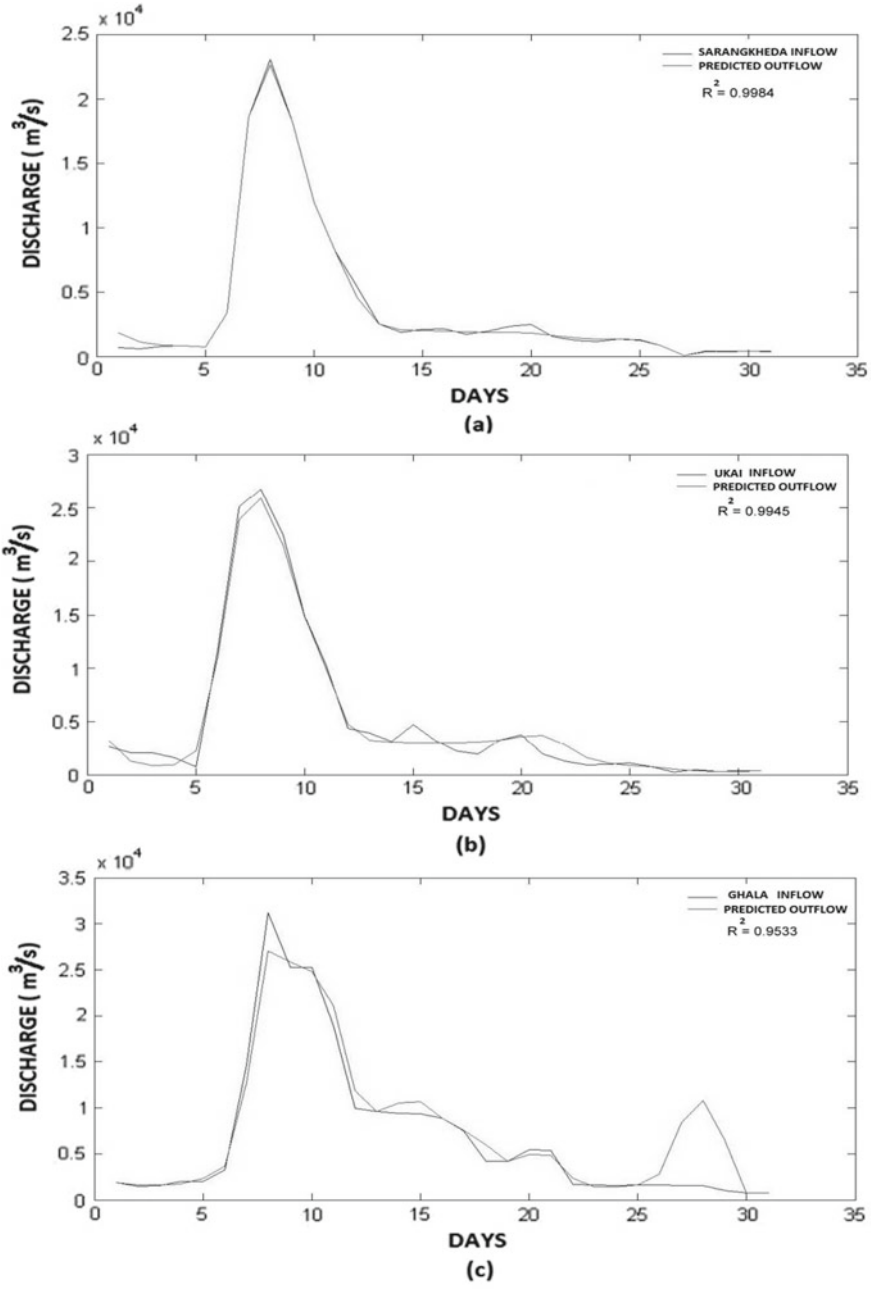

Fig. 6 **a** 2006 actual inflow versus predicted inflow for Sarangkheda (M2); **b** 2006 actual inflow versus predicted inflow for Ukai (M5); **c** 2006 actual inflow versus predicted inflow for Ghala (M8)

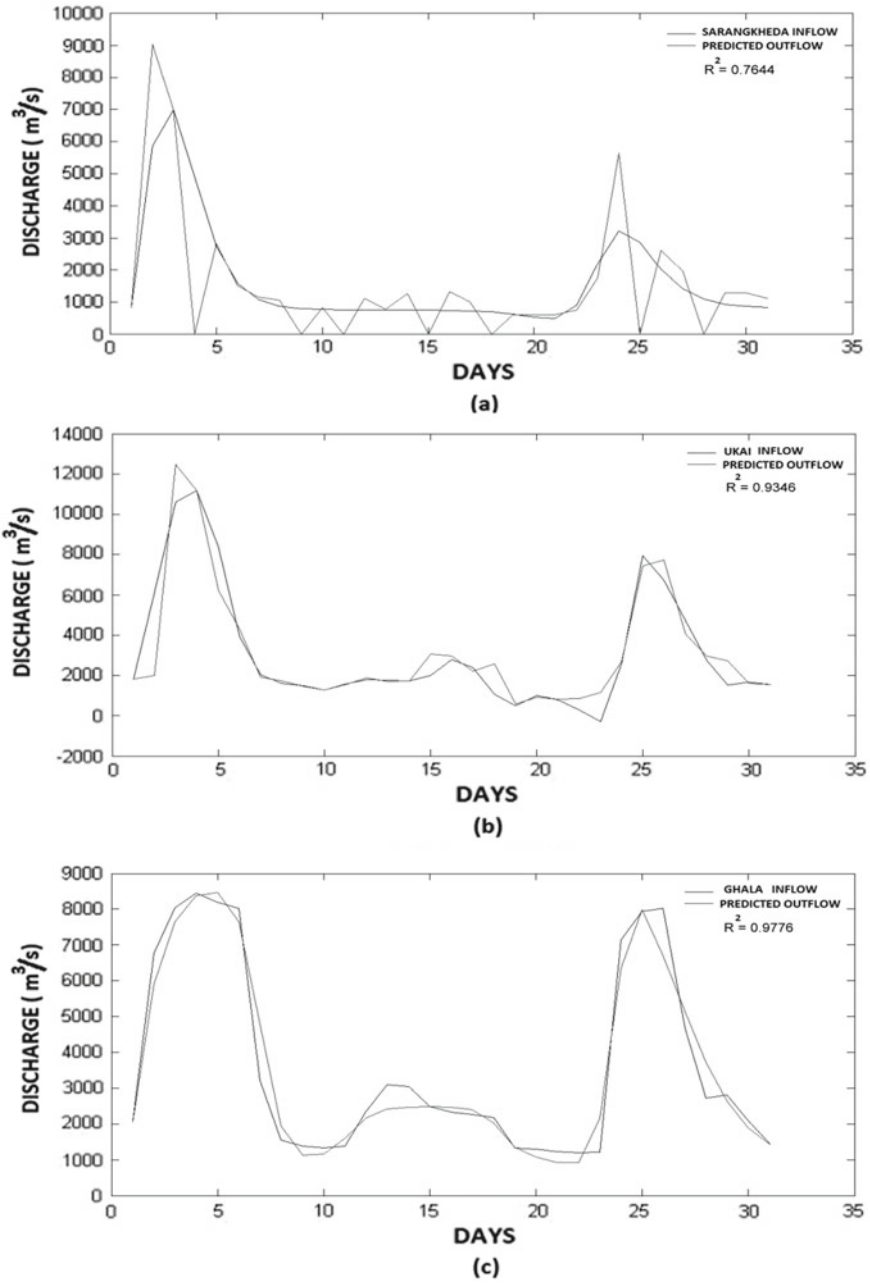

Fig. 7 **a** 2013 actual inflow versus predicted inflow for Sarangkheda (M3); **b** 2013 actual inflow versus predicted inflow for Ukai (M6); **c** 2013 actual inflow versus predicted inflow for Ghala (M9)

Table 3 Correlation coefficient

Model	Year	Location	Hidden layer	Correlation coefficient
M1	1998	Sarangkheda	10	0.9547
M2	2006		10	0.9984
M3	2013		10	0.7644
M4	1998	Ukai reservoir	10	0.9746
M5	2006		10	0.9945
M6	2013		10	0.9346
M7	1998	Ghala	10	0.9909
M8	2006		15	0.9533
M9	2013		15	0.9776

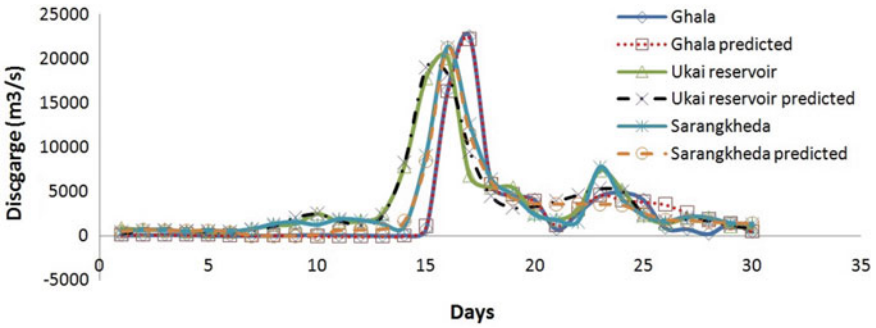

Fig. 8 Flood hydrograph of 1998 actual inflow versus predicted inflow

duration (Fig. 8). On 14 September the Ukai reservoir had a high inflow of 8250 and 1666 m^3/s from Sarangkheda. On 15 September the inflows from Sarangkheda and Ukai were 8476 m^3/s and 19054 m^3/s, respectively. In view of the high inflow to the reservoir, the dam authorities released 11577 m^3/s on 15 September 24:00 h. The inflow from Ghala on 15 September was 1066 m^3/s and the Nehru bridge was 8.4 meters. A peak inflow of 21213 and 18181 m^3/s for Sarangkheda and Ukai was observed on 16 September. The level of the Nehru Bridge was 10.2 m. Parts of the city of Surat have been flooded. Dam authorities decided to increase the releases by 22:00 h on 16 September, released 19822 m^3/s and continued until 7:00 h on 17 September. The peak discharge of 22500 m^3/s was observed at Ghala on 17 September. The flood level at Nehru Bridge reached 11.10 meters at 7:00 h on 17 September and increased to 11.40 m at 16:00 h 60% of the area in the Surat city was severely affected. The inflow decreased on 19 September and the water level began to decline. The level of the Nehru Bridge was reduced to 6.80 m. It could be seen from Fig. 8 the predicted ANN value was very well matched to the actual inflow.

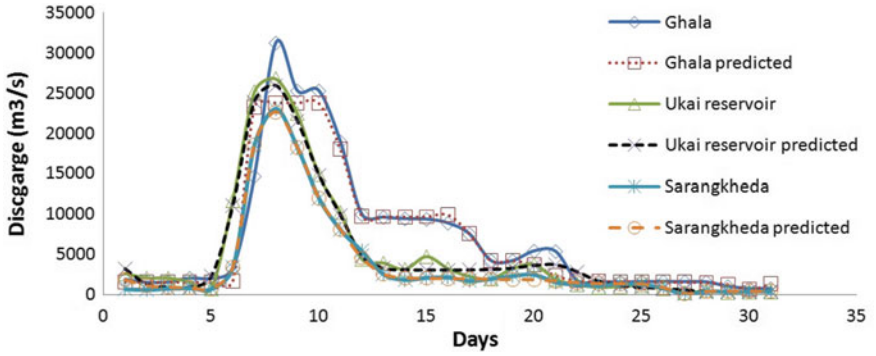

Fig. 9 Flood hydrograph of 2006 actual inflow versus predicted inflow

6 2006 Flood Event

Figure 9 shows actual inflow compared to the predicted ANN inflow for the 2006 flood. High intensity rainfall was reported in the Tapi basin. Ukai reservoir level was 331.54 feet on 1st August and 342.98 feet on 7th August. It increases further to 346.05 feet on 9th August. The inflow to the Ukai reservoir on 6th August was 11030 m^3/s and Sarangkheda was 3395 m^3/s, respectively. Releases from the Ukai dam on 6th August 22:00 h were 7214 m^3/s. It could be seen from Fig. 6a model M2 that Sarangkheda had a high inflow from 7th August and Fig. 6b model M5 represented a high inflow in Ukai reservoir from 6th August. On 7th August 8:00 h the inflow was 24173 m^3/s and the release was 11582 m^3/s from Ukai Dam. On the same day at 22:00 h, the inflow was 30375 m^3/s and the release was 23100 m^3/s, and high inflows being recorded on 8th and 9th August. On 12th August, the inflow reduced and the water level began to decline. At that time, the carrying capacity of the Tapi River downstream of the Ukai Dam was 9910 m^3/s. The flood level at Nehru Bridge had reached a level of 12.40 m. In 2006 the flood caused a catastrophe and a massive destruction of human life and property. According to the Government of Gujarat, a total of Rs 21,000 crores were damaged and 300 individuals died during the 2006 flood. The predicted ANN value was very well matched to the actual inflow.

7 2013 Flood Event

During the 2013 flood, it was noted from the flood hydrograph (Fig. 10) that there was less inflow from Sarangkheda. The highest inflow was from the Ukai catchment area. The highest release of 14158 m^3/s was from the Ukai dam. Ghala was registered with an inflow of 8447 m^3/s on 4th August and the inflow was the same for 3 days. At that time, the carrying capacity of the Tapi River downstream of the Ukai Dam was 8495 m^3/s. Part of the town was flooded. The floods stopped on 8th August 2013 and

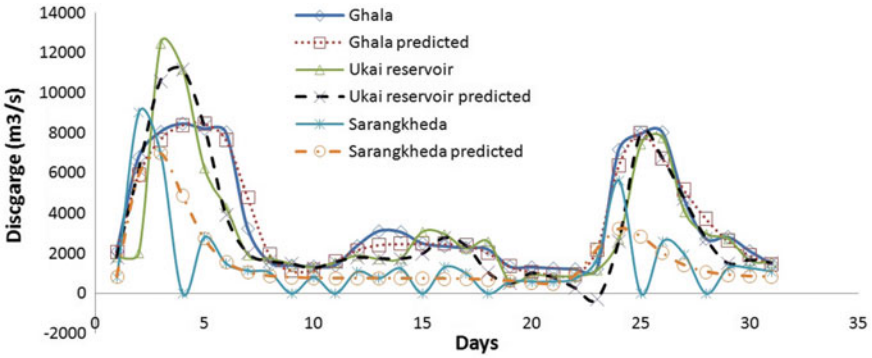

Fig. 10 Flood hydrograph of 2013 actual inflow versus predicted inflow

the water level began to decline. The predicted ANN value was very well matched to the actual inflow for Ukai reservoir and Ghala. While the predicted ANN value was slightly lower than the actual inflow for Sarngkheda.

8 Conclusion

The following findings can be summarized from the current analysis.

Predictions of real-time flood hydrographs for Tapi River, India have been developed using the artificial neural network.The feed-forward network is used to develop the artificial neural network models.The ANN-based model does not require physical parameters. The ANN-based flood hydrograph is an alternative technique, where time is a constraint and other necessary data are not available.

Models M1 to M9 demonstrate a nice agreement with the values observed. Model M3 has underestimated the flow in comparison to other models. Predicting flood hydrographs can be used for proper preparation, management, and mitigation. The outcome can be improved by altering the learning rule, the transfer function, the network and the hidden layer.

The ANN-based model will help analyze the flood hydrograph with a very short duration, otherwise, other software such as Mike 11 and Mike 21 will take longer.

Acknowledgments The authors would also like to acknowledge with a deep sense of gratitude the valuable help received from the authorities of Sardar Vallabhbhai National Institute of Technology (SVNIT) and the P. G. Section of Water Resources Engineering.

References

1. Liong SY, Lim WH, Paudyal GN (2000) River stage forecasting in Bangladesh: neural network approach. J Comput Civ Eng 14(1):1–8. https://doi.org/10.1061/(ASCE)0887-3801(2000)14:1(1)
2. Feng LH, Lu J (2010) The practical research on flood forecasting based on artificial neural networks. Expert Syst Appl 37(4):2974–2977. https://doi.org/10.1016/j.eswa.2009.09.037
3. Thirumalaiah K, Deo MC (2000) Hydrological forecasting using neural networks. J Hydraul Eng 5(2):180–189. https://doi.org/10.1061/(ASCE)1084-0699(2000)5:2(180)
4. Leahy P, Kiely G, Corcoran G (2008) Structural optimisation and input selection of an artificial neural network for river level prediction. J Hydrol 355(1–4):192–201. https://doi.org/10.1016/j.jhydrol.2008.03.017
5. Maier HR, Jain A, Dandy GC, Sudheer KP (2010) Methods used for the development of neural networks for the prediction of water resource variables in river systems: current status and future directions. Environ Model Softw 25(8):891–909. https://doi.org/10.1016/j.envsoft.2010.02.003
6. Mukerji A, Chatterjee C, Raghuwanshi NS (2009) Flood forecasting using ANN, neuro-fuzzy, and neuro-GA models. J Hydraul Eng 14(6):647–652. https://doi.org/10.1061/(ASCE)HE.1943-5584.0000040
7. Nanda T, Sahoo B, Beria H, Chatterjee C (2016) A wavelet-based non-linear autoregressive with exogenous inputs (WNARX) dynamic neural network model for real-time flood forecasting using satellite-based rainfall products. J Hydrol 539:57–73. https://doi.org/10.1016/j.jhydrol.2016.05.014
8. Panda RK, Pramanik N, Bala B (2010) Simulation of river stage using artificial neural network and MIKE 11 hydrodynamic model. Comput Geosci 36(6):735–745. https://doi.org/10.1016/j.cageo.2009.07.012
9. Pramanik N, Panda RK (2009) Application of neural network and adaptive neuro-fuzzy inference systems for river flow prediction. Hydrol Sci J54(2):247–260. https://doi.org/10.1623/hysj.54.2.247
10. Eli Smith RN (1995) Neural-network models of rainfall-runoff process. J Water Resour Plan Manag 121(6):499–508. https://doi.org/10.1061/(ASCE)0733-9496(1995)121:6(499)
11. Tripura J, Roy P (2017) Flow forecasting in multiple sections of a river system. KSCE J Civ Eng 21(2):512–522. https://doi.org/10.1007/s12205-017-1514-9
12. Yazdani MR, Zolfaghari AA (2014) Monthly river forecasting using instance-based learning methods and climatic parameters. 1–11. https://doi.org/10.1061/(ASCE)HE.1943-5584.0001490
13. Chau KW (2006) Particle swarm optimization training algorithm for ANNs in stage prediction of Shing Mun river. J Hydrol 329(3–4):363–367. https://doi.org/10.1016/j.jhydrol.2006.02.025
14. Sahay RR, Srivastava A (2014) Predicting monsoon floods in rivers embedding wavelet transform, genetic algorithm and neural network. Water Resour Manag 28(2):301–317. https://doi.org/10.1007/s11269-013-0446-5
15. Wu CL, Chau KW, Fan C (2010) Prediction of rainfall time series using modular artificial neural networks coupled with data-preprocessing techniques. J Hydrol 389(1–2):146–167. https://doi.org/10.1016/j.jhydrol.2010.05.040
16. Seo Y, Kim S (2016) River stage forecasting using wavelet packet decomposition and data-driven models. Procedia Eng 154:1225–1230. https://doi.org/10.1016/j.proeng.2016.07.439
17. Yaseen ZM, El-Shafie A, Afan HA, Hameed M, Mohtar WHMW, Hussain A (2016) RBFNN versus FFNN for daily river flow forecasting at Johor River, Malaysia. Neural Comput Appl 27(6):1533–1542. https://doi.org/10.1007/s00521-015-1952-6
18. Yaseen ZM, Kisi O, Demir V (2016) Enhancing long-term streamflow forecasting and predicting using periodicity data component: application of artificial intelligence. Water Resour Manag 30(12):4125–4151. https://doi.org/10.1007/s11269-016-1408-5
19. Atiaa AM (2015) Modeling of stage-discharge relationship for Gharraf River, southern Iraq by using data driven techniques a case study. 31–46

20. Nikoo M, Ramezani F, Hadzima NM, Nyarko EK (2016) Flood-routing modeling with neural network optimized by social-based algorithm. Nat Hazards 82(1):1–24. https://doi.org/10.1007/s11069-016-2176-5
21. Fu JC, Hsu MH, Duann Y (2016) Development of roughness updating based on artificial neural network in a river hydraulic model for flash flood forecasting. J Earth Syst Sci 125(1):115–128. https://doi.org/10.1007/s12040-015-0644-z
22. Kumar V, Yadav SM (2018) Optimization of reservoir operation with a new approach in evolutionary computation using TLBO algorithm and jaya algorithm. Water Resour Manag 32(13):4375–4391. https://doi.org/10.1007/s11269-018-2067-5
23. Agnihotri PG, Patel JN (2008) Construction of digital elevation model and contour map for 2006 flood at Surat (India). World Appl Sci J5(3):318–323
24. Kumar V, Yadav SM, Zore P, Venkateswarlu T (2014) ANN and MLR based stage-discharge models for Dehli Gauging station of kim river, Gujarat
25. Central Water Commission. http://cwc.gov.in/

Development of Synthetic UH by Using Geomorphologic Instantaneous Unit Hydrograph (GIUH) Based Nash Model

A. Agrawal and R. K. Shrivastava

Abstract The present study is aimed at developing a methodology suitable for the development of unit hydrograph for un-gauged catchments. As we know in developing countries like India, there is a paucity of the gauged catchment. Research has been done to seek out this problem. In this research, we have found different ways to find the geophysical characteristics of un-gauged catchment. In previous times, there were certain methods to find the geomorphologic characteristics, but these methods were very difficult to apply and time consuming, so our first need was to overcome these problems. There were certain softwares like ILWIS, GRASS, and ERDAS which were introduced and used to find the characteristics in much less time than before and with much more ease. In this research, data is evaluated from DEM through Arc-GIS. This research uses GIUH-based NASH model. Through this model, better instantaneous unit hydrograph was found as compared to any other techniques that were applied in previous time. The curve found through this model is exactly same as the ideal curve.

Keywords Geomorphologic instantaneous unit hydrograph · Nash model · GIS · Arc-GIS · DSRO · Rainfall-runoff · Un-gauged catchment

A. Agrawal (✉)
Department of Civil Engineering, Shri Govindram Seksaria Institute of Technology and Science, Indore, India
e-mail: abhidrakchas@gmail.com

R. K. Shrivastava
Prof & Ex Director, Shri Govindram Seksaria Institute of Technology and Science, Indore, India
e-mail: rk.shrivastav@gmail.com

© Springer Nature Singapore Pte Ltd. 2021

K. K. Pathak et al. (eds.), *Recent Trends in Civil Engineering*, Lecture Notes in Civil Engineering 77, https://doi.org/10.1007/978-981-15-5195-6_72

1 Introduction

1.1 General

Water is considered as the necessary element for any kind of survival. There is a need of a lot of engineering works to maintain the balance between the demand and its supply. The engineering is required in the planning design and construction of dams and barrage, etc. These safeties mainly depend on the flow of discharge and are also required to be protected against the flurry flood. During floods these structures are really helpful because these structures are designed on the basis of chosen design flood and proper operation of the reservoir [1].

In developing countries, watershed is either ungauged or poorly gauged because of which modeling task gets difficult. For the modeling of watershed, we require huge data and information but if data is unavailable then the modeling will become very difficult. These are many researchers for developing synthetic mild hydrograph for the evolution of design flood [2, 3]. However, there are some limitation due to which it becomes very difficult to develop rational unit hydrograph.

During these years there are many attempts which are made to develop the method of synthetic unit hydrograph which will help to overcome the limitation of previous techniques that are being used before.

Determination of flood peak and runoff volume especially from the un-gauged watershed, Synthetic unit hydrographs (SUHs) is used. A comprehensive review of several methods dealing with the SUH derivation is provided by Singh (1988). Their simplicity and ease in the development can be characterized by their synthetic unit hydrographs [1, 2, 4–7].

IUH- At a discrete point in time, the input rainfall is assumed for an IUH. Duration $D \rightarrow 0$ is basically indicated by a finite unit hydrograph& the hydrograph of zero duration in a limiting case is known as instantaneous unit hydrograph [6].

1.2 Objectives

The present study is aimed at developing a methodology suitable for the development of unit hydrograph for un-gauged catchments of Lower Narmada Zone-based. The main objectives of the study are as follows:

- To review various techniques used for Unit Hydrograph generation and develop a report in the form of literature review.
- To identify an appropriate technique from the reviewed literature for developing Unit Hydrograph in a region.
- To identify a suitable area and to procure relevant data for the identified area for problem formulation.

- To process the acquired data so as to prepare it as input to the program for the identified technique.
- To develop strategies for developing Unit Hydrograph in the study area.
- To derive the conclusions on the basis of developed strategies.

1.3 Prologue

This study is described in the following steps:

- Chapter 2 deals with the details of the study area and data acquisition.
- Chapter 3 gives the description of the methodology for producing the Instantaneous Unit Hydrograph at the river site.
- Chapter 4 explains the Result and Discussion.
- Chapter 5 deals with the Conclusion.
- Finally, References and Appendices are given.

2 Study Area and Data Acquisition

2.1 General

In this study we took the Narmada river as our study area. It is the largest river that is flowing in the direction from east to west. This river flow in the Amarkantak plateau of maikala range in the shahdol district of Madhya Pradesh at an elevation of 1057 meters above mean sea level at latitude 22°40' north and a longitude of 81°45' east. The total no. of distance traveled by the river is 1312 km before it falls in the gulf of Cambay in the Arabian sea near Bharuch in Gujrat. There are total of 41 tributaries and each tributary has a catchment area of 500 km^2.

These tributaries are in two directions, i.e., southern and the northern side. Basically 22 are on the southern side and 19 are on the northern side. Out of 41, 39 are present in Madhya Pradesh and two are present in Gujrat [8].

2.2 Study Area

In the Seoni district of Madhya Pradesh the Sher rises. It is present in the Sapura range near Patna. The elevation of Sher is 600 m at a North latitude of 22° 31' and an East longitude of 79° 25'. The direction of the flow of Sher is north-westerly with a total length of 129 km and finally merges into the Narmada. The total area of Sher is 2,901 km^2.

There is another tributary of Narmada river in the Vindhya range of Madhya Pradesh Uri River, at an elevation of 450 m at latitude 22° 36' N and longitude of 74° 47' E with the total length of 74 km.

2.3 Geomorphologic Characteristics

The runoff hydrologic response of a drainage basin basically depends on the characteristics of the watershed. So it is mandatory to understand the different characters of the river basin. As far as the runoff estimation is concerned, geomorphological characteristics of a basin are the most important parameters. The geomorphological characteristics deal with the physical characteristics which include watershed shape, drainage area, ground slope, and centroid of the watershed, and the channel characteristics; include the channel length, channel order, channel slope, and drainage density. Like watershed slope, stream order, watershed areas, length of the stream, the number of streams are used in this paper work [1, 9, 10].

2.4 Data Collection

General. Extreme of the rainfall-runoff modeling requires properly measured and reliable streamflow and precipitation data. In addition, data of soil type, land use, temperature, humidity, and other parameters are also required in some models. In the present study, without using rainfall data, it is possible to develop unit hydrograph with a great accuracy.

Physiographic Characteristics. The whole data regarding the identified catchment, physiographic catchment are basically collected for NCA. The computed data is tabulated in Table 1.

Table 1 Physiographic details of identified catchments

S. No.	River	Area (km^2)	Length (km)		Slope (m/km)
1	Sher	1615	112.6		2.95
2	Uri	784	74		7.14

3 Methodology

3.1 Introduction

We use the GIS layer combined with physical data and the Nash model for current research. The whole study is based on two methodologies first the requirement of data and after that these data were used as input to GIUH based NASH model [3].

3.2 Extraction of Geomorphological Characteristics and Processing of Digital Elevation Model from Digital Elevation Model (DEM)

By processing the toposheets of catchment, the extraction of geomorphological characteristics is possible. But this process is difficult & slow. So, to overcome this difficulty, there are certain software like ILWIS, GRASS, ERDAS, etc., that are used. These do not take too much time and are effortless. There is a new process known as DEM hydroprocessing module allow to extract, through several steps, i.e., by the number. of streams, the average length of streams, and the average area of the catchments of a given order and even for the Horton ratios R_B, R_L, and R_A [5, 7, 11].

Digital Elevation Model is a topographic map or satellite picture, which contains grading of all the points located in the area. Area of DEM data was obtained from Global DEM Explorer. Uri and Sher river basin extraction was operated in Arc-GIS.

The DEM of the catchment of the Narmada river basin extracted following the above procedure was imported by Arc GIS to determine the Horton's ratio and other geomorphological parameters.

3.3 Geomorphological Parameters and Horton's Ratio Computation

The geomorphological parameters of the required catchment and Horton's ratios, i.e., bifurcation ratio (R_B), stream length ratio (R_L), and stream area ratio (R_A) are unique representative parameters for a given watershed [1, 6, 7, 11].

Bifurcation Ratio (Rb)
The bifurcation ratio is given as follows.

$$R_B = N_i / N_{i+1} \tag{1}$$

where, R_B is the bifurcation ratio, and Ni and N_{i+1} = the numbers of streams in order i and $i + 1$, respectively.

Stream Length Ratio (Rl)
The R_L expressed are as follows:

$$R_L = L_{i+1}/L_i \tag{2}$$

where L_i and $L_i + 1$ is average length of order ith and $i + 1$th order, respectively.

Stream Area Ratio (Ra)
The R_A expressed are as follows:

$$R_A = A_{i+1}/A_i \tag{3}$$

where, A_i and $A_i + 1$ is the average area of order i and $i + 1$, respectively.

The complete shape of the GIUH can be obtained by linking q_p and t_p of the GIUH with the scale (k) and shape (n) parameters of the Nash IUH model.

$$\frac{\partial}{\partial t} \ln[U(t)] = \left[-\frac{1}{K} + \frac{n-1}{t}\right] \tag{4}$$

If we equate the first derivation of the equation with zero, then time t will convert into t_p and after differentiating with respect to t and simplifying we get Eq. (4) to zero results in the following expression, where t is equal to t_p.

$$\left[-\frac{1}{K} + \frac{n-1}{t}\right] = 0 \tag{5}$$

And hence

$$t = t_p = K(n-1) \tag{6}$$

Substituting the value of tp from Eq. (6) in Eq. (4) and simplifying, we get

$$q_p = \frac{1}{K\Gamma n} * e^{-(n-1)} * (n-1)^{n-1} \tag{7}$$

From Eqs. (6) and (7), we get

$$q_p t_p = \frac{n-1}{\Gamma n} * e^{-(n-1)} * (n-1)^{n-1} \tag{8}$$

Equating Eq. (10) with Equation

$$qptp = 0.5764 * \left[\frac{RB}{RA}\right]^{0.55} * RL^{0.05}$$

we get

$$\frac{n-1}{\Gamma n} * e^{-(n-1)} * (n-1)^{n-1} = 0.5764 * \left[\frac{RB}{RA}\right]^{0.55} * RL^{0.05} \quad (9)$$

All the terms in the right-hand side of Eq. (9) are known. The only unknown term is the Nash model parameter n, which is obtained by solving Eq. (9) using the Newton Rapson method of nonlinear optimization. The Nash model parameter k for the given velocity V is obtained using Equations ($tp = \frac{0.44L}{V} * \left[\frac{RB}{RA}\right]^{0.55} * RL^{-0.38}$) and (6) and the known value of the parameter n is as follows:

$$K = \frac{0.44L}{V} * \left[\frac{RB}{RA}\right]^{0.55} * RL^{-0.38} * \frac{1}{n-1} \quad (10)$$

We get the dynamic velocity relation from the equation below

$$V = 0.8562 * L^{0.23} * S^{0.385} \quad (11)$$

Here L = length of the stream/ditch from headwater to the outlet or main stream length in meter (m), S = mean watershed slope, and V = dynamic parameter velocity in m/s.

4 Results and Discussions

4.1 Geomorphological Characteristics of the Catchment

The DEM map of India was used to delineate the catchment of Sher and Uri river basin using ArcGIS application. The DEM map of Sher and Uri river catchment shown in Fig. 1 was imported by the GIS in order to determine the necessary geomorphological parameters of the catchment, following the procedures and steps specified in the section of methodology.

The stream ordering map of the catchment is shown in Fig. 2 and both the river is found to be 5th order according to the stream ordering definition (Figs. 3, 4 and 5).

Based on the analysis while developing Synthetic Unit Hydrograph using GIUH model for Sher and Uri Catchment are mention below.

- Using the DEM of the study area the following catchment characteristics were determined. By using various characteristics like area, highest order stream length,number of stream and stream order, etc.; GIUH parameter such as Stream

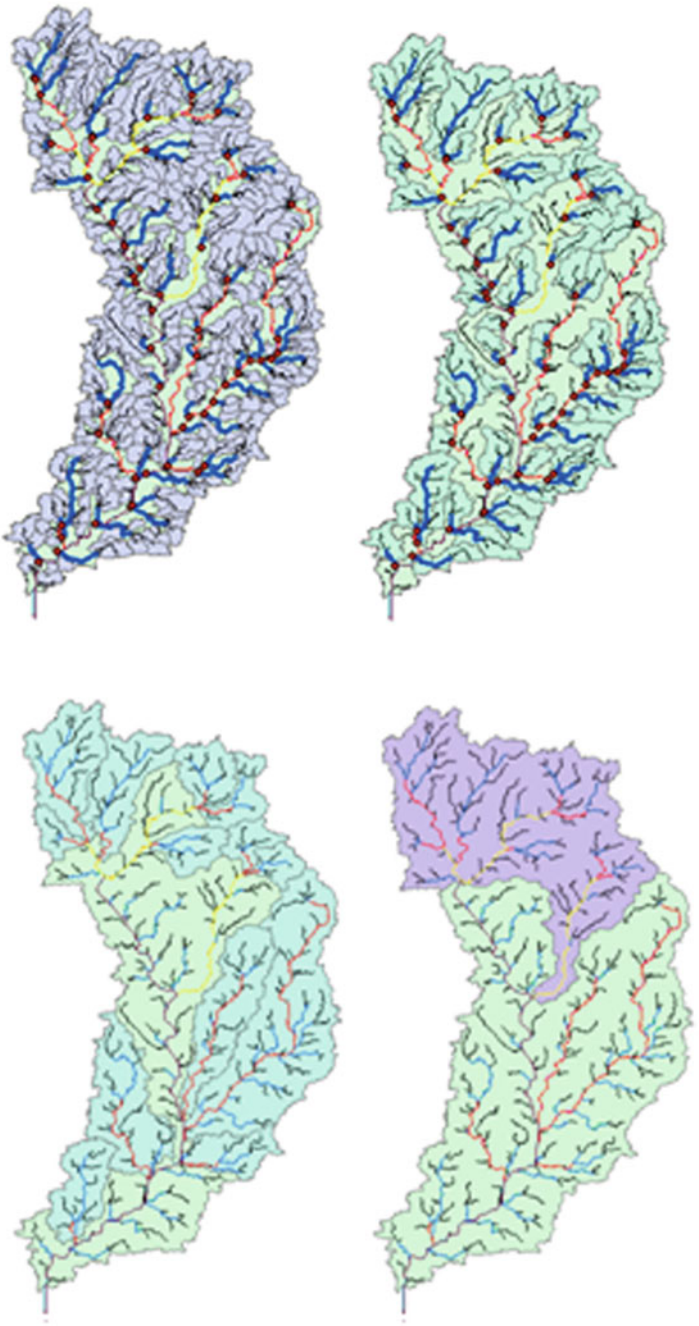

Fig. 1 Uri catchment shows different stream orders covering different areas. Where black, blue, red, yellow, purple line show stream order 1, 2, 3, 4, 5, respectively

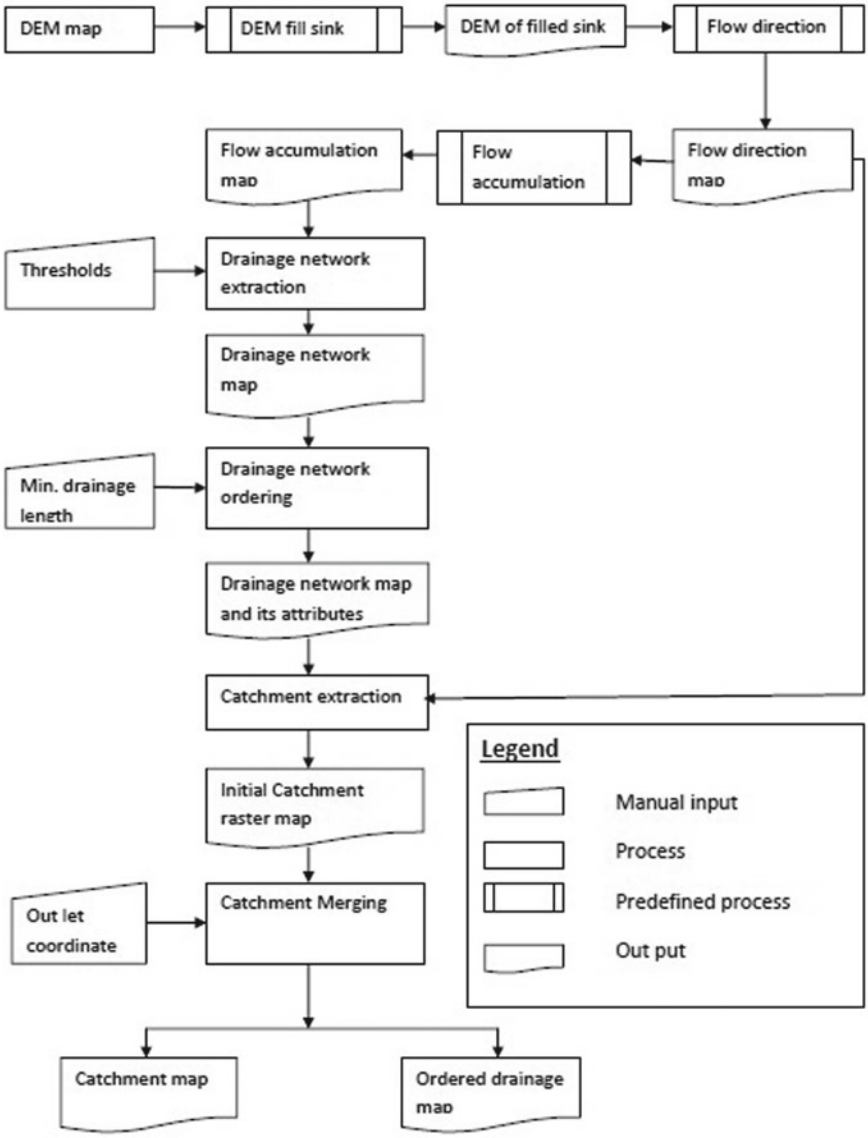

Fig. 2 DEM processing flowchart

Area ratio (RA), Stream Length Ratio (RL), and Bifurcation ratio (RB) can be estimated (Table 2).

- The synthetic unit hydrograph derived based on the GIUH based Nash model approaches considering the SHER basin as gauged has been compared with observed hydrograph and 2PGD model as shown in Figs. 6 and 7.

Fig. 3 Uri river catchment DEM map

- URI basin (ungauged catchment) Unit hydrograph has been derived using the GIUH model.
- Relative error of the developed Synthetic Unit Hydrograph calculated for the GIUH model is 1.14466 while for 2PGD model is 3.761062.

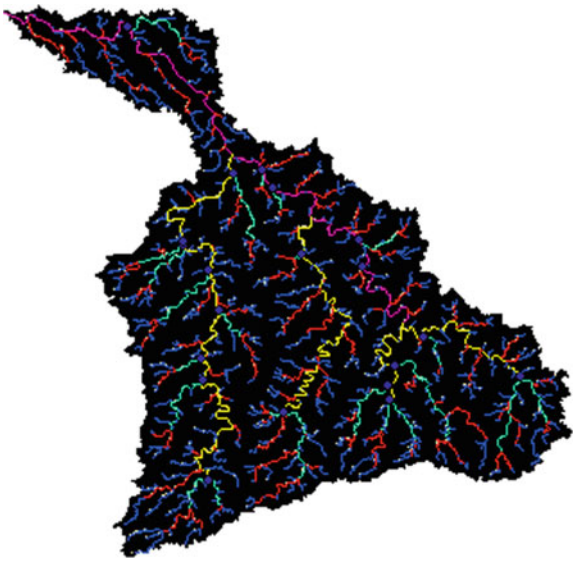

Fig. 4 Sher river basin stream ordering map

5 Conclusions

Based on the above analysis and the results obtained after applying the proposed methodology, the following conclusions were drawn:

- The SUH for ungauged catchment were determined using the GIUH based Nash model for the present study.
- GIUH model performs better than 2PGD on the basis of RE (relative error for peak discharges) when compared with 2PGD.
- All the parameters used for the model are explored from Arc GIS and are further used to derived Unit hydrograph.
- The parameter used in the GIUH model for Sher Basin (gauged) was "*n*" as 4.7652 and "*k*" as 2.07161 depending on catchment characteristics like RA, RB, and RL.
- The parameter used in the GIUH model for Uri Basin (gauged) was '*n*' as 5.2412 and '*k*' as 1.30188 depending on catchment characteristics like RA, RB, and RL.
- GIUH model requires a Digital Elevation Model (DEM) only for generating SUH, while 2PGD does not. 2PGD requires a set of data that includes Area, Slope, and length of the river. The SUH for ungauged catchment was determined using the GIUH based Nash model.

Scope for Further Studies. Based on the experience gained in the present study following extensions of the present study are suggested

- Other methods of Synthetic Unit Hydrograph generation (e.g., GIUH based Clark model, HEC-1, Nakayasu Method, etc.) can also be attempted for Narmada catchments.

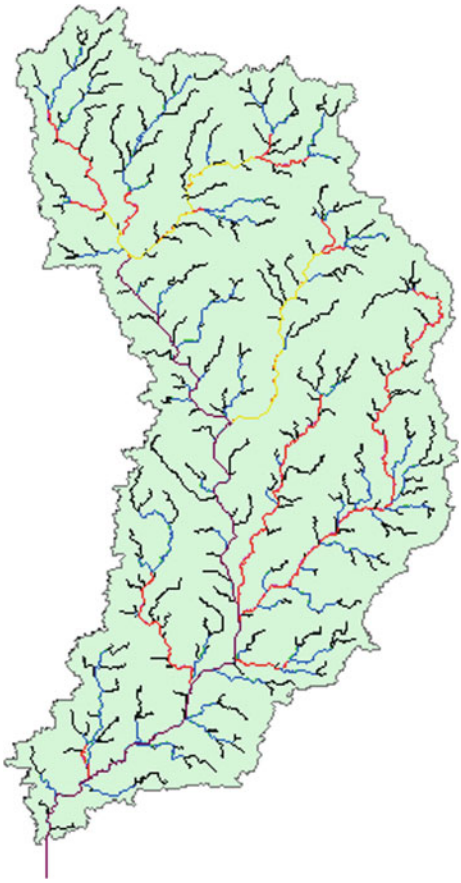

Fig. 5 Uri river basin stream ordering map

Table 2 Calculated catchment characteristics of URI and SHER

Catchment	Area (km)	Highest order stream length (km)	No. of stream	Stream order
SHER	1658	81.598	779	5
URI	826	56.66	367	5

- Similar studies can be conducted for other river basins.
- Same technique may be used for developing synthetic unit hydrograph for another subbasin of the Narmada river.

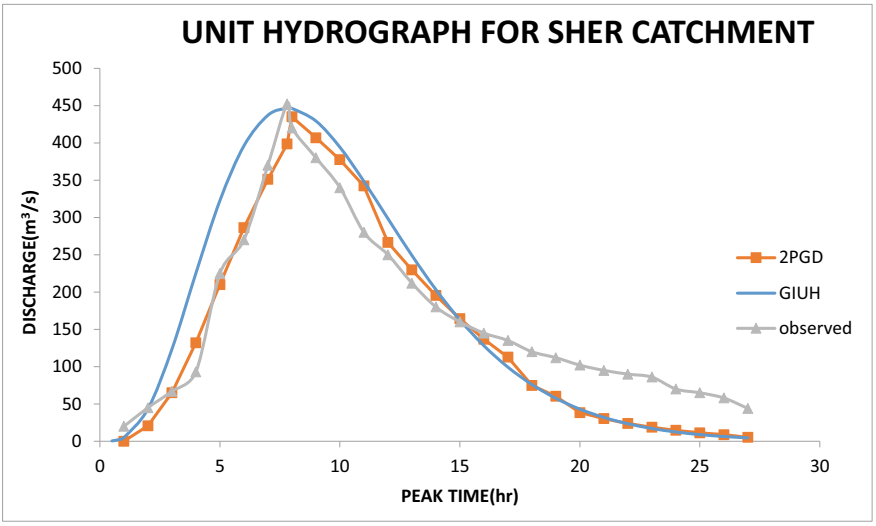

Fig. 6 Synthetic unit hydrograph of SHER catchment

Fig. 7 Synthetic unit hydrograph of URI catchment

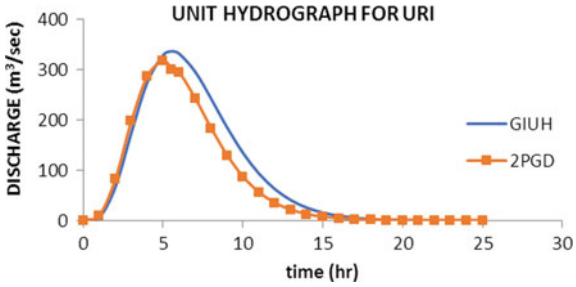

References

1. Alemngus A, Mathur BS (2014) Geomorphologic instantaneous unit hydrographs for rivers in eritrea (east africa). J Ind Water Resourc Soc 34(1):1–14
2. Flores I, Sordo-Ward A, Mediero L, Garrote L (2013) Synthetic generation of arbitrarily long series of flood hydrographs for flood risk assessment. J Geophys Res Abst 15
3. Jain V, Sinha R (2003) Derivation of unit hydrograph from GIUH analysis for a Himalayan River. J Water Resourc Manage 17:355–375 Kluwers Academic Publishers
4. Dhahir MR (2011) Two Parameter gamma distribution and log normal distribution for derivation of synthetic unit hydrograph. J Eng 17:142–148
5. Ellouze-Gargouri E, Bargaoui Z.(2012). Runoff estimation for an ungauged catchment using geomorphological instantaneous unit hydrograph (GIUH) and copulas. J Water Resour Manage 26:1615–1638
6. Jain SK, Singh RD, Seth SM (2000) Design flood estimation using GIS supported GIUH approach. J Water Resourc Manage, Kluwers Academic Publishers 369–376

7. Khaleghia MR, Gholamib V, Ghodusic J, Hosseinia H (2011) Efficiency of the geomorphologic instantaneous unit hydrograph method in flood hydrograph simulation. J Hydrol Eng Elsevier 87:163–171
8. Ghorbani MA, Hasanpour-Kashania M, Zeynalia S (2013) Development of synthetic unit hydrograph using probability models. Res Civil Environ Eng 1:54–66
9. Jotish N, Choudhury P, Nazrin U, Singh K (2011) A geomorphologic based rainfall-runoff model for un-gauged watersheds. Int Gen Geomat Geosci 2(2):676–687
10. Rai RK, Upadhyay A, Sarkar S, Upadhyay AM, Singh VP (2009) GIUH based transfer function for gomti river basin of India. J Spat Hydrol 9(2)
11. Jain SK, Agarwal PK, Singh VP (2007) Narmada basin. In: Hydrology and water resources of india. water science and technology library, vol 57. Springer, Dordrecht

Environmental Engineering

The Selection of Wastewater Treatment Units Based on Analytical Hierarchical Process

Atul Sharma and Nekram Rawal

Abstract Nowadays, various recognized technologies exist for the treatment of municipal wastewater. Each technology has its own advantages and limitations depending on appropriateness to fulfill the desired requirements. In this study, an effort is made to use the MCDM tool to select the most appropriate technology for municipal wastewater treatment in a small to medium city, where availability of land is not a major constraint. The Analytical hierarchy process (AHP) has been used as a decision-making tool, the expert opinions and judgments are used to assign quantitative and qualitative weights to different criterion and sub-criterion. The available options were compared based on three main criteria, i.e., economical aspects, technological aspects, and environmental and health aspects, and thirteen sub-criteria. In the present scenario in India, the three simple and effective treatment technologies were used in this study: (A) Trickling filter system (B) Waste stabilization pond system, and (C) Activated sludge process. The AHP analysis on three options revealed that the waste stabilization pond technology is an appropriate technology with the highest priority value of 40% among the other options.

Keywords Wastewater technology selection · AHP · Trickling filter · Waste stabilization pond · Activated sludge process

1 Introduction

The population in urban boundaries is increasing exponentially. Water is one of the most essential needs of every living entity. Nowadays, the disposal of untreated wastewater is becoming one of the major concerns for society. Since many municipal corporations in India still don't have a wastewater treatment facility, they directly disposed off wastewater into local water bodies or streams, which in due course

A. Sharma (✉) · N. Rawal
Motilal Nehru National Institute of Technology Allahabad, Prayagraj, India
e-mail: atul@mnnit.ac.in

N. Rawal
e-mail: nrrawal@mnnit.ac.in

© Springer Nature Singapore Pte Ltd. 2021

K. K. Pathak et al. (eds.), *Recent Trends in Civil Engineering*, Lecture Notes in Civil Engineering 77, https://doi.org/10.1007/978-981-15-5195-6_73

of time meet to main rivers and pollute them. Since conventional sewage treatment methods are costly and require skilled manpower for their operation and maintenance, many small municipal corporations do not give sufficient weightage to sewage treatment. As per CPHEEO, approximately 70–80% of domestic water supplied becomes discharged as wastewater. There is a significant gap between wastewater generation and available installed wastewater treatment plant capacity. The CPCB 2009 reports, urban areas are generating 35254 MLD sewage while treatment facilities for 11777 MLD only available. Recently, the answer to Lok Sabha's question given by the Ministry of Environment and Forest, Government of India revealed that total wastewater generation from urban areas in the country has grown up to 61948 MLD and the available installed treatment capacity is 23277 MLD only. i.e., total of 920 numbers of STPs are working to treat wastewater. There is a huge gap between the generation and wastewater treatment system and numbers of STPs are required to fill these gaps by choosing appropriate treatment technologies.

In India, The local authorities, i.e., Nagar Nigam are mainly responsible for the collection and treatment of wastewater in the city. The insufficient funds and lack of infrastructural facilitates are quite negligent toward wastewater collection and its treatment. In this situation, the selection of the most suitable municipal wastewater treatment options among the alternatives is a complex decision-making problem with limited available resources. The various treatment technologies options like Activated Sludge Process, Trickling Filter, Rotating Biological Contactor, Oxidation ditch, Waste Stabilization Pond, etc., are commonly used to treat wastewater. The MCDM tools can be used to deal with such a problem choosing appropriate treatment technologies. There are numerous MCDM tools that are available and used, depending upon the nature of the decision-making problem [1]. The MCDM tools are used by different researchers for addressing complex decision-making problems for several decades. Many researchers used numbers of MCDM tools like AHP, ANP, Fuzzy set theory, case-based reasoning, MAUT, simple multi-attribute rating technique, goal programming, SAW and ELECTRE, etc., and each tool has its own merits and shortcomings and limitation in the area of applications. The MCDM techniques also applied in many areas like environmental sciences, management, economics, and product design and in business for giving ranking to alternatives available [2]. An important step of these methods is the involvement of decision makers and their opinion in the whole process of evaluation [3]. ELECTRE is one of the MCDM techniques applied in water management, transportation problems, energy, and environmental field. Uncertainty and vagueness in problem can be addressed through this method [4]. The environmental problem of contaminated groundwater assessment used the cost-benefit method [5]. The AHP tool used for the urban water supply system in Nigeria [6]. The selection of hospital waste suppliers by the AHP tool [7]. The AHP and PROMETHEE tools were used for the selection of proper excavation machines and concluded that the final results of both the method are identical [8].

The AHP tool is one of the most widely used and internationally accepted techniques developed by Prof. Satty [9] in the decision-making problem. The AHP tool allows qualitative and quantitative elements in analysis through field data and experts' subjective judgments. The parameters related to environmental, social, and

human health can easily incorporate through the use of AHP [10]. The provision of consistency checks makes it more reliable than in another method like TOPSIS which doesn't allow such facility [11]. The selection of best municipal solid waste disposal site facility by AHP tool and different sustainability criteria [12]. In this study, an attempt has been made to select the most appropriate wastewater treatment technology from Activated Sludge Process (ASP), Trickling Filter (TF), and Waste Stabilization Pond (WSP) options by Economic, Technological, and Environmental Aspects. The Expert Choice software was used for the AHP analysis.

2 Methodology

2.1 Identification of Design Options

This study is used to select the appropriate wastewater technology among the three technologies for WWT plant in central India. The three technologies are [13, 14]:

(A) Option 1: Wastewater Treatment Plant with trickling filter (TF)
(B) Option 2: Waste Stabilization Pond (WSP)
(C) Option 3: Activated Sludge Process (ASP).

Option 1. Trickling filter (TF) has various advantages like low initial and maintenance cost, low sludge production, and good performance for developing countries like India (Metcalf and Eddy 2003).

Option 2. Waste stabilization pond (WSP) has advantages of low construction cost and uses low energy-consuming systems that treat by natural processes (Metcalf and Eddy 2003).

Option 3. Activated sludge process (ASP) is a suspended-culture system that has been in use since the early 1900s. It has high removal efficiency and the quality of effluent is better than other conventional treatment methods. (Metcalf and Eddy 2003).

A comprehensive judgment is prepared for the collection of information from experts, the practitioner (consultants and plant designers), academicians, and government officials working in WWT and management.

2.2 Analytical Hierarchical Process

The AHP tool developed by Saaty in 1980 is one of the most accepted and widely used MCDM tools for many complex decision-making problems. It is a systematic approach that considers feeling intuition and logic in the final decision-making and

the relation of the importance of different criteria and sub-criteria are taken through questionnaires and expert judgments. The subjective decision of an individual can be easily handled through the AHP tool. The basic steps involved in AHP tool are [9]:

(1) Firstly the decision problem is broken down into simple elements.
(2) Place each of the elements in a proper hierarchic level.
(3) Assign a weight to subjective judgment.
(4) Synthesize the judgment for getting the final ranking of performances through the aggregation of relative weights.

The Pair-wise comparison is the most important part of the analysis. In AHP relative preferences are assigned from 1 to 9 in Table 1, where a higher value indicates increasing importance. Consistency index (CI) value Eq. 1 and randomness index value Table 2 is used to find CR. Consistency ratio (CR) Eq. 2 is the indicator of consistency in judgments. If CR value exceeds 0.10 it indicates inconsistent judgment. Higher values of inconsistency reflect a lack of understanding or information.

$$\mathrm{CI} = (\lambda_{\max} - \mathrm{n}) \big/ (\mathrm{n} - 1) \tag{1}$$

where:

$\lambda_{\max}$ = maximum Eigenvalue and
n = matrix size

.. (2)

Development of priority ranking: the overall ranking of the alternatives is obtained by constructing a decision matrix, which contains different criteria and sub-criteria

Table 1 Pair-wise comparison scale

Numerical rating	Judgments of preferences
9	Extremely important
7	Very strongly preferred
5	Strongly preferred
3	Moderately preferred
1	Equally preferred
2,4,6,8	Intermediate values

Table 2 Average randomness (RI)

Size of matrix	1	2	3	4	5	6	7	8	9	10
Random consistency	0.0	0.0	0.58	0.90	1.12	1.24	1.32	1.41	1.45	1.49

and their relative weighting. So by multiplying their priority vector with weight and adding all of them together, the final priority value of alternatives is obtained.

2.3 Criteria and Sub-criteria Selection

The three main criteria, i.e., economic aspect, technological aspect, and environmental and social aspect, respectively, with respect to the goal, are formed using literature and considering expert opinions [15, 16]. The brief description of criteria and sub-criteria are given in Table 3.

Using selected criteria and sub-criteria the AHP decision network is formed following the basic steps in analyzing procedure and represented in Fig. 1.

3 Results and Discussion

The pair-wise comparisons were conducted by the decision maker for different criteria and sub-criterion. Then normalized priority vectors and consistency ratios are calculated which is presented in Tables 4, 5, 6, 7, 8, 9, and 10.

It is depicted from the graphical representation of Fig. 2 that among the criteria aspects the environmental and social aspects are acquired the highest priority (0.49) than the economic aspects (0.31) and technological aspects which has less priority (0.20). In making comparisons between sub-criteria Figs. 3, 4, and 5, in Economic aspects criteria O & M cost sub-criteria, has the highest priority vector (0.439), similarly effluent quality has the highest priority (0.334) in technological aspect and public acceptance has the highest priority (0.414) in the environmental and social aspect. The overall weighting of Option 2 waste stabilization pond is highest (0.40) considering all the criteria and sub-criteria.

Considering normalized priorities of all the criterion and sub-criterion, decision matrix (Table 11) is formed and priorities of alternatives are determined. The final priorities of alternatives are presented through Table 12 and Fig. 6.

3.1 Sensitivity Analysis

The final outcomes of AHP analysis reveal that WSP has a priority of 40% while ASP and TF have priorities of 31% and 29%, respectively. These final priorities of alternatives are dependent on the weightage of different criteria which are assigned through experts' opinion. Therefore, any change in assigned weightage will affect the final choice of alternative. So sensitivity analysis is conducted to check the impact of variation in weightage of key criteria parameters. The sensitivity graphs are prepared by varying the weightage from 0 to 1 for all three criteria with respect to our goal than

Table 3 Selection of criteria and sub-criteria

Criteria	Sub-criteria	Description
1. Economic aspects	1.1 Capital investment	It includes expenses for the construction of the plant
	1.2 Residual value	Monitory value at the end of the utility period
	1.3 O & M	Related to expenses in the operation and maintenance of the treatment plant
	1.4 Electricity	Expenses on electricity requirements for various processes
2. Technological aspects	2.1 Effluent quality	BOD, Nitrogen, and Phosphorus removal efficiency
	2.2 Sludge handling	The processing, reuse, and disposal of sewage sludge
	2.3 Flow variation	The sensitivity of plant due to variation in wastewater flow rate
	2.4 Simplicity	Simplicity in operation, the requirement of skilled manpower for operation
3. Environmental and social aspects	3.1 Odor	Smell impact, foul smells surrounding the treatment facility
	3.2 Noise	Production of noise on the surrounding area
	3.3 Visual impact	Aesthetic appearance affects due to the sitting of the plant in the surrounding area
	3.4 Public acceptance	The opinion of the local people affected by the plant
	3.5 Use of natural resources	Consumption of natural resources (technology which consumes more resources will have an adverse impact on the environment)

from each criterion one sub-criterion is chosen which has the highest priority in that criteria aspect and sensitivity analysis with respect to the goal is performed similarly. From the sensitivity analysis, it is found that the choice of WSP remains stable in a wide range. So the stability of ranking can arrive through sensitivity analysis and sensitive parameters are identified which needs careful attention. Sensitivity analysis is performed with goal node and various criterions so that the results to be interpreted are described and shown here through Figs. 7, 8, 9, 10, 11, 12, and 13. Now considering the sub-criteria node in economic aspect O & M has a weight of

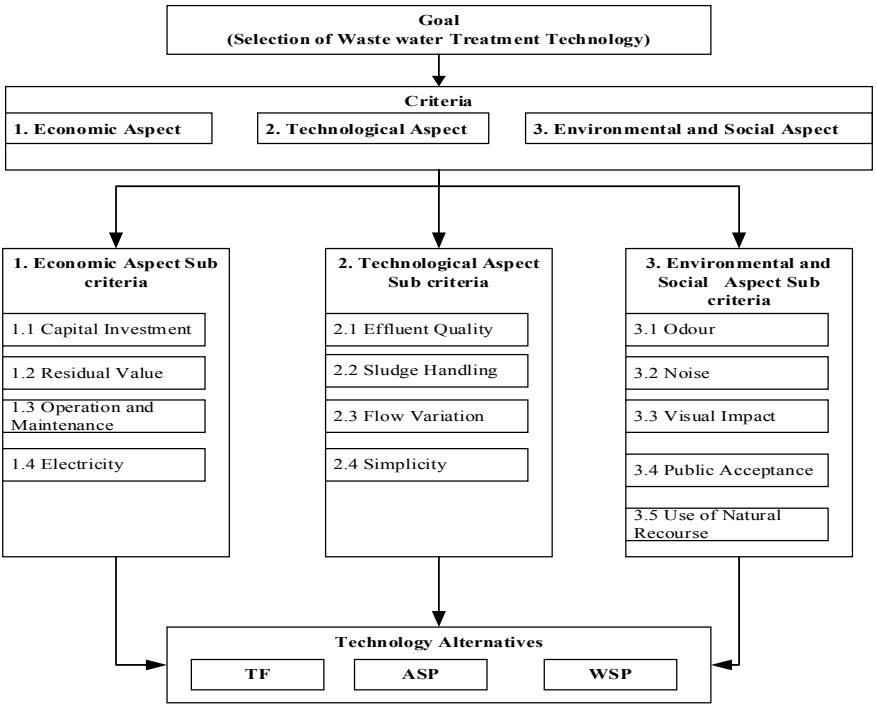

Fig. 1 Systematic representation of AHP decision model

Table 4 Pair-wise comparison matrix for criteria aspect with respect to the goal

Main criteria	1. Economic aspects	2. Technological aspects	3. Environmental and social aspects	Normalized priority vector	
1. Economic aspects	1	2	1/2	0.31	Consistency ratio (CR) = 0.05
2. Technological aspects	1/2	1	1/2	0.20	
3. Environmental and social aspects	2	2	1	0.49	

0.439 (Fig. 3) but the sensitivity graph is flatter and any change in parameter value does not affect the alternative ranks.

The effluent quality has a weightage of 0.334 (Fig. 8) in the technological aspects but with respect to goal node any change in this value will not affect the final choice of alternatives. The public acceptance having a weightage of 0.414 (Fig. 9) and it belongs to environmental and social aspects having the highest importance. From the sensitivity graph, it is found that at a parameter value of 0.85 ASP becomes the first choice and WSP comes down to the second. On the other hand, decreasing the

Table 5 Pair-wise comparison matrix for economic aspect

Economic aspects	1.1 Capital investment	1.2 Residual value	1.3 Operation and maintenance	1.4 Electricity	Normalized priority vector	
1.1 Capital investment	1	1/2	1/3	1/3	0.10	Consistency ratio (CR) = 0.05
1.2 Residual value	2	1	1/3	1/3	0.15	
1.3 Operation and maintenance	3	3	1	2	0.44	
1.4 Electricity	3	3	1/2	1	0.31	

Table 6 Pair-wise comparison matrix for technological aspect

Technology aspect	2.1 Effluent quality	2.2 Sludge handling	2.3 Flow variation	2.4 Simplicity in operation	Normalized priority vector	
2.1 Effluent quality	1	2	1	2	0.33	Consistency ratio (CR) = 0.09
2.2 Sludge handling	1/2	1	2	1	0.25	
2.3 Flow variation	1	1/2	1	2	0.24	
2.4 Simplicity in operation	1/2	1	1/2	1	0.17	

Table 7 Pair-wise comparison matrix for environmental and social aspect

Env. and social aspect	3.1 Odor	3.2 Noise	3.3 Visual impact	3.4 Public acceptance	3.5 Use of natural resources	Normalized priority vector	
3.1 Odor	1	3	2	1/3	1/2	0.17	Consistency ratio (CR) = 0.05
3.2 Noise	1/3	1	1/2	1/3	1/2	0.08	
3.3 Visual impact	½	2	1	1/3	1/2	0.12	
3.4 Public acceptance	3	3	3	1	3	0.41	
3.5 Use of natural resources	2	2	2	1/3	1	0.21	

parameter value WSP remains the first choice while a value below 0.15 TF becomes the second choice, and ASP becomes the last alternative.

The weight of economic aspects is 0.311 if this weight is increased beyond 0.311 the WSP is the best choice (Fig. 10), however, if the weightage is reduced then still WSP remains the first choice up to a weight of 0.11 then ASP becomes the first choice. At a weight of 0.55 among ASP and TF, trickling filter becomes second choice and ASP the last alternative. In technological aspects weight is 0.196 (Fig. 11) this parameter is insensitive, any change in this value does not affect the choice of alternatives.

In environmental and social aspect weight is 0.493 (Fig. 12) if this value is reduced no change in alternatives but at the value lower than 0.27 TF becomes the second choice and value higher than 0.72 ASP becomes the first choice and WSP comes down to the second alternative. So from sensitivity analysis in AHP, we can conclude that even doing substantial changes in different parameter values the final choice remains the same and ranking of the alternatives is highly stable.

Table 8 Pair-wise comparison matrix for economic aspects sub-criterion parameters and alternatives

Capital cost					Consistency ratio (CR)
	1 TF	2 WSP	3 ASP	Normalized priority vector	
1 TF	1	11/5	1	0.34	0.0
2 WSP	5/6	1	7/9	0.29	
3 ASP	1	1 2/7	1	0.37	
Residual value					0.0
1 TF	1	1/3	1	0.2	
2 WSP	3	1	3	0.6	
3 ASP	1	1/3	1	0.2	
O & M					0.01
1 TF	1	1/2	2	0.3	
2 WSP	2	1	3	0.54	
3 ASP	½	1/3	1	0.16	
Electricity					0.02
1 TF	1	1/4	2	0.2	
2 WSP	4	1	5	0.68	
3 ASP	½	1/5	1	0.12	

Table 9 Pair-wise comparison matrix for technological aspects sub-criterion parameters and alternatives

Effluent quality					Consistency ratio (CR)
	1 TF	2 WSP	3 ASP	Normalized priority vector	
1 TF	1	2	1/3	0.2631	0.1
2 WSP	1/2	1	1/2	0.1897	
3 ASP	3	2	1	0.5472	
Sludge handling					0.1
1 TF	1	1/2	2	0.3	
2 WSP	2	1	3	0.54	
3 ASP	1/2	1/3	1	0.16	
Flow variation					0.05
1 TF	1	1/2	2	0.31	
2 WSP	2	1	2	0.49	
3 ASP	1/2	1/2	1	0.2	
Simplicity					0.02
1 TF	1	1/3	2	0.24	
2 WSP	3	1	4	0.63	
3 ASP	1/2	1/4	1	0.14	

Table 10 Pair-wise comparison matrix for environmental and social aspects sub-criterion parameters and alternatives

Odor					Consistency ratio (CR)
	1 TF	2 WSP	3 ASP	Normalized priority vector	
1 TF	1	2	1	0.4	0.01
2 WSP	1/2	1	1/2	0.2	
3 ASP	1	2	1	0.4	
Noise					0.05
1 TF	1	1/3	2	0.25	
2 WSP	3	1	3	0.59	
3 ASP	1/2	1/3	1	0.16	
Visual impacts					0.05
1 TF	1	2	1/2	0.31	
2 WSP	1/2	1	1/2	0.2	
3 ASP	2	2	1	0.49	
Public acceptance					0.01
1 TF	1	2	1/2	0.3	
2 WSP	1/2	1	1/3	0.16	
3 ASP	2	3	1	0.54	
Use of natural resources					0.02
1 TF	1	1/2	1	0.24	
2 WSP	2	1	3	0.55	
3 ASP	1	1/3	1	0.21	

Fig. 2 Criteria priorities

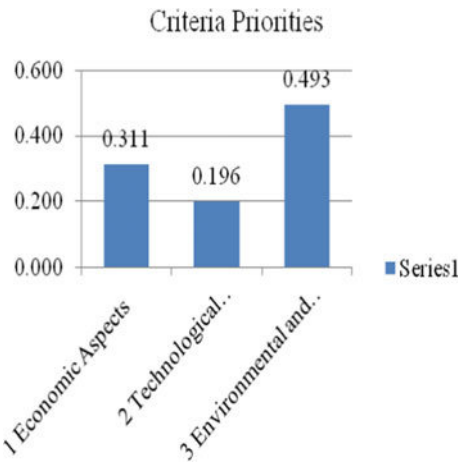

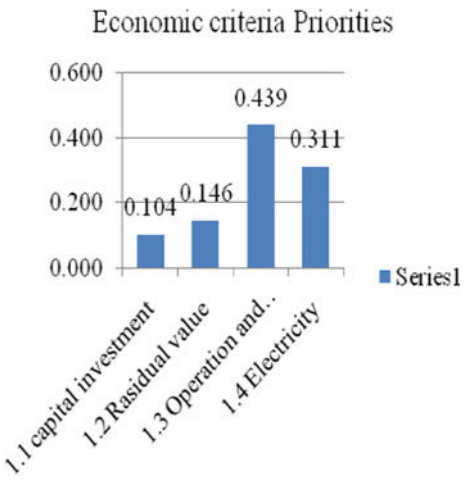

Fig. 3 Economic criteria priorities

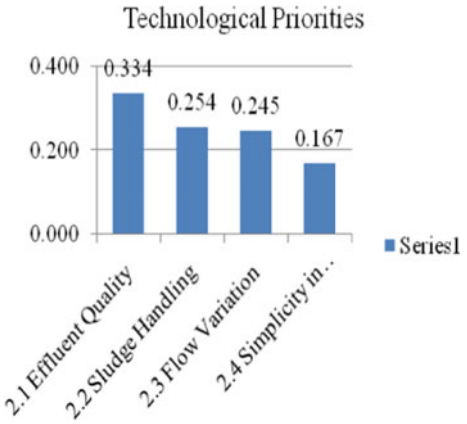

Fig. 4 Technological criteria priorities

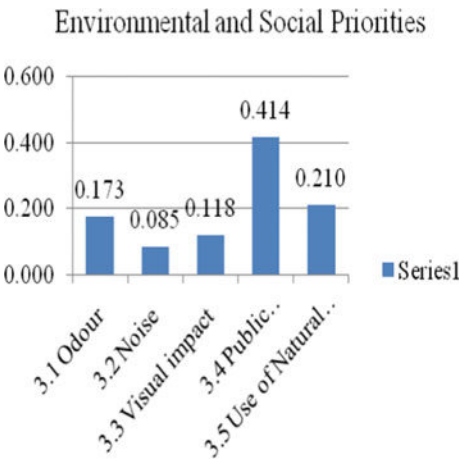

Fig. 5 Environ. and social criteria priorities

Table 11 Decision matrix

Criteria	1 Economic aspects (0.311)				2 Technological aspects (0.196)				3 Environmental and social aspects (0.493)				
Sub-criteria	1.1 Capital investment	1.2 Residual value	1.3 Operation and maintenance	1.4 Electricity	2.1 Effluent quality	2.2 Sludge handling	2.3 Flow Variation	2.4 Simplicity in operation	3.1 Odor	3.2 Noise	3.3 Visual impact	3.4 Public acceptance	3.5 Use of natural resources
Option ↓	**0.104**	**0.146**	**0.439**	**0.311**	**0.334**	**0.254**	**0.245**	**0.167**	**0.17**	**0.085**	**0.118**	**0.414**	**0.210**
1 TF	0.34	0.20	0.30	0.20	0.26	0.30	0.31	0.24	0.40	0.25	0.31	0.30	0.24
2 WSP	0.29	0.60	0.54	0.68	0.19	0.54	0.49	0.63	0.20	0.59	0.20	0.16	0.55
3 ASP	0.37	0.20	0.16	0.12	0.55	0.16	0.20	0.14	0.40	0.16	0.49	0.54	0.21

Table 12 Alternative priorities

Options	Priorities
1 TF	**0.28**
2 WSP	**0.40**
3 ASP	**0.31**

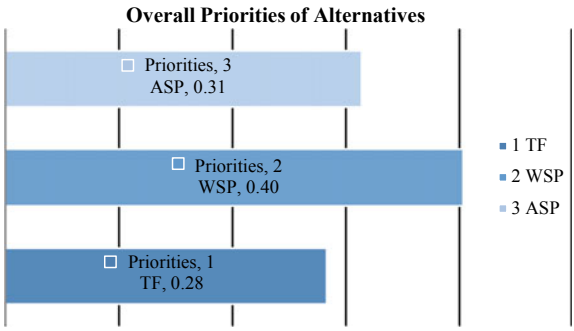

Fig. 6 Final priorities of alternatives

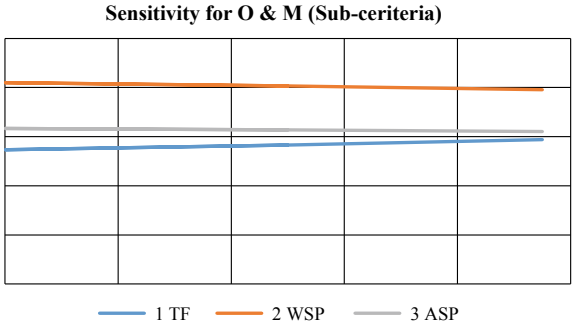

Fig. 7 Sensitivity of goal with operation and maintenance

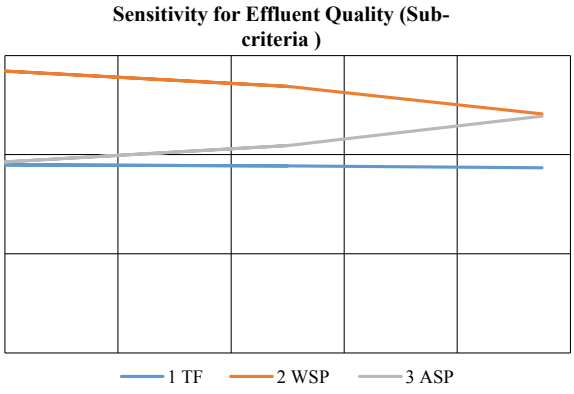

Fig. 8 Sensitivity of goal with effluent quality

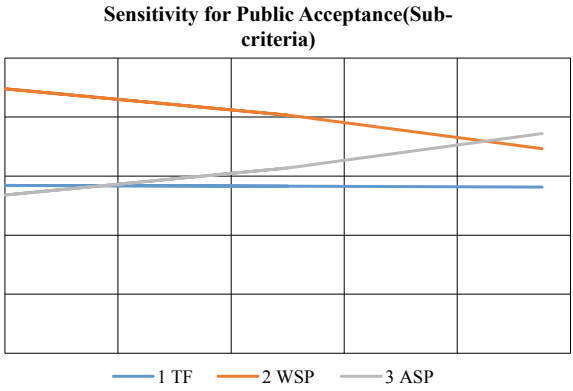

Fig. 9 Sensitivity of goal with public acceptance

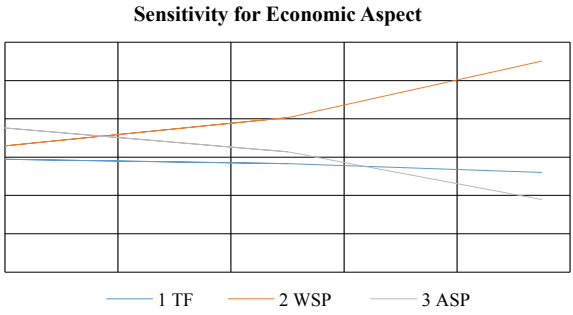

Fig. 10 Sensitivity of goal with economic aspects

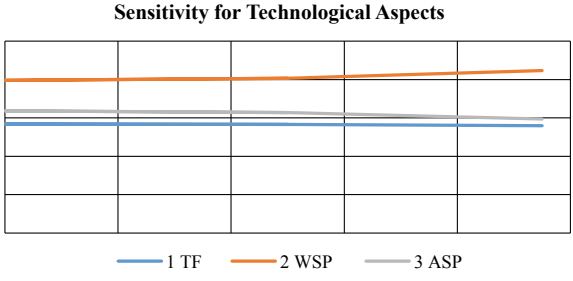

Fig. 11 Sensitivity of goal with technological aspects

4 Conclusions

Presently numerous wastewater technologies are available to treat municipal wastewater. But for Municipal Corporation where funds and skilled manpower is scarce, selection of most suitable and efficient treatment alternative is a complex decision-making task.

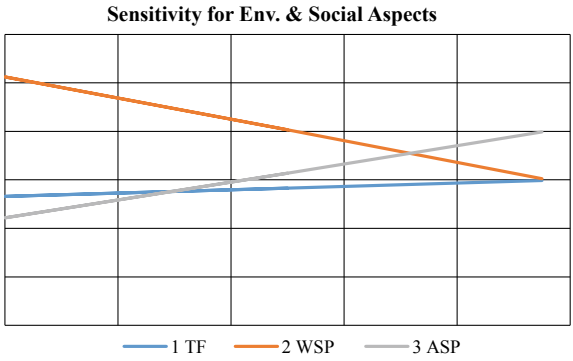

Fig. 12 Sensitivity of goal with environmental and social aspects

The aim of the present study was to evaluate different alternatives to municipal wastewater treatment alternatives for small Municipal Corporation. For the evaluation of alternatives, AHP methods are used, which is based on qualitative and quantitative expert's opinions and feedbacks. The assessment criteria are selected from the literature reviews and from practical field observations. The three main criteria aspects such as economic, technological, and environmental and social are considered. Among each aspect relevant sub-criteria are considered and based on these final choices of alternative is arrived. For comparison of alternatives most commonly used technologies in India are considered. This is trickling filter (TF), activated sludge process (ASP), and waste stabilization pond (WSP), respectively. AHP method is used to rank the alternatives. From the analysis, outcomes are obtained as:

- AHP recommend Option 2 [WSP] is best performance than Option 1 [TF] and Option 3 [ASP].

Since results are widely dependent on expert's subjective judgment and prone to change, so sensitivity analysis is also conducted for criteria having the highest impact on the final ranking of alternatives. Sensitivity analysis reveals the final ranking is consistent even substantial variation is made in key criteria parameters. It shows that expert opinions are consistent and the method used is robust and reliable for decision-making.

Acknowledgments The authors would like to thank all experts from various institutions, field engineers, and research scholars for their valuable suggestions and feedback for rating different wastewater treatment technologies.

References

1. Temiz I, Calis G (2017) Selection of construction equipment by using multi-criteria decision making methods. Procedia Eng 196(June):286–293

2. Zeng G, Jiang R, Huang G, Xu M, Li J (2007) Optimization of wastewater treatment alternative selection by hierarchy grey relational analysis. J Environ Manage 82(2):250–259
3. Figueira J, Greco S, Ehrogott M (2005) Multiple criteria decision analysis: state of the art surveys, vol 78
4. Konidari P, Evaluation method for climate change mitigation instruments. *Cgi.Di.Uoa.Gr*
5. Khadam IM, Kaluarachchi JJ (2003) Multi-criteria decision analysis with probabilistic risk assessment for the management of contaminated ground water. Environ Impact Assess Rev 23(6):683–721
6. Okeola OG, Sule BF (2012) Evaluation of management alternatives for urban water supply system using multicriteria decision analysis. J King Saud Univ—Eng Sci 24(1):19–24
7. Ishtiaq P, Khan SA, Haq MU (2018) A multi-criteria decision-making approach to rank supplier selection criteria for hospital waste management: a case from Pakistan. Waste Manag Res 36(4):386–394
8. Tramarico CL, Salomon VAP, Marins FAS (2017) Multi-criteria assessment of the benefits of a supply chain management training considering green issues. J Clean Prod 142:249–256
9. Saaty TL (2006) Rank from comparisons and from ratings in the analytic hierarchy/network processes I, vol 168, pp 557–570
10. Bottero M, Comino E, Riggio V (2011) Environmental modelling & software application of the analytic hierarchy process and the analytic network process for the assessment of different wastewater treatment systems. Environ Model Softw 26(10):1211–1224
11. Kalbar PP, Karmakar S, Asolekar SR (2012) Selection of an appropriate wastewater treatment technology: a scenario-based multiple-attribute decision-making approach. J Environ Manage 113:158–169
12. Antonopoulos I, Perkoulidis G, Logothetis D, Karkanias C (2014) Resources, conservation and recycling ranking municipal solid waste treatment alternatives considering sustainability criteria using the analytical hierarchical process tool. Res Conserv Recycl 86:149–159
13. Rawal N, Duggal SK (2016) Life cycle costing assessment-based approach for selection of wastewater treatment units. Natl Acad Sci Lett 39(2):103–107
14. Von Sperling M (1996) Comparison among the most. Water Sci Technol 33(3):59–72
15. Karimi AR, Mehrdadi N, Hashemian SJ, Nabi Bidhendi GR, Tavakkoli Moghaddam R (2011) Selection of wastewater treatment process based on the analytical hierarchy process and fuzzy analytical hierarchy process methods. Int J Environ Sci Technol 8(2):267–280
16. Molinos-Senante M, Gómez T, Garrido-Baserba M, Caballero R, Sala-Garrido R (2014) Assessing the sustainability of small wastewater treatment systems: a composite indicator approach. Sci Total Environ 497–498:607–617

Bibliometric Analysis of Constructed Wetlands in Wastewater Treatment

Nandini Moondra, Robin A. Christian, and Namrata D. Jariwala

Abstract Constructed wetlands, an eco-friendly and green wastewater treatment technology has been proven to be an effective alternative for conventional wastewater treatment technologies. The bibliometric analysis was conducted in the field of constructed wetlands to investigate its progress and future research trends during the years 1998–2017 based on the Science Citation Index Expanded (SCI-Expanded) of Web of Science (WOS). Co-word analysis along with top countries and institutes were determined. The analysis of author keywords indicates that the significant hotspots of constructed wetlands include "nutrients" "aquatic plants" "removal," etc., based on centrality. The USA is the country that has contributed the most in the field of constructed wetlands followed by China. Chinese Academy of Sciences is the topmost institute which has a maximum number of publications. Scientists and researches can also explore the utility of constructed wetlands in river water treatment, heavy metal extraction from various wastewaters, petroleum refinery wastes, fish pond discharges, and pre-treated industrial wastewaters, in future. The results provide a comprehensive understanding of constructed wetlands research and help readers to establish future research directions in the field of environment.

Keywords Treatment · Bibliometric · Constructed wetlands · Hotspots

1 Introduction

Constructed wetlands are sustainable and green technology to expel pollutants from contaminated water through physical, chemical, and biological mechanisms [1–5]. Microorganisms present in constructed wetlands are capable of mineralizing organic matter under both aerobic and anaerobic conditions, hence are considered as driving force for the treatment [6–9]. It is found that higher the surface area, more is the substrate available, hence larger the biomass. Plants grown in the wetlands also play a vital role in treatment by enhancing sedimentation via controlling wind speed.

N. Moondra (✉) · R. A. Christian · N. D. Jariwala
Sardar Vallabhbhai National Institute of Technology (SVNIT), Surat, Gujarat, India
e-mail: nandini7808@yahoo.in

© Springer Nature Singapore Pte Ltd. 2021

K. K. Pathak et al. (eds.), *Recent Trends in Civil Engineering*, Lecture Notes in Civil Engineering 77, https://doi.org/10.1007/978-981-15-5195-6_74

Plants also release oxygen required for nutrient removal [10]. Nitrogen and phosphorus are generally removed in constructed wetlands. For the sustainability of a typically constructed wetland land acquisition, investment, and operation costs, energy utilization, ecological benefits should also be studied [5]. Bibliometric is an indicator that helps to measure the impact of the research, journals, institutes on the society through mapping, visualizing, and understanding of various scientific fields and citations in a particular area [11].

2 Methodology

The articles analyzed in this study were taken from the Web of Science center accumulation database, which is the powerhouse of the most vital and influential journals on the planet [12, 13] and incorporates top productions on constructed wetlands. After pre-investigation and examination, the accompanying recovery code utilized as a part of the WOS center gathering was: TS = (constructed wetlands*). Here, "*" signifies an inquiry and "TS" implies topic search. In this examination, only journal articles (review and research) were considered as they give maximum complete and higher quality data than different sorts of distributions. In the study, a sum of 3151 bibliographic records was gathered from the Web of Science database for the time traverse of 1998–2017. Figure 1 demonstrates the conveyance of the 3151 bibliographic records in 1998–2017. The aggregate number of records radically expanded in 2012–2017, with most high records in 2017. The programming bundle CiteSpace was used to envision and break down the writing of a logical learning space. Bibliometric strategies connected in this examination were: (i) Co-cited authors, co-cited journals, and co-cited documents. (ii) Co-word analysis which processes research trends, keywords. (iii) Networks of top countries and institutes.

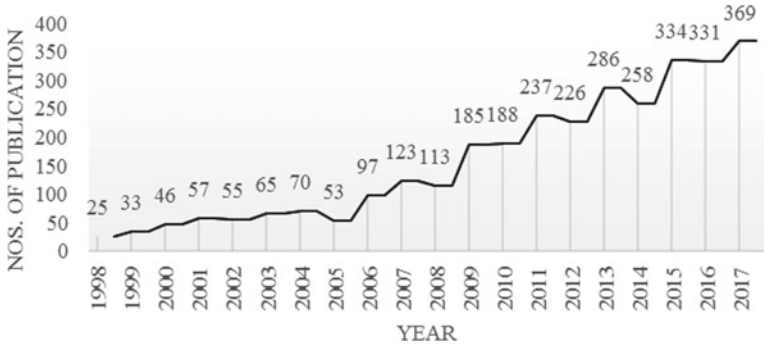

Fig. 1 Number of articles on constructed wetlands in WOS database 1998–2017

3 Results and Discussion

3.1 Document Co-citation

Document co-citation gives an idea about the frequency with which various documents are cited together by other papers as shown in Fig. 2. The top-ranked article titled "Removal of nutrients in various types of constructed wetlands" by Vymazal J [14], in the journal Science of the Total Environment, with citation counts of 272. The second most-cited article is "Microbial Processes Influencing Performance of Treatment Wetlands: A Review" by Faulwetter JL [1], in the Journal of Ecological Engineering, with citation counts of 163. The third most-cited article is by Vymazal J titled as "The Use Constructed Wetlands with Horizontal Sub-Surface Flow for Various Types of Wastewater" in the Journal of Ecological Engineering, with citation counts of 126 [15]. The fourth most-cited article is again by Vymazal J titled as "Constructed Wetlands for Wastewater Treatment: Five Decades of Experience in Environmental Science and Technology" with citation counts of 110 [2]. The fifth most-cited article is also by Vymazal J, in the Journal of Ecological Engineering titled as "Horizontal Sub-Surface Flow and Hybrid Constructed Wetlands Systems for Wastewater Treatment" with citation counts of 109 [16]. The top-ranked article by bursts is "Removal of nutrients in various types of constructed wetlands" by Vymazal J, with a burst of 49.20 [14]. The second is by Stottmeister U, titled as "Effects of Plants and Microorganisms in Constructed Wetlands for Wastewater Treatment" with bursts of 32.85 [17]. The third is by Vymazal J titled as "Horizontal Sub-Surface Flow and Hybrid Constructed Wetlands Systems for Wastewater Treatment" with bursts of 30.55 [16]. The fourth is again by Vymazal J titled as "Constructed Wetlands for Wastewater Treatment: Five Decades of Experience," with bursts of 24.40 [2]. The fifth is by Wu SB, titled as "Development of constructed wetlands in performance

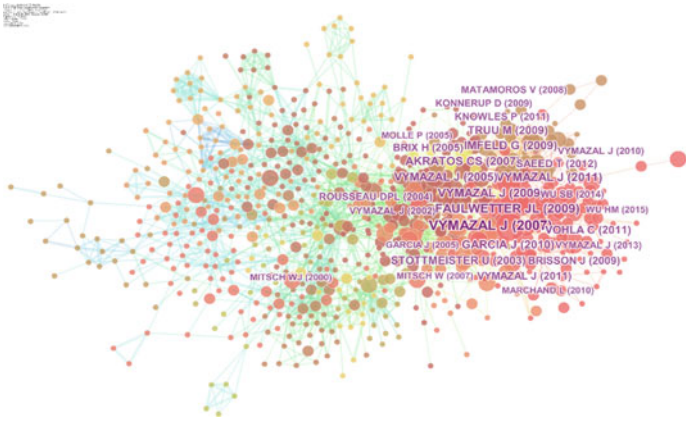

Fig. 2 Document co-citation network

intensifications for wastewater treatment: a nitrogen and organic matter targeted review" with bursts of 20.81 [3].

3.2 Co-word Analysis

In the current years, there have been different subjects and topics in constructed wetlands research. Co-word investigation can enable us to comprehend patterns and frontiers of constructed wetlands to inquire about.

3.3 Co-occurring Subject Categories

In the Web of Science center accumulation database, every journal production was doled out with at least one subject class as per the corresponding journal. Investigation and comprehension of different developing patterns in constructed wetlands inquire about, was finished by making a system of the co-happening subject classes in constructed wetlands research as appeared in Fig. 3. The node size measures the number of articles inside every category. Environmental Sciences Ecology (2711 articles), Engineering (1625 articles), Water Resource (837 articles), Marine Freshwater Biology (156 articles), Agriculture (91 articles), and Biotechnology Applied Microbiology (90 articles) were found to have the most abundant publication records.

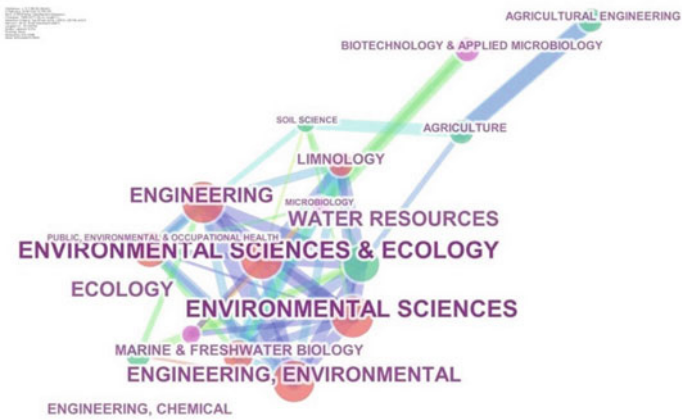

Fig. 3 Co-occurring subject network

3.4 Co-occurring Keyword Network

The node size estimate in the system below speaks to the recurrence with which a keyword occurred in the informational collection. The best ten high-recurrence keywords were "constructed wetlands" (frequency = 2042), "removal" (frequency = 708), "wastewater treatment" (frequency = 547), "wastewater" (frequency = 518), "performance" (frequency = 488), "system" (frequency = 460), "nitrogen" (frequency = 379), "plant" (frequency = 311), "soil" (frequency = 303), "phosphorus" (frequency = 299). In addition, some keywords received relatively high centrality scores, such "nutrient" (centrality = 0.10), "aquatic plant," "water quality," "performance," "removal," "macrophyte," "accumulation" (centrality = 0.08), "retention," "soil," "effluent" (centrality = 0.07). These words significantly connected different researchers and influenced the development of constructed wetlands research. Furthermore, keywords were also found to be citation bursts "reed bed" (burst = 16.83), "subsurface flow"(burst = 12.50), "management" (burst = 12.30), "biomass" (burst = 10.91), "substrate" ((burst = 10.56), "aquatic plant" (burst = 8.96), "artificial wetland" (burst = 8.49), "vertical flow"(burst = 8.41), "pond" (burst = 7.77), and "biofilm"(burst = 7.58) indicating that these are the hot topics in constructed wetlands research (Fig. 4).

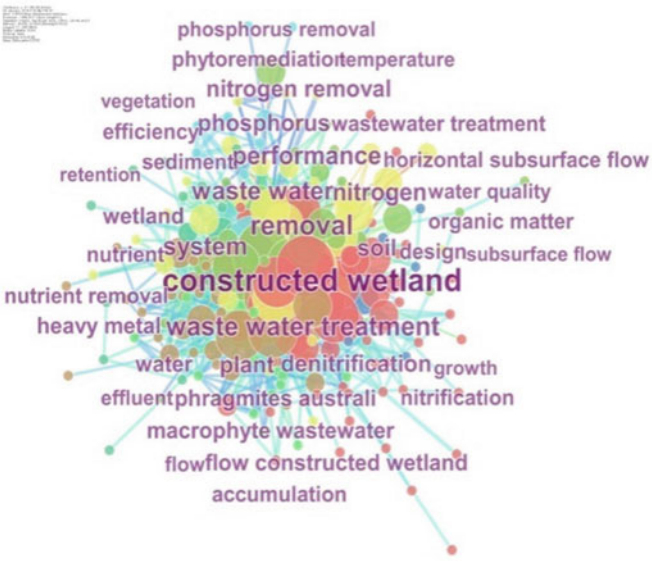

Fig. 4 Co-occurring keyword network

3.5 Network of Countries and Institutions

A network was created considering the commitments of nations and institutions to investigate the circulation of articles on constructed wetlands. The total number of articles distributed in 1998–2017 is denoted by the size of the node. As shown in Fig. 4, the USA (752 articles), China (673 articles), Spain (189 articles), Canada (176 articles), Germany (167 articles), England (145 articles), France (139 articles), Australia (112 articles), Italy (95 articles), and Brazil (75 articles) have made major contributions to the articles on constructed wetlands. Besides, the nodes with high centrality were identified and highlighted such as the USA (centrality = 0.37), Germany (centrality = 0.20), China (centrality = 0.16), England (centrality = 0.11), and the Netherlands (centrality = 0.11). Besides, reference bursts speaking to remarkable add-ons over a brief period were found in nations, for example, the USA (burst count = 101.58), England (burst count = 14.92), Japan (burst count = 8.6), France (burst count = 6.89), Sweden (burst count = 5.20), Thailand (burst count = 4.84), Colombia (burst count = 4.68), Australia (burst count = 4.46), Estonia (burst count = 4.31), and Malaysia (burst count = 4.23). These results demonstrated that these countries have pulled in a remarkable level of consideration in the area of constructed wetlands in corresponding years. It can also be concluded that the USA is a single country which has found to get high references over a brief timeframe even though it was not the discoverer of the constructed wetlands. Studies on the utilization of constructed wetlands for wastewater treatment started in the 1950s at the Max Planck Institute in Germany.

The study also inquire about advance had been exceptionally dynamic at organizations w.r.t constructed wetlands, for example, Chinese Academy of Sciences, China (139 articles); Helmholtz Association, Germany (94 articles); Helmholtz Center For Environmental Research UfZ, Germany (88 articles); the University Of California System, USA (86 articles); Polytechnic University of Catalonia, Spain, (76 articles); United States Department Of Agriculture, USA (72 articles); Aarhus University, Denmark(55 articles); IRSTEA, France (55 articles); the State University System of Florida, USA (53 articles); the University Of Chinese Academy Of Sciences, China (52articles) as shown in Fig. 5. These organizations can be set apart as the production habitats for constructed wetlands research around the globe.

4 Conclusions

Constructed wetland is one of the most suitable engineered green technologies which has great acknowledgment among developing nations for decentralized waste treatment. This examination gives a bibliometric audit to investigate the status and patterns of developed wetlands inquire about around the world. A sum of 3151 bibliographic records was gathered from the WOS center accumulation database. A few core journals have distributed most critical discoveries in constructed wetlands research, such

Fig. 5 Network of countries

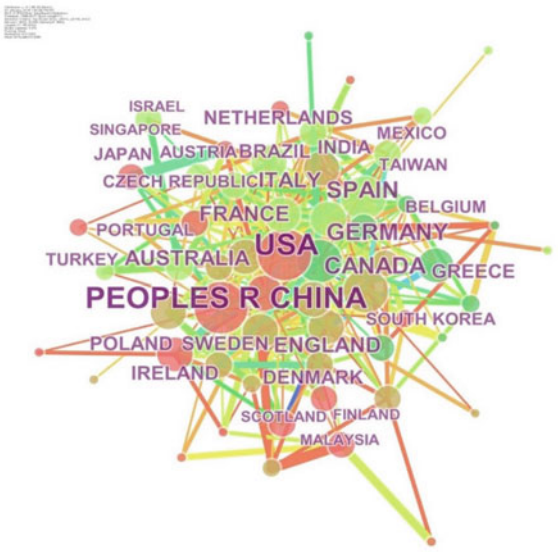

as Ecological Engineering, Water Science and Technology, and Water Research. The majority of the top highly cited articles were published in these journals. Some hot topics of constructed wetlands research that could be understood by relating keywords can be summarized as wastewater treatment, nutrient removal, and phytoremediation removal of toxic metals.

Constructed wetlands have proved its effectiveness in the treatment of industrial wastewater, domestic wastewater, coal water drainage stormwater, etc., so far. Scientists and researches can also explore the utility of constructed wetlands in river water treatment, heavy metal extraction from various wastewaters, petroleum refinery wastes, compost, and landfill leachate, fish pond discharges, and pre-treated industrial wastewaters, such as those from pulp and paper mills, textile mills, and seafood processing in the future. This examination gives essential data to the specialists and practitioners in the field of constructed wetlands research. The principal researchers and foundations, the condition of the exploration field, and hotly debated issues on developed wetlands were recognized by analysts. In addition, this investigation will enable experts to get fundamental discoveries to improve their comprehension of constructed wetlands. The bibliometric survey strategy can likewise be utilized to image the exploration incline in different topics.

References

1. Faulwetter JL (2009) Microbial processes influencing performance of treatment wetlands: a review. Ecol Eng 35(6):987–1004
2. Vymazal J (2011) Constructed wetlands for wastewater treatment: five decades of experience. Environ Sci Technol 45(1):61–69
3. Wu S, Kuschk P, Brix H, Vymazal J, Dong R (2015) Development of constructed wetlands in performance intensifications for wastewater treatment: a nitrogen and organic matter targeted review. Water Res 57:40–45
4. Saeed T, Sun G (2012) A review on nitrogen and organics removal mechanisms in subsurface flow constructed wetlands: dependency on environmental parameters, operating conditions and supporting media. J Environ Manage 112:429–448
5. Wu H et al (2015) A review on the sustainability of constructed wetlands for wastewater treatment: design and operation. Biores Technol 175:594–601
6. Chen Y, Wen Y, Tang Z, Huang J, Zhou Q, Vymazal J (2015) Effects of plant biomass on bacterial community structure in constructed wetlands used for tertiary wastewater treatment. Ecol Eng 84:38–45
7. Truu M, Juhanson J, Truu J (2009) Microbial biomass, activity and community composition in constructed wetlands. Sci Total Environ 407(13):3958–3971
8. Mander U (2014) Greenhouse gas emission in constructed wetlands for wastewater treatment: a review. Ecol Eng 66:19–35
9. Zhao Z (2016) Effects of plant diversity and sand particle size on methane emission and nitrogen removal in microcosms of constructed wetland. Ecol Eng 95:390–398
10. Vymazal J (2013) Emergent plants used in free water surface constructed wetlands: a review. Ecol Eng 61:582–592
11. Leydesdorff L, Milojevic S (2015) Scientometrics. Int Encycl Soc Behav Sci (second ed., pp 322–327)
12. Pouris A, Pouris A (2011) Scientometrics of a pandemic: HIV/AIDS research in South Africa and the World. Scientometrics 86(2):541–552
13. Song J, Zhang H, Dong W (2016) A review of emerging trends in global PPP research: analysis and visualization. Scientometrics 107(3):1111–1147
14. Vymazal J (2007) Removal of nutrients in various types of constructed wetlands. Sci Total Environ 380(1–3):48–65
15. Vymazal J (2009) The use constructed wetlands with horizontal sub-surface flow for various types of wastewater. Ecol Eng 35(1):1–17
16. Vymazal J (2005) Horizontal sub-surface flow and hybrid constructed wetlands systems for wastewater treatment. Ecol Eng 25(5):478–490
17. Stottmeister U (2003) Effects of plants and microorganisms in constructed wetlands for wastewater treatment. Biotechnol Adv 22(1–2):93–117

Assessment of Carbon Foot Print: A Case Study of SVNIT Campus

Bibin K. Suresh, Nandini Moondra, and Bhaven N. Tandel

Abstract The carbon footprint is one of the main methods used to quantify the anthropogenic impact on the environment and to help combat the threat to climatic change. If carbon footprint analysis is being done for the first time, it is curtained to be stuck by wide range of definitions, approaches, and terminology of neighborhood. This study quantified the carbon emission from different sources and carbon absorption by vegetation cover inside the SVNIT campus. The estimation of total carbon sequestration by vegetation cover of SVNIT was around 392 to 400-ton CO_2/year. The total carbon emission by indirect source (electricity) was estimated from 2953.58 to 2506.71 tons of CO_2/year, and from direct sources was 474–520 tons of CO_2/year. The green belt, in the campus, is absorbing 76.92 to 84.63% CO_2 emission annually. In the present paper, an attempt was made to provide an introductory guide on some preliminary concepts of carbon footprint for researchers and interested ones in this area. Each step is presented for calculating the carbon footprint, and an introduction to the main methodologies is presented. An approximate framework of procedures for calculating carbon footprint on different topics is also presented.

Keyword Footprint · IPCC · UNFCCC · CNG · PNG

1 Introduction

After 1950s because of the rapid development in industrial activity, the climatic change and its effects on earth turned out to be more relevant. The major reason for climatic change is increase in concentration of greenhouse gas in the atmospheric air. Even if Carbon dioxide emission is stopped now, it is professed that the effect of the climatic change can be reversed in 1000 years time [1]. The concentration of atmospheric gases such as CO_2, CH_4, and N_2O have increased gradually for many years and in 2014 concentration of CO_2 has increased to 398.78 from 315.71 ppm in 1956 [2]. Ocean acidification is occurring because of the absorption of 30% of

B. K. Suresh (✉) · N. Moondra · B. N. Tandel
Sardar Vallabhbhai National Institute of Technology (SVNIT), Surat, Gujarat, India
e-mail: bibin18021@gmail.com

© Springer Nature Singapore Pte Ltd. 2021

K. K. Pathak et al. (eds.), *Recent Trends in Civil Engineering*, Lecture Notes in Civil Engineering 77, https://doi.org/10.1007/978-981-15-5195-6_75

emitted CO_2 and that is badly affecting the marine organisms. Day by day the increase in GHG gas emission is because of the anthropogenic activities. If the emission is uncontrollably increasing, the GHG emission amounts will rise, and subsequently the climate change would cause a conversion in the whole climate system. So, it is very important to be aware of the present condition of GHG emissions that it became pronounced as the denouement turnout efficaciously apparent.

Various global organizations around the world characterized climatic changes as indicated by their worries. Intergovernmental Panel on Climate Change (IPCC) is one of the major global organization, which characterizes the climatic change as "a drastic change in the condition of the atmosphere which can be recognized by changes of its properties, and that endures for an all-inclusive period, ordinarily decades or more." Another global organization, United Nations Framework Convention on Climate Change (UNFCCC) defines climatic change as "a difference in atmosphere condition which is credited legally or because of human action that changes the arrangement of the air quality across the world and that is not hold out against characteristic atmosphere fluctuation in the past timeframes." These definitions given by the two organizations are predictable about the immediate or gradual impacts of the artificial activites. In other words, climate change can be explained as one of the major challenges faced by countries globally. Green House Gases (GHG) emitted by humans are having a negative impact on the environment and it is globally accepted. Carbon dioxide is one of the major GHG, emerging from various anthropogenic activities. Also, CO_2 emissions by human activities prompt the environmental change. The major sources of CO_2 emissions are occurred by the burning of fossil fuels from thermal power stations, especially coal and diesel and also from vehicle exhaust. The main source of energy is required for the manufacture, transport and transfer of, each product, goods, or service that indirectly produces CO_2 emissions, and the major amount of global energy requirement is fulfilled from non-renewable energy sources and its subsidiaries. Because the burning of fossil fuel carbon dioxide is emitted into the atmosphere. Carbon impression can be defined as complete emissions of GHG caused directly and indirectly by an individual, association, occasion, or item on a regular basis. Finding out the carbon impression of an association can be the initial phase in a program to decrease the outflows and its causes. Carbon in the environment as carbon dioxide is approximately (2% of total air content), and about 5% as biomass in terrestrial plants and soils, approximately (8%) as non-renewable energy sources in an assortment of geologic reservoirs and as a collection of ions in the sea (85%) [3]. Significant amount of GHG emitted from various human activities is carbon dioxide by 54.7%, pursued by methane with 30%, different gases with 9.8%, nitrous oxide with 4.9%, and fluorinated gases with 0.6% [4]. The initial step toward the reduction of carbon dioxide emission is to quantify the amount in the current condition. Evaluation by utilizing the carbon dioxide impression idea gives carbon dioxide emission which is the most bottomless ozone harming substance [5]. Carbon footprint is the subset of ecological footprint. Carbon footprint can be explained as the land area required to assimilate the entire CO_2 produced by the mankind during its lifetime. Global warming issue becomes more and more crucial day by day, and the use of carbon footprint becomes more common, but in its modified form. A

carbon footprint is the total greenhouse gas (GHG) emissions caused directly and indirectly by an individual, organization, event, or product, and is expressed as a carbon dioxide equivalent (CO_2e) [6].

2 Objectives

To estimate the total carbon footprint of the Sardar Vallabhbhai National Institute of Technology (SVNIT), Surat Gujarat. Quantifying GHG emission sources will help to understand the impact the organization is having on climate change and also to identify and prioritize areas for reducing emissions. To create awareness about carbon footprint because of daily human activities and quantify the impact of daily activities of humankind contributing to carbon footprint.

3 Methodology

3.1 Study Area

The Sardar Vallabhbhai National Institute of Technology, Surat is a national level Institute built up mutually by State Government and Central Government in 1961 with a goal to fill in as a benchmark of excellence in technical education in the nation. At present, the organization having nine inns, out of nine six are men lodgings, one women inn, one Ph.D. Scholar family staying, and one is Guest House. The establishment has 183 scholarly employees in different offices against the endorsed quality of 220. Directly, more than 170 research researchers are seeking after their Ph.D. programs in the organization from different specialized establishments and enterprises in the nation. SVNIT is one of the renowned Institutes among the 30 National Institute of Technology all over India. The campus of SVNIT is spread over more than 250 acres of land. Satellite image of SVNIT campus is shown in Fig. 1.

3.2 Data Collection

3.2.1 Electricity Consumption

Electricity consumption data was collected from the concerned Electric Department of SVNIT from the period of Aug 2016 to July 2017 for the whole campus. Average electricity consumption of SVNIT Campus in the study period was found as 5025960 $\pm$ 73043 KWh. Due to less Variation ($\pm$15 KWh) in order to decide the range of Electricity Consumption, 50% confidence interval is considered accordingly, and

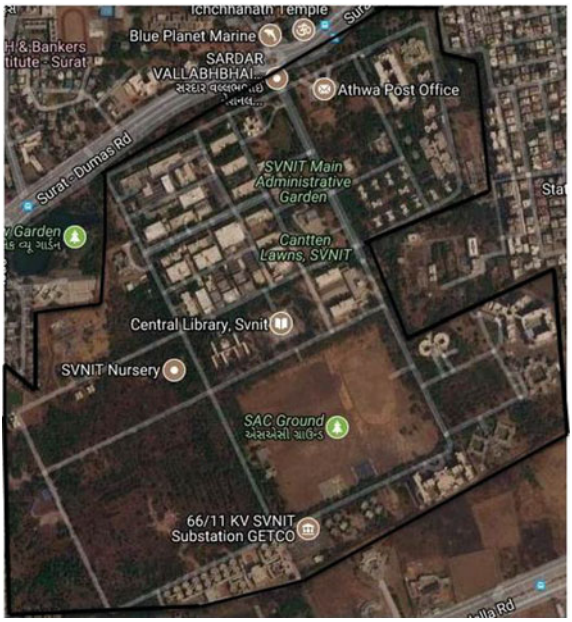

Fig. 1 Satellite image of SVNIT campus showing study area

maximum and minimum of a month were found to be 517936 KWh and 487985 KWh. Similarly, maximum and minimum yearly consumption was 6215232 and 5855820 KWh.

3.2.2 Diesel Consumption of DG Set in SVNIT

In SVNIT campus there are a total of 13 numbers of diesel generator sets which are being used during power failure and emergency situations. Diesel consumption data also collected from Electric Department of SVNIT from the period of Aug 2016 up to July 2017. Average monthly consumption of diesel was found as 1000 $\pm$ 733 L/Month. Considering the confidence interval of 95% max and minimum monthly was found to be 1414 L and 585 L, respectively.

3.2.3 PNG Consumption in SVNIT

There are a total of 58 PNG (Pipe Line Natural) Connection in SVNIT. PNG connections are provided in all hostels except Narmad Bhavan and Raman Bhavan (guest houses), Departments (Civil, Applied Chemistry and Chemical), and at Main Canteen. The total consumption of PNG is 220998 standard cubic meters during the study period.

3.2.4 Food Waste Generation in SVNIT

In order to find out the amount of food waste on a daily basis, a survey was conducted at Gajjar Bhavan (hostel) for a one week period (October 31, 2017 to November 6, 2017). Average food waste generated from Gajjar Bhavan was found 254.5 ± 13.5 kg/day. Based upon the number of food consumers, food waste per consumer per day was calculated, which was found in the range of 0.247–0.265 kg/Person/day by considering the total number of students in various hostels of SVNIT.

3.2.5 LPG Consumption in Campus Survey in Raman Bhavan (Hostel)

A Survey was conducted in Raman Bhavan (hostel) to collect information about LPG consumption by Ph.D. scholars' family. Based upon those responses, average LPG consumption per family per year was calculated, which was found to be 46.88 to 33.68 kg/year.

3.2.6 Fuel Consumption for Internal Transportation Within SVNIT

Based upon the distance of destination from college and weekly trip, total distance travel by individuals was calculated. Based upon mileage of vehicle, total fuel consumption was calculated. Average fuel consumption per family was found to be 0.50 ± 0.38 L/week. Due to the large variation of data in order to find a range, 95% confidence interval was considered. Total fuel consumption per year was calculated considering 84 families and 349 working days in a year.

3.3 CO_2 Sequestered by Vegetation Cover in SVNIT Campus

3.3.1 Area Coverage

These categories cover all those vegetation samples forming a particular polygonal area. From each batch a representative sample was selected and a survey was carried out regarding measurement of tree diameter and height for calculation of CO_2 sink per year by selected batch.

3.4 Carbon Emission Factors

In order to calculate the carbon footprint for Electricity, Diesel, LPG, PNG, Petrol consumption, and Food waste generation following standards were considered. Each

of these standards has specified different carbon emission factors which are used for calculation of carbon footprint for various elements.

3.4.1 ISO 14064 Standards

ISO 14064 is a balanced convention and autonomous, intentional GHG task accounting standard assistance to measure GHG emanation of the association, occasion, item, or individual. For electricity, petrol, diesel, and LPG emission factors are 0.85, 2.296, 2.653 and 2.983, respectively. Calculation of carbon footprint is done by multiplying the consumption of each source with respect to its emission factors. Carbon footprint for electricity in Kg of CO_2 is obtained by the emission factor (0.85) with electricity consumption in KWh. Similarly, carbon footprint in Kg of CO_2 is obtained for petrol, and diesel in liters is calculated by multiplying the respective emission factors; and in the case of LPG carbon footprint in Kg of CO_2 is calculated by multiplying with 2.983 (emission factor) with LPG consumption in Kg. Total carbon footprint is obtained by adding carbon footprint of each source.

Carbon footprint is also calculated by IPCC 2006, US EPA, and Inventory control of greenhouse gases in a similar manner as stated above.

3.5 Calculation of Carbon Footprint

Total Consumption of Electricity, Diesel, LPG, PNG, Petrol, Food waste generation was calculated during the study period; seasonal variation in consumption occurs in each quantity, e.g., in the case of electricity consumption less consumption during the monsoon season and winter season, and more usage of electricity in the summer season. So, there is an upper limit and lower limit for Electricity, Diesel, LPG, PNG, Petrol, Food waste generation, and their corresponding conversion factor given in the above-mentioned methods, and total Carbon footprint was calculated and is shown in Tables 1, 2, 3, 4, 5, and 6.

Table 1 Calculation of carbon footprint due to electricity consumption

Sr. no.	Reference	CO_2 emission factor	Annual Consumption in Kwh		Amount eq. CO_2 in Kg	
			Upper limit	Lower limit	Upper limit	Lower limit
1.	ISO 14040	0.85 kg of CO_2/Kwh	6553512	5517540	5570485	4689909
2.	IPCC	0.45 kg of CO_2/Kwh for purchased electricity	6563512	5517540	2953580.4	2506718.25

Table 2 Calculation of carbon footprint due to diesel consumption

Sr. no.	Reference	CO_2 emission factor	Annual consumption in liters		Amount eq. CO_2 in Kg	
			Upper limit	Lower limit	Upper limit	Lower limit
1	IPCC	74.10 kg CO_2/GJ	16980	7020	49436	20547
2.	ISO 14040	2.63 kg CO/liters/year	16980	7020	44420	15856
3.	EPA (2009)	102.10 kg CO_2/GJ	16980	7020	68523	28460

Table 3 Calculation of carbon footprint due to PNG

Sr. no.	Reference	CO_2 emission factor	Annual consumption in m^3	Amount CO_2 in Kg
1.	IPCC (1996)	56.06 kg of CO_2/GJ	222261	394557.72
2.	EPA (2000)	0.054 kg of CO_2/SCF		424153.962

Table 4 Calculation of carbon footprint due to LPG consumption

Sr. no.	Reference	CO_2 emission factor	Annual consumption in Kg		Amount CO_2 in Kg	
			Upper limit	Lower limit	Upper limit	Lower limit
1.	(GREET)	4.46 kg of CO_2/gal	4301	3587	11535.75	9620.72
2.	IPCC	63.10 kg CO_2/GJ			15335.56	12789.2
3.	Green house gas emission and sinks	57.9 kg CO_2/GJ			14071.72	11735.75
4.	US EIA	56.8 kg CO_2/GJ			13804.38	11524.15

Table 5 Calculation of carbon footprint due to CNG consumption

Sr. no.	Reference	CO_2 emission factor	Annual consumption in Kg		Amount CO_2 in Kg	
			Upper limit	Lower limit		
1.	IPCC (2006)	56.06 kg of CO_2/GJ	348	241	1045	724

3.5.1 Electricity

Calculation of Electricity Consumption was done based on ISO 14040 and IPCC.

Table 6 Calculation of carbon footprint due to petrol consumption

Sr. no.	Reference	CO_2 emission factor	Annual consumption in liters		Amount CO_2 in Kg	
			Upper limit	Lower limit	Upper limit	Lower limit
1.	IPCC (2006)	69.25 kg CO_2/GJ	3890	3027	8781.86	6833.60
2.	ISO 14040	2.296 Kwh/year			8931.44	6949.99
3.	EPA (2009)	87.8 kg CO_2/GJ			11134.26	8664.10

3.5.2 Diesel

Calculation of Electricity Consumption was done based on ISO 14040, IPCC, EPA Standards.

3.5.3 PNG

Calculation of Electricity Consumption was done based on IPCC, EPA Standards.

3.5.4 LPG

Calculation of Electricity Consumption was done based on IPCC, GREET, US EIA, Green House gas Emission and Sinks Standards.

3.5.5 CNG

Calculation of Electricity Consumption was done based on IPCC Standards.

3.5.6 Petrol

Calculation of Electricity Consumption was done based on ISO 1440, IPCC, EPA Standards.

4 Results and Discussions

The carbon footprint is calculated by the data that is obtained by conducting surveys in the campus, and the amount of CO_2 emission is calculated based on the standards such as ISO 14040, IPCC 2006, US EPA, Inventory control of greenhouse gases.

The results that were got after calculation do not represent the complete footprint of the campus due to the incomplete nature of the data and other constraints occurred during the data collection. Primary sources such as PNG, Diesel, Petrol, and CNG cause direct emission of CO_2 to the atmosphere, whereas secondary sources include electricity which does not cause any direct emission of CO_2. Vegetation present in the campus absorbs the CO_2 emitted from the various sources, so the amount of emission will give the carbon footprint of the study area.

4.1 PNG (Pipeline Natural Gas)

PNG is one of the primary sources which causes direct emission of CO_2. From the analysis, it is clear that the major part of CO_2 emission is due to the combustion of PNG (pipe natural gas). The amount of CO_2 emitted is in the range of 394 tons to 424 tons per year. The reason for this much emission is due to the food production in each mess of the hostels. During vacation time, PNG consumption is less during an academic year.

4.2 Vegetable Waste

The main source of vegetable waste is coming from the mess of each hostel. The total amount of vegetable waste produced is in the range of 57 to 62 tons in an academic year. Variation in the quantity of food waste obtained is comparatively very less comparing with other sources. Because in an academic year holidays are maximum up to two months, in that duration food consumption is at its minimum. In the mess vegetarian food is prepared that is the reason due to which the amount of carbon footprint is less as compared to non-veg food.

4.3 LPG (Liquid Petroleum Gas)

In SVNIT, campus consumption of LPG is very less, why, because PNG connections are provided to the most energy-consuming sectors; LPG consumers are mainly Ph.D. scholars and family residing in the Raman Bhavan. The consumption of LPG and CO2 emitted from the combustion of LPG is in the range of 14000 to 7000 kg. The reason for the small quantity is that less number of consumers are there for the LPG.

4.4 Transportation

Fossil fuel consumed in transportation within the SVNIT campus is mainly petrol and CNG. The main reason behind the less consumption of fossil fuel such as petrol and CNG is due to the restriction of vehicle usage by students in the college campus. Only faculty members, Ph.D. scholars residing in the Raman Bhavan are supposed to use vehicles. Apart from this, vehicles are allowed to enter into the campus for various services. Most vehicles driven within the campus are of petrol engines including two-wheelers and four-wheelers. CNG is mainly used in the autorickshaws and some fours-wheelers.

The amount CO_2 emitted in case of CNG is comparatively less than petrol. The reason for comparatively more consumption of petrol is because of students and staff members generally use two-wheelers for traveling inside the campus. CO_2 emitted in case of petrol is in the range of 9700 to 7500 kg per year, and in case of CNG is in the range of 1075 to 724 kg.

4.5 Electricity

In SVNIT campus electricity is a secondary source as it is not produced inside the campus. The demand for electricity is large in the case of SVNIT. DG sets are operated when the electricity is not available in the campus and if there is any repair of the system.

There is emission of CO_2 from electricity starting from the point of production to the point of consumption. Major amount of CO_2 production will take place during the time of production of electricity. In the study area only electricity consumption has to be considered. Annual emission of CO_2 from the electricity source is in the range of 2953.5 to 2506.71 tons per year.

4.6 Diesel

Carbon footprint through diesel consumption is in the range of 6400 to 9600 kg of CO_2/Year. By considering the total emission from each source, they are in the range of 3510 to 2970 tons of CO_2 per year.

4.7 Vegetation Cover

From different sources CO_2 is emitted to the SVNIT premises and similarly the vegetation covers or the green belt present in the campus is absorbing the CO_2 from

the emitting sources. Around 390 to 400 tons of CO_2 is absorbed by the campus in one year as per the calculation.

5 Conclusion

By conducting a study on the carbon footprint of SVNIT campus, it was understood that the emission of CO_2 from the different sources is different and it depends upon the consumption. The major part of CO_2 emission was due to the combustion of PNG (pipe natural gas) and least from the CNG. The food waste emitted 52 to 67 tons of CO_2 because around 224 to 260 tons of food waste is produced annually. Definitely, we can reduce the food waste by adopting optimization in the cooking according to the requirement. Comparing with other emitting sources fossil fuel except for PNG and LPG, consumption of petrol and CNG is less, i.e., because of the restriction in the usage of vehicle by students inside the campus. Total CO_2 emission is in the range 474–520 tons per year, and annually CO_2 is absorbed by the campus 390–400 tons of CO_2. The green belt, which is present in the campus, is absorbing 76.92 to 84.63% from annual CO_2 emission.

References

1. Solomon S, Qin D, Manning M, Marquis M, Tignor MMB, Leroy H (2007) Climate change 2007
2. EPA (2016) Direct Emissions from Stationary Combustion Sources 2016
3. Schuster U et al. (2013) An assessment of the Atlantic and Arctic sea–air CO_2 fluxes, 1990–2009 Biogeosciences 10(1):607–627
4. Climate Change 2007: Impact, adaption and vulnerablity (2007)
5. Asumadu-Sarkodie S, Owusu PA (2016) Carbon dioxide emissions, GDP, energy use, and population growth: a multivariate and causality analysis for Ghana, 1971–2013. Environ Sci Pollut Res Int 23(13):13508–13520
6. Galli A, Wiedmann T, Ercin E, Knoblauch D, Ewing B, Giljum S (2012) Integrating ecological, carbon and water footprint into a 'Footprint Family' of indicators: definition and role in tracking human pressure on the planet. Ecol Indic 16:100–112

Removal Efficiency of Heavy Metals by Washing the Contaminated Soil Using Effective Leaching Agents

J. Sumalatha, R. Prabhakara, and P. V. Sivapullaiah

Abstract Unscientific disposal of industrial waste pollutes the surrounding soil and groundwater during the contamination of heavy metals through leachates. It has been observed from the sample tests conducted on soil and groundwater from various cities that the concentration levels are above the threshold levels. If not addressed, this will result in very serious consequences on the health of human beings and animals. Immediate action is required to prevent contaminated soils from further damage and reduce the contaminant concentrations in the soil. Many researchers have developed different soil remediation methods such as immobilization, phytoremediation, and soil washing. In this research work, an attempt has been made to establish more suitable leaching agents to wash the contaminated soil in bringing down the concentration. In the present study, the use of the soil washing technique with respect to zinc contaminated soil is demonstrated. Column leaching tests on contaminated soil samples were conducted to know the removal efficiencies with mono and combined chemical solutions. Contaminant transport parameters were determined using analytical method of plotting the elution curves of analytical and experimental values. It was observed from the results that leaching with 0.1 Normal Ferric Chloride ($FeCl_3$) is very effective with a removal efficiency of 99.8% compared to the other chemical agents. Further study is very much required in this regard in different soils and for different heavy metals to treat the contaminated sites using soil washing technique.

Keywords Removal efficiency · Transport parameters · Column leaching test · Contaminated soil · Heavy metals

J. Sumalatha (✉)
Ramaiah Institute of Technology, Bengaluru, Karnataka, India
e-mail: latha.msrit@gmail.com

R. Prabhakara
Visvesvaraya Technological University, Belgaum, India
e-mail: r.prabhakara@gmail.com

P. V. Sivapullaiah
GITAM University, Bengaluru, Karnataka, India
e-mail: sivapullaiah@gmail.com

© Springer Nature Singapore Pte Ltd. 2021

K. K. Pathak et al. (eds.), *Recent Trends in Civil Engineering*, Lecture Notes in Civil Engineering 77, https://doi.org/10.1007/978-981-15-5195-6_76

1 Introduction

The soil contamination may happen due to various activities like mining, industrial activities, emissions from transport, use of pesticides and fertilizers, disposal of wastes and sludges, etc. Generally, the heavy metal polluted sites originate in manufacturing areas [1]. As most of the heavy metals do not endure degradation [2], they cause severe problems to humans and the environment in different ways, such as by direct contact with the contaminated soil, by contaminating the water resources, by entering the food chain, or by reducing the agricultural land [3–6]. Hence, suitable treatment methods are required to clean the heavy metal contaminated sites and to protect the human health. The average ranges of heavy metal contents in urban soils worldwide are 66.08 (Cr), 49.60 (Cu), 1733.94 (Pb), 289.78 (Zn), 29.14 (Ni), and 1.52 mg/kg (Cd) which are posing serious threats to many countries (Su 2014). Soil washing is the most widely used technique as it completely eliminates the contaminants. Most of the metal removal rates from soils are too slow to be removed by washing with water alone and need several enhancement schemes such as use of dilute acids and ore complexing agents. Most metal ions in natural stage may not be easily soluble in water and hence dilute acids are used to enhance the solubility of metal ions. Ethylene Diamene Tetra Acetic Acid (EDTA) is an efficient chemical solution which can react with almost all heavy metals [7–9]. Oustan et al. [10] used Oxalic and Acetic acids to treat a calcareous soil which was contaminated. The cadmium contaminated soil can be treated with a diluted Ferric chloride solution [11–14].

For the present study, zinc contaminated soil was collected at the purification plant of Hindustan Zinc Limited (HZL) located near Udaipur in Rajasthan State of Western India. The contamination has happened due to the leakage of a chemical storage tank at Chanderiya smelter. The undisturbed soil samples from four locations were collected at a depth of 0.5 m below ground level. The four locations 1, 2, 3, and 4 are at distances of 5, 10, 15, and 20 m, respectively, from the point of leakage. It was proposed to assess the removal efficiency of selected leaching solutions to remove zinc from the soil. To simulate the soil washing technique, column leaching tests were conducted on contaminated soil with the selected chemical solutions, i.e., 0.1 Normal Hydrochloric acid, 0.1 Normal Ethylene Diamene Tetra Acetic Acid, 0.1 Normal EDTA + HCl, and 0.1 Normal Ferric Chloride solutions; these four chemical solutions here onwards represented as CHS-1, CHS-2, CHS-3, and CHS-4, respectively. The experimental results of leaching tests were modeled using leaching mass ratio approach and thus the contaminant transport parameters were estimated. These models can be used to propose the soil washing program in the field in selecting a suitable leaching solution and to estimate its quantity required in the field (in terms of pore volumes) to remove zinc from a similar type of soil. These models are also useful to estimate the probable time period for the contaminant to reach the water source and its concentration level.

Table 1 Geotechnical properties of the undisturbed soil samples

Location	Bulk density (g/cc)	Water content (%)	Dry density (g/cc)	Specific gravity (G)	Void ratio (e)	Porosity (n)	Zinc content in soil (mg/kg)
1 (sample 1)	1.92	28.2	1.50	2.77	0.85	0.46	23616
2 (sample 2)	2.02	18.5	1.70	2.75	0.61	0.38	19796
3 (sample 3)	2.15	22.4	1.76	2.70	0.54	0.35	5823
4 (sample 4)	1.97	19.8	1.64	2.68	0.63	0.39	189

2 Materials and Methods

2.1 Characteristics of Zinc Contaminated Soil

The composition of the field soil is 84% sand, 4% clay, and 12% silt. The liquid limit of the soil is 26.2% and plastic limit is zero. The soil is classified as "Silty Sand (SM)" as per Indian Standard classification. The geotechnical properties of the soil samples tested are presented in Table 1.

2.2 Batch Leaching Test

From the results of the batch leaching test, the total mass of zinc (m_0) which is the sum of the adsorbed mass (m_s) and pore fluid mass (m_0) presented in each sample was found. The batch leaching test was conducted according to the procedure specified in ASTM D5233-92. As the zinc presented in the soil was not soluble in distilled water, CHS-3 was used as leaching solution. The soil suspension was prepared with twenty grams of dry soil and 100 ml of CHS-3. The mixture was kept on shaking machine for about 24 h and then heated up to boiling point to dissolve the crystalline forms of metals presented in the soil. The mixture was centrifuged to collect the supernatant solution and then filtered using a 0.45-μm size filter film. The effluent was then analyzed with Atomic Absorption Spectrometer (AAS) to estimate the initial concentration of zinc presented in the samples of soil.

2.3 Column Leaching Test

To simulate the soil washing conditions at the field, the column leaching tests on soil samples were conducted according to the procedure given by [15]. The number of pore volumes of fluid required for the removal of zinc from the soil and removal efficiency in a given condition were determined with four leaching solutions, viz., CHS-1, CHS-2, CHS-3, and CHS-4. The photograph of the column leaching test apparatus is shown in Fig. 1.

The leaching solution was placed in the overhead tank and permitted to navigate the soil sample in the column. At regular time intervals, the effluent samples were collected and its cumulative quantity was measured. The concentration of zinc was determined and the mass of zinc leached out with respect to time increment (Δm) was estimated. The governing equation of Advective–Dispersive leaching to model column leaching test which was given by [16] is as shown below (Eq. 1).

$$\mathrm{LMRm} = \frac{\sum \Delta m}{m_0} = \frac{\mathrm{PV}}{\mathrm{RF}} - \frac{1}{2}\left\{\left(\frac{\mathrm{PV}}{\mathrm{RF}} - 1\right) erfc\left(\frac{RF - PV}{\sqrt{\frac{PV.RF}{P_L}}}\right) + \left(\frac{\mathrm{PV}}{\mathrm{RF}} + 1\right)\exp\left(P_L\right) erfc\left(\frac{RF + PV}{\sqrt{\frac{PV.RF}{P_L}}}\right)\right\} \quad (1)$$

RF = Retardation factor;

Fig. 1 Photograph of the experimental setup

P_L = Column Peclet Number = VsL/D;
Vs = Seepage velocity;
L = Length of the soil sample;
D = Dispersion coefficient;
PV = number of pore volumes of leaching solution;
LMRm = Leaching Mass Ratio (Cumulative).

The experimental elution curves were obtained by plotting LMR_m values (calculated from the leaching test with respect to time increment) on x-axis and their corresponding pore volumes (PV) on y-axis [16]. To obtain the contaminant transport parameters (D and RF), the theoretical elution curve was first prepared by substituting trial values of D and RF and experimental values of PV and P_L in Eq. 1. This curve was then matched with the experimental elution curve obtained from the column leaching test. The trials were continued till both the curves match with each other and when the curves were matched, the corresponding trial values were reported as transport parameters. A MATLAB program is created for the above equation to perform iterative calculation and plot the graphs.

3 Results and Discussion

3.1 Experimental Elution Curves

The experimental elution curves obtained from the experimental results are shown in Figs. 2, 3, 4, and 5. It can be observed that higher removal efficiencies were achieved with CHS-4 and CHS-3 solutions. The CHS-1 has showed less removal efficiency and CHS-2 showed moderate efficiency in removal of Zinc from this contaminated

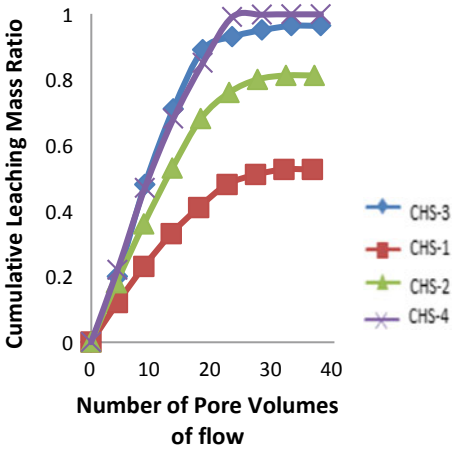

Fig. 2 Elution curves (experimental) of sample 1

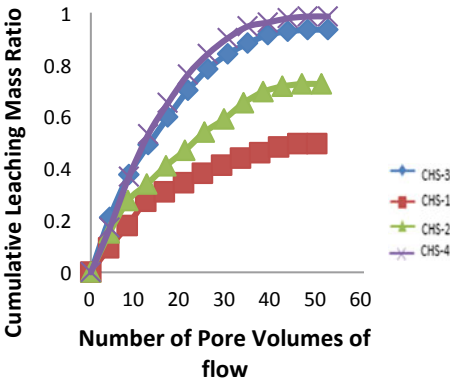

Fig. 3 Elution curves (experimental) of sample 2

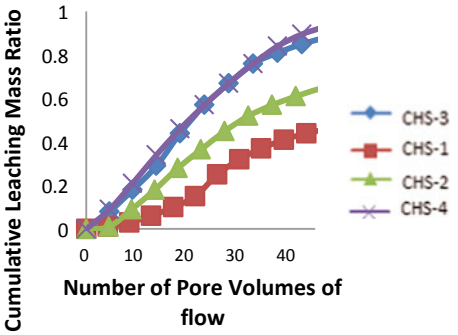

Fig. 4 Elution curves (experimental) of sample 3

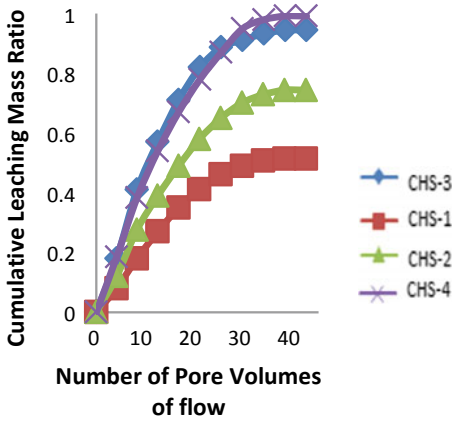

Fig. 5 Elution curves (experimental) of sample 4

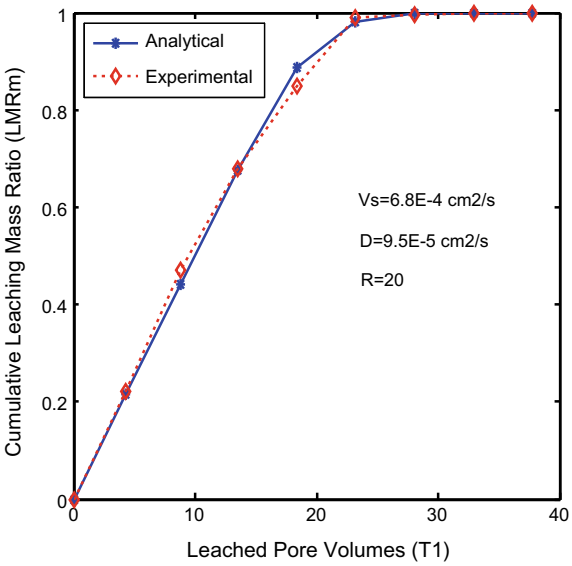

Fig. 6 Elution curves for sample 1

soil. The number of pore volumes required to leach a particular amount of Zinc has also increased with increasing density of soil sample.

3.2 Theoretical Elution Curves and Transport Parameters

As the removal efficiencies are high with CHS-4, the transport parameters of zinc were estimated from the results of column leaching test conducted with this leaching solution only. The theoretical elution curves along with their experimental curves are shown in Figs. 6, 7, 8, and 9, respectively, for samples 1, 2, 3, and 4. The migration rates of zinc through each sample are given in Table 2. These rates are useful to estimate the probable time period for the groundwater contamination to occur at this site and are also helpful to plan the soil washing remediation at the site. The dispersion coefficients of zinc, thus obtained were in the range of $3.8 \times 10^{-5} - 9.5 \times 10^{-5}$ cm^2/s and the retardation factors were in the range of 20–25.5 (Distribution coefficients, $K = 4.7$–5.8).

4 Analysis of Results

The removal efficiencies corresponding to 36 pore volumes of leaching with various solutions to each sample were compared (Figs. 2, 3, 4, and 5) and the percent removal of Zinc from each sample with respect to number of pore volumes is as given below.

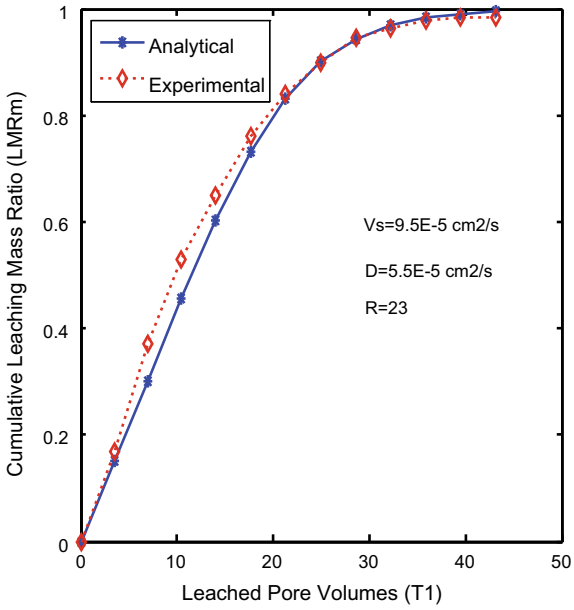

Fig. 7 Elution curves for sample 2

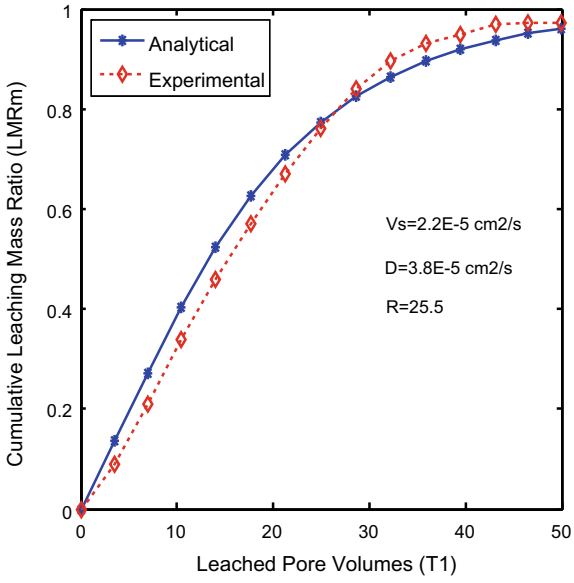

Fig. 8 Elution curves for sample 3

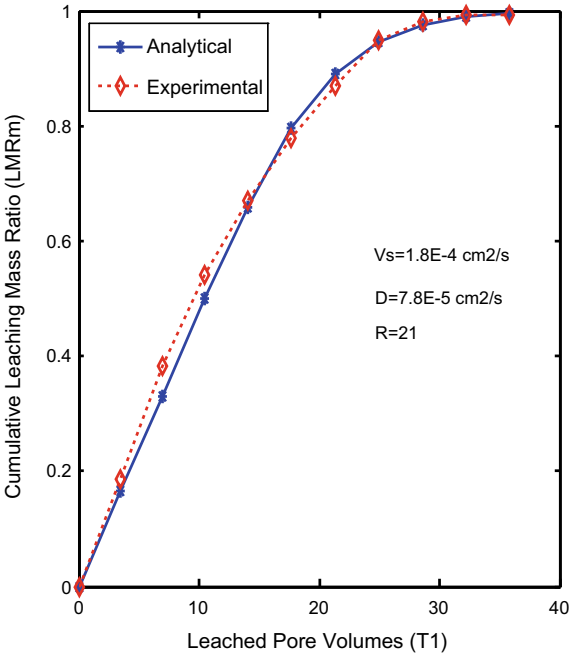

Fig. 9 Elution curves for sample 4

Table 2 Contaminant transport parameters of zinc in soil

Sample	Dry density (ρ_d) (g/cc)	Porosity (n)	Seepage velocity (Vs) (cm/s)	Dispersion coefficient (D) (cm^2/s)	Retardation factor (RF)
1	1.50	0.46	6.8E-4	9.5E-5	20
2	1.70	0.38	9.5E-5	5.5E-5	23
3	1.76	0.35	2.2E-5	3.8E-5	25.5
4	1.64	0.39	1.8E-4	7.8E-5	21

Sample 1: The % removal of zinc from sample 1 with CHS-1, CHS-2, CHS-3, and CHS-4 are 52.6, 81.2, 96.3, and 99.8%, respectively, corresponding to 36 pore volumes of flow. There was no increase in the efficiencies with further washing.

Sample 2: For sample 2, the removal efficiencies with CHS-1, CHS-2, CHS-3, and CHS-4, are 45.5, 67.6, 89.3, and 95.2%, respectively, for 36 pore volumes of flow. The highest efficiencies were achieved corresponding to 52 pore volumes of leaching. The efficiencies with 52 pore volumes of leaching were 49.5, 72.5, 93.4, and 98.5%, respectively, with CHS-1, CHS-2, CHS-3, and CHS-4.

Sample 3: The % removal of zinc from sample 3 with CHS-1, CHS-2, CHS-3, and CHS-4 are 38.5, 56.5, 79.4, and 81.4%, respectively. The highest efficiencies were achieved corresponding to 65 pore volumes of leaching. The efficiencies

corresponding to 65 pore volumes of leaching were 47.3, 69.3, 91.2, and 97.3%, respectively, with CHS-1, CHS-2, CHS-3, and CHS-4.

Sample 4: For sample 4, the removal efficiencies with CHS-1, CHS-2, CHS-3, and CHS-4 are 51.1, 73.6, 93.9, and 98.6%, respectively. The highest efficiencies were achieved corresponding to 43 pore volumes of leaching. The efficiencies with 43 pore volumes of leaching were 51.4, 74.4, 94.5, and 99.2%, respectively, with CHS-1, CHS-2, CHS-3, and CHS-4.

These results were similar to the observations of [12], where the high removal efficiencies were reported as 98.2 and 90%, respectively, with CHS-4 and CHS-2. Hence, it can be observed that the chemical solutions CHS-4 and CHS-3 can be used to treat the zinc contaminated soil with a quantity of 30–50 pore volumes depending on the density of soil. The removal efficiencies varied with the density of soil. The efficiencies were observed decreasing with increasing density. This may be due to the decrease in seepage velocity, which decreases the addictive component of contaminant migration. The dispersion coefficient and retardation factor were obtained by comparing the theoretical and experimental elution curves. The dispersion coefficients decreased and retardation factors increased with the increase in density. The decrease in dispersion is due to the decrease in seepage velocity and the increase in retardation factor is due to the increase in reaction time associated with the slow movement of pore fluid. The contaminant migration rates determined are handy to model the contaminant transport at the site to predict the probable contamination of nearby water sources.

5 Conclusions

1. To find the effective leaching solution for treating a zinc contaminated soil using soil washing technique, column leaching tests with four leaching solutions were conducted on undisturbed samples. The removal efficiencies of selected solutions varied in the order given below. CHS-4 > CHS-3 > CHS-2 > CHS-1
   CHS-4 has shown the best results with the highest removal efficiency of 99.8%. The CHS-4 was also very effective with the highest % removal of 96.3%.
2. It was observed that the removal efficiencies decreased with the increase in density of soil.
3. Estimation of number of pore volumes of leaching fluid required to remove the contaminants varies depending on the density of soil and the velocity of the washing fluid through the soil.
4. To obtain the contaminant transport parameters of zinc, the theoretical and experimental elution curves were matched with the trial values of D and RF. These parameters are useful in estimating the probable time period for groundwater contamination to occur at the site.
5. Use of contaminant transport parameters for the estimation of the rate of removal of zinc in the field soils with different fluids and densities has been demonstrated.

References

1. Gusiatin ZM, Klimiuk E (2012) Metal (Cu, Cd and Zn) removal and stabilization during multiple soil washing by saponin. Chemosphere 86(4):383–391
2. Kirpichtchikova TA, Manceau A, Spadini L, Panfili F, Marcus MA, Jacquet T (2006) Speciation and solubility of heavy metals in contaminated soil using X-ray microfluorescence, EXAFS spectroscopy, chemical extraction, and thermodynamic modeling. Geochimicaet Cosmochimica Acta 70(9):2163–2190
3. McLaughlin MJ, Hamon RE, McLaren RG, Speir TW, Rogers SL (2000) A bioavailability-based rationale for controlling metal and metalloid contamination of agricultural land in Australia and New Zealand. Soil Res 38(6):1037–1086
4. McLaughlin MJ, Zarcinas BA, Stevens DP, Cook N (2000) Soil testing for heavy metals. Commun Soil Sci Plant Anal 31(11–14):1661–1700
5. Ling W, Shen Q, Gao Y, Gu X, Yang Z (2007) Use of bentonite to control the release of copper from contaminated soils. Aust J Soil Res 45(8):618–623
6. Wuana RA, Okieimen, FE (2011) Heavy metals in contaminated soils: a review of sources, chemistry, risks and best available strategies for remediation. ISRN Ecol 1–20
7. Zou Z, Qiu R, Zhang W, Dong H, Zhao Z, Zhang T, Cai X (2009) The study of operating variables in soil washing with EDTA. Environ Pollut 157(1):229–236
8. Khalkhaliani ZN, Mesdaghinia AR, Mahvi A, Nouri J, Vaezi F (2006) An experimental study of heavy metal extraction using various concentration of EDTA in a sandy loam soils. Pak J Biol Sci 9(5):837–842
9. Gebreyesus ST (2015) Heavy metals in contaminated soil: sources & washing through chemical extractants. Am Sci Res J Eng, Technol, Sci (ASRJETS) 10(1):54–60
10. Oustan S, Heidari S, Neyshabouri MR, Reyhanitabar A, Bybordi A (2011) Removal of heavy metals from a contaminated calcareous soil using oxalic and acetic acids as chelating agents. In: Proceedings of the international conference on environment science and engineering IPCBEE, vol 8, pp 152–155
11. Ma F, Zhang Q, Xu D, Hou D, Li F, Gu Q (2014) Mercury removal from contaminated soil by thermal treatment with $FeCl_3$ at reduced temperature. Chemosphere 117:388–393
12. Bilgin M, Tulun S (2016) Removal of heavy metals (Cu, Cd and Zn) from contaminated soils using EDTA and $FeCl_3$. Global NEST J 18:98–107
13. Akahane I, Makino T, Maejima Y, Kamiya T, Takano H, Ibaraki T, Inahara M (2013) Remediation of cadmium-contaminated paddy soils by washing with ferric chloride ($FeCl_3$): effect of soil washing on the cadmium concentration in soil solution and spinach. Jpn Agric Res Q: JARQ 47(3):273–281
14. Hirokazu O, Shingo I, Jian P, Yanfeng Z, Chunxiao J, Hongwen S, Kensuke F (2010) Cadmium extraction from contaminated soil using an iron chloride solution in asian countries. Sustain Food Water 417–424
15. Rowe RK (1988) Contaminant migration through groundwater: the role of modelling in the design of barriers. Can Geotech J 24(4):778–798
16. Shackelford CD, Glade MJ (1997) Analytical mass leaching model for contaminated soil and soil stabilized waste. Groundwater 35(2):233–242
17. Su C (2014) A review on heavy metal contamination in the soil worldwide: situation, impact and remediation techniques. Environ Skeptics Critics 3(2):24

Pre-monsoon Analysis of Vehicular Pollution on Highly Traffic Loaded Squares of Indore City

Ruchir Lashkari and Ramakant Agrawal

Abstract RSPM (PM_{10}) Gaseous pollutant like SO_2, NO_2 and Air Quality Index has been simultaneously measured during the pre-monsoon month of April and May 2019 at the busiest squares of Indore city which are Palasia and Palsikar. Sampling was conducted with the help of respirable dust sampler and was followed by CPCB norms. The lowest RSPM has been observed in the morning time at Palsikar square that is 61 $\mu g/m^3$ and highest in the morning that is 123 $\mu g/m^3$; similarly, at Palasia square the RSPM concentration in morning detected as lowest was 104 and 127 $\mu g/m^3$ as highest during the month. At evening peak hours the concentration at Palsikar square have been observed 117 $\mu g/m^3$ as lowest and 186 $\mu g/m^3$ as highest. On the other end the concentration at Palasia square has been observed 181 $\mu g/m^3$ as lowest and 187 $\mu g/m^3$ as highest. It is observed that the gaseous pollutant concentration was lowest at Palsikar and highest at Palasia and AQI remains moderate except Palasia. This data can help to analyze the present status of vehicular pollution with the respective squares and can also help in the future for making some policies to prevent it.

Keywords RSPM · PM10 · AQI · RDS · CPCB · Gaseous pollutant

1 Introduction

Air pollutants as solid, liquid, or gas present in the atmosphere in such concentrations may be or tend to be injurious to humans, other living creatures, and so to the environment, Air (prevention and control of pollution) Act 1981 [1]. The increase in population resulted in increase in the number of vehicles which is contributing to high level of vehicular pollution in Indore city, and that is responsible for human

R. Lashkari (✉) · R. Agrawal
Department of Civil Engineering, Medi-Caps University, Indore, Madhya Pradesh, India
e-mail: ruchirchamp@gmail.com

R. Agrawal
e-mail: rkagrawal0017@gmail.com

© Springer Nature Singapore Pte Ltd. 2021

K. K. Pathak et al. (eds.), *Recent Trends in Civil Engineering*, Lecture Notes in Civil Engineering 77, https://doi.org/10.1007/978-981-15-5195-6_77

health hazard. Hence, it is very essential to assess the vehicular pollution load on the typical traffic-congested square of the city.

This data can help to analyze the present status of vehicular pollution with the respective squares according to the prescribed limit of CPCB as well as this data can also help in future for making some policies regarding road infrastructure, traffic management, and important strategy for reducing the traffic volume. Transportation plays a significant role in overall development of a country; availability, intensity, frequency, efficiency, and cost of transportation are considered as an index of development [2]. But as the numbers of vehicles are increasing rapidly, it has surely started hindering our atmospheric purity with the vehicular pollution. Vehicular is mainly an urban problem. Vehicular exhaust, a byproduct of fuel combustion contains chemical compounds such as NO_x, SO_x, CO, and HC [3].

2 Causes of Vehicular Pollution

1. High population in the city has also resulted in increase in the number of vehicles, rising vehicular air pollution.
2. Older vehicles (2-stroke 2/3-wheelers) are a significant contributor to air pollution.
3. Inadequate inspection and maintenance facilities of vehicles.
4. Adulteration of fuel and fuel products.
5. Improper traffic management system and road conditions.
6. Absence of an effective mass rapid transport system and intra-city railway networks [4].

3 Objective of the Study

- To identify the sources causing vehicular pollution.
- To assess the pollution level on high traffic loaded square of the city.
- To determine the changes in vehicular pollution due to variations in traffic load respective to the square of the city.
- To Calculate the Air Quality Index for both the square of the city.

4 Methodology

The methodology which had been adopted during the monitoring and analysis of pollutant concentration has been shown in Fig. 1.

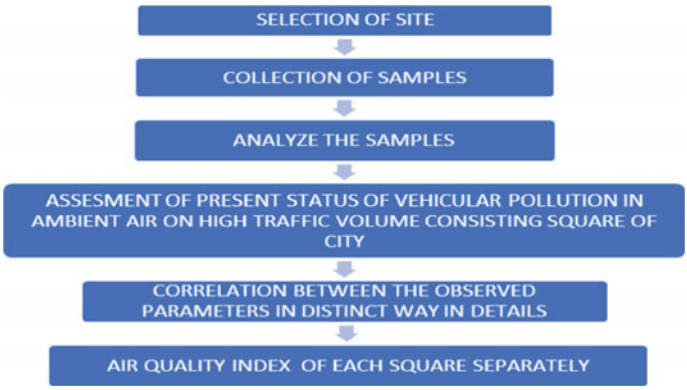

Fig. 1 Methodology flow chart

4.1 Sampling Methodology and Principle

- The samples have collected continuously two times in a week for a single station up to one month according to CPCB sampling guidelines.
- Sampling on each station has been conducted for four hours in the morning and on the same day four hours in the evening according to CPCB guidelines for assessment of vehicular pollution.
- Gravimetric and Absorption principles will be employed for sampling analysis [5].

4.2 Site Selection Criteria

Traffic/Commercial Areas may meet the following Criteria.

- Monitoring site, representing traffic/commercial zone should not be very near with undue influence of traffic emissions.
- It should be near the center of heavy commercial activities.
- The monitoring station must be located near traffic roads with at least 10,000 vehicles/day.

5 Air Quality Index (AQI)

Air Quality Index (AQI) is developed to provide the information about air quality. Air Quality Index (AQI) was introduced by the Environmental Protection Agency (EPA) in USA to measure the levels of pollution due to major air pollutants. It is

one of the important tools available for analyzing and representing air quality status uniformly [6].

6 Location of Air Monitoring Stations in Indore City

The main concern of the project is to measure the concentration of Sulphur dioxide, NO_X, and PM_{10}—the main source of vehicular pollution on typical traffic-congested square with the help of respirable dust sampler. These two critical gaseous pollutants and the particulate pollutants are in very high concentration at both the squares.

Palasia Square. Palasia square is situated on national highway no. 3. This consists of heavy traffic load throughout the day.

Palsikar Square. Palsikar square is situated in the heart of Indore city which connects all four areas of Indore city.

Areas connected with Palsikar Square are Juni Indore (Toward East), Collectorate office (Toward West), Pagnispaga (Toward North), and Manik Bagh (Toward South).

7 Result and Discussion

The average concentration level of respirable suspended particulate matter for Palsikar square has been shown in Table 1.

The average concentration level of respirable suspended particulate matter for Palasia square has been shown in Table 2.

The concentration of RSPM is ranging from 61 to 187 $\mu g/m^3$ for both the stations, i.e., at Palasia square and Palsikar square.

Palsikar square sampling station detects low concentration compared to the Palasia square station which is on national highway no. 3. The lowest RSPM has been

Table 1 Average concentration of RSPM (PM_{10}) at Palsikar square

RSPM-Palsikar		
Date	Morning ($\mu g/m^3$)	Evening ($\mu g/m^3$)
20.4.19	110.39	125.31
21.4.19	102.30	143.68
27.4.19	96.15	117.01
28.4.19	68.41	124.38
4.5.19	123.33	173.86
5.5.19	90.58	165.82
11.5.19	110.12	186.57
12.5.19	61.73	140.89

Table 2 Average concentration of RSPM (PM_{10}) at Palasia square

RSPM-Palasia		
Date	Morning ($\mu g/m^3$)	Evening ($\mu g/m^3$)
24.4.19	109.65	183.82
25.4.19	124.38	185.19
30.4.19	104.17	158.58
1.5.19	127.49	181.16
7.5.19	145.06	181.16
8.5.19	122.55	185.52
14.5.19	106.32	183.82
15.5.19	125.31	187.97

observed in the morning time at Palsikar square that is 61 $\mu g/m^3$ and highest in the morning that is 123 $\mu g/m^3$; similarly at Palasia square the RSPM concentration in morning detected as lowest was 104 and 127 $\mu g/m^3$ as highest.

The concentration of RSPM in the evening at both the squares has been observed higher according to the prescribed guidelines of CPCB. The concentration at Palsikar square have been observed 117 $\mu g/m^3$ as lowest and 186 $\mu g/m^3$ as highest, On the other end the concentration at Palasia square have been observed 181 $\mu g/m^3$ as lowest and 187 $\mu g/m^3$ as highest concentration.

Palasia square is on national highway no. 3 so number of vehicles which passes from there is high as well as the retention time of vehicles on the square is more as compared to the other square of the city. Hence the concentration level of RSPM in evening and morning has been observed higher as compared to the limit prescribed by CPCB.

The Center pollution control board guidelines for the ambient air pollutants has been shown in Table 3 [7].

Palsikar square is in the center of the city; it is also one of the typical traffic-congested square of the city. concentration in the morning at Palsikar squareHere the traffic load observed was less in morning peak hours as compared to evening peak hours as evident from data. Hence, the concentration of PM_{10} has been observed less in morning peak hours and higher in evening peak hours. This trend has been shown in Figs. 2 and 3.

Palasia square is the heart of the city; it is also one of the typical traffic-congested square of the city. Here the traffic load observed was less in morning peak hours as compared to evening peak hours as evident from data. Hence the concentration of PM_{10} has been observed above from the permissible guideline in morning peak hours and higher in evening peak hours, it just doubled the permissible limit. This trend has been shown in Figs. 4 and 5.

The average concentration of SO_2 and NO_2 has been observed at Palsikar square (morning and evening) below the permissible limit prescribed by CPCB. Considering the morning traffic peak hours, the concentration varied from 11 to 15 $\mu g/m^3$ for SO_2 $\mu g/m^3$ and 18 to 23 $\mu g/m^3$ for NO_2 but both the gaseous pollutant found was

Table 3 Permissible guideline prescribed by CPCB

Pollutant	Time weighted average	Industrial, residential, rural and other areas	Ecologically sensitive area (notified by central government)
Sulphur Dioxide (SO_2), $\mu g/m^3$	Annual* 24 h**	50, 80	20, 80
Nitrogen Dioxide (NO_2), $\mu g/m^3$	Annual* 24 h**	40, 80	30, 80
Particulate Matter (size less than 10 μm) or PM_{10} $\mu g/m^3$	Annual* 24 h**	60, 100	60, 100
Particulate Matter (size less than 2.5 μm) or $PM_{2.5}$ $\mu g/m^3$	Annual* 24 h**	40, 60	40, 60
Lead (Pb) $\mu g/m^3$	Annual* 24 h**	0.50, 1.0	0.50, 1.0
Carbon Monoxide (CO) mg/m^3	8 h* 1 h**	02, 04	02, 04

*defined as Annual Arithmetic mean of minimum 104 measurements in a year at a particular site taken twice a week 24 hourly at uniform intervals
**defined as 24 hourly or 8 hourly or 1 hourly monitored values, as applicable, shall be complied with 98 % of the time in a year. 2 % of the time, they may exceed the limits but not on two consecutive days of monitoring

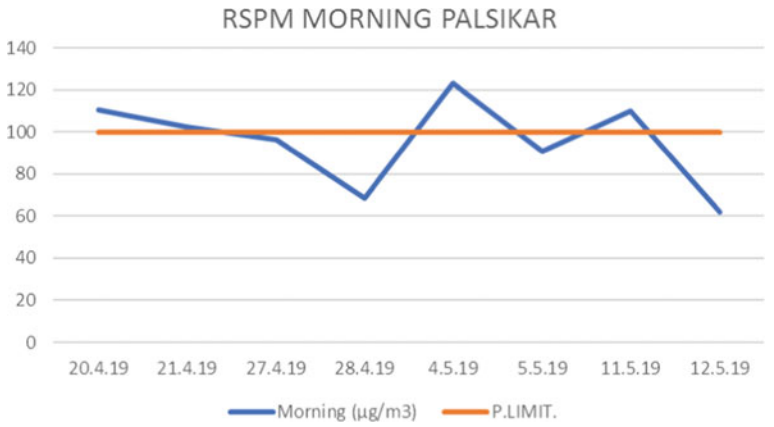

Fig. 2 Variation of RSPM during the month (Palsikar in morning)

low as compared to the evening traffic peak hours. The concentration varies from 17 to 22 $\mu g/m^3$ for SO_2 and 28 to 32 $\mu g/m^3$ for NO_2 at Palsikar square in the evening. It was because of the number of vehicles plying in the evening was higher than the morning. It has also been observed that the concentration level of SO_2 is less then

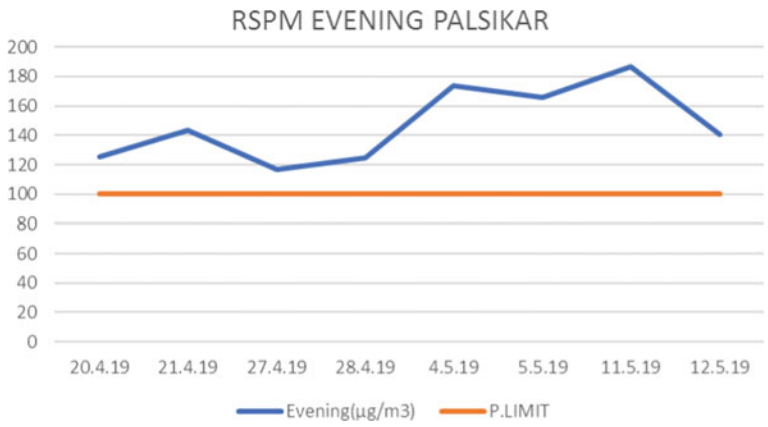

Fig. 3 Variation of RSPM during the month (Palsikar in evening)

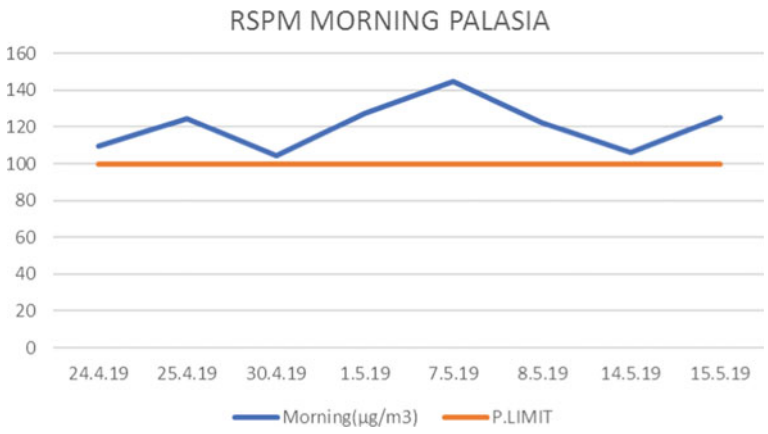

Fig. 4 Variation of RSPM during the month (Palasia in morning)

NO_2 because the petrol engine vehicles eject more nitrogen dioxide than the diesel engine vehicles. The details of concentration have been shown in Table 4.

The average concentration of SO_2 and NO_2 has been observed at Palasia square (morning and evening) below the permissible limit prescribed by CPCB. Considering morning traffic peak hours the concentration has varied from 19 to 23 $\mu g/m^3$ for SO_2 and 30 to 34 $\mu g/m^3$ for NO_2, respectively, but both the gaseous pollutant found less in morning traffic peak hours as compared to the evening traffic peak hours. The concentration varies from 24 to 30 $\mu g/m^3$ for SO_2 and 37 to 40 $\mu g/m^3$ for NO_2 at Palasia square in the evening. It is because of number of vehicles plying in the evening are more than in the morning. It has been also observed that the concentration level of SO_2 is less than NO_2 because the number of petrol engine vehicles are passing

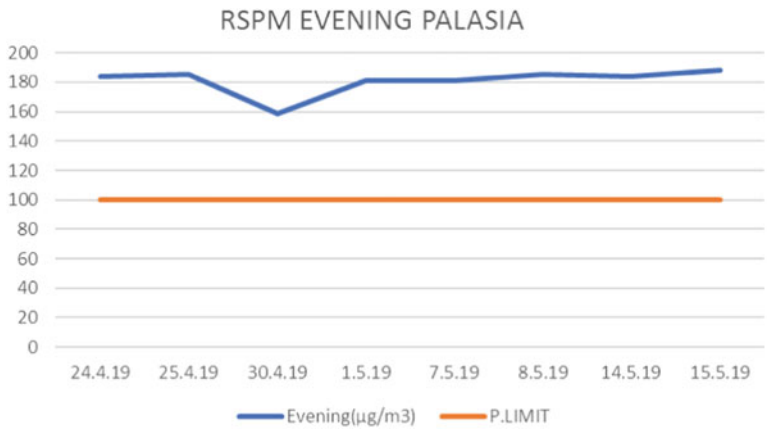

Fig. 5 Variation of RSPM during the month (Palasia in evening)

Table 4 Average concentration of SO_2 and NO_2 at Palsikar square

Palsikar square				
	Morning		Evening	
Date	SO_2 ($\mu g/m^3$)	NO_2 ($\mu g/m^3$)	SO_2 ($\mu g/m^3$)	NO_2 ($\mu g/m^3$)
20.4.19	11.87	18.35	19.61	30.2
21.4.19	14.53	20.18	19.71	31.61
27.4.19	16.65	23.47	18.68	29.47
28.4.19	14.47	19.71	20.29	29.76
4.5.19	14.28	20.98	22.4	31.72
5.5.19	15.46	21.18	20.83	32.05
11.5.19	15.04	21.72	20.91	30.32
12.5.19	13.7	19.67	17.41	28.23

more than the diesel engine vehicles from the square. The details of concentration have been shown in Table 5.

The air quality index for both the locations Palasia and Palsikar has been observed during morning as well as evening peak hours according to the concentration of particulate matter and gaseous pollutant that has been shown in Table 6.

Table 5 Average concentration of SO_2 and NO_2 at Palasia square

Palasia square				
	Morning ($\mu g/m^3$)		Evening ($\mu g/m^3$)	
Date	SO_2	NO_2	SO_2	NO_2
24.4.19	19.67	31.26	25.97	38.73
25.4.19	18.98	30.90	26.31	37.06
30.4.19	19.73	30.24	26.81	39.17
1.5.19	19.08	31.79	23.61	37.10
7.5.19	23.00	34.74	30.40	40.23
8.5.19	19.94	28.94	28.09	39.81
14.5.19	22.21	34.29	26.34	40.23
15.5.19	19.35	30.80	24.92	38.39

Table 6 Air quality index for both the squares during morning and evening peak hours

S. no	Sampling station	PM_{10} in ($\mu g/m^3$)	SO_2 in ($\mu g/m^3$)	NO_2 in ($\mu g/m^3$)	AQI value	Remarks
1	Palsikar morning	95.38	14.5	20.66	46.45	Light air pollution (LAP)
2	Palsikar evening	147.17	19.98	30.42	70.06	Moderate air pollution (MAP)
3	Palasia morning	120.62	20.25	31.62	61.18	Moderate air pollution (MAP)
4	Palasia evening	180.9	26.56	38.84	87.55	High air pollution (HAP)

8 Conclusions

The RSPM concentration in the morning at Palsikar square was observed below the permissible limit but at the same place, the RSPM concentration in the evening was observed above the permissible limit prescribed by CPCB.

The RSPM concentration in the morning at Palasia square is higher as well as crossing the permissible limit. On the other side, the concentration in the evening at Palasia is highest and reaching to the double of the Permissible limit of RSPM prescribed by CPCB.

The concentration pattern of SOx in Palasia square is below the permissible limit in the morning as well as evening but it can cross the limit if the vehicular pollution will be in the same increasing trend.

The concentration pattern of SOx in Palsikar is below the permissible limit in the morning as well as evening but it can cross the limit if the vehicular pollution will be in the same increasing trend.

The concentration pattern of NOx in Palasia Square is acceptable in the morning. On the other end in the evening, it is high but not crossing the permissible limit prescribed by CPCB.

The concentration pattern of NOx in Palsikar Square is acceptable in the morning. On the other end in the evening, it is high but not crossing the permissible limit prescribed by CPCB.

Air quality index for both the locations during the study period was found out to be in the moderate air pollution category. However, at Palasia square in the evening it was observed that is in high air pollution category.

References

1. The Air (Prevention and control of pollution) ACT, 1981
2. National Academics of science, engineering and medicine key transportation indicator; summary of a workshop (2002): PP 22,27
3. Wagela DK (1998) Assessment of air pollution effect on plants and soil due to automobile emissions in and around Indore City. A Doctoral Thesis of Env. Sce. Div, M.B. Gujarati Sci. Coll., DAVV, Indore, India
4. Probes/136/2010 Central pollution control Board (Ministry of Environment & Forests, Govt. Of India) East Arjun Nagar, Delhi—110032 "Status of the vehicular pollution control programme in India. (March 2010)
5. NATIONAL Ambient air quality monitoring series: NAAQMS / / 2003-2004
6. Air Quality EPA-456/F-98-005. Environmental protection agency. U.S 7/2010
7. National Ambient air quality series: NAAQMS 137/2012-2013

Stress–Strain Behavior of Municipal Solid Waste in Undrained Loading Condition

Sandeep Kumar Chouksey

Abstract Shear strength property of municipal solid waste (MSW) reveals important information with reference to the various stability issues in landfill engineering. In this context, the undrained behavior of MSW plays significant role for the short-term stability issues of landfill. The shear strength parameters derived from stresses–strain response of MSW during loading at failure state is important to assess the stability of landfill in undrained condition. The stress–strain analysis of MSW depends upon composition of MSW, water content, unit weight, size and shape of particles, loading history, etc., as the results of all above parameters are clearly visible in nature of stress–strain response of MSW. Due to these issues, analysis of MSW becomes complex, and improper investigation of strength, compressibility parameters, and design may lead to catastrophic failure. Therefore, the stress–strain behavior plays significant role for better understanding of assessment of landfill slope stability in undrained loading condition. In this paper, experimental observation of stress–strain behavior of MSW under undrained loading condition is presented for the waste collected from Bangalore landfill site. The results obtained from experiments are interpreted in the form of stress–strain response and pore water pressure.

Keywords Stress–strain · Pore water pressure · Undrained loading · Slope stability

1 Introduction

Slope failures of landfill have become greatest challenges in the stability analysis of MSW all around the world. The stability issue of landfills mainly depends upon shear strength parameters which are derived experimentally from stress–strain response of MSW under undrained loadings at failure for different confining pressures. The nature of stress–strain response of MSW depends upon number of input parameters such as its composition (component present in waste), water content, unit weight, size and shape of particles, loading history, etc., and the influences of all the parameters

S. K. Chouksey (✉)
National Institute of Technology, Raipur, India
e-mail: schouksey.ce@nitrr.ac.in

© Springer Nature Singapore Pte Ltd. 2021

K. K. Pathak et al. (eds.), *Recent Trends in Civil Engineering*, Lecture Notes in Civil Engineering 77, https://doi.org/10.1007/978-981-15-5195-6_78

are clearly observed in the peculiar behavior of stress–strain response of MSW. Due to these issues, analysis of MSW becomes complex and improper investigation of strength, compressibility parameters, and design which may lead to catastrophic failure. Several failures occurred in various parts of the world such as Rumpke in the USA Dona Juana in Columbia Payatas in Philippines [1, 2] are due to the presence of undrained conditions behavior of landfill material. Therefore, it is very necessary to understand the complex behavior MSW in undrained loading condition for the slope stability assessment of landfill.

2 Consolidated Undrained (CU) Tests

The consolidated undrained (CU) tests are conducted in a standard triaxial apparatus as per ASTM D4767—11 standards. Shear strength of MSW is influenced by various parameters like initial condition, moisture content, its bulk density, etc. Table 1 presents MSW composition, and Table 2 presents basic properties of MSW, respectively.

Tests are carried out by keeping the initial conditions same for all the samples. Tests are performed on cylindrical specimens of size 100 mm height and 50 mm diameter. The tests are carried out in three phases; they are (i) firstly, the sample is saturated and (ii) then it is isotopically consolidated under different confining

Table 1 Composition MSW passing through 100 mm trommel

Type of waste	Quantity in kg	Percentage (%)
Clothes	6.34	6.34
Plastics	28	28
Glass	1.28	1.28
Leather	0.8	0.8
Coconut	5.56	5.56
Metal	–	–
Stones	1.96	1.96
Rubber	0.88	0.88
Wood	0.16	0.16
Compost	54.2	54.2

Table 2 Basic properties of MSW

S. no.	Specific gravity	Water content (%)	Unit weight (γ) kN/m^3	Compression index (c_c)	Recompression index (c_r)
1	0.85	25	7.4	0.56	0.055
2	0.97	44	10.5	0.50	0.080

pressures, and finally the sample is shear under undrained condition at 0.5 mm/min constant strain rate. Shearing deviatoric stress and excess pore water pressures are measured. Figure 1a, b presents experimental observations of stress–strain and pore water pressure results of MSW sample having unit weight of sample 7.4 kN/m^3. Similarly, Fig. 2a, b presents results for MSW sample of unit weight of 10.5 kN/m^3.

It is noted that the behavior of stress–strain response of MSW shows continuously increase in deviatoric stress without reaching ultimate or peak stress level for all the confining pressures, and increase in deviatoric stress is higher for higher confining pressures. This peculiar behavior continuously increases deviatoric stress due to the presence of fibrous effect which is present in the form of textile, rubber, grass, etc. The other important observation in undrained condition is the variation of pore water

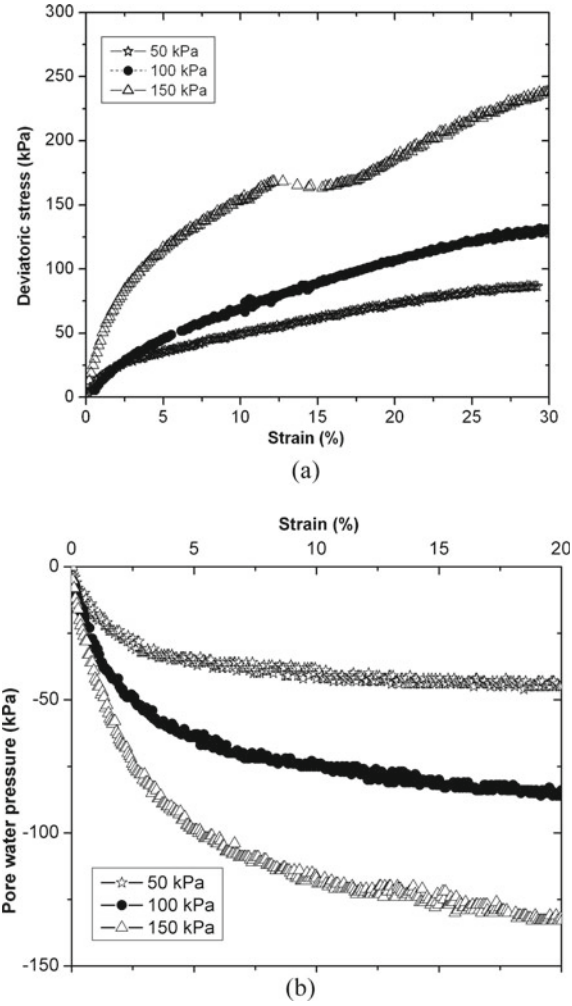

Fig. 1 Experimental response of stress–strain and pore water pressure of MSW at different confining pressures for unit weight of 7.4 kN/m^3

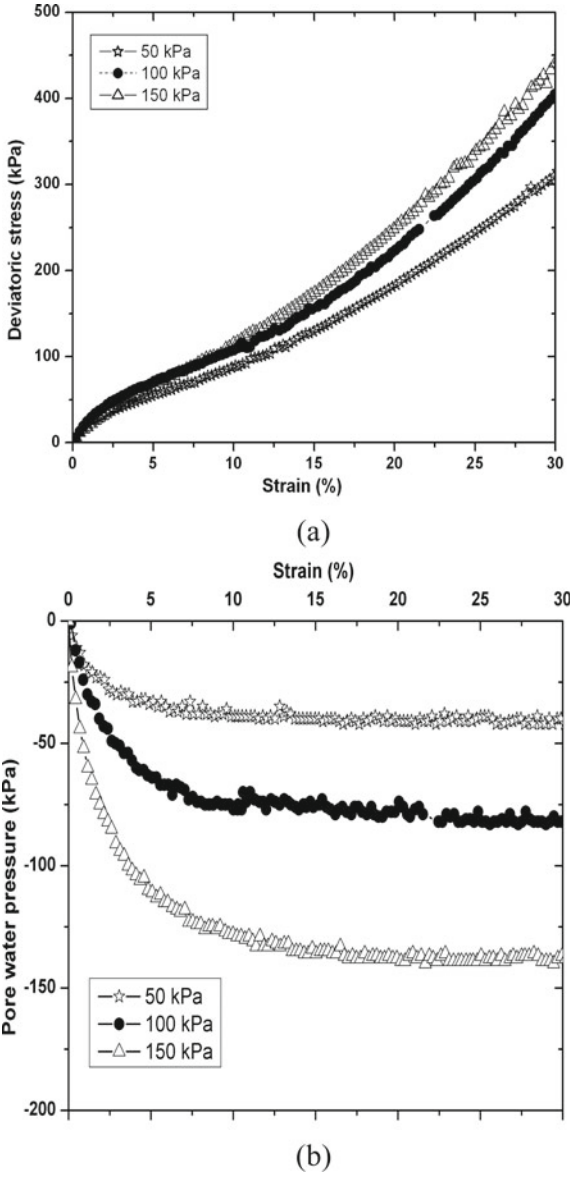

Fig. 2 Experimental response of stress–strain and pore water pressure response of MSW at different confining pressures for unit weight of 10.5 kN/m^3

pressures with strain and confining pressures. It was observed that the pore water pressure of MSW in undrained condition is increased initially and subsequently becomes constant after strain levels of 12–15%. These results are similar to the results reported by [3] for the MSW samples from Bandeirantes Sanitary landfill.

3 Conclusions

In general, the above experimental results show response similar to the results reported in [3–7]. The conclusions drawn from the above study are as follows:

The stress–strain behavior of MSW in undrained condition increases continuously without achieving any peak or ultimate value with reference to the strain value for all the confining pressures (50, 100, and 150 kPa) at unit weights of 7.4 and 10.5 kN/m^3, respectively. This is one of the unique features of experimental observation of MSW under undrained loading condition.

The pore water pressure increases continuously and become constant after strain level of 12–15%.

References

1. Merry SM, Kavazanjian E, Fritz WU (2005) Reconnaissance of the July 10, 2000, Payatas Landfill failure. J Perform Constructed Facil, ASCE 19(2):100–107
2. Blight GE, Fourie AB (2005) Catastrophe revisited—disastrous flow failures of mine and municipal solid waste. Geotech Geol Eng 23:219–248
3. Vilar OM, Carvalho MF (2004) Mechanical properties of municipal solid waste. ASTM Geotech Test J 32(6):1–12
4. Gabr MA, Valero SN (1995) Geotechnical properties of municipal solid waste. ASTM Geotech Test J 18(2):241–251
5. Reddy KR, Hettiarachchi H, Parakalla N, Gangathulasi J, Bogner JE, Lagier T (2009) Geotechnical properties of landfilled municipal solid waste under short-term leachate recirculation operations. Waste Manage Res 27(6):578–587
6. Reddy KR, Hettiarachchi H, Parakalla N, Gangathulasi J, Bogner J (2009) Geotechnical properties of fresh municipal solid waste at Orchard Hills Landfill, USA. Waste Manag 29(2):952–959
7. Reddy KR, Hettiarachchi H, Parakalla N, Gangathulasi PJ, Bogner J, Lagier T (2009c) Hydraulic conductivity of municipal solid waste in landfills. ASCE J Environ Eng 135(8):677–683

Settlement Behavior of Municipal Solid Waste Using Constitutive Modeling Approach

Sandeep Kumar Chouksey

Abstract Settlement behavior of municipal solid waste (MSW) is very important to understand the short- and long-term operations of landfill systems. It provides information about the landfill capacity and also possible to plan the post-closure development at the site activities. Therefore, in this paper, settlement behavior of MSW is calculated for the typical landfill of 30 m height filled in 10 layers and compared with various other existing available models in literature. The result shows that the settlement behavior of MSW varies largely depending upon the assumptions made for the development of models and consideration of various mechanisms.

Keywords MSW · Settlement · Municipal solid waste · Landfill · Short- and long-term operations

1 Introduction

Stability issues of municipal solid waste have become one of the leading problems all over the world, as several failures have occurred due to improper investigation of geotechnical properties of MSW and consideration of various mechanisms which occur simultaneously during the process of filling of landfill. In order to safe disposal waste, it requires knowledge of various disciplines such as geotechnical engineering, environmental engineering, etc. The design of landfill requires various components such as bottom liners, leachate removal and collection system, final cover, etc. Settlement of MSW occurs due to its self-weight and external or surcharge loads placed on it. External loads are coming due to topsoil cover, loads due to the number of layers of waste (lift thickness), final cover, and applicability of site requirement for the future or recreational activates such as park, buildings, etc. Settlement behavior of MSW mainly comes from the following methods: (1) reorientation of particles due to physical process, (2) chemical processes that includes reactions as a result corrosion, combustion, and oxidation; (3) dissolving soluble substances due to dissolution

S. K. Chouksey (✉)
National Institute of Technology, Raipur, India
e-mail: schouksey.ce@nitrr.ac.in

© Springer Nature Singapore Pte Ltd. 2021

K. K. Pathak et al. (eds.), *Recent Trends in Civil Engineering*, Lecture Notes in Civil Engineering 77, https://doi.org/10.1007/978-981-15-5195-6_79

process as a result percolation of liquids occurs from leachate; and (4) biodegradation process which depends upon types and amount of organic present as well as the local environmental conditions. Significant amount of waste settlement takes place during waste placement and due to reorientation of particles as results of mechanical process due to self-waste of waste and surcharge loads. Substantial amount of settlement takes place due to biodegradation processes which is function of organic content, and time is often called secondary settlement.

Therefore, it important to evaluate MSW settlement for the design of final cover for recreational activities. In addition, knowledge of settlement provides information about the stability of landfills and its components such as gas and leachate collection piles, system required for the drainage of leachate, storage capacity, and the overall cost of operation and maintenance of landfill and its systems. Failure of cover systems takes place as a result of excessive settlement and damage of drainage, and gas collection piles take place.

In this context, number of researchers carried out various experiments, and analytical work understands the complex behavior of MSW in order to calculate the settlement behavior of MSW by considering that different mechanisms occur in landfill such as [1–3] addressed these issues. Most of the methods are based on consolidation theory which incorporates primary- and time-dependent secondary compression processes. The models for the settlement of MSW which accounts mechanical response of MSW under different loading conditions have been addressed by very few authors, and continuous efforts have been made to further develop general model for better understanding of MSW behavior with reference to the time and stress.

2 Constitutive Model for MSW

A generalized constitutive model is developed which incorporates the mechanical behavior, time-dependent biological process, and creep in calculation of settlement. The applicability of proposed model is presented with reference to typical landfill site of 30 meters high as shown in Fig. 1 for a period of 30 years which is a closing period of any landfill site. Based on the proposed model of [4], the final expression of yield surface from the proposed model is expressed as follows: The detailed derivation of proposed model is presented in [5].

$$q = Mp\sqrt{\left(\frac{p_0'}{p'}\right)^{\frac{\lambda}{\lambda-\kappa}} \exp\left[\left(\varepsilon_v^c + \varepsilon_v^b\right)\left(\frac{\lambda-\kappa}{1+e_0}\right)\right] - 1} \tag{1}$$

The objective is to calculate the landfill settlement for 10950 days after closure in order to help plan the post-closure development at the site. Points P1 to P10 are the points of interest of each layer for settlement computation. The detailed procedure for the settlement calculation from proposed approach is presented in [3]. Table 1 presents MSW composition.

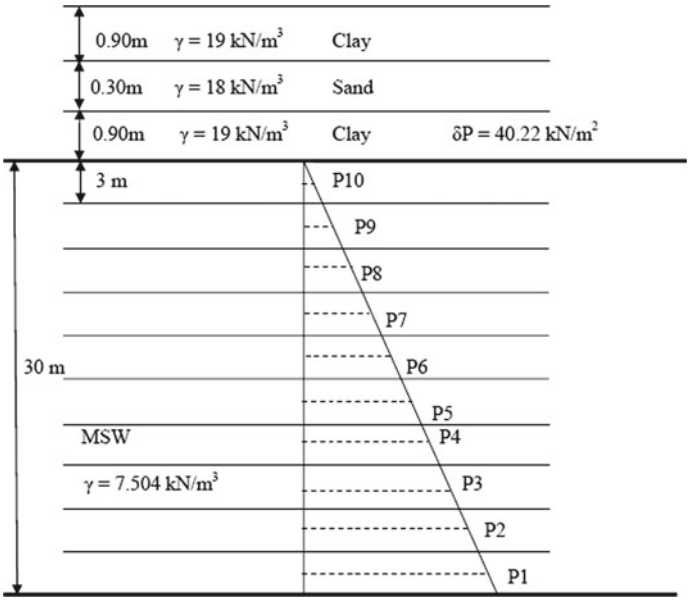

Fig. 1 Typical landfill for calculation of time versus settlement

Table 1 MSW composition

Type of waste	Quantity in kg	Percentage (%)
Clothes	6.34	6.34
Plastics	28	28
Glass	1.28	1.28
Leather	0.8	0.8
Coconut	5.56	5.56
Metal	–	–
Stones	1.96	1.96
Rubber	0.88	0.88
Wood	0.16	0.16
Compost	54.2	54.2

The applicability of proposed model is presented with reference to the model parameters obtained from odometer tests (one-dimensional compression tests) and triaxial compression tests. The input parameters required for the comparison of time–settlement response of MSW are obtained from [6]. The coefficient of earth pressure at rest (K_o), friction angle in terms of material constant (M), and over-consolidation ratio (OCR) are used for the MSW settlement. The method reflects the influence of pre-consolidation pressure and evolution of change in strain with respect to time which gives information of final void ratio. Table 2 presents parameters required for

Table 2 Input parameters used for the validation of proposed

Model	C_c'	b	c	Edg	d	K_o
Marques et al. [6]	0.106	5.7×10^{-4}	1.7×10^{-3}	0.158	1.1×10^{-3}	1
Marques [7]	0.106	5.7×10^{-4}	1.7×10^{-3}	0.158	1.1×10^{-3}	1
Proposed model	0.106	5.72×10^{-4}	1.7×10^{-3}	0.158	1.1×10^{-3}	1

the applicability of proposed model in comparison with [5, 6].

3 Results

The validation of constitutive proposed model for the calculation of time-settlement behavior of MSW is shown in Fig. 2 with reference to the published model of [5, 6]. The obtained results from proposed approach give good agreement with published results of [5, 6]. It may be noted that the approach of [6] accounts depth of lift like the approach presented herein, and hence there is a better agreement between the predictions from the present approach and that of [6].

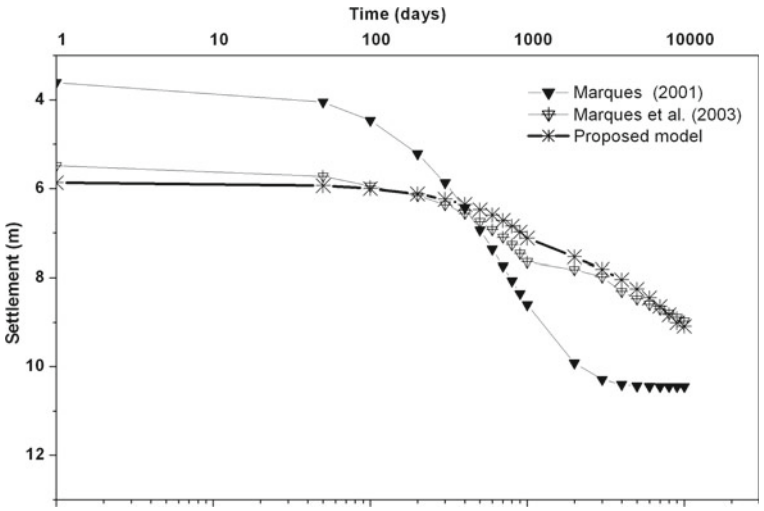

Fig. 2 Settlement behavior of MSW with reference to the time for landfill using [5, 6] and proposed model

4 Conclusions

The above study addresses the following conclusions with reference to the proposed model.

Based on the above approach, it was observed that the total settlement form proposed is in the similar range as those of [5, 6] that accounts all the three mechanisms for the settlement.

The input parameters required for the applicability of proposed model are calibrated from one-dimensional consolidation and triaxial compression tests.

References

1. BabuSivakumar GL, Reddy KR, Chouksey SK (2010) Constitutive model for municipal solid waste incorporating mechanical creep and biodegradation-induced compression. Waste Manage J 30(1):11–22
2. BabuSivakumar GL, Reddy KR, Chouksey SK (2011) Parametric study of parametric study of MSW landfill settlement model. Waste Manage J 31(1):1222–1231
3. Babu Sivakumar GL, Reddy KR, Chouksey SK, Kulkarni H (2010) Prediction of long-term municipal solid waste landfill settlement using constitutive model. Pract Periodical Hazard, Toxic, Radioactive Waste Manage, ASCE 14(2):139–150
4. Chouksey SK, Babu Sivakumar GL (2013) Constitutive model for strength characteristics of municipal solid waste. Int J Geo-mech 15(2):04014040-1–04014040-14
5. BabuSivakumar GL, Reddy KR, Chouksey SK (2010) Constitutive model for MSW considering creep and biodegradation effects. In: 6ICEG international conference at New Delhi, pp 451–456
6. Marques ACM, Filz GM, Vilar OM (2003) Composite compressibility model for municipal solid waste. J Geotech Geo-environmental Eng, ASCE 129(4):372–378
7. Marques ACM (2001) Compaction and compressibility of municipal solid waste Ph.D. Thesis, Sao Paulo University, Sao Carlos, Brazil

Performance Comparison of Microbial Fuel Cell: A Case Study with Different Effluents

Prateek Jyotishi and Dal Chand Rahi

Abstract The numerous ability function of microbial fuel cells creates them more generative in research field at current era. This experimental study includes construction of fuel cell using microorganism in an efficient manner, and the test was carried out in dual chamber microbial fuel cell. In the investigation, dairy wastewater, sugar mill wastewater, and domestic waste effluent were used as waste matter substance. Wastewater characteristics such as total dissolved solids, chemical oxygen demand, and biochemical oxygen demand were observed prior to and later than process the wastewater effluent in microbial fuel cell using yeast as accelerator. In this case study, chemical oxygen demand and biochemical oxygen demand after deduction were established to be 82.68 and 57.52% for dairy wastewater effluent, 91.65 and 80.90% for sugar mill wastewater, 84.19 and 81.08% for domestic wastewater, respectively. The highest voltage generated throughout the experimental run of dairy wastewater was found to be 1.03, 0.098 and 0.081 V generated for the duration of the experimental run of domestic and sugar mill wastewater. In the experimental run, voltage generated during the treatment of dairy wastewater is more. The overall production showed that the organic matter has been successfully treated higher in the dairy wastewater and produces additional electrons when correlated to leather and domestic wastewater in the experimental run.

Keywords Microbial fuel cell · Total dissolved solid · Chemical oxygen demand · Biochemical oxygen demand

1 Introduction

The tremendous challenges we are facing in this era are energy crisis due to continuous reduction of fossil fuels, rising price of fuels, and global heat [1]. Increasing pollution level in terms of CO_2 emissions are not on track which causes global warming. As the world's population increased day-by-day, the demands such as

P. Jyotishi (✉) · D. C. Rahi
Jabalpur Engineering College (JEC), Jabalpur, Madhya Pradesh, India
e-mail: er.prateekjyotishi@gmail.com

© Springer Nature Singapore Pte Ltd. 2021

K. K. Pathak et al. (eds.), *Recent Trends in Civil Engineering*, Lecture Notes in Civil Engineering 77, https://doi.org/10.1007/978-981-15-5195-6_80

water, food, and energy sources are also rising. The Energy–Water–Food Nexus is the biggest challenge in the world. If it is possible to find a better solution to resolve, one challenge could improve the others. To fulfill the India's energy requirement, it is requested to find alternative energy solution which comes under limitless energy sources. As the quantity of nonrenewable fuel source decreases, the market price gets increased [2]. Numbers of researches are carries out in this era related to renewable energy in order to find better suitable technology to fulfill our energy requirement. Along with important renewable energy sources such as solar and wind, biomass, bio-fuel, etc., have also gain attention in the recent era. But it is required to eliminate the limitations of all available renewable sources of energy. Increase in number of industry results in not only high production, but also increased water usage as well as waste generation. Energy recovery from waste generation from different waste generation sources is one of the hot topics for research. Energy can be recovered in different forms such as electrical energy, heat, or natural gas. Comparing with other forms of waste, wet waste (wastewater) is the one from which energy recovery can be done efficiently. Almost several organic materials could be used to feed the fuel cell [3]. This technology is under supervision for large-scale economic output. Multiple applications of this method made it feasible for small case study. This reaction occurs in the absence of free oxygen, and organisms used are termed as electricizers [4]. The gain of using MFC is that it can be effective at room temperature itself [5]. The loss is that it is not able to produce desirable current, and scale-up process is the major issue [6]. Microbial fuel cell is used for wastewater treatment, electricity generation, and as a biosensor in different fields [7]. In cathode chamber, it is seen that electron, proton, and oxygen join to form water [8]. It is also seen that not all of the organisms transfer toward anode [9]. There are mainly three ways by which electrons can be moved: a. through artificial arbiter, b. through microorganism's self-arbiter, and c. through direct transfer of electrons [10]. Most frequently available arbiters are methyl blue, thionine, and neutral red [11]. Microorganisms can be used as pure culture or mixed culture. But mixed culture produces more current when compared to pure culture. Some frequently available microorganisms are Shewanella Escherichia coli, Clostridium butyricum [12] (Fig. 1).

1.1 Agar Salt Bridge Assembly

Salt bridge was prepared by 0.4 c.m. diameter-level cylinder. This salt bridge was arranged with sodium chloride, and 5.5% of agar is added; then the solution was boiled for some time. The concoction was put into the tube and permitted to harden. This salt bridge was used to insert into the consequent microbial fuel cell and potted with help of tape.

Fig. 1 Voltage generated by microbial fuel cell

1.2 MFC Mechanism

MFC is assembly of different electrodes, anode chamber, cathode chamber, and salt bridge. The effluent is filled in anodic chamber, to form a bridge between cathodic and anodic chamber; the salt bridge is fabricated. Make possible the movement of ions (protons). Steel and graphite are used as electrodes of different cross-sectional areas (Fig. 2).

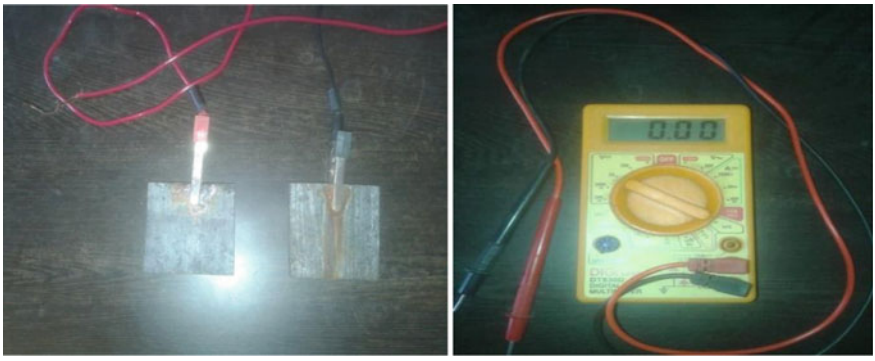

Fig. 2 A multimeter and electrode

Fig. 3 Image of salt bridge

1.3 MFC Assembly

In this case study, two-chambered fuel cell was used. Two plastic bottles of 1000 ml capacity with radius 10 mm were used for the experiment and indicated as cathode and anode. Two holes were made of diameter 5 and 1.6 mm on both the plastic bottles for the introduction of the salt bridge and electrodes. To fill anode chamber, distilled water is used and for the cathode chamber dairy wastewater with activated yeast was used and both chamber lids were bunged airtight and potted with the help of tape (Fig. 3).

2 Collection of Waste Effluent and Analysis of Characteristics

Dairy wastewater effluent is passed down as fuel in microbial fuel cell, and the sample is collected from Mishra Dairy, katra mandla city. Sugar mill waste sample effluent is taken from purvakudwan near mandla. Permissions are taken from each of them to collect waste and domestic effluent from model science school hostel. More than two wastewater effluent samples are taken from source. Collected sample of wastewater effluent is put in the refrigerator at 4 °C for the process of slow down the microbial activity. This wastewater sample is non-noxious and wealthy in organic matter, and this effluent is analyzed in the laboratory to come across the preliminary personality of the wastewater effluent which are total dissolved solid, chemical oxygen demand, biochemical oxygen demand, and the experiment [4]. Outcomes are revealed in Table 1 (Tables 2 and 3).

Table 1 Preliminary characteristics of dairy wastewater

Point	Characteristics	Results
1.	Color	Milky white
2.	Odor	Bad
3.	pH	5.9
4.	BOD (mg/L)	543
5.	COD (mg/L)	1659
6.	TDS (mg/L)	1987

Table 2 Preliminary characteristics of sugar mill wastewater

Point	Characteristics	Results
1.	Color	Grayish black
2.	Odor	Bad
3.	pH	6.1
4.	BOD (mg/L)	623
5.	COD (mg/L)	1786
6.	TDS (mg/L)	1891

Table 3 Preliminary characteristics of domestic wastewater

Point	Characteristics	Results
1.	Color	Light green
2.	Odor	Bad
3.	pH	6.4
4.	BOD (mg/L)	310
5.	COD (mg/L)	607
6.	TDS (mg/L)	490

3 Experimental Setups

The basic arrangement of double-chamber microbic cell for wastewater treatment and electricity generation contains the following items:

- Two plastic bottles of 1000 ml capacity.
- Salt bridge to interconnect the bottles.
- Two electrodes.
- Multimeter for voltage measuring.
- Yeast as an accelerator (Fig. 4).

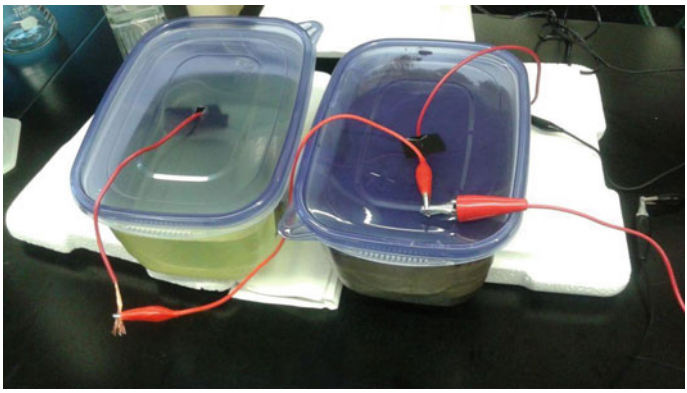

Fig. 4 Image of double-chamber MFC

Table 4 Characteristics of different effluents for result

SL. no.	Parameters	Dairy wastewater effluent	Sugar mill wastewater effluent	Domestic wastewater effluent
1.	Color	Milky white	Light black	Faded green
2.	Odor	Bad	Bad	Bad
3.	pH	6.7	6.4	6.6
4.	BOD (mg/L)	492	571	261
5.	COD (mg/L)	1558	1493	492
6.	TDS (mg/L)	1143	1817	349
7.	Maximum voltage (V)	1.03	0.081	0.098

4 Results and Discussions

Removal efficiencies of wastewater treatment adjacent with the generation of electrical potential are observed for every number of case study. Experimental setup is shown below (Table 4).

5 Conclusion

The experiment named "Performance Comparison of Microbial Fuel Cell" was done, a case study with different effluents. The subsequent conclusions have been prepared.

This case study of microbial fuel cell for dairy, leather, and domestic wastewater treatment productively expresses the microbial fuel cell as a better alternative for recovery of resource. This method is under process in the large amount

of dairy wastewater effluent treatment and electricity production. Domestic wastewater effluent of case study had produced much higher potential as two others. And treatment of effluent shows victorious representation of MFC technology.

References

1. Coyle ED, Simmons RA (2014) Understanding the global energy crisis. Purdue University Press
2. Vernona C, Thompson E, Cornella S (2011) Carbon dioxide emission scenarios: limitations of the fossil fuel resource. Procedia Environ Sci 6:206–215
3. Potte MC (1911) Electrical effects accompanying the decomposition of organic compounds. Roy Soc (Formerly Proceedings of the Royal Society) 84:260–276
4. American Public Health Association (2005) Standard methods for the examination of water and wastewater, 19th edn. APHA, Washington, DC, USA
5. Allen RM, Bennetto HP (1993) Microbial fuel-cells: electricity production from carbohydrates. Appl Biochem Biotechnol 39:27–40
6. Davis F, Higson SPJ (2007) Biofuel cells: recent advances and applications. Biosens Bioelectron 22:1224–1235
7. Rahimnejad M, Adhami A, Darvari S et al (2015) Microbial fuel cell as new technology for bioelectricity generation: a review. Alexandria Eng J 54:745–756
8. Das S, Mangwani N (2010) Recent developments in microbial fuel cells: a review. J Sci Indus Res 69:727–731
9. Shrivastava S, Bundela H (2013) Power generation through double chamber MFC operation by slurry mixed with different substrates. Int J Eng Trends Technol 4:4201–4205
10. Alterman P, Rabaey K, Clauwaert P et al (2006) Microbial fuel cell from wastewater treatment. Water Sci Technol 54:9–15
11. Reddy LV, Kumar SP, Wee YJ (2010) Microbial fuel cells (MFCs): a novel source of energy for new millennium. Curr Res Technol Edu Topic Appl Microbiol Microb Biotechnol 3:956–964
12. Chandra I (2012) Waste to energy: microbial fuel cell a novel approach to generate bio-electricity. Int J adv Biotechnol Bioinf 1:33–40

Microbial Fuel Cell: An Application for Dairy Wastewater Treatment and Electricity Generation

Prateek Jyotishi and Dal Chand Rahi

Abstract Microbial Fuel Cell (MFC) is an alternative to convent Victorian wastewater treatment approach. This case study work shows the MFC as an appreciable approach in the treatment of dairy waste effluent and electricity generation. The better design results are calculated by appraising the practical by taking distinct electrodes, with different electrodes, and their surface area with separate detention time. MFC in graphite, carbon rods, aluminum rod, and stainless steel are used as electrode, and Agar + Sodium Chloride salt bridge issued as protonex change membrane bridge and established as the better design at 10 days of detention time and generated energy of 359 mV to 1106 mV, respectively. The amount of removal efficiencies accomplished in this case study experimental setup for different wastewater parameters which are COD, BOD, and TDS are 93.98%, 90.63%, and 57.52%, respectively. Finally, the result is concluded that "Microbial Fuel Cell Technology" is good alternative for dairy wastewater treatment and simultaneous energy production.

Keywords Total dissolved solid · Chemical oxygen demand · Biochemical oxygen demand · Microbial fuel cell

1 Introduction

The tremendous challenges India is facing in this era are energy crisis due to continuous reduction of fossil fuels, rising price of fuels, and global heat [1]. Increasing pollution levels in terms of CO_2 emissions are not on track which causes global warming. As the world's population increases day-by-day, the demands such as water, food, and energy sources are also rising. The Energy–Water–Food Nexus is the biggest challenge in the world. If it is possible to find a better solution to resolve, one challenge could improve the others [2]. To fulfill India's energy requirement, it is requested to find alternative energy solution which comes under limitless energy sources. As the quantity of nonrenewable fuel source decreases, the market price gets

P. Jyotishi (✉) · D. C. Rahi
Jabalpur Engineering College (JEC), Jabalpur, Madhya Pradesh, India
e-mail: er.prateekjyotishi@gmail.com

© Springer Nature Singapore Pte Ltd. 2021

K. K. Pathak et al. (eds.), *Recent Trends in Civil Engineering*, Lecture Notes in Civil Engineering 77, https://doi.org/10.1007/978-981-15-5195-6_81

increased. Numbers of researches are carrying out in this era related to renewable energy in order to find better suitable technology to fulfill our energy requirement. Along with is, important renewable energy sources such as solar and wind, biomass, bio-fuel, etc. have also gain attention in the recent era. [3]. But it is required to eliminate the limitation so fall available renewable sources of energy. Increase in number of industry results in not only high production, but also increased water usage as well as waste generation. Energy recovery from waste generation from different waste generation sources is one of the hot topics for research. Energy can be recovered in different forms such as electrical energy, heat, or natural gas. Comparing with other forms of waste, wet waste (wastewater) is the one from which energy recovery can be done efficiently. Almost several organic materials could be used to feed the fuel cell. This reaction occurs in the absence of free oxygen, and organisms used are termed as electricigens [4]. The gain of using MFC is that it can be effective at room temperature itself, [5]. The loss is that it is not able to produce desirable current, and scale-up process is the major issue [6].

Microbial fuel cell is used for wastewater treatment, electricity generation, and as a biosensor in different fields [7]. In cathode chamber, it is seen that electron, proton, and oxygen join to form water [8]. It is also seen that not all of the organisms transfer toward anode [9]. There are mainly three ways by which electrons can be moved: a. through artificial arbiter, b. through microorganism's self-arbiter, and c. through direct transfer of electrons [10]. Most frequently available arbiters are methyl blue, thiamine, and neutral red [11]. Microorganisms can be used as pure culture or mixed culture. But mixed culture produces more current when compared to pure culture. Some frequently available microorganisms are *Shewanella Escherichia coli* and *Clostridium butyricum* [12]. This technology is under supervision for large-scale economic output. Multiple applications of this method made it feasible for small case study. Some types of mfc basically used are as follows.

- Single-chamber microbial fuel cell;
- Double-chamber microbial fuel cell;
- Multiple-chamber microbial fuel cell.

1.1 MFC Mechanism

MFC is assembly of different electrodes, anode chamber, cathode chamber, and salt bridge. The effluent is filled in anodic chamber. To form a bridge between cathodic and anodic chamber, the salt bridge is fabricated. Make possible the movement of ions (protons). Steel and graphite are used as electrodes of different cross-sectional areas.

1.2 MFC Assembly

In this case study, two-chambered fuel cell was used. Two plastic bottles of 1000 ml capacity with radius 10 mm were used for the experiment and indicated as cathode and anode. Two holes were made of diameter 5 and 1.6 mm on both the plastic bottles for the introduction of the salt bridge and electrodes. To fill anode chamber, distilled water is used and for the cathode chamber and dairy wastewater with activated yeast was used, and both chamber lids were bunged airtight and potted with the help of tape.

1.3 Agar Salt Bridge Assembly

Salt bridge was prepared by 0.4 c.m. diameter-level cylinder. This salt bridge was arranged with sodium chloride and 5.5% of Agar is added; then the solution was boiled for some time. The concoction was put into the tube and permitted to harden. This salt bridge was used to insert into the consequent microbial fuel cell and potted with the help of tape (Figs. 1 and 2).

Collection of Waste effluent and Analysis of Characteristics. Dairy wastewater effluent is passed down as fuel in microbial fuel cell, and the sample is collected from Mishra Dairy, katra mandla city. Specific permission is taken from the owner of dairy. More than two wastewater effluent samples are taken from source. Collected sample of wastewater effluent is put in the refrigerator at 4 °C for the process of slow down the microbial activity. This wastewater sample is non-noxious and wealthy in organic matter, and this effluent is analyzed in the laboratory to come across the preliminary personality of the wastewater effluent which are total dissolved solid, chemical oxygen demand, biochemical oxygen demand, and the experiment outcome [4] which are revealed in Table 1 (Fig. 3).

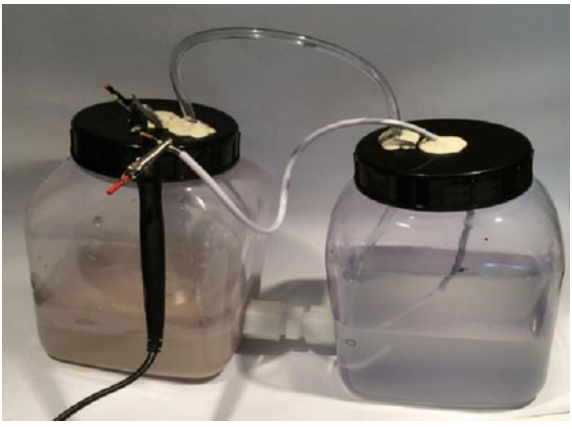

Fig. 1 Double-chamber MFC

Fig. 2 Salt bridge

Table 1 Preliminary characteristics of dairy wastewater sample

Point	Characteristics	Results
1.	Color	Milky white
2.	Odor	Bad
3.	pH	5.9
4.	B.O.D (mg/l)	543
5.	C.O.D (mg/l)	1659
6.	TDS (mg/l)	1987

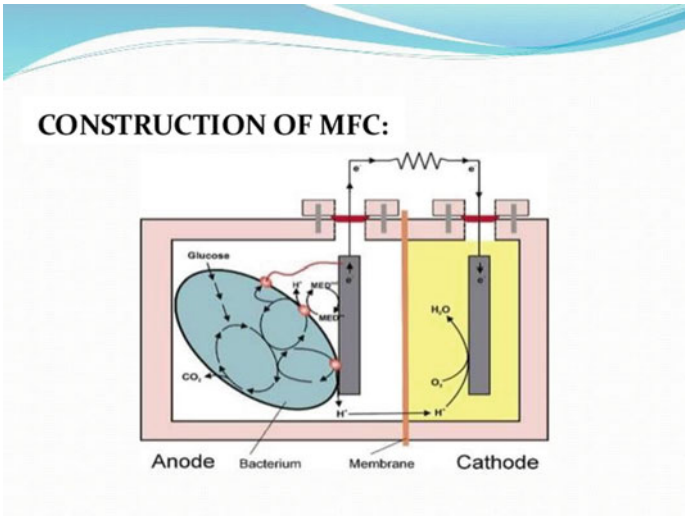

Fig. 3 Block diagram of MFC

Table 2 Characteristics of dairy wastewater

Point	Characteristics	Before	After
1	Color	Milky white	Milky white
2.	Odor	bad	bad
3.	pH	5.9	6.7
4.	BOD (mg/L)	543	492
5.	COD (mg/L)	1659	1558
6.	TDS (mg/L)	1987	1143

2 Experimental Setup

The basic arrangement of double-chamber microbe cell for wastewater treatment and electricity generation contains the following items:

- Two plastic bottles of 1000 ml capacity.
- Salt bridge to interconnect the bottles.
- Two electrodes.
- Multimeter for voltage measuring.
- Yeast as an accelerator.

3 Results and Discussions

Removal efficiencies of wastewater treatment adjacent to the generation of electrical potential are observed for every number of case study. Experimental setup and case study with electrode of stainless steel of higher surface area showed superior capacity of waste removal efficiency and steady electrical potential generation. The scope of COD elimination is observed as 93.98%, and removal efficiency of BOD is noted 90.63% as compared with all case study results. Results of electricity potential generation with respect to different case study experimental setups are revealed in Table 2 (Table 3 and Fig. 4).

4 Conclusions

From the experiment done named "Microbial Fuel Cell an Application for Dairy Wastewater Treatment and Electricity Generation", the subsequent conclusions have been prepared.

This case study of microbial fuel cell for dairy wastewater treatment productively expresses the microbial fuel cell as a better alternative for recovery of resource. This method is under process in the large amount of dairy wastewater effluent treatment and electricity production. The superior outcomes and cost of using various types

Table 3 Efficiency of electricity generation

Number of days	Steel electrode (mV)	Graphite (mV)
1	646	359
2	671	428
3	819	571
4	968	693
5	972	880
6	1106	821
7	894	715
8	596	636
9	348	416
10	188	264

Fig. 4 Double-chamber MFC complete assembly

of electrodes (Steel and copper) as anodic and cathodic electrodes in this case study of double-chamber microbial fuel cell are observed, and stainless steel is established appreciably superior in conditions of both treatment efficiency and electricity generation from the waste effluent.

References

1. Coyle ED, Simmons RA (2014) Understanding the global energy crisis. Purdue University Press
2. Vernona C, Thompson E, Cornella S (2011) Carbon dioxide emission scenarios: limitations of the fossil fuel resource. Procedia Environ Sci 6:206–215
3. Potte MC (1911) Electrical effects accompanying the decomposition of organic compounds. Roy Soc (Formerly Proceedings of the Royal Society) 84:260–276
4. American Public Health Association (2005) Standard methods for the examination of water and wastewater, 19th edn. APHA, Washington, DC, USA

5. Allen RM, Bennetto HP (1993) Microbial fuel-cells: electricity production from carbohydrates. Appl Biochem Biotechnol 39:27–40
6. Davis F, Higson SPJ (2007) Biofuel cells: recent advances and applications. Biosens Bioelectron 22:1224–1235
7. Rahimnejad M, Adhami A, Darvari S et al (2015) Microbial fuel cell as new technology for bioelectricity generation: a review. Alexandria Eng J 54:745–756
8. Das S, Mangwani N (2010) Recent developments in microbial fuel cells: a review. J Sci Indus Res 69:727–731
9. Shrivastava S, Bundela H (2013) Power generation through double chamber MFC operation by slurry mixed with different substrates. Int J Eng Trends Technol 4:4201–4205
10. Alterman P, Rabaey K, Clauwaert P et al (2006) Microbial fuel cell from wastewater treatment. Water Sci Technol 54:9–15
11. Reddy LV, Kumar SP, Wee YJ (2010) Microbial fuel cells (MFCs): a novel source of energy for new millennium. Curr Res Technol Edu Topic Appl Microbiol Microb Biotechnol 3:956–964
12. Chandra I (2012) Waste to energy: microbial fuel cell a novel approach to generate bio-electricity. Int J adv Biotechnol Bioinf 1:33–40

Construction Technology and Management

Analyzing Labor Productivity for Reinforcement Installation Using Artificial Neural Network in India

Jignesh M. Mistry and Geetha K. Jayaraj

Abstract The current investigation study aims to develop a productivity model analyzing the prediction performance for reinforcement installation activity for building projects using artificial neural networks. Fifty-six data were collected from Real Estate Regulatory Authority (RERA) registered residential projects across India. Soft computing tool of MATLAB was utilized for developing the productivity model. A multilayer feedforward network trained with backpropagation algorithm was used as basis, and further optimization of the network was done using Levenberg–Marquardt training function. Different network architectures and data points were tested for obtaining the superlative network for predicting labor productivity. The optimum network comprised of 16 input neurons, followed by 15 hidden neurons and single output fully connected. The developed model showed a respectable regression value between the predicted and the actual output with mean square error of less than seven. The findings of this research study provide awareness of the importance of documenting historical data for prediction of labor productivity.

Keywords Productivity · Artificial neural network (ANN) · Processing element (PE)

1 Introduction

The construction industry in developing nations faces various constraints in the different phases of the project. One of the major constraints is associated with construction labor, i.e., productivity. Construction labors are the most prominent choice for the various agencies involved in the industry for carrying out work, as

J. M. Mistry (✉)
P.G. Student, Department of Civil Engineering, Shivajirao S. Jondhle College of Engineering and Technology, Asangaon (E), Tal. Shahapur, Thane 421601, Maharashtra, India
e-mail: jigneshmistry1507@gmail.com

G. K. Jayaraj
Principal and Professor, Department of Civil Engineering, Shivajirao S. Jondhle College of Engineering and Technology, Asangaon (E), Tal. Shahapur, Thane 421601, Maharashtra, India
e-mail: jayaraj.geetha@gmail.com

© Springer Nature Singapore Pte Ltd. 2021

K. K. Pathak et al. (eds.), *Recent Trends in Civil Engineering*, Lecture Notes in Civil Engineering 77, https://doi.org/10.1007/978-981-15-5195-6_82

they are effortlessly available and for affordable price [1]. Consequently, with the involvement of the labor for execution of the construction works, monitoring of the task work becomes indispensable to ensure that the work is completed effectively, within the specified limits of tolerance and of the required quality. The productivity of labor is often estimated by the senior execution engineer and/or project manager based on experience of the previous work of similar nature, but they are unable to structure a forecasting model for determination of productivity using statistical analysis, neither reflect upon the factors impacting the construction labor productivity [2]. Also, one of the major drawbacks in the developing nation is lack of proper documentation of the construction works which often leads to difficulty in the investigation of productivity of labor. The complex nature of productivity associated with the multiple factors and their interrelationship is determined based on previous works and knowledge by experienced personnel. Analogous to the functioning of the human brain to learn from previous experience [3], a similar soft computing technique could be utilized for prediction of labor productivity. Artificial Neural Network (ANN) has gained a lot of popularity among the researchers with its applications in various engineering problems over the past few decades, and the same can be utilized for the prediction performance of labor.

The working of the ANN is motivated from working of the human brain [3]. The human brain acquires knowledge and learns from huge set of memories in the past and generalizes the output to a new situation in comparison to the previous events from the past. Similarly, ANN has competence to learn from a given set of parameters for a defined problem and its associated output patterns (representing the decision). The network is trained with adequate amount of sample sets until the network is able to generalize the knowledge for the defined problem and becomes proficient in providing a solution for an entirely new problem of similar nature even if there are variations or noise in the dataset is available [4]. Variation in the productivity is caused because of the multiple factors, and resulting relationship between the influential parameters and productivity could be quantified using productivity model. ANN has also been successfully utilized by many researchers in the past for various prediction performances of labor for formwork installation, reinforcement installation, and concrete pouring and finishing works [4–8].

The current research study focuses on developing a simple yet effective prediction model of labor productivity for reinforcement installation activity across India for residential projects with the application of ANN.

2 Literature Review

Starting in the late 1990s, several researchers have made a remarkable work for estimating the productivity of construction works using ANN model. Jason and Simaan [2] in Canada developed a model forecasting formwork for columns, slabs, and walls [2]. After conducting numerous tests on the different network architectures, a three-layered network with a fuzzy output was selected for the study. The selected model

was then tested in a workshop, wherein only 2 out of 12 estimators were able to estimate the formwork productivity for foundation wall within 5% error range. In the following year, Rifat and James [4] in Iowa, United States of America made a comparison of regression model and ANN model for prediction of concrete pouring, concrete finishing, and formwork task [4]. The inputs were varied for different regressions and ANN model. Based on the tests performed on both models, ANN had a better prediction performance for formwork and concrete finishing activity, while regression model had better forecasting performance for concrete pouring activity. Later, Samer and Lokman [5] structured a productivity model for formwork erection, steel fixing, and concrete pouring task in Egypt [5]. Data for the study were collected from residential, commercial, and industrial projects of similar attributes of work. A feedforward network trained with backpropagation algorithm was utilized for developing ANN model for all three concreting activities. From sensitivity analysis factors like hot weather condition and skills of labor had a significant impact on productivity. Further, depending on accessibility to materials, the productivity is enhanced by 30% and with repetitive nature of work the productivity is excelled by 20% enhanced. Self-Organizing Map (SOM) model was developed for prediction of construction crew productivity for concrete pouring, formwork, and reinforcement activities by Emel and Mustafa in Turkey [9]. SOM-based model was able to effectively cluster the data into two-dimensional maps. Further, with the colorful maps guided, a visual environment for data analysis and the prediction performance of SOM-based model is analogous to similar preceding ANN model. In the succeeding year, Dikmen and Murat [6] developed ANN model in Turkey for forecasting man-hour required for formwork installation activity [6]. A multi-layered feedforward network trained with backpropagation was selected for the model. The selected model was then tested over two live projects of similar attributes. The errors in prediction of two projects were 5% and 15%, respectively, which were less in comparison to estimating using Turkish Ministry of Public Works and Settlement (MP + S). Sana et al. [7] developed a productivity model for forecasting production rates of formwork for high-rise structures in Malaysian construction industry [7]. The data were collected from seven different projects of similar nature. The forecasted model had a precise production rate estimation with minimum error in comparison to similar study conducted by Samer and Lokman [5]. Gholamreza and Ehsan constructed ANN model for predicting productivity of labor for concrete works in Iranian construction industry [8]. A total of 15 factors were identified, and the data for the same were collected from 39 different projects for concreting of foundation of gas, steam, and combined cycle power plant. A multi-layered feedforward network trained with backpropagation algorithm was used to develop the network. For optimization, Bayesian regularization had a better prediction performance than early stopping for the two projects which were utilized to test the network proficiency. As observed, several researchers have been able to successfully deploy ANN model to forecast production rates of labor for various concreting activities like steel fixing, formwork installation, concrete pouring, etc., in different countries; a similar research can be conducted for Indian construction industry. Thus, the study aims to utilize ANN for prediction of labor production rates for reinforcement installation activity in India.

3 Methodology

As shown in Fig. 1, the research conducted comprises four intervals: (1) identifying the significant factors; (2) formulating the data collected; (3) designing the neural network; and (4) post-training analysis.

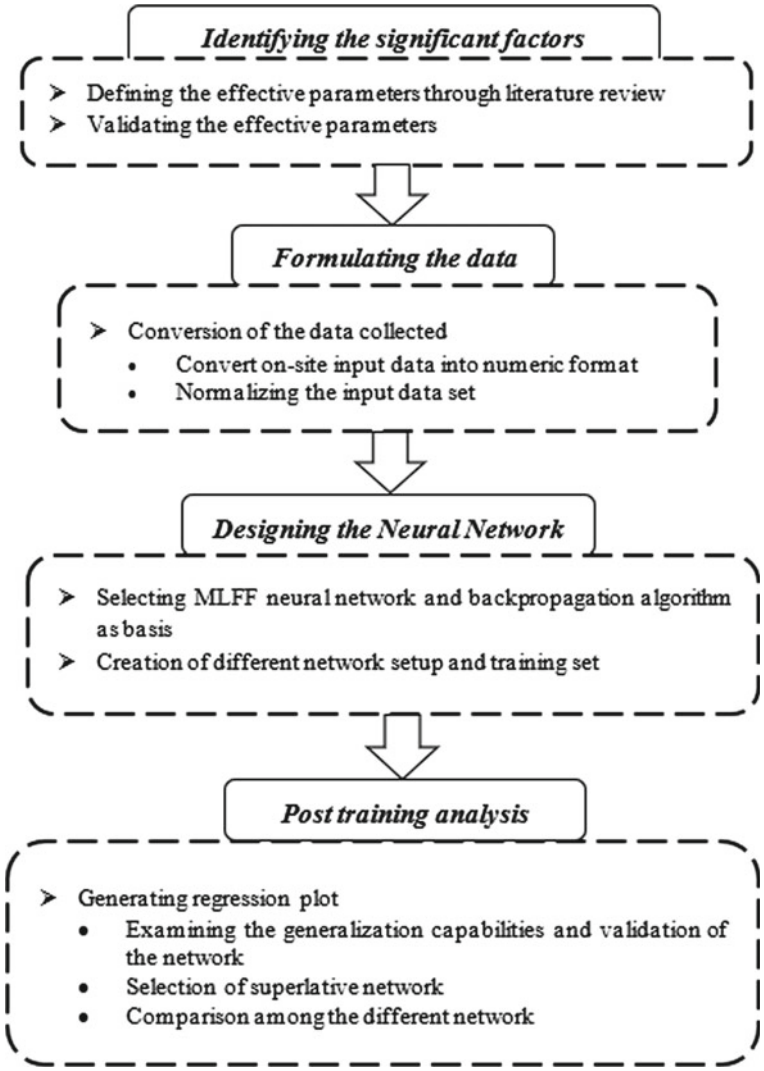

Fig. 1 Research method's detailed structure

3.1 Identification of Significant Factors Affecting Productivity of Labor

The primary task to structure the proposed productivity model is to identify the parameters impacting the labor productivity for reinforcement installation task. The foremost 10 significant factors impacting the reinforcement installation activity in India were identified using relative importance index (RII) and ranked accordingly, and the details for the same ARE represented by Jignesh and Geetha [1].

3.2 Formulating the Data Collected

Conversion of the data collected. Productivity is simply defined as ratio of unit output per given unit input in theoretical terms [9]. But as mentioned by Abdulaziz and Camille [10], based on measurement objective and availability of the data, several definitions of productivity can be encountered [10]. Correspondingly, the measure of productivity for the same task work is conducted in different manners for varied region, thus making the resulted productivity not directly analogous [9]. For this study, the definition of productivity of labor is shown in Eq. 1 [5]:

$$\text{Labor Productivity} = \frac{\text{Crew Size} * \text{Duration}}{\text{Quantum of work}} (\text{man} * \text{days/unit}) \tag{1}$$

where units for measurement of productivity of labor for reinforcement installation are (man*days/tones). Initial questionnaire was prepared based on literature review. The survey form was rectified by three experts from construction industry registered with ISTE (Indian Society of Technical Education) membership to ensure that the factors are relatable for Indian construction industry for finalizing the questionnaire. The final survey form consisted of four sub-sections, viz., (i) general background of the respondent, (ii) general description of the project under execution, (iii) description of structural member under consideration for productivity measurement, and (iv) 23 factors listed affecting reinforcement installation activity. Under the third section, i.e., the description of the structural member considered for productivity measurement involved six questions: (1) structural member under consideration, (2) quantum of the work (ton), (3) duration of the task (days), (4) number of labors required to complete the task (nos.), (5) working condition, and (6) temperature consideration. Three factors, i.e., structural member under consideration, working condition, and temperature condition were in a linguist manner. The data points were converted into numeric format in order to develop ANN model. Table 1 depicts the scalar value for three factors.

Normalizing the input data. A total of 56 data were collected from residential projects registered under Real Estate (Regulation and Development) Act (RERA) in India [11]. The data collected were normalized which is a standard practice

Table 1 Scalar value for factors to convert into numeric format

Scaled value → Factors ↓	5	4	3	2	1
Structural member	Overhead water tank	Prestressed slab	Slab	Column	Footing
Working condition	Mild	–	Moderate	–	Harsh
Temperature	Hot (26 to 42 °C)	–	Moderate (13 to 25 °C)	–	Cold (5 to 12 °C)

for constructing ANN model. The numeric data were normalized in a range of (−1,1), because of such scaling an improvement is made over the data for the confined problem domain [12] allowing the neural network to pace up with the better generalized output results. The data is normalized using Eq. 2 given by [12, 13]

$$\text{Scale value} = \left(2 * \left[\frac{\text{Unscaled value} - \text{VariableMinimum}}{\text{VariableMaximum} - \text{VariableMinimum}}\right]\right) - 1 \quad (2)$$

where unscaled value is the value provided by the respondent on Likert scale, variable maximum is the maximum value of Likert scale, and variable minimum is the minimum value of Likert scale, respectively, for an individual factor. The total number of input parameters is 16, out of which 10 were identified determining the RII [1] as shown in Table 2 and 6 factors (structural member under consideration, quantum of the work, duration of the task, number of labors, working condition, and temperature) are also referred by [5] for developing ANN prediction model for concreting activities as shown in Table 3, respectively.

Table 2 List of top 10 factors affecting labor productivity with RII [1]

Factors	RII (%)	Rank	
Skills of labor [2, 5, 7, 8]	87.50	1	$\mathbf{X_1}$
Supervision of foremen [8]	85.00	2	$\mathbf{X_2}$
Stringent inspection by engineers and supervisor [8]	84.29	3	$\mathbf{X_3}$
Material supplies on time [7, 8]	83.57	4	$\mathbf{X_4}$
Overtime provision [4, 5, 8]	82.86	5	$\mathbf{X_5}$
Safety measures [8]	82.50	6	$\mathbf{X_6}$
Size of crew [2, 4, 5, 8]	80.71	7	$\mathbf{X_7}$
Accuracy rates and details in design [2, 8]	80.36	8	$\mathbf{X_8}$
Method of hauling [2, 7, 8]	79.29	9	$\mathbf{X_9}$
Height of work [6]	78.21	10	$\mathbf{X_{10}}$

Table 3 Other factors for ANN model development [5]

Other 6 factors used for developing ANN model	
Structural member under consideration [4, 5]	$\mathbf{X_{11}}$
Quantum of the work [2, 4, 5]	$\mathbf{X_{12}}$
Duration for task completion [5]	$\mathbf{X_{13}}$
Number of labors [2, 4, 5, 7]	$\mathbf{X_{14}}$
Working condition [2, 5, 8]	$\mathbf{X_{15}}$
Temperature [2, 4, 5, 7, 8]	$\mathbf{X_{16}}$

3.3 Designing the Neural Network

For this investigation study, the network architecture of multilayer feedforward trained with backpropagation algorithm is utilized for developing the ANN model as shown in Fig. 2, as this has been successfully implied in various prediction models for concreting activities [2, 4, 6–8].

Network architecture and learning algorithm for developing the network. *Multilayer Feedforward network* (MLFF). A network comprising more than one computational node is referred to as multilayer feedforward network. These computational nodes are corresponding to the hidden neuron (processing elements) in the hidden layer. Hence, an MLFF network comprises input–hidden–output node, where each layer consists of processing elements (PEs) depending upon the model to be constructed. The PEs in each layer are characterized by a weight known as connection weight. The weighted sum of all the PEs is processed through each of the nodes with the help of activation (squashing/transfer) function, which is fundamental operation for mapping the inputs with the output. If the net input at each of the summing junctions is lesser/greater in order to acquire the desired output, an external bias is applied to increase/decrease the net input at the summing junction [3]. A precise detail for various network architectures and its fundamental is illustrated by Simon [3].

Backpropagation (BP) Algorithm. Also popularly known as the delta rule is one of the most popular training algorithms used for MLFF network. The network with multivariate random inputs with linear and non-linear computation and approximating any continuous function with the desired output can be efficiently performed using MLFF with BP algorithm [14]. One of the common problems for BP algorithm is that it may cause overfitting [8, 14], which simply implies that the error of the training set is driven to a very small value, but when a new set of data is presented to the same network, the error is large, indicating that NN has memorized the training dataset, but has not learned to generalize a new situation. In order to overcome this limitation, a faster BP algorithm, i.e., Levenberg–Marquardt (LM) is used [14]. This algorithm acquires a lower mean squared error (MSE) for function approximation problem in comparison with any other algorithm [15].

Creation of different network setups and training set. A commercial tool of neural network toolbox MATLAB R2019 [16] software is utilized to train, validate,

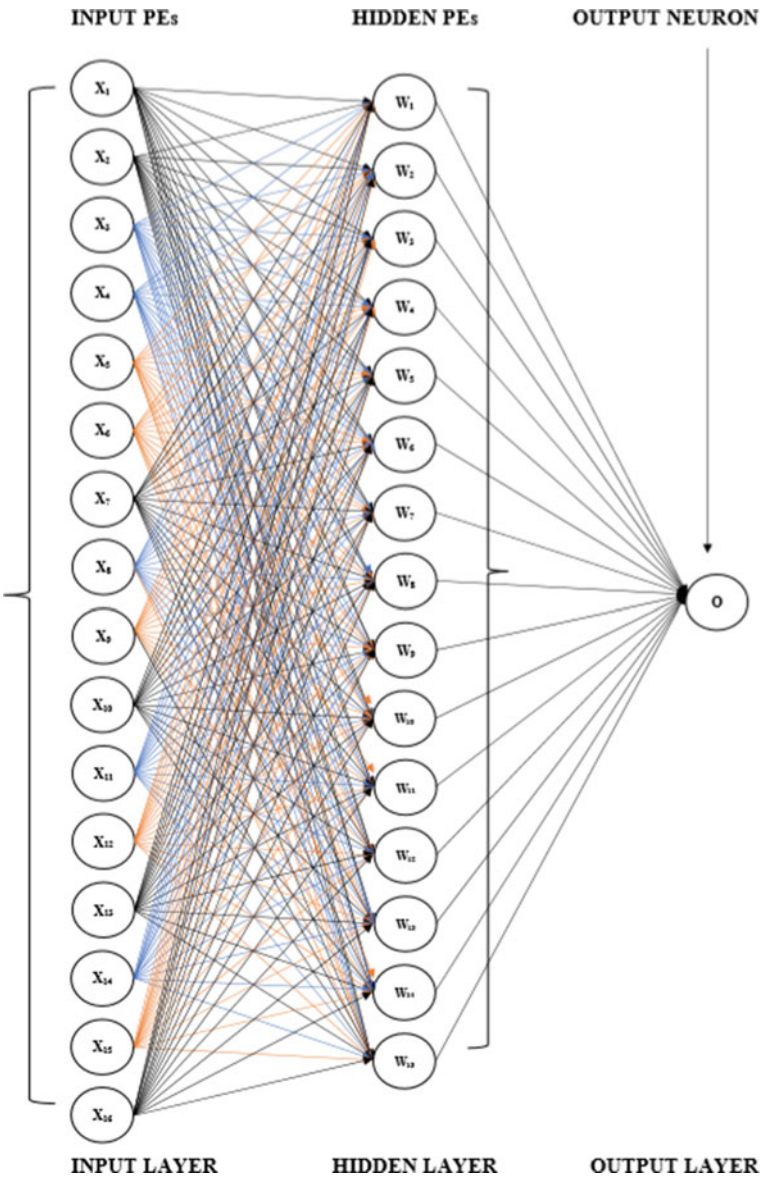

Fig. 2 A multilayer feedforward NN

and test the networks for labor productivity. Network development is an experimental process, and a lot of trials and the various configurations were investigated in order to achieve the most appropriate network. Following are details of the configuration undertaken while developing the neural network model.

Network Architecture and Learning Algorithm. The neural network for this investigation study is an MLFF network with backpropagation algorithm in which the PEs for each of the nodes are fully connected.

Training Function. The network is trained with Levenberg–Marquardt (LM) backpropagation algorithm, i.e., "*trainlm*". For this type of network training function, the weights and biases are updated as stated to LM optimization. In comparison for the other training function for moderate-sized feedforward NN (i.e., up to several hundredweights), it is the fastest and requires more memory.

Number of Layers. The common practice to structure a neural network model for most of the problems is to initially start with two layers (one hidden) and then increase to 3 layers (two hidden layers) provided the network performance with two layers is not satisfactory. The performance of the network was adequate at two layers (one hidden), and the same was selected for this study.

Number of Neurons. The PEs for the input nodes are 16 and for the output node was 1. The PEs in the hidden node were varied, in order to compare the computational performance potential of the network under diverse condition. But too many PEs in the hidden node lead to complexity and requires more time for computation. To overcome this problem, [17] recommended as a thumb rule, the number of hidden neurons should be less than 2x the number PEs in the input node. The hidden neurons were varied starting from 5, and the performance of the network for its mean squared error was checked at each of the intervals for training, validating, and testing.

Training, Validation, and Test Data. The raw data for the test were distributed using different sampling points for input parameters, and the outcome of this sampling on the output parameters was consequently noted. The raw data were distributed into three parts: training, validation, and testing. The varied combinations for training data set were 90%, 85%, and 80%; for validation 5%, 10%, and 10%; and for testing the network 5%, 5%, and 10%, respectively.

Activation Function. The commonly implied activation functions for MLFF networks are the log-sigmoid (*logsig*), tan-sigmoid (*tansig*), and linear (*purelin*) in MATLAB. A combination of this activation function is used in various research studies for solving a variety of problems [8]. Since the inputs varied in the range of −1 to 1, *tansig* function was utilized between the input and hidden nodes to limit the inputs to the hidden layer. While *purelin* function was used between hidden and output nodes, as the output layer of the MLFF is function approximator. The details of the activation function and its use for solving various approximation problems are given in [3].

3.4 Post-training Analysis

Generation of Regression Plot. After several trials and variations made in the network architecture and data points for training, the most significant network was opted which had a better generalization capability and validation of the network grounded on regression plot. Following are few observations made with respect to

the network training and validation: (1) the PEs in the hidden node were varied in the interval of five, as the performance of the network at other intervals had a catastrophic failure; (2) out of three data points, the most significant results were generated at 85 − 10 − 5% for variation made in consideration to all the PEs in the hidden node; (3) the network performance is based on regression and mean square error (MSE), the data point 80 − 10 − 10% had significant results at $(2n - 1)$; 85 − 10 − 5% at $(n - 1)$; and for 90 − 5 − 5% at $(2n - 2)$ where n is the number of inputs. The details of varied network characteristics and its performance are represented in Table 4.

4 Results and Discussion

The network with the most significant results was selected based on the generalizing competency and test performance of the network using the regression plot. The significant results were obtained at 85% training (47 samples), 10% validation (6 samples), and 5% testing (3 samples) dataset. The performance measure for the network was mean square error (MSE)—which is the ratio of total sum squared of difference between the actual output and the predicted output to the total number of samples. With variation in the PEs, i.e., from 20 to 31 had a decent network performance, but the testing of the network had a very low rate of performance measure (MSE), followed to which the performance measure further degraded with PEs of 10 and 5. At 15 hidden PEs, the MSE of 0.07 for training, testing, and overall performance of the network indicating a stronger correlation between the predicted output and the actual output. The regression plot is shown in Fig. 3 which is the correlation between the targeted output and the predicted output.

For perfect fit, the data points should lie at 45° line (dotted line), where the regression value is 1 and MSE is minimum, i.e., 0 [15], and for this case is 0.07. The network is first trained with a set of parameters (training set), after which the performance of the trained network is validated (validation set), and finally a new set of data is represented (testing set) to incorporate how the network response to entirely new data points not utilized for its training and validation (generalization capability).

Table 5 represents the performance of the network over testing data points. The prediction error for the second and third project is lesser than 0.07, while that for the first project is of 0.12. The predicted output for all the three projects is marginally greater than the actual output, indicating that the performance of the network for an entirely new data points had a respectable prediction performance.

5 Conclusion

The purpose of this investigation study was to develop a model for quantifying and predicting the construction labor productivity for reinforcement installation activity

Table 4 Statistical analysis of the ANN productivity model using different network architectures and data points

Hidden PEs	Datasets	90 − 5 − 5%		85 − 10 − 5%		80 − 10 − 10%	
		Statistical parameters					
		R^2	MSE	R^2	MSE	R^2	MSE
5	Training	0.597	0.2723	0.941	0.0970	0.952	0.0349
	Validation	0.605	0.1232	0.981	0.0919	0.184	0.3749
	Testing	0.779	0.4382	0.855	0.2396	0.928	0.1917
	Overall	0.577	0.2732	0.935	0.1041	0.834	0.0881
10	Training	0.924	0.0404	0.983	0.0232	0.880	0.0920
	Validation	0.466	0.1050	0.770	0.3237	0.836	0.1482
	Testing	0.924	0.0404	0.778	0.5348	0.836	0.1170
	Overall	0.912	0.0465	0.938	0.0828	0.800	0.1007
15	Training	0.861	0.0954	0.948	0.0726	0.915	0.0482
	Validation	0.299	0.2062	0.967	0.1002	0.638	0.1564
	Testing	0.498	0.5025	0.999	0.0075	0.478	0.1336
	Overall	0.824	0.1231	0.945	0.0721	0.830	0.0882
20	Training	0.935	0.0427	0.996	0.0055	0.725	0.1360
	Validation	0.955	0.1932	0.815	0.3030	0.647	0.2241
	Testing	0.972	0.0884	0.936	0.1771	0.628	0.2427
	Overall	0.912	0.0532	0.968	0.0465	0.681	0.1569
25	Training	0.861	0.1247	0.996	0.0053	0.745	0.1360
	Validation	0.470	0.2446	0.829	0.2826	0.421	0.2307
	Testing	0.994	0.1664	0.980	0.1390	0.673	0.1225
	Overall	0.833	0.1334	0.969	0.0422	0.693	.01447
30	Training	0.997	0.0022	0.880	0.1902	0.999	0.0009
	Validation	0.931	0.0307	0.884	0.1760	0.353	0.7500
	Testing	0.997	0.1225	0.966	0.0887	0.579	0.2287
	Overall	0.956	0.0250	0.864	0.1833	0.834	0.1056
31	Training	0.620	0.2223	0.999	0.0017	0.996	0.0026
	Validation	0.713	0.5860	0.948	0.1337	0.698	0.2148
	Testing	0.146	0.3023	0.879	0.2321	0.725	0.4385
	Overall	0.517	0.2461	0.981	0.0277	0.902	0.0720

for residential projects in India, using ANN. The factors impacting the labor productivity were identified through literature review and consulting the experts from the industry. These factors were scaled and normalized in order to be utilized for the developed model. Furthermore, to quantify the non-linear and complex relationship between the productivity of the labor and the factors identified, a multilayer feedforward network trained with backpropagation algorithm was used as a basis

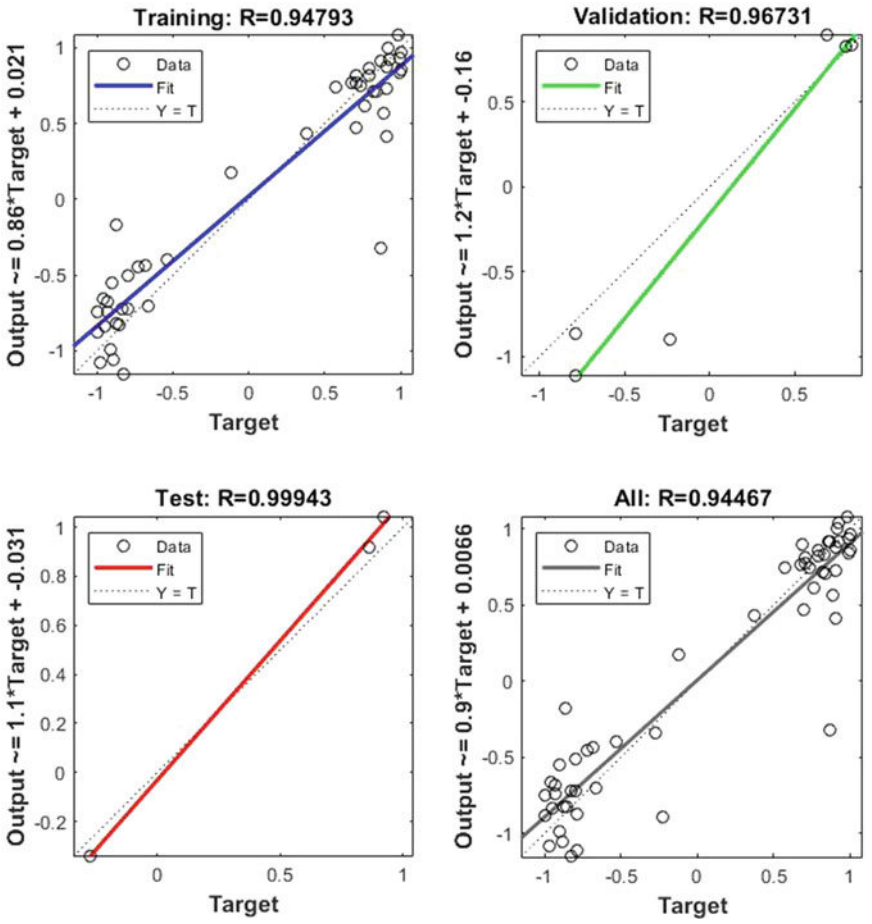

Fig. 3 Regression plot of the optimum developed productivity model

Table 5 Actual output and predicted output of the developed model over test data

Projects →	I	II	III
Actual output (normalized output in man*days/tons)	0.9222	0.8599	−0.2737
Predicted output (normalized output in man*days/tons)	1.0421	0.9196	−0.3409
Error (normalized output in man*days/tons)	0.1199	0.0597	0.0672

and trained with Levenberg–Marquardt training function. The network architecture and the data point for training the network were varied and compared for obtaining the superlative outcomes. The most significant network for the prediction of the labor productivity was verified by performing network estimate on a test data, which

had a virtuous prediction performance of the construction labor productivity for reinforcement installation activity.

The forecasting of work performed by labor is conducted by the senior engineers and project managers based on their experience of their previous works. The data of these previous works need to be carefully documented, such that future investigation related to labor performance could be made possible. Also, ANN as soft computational technique can be utilized for estimating the labor productivity of the labor during the different phases of the construction and the same could also be verified for the ongoing projects. The limitation of this investigation study was for prediction of productivity of labor for reinforcement installation task; it could be also utilized for forecasting formwork installation task, concrete pouring and finishing, masonry work, floor finishing, and overall factors impacting labor productivity.

References

1. Jignesh M, Geetha KJ (2019) Recognition of factors impacting labor productivity for reinforcement installation activity in India. Int Res J Eng Technol 6(2):2334–2342. https://www.irjet.net/archives/V6/i2/IRJET-V6I2463.pdf
2. Jason P, Simaan A (1997) Neural network model for estimating construction productivity. J Constr Eng Manage, ASCE 123(4):399–410. https://doi.org/10.1061/0733-9364
3. Simon H (2001) Neural networks a comprehensive foundation, Second ed., Pearson Education (Singapore) Pte. Ltd., Delhi, Indian Branch, 482 F.I.E Patparganj. 6–15, 21–23, 161–166
4. Rifat S, James R (1998) Construction labor productivity modeling with neural networks. J Constr Eng Manage, ASCE 124(6):498–504. https://doi.org/10.1061/0733-9364
5. Samer A, Lokman M (2006) Neural network for estimating the productivity of concreting activities. J Constr Eng Manage, ASCE 132(6):650–656. https://doi.org/10.1061/0733-9364
6. Dikmen S, Murat S (2011) An artificial neural network model for the estimation of formwork labour. J Civ Eng Manage, Taylor and Francis 17(3):340–347. https://doi.org/10.3846/13923730.2011.594154
7. Sana M, Arazi I, Khamidi FM, Jale Bin A, Saiful Bin Z (2011) Construction labor production rates modeling using artificial neural network. J Inf Technol Constr 16(1):713–725. http://www.itcon.org/2011/42
8. Gholamreza H, Ehsan E (2015) Applying artificial neural network for measuring and predicting construction labour productivity. J Constr Eng Manage, ASCE 141(10):1–11. https://doi.org/10.1061/1943-7862.0001006
9. Emel O, Mustafa O (2010) Predicting construction productivity by using self organizing maps. Autom Constr 19(6):791–797. https://doi.org/10.1016/j.autcon.2010.05.001
10. Abdulaziz J, Camille B (2012) Factors affecting construction labour productivity in Kuwait. J Constr Eng Manage, ASCE 138(7):811–820. https://doi.org/10.1061/1943-7862.0000501
11. Real Estate (Regulation and Development) Act (2016) (RERA). https://www.icsi.edu/media/webmodules/REAL_ESTATE_REGULATION_AND_DEVELOPMENT_ACT.pdf
12. Graham LD, Forbes D, Smith S (2006) Modeling the ready mixed concrete delivery system with neural networks. Autom Constr, Elsevier 15(5):656–663. https://doi.org/10.1016/j.autcon.2005.08.003
13. Hegazy T, Ayed A (1998) Neural network model for parametric cost estimation of highway projects. J Constr Eng Manage, ASCE 124(3):210–218. https://doi.org/10.1061/0733-9364
14. Patel D, Jha K (2015) Neural network model for the prediction of safe work behavior in construction projects. J Constr Eng Manage, ASCE 141(1):1–13. https://doi.org/10.1061/1943-7862.0000922

15. Demuth D, Beale M (2000) Neural network toolbox for use with MATLAB in User's Guide version 3.0, vol 3, NAtick, MA, pp 31–36
16. MATLAB R2019 [Computer Software]. Natick, MA, MathWorks
17. Berry MJA, Linoff G (1997) Data mining technique. Wiley, New York